17th International Conference on Sustainable Energy Technologies

21st to 23rd August 2018, Wuhan, China

Sustainable Energy Technologies for Eco Cities and Environment

Conference Proceedings Volume 2

Proceedings of the
17th International Conference on
Sustainable Energy Technologies – SET 2018
21st to 23rd August 2018, Wuhan China

Sustainable Energy Technologies for Eco Cities and Environment

Volume 2

Edited by

Professor Saffa Riffat, Dr Yuehong Su,
Professor Defu Liu and Professor Yingjiang Zhang

SET 2018 Admin Support
Department of Architecture and the Built Environment
Faculty of Engineering, University of Nottingham

Reference to a conference paper:

To cite a paper published in these conference proceedings, please substitute the highlighted sections of the reference below with the details of the article you are referring to:

Author(s) Surname, Author(s) Initial(s), 2018. 'Title of paper'. In: Riffat, Su, Liu & Zhang, ed, **Sustainable Energy Technologies for Eco Cities and Environment**: Proceedings of the 17th International Conference on Sustainable Energy Technologies, 21-23 August 2018, Wuhan, China. University of Nottingham: Buildings, Energy & Environment Research Group. Volume X, pp XX-XX. Available from: nottingham-repository.worktribe.com/ [Last access date].

ISBN-13 9780853583271

Version: 26.02.2019

Foreward

The 17th International Conference on Sustainable Energy Technologies was a significant international academic conference in the domain of world sustainable energy technologies with a theme of *Sustainable Energy Technologies for Eco Cities and Environment*. The conference aimed to provide a forum for the exchange of latest technical information, the dissemination of up-to-date research results, and the presentation of major issues that may shape future directions of human society, such as sustainable energy technology research, its application and energy security.

Held from August 21st to August 23rd, 2018, in Wuhan, China, the conference was a collaboration between the World Society of Sustainable Energy Technologies (WSSET) and the Hubei University of Technology. World-renowned experts and scholars in the area, representatives of prominent enterprises and universities attended to discuss new developments and achievements in the field, as well as promoting academic exchange, application of scientific results, university-industry collaboration and government-industry collaboration.

The papers contained in these proceedings focus on topics such as Energy Storage for the Age of Renewables; Research, Innovation and Commercialisation in Sustainable Energy Technologies; Integrating Planning & Policy, Architecture, Engineering & Economics; Energy and Environment; Engineering Thermo-physics; and Systemic Change for Cities.

Over 300 delegates from 27 countries attended SET2018; over 400 abstracts were received and 251 papers have been published in the conference proceedings. The proceedings have therefore been divided into four volumes. I hope you enjoy as much as I did the breadth of work you will find in this book.

We would like to thank all participating authors for their contributions to both the conference and to the publishing of this book. We are also indebted to our international scientific committee for their advice and seemingly endless review of papers. We would also like to thank unreservedly Celia Berry, Zeny Armante-Roberts, Amy Long, Dustin Chen for their tireless efforts in making SET2018 one of the most successful conferences we have held. Also a huge thanks to our sponsors PCM Products Ltd., Solar Ready Ltd., Positive Homes, Hubei Provincial Department of Education, Oxford University Press and MDPI.

Professor Saffa Riffat
Chair in Sustainable Energy Technologies
President of the World Society of Sustainable Energy Technologies
SET 2018 Chairman

CONTENTS

Paper Reference # **List of Papers** **Page Number**

104: Experimental study on the control strategies of DC power supply and storage in buildings 1
106: Comparative analysis of biogas and yields from cattle, sheep, poultry wastes and their combinations 7
111: Evaluation of daylighting levels in heritage buildings turned into museums in UAE 18
113: Sugar cane bagasse flow control using bifurcated chute 26
114: Investigation of an innovative PV/T-ORC system using amorphous silicon solar cells and evacuated flat plate collectors: a comparison study 37
116: Generation of typical weather data (TWD) for urban heat island (UHI) 45
117: Theoretical and experimental analysis on the performance of a solid desiccant air-conditioning system under the tropical climate 52
121: Feasibility study of thermochemical energy storage applied in Tibet, China 60
122: Experimental study of the thermal behaviour of nano-enhanced phase change materials (NPCMs) 71
125: Development of a cooling load prediction model for air-conditioning system operation control 80
127: Single-phase PWM rectifier based on PR controller 86
128: Frequency conversion control of photovoltaic grid-connected inverter based on LCL filtering 94
132: Effects of thermal and rheological properties of biodiesel from microalgae and feedstocks 102
134: Experimental study on the thermal performance of solar collectors applied to air conditioning system 115
137: Research of three-level DC/DC converter 121
141: Synchronous control method for combined verification power supply for GIS current transformer based on frequency adaptive PR controller 128
142: Towards a new paradigm for biodiesel production 136
143: Indigenous solar desalination technologies for sustainable potable water supply 144
144: Fermentative production of optically pure d-lactic acid from rice straw hydrolysate by a genetic engineered escherichia coli DX03 153
146: Research on combined power supply control of solar power grid and municipal power grid 158
147: Using COMSOL to simulate the transmittance of PV-VG 167
150: Li-SC HESS power coordination allocation based on PCDH real-time tracking control strategy 175
152: Study on the method of hybrid energy storage to stabilise the power fluctuation of DC microgrid 185
153: Research on energy management strategy of EV HESS based on fuzzy control 195
155: Research on 1D photonic crystal filter applied to solar thermophotovoltaic system 205
157: Discount of living – research on greenhouse gas emissions 211
160: The power quality analysis of the PV access system based on DIgSILENT software 222
161: Research on capacity allocation of hybrid energy storage system based on improved particle swarm optimisation 228
162: Research on photovoltaic grid-connected inverters with unbalanced load compensation 238
163: Review on solid desiccant materials for humidity control in buildings 245
164: Power design for detection of three-phase combined transformer 256
165: Photovoltaic wave power suppression control method based on improved wavelet packet transform 263
166: Research on SOC estimation method of electric vehicle battery based on double fuzzy-variant filter 273
167: HESS power distribution control strategy for DC microgrid based on droop method 284
168: Research on a balanced circuit and control strategy 294
169: Calculation method of convective heat transfer coefficient in air-cooled radiator temperature field simulation 303
170: Research on active equilibrium with balanced power supply 310
171: Research on SOC estimation method of multi-rotor UAV battery based on improved extended Kalman filter 319
172: A study on force-bearing capacity of joints of transmission tower subjected to wind loads 329
173: Control optimisation of hybrid energy storage system based on H-bridge convert 338
174: Research on cascaded bidirectional DC-DC converter based on model predictive control 346
175: Capacity allocation of HESS in microgrid based on fuzzy control and ABC algorithm 355
176: A method of power distribution network classification based on improved grey cluster 365
177: Application of PID optimisation control srategy based on particle swarm optimisation (PSO) for battery charging system 373
179: The development of data acquisition terminal based on ARM 383
180: Study on three-level DC-DC converter for microgrid energy storage system 390
181: Automatic generation control based on improved particle swarm optimisation algorithm 398
182: Research on large scale electric vehicle charging scheme based on improved genetic algorithm 406
183: A lithium-ion battery active equalisation optimisation method 416
184: Multi-energy body DC micro-grid parallel operation energy management strategy 424
185: DC micro grid coordination control strategy based on hybrid energy storage 434
186: Li-ion battery SOC estimation based on RTS - IEKPF algorithm 442
187: Study on photovoltaic grid-connected fast harmonic compensation technology for three-phase voltage unbalance 451
189: Constant power constant voltage startup procedures for VSC-LCC based hybrid pseudo bipolar HVDC system 461

190: Online parameter identification based on split battery model 470
191: HESS power optimised distribution based on genetic algorithm 480
192: Research on self-compensating dynamic droop control strategy of microgrid energy storage system 490
193: Control strategy of bidirectional convertor in DC/AC hybrid microgrid 500
195: A fuzzy control constant polarisation voltage charging method for lithium-ion batteries 509
196: An improved voltage feedforward SVM method for STATCOM in wind plant with multi cells cascaded 519
198: Research on the optimal operation strategy of CCHP-ORC systems 526
200: Research on key techniques for surface defect detection of solar cells based on convolutional neural network 536

104: Experimental study on the control strategies of DC power supply and storage in buildings

Fulin WANG[1], Zeyu SUN[2], Rui YAN[3]

[1] *Beijing Key Laboratory of Indoor Air Quality Evaluation and Control, Department of Building Science, Tsinghua University, Beijing, China, flwang@tsinghua.edu.cn*
[2] *Beijing Key Laboratory of Indoor Air Quality Evaluation and Control, Department of Building Science, Tsinghua University, Beijing, China, 552459677@qq.com*
[3] *Beijing Key Laboratory of Indoor Air Quality Evaluation and Control, Department of Building Science, Tsinghua University, Beijing, China, yanruiqq135@163.com*

In order to improve the electricity generation and distribution efficiency, it is very import to shave electricity load peak and to fill the load valley. Direct current (DC) power supply and distributed electricity storage is considered to be a promising way to achieve the electricity load shift. This paper studies the control strategies of the DC power supply and distributed electricity storage in buildings. Three types of control strategies are developed, which are constant power from grid, demand response mode, and minimum electricity cost mode. The three control strategies are verified both at a small test bed and at an actual office building using DC power. Experiment results show that the developed three control strategies all can achieve the expected load shift purposes. In addition, through the power supply performance test of the DC power supply and distributed electricity storage system at the test bed and actual DC power building, the power supply stability and energy saving potential of the DC power distribution system as well as the applicability of the three control strategies are further verified.

Keywords: Direct current power, Distributed electricity storage, Control strategy, Energy saving, Load shift

1. INTRODUCTION

Electricity is the main energy type used in cities. City electricity load has the characteristic of large gap between peak and off-peak, which is not good for the efficient operation of power plant and grid. The large load gap between peak and off-peak is mainly caused by building electricity load. The situation is getting worse with the large-scale the development of urbanisation. The proportion of the total civil building electricity consumption in urban is gradually increased year by year approaching 40% in China (Beijing Municipal Bureau of Statistics, 2014). Due to the electricity is mainly generated from coal-fire in China, which is difficult to deal with the electricity peak-valley gap, as a result the efficiency of power generation and power distribution is very low. Further it causes the curtailment of renewable energy, such as photovoltaic power and wind power. The Direct Current (DC) power supply and distributed electricity storage is considered as an promising way to fundamentally solve the problem of peak-valley gap of urban electricity load, accept the renewable electricity as much as possible, and benefit the society greatly with economic and environmental rewards. This paper focuses on studying the control strategies for the (DC) power supply and distributed electricity storage. Three types of control strategies are developed, which are constant power from grid, demand response mode, and minimum electricity cost mode. The three control strategies are verified both at a small test bed and at an actual office building using DC power. The following parts describe the details of the control strategies and experimental results.

2. CONTROL STRATEGIES

Three types of control strategies are studied, which are constant power from grid, demand response mode, and minimum electricity cost mode. The basic objectives of these three control strategies are similar, which are to achieve load shift. The control set points are different.

2.1. Constant power from grid

This control strategy is to maintain a constant power induction from grid, so the peak-valley gap can be totally eliminated if all buildings use this control strategy. The method to maintain the power introduced from grid constant by adjusting the battery charge/discharge power to make up the gap between power load and power introduced from grid.

The first step of control strategy of constant power from grid is to predict the electricity load of the next day. Neural network or detailed simulation modelling of buildings can be used to predict electricity loads.

The second step of this control strategy is to decide the set point of power introduced from grid, as shown in Equation 1. The control objective is to maintain constant power introduced from the grid, so the set point of power from grid is the average of the predicted loads.

The third step is to control the battery charge/discharge power, according to Equation 2, to make up the gap between the power load and power introduced from grid.

Equation 1: Set point of power introduced from grid

$$P_{gridset} = \kappa \frac{\int_0^T P(t)dt}{T}$$

Where:

$P_{gridset}$ = set point of power from grid (kW)

P(t) = predicted load at time t (kW)

k = line loss factor (-)

T= time cycle of control (hour)

Equation 2: Battery charge/discharge power

$$P_{bat} = P_{gridset} - P(t)$$

Where:

P_{bat} = battery charge/discharge power (kW)

$P_{gridset}$ = set point of power from grid (kW)

P(t) = predicted load at time t (kW)

2.2. Demand response mode

Demand response is the grid side sends the signal of power limitation to user side and the user side switches off some appliances to meet the limitation (General Administration of Quality Supervision, Inspection and Quarantine of the People's Republic of China, 2016). Demand response is an effective way to achieve demand shift to prevent power failure caused by overload. However the switch off of some appliance might decrease the satisfaction levels and even productivities of users. While the DC power supply and distributed electricity storage system can meet the demand limitation requirement without sacrificing the users' satisfaction levels and productivities.

The demand response control is to change the set point of power introduced from grid according to the grid power limitation signals and to adjust the discharge of battery to make up the gap between demand and grid power supply. The set point of power introduced from grid is calculated as shown in Equation 3 and the battery charge/discharge power is same as shown in Equation 2.

Equation 3: Set point of power introduced from grid for demand response mode

$$P_{gridset} = \eta P(t)$$

Where:

$P_{gridset}$ = set point of power from grid (kW)

P(t) = load at time t (kW)

η = demand response factor (-)

2.3. Minimum electricity cost

In order to achieve demand shift with cost incitement, many electricity grid companies implement time-of-use tariff. Figure 1 shows the time-of-use tariff in Beijing. The electricity price are divided into four categories, i.e. peak (1.5065 RMB/kWh), high (1.3782 RMB/kWh), flat (0.8595 RMB/kWh), and valley (0.3658 RMB/kWh).

The minimum electricity cost control strategy is to utilise this time-of-use tariff to achieve minimum electricity cost. The minimum electricity cost is an optimisation problem that can be solved by dynamic planning. The first step is to predict the time-series load in the following control period. The second stop is to solve the optimisation problem, as shown in Equation 4 to obtain the time-series battery charge/discharge power. Finally control the battery charge/discharge power according to the optimal solution.

Equation 4: Optimisation problem of minimizing electricity cost

$$O: \min C_e = \sum_{t=0}^{23} Pr(t)[P(t) + P_{bat}(t)]$$

Where:

C_e = electricity cost (currency)

Pr(t) = electricity price at time t (currency/kWh)

P(t) = electricity load at time t (kW)

$P_{bat}(t)$ = battery charge/discharge power at time t (kW), plus values represent charge, and minus values represent discharge.

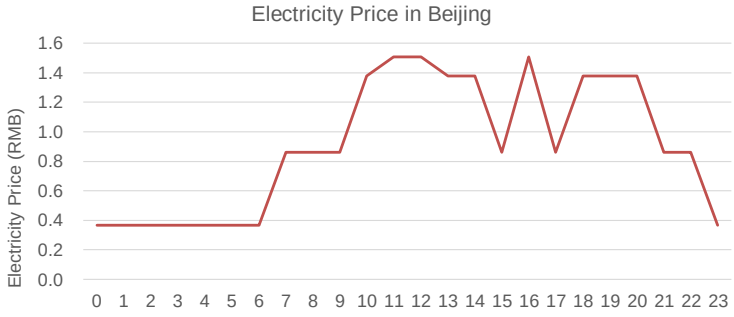

Figure1: Time-of-use tariff in Beijing

3. EXPERIMENTAL STUDY ON THE CONTROL STRATEGIES

3.1. Introduction of test bed

For the purpose of verifying the developed three control strategies, experiments were conducted at a small test bed. The components of the test bed is shown in Figure 2, including 220V alternative current (AC) power from grid, Photovoltaic (PV) panel, AC/DC rectifier, battery, 220V DC bus to supply power, and personal computer (PC), Light-emitting diode (LED) light, and an air-conditioner.

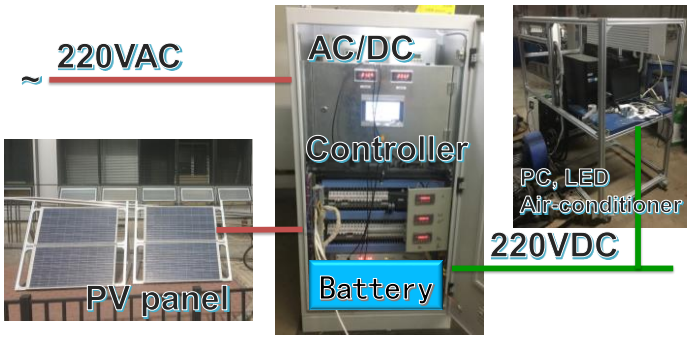

Figure 2: Components of test bed

3.2. Experiment results

The first two types of developed control strategies, i.e. constant power introduced from grid and demand response mode were studied using the small test bed.

Constant power from grid

The experiment results of constant power introduced from grid are shown in Figure 3. From Figure 3, it can be found that although the electricity loads changed from 600 to 1000W and PV power generation changed from 0 to 130W, depending on the battery discharging, the electricity uses from grid were controlled with the range between 600W and 660 W, showing an acceptable control accuracy of ±5%. It should be noted that during this experiment the set point of constant power from gird was relatively small, so most time the battery was at the sate of discharge, as shown by the minus values in the left bottom subfigure of Figure 3.

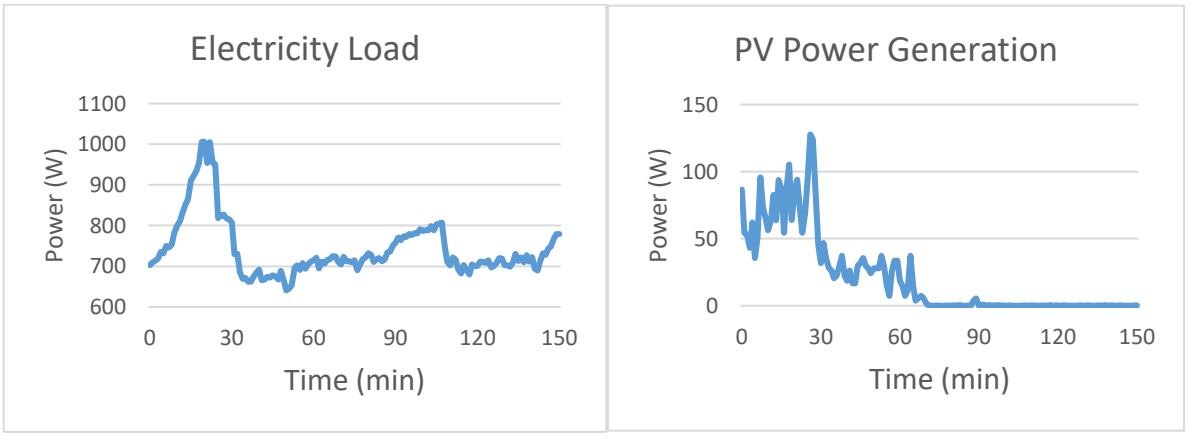

Figure 3: a) & b) Experiment results of constant power from grid

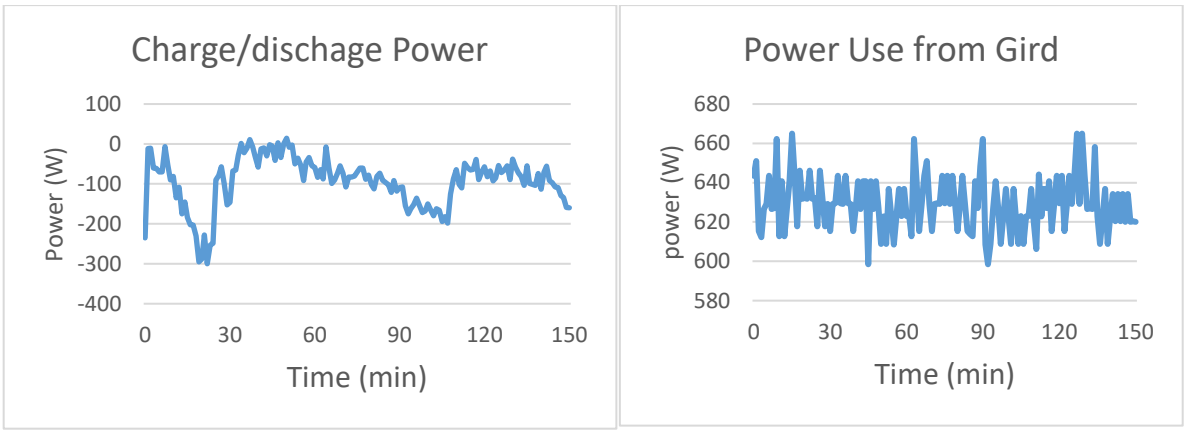

Figure 3: c) & d) Experiment results of constant power from grid

Demand response mode

The experiment results of demand response mode control are shown in Figure 4. From Figure 4, it can be found that the electricity loads changed from 500 to 1040W and PV power generation changed from 0 to 310W. The demand response factors changed from 1, 1.01, 1.75, and 4.12 corresponding to the time-of-use tariff. Correspondingly the battery discharged when power introduced from grid was small, i.e. from time 0 to time 500 min, and charged when the power introduced from grid is large, i.e. after time 500 min. From Figure 4 it can be seen that corresponding to demand response requirements, the control strategy can tune the battery charge/discharge rationally to fulfil the demand response requirements.

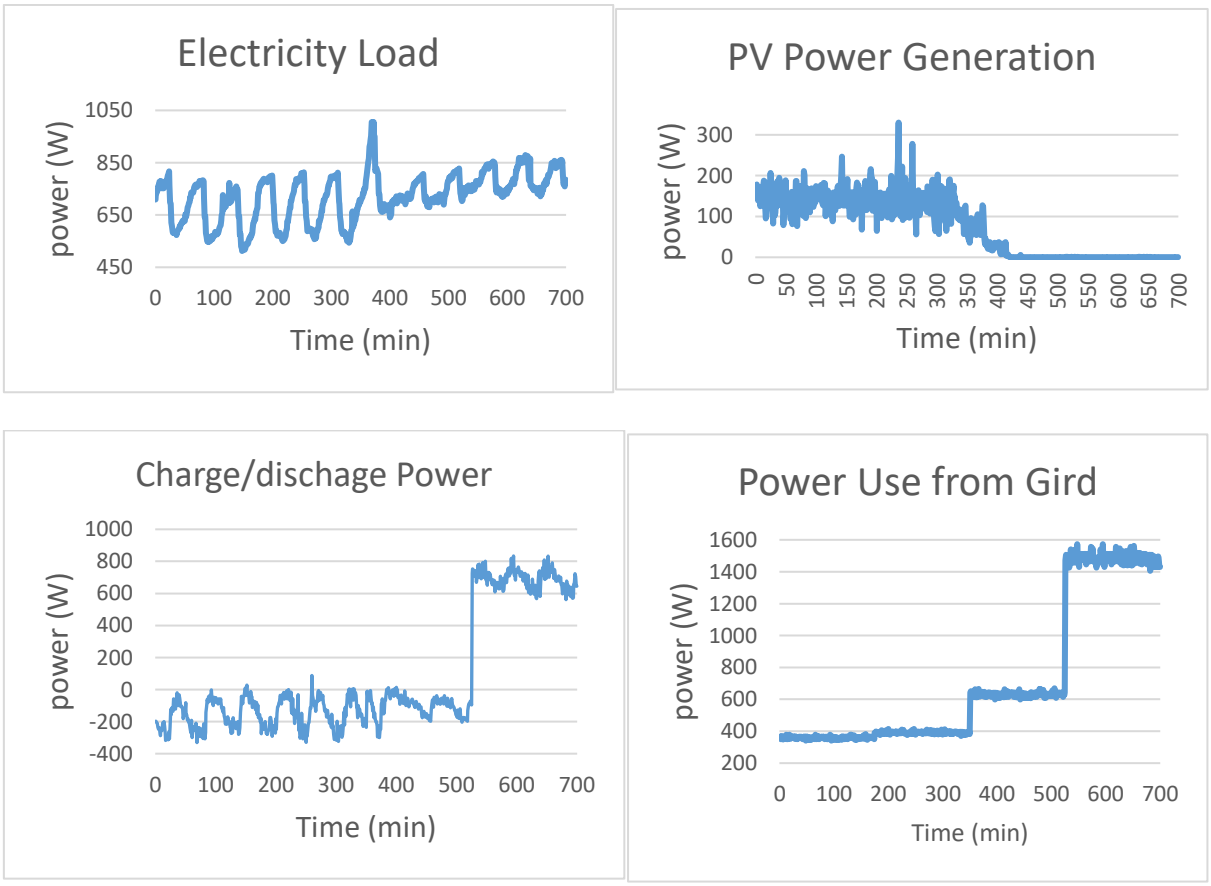

Figure 4: Experiment results of constant power from grid

4. CONCLUSION

DC power supply and distributed electricity storage is an effective way to achieve demand shift while maintain comfortable indoor comfort level and building users productivities. In order to achieve this objective, three control strategies are developed, i.e. constant power introduced from grid, demand response mode, and minimum electricity cost. The first two control strategies were verified at a small test bed. Experiment results show that the two control strategies can achieve the objective of demand shift with an acceptable control accuracy.

5. ACKNOWLEDGEMENT

This research is supported by National Key R&D Program of China, Research and Demonstration of Key Technology of Net-Zero Energy Building (Project Number 2016YFEOI02300) and Innovative Research Groups of the National Natural Science Foundation of China (Grant number 51521005). This research takes part in IEA EBC Annex 67 Energy Flexible Buildings.

6. REFERENCES

Beijing Municipal Bureau of Statistics. 2014, Beijing Statistical Yearbook 2014. Beijing: China Statistical Press.

General Administration of Quality Supervision, Inspection and Quarantine of the People's Republic of China, 2016. GB/T32672-2016 General Technical Specification of Power Demand Response System. Beijing: China Statistical Press.

Wang F, Jiang Y, 2016, Analysis of Key Technology and Benefits of DC Power Supply and Distributed Electricity Storage in Buildings, *Building Electricity,* 35(4), 16-20.

106: Comparative analysis of biogas and yields from cattle, sheep, poultry wastes and their combinations

Alex EDEOJA[1], Andrew ELOKA-EBOKA[2]

[1] *Department of Mechanical Engineering, Federal University of Agriculture, Makurdi, Nigeria, aoedeoja@gmail.com*
[2] *Discipline of Mechanical Engineering, University of KwaZulu-Natal, Durban, South Africa, fatherfounder@yahoo.com*

A comparative analysis of biogas yields from cattle, sheep and poultry wastes as well as that of their blends was carried out at the mesophilic temperature range (30°C – 40°C) in a laboratory scaled conventional digestive system - batch flow micro digesters made of air- impermeable plastic containers with effective volume of about 4 litres. The Experiments was carried out in three replicates at varying total solid concentrations (5%, 15% and 25%) and monitored for 8 days detention period (anaerobically digested) with a one day lag period observed for bacteria activation on the slurries. The biogas yields from these livestock wastes were compared as well as the variation of the total solid (TS) concentration with the biogas yield from the wastes together with their combinations. Seven batch type anaerobic laboratory – scale digesters were used. Biogas measurement was by the water displacement method. Hydrogen ion concentration (pH), ash content of the pulverized materials before and after digestion was determined The result showed that the composite blend of the three livestock (cattle + sheep + poultry) wastes has the highest biogas potential at 15% total solids concentration which peaked during the fourth day. There was a significant difference at 5% confidence level (P > 0.05) between the digestion of carbon before and after digestion and hence increase C:N ratio which favoured complete digestion. There was positive correlation of all the proximate analysis parameters before and after digestion. This shows good prospects for utilizing the blend of these wastes to produce biogas for useful applications in the farms as well as for normal domestic heating purposes.

Keywords: Biogas, yields, poultry, waste, combinations, anaerobic digestion

1. INTRODUCTION

Biogas is a methane-rich gas that is produced from the anaerobic digestion of organic materials (biomass). It is colourless, blue burning gas that can be used for cooking, heating, lighting and other engineering applications. It is odourless and can be obtained from various feedstocks such as cattle dung, poultry and piggery wastes. Methane is a high grade fuel of 22MJ/m^3 (15.6MJ/kg) with a density of 1.2kg/m^3. For almost half a century, engineers and scientists around the world have been advocating the utilisation of locally available renewable energy resources especially in developing countries. With energy being the central and vital issue at the intersection of environment and development, it is true then to say that if energy is got right, other environmental problems will be solved. A count down to this goal and a step towards development is the actualisation of optimisation of anaerobic digestion of organic wastes. The anaerobic digestion of animal, human, municipal and factory wastes as well as vegetables produces biogas, an alternative source of energy. To date there is a global energy crisis as a consequence of declining quantity of fossil fuels coupled with the unprecedented rising crude oil prices. The crisis demands greater attention to alternative energy sources and revision of existing technologies. Hence, it is critical now not only to focus on sustained economic use of existing limited resources but to identify new technologies and renewable resources that have the potential to cater for the increasing energy demand. As, there are large turn-ups of agricultural wastes yearly which are to be properly harnessed to produce energy cheaply for the use of the society, there is the need to convert them (wastes) to wealth. The high premium biogas generated can be commercialised to generate revenue since energy is paramount to every economic sector and as the power take-off to any mechanical operation. Biogas could play a phenomenal role for future energy supply through thermochemical, physico-chemical and biochemical transformations as well as conventional combustion. However, in terms of technology and social economic considerations, biogas technology is more preferred due to its economic feasibility and sustainability potential in addition to possessing other positive attributes such as being globally available, easy to exploit as well as having the capacity to positively contribute towards actualisation of the United Nations Millennium Development Goals (MDGs). Besides, biogas technology offers a very attractive route to utilise diverse categories of biomass and bio-water for meeting energy needs as well as contributing to resources and environmental conservation.

Biogas is particularly suited for meeting small off grid scale energy needs; can contribute to environmental sanitation and biogas technology is also simple enough to avoid production limitations. Fossil fuel energy which is the main energy stay of Nigeria is estimated to be declining, a trend that will intensify after the year 2050 (Pimentel et al., 1998). This is because the world supply of oil (crude) is projected to last fifty years (50 years) approximately at the current production rate, a projection that is based on current consumption rate and population. It is estimated that, if the world population continues to grow at the rate of 15% and if all the people in the world were to enjoy a standard of living and energy consumption rate similar to that of the average American, then the world fossil reserves would last only about 15 more years (Pimentel, 1999). In order to address this anticipated energy crisis, the World Energy Council and the Food and Agricultural Organisation (FAO) have called on governments to promote renewable and sustainable technologies in rural areas (Stout and Best, 2001). In Nigeria, large quantities of animal wastes are produced annually (Table 1) and are underutilised, which can be gasified to produce heat (Jekayinfa and Omisakin, 2005). The biological gasification of biomass material is one of the affordable methods of providing energy for in-situ application in Nigerian farms and villages. Typically, a kilogram of cow's dung yields about 0.09m^3 of biogas per day (Sasse, 1988). In 2006, about 18% of global final energy consumption came from renewable energy sources with 13% coming from traditional biomass such as wood burning and agricultural wastes. Hydroelectricity was the next largest renewable source, providing 3% (15% of global electricity generation), followed by solar hot water/water heating with contributed 1.3%. Modern technologies such as renewable energy geothermal energy, wind power, solar power and ocean energy together provided some 0.8% of final energy consumption. The objectives of this study therefore is to compare biogas yields from three livestock wastes, poultry, cattle and piggery and to compare the variation of the total solid (TS) with biogas yields from the water types thus understanding the influence of animal manure types. It is also aimed at averting the national demand for alternative and renewable source of energy and a contribution to National Development Goals (MDGs) in Nigerian energy environment. The scope of this research work encompasses the evaluation of biogas potential of selected bio-waste from Makurdi metropolis, Nigeria where these animal wastes are readily available. More specifically, the study will screen and evaluate/compare the biomass potentials of cattle, swine and poultry by means of bio-methane potential (BMP) analysis as well as carrying out other tests such as hydrogen ion concentration (pH), ash content, moisture content, volatile matter, carbon content (carbon to nitrogen ratio) and crude fibre content which proffer understanding on the influence of animal manure type on the biogas yield.

1.1. Factors affecting biogas production

The production of biogas is affected and influenced by temperature composition of the feedstock, pH of the waste and toxicity in the form of ammonia aromatic compounds, presence of heavy metals and volatile acids. Other factors are loading rate of feedstock into the digester, retention time of the waste in the digester and the nutrient availability of microorganism responsible for the bioconversion.

Temperature

Temperature is an important parameter that affects biogas production. This is because it affects the enzymatic activities of the micro-organisms responsible for the bioconversion of substrates into gas. Biogas can be produced at the psychrophilic (below 20^{o}C), mesophilic (20 – 40^{o}C) and thermophilic (40 – 65^{o}C) temperatures. Production at temperature below 20^{o}C is not encouraged because the conversion of solid materials within this range of temperature is slow and incomplete. Where production at the psychophilic temperature range is feasible, a longer detention time is required for the degradation process to enable an almost complete conversion of the feedstock. Biogas can also be satisfactorily produced at the mesophilic and thermophilic temperatures. Many advantages have been reported for the production of biogas at the thermophilic temperature. These are:

(i) Higher rate of biogas production because of the high rate of organic conversion at the elevated temperature which allows for heavier organic loading concentration and reduced detention time of substrate in the digester;
(ii) Smaller size anaerobic digester will employ in biogas production implying less capital investment. Due to the faster rate of bioconversion at this temperature, the residence time of the substrate in the digester is reduced, as fresh waste has to be added;
(iii) Thermophilic digestion of waste is much more sanitary than conversion at the other temperature the effluent from an anaerobic digester operated at thermophilic temperature contains very few pathogens because only few pathogens can survive at such temperature; and
(iv) Easy and mechanical transport and handling of the digester mixture because the substrate is less viscous at the elevated temperature.

A major disadvantage of producing biogas at thermophilic temperature is the fact that digestion at this temperature is known to be more easily upset than digestion at other temperatures. This is due to the upset number of microbial species capable of operating at elevated temperatures. Biogas production at the mesophilic temperature can sometimes be quite high because at higher temperatures, only the easily converted carbon is transformed to methane because of the shorter detention time associated with digestion at elevated temperatures. The materials which are more difficult to degrade is left behind in the sludge; the longer detention time which characterises conversion at the lower temperature results in conversion of a digester of carbon content to methane.

Total solid concentration of slurry

Slurries of waste feedstock used in the anaerobic digestion process to produce biogas are usually classified as low (less than 10% TS and high, TS > 20%). Slurry is diluted by the addition of liquid and concentrated by the addition of slurry solids. Slurries of low TS are easier to handle by pumps and pipe works compared to those of high total solid. The quality of biogas yield from slurry depends on the amount and digestibility of solids present in the slurry. If the slurry is too thin, the solid matter separates and falls to the bottom instead of remaining in suspension. If it is too thick, the biogas produced is trapped within the slurry and rises to the surface with difficulty. In both cases, the biogas yields from the digester are reduced. In situations where slurries of low are used, there is reduced conversion efficiency, unstable digester conditions and reduced methane production because of the high water content of the feedstock causes washout of the influent solids and the slow growing methanogenic bacteria from a continuous flow plant. Researches on the effects of varying concentrations of TS on biogas yield have shown that as the concentration of slurries increases, the biogas yield decreases. Therefore, slurries of high concentration should not be used in the anaerobic digestion process for biogas production. This is because at high concentration, there is an accumulation of inhibitory acids produced during digestion. The most advantageous TS for a continuous flow type biogas plant are 5 – 10% compared to as much as 25% for a batch operated plant. The TS concentration of slurry is determined from Equation (1).

$$W_c(\%) = \frac{W_i - W_f}{W_i} \text{ and } TS = 100\% - W_c(\%) \qquad (1)$$

Where W_c, W_i and W_f are the respective water contents of the slurry at any given time, initially and at the end of the period.

Retention time

The retention time in a batch digestion process or HRT as in the continuous flow digestion process has a direction relationship with gas yield, digester size, quantity of waste added and removed from the digester and the efficiency of the biodegradation process. The retention time of the slurry in the digester determines the efficiency of conversion of the acid intermediate (which will be converted into biogas) produced during the anaerobic digestion process. The critical RT will vary with the chemical and physical characteristics of the wastes. In general, 30 days is considered as a minimum time frame for optimum bacterial decomposition to take place to produce biogas and destroy the toxic pathogen found in waste.

pH

The pH value of the slurry in the digester is an important indication of methanogenic performance. In the absence of any other indicator, pH value alone has been used to check the digester environment. Gas will be produced if the pH is between 7.0 and 7.2 beyond this pH limit, digestion can proceed but with less efficiency. pH has been found to affect biogas quality, which may be because the acid produced during the anaerobic digestion process are precursors for the methanogens that produce biogas; process failure will occur if the acidity of substrate in the acetic acid produced during the anaerobic digestion process usually results in a drop of pH value. This makes the substrate unsuitable for the action of the methane forming bacteria. In instances where inefficient amounts of natural alkalinity are not present in the waste, the acidity can be controlled by reducing the loading rate of waste into the digester, which will allow the volatile acids already present to be utilised thus decreasing its concentration. Natural alkalinities in wastes are due to the presence of hydroxides, carbonates and bicarbonates of elements such as Ca, Mg, Na, and NH_3. Of these, Ca and Mg bicarbonates are the most common. An alternative method of controlling the alkalinity of pH of the substrate is by adding alkaline materials such as lime and NaOH to it.

Loading rate

The quantity of waste that is fed into a digester depends on the capacity of the digester, the temperature, the retention time and the efficiency of bioconversion of the waste into biogas. The yield is related to the loading rate of the digester. Although biogas production increases with loading rate, it is known that as loading rate increases, the solid destruction efficiency begins to decrease. This means that for any digester size and operating temperature, biogas yield increases as the loading rate increases up to an optimum value. On attainment of this value, gas yield begins to decrease. This is because; increasing the loading rate after the optimal value increases the total solid concentration of the slurry which results in an accumulation of some inhibitory compounds that reduce the rate of gas yield. Also, the plant digestion process remains in the acid phase since there are more feed materials than methane bacteria can handle. In a simple biogas plant, 1.5kg/m^3/day is already quite a high loading rate. Temperature controlled and mechanically stirred large scale plants can be located at about 5kg/m^3/day.

Carbon-nitrogen ratio of the slurry

The microbial population involved in anaerobic digestion requires sufficient nutrient to grow and multiply. Each species requires both a source of carbon and nitrogen. If there is insufficient quantity of nitrogen present, the bacteria will be unable to produce the enzymes which are needed to utilise the carbon. If there is too much nitrogen particularly in the form of NH_3, it can inhibit the growth of bacteria. An optimum ratio of C:N between 20:1 and 30:1 is recommended for optimum methanogenic performance. Animal manure performs satisfactorily in terms of gas yield when used in the anaerobic digestion process because they contain carbon and nitrogen in the required proportion. A deficiency in the carbon content of animal manure used for anaerobic digestion can be corrected by the addition of plant wastes which are high in carbon content.

Toxicity

Many compounds can be toxic to methanogens if present in sufficient concentration in digester although some are needed, they quickly become inhibitory. These compounds includes various salts, heavy metals such as copper, zinc and nickel present in the waste, antibiotics in the feed for animals that produce the waste sued in the anaerobic digestion and ammonia concentration of the slurry in excess of 300mg/L, the effects of these compounds on the digestion process largely depends on the chemical composition of the waste. The presence of other compounds that are antagonistic (particularly heavy metals) through precipitation as sulphides is also a factor. Another important factor that determines the effects of these compounds system to tolerate and become use to their presence. A minimum amount of ammonia is always required in order to achieve a favourable condition for growth.

1.2. Anaerobic treatment process

The anaerobic degradation of organic matter to methane involves a complex interaction of three groups of bacteria and is illustrated in Figure 4. The first group of bacteria is the fermentive bacteria, which hydrolyses complex long chain organics and ferments them to fatty acids, alcohols and other soluble organics. The second group of bacteria, the acetogenic bacteria has been found to degrade propionate and longer chain fatty acids to acetate, hydrogen and carbon dioxide; presently this is the only known biological degradation pathway for long chain fatty acids and alcohols, since there are no documental cases of methogenic bacteria being isolated which can degrade these organics directly to methane (Mclnerney, et al, 1979). As for the third group of bacteria, the methanogens, the substrates for growth which have been determined to date are hydrogen, acetate, formate and methanol. The activities of these degradable bacteria can be simplified into three-phase processes namely – the hydrolysis, acid forming and methane forming phases. In the hydrolysis phase, extracellular enzymes secreted by acidogens breakdown the complex organic material into simple, soluble molecules. These molecules are broken down into volatile fatty acids VFAs (e.g. propionic and butyric acids), carbon dioxide, ammonia and hydrogen by acidogens in the acid forming phase. In the methane forming phase, methanogens or methane-formers convert the VFA into

CH_4, CO_2, N_2 and H_2S. In this phase too, a synthesis of CO_2 and H_2 takes place to also form CH_4 and water. Figure 5 is a flow diagram of the biogas production process. McCarty (1964) had suggested that the rate limiting step in anaerobic digestion is the conversion of propionic and acetic acid to methane gas. However, Pfeffer (1979) has indicated that at high solid retention time (greater than 10 days), the rate limiting step in the digestion of sewage sludge at 35°C is the hydrolysis of organic solids. In addition, Pfeffer (1979) found that cellulose hydrolysis was the rate limiting step in the digestion of municipal wastes. Figure 2 shows the anaerobic conversion of organic matter to methane while Figure 3 shows a diagram of the biogas production process.

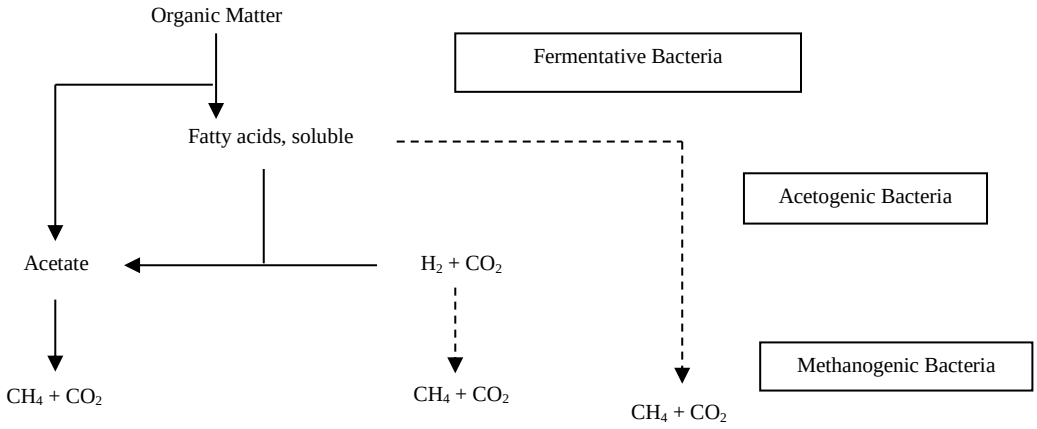

Figure 2: Anaerobic Conversion of Organic Matter to Methane

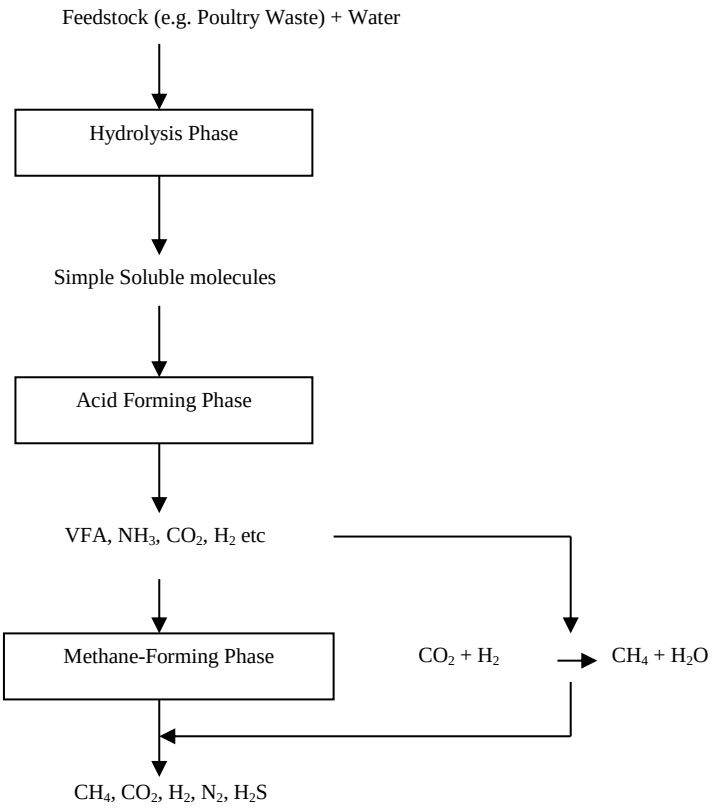

Figure 3: Schematics of a biogas production process

2. MATERIALS AND METHODS

2.1. Feed materials

Three different types of raw materials (animal wastes) comprising of cattle, sheep and poultry as well as their individual combinations were used in this research. The animal wastes not later than two days old were collected from the Research Farm of the Federal University of Agriculture, Makurdi, Nigeria and were stored in black containers for adequate preservation. The initial parameters analysed were moisture content, volatile solids, alkalinity, and carbon - nitrogen ratio as well as the pH of the solution, ash and fibre contents. Experiments were carried out on a laboratory scale using batch flow micro digesters made of air- impermeable plastic containers with effective volume of about 4 litres. It is an upright air tight tank charged with shiny and sealed for digestion to take place. The digester consists of a cylindrical drum sealed at both ends but with opening for feeding the slurry and discharging of the effluent. A fitting that combined a hose was mounted on each digester. The hose (gas collection tube) was used for biogas collection by means of which the digester is linked to the water displacement can. The bio-digesters were incorporated with a stirrer to mix the materials inside manually. This is necessary in order to prevent settling and to maintain contact between bacteria and manure, maintain uniform temperature, prevent surface scum formation and facilitate release of biogas.

2.2. Method

Fresh wastes of cattle, sheep and poultry were collected and weighed in equal proportion. 2.0kg of each sample were collected and open dried to determine the moisture content and the volatile solid composition of the raw materials. The wastes after drying were pulverised and 280m^3, 170m^3 and 57m^3 of tap water was measured using a measuring cylinder and mixed with 2.0kg of the wastes to make a total solid concentration of 5%, 15% and 25% respectively and were charged into the digesters and mixed thoroughly to remove all traces of oxygen, which will ensure good anaerobic condition. The combined blends were also measured proportionally to make a total of 2.0kg waste. Water was warmed to about 65^{o}C to maintain the initial mesophilic temperature for the digestion process to be effective. The digesters were provided with a manual stirring mechanism and the daily temperature readings were taken using mercury thermometer. The experiment was carried out in three replicates (experiments A, B and C) at varying total solid concentrations. The individual digesters were also numbered and labeled accordingly. The whole system was monitored for 8 days detention period with a one day lag period for the bacteria to act on the slurries. Notwithstanding, the period (days) of effective biogas yield were actually noted.

Biogas measurement

The quantity of biogas produced from the digesters was measured using the water displacement method. The digesters were fitted with a drain pipe which was then connected to the inverted burettes inserted into beakers containing water. The pipe incorporates a control valve which was opened only when the biogas measurement is to be taken. The set-up is shown in Figure 4. The volume of biogas produced in a given time is equal to the volume of water displaced and the slurries obtained were measured before and after digestion. Hydrogen ion concentration (pH), ash content of the pulverised materials before and after digestion was determined. 2.0g sample was heated in an electric oven at temperature between 200 – 300^{o}C for about 3 hours. The difference in weight of the ash was determined by weighing. Moisture content was determined using 2.0kg of the samples before and after the digestion. The fresh samples were open air dried to a constant weight to determine the quantity of water lost. The volatile matter of each sample was determined from the ash content of the samples.

Figure 4: Biogas experimental setup

The difference in weight of the burnt fibre and the ash was determined. The carbon content was determined using Equation (3).

$$\text{Carbon Content} = \text{Standard Value}(0.58) \times \text{Volatile Matter (\%)} \quad (3)$$

The crude fibre content of the samples was determined using 2.0g of each sample. 200ml of 1.25% H_2SO_4 was added to 2.0g of the samples contained in a flat bottom flask and boiled for 30 minutes, cooled, filtered and washed dry of the acid. The residues were dried and weighed. Then 200ml of 1.25% NAOH was used to wash the dried residues, boiled for 30 minutes, cooled filtered and weighed. The resultant residues were ashed, cooled and weighed. The crude fibre content (CFC) was determined from the Equation 4.

$$\text{CFC} = \frac{W_{ab}\text{-}W_a}{W_s} \quad (4)$$

Where W_{ab} = weight after acid - base treatment, W_a = weight after ashing and W_s = weight of sample.

3. RESULTS AND DISCUSSIONS

The result of the tested parameters before and after the digestion processes are presented in the Tables, Figures and Graphs. Tables 3 and 4 are respectively the proximate analysis of the raw materials before and after digestion**.** The temperature variation in the digesters during the experimental period is computed in Tables 8, 9, and 10. Correlation analyses of proximate analysis parameters before and after digestion are presented in Table 5. Table 6 is the analysis of variation of the interaction of parameters of proximate analysis before and after digestion while Figure 5 represents the analysis of variation of carbon depletion before and after digestion with Table 7 being the analysis of variation before and after digestion. Table 11, Figures 6 and 7 are the biomass yields at different total solid concentrations. Figure 8 is the cumulative. Table 5 and 6 is the correlation analysis of variation of the interaction.

Table 3: Proximate analysis of the samples before digestion

Wastes	Moisture Content %	Ash Content %	Volatile Matter %	Carbon Content %	pH	Nitrogen Content %	Crude Fibre %	C:N Ratio
Cattle	86.50	24.51	75.49	43.78	6.3	1.10	9.04	40:1
Sheep	82.60	20.38	79.62	51.98	6.9	1.50	8.56	35:1
Poultry	87.30	12.14	87.96	55.21	6.4	2.13	8.82	28:1
Cattle + Sheep	86.00	16.53	83.47	49.61	6.5	1.48	8.65	34:1
Cattle + Poultry	87.15	18.68	81.52	44.39	6.4	1.11	9.25	40:1
Sheep + Poultry	84.70	17.57	82.53	43.42	6.7	1.23	8.61	35:1
Cattle +Sheep+Poultry	85.60	11.56	88.64	47.52	6.5	1.54	9.12	30:1

Table 4: Proximate analysis of the samples after digestion

Wastes	Moisture Content %	Ash Content %	Volatile Matter %	Carbon Content %	Nitrogen Content %	Crude Fibre %	C:N Ratio %
Cattle	92.31	38.64	61.36	35.59	0.93	7.73	38:1
Sheep	87.53	29.46	70.64	37.11	1.34	5.49	27:1
Poultry	89.14	46.82	53.18	38.70	1.40	5.84	23:1
Cattle + Sheep	91.20	41.41	58.59	34.13	1.50	6.25	23:1
Cattle + Poultry	90.75	33.57	66.43	38.42	1.21	6.73	32:1
Sheep + Poultry	88.36	37.85	62.15	36.00	1.30	5.15	28:1
Cattle+ sheep + Poultry	89.37	42.58	57.42	34.57	1.40	6.24	25:1

The comparative analysis of the result showed that the composite blends of the wastes at 15% total solid concentration has the peak biogas yield of 67.90cm^3 and the least cumulative biogas yield of 24.70cm^3 was recorded at 5% total solid concentration. In the first set-up, the biogas yield ceased in digester A1 after day 5 and in digester A2 and A3 after day 6. This may be due to the presence of single raw material and as a result of a very low total solid concentration.

Table 5: Correlation analysis of proximate analysis parameters before and after digestion

Before After	Moisture Content %	Ash Content %	Volatile Matter %	Nitrogen Content %	Crude Fibre %	C:N Ratio
Moisture Content %	1					
Ash Content %	-0.22388	1				
Volatile Matter %	0.228805	-0.99987	1			
Nitrogen Content %	0.108816	-0.71654	0.708625	1		
Crude Fibre %	0.646867	-0.03766	0.05029	-0.28287	1	
C:N Ratio	0.005136	0.878673	-0.87237	-0.89892	0.275081	1
Moisture Content %	0.682898	0.36686	-0.36515	-0.40143	0.536167	0.494759
Ash Content %	0.62481	-0.65036	0.646377	0.602236	0.114708	-0.66726
Volatile Matter %	-0.6274	0.649323	-0.64539	-0.59902	-0.11737	0.664491
Nitrogen Content %	-0.18731	-0.77423	0.768241	0.618244	-0.43819	-0.73365
Crude Fibre %	0.559835	0.468599	-0.46461	-0.41725	0.69348	0.541661
C:N Ratio	0.145047	0.823157	-0.81595	-0.75489	0.463986	0.847118

Table 6: Analysis of variation of proximate analysis parameters before and after digestion

ANOVA

Source of Variation	*SS*	*df*	*MS*	*F*	*P-value*	*F crit*
Rows	7.761363	6	1.293561	0.124665	0.992953	2.23948
Columns	104107.7	11	9464.336	912.1092	1.45E-67	1.936958
Error	684.8371	66	10.37632			
Total	104800.3	83				

Ho: F ≤ Fcrit **α = 0.05**

Ha: F > Fcrit

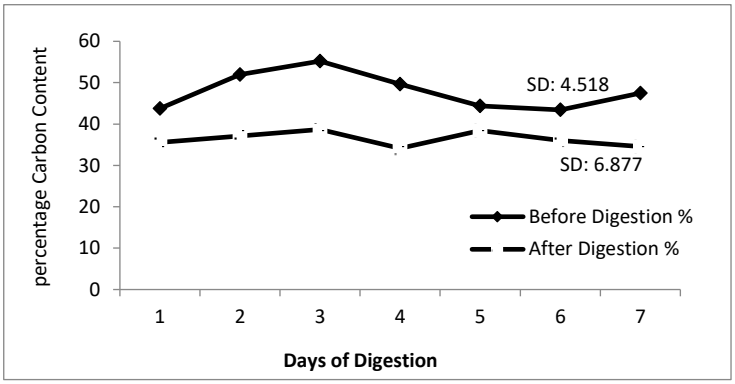

Figure 5: Carbon percentage depletion during digestion

This may also be due to the high carbon-nitrogen ratios of these raw materials which might be complex for the digestive bacteria to breaking as reviewed from past literature. The raw materials that are blended with each other showed a progressive biogas production of 61.90cm^3, 67.90cm^{3}and 46.50cm^3 in experiment A, B and C respectively is 59.30cm^3. This reveals that the blend of the raw materials inoculates each other and thereby inoculants as can be seen from the composition of its carbon-N ratio as recommended by literature (Source). The analysis of variation of the degradation of carbon before and after digestion indicated that there was a significant different at 5% significant level before and after digestion (P > 0.05) (Table 7, Figure 5) but the difference amongst the different animal wastes for carbon depletion was not significant at 5% confidence level (P ≤ 0.05).

Table 8: Temperature results at 5% total solid concentration

	Temperature Values (°C)						
Wastes	**Day 1**	**Day 2**	**Day 3**	**Day 4**	**Day 5**	**Day 6**	**Day 7**
Cattle	32	34	37	37	35	34	31
Sheep	31	33	35	36	36	35	33
Poultry	32	34	34	35	34	33	30
Cattle + Sheep	33	36	36	37	36	34	33
Cattle + Poultry	32	34	36	36	35	34	32
Sheep + Poultry	31	33	35	36	37	35	34
Cattle + Sheep + Poultry	34	35	37	38	38	37	35

Table 9: Temperature results at 15% total solid concentration

	Temperature Values (°C)						
Wastes	Day 1	Day 2	Day 3	Day 4	Day 5	Day 6	Day 7
Cattle	34	34	36	37	36	34	32
Sheep	32	33	35	36	37	35	33
Poultry	33	34	35	37	37	36	34
Cattle + Sheep	31	32	34	35	36	35	32
Cattle + Poultry	34	34	36	36	36	34	33
Sheep + Poultry	35	34	35	36	35	33	31
Cattle+ Sheep + Poultry	35	35	37	38	38	37	35

Table 10: Temperature results at 25% total solid concentration

	Temperature Values (°C)						
Wastes	Day 1	Day 2	Day 3	Day 4	Day 5	Day 6	Day 7
Cattle	29	30	32	34	34	32	30
Sheep	30	31	33	35	33	32	32
Poultry	28	28	30	32	33	31	29
Cattle + Sheep	29	30	31	31	31	30	29
Cattle + Poultry	30	31	32	34	34	32	32
Sheep + Poultry	31	31	33	35	35	33	31
Cattle + Sheep + Poultry	32	34	34	36	36	34	32

There is also significant difference in the interaction of the overall proximate parameters during and after digestion of feedstocks ($P > 0.05$) but this significant difference did not extend to the individual parameters in the cause of the digestion ($P \leq 0.05$) (Table 6). Each parameter was significantly different to each other during the process. This implication has a huge impact in the overall production of bio-gas (methane) whose principle contribution is from carbon as it relates to the C:N which is dependent on the feedstock and this case the synergy of the combined feedstock contributed to this significant difference and hence great biogas yields. Correlation analysis recorded positive results among parameters before and after digestion (Table 5). That means, the parametric losses of the feedstock were gained in the production of the product. Figure 7 show the synergistic potential of the combined waste which peaked during the fourth day in the total solid concentration and the weakness in the single feedstock substrates for all the three percentage concentration of 5%, 15% and 25%. In Figure 8 where the cumulative biogas yields were presented, 15% concentration peaked as earlier established with contribution more from the synergy of the combined waste/feedstock. In the third experimental set up, the biogas yield ceased after day 6. This may be traced to the high total solid concentration of the slurry. In all the digesters, the biogas production showed a rapid increase until day 4 in each digester followed by a slow decrease between day5 and 7.

Table 11: Biogas yields at 5% total solid concentration

Wastes	Day 1	Day 2	Day 3	Day 4	Day 5	Day 6	Day 7	Cumulative
Cattle	4.50	5.60	6.10	6.00	3.50	-	-	24.70
Sheep	5.00	6.40	7.00	7.30	5.90	2.70	-	34.30
Poultry	4.50	5.50	6.80	7.60	4.00	3.10	-	31.50
Cattle + sheep	6.00	7.50	9.40	9.20	7.50	4.50	4.50	48.60
Cattle + poultry	6.50	8.00	9.60	10.20	9.70	8.30	5.80	58.10
Sheep + poultry	5.20	6.30	7.40	8.40	7.80	7.50	6.00	48.60
Cattle + sheep + poultry	6.80	8.40	10.20	10.60	9.30	9.00	7.60	61.90

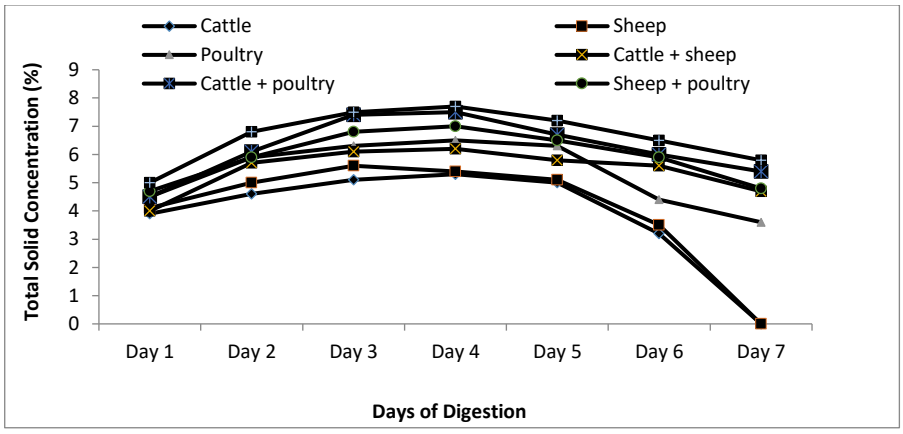

Figure 6: Biogas yields at 15% total solid concentration

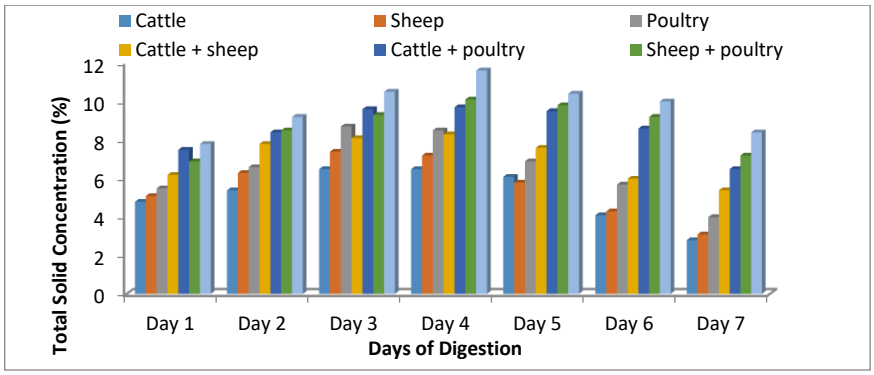

Figure 7: Biogas yields at 25% total solid concentration

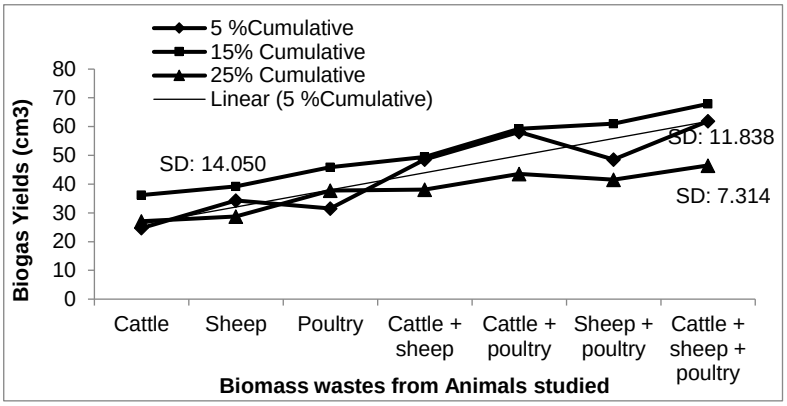

Figure 8: Cumulative biogas yield at 5%, 15% and 25% total solid concentrations

4. CONCLUSION AND RECOMMENDATION

The overall result of the anaerobic digestion of cattle, sheep and poultry wastes as well as their composite blends at mesophile condition indicates that the composite mixture of the wastes proved to have the highest biogas production potential. This result was favourable at 15% total solid concentration of the slump. In contrasts, due to unavailability of inoculants in singular raw material digesters, the biogas production is poor. As a result the daily temperature in these digesters seemed to be heightened. The quantity of biogas yield depends on the type of livestock manure digested and also on the diet and method of storage prior to digestion as well as Carbon-Nitrogen ratio of the livestock manure. Anaerobic digestion technology has the potential of being applied to the management of animal waste which is cheap and cost-effective supply of feed stock for renewable energy generation. Anaerobic digestion can greatly reduce the bulk waste and odour emission while producing energy. The technology of biogas generation from cheap raw materials (animal wastes) is contemporary, right on target and easy to manage. In view of this, the government, private sectors, industries and individuals should applaud and uphold the system as a means of pure energy generation. For optimum yield and best performance of the system, raw materials should be blended together (Inoculated) and at neither too low nor too high total solid concentration. The government of the day through her various organs of development – the Millennium Development Goals MDGs and Energy for Sustainable Development Agency should conduct public enlightenment programs to educate the populace on the potential and lucrativeness of the biogas production to further substantiate the diversification of energy sources from exhaustible fossil fuels to renewable sources. This technology is multi-beneficiary. The utilisation of the system for energy production could impact positively on the country's economy through income generation, job creation and alleviation of poverty. Besides, the methane derived electricity could replace the fossil fuel based electricity, hence contributing to the preservation of the environment. In addition, a suitable design that minimises the energy required should also be looked into and developed.

5. REFERENCES

Anderson, T. Doig A. Rees D. and Khennas, S. (1999), Rural Energy Services; a Handbook for Sustainable Energy Development. ITDG Publishing.

Biogas-africa. Biogas for better life-an African initiative available from: http://www.biogasafrica.org.

Demirel, Y. (2006). Energy Production, Conversion, Storage, Conservation and Coupling XXVI, 616p. 159 illus.

Duncan, M. (1986). Sewage Treatment in Hot Climates. English Langue Book Society/JOHN Willey and Sons.

Itodo, I. N. (2007). Agricultural Energy Technology. Aboki Publishers Makurdi, Nigeria.

Itodo, I. N. and E. I. Kucha, 1997. The Prospects of Biogas Technology in the Agricultural Development of Nigeria. Nigeria Journal of Renewable Energy. Vol. 5.

Itodo, I. N: Lucas, E. B; and Kucha, E. J. (1995). The Effects of using Solar Energy in the Thermophilic Digestion of Poultry Waste. Nigerian Journal of Solar Energy. Vol 13.

Jekayinfa, S. O. and O. S. Omisakin. 2005. The energy potentials of some agricultural waste as local fuel materials in Nigeria CIGR E Journal. Vol. 7.

Khandewal, K. C. and Mahdi, S. S. (1986). Biogas Technology. A practical Handbook. Tata McGrawhill Publishing Company Ltd.

Lettinga, G. A., T. Geest, S. Hobma and J. V. D. Loan, 1979. Anaerobic treatment of methanolic waste water research, vol. 13.Merkel, A. J. (1981). Managing Livestock Wast AVI Publishing Company Inc.

Nzila, C. Wambua P. Githaiga. The Potential of a low Cost EPAD System in the Treatment of Textile Mill Effluents. Journal of Mechanical Engineering. Vol 4.

Pimentel, D. M. Pimentel and O. Karpenstein-Mahan, 1999. Energy use in Agriculture. Invited Overview. Vol, 1 Dec.

Sasse, L. 1988. Biogas Plants. 2nd Edition. Vieweg and Sohn, Germany.

Solar Energy Society of Nigeria. National Solar Energy Forum (2009). University of Agriculture, Makurdi.

Stout, B. A. and G. Best. 2001. Effective Energy use and Climate Change. Needs of Rural Areas in Developing Countries. Invited Overiview. Vol. III.

111: Evaluation of daylighting levels in heritage buildings turned into museums in UAE

Khaled A. AL-SALLAL[1], Amira ABOUELHAMD[2]

[1] UAE University, Al-Ain, k.sallal@uaeu.ac.ae
[2] UAE University, Al-Ain, 200734405@uaeu.ac.ae

The UAE authority has converted many of its heritage buildings into museums due to the cultural value of these buildings and their potential to promote tourism economy. Nevertheless, these buildings were not designed to host valuable artefacts and thus ensuring their operation as museums is a crucial question that is investigated in this research. The objective is to evaluate the daylighting levels in the display room using different Window-To-Wall ratios (WWRs) and the potential risks on the historical artefacts. At the outset, the study conducted several site visits to collect information and take measurements in the real lighting environment of these buildings. This helped to survey the displayed artefacts and classify them into categories based on their sensitivity to light and define the lighting characteristics of the display room. Statistical analysis was performed on building data gathered from images and architectural drawings to identify the measures of the different spatial and building elements. To investigate the daylight performance as a function of WWR change, 3D models with three ranges of WWRs (5%, 9%, and 15%) were developed applied to a medium size exhibited space with courtyard windows on the southwest orientation. Simulations were performed for each category of the artefacts considering a large number of sensors distributed horizontally in the room to cover all possible locations of artefacts. The tested metrics were Daylighting Autonomy (DA) and the Useful Daylighting Illuminance (UDI). The results revealed high levels of illuminance in the exhibited spaces for all tested ranges of WWRs, especially for the high sensitive artefacts; and confirmed that the change of WWR from 5-15% could lead to extreme risks. The study recommends minimise WWR and provide shading in order to enhance the overall lighting environment and reduce light exposure on the artefacts.

Keywords: Museum, daylight autonomy, heritage, courtyard

1. INTRODUCTION

The heritage buildings in the United Arab Emirates (UAE) were built to adapt to the harsh desert climate of the region and to respect the traditions. The construction of these buildings used the available local materials such as coral stones, gypsum, burnt mud (surooj), and palm trunks and fronts. However, after the discovery of oil in the gulf region by 1650s, new methods of construction emerged that replaced the traditional methods of construction. Later on, the UAE authorities realised the significance of the heritage buildings in representing the identity of the country and thus enforced laws to preserve them. Buildings that were once used as residences for rulers or high-status families were retrofitted to serve as museums, restaurants, governmental offices, homes for non-profit corporations, and galleries.

The mission of a museum is: 1-Collect and exhibit art and historic artefacts for public education and enjoyment, 2-Protect the collection from damage, 3-Do this all as efficiently as possible (Miller and Miller, 2005). Natural lighting in museums plays a very significant role owing to the numerous advantages it offers, such as effective colour rendering of artefact, positive psychological impact on visitors, greater satisfaction through artwork gratitude, reduction of energy consumption and electric lighting load (Li et al., 2005, Mueller, 2013, Engineer, 2015, Hefferan, 2008). A major challenge is that natural lighting is not easy to control as it changes depending on the change in time and/or weather conditions. Poor natural lighting in museums could deteriorate exhibited artefacts and possibly cause a non-reversible damage to them due to high radiant energy (Lee et al., 2013, Lithgow et al., 2006, IESNA, 1999). The extent of this damage depends on the sensitivity of the exhibited material, the intensity of light that reaches it, and the exposure time. Long time of exposure and high illuminance levels accelerates the deterioration of artefacts (Pinilla et al., 2016, Domenech-Carbo et al., 2011).

Museums designers can control artefacts' damage caused by natural light by implementing different aspects such as controlling the overall light levels to ensure good lighting, utilizing a full visible spectrum lighting that represents all colours, ensuring the elimination of shadows, glare, and reflections. The lighting authorities such as the Illuminating Engineering Society of North America (IESNA) provide design guidelines that help to consider the sensitivity of the artefacts and eliminate the non-visible radiation caused by high energy. The values given in these guidelines help to control the amount of energy absorbed by the artefacts and thus preserve them. The IESNA guidelines state the maximum illuminance limits for each type of artefacts' category depending on their sensitivity to light. Table 1 specifies these limits for each artefact's category.

Table 1: Recommended illuminance limit for each artefact's category, adopted from IESNA Lighting Handbook (DiLaura et al., 2011).

Artefact category	Illuminance Limit (Lux)
High sensitive to light Books, botanical, specimens, costumes, cotton, drawings, dyed, leather, feathers, fugitive dyes, fur, gouache, insects, manuscripts, miniatures, paintings in distemper media, paper, prints, silk, skins, some minerals, some photographs, stamps, tapestries, textiles, wallpapers, watercolours, wool, and writing inks.	50
Low sensitive to light Bone, horn, ivory, lacquer, leather, oil paintings, some plastics, some photographs, tempura painting, textiles with stable dyes, and wood finishes.	200
No sensitive to light Ceramics, enamel, glass, jewels, metal, most minerals, stone, and wood	1000

The illuminance in a space is not constant, but it rather changes at different times of the day, month and year and depends on the sky conditions. A limited insight is provided when a point-on-time measurement of the average illuminance over a period of time is used to analyses the daylighting in a space (Al-Sallal, 2016). Climate-based metrics such as daylight autonomy (DA) and Useful Daylight Illuminance (UDI) present a more comprehensive picture of the yearly daylight performance over time. The DA is defined as the percentage of a defined period during which interior illuminance exceeds a threshold illumination level (IESNA, 2011), while the UDI gives the percentage of time at which the daylight is considered useful for three range of illuminance limits.

The tourism economy and the need to preserve the country's identity have encouraged the idea of transforming many heritage buildings into museums. Nevertheless, these buildings were not designed for this purpose, which raises the question "are these buildings suitable for museum functions?". The authors have been investigating daylighting performance in heritage museums. Al-Sallal and Bin-Dalmouk (2011) used on-site measurement and computer simulation based on illuminance levels in the display spaces. The results revealed several daylighting problems such as the existence of high illuminance levels and direct sunlight in the display rooms. In another study, Al-Sallal and AbouElhamd (2018) applied a more comprehensive methodology based on yearly analysis of daylighting in the heritage museum using the climate daylight metrics "Daylight Autonomy" (DA) (Al-Sallal and AbouElhamd, 2018). The results helped to understand the daylighting performance in a selected case with WWR = 7%. Both studies have revealed the significance of adding shades to reduce the overall illuminance in UAE heritage museums. The current study aims at investigating daylighting performance as a function of the WWR change. It relies on the climate-based metrics DA and UDI.

2. METHODOLOGY

The study went through several steps: (1) conduct site visits to several heritage museums to collect information and take measurement of the lighting environment; (2) categorise the existing artefacts based on their lighting sensitivity based on the limits on IESNA guidelines; (3) survey the architectural drawings and photographs of several heritage buildings to extract design information; (4) define parameters that help to prototype the 3D geometry of the heritage museums; (5) develop the 3D model; (6) carry out the simulation runs using Diva-For-Rhino computer simulation; (7) interpret the simulation output and discuss the results.

At the outset, site visits were conducted to several UAE heritage museums that included H.H. Sheikh Saeed House Traditional Museum (Dubai), The Heritage House (Dubai), Al Ahmadiya School (Dubai), Al Ain National Museum (Al Ain), Qasr Al-Hosn Fort (Abu Dhabi), and Sharjah Heritage Museum (Sharjah). This helped to experience the lighting environment in these buildings. The UAE heritage buildings consist of several rooms that are arranged around a central courtyard with a midway arcade between the courtyard and the rooms (see Figure 1 for the architectural drawing of H.H. Sheikh Saeed House Heritage Museum, Dubai). They are located in coastal areas with locations to capture the natural wind that usually comes from the Northwest orientation. This explains why the form of these buildings (usually rectangle in their shape) takes the Northwest/Southeast axis and results in walls orientated towards Northwest, Southeast, Northeast, and Southwest. The rooms of these buildings are used as exhibit spaces; which have double shutter windows called Dreesheh towards the courtyard and to the public alleys. The number of these windows depends on the size of the room. Most of the heritage museums operate from 8 am to 6 pm, which gives total operation hours of 3650 hr/year. Konica Minolta luminance meter (model LS-110) and Kodak Grey Card were used to conduct on-site measurements to find the reflectance of the interior and exterior surfaces. These values are listed in Table 2.

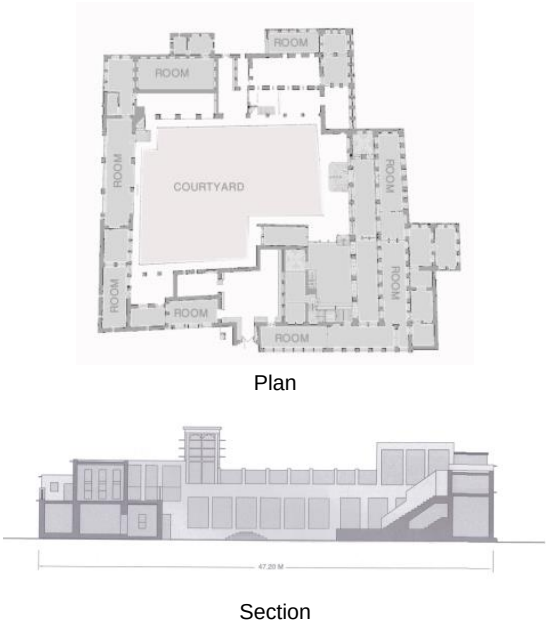

Figure 1: Architectural drawings showing the courtyard, the rooms, and the midway arcade of H.H. Sheikh Saeed House Heritage Museum, Dubai.

Table 2: On-site reflectance vales for different surfaces in UAE heritage museums

Material Name	Reflectance (%)
Sand	35.7
Carpet	19
Local paint (Sarooj)	86
Chandal Wood	29.8
Light grey floor tiles nonslip	41.8
Pavements	20%

During the site visits, the typical artefacts that were found in the UAE heritage museums and their method of display were recorded. The artefacts were classified into groups, as follows:

1. Invaluable documents and manuscripts such as letters, treaties, agreements, decrees and maps that have literally shaped the history of the country.
2. Old currency notes, stamps, and postal stationery.
3. Traditional clothing and textiles.

4. Human skeletons and bones from several excavations recovered from graves that date back to the third millennium B.C.
5. Female jewellery, some of which are prehistoric consisting mostly of bead necklaces agate, bronze, and soft stone.
6. Some of the earliest coinage, silver ornaments, and costume accessories.
7. Traditional weapons including rifles, and guns; in addition to bronze daggers and arrow heads that date back to the first, second, or third millennium B.C.
8. Ceramic and basalt pottery, some of which are prehistoric consisting mostly of vessels and plates
9. Old currency coins
10. Tombs made of stone
11. Utensils made of bronze and stone

Some of these artefacts are shown in Figure 2. These groups were classified to high sensitive, low sensitive, and no sensitive artefacts depending on light sensitivity of their material based on IESNA limits, as listed in Table 1.

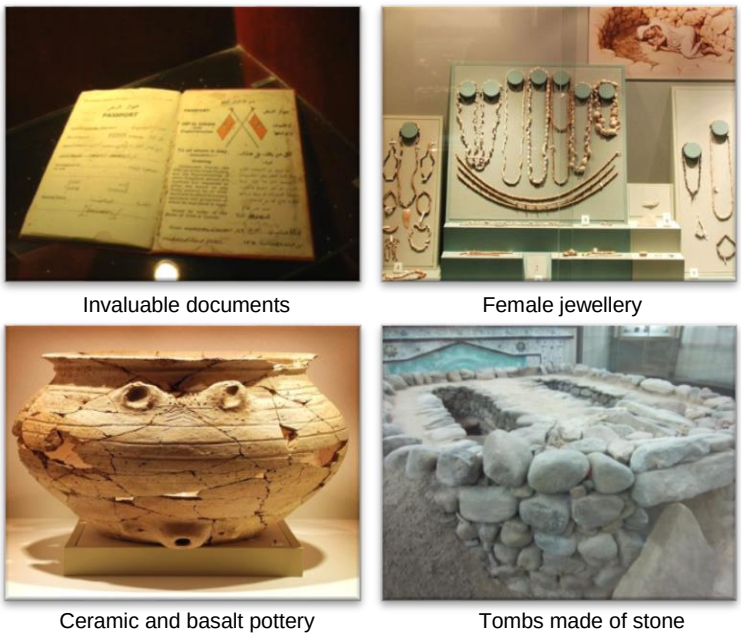

Figure 2: Typical artefacts in UAE heritage museums.

The architectural drawing of the heritage museums, which include the plans, sections, elevations, and details, were surveyed to analyse the spatial distribution of the spaces in these buildings and to extract the range of dimensions for the building elements like the display rooms, the courtyard, and the verandas. The extracted building information included measures such as length, width, depth, height, and thickness. Figure 3 illustrates a box chart that shows the ranges of the depth, length, and height of the display room. The average values were calculated and used to generate a 3D model for the geometry of the heritage museum; some of which are as follows:

(a) Courtyard geometry: rectangle 18 × 12 × 8 m.
(b) Display room: rectangle 8 × 3 × 4 m.
(c) Veranda width: 3 m.
(d) Number of windows: 3.

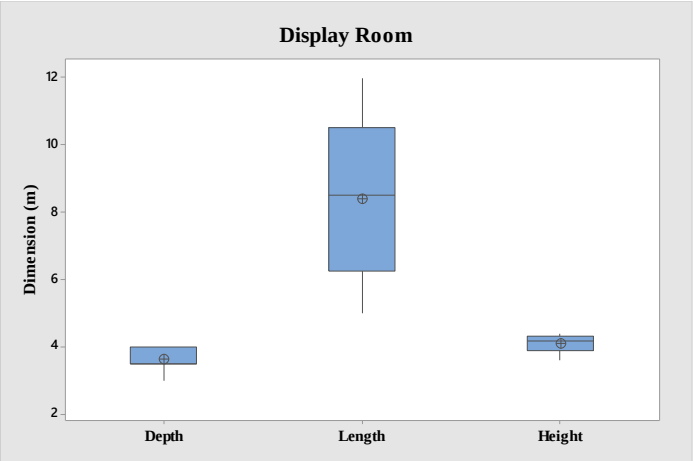

Figure 3: Box chart of the building information for the display rooms in the UAE heritage museums.

Diva-For-Rhino was used to develop the needed 3D geometrical models; which included three models for the three ranges of the tested Window-To-Wall ratios (WWRs). These WWR ranges are WWR = 5%, 9%, and 15%. The display room in these models has windows oriented towards the Southwest (SW) direction. A large number of sensors (20 × 8 sensors) were distributed horizontally in the display room to maximise accuracy of generated results. The location of the sensors was chosen at a height of 0.81m to simulate the actual location of the horizontally displayed artefacts.

The study utilised Diva-For-Rhino to perform the daylighting analysis IN the display room of each model. The analysis depended on climate-based daylight metrics; the Daylighting Autonomy (DA) and Useful Daylight Illuminance (UDI). The illuminance threshold was set in each simulation run according to the artefact's sensitivity to light based on the categories listed in Table 1. The entered thresholds were 50 Lux for the high sensitive, 200 Lux for the low sensitive, and 1000 Lux for the no sensitive materials according to the recommendations in the IESNA lighting handbook (IESNA, 2011).

3. RESULTS AND DISCUSSION

3.2. Daylighting Autonomy (DA)

The DA is calculated for each sensor as the percentage of the museum's operation hours in which the interior illuminance exceeds the defined threshold (IESNA, 2011). Figure 4 illustrates visually the DA in each module of the evaluation grid and throughout the room area for the simulated WWRs (5 %, 9 %, and 15 %) and the three sensitivity to light categories, using a colour scale. The grid with the red colour represents a very high percentage of time in which the illuminance levels exceeded the threshold Lux level (nearest to 100%) while the blue colour represents a very low percentage of time in which the illuminance levels exceeded the threshold Lux level (nearest to 0%). The spatial DA (sDA) gives the percentage of the room area in which the illuminance levels exceeded the Lux threshold for 50% of the time. It can be noticed from Figure 4 that the sDA for the high sensitive materials are very high (> 50%) while that for the no sensitive materials are very low (around 0%), regardless of the WWR. This is because the Lux threshold level for the high sensitive materials is very low (50 Lux) while it is high value for the no sensitive materials (1000 Lux). It is also noticeable that the sDA value increases gradually as the WWR increases for each category of artefacts.

The $DA_{(high\ sensitive)}$ simulations in Figure 4 illustrates that 66% of the display room will experience illuminance levels ≥ 50 Lux, for 50% of operation hours when WWR = 5% (34% only dalylight safety). As the WWR increases for the same materials (high sensitive), the percentage of the operation hours that will not be safe will increase to 90% and 100%, for WWR = 9% and 15% respectively; because (almost) the whole room will be exposed to illuminance levels greater than the safe 50 Lux threshold, for 50% of the operation hours. The $DA_{(low\ sensitive)}$ simulations reveals that 0% of the room area will experience illuminance levels ≥ 200 Lux, for 50% of the operation hours (100% is safe) when WWR = 5%. The percentage of the operation hours that will experience illuminance level ≥ 200 Lux, for 50% of the occupied hours when WWR = 9% was 30% (70% is safe), while when WWR = 15%, this percentage increased to 67% (33% only is safe) for the low sensitive category. This means that the percentage of the operating hours that will not be safe will increase as the WWR increases for this category also. The $DA_{(no\ sensitive)}$ simulations for the three ranges of WWR (5%, 9%, and 15%) results in 0% of the operating hours that will experience illuminance level ≥ 1000 Lux, for 50% of the operation hours in the room (100% safe). This directs a high level of safety with regards to the sun exposure for this category.

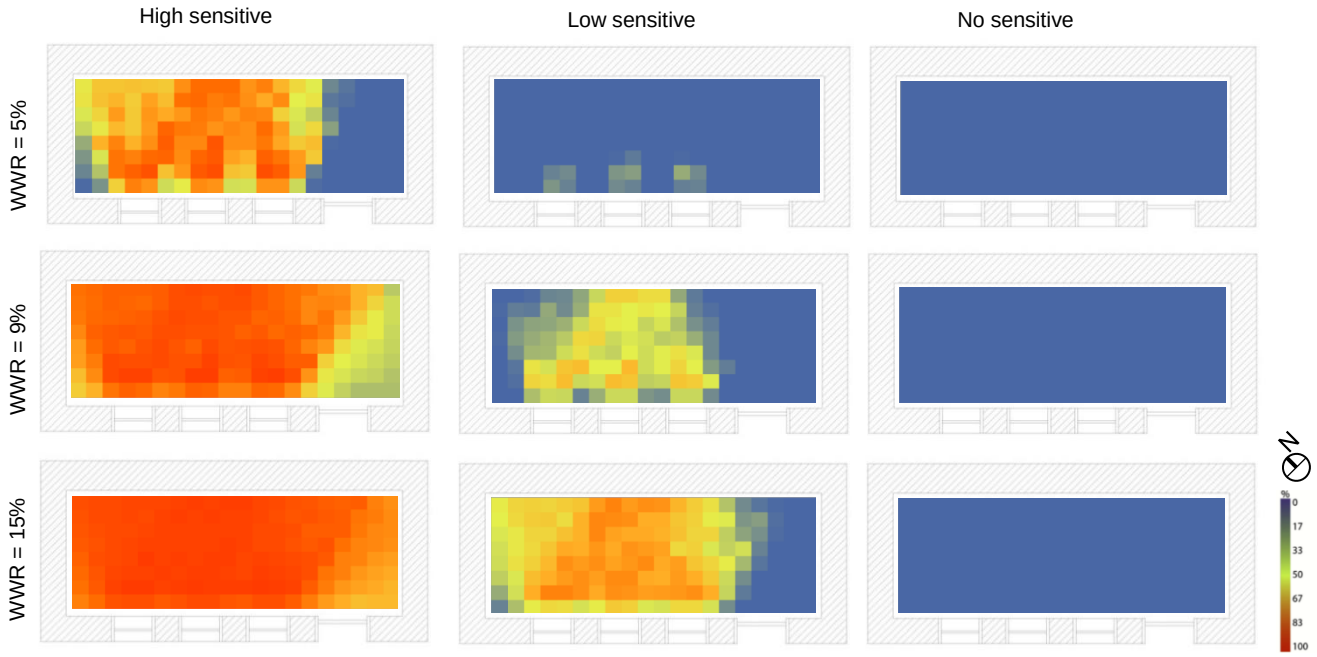

Figure 4: Daylighting Autonomy (DA) results for the exhibit space with WWR = 5%, 9%, and 15%.

3.2. Useful Daylighting Illuminance (UDI)

The Useful Daylight Illuminance (UDI) calculations show the percentage of time in which the daylight in a space is considered useful. The known approach in calculating UDI considers the values that are less than 100 Lux as "too little" light, the values that are between 100-2000 Lux as "useful daylight", and the values that are more than 2000 Lux as "too much" light (IESNA, 2011). This approach is useful in designing office buildings since tasks such as reading, writing and typing require high levels of illuminance. In museum buildings, however, where the conservation of the precious artefacts is the main goal, the values less than 100 Lux can are the safest since these values ensure high protection of the historical artefacts. Figure 5 illustrates visually the ranges of $UDI_{(<100\ Lux)}$, $UDI_{(100\text{-}2000\ Lux)}$, and $UDI_{(>2000\ Lux)}$ for the different WWRs using a colour scale. The grid with the red colour represents a very high percentage of time in which the illuminance levels exceeded the defined range of Lux level (nearest to 100%) while the blue colour represents a very low percentage of time in which the illuminance levels exceeded the defined range of Lux level (nearest to 0%). It shows that while the useful daylight area for museums that have illuminance levels < 100 Lux decrease as WWR increases, the percentage of the room that have illuminance levels between 100-2000 increases as WWR increases, for at least 50% of operation time. The $UDI_{(>2000\ Lux)}$ simulations revealed a zero value for all WWRs; which indicate a high level of safety in the room with regards to the sunlight exposure.

The percentage of the area of the room that receives illuminance levels < 100 Lux is 84% for WWR = 5%, 31% for WWR = 9%, and 14% for WWR = 15%, for at least 50% of the operation time. This indicates that as WWR increases, the useful daylight area in the room that receive illuminance levels < 100 Lux decrease. The high value of the useful daylight $UDI_{(<100\ Lux)}$ (84%) at WWR = 5% indicates that the room will be safe at this WWR, especially for the high sensitivity category. The same figure illustrates that the percentage of the room area that received illuminance levels between 100-2000 Lux is 16% for WWR = 5%, 69% for WWR = 9%, and 88% for WWR = 15%%, for at least 50% of the operation time. A low WWR percentage (WWR = 5%) is recommended to reduce the range of the not safe range of illuminance levels at $UDI_{(100\text{-}2000\ Lux)}$ in museums. Figure 5 also shows that the percentage of the room area that receives illuminance levels > 2000 Lux for at least 50% of the operation time is zero for WWR = 5%, 9%, and 15%. This zero value of the $UDI_{(>2000\ Lux)}$ shows a high level of sunlight exposure safety in the room regardless of the WWR value. These results indicate that low WWR at 5% is the safest to ensure useful daylight levels in museums for artefacts protection, especially for the high sensitive category.

The UDI results along with the DA results can assist museums' designers to locate the artefacts in the safest area of the room depending on the sensitivity of the material. The safest location should be allocated for the high sensitive category while the second safest should be allocated for the low sensitive category. The remaining part of the room can be allocated for the no sensitive category. The high sensitive artefacts could be isolated in separate rooms with small WWR and controlled shading if the entire room is not safe for this category. Adding external and/or internal shading in the display room, and considering shading provided by local trees are recommended to lower the overall illuminance levels in the display rooms.

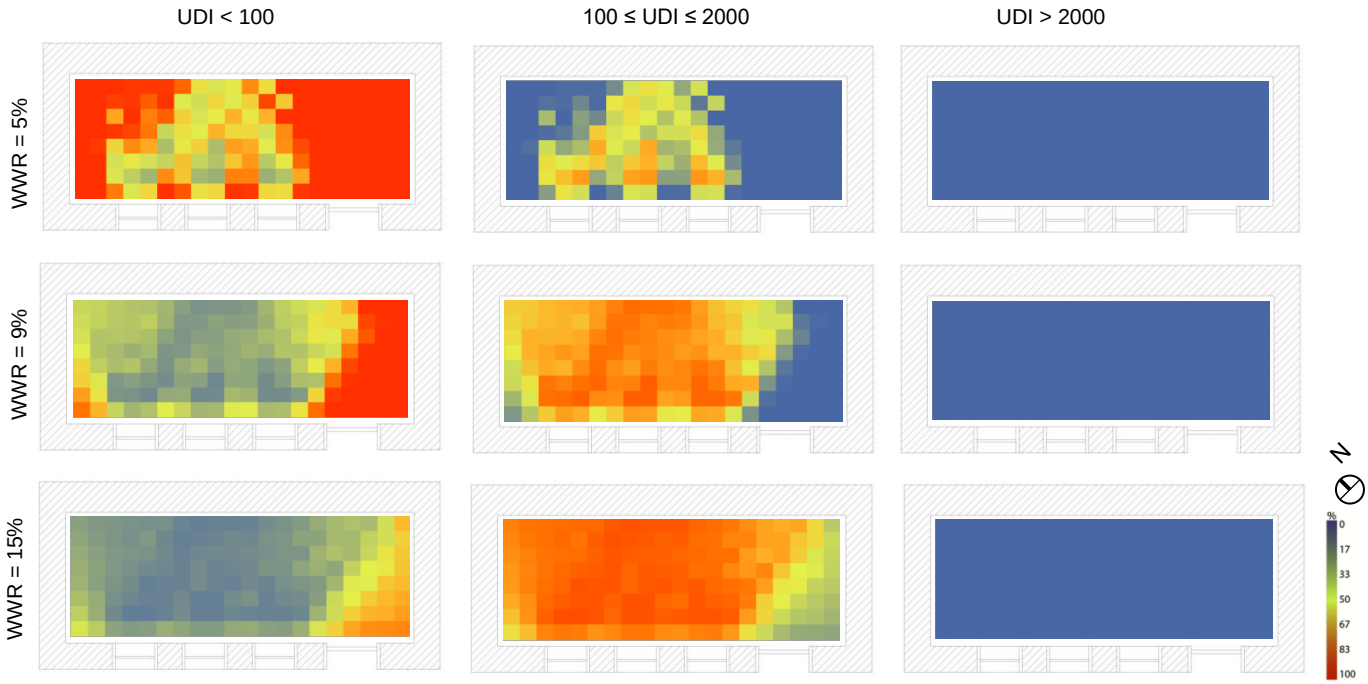

Figure 5: Useful Daylight Illuminance (UDI) results for the exhibit space with WWR = 5%, 9%, and 15%.

4. CONCLUSION

The on-site measurements helped to experience the heritage museums in its real surrounding. The classification of the artefacts assisted in associating the acceptable illuminance with the artefact category and thus helped in choosing the best location in the display room for each category. This study investigated the daylight performance as a function of WWR change for an averaged size display room with SW windows overlooking a central courtyard. The study found several issues after carrying a comprehensive daylighting analysis. Recommendations to minimise the danger of these issues were proposed for museums designers. The main issues that are pointed out in this study are as follows:

- Daylight Autonomy (DA) – Generally, the high sensitive and low sensitive categories perform better for lower WWRs, while the performance for the no sensitive category was very safe (100% is safe) and was not affected by the change in WWR. The high sensitive materials experience a high level of unsafe area for 50% of operation time even for the very low WWR of 5% (66% is not safe); which suggests the need for better shading methods for this category. The low sensitive category, on the other hand, is the safest with 100% safe area when WWR is very low are 5%. None of the WWR for the exhibited spaces recorded any illuminance results greater than 2000 Lux (0% spatial DA).
- Useful Daylight Illuminance (UDI) – The UDI results indicated that the room with low WWR (5%) was the safest compared to the rooms with higher WWRs for both the high sensitivity and low sensitivity categories ($UDI_{<100Lux}$ of 84% for WWR = 5%, versus $UDI_{<100Lux}$ of 31% for WWR = 9%, and $UDI_{<100Lux}$ of 14% for WWR = 15%). The zero value of the $UDI_{(>2000\ Lux)}$ for all WWRs shows a very safe level with regards to sunlight exposure.
- The results suggest high levels of illuminance in the exhibit space for all WWR. Some of the high sensitive materials need special considerations to prevent their damage over time. Using shading elements, both exterior and interior could reduce the illuminance levels inside the display space. Another approach to reducing the overall illuminance in the exhibited space is to use natural shading by trees.

5. ACKNOWLEDGEMENT

This research is funded by UAE University under UAEU Program for Advanced Research (UPAR), Grant # G00001939-UPAR (9) 2015.

6. REFERENCES

Al-Sallal, K. A. 2016. Low Energy Low Carbon Architecture: Recent Advances & Future Directions, CRC Press.

Al-Sallal, K. A., & Abouelhamd, A. R., & Bin-Dalmouk, M. M. (2018). Daylighting performance in UAE traditional buildings used as museums. *International Journal of Low-Carbon Technologies*, *13*(2), 116-121. https://doi.org/10.1093/ijlct/cty003.

Al-Sallal, K. A. & Bin-Dalmouk, M. M. B. 2011. Indigenous buildings' use as museums: Evaluation of day-lit spaces with the Dreesheh double panel window. *Sustainable Cities and Society,* 1**,** 116-124.

Domenech-Carbo, M. T., Silva, M. F., Aura-Castro, E., Fuster-Lopez, L., Kroner, S., Martinez-Bazan, M. L., Mas-Barbera, X., Mecklenburg, M. F., Osete-Cortina, L. & Domenech, A. 2011. Study of behaviour on simulated daylight ageing of artists acrylic and poly (vinyl acetate) paint films. *Analytical and bioanalytical chemistry,* 399(9)**,** 2921-2937.

IESNA .2011. The lighting handbook (10th ed.). DiLaura, D. L., Houser, K. W., Mistrick, R. G., & Steffy, G. R. (eds.). New York: Illuminating Engineering Society of North America.

IESNA. 1999. Lighting handbook. (9th ed.). Rea, M. (ed). New York, USA: Illuminating Engineering Society of North America

Engineer, A. 2015. Museums additions and their impact on occupant experiment. Doctor of Philosophy in Architecture, University of Illinois, Champaign, IL, USA, www.ideals.illinois.edu.

Hefferan, S. 2008. Working with daylight in the museum environment. WAAC newsletter*,* 30(1)**,** 22-24.

Lee, S., Bogaard, J. & Feller, R. 2013. Darkening of paper following exposure to visible and near-ultraviolet radiation. *Journal of the American Institute for Conservation*.

Li, D. H., Lam, J. & Wong, S. 2005. Daylighting and its effects on peak load determination. *Energy,* 30(10)**,** 1817-1831.

Lithgow, K., Lloyd, H., Parry, J., Staniforth, S. & Seeley, N. 2006. The National Trust Manual of Housekeeping: The Care of Collections in Historic Houses Open to the Public. Oxford: Butterworth-Heinemann an imprint of Elsevier.

Miller, J. V. & Miller, R. E. 2005. Museum Lighting Pure and Simple (p. 8). Seaford, DE, US: NoUVIR Research Inistitute. Retrieved from http://www.nouvir.com/pdfs/MuseumLighting.pdf.

Mueller, H. F. 2013. Energy efficient museum buildings. *Renewable energy,* 49**,** 232-236.

Pinilla, S. M., Vazquez, D., Fernandez-Balbuena, A. A., Muro, C. & Munoz, J. 2016. Spectral damage model for lighted museum paintings: Oil, acrylic and gouache. *Journal of Cultural Heritage*.

113: Sugar cane bagasse flow control using bifurcated chute

Chiemela ONUNKA[1], Andrew ELOKA-EBOKA[2]

[1] *Department of Mechanical Engineering, Mangosuthu University of Technology, Umlazi, Durban, South Africa, connadoz@gmail.com*
[2] *Discipline of Mechanical Engineering, University of KwaZulu-Natal, Durban, South Africa, fatherfounder@yahoo.com*

In existing ethanol factories across Southern Africa, the optimisation of bagasse flow is of critical importance to optimum performance of ethanol factories. One of the key strategies in optimisation is the addition of a re-circulation system to the current bagasse conveying system, which feeds a 120 ton/hr steam generating boiler. The focus of this paper is to propose the use of a mechanical diverting chute, which will integrate into the upgraded bagasse conveying system. The chute will enable automated variable flow control of bagasse, through the existing Distributed Control System (DCS), between the re-circulation conveyors and discharge to ground for stock piling. The variation in flow will be controlled by monitoring the feed rate of sugar cane, measured by a belt scale, to the crushing mills. The purpose of this upgraded system is to reduce the required operating hours of a front-end loader, which currently performs the re-circulating function, but also allows surplus bagasse to be stock piled for future use in the factory outside of the crushing season.

Keywords: Bagasse, Sugar cane, Ethanol, Chute control

1. INTRODUCTION

The current conveyor system, which handles the fibrous material discharged from the last cane crushing mill (commonly known as bagasse), is made up of a series of belt conveyors (BC1 & BC2), which discharge to a chain slat conveyor (BC3), and in turn feeds a 120 t/h steam boiler unit. The excess bagasse that passes over the boiler feed chutes is discharged to the ground to prevent fouling up to the end of BC3. The excess bagasse is then stock piled using front-end loaders (FELs). The excess bagasse is also reclaimed, using the same FELs, onto a chain slat conveyor and belt conveyor (RC1 & RC2). As part of a factory optimisation project, for an ethanol plant of this nature, an upgrade was required in the current bagasse handling system. It was proposed to re-circulate bagasse, as opposed to the current once through and discharge to ground operation. The conveyor system upgrade requires that excess bagasse be re-circulated, as well as discharged to ground. It is kept in mind that the purpose of the upgrade is to reduce the operating hours of reclaiming by FELs. The discharge flow rate must be regulated to keep as much bagasse re-circulating without overburdening the existing conveyors. The purpose of the reclaim system is to provide a regular flow of bagasse back to the boiler and to mitigate risk of starving the boiler. However, the long term operating costs for the FELs has made the reclaiming operation too expensive to maintain. The upgraded bagasse system will reduce operation time of the FELs reclaiming bagasse and still fulfils the required feed rate to the boiler. A portion of the re-circulating bagasse must be discharged to ground to avoid overburdening the conveyors. This requires that the discharge flow rate be variable and dependent on the bagasse feed from the mills. As the load from the mill increases, more bagasse must be discharged to ground and no reclaim from the stockpile. Conversely a decrease in mill load with result in more bagasse being re-claimed from the stock pile and increased re-circulation flow rate. In Figure 1, the diverter chute is indicated between conveyors RC2 (existing belt) and RC3 (new belt). Legend describes bagasse flow, existing and new units respectively.

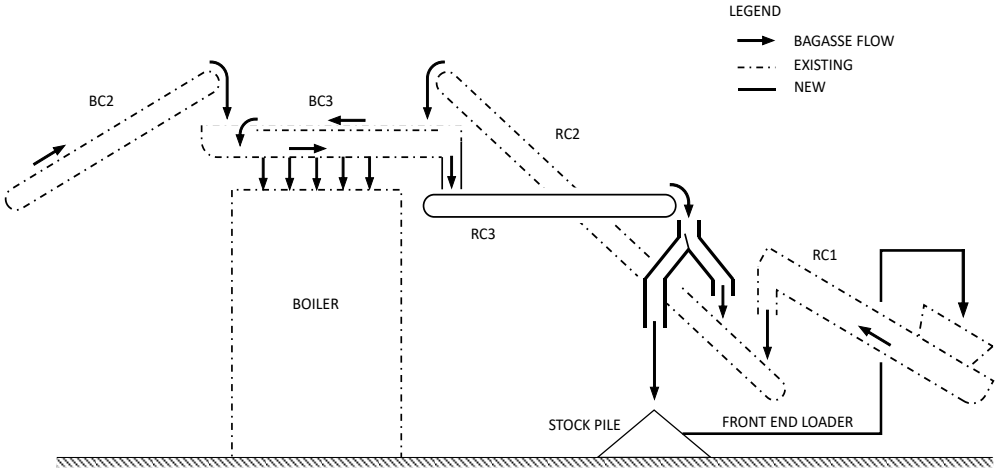

Figure 1: Modified bagasse flow diagram (SiVEST SA Pty Ltd 2015)

A new design was developed to minimise the use of FELs to reclaim excess bagasse from BC3 overflow. The design was to provide a by-pass stream to discharge re-circulating bagasse to ground for stock piling. The design has an automated variable flow linked to the DCS. The new design is modular, cost effective, easy to install-designed and requires simple construction that can be carried out with a standard fitted workshop. The motivation behind this project is to minimise the operating hours of FEL's reclaiming bagasse from the stock pile, but still provide a regular feed rate of bagasse to the boiler. This project will reduce the operating cost of the plant. This paper is therefore focused on the design of a mechanical device, which is operated through the existing control infrastructure, and will regulate the quantity of excess bagasse returning to the boiler. The control system will adjust the chute and divert the flow of bagasse, based on crush rate and boiler feed chute level readings given by the plant distributed control system (DCS).

1.1. Physical properties of bagasse

Bagasse is the fibrous and pith material which remains after sugar juice has been extracted from a sugar cane stalk (Encyclopædia Britannica 2013). Typically the name bagasse is given to the fibre and pith that passes out the last of a series of crushing mills. Bagasse is burned as fuel in a steam-generating boiler. They can also be briquetted to produce biomass fuels. The high temperature and pressure steam is used to drive a turbine alternator to generate electrical power, which is enough to energise the entire sugar factory and have export capacity to supply external users (Austin A, 2011). The exhaust steam from the turbine is used to drive the production process of sugar. If not handled correctly, bagasse has the tendency to choke at transfer points, particularly if chutes converge or if there are surfaces on which bagasse can build up and bridge (Rein P, 2007). The bulk density of bagasse does vary considerably depending on the conditions, however the value indicated below is a good average for this application from few researchers. Bulk Density is 130kg/m3 (Belt Conveyor) (Hugot E, 1986); Bagasse Moisture 50g Water

/100g Bagasse (Rein P, 2007); 275kg Bagasse per Ton of Cane (Hugot E, 1986); Angle of Repose 45-50° (Hugot E, 1986); and Surcharge Angle 30° (Rein P, 2007).

1.2. Bagasse handling devices

Bagasse handling starts from the final crushing mill in a milling tandem, and in South Africa, this is typically done using series of belt conveyors. The conveyors transfer the bagasse to a slat conveyor, which feeds a single boiler or multiple boilers (Chen J and Chung CC, 1993). The excess bagasse is then transferred into a bagasse store, where a continuous reclaiming scrapper loads a belt conveyor that goes back to the boiler. This arrangement is a typical type installation in South African sugar mills. Diverter chutes, also known as bifurcated chutes, are typically placed in complex bagasse handling systems to enable optional change of bagasse flow. Diverter chutes tend to be manually operated and will transfer flow of bagasse from one stream to another based on desired operating scenarios. Another diverting method, which stems from the application to boiler bagasse feed chutes, is to use ploughs on a belt conveyor. Typically boilers are feed using chain-slat conveyors with slots in the deck, however, due to the higher cost of chain-slat conveyors, increases in cane throughput and changes in technology that yield finer bagasse outputs, the use of belt conveyors and ploughs to feed the boilers have since become feasible [8]. This application requires that the plough zone on the belt conveyor be contained within a flat based trough, which means that inclined idlers are removed at plough locations and replaced with a flat plate. A plough design concept was introduced in 1985, by the Felixton II design team lead by R. Renton (Moor BS, 2000). Figure 2 depicts a schematic diagram to showcase its working principles.

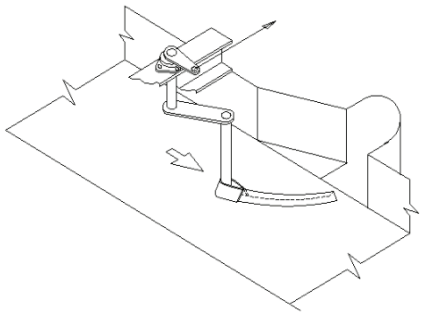

Figure 2: The 'Renton' Plough Design (Moor, 2000)

A flap type pneumatic cylinder can be used to perform the diverting function. This is Bulkmatic diverter chutes. The Diverter Chutes - Flap Type Pneumatic Cylinder Operated shows a three-way diverting chute with two linear actuators that can move diverting plates to direct material flow through one of three discharge ports (Bulkmatic, 2014). Figure 3 gives a pictorial image.

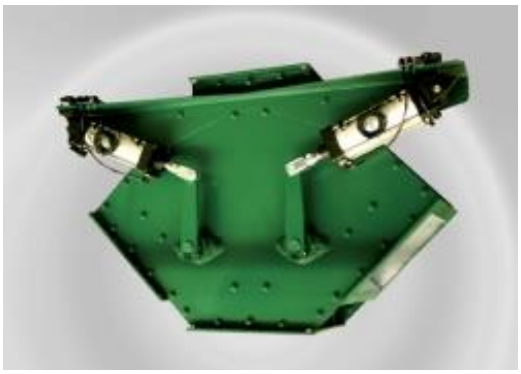

Figure 3: Bulkmatic Diverter Chutes - Flap Type Pneumatic Cylinder Operated (Bulkmati, 2014)

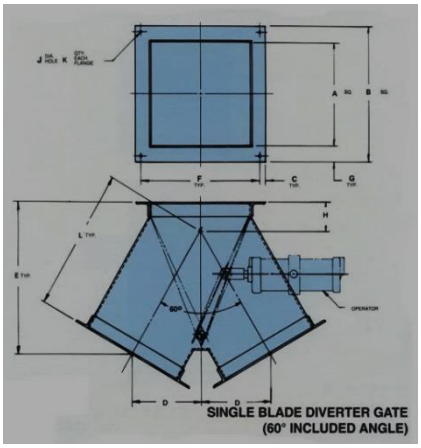

Figure 4: Single Blade Diverter Gate 60° Included Angle (PEBCO, 2013)

A standard diverter chute designs with many varieties and configurations is also used in bagasse handling. The "Single Blade Diverter Gate 60° Included Angle" (PEBCO, 2013) provides the necessary options and configuration as in Figure 4. In consideration of diverting ploughs, an all in one solution can be offered by VHV Anlagenbau GmbH, in the form of a scraper plough (VHV Anlagenbau GmbH, 2015) as shown in Figure 5. The unit is an integrated plough and frame arrangement, which would either require the purchase of a VHV conveyor system, or for the unit to be retrofitted to an existing belt conveyor. This required modification to the conveyor is an unnecessary expense and will therefore not be considered as a feasible solution mainly due to the cost.

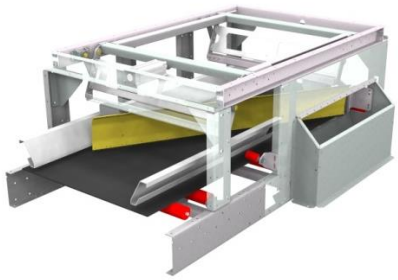

Figure 5: VHV Scrapper Plough (VHV Anlagenbau GmbH)

When considering the options available to handle bagasse, the choices are limited due to the high risk of bagasse choking at transfers. The least risky option is by diverting the bagasse inside the transfer chute. This is also the cheaper option when considering the material cost involved.

2. CONCEPT DEVELOPMENT

The following concepts that have been generated are configurations of the chute and diverter, as this will define the core function of the final product. The actuation and control devices were selected based on the best concept. Due to the fibrous and pit consistency of bagasse, slide gates as diverting methods will not be considered. When developing the concepts, there are a few constraints that must be incorporated:

- Chute Throat Dimensions 1225 x 1090 mm
- As a minimum chute angle not less than 60°
- With minimal throat constriction to reduce chocking risk.
- To minimise capital cost.

2.1. Functional decomposition

The device's core functions have been defined in the following categories:

- Receive Bagasse from RC3 Belt Conveyor
- Divide Bagasse
- Regulate Bagasse Split Flow
- Actuation
- Actuator Positioning
- Position Feedback to DCS
- Operator Input to DCS for Discharge Flow Rate

2.2. Concept one

The first concept shows a trouser leg construction which includes a diverting plate along the inlet centreline, which is hinged near the bottom inverted "V". The plate will swing from one side to the other allowing the bagasse to be diverted onto two separate streams. With reference to the drawing, it can be see that the chute inlet throat dimensions have been carried forward to the outlets. The diverting plate also adheres to the minimum chute angle in all positions. By hinging the diverting plate near the inverted "V", it makes the plate longer and will require more power to move as a result as indicated in Figure 6.

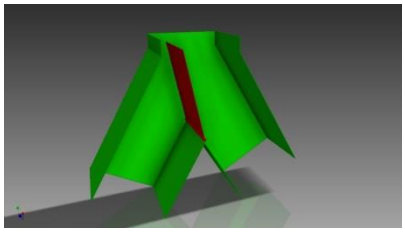

Figure 6: Chute Concept 1

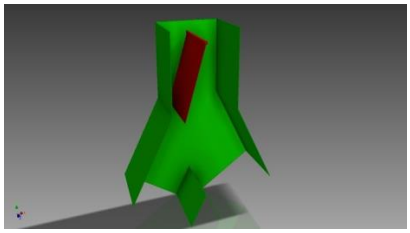

Figure 7: Chute Concept 2

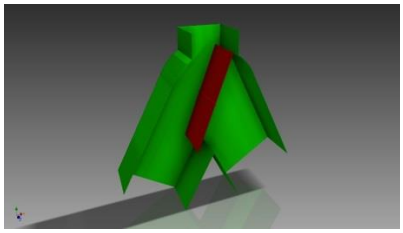

Figure 8: Chute Concept 3

2.3. Concept two

The second concept retains the same dimensional shape as concept 1, except that the inlet has been made longer to accommodate a different diverting plate arrangement. The diverting plate has been made shorter to achieve the

same chute angle, however with this configuration, only half the flow of bagasse would be diverted if the plate were fully closed on one side. Furthermore the risk of choking is far greater with this configuration (See Figure 7).

2.4. Concept three

The third and final concept is a much larger design as a result of hinging the diverter plate in the centre. To adhere to the minimum chute angle, the plate length is double that of concept 2, and if the throat dimensions are honoured, the outlets are required to be much larger. The main disadvantage to this design is that it has much larger geometry and as a result will be more expensive to fabricate. Figure 8 gives showcases these features.

2.5. Concept ranking and selection

The concepts have been evaluated based on the criteria indicated in Table 1. The criteria chosen for evaluation are key requirements for the functional operation, as well as requirements expressed by plant requirement and operational needs.

Table 1: Concept Ranking and Selection Chart

			Concepts		
Selection Criteria	Baseline	Weight	1	2	3
Inlet and Outlet Dimensions	0	5	+1	+1	-1
Size of Diverting Plate	0	2	-1	+1	-1
Overall Size of Chute	0	3	0	-1	-1
Power required to Rotate Plate	0	3	-1	+1	+1
Chute minimum Angle	0	5	+1	+1	+1
Cost to Manufacture	0	4	0	-1	-1
Chocking Potential	0	5	0	-1	-1
Total Plus			2	4	2
Total Minus			2	3	5
Overall Weighted Score			5	3	-11

2.6. Concept evaluation

Based on weighted score as shown in 1, Concept 1 was developed further. This concept has been selected mainly on the reduced risk of chocking, which means a much longer continuous operating cycle without the need for operator maintenance and cleaning is required. The cost to manufacture will also be much less than the other two concepts based on the required dimensions. As a negative, the diverting plate is larger which means more material and a larger power requirement to actuate the plate motion and resist bagasse impact at a larger distance from the fulcrum will be of essence. Each of the concepts generated have potential capacity, however for this application the options are severely limited due to the fibrous consistency of bagasse and its propensity to bridge and choke in chutes. Any convergence of the chute or even protruding objects, such as bolts or welds, in the flow path of bagasse increases the risk of bridging and choking which is not operationally cost-effective.

3. DESIGN APPROACH

The following is the layout of the process and approach for the final detailed design of the concept selected bifurcated chute for the modification of the ethanol plant. A bagasse trajectory and resulting velocity is a factor to use in determining the impact force of the falling material on the diverting plate. The holding torque and subsequent force required to drive the plate about its pivot was established. The shaft size was also determined based on the maximum system load, and fatigue allowance to be factored. Since the design will make use of a linear actuator, a linkage mechanism was employed. The linkages and anchor points were evaluated using Finite Element Analysis (FEA) to determine a suitable design. As for the automation of the chute, a control philosophy is described and a simple process flow chart will show how the system will be eventually controlled.

3.1. Bagasse transfer chute trajectory

The design of the chute begins with determining the bagasse flow path as it leaves the belt conveyor and travels down through the chute. Knowing the flow path of the material indicates the impact zone. The C.E.M.A. Handbook – Belt Conveyors for Bulk Materials was used to calculate the bagasse trajectory (CEMA, 2002). The units given in the C.E.M.A. Handbook are imperial, however they may be converted to metric values and remain accurate (CEMA, 2002).

3.2. Centre of mass, tangential velocity & initial tangent angle

Figure 9 indicates the terms used to express the equation for the cross-sectional center of mass on the belt, tangential velocity and the initial tangent angle at the moment the mass leaves the belt. The tangential velocity (V_s), m/s, of the cross-sectional centre of gravity of load shape must be calculated in order to plot the trajectory. The tangent angle gives a starting point for the plot.

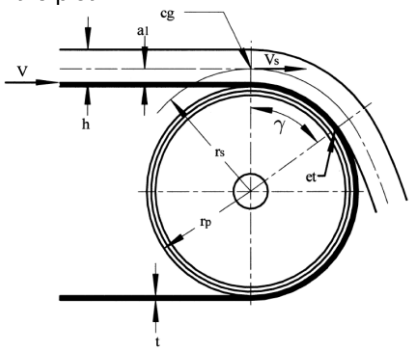

Figure 9: Diagram indicating terms used to plot the material trajectory at the transfer end.

The belt velocity of 1.5 m/s (V_b) may not be used as the tangent velocity; therefore the angular velocity (ω_p) of the pulley is required for the calculation.

$$\omega_p = \frac{60V_b}{2\pi r_p}; \qquad \omega_p = \frac{60\times1.5}{2\pi\times238\times10^{-3}}; \qquad \omega_p = 60.2\ rpm$$

The center of mass can be determined from Table 12-2 in the C.E.M.A. Handbook. For a belt conveyor of width 36" (900 mm) a 35° troughing angle and 30° surcharge angle the follows values are used:

$$h = 180.34\ mm; \qquad a_1 = 73.66\ mm$$

The distance from the center of pulley to the center of mass is:

$$r_s = r_p + t + a_1 = 238 + 12 + 73.66$$

$$r_s = 323.66\ mm$$

The tangential velocity is expressed as:

$$V_s = \frac{2\pi r_s \omega_p}{60}; \qquad V_s = \frac{2\pi\times323.66\times10^{-3}\times60.2}{60}; \qquad V_s = 2.04\ m/s$$

And the tangent angle is given by:

$$\cos\gamma = \frac{{V_s}^2}{gr_s} = \frac{2.04^2}{9.81\times323.66\times10^{-3}} = 1.31$$

However where, $\frac{{V_s}^2}{gr_s} \geq 1$, $\gamma = 0$, therefore, the material will start its trajectory from the top of the belt pulley.

In order to plot the trajectory relative to distance, a suitable time interval must be used. The C.E.M.A. handbook uses 1/20th second intervals. For a constant tangential velocity of 2.04 m/s and time intervals of 1/20th seconds, the linear horizontal distance intervals are 102 mm. The linear vertical distance of the material falls at the same given time intervals. The graph in Figure 10 gives the trajectory plot of the material at the transfer chute.

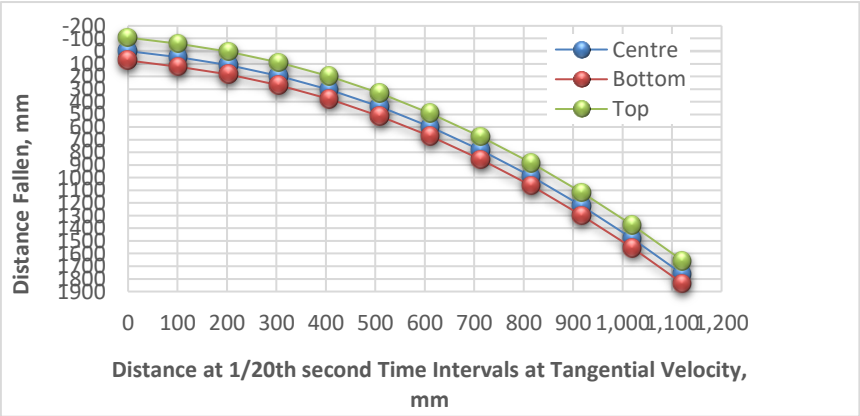

Figure 10: Trajectory plot for 900 mm wide belt operating at 1.5 m/s.

3.3. Diverting plate holding torque

From the data, the time it takes for the material to fall free and impact the chute can be determined and as a result the impact velocity which may be calculated. Assuming negligible deceleration in the horizontal plane and the gravitational acceleration acting in the vertical the following equations may be used to calculate the horizontal and vertical components of the final impact velocity.

$$a_x = 0\,m/s^2$$

$a_y = g = 9.81\,m/s^2$

$$V_x = a_x t + V_s cos\gamma = 0 + 2.04 cos0 = 2.04\,m/s$$
$$V_y = gt + V_s sin\gamma = 9.81 \times 0.5 + 2.04 sin0 = 4.91\,m/s$$

From, $r = \sqrt{(a^2 + b^2)}$

$$V = \sqrt{\left({V_x}^2 + {V_y}^2\right)} = \sqrt{(2.04^2 + 4.91^2)} = 5.31\,m/s$$

By calculating the impact velocity, the impact force of the material on the diverting plate can be calculated using conservation of momentum. To be conservative in the calculation, it is assumed that all momentum is transferred to the plate on impact, which means the final velocity will be zero.

$$F_i = \dot{M}\Delta V = 22.2 \times (5.31 - 0) = 117.9\,N$$

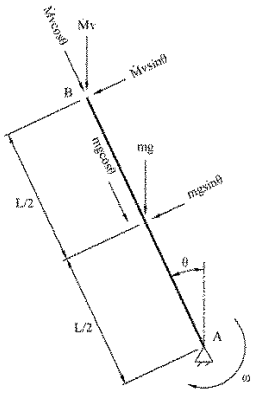

Figure 11: Diverting Plate F.B.D.

When considering the free body diagram in Figure 11, it can be noted that the falling bagasse is impacting at the tip of the plate, this allows a much more conservative estimate on the reaction torque required. The mass of the plate contributes to a significantly higher reaction force due to the overall length. From the 3D model the total weight of the diverting plate assembly is 200 kg. Because of the shape of the plate assembly, the center of mass is closer to the pivot; however the initial calculation will be done using the plate middle point as the center of mass.

$$T_B = F_i L \sin\theta + \frac{mgL\sin\theta}{2}$$
$$T_B = 117.9 \times 1.49 \sin 25 + \frac{200 \times 9.81 \times 1.49 \sin 25}{2}$$
$$T_B = 692\,Nm$$

Due to the shock load of the system, a shock factor of safety is included to ensure smooth actuation at all times, and to ensure a constant operating speed for the actuator.

Therefore the maximum torque required at the shaft is,

$$T = T_B S_f = 692 \times 1.5 = 1038\,Nm$$

In reference to Table 2 for results of concentrations stress over various planes along the shaft body from the results, it can be seen that the chosen geometry for the shaft is adequate for use.

Table 2: Stress along Planes of Shaft Body

Description	Value	Value	Value	Value	Value	Value	Unit
Plane	**A**	**B**	**C**	**O**	**E**	**F**	
Distance	0	109	155	740.98	1245	1315	mm
D	60	60				40	mm
B			80	80	80		mm
H			80	80	80		mm
J	1.27E+06	1.27E+06	6.83E+06	6.83E+06	6.83E+06	2.51E+05	mm^4
I	6.36E+05	6.36E+05	3.41E+06	3.41E+06	3.41E+06	1.26E+05	mm^4
Z	2.12E+04	2.12E+04	8.53E+04	8.53E+04	8.53E+04	6.28E+03	mm^3
A	2.83E+03	2.83E+03	6.40E+03	6.40E+03	6.40E+03	1.26E+03	mm^2
E	205000	205000	205000	205000	205000	205000	MPa
BM	0	44900	44900	308300	40400	0	Nmm
V	0	976.8	976.8	-985.2	-985.2	0	N
T	1038000	1038000	1038000	1038000	0	0	Nmm
Σ	0.00	2.12	0.53	3.61	0.47	0.00	MPa
τ_t	24.47	24.47	6.08	6.08	0.00	0.00	MPa
τ_v	0.00	0.35	0.15	-0.15	-0.15	0.00	MPa
$\tau=\tau_t$ & τ_v	24.47	24.48	6.08	6.08	0.15	0.00	MPa
σ & τ	24.47	25.56	6.35	8.15	0.52	0.00	MPa
K_t	1.8	1.6	1.6	1	1	1.8	
Conc Stress	44.05	40.89	10.16	8.15	0.52	0.00	MPa

3.4. Actuator design

Actuator mechanism

Pneumatic linear and rotary actuators were considered, however this would require installation of compressed air pipework, which would tie into the existing reticulation. This may place a higher demand on the air supply system than it is capable of and would need a redesign of the compressed air plant. A hydraulic system was not the best choice either, since the forces required are not huge. Besides the load issue, electrical power would still be needed to pump the hydraulics, adding more unnecessary costs. Finally, electric actuators offer a fairly large range of loads. The actuator to be used to is an electric linear ball and screw type actuator. Using the catalogs available for SKF, the best suited actuator is a SKG 6005. This actuator offers a top end push load of 6500 N at a speed of 55 mm/s at full load. Considering Figure 12 below, if the stroke is chosen to be 400 mm and the total extended length of the actuator is 1206 mm then the length of the lever AB and position of the anchor point C can be calculated.

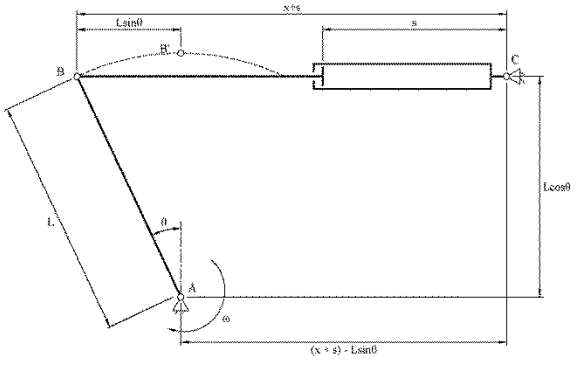

Figure 12 – Actuator Mechanism Diagram

The following equations are determined from Figure 12.

For Lever,

$$L = \frac{s}{2\sin\theta}, \quad where\ s = 400\ mm$$

$$\therefore L = \frac{400}{2\sin 25} = 473.24\ mm$$

For Point C,

$$C_x = (x + s) - L\sin\theta = 1206 - 473.24\sin 25 = 1006\ mm$$
$$C_y = L\cos\theta = 473.24\cos 25 = 428.9\ mm$$

Actuator lever

The actuator mechanism dimensions have been determined, as well as the reactions forces that will occur during operation. The actuator lever must be designed to withstand the applied forces and allow for a safety factor for an overload condition. The length of the lever will be 473 mm as determined above. Using a finite element analysis package, the lever geometry can be determined. To start, a test was done on a general design and a plate thickness of 20 mm; this made it easier to make a clevis at the top of the lever to accept the actuator rod eye. This test indicated a minimum Von Mises Stress (based on steel Yield Stress 350 MPa) safety factory of 15, which is well oversized. The second test was done on a refined design, yet still simple to construct. The plate thickness could be decreased to 12 mm. The simulation returned a result of minimum safety factor of 9; however the maximum deflection at the actuator rod eye was 0.44 mm. For a more optimised view of the results a few more FEA were run with various values for the plate and clevis thickness, these are tabulated in Table 3 below. The results indicate that a 6 mm plate could comfortably be used; however the displacement of the lever end at the clevis start to approach 1 mm and this may affect the actuator rod especially when the actuator is at full extension. The plate thickness 10 mm will be sufficient for the job and this plate size is commonly used for such applications.

Table 3: FEA Results – actuator lever

	Plate Dimensions (mm)			
Design Criteria	**6**	**8**	**10**	**12**
Max. Von Mises Stress (MPa)	77.07	57.68	**46.11**	38.44
Min. Safety Factor	4.54	6.07	**7.59**	9.1
Max. Displacement (mm)	0.87	0.65	**0.53**	0.44

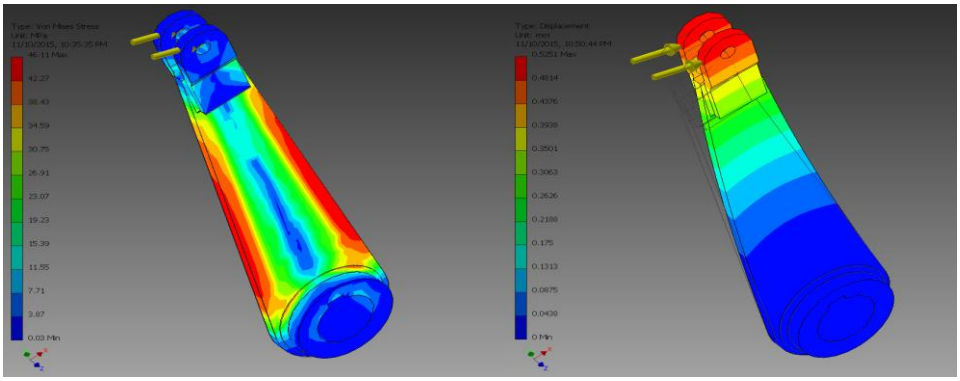

Figure 13:Actuator Lever Von Mises Stress (Left) and Displacement (Right)

Actuator bBase

The actuator base provides an anchor point for the actuator to apply its force into the lever. As such, the base has been through an iterative FEA optimisation process. The benchmark test was completed on a plate thickness of 10 mm, since this was the optimum thickness used for the lever. Further optimisation tests were completed using varying material thickness. The result of the FEA are tabulating in Table 4 below. When examining the results even the 5mm plate could withstand the force, however the decision to use 10 mm plate instead was based on the requirement for the design to be robust.

Table 4: FEA Results – actuator base

Design Criteria	Plate Dimensions (mm)			
	5	6	8	10
Max. Von Mises Stress (MPa)	54.27	45.61	34.45	27.7
Min. Safety Factor	6.45	7.67	10.16	12.64
Max. Displacement (mm)	0.0555	0.0455	0.0330	0.0255

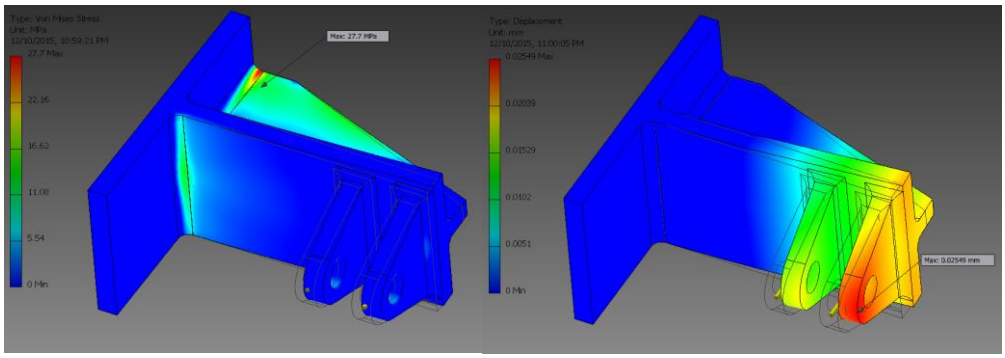

Figure 14: Actuator base Von Mises stress (Left) and displacement (Right)

3.5. Control philosophy

The bifurcated chute will have a modulating control. Using the linear actuator to position the plate in various positions based on the flow of bagasse from along RC3. The use of measurement instruments, like a belt scale or IR sensors to measure the bed height on the belt would give accurate reading, but these instruments are costly and the degree of accuracy for the measurement does not need to be precise. An alternative method, and the one chosen for this project, would be to use RC3 conveyor motor current feedback to the DCS as a way to determine a load change, and hence estimate an approximate mass flow rate. This approximate flow rate could provide the input to the program that controls the position of the linear actuator. The actuator would be fitted with a 1kΩ potentiometer to provide a feedback loop to the DCS as to the position of the actuator along its 400 mm stoke path. To describe the actuator positions, some terms are to be clarified. When the actuator is retracted, the chute is said to be closed, this means all bagasse will fall to ground. When the actuator is fully extended the chute is open and all bagasse will recirculate. The optimum operating condition is for the chute to be 75% open. This will allow 25% of the mass flow to drop to ground and 75% to recirculate. Due to the length of the conveyor system, the affect to a change in position will have an extended lag period. It may take about 120 seconds for material to make a round trip. The calibration of the system will determine the latency response times.

The procedure for the initial calibration of the system should be as follows:

Close all overflows and fully load the conveyor system allowing the bagasse to recirculate with minimal loses. Take note of motor current at maximum load.

Use the DCS to position the diverter to 75% open, allowing some bagasse to fall to ground. Continue this until the motor current is half of the peak value and record the time.

By performing the previous steps the operating current range has been established and the time it takes to drop half the mass flow rate over a recorded period of time at 75% open.

Set the chute position to 50% open and the target current to be 75% of the peak value. Start the Mills and Boiler.

Ensure that as the motor current increases, the chute closes and vice versa.

Some overrides are required to be setup as well. In the event of any of the boiler feed chute level's alarming on the DCS; the actuator is to immediately open. When the alarm has been cleared, the chute is to return to the previous set point. The actuator is to be programmed with an overload, and this must not exceed 3000 N of thrust.

4. CONCLUSION

The goal of this project was to design a mechanism that will divert sugar cane bagasse from one stream to two alternate streams and do this while being automated by the DCS. Overall, that goal has been achieved, however there is a large component that needs refining and that is the control of the unit itself. This can only be done during operation once this unit has been installed and commissioned in the plant. Perhaps further optimisation work could be done on the chute parts in order to shave off material cost, but this may be marginal and at the cost of a robust low maintenance design for energy conservation and waste conversion to energy.

5. REFERENCES

SiVEST SA Pty (Ltd), *Zimbabwe Ethanol Plant, Boiler & Bagasse Pile Aerial Photograph,* Chisumbanje: Unpublised, 2013.

SiVEST SA Pty (Ltd), *Modified Bagasse Flow Diagram,* Durban: Unpublised, 2015.

T. E. o. E. Britannica, "Bagasse," Encyclopædia Britannica, 08 14 2013. [Online]. Available: http://global.britannica.com/EBchecked/topic/48728/bagasse. [Accessed 10 03 2015].

A. Austin, "Bagasse Power," Biomass Magazine, 25 01 2011. [Online]. Available: http://biomassmagazine.com/articles/5247/bagasse-power. [Accessed 10 03 2015].

P. Rein, Cane Sugar Engineering, Berlin: Verlag Dr. Albert Bartens KG, 2007, p. 601.

E. Hugot, Handbook of Cane Sugar Engineering, Amsterdam: Elsevier Science Publishers B.V., 1986, pp. 915-916. (Austin, 2011)

J. Chen and C. C. Chung, Cane Sugar Handbook, 12th ed., John Wiley & Sons, Inc, 1993.

B. S. Moor, "Belt vs. Chain-Slat Bagasse Conveyors for Boiler Feeding," *Proceedings of The South African Sugar Technologists' Association,* vol. I, no. 74, pp. 285-289, 2000.

Bulkmatic, "Diverter Chutes - Flap Type Pneumatic Cylinder Operated," Bulkmatic, 01 06 2014. [Online]. Available: http://www.bulkmatic.co.za/PRODUCTS/DiverterChutes.aspx. [Accessed 10 03 2015].

PEBCO®, "Diverter Gates," PEBCO®, 01 12 2013. [Online]. Available: http://catalog.pebco.com/category/diverter-gates. [Accessed 09 03 2015].

VHV Anlagenbau GmbH, "Material deflection in the carrying strand," VHV Anlagenbau GmbH, 01 06 2015. [Online]. Available: http://www.vhv-anlagenbau.info/products/stripper-techniques/material-deflection-in-the-carrying-strand/. [Accessed 10 06 2015].

R. Beardmore, "BS 970 Steels," Roymech, 25 03 2008. [Online]. Available: http://www.roymech.co.uk/Useful_Tables/Matter/Strength_st.htm. [Accessed 05 05 2015].

CEMA (2002). Belt Conveyors for Bulk Materials 5th Edition: CEMA Engineering Conference, USA.

114: Investigation of an innovative PV/T-ORC system using amorphous silicon solar cells and evacuated flat plate collectors: a comparison study

Cagri KUTLU[1], Jing LI[1,2], Yuehong SU[1], Yubo WANG[3], Gang PEI[2], Saffa RIFFAT[1]

[1]Department of Architecture and Built Environment, University of Nottingham, University Park, Nottingham NG7 2RD, UK
[2]Department of Thermal Science and Energy Engineering, University of Science and Technology of China, 96 Jinzhai Road, Hefei, Anhui, 230026, China
[3]School of Economics and Management, Hubei University of Technology, Wuhan, Hubei, 430068, China

Solar-driven organic Rankine cycle (s-ORC) is promising technology with flexible operation capacity and storage ability (adjustable output and night operation) to meet domestic users' electricity demands. However, this technology suffers from low efficiency. Beside the s-ORC, photovoltaics use semi-conductors to convert solar radiation directly into electricity. This direct conversion efficiency is about 5 to 25% in applications. Moreover, the rest of the collected solar energy can be converted into useful thermal energy by using photovoltaic thermal (PV/T) collectors. However, PV/T systems cannot produce electricity at night time. Therefore, in this study, s-ORC, stand-alone PV and PV/T-ORC systems are analysed and their performances are compared. The s-ORC is driven by evacuated flat plate (EFP) collectors and sensible heat storage unit is implemented to produce smooth generation and maintain heat for the ORC during the night time period. By using amorphous silicon (a-Si) and polycrystalline silicon (poly-Si) cells, EFP collectors are converted into PV/T collectors. These PV/T collectors are replaced with EFP collectors in the s-ORC and PV/T-ORC systems are implemented. It is the first time the EFP collector has been used for PV/T application because EFP is very expensive. However, it will benefit from the use of PV cells to increase its annual yield. Related mathematical models are built and presented in the paper. Transient daily analysis is conducted for two weather data and results are compared for aforementioned systems. Combining PV/T collectors with the ORC gives better performance than stand-alone PV and s-ORC. For summer applications, a-Si based system shows the best performance over other compared systems.

Keywords: Solar ORC, PVT, sensible heat storage, a-Si and poly-Si cells

1. INTRODUCTION

The solar-driven organic Rankine cycle (s-ORC) has a great potential for meeting the residential electricity demand. Its flexible operation capacity with easier collection and storage ability make it promising technology in sustainable energy studies. By combining with a heat storage unit, power generation is not intermitted from solar radiation alterations and it is possible to continue power generation during night. Additionally, the s-ORC allows adjustment to outputs according to resident's electricity demand (Kutlu et al., 2018). However, low power efficiency is one of the main problems in the application of the low-mediate temperature s-ORC. The power efficiency is expected to be lower than 8 % for low temperature s-ORC operations. In contrast, PV cells convert solar energy into electricity with an efficiency of about 5 to 25 % and photovoltaic modules have been used for years and have an important role in future electricity generation systems (Aste et al., 2015). PV technology requires very low maintenance and repair expenses make this technology operationally one of the most low-cost options, however, it also comes with the highest capital costs (Sharma, 2011). A PV/T system consists of a solar collector and PV module as major components. In the PV system, the PV module constitutes 70% of the capital costs. Research into PV technologies has been ongoing for years, resulting in improvement in the performance of cells and the significant reduction of capital costs (Kumar & Kumar, 2017). This study focuses on crystalline silicon type and thin film PV cells. Given their higher conversion efficiency and low cost, crystalline silicon cells have become the most preferred cell material in the world market. However, the use of thin film cells has the potential to become widespread. The percentage of production of thin film amorphous cells and silicon cells in world markets is presented in a report (Fraunhofer, 2016), according to which, thin films have 4.2 percent of the total production, whilst mono-Si and poly-Si are 15.1 and 43.9 percent, respectively. Cells made up of a single silicon crystal are more efficient but expensive as compared to the polycrystalline and thin film cells. The advantages of these solar cells are high conversion efficiency rates, which vary between 15-20%, space-efficiency and a relatively longer lifespan. However, mono-Si has some disadvantages such as expensive capital cost caused by the production process, as a result of which manufacturers are looking for other materials such as polycrystalline, which has a lower production cost in comparison. Although these are less efficient than mono-Si cells, poly-Si cells are widely used in manufactured modules due to their lower production cost, resulting in a subsequent high demand thereof amongst investors. Amorphous silicon cells are widely used and are the most developed thin film cells. In China more than 2.0 GW of a-Si cells can be produced annually (Hanergy 2015). One advantage of amorphous cells is their flexibility which helps prevent fractions (breakup) of cells. For example, PV cells are coupled with copper or other metals in practice. Temperature fluctuations cause the metal to expand and shrink which results in production of tension stress on the cells. Silicon cells are weak in their ability to carry this thermal stress resulting in their shortened lifespan. Moreover, this a-Si flexibility facilitates its ease of integration into building components. Another advantage of a-Si is that it is relatively cheap in comparison to mono-Si and poly-Si. A disadvantage, however, is its low conversion efficiency compared to other silicon based cells which also results in a lower space-efficiency (Nikolaeva-Dimitrova et al., 2010). Table 1 provides a very useful reference, showing a comparison of the cells.

Table 1: Comparison of cells (Energy informative 2015)

	mono-Si	**poly-Si**	**a-Si**
Module efficiency	15-20%	13-16%	6-8%
Area required for 1 kWp	6-9 m^2	8-9 m^2	13-20 m^2
Lowest price*	0.75 $/W	0.62 $/W	0.69 $/W
Temperature resistance of performance	Drops 10-15% at high temperatures	Less than monocrystalline	Tolerates extreme heat

*Lowest price values are taken from reference website; data was collected in 2013.

Solar ORC systems have been compared with PV/T technology to clarify its advantages and disadvantages in terms of electricity and heating (Guarracino et al., 2016). Nonetheless, combination of these two systems can be more attractive. Li et al. (Li et al., 2015) studied a hybrid solar power generation system which consists of a PV/T based on a-Si cells and presented a-Si cells are a good choice for solar cogeneration systems. These cells allow for higher operating temperatures to be reached with a high resistance temperature during the operation.

The evacuated flat plate (EFP) collector is a relatively new technology and its capital cost is higher than conventional collectors. Although it has a high capital cost, EFP collector studies have focused on the fluid heating applications such as district heating and s-ORC. Therefore, the payback periods of these kinds of applications are expected as quite long. However, combining the EFP with PV cells may result in an increment of electricity yield and payback period will be considerably decreased. To prove that statement, a performance comparison is made between four different systems in this study. The models are built and investigation of the systems has been conducted from the point of view of electricity output and its profile. The first one is the s-ORC by using EFP collectors and heat storage unit. Secondly, EFP collectors are covered with a-Si cells with a 0.85 cover ratio, namely a-Si PV/T-ORC system. Thirdly, conventional EFP collectors are covered with poly-Si cells with a 0.85 cover ratio, namely poly-Si PV/T-ORC and finally, stand-alone PV collectors with poly-Si cells. These systems will be compared according to thermal and electrical efficiencies and power outputs considering thermocline behaviour of the water tank in transient state for moderate and high irradiance weather data. Compared systems and parameters are summarised in Figure 1.

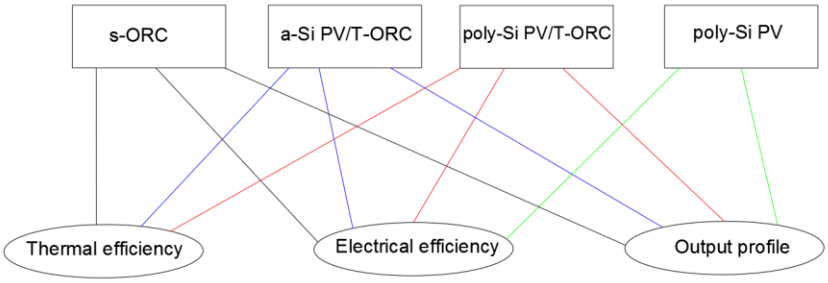

Figure 1: Compared systems and parameters

2. SYSTEM DESCRIPTION AND THERMODYNAMIC MODELLING

The proposed s-ORC as shown in Figure 2 is composed of solar field, heat storage unit and ORC block. TVP SOLAR HT-Power EFP collectors (TVPSOLAR 2013) are used for heating water which comes from the bottom of the tank, then it is discharged into the top of the water tank. A water tank is used as a heat storage unit to provide heat for the ORC. Moreover, it allows to drive ORC when solar radiation is not sufficient or not available. In the ORC block, there are four main components namely pump, evaporator, expander and condenser.

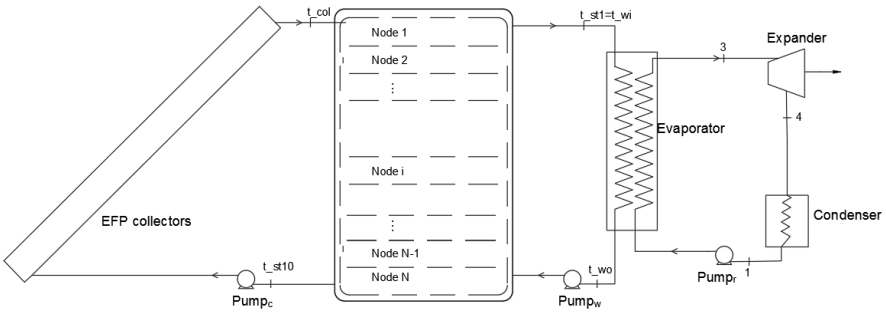

Figure 2: Schematic view of the system

2.1. PV and PV/T system model

Poly-Si type modules are used in stand-alone PV systems. Electrical characteristics of the modules are taken from the manufacturer's data and presented in Table 2. The most common equation to determine the cell temperature is using Normal Operating Cell Temperature (NOCT). This value is given by the manufacturer and Equation (1) is used for calculating the cell temperature (Mattei et al., 2006).

$$T_c = T_a + (NOCT - 20) \cdot \frac{G}{800} \quad (1)$$

Photovoltaic module efficiency is calculated by most known model:

$$\eta_{PV} = \eta_r[1 - \beta_r \cdot (T_c - T_r)] \quad (2)$$

The parameters are given by producer and η_r indicates efficiency at reference temperature. Global electrical efficiency of the PV system can be calculated as Equation (3):

$$\eta_{gPV} = \eta_{PV} \cdot \eta_{DC-AC} \quad (3)$$

Where η_{DC-AC} is conversion efficiency of DC to AC and it is reported as between 80-95% depending on solar irradiance (Ungureşan et al. 2016), (Mulcué-Nieto & Mora-López 2014). For $< 300\ W/m^2$, η_{DC-AC} is 80%. For $300\ W/m^2 < G < 500\ W/m^2$, η_{DC-AC} is 85%. For $500\ W/m^2 < G < 800\ W/m^2$, η_{DC-AC} is 90%. For $> 800\ W/m^2$, η_{DC-AC} is 95%.

General thermal efficiency equation of a solar collector is given in Equation (4). T indicates mean water temperature in collector, G is solar irradiance, A and B are heat loss coefficients. For EFP collectors η_0 is 74.62, A and B are 39.9 and 0.67, respectively.

$$\eta_c(T) = \eta_0 - A \cdot \frac{T - T_a}{G} - B \cdot \frac{(T - T_a)^2}{G} \quad (4)$$

The power output of PV cell is calculated by Eq. (5):

$$W_{PV} = \eta_{PV}(T) \cdot G \cdot A_{col} \cdot x \quad (5)$$

x indicates cover area ratio and it is taken as 0.85. The heat collection efficiency of a PV/T collector can be deduced as:

$$\eta_{PVT}(T) = \eta_c(T) - \eta_{PV}(T) \cdot x \quad (6)$$

$\eta_{PV}(T)$ is assumed as second order equation and can be expressed by

$$\eta_{PV}(T) \cdot x = \eta_{PV,0} + a \cdot T + b \cdot T^2 \quad (7)$$

$$\eta_{PV/T}(T) = \eta'_{c,0} - A' \cdot \frac{T - T_a}{G} - B' \cdot \frac{(T - T_a)^2}{G} \quad (8)$$

$\eta'_{c,0}$, A' and B' are the modified coefficients of the collector.

$$\eta'_{c,0} = \eta_{c,0} - \eta_{PV,0} - a \cdot T_a - b \cdot T_a^2 \quad (9)$$

$$A' = A + (a + 2 \cdot b \cdot T_a) \cdot G \quad (10)$$

$$B' = B + b \cdot G \quad (11)$$

Table 2. Some of the PV module technical specifications (Santiago et al., 2018)

PV	**Specifications**
Model	Atersa A-214P
Type	Polycrystalline Silicon
Module efficiency	12.64 %
Power temperature coeff.	-(0.46)%K
NOCT	47

2.2. Tank and ORC model

The transient heat storage unit is modelled by considering thermocline behaviour. It is analysed using a one-dimensional temperature distribution model (Bellos et al., 2017). The cylinder volume has been divided into 10 equal nodes to obtain temperature distribution in the storage tank. An energy balance equation can be written considering the heat loss to the environment in every control volume. Equation (12) shows the energy balance equations for the nodes:

$$M_{st,i} \cdot c_{p,w} \cdot \frac{\partial T_{st,i}}{\partial t} = \dot{m}_{cw} \cdot c_{p,cw} \cdot \left(T_{st,i-1} - T_{st,i}\right) + \dot{m}_w \cdot c_{p,w} \cdot \left(T_{st,i+1} - T_{st,i}\right) - U_t \cdot A_{st,i} \cdot \left(T_{st,i} - T_{am}\right) \quad (12)$$

Where $\dot{m}_{cw}$ and $\dot{m}_w$ indicate water mass flowrate coming from collector and evaporator respectively, T_{wo} is the water temperature coming from the evaporator to the tank bottom node. U_t indicates the thermal loss coefficient of the well-insulated tank.

It was decided that a scroll type expander would be used in the analysis, as this is particularly well-adapted to small-scale Rankine cycle applications. An empirical model was adapted from (Declaye et al. 2013). Since the heat source temperature is not constant during day, the system operates at off-design conditions. Therefore, the evaporator is designed according to the NTU method. Related equations and a detailed investigation about the effects of circulation water mass flow rate on system performance is given in our previous study (Kutlu et al. 2018). Used ORC design parameters are given in Table 3.

Table 3. Design parameters of s-ORC

Collector area	550 m^2	**Tank volume**	87 m^3
Collector mass flowrate	0.02 kg/s	**Water mass rate**	2 kg/s
Evaporator length	51 m	**Condensing temp**	T_a +10

3. RESULTS AND DISCUSSIONS

Before conducting the daily simulations, conventional EFP collectors are covered with a-Si and poly-Si cells (a-Si PV/T, poly-Si PV/T) and their thermal efficiencies are determined by using Equations (5-11). Figure 3 shows the results of the analysis and compares the efficiencies according to various solar irradiances and operating temperatures. Figure 4 gives electrical efficiencies of a-Si and poly-Si cells in PV/T. Figure 4 presents that electrical efficiency lines intercept at 99 ℃; it means that using the a-Si PV/T at operation temperature of over 99 ℃ has better

electrical performance than poly-Si PV/T. Moreover, it is seen from Figure 3 that poly-Si PV/T has a higher thermal efficiency at higher operation temperatures since rest of the electrical conversion energy is converted into thermal energy. Thus, using poly-Si PV/T has better thermal performance but less electrical performance at high temperature operations.

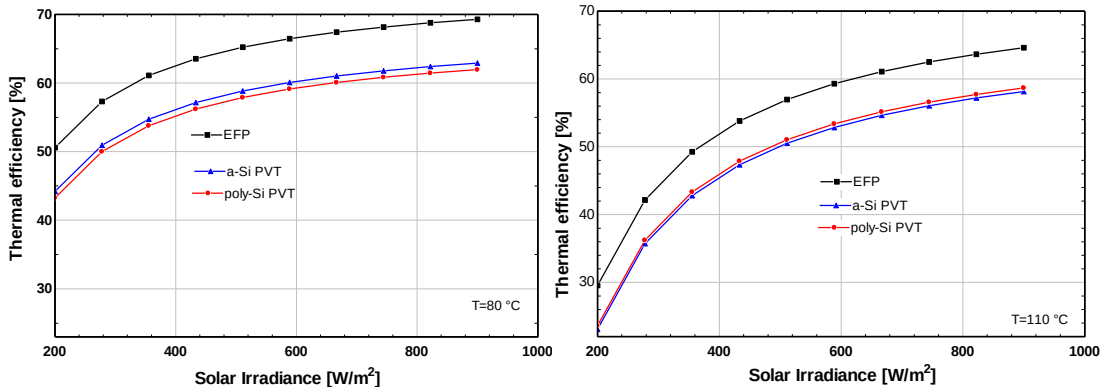

Figure 3: Thermal efficiency comparisons

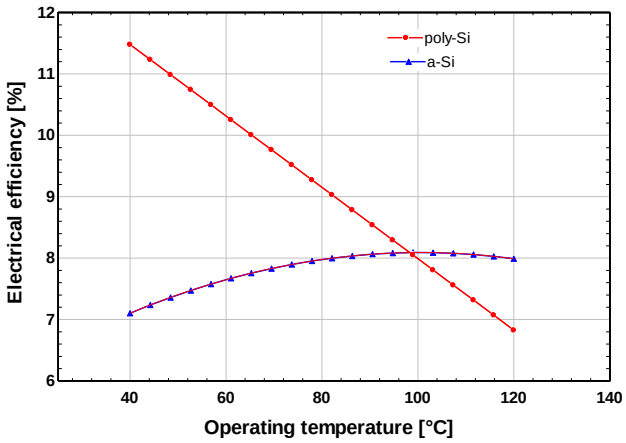

Figure 4: Electrical efficiency of poly-Si and a-Si cells

3.1. Simulations

The weather data in this paper relates to the climate conditions of Istanbul, Turkey. Relevant parameters such as solar irradiance and ambient temperature profiles are obtained by using the software EnergyPlus (Crawley et al., 2000). In the study, two different weather data are used to test the proposed system's performance. One of the weather data is chosen as very good solar irradiance, the other is chosen as moderate solar irradiance with relatively low ambient temperature. Figure 5 shows the used weather data which are statistical days of Istanbul in April and July.

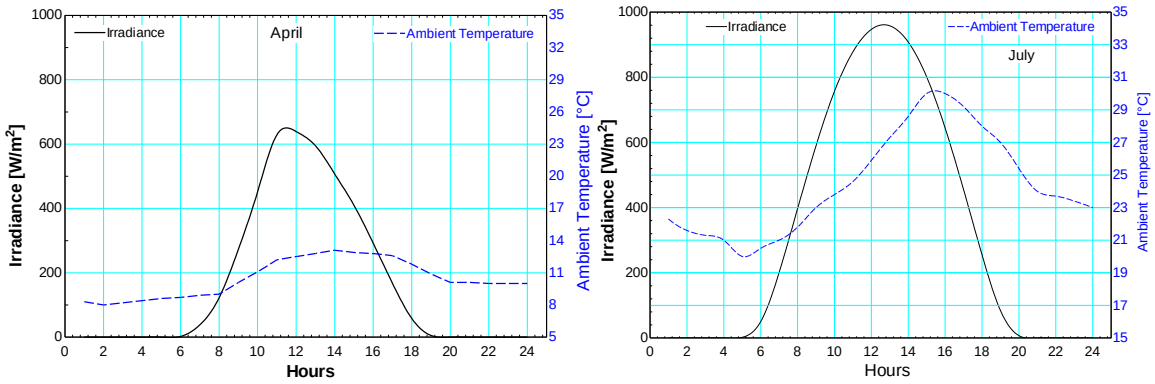

Figure 5: Weather data for a typical day in April and July

As simulations are conducted for selected weather data, the initial tank temperature needs to be determined by using the method of repeating the simulations. To provide operation at close value of the design parameters, the stop criterion is also defined. The fifth element of the tank is selected as stop consideration; this is activated, the refrigerant pump is shut off and the tank is switched to static mode for the particular simulation. Stop temperature is chosen as 80 ℃ and 100℃ for April and July, respectively. Simulations have been conducted for different systems such as s-ORC (EFP collectors are used), a-Si PV/T-ORC, poly-Si PV/T-ORC and stand-alone PV (poly-Si collectors are used). For s-ORC system, electricity is only produced by the expander thus system operation is continued throughout the day. However, for a-Si PV/T-ORC and poly-Si PV/T-ORC systems, electricity is produced by the cells during day time. After the sun sets, stored heat energy in the tank is converted into electricity by the expander. To test the given systems, investigated parameters are compared in relevant figures.

Collector operation temperature which is the mean temperature of the collector inlet and outlet has an influence on collector performances such as thermal and electrical efficiencies. Therefore, Figure 6 is plotted to compare operating temperatures of the s-ORC, a-Si PV/T-ORC and poly-Si PV/T-ORC for April and July. The main difference between the two months' study is temperature values. In April, all systems' operating temperatures are lower than in July as the lower solar irradiance does not allow an increase in tank temperature as high as that in July. It is also seen from the figure that, s-ORC operation temperature is lower for both months. Since only the s-ORC consumes stored heat during the day time, tank temperature of this system stands lower than hybrid systems.

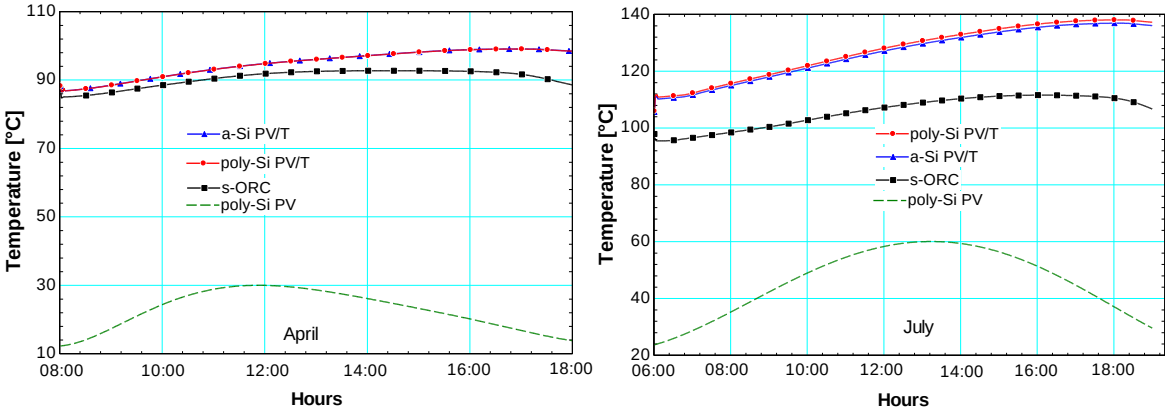

Figure 6: Operating temperatures

Thermal efficiency of the collector is another parameter to be compared. It is known that thermal efficiency of that kind of collector depends on operating temperature, irradiance and ambient temperature. However, in the analysis, weather conditions are identical for specific months and only operating temperatures are different. Therefore, thermal efficiency of the collectors of the s-ORC system is higher for two months. Moreover, all systems' performances are better in July because of higher irradiance and ambient temperature.

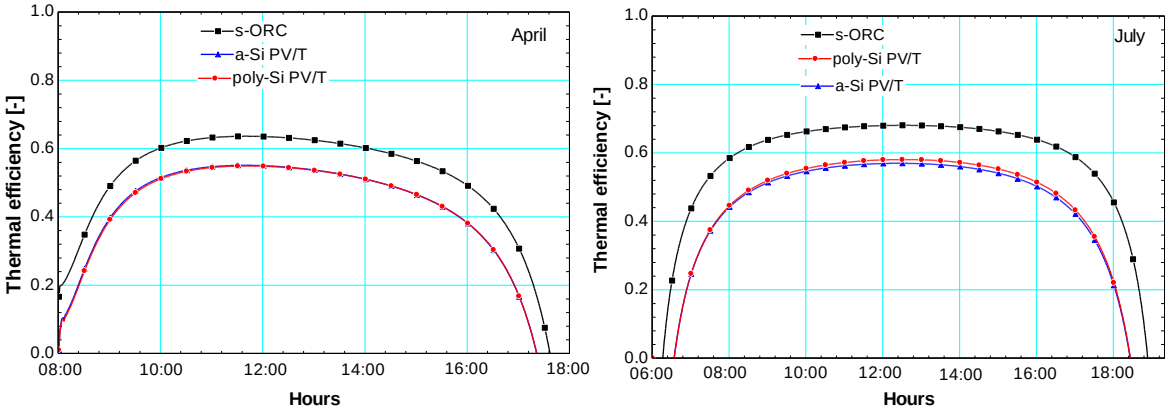

Figure 7: Thermal efficiencies

Figure 8 shows electrical efficiencies of cells for a-Si PV/T-ORC, poly-Si PV/T-ORC and stand-alone PV during the days of April and July. It is evident that the electrical performance of stand-alone PV is better than PV/T-ORC systems. The electrical efficiency depends on cell temperature; the PV cell temperature is lower in stand-alone PV as the heat generated in the PV cells is transported via convection through the ambient by external surfaces. However, in the hybrid systems, cell temperature is totally dependent on collector operating temperature. Thus, stand-alone PV performance is only affected by ambient conditions such as better performance as observed in April. According to Figure 4, poly-Si cells have better performance when operating under 99℃, which is why poly-

Si PV/T have higher electrical efficiency until noon as operating temperature is increasing from 87℃ to 100℃ in April. In contrast, operating temperature increases from 110℃ to 140 ℃ in July and the poly-si cell efficiency decreases in the period of day time.

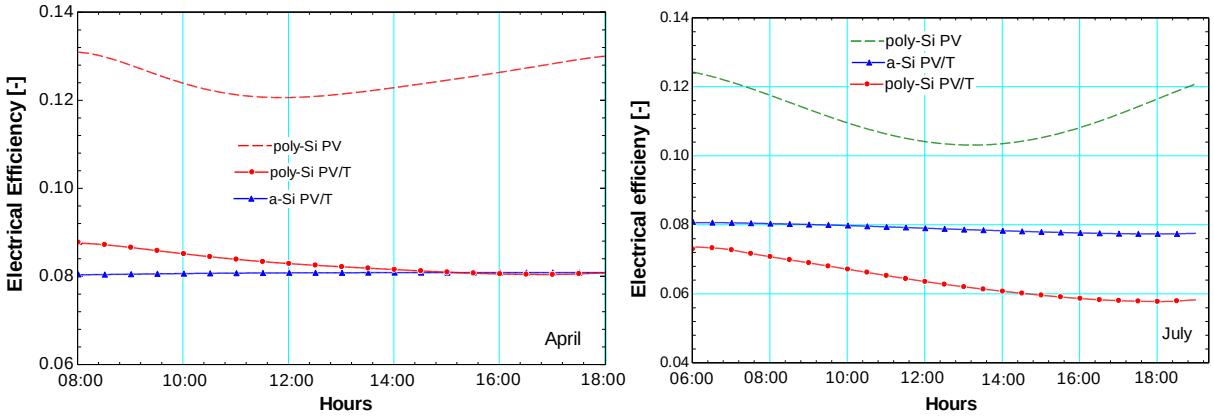

Figure 8: Electrical efficiencies

Figure 9 shows the comparison of the instant electricity outputs for four examined systems. Since the solar irradiance profile is weaker and solar time is shorter in April, electricity production is lower for all systems. Moreover, none of the systems can produce electricity for 24 hr. For both months, stand-alone PV is the highest and s-ORC is the lowest producing systems. poly-Si PV/T-ORC system generates slightly higher electricity in day time because of better electrical efficiency, however, in July, the poly-Si PV/T-ORC system produces considerably more. As both collectors have very close thermal efficiencies, their ORC performances are quite close.

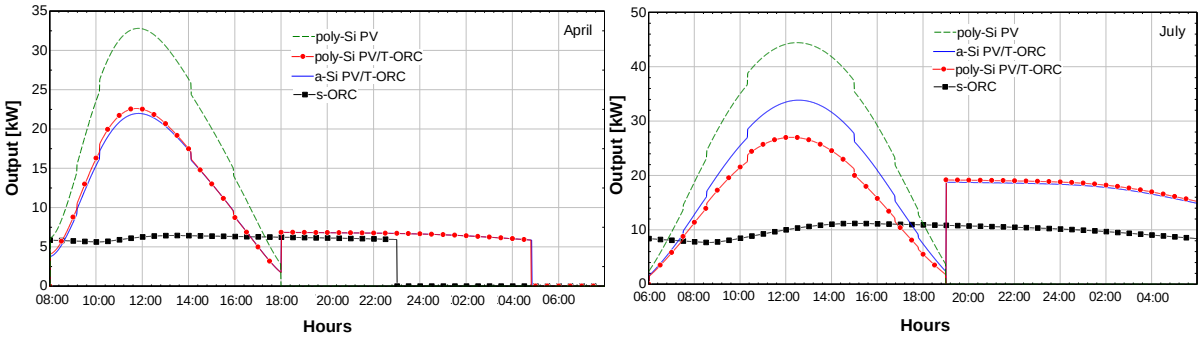

Figure 9: Electricity outputs

Cumulative daily performances of the systems are given in Table 4. Compare to April, the daily produced electricity values increase in July. The s-ORC has the worst performance for both months. a-Si PV/T-ORC, poly-Si PV/T-ORC and stand-alone PV systems produce almost same electricity in April. However, the a-Si PV/T-ORC system produces more power in July. Thus, it can be concluded that hybrid systems have an advantage over conventional s-ORC and PV systems. Moreover, the a-Si PV/T-ORC is promising when combining PV technology and ORC.

Table 4: Daily Produced electricity

	s-ORC	**a-Si PV/T-ORC**	**poly-Si PV/T-ORC**	**poly-Si PV**
Daily Output [kWh]- April	91.86	205.23	208.43	204.62
Daily Output [kWh]- July	235.366	462.11	413.95	365.15

4. CONCLUSION

In this study, the mathematical models for the s-ORC, a-Si PV/T-ORC, poly-Si PV/T-ORC and stand-alone PV systems have been built and their performance parameters have been compared in transient daily state analysis. Although the s-ORC has advantages such as flexible operation and continuous production even at night, its electricity output has been found to be much lower than stand-alone PVs. Combination of these two technologies has given promising results as all their advantages are combined in hybrid systems. Hybrid systems outputs were almost same as stand-alone PV in April simulations but their night long production made them a better option over stand-alone PVs. In July, even daily outputs have been found as better than others. Finally, using a-Si cells in the hybrid system showed great results in summer applications, since it can tolerate excessive temperatures with a stable electrical efficiency.

5. REFERENCES

Aste, N., Leonforte, F. & Pero, C. Del, 2015. Design , modeling and performance monitoring of a photovoltaic – thermal (PVT) water collector. *Solar Energy*, 112, pp.85–99.

Bellos, E. et al., 2017. Energetic , exergetic and financial evaluation of a solar driven absorption chiller – A dynamic approach. *Energy Conversion and Management*, 137, pp.34–48.

Crawley, D.B. et al., 2000. EnergyPlus: Energy Simulation Program. *ASHRAE Journal*, 42(4), pp.49–56.

Declaye, S. et al., 2013. Experimental study on an open-drive scroll expander integrated into an ORC (Organic Rankine Cycle) system with R245fa as working fl uid. *Energy*, 55, pp.173–183. Available at: http://dx.doi.org/10.1016/j.energy.2013.04.003.

Energy informative, 2015. Which Solar Panel Type is Best? Mono- vs. Polycrystalline vs. Thin Film. Available at: http://energyinformative.org/best-solar-panel-monocrystalline-polycrystalline-thin-film/.

Fraunhofer, 2016. Photovoltaics report. , (November), pp.1–43. Available at: https://www.ise.fraunhofer.de/content/dam/ise/de/documents/publications/studies/Photovoltaics-Report.pdf.

Guarracino, I. et al., 2016. Performance assessment and comparison of solar ORC and hybrid PVT systems for the combined distributed generation of domestic heat and power. *International Conference on Heat Transfer, Fluid Mechanics and Thermodynamics*, (August).

Hanergy, 2015. Thin-film Solar Power Generation. Available at: http://www.hanergy.com/en/industry/industry_310.html.

Kumar, M. & Kumar, A., 2017. Performance assessment and degradation analysis of solar photovoltaic technologies: A review. *Renewable and Sustainable Energy Reviews*, 78(November 2016), pp.554–587. Available at: http://linkinghub.elsevier.com/retrieve/pii/S1364032117305919.

Kutlu, C. et al., 2018. Off-design performance modelling of a solar organic Rankine cycle integrated with pressurized hot water storage unit for community level application. *Energy Conversion and Management*, 166(15), pp.132–145.

Li, J. et al., 2015. A Novel Hybrid Solar Power Generation System Using a-Si Photovoltaic / Thermal Collectors and Organic Rankine Cycle. In *Proceedings of the 3rd International Seminar on ORC Power Systems*. pp. 1–10.

Mattei, M. et al., 2006. Calculation of the polycrystalline PV module temperature using a simple method of energy balance. *Renewable Energy*, 31(4), pp.553–567.

Mulcué-Nieto, L.F. & Mora-López, L., 2014. A new model to predict the energy generated by a photovoltaic system connected to the grid in low latitude countries. *Solar Energy*, 107, pp.423–442.

Nikolaeva-Dimitrova, M. et al., 2010. Seasonal variations on energy yield of a-Si, hybrid, and crystalline Si PV modules. *Progress in Photovoltaics: Research and Applications*, 18(5), pp.311–320.

Santiago, I. et al., 2018. Modeling of photovoltaic cell temperature losses: A review and a practice case in South Spain. *Renewable and Sustainable Energy Reviews*, 90(June 2017), pp.70–89. Available at: https://doi.org/10.1016/j.rser.2018.03.054.

Sharma, A., 2011. A comprehensive study of solar power in India and World. *Renewable and Sustainable Energy Reviews*, 15(4), pp.1767–1776. Available at: http://dx.doi.org/10.1016/j.rser.2010.12.017.

TVPSOLAR, 2013. HT Power product datasheet. , 2013. Available at: http://www.tvpsolar.com/files/pagine/HT-Power Datasheet (v4.2x)(ver3).pdf.

Ungureşan, P. et al., 2016. Potential of Solar ORC and PV Systems to Provide Electricity under Romanian Climatic Conditions. *Energy Procedia*, 85(November 2015), pp.584–593.

116: Generation of typical weather data (TWD) for urban heat island (UHI)

Kwanho LEE[1], Geoffrey J. LEVERMORE[2]

[1] School of Building & Environment Design, Ulsan College, Bongsuro 101, Donggu, South Korea, ghlee@uc.ac.kr
[2] School of Mechanical, Aerospace and Civil Engineering, Manchester University, geoff.levermore@manchester.ac.uk

Typical weather data (TWD) consists of 8760 values of various selected meteorological parameters and are derived initially from long-term data. At present, the weather data currently used by designers are invariably derived from meteorological measurements taken at semi-rural sites often at airfields, away from the urban centre. This paper looks at the method of the TWD and urban heat island intensity (UHII) by analyzation and estimation. This study can provide the TWD for urban heat island (UHI) estimate to the heating and cooling load using the UHII models and the TWD in Ulsan, South Korea and Manchester, UK. Comparing the loads between the core area and the Met-office, Manchester showed an increase of 9.2% in Ulsan showed an increase of 11.2%. Energy consumption following the urban heat island in Ulsan was more serious than in Manchester. The core area of Ulsan requests significant measures to reduce the cooling load in summer. The relationship between the wind speed of the meteorological station and the core should be investigated and analyzed for the UHI of the core area.

Keywords: Typical weather data(TWD), Urban heat island (UHII), Urban heat island intensity (UHII), Dry air temperature, wind speed

1. INTRODUCTION

The typical weather data (TWD) consists of 8760 values of various selected meteorological parameters such as ambient temperature, solar radiation, relative humidity and wind velocity and are derived initially from long-term data. Several methods for generating typical data have been developed they are also essential for the numerical analysis of sustainable and renewable energy systems. The urban heat island (UHI) is the urban area compared to the surrounding rural area. The urban heat island intensity (UHII) is the actual temperature difference between the urban area and the rural area. The reason for the UHII can be explained in part by the buildings, how they absorb shortwave solar irradiance during the day and reradiate longwave radiation, especially at night on clear cloud-free nights. The proposed models can provide the typical weather data for estimation of the heating and cooling load using the measured data from Manchester, UK, and Ulsan, South Korea. This study is made to generate TWD using the ISO TRY (ISO, 2005:2-4, LEE et al., 2010: 959-962) for the UHI and the data for this study from Ulsan in South Korea over 30 years (1986-2015). A TWD consists of individual months of meteorological data sets selected from different years over the available data period, which is called a long-term measured data series. The most average months are commonly selected using the Finkelstein-Schafer statistic (Finkelstein and Schafer, 1971: 642).

Urban heat island intensity models are generated using the major climatic factors such as air temperature, horizontal solar irradiation, wind speed and cloud cover among the measured Ulsan meteorological station weather data and field measurements data in 2016. Air temperature of field measurements were carried out in 44 locations and were collected every 30 min. Wind speed of field measurements were carried out in 2 locations of the city centre and east coastal area. Sensors were placed inside a solar shield that protected them from solar radiation (See Figure 1). They were installed on lamppost at approximately 4 m above the ground (KIM et al., 2018: 472-473). In the case of Ulsan, solar irradiation data not measured by the Ulsan meteorological station, so the University of Ulsan uses the horizontal solar irradiation data measured data in 2016, and direct normal irradiation data was calculated using the recent research work (LEE et al., 2013: 196). This study examines the implications of the effect of the UHI available to designers and planners for buildings and urban environment in Ulsan, South Korea and Manchester, UK.

Figure 1: Radiation shield, hook and lamppost for air temperature and wind speed

2. METHODOLOGY

2.1. Typical weather data (TWD) using ISO TRY

The TWD using ISO TRY shall contain hourly values of at least the following meteorological parameters.

- dry-bulb air temperature;
- global and direct normal or diffuse solar irradiance;
- relative humidity or absolute humidity, water vapor pressure or dewpoint temperature;
- wind speed at a height of 10 m above ground.

In the procedure described below, dry-bulb temperature, total solar radiation on the horizontal plane and relative humidity are taken as the primary parameters for selecting the “best” months to form the reference year, with wind speed as a secondary parameter.

a) From 30 years of hourly values, calculate the daily means.

b) For each calendar month, calculate the cumulative distribution function of the daily means overall years in the data set.

c) For each year of the data set, calculate the cumulative distribution function of the daily means within each calendar month.

d) For each calendar month, calculate the Finkelstein-Schafer statistic and rank the individual months from the multiyear record.

f) For each calendar month and each year, add the separate ranks for the three climate parameters.

g) For each calendar month, for the three months with the lowest total ranking, calculate the deviation of the monthly mean wind speed from the corresponding multi-year calendar-month mean. The month with the lowest deviation in wind speed is selected as the “best” month to be included in the reference year.

h) Adjust the parameters in the last eight hours of each month and the first eight hours of the next month by interpolation to ensure a smooth transition when the “best” months are joined to form the reference year.

2.2. UHII MODELS

In this study, we selected the main climate factors affecting the UHI and proposed a model to predict the UHII between the core areas (radius 1.5km from the city centre) and Ulsan meteorological station using the regression equation and the heat balance equation. Regression models (RM) of the main climate parameters are as follows.

Equation 1: Regression model (RM1) with wind speed of the core area.

$$RM_1 = (a \times G + b \times L + c \times W_u + d \times 5hG + e \times 5hL + f) \times \cos(SA)$$

Where:

G = short wave irradiation (W/ m^2)

L = long wave irradiation (W/ m^2)

Wu = wind speed of the core area (m/s)

5hG = sum of G over the past 5 hours (W/ m^2)

5hL = sum of L over the past 5 hours (W/ m^2)

SA = solar altitude (°)

Equation 2: Regression model (RM_2) with wind speed of Ulsan meteorological station

$$RM_2 = (a \times G + b \times L + c \times W_r + d \times 5hG + e \times 5hL + f) \times \cos(SA)$$

Where:

Wr = wind speed of Ulsan meteorological station (m/s)

Equation 3: Longwave irradiation

$$L = 93 - 79 \times (CC \div 8)$$

Where:

CC = cloud cover (Octa)

Single energy balance models (SEBM) using the concept for sol-air temperature (CIBSE, 2008: 5-54) and the energy balance (OKE, 1987: 17) are as follows.

Equation 4: Single energy balance model ($SEBM_1$) with wind speed of the core area.

$$SEBM_1 = (a \times G + b \times L + d \times 5hG + e \times 5hL + f) \div (4 + 4 \times c \times W_u)$$

Equation 5: Single energy balance model ($SEBM_2$) with wind speed of Ulsan meteorological station

$$SEBM_2 = (a \times G + b \times L + d \times 5hG + e \times 5hL + f) \div (4 + 4 \times c \times W_r)$$

The double energy balance model (DEBM) of urban (core of Ulsan) and rural area (Ulsan meteorological station) is as follows (See Figure 2).

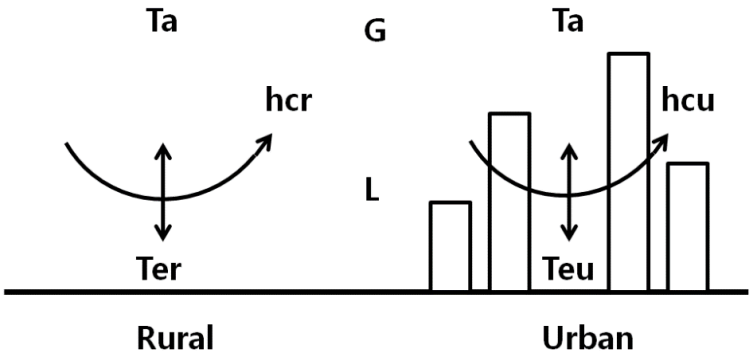

Figure 2: UHII model (DEBM) concept for rural and urban area

Equation 6: Double energy balance model (DEBM)

$$DEBM = (a \times G \times (\alpha_u \times H_{cr} \div H_{cu} - \alpha_r) + b \times L \times (H_{cr} \div H_{cu} - 1) + (d \times 5hG + e \times 5hL) \times H_{cr} \div H_{cu} + f) \div (4 + 4 \times c \times W_u)$$

Where:

$\propto_u$: urban short-wave absorptivity

$\propto_r$: rural short-wave absorptivity

$H_{cr} = 4 + 4 \times W_r$ (m/s)

$H_{cu} = 4 + 4 \times W_u$ (m/s)

3. EVALUATION OF UHII MODELS

To quantify the performance of the models, the mean bias error (MBE) and root mean square error (RMSE) determined for the two models in Manchester. Because there was no wind speed data in Manchester core area, three models (RM1, SEBM1, and DEBM) were excluded to predict UHII. The regression model (RM2) and the single energy balance model (SEBM2) were compared using the MBE, RMSE to assess the feasibility of UHII forecasting models. The evaluation of the two models and constants a, b, c, d, e, f values showed in Table 1.

Table 1: MBE and RMSE of predicting UHII in Manchester

	RM2	SEBM2
MBE (%)`	2.494	5.414
RMSE (%)	90.611	90.649
Average UHII (°C)	1.716	1.716
a: shortwave coefficient	-0.02578	-0.08970
b: longwave coefficient	0.00066	0.00100
c: wind speed coefficient	-0.20668	0.34486
d: shortwave thermal storage coefficient	0.00250	0.00588
e: longwave thermal storage coefficient	0.00115	0.00147
f: constant	15.49279	9.20546

The MBE provides information on the long-term performances of the regression equations, and the RMSE offers information on the short-term performances and the scattering of data around the linear regression. The MBE and the RMSE values of the energy balance model (SEBM2) were relatively higher than the regression model (RM2). The RM2 presented from the above results is a useful tool for predicting the annual UHII using hourly data of solar

irradiation, cloud cover, wind speed and the air temperature of Met-office. The MBE and the RMSE determined for the five models in Ulsan. The regression model (RM1 and RM2), the single energy balance model (SEBM1 and SEBM2) and the double energy balance model (DEBM) compared the feasibility of UHII forecasting models. The evaluation of the five models and constants a, b, c, d, e, f values shown in Table 2.

Table 2: MBE and RMSE of predicting UHII in Ulsan

	RM_1	RM_2	$SERM_1$	$SEBM_2$	DEBM
MBE (%)`	6.660	6.695	0.057	13.968	0147
RMSE (%)	61.811	62.526	54.436	65.584	54.729
Average UHII (°C)	1.374	1.374	1.374	1.374	1.374
a: shortwave coefficient	-0.00483	-0.00483	-0.00657	-0.00657	-0.00932
b: longwave coefficient	0.0.6142	0.06142	0.02939	0.02939	0.01631
c: wind speed coefficient	-1.85883	-0.18818	1.01691	0.50919	1.04586
d: shortwave thermal storage coefficient	0.00310	0.00374	0.00244	0.00367	0.00243
e: longwave thermal storage coefficient	-0.01186	-0.01261	-0.00502	-0.00450	0.00070
f: constant	18.55388	13.02977	5.31383	4.36236	5.27518

The MBE and RMSE values of the regression models (RM1 and RM2) and the single energy balance model (SEBM2) are relatively higher than the other two models (SEBM1 and DEBM). Also, it factors a, b, c, d, e, and f showed changes in the similarity of three models (SEBM1, SEBM2, and DEBM). Both models (SEBM and DEBM) presented a useful tool for predicting the annual UHII using hourly data of solar irradiation, cloud cover, air temperature of rural area and wind speed of the core area. Because there is no urban wind data in the typical weather data, the TWD of the core area could be generated using the regression model (RM2) with wind speed of Ulsan meteorological station. Comparing the MBE and RMSE of Manchester and Ulsan, the MBE was similar, but the RMSE was significantly different Future research on the relationship between the wind speed of the Ulsan meteorological station, and the core area is required. The modified TWD will be a useful tool for estimating the heating and cooling load considering the urban heat island using the wind speed of the core area.

4. TWD FOR UHI

We made TWD for the core area and compared the heating and cooling loads with the TWD and the proposed TWD in Manchester and Ulsan.

4.1. TWD for the core area

ISO TRY in Ulsan was selected using the Finkelstein–Schafer statistic, from 30 years of meteorological data recorded during the period 1986-2015. Ulsan Met-office has not measured the hourly solar irradiance data. We used the formulation (KASTEN & CZEPLAK, 1980: 180-181) to generate hourly horizontal solar irradiation based on cloud cover data. Diffuse irradiation data was calculated using the recent research work. The TWD for the core area made using ISO TRY in Ulsan and the regression model (RM2) with the wind speed of Ulsan meteorological station. The UHII of the core area TWD and ISO TRY in Ulsan (meteorological station) was 1.524°C, the value showed a slight difference the UHII in 2016. We used the TRY provided by CIBSE and the regression model (RM2) with the wind speed of Manchester meteorological station for the TWD of Manchester core area. The UHII of the core area TWD and TRY in Manchester (meteorological station) was 2.723°C, and the value showed a significant difference to the UHII in 2010. This difference may be due to the RMSE of the regression model (RM2).

4.2. Heating and cooling load for core area

The heating and cooling loads concerning the office building having the following conditions was simulated to evaluate the influence of the buildings on the urban heat island in Manchester and Ulsan. The loads were calculated using a dynamic thermal analysis program ISE-VE and variables such as set point temperature, operating hours, an internal heat. The following Table 3 is a typical air-conditioned office building envelope parameters and initial system conditions for annual heating and cooling load simulation (LEE & LEVERMORE, 2016: 5).

Table 3: MBE and RMSE of predicting UHII in Manchester

	Area (m²)	U-value ()
Floor	450	0.2497
Ceiling	450	0.2497
External wall	135	0.3495
Window	135	1.9773

※Height(m): 3, Story: 3, Set point temperature (21°C: winter, 24°C: summer), Control switch: 8 to 6 weekday, Wall-window ratio: 50% and Internal heat gain: 44W/m2

Heating and cooling loads of Manchester and Ulsan for the core area and the Met-office showed in Figure 3. Comparing the loads between the core area and the Met-office, Manchester showed an increase of 9.2% in Ulsan showed an increase of 11.2%. Energy consumption following the urban heat island in Ulsan was more serious than in Manchester. The core area of Ulsan requests significant measures to reduce the cooling load in summer.

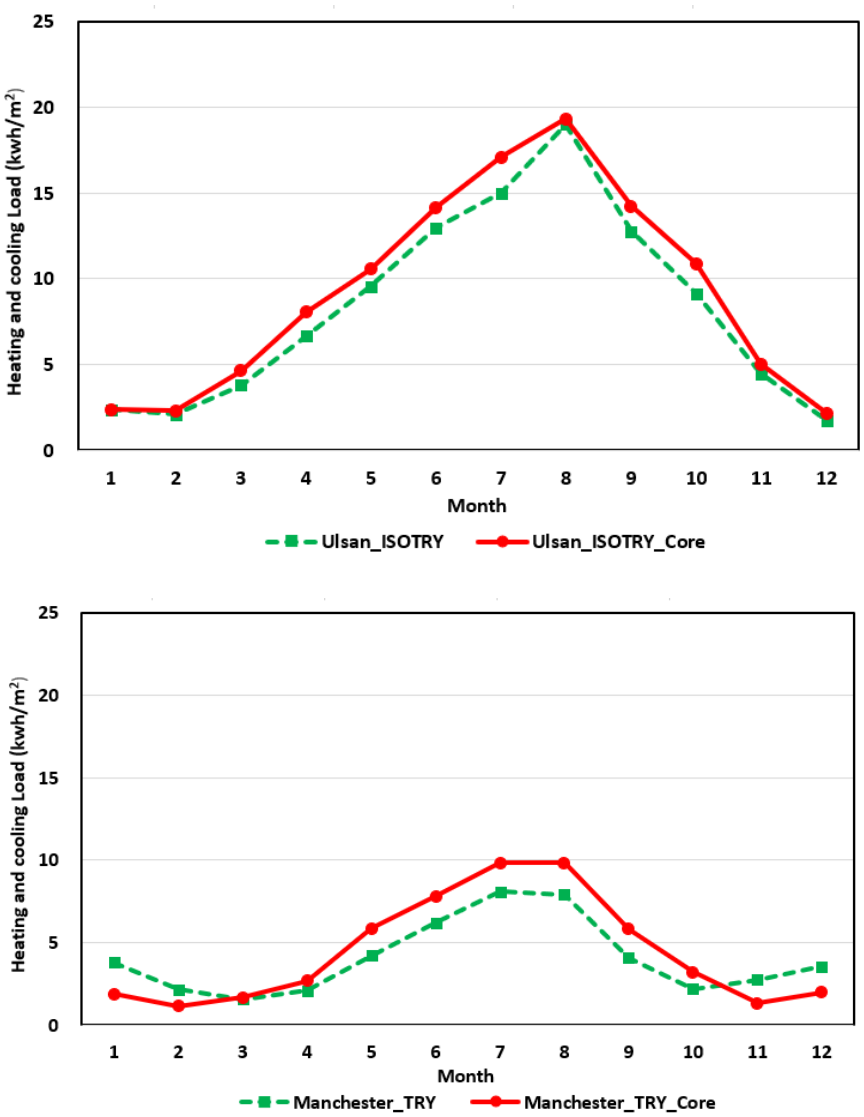

Figure 3: Compare to the heating and cooling load for the core area and the Met-office

5. CONCLUSION

This study can provide the TWD for urban heat island (UHI) estimate to the heating and cooling load using the UHII models and the TWD in Ulsan, South Korea and Manchester, UK. ISO TRY in Ulsan was selected using the Finkelstein–Schafer statistic, from 30 years of meteorological data recorded during the period 1986-2015. Both models (SEBM and DEBM) presented a useful tool for predicting the annual UHII using hourly data of solar

irradiation, cloud cover, air temperature of rural area and wind speed of the core area. Because there is no urban wind data in the typical weather data, the TWD of the core area could be generated using the regression model (RM2) with wind speed of Ulsan meteorological station. The long-term measurement was requested in urban and rural areas to assess the impacts and vulnerability of the UHI. Comparing the loads between the core area and the Met-office, Manchester showed an increase of 9.2% in Ulsan showed an increase of 11.2%.

The main conclusions from this study were:

1. The two TWD are useful for the heating and cooling load in Ulsan, South Korea and Manchester, UK.

2. Two regression models and three energy balance models generate for the predicting of the core area temperature.

3. The wind speed of the core area is an important parameter inaccurate prediction model of urban heat island.

4. Energy consumption following the urban heat island in Ulsan was more serious than in Manchester.

More works are required. The relationship between the wind speed of the meteorological station and the core should be investigated and analysed. Then, the modified TWD will be a useful tool for estimating the heating and cooling load considering the UHI of the core area.

6. ACKNOWLEDGEMENT

This research was supported by Basic Science Research Program through the National Research Foundation of Korea (NRF) funded by the Minister of Education (NRF-2015R1D1A1A01061049)

7. REFERENCES

CIBSE, 2000. CIBSE Guide J. London: Chartered Institution of Building Services Engineers.

ISO, 2005. ISO 15927-4: Hourly data for assessing the annual energy use for heating and cooling.

Finkelstein, JM. and Schafer, RM, 1971, Improved goodness of fit tests, *Biometrika*, 58, 641-645

Kasten, F and Czeplak, G, 1980. Solar and terrestrial radiation dependent on the amount and type of cloud. *Solar Energy*, 24, 177-189

Kim, M. Lee, K. & Cho, G-H, 2018. Temporal and spatial variability of urban heat island by geographical location: A case study of Ulsan, Korea. *Building and Environment*, 126, 471-482

Lee, K. & Levermore, G, 2016. 4th International Conference on Countermeasures to Urban Heat Island/ Evaluation of Urban Heat Island Intensity and Heating and Cooling Load on the Urban and Rural Area. Singapore: National University of Singapore.

Lee, K. Yoo, H. & Levermore, G, 2010. Generation of typical weather data using the ISO Test Reference Year (TRY) method for major cities of South Korea. *Building and Environment*, 45, 956-963.

Lee, K. Yoo, H. & Levermore, G, 2013. Quality control and estimation hourly solar irradiation on inclined surfaces in South Korea. *Renewable Energy*, 57, 190-199.

Oke, T. 1987. Boundary layer climates (2nd ed.). London and New York: Methuen.

117: Theoretical and experimental analysis on the performance of a solid desiccant air-conditioning system under the tropical climate

Kum Ja M[1], Qian CHEN[2], Seung Jin OH[3], T.D. BUI[4], M.D. Raisul Islam[5], K.J. Chua[6]

1 Department of Mechanical Engineering, National University of Singapore, 9 Engineering Drive 1, Singapore, 117575, Singapore, mpemkj@nus.edu.sg
2 Department of Mechanical Engineering, National University of Singapore, 9 Engineering Drive 1, Singapore, 117575, Singapore, chen_qian@u.nus.edu
3 Water Desalination and Reuse Centre, King Abdullah University of Science and Technology, Thuwal, Kingdom of Saudi Arabia, seungjin5111@gmail.com
4 Department of Mechanical Engineering, National University of Singapore, 9 Engineering Drive 1, Singapore, 117575, Singapore, mpebuid@nus.edu.sg
5 Department of Mechanical Engineering, National University of Singapore, 9 Engineering Drive 1, Singapore, 117575, Singapore, mpemdrs@ nus.ed.sg
6 Department of Mechanical Engineering, National University of Singapore, 9 Engineering Drive 1, Singapore, 117575, Singapore, mpeckje@nus.edu.sg

If thermal energy source like solar or waste heat with even low temperature (between 50℃ and 80℃) is available, solid desiccant air conditioning system is an alternative solution to substitute the conventional vapor compression refrigeration air conditioning for tropical climate region. A pilot scale Solid Desiccant Coated Heat Exchanger-Dehumidifier (SDHED) integrated with dew point evaporative cooler has been developed and experimentally investigated on its performance under tropical climate. A number of experiments were carried out to determine the optimal operation parameters of the system depending on the weather condition (outside air temperature and humidity ratio) and availability of waste heat grade (regeneration temperature). The experimental result shows that the optimum COP is achieved when the switching time, i.e., dehumidification/regeneration time, is 300 seconds.

Keywords: Solid Desiccant Coated Heat Exchanger-Dehumidifier; dew point evaporative cooler; tropical climate

1. INTRODUCTION

Singapore's building sector, the second largest electricity consumer after industry sector, consumes up to 38% of the nation's electricity (BCA Building Energy Benchmarking Report, 2014). In tropical country like Singapore, year round average temperature and relative humidity are 30°C and 84%, respectively (www.nea.gov.sg, 2018). Energy consumption for removing latent load of air conditioning to achieve standard comfort condition is always very high and that is 40 to 60 % of building energy consumption. Traditionally, air conditioning systems are running with an evaporator temperature which is lower than dew point temperature to remove the moisture from the air to meet human comfort, and to avoid building material degradation and mould growth. Deep cooling of the processed air running with low evaporator temperatures results in poor performance of the air conditioning system (Oh et al, 2017). Furthermore, traditional vapour compression air conditioners have created many environmental issues such as global warming caused by the greenhouse gas emission from the electrical power plant and creating micro climate due to the release of heat from the multi condensers of air conditioners to the environment (Jones, 1992). Hence, many researchers are finding alternative ways to improve the performance of the system by splitting the latent and sensible loads to run air conditioning system with high evaporator temperature. In splitting process, desiccant dehumidification has very high potential if waste heat or renewable energy is available.

Packed-bed desiccant dehumidifier is the most conventional dehumidification system. In packed-bed systems, the desiccant matrix is packed on a stationary bed, and moist air flows through the bed. The system requires large surface area due to poor heat and mass transfer, resulting in a big footprint size. Additionally, the pressure drop of the air stream is high. An alternative solution is to impregnate the desiccant into a wheel. The moist air gets dehumidified in one portion of the wheel, while in the other portion, hot air is passed through the desiccant for regeneration. Compared with packed-bed systems, desiccant wheels possess better heat and mass transfer between air and desiccant. However, the dehumidification capacity is still limited due to heat released during the adsorption process, which increases the desiccant temperature and reduces the adsorption capacity. Additionally, desiccant wheels can only be regenerated by hot air. Thus, an additional air-heater is required (Pesaran, 1994; Ramzy, Elawady & Abdelmeguid, 2014; Ramzy, Kadoli & Ashok Babu, 2011; Hamed, Abd-Elrahman, El-Emam & Awad, 2013).

Desiccant coated heat exchangers (DCHEs) are developed for addressing the drawbacks of the fixed-bed and rotary desiccant systems. In DCHEs, desiccants are coated on the fins, and the process air flows over the fin side of the heat exchanger. A cooling fluid is passed into the tubes during dehumidification, which removes the sorption heat and reduces the desiccant temperature, thus promoting moisture removal. The regeneration is achieved by circulating hot water (50-90 °C), which can be achieved from industry waste heat or renewable energy sources (Weixing, Yi, Xiaoru & Xiugan, 2008; Zheng, Yuan, Wang & Yuan, 2006; Fathalah, 1996).

This paper investigates the performance of a DCHE in tropical region. A pilot scale Solid Desiccant Coated Heat Exchanger-Dehumidifier (SDHED) integrated with dew point evaporative cooler will be developed. A number of experiments will be carried out to determine the optimal operation parameters of the system.

2. EXPERIMENTAL SET UP

A pilot scale Solid Desiccant Coated Heat Exchanger-Dehumidifier (SDHED) integrated with dew point evaporative cooler had been developed, as shown in Figure 1(a), to recover the waste heat from the exhaust gas of micro turbine (Capstone Microturbine Model: C65). Fresh air is first passed through a SDHED to get dehumidified. Then the dry air is directed to a crossflow dew-point evaporative cooler, Coolerado cooler Model: M30, shown in Figure 1(d), to get cooled. The SDHED, shown in Figure 1(b) schematic diagram and (c) photographical view, comprises of two beds. Each bed has two desiccant coated heat exchangers arranging in 30° tilt position, see Figure 1(b) in the direction of the air flow in order to increase the interaction area between desiccant and humid air, and also to be low air flow rate with a low Reynolds number and thus laminar flow that increase heat transfer rate.

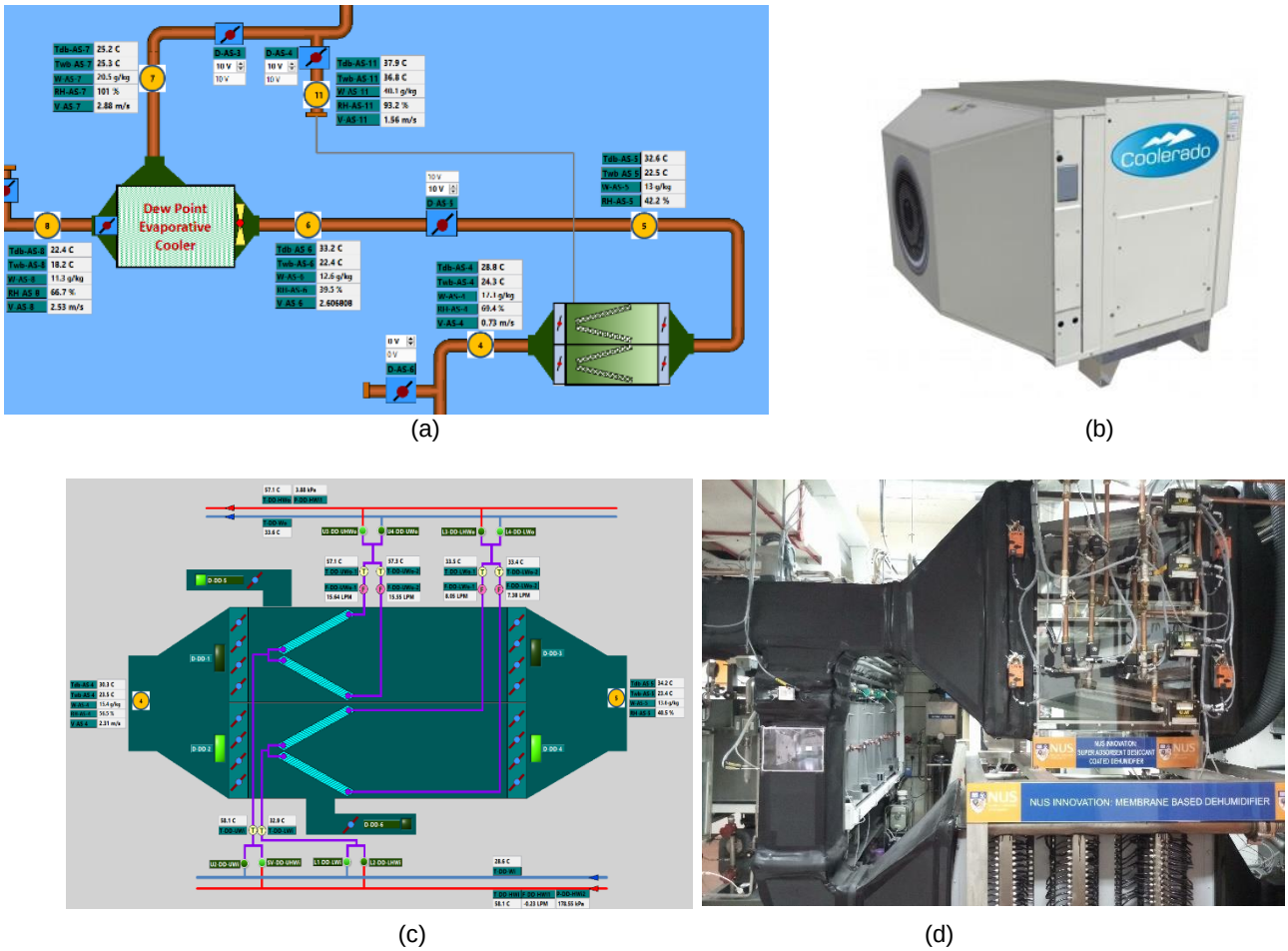

(a) (b)

(c) (d)

Figure 1: (a) Schematic of a Solid Desiccant Coated Heat Exchanger-Dehumidifier (SDHED) integrated with dew point evaporative cooler, (b) dew-point evaporator cooler, Coolerado cooler Model: M30 (b) schematic diagram and (d) photo graphical view of SDHED.

The two beds operates as batch mode: operating adsorption and desorption alternatively. Each bed comprises with two heat exchangers coated with type-RD silica gel. The fine silica-gel powder mixed with Hydroxyethyl cellulose (HEC) used as a binder since it has the best binding force between the type silica-gel powder and the metal fins as well as it didn't affect the adsorbate uptake capacity [24]. During the dip-coating process, the heat exchanger was mounted onto a rotation machine to ensure the uniform coating layer. After that, the heat exchanger was placed into an oven for curing at 120 °C for 12 hours. In adsorption batch of dehumidification process, the silica gel coating on heat exchanger adsorbs the moisture when the air passing through on it. The adsorption heat, generating from adsorption process, is carried away by the cold water flowing from cooling tower to the heat exchanger. In desorption batch of regeneration process, the hot water from the waste heat recovery system heat up the silica gel to regenerate the moisture from the adsorbent. After a moment long the silica gel is dried and ready to adsorb the moisture again in the dehumidification process. In this way two beds are operating alternatively in adsorption and desorption process.

In this test run, dry bulb temperature, wet bulb temperature, flow velocity and pressure drop of inlet and outlet air, and temperature and flow rate of inlet and outlet water are measured, and the measurement data are log into the computer by a data acquisition instruments National Instrument CRio-9067 and LabVIEW software. Dry and wet bulb temperature of air and water is measured with PT 100 RTD 1/10 din temperature sensors with accuracy of ±0.01 °C. A hot-wire anemometer is employed, with an accuracy of ±0.004 m/s of measured value, then the air flow rate can be calculated. The mass flow rate of water is obtained based on the readings of the electromagnetic flowmeter.

3. THEORETICAL ANALYSIS

There are three aspects to evaluate the performance of SDHED; heat transfer, moisture removing rate and coefficient of performance. There are two heat transfer process in SDHED. Heat transfer process in dehumidification mode is that the adsorption heat generating in adsorbent due to moisture adsorption process is required to be

removed by cooling water. In regeneration mode, heat from hot water is required to transfer to the adsorbent to increase its temperature, so that moisture from the adsorbent can be desorbed. In order to evaluate the heat transfer performance of solid desiccant coated heat exchanger, we focused on the impact of air velocity on the effectiveness of heat exchanger ε and number of transfer unit (NTU) to determine the optimal air velocity. Heat transfer coefficient and regeneration heat are needed to calculate to do the analysis of the ε-NTU guide. Heat transfer coefficient can be calculated as follow;

$$U = \frac{\dot{Q_{RH}}}{A\ .\ LMTD} \tag{1}$$

Where:

Q_{RH} = regeneration heat (kW)
A = heat transfer area (m^2)
$LMTD$ = log-mean temperature difference (K)
U = heat transfer coefficient ($kW/m^2.K$)

The total input thermal energy is the heat energy of hot water to heat up silica gel to release the moisture. The time average of the transient regeneration heat during the dehumidification process (tcycle) can be calculated as follows;

$$\dot{Q_{RH}} = \frac{\int_0^{t_{cycle}} \dot{m}_{hw} c_{pw} (T_{hwi} - T_{hwo}) dt}{t_{cycle}} \tag{2}$$

Where:

m_{hw} = hot water flow rate (kg/s)
c_{pw} = specific heat capacity of water (kJ/kg.K)
T_{hwi} = hot water inlet temperature (K)
T_{hwo} = hot water outlet temperature (K)
t_{cycle} = cycle time (s)

ε and NTU are key parameters to evaluate heat transfer performance of SDHED. ε is the ratio between the actual heat transfer amount and the ultimate heat that transfer when area is infinity. NTU is the ratio between total thermal conductance (UA) and the heat capacity $(m\ cp)_{min}$ of fluid. ε-NTU guides the design and calculation of heat exchanger. For comparison, ε and NTU are defined by equations. The heat exchanger effectiveness and the heat transfer unit are derived as

$$\varepsilon = \frac{(T_{hwi} - T_{hwo})}{(T_{hwi} - T_{ai})} \tag{3}$$

$$NTU = \frac{UA}{(\dot{m_{hw}} c_{pw})} \tag{4}$$

Where:

ε = effectiveness of heat exchanger (-)
NTU = heat transfer unit (-)
T_{ai} = inlet air temperature (K)
T_{hwo} = hot water outlet temperature (K)
T_{cycle} = cycle time (s)

The coefficient of performance for the dehumidification process is defined as the latent load divided by the total thermal energy input employed for regeneration process, and it represents the overall system capacity and energy efficiency. It can be calculated as;

$$COP_{DD} = \frac{m_{MRR}\ \ h_{fg}}{\dot{Q_{RH}}} \tag{5}$$

The moisture removing rate of SDHED can be defined as the time average of the transient moisture removal during the dehumidification process (t_{cycle}), and can be calculated as follows;

$$m_{MRR} = \frac{\int_0^{t_{cycle}} \dot{m}_a (w_{in} - w_{out}) dt}{t_{cycle}} \tag{6}$$

Where:

COP_{DD} = coefficient performance of desiccant dehumidifier (-)
m_{MRR} = moisture removing rate ($kg_{moisture}/s$)
ma = mass flowrate of air (kg_{dryair}/s)
h_{fg} = latent heat of vaporisation (kJ/kg)

w_{in} = humidity ration of inlet air (kg/kg)
w_{out} = humidity ration of outlet air (kg/kg)

The overall electrical *COP* of the integrated dehumidification-evaporative cooling process is calculated as

$$COP_{DD+DEC} = \frac{\dot{m}_a (h_{a,in} - h_{a,out})}{W_{Fan} + W_{Pump}} \quad (7)$$

Where:
COP_{DD+DEC} = electrical COP of desiccant dehumidifier and dew point evaporative cooler (-)
W_{Fan} = electricity consumed by the fans (kW)
W_{Pump} = electricity consumed by the pumps (kW)
$h_{a,in}$ = enthalpy of the air at the dehumidifier inlet (kJ/kg)
$h_{a,out}$ = enthalpy at the evaporative cooler outlet (kJ/kg)

4. RESULT AND DISCUSSION

In this study dynamic performance in terms of outlet air conditions is tested under various operating conditions. The experimental results of the desiccant dehumidifier equipped with the adsorbent coated heat exchangers are analysed. The operation parameters are as follows: the inlet air, 28 °C, 19.5 g/kg, velocity of inlet air is varied from 0.5 to 5.5 m/s, and hot water temperature is ranging from 55 to 82 °C. The sampling interval is 1s and the cycle switch time is ranging from 150 to 450 second. The average values of outlet air temperature as well as humidity ratio are adopted. Figure 2 shows the transient temperature and humidity profiles for the air. At the beginning of each cycle, the air humidity drops significantly due to the high adsorption capacity of the desiccant. Accordingly, the air temperature increases due to the released adsorption heat. With the desiccant getting saturated, the moisture removal capacity degrades, and the variations of air temperature and air humidity become smaller.

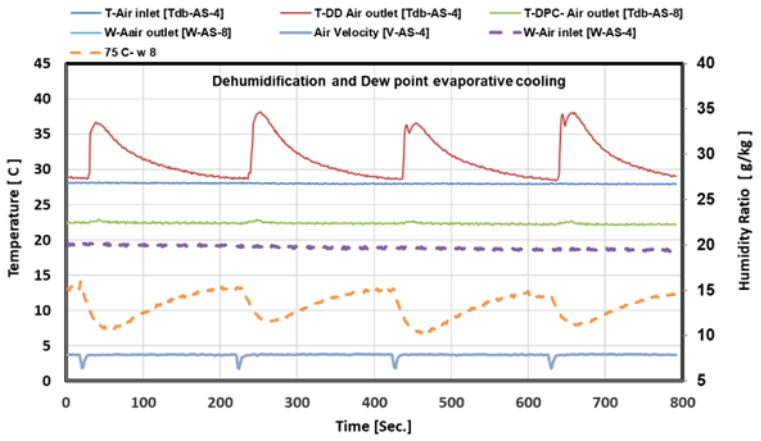

Figure 2: Transient temperature and humidity profiles of the air

Figure 3 shows the transient temperature profiles for the water side. The outlet temperatures for both hot water and cooling water deviate significantly from the inlet values at the beginning of each cycle due to high adsorption/regeneration rates. At the end of each cycle, the water temperatures become stable when the adsorption and desorption slow down.

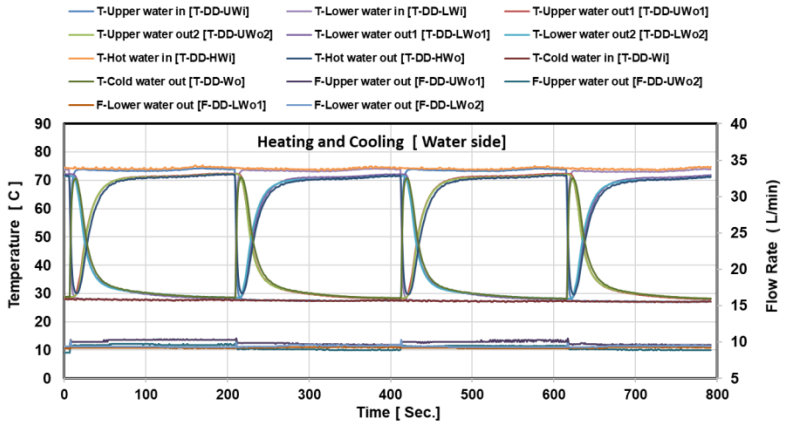

Figure 3: Transient temperature profiles for water side

Figure 4 shows the temperature and humidity ratio of the air at different locations. The humidity ratio of the air drops significantly after dehumidification. However, its temperature increases due to the sorption heat. The higher the moisture removal rate, the higher the air temperature is. On the other hand, the indirective evaporative cooler is able to cool down the air to 22.5 °C regardless of the inlet air temperature and humidity ratio. It is also worth noticing that the humidity ratio of the air remains unchanged after the cooler, since the air is not in contact with water.

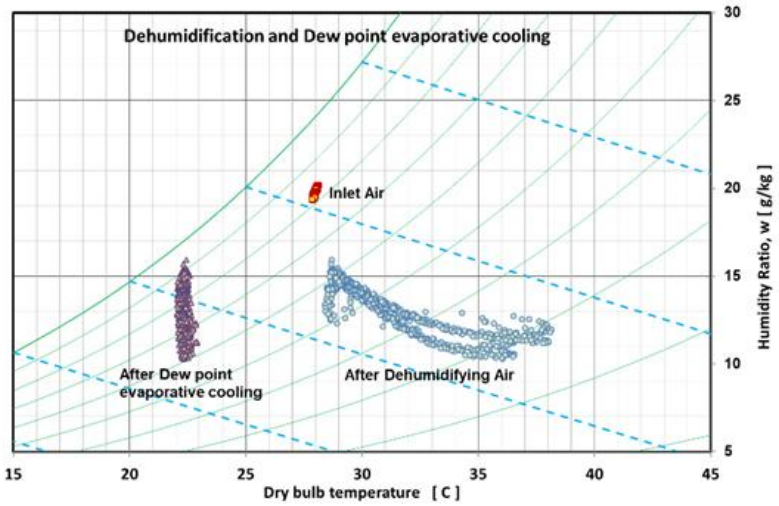

Figure 4: Temperature and humidity ratio of the air at different locations

Figure 5 depicts the transient heating power and moisture removal rate. The heating power has a peak value during the switching period. This is because the coated heat exchanger has to be heated from the adsorption temperature to the desorption temperature. Such a thermal inertia results in substantial energy consumption. On the other hand, the moisture removal rate is high at the beginning of each cycle, because the uptake of the desiccant is small after regeneration.

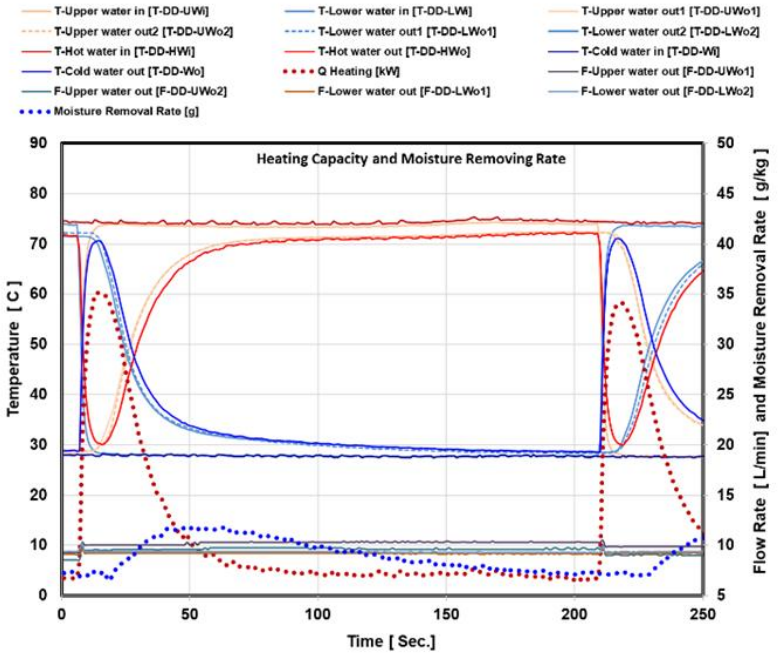

Figure 5: Transient heating power and moisture removal rate

Figure 6 plots the heat transfer unit and heat exchanger effectiveness under varying air velocities. The *NTU* is higher under higher air velocities. The reason is that a higher air velocity promotes heat transfer coefficient. In contrast, the heat exchanger effectiveness degrades at higher air velocities. This is because the residence time for heat and mas transfer decreases at higher air velocities, resulting in incomplete heat transfer between the air and the water.

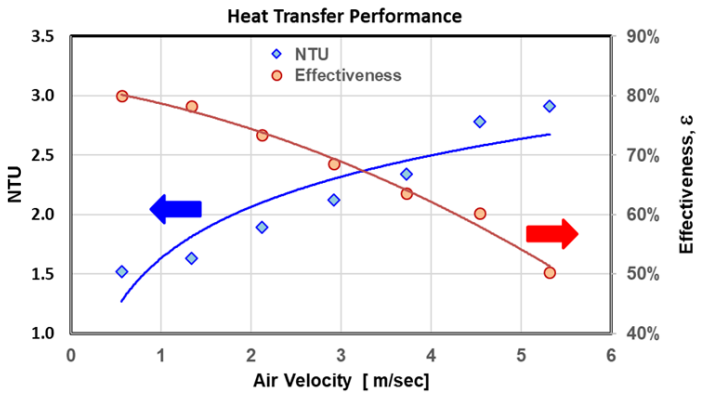

Figure 6: Heat transfer unit and heat exchanger effectiveness under varying air velocities

Figure 7 summarises the moisture removal rate and dehumidification COP under varying hot water temperatures. The moisture removal rate is promoted by higher hot water temperatures. The reason is that a higher hot water temperature enables a more complete regeneration, improving the regeneration capability of the desiccant. In contrast, the dehumidification COP degrades at higher hot water temperatures due to more heat losses.

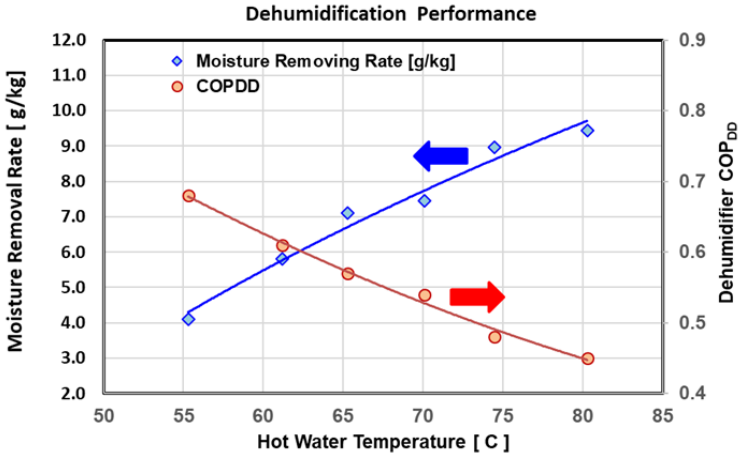

Figure 7: Moisture removal rate and dehumidification COP under different hot water temperatures

Figure 8 plots the COP of the integrated dehumidification-evaporative cooling process under different cycle times. The overall COP first increases with increasing the cycle, because a longer cycle time allows more thorough utilisation of the desiccant's adsorption potential. However, the moisture removal rate becomes smaller when the desiccant gets saturated, leading to a higher air humidity. The performance of the evaporative cooler degrades at a higher air humidity, resulting in the degradation of the overall COP. Consequently, the overall system COP is maximised at a medium cycle time of around 300 s.

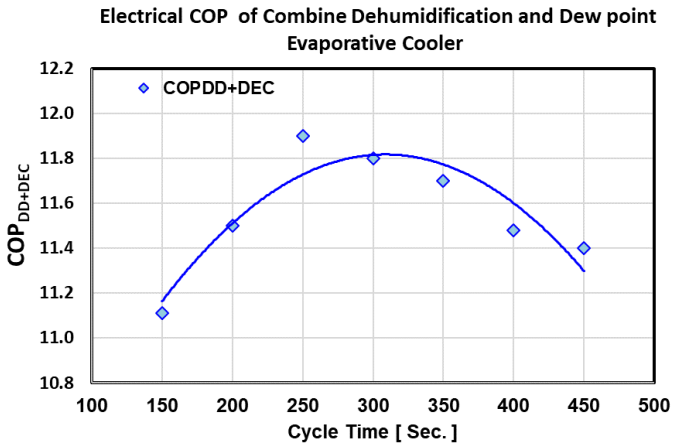

Figure 8: Overall system COP under varying cycle times

5. CONCLUSIONS

A pilot scale Solid Desiccant Coated Heat Exchanger-Dehumidifier (SDHED) integrated with dew point evaporative cooler has been developed and experimentally investigated. A number of experiments were carried out to determine the optimal operation parameters of the system depending on the weather condition (outside air temperature and humidity ratio) and availability of waste heat temperature. The heat transfer unit of the desiccant coated heat exchanger was observed to be higher at higher air velocities, while a higher air velocity results in a lower heat exchanger effectiveness. Additionally, a higher hot water temperature promotes the moisture removal rate while leading to a lower dehumidification COP. For the integrated dehumidification-evaporative cooling process, the optimum COP is achieved when the switching time is 300 s.

6. REFERENCES

BCA building energy benchmarking report 2014. Building construction Authority, Singapore. 2014.

http://www.nea.gov.sg/weather-climate/climate/local-climatology, May, 2018.

Oh SJ, Ng KC, Thu K, Ja MK, Islam MR, Chun W & Chua KJE, Studying the performance of a dehumidifier with adsorbent coated heat exchangers for tropical climate operations, Science and Technology for the Built Environment (2017) 23, 127–135.

Jones RR. Ozone depletion and its effects on human populations. Br J Dermatol 1992;41:2e6.

Pesaran AA. Review of desiccant dehumidification technology. 1994. http://dx.doi.org/10.2172/934386.

Ramzy A, Elawady WM, Abdelmeguid H. Modelling of heat and moisture transfer in desiccant packed bed utilizing spherical particles of clay impregnated with CaCl2. Appl Therm Eng 2014;66:499e506.

Ramzy KA, Kadoli R, Ashok Babu TP. Improved utilisation of desiccant material in packed bed dehumidifier using composite particles. Renew Energy 2011;36:732e42. http://dx.doi.org/10.1016/j.renene.2010.06.038.

Hamed AM, Abd-Elrahman WR, El-Emam SH, Awad MM. Theoretical and experimental investigation on the transient coupled heat and mass transfer in a radial flow desiccant packed bed. Energy Convers Manag 2013;65:262e71.

Weixing Y, Yi Z, Xiaoru L, Xiugan Y. Study of a new modified cross-cooled compact solid desiccant dehumidifier. Appl Therm Eng 2008;28:2257e66.

Zheng Y, Yuan W, Wang H, Yuan X. Experiments on dynamic dehumidification of internally cooling compact solid dehumidifier. J Beijing Univ Aeronaut Astronaut 2006;32:1100e3.

Fathalah K, Aly SE. Study of a waste heat driven modified packed desiccant bed dehumidifier. Energy Convers Manag 1996;37:457e71.

121: Feasibility study of thermochemical energy storage applied in Tibet, China

Liu YANG [1], Cheng ZENG[2], Xiaojing HAN[1], Ming SONG[1], Yongliang SHEN[1], Ashish SHUKLA[2], Shuli LIU[1, 2]

1 Beijing Institute of Technology, Beijing 100081, China, yangliu0620@126.com
2 Coventry University, Coventry CV1 2HF, United Kingdom, zengc3@coventry.ac.uk

In the southwest border of China, there is Tibet, the 'Roof of the world'. While its fragile environment is damaging due to widespread utilisation of biomass in its domestic sector. However, Tibet has abundant solar energy, posing a huge potential for its utilisation in domestic sector to tackle the environmental issues and maintain healthy indoor environment. As a diurnal resource, energy storage systems are critical. Over the last decade, thermochemical energy storage (TCES), as a version of thermal energy storage, is taking a surge in research of solar energy storage owing to the advantages of high energy density and ambient temperature storage without degradation. However, some challenges remain to be addressed including suitable environmental conditions and materials, relatively high capital cost and system complexity. In this paper, a feasibility study of TCES applied in Tibetan climate is conducted. It demonstrates the suitability of TCES in Tibet, reviews thermochemical materials for building applications and analyses the required storage volume to fully compensate the heating demand of a typical Tibetan home in winter. Additionally, an analysis is conducted on TCES's economical and CO_2 savings comparing against electric heaters, air conditioners and natural gas boilers that are the popular heating methods in Tibet.

Keywords: Thermochemical energy storage; Heating; Tibet; Feasibility study

1. INTRODUCTION

1.1. Background of the energy and environment in Tibet

Tibet, known as 'the Roof of the World', is at the southwest border of China. The high-altitude geography cultivates its characteristics, including the energy resources, the climate features, and the fragile eco-environment. The outdoor air temperature is low in Tibet with the annual average temperature at 8.1 °C and winter average temperature at 3 °C. This has led to an increasing space heating demand, especially in winter. According to the survey (Zhou et al., 2009: p187-193), energy consumed by domestic heating has been increased to 42% of total energy consumption of Tibet in 2005.

However, Tibet is short in primary energy sources. Taking Lhasa as an example, it is suffering severe shortage of primary energy sources; as a result, energy supply such as coal, gas, and oil requires long-distance transportation, mainly from Qinghai Province and Sichuan Province in 2000 km away. This has pushes the price of coal and natural gas in Lhasa to about 2000 CNY/tonne and 6-7CNY/m^3 respectively. Instead, biomass has been widely used. Reported in the study (Ping et al., 2011: p514-523), the share of biomass in total energy consumption of Tibet account for nearly 80% in urban and 95% in rural areas. Specifically, yak dung has been widely used in heating in rural areas (Xiao et al., 2015: p406-412).

With heavily relying on biomass and fossil fuel, environmental issues have become critical. Air pollutants, including nitrogen oxides (NOx) and volatile organic compounds (VOCs), emit to environment during combustion, then react and produce ozone under the strong sunshine catalysis. Nitrogen oxides can then react with the ozone and form aerosol pollutants. While Tibet stands out for abundant solar energy resource. It is the region taking up the most solar energy radiation in China, sharing more than 60% of total solar energy with annual solar radiation at 7000-8000 MJ/m^2. The annual hours of average sunlight ranges between 1600 and 3400 hours, with 275-330 days having over 6 hours of sunshine.

The government has been supporting the development of solar thermal utilisation in Tibet. The 13th Five-Year Plan for the Construction of Urban Centralised Heating Facilities in the Tibet has been formulated to promote the construction of the solar energy heating and encourage clean energy utilisation. Many regional guidelines are aimed to develop heat supply infrastructures and promote corresponding technology innovations. Additionally, to support the development, some financial subsidy policies have been provided by the local government. Therefore, in Tibet, utilising solar energy in domestic sector is of significance in tackling the current environmental issues and providing a sustainable approach to meet the increasing space heating demand.

1.2. A short review of the thermochemical energy storage and why introduce it to Tibet

Thermal energy storage can be classified into three categories, namely, sensible, latent, and thermochemical energy storage (TCES). Thermochemical energy storage has been gaining research attention due to the principle of reversible reactions.

In a cycling reaction, thermal energy is stored in an endothermic reaction and released in the reversible exothermic reaction. Compared to sensible and latent thermal storage, the features of TCES are follows.

- During charging/desorption process, additional heat is required to break the binding force between the sorption couple, which is much higher than the evaporation heat of sorbate itself, leading to remarkable energy density;
- In discharging/sorption process, the recombination of bond would not occur until the direct contact between sorption couples. This enables the charged energy to be stored for theoretically unlimited time with little heat loss (Tatsidjodoung et al., 2013: p327-349, N'Tsoukpoe et al., 2009: p2385-2396); and
- The flexible reaction temperature of TCES is another potential advantage for practical applications. The charging and discharging temperature of TCES are determined by the working conditions, allowing flexibility in applications (Yu et al., 2013: p489-514).

However, drawbacks have been reported as the challenges for commercialising the TCES in domestic applications. These are low heat and mass transfer rates, high-pressure drops when using air to solid material pairs (Aydin et al., 2015: p356-367), the system complexity, and relative large capital cost (Yu et al., 2013: p489-514).

While the TCES performance, especially heat and mass transfer, is strongly influenced by ambient conditions. Applying the technique in Tibet can help mitigate the challenges and improve system performance. For an open TCES system (system connects to the ambient), its operating performance depends on solar radiation, air temperature, humidity and air pressure. In charging, the strong solar radiation in Tibet can boost the desorption performance with sufficient energy supply. Meanwhile, it is noted that the pressure difference between vapour and thermochemical materials is increased theoretically due to the high altitude and lower air pressure (Molenda et al., 2013: p76-81, van Essen et al., 2009: p514-524). Take Lhasa as an example, the average vapour partial pressure

is 40% lower than that of plain regions, ranging from 0.24kPa to 1.22 kPa (Zhang et al., 2000: p207-212), which is desirable for the heat and mass transfer process.

Overall, TCES technology has shown the potential for solar energy storage in Tibet with improved performance. Considering the energy, environment and governmental support in solar energy utilisation, it is of significant importance to apply the TCES technology in domestic sector of Tibet.

1.3. A statement of paper content

This paper reviews the energy storage techniques, especially the thermochemical energy storage and the relevant thermochemical materials for building applications. Investigations have been conducted on Tibet climate, local heating demand, and the relevant thermochemical parameters. The feasibility study of using TCES technique in Tibet as a diurnal energy storage method has been stated. The system description and required volume thermochemical material are also given. Additionally, CO_2 and economic analysis of the TCES system in Tibet are conducted with the comparison of electric heaters, air conditioner, and boiler.

2. MATERIALS SELECTION ACCORDING TO TIBET CLIMATE AND APPLICATION

There are various thermochemical materials which can be categorised into chemical reaction, solid adsorption, composites and liquid sorption (Figure 1). This section demonstrates the selection of suitable thermochemical material for the application of Tibet domestic sector.

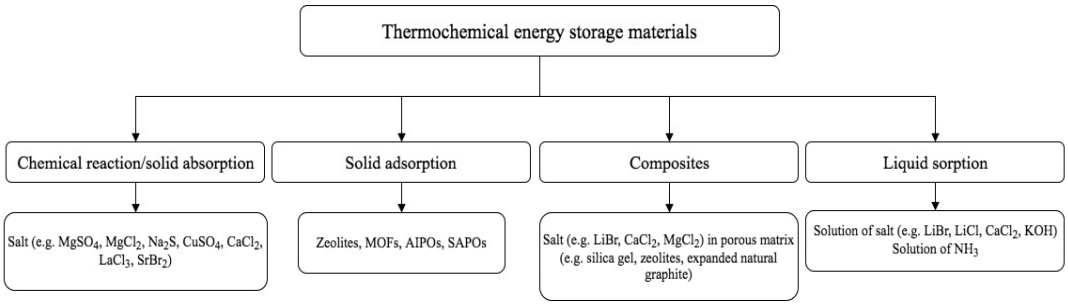

Figure 1: Sorption thermal storage methods and materials (Yu et al., 2013: p489-514)

2.1. Geography and weather condition in Tibet

Tibet features high solar radiation, low temperature, and low atmospheric pressure. These conditions can improve TCES performance and outline material selection criteria.

For thermochemical materials in the open system, since charging is supported by solar radiation, the required charging temperature should be reachable by the relevant solar collectors. Considering outdoor air temperature in Tibet, it fluctuates greatly between day and night, with diurnal temperature difference recorded reaching up to 17 °C (Wang *et al.*, 2013: p110-117). This leads to the necessity of charging the thermochemical materials in the sunny days and discharging in cold nights. Additionally, heating period in a year is remarkably longer than other plain regions. Thus, the materials should offer a good mechanical and chemical stability during charging and discharging cycles. Furthermore, since the system is connect to ambient, the thermochemical materials should be safe and easy to control.

Heating demand based on the high-altitude area

In addition to the climatic features, domestic space heating demand should be considered. To calculate space-heating demand, space heating power index has been used.

Table 1 shows the space heating power index for cities in Tibet (Liu *et al.*, 2011: p40-46). These figures are suggested by the *Design Code of City Heating Network* (2010).

Table 1: Space heating power indexes of residential buildings for typical cities in Tibet

City	Average outdoor air temperature in winter (°C)	Space heating power index (W/m^2)
Lhasa	1.0	56.0
Linzhi	2.3	60.9
Zuogong	-1.4	67.6
Dingri	-2.4	66.9
Cuona	-3.5	72.8
Naqu	-5.0	70.2
Anduo	-5.9	66.7

2.2. Materials selection based on the available energy, energy demand, and limitation of the materials

Thermochemical material is the key element of a TCES system. Table 2 illustrates the properties of some thermochemical materials studied in literature. Figure 2 compares the materials using their theoretical energy density and required charging temperature. According to Table 2 and Figure 2 when apply the materials in Tibet, advantages and disadvantages of the materials are demonstrated as follow.

Chemical reaction/solid absorption materials

- Chemical reaction materials have shown high theoretical energy density ranging from 500 kWh/m^3 to 750 kWh/m^3 and reachable charging temperature with less than 150 °C;
- However, their performance in hydration and dehydration tests is problematic including possible deliquescence behaviour, agglomeration phenomenon, drop of reaction kinetics (Donkers *et al.*, 2016: p25-32), toxic behaviour (Donkers et al., 2016: p25-32), formation of irritation gas (Fopah-Lele and Tamba, 2017: p175-187), high vacuum requisition, severe corrosion (de Boer *et al.*, 2003: p3-19), etc.

Liquid sorption materials

- Energy density of liquid sorption material is notable with KOH/H_2O, $LiCl/H_2O$, and $LiBr/H_2O$ at over 300 kWh/m^3;
- The charging temperature are relatively low ranging from 60°C to 70°C which are suitable for solar collectors.
- However, materials like NaOH and KOH is severely corrosive; and
- The costs of some liquid materials are high. For instance, the price of LiCl and LiBr is around 44 and 27 CNY/kg which is 3 to 10 times higher than that of chemical reaction materials.

Composite materials

- Composite materials are aimed to overcome issues of chemical reaction materials. Improvements in thermal conductivity are appealing when comparing that of chemical reaction materials;
- Also, theoretical energy storage density can be improved compared to solid adsorption materials;
- However, the composites are in material research level. Researchers are finding suitable host matrix and chemical reaction material pairs for diverse application conditions.

Solid adsorption materials

- Solid adsorption materials take advantages in relatively high water uptake capacity with zeolites at about 240 g/kg;
- Materials are easy to control in reversible cycles without report of decomposition or hazardous products;
- However, solid adsorption materials are relatively low in energy density ranging from 160 kWh/m^3 to 220 kWh/m^3;
- The required charging temperature can be over 150 °C. Especially for zeolite 4A and 13X, the suggested charging temperature is 180 °C.

Overall, each material has its own characteristics and compromises may have to be made in selecting the most suitable material. For the application in Tibet, as stated, an open TCES system with ability in short-term energy storage has been targeted. For TCES materials, therefore, safety and stability in charging and discharging cycles should be carefully considered. Additionally, energy storage density should be relatively high to ensure system simplicity and compactness.
Based on the review of the thermochemical materials, zeolites stand out due to its good cycling stability, high water uptake capacity and suitable adsorption temperature for domestic heating.

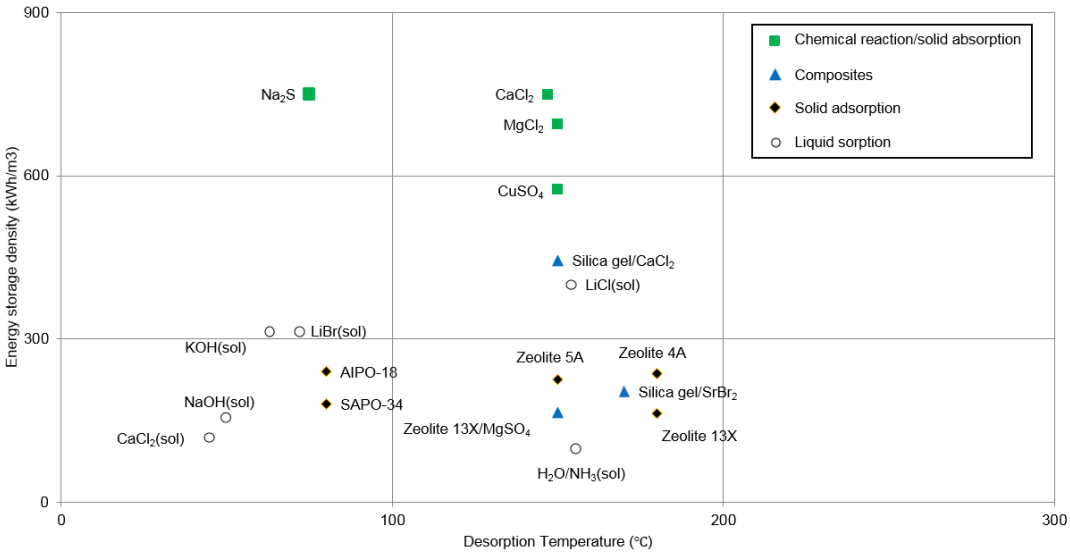

Figure 2: Energy density and charging temperature of typical thermochemical materials

Table 2: Parameter analysis of typical thermochemical materials

	Material	Theoretical energy density (kWh/m^3)	Desorption temperature (°C)	Price (CNY/kg)	Remarks	Refs.
Chemical reaction /solid absorption	$MgCl_2$	694.4	68 - 150	0.61-0.87	• Deliquescence at 20 - 100 °C; forms HCl gas at 140 - 150 °C.	(Glasser, 2014: p526-530)
	$SrBr_2$	628	45 - 52	6.62 - 13.32	• Good cycling stability; • Relatively high in price; cause skin and eye irritation.	(N'Tsoukpoe *et al.*, 2014: p1-16)
	Na_2S	750	66 - 75	2.09 - 2.79	• High theoretical energy density; • Forms H_2S in hydration; severely corrosive to copper, etc.	(Donkers *et al.*, 2017: p45-68)
	$CuSO_4$	574	28 - 150	5.14 - 15.50	• Toxic; reaction kinetics drop substantially in cycles.	(Glasser, 2014: p526-530)
	$CaCl_2$	750	32 - 147	3.22 - 8.45	• Substantial temperature gap between $CaCl_2{\cdot}4H_2O$ and $CaCl_2{\cdot}2H_2O$ at over 120 °C; over-hydration	(Glasser, 2014: p526-530
Solid adsorption	Silica gel	50	88	9.91 – 11.89	• Low in energy storage density and temperature-lift.	(N'Tsoukpoe et al., 2009: p2385-2396)
	Zeolite 4A	236	180	6.61 – 26.42	• High water uptake property and achievable charging temperature; • Relatively low energy storage density than solid absorption materials.	(Demir *et al.*, 2008: p2381-2403)
	Zeolite 5A	226	30 - 350	5.28 – 7.93		
	Zeolite 13X	163	180	9.91 – 16.52		(N'Tsoukpoe et al., 2009: p2385-2396)
	SAPO-34	180	80	33.03-99.09	• Molecule sieve property, with the water uptake up to 250 g/kg; • Degradation reported in charging and discharging cycles.	(Henninger *et al.*, 2010: p1692-702,)
	AlPO-18	240	80	n.a.		
Liquid sorption	$CaCl_2$(sol)	119	44.8	2.53	• Low charging temperature; • Relatively low cost than other liquid materials.	(Hui *et al.*, 2011: p2427-2436)
	NaOH(sol)	154	50	22.06	• High water uptake property; however, strong corrosion.	
	KOH(sol)	313	63	8.81	• High theoretical energy density and high water uptake property; • Achievable charging temperature; • Strong corrosion.	
	LiCl(sol)	400	65.6	44.1	• High theoretical energy density and achievable charging temperature; • Relatively high in price.	
	LiBr(sol)	313	72	26.79	• High theoretical energy density and achievable charging temperature; however, relatively high in price.	
	H_2O/NH_3(sol)	98	155.5	2.96	• Low cost and low energy density; • Suitable for the refrigeration with the evaporator temperature lower than 0°C.	

	Material	Theoretical energy density (kWh/m^3)	Desorption temperature (°C)	Price (CNY/kg)	Remarks	Refs.
Composites	Silica gel/$SrBr_2$	203	170	n.a.	• Improved energy density and water uptake at 203 kWh/m^3 and 0.22 kgH_2O/kg respectively; • The composite is reported stable during 14 charging and discharging cycles.	(Courbon *et al.*, 2017: p1184-1194)
	Silica gel/$CaCl_2$	445	150		• For the host material of $CaCl_2$, silica gel is suggested being better than alumina and bentonite due to lower pore blocking and higher water storage values.	(Jabbari-Hichri *et al.*, 2017: p177-185)
	Zeolite 13X/$MgSO_4$	166	150		• Optimum percentage of $MgSO_4$ is 15 wt%; • Energy density remains stable in 3 charging and discharging cycles.	(Hongois *et al.*, 2011: p1831-1837)

3. THEORETICAL ANALYSIS

3.1. System description

A schematic diagram of the TCES energy storage system is shown in Figure 3(a). The system is comprised of concentrated solar power collectors, TCES reactor, heat exchanger, evaporative humidifier, air to air heat exchangers, fan and pumps. The system operates in charging and discharging modes in winter (November to February). It charges the TCES reactor in the day and discharge the reactor in the night.

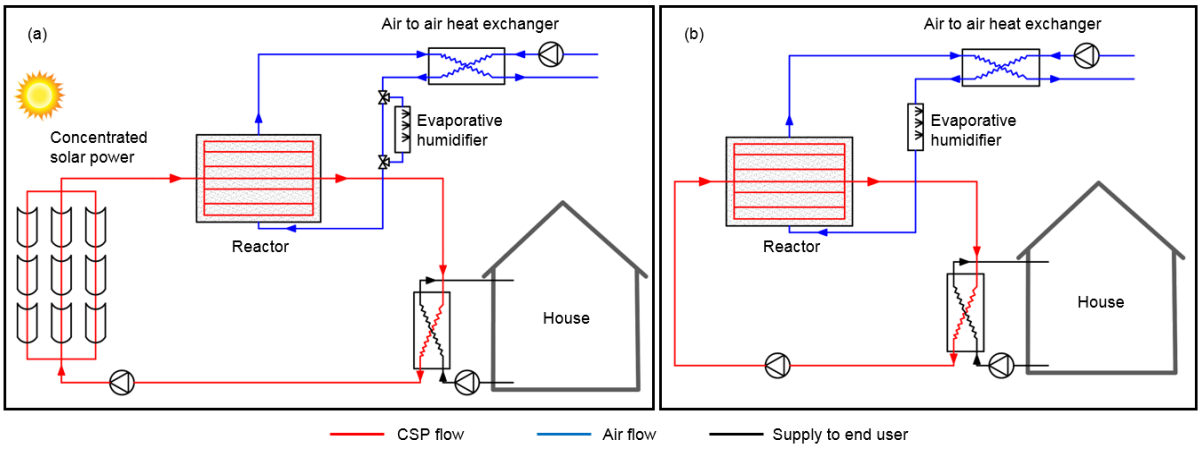

Figure 3: Schematic of the TCES system in (a) charging and (b) discharging focusing on CSP and airflow

In sunny times the system operates in charging mode, where the concentrated solar collectors heat its working fluid (CSP flow) by absorbing solar radiation with the ability in reaching to 200-300 °C (Schaube et al., 2011: p1006-1012, Lei et al., 2013: p107-115). The heated CSP fluid flows across the TCES reactor and heats up the TCES material before flowing through the end user side heat exchanger and back to the solar collectors. While the CSP fluid is being circulated, the airflow is being driven from the ambient and blown through the TCES reactor (bypass the evaporative humidifier in charging mode). The airflow takes out any moisture from the heated TCES material due to water vapour pressure difference between the airflow and TCES material. Therefore, the system is charged by heating the TCES material and removing its adsorbed moistures.

In cold times (such as the morning and midnight), when the end user requires space heating, the stored energy within the system can be discharged through rehydrating the TCES material. Shown in Figure 3(b), in discharging, ambient air flows through the evaporative humidifier before entering the reactor. The humidifier is used to introduce moisture to the air stream. The airflow then takes the moisture to the reactor and hydrates the TCES material. The released energy from the TCES material is extracted by the circulated CSP flow and supplies to the end user.

3.2. Required volume of thermochemical energy storage material for a typical dwelling in Tibet

A two-floor dwelling with total floor area at 100 m^2 has been chosen as a representative dwelling for the theoretical analysis. To calculate space-heating demand, according to Table 1, the average heating power index is 63 W/m^2, which is used in this paper. For a typical day in winter, there are around 8 hours, from 0:00 to 8:00, when the outdoor temperature is lower than that of the indoor temperature with the difference at around 10 °C. The TCES system is designed to provide space heating in this period. Therefore, the space heating demand for the dwelling per heating period is 50.4 kWh.

Energy density of the thermochemical material zeolite 13X is determined based on its adsorption isotherm, charging temperature and climate conditions. The adsorption isotherm for zeolite 13X has been calculated using the Dubinin-Astakhov equation (Mette et al., 2014: p555-561, Gorbach et al., 2004: p29-46) (Figure 4).

According to National Bureau of Statistics of China (2016), the average outdoor air temperature of Tibet winter is 2.6 °C; and the daily average partial water vapour pressure is 7.3 mbar (Zhang et al., 2000: p207-212). In charging, the initial state of the thermochemical material, zeolite 13X, is assumed equilibrium with its ambient. The initial charging point can be found the isotherm at 0.34 $kg_{H2O}/kg_{zeolite}$. When assume the temperature of zeolite 13X reaches to 180 ºC in charging, its water uptake can drop to 0.078 $kg_{H2O}/kg_{zeolite}$, as marked in Figure 4. Therefore, the change of water uptake ΔX is 0.262 $kg_{H2O}/kg_{zeolite}$.

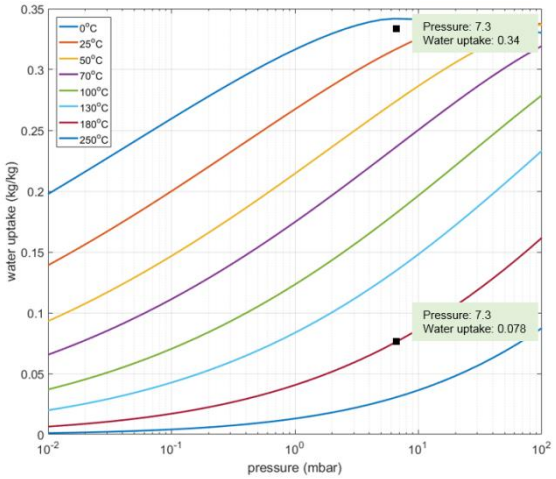

Figure 4: Calculated water vapour adsorption isotherms of zeolite 13X

As enthalpy of adsorption strongly dependent on zeolites water uptake, a polynomial fitting of the measured enthalpy of adsorption of zeolite 13X, reported by (Kim *et al.*, 2016) is used to determine the enthalpy of adsorption at the change of water uptake ΔX. The polynomial fitting is written in Equation 1 1. With a bulk density of zeolite 13X at $\rho = 650\ \mathrm{kg/m^3}$, energy storage density of zeolite 13X can be calculated in Equation 2 2.

Equation 1: The polynomial fitting of the measured adsorption enthalpy of zeolite 13X

$$h_r = 7E+07x^6 - 7E+07x^5 + 3E+07x^4 - 7E+06x^3 + 899951x^2 - 69983x + 6491.3 \qquad \textit{Equation 1}$$

Equation 2: Calculation of the energy storage density

$$E = \frac{\int_{0.078}^{0.34} h_r \times \rho}{3600} = 121\ kWh/m^3 \qquad \textit{Equation 2}$$

Where:

- x = water uptake of zeolite 13X ($kg_{H2O}/kg_{zeolite}$)
- h_r = the measured adsorption enthalpy of zeolite 13X (kJ/kg_{H2O})
- ρ = energy storage density of zeolite 13X ($\mathrm{kg/m^3}$)

Additionally, reactor efficiency, heat exchanger efficiency and heat loss are the main factors for the stored energy calculation. It can be assumed that the energetic efficiency for reactor in discharging at 55% (Johannes *et al.*, 2015: p80-86) and the efficiency/heat loss for the heat exchanger and facilities such as pipes at 70% (Fakheri, 2007: p1268-1276). To meet the space heating demand at 50.4 kWh per heating period, the required energy to be stored in the thermochemical material is 130.9 kWh. The related volume and weight of thermochemical material zeolite 13X is 1.08 m^3 and 702 kg respectively.

3.3. CO_2 savings and economic evaluation of the system

The environmental challenges in Tibet have been gaining importance in controlling greenhouse gas emissions, especially for CO_2 emissions. Applying clean and renewable energy sources in Tibet is a promising solution to tackle the issues. In the domestic sector of Tibet, popular heating methods are electric heaters (EH), natural gas-fired boilers (BO), and air conditioning units (AC). In this section, calculations have been conducted on CO_2 emissions and cost savings of these conventional heating methods, and compared with that of the proposed TCES system. The CO_2 emissions are calculated using Equation 3 and Equation 4 (IPCC, 2006).

Equation 3 and Equation 4 : CO2 emissions calculation

$$CO2_{EH,AC,TCES} = \sum_{N=0}^{N=15} \xi_{EH,AC,TCES} \times K_e \qquad \textit{Equation 3}$$

$$CO2_{BO} = \sum_{N=0}^{N=15} \xi_{BO} \times K_g \qquad \textit{Equation 4}$$

Where:

- ξ = annual energy consumption (kWh)
- K = CO_2 emission conversion factor ($kgCO_2/kWh$)

The annual energy consumption for the conventional heating methods are calculated as referred to Zottl et al. (2011). For the proposed TCES system, the electricity consumed by the fan, humidifier, and pump is assumed at 150 W. The conversion factor, in Tibet, is 0.78 $kgCO_2/kWh$ for electricity and 0.2 $kgCO_2/kWh$ for natural gas (China National Development and Reform Commission, 2015).

According to the calculations, Figure 5 illustrates the CO_2 savings of the TCES system in 15 year's operation. The TCES system allows for a savings of 4.5, 2.4 and 1.5 tonnes of CO_2 emission saving per year compared to that of electric heater, air conditioning, and boiler. For 15-year operation, noticeably, the TCES system is expected to provide a total 67.9 tonnes of CO_2 saving when compares to electric heaters.

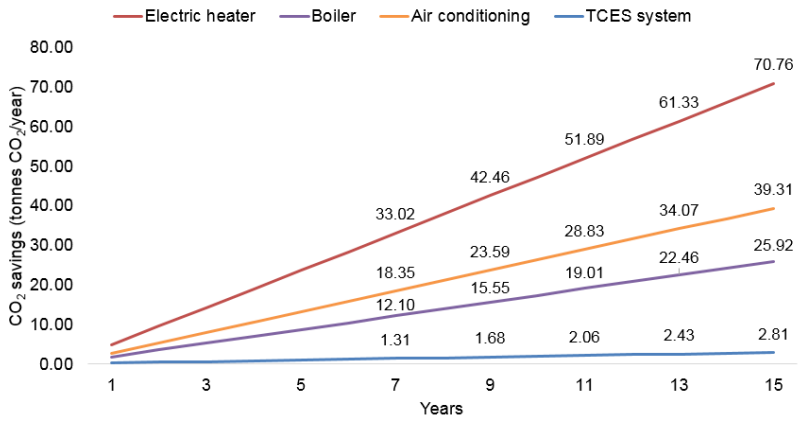

Figure 5: Total CO_2 savings using TCES system comparing with popular heating methods in Tibet

When calculating costs and savings of the proposed TCES system, present worth method has been used. The present value factor (PVF) is given in Equation 5 5.The PVF factor can then be used to calculate the present value of the money for the N^{th} year. The total cost of the TCES system is calculated in

Equation 6.

Equation 5: PVF calculation

$$PVF = \frac{1}{(1+r)^N} \qquad \textit{Equation 5}$$

Equation 6: Total cost calculation

$$\beta_{TCES} = C + \sum_{N=0}^{N=25} (\beta_O + \beta_M) \times PVF$$ *Equation 6*

Where:

- r = the interest rate of USD at 2.00%
- N = year
- C = the system capital cost (USD)
- β_O = operational cost (USD)
- β_M= maintenance cost (USD)

The system capital cost is shown in Table 3. Since the operational and maintenance cost are expected to be low, it is assumed as 3% of the system capital cost, written in Equation 7 7.

Equation 7: Operational and maintenance cost calculation

$$\beta_O + \beta_M = C \times 3\%$$ *Equation 7*

Table 3: Estimation of TCES system capital cost

System components	Price (USD)	System components	Price (USD)
Solar panels (20 m^2)	377	Fan	60
Energy storage tank (1.5 m^3)	90	Pumps	151
TCES material (1.08 m^3)	1016	Pipes, valves, fittings	166
Evaporative humidifier	20	Insulation	121
Heat exchangers	422	System installation cost	377
Total			2800

For the costs of the conventional heating methods, their operational cost can be determined by using Equation 8 8 and Equation 9.

$$\beta_{EH,AC} = \sum_{N=0}^{N=25} \xi_{EH,AC} \times f_e \times PVF$$ *Equation 8*

$$\beta_{BO} = \sum_{N=0}^{N=25} \xi_{BO} \times f_g \times PVF$$ *Equation 9*

Where:

- β = operational cost (USD)
- ξ = the yearly total energy consumption (kWh or m^3)
- f_e= the electricity price (0.075 USD/kWh) (XISANG-GOV, 2014)
- f_g= the natural gas price (0.68 USD/m^3) (XISANG-GOV, 2014)

The cost analysis results are shown in Figure 6. The analysis is conducted based on the total cost of the proposed TCES compared to the cumulative operation cost of the conventional heating methods in 25 years. Comparing with boiler and electric heater, the TCES system can provide an average saving of 537 and 341 USD/year respectively. This makes the cumulative savings of the TCES system exceeds its total cost in 6 and 9 years respectively. After the payback year, when considering operation for 25 years, the cumulative profit for using the TCES system is 8,532 and 4,508 USD compared to that of boiler and electric heater respectively. When comparing with air conditioning, however, the saving for using TCES cannot compensate its total cost until operating for 20 years with 140 USD/year. This is due to the relatively low electricity price in Tibet.

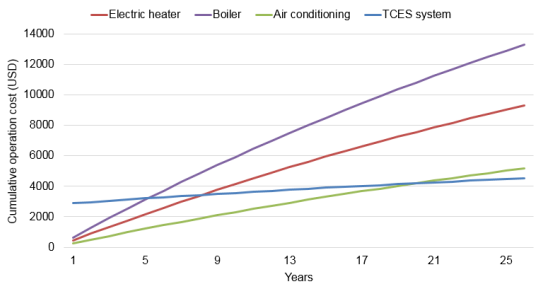

Figure 6: Space heating cost of TCES and conventional heating methods

4. CONCLUSION

In this work, feasibility study of thermochemical energy storage applied in Tibet has been conducted. Investigations have been conducted on Tibet climate features, residential heating demand, thermochemical material selection, TCES system as well as its CO_2 and economic evaluations. According to the climate features, Tibet can be promising in utilising TCES technology with improved performance. To select a suitable material, typical thermochemical materials are evaluated. Zeolite 13X has been selected in diurnal energy storage for space heating of a typical dwelling located in Lhasa. Additionally, theoretical analysis of the system is carried out for the dwelling. Compared to conventional heating methods, it can be concluded that the payback period of the proposed TCES system can be 6 and 9 years compared to natural boilers and electric heaters respectively. Compared to the air conditioning units, the profit margin for the TCES system is unappealing due to the relative high COP level. Considering its advantage in reducing CO_2 emission, however, the proposed TCES system can be a promising solar energy storage technique for domestic heating in Tibet.

5. REFERENCES

Aydin, D., Casey, S. P. & Riffat, S. (2015), "The Latest Advancements On Thermochemical Heat Storage Systems", *Renewable & Sustainable Energy Reviews,* Vol. 41, p.356-367.

China National Bureau of Statistics (2016), China Statistical Yearbook.

China National Development and Reform Commission,'CO_2 Emission Calculation Conversion Factors'. http://qhs.ndrc.gov.cn/zcfg/201605/w020160525509544574361.pdf

Courbon, E., D'ans, P., Permyakova, A., Skrylnyk, O., Steunou, N., Degrez, M. & Frere, M. (2017), "A New Composite Sorbent Based On $Srbr_2$ and Silica Gel for Solar Energy Storage Application with High Energy Storage Density and Stability", *Applied Energy,* Vol. 190, p.1184-1194.

De Boer, R., Haije, W. G. & Veldhuis, J. (2003), "Determination of Structural, Thermodynamic and Phase Properties in The Na_2S-H_2O System for Application in A Chemical Heat Pump", *Thermochimica Acta,* Vol. 395, p.3-19.

Demir, H., Mobedi, M. & Ulku, S. (2008), "A Review On Adsorption Heat Pump: Problems and Solutions", *Renewable & Sustainable Energy Reviews,* Vol. 12, p.2381-2403.

Donkers, P. A. J., Pel, L. & Adan, O. C. G. (2016), "Experimental Studies for The Cyclability of Salt Hydrates for Thermochemical Heat Storage", *Journal of Energy Storage,* Vol. 5, p.25-32.

Donkers, P. A. J., Sogutoglu, L. C., Huinink, H. P., Fischer, H. R. & Adan, O. C. G. (2017), "A Review of Salt Hydrates for Seasonal Heat Storage in Domestic Applications", *Applied Energy,* Vol. 199, p.45-68.

Fakheri, A. (2007), "Heat Exchanger Efficiency", *Journal of Heat Transfer-Transactions of The Asme,* Vol. 129, p.1268-1276.

Fopah-Lele, A. & Tamba, J. G. (2017), "A Review On the Use of $Srbr_2$ $6H_2O$ as A Potential Material for Low Temperature Energy Storage Systems and Building Applications", *Solar Energy Materials and Solar Cells,* Vol. 164, p.175-187.

Glasser, L. (2014), "Thermodynamics of Inorganic Hydration and of Humidity Control, With an Extensive Database of Salt Hydrate Pairs", *Journal of Chemical and Engineering Data,* Vol. 59, p.526-530.

Gorbach, A., Stegmaier, M. & Eigenberger, G. (2004), "Measurement and Modeling of Water Vapor Adsorption On Zeolite 4a-Equilibria and Kinetics", *Adsorption-Journal of The International Adsorption Society,* Vol. 10, p.29-46.

Henninger, S. K., Schmidt, F. P. & Henning, H. M. (2010), "Water Adsorption Characteristics of Novel Materials for Heat Transformation Applications", *Applied Thermal Engineering,* Vol. 30, p.1692-702.

Hongois, S., Kuznik, F., Stevens, P. & Roux, J. (2011), "Development and Characterisation of a New $Mgso_4$-Zeolite Composite for Long-Term Thermal Energy Storage", *Solar Energy Materials and Solar Cells,* Vol. 95, p.1831-1837.

Hui, L., Edem, N. K., Nolwenn, L. P. & Lingai, L. (2011), "Evaluation of A Seasonal Storage System of Solar Energy for House Heating Using Different Absorption Couples", *Energy Conversion and Management,* Vol. 52, p.2427-2436.

Ipcc (2006) Task Force On National Greenhouse Gas Inventories.

Jabbari-Hichri, A., Bennici, S. & Auroux, A. (2017), "Cacl2-Containing Composites as Thermochemical Heat Storage Materials", *Solar Energy Materials and Solar Cells,* Vol. 172, p.177-185.

Johannes, K., Kuznik, F., Hubert, J., Durier, F. & Obrecht, C. (2015), "Design and Characterisation of a High Powered Energy Dense Zeolite Thermal Energy Storage System for Buildings", *Applied Energy,* Vol. 159, p.80-86.

Kim, H., Cho, H. J., Narayanan, S., Yang, S., Furukawa, H., Schiffres, S., Li, X., Zhang, Y., Jiang, J., Yaghi, O. M. & Wang, E. N. (2016), "Characterisation of Adsorption Enthalpy of Novel Water-Stable Zeolites and Metal-Organic Frameworks", *Scientific Reports*.

Lei, D., Li, Q., Wang, Z., Li, J. & Li, J. (2013), "An Experimental Study of Thermal Characterisation of Parabolic Trough Receivers", *Energy Conversion and Management,* Vol. 69, p.107-115.

Liu, J., Yang, L., Liu, Y. & Tian, G. (2011), "Key Technological Research and Application of Low Energy Consumption Building Design in Tibet", *Engineering Sciences,* Vol. 13, p.40-46.

Mette, B., Kerskes, H., Drueck, H. & Mueller-Steinhagen, H. (2014), "Experimental and Numerical Investigations On the Water Vapor Adsorption Isotherms and Kinetics of Binderless Zeolite 13x", *International Journal of Heat and Mass Transfer,* Vol. 71, p.555-561.

Ministry of Housing and Urban Rural Development (2010) Design Code of City Heating Network.

Molenda, M., Stengler, J., Linder, M. & Woerner, A. (2013), "Reversible Hydration Behavior of $CaCl_2$ at High H_2O Partial Pressures for Thermochemical Energy Storage", *Thermochimica Acta,* Vol. 560, p.76-81.

N'tsoukpoe, K. E., Liu, H., Le Pierres, N. & Luo, L. (2009), "A Review On Long-Term Sorption Solar Energy Storage", *Renewable & Sustainable Energy Reviews,* Vol. 13, p.2385-2396.

N'tsoukpoe, K. E., Schmidt, T., Rammelberg, H. U., Watts, B. A. & Ruck, W. K. L. (2014), "A Systematic Multi-Step Screening of Numerous Salt Hydrates for Low Temperature Thermochemical Energy Storage", *Applied Energy,* Vol. 124, p.1-16.

Ping, X., Jiang, Z. & Li, C. (2011), "Status and Future Perspectives of Energy Consumption and Its Ecological Impacts in The Qinghai-Tibet Region", *Renewable & Sustainable Energy Reviews,* Vol. 15, p.514-523.

Schaube, F., Woerner, A. & Tamme, R. (2011), "High Temperature Thermochemical Heat Storage for Concentrated Solar Power Using Gas-Solid Reactions", *Journal of Solar Energy Engineering-Transactions of The Asme,* Vol. 133, p.1006-1012.

Tatsidjodoung, P., Le Pierres, N. & Luo, L. (2013), "A Review of Potential Materials for Thermal Energy Storage In Building Applications", *Renewable & Sustainable Energy Reviews,* Vol. 18, p.327-349.

Van Essen, V. M., Zondag, H. A., Gores, J. C., Bleijendaal, L. P. J., Bakker, M., Schuitema, R., Van Helden, W. G. J., He, Z. & Rindt, C. C. M. (2009), "Characterisation Of Mgso(4) Hydrate For Thermochemical Seasonal Heat Storage", *Journal Of Solar Energy Engineering-Transactions Of The Asme,* Vol. 131, p.514-524.

Wang, S., Zhang, M., Wang, B., Sun, M. & Li, X. (2013), "Recent Changes in Daily Extremes of Temperature and Precipitation Over the Western Tibetan Plateau, 1973-2011", *Quaternary International,* Vol. 313, p.110-117.

Xiao, Q., Saikawa, E., Yokelson, R. J., Chen, P., Li, C. & Kang, S. (2015), "Indoor Air Pollution from Burning Yak Dung as A Household Fuel in Tibet", *Atmospheric Environment,* Vol. 102, p.406-412.

Xisang-Gov, http://www.xisang.gov.cn/zwgk/xxgk/201610/t20161018_90507.html

Yu, N., Wang, R. Z. & Wang, L. W. (2013), "Sorption Thermal Storage for Solar Energy", *Progress in Energy and Combustion Science,* Vol. 39, p.489-514.

Zhang, X. Z., Zhang, Y. G. & Zhoub, Y. H. (2000), "Measuring and Modelling Photosynthetically Active Radiation in Tibet Plateau During April-October", A*gricultural and Forest Meteorology,* Vol. 102, p.207-212.

Zhou, Z., Wu, W., Wang, X., Chen, Q. & Wang, O. (2009), "Analysis of Changes in The Structure of Rural Household Energy Consumption in Northern China: A Case Study", *Renewable & Sustainable Energy Reviews,* Vol. 13, p.187-193.

Zottl, A., Lindahl, M., Nordman, R., Rivière, P. & Miara, M. (2011) Evaluation Method for Comparison of Heat Pump Systems with Conventional Heating Systems.

122: Experimental study of the thermal behaviour of nano-enhanced phase change materials (NPCMs)

Xiaoqin SUN*, Yajing MO, Youhong CHU, Siyuan FAN, Changchuan LI, Baoshan XIE

Energy and Power Engineering,Changsha University of Science&Technology, Changsha,Hunan 410004,PR China, xiaoqinsun@csust.edu.cn

Highly conductive particles have been used to improve the inherent thermal conductivity of phase change materials (PCMs). To investigate the heat transfer process of PCMs enhanced by nano-particles, the melting process of 15 kinds of nano-particles PCMs (NPCMs) was observed in test tubes with different nano-particles and particle concentrations. The NPCMs were prepared by dispersing nano-coconut shell charcoal with mass fraction ranged from 0.02 wt % to 18.5 wt.% and nano-graphite with mass fraction from 0.02 wt.% to 1.0 wt.% in paraffin-based PCM with a nominal melting temperature range of 26-28 °C. Type T thermocouples were used to monitor the temperature variation of each material under different boundary temperatures in a climate chamber. Thermovision tests were conducted to illustrate the temperature distribution. It was found that Nano-particles was able to enhance the heat transfer of PCMs. The addition of nanoparticles within 0.1 wt.% didn't affect the phase change characteristics of paraffin.Dispersant was able to enhance the heat transfer of NPCMs. However, when the concentration increased to 18.5 wt.%, more particles were observed at the bottom of the test tubes, causing heat transfer dead zones.

Keywords: nano-particles phase change materials (NPCMs); nano-coconut shell charcoal; nano-graphite; heat transfer

1. INTRODUCTION

Solid-liquid phase change material (PCM) has been widely used in energy storage and other fields in recent years. Thermal energy storage with PCMs has become an important research area and has attracted an increasing attention in areas such as air conditioning systems (Al-Abidi et al.,2012), building materials (Memon et al.,2015), and electronic cooling (Khateeb et al.2005; Sabbah et al.2008). PCMs have a large latent heat for phase change and can store large amounts of energy. However, due to its small thermal conductivity, the efficiency of phase change systems is limited. Therefore, scholars have explored the methods for enhancing phase transition heat transfer, among which highly conductive particles have been used to improve the inherent thermal conductivity of PCMs. Ghazy et al. (2007) studied the absorption of solar energy by paraffin and paraffin added with aluminium powder, founding that after the addition of aluminium powder, the heat obtained by solar collectors increased obviously, and the highest solar energy utilisation rate of composite energy storage was 94%. Wu et al. (2010) added metal nanoparticles in paraffin to increase the heat transfer rate. Cu, Al, and C/Cu nanoparticles were used in their experiments. It was found that composite PCM with Cu particles has the best heat transfer performance. Vellaisamy et al. (2013) prepared the nanofluid PCM by dispersing multi-wall carbon nanotubes in liquid paraffin to enhance the heat transfer properties during solidification process. They prepared the stable PCM by dispersing multi-walled carbon nanotube (MWCNT) in liquid paraffin at 30 ºC with volume fractions 0.15%, 0.3%, 0.45% and 0.6%. They recommended the best volume fraction of 0.6% because of its appreciable increase in heat transfer properties. Murugan et al. (2017) reported that adding 0.3 wt.% MWCNT into paraffin resulted in a reduction of 30% of the melting time. However, further addition resulted longer melting time due to predominant increase in viscosity of the PCM and reduction of natural convection in the liquid state.

It is a common method to improve the heat transfer performance of PCMs by adding carbon materials. However, in practical applications, the selection of suitable types of carbon materials, addition methods, and carbon addition amounts are needed to be further explored. To explore the effects of nano-additives on the heat transfer performance of phase change materials, nano-graphite and nano-coconut shell charcoal were utilised to synthesise nano-particles PCMs (NPCMs). The effects of different concentrations of nano-additives, dispersants, and synthesizing procedure on the melting process were compared. The temperature variation of the NPCMs in the melting process under dynamic temperature boundary conditions was monitored. The temperature distribution was obtained under the constant temperature boundary conditions using an infrared camera.

2. MATERIALS AND METHODS

2.1. Material preparations

Pure paraffin 1 with a phase change temperature of 26-28 ºC was selected as the base PCM. The DSC test result is shown in Figure 1. The enthalpy changed from 20.8 kJ/kg to 240.2 kJ/kg during melting. The peak temperature for melting was 26.4 ºC. Nano-graphite with a size of 20 nm was used as the nano-additives. Nano-coconut charcoal was obtained after a 30-hr milling process within a 20-Hz ball mill. Figure 2 shows the synthesizing process of NPCMs. The detailed information of these NPCMs is shown in Table 1.

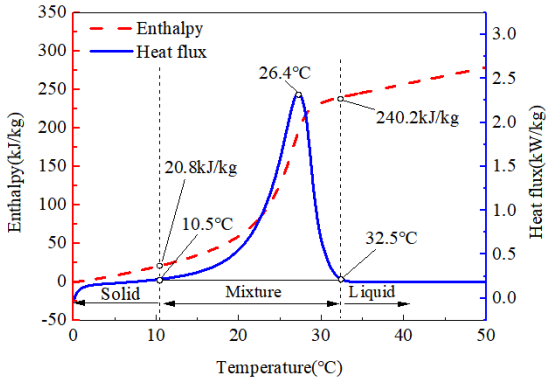

Figure 1: DSC results for pure paraffin

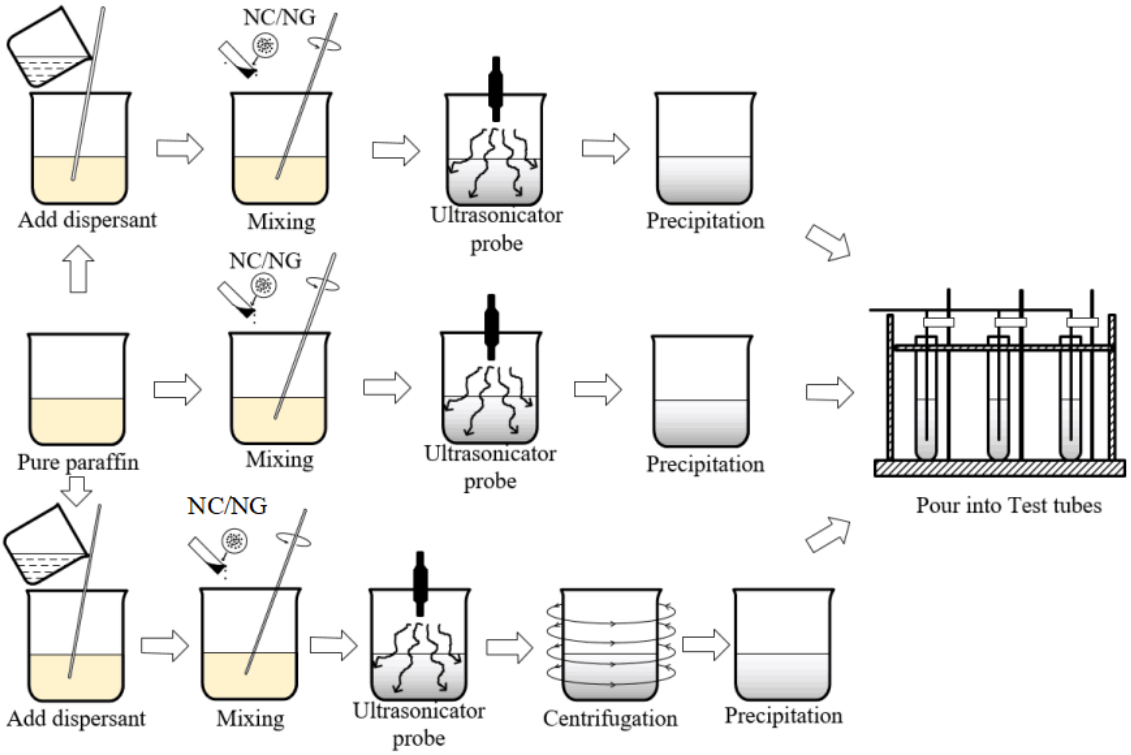

Figure 2: NPCM synthesizing methods

Table 1: Information of NPCMs

Number	Nano-additive	Concentration	Dispersant	Precipitation	Note
A1	NG	0.02 wt.%	/	120 h	Upper layer
A2	NG	0.06 wt.%	/	120 h	Upper layer
A3	NG	0.1 wt.%	/	120 h	Upper layer
A4	NC	0.02 wt.%	/	120 h	Upper layer
A5	NC	0.1 wt.%	/	120 h	Upper layer
A6	NC	18.5 wt.%	/	120 h	Upper layer
A7	NC	18.5 wt.%	/	120 h	Lower layer
A8			Pure paraffin 1		
B1	NG	0.06 wt.%	Oleic acid	120 h	/
B2	NG	0.06 wt.%	Span 80	120 h	/
B3	NG	0.06 wt.%	/	120 h	/
B4	NG	0.06 wt.%	Oleic acid	24 h	Centrifugation
B5	NG	0.06 wt.%	Span 80	24 h	Centrifugation
B6	NG	0.06 wt.%	/	120 h	Centrifugation
B7			Pure paraffin 2		

2.2. Test apparatus

To test the melting process, NPCMs and a pure paraffin were placed in an environmental chamber where the temperature raised from 15 ^{o}C to 50 ^{o}C. Type T thermocouples were fixed in the materials to monitor the temperature variation during the melting of the NPCMs. The experimental apparatus is shown in Figures 3 and 4. To observe the temperature distribution, the melting process was observed using an infrared camera (FLIR T420) with a temperature range of -20 ^{o}C to 120 ^{o}C and accuracy of ±2 ^{o}C. The experiments were divided into four sets, which were the test for same additive with different concentrations, test using NC and NG additives with same concentration, test for NPCMs with different dispersants, and test for upper and lower NPCMs with 18.5 wt.% NC.

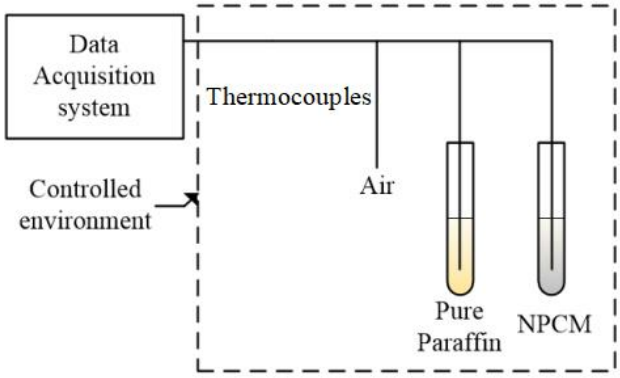

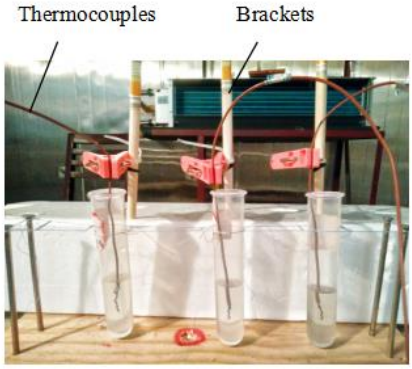

Figure 3. Experimental apparatus

Figure 4. NPCMs test tubes

3. RESULTS AND ANALYSIS

3.1. Tests for same additive with different concentrations

As shown in Equation 5, the melting process of NPCMs increased with the increase of the additive mass fraction. For example, the temperature of sample A3 with 0.1 wt.% NG was higher than it of samples A1 and A2. Same phenomenon was observed for samples A4-A6. This is because the thermal conductivity of the phase change material increased with nano-particles. More nano-particles accelerated the melting process.

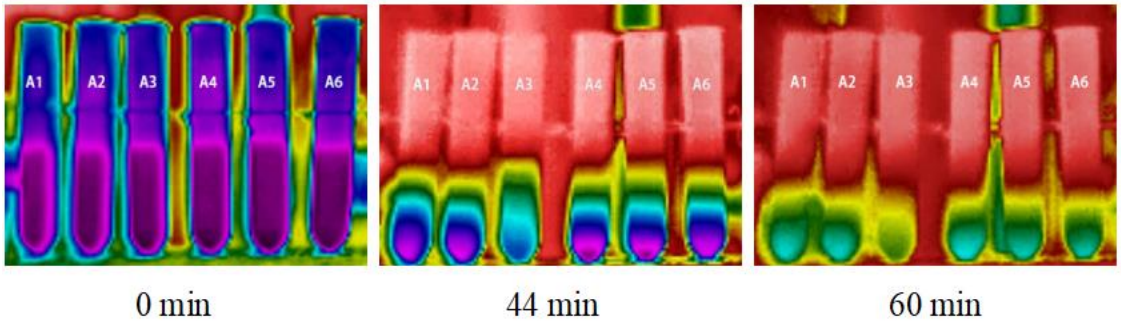

Figure 5. Thermal image of NPCMs with different nano-particle concentrations

Figure 6(a) shows the temperature variation of NPCM with different concentrations of NG.It was observed that the initial temperature of 0.02 wt.% NG-PCM(sample A1) was higher than 0.06 wt.% NG-PCM(sample A2), and both were higher than 0.1 wt.% NG-PCM(sample A3). But the three kinds of NPCMs had no significant difference in the heating rate, phase change temperature and phase transition time during the heating process, and the temperature relationships of the three materials remained unchanged. Compared with pure paraffin 1, the addition of NG within 0.1 wt.% didn't affect the phase change characteristics of paraffin.

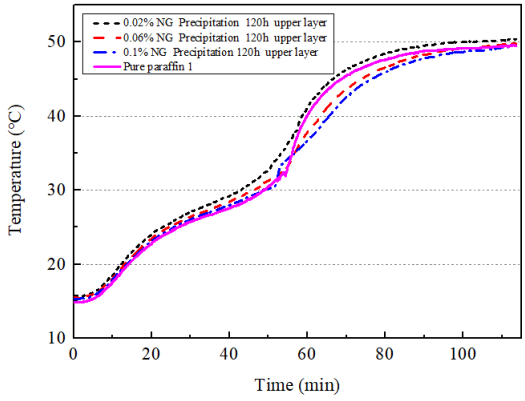

Figure 6(a). Temperature profile of NPCMs with different concentrations of NG

Figure 6(b) shows the temperature of NPCMs with different concentrations. The temperature of NPCM with 18.5 wt.% NC (sample A6) was always higher than that of the other two NPCMs and its melting time was the shortest.The addition of NC within 0.1 wt.% didn't affect the phase change characteristics of paraffin.

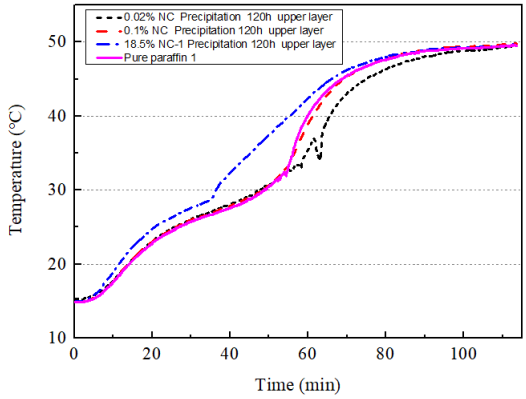

Figure 6(b). Temperature profile of NPCMs with different concentrations of NC

From above analysis, the heat transfer of the NPCMs was related to the concentration of the nano-addictives. In general, the heat transfer increased with the increase of the concentrations. When the additive concentration was less than or equal to 0.1 wt.%, the enhancement phase change heat transfer were not obvious.

3.2. Test using NC and NG additives with same concentration

The temperature distributions during the melting process are shown in Figure 7. Figure 8(a) and (b) is the result for NPCMs with 0.1 wt.% NG (sample A3) and 0.1 wt.% NC (sample A5) and 0.02 wt.% NG (sample A1) and 0.02 wt.% NC (sample A4), respectively.

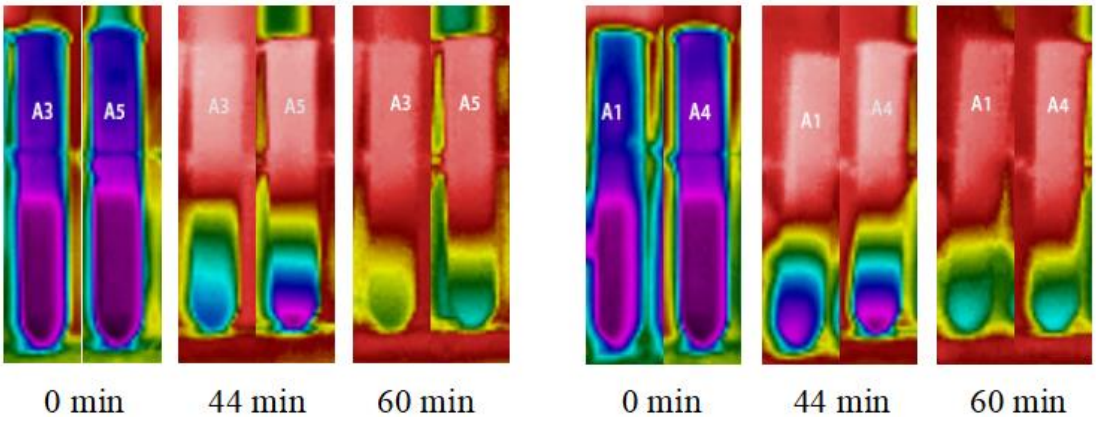

(a) Samples A3 and A5 *(b) Samples A1 and A4*

Figure 7. Temperature distribution of NPCM using NC and NG additives with same concentration

It was observed that the temperature of the NG-PCM was higher than that of the NC-PCM. This is because the thermal conductivity of graphite was higher than that of coconut shell charcoal, which accelerated the heat transfer between the NPCM and surrounding environment. Figure 8 presents the temperature variation of the two kinds of NPCMs with 0.02 wt.% and 0.1 wt.% additives. The results were consistent with the results in Figure 7. When the additive concentration is 0.02 wt.% , compared with the pure paraffin, the phase change temperatures of the NG-PCM and the NC-PCM remained unchanged . Before the phase transition was completed, the NG-PCM accelerated the temperature rise and shortened the phase transition time. The heat transfer characteristics of the NC-PCM were consistent with the pure paraffin before the phase change was completed. However, after the phase change was completed, the thermocouple position was slightly offset due to external disturbance, causing temperature fluctuations. Therefore the temperature of the NC-PCM after phase transition was lower than that of pure paraffin. When the additive concentration was 0.1 wt.% , there was no significant difference in heat transfer characteristics between the two NPCMs before the phase transition was completed. After the phase change was completed, the thermocouple in the NG-PCM was disturbed to cause temperature fluctuation, which made the temperature lower than that of pure paraffin and NC-PCM.

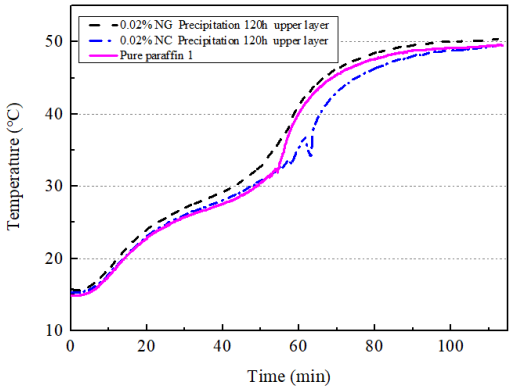

Figure 8. (a) Temperature profile of NPCMs with 0.02 wt.% additives

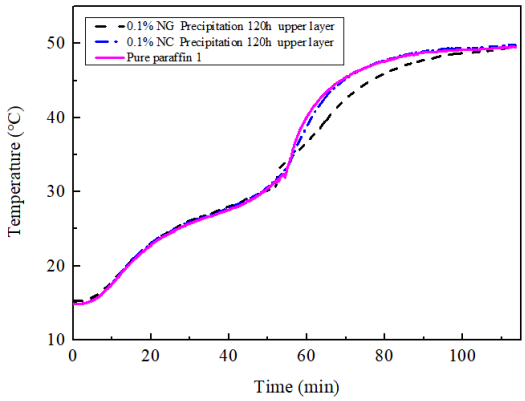

Figure 8. (b) Temperature profile of NPCMs with 0.1 wt.% additives

Compared Figures 7 and 8, the temperature increase rate of the NG-PCM was faster than that of the NC-PCM. When the addictive concentration was 0.02 wt.%, the phase change process of the NG-PCM was shorter than that of the NC-PCM; when the additive concentration was 0.1 wt.%, the phase change processes of NPCMs had no significant difference. Considering the results in Section 3.1, NG was more beneficial to the phase change heat transfer.

3.3. Test for NPCMs with different dispersants

Dispersant is a surfactant, which can increase the surface activity of nanoparticles and increase the contact area between the nanoparticles and the base material. To realise a uniform dispersion and suspension of the nanoparticles in pure PCM, oleic acid and span 80 were used as dispersants. Figure 9 shows the temperature distributions of NPCMs with dispersants. The selected NPCMs are NG-PCM with a concentration of 0.06 wt.%, precipitation for 120 h and the NC-PCM with a concentration of 0.06 wt.% and precipitation for 24 h after centrifugation.

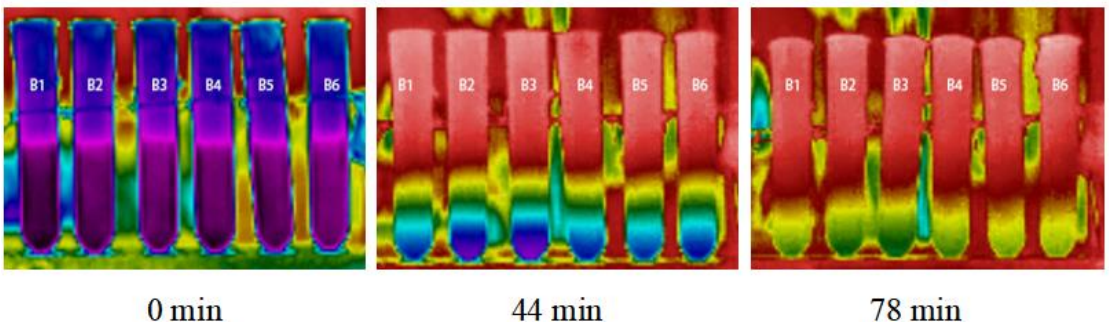

Figure 9. Temperature distribution of NPCMs with different dispersants

Figure 10 shows that the NPCM using oleic acid as a dispersant had the highest heating rate, followed by the NPCM using Span 80 and the NPCM without dispersant. Oleic acid was more oleophilic than Span 80, resulting in a better mixture with paraffin. It enhanced the surface contact between nanoparticles and PCMs and enhanced the heat

transfer. Figure 11 shows the temperature variations of NG-PCMs using different dispersants.The phase change process of the NG-PCM with oleic acid as a dispersant was shortened; the NPCM with the span 80 had no obvious affect on its heat transfer characteristics.

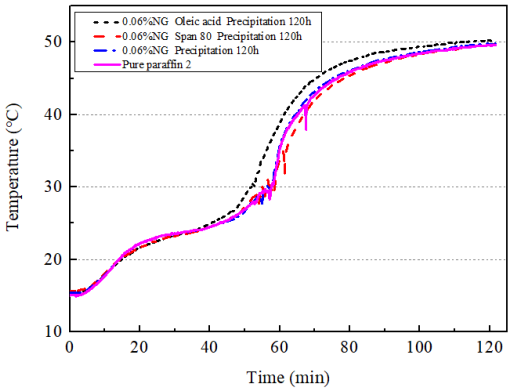

Figure 10(a). Temperature profile of NG-PCM

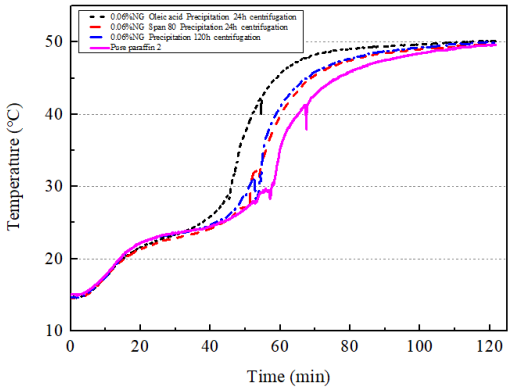

Figure 10(b). Temperature profile of NG-PCMs with centrifugation

From Figures 9 and 10, it was observed that in this set of experiments, the NPCM using oleic acid as a dispersant had the best heat transfer performance and the phase transition time is the shortest, followed by the NPCM using Span 80. NG-PCM using oleic acid was the best selection.

3.4. Test for upper and lower NPCMs with 18.5 wt.% NC

Figure 11 shows the temperature distributions during the melting process of upper and lower layers of NPCMs with 18.5 wt.% NC. According to the test results, the heating rate of the lower layer of the NC-PCM with a concentration of 18.5 wt.% was higher than that of the upper layer. This is because the distribution of nanoparticles in the base PCM is not uniform. The mass fraction of nanoparticles in the lower layer was larger than that in the upper layer because of the gravity. Therefore, the heat transfer in lower layer was superior to the heat transfer in upper layer liquid. However, the temperature of the upper liquid was higher than the temperature of the lower liquid (Figure 12). The heat transfer occurred mainly at the bottom of the test tube for the lower layer NPCM. The thermocouples were placed in the middle of the NPCMs, which did not tell the melting of the material at bottom. When the concentration of NC was 18.5 wt.%, the nanoparticle distribution in the NPCM was uneven, causing heat transfer dead zone.

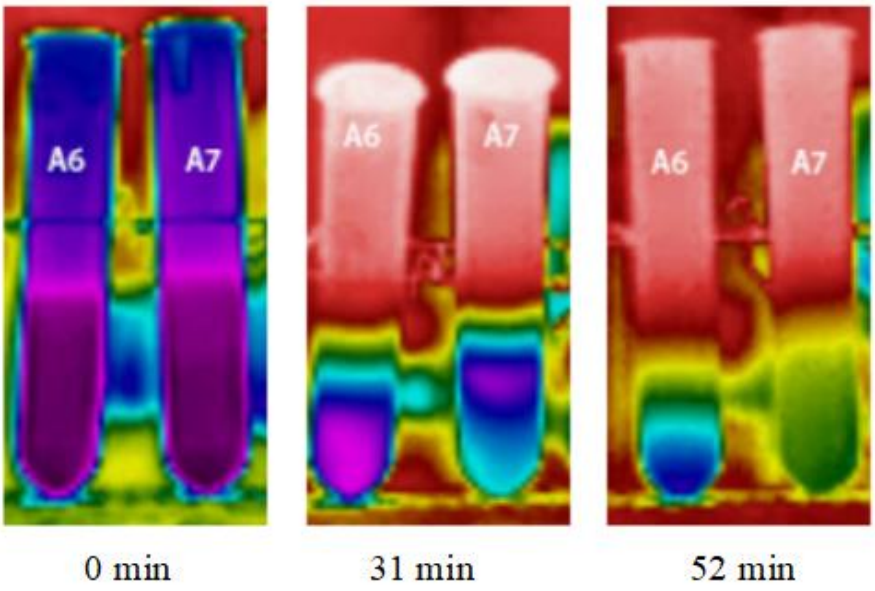

Figure 11: Temperature distribution of NPCM with 18.5 wt.% NC

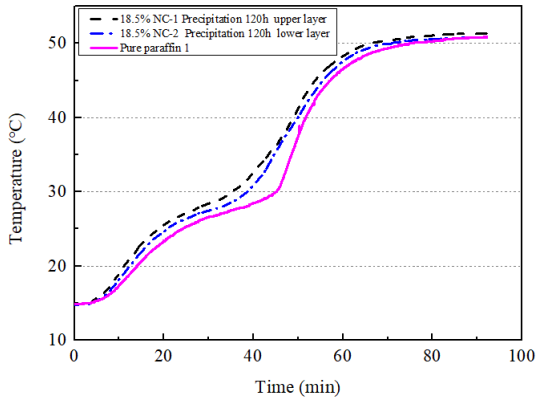

Figure 12: Temperature profile of NPCM with 18.5 wt.% NC

4. CONCLUSION

Tests for PCMs with nano-additives were conducted in this paper. The temperature distribution and variation were observed during melting with different nano-additive concentrations, dispersants, and material preparation processes. The conclusions are as follows:

(1) Nano-particles was able to enhance the heat transfer of PCMs. But The addition of nanoparticles within 0.1 wt.% didn't affect the phase change characteristics of paraffin.

(2) The NPCMs using oleic acid as dispersant had the best heat transfer performance, followed by Span 80. The dispersant was beneficial to the heat transfer process of PCMs.

(3)When the addictive concentration increased to 18.5wt.%, precipitation was observed, which lead to uneven temperature distribution.

5. ACKNOWLEDGEMENTS

This work was supported by the National Natural and Science Funding (51308051), the Science and Technology Department of Hunan (2017RS3036), Hunan Association for Science and Technology (2017TJ-Q05), Changsha City Fund for Distinguished and Innovative Young Scholars (KQ1707013) and Hunan Province 2011 Collaborative Innovation Center of Clean Energy and Smart Grid.

5. REFERENCES

Al-Abidi, A A., Mat, S B, Sopian, K., Sulaiman, M. Y., Lim, C. H., & Th, A. 2012. Review of thermal energy storage for air conditioning systems. *Renewable & Sustainable Energy Reviews*, 16(8), 5802-5819.

Memon, S. A., Liao, W., Yang, S., Cui, H., & Shah SFA,. 2015. Development of composite PCMs by incorporation of paraffin into various building materials. *Materials*, 8(2), 499.

Khateeb, S. A., Amiruddin, S., Farid, M., Selman, J. R., & Al-Hallaj, S. 2005. Thermal management of li-ion battery with phase change material for electric scooters: experimental validation. *Journal of Power Sources*,142(1), 345-353.

Sabbah, R., Kizilei, R., Selman, J. R., & Al-Hallaj, S. 2015. Active (air-cooled) vs. passive (phase change material) thermal management of high power lithium-ion packs: limitation of temperature rise and uniformity of temperature distribution. *Journal of Power Sources*, 182(2), 630-638.

Mettawee, E. B. S., & Assassa, G. M. R. 2007. Thermal conductivity enhancement in a latent heat storage system. *Solar Energy*, 81(7), 839-845.

Wu, S., Zhu, D., Zhang, X., & Huang, J. 2010. Preparation and melting/freezing characteristics of cu/paraffin nanofluid as phase-change material (PCM). *Energy & Fuels*, 24(3).

Kumaresan, V., Velraj, R., & Das, S. K. 2012. The effect of carbon nanotubes in enhancing the thermal transport properties of pcm during solidification. *Heat & Mass Transfer*, 48(8), 1345-1355.

Murugan, P., Ganesh, K. P., Kumaresan, V., Meikandan, M., Malar, M. K., & Velraj, R. 2017. Thermal energy storage behaviour of nanoparticle enhanced PCM during freezing and melting. *Phase Transitions*(4), 1-17.

125: Development of a cooling load prediction model for air-conditioning system operation control

Chengliang FAN[1], Yundan LIAO[1,2,*], Yunfei DING[1,2], Zhenbing CAI [1]

[1]School of Civil Engineering, GuangZhou University, Guangzhou 510006, China
[2]Guangdong Provincial Key Laboratory of Building Energy Conservation and Application Technology, Guangzhou 510006, China

Building cooling load prediction is of critical importance for achieving energy saving of air-conditioning system in high-rise buildings. It not only benefits the energy-efficiency operation of the air-conditioning system, but also great important for the system stability. Many techniques have been developed for building cooling load prediction and these methods are normally arranged into three categories: regress analysis, energy simulation and artificial intelligence. Different from the last two categories, which may have better prediction accuracy but be much complicated, the regression analysis methods are much practical for real applications. It is suggested to use the regression models in the air-conditioning system control for achieving a better operation. However, traditional regression models are often helpless to manage multi-parameter dynamic changes, and the effect of outliers in cooling load prediction has not been considered seriously, accuracy of building hourly cooling load prediction is not satisfied. To promote the application feasibility of regression cooling load prediction models, this study developed an efficient hourly cooling load prediction model based on sensitivity analysis and the traditional auto-regressive with exogenous (ARX) model. The developed cooling load prediction model kept the constitution of ARX model, but used different variables from sensitivity analysis as inputs, also the quadratic term of key variables was included in the model. The prediction accuracy of the developed was validated by compared it to the model established in EnergyPlus, which is a widely acknowledged software for energy modeling. Case studies showed that the deviations between the developed method and EnergyPlus were less than ±10%. The high accuracy ensured that the developed method could provide a reliable prediction for air-conditioning system control. Since the developed method is much less complicated than the energy simulation, it will be much suitable for real operational controls.

Keywords: Cooling load prediction; Operational control; ARX model; Regression analysis; Sensitivity analysis

1. INTRODUCTION

Building energy consumption has been a major section of social energy consumption. In office buildings that have large energy intensity, the heating, ventilation and air-conditioning (HVAC) system takes a proportion of 68% energy consumption (Jing, 2017; Deng, 2018; Cao, 2017). The reduction of HVAC system energy has been one of the primary topics in energy research field. Optimal control offers a potential to reduce HVAC system energy consumption in commercial office buildings by using Building Energy Management (BEM) systems to control the HVAC system. Building cooling load prediction has been regarded as one important technology for HVAC system optimal operation and controls (Yao, 2010).

To promote system optimal control, an accurate and quick cooling load prediction method could be conducive. Cooling load prediction can be a control variable directly used in the control strategy of HVAC system or be used as a reference for improving the control performance. With cooling load prediction, the peak load demand and the variations of cooling load can be predicted advanced and thus the system can be controlled to its working conditions beforehand. For example, cooling load of office buildings may be decreased during noon time, but the controller would detect this variable after people leaving the office, which is delayed. Superfluous energy is consumed for this unnecessary cooling supply. But with the cooling load prediction, this superfluous energy waste can be reduced.

Different methods have been studied in recent years to capture the accuracy of prediction, which can be broadly arranged into three categories: regression analysis, energy simulation, and artificial intelligence (AI) analysis (Ding, 2018). Energy simulation software, including DOE-2, ESP-r, TRNSYS EnergyPlus, can simulate cooling loads when detailed building information, such as physical constructions, windows performance, occupancy, etc. Artificial intelligence (AI) analysis can be introduced to artificial neural network (ANN) and support vector machine (SVM) (Li, 2009). AI analysis uses extensive relation of input and output variables by a set of many processing units arranged in layers, which are selected to operate like neurons in brain. A major disadvantage of AI methods is that a large number of historical load data and weather data are needed to finish training. Simulation methods are acknowledged as specific methods which use more details of buildings and system for prediction. However, data of buildings and systems are often difficult to obtain or hard to identify accurately, especially for older buildings, limiting their accuracy (Pedersen, 2007).

Compared with other categories, regression analysis is considered to be less accuracy, but it tends to be simple and easily implement to any type of building (Aranda, 2012), making them more practical for real applications. Regression methods aim to predict building cooling load by finding out appropriate coefficients, which associated with the most influential inputs or historical load data (Guo, 2014). At present, the main forms of regression analysis used for building cooling load prediction models are the multiple linear regressive (MLR) models (Shin, 2016), auto regressive (AR) models, and autoregressive with exogenous inputs (ARX) models. Some researchers show that the prediction accuracy can be effectively improved if input variables are chosen properly (Qiang, 2015).

Based on the previous studies, the objective of this paper is to make improved ARX model adapt nonlinear condition and provide the capability to reduce the influence of outliers. The first and most important contribution of this paper is that significant variables are selected by sensitivity analysis. Second, higher order term of temperature and interaction term among exogenous variables in improved ARX model to enhance the ability of adapting dynamic changes.

2. SENSITIVITY ANALYSIS

Before conducting the parametric simulation, it is significant to determine what input independent variables are to be study. Sensitivity analysis can show how different values of an independent variable affect the building cooling load in this study. Selecting the key input variables by sensitivity analysis is a good way to understand the improved ARX model. EnergyPlus is used to simulate the building hourly cooling load based on CSWD weather data in Guangzhou. CSWD weather data consisting 8760 hourly records of dry-bulb temperature, relative humility, solar radiation, wind speed and other meteorological parameters. EnergyPlus has been researched and proven to have extremely high calculation accuracy and reliability with a maximum calculation deviation of no more than 5.2% (Henninger, 2013). A list of the input variables was prepared in two groups (Huang, 2015).

(1) External weather: dry-bulb temperature (Temp), relative humidity (RH), wind speed (WS), direct radiation (Rad).

(2) Internal gains: occupancy (Occ), lighting power (LP), equipment power (EP), ventilation rate (VR).

In this paper, influence coefficient (IC) was utilised to quantitatively assess how sensitive the predicted building cooling load would be to changes in input variables (Lam, 2010), Each the input variables were introduced by assigning a range of different values, one at a time. IC was determined as follows:

Equation 1: Influence coefficient value

$$IC = \frac{CL - CL_{bs}}{CL_{bs}} \div \frac{IV - IV_{bs}}{IV_{bs}}$$

Where:

CL = output of building cooling load (kW)
IV = the value of input variables
bs = basic-set value of input variables

The specifications of the office building model are shown in Table 1. Table 2 shows the office building envelope basic-set parameters in Guangzhou. The operating time is from 8:00 to 19:00.

Table 1: Description of the office building model.

Floor area	1337.6 m^2
Number of floors	11
Ceiling height	3 m
Window-to-wall ratio	0.4
Light	20 W/m^2
Equipment	13 W/m^2
Occupancy	10 m^2/person
Light average usage	Until[a] (fraction[b]): 7 (0.05), 8 (0.3), 12 (0.9), 14 (0.8), 18 (0.9), 19 (0.3), 20(0.2), 24(0.05)
Equipment average usage	Until[a] (fraction[b]): 8 (0.4), 12 (0.9), 14 (0.8), 18 (0.9), 19 (0.5), 24 (0.4)
Occupancy schedule	Until[a] (fraction[b]): 7 (0.05), 8 (0.3), 12 (0.9), 14 (0.5), 18 (0.9), 19 (0.3), 20(0.2), 24(0.05)

a The hour of the day until specified fraction is considered.

b The fraction of total value of the variable that is considered in calculation for that specific period of time.

Table 2: Office building envelope basic-set parameters.

Wall	Window	Roof	Overall shading coefficient
	U-value(W/m^2K)		
1.56	4.00	0.54	0.40

The results of sensitivity analysis for the different variables are shown in Table 3. The external weather variables, such as outdoor dry-bulb temperature and direct radiation, have strong correlation with cooling load. The largest influence of variables is dry-bulb temperature, the IC value is 1.29, the next is lighting power, direct radiation and equipment power, the IC value is 0.394, 0.346 and 0.316 respectively. The IC value of wind speed is -0.0126, lower than other input variables. Besides, occupancy and ventilation rate are dynamically changed by subjective behavior or setting, these variables are also closely related with cooling load.

Table 3: The sensitivity analysis summaries of different variables.

Input variables	Unit	Basic-set value	Range	Interval	Influence coefficient
Dry-bulb temperature	℃	28	24-35	1	1.29
Relative humidity	%	70	40-90	5	0.244
Wind speed	m/s	1.7	0.5-4.8	0.3	-0.0126
Direct radiation	W/m^2	350	50-700	50	0.346
Occupancy	m^2/psn	10	2-20	2	-0.117
Lighting power	W/m^2	20	8-30	2	0.394
Equipment power	W/m^2	13	5-25	2	0.316
Ventilation rate	m^3/h/psn	30	20-40	2	0.210

3. DESCRIPTION OF IMPROVED ARX MODEL

Significant input variables on building cooling load had been defined by sensitivity analysis in this improved ARX model. Based on traditional ARX model, to improve prediction accuracy of hourly cooling load, higher order term and interaction term are also included to model nonlinearity and inter-correlation between input variables in this study. As shown of sensitivity analysis summaries, internal gains, such as lighting power, equipment power and ventilation rate, have strong relation with cooling load. The improved ARX model is consist of components introduced in Equation 2.

Equation 2: The improved ARX model

$$CL_{pre,t} = w_1 \cdot CL_{act,t-\tau} + w_2 \cdot Temp_t + w_3 \cdot Temp_t^2 + w_4 \cdot RH_t + w_5 \cdot Temp_t \cdot RH_t + w_6 \cdot Rad_t + w_7 \cdot Occ_t + w_8 \cdot VR_t + w_9 \cdot LP_t + w_{10} \cdot EP_t + w_{11}$$

Where:

τ = predicted time step

t = predicted time

w = weight coefficient for input variables

CL_{pre} = predicted cooling load

The initial weight coefficient matrix '*W*' can be found by Equation 4-7 as shown in Equation 3. '*W*' could be modified and updated. This means that weight coefficients obtained from different time steps are used along with hourly actual weather and historical load data.

Equation 3: The weight coefficient

$$W = [w_1 \quad w_2 \quad \cdots \quad w_{11}]^T$$

Equation 4: The matrix for all input variables

$$A = [A_1 \quad A_2 \quad \cdots \quad A_t]^T$$

Equation 5: The matrix of building cooling load

$$CL = [CL_1 \quad CL_2 \quad \cdots \quad CL_t]^T$$

Equation 6: The matrix of building cooling load

$$CL = A \cdot W$$

Equation 7: The weight coefficient calculation

$$W = (A^T \cdot A)^{-1} \cdot A^T \cdot CL$$

Where:

A_t = [x_1, x_2,…,x_{10}, 1],x_1,x_2,…,x_{10} are 10 vectors of input parameters

The subscript *t* ≥11 for the 11×11 matrix [$A^T \cdot A$] to be invertible.

4. RESULTS

4.1. Solution of weight coefficient matrix

The time span of training cooling load is during July based on EnergyPlus weather file. A special rule for target hour 8:00 is defined. For example, if the target hour is 8:00 on Tuesday, *t*-1 is 8:00 on Monday. If the target hour is 8:00 on Monday, *t*-1 is 8:00 on Friday of the previous week. If the target hour is not 8:00, the calculation rule for *t*-1 is one hour in advance normally. As shown in Table 4, an example of the weight coefficients and relevant statistics is time for 120-h (five consecutive weekdays). The accuracy of proposed model in four cities is evaluated using the following statistical criteria: root mean squared error (RMSE), expected error percentage (EEP), coefficient of variation (CV) and mean absolute error (MAE).

Table 4: An example of the weight coefficients.

Weight coefficients	w1	w2	w3	w4	w5	w6	w7	w8	w9	w10	w11	R^2	RMSE (kW)
Values	0.30	103.6	-0.83	14.5	-0.42	0.09	-17.1	-1.80	-8.1	79.3	-2612.3	0.995	17.3

4.2. Prediction model validation

A low training error cannot guarantee a low prediction error in practice. To verify that the weight coefficient values obtained by training are still used to valid for different weather conditions, the data of August 20 to August 24 is used to validation. At the same time, in order to figure out the effect of adding the higher order term of temperature ($Temp^2$) and interaction term among exogenous variables (Temp•RH) on cooling load prediction results, improved

ARX model was used to make predict before and after removing $Temp^2$ and Temp•RH terms. The results show in Figure 1. Examining Figure 1, we can see that the predicted cooling load does not respond well to some load sudden changes condition after removing $Temp^2$ and Temp•RH terms. As shown in Table 5, the *RMSE* values increased from 33.1kW to 53.8kW, and other evaluation indices values (*EEP*, *CV*, and *MAE*) were increased with different degrees. The R^2 value dropped from 0.982 to 0.953. Results of statistical evaluation show that the higher order term and interaction term can improve accuracy of development prediction method.

Table 5: Statistical evaluation of removing adding terms.

Model	R^2	RMSE (kW)	EEP (%)	CV (%)	MAE (kW)
Improved ARX	0.982	33.1	3.2	4.8	28.3
Removing terms ARX	0.953	53.8	5.1	7.5	41.0

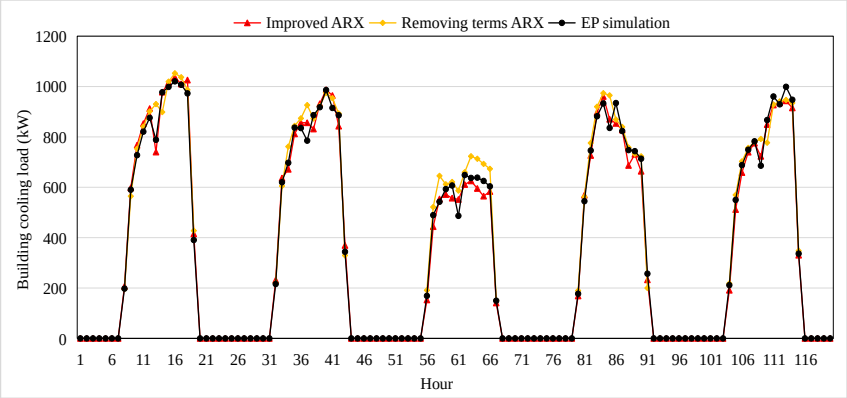

Figure 1: The comparison of improved ARX model before and after removing terms.

5. CONCLUSION

This paper developed an improved ARX model for office buildings cooling load prediction. The developed cooling load prediction model kept the constitution of ARX model, but used different variables from sensitivity analysis as inputs, also the quadratic term of key variables was included in the model. Different from the traditional model is that higher order term and interaction term are included in improved ARX model to adapt nonlinearity and inter-correlation. This case study showed that the deviations between the developed method and EnergyPlus were less than ±10% according to the relative error. The high accuracy ensured that the developed method could provide a reliable prediction for air-conditioning system control.

6. ACKNOWLEDGEMENTS

The work was financially supported by a grant from National Science Foundation of China (Grant No. 51708139) and a special innovation project from Department of Education of Guangdong Province (Grant No. 2017KTSCX144).

7. REFERENCES

Jing, R, Wang, M, Zhang, R, Li, N, Zhao, Y, 2017. A study on energy performance of 30 commercial office buildings in Hong Kong. *Energy and Buildings*, 144(6), 117–128.

Deng, Y, Feng, Z, Fang, J, Cao, S, 2018. Impact of ventilation rates on indoor thermal comfort and energy efficiency of ground-source heat pump system. *Sustainable Cities and Society*, 37, 154-163.

Cao, S, Kong, X, Deng, Y, Zhang, W, Yang, L, Ye, Z, 2017. Investigation on the thermal performance of steel heat exchanger for ground source heat pump systems using full-scale experiments and numerical simulations. *Applied Thermal Engineering*, 115, 91-98.

Yao, Y, Chen, J, 2010. Global optimisation of a central air-conditioning system using decomposition coordination method. *Energy and Buildings*, 42(5), 570–83.

Ding, Y, Zhang, Q, Yuan, T, Yang, F, 2018. Effect of input variables on cooling load prediction accuracy of an office building. *Applied Thermal Engineering*, 128, 225-234.

Li, Q, Meng, Q, Cai, J, Yoshino, H, Mochida, A, 2009. Predicting hourly cooling load in the building: a comparison of support vector machine and different artificial neural networks, *Energy Conversion and Management*, 50(1), 90–96.

Pedersen, L, 2007. Use of different methodologies for thermal load and energy estimations in buildings including meteorological and sociological input parameters, *Renewable and Sustainable Energy Reviews*, 11(5), 998–1007.

Aranda, A, 2012. Multiple regression models to predict the annual energy consumption in the Spanish banking sector, *Energy and Buildings*, 49, 380–387.

Guo, Y, Nazarian, E, Ko, J, Rajurkar, K, 2014. Hourly cooling load forecasting using time-indexed ARX models with two-stage weighted least squares regression. *Energy Conversion and Management*, 80, 46-53.

Shin, M, Do, S, 2016. Prediction of cooling energy use in buildings using an enthalpy-based cooling degree days method in a hot and humid climate. *Energy and Buildings*, 110, 57-70.

Guo, Q, Tian, Z, Ding,Y, Zhu, N, 2015. An improved office building cooling load prediction model based on multivariable linear regression. *Energy and Buildings*, 107, 445-455.

Henninger, RH, 2013. EnergyPlus Testing with Building Thermal Envelope and Fabric Load Tests from ANSI. ASHRAE standard, 140.

Huang, P, Huang, G, Wang, Y, 2015. HVAC system design under peak load prediction uncertainty using multiple-criterion decision making technique. *Energy and Buildings*, 91, 26-36.

Sarwar, R, 2017. Field validation study of a time and temperature indexed autoregressive with exogenous (ARX) model for building thermal load prediction. *Energy*, 119, 483-496.

Lam, J C, 2010. Multiple regression models for energy use in air-conditioned office buildings in different climates. *Energy Conversion and Management*, 51(12), 2692-2697.

127: Single-phase PWM rectifier based on PR controller

Jian PAN[1], Yusi FENG[1], Xiaolei ZHANG[1] , Dongchu LIAO[1] , Tianjun LIU[1]

1Hubei Collaborative Innovation Center for High-efficiency Utilisation of Solar Energy, Hubei University of Technology, South Lee Road, No.28, Wuhan, China, feng_yusi@163.com

For a three-phase PWM rectifier, the input current signals can be converted to a synchronous d-q coordinate system, and the DC component can be controlled in zero steady-state error by PI control adjustment. But for a single-phase PWM rectifier, it is difficult to achieve this conversion after the pi regulator and to track the zero steady-state error of a given signal's sinusoidal current. To overcome these problems, an improved PR controller based on ideal proportion-resonant controller is proposed in this paper. The controller is superior to the PI controller in tracking sinusoidal signals and the DC bus voltage has good stability and anti-interference ability. The MATLAB simulation results verify the effectiveness of the proposed improved PR controller.

Keywords: single-phase PWM rectifier, current control, proportional-resonant controller, harmonic elimination, zero steady-state error

1. INTRODUCTION

Single-phase PWM rectifier has many excellent dynamic characteristics, such as sinusoidal current of power grid, unity power-factor, dual energy flow, fast dynamic control response and so on. It is widely used in UPS, traction locomotive and some other occasions. One of the main goals of controlling single-phase PWM rectifiers is to stabilise the DC bus output voltage. The other is to obtain the unit input power factor, inhibit harmonic current component (Ma, Song, Wang & Feng, 2018; Pu, Nguyen, Lee & Lee, 2010). Achieving these two objectives is closely related to the input current characteristics, so controlling current of power grid is the key to control the single-phase PWM rectifier controller. In this paper, using direct current control can effectively lessen the control performance dependence on the main circuit parameters and improve the dynamic response. In addition, there are many ways to control current of PWM rectifier on the grid-side, for example, hysteresis current controller, PI controller, repetitive controller, fuzzy controller, etc. By Clark transform and Park transform, the sinusoidal current of three-phase PWM rectifier can be converted to a synchronous d-q coordinates (Guo, Liu & Zhang, 2015; Jing & He, 2017). Then the straight flow decomposition is PI regulator to achieve no static error control. But for single-phase PWM rectifier, it is difficult to get DC component by a similar transformation and achieve current PI regulator with no static error control (Taha, Beig & Boiko, 2018). To solve the problem, this paper presents a modified PR regulator to control sinusoidal current (Alemi, Jeong & Lee, 2015). The method avoids the tedious coordinate conversion, reduces the requirements of the switching frequency, and gets a more stable and excellent dynamic performance.

2. CONTROL STRATEGY AND CONTROLLER

2.1. The strategy of single-phase PWM Rectifier Control

Figure 1 presents the topology and control block diagram of single-phase PWM rectifier. The AC circuit of power grid, the IGBT switch bridges and the DC circuit make up the single-phase PWM rectifier. The AC circuit of power grid includes AC power supply u_s, the inductance L and the equivalent resistance R, etc. The DC circuit includes load resistance R_0 and the support capacitor C. The switch arm topology is a voltage source PWM rectifier (VSR).

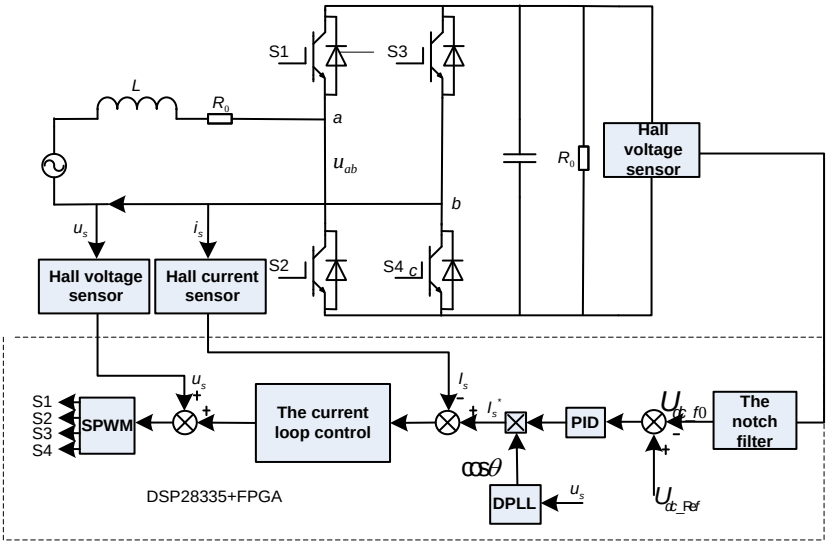

Figure 1: single-phase PWM rectifier control block

A dual- loop control strategy including inner current loop and outer voltage loop is commonly adopted in the rectifier. The outer voltage error value between the given voltage and the feedback voltage is taken as the input of the PI controller, making the DC voltage follow a given voltage with no static error ultimately (Chen, Luo, Shuai & Xie, 2013; Chowdhury, 2016). Then the voltage loop output value is used as the internal current loop reference value. To prevent excessive current, the output value is taken limiting process in the program. The current loop reference value is multiplied the synchronisation signal acquiring by DPLL (Digital Phase Locked Loop), thus getting the input current reference value as the same phase as the grid voltage (Lin, Huang & Wan, 2016). Then the input current feedback goes similar with the current reference value after Comparison between them. This will ensure that the unit input power factor. The error value between the grid voltage and inner current loop output is taken as the modulation wave for generating SPWM signal, ultimately driving four IGBT switching devices (Li, Qi, Tan & Hui, 2018).

2.2. The strategy of inner current loop control

It is mentioned in (Ye, Dai, Lam, Wong & Guerrero, 2016) that the system which theoretically adopts the traditional PI control strategy to track the rapidly changing sinusoidal signal in the internal current loop has static error and poor anti-jamming performance. Both of which severely restricts the PI control application on sinusoidal tracking. Therefore, to improve the control effect, a Proportion - Resonant (PR) controller is design for inner current loop controller (Gao, Wu, Huang, Zhang & Xiao, 2017). The principle is to introduce infinite gain at the fundamental signal frequency to eliminate control system errors.

Equation 1: The transfer function of ideal PR controller

$$G(s) = k_p + \frac{2k_R s}{s^2 + \omega^2}$$

Where:

k_p = coeffcient of proportionality

k_R = resonance coefficient

ω = resonant angular frequency

When taking the coeffcient of proportionality $k_p = 1$, the resonance coefficient $k_R = 1$, the resonant angular frequency ω = 314rad/s. The Bode diagram is shown in Figure 2. The gain can be seen infinity at the resonance frequency. When using PR inner current loop controller, the ideally steady-state error is zero (Komurcugil, Altin, Ozdemir & Sefa, 2016; Nian, Shen, Yang & Quan, 2015; Stojic, Tarczewski & Klasnic, 2017). Due to the substantial increase in resonant frequency, the response is faster when the amount of sinusoidal is being tracked. In short, PR controllers outperform PI controllers in steady-state performance.

However, the controller is difficult to obtain an infinite gain in practical applications, and there are problems in terms of system stability. In addition, when the frequency near the resonance point drops too fast, it adversely affects the frequency of the line side voltage. Thus, people often use a modified PR controller in practice which adds a cut-off frequency based on the ideal resonant controller to adjust the gain and broadband at the resonance frequency.

Equation 2: The transfer function of ideal PR controller which adds a cut-off frequency

$$G(s) = k_p + \frac{2k_R\omega_c s}{s^2 + 2\omega_c s + \omega^2}$$

When taking the scale factor $k_p = 1$, the resonance factor $k_R = 10$, the resonant angular frequency $\omega = 314rad/s$, the cut-off frequency $\omega_c = 5rad/s$. The Bode diagram is shown in Figure 3. The gain is 56 dB at resonance frequency for the improved PR controller when take Figure 2 and Figure 3 into comparison, which can reduce steady-state error, widen the resonant band width, and enhance the anti-jamming capability while tracking the sinusoidal amount.

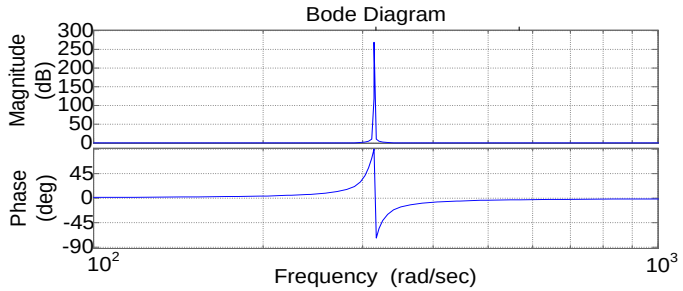

Figure 2: The bode plot of ideal PR function

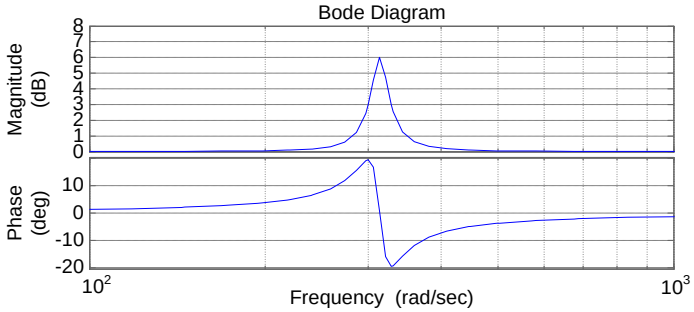

Figure 3: The Bode plot of improved PR function

The Equation 2 shows the performance of the improved PR controller is closely related to k_p, k_R, ω_c. To analyse how each variable influence PR controller, change one of the three variables and keep the other two variables constant.

As can be seen in Figure 4, when keep k_R, ω_c constant and change k_p, the gain and bandwidth of the controller at the resonant frequency hold constant while the gain at other frequencies change significantly. when keep k_p, ω_c constant and change k_R, the gain of the controller at the resonant frequency increases with the growth of k_R, but the bandwidth does not change. When keep k_p, k_R constant and change ω_c, the bandwidth at the resonant frequency widens as ω_c becomes large, but the resonant gain is constant.

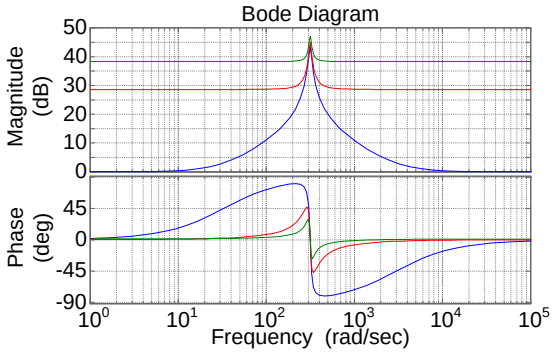

(a) k_R = 150, ω_c = 10, k_p changed

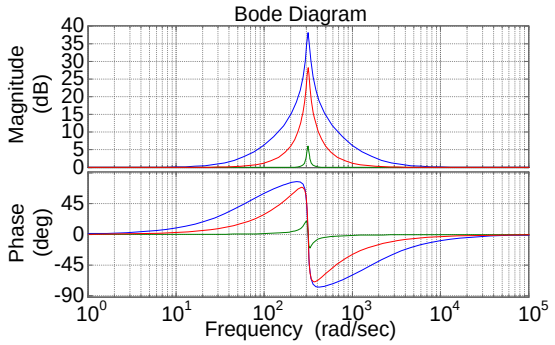

(b) k_p = 1, ω_c = 10, k_R changed.

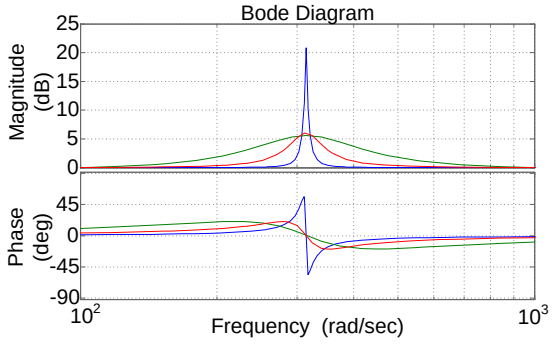

(c) k_p = 1, k_R = 1, ω_c changed.

Figure 4: The Bode diagram of PR controller, when k_p, k_R and ω_c take different values

Therefore, it can be concluded that adjusting coefficient k_p could change the amplitude, phase margin and the dynamic performance of PR controller, which is analogous to the of PI controller. Coefficient k_R adjusts the resonance gain of PR controller. Coefficient ω_c adjusts the resonance bandwidth of PR controller. With the increasing of bandwidth at the resonant frequency while ω_c doing up, it will weaken the PR controller's ability to control input signal.

2.3. The discrete of improved PR controller

In order to make the parameters of the controller facilitate adjustment in practical applications, digital discretisation controller is often used. There are many ways in obtaining discretisation continuous domain function, such as Forward Fourier Approximation, Backward Fourier Approximation, Bilinear Transformation and so on. Bilinear

Transformation is more facilitate implement (Vidal et al., 2013). Putting the Formula $s = \frac{2}{T_s} \cdot \frac{1-z^{-1}}{1+z^{-1}}$ into Equation 2, we can obtain the transfer function of discretisation PR controller as Equation 3.

Equation 3: The transfer function of ideal PR controller which adds a cut-off frequency

$$G(z) = \frac{a_0 + a_1 z^{-1} + a_2 z^{-2}}{1 + b_1 z^{-1} + b_2 z^{-2}}$$

Where:

a_0, a_1, a_2, b_1, b_2 = associated coefficients with $G(z)$

k_p, k_R, ω_c, T_s = made up of a_0, a_1, a_2, b_1, b_2

Equation 4: Differential equation

$$y(k) = a_0 u(k) + a_1 u(k-1) + a_2 u(k-2) - b_1 y(k-1) - b_2 y(k-2)$$

Where:

$y(k)$ = output of the controller

$u(k)$ = error value of the line-side input current

Digital realisation of the dual closed-loop controller

To a certain extent, dual loop control can increase the stability margin of the control system and improve the dynamic response of load disturbances (Nguyen & Lee, 2013; Dou et al., 2015). In this study, the controlling motherboard constituted of DSP chip and FPGA chip. The DSP chip used TI Corporation TMS320F28335 and the FPGA chip used ALTERA Company EP1C20F324I7. The line-side input voltage, current, and intermediate DC voltage were put into the FPGA by AD treatment as analogy sampled value. On one hand, the line-side input voltage was locked phase by FPGA, and real-time phase value of voltage is calculated and sent to DSP. On the other hand, the PWM pulse emitted by the DSP was addressed through the redistribution and protection logic processing by FPGA. Start-up logic and shutdown logic control, pre-charge logic control, rectification control algorithms, fault detection, and communication functions are completed by DSP. The software flow chart of single phase PWM rectifier was shown in Figure 5.

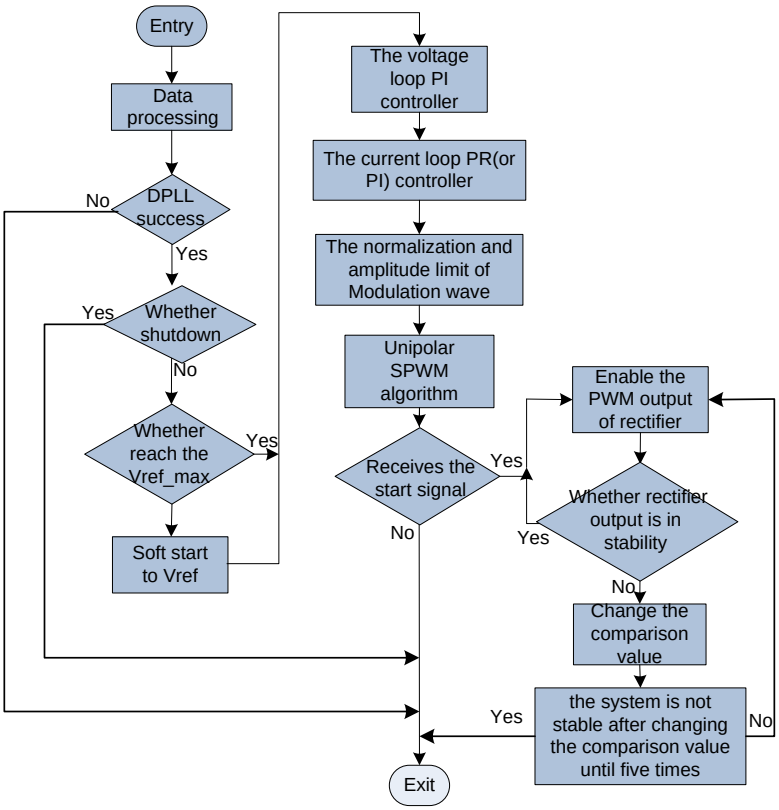

Figure 5: The software flow chart of single phase PWM rectifier

The system analogy signals are taken as the input signals after sampling by AD7606 for fault diagnosis and PLL. First, the system determines whether the phase-locking is successful and if the stop command is received. It starts the rectification control only if both satisfy the conditions and then determines whether a given voltage achieve a given maximum value, otherwise the reference voltage is soft given. The error of given voltage and feedback voltage is limited after the PI controller, taken as the input modulation wave of unipolar SPWM modulation and compared with the triangular carrier in the DSP to generate a PWM wave. Then, determine whether the system is faulty. If not, a starting signal starts rectifier and enable the PWM output. Finally, determine whether the output DC voltage is stable within a certain range. If not, the system is delayed stop after changing the comparison value until five times. If the system is in stability, do return to the previous cycle.

3. SIMULATION

Figure 1 shows the simulation model of the single-phase PWM rectifier in MATLAB /Simulink is built. As shown in Figure 6, unipolar SPWM modulation is used in direct current control strategy. PI controller is used in controlling outer voltage loop while PI controller and PR controller are used in controlling inner current loop respectively. k_p = 1, k_R = 1, ω = 314*rad/s*, ω_c = 5*rad/s* when PR controller is used. k_p = 0.5, k_i = 300 when PI controller is used. u_s = 335*V*/50*Hz*, L = 1.5*mH*, C = 18800*uF*, R_o = 8Ω.

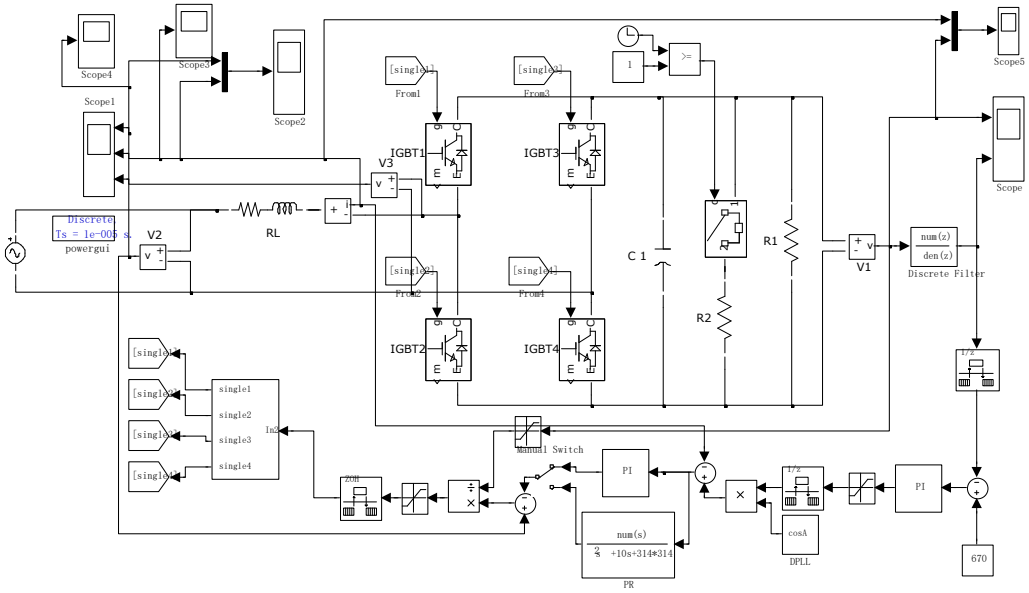

Figure 6: The simulation structure of single phase PWM rectifier

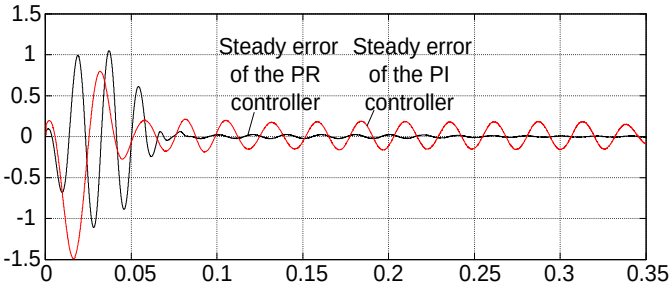

Figure 7: The steady-state error waveform of PI controller and PR controller

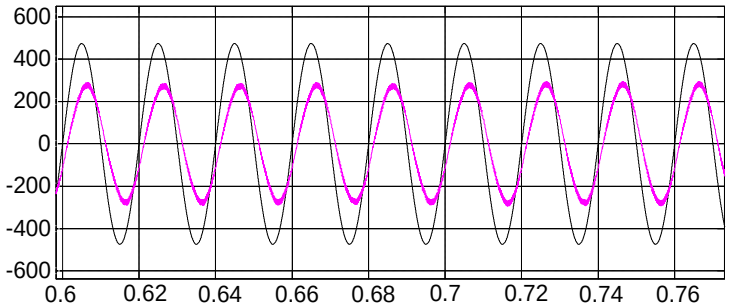

Figure 8: The current and voltage simulation waveform of PI controller

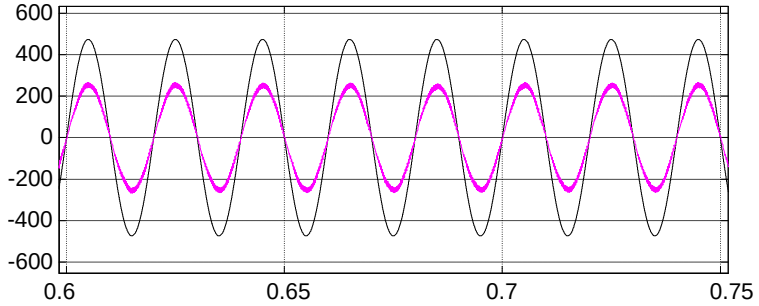

Figure 9: The current and voltage simulation waveform of PR controller

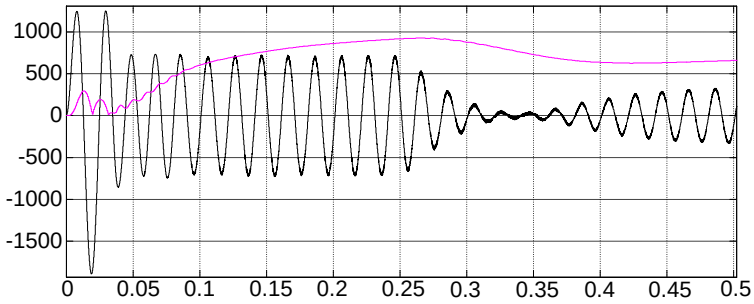

Figure 10: The current and the DC bus voltage simulation waveform of PI controller

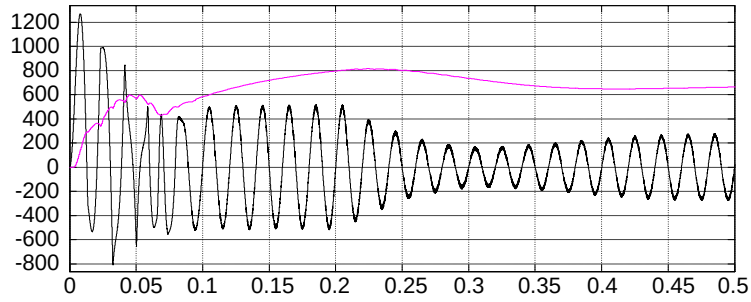

Figure 11: The current and the DC bus voltage simulation waveform of PR controller

Figure 7 presents simulation waveform of error values using PI controller and PR controller respectively. It can be clearly seen that the steady-state error of the input current using PI controller is bigger than that of PR controller. Figure 8 and Figure 9 are simulation waveforms that the input voltage tracks the input current at steady state when PI controller and PR controller are used respectively. The voltage lagged the current 16.7ms and the power factor is 91.7% in Figure 8. In Figure 9, the voltage can be fully tracked by the current so that their zero crossings are overlap, and the power factor is reached 1. Taking Figure 10 and Figure 11 into Comparison, the DC bus voltage using PR controller is quicker in reaching than that of PI controller. And the line-side input current changes much more consistent and smoother. What's more, the better dynamic response is obtained.

4. CONCLUSIONS

In this paper, an improved cut off frequency-added PR controller is applied to a single-phase PWM rectifier based on the ideal PR controller, which increases the bandwidth and gain. It overcomes the shortcomings that the ability of tracking sinusoidal current signal is poor when the steady-state error is zero when the traditional PI controller is applied. And the power factor is closer to 1. The harmonic near the fundamental is effectively suppressed and the quality of the current waveform is obviously improved while the stability and anti-jamming capability of the system are raised.

5. REFERENCES

Alemi, P., Jeong, S. Y., & Lee, D. C. (2015). Active damping of LLCL filters using PR control for grid-connected three-level T-type converters. Journal of Power Electronics, 15(3), 786-795.

Chen, Y., Luo, A., Shuai, Z., & Xie, S. (2013). Robust predictive dual-loop control strategy with reactive power compensation for single-phase grid-connected distributed generation system. IET Power Electronics, 6(7), 1320-1328.

Chowdhury, M. A. (2016). Dual-loop H∞ controller design for a grid-connected single-phase photovoltaic system. Solar Energy, 139, 640-649.

Dou, X., Yang, K., Quan, X., Hu, Q., Wu, Z., Zhao, B., ... & Jiao, Y. (2015). An optimal PR control strategy with load current observer for a three-phase voltage source inverter. Energies, 8(8), 7542-7562.

Gao, J., Wu, X., Huang, S., Zhang, W., & Xiao, L. (2017). Torque ripple minimisation of permanent magnet synchronous motor using a new proportional resonant controller. IET Power Electronics, 10(2), 208-214.

Guo, Q., Liu, H., & Zhang, Y. (2015). A new control strategy for a three-phase PWM current-source rectifier in the stationary frame. Journal of Power Electronics, 15(4), 994-1005.

Jing, F., & He, F. Y. (2017). A Simplified Carrier-Based Pulse-Width Modulation Strategy for Two-level Voltage Source Inverters in the Over-modulation Region. Journal of Power Electronics, 17(6), 1480-1489.

Komurcugil, H., Altin, N., Ozdemir, S., & Sefa, I. (2016). Lyapunov-function and proportional-resonant-based control strategy for single-phase grid-connected VSI with LCL filter. IEEE Transactions on Industrial Electronics, 63(5), 2838-2849.

Li, S., Qi, W., Tan, S. C., & Hui, S. Y. (2018). Enhanced automatic-power-decoupling control method for single-phase AC-to-DC converters. IEEE Transactions on Power Electronics, 33(2), 1816-1828.

Lin, Z., Huang, S., & Wan, S. (2016). A novel control scheme for T-type three-level SSG converters using adaptive PR controller with a variable frequency resonant PLL. Journal of Power Electronics, 16(3), 1176-1189.

Ma, J., Song, W., Wang, S., & Feng, X. (2018). Model Predictive Direct Power Control for Single Phase Three-Level Rectifier at Low Switching Frequency. IEEE Transactions on Power Electronics, 33(2), 1050-1062.

Nguyen, T. H., & Lee, D. C. (2013). Control strategy for three-phase grid-connected converters under unbalanced and distorted grid voltages using composite observers. Journal of Power Electronics, 13(3), 469-478.

Nian, H., Shen, Y., Yang, H., & Quan, Y. (2015). Flexible grid connection technique of voltage-source inverter under unbalanced grid conditions based on direct power control. IEEE Transactions on Industry Applications, 51(5), 4041-4050.

Pu, X. S., Nguyen, T. H., Lee, D. C., & Lee, S. G. (2010). Identification of DC-link capacitance for single-phase AC/DC PWM converters. Journal of Power Electronics, 10(3), 270-276.

Stojic, D., Tarczewski, T., & Klasnic, I. (2017). Proportional-integral-resonant AC current controller. Advances in Electrical and Computer Engineering, 17(1), 81-89.

Taha, W., Beig, A. R., & Boiko, I. (2018). Quasi optimum PI controller tuning rules for a grid-connected three phase AC to DC PWM rectifier. International Journal of Electrical Power & Energy Systems, 96, 74-85.

Vidal, A., Freijedo, F. D., Yepes, A. G., Fernandez-Comesana, P., Malvar, J., López, Ó., & Doval-Gandoy, J. (2013). Assessment and optimisation of the transient response of proportional-resonant current controllers for distributed power generation systems. IEEE Transactions on Industrial Electronics, 60(4), 1367-1383.

Ye, T., Dai, N., Lam, C. S., Wong, M. C., & Guerrero, J. M. (2016). Analysis, design, and implementation of a quasi-proportional-resonant controller for a multifunctional capacitive-coupling grid-connected inverter. IEEE Transactions on Industry Applications, 52(5), 4269-4280.

128: Frequency conversion control of photovoltaic grid-connected inverter based on LCL filtering

Jian PAN[1], Kun LI[2], Dongchu LIAO[3]

[1]Jian Pan, Hubei University of Technology, jpan12@126.com
[2]Kun Li, Hubei University of Technology, 834435731@qq.com
[3]Dongchu Liao, Hubei University of Technology, liaodc63@126.com

Aiming at the problem that the filtering effect of LCL filter becomes worse when the PV system works at low power, this paper presents a control strategy to change the switching frequency according to the instantaneous output power of the inverter. By analysing the design method of each parameter of LCL filter, a single-stage PV grid-connected inverter structure is used to establish the frequency loop based on grid voltage oriented vector control (VOC) to determine the optimal switching frequency under the current power state .The design methods of power detector, frequency calculation and frequency hysteresis comparator are analysed in detail. Finally, the waveforms of grid-connected current before and after frequency conversion are contrasted by MATLAB simulation to verify the feasibility and effectiveness of the inverter control strategy.

Keywords: frequency conversion control; LCL; frequency loop; power quality

1. INTRODUCTION

In the photovoltaic grid-connected inverter based on LCL filter, the filter parameters are designed according to the rated power of the grid-connected inverter (Ruan, Wang & Pan, 2017). However, the power generated by PV modules is closely related to the intensity of solar radiation. Since the intensity of solar radiation changes with time and season, the inverter will not always operate at rated power. When the output power of the PV module gradually decreases, the filtering performance of the LCL filter circuit designed according to the rated output power will decrease as the output current decreases (Xu, Ji, Ge et al, 2016), so that the output current harmonic will increase. Harmonic current injection into the grid will distort the grid voltage and grid current, and harmonics of the grid voltage will increase the harmonics of the local grid-connected current. Therefore, the current harmonics of grid-connected power must be limited to improve the grid-connected power quality.

For current grid-connected power quality problems, the literature (Lai & Kim, 2016) adopts an improved current control method to separate the harmonic components by the sliding average filter from grid-connected current and the grid voltage, and then perform the prediction and compensation on the harmonics, but this method has calculation delay, so that it cannot be fully synchronised with the grid voltage. The literature (Judewicz, González, Echeverría et al, 2016) adopts the predictive current control method, which can effectively reduce the current harmonics of the grid connection. However, the control parameters that affect the system bandwidth and robustness in the control method are difficult to determine, and it is unable to achieve better results.

In order to reduce the switching losses of the power device, the inverter generally selects a lower switching frequency according to the rated power (Huang, 2011). When the inverter operates at lower power, the switching loss of the power device is no longer a limiting factor. Therefore, increasing the switching frequency of the power device according to certain constraints as the output power is reduced helps to reduce the harmonic content of the grid current and improve the grid-connected power quality.

2. INVERTER MODEL AND FILTER DESIGN

2.1. LCL type inverter structure

Three-phase LCL grid-connected inverter topology is shown in Figure 1. The DC power generated by the PV array is filtered by the DC bus capacitance C_1, it is modulated by the switch $s_1 \sim s_6$ to obtain an inverted modulated square wave. After being filtered by the LCL, a sine wave with the same frequency as the grid voltage is obtained, and finally injected into the grid (Xu, Xie & Zhang, 2015).

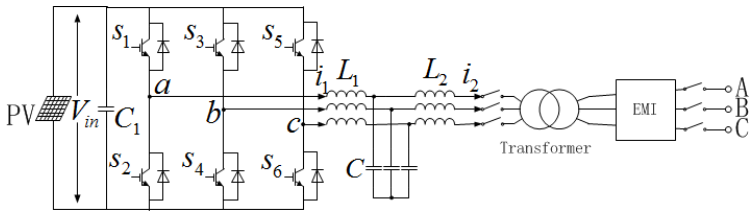

Figure 1: Three-phase LCL inverter circuit structure

2.2. Three-phase LCL Filter Design

LCL filter capacitor design

The larger the LCL filter capacitor is, the larger the reactive power introduced by the filter is, and the larger the current flowing through the inductor L_1 and the switch tube, so the conduction loss of the switch tube will also increase. Defining the ratio of the reactive power introduced by capacitor C in the entire inverter to the output rated active power is λ_c, and it is generally stipulated that its value is less than or equal to 5% (Liserre, Blaabjerg & Hansen, 2005). The maximum value of filter capacitor C is Equation 1.

Equation 1: The maximum value of filter capacitor C.

$$C = \frac{\lambda_c P_{one}}{\omega_0 V_g^2}$$

Where:

P_{one} = the power of one phase of the three-phase LCL inverter

ω_0 = the corner frequency of the power grid

V_g = the effective value of the phase voltage of the power grid

Inverter side inductance L_1 design

As can be seen from Figure 1, the current flowing through the inductor L_1 is also the current flowing through the switch. The current ripple of the inductor L_1 is too large to cause a large loss of the inductor and also increases the current stress of the switch tube, resulting in an increase in the conduction loss and the switching loss of the switch tube. Define the ripple factor of inductor L_1 as λ_{L_1}. At a grid frequency of 50Hz, the minimum value of filter inductance L_1 is Equation 2 (Ruan, Wang & Pan, 2017).

Equation 2: The minimum value of filter inductance L_1.

$$L_{1\_\min} = \frac{\sqrt{3} M_r V_{in} V_g}{4 \lambda_{L1} P f_{sw}}$$

Where:

V_{in} = the DC bus voltage

M_r = the modulation ratio, $M_r = \frac{2\sqrt{2} V_g}{V_{in}}$

P = the total power of the inverter

f_{sw} = the carrier frequency of the switch

Net side inductance L_2 design

The main purpose of the net side inductance L_2 is to eliminate the higher harmonics generated by the inverter, so the main harmonic of the inverter output current can be found through the simulation model, and then the size of the inductor L_2 is selected, and its minimum value (Equation 3) is as follows:

Equation 3: The minimum value of filter inductance L_2.

$$L_{2\_\min} = \frac{1}{L_1 C \omega_h^2 - 1} \left(L_1 + \frac{\left| V_{aN}(j\omega_h) \right|}{\omega_h \lambda_h I_2} \right)$$

Where:

ω_h = the main harmonic frequency

$\left| V_{aN}(j\omega_h) \right|$ = the main effective harmonic value

λ_h = the ratio of the main harmonic current of the rated grid-connected current

I_2 = the effective value of the rated grid-connected current

LCL filter frequency analysis

When the parameter design of the LCL filter is completed, its resonant frequency f_{res} is also determined. Generally, the resonant frequency is greater than 10 times the grid frequency and less than half of the switching frequency f_{sw}. Figure 2 shows the Bode plot of the LCL filter. At the right side of the resonant frequency, the LCL filter has a stronger ability to suppress high frequencies. Therefore, the higher the switching frequency, the larger the LCL filter's attenuation factor. Therefore, increasing the switching frequency helps to enhance the filtering effect of the LCL filter.

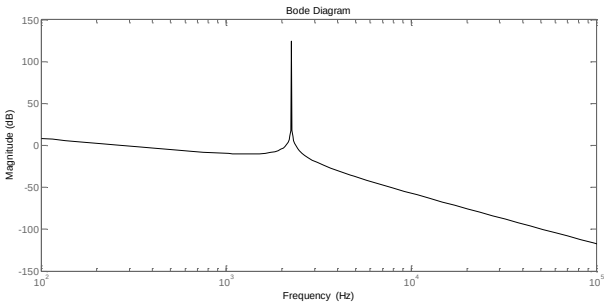

Figure 2: Three-dimensional LCL filter Bode diagram

3. VARIABLE FREQUENCY CONTROL OF LCL TYPE GRID-CONNECTED INVERTER

3.1. LCL type inverter structure

In the LCL filter design, the inductor L_1 is usually larger than the inductor L_2 [1], so the inductor L_1 becomes the main limiting factor for the filter volume and economy. From Equation 2, it can be seen that the minimum value of L_1 is inversely proportional to the rated power of the inverter and the carrier frequency of the switch. According to the foregoing, the parameters of the LCL filter are designed based on the rated power of the inverter. However, the photovoltaic inverter does not always operate at the rated power throughout a whole day, especially in the morning and evening. Due to low output power, the filtering effect of LCL filter becomes worse. To this end, a control strategy for a variable switch tube carrier frequency is proposed, as shown in Figure 3.

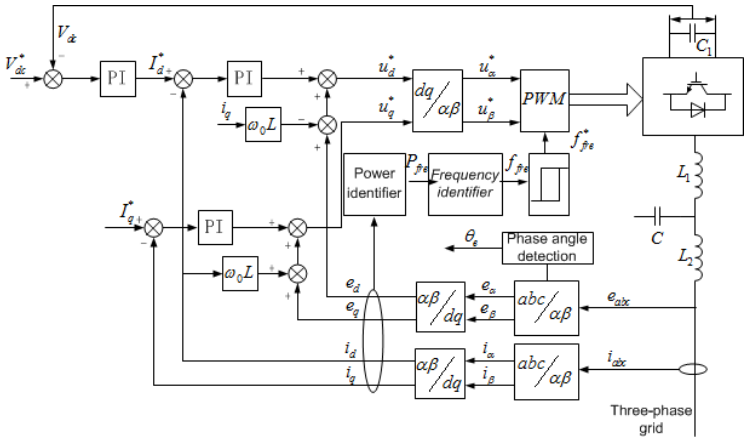

Figure 3: Three-phase LCL inverter control strategy，$e_{abc}=[e_a,e_b,e_c]$ is the grid phase voltage, $i_{abc}=[i_a,i_b,i_c]$ is the grid-connected phase current, i_q^* is the given value of the reactive current, V_{dc}^* is the given value of the bus voltage, ω_0 is the corner frequency of the grid, and L is the sum of the inductances L_1 and L_2.

This strategy adds a frequency loop to the voltage-oriented control (VOC) (Wang, Xiao, Yao et al, 2007; Guo, Xu & Xie, 2008) of the grid. In the three control loops, the current loop is fastest, the voltage loop is second, and the frequency loop is the slowest. In the current loop, mainly including Clark transform, Park transform and feed forward decoupling, the purpose is to quickly track the grid voltage and ensure grid-connected power quality; the output of the voltage loop is used as a reference for the active current in the current loop, and the purpose is to stabilise the DC bus voltage; the frequency loop mainly includes three parts, namely power identifier, frequency identifier and frequency hysteresis comparator. The function of the power identifier is to obtain the output power of the current inverter. The role of the frequency identifier is to determine the optimal carrier frequency of the switch based on the current power. The frequency hysteresis comparator mainly prevents frequency jitter caused by sensor measurement errors.

3.2. Frequency Ring Design

Power identifier

The purpose of the power identifier is to calculate the plural power of the grid-connected inverter currently injected into the grid. From the instantaneous power theory (Zhang X, Cao R, 2011)[11], the instantaneous active power P_d and reactive power P_q of the three-phase LCL grid-connected inverter are Equation 4.

Equation 4: The instantaneous active power P_d and reactive power P_q of the three-phase LCL grid-connected inverter.

$$P_d = \frac{3}{2}(e_d i_d + e_q i_q)$$

$$P_q = \frac{3}{2}(e_d i_q - e_q i_d)$$

The instantaneous reactive power and instantaneous active power can be used to derive the plural power P_s injected into the grid by the three-phase LCL grid-connected inverter.

Equation 5: The plural power injected into the grid.

$$P_s = P_d + jP_q = \frac{3}{2}(e_d i_d + e_q i_q) + j\frac{3}{2}(e_d i_q - e_q i_d)$$

Since the voltage-oriented control method is adopted, so $e_q = 0$, Equation 4 and Equation 5 can be simplified as Equation 6 and Equation 7.

Equation 6: The simplified instantaneous active power P_d and reactive power P_q.

$$P_d = \frac{3}{2}e_d i_d$$

$$P_q = \frac{3}{2}e_d i_q$$

Equation 7: The simplified plural power.

$$P_s = \frac{3}{2}e_d i_d + j\frac{3}{2}e_d i_q$$

Frequency identifier

From Equation 2 we can see that in the case of PV inverter power change, in order to ensure the filter performance of the filter, the product Pf_{sw} of the current power P and the current frequency f_{sw} should be a constant value. Set the rated power of the photovoltaic grid-connected inverter to be P_R, and the switching frequency at rated power is f_R. The Equation 8~10 can be obtained.

Equation 8: The relationship between power and frequency.

$$Pf_{sw} = P_R f_R$$

Equation 9: The apparent power $|P_s|$ can be obtained from Equation (7).

$$|P_s| = \frac{3}{2}\sqrt{e_d^2 i_d^2 + e_d^2 i_q^2}$$

Equation 10: Substituting Equation (9) into Equation (8).

$$f_{sw} = \frac{2P_R f_R}{3\sqrt{e_d^2 i_d^2 + e_d^2 i_q^2}}$$

The switching loss of the switch is also related to its switching frequency. The switching loss of the switch is calculated as Equation 11 (Wang, 2014).

Equation 11: Switching loss.

$$P_{switch\_on} = \frac{1}{2}V_{DS} I_D t_r f_{sw}$$

$$P_{switch\_off} = \frac{1}{2}V_{DS} I_D t_f f_{sw}$$

Where:

V_{DS} = the voltage drop when the switch is fully turned off

I_D = the current flowing when the switch is turned on

t_r = the sum of the current rise time and voltage drop time

t_f = the sum of the current drop time and voltage rise time

P_{switch_on} = the opening loss of the switch

P_{switch_off} = the turn-off loss of the switch

From Equation (11), it is known that the switching loss of the switch tube is proportional to its switching frequency. When the system power is reduced, although the current flowing through the switch tube is decreasing at this time, the efficiency of the system will decrease with the increase of the switching frequency from the Equation 12.

Equation 12: the efficiency of the system.

$$\eta = \frac{P_{switch\_on} + P_{switch\_off} + P_{on}}{P} = \frac{V_{DS} I_D (t_r + t_f)}{2P} f_{sw} + \frac{P_{on}}{P}$$

Where:

P_{on} = the conduction loss of the switch tube

To ensure system efficiency, the switching frequency must have an upper limit.

Frequency Hysteresis Comparator

In order to prevent frequency jitter due to sensor sampling errors, a frequency hysteresis comparator is required, as shown in Figure 4.

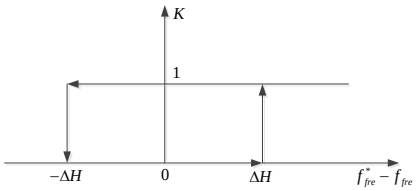

Figure 4: Frequency Hysteresis Comparator

Among them, $2\Delta H$ is the frequency hysteresis width, f_{fre}^* is the switching frequency of the current switch tube, and f_{fre} is the switching frequency identified by the frequency *identifier*. K is the frequency selection switch. When $K=1$, the switching frequency of the switch tube is f_{fre}; when $K=0$, the switching frequency of the switch tube is f_{fre}^*. When $f_{fre}^* - f_{fre} > \Delta H$, $K=1$; When $-\Delta H < f_{fre}^* - f_{fre} < \Delta H$ and $\frac{d(f_{fre}^* - f_{fre})}{dt} < 0$, $K=1$; When $f_{fre}^* - f_{fre} < -\Delta H$, $K=0$; When $-\Delta H < f_{fre}^* - f_{fre} < \Delta H$ and $\frac{d(f_{fre}^* - f_{fre})}{dt} > 0$, $K=0$. The output of the frequency hysteresis comparator reflects the amount of switching state where the actual switching frequency deviates from the calculated switching frequency.

4. SIMULATION ANALYSIS

In order to verify the correctness of the above analysis, a simulation model was built on MATLAB. Set the reactive power to 0. Using the LCL filter parameter design method, design the inductor L_1, L_2 and capacitance parameters with a rated power of 46.6 kW as shown in Table 1.

Table 1 Simulation Parameters of Three-phase LCL Grid-connected Inverter

Parameters	Symbol	Value	Units
Rated power	P_R	46.6	kW
Grid voltage	V_g	220	V
Grid frequency	f_0	50	Hz
DC bus voltage	V_{in}	650	V
Inverter side inductance	L_1	500	μH
Filter capacitor	C	60	μF
Net side inductance	L_2	100	μH
Rated switching frequency	f_R	10	kHz

According to the LCL filter parameters to draw its Bode diagram as shown in Figure 5 Shown, when the switching frequency f_{sw} = 10kHz, LCL filter attenuation factor of 57dB; when the switching frequency becomes 20kHz, LCL filter attenuation multiple of 75.3dB. This shows that the LCL filter has a better filtering effect at high frequencies.

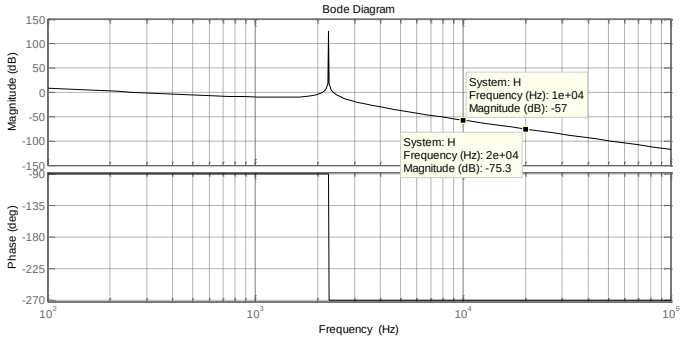

Figure 5: LCL Filter Bode Diagram

The three-phase LCL grid-connected inverter has a rated output power (46.6 kW) and the grid-connected current THD is 0.8% when the switching frequency is 10 kHz. The output power of the inverter is reduced by half (23.3 kW) at 0.05s, as shown in Figure 6(a). From the waveform, it can also be seen that the THD of the grid connection current increases to 1.65% at $P_R / 2$.

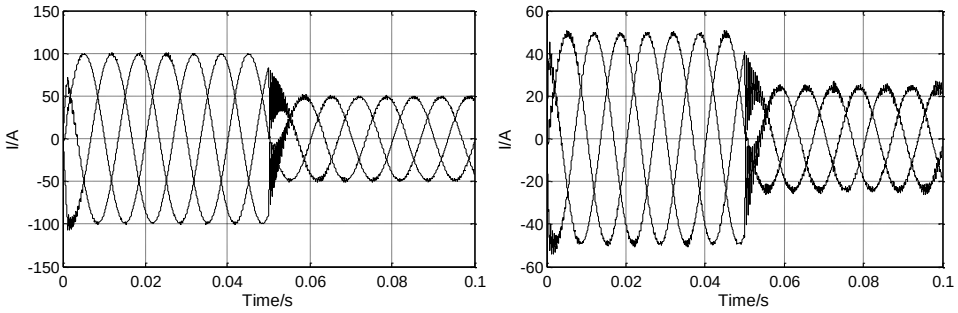

(a) Power dropped from P_R *to* $\frac{P_R}{2}$ *(b) Power dropped from* $\frac{P_R}{2}$ *to* $\frac{P_R}{4}$

Figure 6: Fixed frequency grid current waveform

Figure 6(b) shows the inverter's grid-connected current waveform when the output power of the inverter is reduced from 1/2 rated power (23.3 kW) to 1/4 rated power (11.6 kW). Due to the large difference between the output power and the rated power of the system at this time, the THD of the grid-connected current rapidly rises to 2.77%.

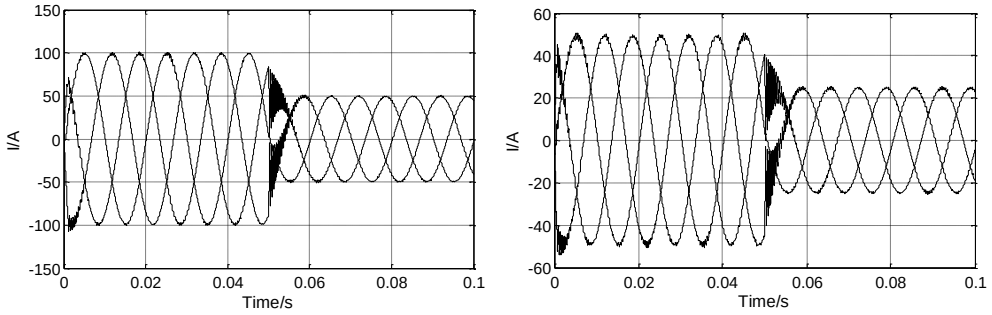

(a) Power dropped from P_R *to* $\frac{P_R}{2}$ *(b) Power dropped from* $\frac{P_R}{2}$ *to* $\frac{P_R}{4}$

Figure 7: Waveform of grid-connected current under frequency control

The simulation parameters of the frequency conversion control strategy are shown in Table 1, and the waveform of the grid-connected current is shown in Figure 7. Figure 7(a) reduces the rated power of the system to 1/2 of the rated power at 0.05s. At the same time, the switching frequency of the switching tube is changed to 20 kHz according to the conversion strategy of this paper. At this time, the grid-connected current waveform THD is 1.05%. Compared with the control method without changing the frequency in Figure 6(a), it is much lower. In order to more

clearly reflect the advantages of the frequency conversion control strategy, the waveform shown in Figure 7(b) adopts a grid-connected current waveform with a rated frequency of 10 kHz at 1/2 rated power, and the output power of the inverter is reduced to 1/4 of the rated power at 0.05s, while changing the switching frequency of the switching tube to 20 kHz, the THD of the grid-connected current at this time was changed from 1.65% to 1.71%, which was greatly improved compared to 2.77% of Figure 7(b).

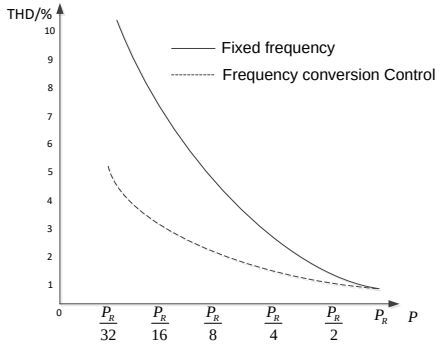

Figure 8: THD of fixed frequency control and frequency conversion control under non-rated power

Figure 8 shows the variation of the THD of the grid-connected current under the non-rated power state in the fixed frequency control method and the frequency conversion control method. It can be seen from the figure that as the instantaneous power of the system decreases, the THD of the grid-connected current of the fixed-frequency control method rises rapidly, and the variation of the grid-connected current THD under the frequency conversion control strategy is small.

5. CONCLUSION

This paper combines the design method of LCL filter for grid-connected inverter and the vector control strategy based on grid voltage orientation, adds frequency control loops with power determiner, frequency identifier, and frequency hysteresis comparator. Detailed derivation proves theoretically the feasibility and effectiveness of the frequency conversion control strategy. The MATLAB simulation experiment gives a comparison of the simulation experiment of the fixed frequency control and the variable frequency control. It is verified that the frequency conversion control method can reduce the grid-connected current THD in the low power state of the inverter and effectively improve the grid-connected power quality.

2. REFERENCES

Ruan X, Wang X, Pan D, 2017. et al. Control techniques for LCL-type grid-connected inverters[J].

Xu J, Ji L, Ge X, et al, 2016. LCL filter Optimisation Design With Consideration of Inverter-side Current Feedback Control Impacts[J]. Chinese Society for Electrical Engineering, 36(17): 4656-4664.

Lai N B, Kim K H, 2016. An improved current control strategy for a grid-connected inverter under distorted grid conditions[J]. Energies, 9(3): 190.

Judewicz M G, González S A, Echeverría N I, et al, 2016. Generalized predictive current control (GPCC) for grid-tie three-phase inverters[J]. IEEE Transactions on Industrial Electronics, 63(7): 4475-4484.

Huang J, 2011. Design of switching frequency of DC-DC switching converter[J]. Power Technology, 35(5): 574-577.

Xu J, Xie S, Zhang B, 2015. Overview of Current Control Techniques for Grid-connected Inverters With LCL filters in Distributed Power Generation Systems[J]. Chinese Society for Electrical Engineering, 35(16): 4153-4166.

Liserre M, Blaabjerg F, Hansen S, 2005. Design and control of an LCL-filter-based three-phase active rectifier[J]. IEEE Transactions on industry applications, 41(5): 1281-1291.

Wang Z, Xiao L, Yao Z, etc, 2007. Design and Implementation of a High Performance Utility-Interactive Inverter[J]. Chinese Society for Electrical Engineering, 27(1): 54-59.

Guo L, Xu A, Xie S, 2008. Research on Indirect Current Control Algorithm for Grid-connected Inverter[J]. Power Electronics, 42(4): 36-38.

Wang B, 2014. Research on the Loss Calculation Method and Temperature Testing of the IGBTs in AC-DC Converters with Chaotic SPWM Control[D].Beijing: Beijing Jiaotong University.

Zhang X, Cao R, 2011. Solar photovoltaic grid-connected power generation and its inverter control[J].

132: Effects of thermal and rheological properties of biodiesel from microalgae and feedstocks

Andrew C. ELOKA-EBOKA[1], Freddie L. INAMBAO[2], Opeyeolu T. LASEINDE[3]

[1] Discipline of Mechanical Engineering, University of KwaZulu-Natal, Durban, South Africa, fatherfounder@yahoo.com
[2] Discipline of Mechanical Engineering, University of KwaZulu-Natal, Durban, South Africa, inambaof@ukzn.ac.za
[3] Department of Mechanical and Industrial Engineering, University of Johannesburg, Johannesburg, South Africa, tlaseinde@uj.ac.za

Comparative investigation and assessment of thermal and rheological properties of biodiesel fuels from micro algae and other second generation feedstocks were carried out with the aim of assessing micro-algal technology as a viable biodiesel production option. Chlorella vulgaris and Synedesmus spp were collected, cultured and cultivated in the open pond and in photobioreactor differently and inoculated with Agar broth media for twenty-three and sixteen days respectively for biomass production/accumulation. Thermal parameters and rheological properties were studied. Viscosity is one of the most critical features of a fuel or biofuel. It plays a dominant role in fuel spray, fuel-air mixture formation and the combustion process. Fuels are sprayed into compressed air and atomised into small droplets near the nozzle exit in any diesel engine. In the combustion chamber, fuel forms cone-shaped spray at the nozzle exits which impacts the viscosity and also affects the atomisation quality, penetration and size of fuel droplets. Density is an important fuel property that influences the amount of fuel injected into the engine cylinder. Changes in fuel density influences engine output power due to different mass of the fuel being injected, and this directly affects engine performance characteristics and emissions. TGA conducted reveals stability of algal oil and biodiesel after thermal treatment. With studies of viscosity and shear stress at varying speeds and temperature being evaluated, the interaction of viscosity at different torque presented in this study decreases from 20 rpm to 60 rpm but increases in shear stress at temperatures of 40ºC and 60ºC. Across temperature was a general initial decrease and later increase from lower temperatures to higher temperatures. The general conclusion is that shear stress increases with increase in temperature and torque while viscosity generally decreases along the trends.

Keywords: Thermal properties, rheological, viscosity, biodiesel, algae, Chlorella Spp, Synedesmus Spp.

1. INTRODUCTION

Many studies have been carried out about the future possibility of exhausting the planet's resources and its ability to sustain its inhabitants. This century will see great changes, and fossil fuels will be partially replaced by new energy sources that can fulfil current needs, but which have a lower environmental impact. Nature has developed photosynthesis, a very efficient light harvesting and conversion system, which uses sunlight to synthesise chemical energy carriers such as carbohydrates, lipids and proteins. Over millions of years nature has collected the sun's energy and stored it as fossil fuels such as oil, coal and natural gas. Besides the properties of photosynthetically produced fossil fuels, the potential of current photosynthetic systems as a provider of clean CO_2-neutral fuels, so called biofuels, has been recognised (Rupprecht, 2009). Microalgae appear to be the only source of renewable biodiesel that is capable of meeting the global demand for transport fuels. Like plants, microalgae use sunlight to produce oils but they do so more efficiently than crop plants. Oil productivity of many microalgae greatly exceeds the oil productivity of the best producing oil crops (Christi, 2007, Eloka-Eboka and Inambao, 2017; Eloka-Eboka et al. 2018). Microalgae are photosynthetic organisms with relatively simple requirements for growth, when compared to other sources of both biomass and biodiesel. Algae have emerged as one of the most promising sources for biodiesel production. It can be inferred that algae grown in CO_2-enriched air can be converted to oily substances. The carbon source necessary for the cultivation of microalgae represents up to 60% of the costs with nutrients. Through the process of photosynthesis, the algae convert water, carbon dioxide (CO_2) and light into oxygen and biomass. The nutritional requirements for growing these microorganisms may be available in industrial waste, effluents/flare gases thus turning what is considered a problem into raw material for obtaining products with high added value, such as biofuels (Becker and Venkataraman, 1984; Vonshak, 1997). Algal biomass has the potential to be converted into biofuels, yielding a CO_2-neutral energy carrier comparable to biofuels produced from other biomass sources. Ethanol being one of the attractive chemicals and an energy source (Ueno *et al*. 1998), application of high carbohydrate-producing marine microalgae can generate an alternative biomass resource for ethanol production. Biogas is a product of anaerobic digestion of organic matter and can be obtained from terrestrial biomass, such as domestic sewage, animal excrement and solid waste, such as weeds, fruit and vegetable leftovers, leaves or plants, or from aquatic biomass such as macro and microalgae or marine plants (Omer and Fadalla, 2003; Gunaseelan, 1997). The type of digestion that uses microalgal biomass can eliminate the process of harvesting and drying of biomass and the associated costs (Vonshak, 1997). In the latter case, this biomass can be burned for energy, since the calorific value of these microorganisms is higher than certain coals. Among biomass, algae (macro and microalgae) usually have a higher photosynthetic efficiency than other biomass (Shay, 1993). Shay (1993) reported that algae were one of the best sources of biodiesel. In fact algae are the highest yielding feedstock for biodiesel. . It can produce up to 250 times the amount of oil per acre as soybeans. In fact, producing biodiesel from algae may be only the way to produce enough automotive fuel to replace current gasoline usage. Algae produce 7 to 31 time greater oil than palm oil. It is very simple to extract oil from algae.

1.1. Potentials of algal biodiesel

Depending on species, microalgae produce many different kinds of lipids, hydrocarbons and other complex oils (Banerjee et al. 2002; Metzger and Largeau, 2005; Guschina and Harwood, 2006). Not all algal oils are satisfactory for making biodiesel, but suitable oils occur commonly. Using microalgae to produce biodiesel will not compromise production of food, fodder and other products derived from crops as they are generally non-edible though harbinger of important natural organic products. Potentially, instead of microalgae, oil producing heterotrophic microorganisms (Ratledge, 1993; Ratledge and Wynn, 2002) grown on a natural organic carbon source such as sugar, can be used to make biodiesel; however, heterotrophic production is not as efficient as using photosynthetic microalgae. This is because the renewable organic carbon sources required for growing heterotrophic microorganisms are produced ultimately by photosynthesis, usually in crop plants. Production of algal oils requires an ability to inexpensively produce large quantities of oil-rich algal biomass. Clearly, oil crops cannot significantly contribute to replacing petroleum derived liquid fuels in the foreseeable future. This scenario changes dramatically, if microalgae are used to produce biodiesel. Between 1 and 3% of the total U.S. cropping area would be sufficient for producing algal biomass that satisfies 50%of the transport fuel needs as shown in Table 1. The algal oil yields given in Table 1 are based on experimentally demonstrated biomass productivity in photo-bioreactors. Actual biodiesel yield per hectare is about 80% of the yield of the parent crop oil in the table. Microalgae appears to be the only source of biodiesel that has the potential to completely displace fossil diesel. Unlike other oil crops, microalgae grow extremely rapidly and many are exceedingly rich in oil. Microalgae commonly double their biomass within 24 h. Biomass doubling times during exponential growth are commonly as short as 3.5 hrs. Oil content in microalgae can exceed 80% by weight of dry biomass (Metting, 1996; Spolaore *et al.* 2006). Oil levels of 20–50% are quite common as presented in Table 2. Oil productivity, that is the mass of oil produced per unit volume of the microalgal broth per day, depends on the algal growth rate and the oil content of the biomass. Microalgae with high oil productivities are desired for producing biodiesel.

Table 1: Comparison of some Sources of Biodiesel

Crops	Oil yield (L/ha)	Land Area needed (M ha)	Percent of existing US cropping area [a]
Corn	172	1540	846
Soybean	446	594	326
Canola	1190	223	122
Jatropha	1892	140	77
Coconut	2689	99	54
Oil palm	5950	45	24
Microalgae [b]	136,900	2	1.1
Microalgae [c]	58,700	4.5	2.5

[a] For meeting 50% of all transport fuel needs of the United States;
[b] 70% oil (by wt) in biomass;
[c] 30% oil (by wt) in biomass. Source: Chisti (2007).

Table 2: Oil Content of some Microalgae

Microalgae	Oil Content (% dry weight)
Botryococcus braunii	25 – 75
Chlorella spp.	28 – 32
Crypthecodinium cohnii	20
Cylindrotheca spp.	16 – 37
Dunaliella primolecta	23
Isochrysis spp.	25 – 33
Monallanthus salina	>20
Nannochloris spp.	20 – 35
Nannochloropsis	31 – 68
Neochloris oleoabundans	35 – 54
Nitzschia spp.	45 – 47
Phaeodactylum tricornutum	20 – 30
Schizochytrium spp.	50 – 77
Tetraselmis sueica	15 – 23

Source: Chisti (2007).

1.2. Biodiesel production from microalgae

Biodiesel is a potential substitute for conventional diesel fuel and can be obtained from various raw materials by a process called transesterification or esterification. The transesterification reaction can be using super critical fluids, enzymatic, acid-catalysed or alkali-catalysed (Fukuda *et al.,* 2001). In these processes occurs the conversion stage of lipids, in ethyl or methyl esters of fatty acids, using methyl alcohol or ethyl, respectively (Xuan *et al.* 2009). Transesterification reactions occur in the presence of a catalyst, for which sodium hydroxide and potassium hydroxide can be used, among others (Xuan *et al.* 2009). After the transesterification reaction, the final reactional mass is made up of two phases, which are separated by decanting or centrifuging. The heavier phase consists of crude glycerine, containing excess alcohol, water and impurities inherent in the raw material. Due to the low solubility of glycerol in the esters, this separation generally occurs quickly. The phase that contains water and alcohol is subjected to an evaporation process, which eliminates these volatile constituents from the crude glycerine, by liquefying these vapors in an appropriate condenser. The esters are centrifuged and dehumidified, which results in biodiesel that should have characteristics which match the specifications of the technical norms established for biodiesel for use as a fuel in diesel cycle engines (Ma and Hanna, 1999). For the past decade, biodiesel has been gaining worldwide popularity and research interest in utilisation in vehicle engines and other kinds of internal combustion (IC) engines as an alternative energy source to petro-diesel (Sgroi *et al*. 2005). The raw materials from which lipids are currently extracted for biodiesel production consist mainly of oily seeds such as soybeans, palm, castor bean, peanut, sunflower, corn, rapeseed and cotton. However, the cultivation of plants depends on factors that may limit or even preclude the production of biodiesel, such as the need for large available areas, suitable soil, high quality water, seasonality, among others. With this type of cultivation, natural resources are not replaced and it may cause demineralisation, salinisation, desertification, soil erosion and depletion of water sources. Pesticides may also be required, which can cause an even greater negative environmental impact (Gerpen, 2005; Knothe, 2005; Krawczyk, 1996). One of the biotechnological processes that have received increasing interest from companies and researchers is the cultivation of microalgae, which are an excellent source of organic compounds such as fatty acids (Johnson and Wen, 2009; Colla *et al*. 2004). The fatty acids that are produced by microalgae can be extracted and converted into biodiesel (Brown and Zeiler, 1993). Microalgae exhibit a great variability in lipid content. Among microalgae species, oil contents can reach up to 80%, and levels of 20–50% are quite common (Powell and Hill, 2009). The microalga *Chlorella* has up to 50% lipids and *Botryococcus* has 80%. The variations are due to different growing conditions and methods of extraction of lipids and fatty acids. One of the main factors that influences the lipid and fatty acid content of microalgae in terms of cultivation is the CO_2 concentration. In areas where microalgae are grown for biodiesel production alongside fossil fuel power stations, CO_2 release can be significantly reduced and the lipid content increased (Sawayama *et al*., 1995; Brown and Zeiler, 1993). Large growths of microalgae occur in many Chinese lakes such as Lake Chaohu, Lake Taihu and Lake Dianchi. This results in the pollution of water, the death of fish and illnesses that affect the lakeside residents. The reduction of these blooms has become an urgent project and one alternative is to use this large amount of biomass for biofuel production (Miao *et al*. 2004). The analysis of the saturated fraction of biofuel from *Chlorella protothecoides*

demonstrated that the alkane's chain reaches 10 – 30 carbons, while the alkanes' chain of the saturated fraction of biofuels from *Microcystis aeruginosa* presented 10–28 carbons. When these results are compared to the chromatography of mineral diesel, the alkane's chain distribution is very similar to that of microalgae (Miao *et al*. 2004). The carbon and hydrogen content of microalgal biofuel is greater than in plant biofuel, although the oxygen content is lower. The H/C and O/C mean molar ratio of microalgal biofuel was 1.72 and 0.26, while the H/C and O/C molar ratio of plant biofuel was 1.38 and 0.37, respectively. Microalgal biofuel is characterised by lower oxygen content and a higher H/C ratio than biofuel from plants, sunflower and cotton (Miao *et al.* 2004). The oxygen content of microalgal biofuel compared to the oil of higher plants is important because high oxygen content is not attractive for the production of transportation fuels. Biofuel from *C. protothecoides* and *Microcystis aeruginosa* has a calorific value of 30 MJ kg^{-1} and 29 MJ kg^{-1} due to their high carbon and hydrogen content and low oxygen content, which also makes the biofuels from microalgae more stable than biofuel from plants. The high hydrogen content of microalgal biofuel is due to chlorophyll and proteins. Compared with plant biofuel, microalgal biofuels has a high calorific value, low viscosity and low density. These physical properties of microalgae make them more suitable for biofuels than lignocellulosic materials (Miao *et al.* 2004). The mean annual productivity of microalgal biomass in a tropical climate region is 1.53 kg m^{-3} day^{-1}, with a mean 30.0% of lipids extracted from the biomass, the concentration per hectare of total area is around 123.0 m^3 for 90.0% of the 365 days of a year, since the remaining 10.0% are used for maintenance and cleaning of the bioreactors. Thus, the yield of biodiesel from microalgae is 98.4 m3 ha^{-1}, so for the production of 5.4 billion m3 of biodiesel required to transport, the microalgae an area of approximately 5.4 Mha must be cultivated, which represents only 3.0% of the area currently used for cultivation of plants for biodiesel production. This would be a possible scenario even if the concentration of lipids in the microalgal biomass was 15.0% of dry weight (Chisti, 2008). To meet the required demand and add 5.0% biodiesel (B5) to mineral diesel oil, one would have to increase the production of vegetable oils by 50.0 – 100.0%. This is a difficult goal to achieve with these oils alone, since it represents a proportional increase in arable land with oil crops, and the current agricultural productivity has reached values that are difficult to increase. As the concentration of fatty acids and productivity of microalgae are much higher than that of plants, this effort to increase oil production would not be so great (Ma and Hanna, 1999). As an example, biodiesel output per required land area has been estimated to be, corn: 145.0 kg oil ha^{-1}, soybeans: 375.0 kg oil ha^{-1}, palm oil: 5000 kg oil ha^{-1}, algae: 80,000 kg oil ha^{-1} (Skjanes *et al.* 2007). The amount of land needed for the corresponding production using microalgae would be around 100.0–200.0 times less.

1.3. Thermo-chemical conversion

Main thermo-chemical processes include liquefaction, pyrolysis and gasification. Hydrocarbons of algal cells have been separated by extraction with organic solvent after freeze–drying and sonicating the algal cells. However, these procedures are not suitable for separation on a large scale because these are costly. Therefore, an effective method is liquefaction for separating hydrocarbons as liquid fuel from harvested algal cells with high moisture content. The direct thermo-chemical liquefaction can convert wet biomass such as wood and sewage sludge to liquid fuel at around 575 K and 10 MPa using catalyst such as sodium carbonate (Demirbas, 2007). At the same time, the liquid oil can be easily separated (Ogi *et al*. 1990) The feasibility of producing liquid fuel or bio-oil via pyrolysis or thermo-chemical liquefaction of microalgae has been demonstrated for a range of microalgae (Peng *et al.* 2000) Since algae usually have high moisture content, a drying process requires much heating energy novel energy production system using microalgae with nitrogen cycling combined with low temperature catalytic gasification of the microalgae has been proposed. The gasification process produces combustible gas such as H_2, CH_4, CO_2 and ammonia, whereas the product of pyrolysis is bio-oil (Chisti, 2006).

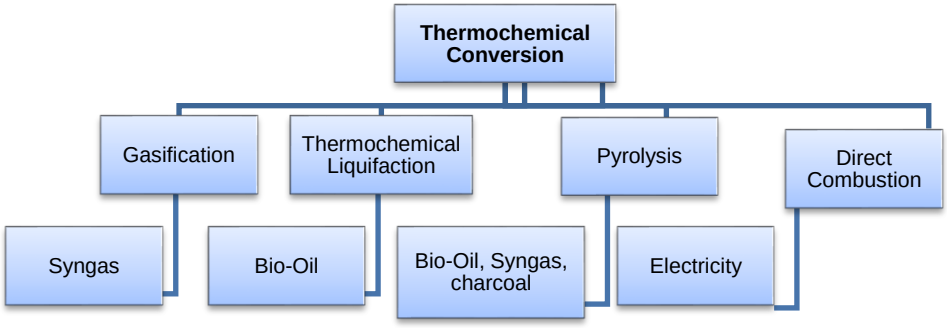

Figure 1: Transesterification of Algal triacyleglyceride in the presence of catalyst. Source: Brennan and Owende (2010).

Thermal and rheological fuel properties

Biodiesel fuel properties vary significantly between feedstocks due to their differing chemical compositions. Table 3 summarises the key fuel properties of various biodiesels reported in the more recent literatures. The factors that influence biodiesel fuel properties are necessary to call to mind and vary from feedstock to feedstock. The relevant rheological and thermal properties in this study include the following:

Kinematic viscosity

Viscosity is the resistance to shear or flow; it is highly dependent on temperature and it describes the behavior of a liquid in motion near a solid boundary such as the walls of a pipe. The presence of strong or weak interactions at the molecular level can greatly affect the way the molecules of an oil or fat interact, therefore affecting their resistance to flow. This is an important rheological property of biodiesel and in this study as it relates to micro-algal biodiesel. It is a key property that differentiates biofuels and fossil fuels and it is usually pegged at 40^{o}C for most biodiesels.

Density

Density is an important fuel property that influences the amount of fuel injected into the engine cylinder. This is because in a diesel engine fuel injection system, pumps and injectors must deliver a precise amount of fuel to provide proper combustion (Boudy and Seers, 2009; Baroutian and Aroua, 2008). However, fuel injection pumps meter is fueled by volume and not by mass, leading to denser fuel which contains greater mass for the same volume. Thus, changes in the fuel density will influence engine output power due to the different masses of the fuel injected, and this directly affects engine performance characteristics (Alptekin and Canakci, 2008). Moreover, density increases the diameter of the fuel droplets in the combustion chamber. Since the inertia of the bigger droplets is relatively large, their penetration in the combustion chamber will be higher as well (Choi and Reitz, 1999). When a fuel with lower density and viscosity is injected, improved atomisation and mixture formation can be attained which consequently affects exhaust emissions. Szybist et al. (2007) found that fuel density correlates with particulate matter (PM) and NOx emissions, with higher densities generally causing an increase in PM and NOx emission in diesel engines. However, while investigating the biodiesel fuel properties on exhaust emission in a light-duty diesel engine, Ng et al. (2012) found that fuel properties moderately affect CO emissions but have no significant impact on NOx, UHC and smoke opacity levels. Density is also a key factor in the design of reactors, separation processes and storage tanks in biodiesel production. Density of biodiesel is closely related to the fatty acid composition and the purity of a biodiesel. Studies have shown that density increases with decreasing chain length and an increasing degree of unsaturation (Blangino et al. 2008; Lang et al. 2001).

Heating (Calorific) value

Heating value is a significant fuel property which influences the suitability of biodiesel as an engine fuel, as it indicates the energy content in the fuel. Due to the high oxygen content of biodiesel, it is generally accepted that biodiesels are about 10% less energy dense as compared with petroleum diesel. The heating value of biodiesel is related to its fatty acid profile. Heating value increases with increasing carbon number in fuel molecules due to mass fraction decreases (Demirbas, 2003). Studies have also found that unsaturated esters have lower mass energy content (MJ/kg). Demirbas (2008) studied the correlation between viscosity and higher heating value (HHV) by performing a linear least square regression analysis. This study found that there is a high correlation between the heating value (thermal) and the viscosity (rheological) of vegetable oils and their methyl esters and that the heating value of vegetables oils and biodiesels increases with viscosity.

Flash point

Flash point is often used as a descriptive characteristic of liquid fuel and is defined as the lowest temperature at which the fuel will start to vaporise to form an ignitable mixture when it comes to contact with air (Ali *et al.* 1995). Hence, flash point is an important parameter for assessing fire hazards during fuel transport and storage. This is reflected by the respective limits within Australian standards (≥120 °C) and the European fossil diesel standard, EN 590 (>55 °C). However, the flash point of biodiesel is approximately double that of petroleum diesel, which makes biodiesel a more acceptable engine fuel in relation to concerns about safety. It is also an important parameter in engine combustion performance. Canakci and Sanli (2009) found that with a high flash point, NOx emission decreased due to low combustion pressure and temperature. Moreover, high flash point is also important in niche applications such as underground mining. On the other hand, studies show that a high flash point can cause cold engine startup problems, misfiring and ignition delay, which increases carbon deposition in the combustion chamber (Ali et al 1995). Biodiesels from animal fat generally have higher flash points than those from vegetable oils. This is the result of the highly saturated fatty acid compounds in biodiesels from animal fats increasing the flash point temperature. Alcohol residue in biodiesel significantly decreases flash point (Canakci and Sanli, 2009).

Lubricity

Lubricity is defined as the ability of fuel to provide hydrodynamic and/or boundary lubrication to prevent wear between engine moving parts. It is an important parameter for diesel engine operation, because poor lubrication leads to the failure of engine parts, such as fuel injectors and pumps as they are directly lubricated by the fuel itself (Lacey and Lestz, 1992). Increasingly strict regulations on the sulphur content of commercial petroleum fuel have resulted in a decrease in fuel lubricity over time. Therefore, the issue of lubricity in fuel is becoming increasingly important with respect to diesel engine operation. Biodiesels typically have superior lubrication properties when compared with petroleum diesel (Hu et al 2008). Studies show that biodiesel derived from vegetable oils can significantly increase diesel fuel lubricity at blend concentrations of less than 1%. Therefore, biodiesel can be used as an additive to improve the lubricity of petroleum fuel (Goodrum and Geller, 2005; Anastopoulos et al 2005; Anastopoulos et al 2001; Van Gerpen et al 2005). Knothe and Steidley (2005) examined the lubricity of biodiesel and petroleum diesel components. They found better lubricity in fatty acid compounds than hydrocarbons in petroleum diesel. This study also reported that pure free fatty acids, monoacylglycerols, and glycerol possess better lubricity than pure esters. The main components responsible for biodiesel lubricity are FAMEs, hydroxyl groups and monoacylglycerols followed by free fatty acids (FFAs) and diacylglycerols, whereas triglycerols do not have any significant effect on the lubricity of biodiesel (Geller and Goodrum, 2004,Hu et al 2005). On the other hand, the structures of fatty acids have an impact on biodiesel lubricity. Increasing saturation leads to a stronger lubrication layer as molecules can align themselves more easily in straight chains and when they are packed closely on the surface. However different results have been reported by Knothe (2005), Anastopoulos et al. (2001) and Bhuyan et al. (2006) who found that lubricity increases with the increase in length of fatty acid chains, while Geller et al. (2004) showed that there is no consistent trend relating chain length to lubricity enhancement.

1.4. Aim of study

The aim of the present study is to comparative investigate and assess of thermal and rheological properties of biodiesel fuels and hybrids from micro algae using micro-algal technology as a viable biodiesel production option and other second generation feedstocks. *Chlorella vulgaris* and *Synedesmus spp were* species of microalgae studied. Studies of viscosity and shear stress at varying speeds and temperature were conducted with direct implications and overall effects in performances. There was interaction of viscosity at different torques as presented in this study and across lower and higher temperatures. The expectation is that shear stress increases with increase in temperature and torque while viscosity generally decreases along the trends.

2. MATERIALS AND METHODS

2.1. Biodiesel preparation and analysis of algal oil, biodiesel and hybrids

The biodiesel was produced after micro-algal production from open pond and by photobioreactor. The micro-algal was extracted from the produced algal biomass and prepared following acceptable method and as adopted by Eloka-Eboka and Inambao (2017a, b). During the production process, two main products, crude biodiesel and crude glycerine, were obtained. Crude biodiesel was refined by washing and drying. Viscosity tests at different temperatures and speeds with shear stress were conducted using Rheometer model TC 202 Bookfield. This is an important parameter for biodiesel processing. In fact, the essence of transesterification is to reduce the viscosity of the crude oil and at the same time break the bond structure for proper atomisation and combustion in the engine cylinder and combustion chamber. Other physiochemical analysis conducted to assess the properties of the produced biodiesel and hybrids are free fatty acid (FFA), total glycerine (TG) and free glycerine (FG), density/specific gravity, calorific values, flash point, cloud point and cetane index which is the measure of the fuel qualities, moisture content, iodine value, fatty acid composition, pour point, Thermal analysis and stability using thermal gravimetric analysis and Fourier infra-red spectroscopy was conducted. Fatty acid composition of the oil samples (crude) and biodiesel was subjected to gas chromatography (GC), using Shidmazu GC-MS analyzer. Randicity was conducted using biodiesel racimat. These were all done in accordance with ASTM standards. These were carried out to analyze thermal and rheological properties of algal oil, biodiesel and hybrids and other second generation feedstocks.

3. RESULTS AND DISCUSSION

3.1. Viscosity and shear stress of algal crude oil and feedstocks at varying temperatures

Table 3: Viscosity and Shear Stress of Oil samples @ 40°C

Sample	Viscosity @40°C (cSt)				Shear Stress @ 40°C (D/cm^2)			
Codes	20rpm	40rpm	50rpm	60rpm	20rpm	40rpm	50rpm	60rpm
A	35.00	34.25	33.95	33.74	9.19	18.09	22.41	26.68
R	26.84	25.79	25.61	25.69	7.09	13.62	16.95	20.35
H	15.90	15.00	15.64	14.55	4.16	7.92	9.66	11.52
J(I)	28.94	27.97	27.77	27.59	7.64	14.81	18.37	21.81
J(N)	31.04	29.92	29.45	29.44	8.12	15.80	19.44	23.32
NM	1.94	1.94	1.99	2.58	1.94	1.95	1.96l	1.98

A: Algal oil (Chlorella); R: Rubber oil; H: Hura crepitans oil; J(I): Indian Jatropha; J(N): Nigerian Jatropha; NM: Natal Mahogany

Table 4: Viscosity and Shear Stress of Oil samples @ 60°C

Sample	**Viscosity @ 60°C (cSt)**				**Shear Stress @ 60°C (D/cm^2)**			
Codes	**20rpm**	**40rpm**	**50rpm**	**60rpm**	**20rpm**	**40rpm**	**50rpm**	**60rpm**
A	19.50	18.75	18.66	18.40	5.15	9.90	12.81	14.53
R	16.65	15.00	14.40	14.20	4.36	7.88	9.56	11.20
H	12.00	10.65	10.14	9.85	3.25	5.54	6.61	7.76
J (I)	18.65	16.76	16.26	15.85	4.87	8.91	10.69	12.51
J (N)	20.00	18.22	17.58	17.10	5.23	9.62	11.56	13.50
NM	6.00	4.65	4.86	4.65	1.52	2.89	3.17	3.72

A = Algae Oil; R = Rubber seedoil; H = Hura crepitans; J (I) = Jatropha (India); J (N) = Jatropha (Nigeria), NM = Natal Mahogany

Table 5: Viscosity and Shear Stress of Oil samples @ 80°C

Sample	**Viscosity @ 80°C (cSt)**				**Shear Stress @ 80°C (D/cm^2)**			
Codes	**20rpm**	**40rpm**	**50rpm**	**60rpm**	**20rpm**	**40rpm**	**50rpm**	**60rpm**
A	18.50	17.65	15.78	14.65	5.31	9.03	10.21	11.55
R	13.00	11.35	10.86	10.40	3.45	5.98	7.05	8.20
H	9.23	7.86	7.38	7.15	2.35	4.24	4.87	5.75
J (I)	13.95	12.25	11.76	11.35	3.72	6.46	7.68	9.02
J (N)	15.15	13.56	12.56	11.90	3.98	7.08	8.20	9.48
NM	4.98	3.98	3.92	3.90	1.38	2.15	2.69	3.09

3.2. Effects of temperature and speed on viscosity and shear stress of algae and feedstock oils

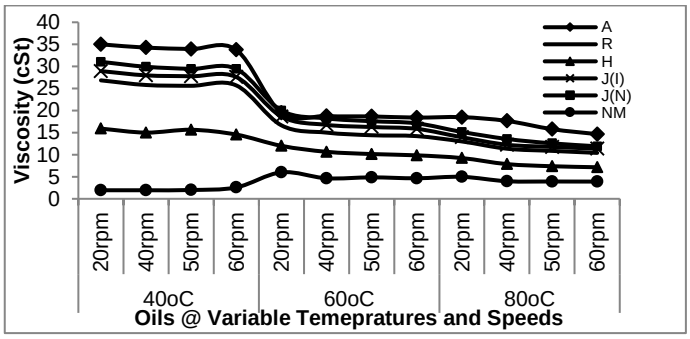

Figure 3: Effects of Temperature and Speed on Viscosity of Algae and feedstock oils

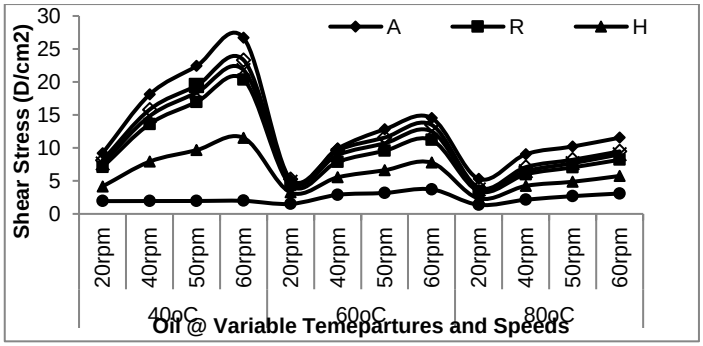

Figure 4: Effects of Temperature and Speed on Shear Stress of Algae and feedstock oils

3.3 Viscosity and shear stress of algal biodiesel, hybrids and feedstocks at varying temperatures

Table 6: Viscosity and Shear Stress of Biodiesel @ 40°C

Samples	Viscosity @40°C (cSt)				Shear Stress @ 40°C (D/cm^2)			
Codes	20rpm	40rpm	50rpm	60rpm	20rpm	40rpm	50rpm	60rpm
B_{100}A	7.05	6.07	5.76	5.55	1.86	3.21	3.80	4.39
B_{100}R	6.30	5.62	4.98	4.75	1.62	2.97	3.29	3.76
B_{100}J(N)	6.30	6.00	5.22	5.05	1.66	3.05	3.44	4.00
B_{100}J(I)	6.60	5.92	4.40	5.20	1.74	3.05	3.56	4.2

B_{100}A = Algae biodiesel (B100), B_{100}R= Rubber biodiesel (B100), B_{100}J (N) = Jatropha biodiesel Nigeria (B100), B_{100}J (I) = Jatropha India biodiesel (B100).

Table 7: Viscosity and Shear Stress of Biodiesel @ 60°C

Samples	Viscosity @ 60°C (cSt)				Shear Stress @ 60°C (D/cm^2)			
Codes	20rpm	40rpm	50rpm	60rpm	20rpm	40rpm	50rpm	60rpm
B_{100}A	20.85	12.45	9.84	8.60	5.37	6.73	6.49	6.77
B_{100}R	19.65	11.85	9.36	8.10	5.19	6.18	6.18	6.41
B_{100}J(N)	19.65	11.70	9.30	8.10	5.17	6.14	6.14	6.37
B_{100}J(I)	19.65	12.07	9.42	8.20	5.19	6.33	6.26	6.49

3.4. Effects of temperature and speed on viscosity and shear stress of algal biodiesel and feedstocks

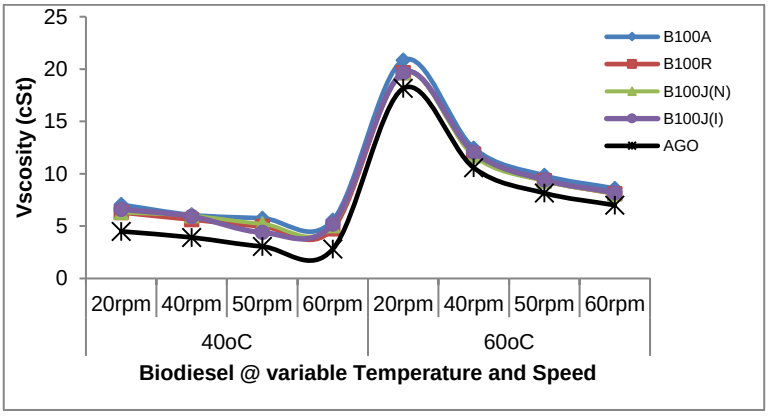

Figure 5: Effect of Temperature and Speed on Viscosity of biodiesel with AGO

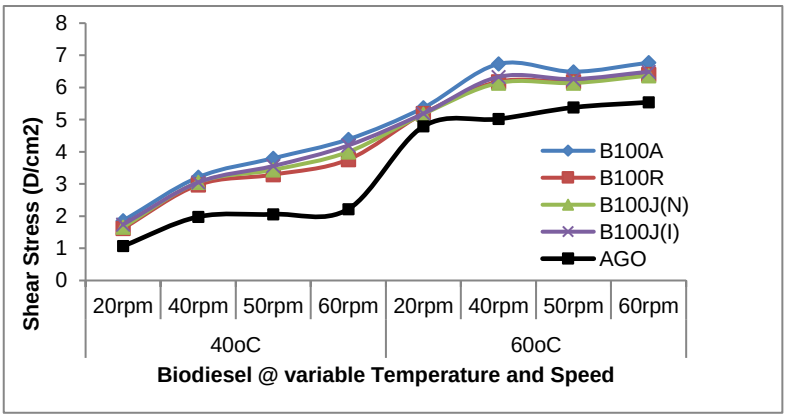

Figure 6: Effect of Temperature and Speed on Shear Stress of biodiesel with AGO

3.5. Viscosity speed and shear stress of biodiesel hybrids and blends

Table 8: Viscosity and Shear Stress of Biodiesel Hybrids and blends @ 40°C

Samples	Viscosity @ 40°C (cSt)				Shear Stress @ 40°C (D/cm²)			
Codes	20rpm	40rpm	50rpm	60rpm	20rpm	40rpm	50rpm	60rpm
$BA_{50}H$	6.90	6.07	5.64	5.45	1.82	3.21	3.72	4.32
$BA_{40}H$	6.90	6.15	5.76	5.60	1.86	3.25	3.84	4.43
$BA_{30}H$	7.05	5.85	5.46	5.25	1.74	3.13	3.48	4.16
$BA_{20}H$	6.60	6.07	5.52	5.35	1.78	3.17	3.64	4.24
$BA_{10}H$	6.75	6.07	5.46	5.25	1.74	3.09	3.60	4.16
$BI_{20}A_{50}$	6.60	4.70	3.42	3.20	1.19	2.18	2.26	2.53
$BI_{20}A_{40}$	4.5	4.62	3.48	3.25	1.23	2.14	2.30	2.57
$BI_{20}A_{30}$	4.65	4.57	3.42	3.20	1.90	2.38	2.26	2.57
$BA_{50}R$	6.60	5.92	5.64	5,45	1.74	3.09	3.72	4.32
AGO	4.50	3.92	3.06	2.80	1.07	2.06	1.98	2.22

$BM_{50}H$ = Algae/Jatropha Hybrid (B50M), $BM_{40}H$= Algae/Jatropha Hybrid (B40M), $BM_{30}H$ = Algae/Jatropha hybrid (B30M), $BM_{20}H$ = Algae/Jatropha hybrid (B20M), $BM_{10}H$ = Algae/Jatropha hybrid (B10M), $BI_{20}M_{50}$ = Blend of Algae/Jatropha Hybrid with AGO ($B_{20}M_{50}H$), $BI_{20}M_{40}$ = Blend of Algae/Jatropha Hybrid with AGO ($B_{20}M_{40}H$), $BI_{20}M_{30}$ = Blend of Algae/Jatropha Hybrids with AGO ($B_{20}M_{30}H$)

Table 9: Viscosity and Shear Stress of Biodiesel Hybrids and blends @ 60°C

Samples	Viscosity @ 60°C (cSt)				Shear Stress @ 60°C (D/cm²)			
Codes	20rpm	40rpm	50rpm	60rpm	20rpm	40rpm	50rpm	60rpm
$BA_{50}H$	20.25	12.85	9.78	8.40	5.34	6.81	6.41	6.61
$BA_{40}H$	20.25	12.45	9.60	8.35	5.38	6.53	6.33	6.61
$BA_{30}H$	19.65	12.22	9.48	8.20	5.23	6.32	6.26	6.53
$BA_{20}H$	20.10	12.30	9.48	8.25	5.31	6.53	6.26	6.53
$BA_{10}H$	19.65	12.07	9.36	8.10	5.23	6.27	6.18	6.41
$BI_{20}A_{50}$	18.45	11.32	8.46	7.25	4.91	5.98	5.58	5.74
$BI_{20}A_{40}$	18.90	11.70	8.46	7.25	4.99	6.37	5.58	5.74
$BI_{20}A_{30}$	18.62	11.70	8.46	7.20	4.91	6.18	5.58	5.70
$BA_{50}R$	19.65	11.77	9.48	8.30	5.19	6.18	6.26	6.57
AGO	18.15	10.57	8.16	7.00	4.79	5.02	5.38	5.54

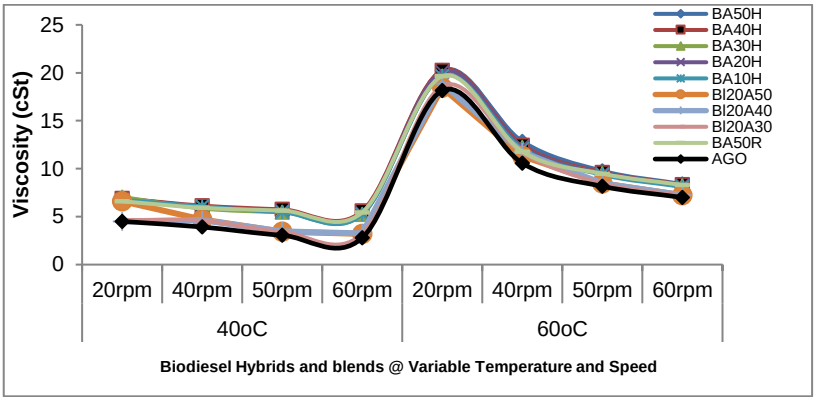

Figure 7: Effect of Temperature and Speed on Viscosity of biodiesel hybrids and Blends

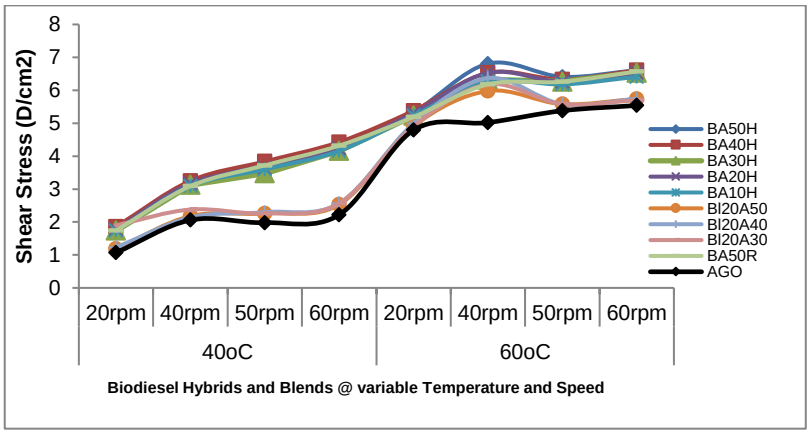

Figure 8: Effect of Temperature and Speed on Shear Stress of biodiesel hybrids and Blends

3.6. Thermal Properties of Algal oil

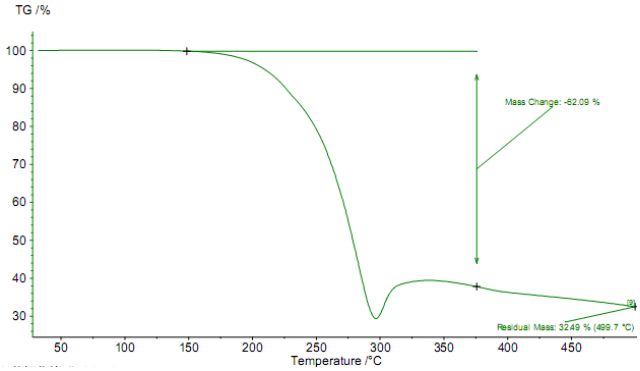

Figure 9: Thermal gravimetric Analysis of Algal oil

Table 10: Thermal Parameters of the Algae Biodiesel and selected feedstock oils

		CN	DU	ΔºC (kJ/kg)	HHV (MJ/kg)	LHV (MJ/kg)	LCSF (ºC)	CFPP (ºC)
CRUDE OIL	A	35.4	52.58	4139.54	40.52	40.22	6.7	4.5
	J(I)	30.2	55.40	40857.15	40.10	40.11	5.4	2.5
	J(N)	29.9	55.98	40540.41	40.10	40.09	5.5	2.8
	H	40.72	60.88	40880.20	40.03	40.03	6.8	3.7
	R	38.49	62.50	39759.41	38.78	39.63	5.8	4.8
	NM	38.02	70.63	39964.85	36.62	37.11	6.9	6.4
BIODIESEL/ FAME	A	56.7	52.58	4139.54	42.51	39.45	1.881	1.881
	J(I)	54.8	55.40	40857.15	42.254	39.27	1.40	1.940
	J (N)	54.1	55.80	40540.41	42.155	39.12	1.50	2.10
	H	52.8	60.88	40880.20	42.180	36.09	2.173	3.173
	R	51.4	62.98	39759.41	39.85	36.85	2.438	3.438
	NM	56.7	69.21	39964.85	38.872	35.18	2.449	5.449

HHV= higher heating value; LHV= lower heating value, CN: cetane number/index, DU: degree of unsaturation, ΔºC: heat of combustion; LCSF: long-chain saturated factor

Table 11: Engine Exhaust Emissions of Algal Biodiesel and AGO

	CO (ppm)		SOx (ppm)		HC (ppm)		NOx (ppm)		VOCs (ppm)	
Engine Load	50 (%)	100(%)	50(%)	100(%)	50(%)	100(%)	50(%)	100(%)	50(%)	100(%)
AGO	0.035	0.018	150	200	171	220	420	660	1.85	3.4
BA100	0.018	0.009	110	140	80	84	435	678	0.50	0.85
BJ100	0.020	0.012	115	146	78	85	438	682	0.50	0.88
$BA_{50}J_{50}$	0.0209	0.0119	116	148	76	87	436	680	0.51	0.89
$BA_{40}J_{10}$	0.0208	0.0118	117	150	75	88	436	681	0.51	0.89
$BA_{30}J_{20}$	0.0207	0.0116	118	152	76	88	435.8	681.7	0.5	0.90
$BA_{20}J_{30}$	0.0206	0.0114	120	153	80	89	435.6	681.5	0.51	0.91
$BM10J_{40}$	0.0205	0.0112	120	154	82	88	435.4	681.2	0.51	0.91
$J_{40}M_{10}$ ME	0.0199	0.010	118	155	83	86	436	672	0.52	0.91
$J_{30}M_{20}$ ME	0.0198	0.011	119	158	84	89	436.6	674	0.52	0.91
$J_{20}M_{30}$ ME	0.0196	0.011	120	158	84	85	436.8	676	0.52	0.91
$J_{10}M_{40}$ ME	0.0190	0.011	121	160	85	86	437	678	0.52	0.91

The fatty acid esters compositions of microalgae sources are different from plant oils. Algal oils contain a high degree of polyunsaturated fatty acids with four or more double bonds when compared to vegetable oils. Free fatty acid composition of the oils show that they all contain mainly saturated, more unsaturated and polyunsaturated fatty acids which compared favourably with common feedstocks like cottonseeds oil composed primarily of unsaturated linolenic and the saturated palmitic acids which gave 98.6% optimum yield. The fatty acid composition obtained were used to determine fuel properties like ignition quality (cetane number), heat of combustion (gross calorific value H), oxidative stability, viscosity and cold flow properties. The results shows all the vegetable oils under study are suitable for biodiesel on the basis of these fuel properties. The identification of lipid composition in selected algae strain is essential for determining the suitability to biodiesel and fuel quality. Different culture conditions play an important role in the lipid composition, like C:N ratio, which is the major factor. In order to improve the fuel properties of algae biodiesel, suitable culture conditions may be used and the properties of biodiesel produced from algae oils must meet the International Biodiesel Fuel Standards. Hybridisation of different feedstock was performed in this study and the properties of the hybrids evaluated and compared are in Tables 8, 9 and 10 and Figures 7 –

8. Hybridisation showed it is another new approach in developing improved biodiesel from different feedstock. The properties as can be seen are comparable with automotive gas oil (AGO) as reference fuel standard. All the chemo-physical properties evaluated fell within ASTM standards with close comparison with AGO. The viscosity of the raw microalgal oil just like other second generation feedstocks is usually higher than that of diesel fuel. Raw oil was converted into biodiesel by means of transesterification process. Viscosity tests at different temperature and speed with shear stress was conducted. Their effects on speed and viscosity for all the algal oil, algal biodiesel and hybrids, selected feedstock and AGO are presented in Tables 3, 4, 5, 6, and 7 and Figures 3 - 8. They were virtually comparable with AGO if evaluated separately and collectively. This is a very important parameter for biodiesel processing. In fact, the essence of transesterification reaction is to reduce the viscosity of the oil and at the same time break the bond structure for proper atomisation and combustion in the engine cylinder and combustion chamber. This was achieved in this study and hence there are comparable viscosities at varying temperatures. The interaction of viscosity at different torques presented decreases from 20rpm to 60rpm but increases in shear stresses at temperatures of 40^{o}C and 60^{o}C. Across temperature was a general initial decrease and later increase from lower temperature to higher temperature. Thermal gravimetric analysis of Algal oil is presented in Figure 9. The influence of total glyceride (%) on temperature was evaluated. There were notable significant mass changes in percentage with increase in temperature. Algal oil was stable in its raw nature and so stability for biodiesel production is not in doubt. At elevated temperatures, the performance of the engine improves with relatively better burning of fuel resulting in decreased CO in Table 11. Oxygen content in biodiesel had direct bearing on the smoke opacity. The smoke opacity was noticed to be reduced as the temperature increased. This trend is mainly due to the presence of internal availability of oxygen content in the biodiesel and neat burning of fuel at elevated temperature (As the oxygen content in the fuel increase, smoke content in the exhaust was noticed to be reduced. Oxygen emission was lower in AGO compared to all the B100. It was noticed that the amount of VOCs obtained were higher in AGO than all the B100. These trends are similar to the results obtained from the analysis using a GCMS.

4. CONCLUSION

The study set to evaluate comparatively the thermal and rheological properties of biodiesel fuels produced from micro algae using micro-algal technology as a viable biodiesel production option. Algal biodiesel and hybrids were produced and the relevant properties evaluated in juxtaposition with other second generation feedstocks and AGO as control using ASTM standards. *Chlorella vulgaris* and *Synedesmus spp* were species of micro-algae studied. Viscosity and shear stress at varying speeds and temperature were conducted and direct implications and overall effects in performances and in emission generation during combustion were established. There were obvious correlations of viscosity at different torques presented across different temperature regimes (low and high temperatures). The general conclusion is that shear stress increases with increase in temperature and torques while viscosity generally decreases along the trends. This is an indication of the importance of these properties in the use of biodiesel for energy application.

5. REFERENCES

Alptekin, E. Canakci, M. (2008). Determination of the density and the viscosities of biodiesel- diesel fuel blends. Renew. Energy, 33, 2623–2630.

Anastopoulos, E.L.; Zannikos, F.; Kalligeros, S.; Teas, C. (2001). Influence of aceto acetic esters and di-carboxylic acid esters on diesel fuel lubricity. Tribol. Int., 34, 749–755.

Anastopoulos, G.; Lois, E.; Karonis, D.; Kalligeros, S.; Zannikos, F. (2005) Impact of oxygen and nitrogen compounds on the lubrication properties of low sulfur diesel fuels. Energy, 30, 415–426

Banerjee A, Sharma R, Chisti Y, Banerjee UC. (2002). Botryococcus braunii: a renewable source of hydrocarbons and other chemicals. Crit Rev Biotechnol 22: 245–79.

Becker, E.N., Venkataraman, L.V. (1984). Production and utilisation of the blue-green alga Spirulina in India. Biomass 20: 105–125.

Christi, Y. (2007). Bioidiesel from microalgae. Biotechnology Advances: 25 (3): 294 – 306.

Chisti, Y. (2008). Biodiesel from microalgae beats bioethanol. Trends Biotechnol. 26, 126–131.

Choi, C.Y.; Reitz, R.D. (1999). A numerical analysis of the emissions characteristics of biodiesel blended fuels. J. Eng. Gas Turbines Power, 121, 31–37.

Colla, L.M., Bertolin, T.E., Costa, J.A.V., 2004. Fatty acids profile of Spirulina platensis grown under different temperatures and nitrogen concentrations. Z. Naturforsch. C 59c: 55–59.

Baroutian, S. and Aroua, M.K. (2008). Estimation of vegetable oil-based ethyl esters biodiesel densities using artificial neural networks. J. Appl. Sci., 8, 3005–3011.

Bhyan, S.; Sundararajan, S.; Yao, L.; Hammond, E.G.; Wang, T. (2006). Boundary lubrication properties of lipid-based compounds evaluated using microtribological methods. Tribol. Lett., 22, 167–172.

Bangino, E.; Riveros, A.F.; Romano, S.D. (2008). Numerical expressions for viscosity, surface tension and density of biodiesel: Analysis and experimental validation. *Phys. Chem. Liq*., 46, 527–547.

Boudy, F.; Seers, P. (2009). Impact of physical properties of biodiesel on the injection process in a common-rail direct injection system. Energy Convers. Manag., 5012, 2905–2912.

Brennan, L. and Owende, P. (2010). Biofuels from microalgae – a review of technologies for production, processing, and extractions of biofuels and co-products. Renew. Sust. Energy Rev. 14, 557–577.

Brown, M.L., Zeiler, K.G. (1993). Aquatic biomass and carbon dioxide trapping. Energy Convers. Manage. 34, 1005–1013.

Eloka-Eboka, A.C. and Inambao, F.L. (2017a). Effects of CO_2 Sequestration on Lipid and Biomass Productivity in Microalgal Biomass Production. Applied Energy195 (2017): 1100 -1111: http://dx.doi.org/10.1016/j.apenergy.2017.03.071

Eloka-Eboka, A.C. and F. L. Inambao (2017b). Performance and Emission Profile of Micro-Algal Biodiesel in Compression Ignition Engine, International Journal of Engineering Research in Africa, Vol. 30, pp. 110-124.

Eloka-Eboka, A., Onunka, C., & Inambao, F. (2018). Detailed design and optimisation of a sustainable micro-algal biofuel process plant. International Journal of Low-Carbon Technologies, https://doi.org/10.1093/ijlct/cty004 Oxford University Press.

Demirbas, A. (2003). Chemical and fuel properties of seventeen vegetable oils. Energy Sources, 25, 721–728.

Demirbas A. (2007). Progress and recent trends in biofuels. Prog Energy Combust Sci 33:1–18.

Demirbas, A. (2008). Relationships derived from physical properties of vegetable oil and biodiesel fuels. Fuel, 87, 1743–1748.

Fukuda, H., Kondo, A., Noda, H. (2001). Biodiesel fuel production by transesterification of oils. J. Biosci. Bioeng. 92, 405–416.

Geller, D.P.; Goodrum, J.W. (2004). Effects of specific fatty acid methyl esters on diesel fuel lubricity. Fuel, 83, 2351–2356.

Gerpen, J.V. (2005). Biodiesel processing and production. Fuel Process. Technol. 86, 1097 – 1107.

Goodrum, J.W.; Geller, D.P. (2005). Influence of fatty acid methyl esters from hydroxylated vegetable oils on diesel fuel lubricity. Bioresour. Technol., 96, 851–855.

Gunaseelan, V.N. (1997). Anaerobic digestion of biomass form methane production: A Review. Biomass Bioenergy 13, 83–114.

Guschina IA, Harwood J.L. (2006). Lipids and lipid metabolism in eukaryotic algae. Prog Lipid Res 45:160–86

Hu, Q.; Sommerfeld, M.; Jarvis, E.; Ghirardi, M.; Posewitz, M.; Seibert, M.; Darzins, A. (2008). Microalgal triacylglycerols as feedstocks for biofuel production: Perspectives and advances. Plant J., 544, 621–639.

Johnson, M.B. and Wen, Z. (2009). Production of biodiesel fuel from the microalga Schizochytrium limacinum by direct transesterification of algal biomass. Energy Fuel 23: 5179–5183.

Knothe, G. (2005). Dependence of biodiesel fuel properties on the structure of fatty acid alkyl esters. Fuel Process Technol. 86: 1059–1070.

Knothe, G.; Steidle, K.R. (2005) Kinematic viscosity of biodiesel fuel components and related compounds Influence of compound structure and comparison to petrodiesel fuel components. Fuel, 84, 1059–1065.

Krawczyk, T. (1996). Biodiesel – alternative fuel makes inroads but hurdles remain. Inform 7: 801–829.

Lacey, P.I.; Lestz, S.J. (1992) .Effect of Low Lubricity Fuels on Diesel Injection Pumps Part I: Field Performance; SAE Technical Paper No. 920823; SAE International: Washington, DC, USA; doi:10.4271/920823.

Lang, X.; Dalai, A.K.; Bakshi, N.N.; Reaney, M.J.; Hertz, P.B. (2001). Preparation and characterisation of bio-diesels from various bio-oils.. Bioresour Technol., 80, 53–62.

Ma, F.; Hanna, M.A. Biodiesel production: A review. Bioresour. Technol. 1999, 70, 1–15.

Metting, F.B. (1996).Biodiversity and application of microalgae. J. Ind. Microbiol: 17 (5 -6): 477 – 89.

Metzger P, Largeau C. (2005). Botryococcus braunii: a rich source for hydrocarbons and related ether lipids. Appl Microbiol Biotechnol 66:486–96.

Miao, X., Wu, Q., Yang, C. (2004). Fast pyrolysis of microalgae to produce renewable fuels. J. Anal. Appl. Pyrol. 71: 855–863.

Ng, J.H.; Ng, H.K.; Gan, S. (2012) Development of emissions predictor equations for a light- duty diesel engine using biodiesel fuel properties. Fuel, 95, 544–552.

Ogi T, Yokoyama S, Minowa T, Dote Y. (1990) Role of butanol solvent in direct liquefaction of wood. Sekiyu Gakkaishi (J Japan Petr Inst) 33:383–9.

Omer, A.M. and Fadalla, Y. (2003). Biogas technology in Sudan. Renew. Energy 28, 499–507.

Peng W.M., Wu QY, Tu P.G. (2000). Effects of temperature and holding time on production of renewable fuels from pyrolysis of Chlorella protothecoides. J Appl Phycol 2000;12:147–52.

Powell, E.E. and Hill, G.A. (2009). Economic assessment of an integrated bioethanol– biodiesel–microbial fuel cell facility utilizing yeast and photosynthetic algae. Chem. Eng. Res. Des. 87, 1340–1348.

Ratledge C. (1993). Single cell oils — have they a biotechnological future? Trends Biotechnol 11:278–84.

Ratledge, C, Wynn, J.P. (2002). The biochemistry and molecular biology of lipid accumulation in oleaginous microorganisms. Adv Appl Microbiol 51:1–51.

Rupprecht, J. (2009). From systems biology to fuel—Chlamydomonas reinhardtii as a model for a systems biology approach to improve biohydrogen production. J. Biotechnol. 142: 10–20.

Shay, E.G. (1993). Diesel fuel from vegetable oils: Status and opportunities. Biomass and Bioenergy Volume 4, Issue 4, 1993, Pages 227-242.

Sgroi, M., Bollito, G., Saracco, G., Specchia, S. (2005). BIOFEAT: biodiesel fuel processor for a vehicle fuel cell auxiliary power unit: study of the feed system. J. Power Sources 149, 8–14.

Skjanes, K., Lindblad, P., Muller, J. (2007). BioCO2 – a multidisciplinary, biological approach using solar energy to capture CO_2 while producing H2 and high value products. Biomol. Eng. 24, 405–413.

Spolaore, P., Joannis-Cassan, C., Duran, E., Isambert, A. (2006). Commercial applications of microalgae. J. Biosci. Bioeng. 101: 87–96.

Szybist, J.P.; Song, J.; Alam, M.; Boehma, A.L. (2007). Biodiesel combustion, emissions and emission control. Fuel Process. Technol., 88, 679–691.

Ueno, Y., Kurano, N., Miyachi, S. (1998). Ethanol production by dark fermentation in the marine green alga, Chlorococcum littorale. J. Ferment. Bioeng. 86: 38–43.

Van Gerpen J. (2005). Biodiesel processing and production. Fuel Process Technol 86:1097–107.

Vonshak, A. (1997). Spirulina platensis (Arthrospira) physiology, cell-biology and biotechnology. Taylor & Francis, London, ISBN 0-7484-0674-3.

Xuan, J., Leung, M.K.H., Leung, D.Y.C., Ni, M. (2009). A review of biomass-derived fuel processors for fuel cell systems. Renew. Sust. Energy Rev. 13: 1301–1313.

134: Experimental study on the thermal performance of solar collectors applied to air conditioning system

Zheng LIN[1], Wei ZHANG[2*], Wei WANG[3], Hao TIAN[4]

[1] Key Laboratory Deep Underground Science and Engineering, College of Architecture and Environment, Sichuan University, Chengdu, China, 610065, zhenglin9374@foxmail.com
[2] Key Laboratory Deep Underground Science and Engineering, College of Architecture and Environment, Sichuan University, Chengdu, China, 610065, xskin821@163.com*
[3] Key Laboratory Deep Underground Science and Engineering, College of Architecture and Environment, Sichuan University, Chengdu, China, 610065, 1005015056@qq.com
[4] Key Laboratory Deep Underground Science and Engineering, College of Architecture and Environment, Sichuan University, Chengdu, China, 610065, 1355358537@qq.com
Corresponding author: Wei Zhang emai: xskin821@163.com

Solar powered air conditioning system is hot issue in the study field of building energy conservation. An experimental platform of solar powered air conditioning system was carried out to test the efficiency of the solar powered air conditioning system and the coupled relation with the solar radiation intensity. The outdoor and indoor environmental test system was used to collect the performance parameter data of the solar powered air conditioning system. According to the analysis result, the transient thermal efficiency would decline with the rising normalised temperature difference. The transient thermal efficiency has the same variation trend with the solar radiation. The research result could help to improve the study of solar powered air conditioning system and its application.

Keywords: solar energy; air conditioning; efficiency; solar collector

1. INTRODUCTION

Because the conventional sources of energy are limited and cannot meet the increasing need of the common activities, also some fossil energy would bring the problem of air pollution, the clean and renewable energy technologies is a prospective way. The solar energy which is coming from the sun in the form of solar radiation is a kind of alternative source of clean renewable energy (Bhowmik H,Amin R, 2017). For example, Air conditioning is important for maintain thermal comfort in indoor environments (Guguloth R, 2015), but there exists lots of electricity energy consumption in the building services system like central air-conditioning system. Nowadays, to solve the building non-renewable energy consumption problem, increase the use of clean and renewable energy, lots of solar energy technologies have been studied especially in the field of air-conditioning system, the solar thermal air-conditioning system have become an important research topic (Xu H, Sze JY, 2017).

Solar thermal collectors could collect the solar radiation energy that can be used to supply the thermal energy to the chiller in the air-conditioning system to offer the building cooling demand or the solar thermal energy can be employed to heat the water which could satisfy the building's heating demand (Li Q, Zheng C, 2017). Wei Zhang (2012) experimentally researched three different solar collectors for the solar ejector air conditioning system for the Mediterranean climate and simulated the system by computer. From his study and analysis, the evacuated tube collector with specific surface would be the most economical way for solar ejector air conditioning system. Martinez-Rodriguez (2018) made a primary network design of evacuated tube type solar collectors for solar thermal energy application. His research could be used at early design stages for assessing the cost benefit of the solar energy system. In his research results, most solar collectors of the evacuated tube have a similar thermal performance according to their independently features. Li Q (2017) used simulation software (Zemax, version 12.EE) simulate the optical efficiency of the concentrator system at different light incident angles, and a ray tracing simulation was carried out by using optical design. The simulation and analysis results showed that the maximum optical efficiency of the system was around 90% when the incident light angle is 0℃.

The previous research works showed that the evacuated tube solar collector has better performance than other collectors. To analysis the efficiency of collector and its relationship with the solar radiation, the solar powered air conditioning system coupled with the solar collectors' experimental rig was carried out.

2. EXPERIMENTAL SET-UP AND PROCEDURES

2.1. Experimental system setup

The experiment here is formed by evacuated tube solar collectors driving a heat exchange machine and an absorption refrigeration machine. The heat exchange machine, driven by solar collectors, while changing the temperature of the fluid, influences the efficiency of the absorption refrigeration machine which powers the air conditioning system. The evacuated tube solar collectors could work at higher temperature than other glass panels. The diagram of solar powered air conditioning experimental system with evacuated tube solar collectors is shown in the Figure 1.

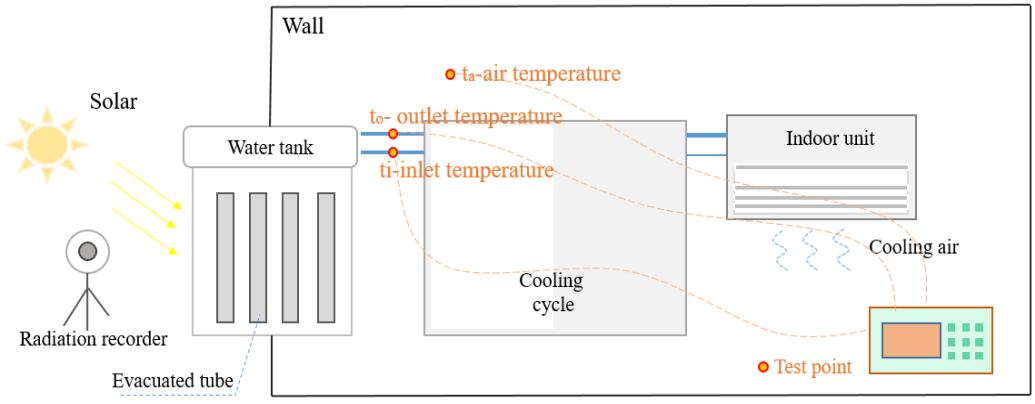

Figure 1: The diagram of a solar powered air conditioning experimental system with evacuated tube solar collectors.

As shown in the Figure 1, there are three test point in this experimental process, t_a was directed as air temperature, to was outlet fluid temperature while t_i was inlet fluid temperature. The test instruments and instrument parameters are as follow in Figure 2. The evacuated tube solar collectors were installed with the air conditioning system and the solar radiation recorder was fixed outside to measure the dynamic solar radiation intensity, a multi-channel temperature heat flow tester was used to record the temperature of those three test points.

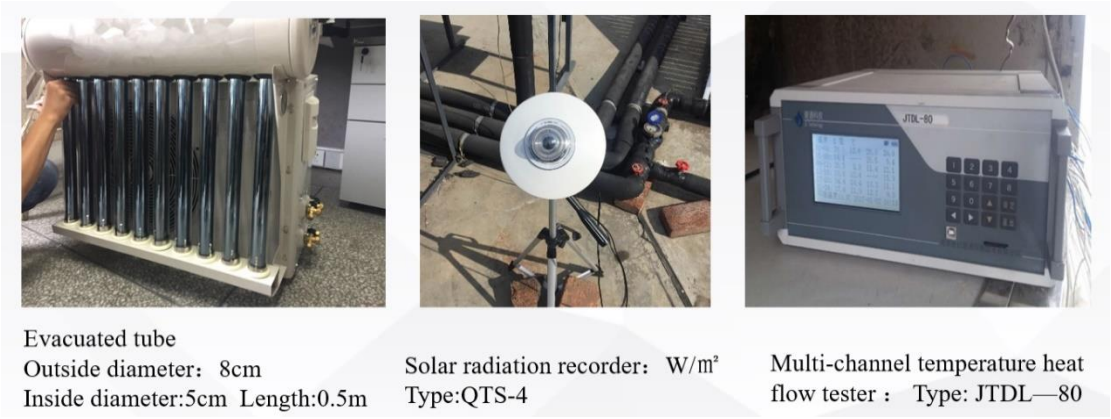

Figure 2: The test instruments of the solar powered air conditioning system with evacuated tube solar collector.

In this experiment, the temperature of three test points was tested and recorded through the specific instruments, the variation situation of the solar radiation was also recorded. The experiment was carried out for one week started from 8:00 AM to 17:00 PM and the experimental data of a typical day conformed to the requirements were chosen for the calculation and analysis. Data were collected when the system was operating stably at a time interval of 3 min.

2.2. Experimental system setup

The transient thermal efficiency of the evacuated tube solar collector can be written as Equation (1) and Equation (2). During the experiment, performance tests were complied with the Chinese standard GB/T 17581-1998, thus the transient efficiency "η" _0of the liquid-tube working reflectorless solar tube solar collector should not lower than 0.62, the total heat loss coeddicient U of the evacuated tube solar collector should not higher than3.0, while this experiment, the "η" _0 was chosen as 0.62 and the U was chosen as 3.0W/（㎡·k）.

$$\eta = \eta_0 - UT_i \qquad \text{Eq (1)}$$

$$T_i = ((t_i + t_o)/2 - t_a)/G \qquad \text{Eq (2)}$$

Where:

η_0=transient thermal efficiency

U=the total heat loss coefficient of the collector based on T_i（W/（㎡·k））

G=total solar radiation (W/㎡)

T_i—normalised temperature difference ℃

ti—tube inlet fluid temperature ℃

ta—air temperature ℃

to—tube outlet temperature ℃

3. EXPERIMENTAL SET-UP AND PROCEDURES

As the weather was always changing with time, the experiments were tested in one week and the experimental data conformed equipment, the experimental data on September 28th was chosen to analyze the performance. The variation of the solar radiation intensity is shown in the Figure 3 and the calculated results of the transient efficiency of evacuated tube solar collectors is shown in the Figure 4. As shown in Figure 3, during the test time, the solar radiation intensity fluctuates with the weather conditions, it is clearly that the solar radiation is declined because of the cloud influence during the 12:33 PM to 13:48 PM, as shown in the Figure 4, the transient efficiency of the evacuated tube solar collector

has the same decline effect at the time around 13:55 PM. The overall trend between the solar radiation intensity and the transient efficiency of the collectors are basically the same, which means that the solar radiation has positive effect on the efficiency of the collectors, furthermore it would deeply influence the solar powered air conditioning system.

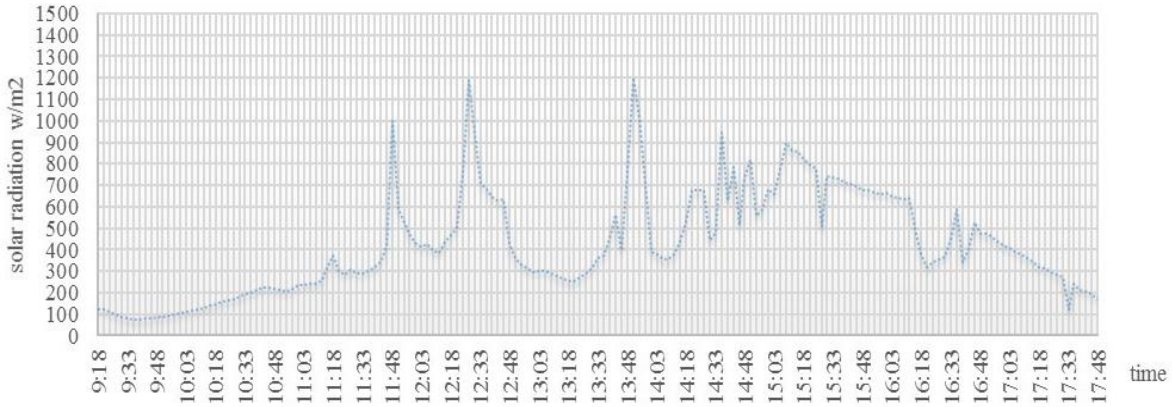

Figure 3: The variation of the solar radiation intensity on 28th Sept.

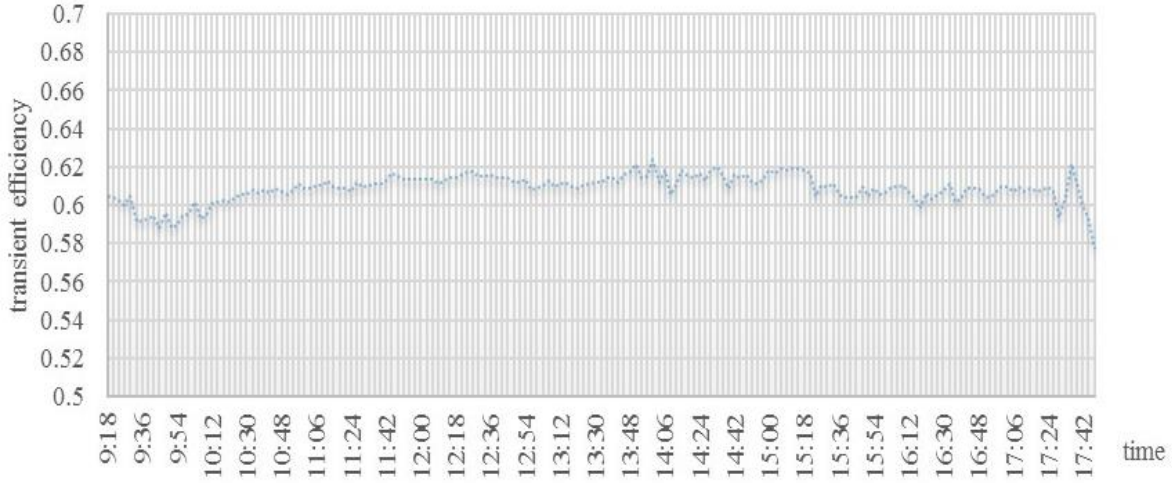

Figure 4: The variation of the solar radiation intensity on 28th Sept.

Comparison between the variation trend of solar radiation density and the calculated results of the transient efficiency of collectors are shown in the Figure 5, when the solar radiation intensity is increasing the morning, the transient efficiency of the collector is also increasing. When the solar radiation is declined because of the weather influence, the transient efficiency has the same variation trend. Base on the overall trend, the variation curve shows that the solar radiation intensity has the positive correlation with the transient efficiency of the evacuated tube solar collectors.

The normalised temperature difference T_i can be obtained from the Equation (2), Figure 6 provides the detailed results, the transient efficiency is also provided. Figure 6 show that with decreasing T_i , the transient efficiency was declined. The result indicates that the transient efficiency has the liner relationship with normalised temperature difference, but the normalised temperature difference is influenced by lots of factors for example the weather conditions, the air temperature and the solar radiation, which means that the climate conditions should be considered as an important condition when studying the efficiency of the solar collectors and the solar powered air conditioning system.

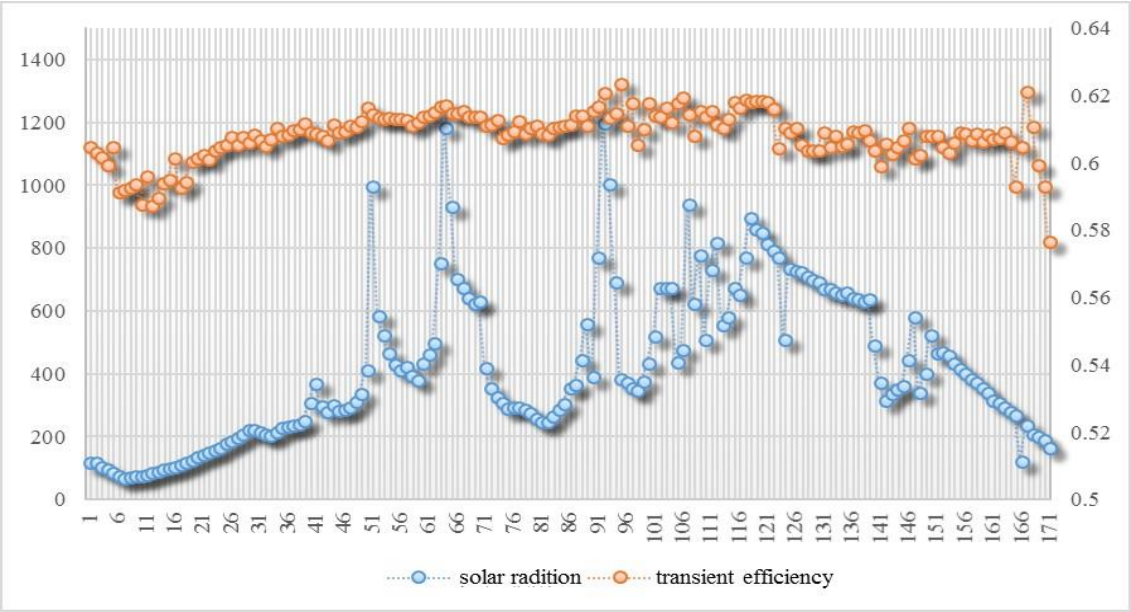

Figure 5: The variation trend of solar radiation density and the calculated results of the collectors 'transient efficiency

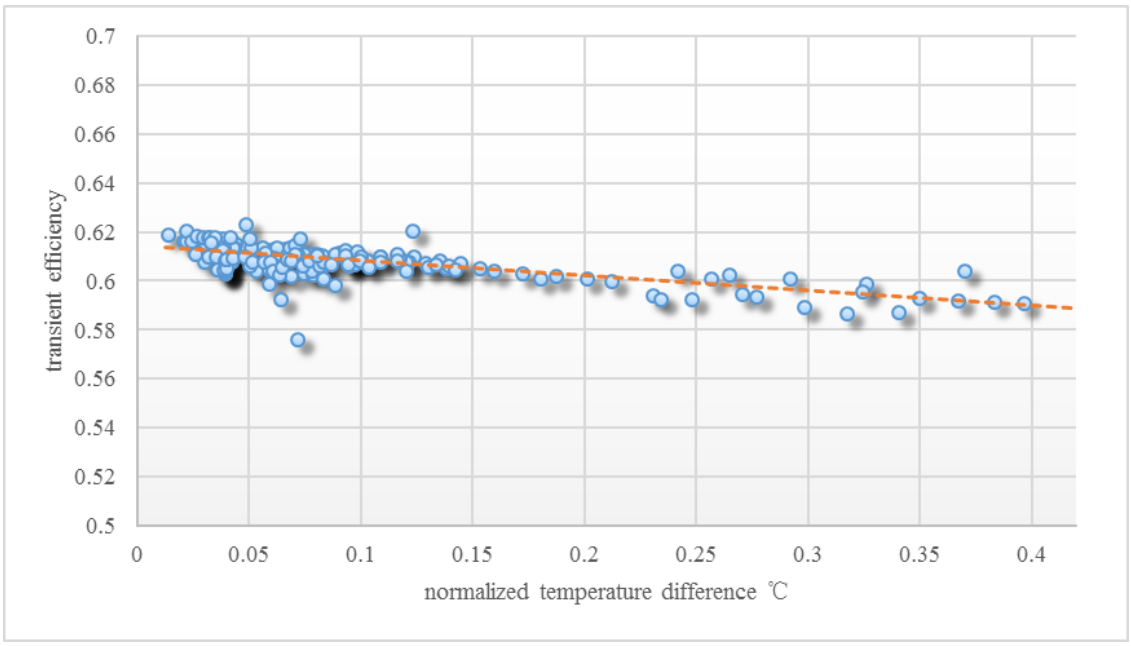

Figure 6: The variation trend of normalised temperature difference and transient efficiency

4. CONCLUSION

A solar powered air conditioning system coupled with the solar collector's experimental rig was constructed and tested at Chengdu, Sichuan on September 28th. It is obtained from the observation that the unit in solar powered air conditioning system are strongly depending on solar radiation. Solar radiation intensity has the positive correlation with the transient efficiency of the solar facilities and the whole system. The effect of climate on system efficiency cannot be negligible. This trend could provide an effective way to improve the efficiency of solar powered air conditioning system, the research on how to re-direct or control the solar beam radiation has important research significance.

5. ACKNOWLEDGEMENTS

This project is funded by the National Natural Science Foundation of China (No. 51508352), Science &Technology Department Foundation of Chengdu City, China (No.2015-HM01-00244-SF) and Key Laboratory Deep Underground Science and Engineering Foundation of Sichuan University, China (No.DUSE201702)

6. REFERENCES

Bhowmik H, Amin R. Efficiency improvement of flat plate solar collector using reflector. Energy Reports. 2017; 3:119-23.

Gugulothu R, Somanchi NS, Banoth HB, Banothu K. A Review on Solar Powered Air Conditioning System. Procedia Earth and Planetary Science. 2015;11:361-7.

Li Q, Zheng C, Shirazi A, Bany Mousa O, Moscia F, Scott JA, et al. Design and analysis of a medium-temperature, concentrated solar thermal collector for air-conditioning applications. Applied Energy. 2017;190:1159-73.

Martínez-Rodríguez G, Fuentes-Silva AL, Picón-Núñez M. Solar thermal networks operating with evacuated-tube collectors. Energy. 2018;146:26-33.

Xu H, Sze JY, Romagnoli A, Py X. Selection of Phase Change Material for Thermal Energy Storage in Solar Air Conditioning Systems. Energy Procedia. 2017;105:4281-8

Zhang W, Ma X, Omer SA, Riffat SB. Optimum selection of solar collectors for a solar-driven ejector air conditioning system by experimental and simulation study. Energy Conversion and Management. 2012;63:106-11.

137: Research of three-level DC/DC converter

Kai FEI[1], Ziqiang XI[2], Changzheng ZHANG[2]

[1] Hubei Collaborative Innovation Center for High efficiency Utilisation of Solar Energy, Hubei University of Technology, Wuhan, 430068,P.R.China,490028022@qq.com
[2]Hubei Collaborative Innovation Center for High efficiency Utilisation of Solar Energy, Hubei University of Technology, Wuhan, 430068,P.R.China,695936405@qq.com
[2]Hubei Collaborative Innovation Center for High efficiency Utilisation of Solar Energy, Hubei University of Technology, Wuhan, longmarch_zhang@163.com

With the expansion of energy demand and the development of environmental protection.The use of new energy has received more and more attention especially the solar energy which plays an very important part in energy system.Three-level DC/DC converter has important significance for improving solar power generation efficiency.Compared to the traditional two-level DC/DC structure, the Three-Level DC/DC has the advantages of small power loss of switching devices and high efficiency of the entire power generation system,but it has unbalanced power problems in the bipolar DC bus which we called neutral point voltage fluctuation.While the voltage of both DC side is unbalanced ,it will increase the harmonics of the system output voltage,and it will also damage the switches. Whether neutral point voltage fluctuation can be handled well is the top priority in research. In order to solve this issue,corresponding modulation strategies and control methods are proposed in this paper.Taking the Three-Level DC/DC converter as research subject,this paper mentions some points as follows.Three-Level DC/DC Converter topology is described and converter operating `principle is introduced in detailed way to make a good foundation for the analysis of the following modulation strategy.After Specif Modulation analysis has been illustrated a Multi-carrier Pulse Width Modulation method is used to keep the bipolar DC bus voltage in balance.Then Select a double closed-loop voltage control strategy to achieve the stability of the whole There-Level DC/DC system.At last we set up models that consists of a voltage input module,a control module and a DC/DC conversion module for simulation.Simulation results are presented to verify the effectiveness of the proposed theory.

Keywords: The solar power,Three-Level DC/DC Converter,Neutral point voltage,modulation strategy,Control method.

1. INTRODUCTION

In the background of the continuous depletion of non-renewable energy, the economy has continued to develop.Solar Power is one important component of new energy transformation (Guerrero J M, 2010). DC/DC conversion is a necessary part in Solar power system.It not only influences voltage stable in DC bus,but also affects the conversion efficiency of the whole systems (Green M, 2006).So it is meaningful for us to do a deep research on it.

At present, the DC/DC converter technology develops from two-level to three-level and multi-level.The level number refers to the output of the DC/DC Before the filter inductors.Levels' classification are determined by the phase voltage of the Neutral N of the bus voltage. If its $\pm U$,the DC/DC converter is two-level and its line voltage is 0, $\pm U$ .It would be Three-Level if N phase voltages are 0, $\pm U/2$, $\pm U$ .Compared with the two levels, the three levels have the following main advantages:It has Low harmonic content and small filter inductance.The switching frequency is lower, the switching loss is smaller, the voltage change rate (du/dt) during the switching operation is smaller which makes electromagnetic interference (EMI) smaller (Grbovic, 2010). It also increases the power system efficiency.However, once the level of the converter becomes more, the output voltage waveform is nearly same to a sine wave,it's topology and control system will be more complex.This paper proposes a kind of modulation strategy and a double closed-loop control system based on the fundamental topology and operating principle.The proposed modulation strategy limits the voltage fluctuations and eliminates the additional circuits in using Multi-carrier Pulse Width Modulation method,thereby improve overall system efficiency.It is introduced exhaustively in the main text.

2. THREE-LEVEL DC/DC CONVERTER

2.1. Topology Description

The topology of the proposed converter is shown in Figure 1. It consists of Three-Level DC/DC converter unit to handle the high current,and the output terminals p,z,n directly connected to DC bus.Each Unit is composed of four switching devices.On the input side there are one diode and one filter capacitor C_f .Each unit consists of four switching device(S_1 、 S_2 、 S_3 、 S_4) with four diodes（ D_1 、 D_2 、 D_3 、 D_4 ）,and two inductors（ L_1 、 L_2 ）.This converter is modular in essence because the parallel DC/DC converters have common input filter capacitors（ C_1 、 C_2 ）and common output side(C_f),So the capacity can be increased easily by connecting more DC/DC converters in parallel (H.Yu,2013).

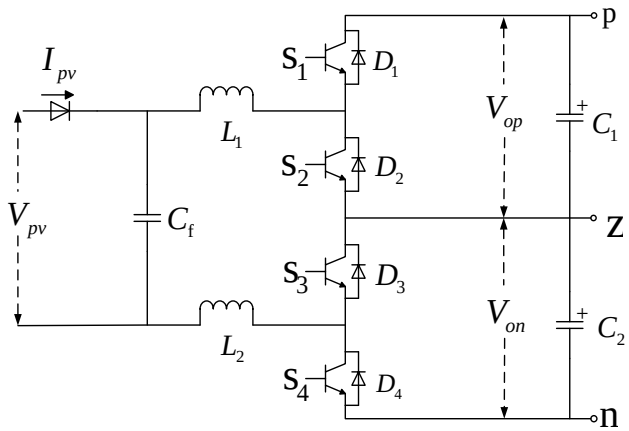

Figure 1: Proposed High-Power Three-Level DC/DC converter topology

2.2. Operating Principle and Modulation

The main topology of the converter selected in this paper can achieve the four operating modes presented in Figure 2 by changing the mode of the switch.According to the position of the switches, we name the four modes (e.g 23 means 2 and 3 switches are turned ON). In the whole working conditions, we find that there are no influence on the balance of Voltage in 23 or 14stage because the output voltage of stage 23 is zero and 14 stage make the DC side

voltage $V_{\text{on}}+V_{\text{op}}$.usually $2V_{\text{i}}$. During the stage 13 24 , there produce the output voltage, but have opposite neutral-point currents. Due to this operating characteristic, when the total voltage at the output remains constant, if the voltage between pn and the voltage between nz is not equal, we can make the switch working on 13 or 24 stage to keep the V_{on} V_{op} the same.For example, if V_{op} is small than V_{on}, the system is turned in the 13 stage to charge C_1 capacitor until the V_{on} and V_{op} are at the same voltage level.On the contrary, if V_{on} is smaller, correspondingly turn on 24 switches.

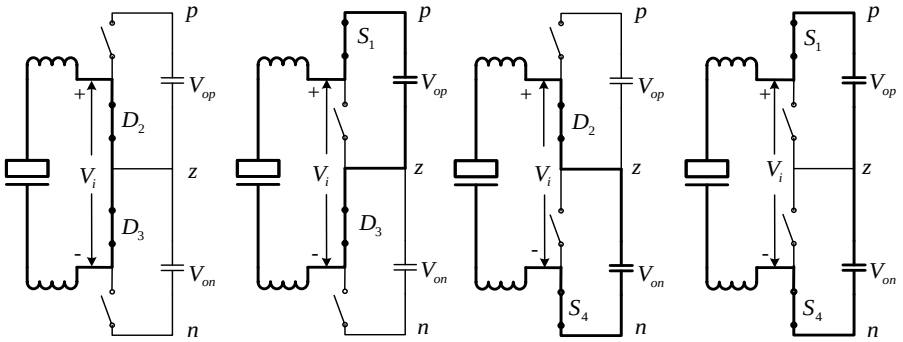

Figure 2: Four operating stages

Based on topology and operating stages.Multi-carrier Pulse Width Modulation (PWM）(TAO Fen, 2016) is selected in this research.The specific method is as follows:the modulation signals are compared with two triangle Carrier signals,the difference between the two triangle Carrier signals are 180°phase deviation. Neutral Point voltage balance can achieve by this feature. The modulation signals d_1 d_4 caused by unbalance voltage. d is duty cycle to equilibrium.In order to distinguish between the output voltage of the balanced and unbalanced, using the voltage between the switch and the inductor V_{i} in Figure 1 to denote the value of the output voltage.

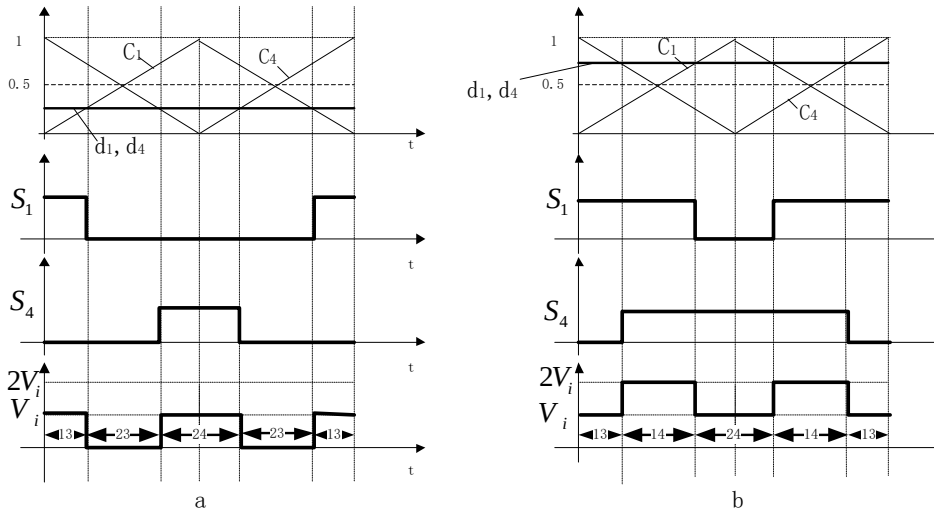

Figure 3: Modulation signal （d≤0.5 d≥0.5）

When Neutral Point voltage is balanced, $d_1=d_4=\text{d}$. Discussing two situations separately Figure 3 shows the converter waveform when $d_1=d_4=\text{d}\le 0.5$ and $d_1=d_4=\text{d}\ge 0.5$ .After the comparison, get the corresponding switch signal S_1 . S_4 .Switching signals are complementary,if S_1 is on then S_2 is off or S_1 is off then S_2 is on.When the duty cycle of the two modulating signals is less than 0.5, the stages of operation are 13, 23, and 24.Simultaneously there are three types of output voltage including V_{op} (13), V_{on} (24),0(23).while d more than 0.5,13. 14. 24 stages are available.The output voltage also has two forms.one is $V_{\text{op}}=V_{\text{on}}=V_{\text{i}}$,the other is $2V_{\text{i}}$.

2.3. Neutral Point voltage balance analyse

When discussing unbalance position, it will be divided into two situations to analyse in a balanced position in order to verify the feasibility of the operating principle.

2.4. d>0.5 when balancing

When d_1 >0.5 d_4 >0.5,the duty cycle is also less than 0.5 after Neutral Point voltage keeps in balance.Compared with Figure 3 a picture,we find that the 24 stage operation time is shorter,and the 13 mode operation time is longer.During the 14 stage,no matter if it is balanced or not,the output voltage is always the same.This also just verified that 14 stage have no effect on the neutral balance.Influenced by the turn-on time of the switch, the output voltage in the 13 and 24 stages are also different.Therefore, in this case we can control the voltage by changing the on-off time of the switch.Part B shows states when exchanging the position of d_1 and d_4.

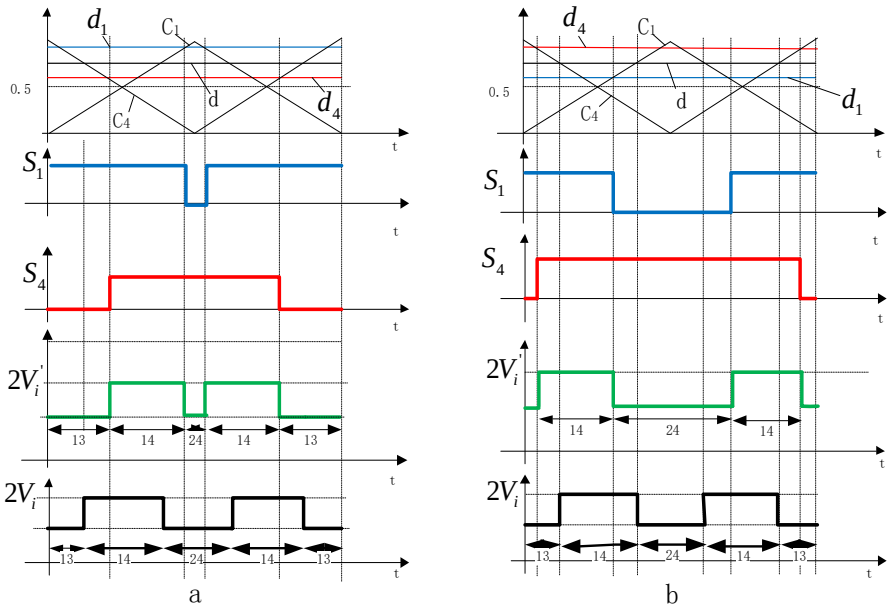

Figure 4: Modulation signal (d1≠d4，d＞0.5)

2.5. D<0.5 in balance

When d_1 <0.5 d_4 <0.5,the duty cycle is also less than 0.5 after Neutral Point voltage keeps in balance.At this moment,the stages of operation are 13, 23, and 24.After calculation the time has not changed in the 23 operating stage, and the output voltage in the 23 operating stage is zero.The process of the output voltage from unbalanced to the equilibrium only increases operating time of 24 stage, the time of the 13 stage is reduced, and the increase time of the 24 mode is the same as that of the 13 mode.Increasing time is the same as decreasing time.Part b in the Figure 5 shows the condition when exchanging the position of d_1 and d_4.

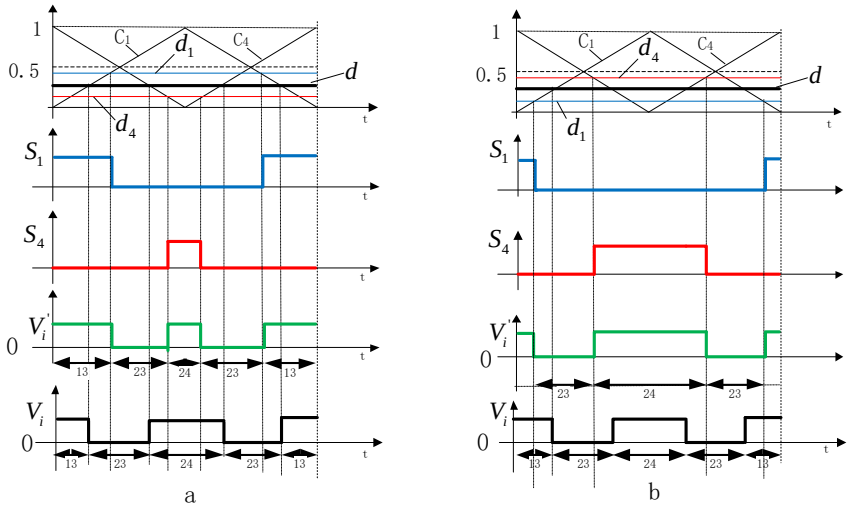

Figure 5: Modulation signal (d1≠d4，d＜0.5)

3. CONTROL THEORY

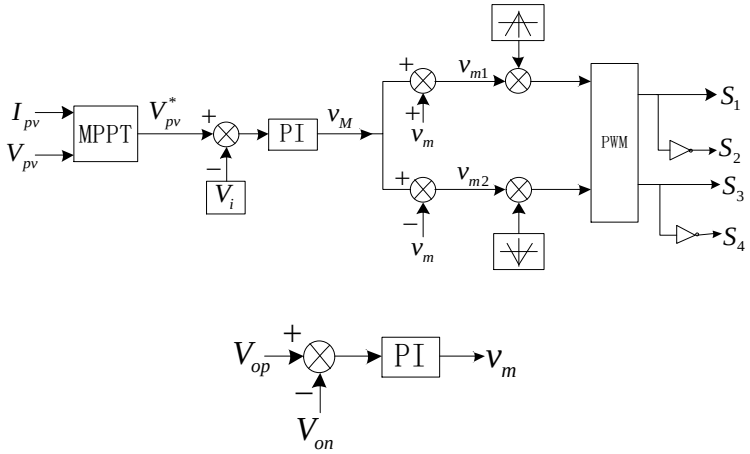

Figure 6: Control diagram

The control theory proposed in this paper is shown in Figure 6.Maximum power point tracking (MPPT) technology is used to improve the conversion efficiency of solar power (J.M.Kwon, 2008).MPPT module only produce the voltage (V_{pv}^{*}) at the maximum power point and does not affect the subsequent research on voltage balance.At present, the technology of maximum power point tracking has been very advanced.And It isn't the point in this research.So the specific algorithm will not be described.

Comparing V_i output voltage when balancing with V_{pv}^{*}, then get the V_M signal after PI. The below PI are used to get the voltage signal V_m by Comparing V_{op} and V_{on} .The reference V_M plus and minus V_m respectively obtaining V_{m1} , V_{m2} .Finally,We transform modulation signal that Generate by comparing two triangular modulated wave carriers with V_{m1} V_{m2} into switching signal S_1 S_3 .It should be noticed that two triangular modulating wave carriers should be phase shifted 180°.

4. SIMULATION RESULT

According to the above modulation strategy and control principle, the entire system is simulated to verify its feasibility, as shown in Figure 7.

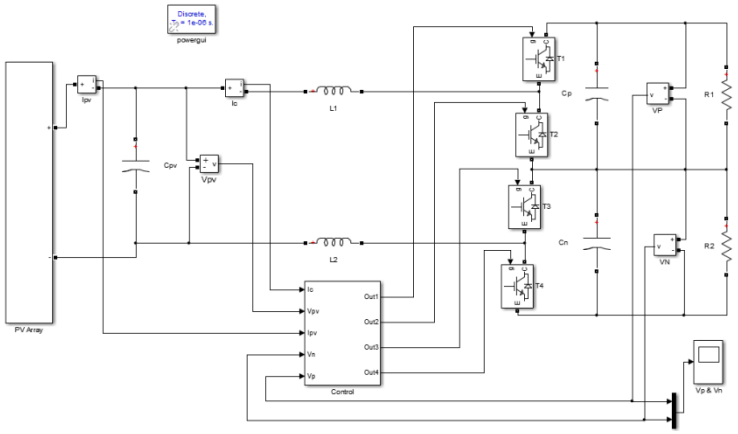

Figure 7: DC/DC system Simulation Structure Diagram

The output voltage of the Photovoltaic using Maximum power point tracking (MPPT) is 600V, the input current of DC/DC converter side is 20A, and the simulation power is 10KW. By setting the resistance of the output terminals R_1 and R_2 differently, the DC bus voltage is unbalanced and the Neutral Point voltage is shifted.

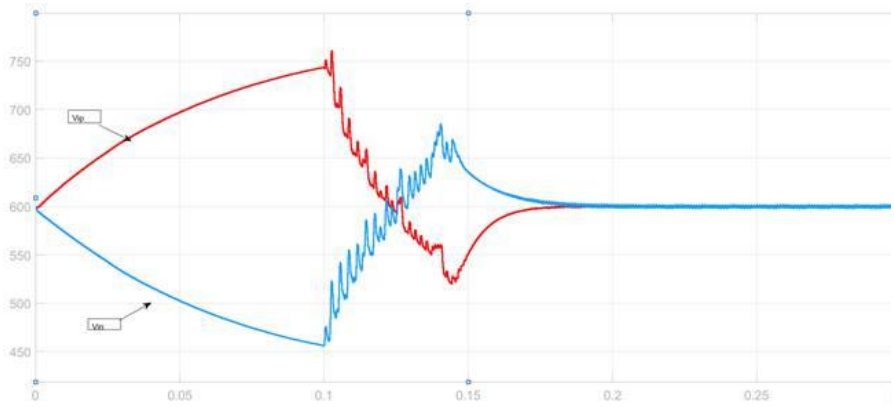

Figure 8: Simulation Result

The simulation waveform is shown in Figure 8.The Blue line represent V_{on} in output side.The red line is V_{op} .Adding the control module at 0.1s,It can be seen that when the Neutral Point voltage control don't work, the output voltage is shifted, and the voltage fluctuations becomes greater with the time increasing. At 0.1s,the voltage will adjust immediately and the both side reach equilibrium nearly 0.18s.This proves that this strategy can accurately and efficiently control the fluctuation of the Neutral Point voltage.

5. CONCLUSION

The Three-Level DC/DC converter based solar power generating system is proposed for high power and voltage situation.Compared with the traditional two-level inverter, the three-level inverter has the advantages of high equivalent switching frequency, good output performance, and good electromagnetic compatibility.Meanwhile the use of three-level DC/DC converters brings lower current stress and lower output current ripples,and the power capacity can be easily scaled up due to its modularity.

The natural problem of three-level structure - Neutral point voltage imbalance is the focus of the research.Analysis of operating principles make it clearly that the causes of Neutral point voltage fluctuations.By the analysis of the classification of modulation Multi-carrier Pulse Width Modulation（PWM） is proposed to assist the DC/DC converter in balancing voltage when the imbalanced voltage is out of its controllable zone.Meanwhile,a double closed-loop control structure is chosen to complete voltage balance task. Through the simulation and results, it has been demonstrated that this Three-Level DC/DC converter can deal with Neutral point voltage imbalance perfectly and is very well in high power voltage transformation area of the solar power.

6. REFERENCES

Guerrero J M, Blaabjerg F,(2010). Distributed generation: toward a new energy paradigm[J].IEEE Transactions on Industrial Electronics Magazine.4(1),52-64.

Green M,(2006). Consolidation of thin-film photovoltaic technology: the coming decade of opportunity[J]. Progress in Photovolaics: Research and Applications.(14):383-392.

Grbovic,P.J.Delarue, (2010). A Bidirectional Three-Level DC/DC Converter for the capacitor Applications.IEEE Transactions on Industrial Electronics Magazine.

Yu H, Xiang X, Zhao C, (2013). Performance analysis of a ZVS bidirectional dc-dc converter with reduced voltage stress on high voltage side. IEEE ECCE.

Kwon JM, Kwon BH, (2008). Three-phase photovoltaic system with three-level boosting MPPT control.IEEE Trans.Power electron.vol.23, no.5, pp.2319-2327.

Tao F, Xie Z, (2016). Fast valve power loss evaluation method for modular multi-level converter operating at high-frequency.Protection and Control of Modern Power Systems.

141: Synchronous control method for combined verification power supply for GIS current transformer based on frequency adaptive PR controller

Guowei CHEN, Ziqiang XI, Lujun WANG

Hubei University of Technology Solar Energy Efficient Use of Hubei Cooperative Innovation Center. Hubei, Wuhan 430068

In order to reliably verify the current transformers, it is generally required that the verification system maintains a high output accuracy within a wide capacity range of 5% to 110%.In order to solve the problem of the low accuracy of the output of the ultra-high voltage gas-insulated enclosed combined electrical type (GIS) current transformer calibration system in a wide range of output. A combination of digital, high-capacity, wide-voltage, and high-precision power solutions is proposed.The scheme uses a combined power supply structure in series with a power electronic power supply and an electrical power supply. The electrical power supply regulates the voltage output through a voltage regulator,used when combining power supply low voltage output.Power electronic power supply adopts single-phase full-bridge inverter structure.When the combined power supply outputs a large voltage, the combined power supply in series can maintain high accuracy over a wide range of voltage output. In order to make the electronic power source and electrical power maintain synchronous operation, a frequency adaptive proportional resonant (PR) controller is used. Added frequency adjustment module based on adaptive notch filter on the basis of traditional PR controller .The PR controller parameters of power electronics are designed as time-varying parameters according to the frequency of electrician power. Then, the frequency and phase of electrician power supply are tracked in real time by adaptive notch filter. The experimental results show that the frequency adaptive PR controller can make the power electronic power supply output high-precision voltage waveform, and synchronise with the electric power supply's frequency and phase at any time, and the output voltage of the combined power supply is stable and THD<3%.

Keywords : current transformer ; calibration system; frequency adaptive; PR controller

1. INTRODUCTION

The current transformer calibration system consists of verification power supply, compensation device, up flow device, standard current transformer, mutual inductor calibrator and current load box. Its main function is to verify the technical performance of current transformer in the field or laboratory.In the early stage of the development of the power grid, the voltage level is not high and the capacity of the current transformer is not large, so the traditional electric power supply is generally used as the verification power.With the development of full control type semiconductor device with IGBT, MOSFET and high performance digital control chip,verification power to begin the development of inverter power supply direction based on power electronic technology.

In recent years, with the continuous development of EHV power grid in China, more and more attention has been paid to the verification system of EHV GIS current transformer in order to ensure accurate measurement and protection design.Because the GIS pipeline has the characteristics of full closure, it is impossible to separate the current transformers at the on-site inspection timing. It is necessary to carry the necessary electrical components and a long pipeline bus to carry out on-site verification. Therefore, the impedance of the test loop at the on-site inspection is too large. The required riser and voltage regulator have large capacity. In order to truly verify the current transformer, it is generally required to verify that the power supply field can maintain high output accuracy within a wide capacity range of 5% to 110%.

In order to solve the above-mentioned problem of wide-capacity output, this article uses a combined power supply structure in which a power electronic power supply and an electrical power supply are connected in series,in which the electrical power supply regulates the voltage output through a voltage regulator,used when combining power supply low voltage output.Power electronic power supply adopts single-phase full-bridge inverter structure.When the combined power supply outputs a large voltage, the combined power supply in series can maintain high accuracy over a wide range of voltage output.

Proportional Integral (PI) controller is the most commonly used single-phase inverter control algorithm, which has the characteristics of simple structure and easy to implement.However, it is pointed out that the PI controller can not achieve steady-state error theoretically when the sinusoidal voltage reference signal is tracked.An improved method is to transform the sinusoidal signal into the DC quantity in the rotating coordinate system, and then to achieve steady-state error tracking.But for single phase voltage, because there is no quadrature component input, it is difficult to directly transform it to the rotating coordinate system. After transforming to the rotating coordinate system, there is a coupling component between the dq axes (Ahmed K H, 2011).

In recent years, proportional resonance (PR) controller has been widely concerned because of its steady-state error sinusoidal signal.However, when the PR controller is calculating the control parameters, a given resonant frequency parameter is usually needed.The frequency of the power electronic power supply in this paper is the same as that of the electric power supply, and it is a time-varying parameter(Zhang Jianpo,2013).In order to ensure the synchronous operation of power electronic power supply and electrical power supply, a frequency adaptive PR controller is proposed in this paper. First, the PR controller parameters of power electronics are designed as time-varying parameters according to the frequency of electrician power. Then, the frequency and phase of electrician power supply are tracked in real time by adaptive notch filter.

In this paper, the structure and principle of the combined verification power supply for GIS current transformer are introduced, and the output current control model is set up.The output voltage control circuit of power electronic power supply is analyzed in detail, and then the adaptive PR controller is analyzed in detail.Finally, the effectiveness of the proposed controller is verified by experiments.The experimental results show that the frequency adaptive PR controller can make the power electronic power supply output high-precision voltage waveform, and synchronise with the electric power supply's frequency and phase at any time, and the output voltage of the combined power supply is stable and THD<3%.

2. STRUCTURE AND PRINCIPLE OF COMBINED VERIFICATION POWER SUPPLY

Figure 1 is the structure diagram of the GIS current transformer combined check power supply. The combined power supply consists of two parts, the power electronic power supply and the electrician power supply. The power electronic power supply is the three-phase input single-phase output inverter structure, the capacity is 150KVA, input connected to 380V power grid, output adjustable 20-300V.The electric power supply is the cascade transformer structure of the voltage regulator.The transformer mainly plays the role of isolation, the output voltage is adjustable from 0 to 20V.

When the output voltage of the combined power supply is less than 20V, the electrician power supply is output, the power electronic power supply is not output, and the output voltage waveform is THD<5%.

When the output voltage of the combined power is greater than 20V, the power electronic power and electrician power output in series, the power electronic power is coarse tuned, the electrician power is fine tuned, and the output voltage waveform is THD<3%.

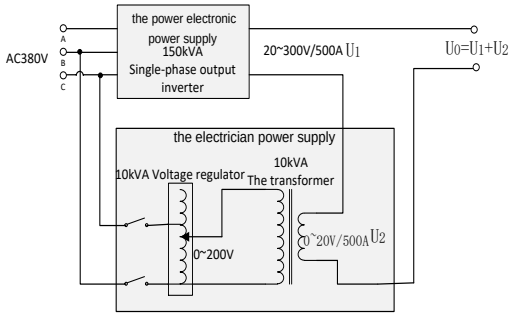

Figure 1: Structure of GIS current transformer combined verify power

The topology of power electronic power supply is shown in Figure 2, and the main circuit is three phase uncontrolled rectifier and single phase full bridge inverter.The output of the inverter is mainly reactive component, and the input is uncontrolled rectification, and its harmonic is not serious.Full bridge inverter is the core part of the whole system. The combined power supply mainly controls the output voltage by controlling the full bridge inverter, and then produces full range verification current.

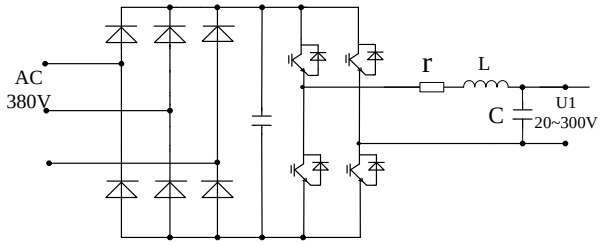

Figure 2: Topology of the electronic power

3. POWER ELECTRONIC POWER SUPPLY MODELING AND CONTROL ALGORITHM ANALYSIS

When the power electronic power supply works stably, the voltage variation of the DC bus capacitor is small, equivalent to a constant voltage source. It is assumed that the output filter inductance is L, the inductor's equivalent internal resistance is r, the filter capacitance is C, the load is Z, the transfer function of the control system is $G_{c(s)}$, and the gain of the inverter is K, then the inverter control block diagram can be expressed as Figure 3. U_{1ref} is the output voltage of the combined power supply minus the actual output voltage of the electrical power supply. $U_{1(s)}$ is the actual output voltage of the power electronic power supply.

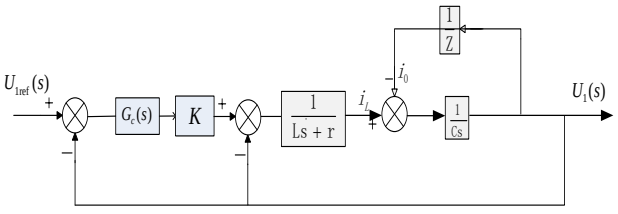

Figure 3: Control block of the electronic power

Equation 1: The open loop transfer function of the system can be expressed as:

$$G(s)=\frac{G_c(s)K}{LCs^2+s\frac{L}{Z}+1}$$

Where:
$G_{c(s)}$= the transfer function of the control system
L = the output filter inductance
Z =the load
$G_{c(s)}$=the transfer function of the control system
K = the gain of the inverter

Equation 2： the control algorithm uses the PR controller, and G_c (s) is expressed as:

$$G_c(s) = K_p + \frac{K_R s}{s^2 + \omega_0^2}$$

Where:
K_P= proportional coefficient
K_R= the coefficient of resonance term
ω_0= the resonant frequency.

Considering the limitation of the parameter accuracy and the accuracy of the digital system of the analog system, the ideal PR controller is not easy to achieve, and the gain is very small at the non fundamental frequency. When the resonance frequency is shifted, the effect is greatly reduced.

Equation 3: quasi resonant controller form:

$$G_c(s) = K_p + \sum_{n=1}^{h} \frac{2K_R \omega_c s}{s^2 + 2\omega_c s + (n\omega_0)^2}$$

Where:

K_P = the proportional term coefficient
K_R=the resonance term coefficient
ω_c=the shear frequency
n = the number of resonance link
ω_0 = the resonant frequency.

In this paper, the frequency adaptive method is used to obtain real time and accurate grid frequency. The Bode diagram of the system's open-loop transfer function is shown in Figure 4. It can be seen from the graph that after introducing the PR controller, the open loop transfer function of the system has obvious spike gain at the power frequency and harmonic frequency, but little change at other frequencies.This can effectively improve the tracking precision of the power frequency voltage, restrain the harmonic interference, and have less influence on the stability and speediness of the system.

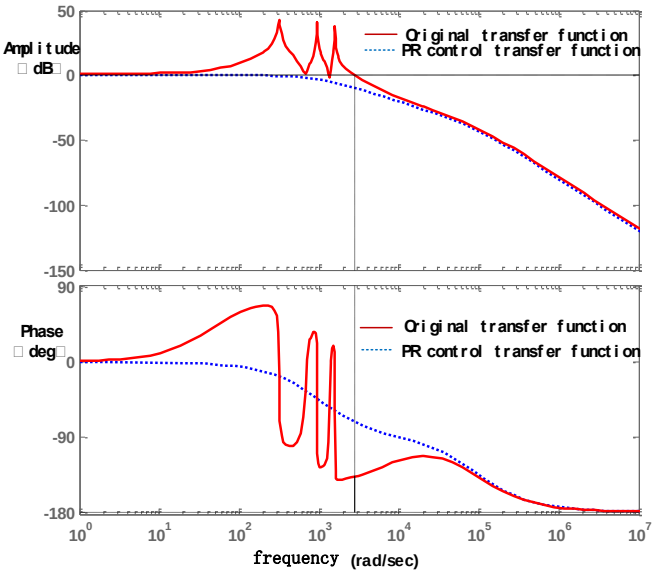

Figure 4: Bode plot of system open loop transfer function

4. ANALYSIS AND DESIGN OF FREQUENCY ADAPTIVE PR CONTROLLER

Discretisation of quasi PR controllers

Equation (3) is a continuous form of quasi-PR controller transfer function. In order for this function to be implemented in an actual numerical control system, the function needs to be discretised.In order to transform the continuous system of transfer function D(s) into discrete system D(z), the following methods can be implemented: reverse difference transform, forward difference transform, impulse response invariant method, zero pole matching method, bilinear transformation method and so on. The bilinear transformation method is used to transform the formula (3) into the form of IIR filter.

Equation 4: The formula of the transformation by the bilinear transformation method

$$s = \frac{2}{T}\frac{1- z^{-1}}{1+ z^{-1}}$$

Where:

T = the sampling period.

Substituting Equation (4) into Equation (3) yields a discrete version of the PR controller:

Equation 5: discrete version of the PR controller

$$G(z) = \frac{b_0 + b_1 z^{-1} + b_2 z^{-2}}{a_0 + a_1 z^{-1} + a_2 z^{-2}}$$

The coefficients a_0, a_1, a_2, b_0, b_1, b_2 are calculated as follows:

Equation 6:

$$\begin{aligned}
a_0 &= 1,\\
a_1 &= \frac{2\omega_0{}^2T^2 - 8}{4 + 4\omega_c T + \omega_0{}^2T^2},\\
a_2 &= \frac{4 - 4\omega_c T + \omega_0{}^2T^2}{4 + 4\omega_c T + \omega_0{}^2T^2},\\
b_0 &= \frac{4K_P + \omega_0{}^2T^2K_P + 4K_R\omega_c T + 4K_P\omega_c T}{4 + 4\omega_c T + \omega_0{}^2T^2},\\
b_1 &= \frac{2\omega_0{}^2T^2K_P - 8K_P}{4 + 4\omega_c T + \omega_0{}^2T^2},\\
b_2 &= \frac{4K_P + \omega_0{}^2T^2K_P - 4K_R\omega_c T - 4K_P\omega_c T}{4 + 4\omega_c T + \omega_0{}^2T^2}.
\end{aligned}$$

From the Equation (6), we can see that after the bilinear transformation is discretised, we can dynamically adjust the parameters of the controller in the substitution mode as long as we get the value of ω_0 in real time, so that the resonant frequency of the control system is consistent with the grid frequency.

Frequency adaptive algorithm

This article uses an adaptive notch filter to obtain the phase of an electrical power supply in real time. Adaptive notch filter is mainly composed of a notch filter module and adaptive module.The role of notch filter module is to extract sinusoidal components of input signal, while adaptive module adaptively adjusts the frequency of notch filter according to some rule.The trap module and the adaptive module are coupled, and the adaptive trap is usually expressed in the form of nonlinear dynamic equations.

Adaptive notch filter has various forms. It will vary with the structure of notch filter and adaptive rules. The adaptive notch filter with global stability can be expressed as the following:

Equation 7:

$$\begin{aligned}
\ddot{x} + 2\zeta\theta\dot{x} + \theta^2 x &= \theta^2 y\\
\dot{\theta} &= -\gamma x(\theta^2 y - 2\zeta\theta\dot{x})
\end{aligned}$$

Where:
y = the input signal
x = the state of the adaptive notch filter
θ = the operating frequency of the notch filter
γ = the parameter for controlling the adaptive frequency of the notch frequency
ζ is the parameter for controlling the bandwidth of the notch filter.

Equation (7) is a strongly nonlinear coupled equation, but due to the small value of the parameter γ that controls the frequency adaptive frequency of the notch filter, the change in θ is slower. When the input signal is y=Asin(ωt), Equation (7) The illustrated kinetic equation has a globally stable running orbit.

Equation 8:

$$p(t) = \begin{pmatrix} \bar{x} \\ \dot{\bar{x}} \\ \bar{\theta} \end{pmatrix} = \begin{pmatrix} -\frac{A}{2\zeta}\cos\omega t \\ \frac{A\omega}{2\zeta}\sin\omega t \\ \omega \end{pmatrix}$$

The orbital parameter $\bar{\theta}$ is the estimated value of the input signal frequency. The rigorous proof of Equation (8) uses the knowledge of adaptive integral manifolds, intuitively understood as follows:

Near the stable working point are:

$$\theta \approx \omega$$
$$\ddot{x} \approx -\omega^2 x$$

The adaptive rule of the notch frequency is:

$$\dot{\theta} = -\gamma x(\theta^2 y - 2\zeta\theta\dot{x}) = -\gamma x(\ddot{x} + \theta^2 x) \approx -\gamma(\theta^2 - \omega^2)x^2$$

Since both x2 and γ are greater than 0 in the above equation, regardless of whether θ is greater than or less than the estimated frequency, the trend of θ tends to gradually approach the actual frequency, which is not related to the size of the actual frequency. Substituting the estimated frequency of Equation (8) into Equation (6) completes the adaptive adjustment of the parameters of the PR controller.

5. EXPERIMENTAL VERIFICATION

In order to verify the effectiveness of the proposed frequency adaptive PR controller in series control of the power electronic power supply and the electrical power supply, an experimental study was performed on the verification power supply of an ultra-high voltage GIS current transformer according to the topology shown in Figure 1.The parameters of the system are shown in Table 1.

The comparison experiments were carried out when the PR controller frequency was fixed and the PR controller frequency was adaptive.

Table 1: Parameter of the combined power

Rated Capacity (kVA)	200
Switching Frequency (Hz)	10K
Sampling Frequency (Hz)	10K
Input Voltage (V)	380

Test situation of PR controller with fixed frequency

The test is shown in Figures 5-7. As can be seen from Figure 5 and Figure 6, using a fixed-frequency PR controller, power electronics output voltage waveform can still maintain a lower THD.

That is, the output voltage of the power electronic power supply itself is not affected. The problem is that there are low-frequency fluctuations in the series voltage output from the electrical power supply and the power electronic

power supply. The fluctuation amplitude is about 15%, as shown in Figure 8, and the transformer will be calibrated at this time. The test brings a lot of error.

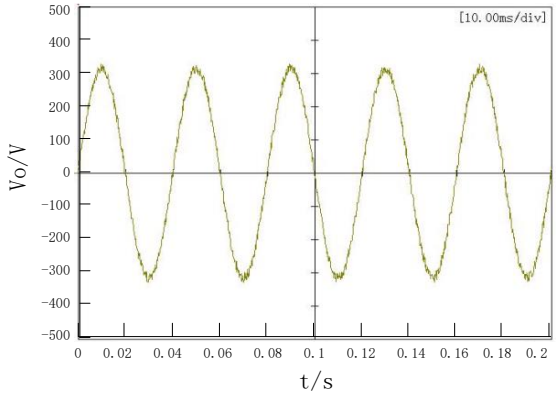

Figure 5: Output voltage of electronic power with fixed freqency PR controller

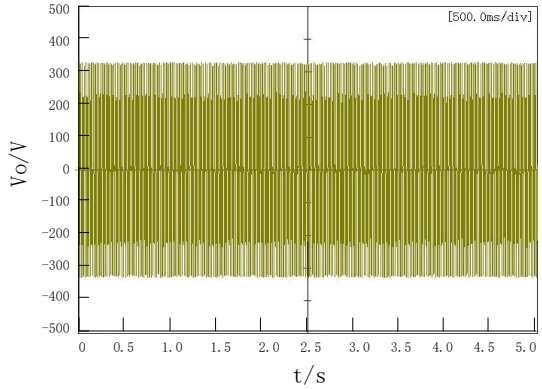

Figure 6: Output voltage of electronic power with fixed freqency PR controller (long time observation)

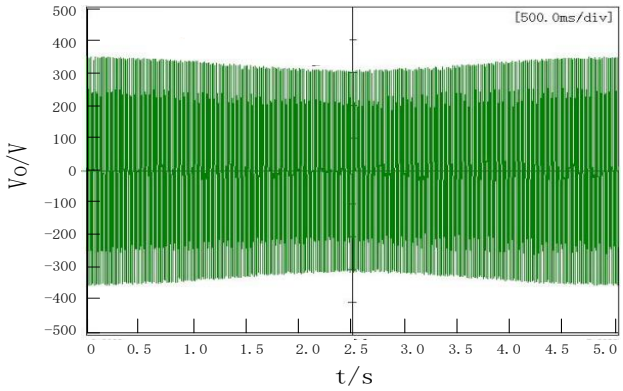

Figure 7: Output voltage of combined power with fixed freqency PR controller

(long-time observation)

Test situation of frequency adaptive PR controller

The test is shown in Figures 8-9. It can be seen from Figure 8 that using a frequency-adaptive PR controller, the output voltage waveform of the power electronics power supply can keep THD low.

The output voltage quality of the power electronics power supply can be guaranteed. The output voltage of the combined power supply is shown in Figure 9. At this time, the output voltage remains stable and there is no problem of low-frequency fluctuations. It can be used as a transformer to verify the power supply.

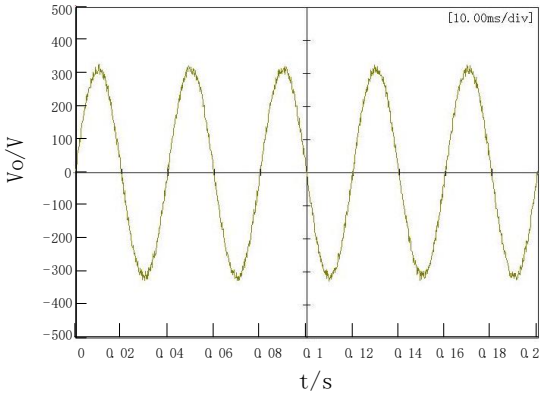

Figure 8: Output voltage of electronic power with variable freqency PRcontroller

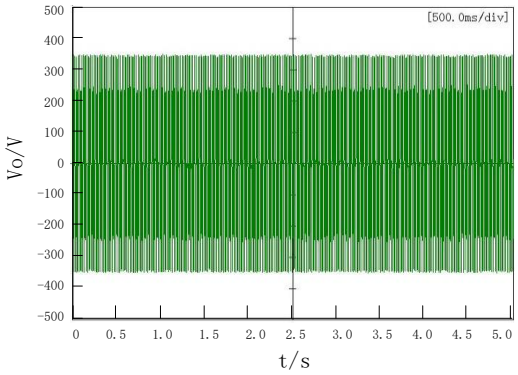

Figure 9: Output voltage of combined power with variable freqency PR controller (long time observation)

6 CONCLUSION

For the ultra high pressure GIS current transformer calibration system, the output in the wide range of 5%~110% is required to maintain high accuracy. This paper adopts a combined power supply structure in which a power electronic power supply and an electrical power supply are connected in series, in order to make the power electronic power supply. The electrical power supply maintains the series synchronous operation and proposes a frequency adaptive proportional resonant controller.

In this paper, the structure of the combined power supply is introduced firstly. The power electronics power supply is modeled and the control system is analyzed. The design method of the frequency adaptive PR controller is given.

Finally, experiments were carried out in the combined power supply proof machine 200kVA. The experimental results show that the frequency-adaptive PR controller can make the power electronic power supply output high-precision voltage waveform and keep the frequency and phase synchronisation with the electrical power supply. The combined power supply output voltage is stable and reliable, THD <3%, can be used as ultra-high pressure GIS Current transformers verify power usage.

7 REFERENCES

Prodanovic M, Green T C, Mansir H, 2000. A survey of control methods for three-phase inverters in parallel connection[Z].472-477.

Ahmed K H, Massoud A M, Finney S J, et al, 2011. A Modified Stationary Reference Frame-Based Predictive Current Control With Zero Steady-State Error for LCL Coupled Inverter-Based Distributed Generation Systems[J]. Industrial Electronics, IEEE Transactions on. 58(4): 1359-1370.

Zhang J, Zhao C, Jing H B, 2013.Simulation study of proportional resonant controller in MMC-HVDC control [J].Proceedings of the Chinese Academy of electrical engineering. 33 (21): 53-62.

Karimi H, Karimi-Ghartemani M, Iravani M R, 2004. Estimation of frequency and its rate of change for applications in power systems[J].Power Delivery, IEEE Transactions on. 19(2): 472-480.

142: Towards a new paradigm for biodiesel production

A proposal from an energy policy and technical perspectives

Gabriel MURILLO[1], Jianzhong Sun[2]

[1] School of Environmental Science and Safety Engineering, Jiangsu University, Zhenjiang, 212013, P. R. China, murillom.gabriel@gmail.com
2 School of Environmental Science and Safety Engineering, Jiangsu University, Zhenjiang, 212013, P. R. China, jzsun1002@hotmail.com

Biodiesel, as source of bio-energy, has the potential to decrease most of the actual greenhouse gas emissions in the transportation sector, creating the conditions for a more global sustainable development. Nevertheless, in the past decades has been the subject of many debates. Its massive world production has been hindered by the lack of sustainable raw materials, as well as the effect of cheap petroleum prices. The actual context compels to find ways to assure its economical, technical and environmental feasibility. The aim of this paper is to propose a new paradigm for biodiesel production and use, to be seen as a strategic and decentralised source of bio energy. Our proposal focuses on 3 main pillars, at using biodiesel as energy back up in case of natural catastrophes and eventual geopolitical conflicts that could give certain level of autonomy to many regions of the world; to massively apply the concept of lipid waste management for biodiesel production and to substitute first-generation lipid sources used to produce biodiesel by waste lipids. Specific tasks should be implemented along short, middle and long-term, which cover the implementation of energy policies, a breakthrough approach in the design of bio-oil harvesting systems from microalgae, and alternative uses of biodiesel as a chemical platform to be used in other sectors of transport, such as maritime shipping and aviation. Different possible scenarios are shown to analyse the challenges and opportunities of biodiesel in the short-term. The future of biodiesel production and use is still not clear because of the complex factors that affect this industry. Our proposals could be useful guides for energy policy makers and researchers to use this source of biofuel in a more feasible and sustainable way.

Keywords: biodiesel, energy backup, feasibility, sustainability, new paradigm.

1. INTRODUCTION

Biodiesel, as an alternative fuel source, is mainly produced from vegetable or animal fats; at commercial scale is mainly produced by the mixture of an alcohol of short chain (methanol or ethanol), a lipid source (vegetal or animal) and a catalyst (typically homogeneous, alkaline, acid catalyst, or a combination of both in a multi-step process). Its main chemical reaction mechanisms are esterification and trans esterification. Depending on the lipid source, and according to the reaction mechanism, the main by-products of biodiesel production could be water or glycerol, respectively.

Some of the main reasons why biodiesel is seen as an attractive and potential source of bioenergy is because can be used in modern cars fed with petroleum diesel, moreover, if produced in a sustainable way can generate a dramatic reduction of pollutants derived from the emissions from the combustion of petroleum diesel, such as CO_2, particulate matter, sulphuric compounds, etc. Biodiesel is less toxic than petroleum-diesel and can be easier to manage in case of spillage.

Some of its advantages are its high cost compared to petroleum diesel depending on the lipid source, is not feasible to use in regions with winter season due to its unfavourable cold filter plugging point and cloud point and the amounts of renewable sources to produce biodiesel are very limited in comparison to the world's demand.

In recent years, the drop of world petroleum prices has produced a strong impact in the industrial and academic sectors, when 10 years ago were stimulated by the high prices of this fossil fuel (see Figure 1). As a response, several countries have established measures to keep the biodiesel industry alive, through the application of incentives and mandates. However, its future does not look certain due to the complexity of factors that are playing a role around this topic.

The objectives of this paper are to discuss the most important factors (positive as negative) where biodiesel has been affected, and to develop key proposals, ranging from technical to also include energy policies, in the short, middle and long-term for biodiesel, as an attempt to create a new paradigm in the production and use of this source of biofuel to assure its feasibility and sustainability.

2. METHODOLOGY

This paper has been written based on a literature review, from scientific publications, reports, and news from specialised magazines related to biodiesel industry or from the sectors related to the key influential topics. The proposals were based on the information obtained by the literature review and from our opinions.

3. RESULTS AND DISCUSSION

3.1. World petroleum prices and production

The elaboration of forecasts to predict petroleum prices is complicated because of its variability that not only depends on market forces, but also on political and geopolitical factors. During the second half of the decade of 2000´s till the first years of the decade of the 2010´s, petroleum prices kept high enough to promote biodiesel production, stimulating numerous researches and generating profitability in the biofuel's industry. Nevertheless, since 2014 its prices collapsed, reaching prices of less than US$ 40 per barrel in 2016 (IEA, 2018, p.1). From Figure 1 can be noted in red dotted line the cost of biodiesel that, without incentives or subsidies, ranges – in average – approximately from US$ 105-115. (Lane, J. 2017, p.1).

Regarding to petroleum production, the scenario is also complex, since the global production of conventional petroleum reached its peak in the year 2011 (Berman, A., 2015, p.1) and the demand keeps rising, reaching almost 100 million barrels per day (OECD/IEA, 2016, p.2). The main factor that has kept a stable supply is the recent development of non-conventional petroleum, called tight light oil (TLO), led by the United States, with recoverable reserves in the order of 78 billion barrels (IEA, 2015, p.1). The technique to extract non-conventional petroleum extracted by some American companies is commonly called *fracking*. Nonetheless, this technology has not demonstrated to be cheap and also has arisen environmental concerns, especially related to the pollution of aquifers and induced seismicity (Erbach, G. 2014, pp.16-19). The main uncertainty in the expansion of this non-conventional source of petroleum in the future is the implementation of the technology in other countries, as the method of extraction utilises directed drilling its use in many countries could be limited. Figure 2 shows the amount of reserves in billions of barrels. While petroleum prices keep below the threshold of the production cost of biodiesel, incentives to promote its use will be necessary.

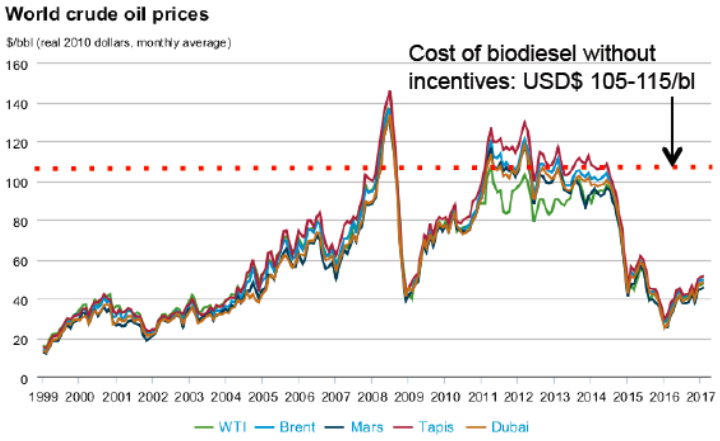

Figure 1: World petroleum prices from 1999 to 2017. Edited from (IEA, 2018, p.1; Lane, J, 2017, p.1).

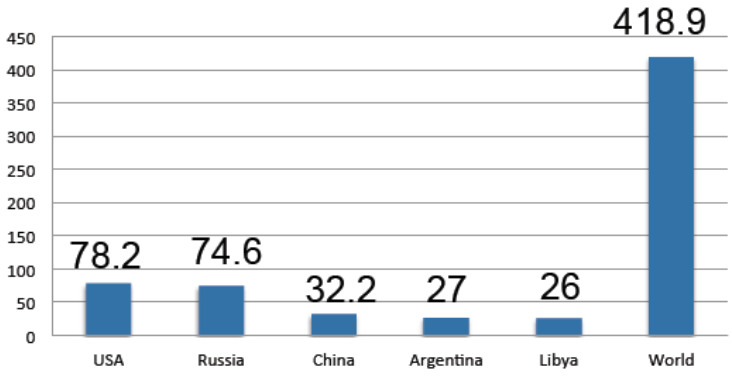

Figure 2: Technically recoverable tight light oil in billions of barrels. Own elaboration from (EIA, 2015, p.1).

3.2. Availability of raw materials

The main constraint for a massive biodiesel production is the availability of raw materials, especially lipid sources. The actual global biodiesel production is estimated in 36.6 billion litres; the main producers are the United States (US), Brazil, Germany, Argentina and Indonesia with 16%, 11%, 9%, 9% and 7%, respectively (REN21, 2018, pp.56-58); however the majority is produced from edible oils, such as soybean, palm, rapeseed, etc. (Araújo, K., Mahajan, D., Kerr, R and da Silva, M., p.3). The limitation of lipid sources relies especially in the yield of lipids per unit of cultivated area. (Gui, M. M., Lee, K. T. and Bhatia, S., 2008, p.1647) reported low yields of the main crops involved in biodiesel production, especially soybean oil and rapeseed (375 and 1,000 kg.ha-1, respectively), the main lipid sources of US, Brazil and the European Union (EU), that in total account for approximately 70% of world´s biodiesel production, respectively. In contrast, palm oil shows an oil yield of 5,000 kg.ha-1, a base line for a more feasible biodiesel production. The main reason why in the US and the EU is mostly used rapeseed and soybean oil is because the molecular structure of biodiesel produced from these kind of lipids (degree of saturated acyl glycerides) allow them to perform better on cold weather conditions, adding a technical complexity in the requirements of the most ideal lipid sources.

Nowadays, the cheapest available lipid source to produce biodiesel is the so-called waste vegetable oil (WVO). Compared to non-used edible oils, WVO usually has higher viscosities and gums and is produced at relative high temperatures and exposed to water. WVO also has high concentration of free fatty acids (FFA), which under the use of conventional catalysts produces high amounts of soap. As a conventional alternative, biodiesel should undergo esterification reactions, and then trans esterification, at using acid and alkali catalysts, stepwise, generating water and glycerol as by-products, respectively. An alternative for these cases is under research and consists in the use of enzymes to catalyse FFA´s to produce biodiesel (Murillo, G., Ali, S. S., Yan, Y-J., Sun, J. Z., et al, 2018, pp. 448-456; Lam, M., Lee, K. T. and Rahman M. A., 2010, pp. 513-514). It is estimated that the worldwide production of WVO is of approximately 29 million tons (Pukakle, D. D., Maddikeri, G. L., Gogate, P. R., Pandit, A. B. and Pratap, A. P., 2015, p.279). Most of those cheap lipid sources have not being valorised, therefore it represents a valuable substrate to be used for biodiesel, if properly pre-treated and converted, with the appropriate catalysts.

Since the decade of the 1970s, the US has invested important economical resources to determine the potential use of lipids coming from microalgae. Since then, many research centres around the world have tried to find suitable

strains, reaction conditions (mostly in open-pond and closed photo bioreactors), substrates, etc., with the aim to achieving a feasible production. In theory, some microalgae species have the potential to produce between 12,000-98,500 L.ha-1.y-1 (Schenk, P. M., Thomas-Hall, S. R., Stephens, E., Marx, U. C., et al., 2008, p. 24).

However, it has not been demonstrated its economical viability, since the average production cost of biodiesel from microalgae oil is near US$ 77-109 per gallon (Richardson, J. W., Johnson, M. D., Zhang, X., Zemke, P., et al., 2014, p.96). The main limitation to make oil from microalgae economically feasible relies in the dewatering step during algal biomass extraction from the aqueous media before oil extraction, because of the high amounts of energy required in this operation (Uduman, N., Qi, Y., Danquah, M. K., Forde, G. M. and Hoadley, A., 2010, p. 012701-1).

3.3. Electric cars

Many companies are investing important efforts and resources to make possible the massive use of electric vehicles; this could make an important contribution in the reductions of greenhouse gas emissions (GHG) (Hwang, R., 2016, p.1); from small vehicles, buses (Cooper, D., 2017, p.1) and even heavy-duty vehicles (Manthey, N., 2018, p.1). The opportunity of electric vehicles relies on their capacity to run long distances with only one charge and fed, ideally, with renewable electricity. Nevertheless, the main drawback that hinders its massive distribution to the global markets is the cost of the electric batteries. Recently, was reported the rapid fall in the cost of Li-ion batteries, the most used kind in electric vehicles (Nykvist, B. and Måns, N., 2015, p.330). However, efforts are still necessary in the fields of material engineering, electro chemistry and other areas to drop the cost from the actual range of approximately US$150-200 to below US$ 100, where the possibility to make popular the electric cars could be real, consequently getting big chances to substitute millions of vehicles that actually are running on internal combustion engines, and achieving important reductions in GHG (Randall, T., 2016, p.1).

3.4. Energy policies

Biodiesel has been promoted through the implementation of especial mechanisms, such as tax exemption, reduction of fossil fuels subsidies, and production targets. One of the most effective measures that has kept alive the biodiesel industry in recent times is the implementation of targets, such as biodiesel mandates. Some examples of biodiesel mandates are summarised in Table 1, taken from (Ren21, 2018, pp. 56-58). In coming years, is expected that many countries will ban the selling of cars fuelled by fossil liquids, such as petroleum diesel. This measure will favour the introduction of electric vehicles more quickly.

Table 1: Summary of biofuel targets and blend mandates

Region	Biodiesel Target/Mandate
European Union	10% of transportation fuels consumed in each member state must come from renewable resources by 2020.
Brazil	Mandate for B8 was increased to B10 in early 2018.
New Zealand	The maximum blend for biodiesel was increased from B5 to B7.
Colombia	Some regions increased their blends from B8 to B9.
US state of Minnesota	In May of 2018, the blend mandate was doubled to B20, being the highest blend mandate worldwide.
Slovenia	Mandated that 10% of all heavy-duty trucks must run entirely on biodiesel.

4. PROPOSALS

4.1. General view for biodiesel as a sustainable fuel in the future based on a paradigm shift perspective

In our specific case, we can understand the actual biofuels paradigm as a set of technological solutions, substrates and processes that lead to the transformation of raw materials to biofuels, under a set of policies and rules to supply the energy needs of a certain market under a reasonable price, under the condition of strong economical incentives and limited production which also limits its positive environmental effects. (Xu, J. and Li, M., 2017, p.49) indicated: “Thomas Khun argued that a paradigm shift occurs because the existing paradigm no longer fits the traditional framework”. In the case of biodiesel, due to the environmental concerns, competition for primary raw materials and water, due to the changes in land use that have occurred in some regions of the world to expand biodiesel production (Jungbluth, N., unpublished, pp. 14-15; Union of Concerned Scientists, 2008, p.1), the need for a paradigm shift became obvious and urgent.

In the context of the construction of a new paradigm, we propose biodiesel as a source of energy back up, this vision is critically important in countries without exploitation of fossil fuels. This energy back up could be essential in cases of natural disasters, and in case of force majeure, such as geopolitical events, where regional or global petroleum supply could be interrupted for some days or weeks, basic biodiesel supply could be vital to repair essential infrastructure, for transportation of food and water to the regions that could be affected.

Biodiesel could be used as a measure for lipid waste management, substituting in a gradual way first-generation biodiesel production. The paradigm shift also includes the idea of not using biodiesel to try to substitute worldwide petroleum diesel production, unless if important breakthroughs on research and industrial development will be achieved in the field of oil extraction from microalgae in terms of efficiency, sustainability and costs.

4.2. Case scenario analyses

In coming paragraphs are shown case scenarios for biodiesel production in the short-term (2018-2015). Some assumptions were made: energy policies will continue to be implemented, and improved, and the industrial capacity of biodiesel production will not be affected by other factors not included in this paper.

Case 1: petroleum prices will remain as usual, and electric car production will start to become massive. Petroleum demand will start to shrink, keeping the prices low, which will be a disadvantage for biodiesel. In order to avoid a competition, biodiesel supply must start focusing on alternative markets, leaving car fleet for electric cars. Favourable energy policies will be necessary to be kept to maintain the biodiesel industry alive, while a new way to produce high and cheap yields of microalgae bio oil must be achieved in coming years.

Case 2: petroleum prices rise and electric car production will start to become massive in the short-term. Assuming that the peak in the supply of conventional petroleum will have a higher impact than the expected, and the supply of TLO will not suffice, markets will continue to demand biodiesel. In the short-term, biodiesel and electric vehicles will satisfy the eventual increasing energy demand, being a good opportunity for both industries.

Case 3: Cost of Li-ion batteries will not reach the threshold of US$ 100/kWh. If petroleum prices rise during this period, biodiesel production will face the critical bottleneck of insufficient amount of lipids to supply its increasing demand, and the objectives to reduce GHG emissions from transportation sector will become seriously limited.

4.3. Measures to promote biodiesel production in the context of the construction of a new paradigm

Short-term measures (2018-2025)

The main measures during the first period include to continue to promote favourable energy policies, such as tax waivers, blend mandates, and the progressive ban in the use of petroleum diesel cars. Municipalities of the main cities of the world should develop strategic policies to incentivise/mandate the efficient collection of WVO, and to promote the job creation with the construction of facilities to convert the lipid wastes to biodiesel. Efforts should focus in places where food waste generation is high. Municipalities must collect WVO without any additional cost than collection; tax incentives to the suppliers of WVO can be created, such as discounts in taxes, patents, etc. Lipid waste collection should be carefully planned at district level. We propose as a standard method, an analogue technology utilised for coffee filtering in some kinds of coffee makers (Maquinas De Cafe.com, 2017, p.1) (see Figure 3). We propose at least 3 filters set in series, the first one with pore size of 25 µm, a second filter of 5 µm, and a third filter of 1 µm, respectively.

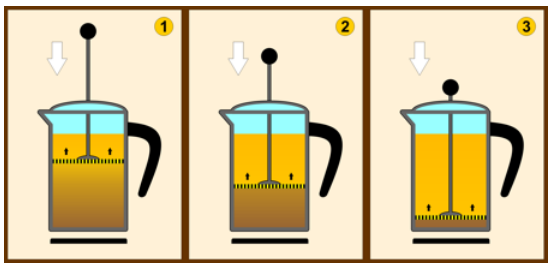

Figure 3: General proposal for a standard method to filter waste vegetable oil. Edited from (Maquinas De Cafe.com, 2017, p.1).

Policy makers should address the use of actual biodiesel production, focusing its use in heavy machinery, related to construction, agriculture and similar activities. Furthermore, biodiesel production can start to be used in rail transport, in small blends (B5) (UIC, unpublished, pp. 52-54), and through R&D, blends can increase along the time to reach B30 and B50 in the middle term. During this term, strong R&D need to start in the maritime shipping sector

in order to overcome the actual obstacles of the implementation of biodiesel (long-term storage stability, treatment in marine environment, supply guarantee, and reliability) (IEA Bioenergy, 2017, pp.71-72).

Furthermore, we suggest alternative design methods for bio oil production from microalgae. In Figure 4 we propose a general scheme for bio-oil extraction from microalgae, which bypasses the step of biomass dewatering; this means that bio-oil could be released before microalgae will be collected in higher concentrations, through this way the lipids can be separated with advanced hydrophobic membranes. Technologies such as hydrodynamic cavitation, ultrasound, and others, can be taken into account. This conceptual proposal requires a thorough and rigorous evaluation before validation.

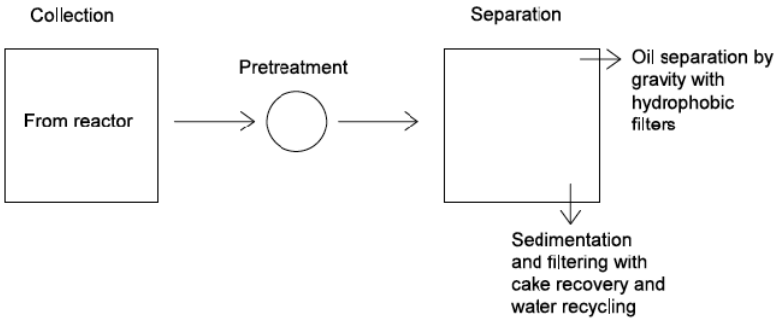

Figure 4: Alternative design step for microalgae bio oil extraction.

Middle term measures (2026-2040)

In this period it is expected that favourable energy policies had achieved the consolidation of the expansion in the production of biodiesel of second generation. Biodiesel might be used progressively in rail transport (B5-B20) in the main cities around the world. It is expected a progress in initial uses of biodiesel in the maritime sector. During this span it is expected a paradigm shifting scheme in the production of microalgae bio-oil. Efforts to integrate economical and technical feasibility could be made. An integrated view in the research of biodiesel as a chemical platform for aviation biofuels could be developed. The efforts could focus to use the high quality fractions for aviation – to produce hydro treated esters and fatty acids –, and part of the by-products used in blends with bunker or similar fuels (IEA Bioenergy, 2017, pp. 71-72).

Long-term measures (2041-2060)

We expect in this period a consolidation in the use of the use of biodiesel for rail transport, with blends higher than B20. If the limitations of bio oil from microalgae are overcome, significant achievements in its use in the maritime and aviation transport sectors are expected. Glycerol valorisation will play an important role at adding economical value to biodiesel. Its molecular structure propitiates to use it as a chemical platform for the production of alcohols, that could be used for the production of biodiesel, biopolymers, substrates for food and pharmaceutical industries and other areas of interest (Fan, X., Burton, R. and Zhou, Y., 2010, pp.17-22; Sathianachiyar and S., Devaraj, A., 2013, pp.1-4).

Figure 5 summarises the main concepts previously discussed. In the case of electric vehicles, some statements – highlighted with the symbol (*) – were based from (Randall, T., 2016, p.1). The red arrows mean the direction of energy flows, or displacement of fuel sources.

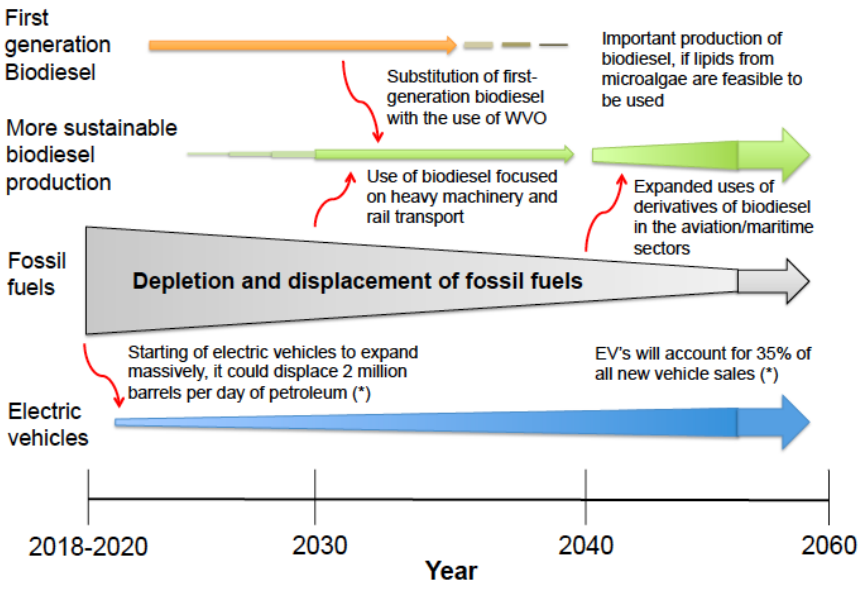

Figure 5: Non-competitive development between biodiesel and electric vehicle industries.

5. CONCLUSIONS

In this paper we proposed three basic pillars for the construction of a new paradigm for biodiesel: to plan the production of this source of biofuel as a measure for lipid waste management, to gradually substitute first-generation biodiesel produced from edible lipids, and to use biodiesel as a strategic energy back up, especially in countries where fossil fuels are not extracted.

In the short-term, the best opportunity will be to systematically collect, treat and produce biodiesel from waste vegetable oil with the support of local governments. In parallel, biodiesel could be redirected to satisfy the demand in the use of construction and agricultural equipment. In the middle and long-terms, It is expected a breakthrough in the production of bio-oil from microalgae, that would facilitate the conditions to create a strong chemical platform for the development of advanced biofuels in the aviation and maritime shipping sectors where a decrease in its GHG emissions is necessary.

May this paper serve as a base for deeper discussions to find consensus among different groups to create the conditions for the construction of a new paradigm for biodiesel production and use.

6. REFERENCES

Aráujo, K., Mahajan, D., Kerr, R. and da Silva, M. (2017) Global Biofuels at the Crossroads: an Overview of Technical, Policy, and Investment Complexities in the Sustainability of Biofuel Development. Agriculture 7,32: pp. 1-22.

Berman, A. (2015) The crude oil export ban--What me worry about peak oil? [online]. Forbes. Available at: https://www.forbes.com/sites/arthurberman/2015/12/27/the-crude-oil-export-ban-what-me-worry-about-peak-oil/#12f1deb31875 (Accessed 13 July 2018).

Cooper, D. (2017) China's Shenzhen city electrifies all 16,359 of its public buses [online]. Engadget. Available at: https://www.engadget.com/2017/12/29/china-shenzhen-public-electric-buses/ (Accessed 14 July 2018).

Erbach, G. (2014) Unconventional gas and oil in North America. The impact of shale gas and tight light oil on the US and Canadian economies and on global energy flows. Report for the European Parliament. European Union.

Fan, X., Burton, R. and Zhou, Y. (2010) Glycerol (By product of Biodiesel Production) as a Source for Fuels and Chemicals – Mini Review. The Open Fuels & Energy Science Journal 3: pp. 17-22.

Gui, M. M., Lee, K. T., Bhatia, S. (2008) Feasibility of edible oil vs. non-edible oil vs. waste edible oil as biodiesel feedstock. Energy 33: pp. 1646-1653.

International Energy Agency Bioenergy (2017) Biofuels for the marine shipping sector [online]. Available at: http://task39.sites.olt.ubc.ca/files/2013/05/Marine-biofuel-report-final-Oct-2017.pdf (Accessed 14 July 2018).

International Union of Railways (UIC) and the Association of Train Operating Companies of the United Kingdom (ATOC) (2007). Railways and Biofuel. First Report. Unpublished.

Jungbluth, N. (unpublished) Life Cycle Analysis and Sustainability aspects of biodiesel. 2nd International Congress on Biodiesel, AOCS, 17 November 2009. Munich.

Lam, M. K , Lee, K. T., Rahman M. A. (2010) Homogeneous, heterogeneous and enzymatic catalysis for transesterification of high free fatty acid oil (waste cooking oil) to biodiesel: a review. Biotechnology Advances 28: pp. 500-518.

Lane, J. (2017) Ethanol and biodiesel: dropping below the production cost of fossil fuels? [online]. Biofuels Digest. Available at: http://www.biofuelsdigest.com/bdigest/2017/05/18/ethanol-and-biodiesel-dropping-below-the-production-cost-of-fossil-fuels/ (Accessed 24 June 2018).

Manthey, N. (2018) Shenzhen: BYD lands large order for electric dump trucks [online]. Electrive.com. Available at: https://www.electrive.com/2018/05/15/shenzhen-byd-lands-large-order-for-electric-dump-trucks/ (Accessed 14 July 2018).

Maquinas de Cafe (2017) Cafetera Francesa [online]. Available at: http://www.maquinasdecafe.com/cafeteras/cafetera-francesa/ (Accessed 14 July 2018).

Murillo, G., Ali, S. S., Yan, Y-J., Sun, J. Z., et al., (2018) Evaluation of the kinematic viscosity in biodiesel production with waste vegetable oil, ultrasonic irradiation and enzymatic catalyst: a comparative study in two reactors. Fuel 227: pp. 448-456.

Nykvist, B. and Nilson, M. (2015) Rapidly falling costs of battery packs for electric vehicles. Nature Climate Change 5 (4): pp. 329-332.

OECD/IEA (2016) Medium-term oil market report 2016 [online]. Available at: https://iea.org/Textbase/npsum/MTOMR2016sum.pdf (Accessed 13 July 2018).

Pukale, D. D., Maddikeri, G. L., Gogate, P. R., Pandit A. B., et al (2015) Ultrasound assisted transesterification of waste cooking oil using heterogeneous solid catalyst. Ultrason Sonochem 22: pp. 278-286.

Randall, T. (2016) Here's how electric cars will cause the next oil crisis. [online]. Bloomberg. Available at: https://www.bloomberg.com/features/2016-ev-oil-crisis/ (Accessed 14 July 2018).

Ren21 (2018) Renewables 2018. Global Status Report [online]. Available at: http://www.ren21.net/gsr-2018-launched (Accessed 22 June 2018).

Retrieved on June 24, 2018. Hwang, R. (2016) Future of electric vehicles is bright [online]. NRDC. Available at: https://www.nrdc.org/experts/roland-hwang/future-electric-vehicles-bright (Accessed 24 June 2018).

Richardson, J. W., Johnson, M. D., Zhang, X., Zemke, P. et al (2014) A financial assessment of two alternative cultivation systems and their contributions to algae biofuel economic viability. Algae Research 4: pp. 96-104.

Sathianachiyar, S. and Devaraj, A. (2013) Biopolymer production by bacterial species using glycerol, a byproduct of biodiesel. International Journal of Scientific and Research Publications. 3(8): pp.1-5.

Schenk, P. M., Thomas-Hall, S. R., Stephens, E., Marx, U. C., et al., (2008) Second generation biofuels: high-efficiency microalgae for biodiesel production. Bioenerg Res 1: pp. 20-43.

Uduman, N., Qi, Y., Danquah, M. K., Forde, G. M. and Hoadley, A. (2010) Dewatering of microalgal cultures: a major bottleneck to algae-based fuels. Journal of Renewable and Sustainable Energy 2, 012701

Union of Concerned Scientists. (2008) Land-use changes and biofuels. The changing landscape of low-carbon fuel risks and rewards. Factsheet.

US Energy Information Administration (2015) World shale resource assessments [online]. Available at: https://www.eia.gov/analysis/studies/worldshalegas/ (Accessed 22 June 2018).

US Energy Information Administration (2018) What drives crude oil prices? [online]. Available at: www.eia.gov/finance/markets/crudeoil/spot_prices.php (Accessed 23 June 2018).

Xu, J. and Li, M. (2017) Innovative technological paradigm-based approach towards biodiesel feedstock. Energy Conversion and Management 141: 48-62.

143: Indigenous solar desalination technologies for sustainable potable water supply

K S REDDY[1], H SHARON[2]

[1] Professor, Heat Transfer and Thermal Power Laboratory, Dept. Of Mechanical Engineering, Indian Institute of Technology Madras, Chennai – 600 036, ksreddy@iitm.ac.in
[2] Research Scholar, Heat Transfer and Thermal Power Laboratory, Dept. Of Mechanical Engineering, Indian Institute of Technology Madras, Chennai – 600 036

Water plays an important role in mankind's day to day life activities and most of the regions of the globe are under severe water scarcity. In India, several regions are under severe water stress and deaths are reported every year due to unsafe water consumption. Desalination of sea water is an effective option to satisfy the fresh water demands. Desalination industry is widely expanding in India and its market value wound be around USD1.9 billion in 2019. The desalination is an energy intensive process and it requires at least a ton of oil to produce 20 tons of fresh water. For every one ton of fresh water produced nearly 25.0 kg of CO_2 is emitted to the atmosphere. Solar energy can be used to power desalination technology there by cut off in carbon emission can be achieved. India receives nearly 3.5 to 6.0 kWh/m^2-d of solar radiation which paves the way for setting up solar thermal or PV based desalination units. Solar stills have been widely used to meet the fresh water demands. Solar stills are a sustainable option for remote and rural locations were access to electricity and fresh water is minimal. Cascaded vertical double slope still and Active multi effect evacuated vertical solar still can produce fresh water of around 20 kg/d from saline water of 5.0 wt% salinity which is fairly sufficient for a family of 4 to 5 members. The units can mitigate at least 80 tons of CO_2 emission during their life time of 20 yrs. Cost of distilled water is around 33.0 USD/kL for 12% interest rate and it can be reduced to 19.0 USD/kL for 5% interest rate. The production cost and environmental benefits of these solar desalination units are highly competitive and viable in rural areas.

Keywords: solar desalination; potable water; enviro-economic analyses; emission mitigation

1. INTRODUCTION

Industrialisation, motorisation, and enhanced life standards of mankind has increased fresh water demand. Naturally available fresh water reserves are not capable of meeting these rising demands because of their less availability and manmade pollution (Gude et al., 2010). India holds nearly 16.0% of world's total population and has only 4.0% of global renewable water. Nearly, 54.0% of Indian states are under high to extremely high water stress. Water supply in urban India is much lower than any other developing countries in the globe. Piped water supply for nearly 10-15 h/d in 1980 has fallen to 1.5 h/d in 2006 (Tortajada, 2016).

The current situation of water scarcity can be tackled only if mankind finds some alternate ways to produce fresh water from available saline water and polluted wastewater. Luckily, desalination technology developed long back resembling natural hydrological cycle has the capability to tackle this problem. Desalination is the process of separating salts and minerals from saline water (Reif and Alhalabi, 2015) and this process can also be utilised for treating wastewater (Rebhun, 2004). Thermal desalination process produces high quality distillate but the process is energy intensive and it emits green house gases (Kalogirou, 2005). Membrane process cannot tolerate high salinity and heavy metal concentration of feed water. Brine discharged from both these large scale units has caused severe impacts on marine aquatic life and inland ground water quality (Roberts et al., 2010).

India has 250-300 clear days and 2300-3200 sunshine hours/year. Nearly, 80% of India receives annual cumulative solar radiation above 1700 kWh/m^2 (Kapoor et al., 2014). Hence, solar thermal energy can be effectively utilised to desalt saline in a sustainable way. Compact solar thermal distillation systems are nearly maintenance free and are highly suitable for meeting the daily drinking water requirements of communities in arid, remote, and rural water deficient regions. In case of compact solar distillation systems, reject brine recycling, concentrating and mineral recovery is highly feasible, which can lead to reduced or no brine disposal. However, the main drawback of compact or small-scale solar distillation systems is their lower distillate productivity (2.0-3.0 L/m^2-d).

The objective of the present work is to compare the performance, environmental benefits and economics of novel compact high yield solar distillation system suitable for rural applications. The yield enhancement techniques adopted for these distillation units are preheating, reuse of latent heat and evacuation.

2. COMPACT SOLAR DISTILLATION UNITS

In case of rural and remote regions, solar energy based distillation systems with low maintenance and operational difficulties are highly preferred. Basin type solar stills developed based on these characters are widely studied in various aspects. Vertical solar still which has reasonable distillate productivity and less ground area occupancy has not been studied widely. High yield and compact solar distillation unit has been developed by modifying vertical solar still.

2.1. Active vertical solar still

The schematic of active vertical solar still along with its energy transfer process is shown in Figure 1. The preheating of feed water in vertical solar still is achieved by incorporating basin solar still instead of feed water storage tank. Water preheated in basin solar still kept above is allowed to flow as thin film over the blackened absorber plate of vertical solar still. Portion of feed water evaporates while flowing over the absorber plate due to high temperate attained by convection from absorber plate. Part of the preheated feed water leaves the unit as reject. The vertical distillation unit with single slope still and double slope still is termed as cascaded vertical single slope still (CVSS) and cascaded vertical double slope still (CVDS) respectively.

2.2. Active multi effect vertical solar still

The schematic of active multi effect vertical solar still along with its energy transport process is shown in Figure. 2. Heated feed water from solar collector is distributed uniformly over the evaporating surface of each effect. Vapours formed by evaporation condenses over the condensing surface there by latent heat of condensation released from the effects is utilised for evaporation in successive effects. The unit is also provided with vacuum pump for operation of the unit under reduced pressure for enhanced evaporation.

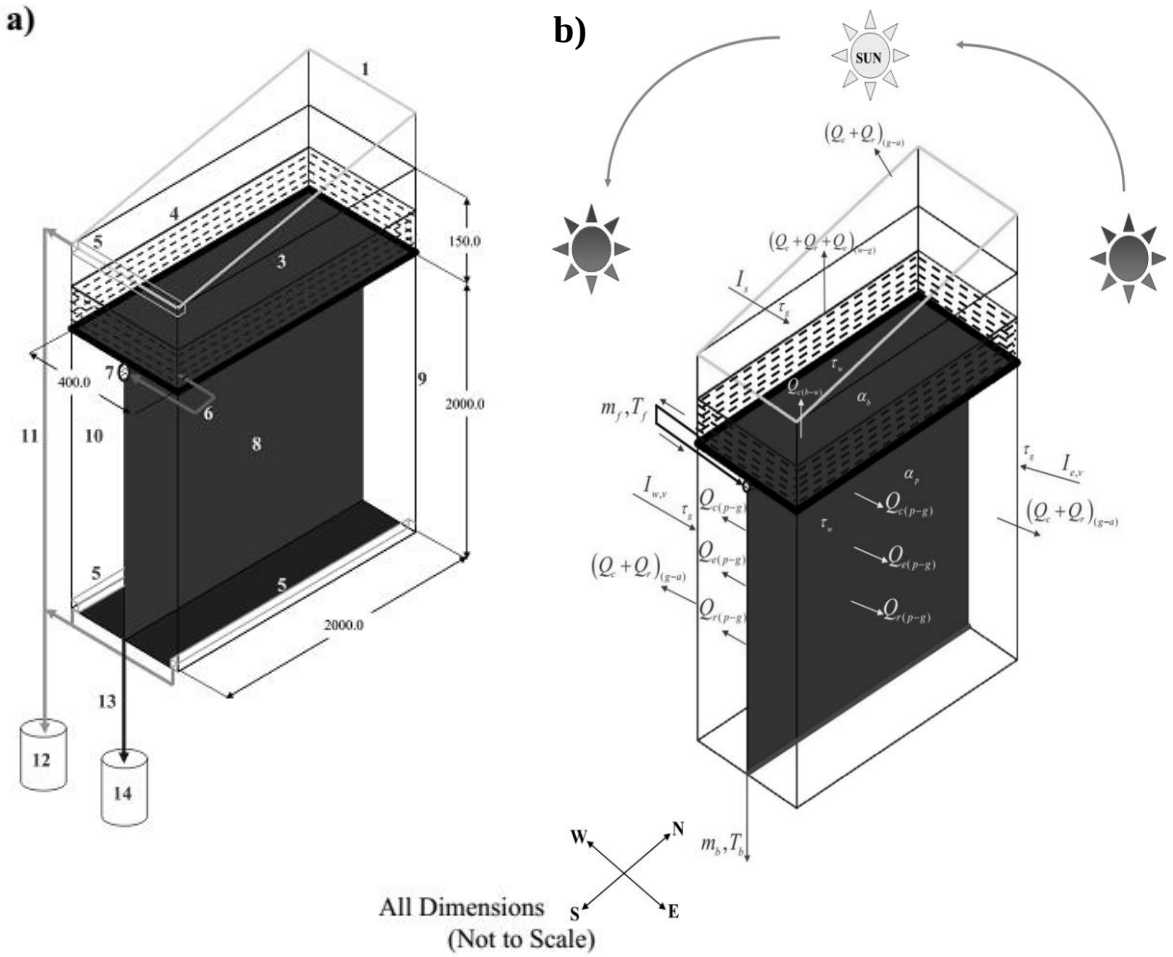

1	Glass Cover of Single Slope Still	8	Absorber Plate of Vertical Still
2	Glass Cover of Double Slope Still	9	East Glass Cover of Vertical Still
3	Absorber Plate of Basin Type Still	10	West Glass Cover of Vertical Still
4	Water Mass in Basin Type Still	11	Distillate Carrying Tube
5	Distillate Collection Trough	12	Distillate Collection Tank
6	Pipe Connecting Feed Water Tank and Feed Water Distributor	13	Brine Carrying Tube
7	Feed Water Distributor	14	Brine Collection Tank

Figure 1: a) Active vertical solar still- schematic b) Energy transport process (Sharon and Reddy, 2015)

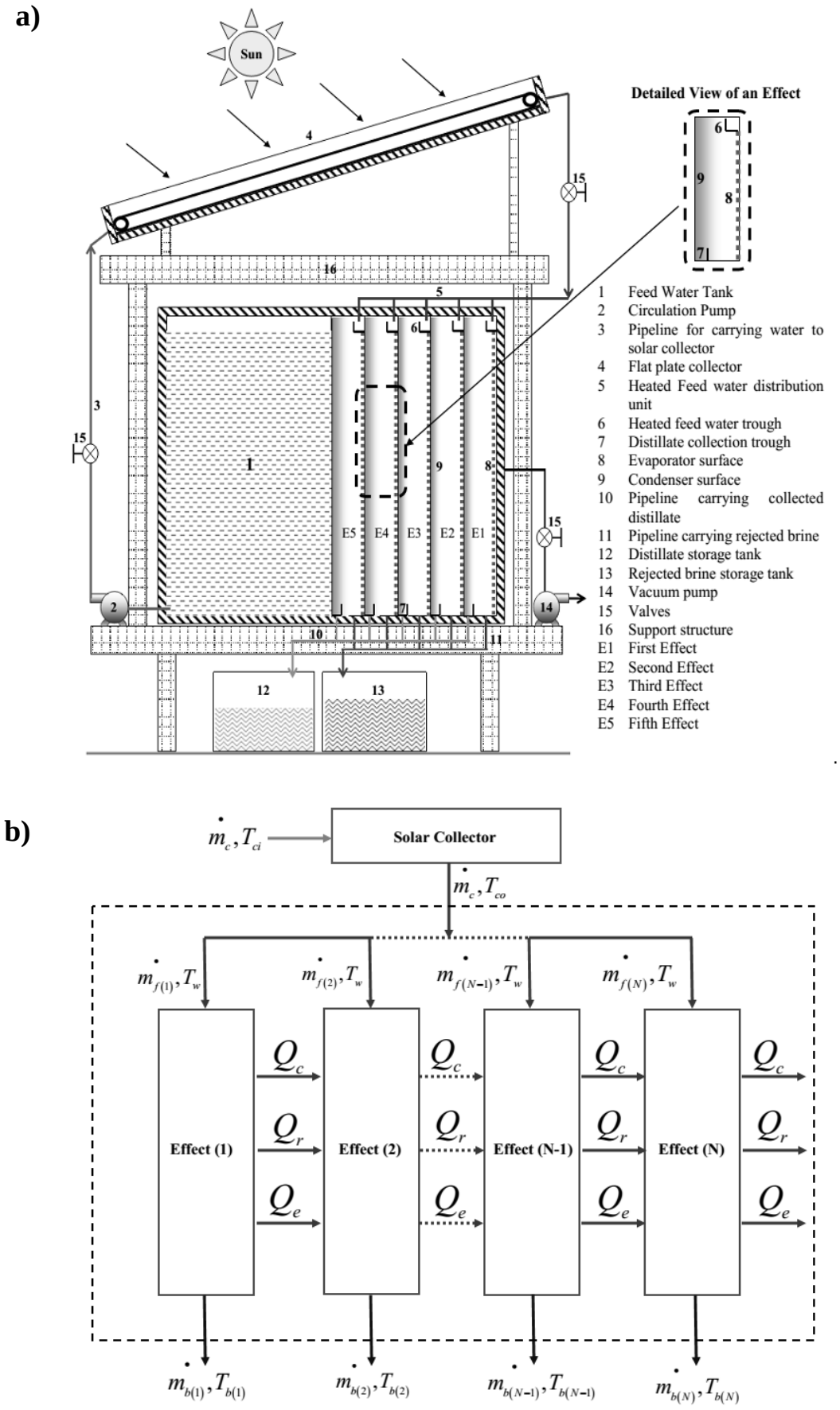

Figure 2: a) Active multiple effect vertical solar still – schematic b) Energy transport process (Reddy and Sharon, 2016)

3. PERFORMANCE AND ENVIRO-ECONOMIC ANALYSES OF COMPACT SOLAR DISTILLATION UNITS

Performance of proposed compact solar distillation units are assessed by their distillate yield, thermal efficiency, solar energy coefficient of performance and performance ratio.

Equation 1: Distillate yield of distillation unit.

$$m_d = \left(\frac{h_c P_t \frac{M_v}{R} \left[\frac{P_{T_e}}{T_e + 273} - \frac{P_{T_c}}{T_c + 273} \right]}{\left(\rho_{av} c_{av} \right) P_{LM}} Le^{-2/3} \right) A_e$$

Where:

A_e = area of evaporating surface (m^2)
m_d = distillate yield (kg/s)
M_v = molar mass of water vapour (kg/kmol)
R = universal gas constant (J/kmol-K)
h_c = convective heat transfer coefficient (W/m^2-K)
P_t= total pressure (Pa)
P_{Te}= partial pressure corresponding to evaporator temperature (Pa)
P_{Tc}= partial pressure corresponding to condenser temperature (Pa)
P_{LM}= partial pressure
T_e = evaporating surface temperature (° C)
T_c = condensing surface temperature (° C)
ρ_{av} = density of air-vapour mixture (kg/m^3)
C_{av} = specific heat capacity of air-vapour mixture (J/kg-K)
Le = Lewis number

Equation 2: Thermal efficiency/solar energy coefficient of performance of distillation unit

$$\eta_{th}(or)SCP = \frac{m_d h_{fg}}{\left(I_{ev} + I_{wv} \right) A_e}$$

Where:

h_{fg} = latent heat of condensation (kJ/kg-K)
I_{ev} = solar radiation over east facing surface of absorber plate (W/m^2)
I_{wv} = solar radiation over west facing surface of absorber plate (W/m^2)
SCP = solar energy coefficient of performance
η_{th} = thermal efficiency (%)

Equation 3: Performance ratio of distillation unit.

$$PR = \frac{m_d h_{fg}}{Q_u}$$

Where:

PR = performance ratio
Q_u = useful heat energy supplied by solar collector (W)

Enviro-economic analyses are necessary for assessing the environmental benefits and economics of proposed compact solar distillation units. Environmental benefits are estimated in terms of energy payback time and net CO_2 emission mitigated potential. Economic feasibility is assessed by distillate production cost and finance payback period.

Equation 4: Energy payback time of distillation unit.

$$EPBT = \frac{E_{in}}{E_{out}}$$

Where:

EPBT = energy payback time (Yr)
E_{in} = embodied energy of distillation unit (kWh)
E_{out} = energy output of distillation unit (kWh)

Equation 5: Net CO_2 emission mitigated by distillation unit.

$$NCM = \frac{\left(\left(E_{out} LT\right) - E_{in}\right)\left(CO_2\right)_{EF}}{1000}$$

Where:

NCM = net CO_2 emission mitigated by distillation unit (tons)
LT = life time (Yr)
$(CO_2)_{EF}$ = carbon-dioxide emission factor (1.58 kg of CO_2 for 1 kWh of electricity generated from Indian coal power plants)

Equation 6: Distillate production cost of distillation unit.

$$CPL = \frac{TAC}{M_Y}$$

Where:

CPL = distillate production cost per litre (Rs./L)
M_Y = annual distillate production (L)
TAC = total annualised cost (Rs.)

Equation 7: Distillate production per USD invested on distillation unit.

$$PPD = \frac{1}{CPL}$$

Where:

PPD = distillate production per USD invested (L/USD)

Equation 8: Finance payback period of distillation unit.

$$FPBP = \frac{\ln\left(\frac{M_Y S_p}{\left(M_Y S_p\right) - \left(\left(CC\right)\left(IR\right)\right)}\right)}{\ln\left(1 + IR\right)}$$

Where:

CC = capital cost (Rs.)
FPBP = finance payback period (Yr)
IR = interest rate
S_p = selling price (Rs./L)

3.1. Performance of compact solar distillation units

The performance of proposed compact solar distillation units are simulated under the climatic conditions of Chennai (13.08° N, 80.27°E), Tamil Nadu, India. The different geometrical parameters of the distillation unit are optimised by parametric study. The optimised system is studied for its effectiveness in desalting feed water of salinity varying from 0 wt% to 10 wt%. The optimum system parameters for active vertical solar still are given below:

Optimum absorber area is 4.0 m^2

Optimum gap between evaporating and condensing surface is 0.2 m

Maximum yield is observed under maximum breadth condition for fixed absorber area

Incorporation of preheating unit enhances the yield by 22.0%

The optimum system and operating parameters for active multi effect vertical solar still estimated by parametric study are given below:

Optimum number of effects is 5

Optimum gap between evaporating and condensing surface is 0.05 m

Optimum feed water flow rate is 0.002 kg/s

Yield enhancement by 51.3% by reducing the operating pressure from 1.0 to 0.5 bar

The yearly average yield and performance parameters for active vertical solar still and active multi effect vertical solar still is shown in Table 1 and Table 2, respectively. The yield is found to drop by around 10.0% for every 5.0

wt% increase in salinity due to boiling point elevation which reduces vapour pressure at evaporating surface. Yield from CVDS unit is nearly 15.0% higher than that of CVSS. The yearly average yield of non-evacuated active multiple effect vertical still drops from 6.8 to 4.6 kg/d with increase in salinity from 0 to 10 wt%. However, the yield of evacuated unit is nearly 3 times higher than non-evacuated unit. The SCP and PR are also higher for evacuated unit compared to non-evacuated unit.

Table 1: Yearly average yield and efficiency of active vertical still under optimised condition (Sharon and Reddy, 2015)

Type of Unit	CVSS Unit		CVDS Unit	
Salinity	Yield	Thermal Efficiency	Yield	Thermal Efficiency
0.0 wt%	15.7 kg/d	50.6%	17.9 kg/d	52.2%
5.0 wt%	14.2 kg/d	45.5%	16.3 kg/d	47.4%
10.0 wt%	12.5 kg/d	40.2%	14.6 kg/d	42.3%

Table 2: Yearly average performance of active multiple effect vertical solar still (Reddy and Sharon, 2016)

Active multiple effect vertical solar still						
Non - Evacuated Unit				Evacuated Unit		
Salinity	Yield	SCP	PR	Yield	SCP	PR
0.0 wt%	6.8 kg/d	0.9	1.8	21.3 kg/d	3.0	5.6
5.0 wt%	5.6 kg/d	0.8	1.5	16.6 kg/d	2.4	4.4
10.0 wt%	4.6 kg/d	0.7	1.2	13.0 kg/d	1.9	3.5

3.2. Environmental benefits of compact solar distillation units

The embodied energy of compact solar distillation units along with their environmental benefits is tabulated in Table 3. The major components of distillation unit proposed in this study are made of stainless steel and tempered glass. Embodied energy is calculated by considering the energy density and mass of the material used for development of distillation unit. Embodied energy of evacuated unit is higher than non-evacuated active multi effect vertical solar still due to incorporation of vacuum pump.

Table 3: Embodied Energy, EPBT & NCEM Potential of Solar Distillation Units (Sharon et al., 2017)

Solar Distillation Unit	CVDS	Active multiple effect vertical solar still		Tilted solar still	
	Non-evacuated	Non -evacuated	Evacuated	With Basin	With Wick
E_{in} (kWh)	4389.8	3744.6	3800.8	1820.8	1397.2
EPBT (Yr)	1.6	4.0	1.4	2.8	2.6
NCEM (tons)	78.9	23.7	81.8	17.7	14.9

Energy payback time is the time taken to regain the energy spent on the unit. Life time of the unit is considered as 20 yr. Evacuated unit has lowest energy payback time and highest net CO_2 emission mitigation potential due to its high distillate output. Environmental benefits of proposed compact solar distillation units are very much better than passive tilted solar still.

3.3. Economics of compact solar distillation units

The summary of economic analysis of proposed solar distillation units is tabulated in Table 4. The economics of compact solar distillation unit is carried for system life time of 20 Yr, interest rate of 12% (private banks) and 5% (government banks). Distillate production cost, production per USD invested and finance payback time is superior for CVDS unit due to its combination of less initial cost and high distillate productivity. Economic viability of proposed units increases with reduction in interest rate. Multiple effect units must be operated in evacuated condition to have

low finance payback time. Even though tilted solar still has lower capital cost, its distillate production cost is higher than active CVDS and evacuated active multiple effect vertical solar still due to their high capacity.

Table 4: Summary of Results on Economic Analysis of Solar Distillation Units (S_P = 0.06 USD/L) (Sharon and Reddy, 2015; Reddy and Sharon, 2016; Sharon et al,, 2017)

Solar Distillation Unit	CVDS	Active multiple effect vertical solar still		Tilted solar still	
	Non -evacuated	Non -evacuated	Evacuated	With Basin	With Wick
Total Cost (Rs.)	51,088	51,509	59,901	20,054	18,544
CPL (Rs./L) (IR = 12%)	1.75	5.54	2.27	3.08	3.41
CPL (Rs./L) (IR = 5%)	0.99	3.16	1.29	1.76	1.94
PPD (L/USD) (IR = 12%)	37.34	11.75	28.65	21.16	19.11
PPD (L/USD) (IR = 5%)	65.47	20.61	50.13	37.10	33.51
FPBP (Yr) (IR = 12%)	3.86	> 20	5.15	8.66	10.39
FPBP (Yr) (IR = 5%)	3.27	12.97	4.17	6.18	6.97

4. SUMMARY AND CONCLUSION

The summary of major results obtained through performance and enviro-economic analyses of compact solar distillation units is tabulated in Table 5. CVDS unit has higher distillation production for lower ground area occupancy. Active multiple effect evacuated vertical solar still has higher distillate productivity/m^2 of solar radiation collected and lower energy payback time. Thermal energy requirement of active multi effect evacuated vertical solar still is nearly 7 to 10 times lower than single effect units. Solar distillation unit of higher capacity is found to have lower environmental impact, energy payback time and distillate production cost. The performance and envoi-economic results indicate the suitability of proposed distillation systems for potable water production in rural and remote coastal regions.

Table 5: Comparison of compact solar distillation units

Solar Distillation Unit		Unit 1	Unit 2	Unit 3
Average daily yield	kg/d	16.30	16.60	3.29
Average daily yield (based on solar collector area)	kg/m^2-d	3.40	16.60	2.86
Average daily yield (based on ground area occupied)	kg/m^2-d	16.30	16.60	2.44
Average useful thermal energy requirement	kJ/kg	3919.13	534.35	5629.29
Average Efficiency/PR	(%)	47.4	4.44 (PR)	33.8
Energy Payback time	Yr	1.6	1.4	2.6
Net CO_2 emission mitigated in lifetime	Tons	78.98	81.8	14.93
Harmful gas emissions mitigated /m^3 of distillate	kg of CO_2	969.0	983.3	907.6
Distillate production cost	USD/L	0.027	0.035	0.048
	Rs./L	1.76	2.28	3.41
Finance payback time	Yr	3.9	5.2	10.4
Unit 1 - CVDS; **Unit 2** - Active multiple effect vertical solar still (Evacuated); **Unit 3** – Tilted solar still (with wick)				
Life time = 20 yrs; **Clear days** = 250; **Interest rate** = 12%; **Selling price** = 0.06 USD/L; **Salinity** = 5 wt%				

5. REFERENCES

Gude, VG., Nirmalakhandan, N., Deng, S., 2010. Renewable and sustainable approaches for desalination. *Renewable and Sustainable Energy Reviews,* 14, 2641-2654.

Kalogirou, S., 2005. Seawater desalination using renewable energy sources*. Progress in Energy and Combustion Science*, 31, 242-281.

Kapoor, K., Pandey, Kk., Jain, Ak., Nandan, A., 2014, Evolution of solar energy in India: A review. *Renewable and Sustainable Energy Reviews*, 40, 475-487.

Rebhun, M., 2004. Desalination of reclaimed wastewater to prevent salinisation of soils and groundwater. *Desalination*, 160, 143-149.

Reddy, Ks., Sharon, H., 2016, Active multi-effect vertical solar still: Mathematical modeling, performance investigation and enviro-economic analyses. *Desalination*, 395, 99-120.

Reif, Jh., Alhalabi, W., 2015. Solar-thermal powered desalination: Its significant challenges and potential. *Renewable and Sustainable Energy Reviews*, 48, 152-165.

Roberts, Da., Johnston, El., Knott, NA., 2010, Impacts of desalination plant discharges on the marine environment: A critical review of published studies. *Water Research*, 44, 5117-5128.

Sharon, H., Reddy, KS., 2015, Performance investigation and enviro-economic analysis of active vertical solar distillation units. *Energy*, 84, 794-807.

Sharon, H., Reddy, Ks., Krithika, D., Philip, L., 2017, Experimental performance investigation of tilted solar still with basin and wick for distillate quality and enviro-economic aspects. *Desalination*, 410, 30-54.

Tortajada, C., 2016. Policy dimensions of development and financing of water infrastructure: The cases of China and India. *Environmental Science & Policy*, 64, 177-187.

144: Fermentative production of optically pure d-lactic acid from rice straw hydrolysate by a genetic engineered escherichia coli DX03

Jia ZHAO[1,2], Hailiang PAN[1,2], Xiao ZHAO[1,2], Wa GAO[1,2], Jinhua WANG[1,2*]

[1]Key Laboratory of Fermentation Engineering, Hubei University of Technology, Ministry of EduucationWuhan 430068 China,237722756@qq.com
[2]Hubei Key Laboratoyr of industry Microbiology, Wuhan 430068 China, jinhwang99@126.com

Lignocellulosic materials, such as rice straw, are utilised as a substrate for microbial fermentation. Rice straw was pre-treated and used for fermentative production of D-lactic acid by genetic engineered Escherichia coli DX03 (ΔfrdBC ΔldhA ΔackA ΔpflB ΔpdhR::pflBp6-acEF-lpd ΔmgsA ΔadhE ΔptsG ΔmglB) in a 7 L fementer. After acid hydrolysis, detoxification and cellulase treatment, 52.4 g of reducing sugars was generated from 100 g of rice straw. Following a 36 h fermentation, 46.7 g of D-lactic acid was produced from the hydrolysate by DX03, achieving an optical purity of 99.8%, and a yield of 89.34%. This results suggests that E.coli strain DX03 has the potentials for fermentative production of green chemicals such as D-lactic acid, using the low-cost hydrolyzed lignocellulosic materials.

Key words: Escherichia coli DX03, Rice Straw, Fermentation, D-lactic acid

1. INTRODUCTION

The globally increasing consumption of fossile fuels and its negative impacts on environments have inspired the development of renewable and sutainable bioenergy, which is regarded as one of the future economic and social developments because of its reproducibility, sustainability and cleanliness (Xie, G and L. Peng, 2014:page1). Utilisation of lignocellulose, an abundant and readily available resource, for production of biofuel and/or green chemicals, has become a current research hotspot (Lin R, 2015; Hill, J, 2007).

Production of rice, a major grain consumed in China, generates a large amount of rice straw every year. Although rice straw is rich in cellulose and hemicellulose which can be saccharified into fermentable sugars such as glucose and xylose (Teeravivattanakit, T, 2017), at present, however, rice straw is under-utilised. Most of them are directly burned or returned to the field which not only wastes resources but also pollutes our environment. Therefore, effectively using rice straw as a fermentation resource has become a research hotspot in fermentation field.

D-lactic acid is an important chiral precursor for the synthesis of many organic compounds. D-lactic acid polymer is an ideal green polymer material with a good heat resistance and other physical properties such as biodegradability (Datta R, 1995). Compared with the traditional polymer, poly D- lactic acid can be degraded into inorganic substances naturally with little pollution to the environment (Zhang Y, 2013). So it belongs to the environment-friendly material. Using lignocellulose to produce D-lactic acid on large scale has great practical potentials (Sasaki C, 2012).

In this paper, we describe fermentative production of D-lactic acid using rice straw hydrolysate as a fermentation substrate by a genetically engineered *E. coli* DX03 strain.

2. HYDROLYSIS OF RICE STRAW

2.1. Materials

Rice straw was obtained from a farmland in Jiangxia District, Wuhan P.R. China. After crushing and grinding, the rice straw powder was screened through an 80 mesh net, then dried at 60^0C to a constant weight, and stored for future use. Cellulase was purchased from Su Kehan Bioengineering Co. Ltd., and all other reagents were purchased in analytical grade.

2.2. Acid hydrolysis

The first acid hydrolysis: 100 g of rice straw powder was soaked into a 10% phosphoric acid solution with a solid:liquid ratio of 1:9, then sterilised for 90 min, followed by 20 min at 50℃. (Dai B L, 2014: page 2). After acid hydrolysis, the mixture was centrifuged to separate the liquid from solid. The solid was washed to neutral pH for second acid hydrolysis. The pH of the combined liquid was adjusted to 6.0.

The second acid hydrolysis: the solid from first acid hydrolysis was mixed with 10% phosphoric acid solution according to the solid:liquid ratio of 1:5. After mixing uniformly, the mixture was then treated for 120 min at 135℃. The subsequent treatment is the same as the first acid hydrolysis.

2.3. Cellulase treatment

The cellulase was added into straw acid hydrolysate according to 30 FPU enzyme per 10 g straw. The mixture was then enzymatically hydrolyzed for 60 h under the conditions of pH 6.0, temperature of 50℃ and agitation of 200 rpm.

2.4. Analysis of sugars

The reducing sugar was determined by 3, 5-Dinitrosalicyic acid method (Wang J, 2008). The determination of glucose and xylose was performed by HPLC (Liu X, 2008). The chromatographic conditions were: Bio-Rad HPX87H column, 4 mM H_2SO_4 as mobile phase, 0.4 mL/min flow rate, 45^0C column temperature and a parallax detector.

3. PRODUCTION OF D-LACTIC ACID IN SHAKE FLASK

3.1. Experimental materials

Escherichia coli DX03 was constructed and stored in our laboratory. The rice straw hydrolysate was prepared as above described. All other reagents were purchased in analytical grade.

3.2. Media

Luria Broth (LB) medium: 2% reducing sugar, 0.5% yeast extract, 1% peptone, 0.5% sodium chloride.

Enzyme supplemented medium: 2% reducing sugar, 0.2% yeast extract, 0.5% cellulase enzyme.

3.3. Fermentation in shaking flask

Flask fermentation was conducted for 24 h using in a 250 ml shaking flask containing 100 ml one of the two different fermentation media under the following conditions: 1% of inoculum, 50^0C, 200 rpm agitation. Each treatment had three or more replicates.

3.4. Fermentation in bioreactor

The fermentation was conducted in a 7 L Biostat A plus fermentor (Sartorius Stedim Biotech Germany) containing 1 L of rice straw hydrolysate which was pre-concentrated by rotary evaporator to obtain higher concentration of sugars. The fermentation conditions were as follows: 10% (v/v) inoculum, 37^0C, 0.1vvm air flow rate, 200 rpm agitation, and pH 6.8 by 3 M $Ca(OH)_2$. Each treatment was repeated three times. Sample was taken every 4 h for analysis of sugar consumption and lactic acid production.

3.5. Analysis

Glucose and xylose were detected by the above described HPLC methods. D- lactic acid optical purity were detected by HPLC using a chromatographic chiral column (EC 250 /4 NUCLEOSIL Chiral-1 (Germany)) with the following condition: mobile phase, 0.2 mM CuSO4; flow rate is 0.5 ml/min; column temperature, 35; and a PDA detector.

4. RESULTS AND DISCUSSION

4.1. Composition of rice straw and sugar released from its hydrolysis

Table 1: Sugar released from rice straw hydrolysis (g / 100 g rice straw)

Sugar	Reducing sugar	Glucose	Xylose
Content	52.42	24.60	19.98

The compositions of the rice straw was analyzed by procedures described by Sluiter (2011). The results indicated that the rice straw used in this study contained 34.7% of cellulose, 26.1% of hemicellulose and 16.7% of lignin. As shown in Table 1, after acid and cellulose hydrolysis, 52.42 g of total reducing sugar, 24.60 g of glucose and 19.98 g of xylose were released from 100 g of rice straw. The content of cellulose in rice straw is higher than that of hemicellulose, which limits the efficiency of saccharification (Xu N, 2012: page 1) because the crystalline cellulose is harder than hemicellulose to be hydrolyzed (AVCI A， 2013). As a result, in the first acid hydrolysis, most xylose was released with a small amount of glucose. Increasing temperature and hydrolysis time in the second acid hydrolysis released more glucose with some xylose. It is worth to mention that separation of liquid and solid after first acid hydrolysis is helpful because it prevents xylose obtained from further conversion into microbial inhibitors such as furfural and acetic acid in the second acid hydrolysis.

4.2. Selection of medium

Table 2: Results of shaking flask fermentation (g/L)

		Reducing sugar	Glucose	Xylose	D-lactic acid	L-lactic acid
LB medium	Initial	19.67	7.96	6.37	0	0.01
	After fermentation	13.35	3.51	5.31	5.47	0.01
Enzyme supplemented medium	Initial	19.75	10.76	4.61	0	0.01
	After fermentation	13.27	5.78	3.58	5.73	0.01

The data is an average of 10 replicated shaking flasks

As shown in table 2, there was no significant difference for consumption of xylose with two different medium. For glucose, however, the enzyme supplemented medium achieved higher consumption rate than that of LB medium; with a conversion rate of 86.33% and 88.43% in LB medium and enzyme supplemented medium, respectively. The optical purity of D- lactic acid were 99.64 % and 99.83%, respectively, in two types of medium. The possible reason of higher glucose conversion rate is that the carbon-nitrogen ratio is higher in the enzyme supplemented medium than in LB medium, resulting in larger metabolic flux to D- lactic acid, a higher conversion rate of sugar and higher optical purity of D-lactic acid. Therefore, enzyme supplemented medium is selected for subsequent fermentation.

4.3. Result of bioreactor fermentation

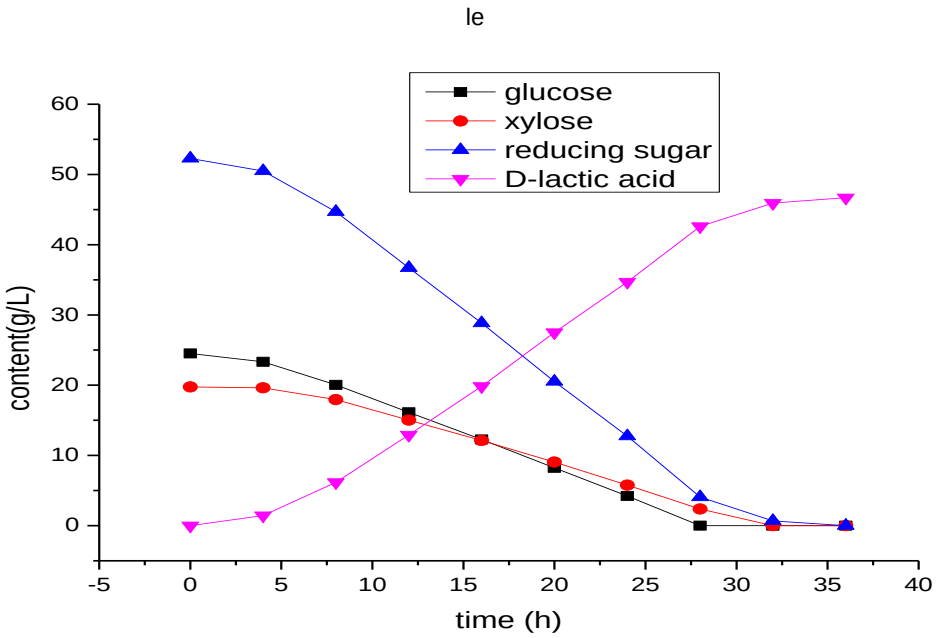

Figure 1: Content of each substance with the fermentive time

As shown in Figure 1, *E.coli* DX3 completed the fermentation in 36h using rice straw hydrolysate as fermentation substrate. The initial glucose, xylose and reducing sugar were 24.52 g/L, 19.75 g/L and 52.27 g/L, were completed fermented in 28 h, 32 h and 36 h respectively. The consumption rates of glucose, xylose and reducing sugar were 0.87 g/(L•h), 0.62 g/(L•h) and 1.45 g/(L•h), respectively. The final titer of D-lactic acid was 46.70 g/L with a volumetric productivity of 1.30g/ (L /h). The conversion rate of sugar and the purity of D- lactate acid reached to 89.34% and 99.8% respectively, which meets the domestic industrial standard. Because the strain *Escherichia coli* DX03 can use pentose and hexose simultaneously, the glucose effect is not obvious in the fermentation, which is beneficial to the production of D- lactic acid using lignocellulosic hydrolysate which contains both C5 and C6 sugars.

5. CONCLUSION

In this study, through a two-step acid hydrolysis and cellulase saccharification of rice straw, 52.42 g reducing sugar, 24.60 g glucose and 19.98 g xylose were obtained from 100 g rice straw. The glucose released from this hydrolysis process is 5 to 6 times than that of traditional one-step acid hydrolysis. The higher glucose released is beneficial to subsequent fermentation. Therefore, hydrolysate of rice straw and enzyme supplemented medium is selected for fermentative production of D-lactic acid.

The fermentation was completed in 36 h. The conversion rate of sugar is 89.34%, and the optical purity of D- lactic acid reaches to 99.8%. These relative short fermentation time, high conversion rate of sugar, and high optical purity of D-lactic acid reach to the general requirement of the domestic industrial standard. These results shows the industrial potentials of *E. coli* DX03 for D-lactic acid fermentation using lignocellulosic hydrolysate.

6. ACKNOWLEDGEMENTS

This study was financially surported by the National Key Technology R&D Program(2012BAD27B03) and Hubei Natural Science Foundation(2015CFB637)

7. REFERENCES

Avci A，Saha B C，Kennedy G J，Et Al. Dilute Sulfuric Acid Pretreatment Of Corn Stover For Enzymatic Hydrolysis And Efficient Ethanol Production By Recombinant Escherichia Coli Fbr5 Without Detoxification[J]. Bioresour Technol，2013，142（13）：312-319.

Datta, R, Et Al. "Technological And Economic Potential Of Poly(Lactic Acid) And Lactic Acid Derivatives. " Fems Microbiology Reviews 16.2–3(1995):221-231.

Hill, Jason. "Environmental Costs And Benefits Of Transportation Biofuel Production From Food- And Lignocellulose-Based Energy Crops. A Review."?Agronomy For Sustainable Development?27.1(2007):1-12.

Lin R, Cheng J, Ding L, Et Al. Subcritical Water Hydrolysis Of Rice Straw For Reducing Sugar Production With Focus On Degradation By -Products And Kinetic Analysis[J]. Bioresource Technology, 2015,186:8-14.

Liu X, Ai N, Zhang H, Et Al. Quantification Of Glucose, Xylose, Arabinose, Furfural, And Hmf Incorncob Hydrolysate By Hplc-Pda–Elsd[J]. Carbohydrate Research, 2012, 353: 111-114.

Sluiter A, Hames B，Ruiz R，Et Al. Determination Of Structural Carbohydrates And Lignin In Biomas [R].Golden C. Dai B L, Zhu A F, Mu F H, Et Al. Effect Of H3po4 Pretreatment On Biogas Production Of Rice Straw During Anaerobic Digestion[J]. Advanced Materials Research, 2014, 953-954:216-219.

Sasaki C, Okumura R, Ai A, Et Al. Effects Of Washing With Water On Enzymatic Saccharification And D -Lactic Acid Production From Steam-Exploded Sugarcane Bagasse[J]. Journal Of Material Cycles & Waste Management, 2012, 14(3):234-240.

Teeravivattanakit, T, Et Al. "Chemical Pretreatment-Independent Saccharifications Of Xylan And Cellulose Of Rice Straw By Bacterial Weak Lignin-Binding Xylanolytic And Cellulolytic Enzymes. " Appl Environ Microbiol (2017):Aem.01522-17.

Wang J, Zhang S, Yang B. Application Of 3, 5-Dinitrosalicyic Acid (Dns) Method To Test The Reducing Sugar And Water-Soluble Total Sugar Content In Sugarcane Internodes[J]. Sugarcane & Canesugar, 2008.

Xu N, Zhang W, Ren S, Et Al. Hemicelluloses Negatively Affect Lignocellulose Crystallinity For High Biomass Digestibility Under Naoh And H2so4 Pretreatments In Miscanthus[J]. Biotechnology For Biofuels, 2012, 5(1):58.

Xie, G And L. Peng. "Genetic Engineering Of Energy Crops: A Strategy For Biofuel Production In China Free Access."?Journal Of Integrative Plant Biology?53.2(2011):143-150.

Zhang, Y, And P. V. Vadlani. "D-Lactic Acid Biosynthesis From Biomass-Derived Sugars Via Lactobacillus Delbrueckii Fermentation." Bioprocess & Biosystems Engineering 36.12(2013):1897-1904.

146: Research on combined power supply control of solar power grid and municipal power grid

Xiaokang ZHAO[1], Jie ZHANG[2], Hui XIAO[3], Fan XIAO[4]

[1] Hubei Collaborative Innovation Center for High-efficiency Utilisation of Solar Energy, Hubei University of Technology, 944146554@qq.com
[2] Hubei Collaborative Innovation Center for High-efficiency Utilisation of Solar Energy, Hubei University of Technology, zjmato@163.com
[3] State Grid Huanggang Power Supply Company, Huanggang, Hubei Province, xh_dzyx@163.com
[4]State Grid Huanggang Power Supply Company, Huanggang, Hubei Province, 67111366@qq.com

Renewable energy sources cannot guarantee long-term and stable output supply when they are given energy consumption at the load end. At the same time, traditional solar and utility power supply system cannot guarantee the priority of using solar energy to generate electricity, which has certain limitations. In this regard, an energy control strategy for achieving smooth and no backflow switching and prioritizing the use of clean energy solar energy under a joint power supply system of a solar power grid and a municipal power grid is proposed, which is used for a conventional combined power supply system of a contactor switching circuit. A new combined power supply topology is proposed, which effectively reduces the impact on the solar power grid and the municipal power grid during the system switching process combined control mode for controlling the current phase and repetitive control at the output end of the solar power grid in the combined power supply mode and adding a feedforward control method for the grid voltage is adopted to ensure that the solar grid and the municipal power, and prioritise the use of clean energy solar energy. And at the same time, ensure the maximum utilisation of solar energy. In order to further validate energy control strategy, this paper chose the combined power supply system with solar power grid and the municipal power grid as the object of this research the topology structure and controlling strategy of the power supply system were comprehensively and deeply researched, and on this basis, the combined power supply system prototype was designed on the foundation of DSP28335 and CPLD. And hardware parameters are designed in the system, and an energy management optimisation algorithm based on the system is developed on the corresponding experimental platform. The experimental results show that the proposed energy control strategy can effectively reduce the impact on the solar power grid and the municipal power grid during the system switching process, ensure that the solar power grid and the municipal power grid have no backflow combined power supply, and give priority to the use of clean energy solar energy.

Keywords: Combined power supply; No backflow; Energy Control; Repetitive Control; Voltage Feed Forward

1. INTRODUCTION

At present, with the outbreak of energy crisis in various countries around the world, global energy resources are facing tremendous pressure and challenges. Under this environment, renewable energy sources such as solar energy, wind energy, and tidal energy have become a rookie and gradually gain people's attention (Nigim, 2006). However, these renewable energy sources cannot guarantee long-term and stable output supply when they are given energy consumption at the load end. This causes renewable energy sources to encounter enormous resistance at the development side, and at the same time, it also leads to a reduction in the effectiveness of renewable energy in mitigating the global energy crisis.

Among all renewable energy sources, solar energy has inexhaustible advantages and is an ideal clean resource. In order to make full use of solar photovoltaic power generation, while ensuring the stability of the load, we must provide additional backup power supply based on the solar photovoltaic power supply system. In the traditional solar power system, battery packs are used for backup energy. Not only is the system structure complex and the cost is high, but also the used batteries are prone to serious environmental pollution, while the municipal power grids do not have the above problems. Therefore, under the conditions of municipal power grids, Use municipal power grid as backup power (Liao, 2009; Khanh, 2010). Liao Zhiling (2009) proposed a control method using contactor switching to realise the joint power supply of the solar grid and the municipal grid, but this kind of control mode can only guarantee the basic power supply of the load, during the frequent switching process of the contactor. It is also easy to impact the grid and affect the stable operation of the municipal grid system. Zhang Chunlong proposed a combined power supply technology between the solar grid and the municipal power grid connected on the DC side (Zhang, 2012). Under this model, it is unable to ensure the maximum use of solar energy when the solar microgrid system has power output.

This paper proposes a new energy control strategy for a non-countercurrent combined power supply system between a solar power grid and a municipal power grid, which includes the hardware topology of the combined power supply system of the solar grid and the municipal grid and the energy control strategy of the system. Under the proposed new topology, the current phase of the output of the solar power grid inverter is controlled, and the composite control method combining the feedforward control of the grid voltage and the repetitive control is added to realise the energy control of the entire power supply system (Yao, 2006; Wang, 2007; Zhang 2011). It not only ensures the priority, full and efficient use of renewable energy solar energy, but also does not feed the municipal grid, and does not have any impact on the electrical energy of the municipal grid system. It can also realise long-term, sustained, stable and efficient work of the load.

2. NO-CURRENT COMBINED POWER SUPPLY SYSTEM TOPOLOGY DESIGN

2.2. Traditional combined power supply system structure

Figure 1 shows another common combined control system for solar power grid and municipal grid. The power of the municipal grid is converted to DC by the power factor correction converter, and then parallel to the output of the DC/DC converter of the solar grid side. The DC load provides power. Although this kind of power supply mode can ensure that the power generated by the solar power grid will not flow back to the municipal power grid, it cannot guarantee the priority of using the power generated by the solar power grid. And the demand for domestic electricity load is mostly 220V AC, so the utility of the power supply system is not strong.

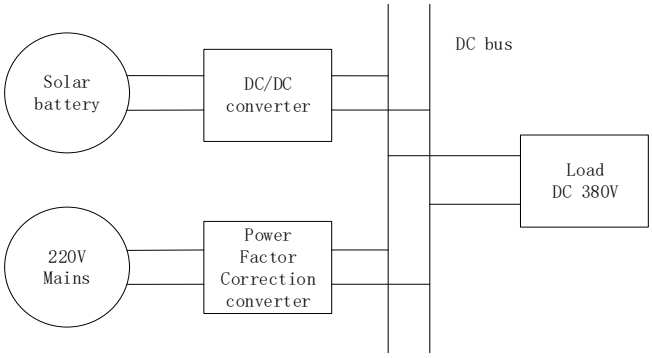

Figure 1: Solar energy and power combined supply system I

2.3. New joint power supply system structure

This paper proposes a new non-reverse combined power supply system for solar grid and municipal grid. The hardware connection structure is shown in Figure 2 below.

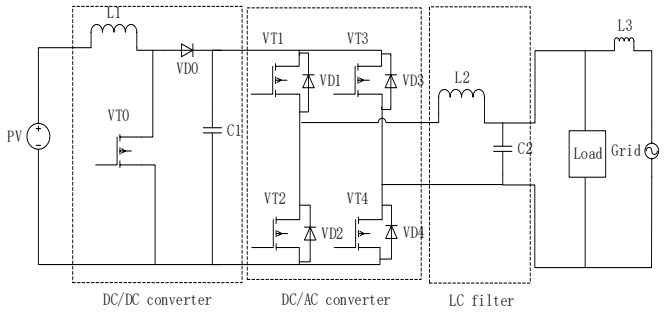

Figure 2: Solar energy and power combined supply system II

The system does not use hard-to-connect switching devices such as contactors, and uses LC to directly couple softly with the load. Through the control of the phase, matching power adjustment can be achieved. It effectively avoids the impact on the municipal power grid when the contactor is switched on, can smoothly switch between different working modes, and ensures the priority use of clean energy solar energy. And because the solar grid will not feed the municipal grid at any time under this mode of operation, it will not have any effect on the power quality of the municipal grid (Wu, 2008).

3. ENERGY CONTROL STRATEGY

3.1. Fuzzy self-tuning PI control

In the combined power supply system of solar grid and municipal grid, the reliability of energy control will directly affect the stability of the entire system. In common photovoltaic power generation systems, PI control, repetitive control and grid voltage feedforward control are ideal control strategies for controlling the effect. The two most important PI control parameters are the proportional and integral coefficients.

Proportional coefficient: It can reflect the sensitivity of the system to the error signal. The greater the sensitivity to the error signal, the smaller the proportional coefficient is, the more stable the system is. The corresponding increase in it can reduce the overall system error, improve the steady-state characteristics of the entire control system, but it will reduce the relative stability of the system. And as it increases, the system's overshoot will increase further. If the value is too small, although the system stability will increase, it will cause the dynamic characteristics to deteriorate. In summary, its value should be selected according to the needs of the system.

Integral coefficient: It has accumulative and memory functions, it can also accumulate deviation signals, and its function is to reduce static errors, so increasing it can improve system stability. Although proper increase can improve the relative steady-state performance of the system, if the phenomenon of integral saturation appears at the beginning of the response process beyond the General Assembly, it will not achieve a significant adjustment effect. Therefore, different suitable parameters need to be selected for different systems.

If the current loop controlling the current phase in the control system is only adjusted using a PI controller, the structure is shown in Figure 3 (Wang, 2009).

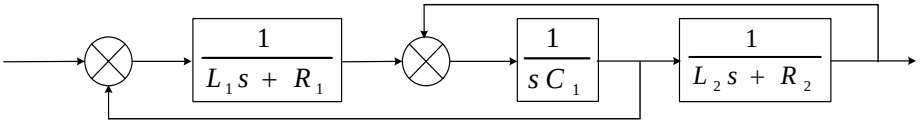

Figure 3: Structure diagram of PI control

The PI controller is $\frac{K_p s + K_i}{s}$, and the inverter part is K_{pwm}.‘

Equation 1: The system's Open loop transfer function.

$$G(s) = \frac{K_p s + K_i}{s} K_{pwm} \frac{1}{(L_1 L_2 C_1 s^3 + (L_1 R_1 C_1 + L_2 R_2 C_1) s^2 (R_1 R_2 C_1 + L_1 + L_2) s + (R_1 + R_2)}$$

Through specific experimental tests to determine the appropriate scale factor and integral coefficient. The first is the selection of the proportional coefficient. Increasing the proportional coefficient increases the gain of the controller, improves the open-loop gain of the system, and reduces the corresponding steady-state error of the

system. The control accuracy of the system is correspondingly improved, but it is also reduced. The relative stability of the system may even cause instability in the closed-loop system, so the selection parameters should not be too large. After experimental verification, P=0.3 is taken here. Secondly, the choice of the integral coefficient and the increase of the integral coefficient can improve the relative steady-state performance of the system and reduce the adverse effects of system stability. After experimental verification, I=103 is taken here.

3.2. Repetitive control

The basic idea of repetitive control comes from the internal model principle in control theory. The internal model principle is to transplant the dynamic mathematical model of the signal external to the entire system into the controller to form a high-accuracy feedback control, the output of this system is then able to track the reference input signal without any difference. Therefore, the repetitive control is a control scheme that can eliminate all the periodic errors contained in the stable closed loop, and the control performance is superior. Commonly used repetitive control system shown in Figure 4.

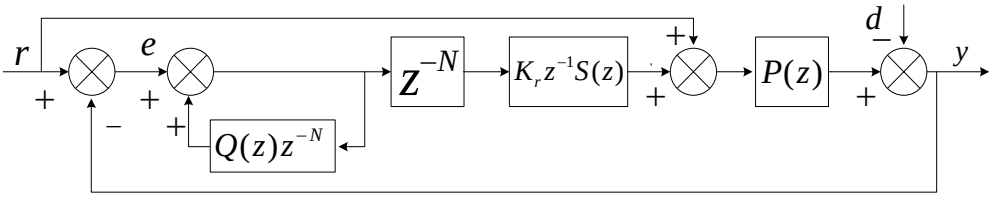

Figure 4: Common repetitive control system

In Figure 4, r is the reference sine signal given by the system; e is the error signal; d is the disturbance signal; P(z) is the SPWM inverter; y is the actual output voltage; Q(z) is the band limit filter; S(z) is the compensator of the repetitive control loop; z^{-N} is the cycle delay; N is the number of samples in a fundamental period; K_r is an adjustable gain (Kwang, 2009).

The basic idea of repetitive control is to assume that the fundamental waveform distortion that occurred in the previous cycle will also reappear at the same time in the next fundamental cycle, so the controller will use the error between the given signal and the feedback signal. The signal is used to determine the correction signal needed by the system, and then this correction signal is superimposed on the original control signal at the same time in the next fundamental wave period to eliminate the repetitive distortion that will occur in the subsequent cycles of the system.

Equation 2: Perturbation input d(k) tracking error e(k) transfer function.

$$F(z^{-1}) = E(z^{-1}) / D(z^{-1}) = 1 \Big/ [1 + \frac{1}{1 - Q(z^{-1})z^{-N}} z^{-N} K_r z^k S(z^{-1}) P(z^{-1})]$$
$$= [1 - Q(z^{-1})z^{-N}] \Big/ \{1 - [Q(z^{-1}) - K_r z^k S(z^{-1}) P(z^{-1})] z^{-N}\}$$

Where:

$E(z^{-1})$ = z transforms of e(k)

$D(z^{-1})$ = z transforms of d(k)

Then we can get:

Equation 3: The corresponding frequency functions.

$$F(j\omega) = F(z^{-1})$$
$$z = e^{j\omega T}$$

Where:

T = The sampling period

If we assume that $Q(z^{-1})$ = 1, and $P(z^{-1})$ is stable, then:

Equation 4: The frequency function when $Q(z^{-1})$ = 1, and $P(z^{-1})$ is stable.

$$F(j\omega) = \frac{1}{1 - [1 - K_r e^{j\omega kT} S(j\omega) P(j\omega)] e^{-j\omega NT}}$$

The reference instruction is a sinusoidal signal with period TS=NT. The period of the disturbance input d(k) is the same as the reference instruction period, and the angular frequency in the corresponding Fourier series can be expressed as $\omega = \frac{2\pi m}{NT}$（$m$=0,1,2…）, then:

Equation 5: The steady-state error of period perturbations below 1/(2T) of the Köhren frequency

$$F(j\omega) = \frac{1-e^{-j2\pi m}}{1-[1-K_r e^{j2\pi mk/N} S(j\omega)P(j\omega)]e^{-j2\pi m}} = 0$$

It is easy to see from the above equation that the repetitive controller has a periodic disturbance of any frequency lower than 1/(2T) of the Nyquist frequency and that the steady-state error is zero.

3.3. Voltage feedforward control

The block diagram of the grid control system without voltage feed-forward control is shown in Figure 5.

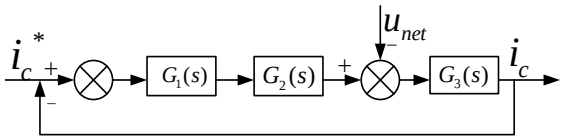

Figure 5: Block diagram of grid connected control system without voltage feedforward

The essence of solar photovoltaic grid-connected power generation system is to convert the DC power generated by photovoltaic cells into AC power, which is an active inverter system. Therefore, the system can easily produce corresponding fluctuations due to internal changes in the power grid system, and the output grid-connected current of the system will be further distorted accordingly, failing to meet the grid connection standards of the relevant national regulations.

As can be seen from Figure 5, when the grid voltage changes by Δ, the system grid-connected current will also change accordingly, and the output is:

Equation 6: When the grid voltage changes Δ, the system grid-connected current output

$$\Delta i_C = \frac{G_3(s)}{1+G_1(s)G_2(s)G_3(s)} \Delta u_{net}(s)$$

It can be seen from the above equation that when the grid voltage suddenly changes, the output current of the grid-connected system will change with it, and the system will lose stability. In order to eliminate the effects of grid voltage instability on the stability of the entire system, effective measures must be taken to suppress this change.

In this paper, the voltage feed forward regulation link is added to the solar photovoltaic grid-connected system to improve the stability of the entire system. The block diagram of the solar photovoltaic grid-connected control system with increased voltage feed-forward control is shown in Figure 6.

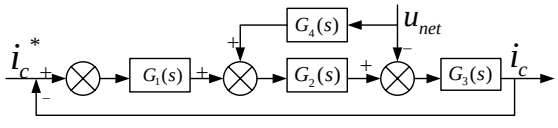

Figure 6: Block diagram of voltage feed forward control system

It can be seen from Figure 6 that after the system is added with the feedforward regulation of the grid voltage, the corresponding current change can be obtained as:

Equation 7: The corresponding current change after adding the feedforward voltage regulation of the mains voltage

$$\Delta i_C = \frac{G_3(s)[G_2(s)G_4(s)-1]}{1+G_1(s)G_2(s)G_3(s)}\Delta u_{net}(s)$$

If we make $G_4(s) = 1/G_2(s)$, then the right part of the equation above can be eliminated, which can eliminate the impact of grid voltage sudden changes on the entire system. By adding a voltage feed forward control link, a suitable duty cycle corresponding to the grid voltage is given, thereby eliminating the influence of the grid voltage change on the entire system.

3.4. Compound Control

Although the fuzzy auto-tuning PI control for controlling the current output phase can make the system have better dynamic characteristics, its control ability is relatively limited. Although the repetitive control can ensure that the output signal accurately tracks the given signal, the control signal obtained by the repetitive control cannot be output immediately, but must be delayed by one reference cycle to be output. If interference has already occurred within the system at this time, then the elimination of the influence of the interference signal on the output requires at least one reference period, and in the period in which the interference signal appears, the system cannot make any adjustment to the interference signal, then within this period the system is almost in the open-loop control state, and the dynamic performance of the control system will also be seriously affected. The addition of grid voltage feedforward control can prevent the system from being influenced by the voltage fluctuations of the grid, and it can also appropriately reduce the gain of the control system, which is beneficial to the further improvement of system stability.

This paper proposes combining fuzzy self-tuning PI control, repetitive control and grid voltage feed forward control to form a composite control. The fuzzy self-tuning PI control is used to reasonably improve the dynamic characteristics of the system, and the repetitive control is used to reasonably improve the steady-state characteristics of the system. Use grid voltage feedforward control to eliminate the effect of changes in grid voltage on the system.

4. EXPERIMENTAL VERIFICATION

In order to further verify the accuracy of the control strategy of the combined power supply system, a prototype based on TI's DSP chip (TMS320F28335) 3000VA was developed. The input voltage of the inverter is 600V, and the switching frequency is f=20kHz. The IGBT of the Infineon company model FF100R12KS4 is selected for the switchgear. The main parameters are: the withstand voltage value is 1200V and the rated current is 100A. Grid voltage = 220V, frequency = 50Hz.

The system is only controlled by the current phase and repetitive control. The resulting grid-connected waveform is shown in Figure 7.

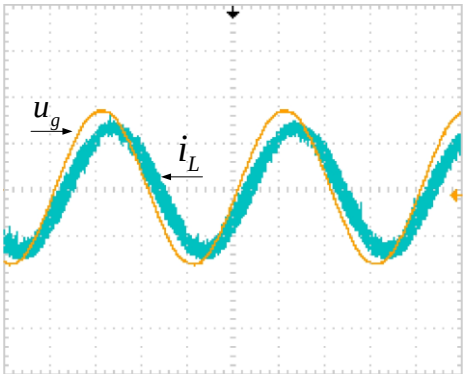

Figure 7: Grid voltage and grid connected current waveform I

The system is under the feedforward control and repetitive control of the grid voltage only. The resulting grid connection waveform is shown in Figure 8.

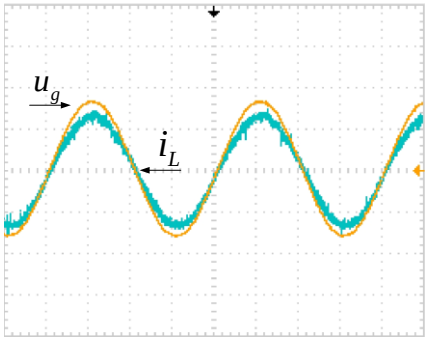

Figure 8: Grid voltage and grid connected current waveform II

The system is under complex control of the current phase control, feedforward control of the grid voltage, and repeat control. The resulting grid-connected waveform is shown in Figure 9.

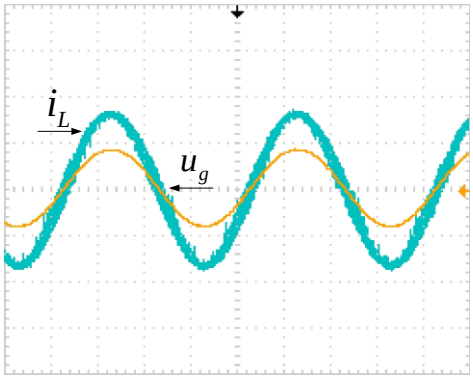

Figure 9: Grid voltage and grid connected current waveform III

Comparing Figure 7, Figure 8 and Figure 9, it is easy to see that when the system only uses current phase control and repetitive control, or only adopts grid voltage feedforward control and repetitive control, the obtained grid-connected waveforms are not ideal. When the system adopts the combined control of current phase control, grid voltage feedforward control and repetitive control, the grid-connected waveform of the system is greatly improved.

During the operation of the combined power supply system between the solar grid and the municipal grid, three analog resistive loads are used on the load side. The resistance value of each channel is 40Ω, the rated power is 2.5kW, the effective operating voltage is 220V, and the actual operating power is 1.2 per channel. kW. When the power consumption of the load side is a single channel of 1.2kW, it is less than the maximum power generation of 3kW on the solar grid side. In order to prioritise the use of clean energy solar energy and ensure that there is no backflow power supply, a reasonable energy control strategy should be adopted to ensure that the power consumed by the load side is all provided by the output power of the solar grid. The output power provided by the municipal grid is 0. After grid connection, the current waveforms of the voltage, current, and solar grid at the municipal grid are shown in Figure 10.

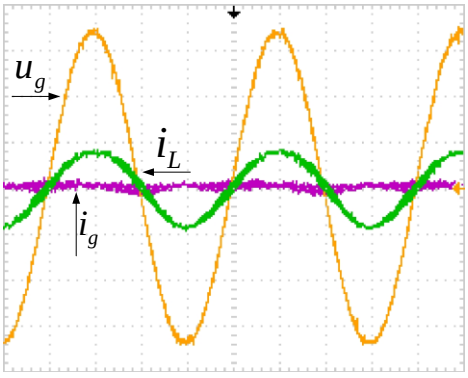

Figure 10: Grid voltage, grid current and grid connected current waveform I

With the increase of power consumption at the load side of the system, the output power of the solar power grid end and the output power of the municipal power grid end are correspondingly changed. When the power consumption of the load side is 2.4 kW, the power consumption at the load end does not exceed the maximum output power of the solar power grid by 3 kW. In order to prioritise the use of clean energy solar energy and ensure that there is no backflow power supply, this should be achieved through a reasonable energy control strategy. The power consumption of the load side is still entirely provided by the output power of the solar grid, while the output power of the municipal grid is always zero. After the grid connection, the current waveforms of the voltage, current, and solar grid at the municipal grid are shown in Figure 11.

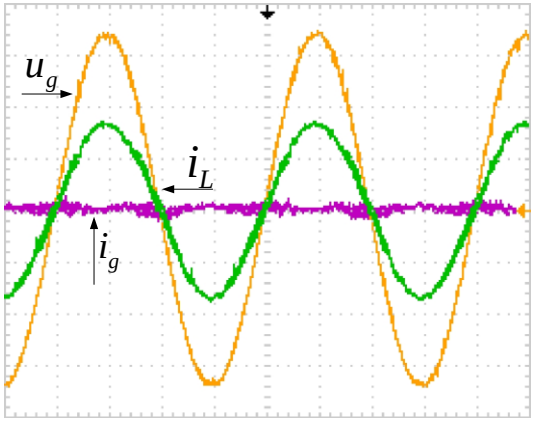

Figure 11: Grid voltage, grid current and grid connected current waveform II

As the power consumption at the load side of the system continues to increase, the output power at the solar grid side and the output power at the municipal grid will also change accordingly. When the power consumption of the load side is 3.6kW three-way, the maximum power of the solar output is still 3kW under the same light conditions. Because the power consumption at the load end exceeds the maximum output power of the solar grid at this time by 3 kW, in order to meet the stability and continuous operation of the load, and to ensure the priority use of clean energy solar energy to achieve non-reverse power supply, a reasonable energy control strategy should be adopted to make the solar grid The output power of the terminal is still maintained at a maximum of 3 kW, and the remaining insufficient 0.6 kW is then provided by the output power of the municipal grid. After the grid connection, the current waveforms of the voltage, current, and solar grid at the municipal grid are shown in Figure 12.

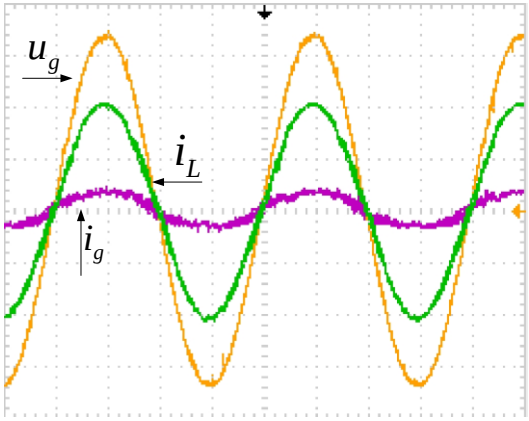

Figure 12: Grid voltage, grid current and grid connected current waveform III

5. CONCLUSION

For the switching circuits in the traditional solar power grid and municipal power grid combined power supply systems, a new type of grid-connected circuit topology for combined power supply is proposed, which effectively reduces the impact on the solar power grid and municipal power grid during the system switching process, and can achieve smooth and no reverse switching. The system control section adopts a reasonable energy control strategy to ensure the coordinated operation of the two power sources, so that the solar power grid and the municipal power grid have no counter-current combined power supply, and they can give priority to the use of clean energy solar energy, making maximum use of solar energy resources. The final experimental results show that the proposed energy control strategy has a good control effect.

6. REFERENCES

Nigim K A, Zobaa A F. 2006. Development and opportunities of distributed generation fuelled by renewable energy sources [J]. International Journal of Global Energy Issues, 26(3):215-231.

Liao Z, Ruan X. 2009, Energy management control strategy for stand-alone photovoltaic power generation system [J]. Chinese Journal of Electrical Engineering, 29(21):46-52.

Khanh L N, Seo J J, Kim Y S, et al. 2010, Power-management strategies for a grid-connected PV-FC hybrid system[J]. IEEE Transactions on Power Delivery, 25(3):1874-1882.

Ding N. 2013, Design of inverter integrated control system for solar photovoltaic solar photovoltaic market [J]. China new technology and new products, (24):2-5.

Zhang C, Shao L, Dai W. 2012, Energy management and control of photovoltaic power supply system [J]. Journal of Nantong University: Natural Science Edition, (03):5-10.

Yao Z, Wang Z, Xiao L, et al. 2006, Research on grid control strategy of a new inverter [J]. Chinese Journal of Electrical Engineering, 26(18): 61-64.

Wang Z, Xiao L, Yao Z, et al. 2007,Design and implementation of high performance inverter for grid connected independent dual mode control [J]. Chinese Journal of Electrical Engineering, 27(1):54-59.

Zhang P, Jin H. 2011, The design of PI+ inverter based on repetitive control [J]. Ship electric technology, 31(8):48-51.

Wu Z, Zou Y, Zhang Y, et al. 2008, Improvement of input current waveform of single phase PWM rectifier [J]. High voltage technology, 3(34):603-608.

Wang C, Xiao Z, Wang S. 2009, Multi loop feedback control strategy for distributed power inverter I microgrid [J]. Journal of Electrical Technology, 24(2):100-107.

Kwang S L, Wangyun W, Jay H L. 2009, Synthesis of run-to-run repetitive control methods using finite impulse models [J] . Science Direct on Journal of process control, 19(2):364-369.

147: Using COMSOL to simulate the transmittance of PV-VG

Xie JINGYU, Chen BENYUAN, Ke AIHUA, Hu XIAOFENG

Solar Energy Efficient Utilisation Cooperative Innovation Center, Technology of Hubei University, Hubei Wuhan,48201954@qq.com

With the gradual deterioration of the environment and the depletion of natural energy, energy-saving and environment-friendly green building materials are considered as important development direction in many countries. In addition to the substantially reducing in building materials, the use of photovoltaic vacuum glazing (PV-VG) in buildings will lead to a gradual reduction in energy consumption / operating costs and carbon dioxide emissions. In this paper, the transmittance of a photovoltaic vacuum glazing is simulated. In addition to transparent conductive glazing and aerogel, there are three functional films: TiO2 nanocrystalline photocatalytic film, amorphous / microcrystalline silicon film and Low-e film are applied. TiO2 film has the advantages of high catalytic activity, good chemical stability, and self-cleaning of glazing. Amorphous / microcrystalline silicon films can absorb infrared light and visible light partially to generate electricity. The low-e film can reflect the infrared light that is not absorbed by the photovoltaic layer. At the same time, it can also block far-infrared rays, thereby enhancing the thermal insulation of glazing. During the simulation process, the geometrical optics physical module of Comsol software is used to study the ray tracing, as well as a series of settings such as geometry structure, material, and dielectric properties that established the permance and ray release range of photovoltaic vacuum glazing. In the simulation, the incident light has a wavelength in the range of 400nm to 800nm. Finally, the absorption coefficient and transmittance of different films were obtained.

Keywords: photovoltaic film; nanometer photocatalytic film; transmittance; photovoltaic vacuum glazing.

1. INTRODUCTION

At present, the earth's energy is decreasing, but the energy consumption has not stopped but keep moving forward. Therefore, all countries in the world will regard as energy-saving and emission-reduction as one of the important research directions. Replacing the traditional glass with photovoltaic vacuum glass in building will reduce carbon dioxide emissions, energy losses and operating costs. Although the glass in our country has made great progress compared with the traditional glass in many aspects, PV-VG's photoelectric conversion efficiency and visiable light transmittance still have many problems. The main reason is that the following three issues have not been solved:

The first is the matching problem of vacuum glass and its seals and supports. After installing the vacuum glass, the durability and reliability of vacuum sealing materials in the actual climate are very important. Destructive, the tensile stress on the outer surface is mainly concentrated on the joint part and support side edge. Vacuum sealing technology has a great influence on the stress distribution, transmittance and photoelectric conversion the efficiency of PV vacuum glass, is for further study.

The second is the temperature control technology of photovoltaic film. Photovoltaic vacuum glass requires low thermal conductivity, and the temperature of the photovoltaic film needs to be controlled within on the appropriate range in order to increase the conversion efficiency of the photovoltaic layer. When the photovoltaic cell generates current supply for an external load, its own internal resistance cause heat generates and temperature. And when the local temperature is so high that it may even cause the cells to burn. The thermal spot distribution and thermal runaway of photovoltaic cells have important influence on the photoelectric conversion efficiency of photovoltaic film. Domestic research on thermal runaway is not yet mature, and foreign countries are still in the initial stage.

Thirdly, the self-cleaning and anti-fouling function of photovoltaic vacuum glass need to be further improvement. The surface of photovoltaic glass is often affected by climate and environmental factors, so it is easy to be attached with dust and other pollutants, which seriously reduces its transmittance and the efficiency of photovoltaic film generation. By preparing a nano-photocatalytic film on the surface of glass, the degradation of organic matters and the function of anti-fogging can be realised in the presence of light. However, the high-activity catalyst and glass-based light emission technology are not perfect. Photovoltaic (PV) load and morphology control of vacuum glass light catalyst is the key problems which must be solved during its practical application.

In this paper, COMSOL is used to simulate the transmittance of PV vacuum glass in its structure, and the geometric structure of the low-e film, nanometer photocatalytic thin film, and amorphous/microcrystalline silicon films are simulated.

2. MAIN GEOMETRY AND CHARACTERISTICS OF PV-VG.

The 3D COMSOL project is set up to simulate the visible light transmittance of PV-VG by using the ray optics module. The main functional film in vacuum glass is TiO2 nano-photocatalytic film, amorphous/microcrystalline silicon film and low-e film.

The TiO2 film has good chemical stability and high catalytic activity. In addition, TiO2 film can also achieve surface self cleaning on photovoltaic glass. The low-e film reflects infrared light that is not absorbed by the PV film. The PV film uses infrared and visible light to generate electricity. Amorphous / microcrystalline silicon films absorbs infrared light and achieves partial visible light generation.

2.1. Geometric

The geometry of PV-VG is shown in Table 1.

Table 1: Geometry parameters of the glazing

Item	*Size(mm)*
Length of the form	*500*
Width of the form	*500*
Thickness of the TCO	*2*
Thickness of the Vacuum glass sheet	*4*
Height of columns	*0.5*
Radius of columns	*0.5*
Distance of columns	*30*
sealing depth	*8*

2.2. Material

Domain

Table 2 lists the main material parameters of each domains.

Table 2: Material of domains

Item	*The real part of refractive index(1)*	*The imaginary part of refractive index (1)*
Glass	*1.5*	*1e-8*
Rarefied gas	*1*	*0*
Aerogel	*1.07*[1]	*0.21*[1]
Resin	*1.58*	*0**

*As an edge-sealing material, the imaginary part of refractive index of the resin is simply set to 0 here, because the sealing area is usually covered by an opaque window frame. The effect of this area on light transmittance is ignored.

Coating

- **ZnO** (Rahul et al, 2014)

The refractive index of ZnO is shown in Figure1 and the absorption coefficient is shown in Figure 2.

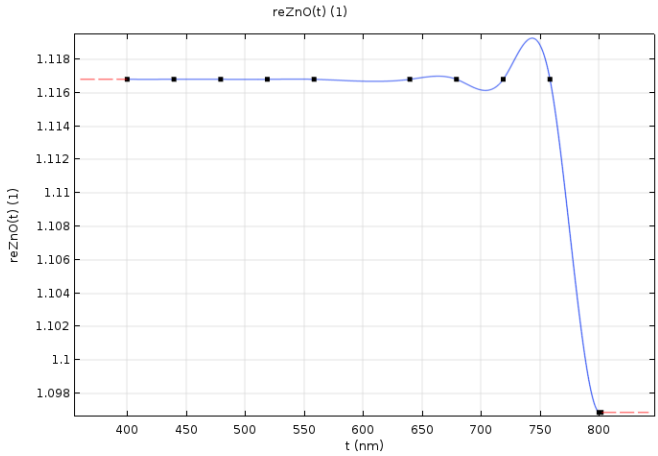

Figure 1: The refractive index of ZnO

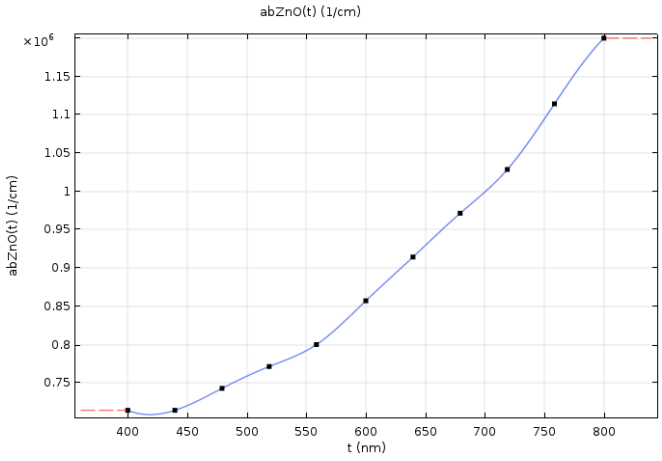

Figure 2: The absorption coefficient of ZnO

- **a-Si** (Tairan et al, 2016)

The refractive index of a-Si is shown in Figure 3 and the absorption coefficient is shown in Figure 4.

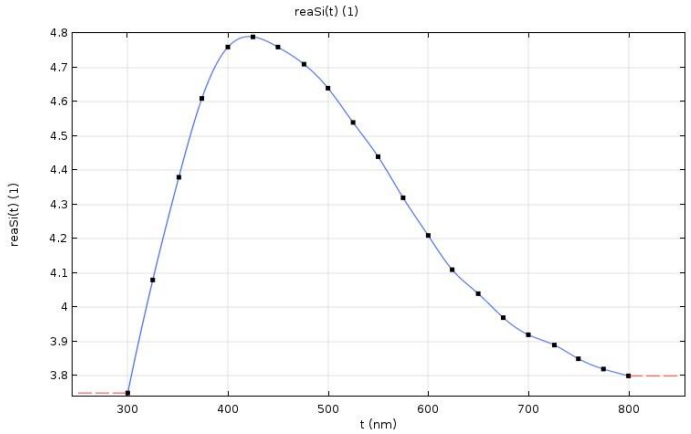

Figure 3: The refractive index of a-Si

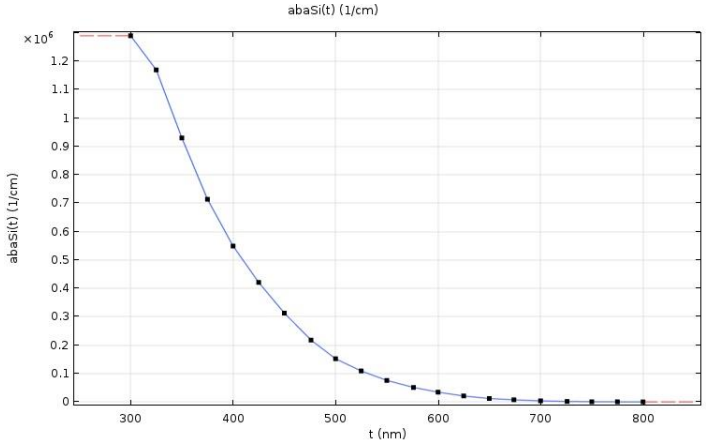

Figure 4: The absorption coefficient of a-Si

- **uc-Si** (Tairan et al, 2016)

The refractive index of uc-Si is shown in Figure 5 and the absorption coefficient is shown in Figure 6.

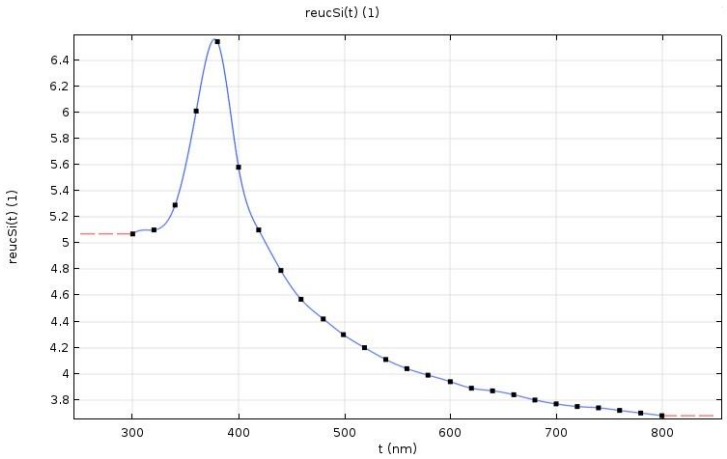

Figure 5: The refractive index of uc-Si

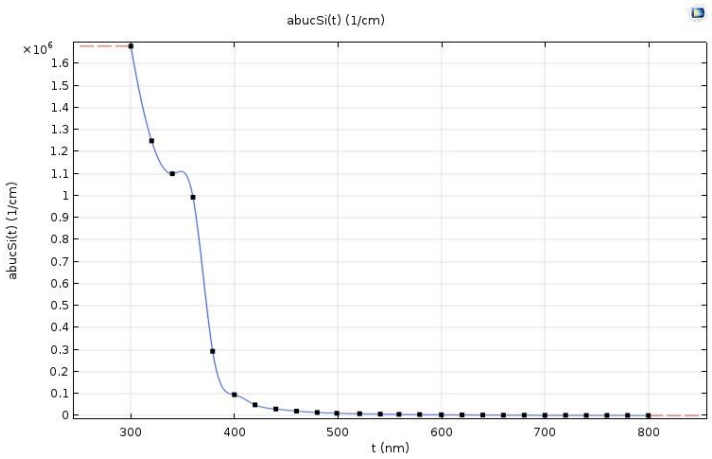

Figure 6: The absorption coefficient of uc-Si

- **TiO2** (Thomas et al, 2016)

The refractive index of TiO2 is shown in Figure 7 and the extinction coefficient is shown in Figure 8.

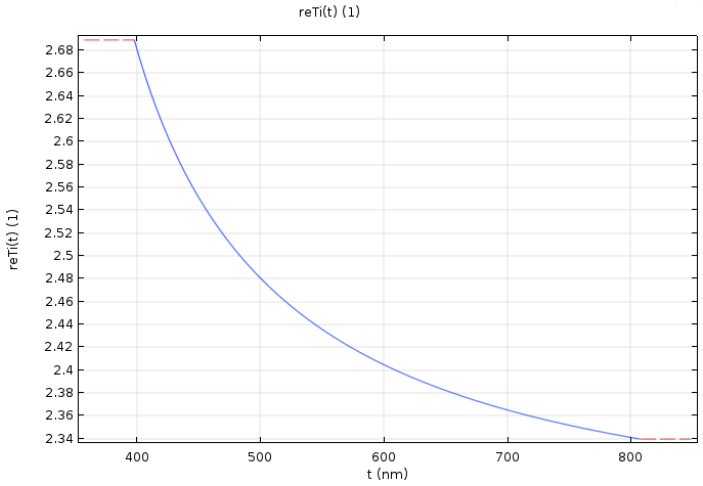

Figure 7: The refractive index of TiO2.

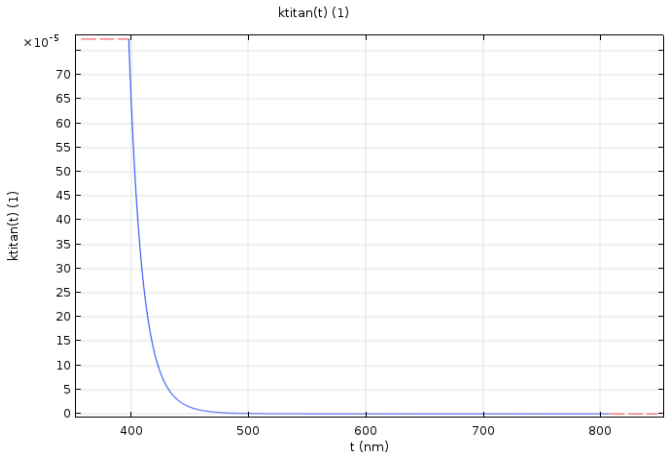

Figure 8: The extinction coefficient of TiO2.

- **Ag** (Arkadiusz et al, 2017)

The refractive index of Ag is shown in Figure 9 and the extinction coefficient is shown in Figure 10.

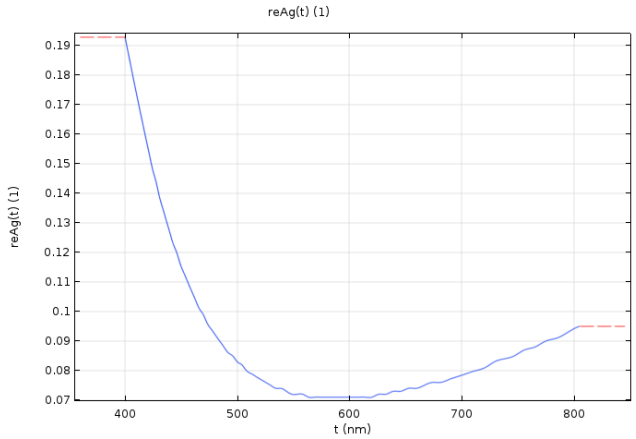

Figure 9: The refractive index of Ag

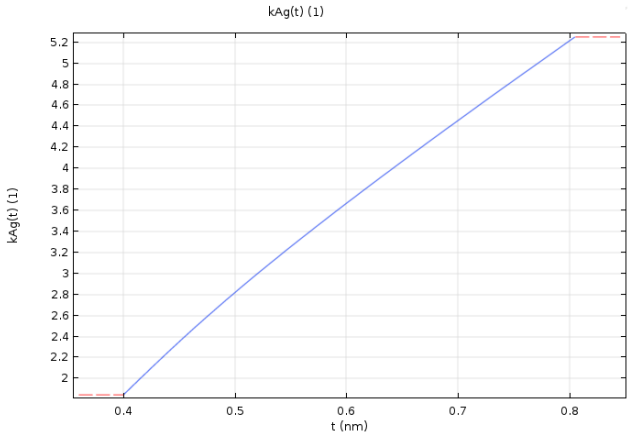

Figure 10: The extinction coefficient of Ag.

Relationship between absorption coefficient and extinction coefficient.

Let the extinction coefficient be k and the absorption coefficient be α. The relationship between them is (Aleš et al, 2000):

$$k = \frac{\lambda}{4\pi}\alpha \qquad (1)$$

2.3. Geometrical optics

Incident ray properties

Wavelength range: 400nm-800nm.
Power: 1 W.

Coatings

Thickness of TiO2 film: 350nm .
Thickness of Low-e film: 20nm.
Structure of PV film(from top to bottom):
ZnO : 500nm;
uc-Si or a-Si: 1um;
ZnO : 500nm;
Ag : 20nm.

3. SIMULATION PROCESS

The main purpose is the "ray tracing" part of geometric optical physics field in COMSOL. The theoretical diagram of photovoltaic vacuum glass is shown in Figure11.

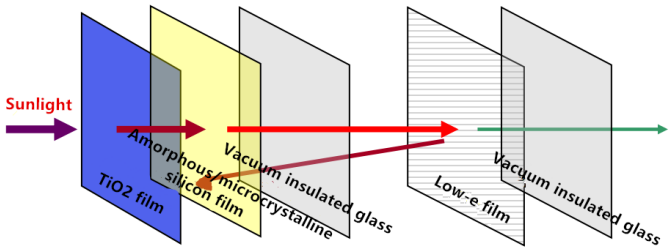

Figure 11: The theoretical diagram of photovoltaic vacuum glass

The first step is to plot the geometry of photovoltaic vacuum glass, and then set the materials (eg, glass, aerogel, resin, etc.). The third step is to set "geometrical optics" physical fields: for example, use the master curvature and radiation power to calculate light intensity; under the coating options in the "material discontinuity" window, select "add layer to surface" and then add the film refractive index and film thickness in the sub-option "dielectric film". Besides, the incident light wavelength range is 400-800nm.

4. RESULTS AND ANALYSIS

From Figures 12-14, the horizontal axis is the wavelength (m) and the vertical axis is the power of exit rays (W).

4.1. uc-Si film

When the PV film is uc-Si film, the power of exit rays is shown in Figure 12.

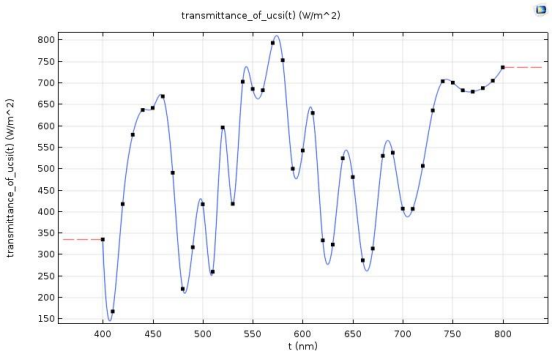

Figure 12: Transmittance of the glazing to different wavelength of incident ray (uc-Si film)

4.2. a-Si film

When the PV film is a-Si film, the power of exit rays is shown in Figure 13.

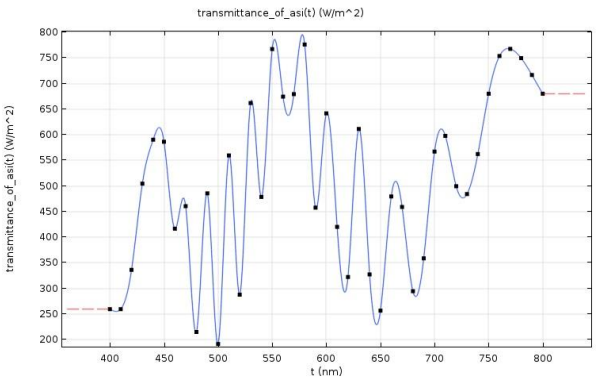

Figure 13: Transmittance of the glazing to different wavelength of incident ray (a-Si film)

4.3. a-Si/uc-Si film.

When the PV film is a-Si/uc-Si film, the power of exit rays is shown in Figure 14.

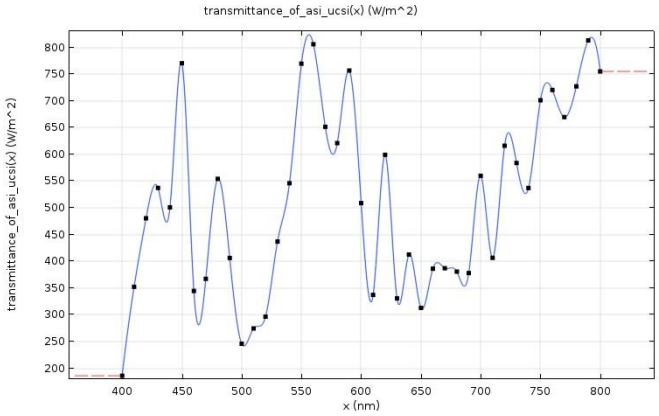

Figure 14: Transmittance of the glazing to different wavelength of incident ray (a-Si/uc-Si film)

5. SUMMARY

In order to cope with the global energy exhaustion and the gradual deterioration of the environment, the design and production of new green materials is imminent. This article describes the design of photovoltaic vacuum glass, using TiO2 film, amorphous/microcrystalline silicon film and low-e film. In theory, full spectrum utilisation and self cleaning capabilities of PV glass are achieved. Finally, the transmittance of three different films were obtained. It is expected that this research will develop high-performance photovoltaic vacuum glass that can replace traditional glass. In addition to energy conservation and emission reduction, photovoltaic glass can create more employment opportunities after it is put intooperation.

6. ACKNOWLEDGEMENTS

The authors would like to express their sincere gratitude to Hubei Collaborative Innovation Center for High-efficiency Utilisation of Solar Energy, Hubei University of Technology, for its Open Foundation under Grant No. HBSKFTD2016001 and No. HBSKFMS2014020. This work was also supported in part by the International Science & Technology Cooperation Program of China under Grant No. 2016YFE0124300, in part by the Doctoral Starting up Foundation of Hubei University of Technology for the project under grant No. BSQD12066 and in part by the Open Foundation of Guangdong Province Digital Signal & Image Processing Key Laboratory under grant No. 2016GDDSIPL-01.

7. REFERENCES

Tairan. Fu, Jiaqi. Tang, Kai. Chen, et al. Determination of Scattering and Absorption Coefficients of Porous Silica Aerogel Composites [J]. Journal of Heat Transfer. 2016, 138(3): 032702-1~032702-7.

Rahul. Dewan, Vladislav. Jovanov, Saeed. Hamraz & Dietmar. Knipp. Analyzing periodic and random textured silicon thin film solar cells by Rigorous Coupled Wave Analysis [J]. Scientific Reports, Nature. 2014, 6029(4): 1-7.

Thomas. Siefke, Stefanie. Kroker, Kristin. Pfeiffer, et al. Materials pushing the application limits of wire grid polarisers further into the deep ultraviolet spectral range [J]. Advanced Optical Materials. 2016, 4(11): 1780-1786.

Arkadiusz. Ciesielski, Lukasz Skowronski, Marek Trzcinski, et al. Controlling the optical parameters of self-assembled silver films with wetting layers and annealing [J]. Applied Surface Science. 2017, 421(2): 1-8.

Aleš. Poruba, Antonín. Fejfar, Zdeněk. Remeš, et al. Optical absorption and light scattering in microcrystalline silicon thin films and solar cells [J]. Journal of Applied Physics. 2000, 88(1): 148-160.

150: Li-SC HESS power coordination allocation based on PCDH real-time tracking control strategy

Zhangqing HE[1], Zhihao CHENG[2], Tiezhou WU[3]

[1] *Hubei Key Laboratory for High-efficiency Utilisation of Solar Energy and Operation Control of Energy Storage System, Hubei University of Technology, 249825398@qq.com*
[2] *Hubei Key Laboratory for High-efficiency Utilisation of Solar Energy and Operation Control of Energy Storage System, Hubei University of Technology, 1038687375@qq.com*
[3] *Hubei Key Laboratory for High-efficiency Utilisation of Solar Energy and Operation Control of Energy Storage System, Hubei University of Technology, zhcheng0107@163.com*

The micro-grids usually use energy storage systems to suppress DC bus power fluctuations caused by load changes. The paper uses a hybrid energy storage system (Li-SC HESS) for lithium batteries and super-capacitors to meet both power and energy requirements due to load changes. This paper proposes a PCDH（Port controlled dissipation Hamiltonian） real-time tracking control method based on the low-pass filter time constant modified Li-SC HESS power coordinated distribution for the DC/DC and DC/AC double-stage conversion structure and the passivity of hybrid energy storage system. Combined with the good dynamic characteristics and strong robustness, the method can quickly track and control the DC side voltage, so that it can quickly adapt to the demand of power coordination allocation and maintain the power balance of the system. In this paper, the hybrid energy storage system model of the optical storage micro-grid is established by Matlab/Simulink software, and compared with the conventional voltage and current double closed loop PI control strategy of the micro-grid. Simulation test results show that the proposed PCDH real-time tracking control method has better ability to track load changes and has strong robustness. At the same time, the power coordination allocation method can correct filter time constants in real time participates in the HESS adjustment and effectively reduce the charge and discharge times of lithium batteries, smooth the charging and discharging process, improve the stability of the DC bus voltage, extend its service life, and improve the performance of the hybrid energy storage system are of great significance in the subsequent in-depth study of the power coordination management of the hybrid energy storage system.

Keywords: micro-grid，HESS；power coordinated allocation；PCDH real-time tracking control

1. INTRODUCTION

In recent years, the capacity of renewable energy generation in micro-grid is on the increase, in order to ensure the power quality security and stability of the system, energy storage device is indispensable. However, a single storage device is difficult to satisfy both the power and energy requirements, for example, when the micro-grid has an energy gap when it is running independently or during a black start, energy-based energy storage (such as lithium batteries, Li) is required to provide main power support; when the load change causes power imbalance or unstable renewable energy or even power quality problems, the super capacitor (SC) is required to assist the main power source to quickly respond to power changes. Hence, taking the quick response characteristic and long cycle life of supercapacitors with a large capacity of the lithium battery storage into consideration, a Li-SC hybrid energy storage system (Hybrid Energy Storage System, HESS) is made, whose coordinated allocation of the internal power have been one of the hot topic studies for scholars at home and abroad. However, the power coordination allocation method of the hybrid energy storage system is not very mature, and the method of prolonging the life of lithium battery still needs to be further improved.

This paper utilises the two-stage transformation structure of hybrid energy storage system, that is DC/DC and DC/AC, puts forward a PCDH real-time tracking control method for power coordinated allocation of Li-SC HESS based on the low-pass filter time constant. Taking battery charge/discharge status into consideration, the strategy real-time traces the remaining charge (SOC) and charge/discharge power to correct filter time constant, and to adjust the power value of each storage element, making a achievement of the purpose of coordination HESS power coordinated allocation. Besides, combined with the energy shaping control method to the side of DC/AC, with which has good dynamic characteristic and robustness, this control can quickly track and control the DC voltage, so that it can quickly adapt to the needs of adaptive power allocation, thus maintaining a power balance.

This kind of control method can effectively smooth lithium battery charge and discharge process, extend the life of lithium batteries to optimise performance HESS.

2. BENEFITS OF INTEGRATING ENERGY STORAGE FOR RAPS SYSTEM

HESS in the topological structure of micro-grid application is shown in Figure 1.

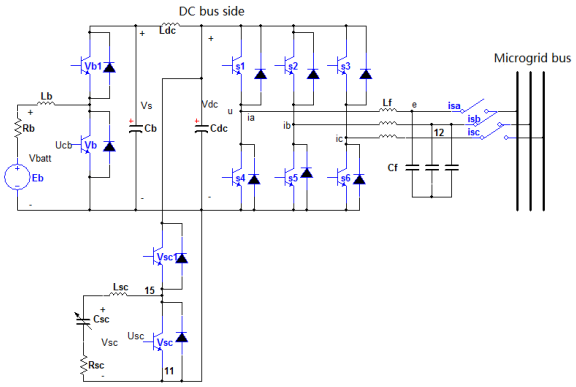

Figure 1: Diagram of HESS main circuit structure

The control module includes the front stage DC/DC bidirectional converter and the post stage DC/AC bidirectional converter; L_b and L_{sc} are lithium battery and super capacitor inductor respectively.The lithium battery state of charge and discharge as state variables, lithium battery parameters are obtained according to discharge characteristic curve, and also fully applicable to the charging characteristics . The controlled voltage source voltage see Equation 1.

Equation 1: The controlled voltage source voltage.

$$\begin{cases} V_{sc} = V_{sc0} - \int_0^t \frac{i_{sc}}{C} dt - R_{sc} i_{sc} \\ V_{bat} = V_{bat0} + R_b \times i_{bat} - K \frac{Q}{Q - \int_0^t i_{bat} dt} + A \exp(-B \int_0^t i_{bat} dt) \end{cases}$$

Type: R_{sc} , R_b respectively for SC, lithium battery internal resistance; SC, lithium batteries of the no-load voltage respectively for the V_{sc} ,V_{bat} ; SC, lithium battery constant voltage respectively for the V_{sc0} , V_{bat0} ; I_{sc} , I_{bat} for

SC and lithium battery open circuit current; C is the capacitance; K for the lithium battery group polarisation voltage; Q for the capacity; A is an amplitude of exponential region; B is the reciprocal of the time constant of the exponential region.

3. PROPOSED COORDINATED CONTROL APPROACH FOR HYBRID STORAGE-BASED RAPS SYSTEM

3.1. The constraint conditions of hybrid energy storage system

Single use lithium batteries as storage can equipment, lithium battery in order to maintain the DC bus voltage constant, often need to frequent the absorbed and emitted a larger power and switching frequently between the state of charging and discharging, and the use of Li-SC hybrid energy storage lithium battery can be a good way of improving working conditions. Due to power with respect to the DC bus voltage, the load changes is more sensitive with the help of the photovoltaic array of micro grid system, according to the load power P_{Load} and P_{PV} array output power difference of Power Coordination Distribution in Li-SC, can well smoothed lithium battery charging and discharging process, and reduce the number of charging and discharging, and achieve the purpose of stable DC bus voltage.Ignore the energy loss of each part of the system, the relationship between the DC bus voltage V_{dc} and the energy unit power see Equation 2.

Equation 2: the relationship between the DC bus voltage V_{dc} and the energy unit power

$$C_{dc}V_{dc}\frac{dV_{dc}}{dt} = P_{PV} - P_{Load} - P_{HESS}$$

Type: the need to adjust the power of HESS.To make the system stable power vacancy for ΔP_{ref} , when the DC bus voltage fluctuations in the demand of the power of the system changes, namely $\Delta P_{ref} \neq 0$, when the voltage fluctuation is small, to prevent HESS frequent charge discharge switch, when HESS is not working, micro voltage can in affordable within the scope of small amplitude changes; if the voltage fluctuation continued to increase, in order to maintain the stability of DC bus voltage and need to regulation P_{HESS} to compensate the system load and the difference between the solar panels power. In order to improve the effectiveness of the HESS operation and stability, need to fully consider the constraints of the energy storage element operation, including the charge and discharge state of each storage element under the changing SOC and charge discharge power limit. At the same time, by using recursive push mode to consider changes in the volume of its influencing factors, including the influence the time energy storage element characteristic of self discharge factors (in which lithium batteries as energy storage elements, self discharge characteristics is very small, this can be ignored, and the energy density of the SC low, with the self discharge characteristics, which can not be ignored) and the charge discharge capacity. So that the energy storage medium self discharge rate σ , the efficiency of bidirectional DC / DC converter storage can charge discharge efficiency η of the element and storage element time t the charging and discharging power of $P_{ESS(t)}$, the charging process, the storage element t the end of the period when the remaining power $E(t)$, $SOC(t)$ and the maximum allowable charging and discharging power of $P_{ESS\_limit}(t)$ and its charge and discharge characteristics, $E(t)$ specific relationship seen in Equation 3.

Equation 3: the storage element t the end of the period when the remaining power $E(t)$, $SOC(t)$ and the maximum allowable charging and discharging power of $P_{ESS\_limit}(t)$ and its charge and discharge characteristics, $E(t)$ specific relationship

$$\begin{cases} E(t) = (1-\sigma)E(t\text{-}1) + P_{ESS}(t)\Delta t\eta \\ SOC(t) = SOC_0 + \dfrac{\int_0^t P_{ESS}(t)dt\eta}{E_{N\_L}} \\ P_{ESS\_limit}(t) = min\left\{P_{maxC}, \dfrac{E_{max} - (1-\sigma)E(t-1)}{\eta\Delta t}\right\} \end{cases}$$

Similarly, the corresponding discharge procedure see Equation 4,

Equation 4: the corresponding discharge procedure

$$\begin{cases} E(t) = (1-\sigma)E(t\text{-}1) - \dfrac{P_{ESS}(t)\Delta t}{\eta} \\ SOC(t) = SOC_0 - \dfrac{\int_0^t P_{ESS}(t)dt}{E_{N\_L}\eta} \\ P_{ESS\_limi}(t) = min\left\{P_{maxD}, \dfrac{[(1-\sigma)E(t-1) - E_{min}]\eta}{\Delta t}\right\} \end{cases}$$

The above two Equations, Δt is calculated each window length, E_{N-L} is the rated energy storage element, $E_{\max}$ 、 $E_{\min}$ are energy storage element allows the upper and lower electricity consumption. SOC_0 is the initial value of the remaining capacity. $P_{\max C}$ and $P_{\max D}$ are respectively the maximum storage charge and discharge power element charge and discharge power characteristics under the decision. $P_{SC\_limit(t)}$ and $P_{bat\_limit(t)}$ are respectively SC and lithium battery charge and discharge time of t the maximum allowable power, $P_{HESS\_limit(t)}$ is the sum of $P_{SC\_limit(t)}$ and $P_{bat\_limit(t)}$.

3.2. HESS based on the low-pass filter time constant correction power allocation policy coordination

In the hybrid energy storage system control technology, the SC system and the lithium battery system need to be coordinated and controlled to give full play to the performance of the HESS. In this paper, a first-order Butterworth low-pass filtering method HESS power command $P_{HESS(t)}$ obtained by filtering the low frequency component as its reference power lithium battery energy storage P_{bat_ref} , after filtering and then the remaining part of the SC-frequency reference power storage P_{SC_ref} , is greater than a predetermined power 0 discharge, less than 0 indicates charging, time-domain relationship shown in Equation 5.

Equation 5: time-domain relationship

$$\begin{cases} P_{bat\_ref}(t) = \dfrac{T_d}{T_f}[\,P_{HESS}(t) - P_{HESS\_ref}(t-1)] + P_{bat\_ref}(t\text{-}1) \\ P_{sc\_ref}(t) = P_{HESS}(t) - P_{bat\_ref}(t) \end{cases}$$

Among them, $P_{HESS\_ref\,(t-1)}$、 $P_{bat\_ref\,(t-1)}$ respectively, of the previous time T of the reference value; T_f is the filter time constant, the size of the system by power fluctuations hybrid energy storage system configuration requirements and the capacity of co-determination; T_d for the control of the low-pass filter constant cycle, and there is $\Delta T = C * T_d$, C is the rate of change of the filter time constants.

To protect the battery-optimised operation of the system in case of power fluctuation meet the requirements, according to the SC on the fast high frequency response characteristics when the system load due to severe power fluctuations caused by mutations when, SC priority objective to stabilise fluctuations in lithium batteries as a back-up storage; Conversely, lithium priority compensation system slow power fluctuations. SOC reaches a critical element in the energy storage (or lower) limit, prohibit its charge (or discharge) electricity; When the SOC has not reached a critical limit value, the battery SOC into normal operation interval (SOC_{low}, SOC_{high}) 、 T_f can be modified interval $\left(SOC_{high}, SOC_{\max}\right) \cup \left(SOC_{\min}, SOC_{low}\right)$.

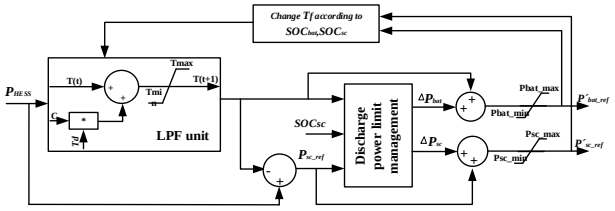

Figure 2: Diagram of power coordinating allocation control

Based on Figure 2, the specific coordination control steps are as follows:

(1) Start the filter time constant for the separation of lithium batteries power P_{bat_set} the current reference HESS power P_{HESS} and SC power reference value P_{SC_ref};

(2) According to the power limit management strategy, to correct the power which is allocated in (1) get P'_{bat_ref}, P'_{SC_ref} and calculate real-time SOC_{bat} 、 SOC_{SC} of lithium and SC;

(3) When $SOC \in \left(SOC_{high}, SOC_{\max}\right)$, the discharge capacity of the energy storage element of strong, weak charge, prior to discharging, and $SOC \in \left(SOC_{\min}, SOC_{low}\right)$, the charging characteristics of priority, by the SOC feedback control HESS real-time tracking and correction T_f, avoid overcharge and over discharge of the energy storage element damage. The corresponding T_f adjustment process as shown in Figure 3.

Among them, $T(t), T\left(t+1\right)$ respectively the current and the next moment ,the upper and lower limits were $T_{\max}$ 、 $T_{\min}$、 ΔP_{bat}、 ΔP_{SC} are the corrected power of lithium battery and SC, respectively, and $\Delta P_{bat} = -\Delta P_{SC}$ (the following process is no longer described in the expression of ΔP_{bat}).Figure 2 charge and discharge power limit management based on SC pre response specific measures are as follows: in normal operation, the super capacitor $SOC_{sc} \in \left(SOC_{low}, SOC_{high}\right)$, $\Delta P_{sc} = 0$, each storage element of power does not change; discharge power is out of the limit, the power correction Equation rules such as Equation 6; Similarly, Equation 7 is used when the charging power exceeds the limit.

Equation 6: Discharge power is out of the limit, the power correction

$$\begin{cases} \Delta P_{sc} = 0, SOC_{sc} > SOC_{sc\_max} \\ \Delta P_{sc} = P_{sc\_ref}\left(\dfrac{SOC_{sc} - SOC_{sc\_high}}{SOC_{sc\_max} - SOC_{sc\_high}}\right) = A, SOC_{sc} \in (SOC_{sc\_high}, SOC_{sc\_max}) \\ \Delta P_{sc} = -P_{sc\_ref}\left(\dfrac{SOC_{sc\_low} - SOC_{sc}}{SOC_{sc\_low} - SOC_{sc\_min}}\right) = B, SOC_{sc} \in (SOC_{sc\_min}, SOC_{sc\_low}) \\ \Delta P_{sc} = -P_{sc\_ref}, SOC_{sc} < SOC_{sc\_low} \end{cases}$$

Equation 7: Charge power is out of the limit, the power correction

$$\begin{cases} \Delta P_{sc} = -P_{sc\_ref}, SOC_{sc} > SOC_{sc\_max} \\ \Delta P_{sc} = -A, SOC_{sc} \in (SOC_{sc\_high}, SOC_{sc\_max}) \\ \Delta P_{sc} = -B, SOC_{sc} \in (SOC_{sc\_min}, SOC_{sc\_low}) \\ \Delta P_{sc} = 0, SOC_{sc} < SOC_{sc\_low} \end{cases}$$

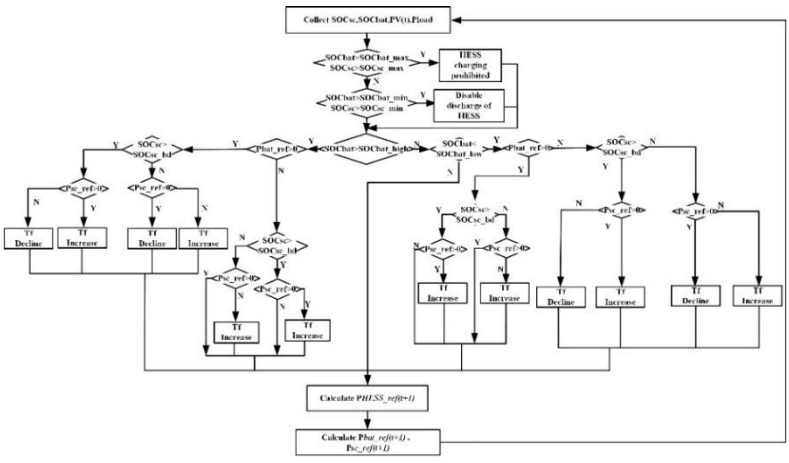

Figure 3: SOC modified low pass filter time constant T_f method based on HESS

3.3. Passive PCDH control strategy for bidirectional DC/AC converter

According to Figure 1, it is known that when the micro-grid system is in the isolated network mode, the system only completes the conversion between the DC power, and when it is in the grid mode, the system can only complete the conversion between the AC and DC power, and the energy is not generated in the two modes. Therefore, the system is a passive system. The traditional PI closed-loop control PWM (or SVPWM) switch pulse wave signal has a certain time delay on the tracking effect, thus reducing the quality of the voltage and frequency of the DC bus side. In this paper, based on the system passivity and the port controlled dissipative Hamilton (PCDH) system model, and combining the principle of constant voltage and constant frequency control (U/F control) under the isolated island mode of micro-grid, the state error energy forming control method of the bidirectional DC/AC converter is established. With its simple control, good robustness and dynamic tracking characteristics, this method can track the change of the power difference of the system in real time in order to optimise the real-time effect of T_f .

Equation 8: The port controlled dissipative Hamiltonian (PCDH) system mode

$$\begin{cases} \dot{x} = [J(x) - R(x)]\dfrac{\partial H(x)}{\partial x} + G(x)u \\ y = G^T(x)\dfrac{\partial H(x)}{\partial x} \end{cases}$$

Among them: $x \in R^n$ is the system state variable; $u, y \in R^m$, u and y are the conjugate input and output port variables of the system respectively, the double integral reflects the system interaction with the outside world power. $J(x) = -J^T(x)$ is the system inline structure matrix, which reflect the structural characteristics of the system; $R(x) = R^T(x) \geq 0$ is the dissipative damping matrix inside the system, which reflect the additional resistive structure on the port; $G(x)$ reflects the system's port features; $H = 0.5x^T Qx$ is a Hamiltonian function that describes the sum of the system's stored energy; Q corresponds to a diagonal matrix with a specific meaning in the PCDH structure of an actual circuit system.

According to Figure 1, the state average model on the DC/AC side under the dq coordinate system (the left of Equation 9) is obtained by the equal power coordinate transformation. Due to $i_{eq} = (1 - U_{cb})i_{batt_{ref}} + (1 - U_{sc})i_{sc_{ref}}$, the duty cycle of the boost/buck converter of the lithium battery is U_{cb} , and the duty cycle of the corresponding SC is U_{sc} . The part of lithium battery applies state space average method to obtain its KCL and KVL respectively. See Equation 9. Due to the internal resistance of battery R_b is small, the energy loss during work can be ignored and after DC bus voltage is stable under the ideal situation, SC neither exports nor absorbs the power, that is, ideally $I_{sc_{ref}} = 0$, $I_{bat_{ref}} = \dfrac{U_{dc}}{U_{bat0}} \cdot \bar{I}_{dc} = \dfrac{U_{dc}}{U_{bat0}} \cdot \bar{I}_0$, $\bar{I}_0 = \mu_d I_d + \mu_q I_q$, so $I_{eq} = (1 - U_{cb}) \cdot I_{bat_{ref}}$.

Equation 9: The state average model (the left of Equation 9) , KCL and KVL (the right of Equation 9)

$$\begin{cases} L_f \dfrac{d i_d}{d t} = \mu_d V_{dc} - R_f i_d - e_d + \omega L_f i_q \\ L_f \dfrac{d i_q}{d t} = \mu_q V_{dc} - R_f i_q - e_q - \omega L_f i_d \\ C_f \dfrac{d e_d}{d t} = i_d - i_{sd} + \omega C_f e_q \\ C_f \dfrac{d e_q}{d t} = i_q - i_{sq} - \omega C_f e_d \\ C_{dc} \dfrac{d V_{dc}}{d t} = i_{dc} - i_0 + (1 - \mu_{sc}) i_{sc} \end{cases} \qquad \begin{cases} C_b \dfrac{d V_s}{d_t} = -i_{dc} + (1 - U_{cb}) i_{batt} \\ L_b \dfrac{d i_{batt}}{d_t} = E_b - R_b i_{batt} - (1 - U_{cb}) V_s \\ C_{sc} \dfrac{d V_{sc}}{d_t} = -i_{sc} \end{cases}$$

Among them: R_f is the equivalent internal resistance of the filter inductor L_f ; μ_d and μ_q are the duty cycle functions of DC/AC, μ_a , μ_b and μ_c are the corresponding duty cycle functions in the dq coordinate system; i_d

and i_q correspond to the components on the dq axis of i on the inverter side, respectively; i_{sd} , i_{sq} are the components of current $\vec{i}_s$ on the dq axis of the micro-grid side, respectively ;the corresponding voltages $\vec{e}$ are e_d , e_q; i_{dc} and i_0 are DC side output current and DC/AC side input current, respectively.

According to $V_d = \mu_d V_{dc}, V_q = \mu_q V_{dc}$, μ_d and μ_q are obtained, then V_d and V_q is obtained, and then $\alpha\beta$ coordinate transformation is used to obtain control voltages V_α and V_β , that is, PWM control bidirectional DC/AC inverter driving signals, So as to control the stability of DC bus voltage amplitude and ensure the reliability of micro-grid system.

4. RESULTS AND ANALYSIS OF RESULTS

According to PCDH real-time tracking control principle coordinated by power, the simulation model of photovoltaic micro-grid isolated-grid model based on hybrid storage system of lithium-ion battery and supercapacitor built under MATLAB/Simulink is shown in Figure 4, and the important simulation parameters are shown in Table 1, Table 2.

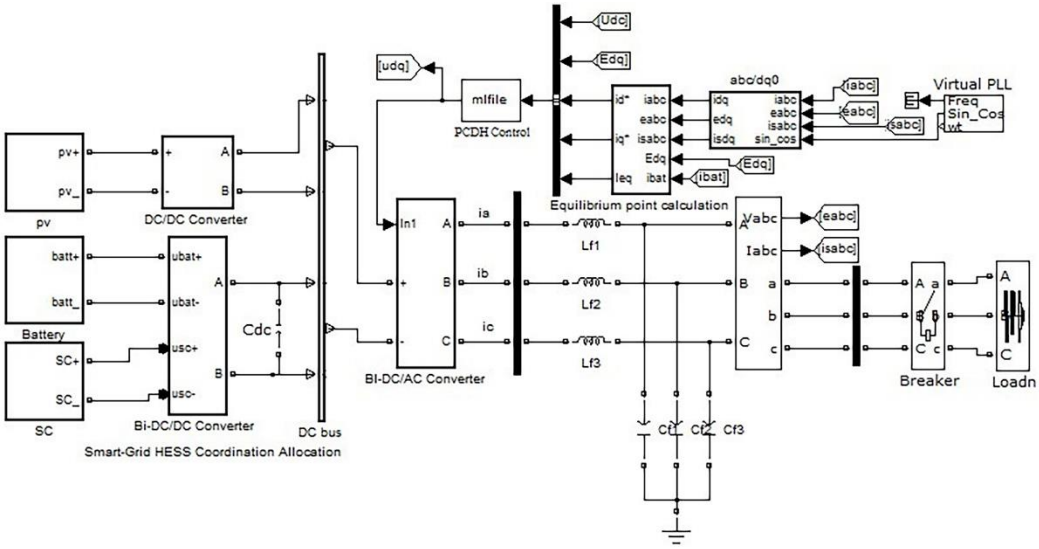

Figure 4: Micro-simulation model based on Li-SC HESS

Table 1: Micro-grid important simulation parameters

Parameter	Numerical value	Parameter	Numerical value
Battery rated capacity ($A \cdot h$)	400	Supercapacitor rated power (kw)	20
Battery rated power (kw)	20	Capacitance value (F)	10
Battery rated voltage (V)	500	Rated voltage (V)	400
Maximum power output time (h)	≥ 10	Maximum power output time (s)	≥ 30
Battery internal resistance (Ω)	0.0014	Micro-grid voltage (V)	380
Battery side energy storage inductor L_b (mH)	0.7	Micro-grid frequency (HZ)	50
L_b equivalent resistance R_b (Ω)	0.1	DC side voltage (V)	50
Photovoltaic solar panel power fluctuation range (kw)	5~15	Voltage regulated capacitor C(mF)	5
Reference temperature ($^\circ C$)	25	Filter capacitor C_f (μF)	75

Reference light intensity (W/m^2)	1000	Filter inductor L_f (mH)	0.8
MPPT sampling time (s)	0.0001	damping r_{a1} (Ω)	0.1
Low pass filter time constant T_f initial value	$150 \in (100,200)$	Important load power (kw, kvar)	10,1
		General load power (kw, kvar)	(3 piece)15,2

Table 2: Remaining capacity limit of each storage element (initial values are all 0.70)

Energy storage element	$SOC_{\min}$	SOC_{low}	SOC_{high}	$SOC_{\max}$
Lithium Ion Battery	0.30	0.35	0.85	0.95
Super capacitor	0.25	0.30	0.80	0.90

This article compares and analyzes the PCDH control method of the HESS power coordination allocation combined with the upper-level revisable T_f and the conventional double-closed-loop PI control method of voltage and current. The details are as follows:

(1) To make the output power P_{pv} of the shilling PV array remains unchanged when the system is connected to a certain amount of load. At $t = 0.2s$, the absorbed power P_{load} of the system load is reduced. The power vacancy Δp_{ref} of the system suddenly drops from 12kw to -3kw and then rapidly rises to 5kw. At $t = 0.8s$, make the load power constant. By changing the temperature of the solar panel and its light intensity, the power vacancy ΔP_{ref} of the system drops from 5kw to 1kw to 4kw at $t = 1s$. Under the system power vacancy, the curve of the output power of the lithium battery with the above two control methods and the output power curve of the supercapacitor in the method presented in this paper are shown in Figure 5(a) and Figure 5(b) respectively. (The graph of system power vacancy is no longer displayed in the graph since the power vacancy of the system is basically the same as the lithium battery power curve under the conventional control strategy. This is also the case in Figure 5(b) below.)

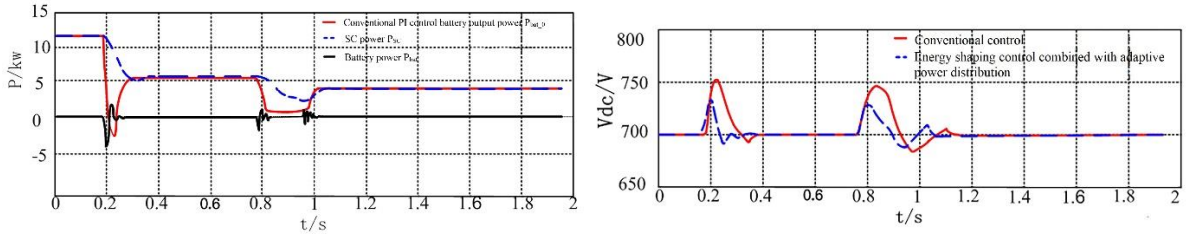

Figure 5: left (a), right (b) respectively the output power graph of HESS and the voltage waveform of micro-grid DC bus side when P_{load} plummeted while P_{pv} unchanged, and when P_{pv} changed while P_{load} unchanged

Through the comparison and analysis of the variation curves of the output power P_{bat} and P_{bat_0} of the lithium battery in Figure 5(a), it is found that when the load of the system is changed suddenly, the lithium battery still needs to pass the zero point once in the conventional PI control mode, that is, complete a lithium battery charge and discharge will give a certain degree of impact on the lithium battery. By using the improved hybrid energy storage control method, the SC can provide short-term support for the system power vacancy more quickly, better smoothing the charging and discharging process of the lithium battery, and reducing the impact on the lithium battery. In particular, the PCDH control method of Figure 5(b) in combination with power coordinated distribution reduces the variation of the voltage V_{dc} on the DC bus side of the micro-grid and effectively reduces the time for restoration of stability, showing its good tracking characteristics. In addition, this kind of control method can also restrain the photovoltaic intermittent fluctuation well, which is helpful to ensure the stability of the system under the micro-grid grid islanding mode.

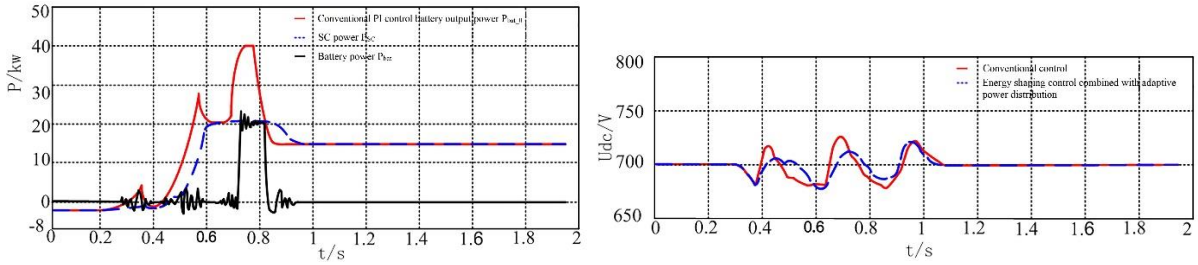

Figure 6: Left (a), right (b) respectively are the output power curve of the HESS and the waveform of the voltage V_{dc} on the DC bus side of the micro-grid when the P_{pv} constant P_{load} gradually increases.

(2) If make the output power of the PV array P_{pv} keep constant, by gradually increasing the amount of general load to increase P_{load} power system load. When the system power vacancy changes, the output power curve of the lithium battery under conventional control and the output power curve of the energy storage device of HESS which under PCDH control of power coordination and distribution shown in Figure 6(a), the corresponding micro-grid DC bus side voltage V_{dc} waveform as shown in Figure 6(b).

As can be seen from Figure 6(a), when P_{pv} is unchanged and P_{load} is increased, the system bus voltage is reduced and the PV array is in MPPT mode. SC preferentially releases power and compensates for DC bus voltage disturbance under PCDH control of power coordination and distribution, by timely tracking the SOC of each energy storage component, determining the discharge strength to correct T_f , and effectively smoothing the power fluctuations of the lithium battery, especially when the system power short-term rapid changes in a short time are more obvious on the output power of the lithium battery. When the lithium battery is increased to a full power state and then continues to increase, the SC can continue to replenish the excess power deficit until the lithium battery and the SC are both operating at full power output and $SOC_{bat} < SOC_{\min}$. If the load power continues to increase, the SC can not operate for a long time Output power, then HESS lost regulatory capacity. In order to ensure the safety of the system, part of the load needs to be cut off (or the system should be shut down in time). In the absence of a voltage protection device, timely shutdown of the system here requires further improvement in the future. Through the simulation results of Figure 6(b), it can be verified that this kind of control method can restrain and effectively reduce the DC bus-side power fluctuations caused by load changes, and has better robustness than conventional PI control.

In addition, the FFT harmonic analysis of the DC side voltage of the DC side of the micro-grid is analyzed by "powergui" with MATLAB, as shown in Figure 7 (a) and Figure 7 (b) respectively, the results show that the micro-grid system voltage which under two kinds of control strategies are less than 5%, both of which can meet the micro-grid harmonic standards, and the harmonics of the PCDH control method that can be coordinated and distributed in real time are smaller than the conventional control, further verifying that the method can improve the stability of the DC bus voltage of the micro-grid Feasibility.

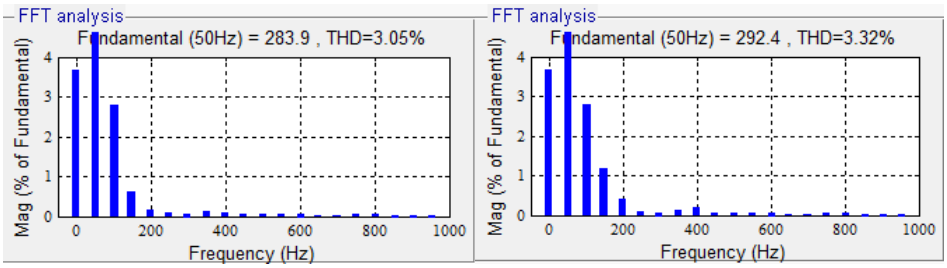

Figure 7: left (a), the right (b) are harmonic analysis diagrams under the power coordinating allocation's PCDH control strategy vs the conventional's

5. CONCLUSION

HESS has a significant restraining effect on the load variation with relatively sensitive to DC bus power fluctuation, so its power coordination is significant to maintain the stable operation of micro-grid, and the requirement to its control method becomes higher. This article applies the characteristics of high power density of SC, rapid charging

and discharging as well as the lithium battery is suitable for the main power supply to stabilise the power fluctuation of long period, establishes two-stage HESS micro-grid simulation model by means of the software platform of Simscape and Simulink, compares and analyzes PCDH energy forming control strategy of this power coordination distribution and regular voltage current double closed-loop PI control strategy. The simulation and experimental results show that the PCDH energy forming control method of such power coordination distribution has a good capacity of tracking the load variation and has strong robustness; Meanwhile, modify the power coordination distribution of filter time constant in real time to participate HESS regulation, which effectively reduces the times of charging and discharging of the lithium battery, smooths the process of charging and discharging, and properly prolongs the working life of lithium battery.

6. REFERENCES

Zhu Y, Zhuo F, Shi H. Power management strategy research for a photovoltaic-hybrid energy storage system[C]. ECCE Asia Downunder (ECCE Asia)： IEEE， 2013:842-848.

Carreira D， Domingos Marques G， Sousa D M. Hybrid energy storage system joining batteries and super-capacitors [C]. Power Electronics for Distributed Generation Systems (PEDG). 2014 IEEE 5th International Symposium on. IEEE， 2014：1-6.

Lahyani A, Venet P, Guermazi A, et al. Battery/Supercapacitors Combination in Uninterruptible Power Supply (UPS) [J]. Power Electronics IEEE Transactions on， 2013， 28(4)：1509-1522.

Damith B. Wickramasinghe A， Branislav H， et al.Single-Phase Grid-Connected LiFePO4 Battery-Supercapacitor Hybrid Energy Storage System With Interleaved Boost Inverter [J].IEEE TRANSACTIONS ON POWER ELECTRONICS，2015，30（10）：5591-5604.

Tian H, Li X. Integrated control strategy of photovoltaic grid-based microgrid operation based on hybrid energy storage [J]. Power System Protection and Control, 2014, 42(19): 122-128.

Ding M， Lin G， Chen Z . A control strategy for hybrid energy storage systems [J]. Proceedings of the CSEE， 2012， 32（7）：1-6.

Li F, Xie K, Zhang X. Control Strategy Design of Hybrid Energy Storage System Based on State of Charge and Discharge of Lithium Battery [J]. Automation of Electric Power Systems, 2013, 37(1): 70-75.

Zhang P, Han X, Zheng R. Research on operation strategy of AC/DC hybrid microgrid based on energy storage control [J]. East China Electric Power, 2013, 41(5): 0967-0972.

Li T, Qin Y, Xiao C. Research on the management and control strategy of hybrid energy storage in isolated grid-operated microgrids [J]. Hydroelectric Energy, 2014, 32(6): 180-184.

Mao M， Liu Y， Jin P， Huang H， Chang L.: Energy coordinated control of hybrid battery-supercapacitor storage system in a microgrid [J].IEEE International Symposium on Power Electronics for Distributed Generation Systems， 2013， 8-11（7）：1-6.

Wang J, Wang J, Wang X, et al. Modeling and Simulation of Photovoltaic Grid-connected Generation Systems in Microgrid [J]. Journal of Beijing Institute of Architecture and Engineering, 2013, 29(1):59-63.

Sang B, Tao Y, Zheng G, et al. Research on the topological structure and control strategy of hybrid capacitor-battery hybrid energy storage [J]. Power System Protection and Control, 2014,2(2):1-6

152: Study on the method of hybrid energy storage to stabilise the power fluctuation of DC microgrid

Tiezhou WU [1], Linxin GUO[1], Yueyang WANG [1]

[1] Hubei Key Laboratory for High-efficiency Utilisation of Solar Energy and Operation Control of Energy Storage System, Hubei University of Technology, guolinxin212@163.com
[1] Hubei Key Laboratory for High-efficiency Utilisation of Solar Energy and Operation Control of Energy Storage System, Hubei University of Technology, 1033823353@qq.com
[1] Hubei Key Laboratory for High-efficiency Utilisation of Solar Energy and Operation Control of Energy Storage System, Hubei University of Technology, 1297362526@qq.com

Currently using hybrid energy storage system to suppress load fluctuation caused by load change is a hot issue. The traditional battery-super capacitor hybrid energy storage system uses low-pass filtering to provide energy and power requirements for each energy storage unit, but it cannot dynamically adjust the filter constant of the filter. The compensation coefficient of the low pass filter changes with the charge and discharge states.Energy storage power is used to determine the target power of the energy storage unit. According to the actual operating conditions of the hybrid energy storage system, an objective function for fluctuations of the DC bus power fluctuations caused by load change is established, and an improved particle swarm algorithm is utilised to find the output power coefficient of each energy storage unit. The output coefficient of the hybrid energy storage control strategy under the improved particle swarm optimisation algorithm has the characteristics of fast convergence and high computational efficiency in the optimisation process. And it will not fall into the local optimal solution;The super capacitor bears more High frequency components and the charge and discharge times of the battery.Comparing with the energy storage coefficient without the compensation coefficient control strategy, the experimental results show that the DC bus power fluctuation caused by the load change can be effectively suppressed, and the peak-to-valley difference of the DC bus is reduced by about 60%.The effectiveness of the control strategy is verified and the service life of the energy storage battery can be lengthened .It has great engineering application value.

Keywords: Hybrid energy storage ; Power fluctuation ; Low pass filter ; Particle swarm optimisation

1. INTRODUCTION

Microgrid is a system consisted of load and micropower.The internal power supply of the microgrid is mainly dependent on the conversion of energy and is controlled by the power electronic devices. It can meet the user's need of power quality and power supply security. In recent years, thanks to the good reliability and controllability of the microgrid. It is becoming more and more widely used. However, the micro-grid capacity is limited, when the strong fluctuations occur within a short time frequently, the micro-grid bus voltage will fluctuate. This situation will greatly affect the power quality of micro-grid, threaten the stable and reliable operation of the microgrid. Hybrid energy storage is considered as one of the measures to solve the problem. In general, energy storage devices are classified two types: power and energy. The former (such as the super capacitor) has a high power density and fast response time, but the energy density is low. The energy density of the latter (such as a battery) is high, but the response is slow and is not suitable for frequent charge and discharge, but the power density is low. After combination of the characteristics of these two energy storage devices, the hybrid energy storage system can give full play to technical complementarity of the two energy storage devices.

The control strategy of hybrid energy storage systems has often been studied and practiced in literature: the output coefficient of the super capacitor is determined by collecting the charge and discharge state of the lithium battery (Chen, 2017); the reference power of the battery is obtained by improving the filter compensation coefficient, and the super capacitor is controlled with constant voltage (Li & Li, 2016); Luo (2016) propose a new hybrid energy storage topology; the advantages and disadvantages of different topology of hybrid energy storage of power type and energy type are analyzed, and the general principles of hybrid energy storage topology selection are summarised. Chong et al (2016) characterised the load in the microgrid by high fluctuation and strong randomness. It has certain controllability and can improve the ability of the traditional grid to accept the distributed renewable energy. In Tian (2016), although the intelligent optimisation algorithm is utilised to solve the problem of low response smoothing response in energy storage, but it can not quickly find the optimal output ratio of the problem.

In this paper, hybrid energy storage system composed of super capacitor (SC) and battery (Battery) is set as an example to firstly illustrate the topology of the control principle. A new control strategy based on two-order filter improved is proposed. It's objective to smooth the load fluctuation and peak-valley difference. The improved particle swarm optimisation is the new method to find the solution to the objective function. and an experimental platform is set up. The experimental results show that the power fluctuation on the DC bus of the microgrid is effectively suppressed and the peak-valley difference of the load curve is reduced after the utilisation of the control strategy proposed in this paper.

2. THE OVERALL STRUCTURE OF A HYBRID ENERGY STORAGE SYSTEM

Hybrid energy storage system composed of micro-network structure is shown in Figure 1, the energy relationship in the figure is as follows.

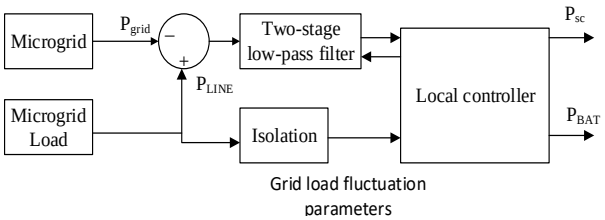

Figure 1: Hybrid energy storage system structure

The characteristics of P_E and P_{LOAD} are shown in Equation (1), (2):

Equation 1: P_E

$$P_E = P_{SC} + P_{BAT}$$

Equation 2: P_{LOAD}

$$P_{LOAD} = P_E + P_{LINE}$$

where,

P_{SC} = the power sharing of the super capacitor in the hybrid energy storage system

P_{BAT} = the power sharing for the battery in the hybrid energy storage system

P_E = the power of the hybrid energy storage system

P_{LOAD} =the load power

P_{LINE} =the BUS power

From the mixed energy storage system structure it can be seen that the load power of micro-grid fluctuations in real time, and the power on the bus will produce with corresponding fluctuations. Thus it exerts negative impacts on the bus power quality. However, with the introduction of hybrid energy storage system, the corresponding control strategy is used to control the different energy storage devices to share difference power fluctuations in storage system (Ma, 2016). The quality of bus power can be effectively improved, but how to quickly and accurately determine the output coefficient of the hybrid energy units in storage system, In order to find the solution the load fluctuations of high frequency, middle frequency, low frequency need to be distinguished. And then according to the characteristics, the energy storage units bear the load of different frequencies. Thus, a two-stage low-pass filter is introduced. And then the filtered parameters is delivered to the local controller. The local controller will collect the parameters of the grid load fluctuation and transform them into the power converter control signal, and finally the super capacitor power and battery power can be obtained.

3. IMPROVED HYBRID ENERGY STORAGE TOPOLOGY AND LOW AYOUT AND LOW-PASS FILTER STRUCTURE ANALYSIS

3.1. Improved hybrid energy storage topology

The traditional hybrid energy storage topology, super capacitors and batteries are paralleled on AC side through the DC/AC converter (Lee & Wang, 2008). In this paper, the topology shown in Figure 2, the super capacitor and battery are in paralleled on the DC bus through the DC / DC power converter group directly. DC/DC power converter group is composed of different power converters, to independently control hybrid energy storage devices in different energy storage units. Compared with the traditional topology, this structure has the advantage that the two different energy storage devices are connected through the current transformation and voltage modulation functions of DC/DC power converter. It's convenient to control the different energy storage devices, to maintain a constant DC bus voltage altogether. At the same time, since the two independent energy storage devices can be controlled independently, the capacity of the battery and the super capacitor can be obtained through the previous research on the microgrid design. And then the design capacity of the system can be optimised, in the absence of cross-border depth of the discharge, its stored energy can be made full use of (Yang, 2015; Granado, Pang & Wallace, 2016; Jiang, 2016). The fluctuation frequency of the load is obtained by real-time on-line detection, and the two-stage low-pass filter is input, and the two-stage low-pass filter filters the high frequency, medium frequency and low frequency load fluctuation. According to the results of filtration, the output coefficient of different energy storage devices is determined by algorithm control. By collecting the parameters of the grid in real time, and adjusting the parameters of the filter in time to achieve the purpose of smoothing the load fluctuation and reducing the peak valley difference of the load curve.

Through the analysis of the topology of the hybrid energy storage, it can be seen that the two-order low-pass filter is the key to maintain the normal and stable operation of the system regardless of whether the hybrid energy storage system is in the state of charge or discharge (Zhang, 2016; Li, 2016; Chen, 2016). Therefore, it is very important to dynamically adjust the parameters of the two-stage low-pass filter to achieve better control effect in order to improve the capacity of the hybrid energy storage system to suppress the load fluctuation and to reduce the peak valley difference of the load curve. In addition, the DC/DC converter is operated by the control signal. In order to generate such a set of control signals, it is necessary to set a controller for the DC/DC converter.

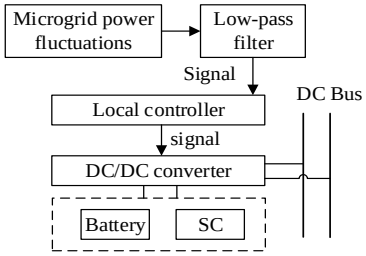

Figure 2: hybrid energy storage structure topology

3.2. Improved low-pass filter

The structure of the two-stage low-pass filter after adding the corresponding compensation and coefficient adjustment in the hybrid energy storage system is shown in Figure 3.

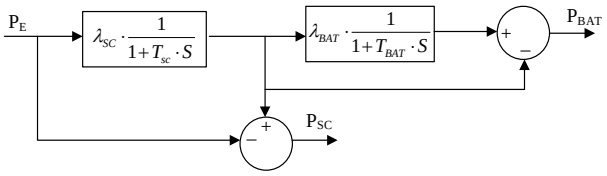

Figure 3: Improved two-stage low-pass filter

From the figure the relationship can be analyzed as follows, as Equation (3) shows:

$$\begin{cases} P_{SC} = \left(\dfrac{\lambda_{SC} - 1 - T_{SC}S}{1 + T_{SC}S} \right) P_E \\ P_{BAT} = \left(\dfrac{\lambda_{SC} \cdot \lambda_{BAT} - \lambda_{SC}(1 + T_{BAT}S)}{(1 + T_{SC}S) \cdot (1 + T_{BAT}S)} \right) P_E \end{cases}$$

Equation 3: P_{SC}、P_{BAT}

where,

$\lambda_{sc}S$ =compensation coefficient of the pre-filter

$\lambda_{BAT}S$ =compensation coefficient of the post-class filter

Due to the characteristic of the Butterworth filter, the signal will be attenuated after filtration, so the compensation coefficient needs to be added. When the hybrid energy storage system is in a different charge and discharge state and power rate, the compensation coefficient is also different.

Due to the characteristics of the first-order Butterworth low-pass filter, the cutoff frequency has a phase delay of -45°, which results in a signal attenuation, which is small or too large. When P_E>0 and dP_E/dt>0 , it is necessary to make the compensation coefficient greater than 1; when P_E>0 and dP_E/dt<0, it is necessary to make the compensation coefficient less than 1;when P_E<0 ,it's on the contray. Specific values of λ_{SC} and λ_{BAT} (to hybrid energy storage discharge as an example) is as Equation (4) shows:

$$\begin{cases} \lambda_{SC} = 1 + k_1(dP_E / dt) \\ \lambda_{BAT} = 1 + k_2(dP_E / dt) \end{cases}$$

Equation 4: λ_{SC}、λ_{BAT}

where,

k_1 =adjustment factors

k_2 = adjustment factors

And the value of T_{SC} and T_{BAT} determine the two-stage low-pass filter cut-off frequency, and it is concerned with the output of various energy storage devices (Chen, 2016). The hybrid energy storage system should have the function of real-time monitoring and fast tracking of load fluctuation. Therefore, it is very important to get the value quickly and accurately.

4. MULTI-OBJECTIVE FUNCTION SOLVING

4.1. Multi-objective function of the proposed

According to the actual operation of the hybrid energy storage system, the objective function of aiming at improving the ability of the load fluctuation smoothing and reducing the daytime peak-valley difference is as follows:

In order to make the control strategy more desirable for the intended purpose, the following rules are made: the period of the control strategy is 1h and it is divided into 60 periods. That is, there are 60 mins. The objective function is shown in Equation (5).

$$\begin{cases} F_1 = \min \sum_{i=1}^{60} (P_{LOAD_i} - P_{LINE_i})^2 \\ F_2 = \min[\max(P_{LINE_j}) - \min(P_{LINE_k})] \end{cases}$$

Equation 5: F_1、F_2

P_{LOADi} =Load power of in its period

P_{LINEi} =DC bus power of microgrid in its period

$\max(P_{LINEj})$ =period with maximum bus power in a control strategy

$\min(P_{LINE_k})$ =period with minimum bus power in a control strategy period

4.2. Improved Particle Swarm Optimisation

Particle swarm algorithm is an overall optimisation algorithm based on group intelligent heuristic. The core idea of the algorithm is to refer to the individuals in the optimal position of the group, and the optimal position that the particle has reached to determine and adjust the direction and size of the next search. The mathematical Equation is shown as Equation (6).

Equation 6: x_{id} 、 v_{id}

$$\begin{cases} x_{id} = x_{id} + v_{id} \\ v_{id} = wv_{id} + c_1 r_1 (p_{id} - x_{id}) + c_2 r_2 (p_{gd} - x_{id}) \end{cases}$$

c_1 =Learning factor
c_2 =Learning factor
r_1, r_2 =Random number between (0,1)
w =Inertia weight factor

Each particle has a dimension of the position vector and velocity vector. At the initial stage of the algorithm, each particle is randomly distributed into the space, and then the fitness of each particle at the current position is calculated. Each particle will adjust and calculate the velocity vector and position of the particle according to its own inertia, experience, and the position of the group's optimal value before each iteration. Until the P_{best} is found.

However, in the process of using traditional particle swarm algorithm to find the solution, although the algorithm has the advantage of fast convergence, there is a phenomenon called "precocious". When a particle is in the local optimal solution, the other particles around will quickly move closer to the particle, making the algorithm into the local optimal solution. Secondly, the value of has great influence on the result of the algorithm, and the larger convergence is beneficial to convergence of the algorithm. The smaller algorithm is helpful to improve the search precision. Combined with the actual work of hybrid energy storage system, a self-adjusting strategy is added, that is setting the maximum times of local search iterations. When the number of iterations has been processed, if P_{best} of group still can not meet the needs of the system error, then the current P_{best} is saved. The particles around the local optimal solution will be initialised again. It is rectified according to Equation (7). Modify the inertia weight factor of the particle swarm algorithm and increase the compensation coefficient. When the particle distance from the overall optimal value is long, the value of is increased to speed up the searching process and convergence of the system. When the particle distance from the overall optimal value is short, the value of is decreased to improve the searching accuracy.

Equation 7: w

$$w = \begin{cases} w' + k' \dfrac{dv_{id}}{dt} & g'_{best} > \Delta error \\ w' - k'' \dfrac{dv_{id}}{dt} & g'_{best} < \Delta error \end{cases}$$

w' =Reference value of w
k' =Compensation coefficients
k'' =Compensation coefficients
vid =Current particle velocity
$\Delta error$ =Current particle velocity

At the same time, in order to play the advantages of optimal particle of all the particles, the efficiency of the algorithm is improved. A phase-out identification strategy is introduced to the algorithm. That is, in each iteration of the system, the particles of continuous deterioration are reset and then return to the location for research.

4.3. Multiobjective function solving

Since there are two objective functions in the system, the objective functions need to be processed. The traditional method is to introduce the proportional coefficient, and take into account the impact of each objective function on particle flight to determine the scale factor. However, this method can not accurately search the overall optimal

value, and when the number of objective functions is further increased, when determine the scale factor the method not only requires a large amount of computation, but also leads to further expansion of the error.

Therefore, in this paper, the overall solution method is utilised, through the multi-objective function to jointly guide the various particles in the decision variable space flight. Because of the existence of multiple objective functions, the particles do not move along the direction of the function F_1 , nor move along the direction of the function F_2 , but move along a certain direction between function F_1 and the function F_2 , thus making it into the inferior solution. The specific process is as follows:

1) First find the overall corresponding extremes of each objective function for each particle. In this case $G_{best}[1]$ and $G_{best}[2]$ should be found.

2) And then find the individual extremes of each corresponding target function of each particle during the movement. In this case $P_{best}[1,i]$ and $P_{best}[2,j]$ should be found.$P_{best}[1,i]$ is the individual extreme of the particle in the first objective function.$P_{best}[2,j]$ is the extreme value of the individual particle in the second objective function.

3) When the algorithm starts, $G_{best}[1]$ and $G_{best}[2]$ are will be used as the "default" value. When the velocity of each particle needs to be updated, the individual extremes of each particle are judged to be superior to the "default" by judging the individual extremes of the particle. Determine whether to select the updated location or select a random value in the individual extremum.

After several iterations, we can determine the overall optimal value under multiple objective functions.

4.4. Algorithm Constraints

After determining the objective function, taking into account the optimal operating characteristics of the battery-supercapacitor and the management strategy of the energy storage system, it is necessary to establish the constraint according to some basic requirements of the hybrid energy storage system. The constraints are as follows:

1) Energy conservation constraints. According to the law of conservation of energy, the contribution of photovoltaic power generation at a given time, the output of the battery and the output of the super capacitor should be equal to the power on the DC bus plus the grid power (Liu, 2014). Mathematical formula is as follows Equation(8):

Equation 8:Energy conservation constraints

$$Q_{Vi} + Q_{SCi} + Q_{BATi} = Q_{linei}$$

Q_{vi} =Photovoltaic output

Q_{sci} =Super capacitor output

Q_{BATi} =Battery output

Q_{linei} =Power of bus load

Q_{gridi} =Microgrid connected power

2) SOC constraint (Chen, 2016). The overcharge and over discharge of the energy storage device have negative effects on the life and performance of the device. Therefore, it is necessary to limit the SOC of the battery and the super capacitor. Mathematical formula is as follows Equation (9)

Equation 9: SOC constraint

$$\begin{cases} 15\% \le SOC_{SCi} \le 90\% \\ 15\% \le SOC_{BATi} \le 85\% \end{cases}$$

SOC_{sci} =SOC of the super capacitor

Q_{sci} = SOC of the battery

3) Maximum power constraint. The output power of the battery and super capacitor should not be greater than its rated power.

4.5. Algorithm specific solution process

The algorithm solution steps are shown in Figure 4.

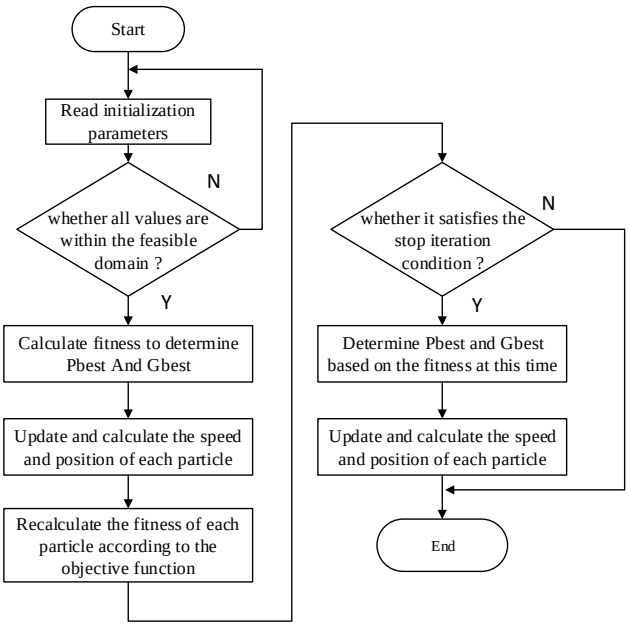

Figure 4: Algorithm control flow chart

5. ANALYSIS OF EXPERIMENTAL RESULTS OF IMPROVED HYBRID ENERGY STORAGE CONTROL STRATEGY

In order to verify the correctness of the output coefficient of each energy storage unit in the improved microgrid, the experimental verification is carried out.

The power demand fluctuation on the micro-grid DC bus is sampled. The parameters are set as follows（Table 2）:

Table 2: Experimental platform construction design index

parameter name	Parameter value
Operating temperature	T_C=25°C
DC bus rated voltage	VDC=500V
Battery rated voltage	VBAT=300V
Battery rated capacity	500Ah
Battery initial state of charge	SOC=60%
Super capacitor rated voltage	VSC=400V
Super capacitor rated capacity	60F
Transmission efficiency	0.95
Sampling frequency	40KHZ
switch frequency	10KHZ

The power smoothing object is the microgrid power plant of 100KW. The typical DC bus power demand curve is shown in Figure 5, in the sampling period of 5 mins, the maximum power requirement is 105KW, the minimum power requirement is 73KW.

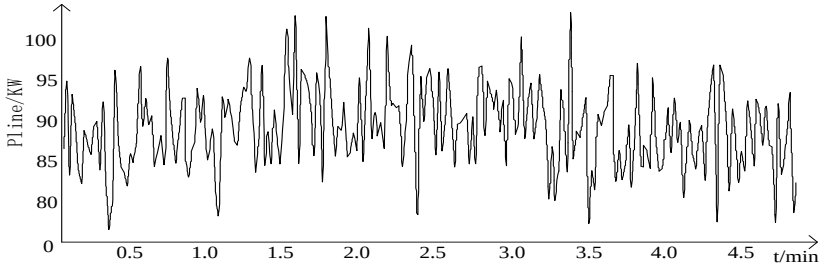

Figure 5: Power demand fluctuation on DC bus

Perform a comparative experiment test. The performance of the improved two-order low-pass filter in the application of the proposed control strategy was tested. It's shown in Figures 6, 7.

In order to verify whether the high frequency and the low frequency components can be distinguished fast and accurately, achieve the objectives of smoothing of the load voltage and reducing the daytime peak valley difference. And ensure SOC of each energy storage unit will not cross.

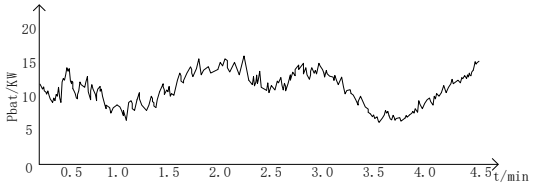

Figure 6: power of the battery after strategy

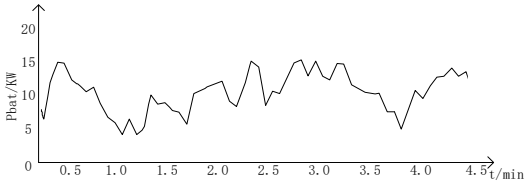

Figure 7: output of the battery before

As shown in Figure 7, when the control strategy proposed in this paper is not added to the system in the hybrid energy storage system, the battery charge and discharge are very frequent and volatile. After using the control strategy proposed in this paper, as shown in Figure 6, fluctuations in the system are significantly suppressed, and the battery output is reduced. The reduction of battery output means that the battery's energy consumption rate is slowed down, and the times of battery charging and discharging is reduced. Therefore, through the comparison of Figure 6 and Figure 7, it can be found that the control strategy can reduce the times of battery charging and discharging and output fluctuations.

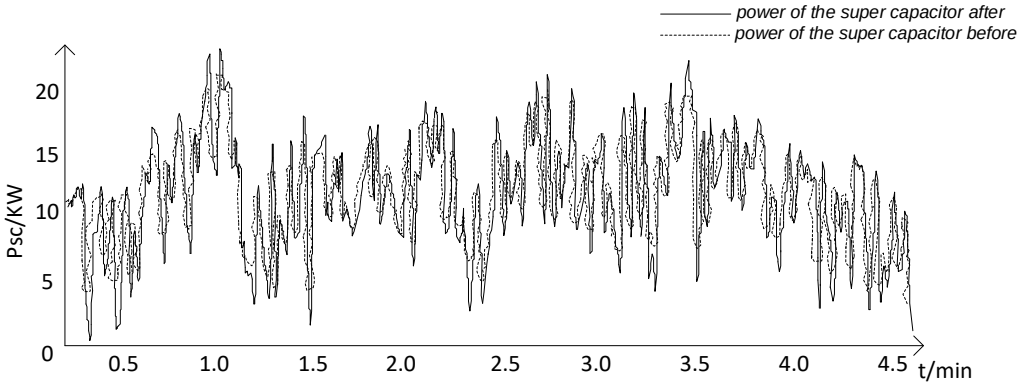

Figure 8: power of the super capacitor after and before

By the comparison Figure 8, It can be seen that after using the control strategy. The super capacitor has the advantages of high power density and fast response, and as much as possible to suppress the power fluctuation of the DC bus, so the Power fluctuations of super capacitor will increase. At this point, the super capacitor takes on more high-frequency fluctuations, reduces the impact of high-frequency fluctuations on the battery, and the desired results is achieved.

Figure 9 is the DC bus on the power fluctuations after using the proposed control strategy. Compared with the power demand fluctuation on the DC bus, not only the fluctuation of the power curve is suppressed, but also the daytime peak-valley difference is also significantly reduced.

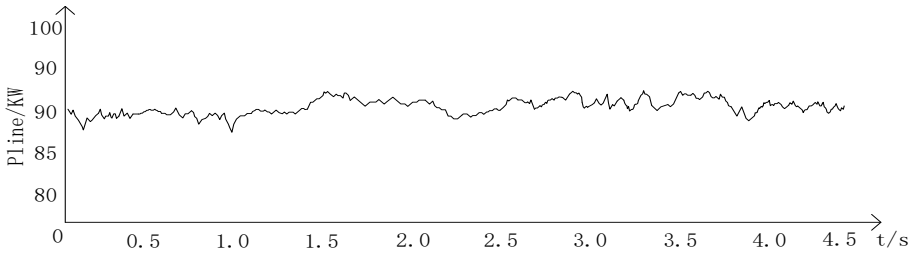

Figure 9: DC power fluctuation after using this control strategy

Comparing Figure 5 with Figure 9 can be seen that after using this control strategy, the DC bus power peak-valley decrease from 30kW down to 10kW. And in the 4.5min control cycle, the DC bus power tend to ease from the previous frequent and violent fluctuations. Figure 6 with Figure 7 ,it can be seen after using the control strategy, the battery no longer needs to bear too much of the high-frequency power fluctuations load side, the discharge curve is more smooth, the work has been greatly improved, The service life has been extended. Comparing power of the super capacitor after and before in Figure 8, it can be seen that after using the control strategy, compared with the traditional control strategy, the super capacitor bears more high-frequency components. It can be seen that the improved control strategy of the hybrid energy storage system can give full play to the advantages of the energy storage units in the hybrid energy storage system.

6. CONCLUSION

This paper first analyzes the characteristics and differences between the different devices in the hybrid energy storage system, and then introduces the concept of different energy storage device withstanding different frequency of the bus load fluctuation. And the objective function is established by using the improved particle swarm algorithm to reduce the load fluctuation and the peak-valley difference. Among them, the improved hybrid control strategy under the improved particle swarm optimisation algorithm has the characteristics of fast convergence speed and high computational efficiency in the process of optimisation, but it will not fall into the local optimal solution. Finally, the experimental data verify that the control strategy proposed in this paper can significantly reduce the battery charge and discharge and output, the super capacitor bears more high-frequency components, thus reducing the DC bus peak-valley difference of about 60%, and smoothing the power fluctuations, The effectiveness of the control strategy is verified.

7. REFERENCES

Chen Z. Optimal Stabilisation Control Strategy of Microgrid Virtual Energy Storage System Based on Continuous State Variables Constraints [J] .Power System Technology, 2017 (01): 55-63.

Li Z, Li M. Power balance control strategy of hybrid-bus microgrid [J]. Journal of Central South University, 2016 (06): 2331-2338.

Luo P. Optimisation of hybrid micro-grid energy storage capacity based on spectrum analysis [J]. Power System Technology, 2016 (02): 376-381.

Chong LW, Wong YW, Rajkumar RK, Rajkumar RK, Isa D. Hybrid energy storage systems and control strategies for stand-alone renewable energy power systems[J]. Renewable & Sustainable Energy Reviews, 2016, 66:174-189.

Tian M. DC microgrid hybrid energy storage based on battery and supercapacitor [D]. Beijing JiaoTong University, 2016:2-5.

Ma S. Volume configuration of hybrid energy storage system to stabilise wind power fluctuation [J] .Power System Protection and Control, 2014(08):108-114.

Lee DJ, Wang L. Small-Signal Stability Analysis of an Autonomous Hybrid Renewable Energy Power Generation/Energy Storage System Part I: Time-Domain Simulations [J]. IEEE Transactions on Energy Conversion, 2008(01):311-320.

Yang J. Research on optimal configuration of hybrid energy storage capacity in independent scenery power generation [J] .Power System Protection and Control, 2015(03):120-128.

Granado PCD, Pang Z, Wallace SW. Synergy of smart grids and hybrid distributed generation on the value of energy storage[J].Applied Energy, 2016,170:476-488.

Jiang W.Space-confined assembly of all-carbon hybrid fibers for capacitive energy storage: realizing a built-to-order concept for micro-supercapacitors[J]. Energy & Environmental Science, 2016,9(2):611-622.

Zhang Q. Capacity Determination of Hybrid Energy Storage System for Smoothing Wind Power Fluctuations with Maximum Net Benefit [J]. Transactions of China Electrotechnical Society, 2016(14):40-48.

Li C. Applying Supercapacitor to the DC Power Supply System of the Smart Substation [D]. Beijing Jiaotong University, 2016:4-8.

Chen S. Research on power management strategy of PV micro-grid with hybrid energy storage system [D]. Jiangsu University, 2016:11-13.

Chen H. Optimal Energy Management and Configuration for Stationary Super capacitor Energy Storage System Applied in Urban Rail Transit Based on Hybrid Particle Swarm Algorithm [D]. Beijing Jiaotong University, 2016:13-17.

Liu Y. Study on low-voltage ride through control strategy of photovoltaic system based on super-capacitor [J]. Power System Protection and Control, 2014(13):109-117.

Choi JW, Heo SY, Kim MK. Hybrid operation strategy of wind energy storage system for power grid frequency regulation [J]. Iet Generation Transmission & Distribution, 2016,10(3):736-749.

153: Research on energy management strategy of EV HESS based on fuzzy control

Honglin BIAN[1], Jiasheng ZHANG[2], Zhihao CHENG[3]

[1] *Hubei Key Laboratory for High-efficiency Utilisation of Solar Energy and Operation Control of Energy Storage System, Hubei University of Technology, 1378733981@qq.com*
[2] *Hubei Key Laboratory for High-efficiency Utilisation of Solar Energy and Operation Control of Energy Storage System, Hubei University of Technology, 852815242@qq.com*
[3] *Hubei Key Laboratory for High-efficiency Utilisation of Solar Energy and Operation Control of Energy Storage System, Hubei University of Technology, 1038687375@qq.com*

Aiming at the real-time distribution of output power of lithium battery and ultracapacitor hybrid energy storage system, in order to improve the accuracy of policy control and prolong the service life of battery, a fuzzy control strategy based on parameter improvement is designed to manage the power of the electric vehicle hybrid energy storage system in this paper, so as to rationally allocate the power of the lithium ion battery and the supercapacitor. A dynamic power model is established based on the real-time charging state of the hybrid energy storage unit. In this method, the power model and the physical quantity of input parameters are unified, and the real time maximum allowable charge discharge power and the system demand power are taken as input parameters, and the more accurate fuzzy control rules are Formulated, thus the power distribution of fuzzy control is realised. The experimental platform is built through the Arbin battery test system, and the fuzzy control strategy with improved parameters is compared with the traditional fuzzy control. The experimental results show that the fuzzy control system improved by the parameters is stable, the average current amplitude of lithium battery is reduced by 5% per unit time, the energy consumption of the battery is reduced, the characteristics of the supercapacitor are better played, and the working efficiency is improved. It can extend the service life of lithium battery, and the input volume is all power value. It is easier to compare and classify, and has higher accuracy for meeting the system power requirement.

Keywords: HESS; fuzzy control; super capacitor; electric vehicle; power model

1. INTRODUCTION

Automobile is a means of transportation which is closely related to people's life. Under the background of the increasing shortage of mineral energy and the upgrading of environmental protection, the Electric Vehicle (EV), with the advantages of low emission and high efficiency, has attracted more and more attention from the society.

After years of research, the endurance capacity of electric vehicles has been greatly improved, and civilian electric vehicle products have gradually expanded the scale of promotion and application. However, as an energy type energy storage device, a lithium battery has a low power density and a short cycle life, and it is difficult to realise rapid output and recovery of instantaneous high power. To solve this problem, a hybrid energy storage system (HESS) system consisting of a lithium battery and a supercapacitor (SC) can be better solved.

The HESS power allocation control strategy is the key to HESS research. At present, domestic and foreign scholars have studied more power distribution strategies, such as filter control, particle swarm optimisation, logic threshold control, and fuzzy logic control. The filter control uses a low-pass filter to divide the demand power into the average power and the peak power, and achieves power distribution by controlling the time constant. However, this strategy cannot adapt well to the actual changing conditions. The particle swarm algorithm controls the use of the HESS model to establish a multi-objective function and optimises the optimal power distribution coefficient, but the algorithm is easily trapped in the local optimal solution. Both the logic threshold control and the fuzzy logic control are rule-based control strategies. The control idea is roughly the same, except that the fuzzy control threshold is blurred. The disadvantage of fuzzy control is that the control accuracy is limited, the flexibility is not enough, and online adjustment cannot be made in time.

Based on the above analysis, an improved parameter fuzzy control strategy is adopted to allocate the power of Li ion battery and super capacitor reasonably. While taking into account the characteristics of fuzzy control stability, in view of the limited control precision in the hybrid energy storage application, the power parameter improvement method is adopted to optimise the problem. This paper first establishes the control structure of the hybrid energy storage system, and then establishes the power mathematical model of the energy storage system, which is improved to the maximum power model on the basis of the traditional state of charge state model. Finally, the fuzzy control of parameter input is improved, the fuzzy control rules and membership functions are Formulated, and the output power distribution coefficient is obtained.

2. HYBRID ENERGY STORAGE SYSTEM TOPOLOGY

Lithium battery is used as power storage and output device, and the voltage changes slowly during vehicle driving. As the main variable, current is one of the control objectives of power allocation strategy. Supercapacitor, as an auxiliary power supply, has the characteristics of high power ratio, the main power output and recovery device. In the stage of vehicle acceleration and braking, high power output and recovery can be realised, which reduces the impact of large current on the lithium battery and reduces the energy dissipation. The hybrid energy storage composed of lithium battery, ultracapacitor and DC/DC converter forms the energy source of EV. Since supercapacitors and lithium batteries are different in voltage properties, in order to improve the control flexibility, the DC/DC converter and the super capacitor are connected in series with the lithium battery in a series manner to form a topology as shown in Figure 1. The controller can not only regulate the terminal voltage of the super capacitor, but also control the charge discharge current of each unit of the hybrid energy storage device.

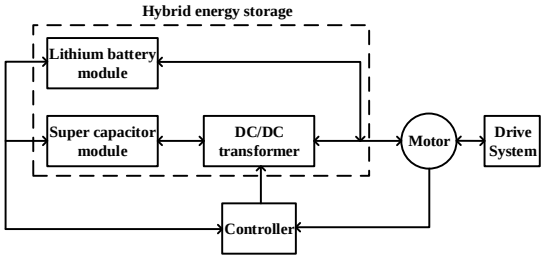

Figure 1: Topological structure of hybrid energy storage system

3. HYBRID ENERGY STORAGE SYSTEM CONTROL STRATEGY

3.1. Working Principle of Hybrid Energy Storage System

In addition to meeting the power demand at any time during the operation of an electric vehicle, the hybrid energy storage system must also recover the braking energy as much as possible. The control part of the hybrid energy storage system uses a three-dimensional input fuzzy algorithm: The fuzzy controller will fuzzify the input parameters

such as system demand power $P_{req}(t)$, lithium battery real-time maximum allowable power $P_{B\_limit}(t)$, and supercapacitor real-time maximum allowable power $P_{SC\_limit}(t)$, and classify and classify the fuzzy rules; Then unambiguously, the controller finally outputs the power distribution coefficient λ(t) of the lithium battery and the super capacitor. The DC/DC converter is the implementing agency of the entire control system. The power distribution coefficient λ(t) controls the power switching of the DC/DC converter, which in turn controls the actual power output values of the lithium battery and the supercapacitor to achieve energy control management of the entire hybrid energy storage system (Figure 2).

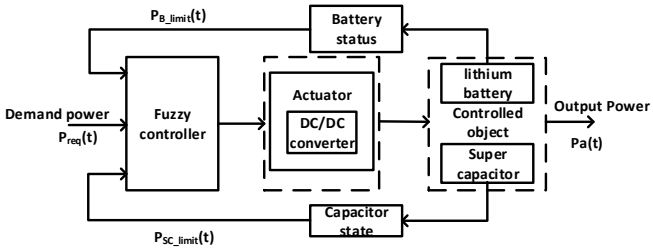

Figure 2: Working principle of hybrid energy storage system

3.2. Power model of hybrid energy storage system

(1) System demand power at t time

In the ideal condition, the power of the system is equal to the output power of the hybrid energy storage. The change of the acceleration in the car reflects the change of the output power of the hybrid energy storage. During operation, the acceleration operation of vehicle can be divided into continuous acceleration, constant power acceleration and maximum power acceleration. From the basic physical and mechanical analysis, we can see that traction, ground friction, air resistance, gravity and supporting force are the driving forces of automobiles. According to Newton's second law, we can get the Equation 1:

Equation 1: the force that the car receives when it is driving

$$\mathrm{m}\frac{\mathrm{dv}}{\mathrm{dt}} = \frac{P_{ref}}{v} - mgf - \frac{\mathrm{C_D}Av^2}{21.25}3.6^2$$

Where:

m = the quality of the car (kg)

$\frac{\mathrm{dv}}{\mathrm{dt}}$= the acceleration of the car(m/s^2)

g= the acceleration of gravity(m/s^2)

P_{ref}= the power demand of the system when the vehicle is traveling(kW)

v= the speed of the car(m/s)

f= the coefficient of resistance of the road when the car is moving

$\mathrm{C_D}$= the air resistance coefficient when the car is traveling

A= the frontal area when the car is driving[11](m^2)

Table 1 shows the relevant simulation parameters when a car is traveling.

Table 1: Simulation parameters in vehicle driving

Parameters	Value
Quality /kg	1000
Road surface resistance coefficient	0.0195
Air resistance coefficient	0.335
Frontal area/m^2	2.0
Gravity acceleration /$\mathrm{m}\cdot s^{-2}$	9.8

Equation 1 and Table 1 can be used to determine the relationship between the vehicle's demand power and speed in Equation 2:

Equation 2: the corresponding demand power of the car at the corresponding speed

$$P_{ref} = 0.003984v^3 + 191.1v + 1000v\frac{\mathrm{dv}}{\mathrm{dt}}$$

Where:

v = the speed of the car(m/s)

P_{ref}= the corresponding demand power of the car at the corresponding speed(kW)

Equation 2 can obtain the corresponding demand power of the car at the corresponding speed, which is helpful for the selection of the hybrid energy storage capacity, and also provides the basis for the power distribution of the energy storage system under different working conditions.

(2) Maximum charging and discharging power of hybrid energy storage at time t

The maximum power that the hybrid energy storage can provide determines the maximum acceleration of the car when it is working. In practical work, lithium batteries and supercapacitors are used as electric energy carriers. In the face of complex and ever-changing operating conditions, the remaining power is constantly changing. The trend of the remaining power has a close relationship with the operating mode of the energy storage carrier t, the ambient temperature and the switching losses. According to the law of conservation of energy, an iterative algorithm is used to obtain the relation of the remaining energy of the hybrid energy storage in the work.

Equation 3: At t time, the remaining capacity of the energy storage carrier during charging process

$$\mathrm{E(t)} = (1 - \sigma_{adr})\mathrm{E(t-1)} + P_{ESS}\Delta t\eta_C$$

Equation 4: At t time, the remaining capacity of the energy storage carrier during discharging process

$$\mathrm{E(t)} = (1 - \sigma_{adr})\mathrm{E(t-1)} + \frac{P_{ESS}\Delta t}{\eta_D}$$

Where:

$\mathrm{E(t)}$ = the remaining power at the end of time of energy storage carrier t(kW)

$P_{ESS}(t)$= the charging and discharging power at time t of the energy storage carrier t(kW)

σ_{adr}= the self-discharge rate of the energy storage carrier

η_C= the charge efficiency of the energy storage carrier

η_D= the discharge efficiency of the energy storage carrier

Δt= the duration of each calculation window(s)

The maximum allowable charge and discharge power at time t of the energy storage carrier t is determined by its own charge and discharge characteristics and the remaining power at time t, and its expression is as follows.

Equation 5: when charging, the maximum allowable charge discharge power of the energy storage carrier at t time

$$P_{ESS\_limit}(t) = \min\{P_{maxC}, \frac{P_{maxC}, E_{max} - (1 - \sigma_{adr})\mathrm{E(t-1)}}{\eta_C\Delta t}\}$$

Equation 6: when discharging, the maximum allowable charge discharge power of the energy storage carrier at t time

$$P_{ESS\_limit}(t) = \min\{P_{maxD}, \frac{[(1 - \sigma_{adr})\mathrm{E(t-1)} - E_{min}]\eta_D}{\Delta t}\}$$

Equation 7: maximum allowable charge discharge power of a hybrid energy storage system

$$P_{ESS\_limit}(t) = P_{SC\_limit}(t) + P_{B\_limit}(t)$$

Where:

$P_{ESS\_limit}(t)$ = the maximum permissible charge discharge power of the energy storage carrier at t time(kW)

$P_{ESS}(t)$= the charging and discharging power at time t of the energy storage carrier t(kW)

P_{maxC}= the maximum charging power determined by the charge discharge power characteristics of the energy storage carrier, Positive value(kW)

P_{maxD}= the maximum discharging power determined by the charge discharge power characteristics of the energy storage carrier, Positive value(kW)

E_{max}= the maximum of the energy storage carrier(kW)

E_{min}=the maximum and minimum of the energy storage carrier(kW)

$P_{B\_limit}(t)$=battery power(kW)

$P_{SC\_limit}(t)$= supercapacitor power(kW)

$P_{ESS\_limit}(t)$= maximum allowable charge discharge power of a hybrid energy storage system(kW)

$\min\{\cdot\}$= allowable charge discharge power of the system.

3.3. Fuzzy control power optimal allocation

In the actual work of electric vehicles, mixed energy storage has two states: discharge and charging. Under different working conditions, the nature of demand power $P_{req}(t)$ is different, and the Formulation of control strategies is also different. The demand power $P_{req}(t)$ can be divided into average power and peak power, lithium battery takes on average power, and super capacitor is responsible for peak power. In the discharge state, the instantaneous large current discharge of the lithium battery must be avoided. In the charging state, the super capacitor should ensure that the braking energy can be recovered as much as possible. The control strategy is designed according to the different characteristics of the two states.

When demand power $P_{req}(t) > 0$

When the demand power is $P_{req}(t) > 0$, the hybrid energy storage is the discharge mode, and the basic control strategy is as follows.

When the demand power $P_{req}(t)$ is very small. If $P_{B\_limit}(t)$ is higher, the lithium battery discharges separately; if $P_{B\_limit}(t)$ is moderate, the lithium battery discharge alone; if $P_{B\_limit}(t)$ is lower, $P_{SC\_limit}(t)$ is moderate or higher, the lithium battery and supercapacitor discharge together, or the lithium battery discharge alone.

When the demand power $P_{req}(t)$ is small. If $P_{B\_limit}(t)$ is higher, the lithium battery discharges separately; if $P_{B\_limit}(t)$ is moderate and $P_{SC\_limit}(t)$ is higher, the lithium battery and supercapacitor discharge together, otherwise the lithium battery can discharge alone. If $P_{B\_limit}(t)$ is low and $P_{SC\_limit}(t)$ is moderate or higher, the lithium battery and supercapacitor will discharge together, otherwise the lithium battery will be discharged separately.

When the demand power $P_{req}(t)$ is moderate. If $P_{B\_limit}(t)$ is higher and $P_{SC\_limit}(t)$ is higher, the lithium battery and supercapacitor will discharge together, otherwise the lithium battery will discharge separately. If $P_{B\_limit}(t)$ is moderate, $P_{SC\_limit}(t)$ is moderate or higher, the lithium battery and supercapacitor discharge together otherwise the lithium battery discharge alone; if $P_{B\_limit}(t)$ is low, the lithium battery and supercapacitor discharge together.

When the demand power $P_{req}(t)$ is large. At this time, the lithium battery and the supercapacitor discharge together.

When demand power $P_{req}(t) < 0$

When the demand power is $P_{req}(t) < 0$, the hybrid energy storage is the charging mode. At this time, the control strategy is not classified according to the size of $P_{req}(t)$, and only the $P_{B\_limit}(t)$ and $P_{SC\_limit}(t)$ states are required. The size of $P_{B\_limit}(t)$ and $P_{SC\_limit}(t)$ is also a reflection of the residual capacity of lithium battery and ultracapacitor, and its basic control strategy is as follows.

If $P_{SC\_limit}(t)$ is very low, super capacitor will be charged separately.

If $P_{B\_limit}(t)$ is low and $P_{SC\_limit}(t)$ is low, the lithium battery and super capacitor will be charged together, otherwise the super capacitor will be charged separately.

If $P_{SC\_limit}(t)$ is moderate, $P_{B\_limit}(t)$ is low or moderate, the lithium battery and super capacitor will be charged together, otherwise the super capacitor will be charged separately.

If $P_{SC\_limit}(t)$ is high, the lithium battery and super capacitor will be charged together.

Equation 8: constraint condition

$$K_B(t) + K_{SC}(t) = 1$$
$$P_{B\_min}(t) < P_B(t) < P_{B\_limit}(t)$$
$$P_{SC\_min}(t) < P_{SC}(t) < P_{SC\_limit}(t)$$

Where:

$K_B(t)$ = the power distribution coefficients of lithium battery

$K_{SC}(t)$= the power distribution coefficients of supercapacitor

$P_B(t)$= output power of lithium batteries(kW)

$P_{SC}(t)$= output power of supercapacitor(kW)

3.4. Fuzzy membership function and rule Formulation

The quantitative description of fuzzy language variables is determined by its membership function, and the membership function is selected correctly. It is the basis of using fuzzy set theory to solve practical problems. For a typical fuzzy controller, when the input fuzzy subset is evenly distributed in the fuzzy universe, the structure of the fuzzy controller is best.

Equation 9: the membership degree interval of lithium battery

$$0 < \frac{P_B(t)}{P_{B\_limit}(t)} < 1$$

Equation 10: the membership degree interval of super capacitor

$$0 < \frac{P_{SC}(t)}{P_{SC\_limit}(t)} < 1$$

Where:

$P_B(t)$ = battery power(kW)

$P_{B\_limit}(t)$= maximum battery charge and discharge power(kW)

$P_{SC}(t)$= super capacitor power(kW)

$P_{SC\_limit}(t)$= maximum super capacitor charge and discharge power(kW)

When $P_{req}(t) > 0$, the electric vehicle is in the discharged output power state. The membership functions of energy devices and distribution factors are shown in Figure 3 (below).

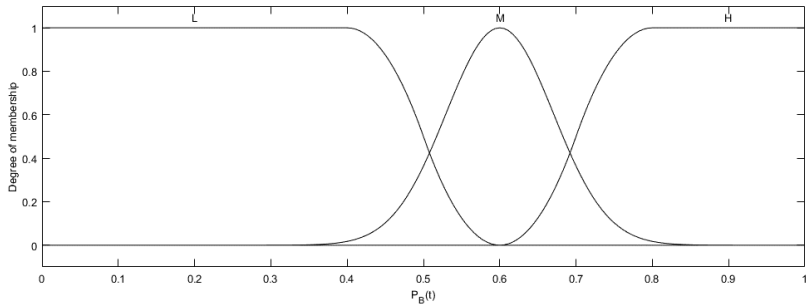

(a) Membership function of Lithium battery

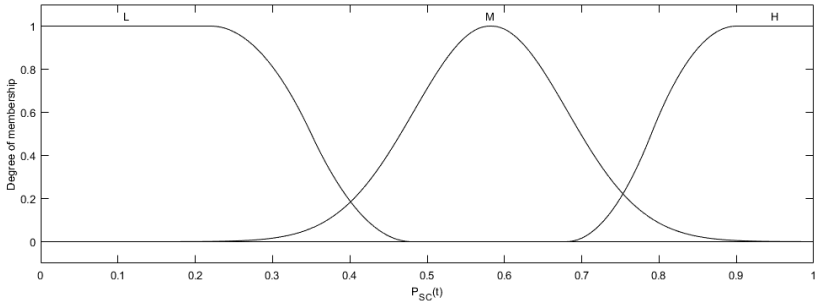

(b) Membership function of supercapacitor

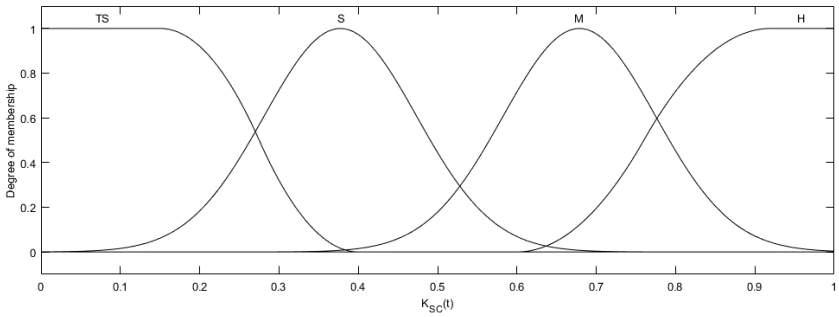

(c) Membership function of distribution factor

Figure 3 Membership function [$P_{req}(t) > 0$]

In this paper, the fuzzy rules are used in the form of if-then:

If $P_{req}(t)$ is A and $P_{B\_limit}(t)$ is B and $P_{SC\_limit}(t)$ is C， Then $K_{SC}(t)$ is D。

The fuzzy control rules for $P_{req}(t) > 0$ are shown in Table 2.

When the vehicle braking energy is recovered to $P_{req}(t) < 0$, the membership function of the lithium battery and the distribution factor is the same as that of the $P_{req}(t) > 0$. The supercapacitor membership function is shown in Figure 4, and the specific rules are shown in Table 2.

Table 2: Fuzzy control table [$P_{req}(t) > 0$]

$K_{SC}(t)$		$P_B(t)[P_{req}(t) = \mathrm{TS/S/M/B}]$		
		L	M	H
$P_{SC}(t)$	H	TS-S/S-S/M-B/B-B	TS-TS/S-S/M-M/B-M	TS-TS/S-TS/M-S/B-S
	M	TS-S/S-S/M-M/B-B	TS-TS/S-TS/M-S/B-M	TS-TS/S-TS/M-TS/B-S
	L	TS-TS/S-TS/M-S/B-M	TS-TS/S-TS/M-TS/B-S	TS-TS/S-TS/M-TS/B-S

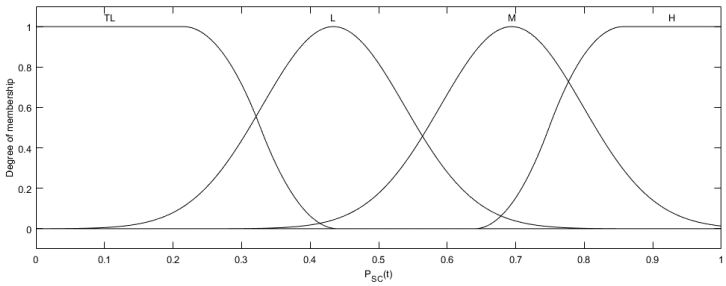

Figure 4: Membership function of Supercapacitor $P_{SC}(t)$ [$P_{req}(t) < 0$]

Table 3: Fuzzy control table [$P_{req}(t) > 0$]

$K_{SC}(t)$		$P_B(t)$		
		L	M	H
$P_{SC}(t)$	TL	B	B	B
	L	M	B	B
	M	S	M	B
	H	TS	TS	TS

4. EXPERIMENTAL VERIFICATION

In order to verify the effectiveness of fuzzy control parameters to improve the optimisation, this paper adopts a comparative method. Under the same experimental conditions, the experiment is carried out by the fuzzy control algorithm before and after the improvement of the parameters. A hybrid energy storage experiment platform is set up as shown in Figure 5. The experimental platform is made up of power lithium battery, super capacitor, bidirectional DC/DC converter, ARBIN multifunctional battery testing system and central control computer. The capacity of the power lithium battery is 48V, 100Ah, the capacity of the super capacitor is 48V, 165F, the maximum continuous current is 100A, and the specific parameters are shown in Table 4.

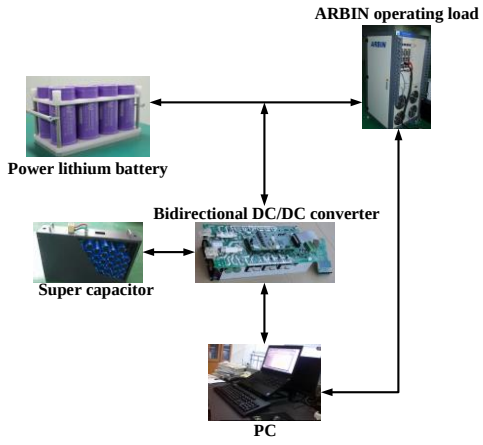

Figure 5: Hybrid energy storage experimental platform

One of the most important functions of the ARBIN battery test system used in this experiment is electric vehicle load test. The test equipment is a dual channel. It can also collect the changes of current and voltage and power of lithium battery and ultracapacitor during load test. The control computer, based on the data collected by the ARBIN equipment, uses the control logic built on the Simulik to control the output signal of the DC/DC converter and realise the management of the energy flow. The gray arrow in Figure 5 represents the flow of energy, and the white arrow represents the flow of the control signal.

Table 4: Parameters of lithium battery and supercapacitor

Parameter type	Lithium battery	Supercapacitor
Rated capacity/kW·h	4.8	2.4
Maximum continuous discharge power/kW	4.8	4.8
Maximum continuous charging power/Kw	4.8	4.8
Permissible discharge depth/%	20-90	25-95
Self discharge rate/%·min^{-1}	0	0.02
Charge discharge efficiency/%	90	95

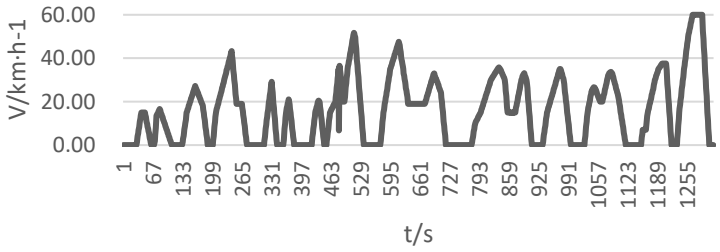

Figure 6: Vehicle speed under CBDC condition

The typical China Bus Driving Cycle (CBDC) was selected as the test condition (Figure 6). Compared with NEDC, the data of CBDC are closer to the actual working conditions, especially in the process of starting and stopping acceleration, which is more in line with the current traffic situation in China's big cities.

Figure 7 is the power demand of vehicle in CBDC condition. Before the experiment, the data is input into the test system to the end of the experiment, and the ARBIN equipment records all the data. The waveform of system demand power, lithium battery power and super capacitor power is shown in Figure 8. Compared with Figures 7 and 8, we can see that the improved fuzzy control strategy is satisfied with the power demand of the system.

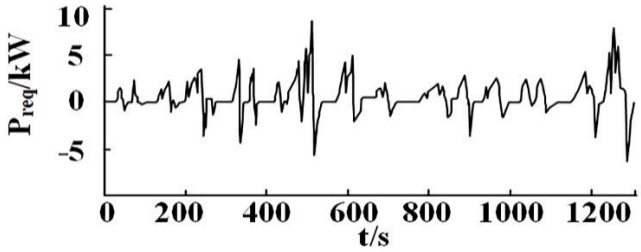

Figure 7: The power demand of the vehicle under CBDC condition

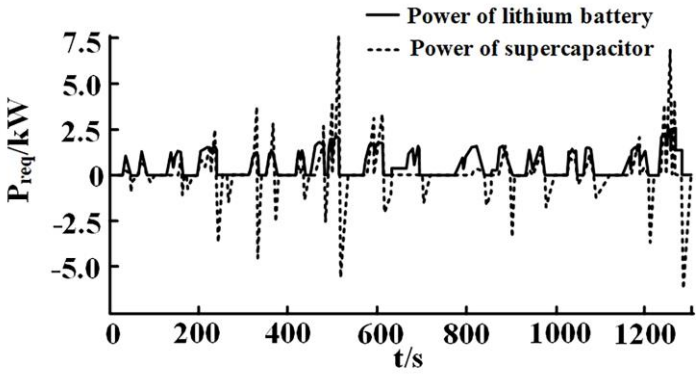

Figure 8: Power chart of parameter improved fuzzy control

For power allocation, combined with data for further comparative analysis. Because the lithium battery and the supercapacitor are parallel structures, in the most cases of the working process, the power is provided together, and the output endpoints are equal at both ends, only the output current of the lithium battery and the supercapacitor is different. The purpose of the hybrid energy storage control is to reduce the amplitude of the output power fluctuation of the lithium battery, suppress the change curve of the output current, and the change of the current of the HESS parameters before and after the improvement of the parameters as shown in Figure 9. In order to show the response of the parameter optimisation to the current more clearly, the current integral method is used to display the electricity consumption per unit time, that is, to reflect the change of current. Figure 10 shows the power consumption before and after the improvement of the parameters.

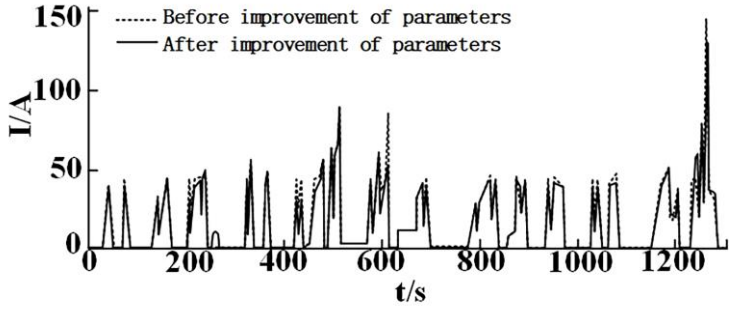

Figure 9: Comparison of the current changes before and after the improvement of HESS parameters

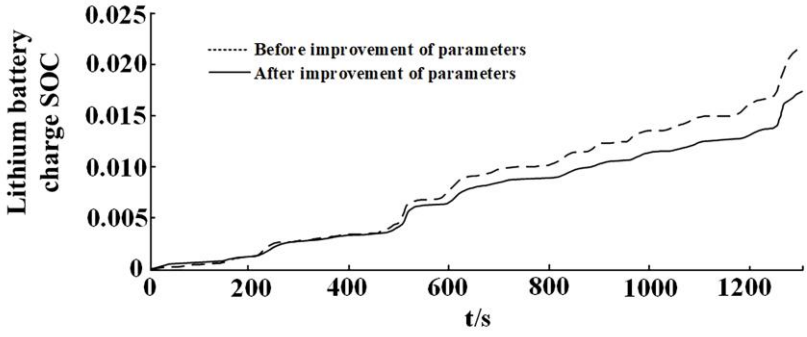

Figure 10: Comparison of energy consumption of lithium ion batteries

When the system demand power has both positive and negative values, when the demand power is negative, the vehicle is the brake state, and the supercapacitor is the main work, and the braking energy is recovered to the maximum. The basic conforms to the control strategy planning shown in Figure 8. From Figure 9 and Figure 10, we can see that the control strategy meets the demand, the super capacitor bears the peak power in the work, the output power of the lithium battery is stable, and there is no big instantaneous change. Through the comparison of power consumption, the average output current of lithium battery after improved parameters is less than that before improvement, and the energy consumption of lithium battery is reduced by about 5%.

5. CONCLUSION

In this paper, the hybrid energy management system of electric vehicle is deeply studied. On the basis of traditional fuzzy control, aiming at the problem of the limited precision of fuzzy control, the power model and the physical quantity of input parameters are adopted to make more precise fuzzy rules. The fuzzy control with improved parameters is the power value, which is easier to compare and classify. At the same time, it has higher accuracy to meet the power requirements of the system. Compared with the traditional fuzzy control power allocation strategy, the fuzzy control management strategy, which is improved by the parameters, reduces the current fluctuation of the lithium battery, reduces the energy consumption of the battery, and improves the performance of the supercapacitor and improves the working efficiency.

6. REFERENCES

Sheikhan M, Pardis R, Gharavian D. State of charge neural computational models for high energy density batteries in electric vehicles [J]. Neural Computing & Applications, 2013,22(6)：1171-1180.

Chang W Y. Estimation of the state of charge for a LFP battery using a hybrid method that combines a RBF neural network,an OLS algorithm and AGA [J]. International Journal of Electrical Power & Energy Systems, 2013,53(4)：603-611.

Xiong R, Cao J, Yu Q. Reinforcement learning-based real-time power management for hybrid energy storage system in the plug-in hybrid electric vehicle[J]. Applied Energy, 2018, 211:538-548.

Cao J, Xiong R. Reinforcement Learning-based Real-time Energy Management for Plug-in Hybrid Electric Vehicle with Hybrid Energy Storage System[J]. Energy Procedia, 2017, 142:1896-1901.

Wang Q, Sun Y, Huang Y. Research on the control strategy and optimisation of energy management system of hybrid energy storage in a hybrid electric vehicle [J].Transactions of China Electrotechnical Society,2014(S1)：155-163.

Sharafi M, Elmekkawy TY. Multi -objective optimal design of hybrid renewable energy systems using PSO -simulation based approach [J].Renewable Energy, 2014,68(68)：67-79.

Bocklisch T. Hybrid energy storage systems for renewable energy applications [J]. Energy Procedia, 2015,73：103-111.

Huang W, Xiong W, Che W. Application of Fuzzy Control in Hybrid Wind/PV Microgrid with Energy Storage [J]. Modern Electric Power, 2017.

Ding M, Lin G, Chen Z et al. A control strategy for hybrid energy storage system [J]. Proceeding of the CSEE, 2012,32(7)：1-6.

Du S, Zuo C. Self -adaptive fuzzy pi control in energy distribution of pure electric vehicle with dual -energy system [J].International Journal of Control & Automation, 2014(7)：273-286.

Qi H, Luo W, Yu J. Study on hybrid energy storage system control strategy and its testing [J]. Science Technology and Engineering, 2016,16 (10)：195-199.

Pan H. An image edge detection algorithm based on fuzzy theory [J].Journal of Chongqing Technol Business University (Sci Ed), 2013,30(7)：53-56.

155: Research on 1D photonic crystal filter applied to solar thermophotovoltaic system

Qiang WANG, Lingyun LIU, Yuan WANG, Jing TONG

Hubei Collaborative Innovation Center for High-efficiency Utilisation of Solar Energy, Hubei University of Technology, Wuhan, 430068, P. R. China;
School of Electrical and Electronic Engineering, Hubei University of Technology, Wuhan, 430068, China

The solar thermophotovoltaic system transforms the radiation emitted by thermal emitter into electrical energy when the emitter is heated by sunlights. The filter in the system reflects the longer wavelengths, and is transparent for the shorter ones. The optical filter can improve the efficiency of the solar thermophotovoltaic system. An 1-dimensional photonic crystal was studied numerically. It is shown that the cutoff wavelength of the filter is 2μm, and the average transmission for shorter wavelengths is > 70%, and the reflectance for longer wavelengths is > 90%. The 1-dimensional photonic crystal filter can improve the efficiency of the solar thermophotovoltaic system.

Keywords: solar thermophotovoltaic; 1D Photonic Crystal; filter

1. INTRODUCTION

Solar Thermophotovoltaic (STPV) is a technology that a absorber heat the radiator by absorbing sunlight, and the energy radiation from radiator is converted into electrical energy by PV. Optical filter is an important part of STPV system. Its main function is that transmission short-wavelength which can be absorbed by PV,and reflection long-wavelength which can not be absorbed by PV to heat radiator. So it can improve the efficiency of the system. The performance of the optical filter directly affects the conversion efficiency of the STPV system. Since the concept of photonic crystals was introduced in the 1980s (Yablonovitch 1987), it has attracted wide attention with its unique properties (Schneider 2003; Hattori 1996; Hattori 1997). Photonic crystal is an artificial dielectric structure with a periodic change of dielectric constant. It can modulate the state mode of photons, make the dispersion curve of light waves into a band structure, and exhibit a photonic band gap similar to the semiconductor band gap. The frequency falls on the forbidden band. The electromagnetic waves in the medium are prohibited from propagating, and the light whose frequency is outside the forbidden band can pass. So far, the theoretical and applied research of photonic crystals has achieved a series of results, such as photonic crystal microcavity and thresholdless lasers (Ye 1999), photonic crystal waveguides and optical fibers (Inouye 2003), photonic crystal polarisers (Liu 2008) and filters (Xue 2009), bistable and optical switch (Tian 2005), super prism (Fang 2004) and low loss mirror (Qin 2003). To be applied to a solar thermal photovoltaic system, the optical filter must meet two conditions: first, the cutoff wavelength should match the photovoltaic cell, and second, the reflected long wave and the transmitted short wave. This paper uses the band gap of photonic crystals.Characteristic (Wu 2006; Liu 2006), a photonic crystal filter with a symmetrical structure composed of high and low refractive index media was designed and the transmission and reflection spectra of the photonic crystal were calculated. The filter has a cut-off wavelength of 2 um, a short-wave average transmittance of more than 70%, and a long-wave average reflectance of more than 90%. The forbidden band width (Mauk 2003) of the GaSb photovoltaic cell is about 0.7 eV, and its corresponding wavelength is about 1.8 um. Most of the transmitted light of the filter can be absorbed by the GaSb battery.

2. STRUCTURAL DESIGN AND OPTIMISATION

The one-dimensional photonic crystal filter designed in this paper is an artificial optical material composed of two different refractive index media (A high-refractive index material and a low-refractive-index material), which are alternately arranged (Leung 1990). It is structurally simpler and easier to prepare than two-dimensional and three-dimensional photonic crystals. The structure of the one-dimensional photonic crystal filter designed in this paper is shown in Figure 1, where A and B are high refractive index TiO2 and low refractive index SiO2, respectively.

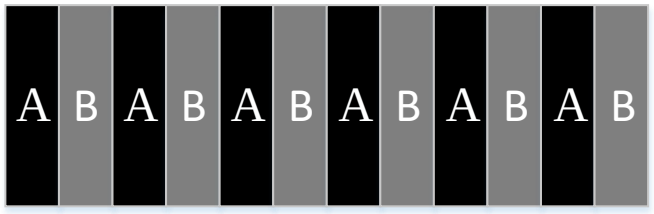

Figure 1: Schematic diagram of one-dimensional photonic crystal filter

The electromagnetic wave propagation characteristics in this structure can be calculated using the transfer matrix method (Yin 1987; Gong 2004). Let A and B have refractive indices n_1 and n_2, respectively, and the film thicknesses are d_1 and d_2, respectively. When the TE wave is incident, the characteristic matrix of each single layer film is:

$$M(z)=\begin{bmatrix}\cos(k_0 nz\cos\theta) & -(i/p)\sin(k_0 nz\cos\theta)\\ -ip\sin(k_0 nz\cos\theta) & \cos(k_0 nz\cos\theta)\end{bmatrix} \quad (1)$$

Where $k_0=2\pi/\lambda=\omega/c$, λ is the wavelength of the incident wave, which ω is the frequency of the incident wave, *c* is the velocity of the light in the vacuum, and $p=\sqrt{\varepsilon/\mu}\cos\theta$, ε is the dielectric constant of the medium, which μ is the magnetic permeability, which θ is when the wave is transmitted to the medium. Incident angle, z is the distance of light transmission.

The characteristic matrix of the entire structure is:

$$M(z_N) = M_1(z_1)M_2(z_2 - z_1)....M_N(z_N - z_{N-1}) = \begin{bmatrix} m_{11} & m_{12} \\ m_{21} & m_{22} \end{bmatrix} \quad (2)$$

Thus, the reflection coefficient and transmission coefficient of the one-dimensional photonic crystal filter for a specific incident wavelength are:

$$r = \frac{(m_{11} + m_{12}p_A)p_B - (m_{21} + m_{22}p_A)}{(m_{11} + m_{12}p_A)p_B + (m_{21} + m_{22}p_A)} \quad (3)$$

$$t = \frac{2p_B}{(m_{11} + m_{12}p_A)p_B + (m_{21} + m_{22}p_A)} \quad (4)$$

$p_A = \sqrt{\varepsilon_A / \mu_A}\cos\theta_A$ Indicates the external environmental factor of the left side of the structure

$p_B = \sqrt{\varepsilon_B / \mu_B}\cos\theta_B$ Indicates the external environmental coefficient of the right side of the structure

so, the reflectance and transmittance are obtained:

$$R = |r|^2 \ , \ T = \frac{p_B}{p_A}|t|^2 \quad (5)$$

If the incident wave is a TM wave, simply change p in Equation (1) to $q = \sqrt{\mu / \varepsilon}\cos\theta$, and the other formulas can be changed accordingly.

The one-dimensional photonic crystal filter was simulated using MacLeod software. The simulation design of the number of cycles and physical thickness on the filter performance of the photonic crystal is optimised. As shown in Figure 2, as the number of cycles increases, the cutoff frequency shifts to the right, the transmittance at the short wave increases, and the reflectance at the long wave increases, that is, the performance of the transmitted short-wave reflected long wave is continuously enhanced.

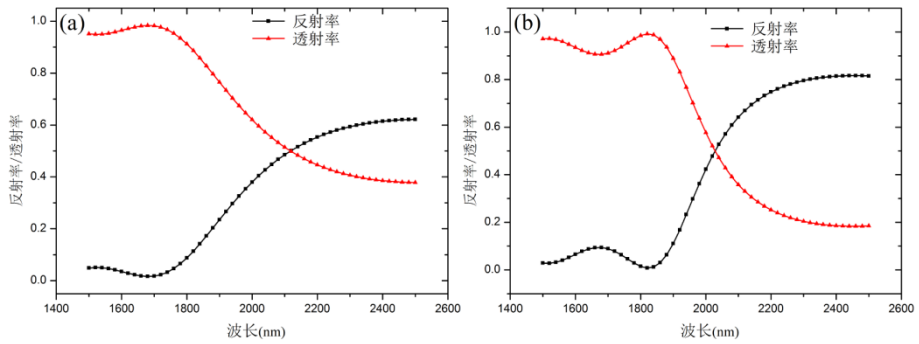

Figure 2: Reflectance and Transmittance for Different Cycle Numbers

The number of cycles is 2; (b) the number of cycles is 3; (c) the number of cycles is 4; (d) the number of cycles is 5

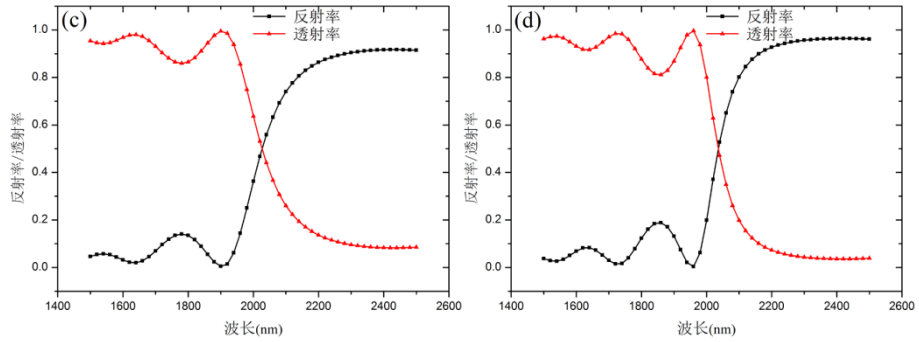

Figure 2: Reflectance and Transmittance for Different Cycle Numbers

The number of cycles is 2; (b) the number of cycles is 3; (c) the number of cycles is 4; (d) the number of cycles is 5.

In the design of photonic crystal filters, how to control the position of the center wavelength of the filter must also be considered, which is mainly related to the cell thickness of the photonic crystal structure. The physical thickness is changed while the number of cycles is kept at 5, and the physical thicknesses of the A and B dielectric layers are taken as 580 nm, 600 nm, 620 nm, and 640 nm, respectively, and the results are shown in Figure 3. It can be seen from the figure that the physical thickness gradually increases while the number of cycles remains constant, and its cut-off frequency will continue to shift to the right, but the reflectance and transmittance will not change in reverse.

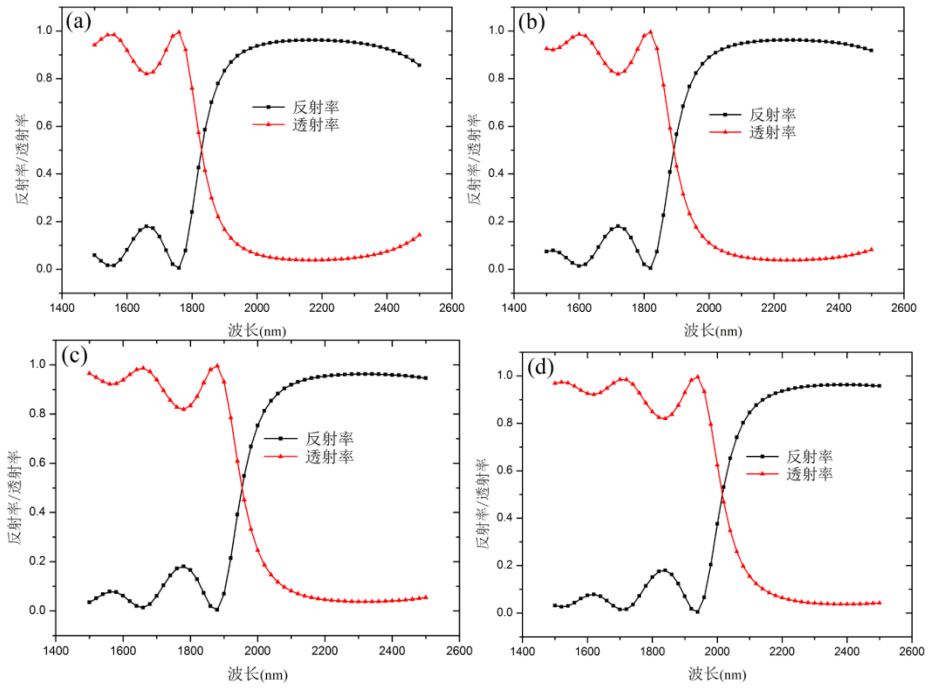

Figure 3: Reflectance and Transmittance of Different Physical Thicknesses

(a) thickness is 580 nm; (b) thickness is 600 nm; (c) thickness is 620 nm; (d) thickness is 640 nm

After continuous simulation optimisation, the model structure of the one-dimensional photonic crystal filter is (AB)6. The refractive indices of TiO2 and SiO2 are recorded as nA and nB, respectively, and the physical thickness is recorded as d_A and d_B. According to the literature [8], n_A = 2.78, n_B = 1.48, d_A = 320 nm, d_B = 330 nm, and center wavelength = 2000 nm.

3. ANALYSIS AND DISCUSSION

The simulation results at an incident angle of 0 are shown in Figure 4(a). It can be seen from the figure that the left side transmittance at 2000 nm is greater than 70%, the reflectance is less than 20%, and the transmittance on the right side is smaller than 10%, reflectivity greater than 90%. That is, the short wave is reflected by the short wave. The above analysis shows that this one-dimensional photonic crystal filter can be GaSb photovoltaic cells are matched and have high filtering efficiency.

The incident and angle of incidence are 10°, 20°, and 30°, respectively. The reflectance and transmittance of the filter in both TE and TM waves are shown in Figures 4(b), (c), and (d). It can be seen from the figure that the incident angle increases the cutoff frequency to a small left shift but the transmittance and reflectance do not change. These characteristics show that the one-dimensional photonic crystal can transmit short-wave and long-wave waves well regardless of the incident angle, and can be used as a filter with good performance and can meet the requirements of solar thermal photovoltaic system.

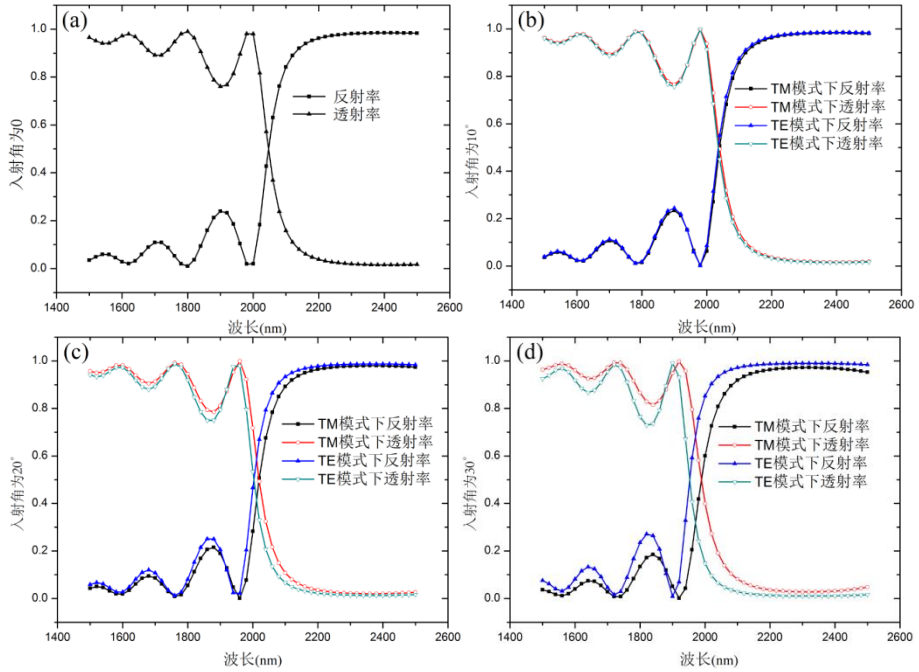

Figure 4: Reflectance and Transmittance at Different Incidence Angles

(a) *the incident angle is 0; (b) the incident angle is 10°; (c) the incident angle is 20°; (d) the incident angle is 30°*

4. CONCLUSION

In this paper, the filter of solar thermal photovoltaic system is studied. A one-dimensional photonic crystal filter is designed by combining the characteristics of one-dimensional photonic crystal with the filter. Through theoretical analysis and simulation, it is found that the filter is insensitive to the incident angle, and can pass through short-wave and long-wave reflection well, which is better matched with GaSb photovoltaic cells. The filter selects TiO_2 and SiO_2 as preparation materials, which has the advantages of simple material and economical advantages, and can well meet the requirements of materials for solar thermal photovoltaic systems.

5. REFERENCES

Yablonovitch E, Inhibited spontaneous emission in solid-state physics and electronics [J]. Phys. Rev. Lett, 1987, 58(20): 2059.

Schneider G J, Watson U H, Nonlinear optical spectroscopy in one-dimensional photonic crystals [J]. Appl. Phys. Lett,2003, 83(26): 5350-5352.

Hattori T, Tsurumachi N, Muroi N, Nakatsuka H, and Ogino E. Enhancement of optical nonlinearity in one-dimensional photonic crystals [J]. Progress in Crystal Growth and Characterisation of Mater, 1996,33(1):183-186.

Hattori T, Tsurumachi N, Nakatsuka H. Analysis ofoptical nonlincarity by defect states in one-dimensionalphotonic crystals [J].J. Opt. Soc. Am. B, 1997, l4(2):348-355.

Ye J Y, Ishikawa M,Yamane Y, Tsurumachi N, and Nakatsuka H. Enhancementof two-photon excited fluorescence using one-dimensional photonic crystals [J]. Appl. Phys. Lett, 1999, 75(23): 3605-3607.

Inouye H, Kanemitsu Y. Direct observation of nonlinear effects in a one -dimensional photonic crystal [J]. Appl. Phys. Lett, 2003, 82(8): 1155-1157.

Liu Q, Design of photonic crystal dual channel tunable polarisation filter[J]. Laser Technology， Acta Photonica Sinica 37, 305. 2008，32(2):84-87. (in Chinese)

Xue H, Zheng Y, Gu P, Zhang J, Shen W, Chen H. A new type of low angle effect filter [J]- Acta Physica Sinica, 2009 - wulixb.iphy.ac.cn 2009, 58(6):3983-3987

Tian G, Wu Y, Wang Z, Two-channel position design and adjustment of one-dimensional photonic crystal [J] Optics Journal 2005, 25(5):661-664.

Fang Y, Shen T, Tan X. Study on Doping Defect Mode of One-Dimensional Photonic Crystal [J].Optics Journal, 2004, 24(11):1157-1160.

Qin Q,Lu H,Zhu S N,et al,Resonance transmission modes in dual-periodical dielectric multilayer films[J].Appl,Phys.Lett, 2003, 82(26):4654-4656.

Wu J, Shi G, Kong M. Influence of basic periodic structure of one-dimensional photonic crystal on photonic band gap [J]. Journal of Changchun University of Science and Technology, 2006, 29(2):45-51.

Liu Q, Response of the forbidden band width of one-dimensional photonic crystal to refractive index [J]. Journal of Chongqing Technology and Business University, 2006, 23(4):14-20.

Mauk M G, Andreev V M. GaSb-related materials for TPV cells [J]. Semicond. Sci. Technol, 2003, 18: 191.

Leung K M, Liu Y F.Photon bands structure the Plane-wavemethod[J].Phys Rev.B, 1990, 41(14):10188-10190.

Yin Shubai. Thin Film Optics [M]. Beijing: Science Press, 1987:78-97.

Gong Yiling, Xu Zhenyu, Band gap analysis of one-dimensional photonic crystal[J] Journal of Tongji University, Natural science newspaper， 2004, 32(7):920-923.

157: Discount of living – research on greenhouse gas emissions

Wei ZENG[1], Junfei AN[2], Shuzhi HONG[3]

[1] WeiZeng,Hubei University of Technology, @shinway126.com
[2] JunFeiAn,Hubei University of Technology, 2223095852@qq.com
[3] ShuZhiHong, Hubei University of Technology, 1441609914@qq.com

The global climate change caused by excessive Greenhouse Gas (GHG) Emissions is posing a threat to human beings' living environment and the public cost of this is generally known as well as accepted. In addition, as a scarce commodity, the right of GHG Emissions has been given the financial features by carbon emission trade, thus forming the emission prices and quantifiable assets. However, GHG Emissions is a kind of asset with its own limitation and prospective upper limit. It is globally recognised that the emission cap, determined by IPCC, refers to the atmospheric GHG concentration and total emission when the global temperature increase will not exceed 2℃ at the end of this century.

Based on Natural Resource and Environmental Economics and Theory of Property, this dissertation defines the GHG Emissions theoretically, and systematically illustrates the scarcity, externalities and positive feedback effect. When it comes to the analytic method, by applying financial method and SRES scenarios analysis model to the environmental technical analysis, we establish a mixed mathematical model of atmospheric temperature-- GHG concentration--total emissions--emission reduction--the price of carbon emission right in combination with the status quo of carbon trade, which can effectively solve the interdisciplinary problem about the GHG emission control by discounting the full-cycle Emissions assets from present to the end of this century based on the global GHG emission cap. The research findings could contribute to the goal-setting of total emission reduction and sensible judgement about the price of carbon emission right.

Keywords: GHG Emission Discounting; Carbon Trade; Discounting Model

1. INTRODUCTION

Since the industrial revolution, the emission and concentration of greenhouse gases have been increasing gradually, and the dramatic increase of greenhouse gas emissions caused by human activities is the main reason for the abnormal warming of the climate system in the last 50 years.

At the United Nations Conference on Environment and Development (UNCED) of Rio in June 1992, more than 150 countries set up a development goal: "stabilised the greenhouse gas content in the atmosphere at an appropriate level to prevent severe climate change from causing harm to human being". Subsequently, <<Kyoto protocol>> was passed in Kyoto, Japan, which regarded “By the end of this century, the global average temperature increase will be limited to less than 2℃” as a goal.<<Kyoto protocol>> tried to use the market mechanism as a new way to solve the carbon dioxide as the representative of the greenhouse gas emission reduction.

In order to achieve this gaol and avoid more economic losses, the amount of greenhouse gas emission reduction corresponding to the 2℃ limitation can be discounted at the moment. From an economic point of view, discounting is the conversion of future income into the present value of equal value. One of the effective discounting means is carbon trading, which can break through the time and space restrictions, make carbon emission reduction take place at some industries with the lowest marginal cost, and achieve the emission control targets at a lower cost.

2. THE CONCEPT AND THEORETICAL BASIS OF CARBON TRADING

2.1. Public goods and scarcity

The atmospheric environment is an indispensable resource for all mankind to survive. It has both non exclusiveness and consumption commonality, so it is considered to be a public pond resource.

In a certain period of time, the atmospheric environment carrying capacity is relatively stable, and the amount of air pollutants and greenhouse gases that can be accommodated is limited. Therefore, the more greenhouse gas emissions will reduce the carrying capacity of atmospheric space, and more public costs will be imposed on the environmental protection. With the improvement of productivity, rapid economic development and rapid population growth, the emission of pollutants has far exceeded the capacity of the environment, resulting in a sharp rise in the scarcity of environmental capacity resources. The scarcity of environmental function resources and the scarcity of environmental capacity and resources are the theoretical basis of total quantity control and the precondition of emissions trading.

2.2. Economic externality theory

Economic externality means that in social and economic activities, the economic behavior of an economic subject has a direct impact on the welfare of another economic subject, but it does not pay the corresponding price or others do not get the corresponding compensation. As a public resource, discharging GHG obviously reduces the amount of the atmospheric emission space that other people can get. Therefore, greenhouse gas emissions are actually an external uneconomic behavior.

The classical lighthouse, traffic, pollution and other examples all illustrate the existence of externality. Kos believes that the market is the most effective means to solve the external problems. It is considered that the improvement of externality should solve the problem of zero transaction costs and try to reduce the social cost by using property rights theory.

2.3. Coase’s theory of property

After the "Pigouvian Taxes" proposed to use tax means to force the internalisation of enterprises to achieve externalities, Ronald Kos (Ronald Coase) proposed a new point of view: in the absence of transaction costs, as long as the property rights (initial rights) are defined clearly, then the resources can be effectively configured or obtained the maximum social output value through negotiation. But in the real world, the transaction cost is always greater than zero. Thus, Kos's second theorem is introduced. That is, when the transaction cost is positive, different initial rights will bring different efficiency in the allocation of resources, that is, if the market transaction has cost, the new definition of rights will have an impact on economic efficiency, which emphasises on the importance of transaction costs.

2.4. Theory of emission trading

In the <<social cost problem>>, Kos obtained the argument of the efficiency of the resource allocation through the clear definition of rights, and used the method of market and property right to solve the externality problem, and put forward the concept of the emission trading theory. That is to meet the requirements of the environment, set up legal pollution emission rights, and allow such rights to be bought and sold like ordinary goods. By using the market mechanism to achieve the optimal allocation of environmental capacity resources, then achieve the purpose of controlling the emission of pollutants.

3. DISCOUNT

3.1. Conception

According to the present value concept, we know that the value of the extra unit price now required is equal to the sum of discounted future value of these environmental governance costs. Therefore, there is an optimal discount factor to maximise the present value of future earnings and the optimal discount factor is the discount rate.

The discount rate is the interest rate that changes the future payment to the present value, which can be expressed in the following Equation:

$$\mathrm{i} = \sqrt[t]{\frac{M_0}{M_t}} - 1$$

The I is the discount rate, and the is the current value, and the is the value of the future t time, and the T is the time between the future and the present.

The discount rate of each income is different, and the time preference rate will be the discount rate for the consumption income, and the marginal capital productivity will be the discount rate for the investment income. Under the condition of complete market and no taxation, the discount rate is the same as monetary interest rate. However, our actual market is incomplete, especially in climate change economics. When it comes to the discounting of the environment, we discount the emission assets to the end of the century with the global greenhouse gas emission limit (2℃), because of market failures and the existance of externalities. The selection of rates is more complex.

3.2. Status and function

The discount rate helps to determine a reasonable discounts for future consumption changes. The higher prices of unit carbon in the carbon trading market reflect the current value of the cost of pollution control in the future for which people would like to pay. The higher cost of the future is known to be paid, and people are willing to minimise the cost in an earlier period of time, and the cost of this reasonable range depends on the forecast of the discount rate.

The high discount rate will discount future disaster losses as a smaller present value and tend to reduce emissions in the future, while the low discount rate will make future losses look very large and tend to reduce the current large emission reduction.

According to the current research, discount rate can be divided into two categories: market discount rate and social discount rate. The market discount rate refers to the discount rate that can effectively balance the current emission reduction costs and the benefits from decreasing future disasters. Social discount rate, also known as social time preference rate, is used to measure the change rate of social welfare or consumption with time, which is mainly used in the cost and benefit analysis of public investment projects.

3.3. Formula and parameter

Ramsey first proposed the decision formula of discount rate when discussing the best savings in society, that is, the Ramsay equation. According to the Ramsay equation, the discount rate (r)depends on three parameters: rate of pure time preference(ρ), elasticity of marginal utility(η) and growth rate of consumption per capita (g)

$$\mathrm{r} = \rho + \eta \mathrm{g}$$

The pure time preference rate (ρ) is a measure calculating the degree of welfare that we discount in the future and the welfare of the offspring is equivalent to the parameter of the contemporary welfare, which is expressed as a percentage per unit time.

On the value of the pure time preference rate (ρ), the <<Stern report>> believes that intergenerational neutrality represented by the discount rate near zero is the minimum ethical requirement, and ρ=0.1% is already a considerable value. But Nordhaus points out that 0.1% of the ρ value will cause the loss after two hundred years to be discounted to now with an astronomical figure, and from the theoretical point of view, the low ρ value requires a very high social optimal saving rate at present which is not reality, so he supports that ρ =3% is more practical. Taking into account the needs of developing countries, Nordhaus used ρ=1.5% in the DICE-2013 model, and Wang Zheng also uses a compromise.

Marginal utility elasticity (η) utility has the marginal elasticity of income, which is to measure the curvature of the utility function with higher value of the η, people become richer, and then they are less concerned with the expenditure of one dollar.

Similarly, there are some conflicting views about the value of the η. The theorists believe that a smaller value should be taken, for example, take 1 in the Stern report and take 1.5 in Cline (1992). The market group believes that reasonable η should be between 2-3, Nordhaus (1994), Arrow (2007), Dasgupta (2007), and Weitzman (2010) support the market view.

The consumption growth rate (g) affects the value of the discount rate by its symbol and size. If the per capita consumption does not increase, the social time preference rate is equal to the pure time preference rate (ρ) if the expected consumption will increase, then the social time preference rate will be higher than the pure time preference rate (ρ).

The present study simply treats the future consumption growth rate as a positive exogenous variable. If the uncertainties of the growth of future climate change, such as the constraints on growth or the undetermined effects of a possible climate catastrophe on the economy, are taken into account, the assumption that the rate of consumption growth is positive will be oppugned and get a lower discount rate.

3.4. The value and dispute of discount rate

By reading three empirical studies of Cline (1992), Nordhaus (1994) and Stern (2006) in global climate change economics. Generality, Cline and Stern have urged immediate and powerful global action to cope with climate change - the Stern added that this is equivalent to an annual expenditure of 2%GDP in rich countries. But Nordhaus believes that even though climate change poses a threat to the global economy, investing in renewable capital and human capital will be fairer and more efficient. The two sides come to a very different conclusion, although they agree that the world's per capita GDP will continue to grow in the next 100 years, usually between 1% and 2%, even more than imagined.

The <<Stern report>> uses the social discount rate, while Nord Moorhouse advocates the use of the market discount rate. The low discount rate will make future losses look very large and tend to enhance the current large emission reduction, while the high discount rate will discount future disaster losses as a smaller present value and tend to reduce emissions in the future. Arrow divides economists corresponding to the two discount rates into prescriptionist and descriptionist.

The prescriptionist emphasises fairness, if we consider the discount rate from an ethical point of view, the pure time preference rate (ρ) and the low marginal utility elasticity (η) will be very low or zero. Then the low discount rate (r) make the discounting of the future climate change very large, so the prescriptionist supports reducing the emissions immediately in the climate policy.

The descriptionist emphasises efficiency, and advocates that the discount rate is determined by adopting the producer interest rate or the consumer interest rate according to the consumer behavior in the market and the real return of capital, so as to achieve the maximisation of social resources. The pure time preference rate (ρ) and the marginal utility elasticity(η) used by the descriptionist are higher, so the discount rate (r) is also relatively high. The higher discount rate makes the loss of the future climate change discounted lower than the result of prescriptionist, so the descriptionist advocates gradual action in the climate policy.

At present, in order to simplify the calculation, the discounting rate is regarded as an external fixed value in a comprehensive evaluation model, while some recent studies suggest that a dynamic discount rate is needed, and the rate of discounting in the long term will decrease to the minimum. Stern pointed out that the discount rate is dependent on consumption growth, so the long-term discount rate is not a fixed value. If future consumption falls, the discount rate can be negative. If inequality increases with time or future uncertainty increases, the discount rate will also decrease. In DICE-2013 the rate of pure time preference was 1.5%, marginal utility elasticity was 1.3, and the annual growth rate of per capita consumption began to be 2.7%, and gradually dropped to 0.77% in 200 years. In addition, the discount rate of 2200 was 2.5% by calculation. At present, the discount rates of some representative scholars are shown in Table 1.

Table 1: comparison of discount rates in the area of climate policy modelling

	Representative scholar	ρ	η	g	r	reference
static discount	Chrishope	1.03%	1.17	1.60%**	2.9%①	PAGE2009
	Stern	0.10%	1	1.30%	1.40%	[18]
	Stern recalibrated	0.10%	2.1	1.30%	3.73%**	DICE2013②
	Cline	0%	1.5	1.30%*	2.05%**	[13]
	Edenhofer	1%%	3.1	1.30%*	5.00%	[19]
	Nordhaus	3%	1	1.30%*	4.30%**	[20]
	Dasgupta	≈0	[2,3]	1.30%*	[2.6%,3.9%]**	[13]
dynamic discount	Nordhaus	1.5%	1.3	2.7%→0.77%	5%→2.5%(200 年)	DICE2013
	Weitzman	0%	3	2%	6%→minimum	[21]
	Gollier	2%	2	2%	5%→minimum	[22]

For the g value that are not given, 1.3% of the Stern report is used for reference. * * * is the result calculated by the author according to the Ramsey equation; the ">" indicates a decline with time; [2, 3] represents a number between them;

① the PTP and EMUC values in the PAGE09 model are smaller than those in DICE2013, resulting in a discount rate of 2.9% and 5% respectively.

② because the real interest rate gained by the Stern report is lower than the assumed level, we adjust the parameters of the preference function to match the real interest rate. On the Ramsey equation, the time preference rate is maintained at 0.1% per year, and the consumption elasticity coefficient is increased to 2.1.

4. INTEGRATED ASSESSMENT MODEL

4.1. Model framework

At present, the cost and benefit accounting in the climate change economy depends on the large Integrated Assessment Model (IMA). By introducing the cost function and loss function of the climate change, the optimal cost reduction path is obtained by maximizing the discounted social welfare function. It can also provide the impact of climate change under different scenarios to support decisions at all levels. It is mainly divided into six steps:

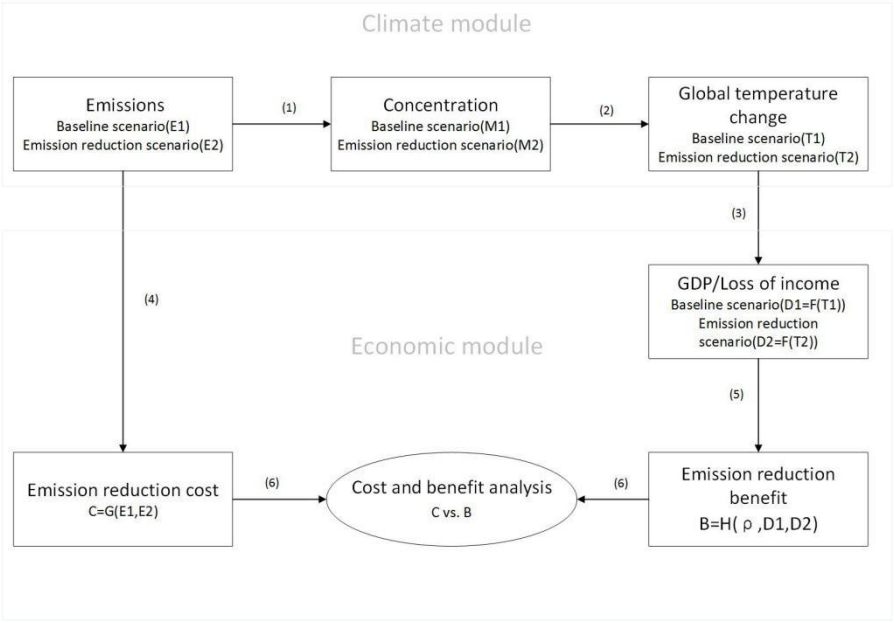

Figure 1: Comprehensive assessment model framework diagram

E, M, T, C, D, B and ρ respectively represent greenhouse gas emission, greenhouse gas concentration, global temperature, emission reduction cost, GDP/ revenue loss, emission reduction benefit and time preference rate. F, G and H respectively represent loss function, emission reduction cost function and welfare function.

4.2. Model classification

The comprehensive evaluation model is divided into global model and regional model according to the different applicable subjects, and according to the different model building methods, it can be divided into optimisation model, computable general equilibrium model (CGE) and simulation model. (such as table 2)

The optimisation model can be divided into the social welfare maximisation model and the cost minimisation model according to the objective function, and the social welfare maximisation model is to maximise the discounted social welfare by selecting the greenhouse gas emission reduction in each period.

The CGE model describes the interactions between multiple markets and their actors, and estimates the direct and indirect effects of policy changes. It reflects the relationship between supply and demand, and gets the total amount and price of the equilibrium market. It focuses on the economic cost of emission reduction and the level of carbon tax necessary to achieve a specific emission reduction target.

The simulation model determines the carbon emissions that can be produced at every time in the future through the exogenic emission parameters, and can assess the social costs of future possible emission scenarios.

Table 2: classification of integrated climate change assessment models

model	model			emission scenarios
	optimisation	CGE	simulation	
global	DICE	JAM		(1) to make GDP predictions consistent with emission forecasts. (2) calculate the effects of important variables based on different assumptions, such as output, emissions, temperature changes and impacts. (3) to track and estimate the costs and benefits of alternative strategies through a uniform way to replace all variables policy implications. (4) estimate the relative uncertainty of substitution variables and strategies. (5) computation reduces the impact of uncertainty on key parameters or variables, and estimates the value of research and new technologies.
	ENTICE	IGEM		
	DEMETER			
	MLND			
	GET-LFL			
	RICE	GTAP-E	PAGE	
	FUND	MIT-EPPA	ICAM-1	
	CETA	CEEPA	IMAGE	
	MERGE	AIM	E3MG	
	GRAPE	GREEN	GIM	
	PRICE	Global2100		
	FEEM-RICE	SGM		
	DNE21+			
regional	MESSAGE-MACRO			
	DIAM			

5. DICE MODEL

5.1. Logic structure

DICE (the dynamic integrated model of climate and economy) is a simplified analysis and empirical model that treats the concentration of greenhouse gases as negative natural capital, reducing emissions as an investment to improve the quality of natural capital (reducing negative capital), reducing emissions by output and reducing economic consumption to prevent the economic danger of climate change, thus increasing the possibility of future reduction of consumption. The following is the main module and logical structure of the DICE model:

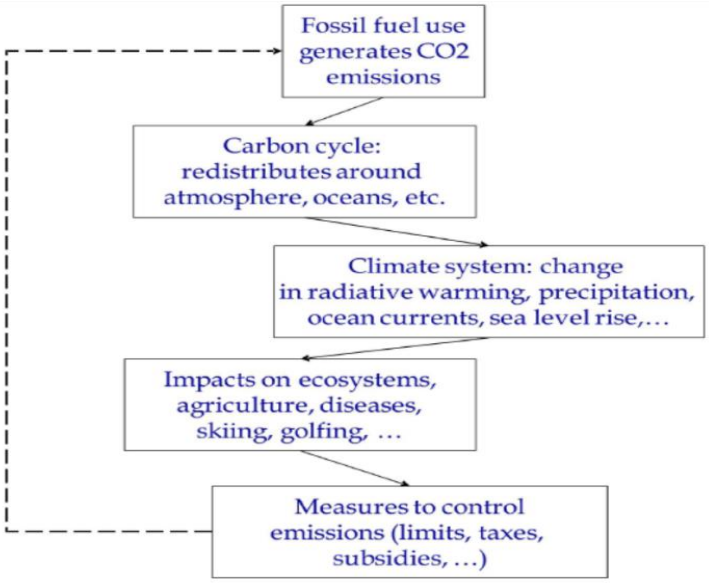

Figure 2: Main modules and logical structure of dice model

The DICE model takes the global or regional assumptions as well-defined preferences, and uses social welfare functions to represent different consumption channels. It chooses the appropriate parameter values, such as the coefficient of the carbon cycle matrix, climatological parameters, economic parameters, discount rate, and regards the discounted value of the population weighted per capita consumption utility as the maximum expression of the

social welfare function (W), then calculates the simulation results of different scenario models. There are mainly the following scenarios:

(1) Base: no climate change policy is adopted. The baseline can be interpreted as not taking action on the status quo of climate policy.

(2) Optimal: climate change policy maximises economic welfare; since 2015, all countries have been fully involved and are not subject to climate restrictions.

(3) Lim2t: the optimal strategy further restrains the global temperature than the average level of 1900 is no more than 2 degrees Celsius.

(4) Stern: "Stern report" advocated the use of very low discount rate of climate change policy. The time discount rate is 0.1%, and the annual consumption elasticity coefficient is 1.

(5) Low time preference with calibrated interest rates: because the actual interest rate caused by the Stern report is lower than the hypothesis level, we adjust the parameters of the preference function to match the actual interest rate of the calibration. The time preference rate is maintained at 0.1% per year, and the consumption elasticity coefficient is increased to 2.1.

(6) Copen: in this case, it is assumed that the high income countries will implement the deep emission reduction in the next forty years, while the developing countries are gradually implementing.

Related parameters:

Parameter	Value
The elastic coefficient of marginal consumption utility	1.3
Annual social time preference rate	0.015
Annual rate of depreciation of capital	0.1
Elastic coefficient of capital output	0.3
HOTELLING rental parameters (every five years)	Value
Hotelling's rent ratio coefficient	100
Hotelling index	12
Cumulative fuel carbon emissions, 2208 (GtC)	90

5.2. Main operation results

Economic variables

The real interest rate (discount rate) is a key variable in determining climate policy. Tables 3, Figure 3 to 5 show the major economic variables in different scenarios. These show the rapid growth of the global economy.

Table 3: the main economic variables in different scenarios

Gross world output (trillions 2005 US$)	2010	2020	2030	2050	2100	2150	2200
Base	63.4	89.3	120.8	200.9	488.9	863.5	1,285.4
Optimal	63.4	89.3	120.9	201.3	499.0	941.0	1,503.4
Limit T < 2 °C	63.4	88.9	119.9	197.6	502.6	962.9	1,532.4
Stern discounting	63.4	95.5	129.7	214.6	552.5	1,052.6	1,667.4
Stern recalibrated	63.4	89.0	120.6	201.8	507.3	978.9	1,576.6
Copenhagen	63.4	89.3	120.7	200.9	498.8	936.8	1,481.7
Per capita consumption (2005 US$)	2010	2020	2030	2050	2100	2150	2200
Base	6,883	8,762	11,005	16,597	36,694	63,206	93,025
Optimal	6,883	8,748	10,985	16,564	37,071	68,160	108,041
Limit T < 2 °C	6,883	8,726	10,905	16,195	37,357	69,736	110,120
Stern discounting	6,883	8,523	10,760	16,184	37,995	70,876	111,755
Stern recalibrated	6,883	8,736	10,943	16,480	37,058	69,042	109,468
Copenhagen	6,883	8,749	10,971	16,517	37,115	67,949	106,609
Real interest rate (% per year)	2010	2020	2030	2050	2100	2150	2200
Base	0.0	5.1	4.9	4.4	3.5	2.9	2.5
Optimal	0.0	5.1	4.9	4.4	3.6	3.1	2.7
Limit T < 2 °C	0.0	5.0	4.8	4.3	3.7	3.1	2.7
Stern discounting	0.0	2.7	2.4	2.1	1.6	1.2	0.9
Stern recalibrated	0.0	5.1	4.9	4.3	3.1	2.4	1.8
Copenhagen	0.0	5.1	4.8	4.4	3.6	3.1	2.7

Table 4: major geophysical variables in different scenarios

Industrial CO2 emissions (GtCO2/yr)	2010	2020	2030	2050	2100	2150	2200
Base	31.1	39.4	48.3	66.2	101.0	110.4	90.4
Optimal	31.1	30.5	34.8	39.2	14.5	0.0	0.0
Limit T < 2 °C	31.1	24.5	24.2	10.4	0.0	0.0	0.0
Stern discounting	31.4	15.7	13.7	1.9	0.0	0.0	0.0
Stern recalibrated	29.9	29.4	32.8	34.3	0.0	0.0	0.0
Copenhagen	30.4	35.3	38.7	38.7	21.9	12.8	13.3
CO2 concentrations (ppm)	2010	2020	2030	2050	2100	2150	2200
Base	384.5	414.9	451.1	540.7	832.1	1,127.8	1,329.1
Optimal	384.5	410.3	435.0	487.6	555.3	484.7	459.2
Limit T < 2 °C	384.5	407.5	424.0	442.0	393.8	380.6	374.0
Stern discounting	384.5	402.8	408.7	407.4	371.3	360.4	356.6
Stern recalibrated	384.5	409.1	432.4	478.9	492.7	440.5	425.3
Copenhagen	384.5	413.4	443.0	499.6	553.8	544.4	553.9
Temperature increase (°C from 1900)	2010	2020	2030	2050	2100	2150	2200
Base	0.83	1.05	1.32	1.97	3.95	5.68	6.84
Optimal	0.83	1.04	1.28	1.80	2.98	3.12	2.90
Limit T < 2 °C	0.83	1.04	1.26	1.66	2.00	1.97	1.90
Stern discounting	0.83	1.03	1.22	1.51	1.73	1.72	1.68
Stern recalibrated	0.83	1.04	1.27	1.77	2.73	2.69	2.53
Copenhagen	0.83	1.05	1.30	1.86	2.99	3.38	3.51

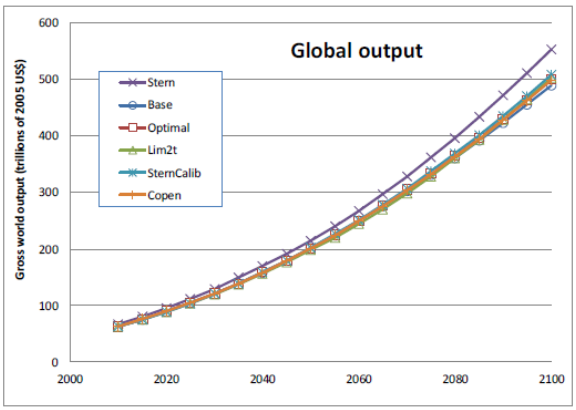

Figure 3 global total output from 2010 to 2100 under the "replacement policy"

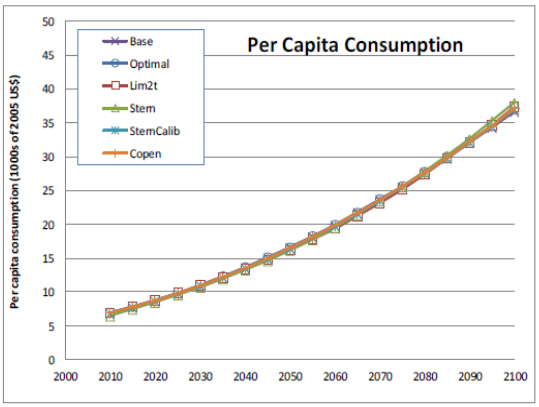

Figure 4 per capita consumption from 2010 to 2100 under the replacement policy

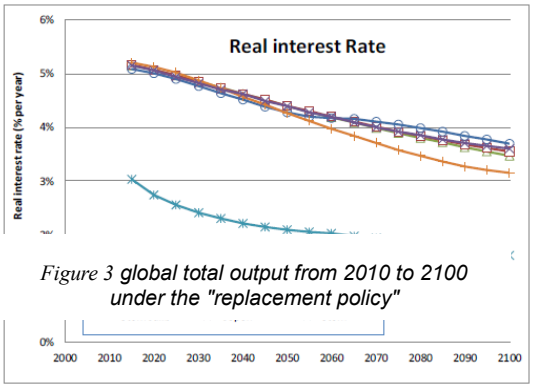

Figure 3 global total output from 2010 to 2100 under the "replacement policy"

Figure 5: real interest rates under alternative policy

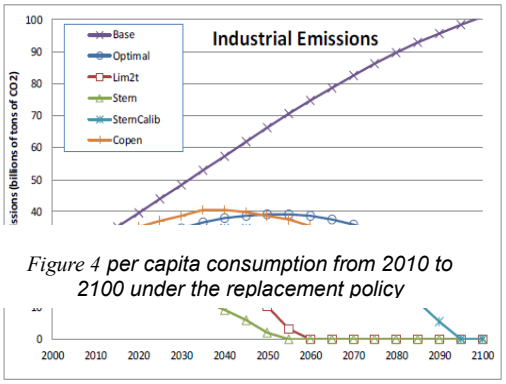

Figure 4 per capita consumption from 2010 to 2100 under the replacement policy

Figure 6: carbon dioxide emissions under alternative policy

Environment variable

Table 4 and Figures 6-8 show the main environmental variables: carbon dioxide emissions from industry, carbon dioxide in the atmosphere, and global average temperature. If we do not take any control, the prediction of the model will increase substantially in the next century and beyond. By 2100, the baseline temperature is expected to be higher than the 1900 level (roughly 4℃) and will continue to rise. It is estimated that the carbon dioxide concentration in the atmosphere will reach 832ppm by 2100, while the CO2-E concentration is estimated to be 920ppm.

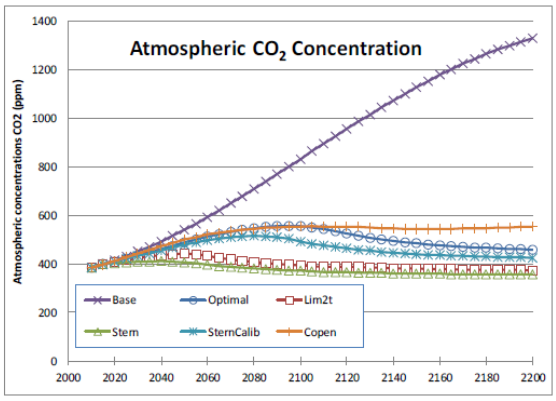

Figure 7: atmospheric carbon dioxide concentration under alternative policy

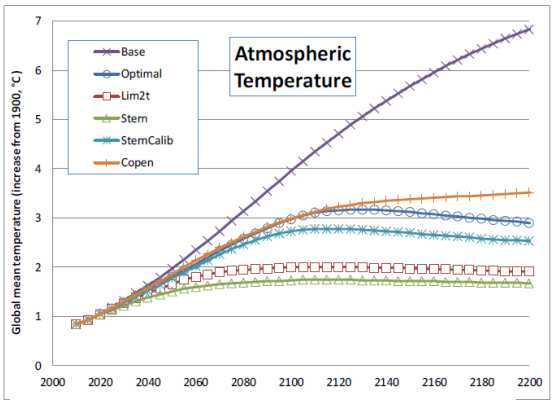

Figure 8: global warming under the replacement policy (C, 1900)

Policy variables

Table 5 and Figures 9-11 show policy variables in different scenarios. If we want to achieve the goal of 2℃, the global emission control rate will reach 50% by 2030, and industrial emissions will reach zero by 2060.

Table 5: major climate policy variables under different scenarios

Emissions control rate (%)	2015	2020	2030	2050	2100	2150	2200
Base	0.4	0.5	0.7	1.2	4.0	11.5	28.7
Optimal	20.6	23.1	28.6	41.7	86.4	100.0	100.0
Limit T < 2 ℃	33.1	38.1	50.3	84.5	100.0	100.0	100.0
Stern discounting	58.2	63.5	74.2	97.4	100.0	100.0	100.0
Stern recalibrated	22.7	25.7	32.5	49.2	100.0	100.0	100.0
Copenhagen	5.6	11.1	20.6	42.4	79.4	90.0	90.0
Carbon price (2005$ per ton CO2)	2015	2020	2030	2050	2100	2150	2200
Base	0.0	0.0	0.0	0.1	0.7	3.4	13.9
Optimal	19.6	23.4	32.7	58.2	167.6	169.3	131.4
Limit T < 2 ℃	45.8	57.6	90.1	207.4	218.1	169.3	131.4
Stern discounting	126.8	144.3	181.5	267.9	218.1	169.3	131.4
Stern recalibrated	23.3	28.4	41.1	78.4	218.1	169.3	131.4
Copenhagen	10.1	35.8	85.4	81.9	144.0	140.1	108.7

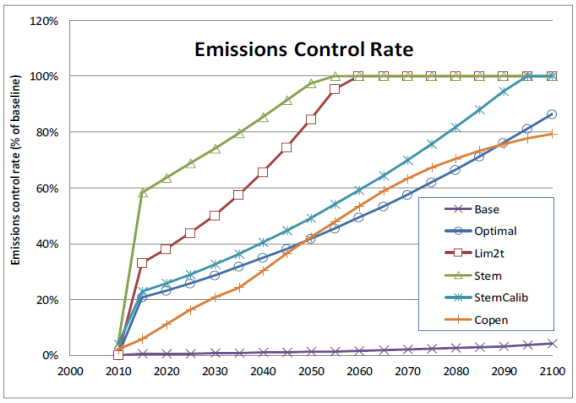

Figure 9: emission control rate under alternative scenarios

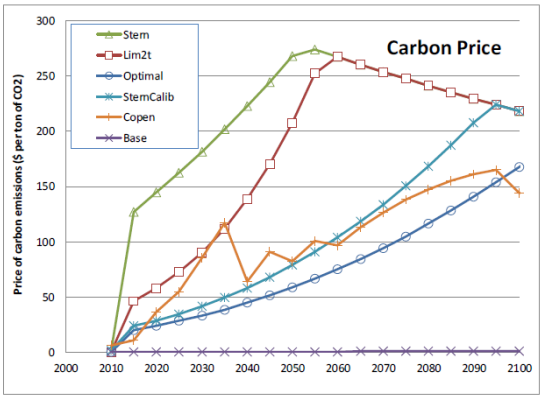

Figure 10: global average carbon prices in alternative scenarios

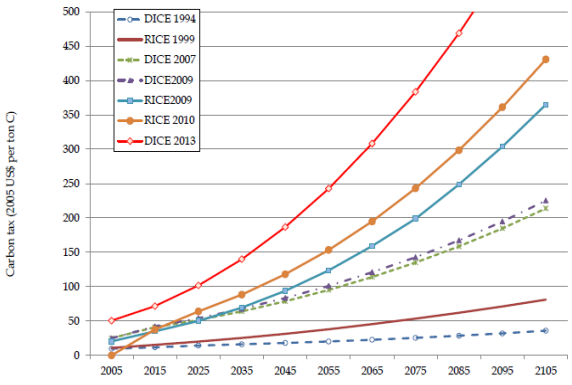

Figure 11: best carbon price (US dollar per ton of carbon, US $2005)

Change of carbon price

Perhaps the most important output of the comprehensive economic model of climate change is the "carbon price" in the short term. This is a market price concept for measuring greenhouse gas emissions. In the market environment, such as "limitation and trading system", the price of carbon is the trading price of carbon emission permits. If policies are optimised, carbon prices are also the social cost of carbon.

Figure 11 shows the trajectory of calculating the optimal carbon price. In the past twenty years, the optimal carbon price has also risen sharply. This is because all the main factors (output, damage equation, temperature rise, discount) work in the same direction.

6. REFERENCES

http://www.tanpaifang.com/tanguwen/2015/1008/47944.html

Xiang Y, Ren J. A Review of the Theory of externality in Western Economic circles [J]. Economic review, 2002(03):58-62.

Scitovsky T, 1954. Two Concepts of External Economics, Journal of Political Economy, Apr. 1954.

Coase RH (1960):"The Problem of Social Cost". Journal of Law and Economics, Vol. 3, PP.1 ─ 44.

Wu J, Ma Z. Coase Theorem's theoretical contribution to Emission Trading Policy [J]. Journal of Xiamen University (philosophy and Social Sciences Edition), 2004(03):21-25.

Kos R, et al. Property rights and institutional changes >[Ml. Shanghai: Shanghai Sanlian Bookstore, 1996.

Stern (2008, pp.12-13)

Ramsey 1928

Nordhaus W D. A review of the Stern review on the economics of climate change[J]. Journal of Economic Literature, 2007,45(3):686-702.

Dasgupta, 2007

Nordhaus 2014

Liu C. The latest Research Progress on discount rate in Climate change Economics [J]. Economic dynamics, 2012(3):123-129.

Partha D. Discounting climate change[J]. Journal of Risk and Uncertainty, 2008, 37(2-3).

Arrow K J, Cline W, Maler K, et al. Intertemporal equity, discounting, and economic efficiency[M]. Cambridge: Cambridge University Press, 1996.

Wei Y, Mi Z, Zhang H. Progress in the study of Integrated Climate change Assessment models [J]. System Engineering Theory and practice, 2013,33(08):1905-1915.

DICE 2013

Zhang X, GE Q. Integrated climate change assessment model [J]. Advances in Geography Science, 1999(01):62-69.

Stern N. The economics of climate change: The Stern review[M]. Cambridge: Cambridge University Press, 2007.

Edenhofer O, Lessmann K, Bauer N. Mitigation strategies and costs of climate protection: The effects of ETC in the hybrid model mind[J]. The Energy Journal, 2006(S): 207-222.

Nordhaus W D. Managing the global commons: The economics of climate change[M]. Cambridge: MIT Press.

Weitzman M L. Risk-adjusted gamma discounting[J]. Journal of Environmental Economics and Management, 2010, 60(1): 1-13.

Gollier C. Expected net present value, expected net future value, and the Ramsey rule[J]. Journal of Environmental Economics and Management, 2010, 59(2): 142-148.

160: The power quality analysis of the PV access system based on DIgSILENT software

Hu YUE[1], Ding Wen FANG[2]

[1] *Hubei Collaborative Innovation Center for High-efficiency Utilisation of Solar Energy, Hubei University of Technology, 452350302@qq.com*
[2] *Hubei Collaborative Innovation Center for High-efficiency Utilisation of Solar Energy, Hubei University of Technology, 523661844 @qq.com*

In recent years, photovoltaic power generation has been widely used due to its clean, pollution-free, low-cost features. When PV is connected to the power grid, there is a dynamic interaction between the inverter control loop and the passive components, so that the amplitude of the grid-side voltage and current harmonics continues to be amplified and severely distorted. This phenomenon has a great impact on the power quality of the power grid. In view of this phenomenon, this paper takes the 60MW agricultural photovoltaic hybrid power station project of Fuxiejie Town, Yangxin County of China Power Investment Corporation as an example, and simulates PV into PV nodes and harmonic sources, and builds a grid-connected photovoltaic system model on the DIgSILENT simulation platform. On this basis, the simulation analysis of the harmonic voltage, current and voltage drop of the internet point was carried out. Then according to the national standard GB/T 19964-2012 "Technical Regulations for Photovoltaic Power Plant Access Power System", GB/T 12325-2008 "Power Quality Supply Voltage Deviation" and GB/T 14549-93 "Power Quality Public Power Grid Harmonics", comparing the simulation results with the allowable values specified by the national standard, the power quality of the Yangxin County power grid was analyzed. The results show that when PV power plants have the greatest impact on the power grid (maximum PV output), voltage deviations and harmonics at various points of the Yangxin County power grid are lower than the allowable values and meet the requirements.

Keywords: DIgSILENT; Photovoltaic; The power quality; Voltage deviation; Power grid harmonics

1. INFLUENCE OF PHOTOVOLTAIC POWER GRID-CONNECTED SYSTEM ON POWER QUALITY

The solar photovoltaic power generation system consists of photovoltaic modules, DC monitoring and distribution boxes, grid-connected inverters, metering devices and on-grid power distribution systems. Solar energy is converted into DC power through photovoltaic modules, and then collected through a DC monitoring distribution box to a grid-connected inverter. Finally, DC power is converted into a sine-wave current with the same frequency and phase in the grid.

The whole photovoltaic power station is composed of several subsystems, a large number of photovoltaic panels are installed on the roofs of each building, and the PV panels are divided into a certain capacity subsystem according to geographical location and capacity arrangement. Each subsystem is relatively independent and consists of a photovoltaic module, a DC monitoring power distribution box, and a grid-connected inverter. Each subsystem is connected to the grid after boosting (isolation) of the transformer.

As a result of these characteristics of solar photovoltaic power generation system, when the PV power station is connected to the power grid, it will have some influence on the power grid and its operation in the large power system, which is mainly manifested in the following aspects:

1) System voltage deviation

The actual output power of a solar photovoltaic power plant varies with the change of the light intensity. When the light intensity in the daytime is the strongest, the output power of the power generating device is the largest, and after the light is almost absent at night, the output power is substantially zero. Therefore, in addition to equipment failure factors, the output power of the power generation device varies with natural factors such as sunshine, weather, season, temperature, etc., so the output power is very unstable

2) Generate a lot of harmonics

Solar photovoltaic power generation system converts solar energy into DC power through photovoltaic modules, and then converts DC power into grid-connected sinusoidal current with the same frequency and phase in the grid through a grid-connected inverter. In the process of converting DC power to AC power through an inverter, a large amount of harmonics are generated.

3) Reactive power balance problem

The power factor generated by solar photovoltaic power plants is relatively high, about 0.98 or more, basically purely active output. According to relevant regulations, in order to meet the principle of layered division and local balance for reactive power compensation, solar photovoltaic power stations should be equipped with appropriate reactive power compensation devices to meet the requirements of the power grid for reactive power, which can improve voltage quality and reduce line losses.

2. MODELING OF GRID-CONNECTED PHOTOVOLTAIC POWER GENERATION SYSTEM

2.2. The principle of grid-connected photovoltaic power generation system

The working principle of photovoltaic cells is based on the photovoltaic effect of the diodes to convert light energy into electrical energy. Due to the small output power of a single photovoltaic cell, large-scale photovoltaic arrays are composed of a large number of photovoltaic cells in series and parallel. Photovoltaic grid-connected power generation system achieves power transmission through photovoltaic arrays and grid-connected inverters. The power of the transmission grid is related to the topological structure of photovoltaic power generation, inverter control, maximum power point tracking (MPPT), etc.

Compared with isolated photovoltaic solar power plants, the incorporation of large grid systems can bring many benefits to solar photovoltaic power generation. First of all, it is not necessary to consider the stability of the load power supply and the quality of the power supply; secondly, the photovoltaic cells can always operate at the maximum power point, so that the large power grid can receive all the power generated by the solar energy and improve the efficiency of solar power generation; Finally, the battery is omitted as an energy storage link, which reduces the energy loss in the charging and discharging process of the battery, eliminates the operating and maintenance costs due to the presence of the battery, and also eliminates the pollution caused by the disposal of the used battery.

Grid-connected photovoltaic systems consist of photovoltaic arrays, inverters, and controllers. The inverter reverses the power generated by the photovoltaic cell into AC power and incorporates it into the grid; The controller controls the maximum power point of the photovoltaic cell to track and control the waveform and power of the inverter grid-connected current, so that the power transferred to the grid is balanced with the maximum power generated by the photovoltaic array. The controller is generally composed of a single-chip microcomputer or a digital signal processing chip as a core device; the voltage-type converter is mainly composed of a power electronic switching device connected with an inductor, and transmits power to the grid in the form of pulse width modulation.

The structure diagram of a typical photovoltaic grid-connected system includes: photovoltaic arrays, DC-DC converters, inverters, and integrated relay protection devices. The structure of a photovoltaic grid-connected system is shown in Figure 1. With a DC-DC boost chopper converter, a DC loop can be established between the converter and the inverter. The boost chopper is used to increase the voltage of the photovoltaic array to a suitable level according to the size of the grid voltage, and the DC-DC converter also serves as a maximum power point tracker, which increases the economic performance of the photovoltaic system. The inverter is used to provide power to the AC system. The relay protection system can ensure the safety of the PV system and the power network.

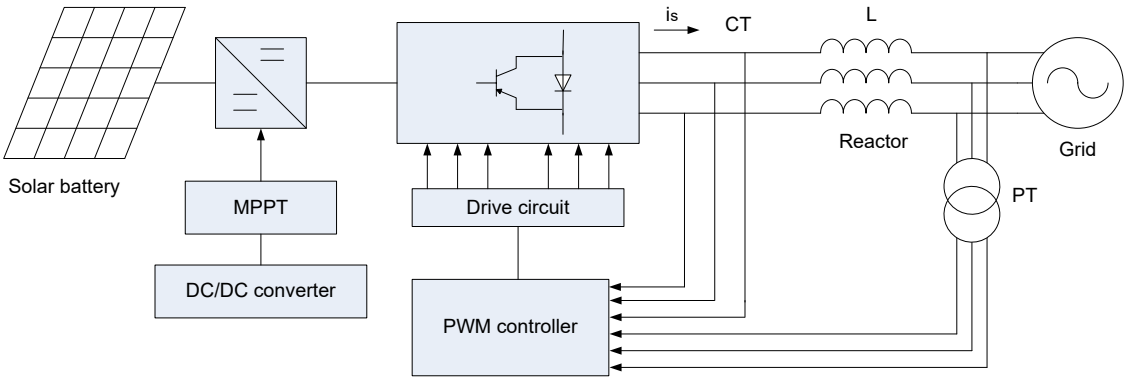

Figure 1: Photovoltaic grid-connected model

2.3. Equivalent model of photovoltaic generation based on power quality test

In general, the regional power system is regarded as an AC voltage source with infinite capacity, and the output of the grid-tied inverter can be controlled as a voltage source or a current source. If the output of the grid-connected system is controlled as an AC voltage source, the solar grid-connected system is actually a parallel connection of two AC voltage sources. To ensure the stable operation of the system, the amplitude and phase of the output voltage of the grid-connected system must be strictly controlled at the same time. Because of the slow response of the phase-locked loop and the inability of the output voltage to be accurately controlled, there may be a circulation between the grid-connected system and the power grid, and the system cannot operate stably and even malfunction. Therefore, the photovoltaic grid-connected system is often designed as a current source system. In this case, the grid-connected system is actually a parallel connection of an AC current source and a voltage source. By controlling the phase synchronisation of the grid-connected current and the grid voltage, the power factor of the system output is guaranteed to be 1. At the same time, the active output and reactive output of the system can also be controlled by adjusting the magnitude and phase of the output current of the grid-connected system.

In the photovoltaic system, the inverter has the following characteristics:

1) The DC power of the photovoltaic cell is converted into AC power suitable for the power grid, and the power factor is approximately unit power factor;

2) The fluctuation range of the DC voltage provided by the photovoltaic cell is relatively large, and the inverter may operate in the environment of a wide input DC voltage;

3) The inverter has high conversion efficiency, low loss and high efficiency.

For photovoltaic power generation models that are mainly used for power quality testing, the following simplifications can be made:

1) The power electronic converter used in photovoltaic systems is a non-linear impedance, causing distortion of the current waveform, so it can be equivalent to a harmonic current source, and the corresponding current harmonic content can be measured by field tests.

2) The most serious condition of the power quality test should be considered, that is, the PV system maintains the maximum output in the minimum mode operation. At this time, PV has the greatest impact on the power system, that is, the PV model maintains the maximum active output. The photovoltaic system application controller allows itself to always operate near the maximum power point and the output voltage is stable, which can be simplified into PV nodes for analysis.

The above simplification basically meets the requirements for photovoltaic models that are mainly used for power quality testing. In addition, for large grid systems with higher voltage levels, they can be approximated as voltage sources. Through the above simplified conditions, a photovoltaic grid-connected model for power quality testing can be built.

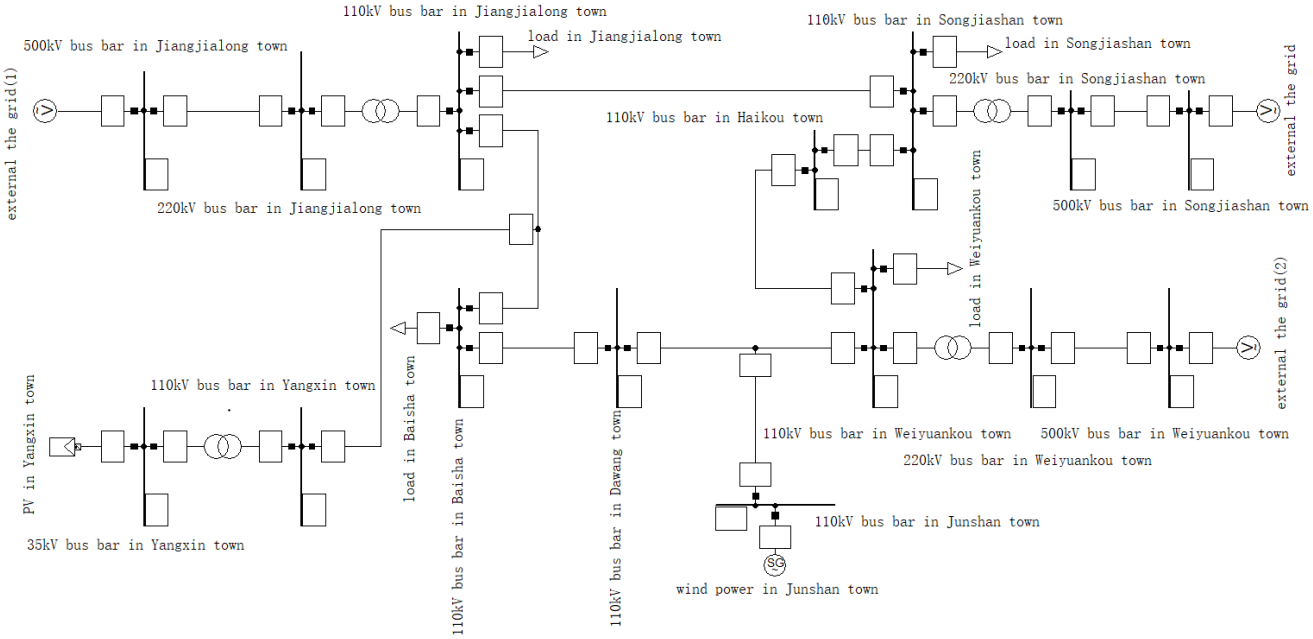

Figure 2: System Simulation Model

3. SIMULATION OF EXAMPLES

Take the 60MW agricultural photo-complementary photovoltaic power station project of Fupingjie Town, Yangxin County, China Power Investment Corporation as an example, this paper builds a grid-connected photovoltaic system model based on DIgSILENT software, in which power electronic devices such as inverters need to be simulated as harmonic sources, and other parameters are based on Electrical primary equipment parameters given. In this model, the PV project is equivalent to a PV power supply point, and the harmonic parameters of the injection system are set up according to the harmonic characteristics of the inverter. The P-Q method and the Newton-Raphson method are used to comprehensively calculate the voltage deviation and harmonics, and the site most affected by the photovoltaic system, ie, the Internet point, is considered. The calculated results are compared with the permissible values, and whether or not they meet the requirements is analyzed.

The system simulation model is shown in Figure 2.

1) Voltage deviation results

According to the operating characteristics of photovoltaic grid-connected power plants, considering the worst case scenario, when the photovoltaic power plant at Futuo Street outputs the maximum power, the voltage deviation at the access point is calculated as shown in Table 1.

Table1: Access point voltage deviation

Operating conditions	Junction
Photovoltaic plant put into operation	-2.132

The percentage of each harmonic current and total current harmonic distortion of the PV grid-connected inverter injected into the common connection point and the calculation results of each harmonic current content of the access point when the photovoltaic grid-connected inverter is in the rated operation state as shown in Table 2, the harmonic current injection value is the maximum value of each harmonic current in the three-phase current taking into account the harmonic injection current of the inverter.

The national standard GB/T 12325-2008 "Power Quality Supply Voltage Deviation" stipulates that the sum of the absolute values of the positive and negative deviations of the supply voltage of 35kV and above does not exceed

±10% of the nominal voltage. Analyzing the calculation results in Table 2 and comparing it with the national standard, we can know that in the worst case, the maximum voltage of the PV power station at Futuo Street was at -2.232% of the rated voltage at the maximum output power. This error range meets the requirements within ±10% of the nominal voltage allowed by the national standard.

Table 2: Access point voltage deviation

Harmonic times	Access point current (A)	Harmonic current allowable value (A)
Fundamental current value	320.59	/
THD(%)	1.113	/
2	2.236	5.99
3	0.221	2.45
4	0.378	2.81
5	1.102	2.61
6	0.535	1.88
7	2.236	2.47
8	0.441	1.41
9	0.19	1.5
10	0.252	1.12
11	0.346	1.17
12	0.189	1.78
13	0.661	1.62
14	0.095	0.77
15	0.063	0.86
16	0.063	0.68
17	0.283	1.28
18	0.063	0.59
19	0.22	1.13

As in GB/T 14549—2093 “Power Quality Harmonics in Public Power Networks”, the utility grid is required to provide a nominal voltage of 110 kV, and the total harmonic distortion limit of harmonics is 2%. The allowable values of the harmonic currents at the common connection point converted from the national standard are shown in Table 2. Under the condition that all PV grid-connected inverters are in the rated operation state at the same time, the harmonic currents injected into the grid point system of the inverter do not exceed the permissible values, and the total harmonic distortion rate of the current is 1.113%, which satisfies the requirements.

4. RESULT ANALYSIS

When the maximum output of the photovoltaic power station at Futuo Street, the voltage deviation and voltage and current harmonics of the network point did not exceed the allowable value, indicating that after the photovoltaic power station was connected, all points of the Yangxin County power grid met the corresponding power quality requirements. Therefore, for the two power quality indicators such as voltage deviation and grid harmonics, it is feasible for this PV power station to access the Yangxin County power grid.

5. CONCLUSION

Based on the DIgSILENT simulation platform, this article uses the 60MW agricultural photovoltaic hybrid power station project of Fuxiejie Town in Yangxin County of China Power Investment Corporation as an example to build a photovoltaic grid-connected model based on power quality testing. Then the influence of the PV system access on the voltage deviation and harmonic current of the power grid is analyzed, and the results are compared with the allowable values of the national standard to judge whether the requirements are satisfied. However, the model of the power grid is relatively simple, and the 220 kV or more power grid is simulated as a voltage source without considering its voltage and frequency changes. Further research is still needed.

6. REFERENCES

Huang W, Dong X, Lei J, Yu i. 2016, Comprehensive Analysis of Large-capacity Distributed Photovoltaic Grid-connected Distribution Networks[J]. Journal of Electric Power Systems and Automation, 28(11):44-49

Mollerstedt E, Bernhardsson B. 2000, Out of control because of harmonics-an analysis of the harmonic response of an inverter locomotive[J]. IEEE Transa-ctions on Control Systems, 20(4): 70-81.

Enslin J H R, Heskes P J M. 2004, Harmonic interaction between a large number of distributed power inverters and the distribution network[J]. IEEE Transactions on Power Electronics, 4(6): 1586-1593.

Zhang X. 2011, Solar photovoltaic grid-connected power generation and its inverter control [M]. Beijing: Machinery Industry Press.

Zou X, Yi L, Zhang M, et al. 2008, A New Method of Constant Frequency Hysteresis Current Control for Photovoltaic Grid-Connected Inverters[J]. Electric Power Automation Equipment, 28(4): 58-62.

161: Research on capacity allocation of hybrid energy storage system based on improved particle swarm optimisation

Li LIAO [1], Xiao SHI[2], TieZhou WU[3], JunJie ZHANG[4]

[1] Hubei Key Laboratory for High-efficiency Utilisation of Solar Energy and Operation Control of Energy Storage Sysetem，Hubei University of Technology, 646352864@qq.com

[2] Hubei Key Laboratory for High-efficiency Utilisation of Solar Energy and Operation Control of Energy Storage Sysetem，Hubei University of Technology, 15671676897@163.com

[3] Hubei Key Laboratory for High-efficiency Utilisation of Solar Energy and Operation Control of Energy Storage Sysetem，Hubei University of Technology, 1297362526@qq.com

[4] Hubei University of Technology, 2978636476@qq.com

In view of optimizing the configuration of each unit's capacity for energy storage in the micro-grid system, in order to ensure that the planned energy storage capacity can meet the reasonable operation of the micro-grid's control strategy, the power fluctuations during the grid-connected operation of the micro-grid are considered in the planning and The economic benefit.of the hybrid energy storage is quantified. This paper uses an improved filter that can dynamically adjust the time constant to distinguish between high frequency and low frequency power fluctuations. Combined with the state of charge and other limiting conditions of the hybrid energy storage system, the target power value of each energy storage unit in the hybrid energy storage is determined.Satisfying the constraint conditions such as the charging and discharging power of the energy storage units,a multi-objective function aiming at minimizing the power fluctuation on the DC bus in the micro-grid and optimizing capacity ratio of each energy storage system in the hybrid energy storage system is established.The improved particle swarm algorithm is used to solve the objective function, and the solution is applied to the micro-grid experimental platform. By comparing the power fluctuations of the battery and the super capacitor in the hybrid energy storage system, the power distribution is directly reflected. Comparing with the traditional mixed energy storage control strategy, it shows that the optimised hybrid energy storage control strategy can save 4.3% of the cost compared with the traditional hybrid energy storage control strategy, and the performance of the power fluctuation of the renewable energy is also improved. It proves that the proposed energy management strategy has certain theoretical significance and practical application value.

Keywords: renewable energy, Hybrid energy storage; Micro power grid

1. INTRODUCTION

In recent years, with the rapid development of micro-grids, it has become a highly efficient and flexible new distributed power grid that can be tightly integrated with existing power systems. The proportion of renewable energy power generation is increasing. However, the output power of renewable energy sources may change due to uncontrollable factors such as weather and seasons, and it is impossible to formulate a precise power generation plan, and the reliability is not high. Especially for stand-alone micro-grids containing renewable energy sources, since they will not be able to feed energy from large grids, these problems may cause serious consequences at the load side (Chen, 2017).

The existing energy storage devices are generally divided into two types, one is a power storage unit with higher power density and lower energy density (Li, 2016), such as super capacitor (Wang. 2010). The other is energy storage unit with higher energy density and lower power density (Hou, et al, 2017), such as battery (Liu et al. 2015; Peng, 2011). When the output power of renewable energy is large, the super capacitor can effectively suppress the short time high frequency power fluctuation, and the battery can suppress the long time low frequency power fluctuation. When the power output of renewable energy is stable and sufficient, the energy storage system is in charge state and can fully absorb renewable energy.When renewable energy can not meet the demand of micro-grid, the energy storage system can also supply power to all or important loads independently (Del Granado et al, 2016). On the basis of using the filter as the power allocation control strategy, the multi-objective function is proposed in combination with the control requirements. After fitting, the target function is solved by the particle swarm optimisation algorithm. The specific capacity parameters of the battery and the super capacitor are obtained. The control signal is produced by the local strategy controller to the optimised storage system, and the final control effect of the micro-grid is achieved.

2. RECONFIGURABLE MICRO-GRID STRUCTURE ANALYSIS

2.1. Renewable energy generation system and hybrid energy storage system structure

For stand-alone operation of micro-grids containing renewable energy, it is mainly composed of wind power generation systems, photovoltaic arrays, hybrid energy storage systems, DC/AC conversion devices, DC/DC conversion devices, and loads (Zhu. 2015). The structural diagram is shown in Figure 1.

The conversion of renewable energy from different properties to electricity has different properties. For example, wind power is alternating current and photovoltaic power is direct current. Therefore, it is necessary to use AC/DC or DC/DC and DC bus respectively to connect. After the DC bus meets the DC load in the micro-grid, the DC/AC module is connected to the AC bus to supply the AC load in the micro-grid. However, the instability of renewable energy will cause great fluctuation of power on DC bus and affect the power quality and reliable operation of micro-grid (Choi et al, 2016). Therefore, the power frequency characteristics of renewable energy are detected in real time and controlled by local policy controller. The power fluctuation is divided into two parts of high frequency and low frequency by the improved low pass filter, and then the power stability on the DC bus is maintained by the reduction of the power distribution of different energy storage units in the hybrid energy storage system. As the core of the control strategy, local strategy controller needs to collect the frequency information of power fluctuation, and then completes the calculation steps in the low-pass filter algorithm and other control strategies. Finally, the control signal is generated to control the DC-DC converter.

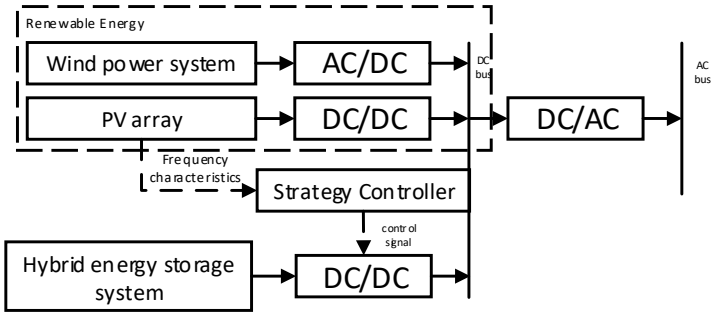

Figure 1: System Structure

2.2. The principle of smooth control strategy of hybrid energy storage system

Different energy storage units in energy storage system are responsible for high-frequency or low-frequency power fluctuations generated by renewable energy (Yang et al. 2016). Combined with the characteristics of the two types of energy storage units, smooth control strategy can use supercapacitors to suppress high frequency part of the

fluctuations in P_{ref} , and batteries to stabilise the low frequency part of P_{ref} . When the output power of the renewable energy fluctuates greatly, the DC bus power of the micro-grid will not fluctuate greatly, and the micro-grid can operate reliably. The principle of filter smoothing control strategy for hybrid energy storage is shown in Figure 2.

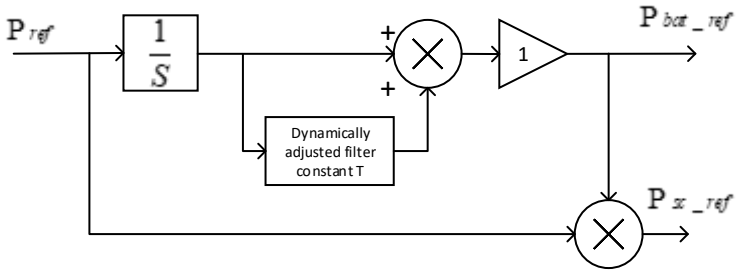

Figure 2: Principle of smoothing control strategy of hybrid energy storage filter

3. THE OBJECTIVE FUNCTION OF HESS

3.1. Objective function

Objective function to reduce the fluctuation of renewable energy power:

Considering that the output power of renewable energy changes rapidly, 1 min is set as a scheduling period. The objective function is established as in Equation 1:

Equation 1: To reduce the power fluctuation of renewable energy as an objective function

$$F_1 = \min \sum_{i=2}^{n} \left| (P_{DG,i} - P_{DG,i-1}) \right|$$

Equation 2: The output power of the renewable energy source

$$P_{DG,i} = P_{dg,i} + P_{bat,i} + P_{sc,i}$$

Where:

F_1 = the power fluctuation of renewable energy (kW)
n = the number of scheduling cycle
$P_{DG,i}$ = the output power of the i dispatching cycle after the hybrid energy storage system is stabilised (kW)
$P_{dg,i}$ = the output power of the renewable energy source that has not been stabilised by the hybrid energy storage system (kW)
$P_{sc,i}$ = the output powers of the super capacitor in the i-th scheduling period (kW)
$P_{bat,i}$ = the output powers of the battery in the i-th scheduling period (kW)

Objective function to meet the minimum cost of construction operation:

At the present stage, the construction and operation of Micro-grid need higher cost. If more hybrid energy storage systems are configured, they can meet the normal operation of the Micro-grid, but they will have high construction, operation and maintenance costs. If fewer hybrid energy storage systems are configured, the normal operation of the Micro-grid cannot be met. Therefore, the objective function is introduced in order to meet the operation of the Micro-grid and the minimum construction operation cost, defined as Equation 3:

Equation 3: To meet the micro-grid operation and minimise construction and operation costs.

$$F_2 = \min(m_1 \frac{E_{bat}}{\eta_{bat}} + m_2 \frac{E_{sc}}{\eta_{sc}} + m_3 P'_{bat} + m_4 P'_{sc})$$

Where:

F_2 = construction and operation costs
m_1 = the cost of each degree of storage unit of battery , including the cost of its supporting equipment
m_2 = the cost of each degree of storage unit of super capacitor , including the cost of its supporting equipment
m_3 = the scheduling costs when the battery participate in the long-term scheduling of the micro-grid
m_4 = the scheduling costs when the super capacitor participate in the long-term scheduling of the micro-grid

E_{bat} = the installed capacity of the battery (A·H)

E_{sc} = the installed capacity of super capacitor (F)

η_{bat} = the energy conversion efficiency of the battery

η_{sc} = the energy conversion efficiency of the super capacitor

P'_{bat} = the average power when the battery participate in the long-term scheduling of the power grid (kW)

P'_{sc} = the average power when the super capacitor participate in the long-term scheduling of the power grid (kW)

3.2. Constraint condition

(1) In order to prevent the overcharge and overdischarge of the energy storage unit, the remaining capacity of the energy storage system is limited, defined as Equation 4.

Equation 4: the remaining capacity of the energy storage system

$$20\% < SOC_{sc} < 90\%$$
$$30\% < SOC_{bat} < 80\%$$

Where:

SOC_{sc} = the SOC of super capacitor in the hybrid energy storage system

SOC_{bat} = the SOC of the battery in the hybrid energy storage system.

(2) Considering the broken state of the renewable energy in the micro-grid, the hybrid energy storage system needs to be able to output relatively large power in a certain time to meet the normal operation of the micro-grid. At the same time, it is also necessary to consider that the maximum allowable output power of each energy storage unit and each power converter cannot be exceeded, described as Equation 5.

Equation 5: The maximum allowable output power.

$$\begin{cases} P_{uc,i} + P_{bat,i} \geq P_{\max} \\ P_{uc,\min} \leq P_{uc,i} \leq P_{uc,\max} \\ P_{bat,\min} \leq P_{bat,i} \leq P_{bat,\max} \end{cases}$$

Where:

$P_{uc,\min}$ = the minimum power that the super capacitor and power converter can withstand (kW)

$P_{uc,\max}$ = the maximum power that the super capacitor and power converter can withstand (kW)

$P_{bat,\min}$ = the minimum power that the battery and power converter can withstand (kW)

$P_{bat,\max}$ = the maximum power that the battery and power converter can withstand (kW)

$P_{\max}$ = the output relatively large power in a certain time to meet the normal operation of the micro-grid (kW)

(3) Energy constraint conditions.

At any time, the power balance must be guaranteed in the micro-grid. The power relation can be described as Equation 6:

Equation 6: Energy Constraints in Reliable Energy-Containing Micro-grids.

$$P_{sc,i} + P_{bat,i} + P_{pv,i} + P_{w,i} = P_{L,i} + P_{loss,i}$$

Where:

$P_{sc,i}$ = the power of the super capacitor at the current sampling time (kW)

$P_{bat,i}$ = the power of the battery at the current sampling time (kW)

$P_{pv,i}$ = the output power of PV at the current sampling time (kW)

$P_{w,i}$ = the output power of wind power at the current sampling time (kW)

$P_{L,i}$ = the power at the DC bus at the current sampling time (kW)

$P_{loss,i}$ = the power consumption of surplus power through the load unloading device (kW)

4. USING PARTICLE SWARM OPTIMISATION TO SOLVE MULTIOBJECTIVE FUNCTIONS

4.1. Adaptive weighted particle swarm optimisation

Particle Swarm Optimisation (PSO) is an intelligent algorithm that simulates the process of flock search for food. Its advantage is that the algorithm process is simple, the parameters are less than other algorithms, and it is easy to implement. Its position and speed are updated according to the formula of Equation 7:

Equation 7: Particle update equation.

$$\begin{cases} v_{ij}^{t+1} = wv_{ij}^{t} + c_1 r_1 (p_{best,ij}^{t} - x_{ij}^{t}) + c_2 r_2 (g_{best,ij}^{t} - x_{ij}^{t}) \\ x_{ij}^{t+1} = x_{ij}^{t} + v_{ij}^{t+1} \end{cases}$$

Where:

t = the number of iterations of the algorithm
w = the inertia weight of each particle during flight
v_{ij}^{t} = the velocity of the particle at the i-th row and the j-th column at t
c_1 , c_2 = the learning factors of the algorithm
r_1 , r_2 = random numbers
p_{best} = the optimal fitness of each particle respectively Optimal fitness
x_{ij}^{t} = The position of the particles in row i and column j at t
g_{best} = the global of each particle respectively Optimal fitness

w is the inertia weight, which plays a role in maintaining the original motion state of the particle. The bigger the w , the stronger the global optimisation ability.

The inertial constant w is a very important constant in the particle swarm algorithm. The larger the value of w , the faster the particle's search speed, but the lower the search accuracy. The smaller the value of w , the slower the particle's search speed, but the higher the search accuracy. Therefore, compared to the particle swarm optimisation algorithm with fixed inertia weights, the adaptive optimisation method of decrementing the inertia weight can guarantee the search accuracy without losing the algorithm speed, so that the value of w can be changed according to Equation 8:

Equation 8: inertial constant.

$$w = \begin{cases} w' + k' \dfrac{dv_{id}}{dt} & g'_{best} > \Delta error \cdot 10 \\ w' - k'' \dfrac{dv_{id}}{dt} & g'_{best} < \Delta error \end{cases}$$

Where:

w' = the reference value of w
k' , k'' = compensation coefficients
v_{id} = the current particle velocity
$\Delta error$ = the allowable error of the system

4.2. Worst particle elimination strategy

In order to exert the advantages that all the particles in the particle should have, and increase the efficiency of the algorithm, in the algorithm, a knock-out judgment strategy is also introduced. That is, in each iteration of the system, the particles with the least fitness are replaced by the particles with the best fitness, new speeds and positions are set, and a re-search step is performed, the optimal particle fitness does not change. After adding the worst particle elimination strategy, the algorithm's convergence and local search capabilities will be significantly improved. The specific steps are as follows:

Step1: algorithm initialisation operation, calculate the initial fitness of each particle, etc;

Step2: Prepare for iterative operations, find out the individual extreme p_{best} and the individual worst fitness p_{worst}, use p_{best} instead of p_{worst};

Step3: Calculate and find the global extreme g_{best} and global worst fitness g_{worst}, replace g_{best} with g_{worst};

Step4: Update the position and velocity of the particle based on the particle velocity update formula and the position update formula;

Step5: Determine whether the loop limit condition is reached (reach the allowable error or the number of iterations reaches the upper limit), and exit the algorithm if it is reached. If it does not, go back to the second step, continue execution.

4.3. Multi-objective function fitting

Since the particle swarm algorithm can only calculate a single objective function, but we proposes multiple objective functions here, so it is necessary to fit multiple objective functions. The conventional practice is to propose a set of parameters $\lambda_i(i=1,2,3\cdots)$, the sum of the parameters is 1, according to the important length of each objective function, artificially relying on the experience of the method to set, doing so in many cases will produce a larger error.

The fitted multi-objective function should be described as in Equation 9.

Equation 9: The fitted multi-objective function.

$$\begin{cases} F = \lambda_1 F_1 + \lambda_2 F_2 + \cdots + \lambda_m F_m \\ \lambda_1 + \lambda_2 + \cdots + \lambda_m = 1 \end{cases}$$

Where:

F = the fitted objective function
λ_m = the weighting coefficient of m
F_m = the objective function of m

Based on the traditional multi-objective function fitting, this paper proposes a method based on the difference between the current value and the average value as the discriminant principle, and uses the entropy weight method to determine the weighting coefficient. The coefficients are determined by weighting all the indices using the entropy weight of each index. The method is as shown in Equation 10.

Equation 10: The weighting coefficient.

$$\Delta_i^j = f_i^j - f_{average}$$

Where:

Δ_i^j = the difference between the current particle and the average fitness
f_i^j = the fitness of the current particle of each objective function
$f_{average}$ = the average of the fitness of all particles of each objective function

The difference reflects the difference between the current particle's flight according to the current flight trajectory and speed and the optimal value. If the difference is larger, the gap between the current configuration and the optimal solution is larger. According to the difference, the method for determining each utility coefficient before each objective function using the entropy weight method is as follows:

1) Determine the loop control variable m according to the number of objective functions, and find the optimal solution for a single objective function as f_i;

2) Bringing the optimal solution of each single goal into a different objective function to obtain the corresponding objective function fitness f_i^j;

3) Calculate the difference Δ_i^j of the optimal solution for each objective function;

4) Calculate the average difference of each objective function: $u_i = \dfrac{\sum_{j=1}^{m} \Delta_i^j}{m} \quad i = 1, 2, \cdots, m$;

5) Calculate the weighting factor for each objective function: $\lambda_i = \dfrac{u_i}{\sum_{j=1}^{m} u_j} \quad i = 1, 2, \cdots, m$;

4.4. Solving multi-objective functions

Using the improved particle swarm algorithm to solve the objective function after fitting. The calculation process is as follows:

Step1: Initialise the algorithm, calculate the fitness of the multi-objective function of each particle based on the objective function after fitting, and input constraint condition;

Step2: Determine the fitness of each particle's multi-objective function is within the range of feasible solutions, and search for g_{best} and p_{best} according to the initial value;

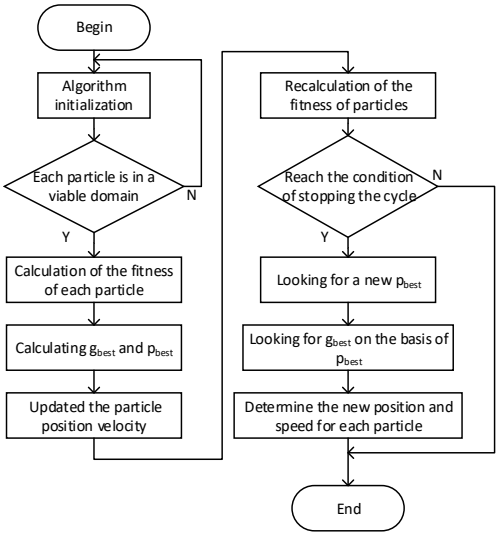

Figure 3: algorithm calculation flow chart

Step3: Calculate the position and velocity of each particle at the next iteration based on the particle velocity and position update formula, and recalculate the fitness of each particle;

Step4: Judge whether the conditions for stopping the iteration has reached, such as reaching the accuracy requirement or reaching the number of iterations. If it is not reached, choose a new p_{best}, and g_{best} is selected from it, and re - execute step 3 n. If the stop iteration condition is reached, the loop is stopped;

Step5: Output algorithm results;

The calculation flow chart of the algorithm is shown in Figure 3.

5. EXPERIMENTAL RESULTS AND ANALYSIS

Table 1: Main parameters of the Micro-grid model

Parameter name	Parameter symbol	Parameter values
Battery voltage	V_{bat}	70-85 (V)
Supercapacitor voltage	V_{sc}	60-75 (V)
DC Bus Voltage	U_{dc}	120 (V)
Maximum output power of battery	$P_{bat\_\max}$	800 (W)
Maximum output power of supercapacitor	$P_{sc\_\max}$	2000 (W)
Transmission efficiency	η	0.95
Sampling frequency	f_{bat}	40kHZ
Switching frequency	T	10kHZ
Rated load of DC bus	P_{load}	3000 (W)

The main parameters of the selected Micro-grid model in the experiment are shown in Table 1.

1) Analysis of Experimental Results of Economic Benefit

Table 2 and Table 3 show the economic analysis of the traditional hybrid energy storage system control strategy and the economic benefits analysis of the traditional hybrid energy storage system control strategy after optimisation.

Table 2: Economic Benefit Analysis of Traditional Hybrid Energy Storage Control Strategy

Parameter name	Parameter values
Equivalent discharge cycles of accumulators in 1 load cycles	3.2
Equivalent discharge cycles of ultracapacitor in 1 load cycles	5.4
Replacement times of battery in the whole life cycle	3.6
Replacement of supercapacitor during the whole life cycle	0.2
Charge per batch of battery per batch / yuan	1592
Cost per unit of super capacitor per batch / yuan	28497
The cost / element of the battery for the whole life cycle	5731
The cost / element of the supercapacitor during the whole life cycle	5699
Cost / yuan of hybrid energy storage system in the whole life cycle	11430

Table 3: Economic Benefit Analysis of Optimised Hybrid Energy Storage Control Strategy

Parameter name	Parameter values
Equivalent discharge cycles of accumulators in 1 load cycles	1.8
Equivalent discharge cycles of ultracapacitor in 1 load cycles	7.4
Replacement times of battery in the whole life cycle	1.5
Replacement of supercapacitor during the whole life cycle	0.3
Charge per batch of battery per batch / yuan	1592
Cost per unit of super capacitor per batch / yuan	28497
The cost / element of the battery for the whole life cycle	2388
The cost / element of the supercapacitor during the whole life cycle	8549
Cost / yuan of hybrid energy storage system in the whole life cycle	10937

The analysis of the calculated results shows that the optimised hybrid energy storage control strategy can save 4.3% of the operating cost in a single operating cycle. And the number of times the battery needs to be replaced is also significantly reduced.

2) Analysis of experimental results of fluctuating power fluctuations in renewable energy sources

The experiment in this area use one day as the scheduling period to observe the suppression effect of the hybrid energy storage system. The contrastive object of the experiment is the traditional hybrid energy storage system to control the power fluctuation of renewable energy. In a Micro-grid operation cycle, the correctness and effectiveness of the improved control strategy can be verified by comparing the control effects of the improved hybrid energy storage system control strategy and the traditional hybrid energy storage system control strategy. The comparison results are shown in Figure 4 and Figure 5.

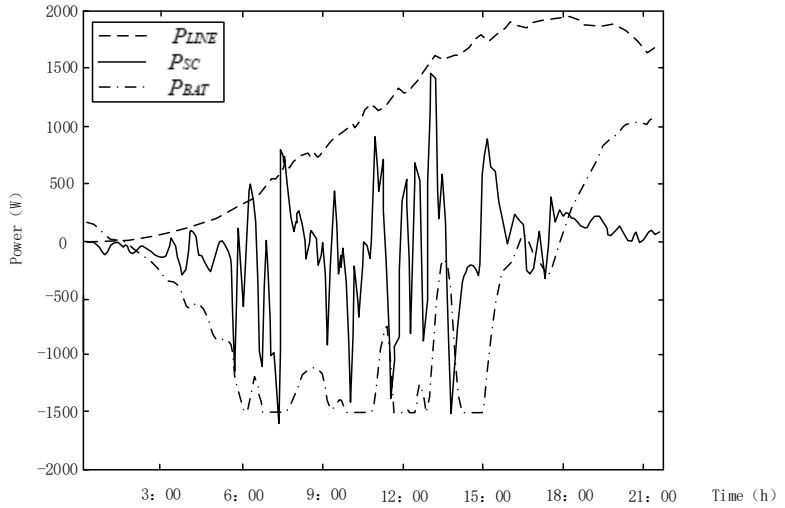

Figure 4: Micro-grid operation without using this control strategy

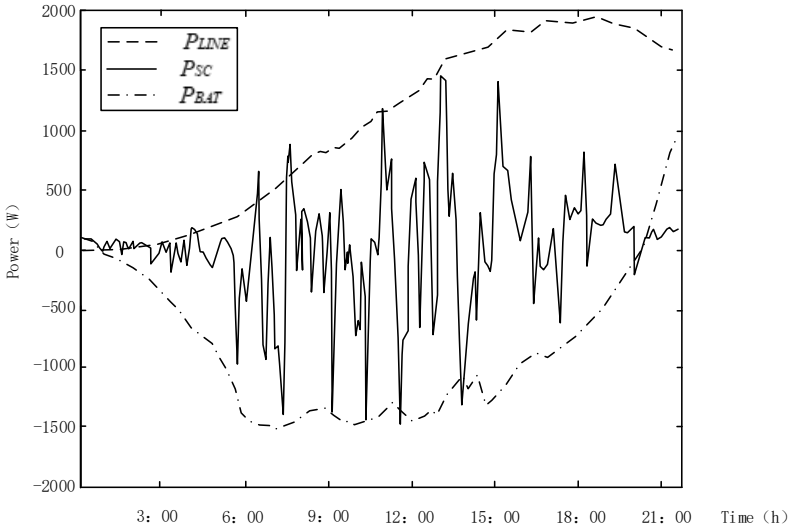

Figure 5: Micro-grid operation when using this control strategy

From the comparison chart, we can see that, when the control strategy is not used, although the super capacitor bears most of the high-frequency fluctuations, the grid-connected power generated by the power generation unit cannot be controlled, causing the battery to be cut off by the safety module because of the excessive discharge power between 6 o'clock and 15 o'clock. From the P_{LINE} curves, it can be seen that the use of this control strategy is more excellent in suppressing bus power fluctuations. The working status of the battery has also been significantly improved. Overcharging and overdischarging are basically avoided, which can effectively extend the service life of the battery. The improved hybrid energy storage control strategy has improved the working conditions of the battery, and basically no overcharge and discharge have occurred.

6. CONCLUSION

This paper uses a hybrid energy storage system consisting of a battery and a super capacitor to suppress the power fluctuation of the Micro-grid caused by renewable energy. Based on the multi-objective function of the minimum power fluctuation on the DC bus and the optimal capacity ratio of each energy storage system in the hybrid energy storage system, the improved particle swarm optimisation is used to solve the objective function. Experiments show that hybrid energy storage control strategy can attenuate power fluctuations on the DC bus, and the fluctuation of the high frequency components of the battery is reduced, the cycle life of battery is extended, and the cost of the system is also reduced. Compared with the traditional hybrid energy storage control strategy, the strategy can save 4.3% of the cost, and the performance of modulating power fluctuations in renewable energy has also been significantly improved. It proves that the proposed energy management strategy has certain theoretical significance and practical application value.

7. REFERENCES

Chen Z Y. 2017. Optimal Smoothing Control Strategy of Virtual Energy Storage System in Micro-grid Based on Continuous State Constraints [J]. Power System Technology, (01):55-63.

Li Z Y, Li M. 2016. Power balance control strategy of hybrid-bus Micro-grid[J]. Journal of Central South University, (06):2331-2338.

Wang X. 2010. Research on the Influence of Supercapacitors on Power Quality of Micro-grid[D]. North China Electric Power University (Beijing).LW C, YW W, RK R, RK R, D I. 2016. Hybrid energy storage systems and control strategies for stand-alone renewable energy power systems[J].Renewable & Sustainable Energy Reviews, 66:174-189.

Hou S Y, Bi X H, Sun W, et al. 2017. Control strategy of hybrid energy storage under islanamg operation state[J]. Journal of Electrical Machines and Controls, 21(5):15-22.

Liu CY, Wang XL, Liu SM, et al. 2015. Micro-grid economic dispatch model considering battery life[J]. Electric Power Automation Equipment, 35(10): 29-36.

Peng SM, Cao YF, Cai X. 2011. Mode and Control Strategy of Large Battery Energy Storage System Accessing Micro-grid[J]. Automation of Electric Power Systems, 35(16): 38-43.

Del Granado PC, Pang Z, Wallace ST. 2016. Synergy of smart grids and hybrid distributed generation on the value of energy storage[J].Applied Energy, 170:476-488.

Zhu YQ, Jia LH, Wang YS. 2015. Basic Principles of Micro-grid Structure Design[J]. Advanced Technology of Electrical Engineering and Energy, 34(9):44-63.

Choi JW, Heo SY, Kim MK. 2016. Hybrid operation strategy of wind energy storage system for power grid frequency regulation[J]. Iet Generation Transmission & Distribution, 10(3):736-749.

Yang W, Luo A, Chen YD, et al. 2016. Secondary ripple current suppression and equalisation control method for two-band pass filter of bidirectional energy storage converter in DC micro-grid[J]. Proceedings of the CSEE, 36(6) :1613-1624.

162: Research on photovoltaic grid-connected inverters with unbalanced load compensation

He XIAO, Xi ZIQIANG, Zhang CHANGZHENG

Hubei Key Laboratory for High-efficiency Utilisation of Solar Energy and Operation Control of Energy Storage System, Hubei University of Technology, Wuhan, 430068, P. R. China
e-mail:315392728@qq.com

The increasing global energy crisis and environmental problems have stimulated the rapid development of renewable energy grid-connected technologies such as wind and light. As an important supplement to traditional large-scale centralised wind power stations, the distributed generation technology of renewable energy has attracted widespread attention at home and abroad. As a special distributed power generation system, the microgrid is an important bridge and link between the power grid and renewable energy, which can effectively reduce the impact of renewable energy grid-connected units on the power grid and improve the reliability of power supply and power quality, which is popular favored. However, most grid-connected inverters in the microgrid can only rigidly inject pure sinusoidal fundamental active current into the grid, which exposes many technical limitations and can hardly meet the needs of many emerging technologies. Among them, auxiliary power demand for grid-connected inverters, such as power quality control, autonomous operation, harmonic resonance suppression, etc., has received the most attention. In this paper, the influence of three-phase unbalance on grid-connected inverters is studied. Based on the photovoltaic system, a three-phase four-wire inverter system structure based on command signal generation is proposed. Through model selection, functional analysis, study of its modulation strategy and establishment of a corresponding simulation model, the working principle of photovoltaic grid-connected inverter system is analyzed in depth. The final simulation results show that the control strategy and modulation method studied in this paper can make PV grid-connected inverters have the function of load imbalance compensation, and effectively compensate for the imbalance produced by composite loads such as pure resistive and harmonic loads.

Keywords:PV inverter; DC microgrid; three level

1. INTRODUCTION

As non-renewable energy sources are depleted, but the economy continues to grow, energy issues have become increasingly serious. The development and utilisation of renewable energy has played a positive role in improving people's quality of life and improving the ecological environment. The development of renewable energy can make full use of our land resources, adjust the energy structure, and promote the production and development of emerging industries. It can be seen that expanding the renewable energy industry in China can accelerate the development of emerging industries and produce huge social and economic benefits. Photovoltaic power generation, as an important component of the development of renewable energy in recent years, has enormous environmental advantages and long-term sustainability. From the energy conservation and emission reduction targets of various countries and the UN's “Renewable Energy Special Report”, we can see that by 2050, achieving a high proportion of renewable energy alternatives is a worldwide trend, which will promote the development of China's solar photovoltaic power generation industry. On October 26, 2012, the State Grid Corporation of China issued the "Opinions on the Implementation of Distributed Photovoltaic Power Grid-connected Services", which significantly reduced the entry threshold for photovoltaic power generation; the National Energy Administration clearly stated that the target for the installation by 2020 is 100 million KW. In the coming years, there will be more than 10 GW of domestic installed capacity. By 2030, the total energy demand will reach 5 billion tons of standard coal, and by 2050 it will reach 5.2 billion tons. Renewable energy will account for 40% of the total energy demand in 2050, and renewable energy will reach 60% of the total electricity demand. Power generation may have a capacity of 1 billion KW. The strong support of national policies will promote the rapid and healthy development of China's solar photovoltaic power generation industry.

In photovoltaic power generation systems, inverters have a very significant role (Wei, 2014:218-225). The quality of the grid-connected PV power system depends largely on the efficiency of the inverter. The three-phase unbalanced problem is also one of the key problems to be solved in the inverter. When the three-phase imbalance occurs in the system, the system will cause serious consequences in the operation, for example, when the rotary electric machine is unbalanced in three phases, it generates a large amount of extra heat and may cause vibration, resulting in abnormal operation and work status. At the same time, since China's power distribution network mainly uses three-phase four-wire power supply, there are a large number of single-phase power units. Therefore, it is of great significance to take appropriate compensation measures for power systems with three-phase imbalance.

This paper studies a new three-phase four-wire photovoltaic system. The system can realise the unbalanced load compensation function while achieving the basic functions of high-power photovoltaic grid-connected power generation. On the basis of in-depth analysis of existing researches, we attempted to make breakthroughs in solving key scientific issues in the field of photovoltaic power generation and unbalanced compensation through structural optimisation and improvement of control.

2. GRID-CONNECTED INVERTER TOPOLOGY SELECTION

In this paper, a diode-clamped three-level inverter topological structure is adopted (Li, 2014:49-54). When the neutral line selects a structure that does not contain an inductor, the three bridge arms can be regarded as three totally independent control systems. The inverter topology is shown in Figure 1.

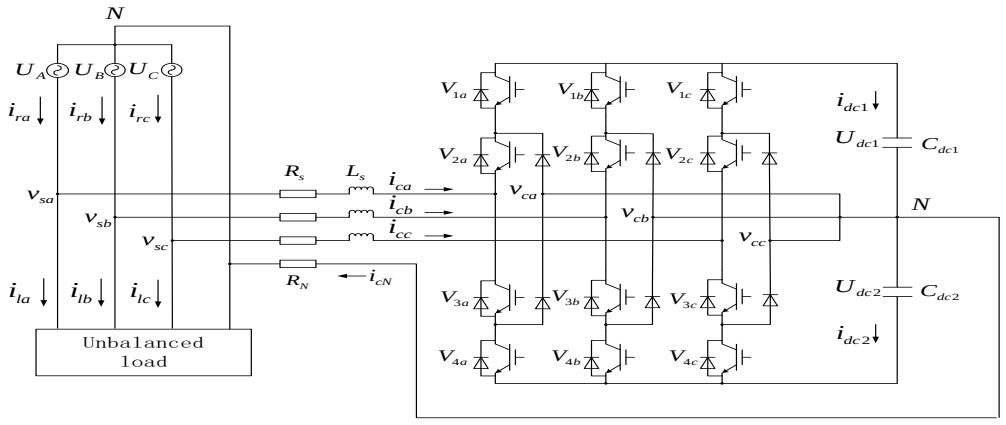

Figure 1: Diode clamped three-level inverter topology

From Figure 1 you can define the switch function as follows:

$$S_j = \begin{cases} 2; & V_{1j}, V_{2j} \ \text{ON} \\ 1; & V_{2j}, V_{3j} \ \text{ON} \\ 0; & V_{3j}, V_{4j} \ \text{ON} \end{cases} \quad (1)$$

In the formula $j = a, b, c$

For the moment, the voltage imbalance of the upper and lower bridge arms on the DC side is not taken into consideration, and the voltages of the neutral points on the power grid can be described as follows:

$$\begin{cases} u_{AN} = (S_a - 1)U_{dc} \\ u_{BN} = (S_b - 1)U_{dc} \\ u_{CN} = (S_c - 1)U_{dc} \end{cases} \quad (2)$$

Where U_{dc} represents one-half of the voltage on the DC side of the inverter, that is, the voltage of a single capacitor in the absence of an offset on the DC side.

According to Figure 1 and Equations 1-2, the relationship between current and voltage on the output inductor can be obtained as shown in Equations (2-3) to (2-5):

$$U_{sa} = (S_a - 1)U_{dc} + L_s \frac{di_{ca}}{dt} + R_s i_{ca} + R_N i_{cN} \quad (3)$$

$$U_{sb} = (S_b - 1)U_{dc} + L_s \frac{di_{cb}}{dt} + R_s i_{cb} + R_N i_{cN} \quad (4)$$

$$U_{sc} = (S_c - 1)U_{dc} + L_s \frac{di_{cc}}{dt} + R_s i_{cc} + R_N i_{cN} \quad (5)$$

Among them: i_{ca}, i_{cb}, i_{cc} is the inverter output current, L_s is the output connection inductance, R_s is the line equivalent resistance, R_N is the middle line equivalent resistance.

3. ANALYSIS OF WORKING PRINCIPLE OF GRID-CONNECTED INVERTER

The following will introduce the working principle from the inverter operation mode and the compensation unbalanced instruction signal generation method.

3.1. Inverter operation mode analysis

In this paper, the inverter topology can achieve the three operating modes shown in Figure 2 by changing the state of the switch (Zhao, 2014:72-78). Because three bridge arms can realise independent control, one of the bridge arms is selected for analysis. According to different combinations of switches, three working states can be obtained: “P” state (or “1” state), and “O” state. (or "zero" state), "N" state (or "-1" state).

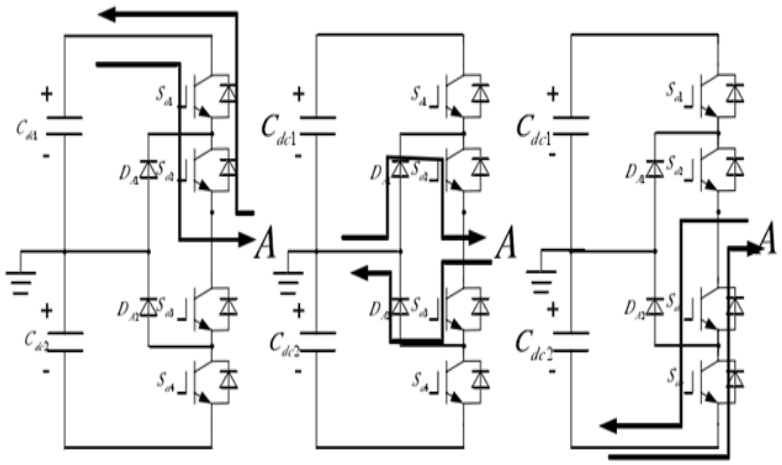

Figure 2: Three operating modes of inverter switch

(1) "P" state: When S_{a1}, S_{a2} are on, S_{a3} and S_{a4} are off, and the current direction flows from the neutral point through the diode to the distribution network side, the voltage at point A is $U_A=1/2U_{dc}$; when S_{a3} and S_{a4} are off, the current direction is from the distribution network. Side through the diode to the neutral point, this time also has the voltage A point $U_A=1/2U_{dc}$.

(2) "O" state: When S_{a2}, S_{a3} are on, S_{a1} and S_{a4} are off, and the current direction flows from the neutral point through the diode to the distribution network side, the voltage at point A is $U_A=0$; There is also a situation where the current flows from A and the direction of the current flows from the distribution network side to the neutral point via the diode, this time also has the voltage A point $U_A=0$.

(3) "N" state: When S_{a3}, S_{a4} are on, S_{a1} and S_{a2} are off, and the current direction flows from the neutral point through the diode to the distribution network side, the voltage at point A is $U_A=-1/2U_{dc}$; when S_{a1} and S_{a2} are off, the current direction is from the distribution network. Side through the diode to the neutral point, this time also has the voltage A point $U_A=-1/2U_{dc}$.

Table 1: Three-phase inverter switching status per phase

MODE	Sa1	Sa2	Sa3	Sa4	Ua
P	ON	ON	OFF	OFF	Udc/2
O	OFF	ON	ON	OFF	0
N	OFF	OFF	ON	ON	-Udc/2

By changing the on-off condition of each bridge switch by a specific rule, the line voltage U_{ab} can be obtained by the phase voltages U_A and U_B after the control. Ensure that the output phase of the inverter system varies among the three potential states of $U_{dc}/2$, 0, and $-U_{dc}/2$.

3.2. Command signal generation method for compensating unbalanced load

The command signal generation method is based on research and analysis of the zero-sequence current separation method (Rivera,2014:1107) in reactive current detection. First, the zero-sequence components of the three-phase load currents i_a , i_b , and i_c are detected, and then the zero-sequence components are respectively taken from this three-phase load current. In the elimination, the current after eliminating the zero sequence is 3/2 converted, and the corresponding active component and reactive component can be obtained. Disconnect I_q channel, I_d get the corresponding DC component $i_a^{'}$, $i_b^{'}$, $i_c^{'}$ after low-pass filter, and then carry out coordinate inverse transformation to get fundamental active component, and use three-phase load current i_a , i_b , i_c minus i_{af} , i_{bf} . i_{cf} , get the required compensation signal i_{ar} , i_{br} , i_{cr} , which contains the three-phase load current reactive power, fundamental negative sequence, zero sequence and harmonic components.

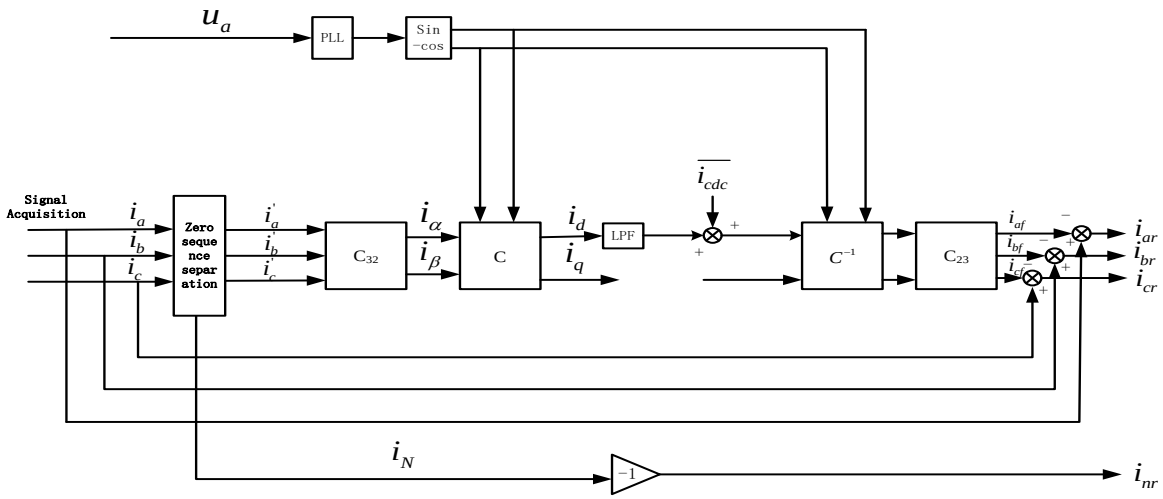

Figure 3: Zero-sequence current separation principle

4. MODULATION METHOD

This article chooses single sine wave double triangle wave modulation as the modulation method of the inverter system (Chen, 2104:3808-3817). The reference sine wave is R_X, the two triangular carriers are T_{r1} and T_{r2}, respectively, and both have the same amplitude and phase. Where T_{r1} is in the positive quadrant and T_{r2} is in the negative quadrant, as shown in the following figure.

At this time, the switching control law is as follows: When R_X>T_{r1}, S_{X1} and S_{x2} are turned on and the output phase voltage is $1/2\,U_{dc}$. When R_X<T_{r1} , S_{X2} and S_{x3} are turned on, and the output phase voltage is 0. When R_X>T_{r2}, S_{X2} and S_{x3} are turned on and the output phase voltage is 0. When R_X<T_{r2}, S_{X3} and S_{x4} are turned on and the output phase voltage is $-1/2\,U_{dc}$. The driving waveform is shown in Figure 4.

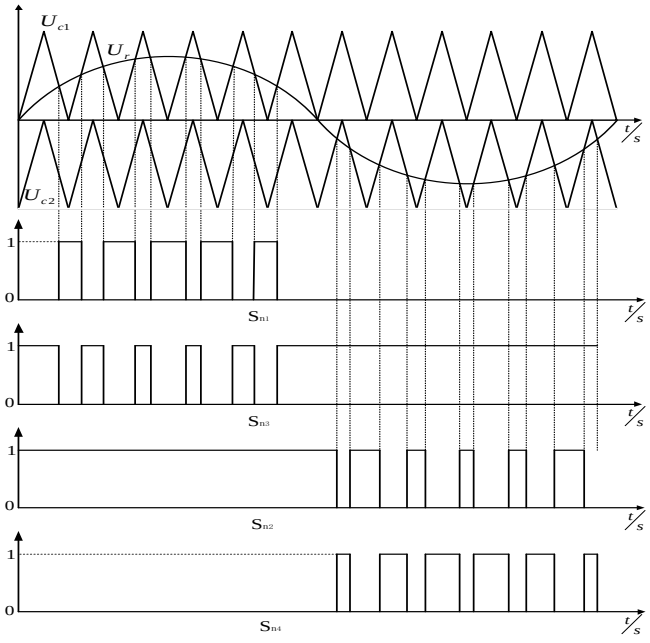

Figure 4: Zero-sequence current separation principle

5. EXPERIMENTAL SIMULATION

Based on the research of the above detection methods and modulation methods, a simulation model was established through Matlab/Simulink and simulation experiments were conducted. Three-phase power supply with a line voltage of 380V and a frequency of 50Hz is used. The load is an unbalanced load case with resistance and inductance for simulation analysis. The resistances of the three-phase load are 4 Ω , 10 Ω , and 10 Ω , the inductance is 4mH, and the switching frequency is 18kHz. The simulation model diagram is shown in Figure 5.

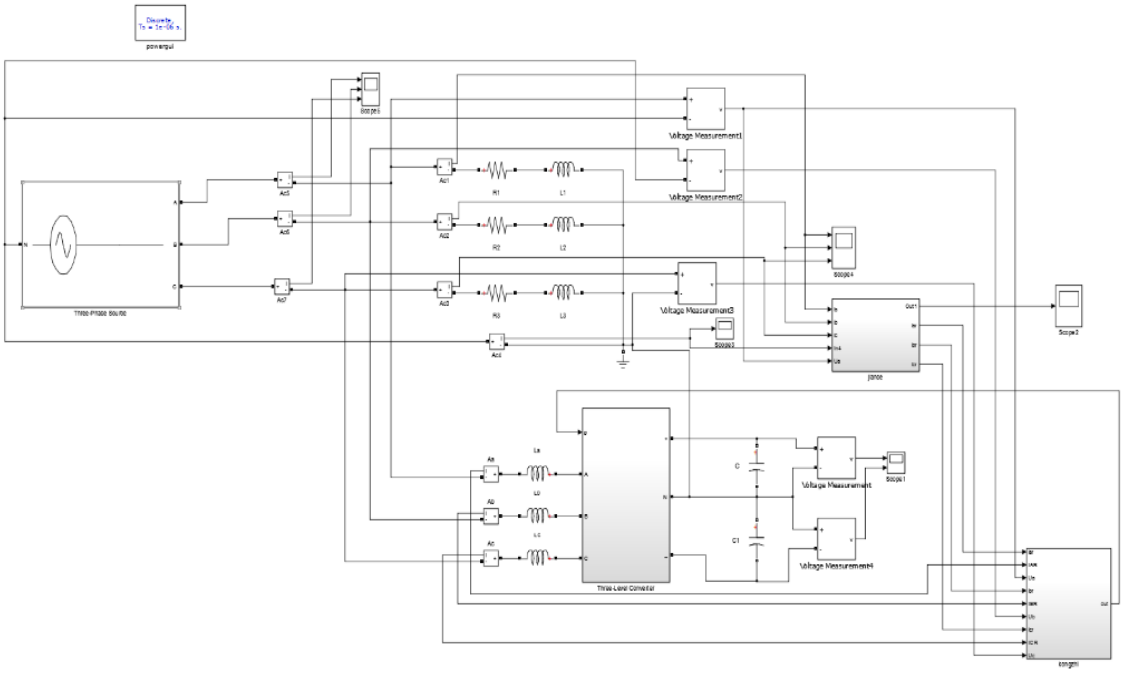

Figure 5: Inverter part of the main circuit simulation

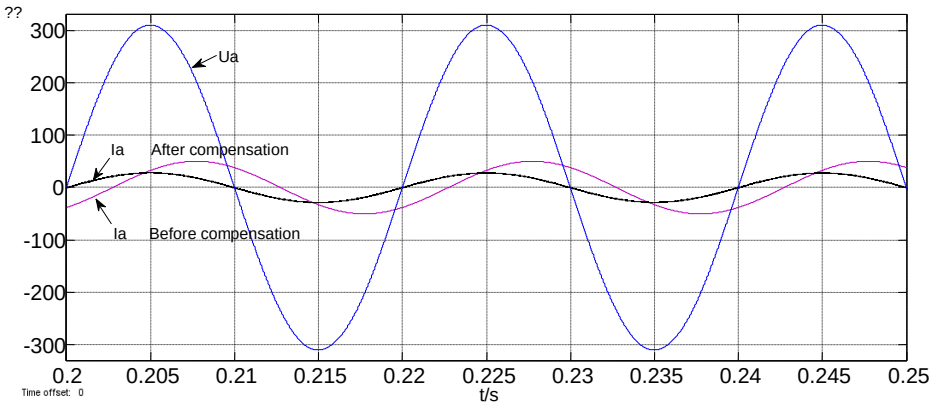

Figure 6: Waveform before compensation

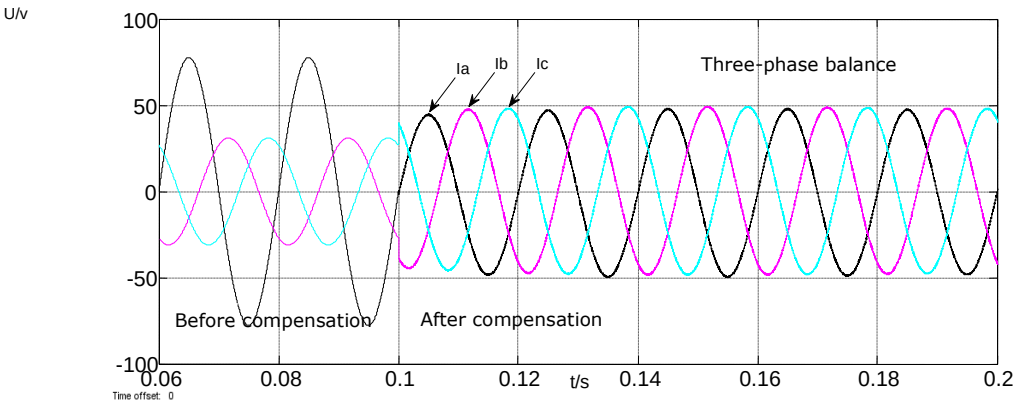

Figure 7: Balanced waveform after compensation

By comparison of voltage waveforms before and after compensation for unbalanced three-phase loads, the current lags behind the voltage before the compensation. After the compensation, the voltage and the current achieve the same phase, achieving the purpose of reactive power compensation. After compensation, the three-phase voltage can also be balanced to verify that this system can achieve compensation under unbalanced load conditions.

6. CONCLUSION

In this paper, a novel compound control strategy based on zero-sequence current-separating instruction signal generation method and SPWM double triangle wave modulation is used to realise three-phase balance for unbalanced load compensation in three-level three-phase four-line photovoltaic inverter. The experimental results show that the method proposed in this paper compensates for unbalanced loads in photovoltaic grid-connected systems through command signal generation methods with good dynamic performance and steady-state performance, which is correct and feasible.

7. REFERENCES

Wei X, Wang X, Gao C .2014. Research on Three-phase T-type Three-level Photovoltaic Inverter Technology.[J]. *Chinese Society for Electrical Engineering*. (34): 218-225.

Li Z, Hu X, Yan H, Yao J, Luo X. 2014. Research and Implementation of Improved SVPWM for Three-level Inverter.[J]. *Computing Technology and Automation,* (04):49-54.

Zhao C, Li L, Zhai X, 2014. Research on Active Power Filter Based on Three-level Inverter. [J]. *Automation of Electric Power Systems*.38(4):72-78.

Rivera S, Wu B, Kouro S, Yaramasu V, and Wang J, 2014. Electric vehiclecharging station using a neutral point clamped converter with bipolar DC bus.[J]. *IEEE Trans Ind Electron.* 10(1109).

Chen HC and Liao J-Y, 2014. Design and implementation of sensorlesscapacitor voltage balancing control for three-level boosting PFC.[J]. *IEEE Trans. Power Electron*. 29(7): 3808–3817.

163: Review on solid desiccant materials for humidity control in buildings

Ziwei CHEN[1], Mariana VELASCO CARRASCO[2], Yate DING[3], Saffa RIFFAT[4]

[1] Ziwei Chen, Department of Architecture and Built Environment, The University of Nottingham, University Park, Nottingham NG7 2RD, UK, Ziwei.chen1@nottingham.ac.uk
[2] Mariana Velasco Carrasco, Department of Architecture and Built Environment, The University of Nottingham, University Park, Nottingham NG7 2RD, UK, ezxmv@nottingham.ac.uk
[3] Yate Ding, Department of Architecture and Built Environment, The University of Nottingham, University Park, Nottingham NG7 2RD, UK, yate.ding@nottingham.ac.uk
[4] Saffa Riffat, Department of Architecture and Built Environment, The University of Nottingham, University Park, Nottingham NG7 2RD, UK, saffa.riffat@nottingham.ac.uk

Thermal comfort in buildings is an essential factor for designing energy efficient systems and a cumulative effect resulting from a variety of environmental and personal factors. High moisture content in indoor air can lead to serious health implications for occupants. Dehumidification in buildings is commonly realised by mechanical vapour compression, while desiccant materials with high affinity for water vapour are a promising technology for handling environmental-friendly indoor air conditioning without overcooling and reheating problems. Solid desiccant materials absorb moisture when vapour pressure of the desiccant surface is less than that of the process air until an equilibrium state is achieved between the desiccant and air. Ideally, the solid desiccant is expected to have large water adsorption capacity at its operative temperature and easily regenerated at a lower achievable regeneration temperature. Silica gel and zeolite are the two widely adopted solid desiccants with strong affinity and extensive researches have been conducted to develop solid desiccant materials with better adsorption and regeneration capabilities as well as long stability, such as nanoporous inorganic material, composite and polymeric desiccants. This review summarises recent researches and developments on available solid desiccant materials that can be utilised in built environment for dehumidification purpose.

Keywords: Dehumidification, Solid desiccant, Humidity control, Desiccant dehumidification

1. INTRODUCTION

As defined by ASHRAE, comfort is “the condition of mind that expresses satisfaction with the thermal environment, it requires subjective evaluation” (ASHRAE, 2013). Thermal comfort can be influenced by a variety of parameters, such as air temperature, air movement, air humidity and personal factors. Owing to the expanding economies, increasing population and higher living standard, more energy has been consumed for air conditioning in buildings to achieve thermal comfort. In particular, air dehumidification plays an important role for indoor thermal comfort in hot and humid regions. A number of dehumidification technologies have been available, such as cooling coil, solid and liquid desiccant dehumidification and electrochemical dehumidification (Zhang, 2008). Conventionally, cooling and dehumidification demands are achieved by mechanical vapour compression, in which dehumidification is accomplished by cooling air to dew point temperature, and extra energy is consumed for re-heating the air to reach the desired supply temperature (Xiao et al., 2011). However, the associated risks appear, such as leakage, bacterial breeding, and fungi due to water condensation on the surface of the cooling coil. Alternatively, the desiccant-based technology has become more attractive for providing energy-efficient and cost-effective dehumidification.

Desiccant is a hygroscopic substance that has strong affinity for water vapour. There are many ways to classify the available desiccant, for instance solid and liquid desiccants (i.e. depending on physical state), physisorption and chemisorption desiccants (i.e. depending on the strength of the bond between the adsorbate and adsorbent), natural and artificial desiccants (i.e. depending on the material), bio and rock-based desiccants, composite and polymer-based desiccant. By comparison, the solid desiccant is safer and economical to utilise for dehumidification. A great number of studies have been conducted for solid desiccant-based technology, for instance advanced desiccant materials (Rajamani and Maliyekkal, 2018, Ahn et al., 2015, Seetapan et al., 2011, Asim et al., 2015, Khedari et al., 2003, Aristov, 2007, Kiatkamjornwong, 2007), experimental investigations of various solid desiccant-based dehumidification systems (Jia et al., 2006, Chen et al., 2016, Cao et al., 2014, Kang and Lee, 2017, Al-Alili et al., 2015, Tu et al., 2018) and development of numerical simulation (De Antonellis et al., 2010, Kang et al., 2015, Narayanan, 2017, De Antonellis and Kim, 2018, Dai et al., 2015, Merabti et al., 2017). Solid desiccant materials are of vital importance to the solid desiccant-based system, because the material characteristics affects the system performance markedly. In recent years, a variety of new solid desiccant has been developed and evaluated, with improvements in water/vapour adsorption, regeneration capacity and stability (Zheng et al., 2014a). The current development of solid desiccant materials mainly focusses on (a) porous physical adsorbent and (b) composite desiccant on the basis of two different desiccant materials.

Extensive literature reviews have been conducted on the solid desiccant-based technology especially for industrial applications, while there are limited review papers discussing the solid desiccant materials for building applications. In this paper, a comprehensive review of the literature is presented regarding the current available solid desiccant materials, in particular the silica-gel based, nanoporous inorganic, composite and polymeric desiccant materials. Additionally, the recent development in the solid desiccant-based system is also reviewed.

2. SOLID DESICCANT MATERIAL

For dehumidification, solid desiccant materials rely on the adsorption of vapour molecules onto their surface to retain moisture, which is different from the liquid desiccant materials absorbing water molecules into the solution (Yang et al., 2015). Basically, solid desiccant materials can be regenerated at specific temperature for cyclic operation. The available solid desiccant materials can be classified into different categories from different perspectives, for instance, with porous structure and form solid crystalline hydrate. Figure 1 presents the detailed classification of the available solid desiccant materials based on the comprehensive review of the literature (Zheng et al., 2014a, Sultan et al., 2015, Jani et al., 2016, Rambhad et al., 2016, Wu et al., 2018, Pallav, 2018, Jani et al., 2015, Henninger et al., 2009). The most commonly encountered conventional solid desiccants are silica gel, activated alumina, molecular sieves, and activated carbon. Among them, molecular sieve, which is also known as zeolite, is capable of dehumidifying air with large exothermic and endothermic reactions at a very low level of humidity (Hong et al., 2016) and require higher regeneration temperature (i.e. above 200℃), while the cyclic operation with silica gel and activated alumina can be realised at relative lower temperatures (Singh and Singh, 1998). More advanced solid desiccants have been developed from those conventional solid desiccants, with improvements in moisture adsorption capability, regeneration ability, cost and long-term durability (Pallav, 2018).

Only few researchers have summarised the available solid desiccant materials for adoption. For instance, Sultan et al. (2015) reviewed the solid desiccant materials by introducing the classification of the solid desiccant materials and presenting detailed reviews on silica gel, molecular sieve, activated alumina, composite and polymer desiccants, activated carbon and clay-based desiccant. Zheng et al. (2014a) reported the recent progress on novel desiccant materials for solid desiccant cooling systems, including composite desiccants, nanoporous inorganic and polymeric desiccants.

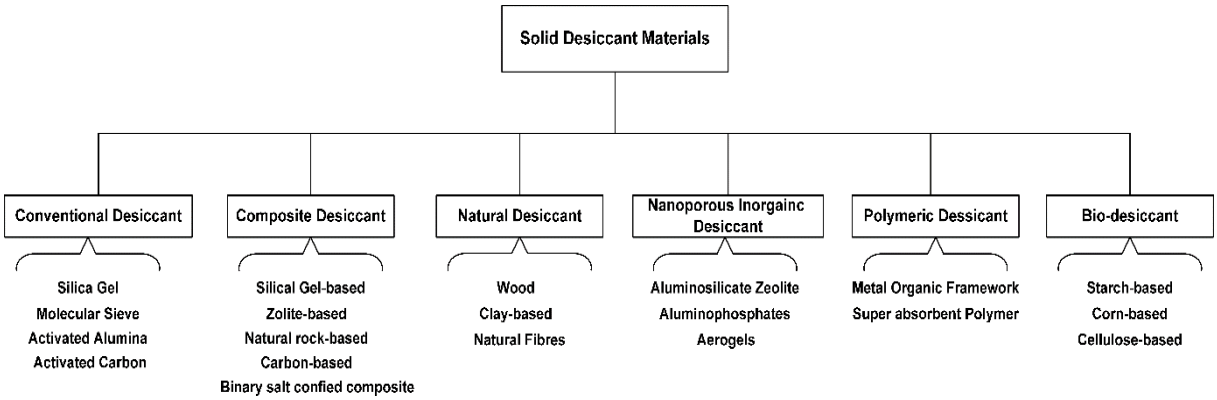

Figure 1: Classification of solid desiccant materials

2.1. Comparison between liquid and solid desiccant materials

Solid desiccant materials contribute to an effective and economical approach for dehumidification, and are less subject to corrosion compared to liquid desiccants. Most of the solid desiccant materials are environmental friendly. In some cases for desiccant cooling, solid desiccant materials are more favourable for adoption, due to their dryness, structure simplicity, chemical inertness and ease of operation (Chua and Chou, 2003) . On the other hand, the liquid desiccant materials requires a complicated packing system for dehumidification and regeneration, while simpler device such as the rotary desiccant wheel can be used to accommodate solid desiccant materials, and without any carry-over problem of desiccant droplets (Jani et al., 2015), which may be harmful for building structure and human health (Huang and Zhang, 2013).

2.2. Silica gel

Silica gel is an amorphous form of silicon dioxide and is presented as porous beads or granules. It absorbs water vapour up to 40% of its dry mass through physical adsorption into its internal pores without any chemical reaction (Zendehboudi et al., 2018). Silica gel is featured with (Lazaar et al., 2017, Zendehboudi et al., 2018, Jain et al., 2013, Barbé et al., 2012):

- Chemical inertness and toxic-free;
- High melting point for safe transportation;
- Long life;
- Low abrasion;
- Low cost;
- Feasibility of application under various operating conditions;
- Resistance to most chemicals.

A number of commercial silica gel are available on the market, for instance Type-RD, Type-A, Type-3A, Type-A++ and Type-A5BW. Alternatively, self-indicating silica gels have been developed by coating with non-toxic and non-flammable indicators to provide a visual indication as to the activity level of the silica gel. Figure 2 presents four different types of silica gel, namely non-indicating, self-indicating and partial-indicating types. The characteristics of silica gel and its application for dehumidification have been intensively investigated by researchers both experimentally and theoretically. It has been stated in the literature (GeeJay Chemicals Ltd, 2013, Barbé et al., 2012) that silica gel is suitable for dehumidification at high relative humidity condition (e.g. 60-90%RH) at an indoor temperature range of 21 to 32℃. However, the regeneration temperature of silica gel is relatively high (i.e. 100-120℃). In order to deal with the high regeneration temperature, a non-heating regeneration method with ultrasonic has been proposed and assessed by Yang et al. (2013), Yao et al. (2014b).

Figure 2: Non-indicating silica gel (upper left), self-indicating silica gel (upper right), partial-indicating (lower right) and non-indicating silica gel with indicator beads (Barbé et al., 2012)

On the other hand, a variety of advanced desiccant materials have been discovered to address the shortcomings of the silica gel, by combining silica gel with other solid or liquid desiccants, like salts lithium chloride (Yu et al., 2014), calcium chloride (Wu et al., 2007) and strontium bromide (Courbon et al., 2017). Zheng et al. (2014b) experimentally tested a novel composite solid desiccant material with significant improvement in the thermal conductivity (i.e. 270 times) compared to pure silica gel, which is made of silica gel and expanded natural graphite treated with sulfuric acid as a host matrix.

2.3. Composite desiccant

Basically, hygroscopic salts can be impregnated to the pores of porous desiccant materials to form composite desiccant materials (Chua et al., 2018). In order to evolve the composite desiccant materials with good performance, various combinations of desiccant and salts have been investigated and nowadays the composite desiccants are typically available in silica-based, mesoporous silicate-based and carbon-based. In particular, silica gel is the most widely used host materials for creating composite desiccant materials. For example, a combination of activated carbon and silica-gel has been investigated by Huang et al. (2010) and Tso and Chao (2012) evaluated a composite adsorbent synthesising from activated carbon, silica gel and calcium chloride and their results demonstrate that the developed composite desiccant can be a good candidate for the low temperature heat-driven dehumidification system. Chen et al. (2015a) combined silica gel with two different types of polymers for dehumidification and found an improvement of 41% in the sorption capacity compared with pure silica gel. Ge et al. (2017) proposed a composite desiccant coated heat exchanger integrating silica gel with potassium formate and their experimental results revealed the utilisation of composite silica gel and potassium formate effectively enhances the adsorption capacity. Another mature solid desiccant, activated carbon has also been a popular host for the composite desiccant materials, because of its large surface area, large pore volume and outstanding heat transfer property (Yuan et al., 2016). With the impregnation of hygroscopic salts, water adsorption of activated carbon can be enhanced markedly. On the other hand, mesoporous silicate-based composite desiccants are formed by hydrothermal formation of the silica gel and available in various porosities with high adsorption capacity (Kumar et al., 2017). Even with narrow pore size , mesoporous silicate can be selected as the host materials for composite desiccants (Vazquez et al., 2017). Additionally, natural mineral clays can be another option as the host due to the material availability and low cost. It is also noteworthy that the dehumidification performance of composite desiccant materials varies significantly depending on the host and immersed salts, which implies the importance of an optimal selection of the component materials and optimisation of material composition.

2.4. Nanoporous inorganic material

In general, nanoporous materials include organic and inorganic based materials with the micro, meso or macro pore size distributions (Abolghasemi Mahani et al., 2018). In terms of the solid desiccant materials, the nanoporous inorganic materials have gained increasing interest, which mainly includes aluminosilicate zeolites, aluminophosphates and aerogels. Among the inorganic materials, aluminosilicate zeolite is artificially synthesised zeolite with higher water adsorption rate and is capable of dehumidifying at a low pressure drop. Wei et al. (2013) compared the dehumidification performance of a hierarchically porous aluminosilicate zeolite with commercial microporous zeolite 3A and silica gel, the synthesised aluminosilicate exhibits desirable absorption capacity of water vapour at various operating conditions. Owing to its features of fast adsorption and desorption rates as well as good

regenerability at low regeneration temperature, the researchers demonstrate the great potential of using aluminosilicate zeolite for building dehumidification purpose. Aerogels are formed by a sol-gel synthesis and drying of the gel and available in different types (i.e. silica aerogel, alumina oxide aerogel and silica oxide aerogel) (Shi et al., 2014). In terms of the building dehumidification, silica aerogel has been proved as a good adsorbents for water and also other organic vapours, because of its better stability, cyclic capability and regenerability (Novak and Knez, 2000).

2.5. Super absorbent polymer

A polyelectrolyte is a polymer with dissociating ionisable and/or ionic groups in their repeat units (Kiatkamjornwong, 2007). Theoretically, the solubility of a polyelectrolyte in water, other polar and hydrogen-bonding liquids is determined by the type of dissociating groups. The cross-linked polyelectrolytes form 3-dimensional structures that swell in and retain a vast amount of liquid relative to their own mass through hydrogen bonding with water molecules (Ahmed, 2015). In practice, polyelectrolytes are commonly called as hydrogels and super absorbent polymers (SAP) when cross-linked, and they can be divided into natural and synthetic types depending on the composed materials. Figure 3 shows three different SAPs and their physical state when absorbing water. Synthetic polyelectrolytes have been regarded as advanced desiccant materials due to their adjustable functionality, ease of regeneration and high adsorption capacity (Jani et al., 2015).

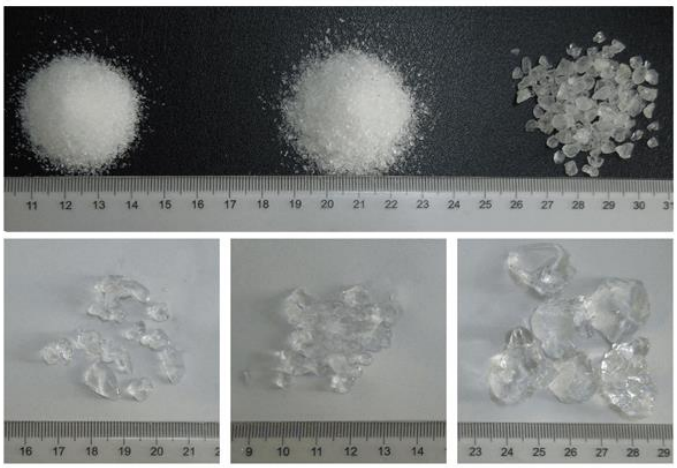

Figure 3: Examples of super absorbent polymer (Ma's Group Inc, 2009)

It has been found that the water uptake of the composite absorbent is commonly limited, while SAPs are capable of absorbing liquid water up to 1000 times of its weight (Gawande and Mungray, 2015). Since early 1970s, SAPs and their associated SAP composites have attracted more and more attention. Figure 4 presents a comparison of dehumidification performance among silica gel, ferroaluminophosphate zeolite and SAP, which was presented in the experimental study of White et al. (2011). The graph shows that the dehumidification performance of SAP is much better than those of silica gel and zeolite at a lower regenerating temperature and higher relative humidity condition.

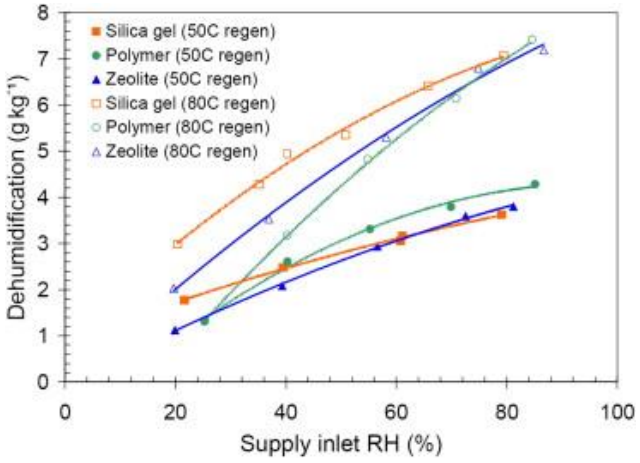

Figure 4: Comparison of dehumidification performance among silica gel, zeolite and super absorbent polymer (White et al., 2011)

Extensive researches have been carried out with a main focus on the development of advanced SAPs and potential applications. Currently, more than 80% of SAPs have been adopted for commercial applications, like as sorbents in personal care products (e.g. disposable diaper, hygiene and incontinence products) (Seetapan et al., 2011). However the sorption of water vapour is comparatively low for SAPs. Different solutions have been developed to address its low ability of vapour sorption. For example, Ahn et al. (2015) enhanced the SAP utilisation by growing mesoporous silica on the surface of swelling SAP and then impregnating calcium chloride in ethanol. Chen et al. (2015a) solved the high pressure drop problem of the solid desiccant-based air conditioning system by using a composite desiccant material, which is composed of silica gel particles and polymer power and proved that the developed composite material has significant energy-saving potential for building application. In addition, Yang et al. (2015) developed a solid super desiccant based on the concept of impregnating a super liquid hygroscopic agent in a SAP to take advantage of the vast vapour absorption capacity of the hygroscopic agent and the liquid withholding capacity of the SAP. Until now, there are limited studies on the development and feasibility assessment of novel SAPs for dehumidification in buildings.

2.6. Metal organic framework

Metal-Organic Framework (MOF) refers to a Coordination Polymer (or alternatively Coordination Network) with an open framework containing potential voids (Batten et al., 2013). Typical MOFs are crystalline and hybrid materials containing metal ions and organic molecules, that together forms a 3-dimensional structure (Fromm et al., 2010). Based on the literature (Wang et al., 2015, Song et al., 2016, Jeong et al., 2011) , MOFs are characterised with: high surface area, large pore volume, diversity of structures and unprecedented physicochemical variability owing to their alterable composition. MOFs have been widely accepted in industrial applications, such as gas and electronics applications. Rising interest has been focussed on MOFs as water adsorbents due to their large adsorption capacity, highly tunable structure, high surface area, and pore volume controlled by change in organic ligands and metal subunits (Henninger et al., 2009). On the other hand, MOFs are capable of adsorbing water vapour at various relative humidity ranges, which makes MOFs more potential for dehumidification demand. For example, MOF-801 can adsorb moisture when relative humidity level below 20%RH, UiO-66 works in 30-40%RH and for MIL-101, the range is between 40-50%RH. Nevertheless, limited investigations have been noted in the existing literature regarding the adoption of MOFs as the solid desiccant materials for dehumidification in building. For example Bareschino et al. (2017) proved the feasibility of using MIL101 in the desiccant wheel system and an improvement of 30% in the dehumidification effectiveness has been achieved compared to the conventional silica gel based desiccant wheel. Shi et al. (2016) used a commercially available MOF, CPO-27(Ni) in a single adsorption bed system and they highlighted the great potential of using MOFs in air conditioning systems as they observed 42% more cooling power can be produced by the system with CPO-27(Ni) than that of zeolite material.

2.7. Material selection

Yet there is no perfect solid desiccant suitable for all kinds of applications. Many parameters can be taken into account when choosing the adopted solid desiccant material, such as thermos-physical properties, availability, economics, process and operation condition. For a better dehumidification and regeneration performance of a solid desiccant-based system, the solid desiccant is expected to have high water adsorption capacity, good regenerability at relatively low regeneration temperature, low desorption energy input and high durability (Wang et al., 2013). Referred to Figure 5 produced by Zheng et al. (2014a), the MOFs have better adsorption capacity with regeneration temperature ranging from 65℃ to 90℃. It can be also seen that relatively high regeneration temperature (more than 60℃) for most composite desiccants. However, clay-based composite solid desiccant materials have relative lower regeneration temperature (e.g. 35℃ to 55℃), which indicates that low-grade heat sources can be utilised for regeneration.

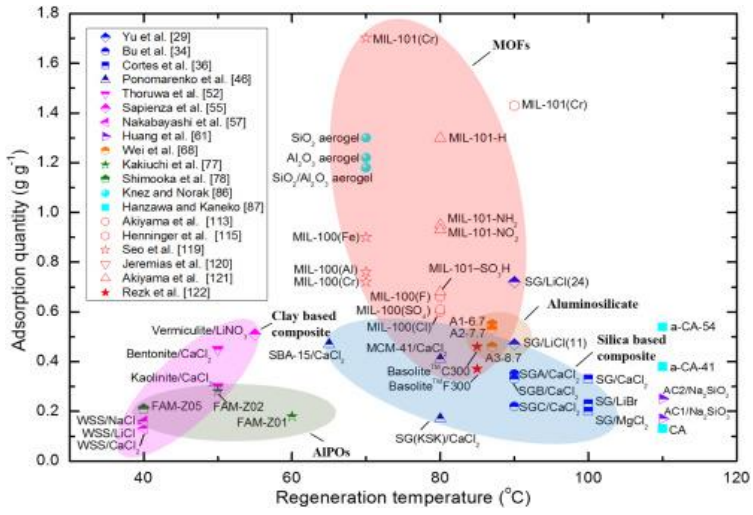

Figure 5: Water adsorption quantity and regeneration ability of desiccant materials (Zheng et al., 2014a)

3. SOLID DESICCANT-BASED TECHNOLOGY

In general, solid desiccant materials can be employed for the desiccant dehumidification system in different configurations like the packed and fluidised beds and desiccant wheel. A solid desiccant-based system commonly uses a solid desiccant embedded in a desiccant wheel or a cross-flow wheel. The channels of desiccant wheel frame can be fabricated in honeycomb, triangular and sinusoidal structures (Yadav and Bajpai, 2011). The majority of the studies conducted on the desiccant wheel system have adopted silica gel as the desiccant material, and examined the system performance in the perspectives of dehumidification effectiveness, moisture removal rate, regeneration capacity, regeneration heat input and sensible energy ratio. And researchers have pointed out that the dehumidification performance is affected by various factors, for example wheel configuration, desiccant material, regeneration method and operating condition (Yao et al., 2014a, Fong and Lee, 2018). Typically, solid desiccant materials are arranged in a honeycomb matrix structure, but it results in a high pressure drop across the device, which requires fans and blowers to provide adequate ventilation. To allow efficient passive ventilation through the wheel, O'Connor et al. (2016) conceptualised a innovative desiccant rotary wheel through re-designing the traditional honeycomb matrix structure to achieve a low pressure drop of below 2Pa. Guan et al. (2015) and Liu et al. (2016) adopted a two-stage desiccant wheel system to improve the dehumidification system and noted the reduction in the regeneration temperature and higher exergy destruction and exergy efficiency.

Ramzy et al. (2010) assessed the cyclic operation of a radial-flow two desiccant bed dehumidification system and they proposed an intercooled packed bed to increase the utilisation of desiccant material in the trailing layer of the packed bed (Ramzy et al., 2015). Chen et al. (2015b) investigated silica gel circulating fluidised beds for air conditioning, with higher dehumidification performance (i.e. 20% improvement) than that of the conventional packed beds. Fernández-Hernández et al. (2015) theoretically evaluated the feasibility of a novel solid desiccant-based system, which incorporates two layers of solid desiccant materials inside each side of a ventilated building façade. Furthermore, the rising demand for air conditioning, particularly in hot and humid regions has resulted in a remarkable increase in energy resources (Cheng and Zhang, 2013). Therefore, different solutions to handle the indoor air conditioning with less energy consumption have been proposed, for instance, the utilisation of renewable energy sources as the alternatives for regeneration heat input and integration of diverse technologies. Recently, solid desiccant-based technology integrated with vapour compression refrigeration is an innovative approach in field of space air conditioning to eliminate environmental and economic issues that associated with the use of stand-alone conventional vapour compression cooling systems (Jani et al., 2018a). Jani et al. (2018b) simulated the performance of a solid desiccant (i.e. in desiccant wheel structure) assisted hybrid space cooling system using TRNSYS and proved that the feasibility of the hybrid cooling system to effectively handle high latent load in hot and humid regions.

4. CONCLUSIONS

This paper reviewed the current available solid desiccant materials for humidity control in buildings, which mainly focused on silica gel-based desiccant, composite, nanoporous inorganic desiccants, super absorbent polymer and MOF. For practical air conditioning applications, a number of requirements should be satisfied however, no perfect solid desiccant materials exist. In recent years, great progress has been noted in the solid desiccant material, for instance the advanced composite desiccant, polymeric desiccant and MOFs. Those novel materials exhibit high adsorption capacity, regenerability and long durability. Regarding the synthesised desiccant materials, what is noteworthy is the optimal selection of the component materials and optimisation of material composition. The solid desiccant-based air conditioning system has been an attractive energy-efficient option. Extensive studies have been conducted on the system design, optimisation and feasibility investigations for industrial applications, while few works have concerned the built environment applications to address latent loads. Hence, more studies on the development of solid desiccant materials for air conditioning in buildings are still needed.

5. REFERENCES

Abolghasemi Mahani, A., Motahari, S. & Mohebbi, A. 2018. Sol-gel derived flexible silica aerogel as selective adsorbent for water decontamination from crude oil. *Marine Pollution Bulletin,* 129**,** 438-447.

Ahmed, E. M. 2015. Hydrogel: Preparation, characterisation, and applications: A review. *Journal of Advanced Research,* 6**,** 105-121.

Ahn, K. W., Jang, S. Y., Hwang, M. H. & Kim, S.-G. 2015. $CaCl_2$-in-Mesoporous Silica Grown on Superabsorbent Polymer to Enhance Water Uptake. *KONA Powder and Particle Journal,* 32**,** 207-216.

Al-Alili, A., Hwang, Y. & Radermacher, R. 2015. Performance of a desiccant wheel cycle utilizing new zeolite material: Experimental investigation. *Energy,* 81**,** 137-145.

Aristov, Y. I. 2007. New family of solid sorbents for adsorptive cooling: Material scientist approach. *Journal of Engineering Thermophysics,* 16**,** 63-72.

ASHRAE 2013. 2013 ASHRAE Handbook - Fundamentals (I-P Edition). American Society of Heating, Refrigerating and Air-Conditioning Engineers, Inc.

Asim, N., Emdadi, Z., Mohammad, M., Yarmo, M. A. & Sopian, K. 2015. Agricultural solid wastes for green desiccant applications: an overview of research achievements, opportunities and perspectives. *Journal of Cleaner Production,* 91**,** 26-35.

Barbé, B., Gillet, P., Beelaert, G., Fransen, K. & Jacobs, J. 2012. Assessment of desiccants and their instructions for use in rapid diagnostic tests. *Malaria Journal,* 11**,** 326.

Bareschino, P., Diglio, G., Pepe, F., Angrisani, G., Roselli, C. & Sasso, M. 2017. Numerical study of a MIL101 metal organic framework based desiccant cooling system for air conditioning applications. *Applied Thermal Engineering,* 124**,** 641-651.

Batten, S. R., Champness, N. R., Chen, X.-M., Garcia-Martinez, J., Kitagawa, S., Öhrström, L., O'keeffe, M., Suh, M. P. & Reedijk, J. 2013. Terminology of metal–organic frameworks and coordination polymers (IUPAC Recommendations 2013). *Pure and Applied Chemistry,* 85**,** 1715-1724.

Cao, T., Lee, H., Hwang, Y., Radermacher, R. & Chun, H.-H. 2014. Experimental investigations on thin polymer desiccant wheel performance. *International Journal of Refrigeration,* 44**,** 1-11.

Chen, C.-H., Hsu, C.-Y., Chen, C.-C. & Chen, S.-L. 2015a. Silica gel polymer composite desiccants for air conditioning systems. *Energy and Buildings,* 101**,** 122-132.

Chen, C.-H., Hsu, C.-Y., Chen, C.-C., Chiang, Y.-C. & Chen, S.-L. 2016. Silica gel/polymer composite desiccant wheel combined with heat pump for air-conditioning systems. *Energy,* 94**,** 87-99.

Chen, C.-H., Ma, S.-S., Wu, P.-H., Chiang, Y.-C. & Chen, S.-L. 2015b. Adsorption and desorption of silica gel circulating fluidized beds for air conditioning systems. *Applied Energy,* 155**,** 708-718.

Cheng, Q. & Zhang, X. 2013. Review of solar regeneration methods for liquid desiccant air-conditioning system. *Energy and Buildings,* 67**,** 426-433.

Chua, K. J. & Chou, S. K. 2003. Low-cost drying methods for developing countries. *Trends in Food Science & Technology,* 14**,** 519-528.

Chua, K. J., Chou, S. K. & Islam, M. R. 2018. On the experimental study of a hybrid dehumidifier comprising membrane and composite desiccants. *Applied Energy,* 220**,** 934-943.

Courbon, E., D'ans, P., Permyakova, A., Skrylnyk, O., Steunou, N., Degrez, M. & Frère, M. 2017. A new composite sorbent based on SrBr2 and silica gel for solar energy storage application with high energy storage density and stability. *Applied Energy,* 190**,** 1184-1194.

Dai, Y., Li, X. & Wang, R. 2015. Theoretical Analysis and Case Study on Solar Driven Two-stage Rotary Desiccant Cooling System Combined with Geothermal Heat Pump. *Energy Procedia,* 70**,** 418-426.

De Antonellis, S., Joppolo, C. M. & Molinaroli, L. 2010. Simulation, performance analysis and optimisation of desiccant wheels. *Energy and Buildings,* 42**,** 1386-1393.

De Antonellis, S. & Kim, D.-S. 2018. Effectiveness of a symmetric desiccant wheel operating in balanced flow condition: Modeling and application. *International Journal of Refrigeration,* 88**,** 347-359.

Fernández-Hernández, F., Cejudo-López, J. M., Domínguez-Muñoz, F. & Carrillo-Andrés, A. 2015. A new desiccant channel to be integrated in building façades. *Energy and Buildings,* 86**,** 318-327.

Fong, K. F. & Lee, C. K. 2018. Impact of adsorbent characteristics on performance of solid desiccant wheel. *Energy,* 144**,** 1003-1012.

Fromm, K. M., Sague, J. L. & Mirolo, L. Coordination Polymer Networks: An Alternative to Classical Polymers? Macromolecular symposia, 2010. Wiley Online Library, 75-83.

Gawande, N. & Mungray, A. 2015. *Superabsorbent polymer (SAP) hydrogels for protein enrichment*.

Ge, T. S., Zhang, J. Y., Dai, Y. J. & Wang, R. Z. 2017. Experimental study on performance of silica gel and potassium formate composite desiccant coated heat exchanger. *Energy,* 141**,** 149-158.

Geejay Chemicals Ltd. 2013. *Uk Supplier Of Silica Gel & Desiccant Products* [Online]. Available: http://www.geejaychemicals.co.uk/silicagel.htm [Accessed 20/60 2018].

Guan, Y., Zhang, Y., Sheng, Y., Kong, X. & Du, S. 2015. Feasibility and economic analysis of solid desiccant wheel used for dehumidification and preheating in blast furnace: A case study of steel plant, Nanjing, China. *Applied Thermal Engineering,* 81**,** 426-435.

Henninger, S. K., Habib, H. A. & Janiak, C. 2009. MOFs as Adsorbents for Low Temperature Heating and Cooling Applications. *Journal of the American Chemical Society,* 131**,** 2776-2777.

Hong, S. W., Ahn, S. H., Chung, J. D., Bae, K. J., Cha, D. A. & Kwon, O. K. 2016. Characteristics of FAM-Z01 compared to silica gels in the performance of an adsorption bed. *Applied Thermal Engineering,* 104**,** 24-33.

Huang, H., Oike, T., Watanabe, F., Osaka, Y., Kobayashi, N. & Hasatani, M. 2010. Development research on composite adsorbents applied in adsorption heat pump. *Applied Thermal Engineering,* 30**,** 1193-1198.

Huang, S.-M. & Zhang, L.-Z. 2013. Researches and trends in membrane-based liquid desiccant air dehumidification. *Renewable and Sustainable Energy Reviews,* 28**,** 425-440.

Jain, V., Bajaj, G. & Avinash, D. 2013. Numerical Analysis of Silica Gel Bed Used In Desiccant Air Cooler and Dehumidifier. *Int. Journal of Engineering Research and Applications* 3**,** 640-644.

Jani, D. B., Mishra, M. & Sahoo, P. K. 2016. Solid desiccant air conditioning – A state of the art review. *Renewable and Sustainable Energy Reviews,* 60**,** 1451-1469.

Jani, D. B., Mishra, M. & Sahoo, P. K. 2018a. A critical review on application of solar energy as renewable regeneration heat source in solid desiccant – vapor compression hybrid cooling system. *Journal of Building Engineering,* 18**,** 107-124.

Jani, D. B., Mishra, M. & Sahoo, P. K. 2018b. Performance analysis of a solid desiccant assisted hybrid space cooling system using TRNSYS. *Journal of Building Engineering,* 19**,** 26-35.

Jani, J. B., Rajput, V. P. & Shukla, M. 2015. A Review on Performance Anyalysis of Different Desiccant Materials for a Desiccant Cooling System. *International Journal of Advance Research in Engineering, Science & Technology,* 2**,** 2394-2444.

Jeong, S., Song, X., Jeong, S., Oh, M., Liu, X., Kim, D., Moon, D. & Lah, M. S. 2011. Metal–Organic Frameworks Based on Unprecedented Trinuclear and Pentanuclear Metal–Tetrazole Clusters as Secondary Building Units. *Inorganic Chemistry,* 50**,** 12133-12140.

Jia, C. X., Dai, Y. J., Wu, J. Y. & Wang, R. Z. 2006. Experimental comparison of two honeycombed desiccant wheels fabricated with silica gel and composite desiccant material. *Energy Conversion and Management,* 47**,** 2523-2534.

Kang, H. & Lee, D.-Y. 2017. Experimental investigation and introduction of a similarity parameter for characterizing the heat and mass transfer in polymer desiccant wheels. *Energy,* 120**,** 705-717.

Kang, H., Lee, G. & Lee, D.-Y. 2015. Explicit analytic solution for heat and mass transfer in a desiccant wheel using a simplified model. *Energy,* 93**,** 2559-2567.

Khedari, J., Rawangkul, R., Chimchavee, W., Hirunlabh, J. & Watanasungsuit, A. 2003. Feasibility study of using agriculture waste as desiccant for air conditioning system. *Renewable Energy,* 28**,** 1617-1628.

Kiatkamjornwong, S. 2007. Superabsorbent Polymers and Superabsorbent Polymer Composites. *ScienceAsia,* 33(s1)**,** 39-43.

Kumar, S., Malik, M. M. & Purohit, R. 2017. Synthesis Methods of Mesoporous Silica Materials. *Materials Today: Proceedings,* 4**,** 350-357.

Lazaar, K., Hajjaji, W., Pullar, R. C., Labrincha, J. A., Rocha, F. & Jamoussi, F. 2017. Production of silica gel from Tunisian sands and its adsorptive properties. *Journal of African Earth Sciences,* 130**,** 238-251.

Liu, X.-H., Zhang, T., Zheng, Y.-W. & Tu, R. 2016. Performance investigation and exergy analysis of two-stage desiccant wheel systems. *Renewable Energy,* 86**,** 877-888.

Ma's Group Inc. 2009. *History of Super Absorbent Polymer Chemistry* [Online]. Ma's Group Inc. Available: https://www.socochem.com/history-of-super-absorbent-polymer-chemistry.html [Accessed 18/06 2018].

Merabti, L., Merzouk, M., Kasbadji Merzouk, N. & Taane, W. 2017. Performance study of solar driven solid desiccant cooling system under Algerian coastal climate. *International Journal of Hydrogen Energy,* 42**,** 28997-29005.

Narayanan, R. 2017. Investigation of Geometry Effects of Channels of a Silica-gel Desiccant Wheel. *Energy Procedia,* 110**,** 20-25.

Novak, Z. & Knez, Z. 2000. Silica aerogels and their application for different adsorption processes.

O'connor, D., Calautit, J. K. & Hughes, B. R. 2016. A novel design of a desiccant rotary wheel for passive ventilation applications. *Applied Energy,* 179**,** 99-109.

Pallav, G. 2018. Advanced Desiccants for HVAC System: A Review. *International Journal of Engineering Technology Science and Research,* 5**,** 221-224.

Rajamani, M. & Maliyekkal, S. M. 2018. Chitosan reinforced boehmite nanocomposite desiccant: A promising alternative to silica gel. *Carbohydr Polym,* 194**,** 245-251.

Rambhad, K. S., Walke, P. V. & Tidke, D. J. 2016. Solid desiccant dehumidification and regeneration methods—A review. *Renewable and Sustainable Energy Reviews,* 59**,** 73-83.

Ramzy, A., Abdelmeguid, H. & Elawady, W. M. 2015. A novel approach for enhancing the utilisation of solid desiccants in packed bed via intercooling. *Applied Thermal Engineering,* 78**,** 82-89.

Ramzy, A., Hamed, A., Awad, M. & Bekheit, M. 2010. Theoretical investigation on the cyclic operation of radial flow desiccant bed dehumidifier. *Journal of Engineering and Technology Research,* 2**,** 96-110.

Seetapan, N., Srisithipantakul, N. & Kiatkamjornwong, S. 2011. Synthesis of acrylamide-co-(itaconic acid) superabsorbent polymers and associated silica superabsorbent polymer composites. *Polymer Engineering & Science,* 51**,** 764-775.

Shi, B., Al-Dadah, R., Mahmoud, S., Elsayed, A. & Elsayed, E. 2016. CPO-27(Ni) metal–organic framework based adsorption system for automotive air conditioning. *Applied Thermal Engineering,* 106**,** 325-333.

Shi, H.-X., Cui, J.-T., Shen, H.-M. & Wu, H.-K. 2014. Preparation of Silica Aerogel and Its Adsorption Performance to Organic Molecule. *Advances in Materials Science and Engineering,* 2014**,** 1-8.

Singh, S. & Singh, P. P. 1998. Regeneration of silica gel in multi-shelf regenerator. *Renewable Energy,* 13**,** 105-119.

Song, X., Zhang, S., Zhao, G., Zhang, W., Chen, D., Yang, Q., Wei, Q., Xie, G., Yang, D. & Chen, S. 2016. Ag (I)-based high-energy metal organic frameworks (HE-MOFs) incorporating coordinated moieties in channels: synthesis, structure and physicochemical properties. *RSC Advances,* 6**,** 93231-93237.

Sultan, M., El-Sharkawy, I. I., Miyazaki, T., Saha, B. B. & Koyama, S. 2015. An overview of solid desiccant dehumidification and air conditioning systems. *Renewable and Sustainable Energy Reviews,* 46**,** 16-29.

Tso, C. Y. & Chao, C. Y. H. 2012. Activated carbon, silica-gel and calcium chloride composite adsorbents for energy efficient solar adsorption cooling and dehumidification systems. *International Journal of Refrigeration,* 35**,** 1626-1638.

Tu, R., Hwang, Y., Cao, T., Hou, M. & Xiao, H. 2018. Investigation of adsorption isotherms and rotational speeds for low temperature regeneration of desiccant wheel systems. *International Journal of Refrigeration,* 86**,** 495-509.

Vazquez, N. I., Gonzalez, Z., Ferrari, B. & Castro, Y. 2017. Synthesis of mesoporous silica nanoparticles by sol–gel as nanocontainer for future drug delivery applications. *Boletín de la Sociedad Española de Cerámica y Vidrio,* 56**,** 139-145.

Wang, T. C., Bury, W., Gómez-Gualdrón, D. A., Vermeulen, N. A., Mondloch, J. E., Deria, P., Zhang, K., Moghadam, P. Z., Sarjeant, A. A. & Snurr, R. Q. 2015. Ultrahigh surface area zirconium MOFs and insights into the applicability of the BET theory. *Journal of the American Chemical Society,* 137**,** 3585-3591.

Wang, W., Wang, X., Song, C., Wei, X., Ding, J. & Xiao, J. 2013. Sulfuric Acid Modified Bentonite as the Support of Tetraethylenepentamine for CO2 Capture. *Energy & Fuels,* 27**,** 1538-1546.

Wei, X., Wang, W., Xiao, J., Zhang, L., Chen, H. & Ding, J. 2013. Hierarchically porous aluminosilicates as the water vapor adsorbents for dehumidification. *Chemical Engineering Journal,* 228**,** 1133-1139.

White, S. D., Goldsworthy, M., Reece, R., Spillmann, T., Gorur, A. & Lee, D.-Y. 2011. Characterisation of desiccant wheels with alternative materials at low regeneration temperatures. *International Journal of Refrigeration,* 34**,** 1786-1791.

Wu, H., Wang, S. & Zhu, D. 2007. Effects of impregnating variables on dynamic sorption characteristics and storage properties of composite sorbent for solar heat storage. *Solar Energy,* 81**,** 864-871.

Wu, X. N., Ge, T. S., Dai, Y. J. & Wang, R. Z. 2018. Review on substrate of solid desiccant dehumidification system. *Renewable and Sustainable Energy Reviews,* 82**,** 3236-3249.

Xiao, F., Ge, G. & Niu, X. 2011. Control performance of a dedicated outdoor air system adopting liquid desiccant dehumidification. *Applied Energy,* 88**,** 143-149.

Yadav, A. & Bajpai, V. 2011. Optimisation of operating parameters of desiccant wheel for rotation speed. *International Journal of Advanced Science and Technology* 32**,** 109-116.

Yang, K., Yao, Y., Liu, S. & He, B. 2013. Investigation on applying ultrasonic to the regeneration of a new honeycomb desiccant. *International Journal of Thermal Sciences,* 72**,** 159-171.

Yang, Y., Rana, D. & Lan, C. Q. 2015. Development of solid super desiccants based on a polymeric superabsorbent hydrogel composite. *RSC Advances,* 5**,** 59583-59590.

Yao, Y., Yang, K. & Liu, S. 2014a. Study on the performance of silica gel dehumidification system with ultrasonic-assisted regeneration. *Energy,* 66**,** 799-809.

Yao, Y., Yang, K., Zhang, W. & Liu, S. 2014b. Parametric study on silica gel regeneration by hot air combined with ultrasonic field based on a semi-theoretic model. *International Journal of Thermal Sciences,* 84**,** 86-103.

Yu, N., Wang, R. Z., Lu, Z. S. & Wang, L. W. 2014. Development and characterisation of silica gel–LiCl composite sorbents for thermal energy storage. *Chemical Engineering Science,* 111**,** 73-84.

Yuan, Y., Zhang, H., Yang, F., Zhang, N. & Cao, X. 2016. Inorganic composite sorbents for water vapor sorption: A research progress. *Renewable and Sustainable Energy Reviews,* 54**,** 761-776.

Zendehboudi, A., Angrisani, G. & Li, X. 2018. Parametric studies of silica gel and molecular sieve desiccant wheels: Experimental and modeling approaches. *International Communications in Heat and Mass Transfer,* 91**,** 176-186.

Zhang, L.-Z. 2008. *Total Heat Recovery : Heat and Moisture Recovery from Ventilation Air,* New York, NY, USA, Nova Science Publishers, Inc.

Zheng, X., Ge, T. S. & Wang, R. Z. 2014a. Recent progress on desiccant materials for solid desiccant cooling systems. *Energy,* 74**,** 280-294.

Zheng, X., Wang, L. W., Wang, R. Z., Ge, T. S. & Ishugah, T. F. 2014b. Thermal conductivity, pore structure and adsorption performance of compact composite silica gel. *International Journal of Heat and Mass Transfer,* 68**,** 435-443.

164: Power design for detection of three-phase combined transformer

Liu GEGE[1] , Xi ZIQIANG [1]

[1]College of Electrical and Electronic Engineering, Hubei University of Technology, Hubei WUhan,970885914@qq.com

The three-phase combination transformer is a strong inspection and metering device, and the accuracy of its gateway measurement is very important for fair settlement in the urban power grid trade. However, so far, the General Administration of Quality Supervision, Inspection and Quarantine of the People's Republic of China (AQSIQ) has not issued a special verification protocol for three-phase combination transformers. Therefore, in the error calibration test of three-phase combination transformers, the testers can only use the phase transformers of the combination transformer. Considered as independent individuals, and then individually perform error checking for each phase element in batches according to the relevant provisions in JJG314-2010 "Voltage Transformer for Measurement" and JJG313-2010 "Current Transformer for Measurement". . In comparison, ignoring the error calibration data obtained from the electromagnetic influences between the phase transformers of the combined transformer does not have a high accuracy. Therefore, a test power source capable of implementing simultaneous error checking on three-phase components has been developed. It is of great significance. This paper takes a 10kV three-phase composite transformer as the object to be measured, and designs a test power supply for three-phase combined transformer calibration, including a three-phase voltage source and a three-phase current source. The three-phase combination transformer is tested by the test power supply. The error check can choose single-phase power output or three-phase simultaneous output and analyze the practicability and reliability of the test power supply's performance test data. The test results show that the designed test power supply for the three-phase combined transformer can meet the test method requirements of the three-phase method and the single-phase method at the same time. The power output range is wide and the adjustment accuracy is high.

Keywords: three-phase combined transformer; three-phase voltage source; three-phase current source

1. INTRODUCTION

Three phase combined transformer is a mandatory calibration equipment. The accuracy of its metering is crucial to fair settlement in the urban power grid trade. But so far, the State Administration of quality supervision, inspection and Quarantine has not issued special verification regulations for three-phase combined transformers. Therefore, in the error calibration test of the three-phase combined transformer, the test personnel can only regard each phase element of the combined transformer as an independent individual. According to the relevant regulations of JJG314-2010 "measuring voltage transformer" and JJG313-2010 "measuring current transformer", the single phase method is used to verify the error of each phase element separately. In comparison, the error data obtained from ignoring the electromagnetic effects between the components of the composite transformer are not highly accurate. Therefore, it is of great significance to develop a test power supply which can realise the error calibration of three-phase components simultaneously. In this paper, 10kV three-phase combined transformer is taken as the test object. A test power supply for three phase combined transformer calibration is designed. The usability and reliability of the test power are analysed through the test data.

2. TEST POWER SUPPLY DESIGN BASIS

Three phase combined transformer is a transformer used for three-phase power system, which is composed of three phase voltage transformer and three single-phase current transformers. According to the requirements of the test method specified in the standard of JB/T 10432-2004 "three phase combined transformer", the test power for three phase combined transformer calibration should meet the following requirements.

(1)The test power supply should be rated frequency, and the symmetrical three phase voltage and three phase current can be output simultaneously.

(2)In the error check, the three-phase voltage of the test power supply can run the three-phase voltage transformer within the range of 80% to 120% rated voltages. The three phase output current allows each phase current transformer to operate within the range of 5% (or 1%) rated current to rated continuous hot current.

(3)The power output is stable and can operate for a long time.

3. EXPERIMENTAL POWER SUPPLY WORKING PRINCIPLE

Test power supply for three-phase combination transformer check that the design of this paper include three-phase voltage source that consist of a three-phase double voltage regulation power supply and three-phase booster, and three-phase current source that consist of another three-phase double voltage controlled power source and three sets of current transformer with standard current transformer.

3.1. Three-phase output adjustment device

Three phase double regulated power supply consists of two main regulating devices and a fine tuning device. The main regulating device consists of three phase voltage regulator. The trimming voltage device consists of three auxiliary voltage regulating units (Ren, 2015). The main regulation and fine-tuning have different adjustment fineness. As shown in Figure 1, the three phase double regulated power supply's input terminal is three-phase four wire system.But the zero line is divided into three after the power is introduced. A phase line and a zero line are connected to each phase input winding end of the three phase voltage regulator 1. The three-phase voltage regulator 1 consists of three input terminals connected to a star type single-phase auto voltage regulator. The output terminals of each phase are connected through the independent auxiliary voltage regulating unit to the outlet end. The auxiliary voltage regulator unit consists of a two stage winding connecting three phase voltage regulator 1 output terminal and a three-phase double voltage regulator outlet transformer. 3. And a single-phase voltage regulator 2 connected with the buck isolation transformer 3 primary winding and the corresponding three-phase three-phase AC inlet terminal.

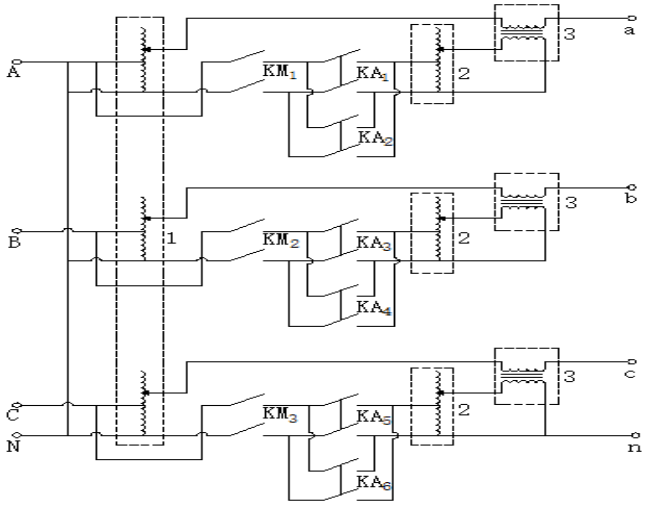

Figure 1: Functional diagram of three phase dual-voltage power

During the error calibration test of three-phase combined transformer, the three phase voltage regulator can be adjusted by the experimenter to realise the three-phase voltage and three-phase current output simultaneously. The relationship between input voltage and output voltage of each phase can be expressed as:

$$\frac{U_1}{U_2} = \frac{N_1}{N_2} \quad (1).$$

Where: U1 and U2 are the single-phase of the three-phase voltage regulators, respectively, for input and output voltages. N1 and N2 are Single phase winding turn number of three phase voltage regulator, respectively, for primary winding and secondary winding. Under the condition of U1 unchanged, adjusting the three-phase voltage regulator to change the ratio of N1 and N2 can synchronously realise U2 in a certain range.

By setting the variable ratio of the buck isolation transformer in the auxiliary voltage regulating unit, the finer adjustment has smaller output adjustment fineness than the main adjustment. Therefore, in order to ensure the three phase output balance and the accurate adjustment of the corresponding output value, the tester can adjust the output of the auxiliary voltage regulating unit to modify the output of the power supply.

In addition, the input and control loop of each auxiliary voltage regulator unit adopts voltage forward and reverse input control design. When the single-phase or multiphase output voltage exceeds the required value during the first boost process, the direction of the input voltage of the auxiliary voltage regulating unit can be changed thus the direction of the output voltage of the auxiliary voltage regulator unit can be changed. In order to reverse the output voltage of three phase double regulated power supply. In this way, the output voltage of the three phase double regulated power supply is reversed.

3.2. Three-phase voltage output

When the three-phase combined transformer is calibrating the error, the output terminal of a three-phase double regulated power supply is connected with the input terminal of the three-phase booster. The output terminal of the three-phase booster is connected with the high voltage terminal of the three-phase voltage transformer in the three-phase combined transformer (Liu, 2010). The number of turns of the secondary winding of the three-phase boost is fixed, and the number of turns of the single-phase secondary winding is more than that of the original winding. Each phase output voltage of the three-phase voltage regulator increases with the increase of the output voltage of the three-phase dual voltage regulator, and finally reaches the required voltage range.

3.3. Three-phase current output

The output of another three-phase dual voltage regulator power supply is connected to the input of three standard current transformers with a current booster. The high current output end of the standard current transformer with a lift is connected to the primary winding outlet end of the three single-phase current transformers in the combined transformer (Zhang, 2012). The standard current transformer with a lift is composed of a combination of a lift and a

standard current transformer. The output terminal of the upconverter is the input end of the standard current transformer. At the same time, the output terminal of the upconverter is also the output terminal of the combined device. The relationship between input current and output current of a standard current transformer with a lift can be expressed as:

$$\frac{I_1}{I_2} = \frac{W_2}{W_1} \tag{2}$$

In the Formula :I1 and I2 are current of upconverter, corresponding to input and output respectively. W1 is the number of turns of the primary winding of the riser; W2 is the number of turns of the secondary winding of the riser. The number of turns on the secondary side of the upconverter is less than that of the original winding, and the power of the primary side and the secondary side is equal. With the increase of the input voltage of the upconverter, the output voltage will be lower and lower, but the load current will be increased. When the error is checked, the tester can adjust the output of the current transformer with the current transformer accurately by adjusting the three phase output of the three-phase dual voltage regulator.

4. 10KV THREE-PHASE COMBINATION TRANSFORMER CALIBRATION TEST POWER SUPPLY DESIGN

In this paper, a JLSJWS-10 type three-phase combined transformer is chosen as the test subject. The working frequency is 50Hz, the rated voltage is 10kV, and the accuracy is 0.2S level. Among them, the voltage capacity of the combined transformer is 3 x 20V A and the voltage ratio is 10kV/100V. The current part of the unit has a capacity of 3 * 10VA and a current ratio of 600A/5A.

4.1. Three-phase dual voltage regulator power supply design

The key point of the design of three phase double regulated power supply is the adjustment and fineness design of the two sets of voltage regulating devices. It is necessary to consider comprehensively the specifications and parameters of the components used in the test power supply and the specifications and parameters of the three-phase combined transformer (Jiang, 2011).

(1) The determination of the fineness of the main adjustment. Based on the safe and stable operation of the equipment and its volume and weight optimisation considerations, the main regulation of the three-phase dual regulated power supply is made up of three single-phase pie type autotransformer with capacity of 3K V. A and rated voltage of 220V.It mainly adjusts input A, B, C and N input three phase AC 220V voltage. Rotating the main handwheel can simultaneously drive the brush of three voltage regulators to slide on the surface of each coil and adjust the voltage. The coil of each single phase automatic coupling voltage regulator is 250 turns, and the potential at each turn is 1 turns / volts. The carbon brush is adjusted by one turn voltage to adjust 1V, and the output voltage can be adjusted to 0~250V with a continuously adjustable voltage of 1V.

(2) Determination of fine adjustment fineness. The three auxiliary voltage regulating units connected in the three phase voltage regulator output loop are regulated by independent auxiliary handwheels. The auxiliary voltage regulator unit consists of a single-phase pie voltage regulator with a capacity of 0.2K V. A and a rated voltage of 220V. After input of each voltage regulator input single-phase AC 220V voltage, the adjustable range and adjusting fineness of the output voltage are in accordance with the single-phase autotransformer voltage regulator consisting of a three-phase voltage regulator. But in the output circuit of the three-phase dual voltage power supply, it is used in conjunction with the buck isolating transformer with a specification of (200V:10V).Therefore, the actual adjustable voltage range of the auxiliary voltage regulating unit is 0~12.5V, and the fineness is 0.05V.

Besides, an AC contactor with switching voltage input direction is arranged in the input control loop of each auxiliary voltage regulating unit. In order to ensure the smooth operation of the commutator, the rated current of the commutator should be greater than the maximum output current of the three-phase double regulated power supply. The maximum output current of the three phase double regulated power supply is about 14A. Therefore, the rated current of the reversing contactor is set to 20A, and after the contactor has skipped. The test personnel can reverse the voltage output of the three-phase dual regulated power supply under the condition that the auxiliary handwheel rotation direction is unchanged.

4.2. Three-phase voltage source design

The structure diagram of the three-phase voltage source is shown in Figure 2. During the error check, in order to ensure the three-phase voltage output by the test power supply, the three-phase voltage transformer in the 10kV three-phase combination transformer can operate within the range between 80% and 120% of the rated voltage, and the selected three-phase voltage booster the input voltage range is 0~230V, the output voltage range is 0~12kV, and the rated operating frequency is 50Hz.

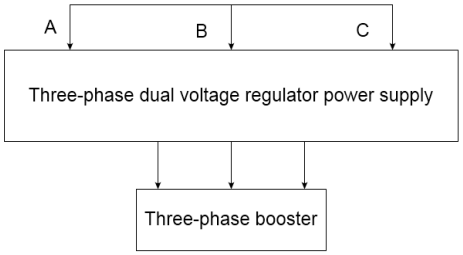

Figure 2: Structure diagram of three phase voltage source

4.3. Three-phase current source design

The accuracy of the three single-phase current transformers in the JLSJWS-10 three-phase combined transformer is 0.2S. When the S-class current transformer is subjected to error checking, three phase double regulated power supply and three three-phase current source with a lift up standard current transformer shall have fine adjustment requirements. It can ensure that the measuring point of 1%IN and 5%IN of current transformer can be adjusted in three phase combined transformer (Yang, 2015). 20%IN, 100%IN and 120%IN measurement points can be adjusted accurately. According to the requirements, the specific parameters of the standard current transformer with the upconverter are chosen as shown in Table 1.

Table 1: Parameters list of standard current transformer with current elevator

parameter name	Value	unit	parameter name	Value	unit
Primary current	5~600	A	Riser voltage	250	V
Secondary current	5	A	Riser capacity	2	kVA
Rated frequency	50	Hz	Rated load	5	VA
Operating Voltage	10	kV	Lower limit load	2.5	VA
Accuracy level	0.02S	level	Power factor	1	

The structure diagram of the three-phase current source is shown in Figure 3. The rated primary current of the selected upconverter is 600A, and the error check is allowed to operate at no more than 120% of its rated current (i.e. 720A). It satisfies the requirements of current transformer for rated current of the current transformer during the error check of 10kV three-phase combined transformer (Ding, 2016). In addition, the rated capacity of the selected upflow device is less than the rated capacity of the three-phase dual voltage regulator, which can ensure the safe use of the three-phase dual voltage regulator.

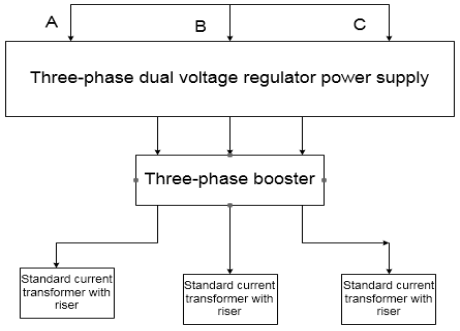

Figure 3: Structure diagram of three phase current source

5. TEST POWER APPLICATION AND ITS PERFORMANCE TEST

Based on the test power supply of the three-phase combined transformer designed in this paper, the principle diagram of the connection of the 10kV three-phase combined transformer for error checking is shown in Figure 4.

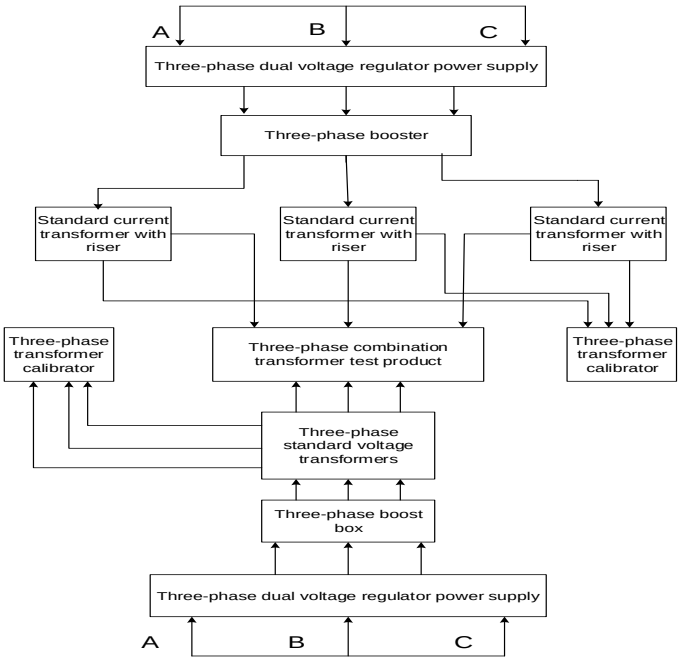

Figure 4: Functional block diagram of three phase detection method

For the error calibration test of three-phase combined transformer, it is necessary for two test personnel to stand in front of the control panel of a three-phase dual voltage power supply. Then according to the test method stipulated in the standard of JB/T 10432-2004 "three phase combination transformer", three phase dual voltage regulation power supply is adjusted to realise the output of three-phase voltage and three-phase current. When the test power is used to check the error of the three-phase combined transformer with single-phase method, on the basis of three phase calibration, we need to pull out the corresponding connection wires of the output voltage two of the two three-phase double regulated power supply.

In order to verify whether the designed test power conforms to the test method specified in the standard. In this paper, the three-phase voltage and three-phase current output of the test power under load are tested and analyzed. The test data table is shown in Table 2 and Table 3.

Table 2: Output of three phase voltage

Standard Requirements Test Voltage (V)			Actual output voltage (V)		
Phase A	Phase B	Phase C	Phase A	Phase B	Phase C
8000	8000	8000	8006.6	8004.7	8004.7
10000	10000	10000	10017.6	10016.6	10017.6
12000	12000	12000	12028.5	12027.6	12025.7

Table 3: Output of three phase current

Standard Requirements Test Current (A)			Actual output current (A)		
Phase A	Phase B	Phase C	Phase A	Phase B	Phase C
6	6	6	6.01	6.01	6.02
30	30	30	30.15	30.11	30.13
120	120	120	120.18	120.21	120.19
300	300	300	300.45	300.51	300.49
480	480	480	480.87	480.92	480.85
600	600	600	601.25	600.98	601.17
720	720	720	721.97	721.87	721.93

After calculation, the maximum deviation of the three-phase voltage output of the designed test power is 0.23%. The maximum deviation of the output of the three-phase current is 0.33%. The test power supply can simulate the actual working state of the 10kV three-phase combined transformer, and at the same time, the error calibration test for the three phase transformer of the transformer is carried out. It meets the requirements of three-phase power transformer in the process of error calibration.

6. CONCLUSION

The three-phase power transformer designed for verification can output symmetrical three-phase voltage and three-phase current at the same time. The adjustment range of power output is wide and the adjustment fineness is small. Using this test power to check the error of 10kV three-phase combined transformer. Aiming at the current transformer in the composite transformer, the measurement points of 1%IN and 5%IN can be adjusted. 20%IN, 100%IN and 120%IN measurement points can be adjusted accurately. Fully conforms to the test method requirements of the three phase combined transformer error calibration stipulated in the JB/T 10432-2004 "three-phase combined transformer" standard. The positive and negative output control design of the auxiliary voltage regulating unit also optimises the output regulation speed of the test power to a certain extent. The stability of the test power and the efficiency of the experimenters are improved.

In addition, the test power supply can meet the requirements of the three-phase and single-phase test methods at the same time. When the single phase method is used to verify the error of the three-phase combined transformer, it is very convenient to remove the two phase connecting wire in the three-phase output of the three-phase double voltage power supply on the basis of the connection between the equipment in the three-phase method check.

7. REFERENCES

Ding W, Jin X, Chen M, 2016. *Analysis of Influence Quantity of Three-phase Combined Transformer Error Checking* [J].Journal of Huaqiao University (Natural Science), 2016, 9(5):622-626.

Jiang W, Yang H, Jiang B, 2011. *Three-phase Verification Method and Its Implementation of High-voltage Three-phase Combined Transformer*[J]. Electrical Measurement & Instrumentation, 2011, 7(7):46-49.

Liu P, Jiang Y, 2010. *Comparative Study on Two Verification Methods of Three-phase Combined Transformer* [J].Sichuan Electric Power Technology, 2010, 2(1):79-81.

Ren L, Liu G, Jiang B, 2015. *Research on Error Influence of Three-element Three-phase Combined Transformer* [J].Auto Control, 2015, 6(2):77-80.

Yang Z, 2015. *Study on verification device of high voltage three phase combined transformer*[J].Acceleration of Electrical Engineering, 2015, 2(9):08-12.

Zhang N, Liao H, Wu Y, 2012.*Study on Three-phase Combined Transformer Verification Device*[J].Automation and Instrumentation, 2012, 3(4):41-43.

Zhang H, Zhang F, Chen Y, 2015. *Analysis of voltage error of three-phase three-element combined transformer* [J].Intellectual Intelligence Application, 2015, 3(8):64-65.

165: Photovoltaic wave power suppression control method based on improved wavelet packet transform

Linzhang WU[1], Wenshan YU[2], Tiezhou WU[3], Junjie ZHANG[4]

[1] *Hubei Key Laboratory for High-efficiency Utilisation of Solar Energy and Operation Control of Energy Storage System, Hubei University of Technology, 430068, China, yws3355@qq.com*
[2] *Hubei Key Laboratory for High-efficiency Utilisation of Solar Energy and Operation Control of Energy Storage System, Hubei University of Technology, 430068, China, 1457575180@163.com*
[3] *Hubei Key Laboratory for High-efficiency Utilisation of Solar Energy and Operation Control of Energy Storage System, Hubei University of Technology, 430068, China, 461821408 @qq.com*
[4] *Hubei Key Laboratory for High-efficiency Utilisation of Solar Energy and Operation Control of Energy Storage System, Hubei University of Technology, 430068, China, 2978636476@qq.com*

The hybrid energy storage system consisting of a lithium-ion battery pack and a super capacitor is currently a common method of suppressing fluctuations in the output power of microgrid photovoltaics. Using the wavelet packet analysis method to decompose the photovoltaic output power, the power components in different frequency bands can be obtained. However, the traditional wavelet packet decomposition method has a fixed number of decomposition layers and cannot follow the change of photovoltaic output power in real time. This paper proposes an improved wavelet packet decomposition method. Considering the fluctuation of solar cell output power and the current working state of the hybrid energy storage system, the fuzzy control algorithm is used to adjust the number of wavelet packet layers in real time to achieve a self-adaptation of the power fluctuations during the stabilisation process. The lithium-ion battery and the supercapacitor state of charge are considered. , The use of fuzzy control to their secondary output power distribution, improve the effect of stabilisation. Experiments show that compared with the control method based on traditional wavelet packet, the control method proposed in this paper improves the control effect by 4.5%.

Keywords: Suppression of photovoltaic output power; Hybrid energy storage system; Improved wavelet packet decomposition; Fuzzy control

1. INTRODUCTION

Since human society entered the age of electronics, energy and the environment have become an urgent problem to be solved by human survival and development. The research and utilisation of various renewable energy sources have been increasingly valued by humans (Amuti, 2014). In modern times, many countries and regions are paying more attention to the development and utilisation of green renewable energy. With the support of governments from various countries, distributed generation technologies have developed rapidly. Currently, mature distributed generation technologies include photovoltaic power generation, fuel cell power generation, micro-turbine power generation, and wind power generation (Wang, 2012). Distributed power sources are widely used in microgrids, which not only satisfy people's demand for electrical energy but also protect the environment (Kang, 2017). However, their inherent high uncertainty and strong volatility contribute to the stability and power supply of power systems. Caused a huge impact and impact (Wang, 2016). How to suppress the output of distributed power supply and improve the overall quality of micro-grid operation has become an issue of increasing concern.

The rapid development of energy storage technology provides a new way of thinking for solving the above problems. Energy-based energy storage (represented by lead-acid batteries, lithium batteries, etc., with high energy density, long energy storage time, but low power density, short cycle life) and power-type energy storage (using supercapacitors, flywheel energy storage, etc. Representative, high power density, fast response, long cycle life, but low energy density, high self-discharge rate are used together to achieve technical complementarity to meet different levels of technical requirements (Hou, 2017). (Huang et al, 2017) proposed a fuzzy control method of variable filter constants, which adjusts the grid-connected power by changing the filter time constant and adjusts the energy distribution of the battery and the super capacitor through fuzzy control to suppress the fluctuation of the microgrid. (Han et al, 2013) uses wavelet packet analysis to analyse the output power of the wind farm and modifies the output fluctuation of the wind farm by allocating battery and super capacitor power. (Wu et al, 2017) proposed a wavelet packet decomposition control strategy based on wind power grid-connected standard, and adjusted the wavelet packet decomposition layer number to fluctuate the wind power fluctuations by evaluating the fluctuation power. (Esmaili A et al, 2013) proposed an energy storage device based on a zinc bromide fluid battery and a lithium ion capacitor, and applied this energy storage device to wind farms to reduce the wind power drop. (Wang et al, 2015) proposed a virtual inertia control strategy for a DC microgrid bidirectional grid converter, which enhanced the inertia of the DC microgrid and stabilised the voltage fluctuation of the DC bus of the microgrid. In (Wang and Yan et al, 2013), a generalised harmonic wavelet packet decomposition algorithm is proposed to perform arbitrary frequency band and hierarchical decomposition of the signal, which better solves the aliasing of the signal spectrum. (Xiong and Wang et al, 2015) established the evaluation index of hybrid energy storage system applied in microgrid, and proposed a hybrid energy storage charge/discharge control strategy with secondary correction, which achieved a better effect of suppressing the fluctuation of microgrid. (Wu and Pan et al, 2013) proposed a power control strategy based on hybrid energy storage based on the characteristics of microgrid operation mode, micro power supply and energy storage system, and established a typical microgrid model to verify the effectiveness. (Ji and Zhang et al, 2017) proposed a microgrid energy optimisation strategy for energy storage stabilisation and load switching, and verified the effectiveness of the energy optimisation strategy through calculation examples.

Based on the characteristics of distributed power supply, this paper improves the wavelet packet analysis method and proposes an adaptive fuzzy wavelet packet power control method for photovoltaic power control. By taking into account the changes of the external environment, the fuzzy control adaptively adjusts the number of wavelet packet decomposition layers. The solar PV output is directly obtained through adaptive wavelet packet decomposition to obtain the grid-connected power, lithium-ion battery power and super-capacitor power, and adaptively adjusts the number of wavelet packet decomposition layers through fuzzy control to achieve real-time adaptive control of photovoltaic fluctuations. The analysis process of the fluctuation power of the microgrid can be optimised, and the analysis effect and efficiency can be improved. Secondly, the secondary fuzzy control can be used to complete the energy distribution within the hybrid energy storage system, improve the effect of power fluctuation fluctuation of the microgrid, and prolong the service life of the hybrid energy storage system.

2. WAVELET PACKET ANALYSIS APPLIED TO PHOTOVOLTAIC POWER DECOMPOSITION

2.1. Wavelet packet time-frequency analysis

When using the hybrid energy storage system to suppress the power fluctuation of the solar cell output, firstly, the output power of the solar panel needs to be analysed to obtain the power components of different frequency bands, and then the distribution is performed according to the characteristics of the grid connection and different energy storage components. The commonly used analysis method is the low-pass filtering method, but it has a single filtering effect and cannot cope with the matching problem when photovoltaic output fluctuations. The wavelet packet decomposition analysis method is a frequency feature extraction method for multi-frequency signals. It is developed from multi-resolution wavelet analysis and can compensate for the fact that wavelet analysis can only decompose low-frequency signals and cannot decompose high-frequency signals. The signal analysis method is shown in Figure 1.

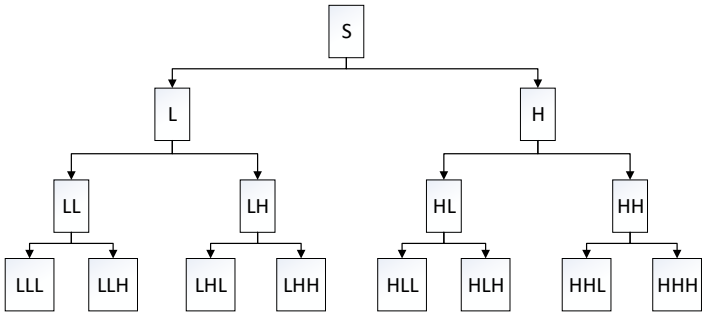

Figure.1: Wavelet packet decomposition analysis

In the Figure 1, S is the original signal, L is the decomposed low-frequency component, and H is the decomposed high-frequency component. The wavelet packet decomposition divides the frequency band into multiple levels and adaptively selects the best basis function according to the characteristics of different frequency components in the analysed signal, thereby improving the accuracy in signal analysis. From the perspective of the filter, wavelet packet decomposition is to pass the analysed signal through a series of band-pass filters with the same bandwidth and different centre frequencies. The wavelet decomposition layer is a crucial parameter. The selection of the decomposition layer directly affects the signal analysis effect. Too large or too small will deviate the analysis result from the optimal result. In the article that has applied the wavelet packet decomposition method to the analysis of solar output power signals, the determination of the number of wavelet packet decomposition layers has not been self-adapted according to fluctuation power changes. In order to solve this problem, the first layer of fuzzy control was introduced to determine the optimal number of wavelet packets based on changes in the output power fluctuation and the frequency range that the hybrid energy storage device can accept, thereby optimizing the PV output power decomposition effect.

2.2. Adaptive fuzzy wavelet packet decomposition

In the wavelet packet decomposition and reconstruction process of the wave power output from the solar panel, the optimal wavelet packet decomposition layer number is obtained in real time, and a fuzzy algorithm is added to consider the wavelet packet decomposition layer number n(t- 1) The normalised output power of the previous period is obtained by fluctuating power of the current period and the current optimal decomposition layer number n(t) is obtained. A schematic diagram thereof is shown in Figure 2.

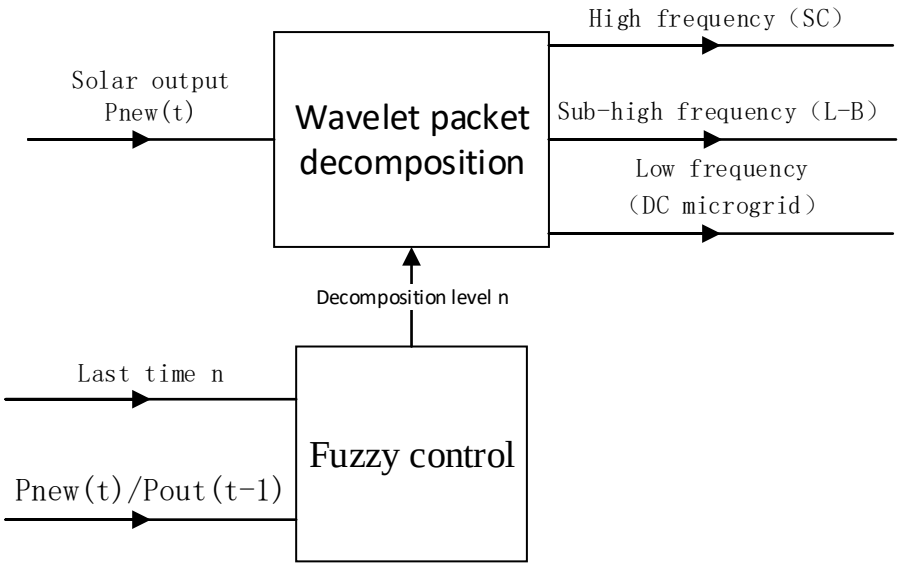

Figure 2: Fuzzy Wavelet Packet Decomposition

The wavelet packet decomposition of the output power of the photovoltaic power supply in the microgrid is converted into high-frequency components, sub-high-frequency components and low-frequency components. The high-frequency components are input to the super-capacitor, and the sub-high-frequency outputs are absorbed to the lithium-ion battery. Output to a DC microgrid or inverting the grid. The level of the decomposition layer and the current power change rate of the fuzzy controller are output at the same time, and the current optimal decomposition layer number of the wavelet packet decomposition is output.

2.3. Secondary power distribution of supercapacitors and lithium batteries

The high-frequency power component and the sub-high-frequency power component obtained by the wavelet packet decomposition do not consider the working state of the lithium battery and the super capacitor. If the direct input may cause the lithium battery and the super capacitor to work in an overcharge or over-discharge state, this will result in the service life of the lithium battery and the super capacitor is greatly reduced. Therefore, it is necessary to perform secondary distribution of the power component in consideration of the current state of charge of the lithium battery and the super capacitor in order to suppress the output of the micro grid photovoltaic power supply and extend the hybrid energy storage system. The goal of service life.

The secondary distribution system diagram of the output power of the hybrid energy storage system is shown in Figure 3. The hybrid energy storage system adopts fuzzy control to achieve secondary distribution of power, supercapacitor current state of charge, current state of charge of the lithium battery, and current wavelet decomposition. The layer number is input, the secondary distribution coefficient k is output, the first frequency band of the power component after decomposition of the wavelet packet is connected to the grid or supplied to the load, and the second to kth input is input to the battery, and the rest is input to the super capacitor.

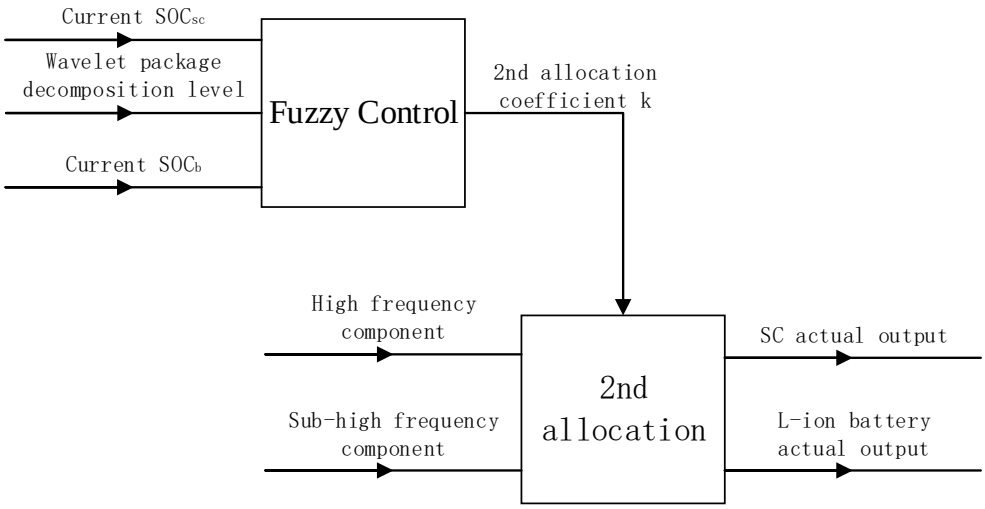

Figure 3: Lithium battery, super capacitor power distribution diagram

3. DUAL ENERGY STORAGE SYSTEM FUZZY CONTROL STRATEGY

3.1. Fuzzy wavelet packet control strategy

The input of the fuzzy wavelet packet controller is the ratio of wavelet packet decomposition layer n(t-1) at the end of the t-1 period and the ratio of the output power of the photovoltaic power source and the output power of the t-1 period at the current microgrid D(t),D(t) can be derived from Equation 1.

Equation 1: The change ratio of the photovoltaic output power .

$$D(t) = \frac{Pout(t)}{Pout(t-1)}$$

Where:

Pout(t) = the current output power of the microgrid photovoltaic power supply

Pout(t-1) = the output power of the microgrid photovoltaic power supply over a period of time

When D(t) is near 1, the output of the microgrid power supply in the previous period is not much different from the current output. Therefore, the wavelet packet decomposition layer number n in the current period can be changed in a small range or not, when D(t) changes. When it is larger, the optimal number of decomposition layers is obtained by fuzzy control according to the number of decomposition layers n(t-1) of D(t) and the previous period.

The fuzzy set of fuzzy control input n(t-1) is {2,3,4,5,6}, and the fuzzy vocabulary is {VS,S,M,B,VB},D(t). The fuzzy universe selection is {0,0.3,0.6,0.9,1,1.1,1.4,1.7,2} and the fuzzy language set is chosen as

{NB,NM,NS,NZ,Z,PZ,PS,PM,PB} The output of the fuzzy controller is the wavelet packet decomposition layer n(t), which is the same as the domain and word set of n(t-1). The fuzzy control rule table is shown in Table 1.

Table 1: fuzzy wavelet packet control rules

n (t)		n (t-1)				
		VS	S	M	B	VB
D (t)	NB	VS	VS	VS	S	M
	NM	VS	VS	S	M	B
	NS	VS	S	S	M	B
	NZ	VS	S	M	B	VB
	Z	VS	S	M	B	VB
	PZ	VS	S	M	B	VB
	PS	S	M	B	B	VB
	PM	S	M	B	VB	VB
	PB	M	B	VB	VB	VB

The membership functions of fuzzy controller input and output are shown in Figure 4 (a), (b) and (c). The design of membership functions and fuzzy control rules for input and output in fuzzy control need to follow the following principle: The membership function allows certain human skills, but it needs to meet the objective conditions of the input, that is, it can correctly reflect the overall characteristics of the elements in the input from the collection to the non-collection; the fuzzy control rules The formulation needs to be combined with the actual situation and based on the existing experience. For example: when the number of wavelet packet decomposition layers in the previous period is small and when the current output power of the photovoltaic power source differs greatly from the output power at the previous moment, it needs to be at the last moment. The number of decomposition layers is added on the basis of the number of decomposition layers to ensure that the low-frequency power component can be decomposed; when the number of layers of wavelet packet decomposition in the previous period is large and the output power of the current photovoltaic power source is not significantly different from the output power of the previous moment, the difference is The number of wavelet packet decomposition layers can be fine-tuned or unchanged on the basis of the last moment.

There are many methods of defuzzification in fuzzy control. Common methods of defuzzification include: centre of gravity method, maximum degree of membership method, maximum degree of membership method, maximum degree of membership method, weighted average method, etc. This article selects the centre of gravity method as double fuzzy. The defuzzification method of the control process is different from the above-mentioned three maximum degree of membership methods. The centre-of-gravity method takes the centre of gravity of the graph area of the membership function and the abscissa axis as the final output value of the fuzzy output. For the continuous membership function, it is calculated.

Equation 2: The continuous the centre-of-gravity method solves the fuzzy equation function .

$$V_{OUT} = \frac{\int_V v\mu_v(v)dv}{\int_V \mu_v(v)dv}$$

Equation 3: The discrete the centre-of-gravity method solves the fuzzy equation function .

$$V_{OUT} = \frac{\sum_{k=1}^{m} v_k \mu_v(v_k)}{\sum_{k=1}^{m} \mu_v(v_k)}$$

Where:

V_k= fuzzy input

$\mu_K(v_k)$= corresponding membership function

V_{OUT}= the output after the center of gravity solution blurring

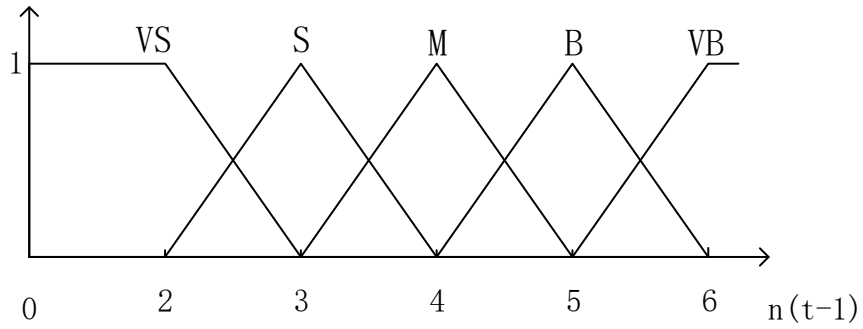

Figure 4(a): wavelet packet decomposition layer n(t-1) membership function

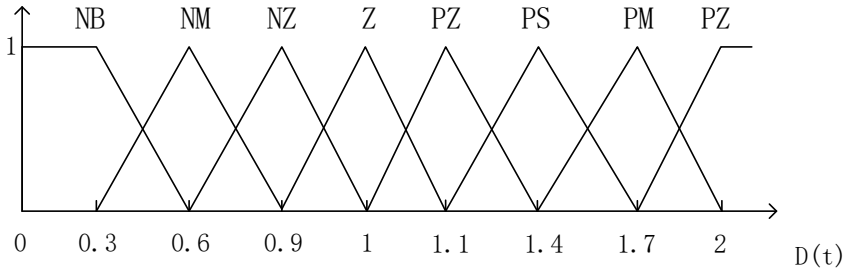

Figure 4(b): Output power ratio D(t) membership function

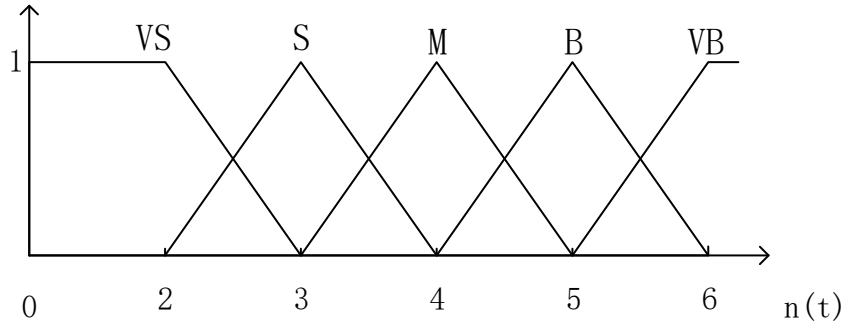

Figure 4(c): wavelet packet decomposition layer n(t) membership function

Figure 4: Membership functions of fuzzy control input and output

3.2. Power secondary batch control strategy

The secondary distribution of the output power of the hybrid energy storage system is fuzzy control input is the current SOC of the super capacitor, the current decomposition level of the current SOC and wavelet packet decomposition of the lithium ion battery, in order to prevent the lithium ion battery and the super capacitor from overcharging or overwork. Put the problem and reserve margin for the hybrid energy storage system. This article sets the SOC of the lithium-ion battery to 25%-75%, that is, if it is lower than 25%, it is regarded as that the lithium-ion battery has been emptied and more than 75% is regarded as lithium ion. The battery is full; the SOC of the super capacitor is set to 10%-90%. Below 10%, the super capacitor is emptied. Above 90% is regarded as the super capacitor is full. The wavelet packet decomposition layer output is controlled by the fuzzy wavelet packet

Equation 4: The SOC of supercapacitor .

$$SOC_{SC} = \frac{C_{SC}^{0} + \int_{0}^{t}\left(\eta_c I_c - \frac{I_d}{\eta_d}\right)}{C_{SC}^{max}}$$

Where:

SOC_{SC} = the SOC of super capacitor at t time (h)

C^0_{sc}= the initial capacity of the super capacitor (Ah)

η_c= charging efficiency

I_c= charging current

η_d= discharge efficiency

I_d= discharge current

C_{sc}^{max}= the maximum capacity of the super capacitor (Ah)

The lithium-ion battery SOC calculation formula is similar to the super-capacitance SOC calculation formula, and will not be repeated here.

The secondary distribution of the output power of the hybrid energy storage system needs to consider the working state of the lithium-ion battery and the super capacitor. When the super capacitor has a high SOC and the solar battery needs to be charged to the super capacitor, the output power of the lithium-ion battery can be adjusted to make the lithium. The ion battery moderately absorbs some high-frequency power so as to protect the supercapacitor from damage caused by overcharging of the supercapacitor; when the lithium ion battery has a low SOC and the lithium ion battery needs to supply power to the load, the supercapacitor output can be adjusted. Power, so that the super capacitor moderately share the power required by part of the load. In addition, within the energy storage system, the lithium ion battery and the super capacitor exchange energy to ensure that the super capacitor SOC is about 50%, so that there is sufficient margin to absorb the excess power of the solar panel, and at the same time. The supercapacitor can follow the power change of the load when the power consumption of the load is high. The fuzzy control strategy for the secondary distribution of output power of hybrid energy storage system is based on the similarity of the input and output membership functions and the establishment of control rules with the above fuzzy wavelet packet control strategy, which will not be described here.

When secondary distribution of the output power of the hybrid energy storage system is performed, it is first determined whether or not secondary distribution is required. In the hybrid energy storage system, the SOC of the super capacitor changes rapidly, so the state of the super capacitor can be used to judge whether secondary power is required. Distribution, when the current SOC or current SOC margin of the supercapacitor can meet its output requirements, no secondary allocation is made. When it is not satisfied, secondary distribution of the hybrid energy storage system is required.

4. EXPERIMENTAL ANALYSIS

In order to verify the proposed fuzzy wavelet packet control strategy, this paper uses a school PV hybrid energy storage project as a platform to carry out control strategy verification test. The microgrid structure in the experiment is shown in Figure 5.

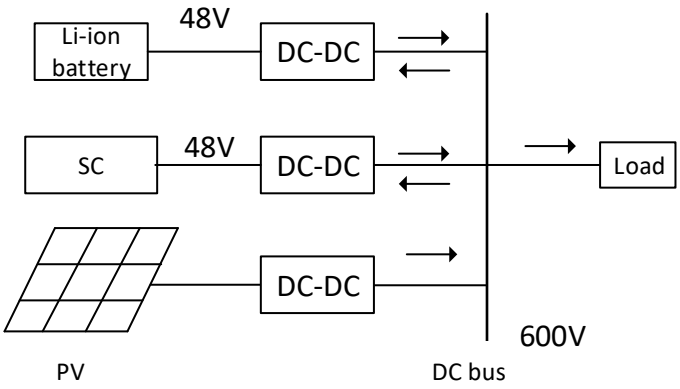

Figure 5: Micro network system structure

The solar battery consists of 70 photovoltaic solar cells with a rated power of 260 W. The rated power of the solar battery is 18.2 KW. The two-way half-bridge DC/DC is connected to the DC bus. The DC bus voltage in the microgrid is 600 V. The hybrid energy storage system consists of Lithium-ion battery packs and ultra-capacitor packs consist of a rated voltage of 48V for lithium-ion battery packs and a rated voltage of 48V for ultracapacitor packs. They are

connected to the DC bus via bi-directional half-bridge DC/DC, and the other end of the bus connects to the microgrid load.

Figure 6 shows the output power of a photovoltaic solar cell on a certain day. It can be seen from the figure that the overall trend of the output power of the solar cell is rising from 6 to 11 o'clock, and the power fluctuation is small. After 11 o'clock, the solar cell is. The output power of the group has large fluctuations, and the fluctuation range is relatively large, which is not conducive to the normal operation of the load end of the micro network.

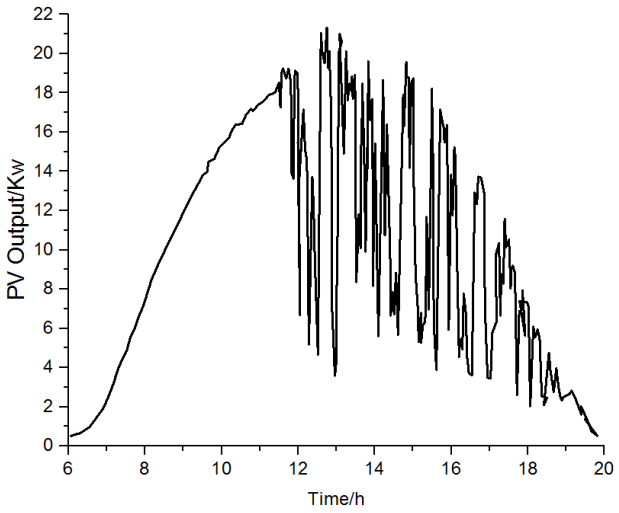

Figure 6: The output power of a photovoltaic solar cell on a certain day

If only the wavelet packet decomposition algorithm is used to decompose the photovoltaic output power and the fuzzy control is used to distribute the power between the supercapacitor and the lithium-ion battery without optimizing the wavelet packet decomposition coefficient in real time, the power after the suppression is shown in Figure 7 . From the figure, we can see that after using the wavelet packet decomposition and power distribution fuzzy control to stabilise the PV output power, the PV output power has been improved, and the suppression effect has reached 91.1% of the target, but due to the failure to adjust the wavelet decomposition in time The decomposition layer, so the effect is not ideal.5

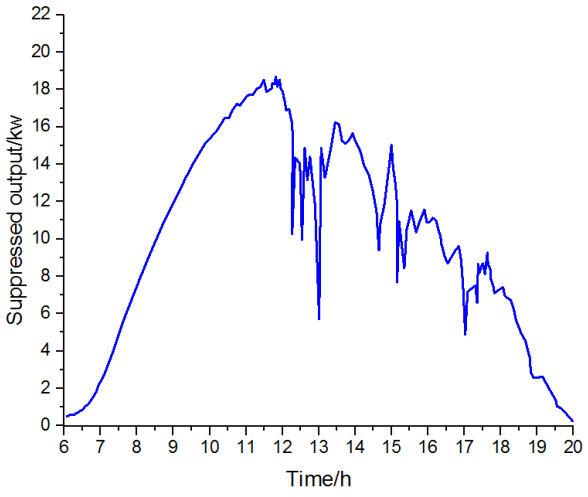

Figure 7: The output power after the suppression without optimizing the number of decomposition layers in real time

After introducing fuzzy control to the wavelet packet decomposition process, the number of decomposition layers of the wavelet packet decomposition can be adjusted in real time according to the change of the photovoltaic output power, its output power after the suppression, and the output power of the supercapacitor and lithium ion battery in the hybrid energy storage system. Figure 8 (a), (b), (c). It can be seen from the figure that after adding the fuzzy control process to the optimal control of the wavelet packet decomposition layer number, the control strategy improves the effect of suppressing the output power fluctuation of the photovoltaic solar battery pack very clearly, and the suppression effect reaches 95.6% of the target of the suppression. The respective output power of the

super-capacitor and lithium-ion battery pack can be seen that the super-capacitor effectively absorbs the high-frequency part of the photovoltaic output power fluctuation, and the lithium-ion battery output power is relatively smooth, avoiding the high frequency of the lithium-ion battery directly absorbing the photovoltaic fluctuation power. The component not only reduces the impact of photovoltaic output fluctuation on the stable operation of the microgrid, but also prolongs the service life of the lithium ion battery in the hybrid energy storage system.

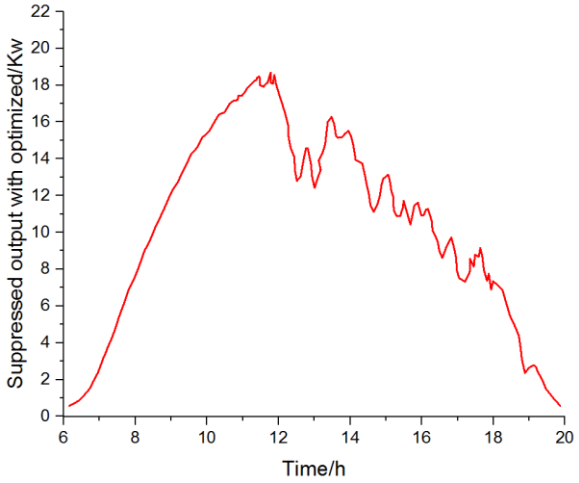

Figure 8 (a) Optimizing the power level of decomposition layers

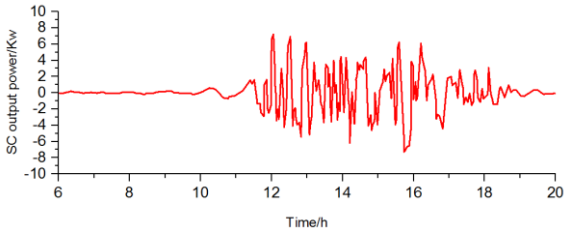

Figure 8 (b) Supercapacitor output power

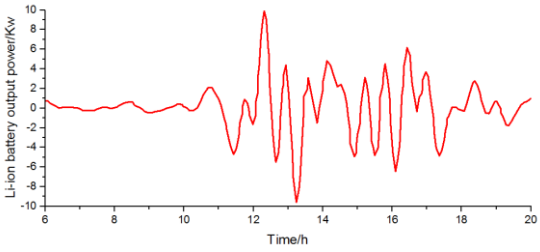

Figure 8 (c) Lithium-ion battery output power

5. CONCLUSION

This paper focuses on the output power fluctuations of photovoltaic solar cells and the stability requirements of microgrid operation. It is based on the combination of wavelet packet decomposition and fuzzy control to adjust the output power of different types of energy storage units in a hybrid energy storage system in a microgrid. The actual fluctuation of the output, while taking into account the actual remaining capacity of each energy storage unit, and real-time adjustment of wavelet packet decomposition layer, to achieve better control results. Through experimental comparison and verification, this method has the following advantages:

1. Considering the fluctuation of output power of photovoltaic solar cells and the need for stable operation of microgrids under island conditions, a hybrid energy storage system is introduced into the microgrid to regulate the energy imbalance between the photovoltaic output and the microgrid load through lithium-ion batteries. The super capacitor suppresses the fluctuation of the PV output power and reduces the impact on the stability of the microgrid.

2. Use the wavelet packet decomposition to process the PV output power to obtain the power components of different frequency bands. Combining the lithium-ion battery and the supercapacitor's tolerance to the power of different frequency bands, the processed power is distributed and the PV output power is combined. The actual fluctuation of the wavelet packet decomposition layer is adjusted by fuzzy control to optimise its decomposition effect.

3. Consider the actual state of charge of the lithium-ion battery and the super capacitor during operation, and use the fuzzy control to perform secondary distribution of the power of the wavelet packet decomposition, so that the lithium-ion battery and the super capacitor can avoid overcharging and overshoot during operation. Releasing, while increasing the service life of the lithium-ion battery, increases the activity of the super-capacitor, thereby improving the stabilisation effect of the hybrid energy storage system.

6. REFERENCES

Alinur A, Yan Q, Tursun Y, et al. 2014 .Research on Forecasting Accuracy of Wind Power with Hybrid Energy Storage. Renewable Energy. 32(7): 978-985.

Wang C, Gao F, Li P, et al. 2012. Research on Low-Voltage Microgrid Control Strategy. Proceedings of the CSEE. 32(25): 2-8.

Kang H, Qu Y, Zhao L, et al. 2017. Research on microgrid control technology with distributed power supply and energy storage device . Power Technology. 41(4):627-629.

Wang Y, Wang S, Jiang J, et al. 2016. Analysis of output power characteristics and smooth control of photovoltaic power generation system. Chinese Journal of Solar Energy. 37(4):847-852.

Hou S, Yu H, Li Q, et al. 2017. Self-adaptive control strategy of hybrid energy storage in micro-grid island operation. Automation of Electric Power Systems. 41(17):15-21.

Huang W, Xiong W, Che W. 2017. Application of Fuzzy Control in Scenery Hybrid Energy Storage Microgrid System. Modern Electric Power. 34(1):30-36.

Han X,Chen Y, Zhang H,et al. 2013. Application of hybrid energy storage technology based on wavelet packet decomposition in power fluctuation modulating wind farm.Proceedings of the CSEE. 33(19):8-13.

Wu J, Ding M. 2017. Adaptive Wavelet Packet Decomposition-based Hybrid Energy Storage Suppression Wind Power Fluctuation Control Strategy. Electric Power System Automation. 41(3):7-12.

Esmaili A, Novakovic B, Nasiri A, et al. 2013. A Hybrid System of Li-Ion Capacitors and Flow Battery for Dynamic Wind Energy Support. IEEE Transactions on Industry Applications. 49(4):1649-1657.

Wang H, Wang D, Jia H, et al. 2015. A Battery and Virtual Energy Storage Coordination Control Strategy for Suppressing Power Fluctuation in Micro-network Connection Lines. Proceedings of the CSEE. 35(20): 5124-5134.

Wang Y, Yan B, Zhang S, et al. 2013. An Improved Generalized Harmonic Wavelet Packet Decomposition Algorithm and Its Application to Signal Feature Extraction. Journal of Yanshan University. (4):358-365.

Xiong X, Wang J, Yang R, et al. 2015. Fuzzy Adaptive Control Strategy of Hybrid Energy Storage in Microgrid. Power System Technology. 39(3):677-681.

Wu Y, Pan W, Feng M, et al. 2013. Microgrid Power Control Strategy Based on Hybrid Energy Storage. Journal of Electric Power Systems and Automation. 25(2):109-114.

Ji Y, Zhang P, Yao X, et al. 2017. Distributed Energy Optimisation Method Based on Market Control for Microgrid. Automation of Electric Power Systems. 41(15):34-41.

166: Research on SOC estimation method of electric vehicle battery based on double fuzzy-variant filter

Zhang-qing HE [1], Lei-ming JIAO [2], Ling-chao ZHANG [3]

1 Hubei Key Laboratory for High-efficiency Utilisation of Solar Energy and Operation Control of Energy Storage System, 136370818@qq.com
2 Hubei Key Laboratory for High-efficiency Utilisation of Solar Energy and Operation Control of Energy Storage System,920462088@qq.com
3 Hubei Key Laboratory for High-efficiency Utilisation of Solar Energy and Operation Control of Energy Storage System,2207433369@qq.com

Power batteries are the power source of electric vehicles，so the estimation precision of the battery SOC directly affects the vehicle's handling and safety. In order to improve the accuracy of the online SOC estimation, a fuzzy rule is introduced in the filtering stage to adjust the filtering parameter β of the variable structure to suppress the buffeting of the convergence stage. This paper utilises double fuzzy-variable structure filtering to estimate the SOC. The first fuzzy-variable structure filter filters the terminal voltage of the power battery. Another fuzzy-variable structure filter uses the filtered terminal voltage data to estimate the SOC. During the simulation, 1%, 2%, and 3% Gaussian noise was added to the experimental data to simulate the sensor error characteristics in the actual industry and to verify the effectiveness of the double-fuzzy variable structure filtering algorithm in practice. The error of terminal voltage and the real voltage before and after fuzzy-variable structure filtering are compared thereby the effectiveness of filtering in reducing the terminal voltage error is verified. Under the three kinds of Gaussian noise conditions, the SOC is estimated by using terminal voltages before and after filtration. The simulation results verifies that the filtered terminal voltage can effectively improve the SOC estimation accuracy. The three kinds of different SOC initial values have proved that the algorithm has little dependence on the initial value. The experiment and simulation show that the double-fuzzy variable structure filtering is suitable for SOC estimation with low sensor accuracy and unknown initial value. It also has high estimation accuracy and high convergence speed. It provides a practical SOC estimation scheme for the battery management systems.

Keywords: state of charge; double fuzzy-variable structure filtering; terminal voltage; Gaussian noise

1. INTRODUCTION

With the increasing emphasis on the environment, energy shortages and energy security, the development of electric vehicles with zero emissions and high energy efficiency is attracting more and more attention. As the power source of electric vehicles, the power battery plays a key role in the running of the electric vehicle. The estimation accuracy of the SOC of the battery state of charge directly affects the use control strategy of the vehicle (Pang, et al, 2017). The power battery SOC is not a directly measurable value and needs to be obtained through indirect estimation of the terminal voltage, current, and other state quantities. Since the error of the battery condition monitoring link is unavoidable, the remaining battery power obtained through indirect estimation is obtained. The existence of errors cannot be avoided.

There are many commonly used SOC estimation algorithms. The Ampere-Hour integral measurement (FAN, et al, 2015:111-115) and the open circuit voltage measurement (Zheng, et al, 2016:513-525) are the most basic algorithms. The Ampere-Hour integral measurement is simple and easy to use. But as cumulative error increases, and the algorithm cannot give the initial SOC value; As for the open circuit voltage method, the collection of the open circuit voltage data requires the battery to stand for a long time to be accurately obtained, and thus is not suitable for SOC online estimation. There are also some advanced algorithms such as: Kalman filtering algorithm (Pan, et al,2014:148-150), particle filtering algorithm (Ye, et al, 2018:789-799), artificial neural network algorithm (Jokar, et al, 2017:73-87), etc. Among them Kalman filtering method is most commonly used for linear SOC estimation; adaptive Kalman filter (Hua, et al, 2017:77-80)(EKF), Unscented Kalman filter (WU, et al, 2017:143-148) (UKF) and other methods recursively estimate the minimum variance of the SOC, but they highly dependent on the model; the particle filter algorithm needs to use a large number of samples to effectively approximate the system after The probability density and computational complexity are too large. The neural network needs to collect a large amount of battery data as training samples. The degree of estimation is largely influenced by the training methods and training data, and the learning time is too long.

In this paper, SOC estimated by using the dynamic stress test (DST) and federal urban driving schedule (FUDS) measurement data. For the problems of accumulated error, nonlinearity of power battery, and low precision of measuring instruments, this paper proposes a simulation algorithm based on double fuzzy-variable structure filtering (Ahmed, et al, 2016:537-548) and adopts a variable structure filter (Sun, et al, 2016:717-726) for battery based on DST operating parameters. The model performs parameter identification (Dang, et al, 2015:356-366). The first fuzzy-variable structure filter filters the battery terminal voltage measurement values of the FUDS condition, reduces the error of the terminal voltage, and improves the SOC estimation accuracy; the second fuzzy-variable structure filter performs SOC estimation has obtained SOC estimation methods with fast convergence, high accuracy, low dependence on initial values, and applicability to low precision measurement instruments.

2. POWER BATTERY MODEL AND PARAMETER IDENTIFICATION

2.1. Thévenin model

The paper uses the Thévenin model (Wei, et al, 2016:291-293) with simple structure, clear physical meaning, and wide application. The model is composed of terminal voltage U, open-circuit voltage U_{oc} (OCV), polarisation response of RC structure, and ohmic resistance R_0 in series. RC structure It consists of a parallel connection of the polarisation resistance R_p of the battery and the polarisation capacitance C_p of the battery. i(t) represents the current flowing through the ohmic resistance R_0; $U_p(t)$ represents the voltage of the polarisation capacitance of the battery, and its model structure is shown in Figure 1.

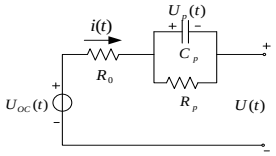

Figure 1:Thévenin model

The Thévenin model is as follows:

Equation 1: Thévenin model math

$$\begin{cases} \dfrac{dU_p(t)}{dt} = -\dfrac{U_p(t)}{R_pC_p} + \dfrac{i(t)}{C_p} \\ U(t) = U_{OC}(t) - R_0 i(t) - U_p(t) \end{cases}$$

Where:

U = terminal voltage(V)
U_{oc}=open-circuit voltage(V)
RC= Polarisation reaction structure
R_p = polarisation resistance(Ω)
C_p = polarisation capacitance(F)
$i(t)$ = Current(A)
$U_p(t)$=Polarisation capacitor voltage(V)

The model is discretised by the backward differential method. Considering the slow charging and discharging process of the power battery, the open circuit voltage Uoc slightly changes ie $U_{oc,k}$=$U_{oc,k-1}$. After arrangement it can be obtained:

Equation 2: Backward differential transformation method to discretise the model

$$U_k = aU_{k-1} + bI_k + cI_{k-1} + (1-a)U_{oc,k}$$

Where:
a=Differential model parameters
b=Differential model parameters
c=Differential model parameters

2.2. Parameter identification of Thévenin model

According to the nonlinearity of the power battery, the coefficient of the terminal voltage U and current I in Equation (2) are chosen as the state variable, that is X_K=[a_k, b_k, c_k, (1-a_k)$U_{oc,k}$]^T , The terminal voltage U_k in Equation (2) is chosen as the observation equation, that is $Z_k = U_k$, variable structure filtering is utilised to identify the parameters of the Thévenin model. The variable structure filtering mathematical model is as follows:

Equation 3: Variable Structure Filtering Mathematical Model

$$\begin{cases} x_k = Ax_{k-1} + BI_{k-1} + w_k \\ z_k = Cx_k + v_k \end{cases}$$

Equation 4:Equation of state

$$x_{k|k\text{-}1} = Ax_{k\text{-}1|k\text{-}1} + BI_{k\text{-}1} \;;\; \begin{bmatrix} \hat{z}_{k|k\text{-}1} \\ \hat{z}_{k|k} \end{bmatrix} = C \begin{bmatrix} x_{k|k\text{-}1} \\ x_{k|k} \end{bmatrix}$$

Equation 5:Priori estimate model

$$x_{k|k} = x_{k|k\text{-}1} + K_k$$

Equation 6:VSF gain equation

$$K_k = C^{-1}(\beta \mid e_{z_{k|k\text{-}1}} \mid + \gamma \mid e_{z_{k\text{-}1|k\text{-}1}} \mid) \circ sat(e_{z_{k|k-1}}, \psi)$$

Equation 7:Observation equation

$$\begin{bmatrix} e_{z_{k|k\text{-}1}} \\ e_{z_{k|k}} \end{bmatrix} = z_k - \begin{bmatrix} \hat{z}_{k|k\text{-}1} \\ \hat{z}_{k|k} \end{bmatrix}$$

Equation 8:Saturation function

$$sat(e_{z_{k|k-1}}, \psi) = [sat(e_{z_{1,k|k-1}}, \psi_1) \quad \dots \quad sat(e_{z_{n,k|k-1}}, \psi_n)]^T$$

Equation 9:Saturation function

$$sat(e_{z_{i,k|k-1}}, \psi_i) = \begin{cases} e_{z_{i,k|k-1}} / \psi_i & e_{z_{i,k|k-1}} \le \psi_i \\ sign(e_{z_{i,k|k-1}}) & e_{z_{i,k|k-1}} > \psi_i \end{cases}$$

Where:

A	=System matrix	n×n
B	=Input matrix	n×p
C	=Output matrix	m×n
C^{-1}	=Inverse matrix	n×m
X_k	=Differential model parameters	
$\hat{X}_{K\|K}$ $\hat{X}_{K\|K-1}$	= A posteriori and a priori state estimates	n×1
$\hat{Z}_{K\|K}$ $\hat{Z}_{K\|K-1}$	= posteriori and a priori output estimates	m×1
w_k	=System noise	n×1

v_k =Measurement noise m×1

K_k =VSF gain n×1

$e_{k|k}$ $e_{k|k-1}$ = Output estimation error calculated by using the a posteriori m×1

k =Calculation step index

Ψ=Boundary layer

sign =Scalar sign function

i =Subscripts used to identify elements of matrices and vectors

β,γ =Constant value 0-1

o =the Schur product

sat =Saturation function

From this identification, you can get the Thévenin model and the open-circuit voltage U_{oc} of the battery.

With reference to the open circuit voltage method, the open circuit voltage (OCV) and the SOC have a good consistency. The mathematical model relationship is as follows:

Equation 10: High Order Polynomial Approximate Fitting into OCV-SOC Function

$$\begin{aligned} U_{oc,k} &= g(SOC) \\ &= h_1 SOC_k^{\ 8} + h_2 SOC_k^{\ 7} + h_3 SOC_k^{\ 6} + h_4 SOC_k^{\ 5} + h_5 SOC_k^{\ 4} \\ &\quad + h_6 SOC_k^{\ 3} + h_7 SOC_k^{\ 2} + h_8 SOC_k^{\ 1} + h_9 \end{aligned}$$

In the Equation: h1~h9 is the coefficient of OCV-SOC high polynomial fitting, after approximation fitting: h_1 = 2.10 × 103, h_2 = -7.38 × 103, h_3 = 9.98 × 103, h_4 = -6.23 × 103, h_5 = 1.40 × 103, h_6 = 3.26 × 102, h_7 = -2.40 × 102, h_8 = 47.98, h_9 = 22.27.

Where:

$h_1 \sim h_9$ = the coefficient of OCV-SOC high polynomial fitting

3. TERMINAL VOLTAGE FITERING

In the experiment, the measured values of the current and the terminal voltage are based on the Arbin platform and the data is obtained by 0.1% high accuracy sensor sampling. Taking into account the low precision of the actual industrial sensor, and in order to effectively verify the effectiveness of the algorithm in practice In the simulation, the 1%, 2%, and 3% Gaussian noise is added to the current and terminal voltage values measured in the FUDS operating conditions in the simulation process to simulate the error characteristics of the sensor measurements in actual industry. The validity of the algorithm is verified in real industry.

3.1. Specifications

In the experiment simulation, for the voltage and current of the FUDS working condition 1%, 2% and 3% of three Gaussian noises are added to them respectively at the same time. The voltage $U_{p,k}$ of the polarisation capacitor C_p and SOC are selected as the state equation of the fuzzy-variable structure filter, ie x_k=[SOC_k $U_{p,k}$]^T. The terminal voltage U_k is an observation equation, that is $Z_K = U_K$, U_k can be represented by the relationship between the KVL of the physical model of the battery and the Equation (10).

The gain of the parameter in updated status $x_{k|k} = x_{k|k\text{-}1} + K_k$:

Equation 11: VSF gain

$$K_k = C^{-1}(\beta \mid e_{z_{k|k-1}} \mid + \gamma \mid e_{z_{k-1|k-1}} \mid) \circ sat(e_{z_{k|k-1}}, \psi) \quad (11)$$

$$K_k = C^{-1}(\beta \mid e_{z_{k|k-1}} \mid + \gamma \mid e_{z_{k-1|k-1}} \mid) \circ sat(e_{z_{k|k-1}}, \psi)$$

A large number of tests have found that β has a greater influence on the gain K value and it can be well controlled the article mainly adjust the value of the parameter β.

In order to suppress the buffeting of the system in the convergence phase and improve the estimation accuracy, fuzzy rules (Deng, et al, 2016: 472) are introduced. In this paper, for the problem that the variable structure filter is easy to produce vibration after convergence which causes larger errors in the estimation result. When variable structure filtering is used to perform SOC online estimation, fuzzy rules are used to adjust the variable structure filter parameter β to increase the gain of the parameter K. Taking into account a large range of β values, can

accelerate the convergence of learning, can eliminate the error of SOC in time, and through the test and simulation, a simple and effective value of β which can ensure SOC accuracy and convergence rate of SOC is selected, the fuzzy rules are as follows:

Equation 12: Fuzzy rules

$$\beta = \begin{cases} 1 & U_{e1} \geq 0.034U_N \\ 0.1 \cdot U_{e1} & 0.034U_N > U_{e1} > -0.034U_N \\ 1 & U_{e1} \leq -0.034U_N \end{cases}$$

Where:

U_{e1} =the error between the measurement of the terminal voltage and the estimated value

U_N = the rated voltage of the battery

3.2. Page size three Gaussian noise filters

Using the fuzzy-variable structure filter to filter the terminal voltage U on the MATLAB platform, the U filtered simulation results are shown in Figure 2:

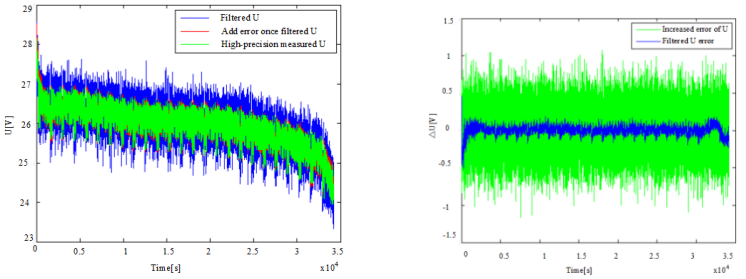

(a) Three types of U with 1% Gaussian filtering error (b) Error between U after filtering and high-precision measured U

Figure.2:simulation after adding 1% Gaussian noise

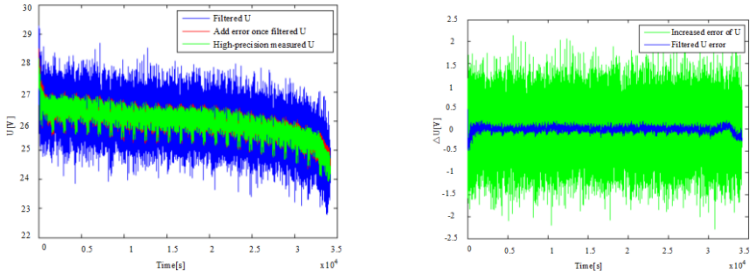

(a) Three U under 2% Gaussian Filtering Error (b) Error between U after filtering and high-precision measured U

Figure.3: simulation after adding 2% Gaussian noise

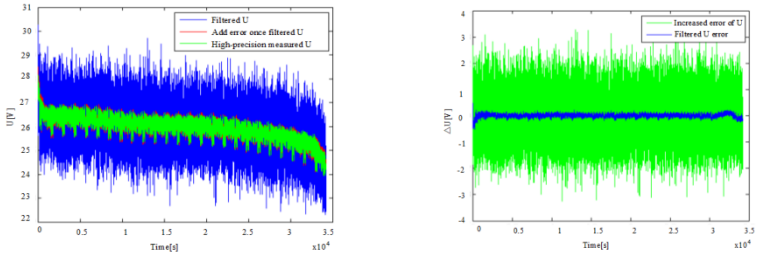

(a) Three U under 3% Gaussian filter error (b) Error between U after filtering and high-precision measured U

Figure.4: simulation after adding 3% Gaussian noise

Table 1: Comparison of U Errors Before and After Filtering three kinds of Gaussian Noise

Gaussian noise		Relative maximum error (V)	Relative mean (V)
1%	Before filtering	1.1658	0.2251
	After filtering	0.5038	0.0431
2%	Before filtering	2.2788	0.4519
	After filtering	0.4939	0.0455
3%	Before filtering	3.2658	0.6719
	After filtering	0.5301	0.0474

Through the comparison between Figure 2, Figure 3, Figure 4 and Table 1, it is proved that the U-filtered errors of three kinds of Gaussian noise interference are obviously reduced; the feasibility of improving SOC estimation accuracy is increased; and the fuzzy-variable structure filtering is verified. The effectiveness of the voltage filtering at the opposite terminal.

4. SOC ESTIMATION SIMULATION

In the SOC estimation, the fuzzy-variable structure filter is used for the second time. The β value is slightly different from the first time. The fuzzy rules are as follows:

Equation 13: Secondary fuzzy rules

$$\beta = \begin{cases} 1 & U_{error} \geq 0.034U_N \\ 0.05 \cdot U_{error} & 0.034U_N > U_{error} > -0.034U_N \\ 1 & U_{error} \leq -0.034U_N \end{cases}$$

Where:

U_{e2} =the error between the measurement of the terminal voltage and the estimated value

4.1. SOC estimation before and after terminal voltage filtering

Referring to the OCV-SOC relationship fitting method of Equation (10), the open circuit voltage value is the independent variable and the SOC value is the dependent variable. The mathematical relationship of fitting SOC-OCV is $SOC_k=f(U_{oc,k})$.

Under FUDS conditions, $U_{oc,1}$ is calculated by Equation (2). Substituting the formula $SOC_k=f(U_{oc,k})$, SOC1=0.985, which is the initial value of SOC, is calculated.

Add 1% Gaussian noise to the current and terminal voltage measurement values, and use the fuzzy-variable structure filtering algorithm to simulate. The SOC estimation value simulation diagram before and after the terminal voltage filtering is as follows:

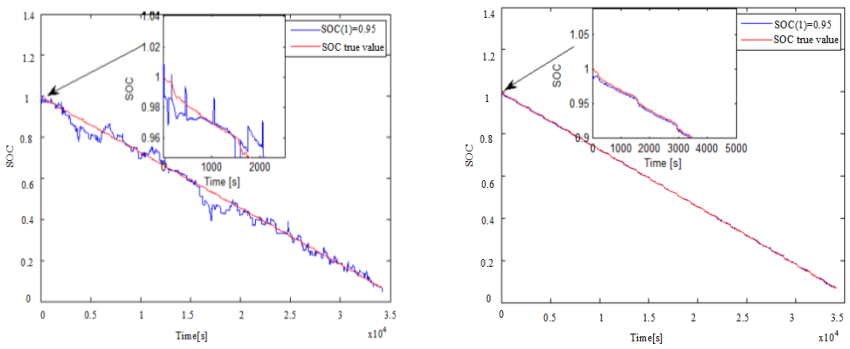

(a) Unfiltered SOC estimation of terminal voltage (b) Filtered SOC estimation of terminal voltage

Figure.5: simulation after adding 1% Gaussian noise

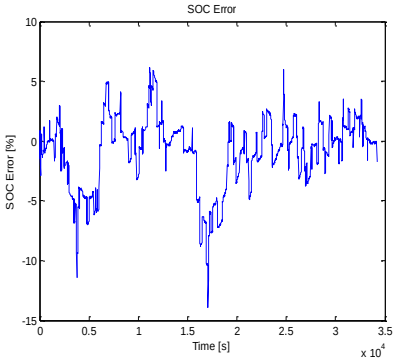

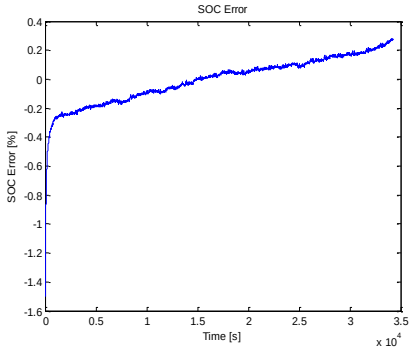

(c) Unfiltered SOC estimation error of the terminal voltage (d) Filtered SOC estimation error at the terminal voltage

Figure.5: simulation after adding 1% Gaussian noise (continued)

Adding 2% Gaussian noise to the current and terminal voltage measurements. The SOC estimation before and after the terminal voltage filtering is simulated as follows:

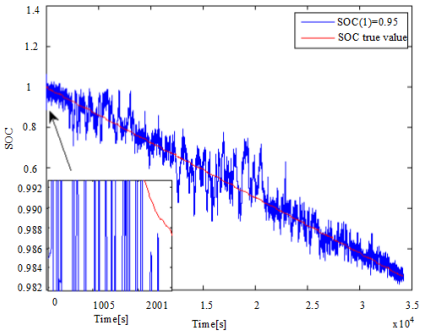

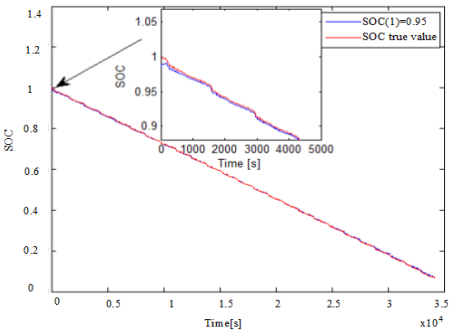

(a) Unfiltered SOC estimation of terminal voltage (b) Filtered SOC estimation of terminal voltage

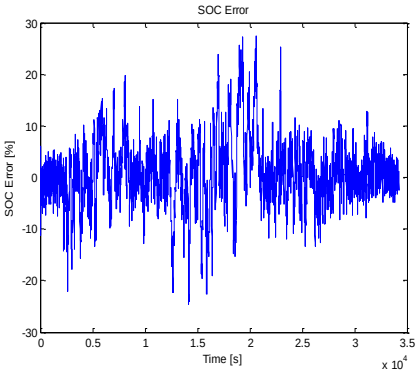

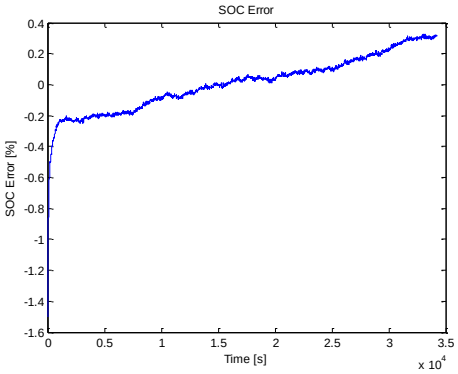

(c) Unfiltered SOC estimation error of the terminal voltage (d) Filtered SOC estimation error at the terminal voltage

Figure.6: simulation after adding 2% Gaussian noise

Add 3% Gaussian noise to the current and terminal voltage measurements. The SOC estimation simulation before and after the terminal voltage filtering is as follows:

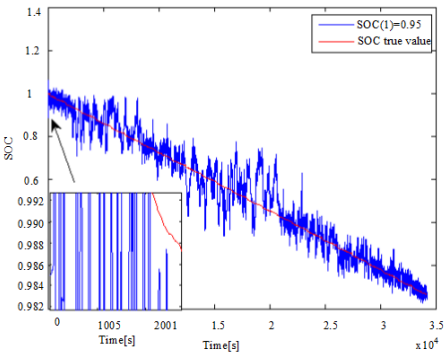

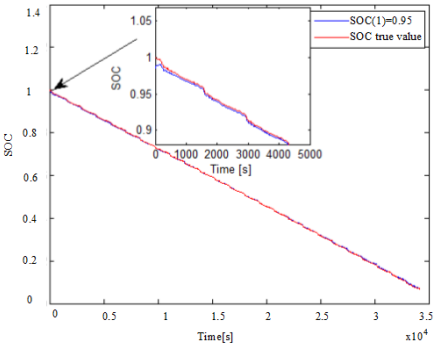

(a) Unfiltered SOC estimation of terminal voltage (b) Filtered SOC estimation of terminal voltage

Figure.7: simulation after adding 3% Gaussian noise

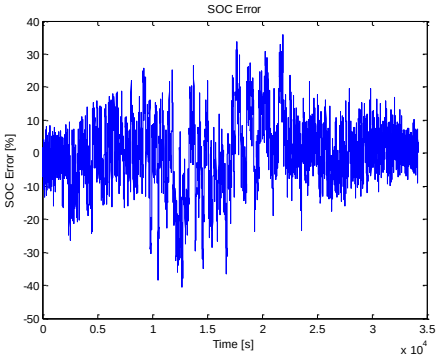

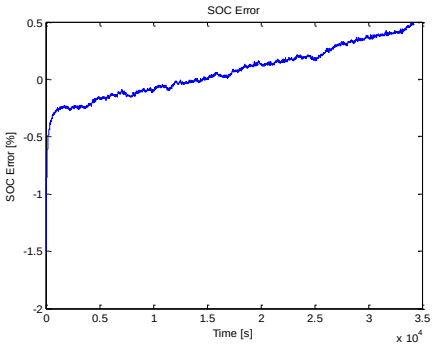

(c) Unfiltered SOC estimation error of the terminal voltage (d) Filtered SOC estimation error at the terminal voltage

Figure.7: simulation after adding 3% Gaussian noise (continued)

Table 2: Comparison of SOC Errors before and after Terminal Voltage Filtering under Three Kinds of Gaussian Noise Conditions

Gaussian noise		Relative maximum error (%)	Relative mean (%)
1%	Before filtering	13.8872	2.2002
	After filtering	1.5	0.1317
2%	Before filtering	27.3125	4.8100
	After filtering	1.5	0.1441
3%	Before filtering	40.4073	7.3666
	After filtering	1.5	0.1919

According to the comparison of the SOC in the conditions of Figure 5, Figure 6, Figure 7 and Table 2, it is proved that the SOC estimation accuracy obtained after U-filtering is significantly improved; and the voltage and current of the Double fuzzy-variable structure filter are verified. The noise caused by the accuracy of the sensor in the acquisition process has good stability, confirming the feasibility of the algorithm in practice.

4.2. The Influence of SOC initial value on double fuzzy variable structure filtering

The initial value of SOC is a value that cannot be directly measured. However, many algorithms have a certain dependence on the initial value during the estimation process. The selection of the initial value directly affects the convergence rate and accuracy of the estimated value, and is subject to the double fuzzy-variable structure. For the study of the influence of initial value of SOC, this paper uniformly selects the initial value of SOC (initial estimated SOC) and 0.5 and 0 test points for comparison.

(1) After simulation data is increased by 1% Gaussian noise, the simulation results of the three initial SOC values are as follows:

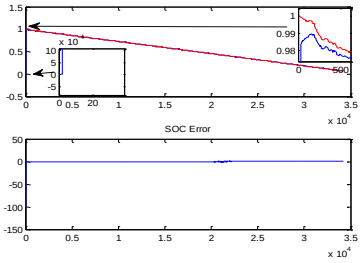

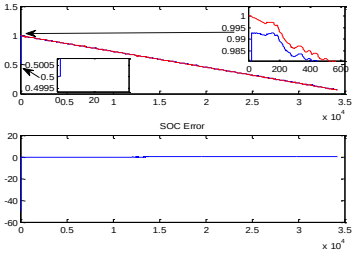

(a) When the initial value of SOC is 0 (b) When the initial value of SOC is 0.5

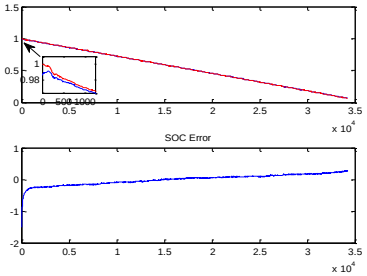

(c) When the initial value of SOC is 0.985

Figure.8: SOC estimation simulation and error

(3) After 2% Gaussian noise is added to the simulation data, the simulation results of the three initial SOC values are as follows:

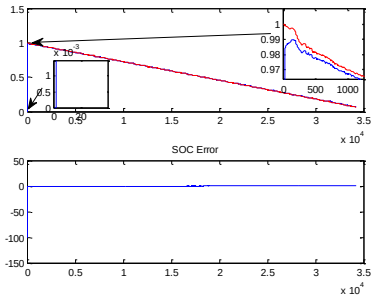

(a) When the initial value of SOC is 0

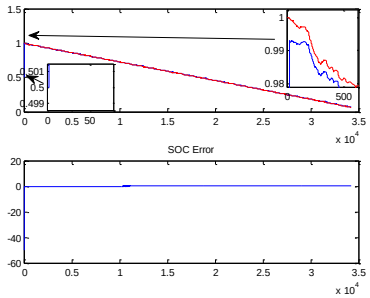

(b) When the initial value of SOC is 0.5

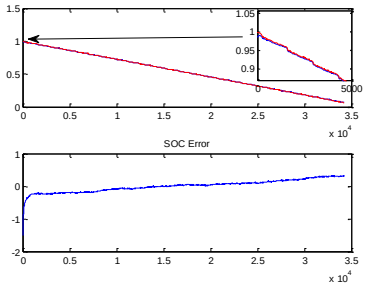

(c) When the initial value of SOC is 0.985

Figure.9: SOC estimation simulation and error

(3) After the simulation data is increased by 3% Gaussian noise, the simulation results of the three initial SOC values are as follows:

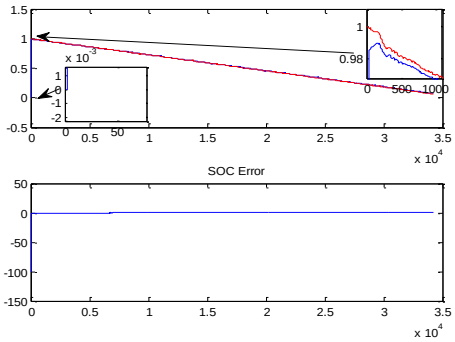

(a) When the initial value of SOC is 0

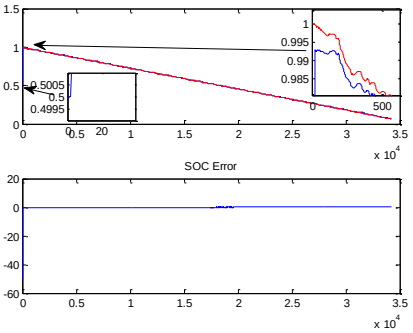

(b) When the initial value of SOC is 0.5

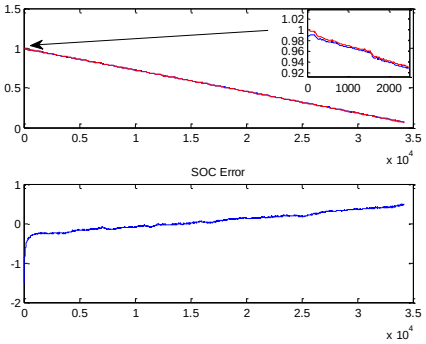

(c) When the initial value of SOC is 0.985

Figure 10 SOC estimation simulation and error

Table 3: error comparisons of three SOC initial values estimation

Gaussian noise	*Initial SOC*	*Relative maximum error (%)*	*Relative mean (%)*
	0	*100*	*0.1688*
1%	*0.5*	*50*	*0.1451*
	0.985	*1.5*	*0.1317*
	0	*100*	*0.1999*
2%	*0.5*	*50*	*0.1612*
	0.985	*1.5*	*0.1441*
	0	*100*	*0.2118*
3%	*0.5*	*50*	*0.1466*
	0.985	*1.5*	*0.1919*

By comparison between Figure 8, Figure 9, Figure 10 and Table 3, we can conclude that in the case of three kinds of Gaussian noise, the SOC estimation based on the double fuzzy-variable structure filter has a small dependence on its initial value, so under the double fuzzy-variable structure filtering algorithm, the initial value of SOC has little influence on the estimation accuracy of SOC. When the initial error is large, it can converge near the true value in a short time.

5. CONCLUSION

Variable structure filtering is based on the characteristics of the sliding mode. It can quickly converge to be close to the true value, approaching the true value and shuttling back and forth around it. However, it will generate large fluctuations and increase the error of the SOC estimation value. Therefore, the fuzzy phase is introduced in the filtering stage. Rule adjustment variable structure filter parameter β can effectively suppress the chattering phenomenon in the convergence phase. By adding Gaussian white noise during the simulation process and selecting three different SOC initial values, the effectiveness of the double fuzzy-variable structure filtering algorithm in practical operation is verified. The simulation results show that the algorithm has good convergence, fast convergence and the estimation accuracy is improved.

6. REFERENCES

Pang C.Research on Battery Management System for Electric Vehicles [J]. Power Technology, (12).

Fan X, Zeng Q, Zhang X. 2015.SOC Estimation and Simulation of Electric Vehicle Battery Based on Improved Ahta Integration Method [J]. Electrical Applications, (8):111-115.

Zheng F, Xing Y, Jiang J, et al. 2016. Influence of different open circuit voltage tests on state of charge online estimation for lithium-ion batteries[J]. Applied Energy, 183:513-525.

Pan W, Liu X. 2014.Research on SOC Estimation of Lithium Battery Based on Improved Kalman Filter[J]. Computer Simulation, 31(3): 148-150.

Ye M, Guo H, Xiong R, et al. 2018.A double-scale and adaptive particle filter-based online parameter and state of charge estimation method for lithium-ion batteries[J]. Energy, 144:789-799.

Jokar A, Rajabloo B, Desilets M, et al. 2017.An On-line Electrochemical Parameter Estimation Study of Lithium-Ion Batteries Using Neural Networks[J]. Ecs Transactions, 75(20):73-87.

Hua J, Shao R, Zhu Y, et al. 2017.Lithium battery SOC estimation based on adaptive Kalman filter algorithm [J]. Science Bulletin, (5):77-80

Wu Y, Zhou Y, Li Q. 2017. Simulation Research on Accurate Estimation of SOC of Three-element Lithium Battery[J]. Computer Simulation, (12):143-148.

Ahmed R, Sayed M E, Gadsden S A, et al. 2016.Artificial neural network training utilizing the smooth variable structure filter estimation strategy[J]. Neural Computing & Applications, 27(3):537-548.

Sun Y, Ma Z, Tang G, et al. 2016. Estimation method of state-of-charge for lithium-ion battery used in hybrid electric vehicles based on variable structure extended Kalman filter[J]. Chinese Journal of Mechanical Engineering, 29(4):717-726.

Dang X, Li Y, Kai X, et al. 2015. Open-Circuit Voltage-Based State of Charge Estimation of Lithium-ion Battery Using Dual Neural Network Fusion Battery Model[J]. Electrochimica Acta, 188:356-366.

Wei Z, Dong B, Liu X, et al. 2016. The Thevenin Model of Lithium Battery Dynamic System[J]. Power Technology, 40(2): 291-293.

Deng Z, Yang L, Cai Y, et al. 2016,.Online Identification with Reliability Criterion and State of Charge Estimation Based on a Fuzzy Adaptive Extended Kalman Filter for Lithium-Ion Batteries[J]. Energies, 9(6):472.

167: HESS power distribution control strategy for DC microgrid based on droop method

Honglin BIAN[1], Changhong SHI[2], Tiezhou WU[3]

[1] *Wuhan Boyu Photoelectric system limited liability company, 1297362526@qq.com*
[2] *Hubei Key Laboratory for High-efficiency Utilisation of Solar Energy and Operation Control of Energy Storage System, Hubei University of Technology, 1312850168@qq.com*
[3] *Hubei Key Laboratory for High-efficiency Utilisation of Solar Energy and Operation Control of Energy Storage System, Hubei University of Technology, 1683248539@qq.com*

Hybrid energy storage system can compensate for the fluctuation of bus power which is caused by the change of output power of power generating unit and load in DC microgrid. In the existing hybrid energy storage coordinated control strategy, using traditional voltage droop method to control the battery to suppress non-high frequency components of bus power fluctuation, and the integral droop method is used to control the super capacitor to suppress the high-frequency fluctuation component of the power fluctuation. The effect of this strategy is similar to that of a filter, which automatically divides the ripple power into high-frequency and non-high-frequency ripple components. However, when the voltage droop method is applied, the difference of the battery SOC in the parallel hybrid energy storage unit is not taken into consideration, and the non-high frequency fluctuation component borne by the battery is not redistributed, which is not conducive to avoiding overcharge and over-discharge of the battery. It is considered that the voltage sag coefficient will be affected by SOC, the voltage droop coefficient is divided by the nth power of the SOC to obtain a new voltage droop coefficient, thereby obtaining an improved voltage droop method in which the voltage droop coefficient is related to the SOC, and then it is combined with the integral droop method to get a new coordination control strategy. Simulation and experimental results show that the proposed control strategy can re-distribute the non-high frequency power according to the SOC of the battery while suppressing the bus power fluctuations, so as to achieve SOC equalisation of the batteries in different energy storage units, the bus voltage fluctuation is small during the entire process.

Keywords: Voltage sagging method; integral sagging method; droop coefficient; SOC; Redistribute

1. INTRODUCTION

In order to realise the energy structure transformation and respond to the sustainable development strategy of energy, distributed generation represented by wind energy and solar energy has quickly become the focus of experts and scholars. Distributed generation is random and intermittent, and its stability is too poor to directly access the large grid. In order to solve the problem of integration of distributed power and large grids, the concept of microgrid came into being. The microgrid is divided into AC microgrid and DC microgrid. Although the former currently occupies a major position, the DC microgrid structure is more simple and does not need to consider factors such as frequency, reactive power, and phase, which is more advantageous than AC microgrid. Therefore, DC microgrids have received people's attention in recent years.

The bus voltage directly reflects whether the power between the DC microgrid power supply and the load is balanced and whether the system can operate stably. Because of the randomness of the output power variation of the distributed power generation unit and the uncertainty of the load change, the hybrid energy storage system plays a crucial role in the regulation of the DC microgrid bus voltage. The battery and the super capacitor have a strong complementarity in their inherent characteristics, and use them to form a hybrid energy storage system, making full use of the advantages of both. Therefore, the study of the power distribution strategy of hybrid energy storage system is the key to ensure the stable operation of DC micro-electricity.

Mi et al (2017) use multiple small-capacity energy storage units to balance bus voltage fluctuations. In order to avoid overcharge and over-discharge of energy storage units, an adaptive droop control strategy is designed to allocate power according to the SOC and maximum power of each energy storage unit. Yang et al (2016) use the first derivative of the voltage instead of the voltage, reduces the influence between the voltage and the current, improves the accuracy of the current distribution, but does not consider the SOC and cannot perform power distribution based on the capacity of the energy storage unit. Zhang, Wang & Wang (2018) divide the operating mode according to the bus voltage information and uses droop control for the photovoltaic array or the battery module of the electric vehicle to achieve power distribution. Li et al (2017) improve the SOC exponent of the voltage droop method during charge and discharge of the energy storage unit and improved the resolution of the SOC. Through this droop control method, the system bus voltage was stabilised, and the system quickly converged to the SOC equilibrium state. Lin et al (2017) propose a novel integral sag method. The integral sag method is used to control the super-capacitor to quickly compensate the high-frequency fluctuation components of the power fluctuation. The traditional voltage sags method is used to control the battery to stabilise the non-high-frequency fluctuation components of the power fluctuation. Through the coordinated control of the two drooping methods achieves the power distribution of the fluctuating power between the energy storage units.

In order to solve the overcharge and over-discharge of the battery in the energy storage unit, it is necessary to redistribute the non-high frequency fluctuation component that the battery bears. Based on the traditional voltage droop method, this paper improves the voltage droop coefficient, and then combines the improved voltage droop method with the integral droop method to obtain a coordinated control strategy. Simulation and experimental results show that the proposed control strategy can suppress the bus voltage fluctuations, and can achieve the battery SOC equilibrium in the energy storage unit.

2. DC MICROGRID HYBRID ENERGY STORAGE SYSTEM

Figure 1 is a schematic diagram of a DC microgrid with a typical hybrid energy storage system. The grid-connected operation mode is not discussed in this paper. Here, only the hybrid storage power allocation strategy when the microgrid is operating in islanding mode is studied.

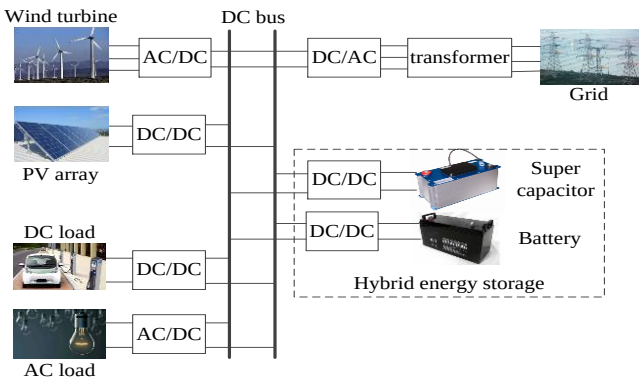

Figure 1: Structure diagram of DC micro grid with hybrid energy storage

There are many kinds of connection modes between the storage battery and the super capacitor in the hybrid energy storage system, and often used are direct parallel connection, single DC/DC parallel connection, and dual DC/DC parallel connection. The disadvantage of direct parallel connection is obviously that the voltage output from the super capacitor and the battery is always the same, resulting in inflexible control of it. There are two situations in which a single DC/DC is connected in parallel. The first is that the battery is first connected to the DC/DC converter and then in parallel with the super capacitor. This method can guarantee the service life of the battery and reduce the requirements on the battery. However, if a single supercapacitor is directly connected to the busbar, its voltage is difficult to reach the DC bus voltage level. When multiple supercapacitors are connected in parallel, there is no doubt that the cost will be increased. The second is that the super capacitor is connected to the DC/DC converter and then connected in parallel with the battery. This method greatly reduces the voltage requirement for the super capacitor, but the battery capacity cannot be fully utilised in this case. The dual DC/DC parallel connection not only can adjust the output power of the energy storage element, but also can control the charging and discharging processes of the super capacitor and the battery separately. In addition, The effect of bus voltage on the voltage of the two types of energy storage elements will also be reduced to a very small degree, more flexible control. In summary, this article decided to use dual DC / DC connection.

In order to more easily and directly study the power interaction between the DC bus and the distributed power generation unit, the hybrid energy storage device and the load, and taking into account that the DC microgrid is in the island operation mode, The structure of the DC microgrid hybrid energy storage system shown in Figure 1 can be simplified to the structural model shown in Figure 2. Regardless of the specific working conditions within each module, only the power interaction between these modules and the DC bus is considered, and each part can be equivalent to a module whose power can be changed, thereby simplifying our research and analysis process. In Figure 2, P_S is the output power of the distributed power generation unit, P_L is the power consumed by the AC-DC load, and P_{ES} indicates the power released or absorbed by the hybrid energy storage system.

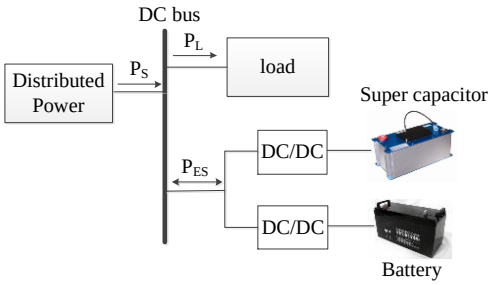

Figure 2: DC micro grid hybrid energy storage system simplified structure diagram

The power difference between the distributed power supply and the AC/DC load is provided by the hybrid energy storage system, so as to stabilise the DC bus voltage and realise the power balance of the DC micro-grid. Then the DC bus power balance needs to meet the following conditions:

Equation 1: DC bus power balance condition.

$$P_S - P_L = P_{ES}$$

Where:

P_S= the output power of the distributed power generation unit (W)
P_L= the power consumed by the AC-DC load (W)
P_{ES}= the power released or absorbed by the hybrid energy storage system (W)

3. THE PRINCIPLE OF DROOP METHOD

Centralised control, master-slave control and other power allocation control strategies based on high-speed communications enable rapid power allocation and ensure that all operating parameters of the microgrid are at rated values. However, such control strategies rely too much on communications facilities. When the communications link experiences serious failures and delays, the control system is prone to failure. Droop control method is one of the most commonly used methods in microgrid power control strategies that do not require interconnected communications. Compared to other control strategies that require communications, there is no problem of communication device failure and system crash. And the droop control method has a simple structure and can also reduce the current between the DC/DC converters. The traditional voltage droop method is shown in Equation 2.

Equation 2: The traditional voltage droop method.

$$u_{ref} = u_n - i_o \cdot R$$

Where:

u_{ref}=the reference output voltage(V)
u_n=the rated voltage of the converter(V)
i_o=the output current of the converter(A)
R=the equivalent output impedance of the converter and also represents the droop coefficient(Ω)

When a sudden power change occurs on the DC bus, the super capacitor can respond quickly, so it can suppress the sharp rise or fall of the DC bus voltage. Figure 3(a) shows the charging circuit diagram for the series connection of capacitors, resistors, and a DC voltage source. Figure 4(b) shows the discharge circuit diagram for a capacitor and resistor connected in series. Figures 3(a) and 3(b) are equivalent to the RC circuit full-response and zero-input response circuit in circuit theory knowledge, where U_S and u_C represent the DC supply voltage and capacitor voltage, respectively.

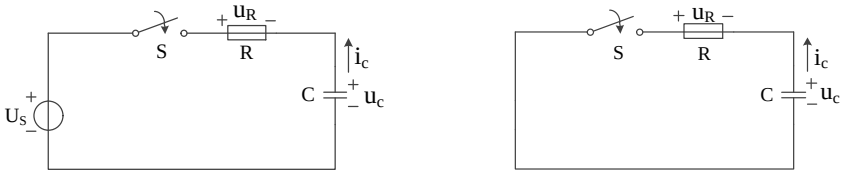

(a) Charging (full response) *(b) Discharging (zero input response)*
Figure 3: Capacitor charging / discharging circuit diagram

In the charging circuit shown in Figure 3(a), the switch S is closed and $u_R+u_C=U_S$ can be obtained according to Kirchhoff's voltage law (KVL). and then the initial condition and the relation of each element are brought into KVL, and the equation shown in the equation can be obtained:

Equation 3: KVL of charging circuit.

$$RC\frac{du_C}{dt}+u_C=U_S$$

Where:

R= Circuit resistance(Ω)
C= Circuit capacitance(F)
u_C=the capacitor voltage(V)
U_S= the DC supply voltage(V)

By solving the differential Equation (3), the capacitor voltage and current expressions as shown in Equation 4 and 5 can be obtained. Where U_O is the initial voltage of the capacitor and U_O is less than the DC supply voltage U_S, so that the capacitor can be charged after the switch S is closed and its voltage will increase to U_S at the end of the charge.

Equation 4: The capacitance voltage of the charging circuit.

$$u_C=U_S+(U_0-U_S)e^{-t/RC}$$

Equation 5: The capacitance current of the charging circuit.

$$i_C=\frac{U_0-U_S}{R}e^{-t/RC}$$

Where:

u_C=the capacitor voltage(V)
U_S= the DC supply voltage(V)
U_O=the initial voltage of the capacitor(V)
i_C= Charging circuit current(V)
t= time(S)

For the discharge circuit shown in Figure 3(b), the solution of the capacitor voltage and current expressions is shown in Equation 6 and 7:

Equation 6: The capacitance voltage of the discharge circuit.

$$u_C=U_0e^{-t/RC}$$

Equation 7: The capacitance current of the discharge circuit.

$$i_C=\frac{U_0}{R}e^{-t/RC}$$

Where:

u_C=the capacitor voltage(V)
U_O=the initial voltage of the capacitor(V)
t= time(S)
i_C= Charging circuit current(V)
R= Circuit resistance(Ω)
C= Circuit capacitance(F)

Combining the voltage and current expressions of the capacitor charging circuit and the discharging circuit, the relationship between the voltage and the current of the capacitor can be expressed by Equation 8.

Equation 8: The relationship between the voltage and current of the capacitor.

$$u_C = U_0 - m\int i_C dt$$

Where:

u_C=the capacitor voltage(V)
U_O=the initial voltage of the capacitor(V)
m=1/c is a constant describing the charge/discharge speed of the capacitor.
i_C= Charging circuit current(A)

4. HYBRID ENERGY STORAGE POWER DISTRIBUTION CONTROL STRATEGY

4.1. The derivation of equivalent formula of voltage sag based on SOC

Since the SOC of the battery is different in the parallel hybrid energy storage unit, the output capability will be different when responding to non-high frequency fluctuation components. In order to redistribute non-high frequency fluctuation components, it is necessary to determine the output size according to the battery SOC. A battery with a large SOC absorbs less power and releases more power. A battery with a smaller SOC absorbs more power and releases less power. This helps avoid overcharging and over-discharging of the battery.

According to the battery calculation model, the calculation formula for the state of charge of the battery can be obtained as shown in Equation 9.

Equation 9: the calculation formula for the state of charge of the battery.

$$SOC = SOC_0 - \frac{1}{C_N}\int_0^t \eta I d\tau$$

Where:

SOC= the state of charge of the battery
SOC_0= the initial state of charge of the battery
C_N= the battery rated capacity (A·H)
t= Charge and discharge time(S)
η= Coulomb's efficiency coefficient
I= the Battery current(A)

Ignoring the power loss of the converter and expecting the output voltage of each battery group to be equal, the input and output power of the converter can be approximately equal to the product of the input voltage and the output current of the converter. According to the above, the SOC calculation formula of Equation 10 can be obtained.

Equation 10:

$$SOC = SOC_0 - \frac{1}{C_N U_i}\int_0^t \eta P_o d\tau$$

Where:

SOC=the state of charge of the battery
SOC_0= the initial state of charge of the battery
C_N= the battery capacity(A·H)
U_i= the input voltage of the converter(V)
P_o= the output power of the converter(W)

The product of the equivalent output resistance R of the converter and the output current i_o in Equation 2 is replaced with the output power P_o to obtain the voltage droop method formula as in Equation 11. Then considering the relationship between droop coefficient and SOC, it can be changed to the voltage droop formula as shown in Equation 12. n takes a positive integer, and the SOC equalisation speed changes when the values are different.

Equation11:

$$u_{ref} = u_n - a_0 P_o$$

Equation12: $$u_{ref}^{'} = u_n - a_0 / SOC^n \cdot P_o = u_n - aP_o$$

Where:

u_{ref}=the reference output voltage(V)
u_n=the rated voltage of the converter(V)
a_0=the initial droop coefficient
P_o=the output power(W)
u_{ref}'= the reference output voltage calculated after considering SOC(V)
SOC^n= the n index of SOC
a=the new droop coefficient

4.2. Hybrid energy storage coordination control strategy

At present, there are many kinds of mixed energy storage power distribution methods, and power distribution methods based on power fluctuation characteristics are most suitable for energy storage element characteristics of hybrid energy storage systems. Among them, the power distribution method based on high-low-pass filtering is the most studied by experts and scholars.

From the derivation process of the integral sagging method, it can be seen that this method is suitable for controlling super capacitors, and the voltage sagging method is suitable for the control method of the battery. Because the voltage sagging method and the integral sagging method require coordinated control to suppress bus power fluctuations, Equations 8 and 12 are rewritten as shown in Equations 13 and 14.

Equation 13: $$u_1 = u_{n1} - aP_D$$

Equation 14: $$u_2 = u_{n2} - b\int P_G$$

Where:

u_1=the reference output voltage(V)
u_2=the reference output voltage(V)
$a=\Delta U_{max}/P_D$ is the voltage droop coefficient
b=the integral droop coefficient
P_D=the non-high frequency component of the fluctuation power
P_G=the high frequency component of the fluctuation power

The power absorbed or released by the hybrid energy storage system is equal to the high-frequency ripple power plus the non-high-frequency ripple power. Laplacian transformations are performed on Equations 13 and 14 and transform it from time domain to complex frequency domain for analysis. You can get expressions like Equations 15 and 16.

Equation15: $$P_G = \frac{s}{s + b/a} P_{ES}$$

Equation 16: $$P_D = P_{ES} - P_G = \frac{b/a}{s + b/a} P_{ES}$$

Where:

P_D=the non-high frequency component of the fluctuation power
P_G=the high frequency component of the fluctuation power
P_{ES}= the power released or absorbed by the hybrid energy storage system(W)

Equations 15 and 16 show that the coordinated control strategy of the voltage sagging method and the integral sagging method can automatically split the ripple power into high-frequency ripple power and non-high-frequency ripple power without using a high-pass/low-pass filter. Then, Laplacian inverse transformation is performed on the above equation to obtain the respective output of the super capacitor and the battery when the DC bus generates power fluctuations.

Equation 17: $$P_G = P_{SC} = P_{ES} e^{-\frac{b}{a}t}$$

Equation 18:

$$P_D = P_{Bat} = P_{ES} - P_G = P_{ES} - P_{ES} e^{-\frac{b}{a}t}$$

Where:

P_{SC}=the power released or absorbed by the supercapacitor (W)

P_{Bat}=the power released or absorbed by the battery (W)

The high-frequency fluctuation component is suppressed by using a super capacitor, and the non-high-frequency fluctuation component is sent to the battery for suppression. The DC/DC converter control block diagram using the voltage sagging method and the integral sagging method is shown in Figure 4. The non-high-frequency ripple power (high-frequency ripple power) is brought into Equations (13a) and (13b) to obtain the reference voltage, The reference voltage is compared with the actual output voltage of the battery (super capacitor) and then through the voltage loop to get the reference current. Then the reference current is compared with the output current of the battery (super capacitor) and the duty cycle of the converter is calculated after the current loop, so that the PWM wave of the switching tube of the DC/DC converter is obtained.

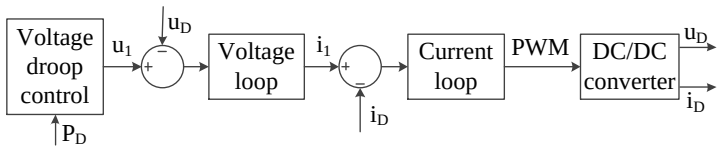

(a)Voltage droop method

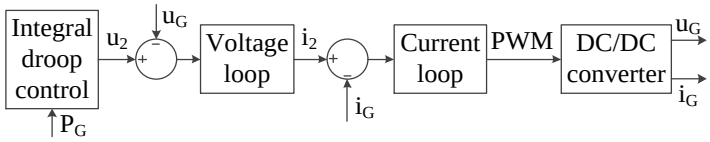

(b)Integral droop method

Figure 4: Converter control block diagram based on droop method

5. SIMULATION ANALYSIS AND EXPERIMENTAL VERIFICATION

5.1. Simulation analysis

This paper validates the correctness of the proposed power distribution control strategy by building a simulation model in MATLAB/SIMULINK. Two sets of distributed power generation units are used for simulation. The maximum output power of the first and second groups is 2000W and 5000W. Two sets of batteries with a rated capacity of 4A•h were used, the SOCs of the first and second groups were 60% and 40% respectively. Two sets of super capacitors with a rated capacity of 25F and two sets of loads of 4000W.

After the simulation began for a period of time, the system was operating in a stable state. The maximum output power of the distributed power supply was changed from 2000W to 5000W, and the load was 4000W. Figure 5 is a simulation result of a DC microgrid when the power of a distributed power generation unit changes.

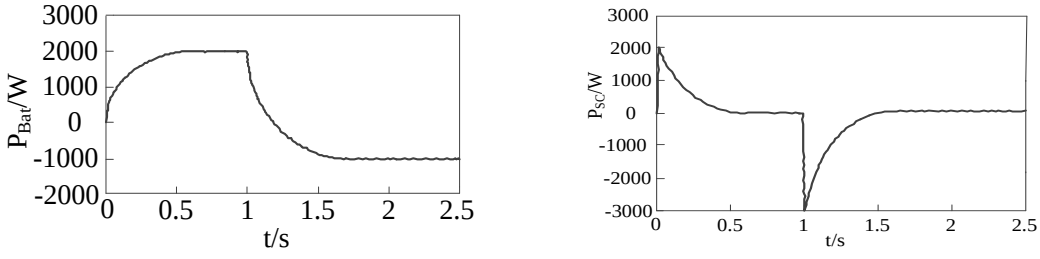

(a) Output power of battery *(b) Output Power of Supercapacitors*

Figure 5: Simulation result diagram of DC microgrid

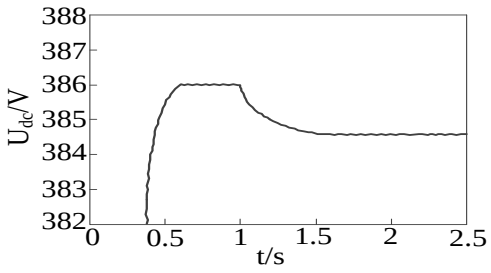

(c) DC bus voltage fluctuation

Figure 5: Simulation result diagram of DC microgrid (continued)

From Figure 5(a) and Figure 5(b), it can be seen that the battery does not have time to act when the simulation is started, and the output power of the supercapacitor mutates from 0 to 2000W to supplement the power shortage. Then the output power of the battery slowly increases to 2000W, and the output power of the super capacitor gradually decreases from 2000W to 0. At about 0.6S, the output power of the energy storage element is fixed, and the DC microgrid is operating in stable state. In 1S, the output power of the distributed power generation unit was changed from 2000W to 5000W, and the battery was still in a state of releasing power because of slow motion. Therefore, the supercapacitor needs to absorb 3000W of power and then decay to 0 in exponential form, and the battery is slowly converted from the original release power to absorbed power and finally tending to be stable.

It can be seen from Figure 5(c) that the bus voltage increases exponentially to 386V, and the voltage remains unchanged when the power balance is reached. Then at 1S, the output power of the distributed generator unit changes, and the bus voltage is quickly adjusted to approximately 384.7V and then remains unchanged. The DC bus voltage fluctuates little during the entire process and responds quickly.

5.2. Experimental verification

A microgrid model was set up in the laboratory for verification. The switching frequency of the DC/DC converter is 10 kHz, the load is a resistive load, the other parameters are the same as those of the simulation model. The experimental results are shown in Figure 6 and Figure 7.

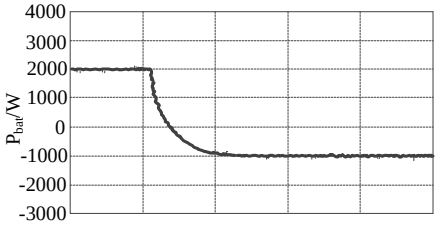

(a) The output power of the battery

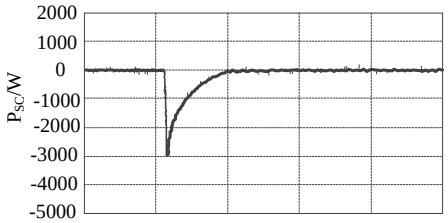

(*b) The output power of the supercapacitor*

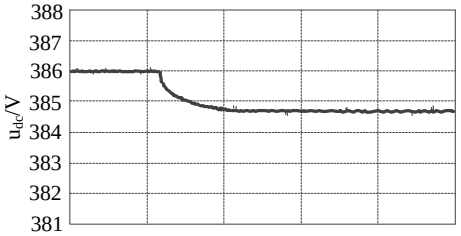

(c) Voltage fluctuation of DC bus

Figure 6: Experimental results of DC microgrid

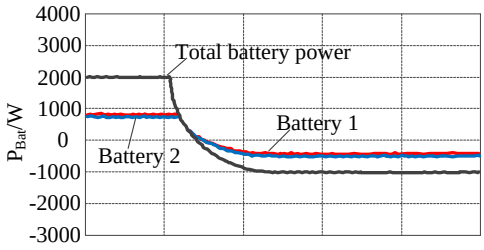

(a) Using the original hybrid energy storage control strategy

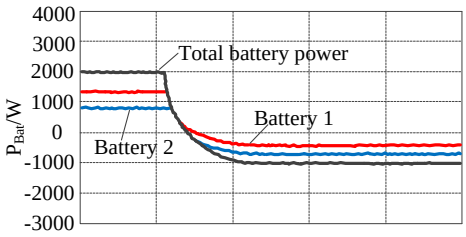

(b) Using the hybrid energy storage control strategy proposed in this paper

Figure 7: Battery power distribution when distributed generation power fluctuation

Figure 6(a) and Figure 6(b) are the output power changes of the battery and the super capacitor. It can be seen from the figure that the change of the battery is relatively slow, while the super capacitor responds quickly to power fluctuations. Figure 6(c) shows that the bus voltage can quickly return to stable after power fluctuations occur, and the voltage fluctuation is small.

Figure 7(a) shows the battery power distribution obtained by using the original hybrid energy storage control strategy. It can be clearly seen that different battery groups always bear the same non-high-frequency fluctuation components, which is detrimental to the battery SOC balance. Figure 7(b) shows the battery power allocation when using the hybrid energy storage control strategy proposed in this paper. It can be seen that the first group of batteries with large SOC discharges more power when discharged, and absorbs less power when charging. The second group has a small SOC. The discharge power is less when discharged, and more power is absorbed when charging.

6. CONCLUSION

The existing hybrid energy storage control strategy can automatically decompose the fluctuating power into high-frequency and non-high-frequency power, the battery bears the steadiness task of the non-high-frequency partial fluctuating power, and the super capacitor is responsible for suppressing the high-frequency part of the fluctuating power. However, this strategy does not take into account the overcharge and over-discharge of the battery. In this paper, in order to solve this problem, based on the original voltage droop method formula, the voltage droop coefficient is divided by the nth power of SOC to obtain a new voltage droop coefficient. This can redistribute non-high frequency ripple power based on battery SOC size, the SOC with large battery has less output when charging, and has more output when discharging. A battery with a small SOC has less output when it is charged, and has more output when discharged. By building a simulation model in MATLAB/SIMULINK and setting up a microgrid model in the laboratory, the simulation and experimental results show that the proposed control strategy can suppress the bus power fluctuations while also achieving the battery SOC balance in the energy storage unit, avoiding overcharge and over-discharge of the battery.

7. REFERENCES

Mi Y, Wu Y, Zhu Y, et al. Coordinated control of independent DC microgrids with automatic distribution of load power[J]. Power System Technology, 2017, 41(2): 440-447.

Yang J, Jin X, Wu X, et al. An Improved Current Load Distribution Control Strategy for DC Microgrid[J]. Proceedings of the CSEE, 2016, 36(1):59-67.

Zhang G, Wang X, Wang S. Research on DCS Microgrid Energy Coordination Control Strategy Based on DBS[J]. High Voltage Apparatus, 2018(3).

Li P, Zhang C, Yuan R, et al. Load current distribution method of distributed energy storage system based on improved SOC droop control [J]. Proceedings of the CSEE, 2017, 37(13): 3746-3754.

Lin P, Wang P, Xiao J, et al. An Integral Droop for Transient Power Allocation and Output Impedance Shaping of Hybrid Energy Storage System in DC Microgrid[J]. IEEE Transactions on Power Electronics, 2017:1-1.

Wen B, Qin W, Han X, et al. DC Micro-grid Hybrid Energy Storage System Control Strategy Based on Voltage Sag Method[J]. Power System Technology, 2015, 39(4): 892-898.

Zhi N, Zhang H, Xiao Y. Research on Improved Droop Control Strategy to Improve Dynamic Characteristics of DC Microgrid[J]. Journal of Electric Engineering Technology, 2016, 31(3):31-39.

Yang J, Jin X, Wu X, et al. Non-interconnection communication network power allocation strategy of hybrid energy storage system in DC microgrid[J]. Journal of China Electrotechnical Society, 2017, 32(10):135-144.

Lu X, Guerrero J M, Sun K, et al. An Improved Droop Control Method for DC Microgrids Based on Low Bandwidth Communication With DC Bus Voltage Restoration and Enhanced Current Sharing Accuracy[J]. IEEE Transactions on Power Electronics, 2013, 29(4):1800-1812.

Oliveira T R, Donoso-Garcia P F. Distributed Secondary Level Control for Energy Storage Management in DC Microgrids[J]. IEEE Transactions on Smart Grid, 2016, PP(99):1-11.

168: Research on a balanced circuit and control strategy

Li LIAO [1], Feng JI [2], Tiezhou WU[3]

[1] *Hubei Key Laboratory for High-efficiency Utilisation of Solar Energy and Operation Control of Energy Storage System, Hubei University of Technology, 430068, China, 925423672@qq.com*

[2] *Hubei Key Laboratory for High-efficiency Utilisation of Solar Energy and Operation Control of Energy Storage System, Hubei University of Technology, 430068, China, 9051617@163.com*

[3] *Hubei Key Laboratory for High-efficiency Utilisation of Solar Energy and Operation Control of Energy Storage System, Hubei University of Technology, 430068, China, 443903093 @qq.com*

For reducing the inconsistent state of charges (SOC) of lithium-ion battery cells and making the full use of battery packs, effective battery balancing technology should be used. In order to achieve the goal of balancing any single cell in the battery pack expediently and considering the cost and the balance efficiency, a balanced circuit is proposed. By changing the action state of Single-Pole Double-Throw (SPDT) relay connected to each of the single cell battery, the balanced single cell battery is in a state of non-load power supply, at this point, the balanced battery is in "charging" state compared with other batteries in the battery pack, thus achieving the balance target of the battery pack. On this basis, this paper also proposes a new balancing control strategy; it is different from the traditional control strategy to balance the SOC of the single cell to the SOC average of the battery pack, considering the different SOC change rates of the cells with different capacity in the battery pack. The balanced control strategy proposed in this paper which allows the set condition of the single cell to end the equilibrium process in advance so as to reduce the unnecessary balance time and then improve the equilibrium speed. In order to verify the feasibility of the proposed circuit and control strategy, 18650 batteries with different initial SOC in series are experimentally verified. The experimental results show that the balanced circuit proposed in this paper can well balance the cell of each single cell and make the battery pack reach a balanced state.

Keywords: battery equalisation, 18650 cell, single pole double throw relay, equalisation strategy

1. INTRODUCTION

Lithium-ion batteries are widely used because of their excellent performance (Lee et al., 2017).However, single lithium-ion battery has low voltage and capacity. It is usually necessary to connect multiple batteries in series to meet load voltage and power requirements (Chen et al., 2016). In order to improve the capacity of the battery and reduce the risk of overcharge or over-discharge of the cell, It is necessary to balance the lithium-ion battery pack (Wang et al., 2016, Ju et al., 2016, Cui et al., 2017).

Passive equalisation is widely applied, but there are some disadvantages such as energy waste and difficulty in heat management (Qi and Lu, 2017). The performance of the traditional active equilibrium circuit is not good (Wei et al., 2017, Song et al., 2016). (Zheng et al., 2017) put the equaliser in different layers to improve the speed and efficiency of equalisation, but the cost is high. (Morstyn et al., 2016) use the LC resonant circuit to achieve a faster balancing speed, but it is not convenient to balance any single cell in the battery pack. (Kim and Lee, 2017) use Bi-directional flyback converter, which can balance battery more convenient, but the equilibrium speed is slower. (Kim et al., 2012) assign different force coefficients for each battery, balanced the arbitrary single cell battery in the battery group. Although it has a good performance in equilibrium efficiency and equilibrium speed, but the cost is high. In the equalisation method, (Bouchhima et al., 2016, Huang and Qahouq, 2015, Han and Zhang, 2017) are more commonly balance the SOC value of the battery to the target value.

A equalisation circuit is proposed in this paper. By controlling the operation state of the SPDT relay, the battery pack can be well balanced. At the same time, considering of battery capacity in the battery group are difference, compared with the traditional equilibrium method, there is a certain margin when the battery is balanced, and the balance speed is accelerated indirectly on the premise of achieving the balance of the battery group. The experiment is carried out to verify the feasibility of the equalisation circuit and the equalisation method.

2. ANALYSIS OF EQUILIBRIUM CIRCUIT

2.1. Equilibrium circuit

Figure 1 shown a balanced circuit containing N cells. B1 corresponds to the SPDT relay K1, determines whether the B1 is supplied to the load, B2 corresponds to the SPDT relay K2, determines whether the B2 is supplied to the load, and so on.

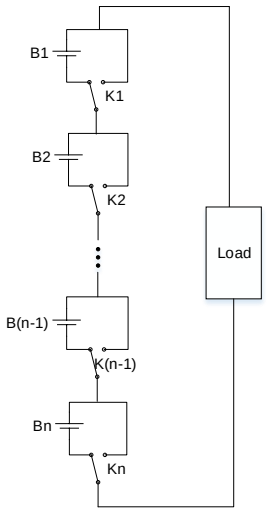

Figure 1: Balance circuit

For the convenience of expression, as shown in Figure 2, all the SPDT relays are normally closed on the left side Normal Connected (NC), the right is Normal Open (NO), the middle is the common terminal Common (COM). When a SPDT relay does not receive the trigger instruction, the COM is connected with the NC. When the SPDT relay receives the trigger instruction, the COM terminal is connected to the NO terminal.

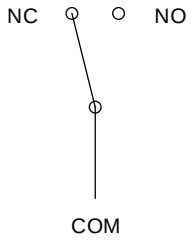

Figure 2: Action state of SPDT relay

As shown in Figure 1, under normal circumstances, the anode of each single cell is connected to the NC terminal of the corresponding SPDT relay. By controlling the operation state of the SPDT relay corresponding to each single cell, it is possible to decide whether the single battery is supplied to the outside power. So as to control the change of the SOC value of the corresponding single cell, and ultimately achieve the purpose of equalisation for the battery pack.

2.2. Analysis of working principle

In order to facilitate the analysis of the working principle of the balanced circuit, it is assumed that the SOC value of the B1 in the battery group is low and needs to be balanced; the SOC value of the other batteries is higher and does not need to be balanced. In order to achieve the target of balancing B1, only change the action state of SPDT relay K1 corresponding to the B1, so that the COM terminal of the SPDT relay K1 is connected to the NO terminal, as shown in Figure 3.

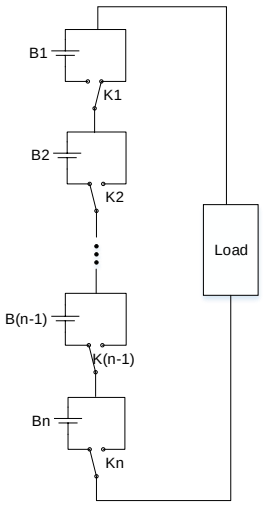

Figure 3: Battery balance diagram

As shown in Figure 3, all batteries except B1 are supplied for load. It can be considered that the B1 is in the "off" state at this time. During this period, the SOC value of B1 remained unchanged while the SOC value of other batteries gradually decreased. Take B2 as an example, when the B1 is in the "disconnected" state.

Equation 1: The variation of the SOC value of the B2 battery.

$$\Delta SOC_{B2} = -\frac{1}{Q_{B2}}\int_0^T I_{out}dt$$

Where:

ΔSOC_{B2}= the SOC change of B2 battery

Q_{B2}= the capacity of the B2 battery (Ah)

T= equilibrium time (h)

I_{out} = the current provided by the battery pack for the load (A)

The minus sign indicates that the SOC value of the B2 is decline. It can be understood that the SOC value of the B2 varies from 0 to T is ΔSOC_{B2}, the SOC value of the B1 is 0. In turn, if the SOC value variation of the B2 is 0 and the SOC value variation of the B1 is shown in Equation 2.

Equation 2: The variation of the SOC value of the B1 battery

$$\Delta SOC_{B1} = -\frac{Q_{B2}}{Q_{B1}} \Delta SOC_{B2}$$

Where:

ΔSOC_{B1}= the SOC change of B1 battery

Q_{B2}= the capacity of the B2 battery (Ah)

Q_{B1}= the capacity of the B1 battery (Ah)

ΔSOC_{B2}= the SOC change of B2 battery

The minus sign indicates that the SOC value of B1 is in an ascending state compared to B2 at 0 to T. It can be understood that between 0 to T, the other batteries are not discharged, while B1 is in a "charging" state. If the SOC value of the B1 is SOC_{B1} before equalisation, the SOC value of the B2 is SOC_{B2}. To make the SOC value of the B1 and the SOC value of the B2 reach the same level, for B1, it is necessary to "charge" Q_n as shown in Equation 3.

Equation 3: Q_n should be "charge" of B1 battery

$$Q_n = Q_{B1}(SOC_{B2} - SOC_{B1})$$

Where:

Q_n= the capacity should be change of the B1 battery (Ah)

Q_{B1}= the capacity of the B1 battery (Ah)

SOC_{B2}= the initial SOC of B2 battery

SOC_{B1}= the initial SOC of B1 battery

When the SOC value of B1 reaches the set equilibrium completion condition, the COM terminal of the SPDT relay K1, which corresponds to the B1 battery, is connected to the NC terminal, ending the equalisation process of the B1 battery.

Through the analysis of the balance process of the B1 battery, the balanced circuit proposed in this paper is to balance the corresponding single cell by changing the action state of the SPDT relay, so that the circuit can balance the battery of any single cell in the battery pack more conveniently. At the same time, it can be seen that, because there is no energy transfer process, it will not exist in the traditional active equilibrium circuit, when the battery pack is balanced, the loss is unavoidable and the equilibrium efficiency is not ideal. Therefore, the equilibrium efficiency can be close to the ideal value of the traditional active equilibrium circuit.

3. Equilibrium method

(Huang and Qahouq, 2015) show that

Equation 4: The SOC change of battery

$$\frac{\Delta SOC}{\Delta T} = \frac{I}{Q}$$

Where:

ΔSOC= the SOC variation of the battery

ΔT= the time variation (h)

I= the current of the battery (A)

Q= the capacity of the battery (Ah)

For each series battery, the SOC change rate of each battery is only related to its capacity Q. If the SOC value of B1 is larger than B2, but the capacity Q is smaller. When B2 is balanced, the SOC change of the two batteries are shown in Figure 4.

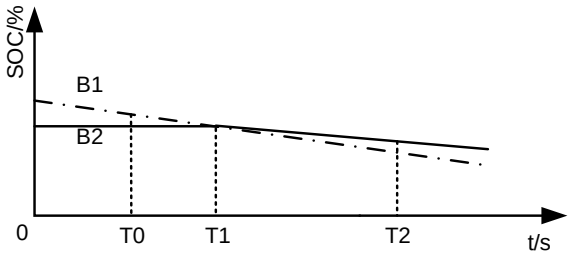

Figure 4: The SOC change of B1 and B2

The traditional equalisation method will make the equalisation circuit work to T1. But as shown in Figure 3, after T1, the difference between the SOC of B2 and B1 will gradually increase. At T2, if the difference between the SOC of B1 and B2 is equal, the equalisation of B2 at T0 to T1 is unnecessary. Considering the battery parameters obey the normal distribution (Campestrini et al., 2016), when the equilibrium process of the battery is finished at the end of the T0, about half of the battery will change to the target value because of the difference of the battery capacity.

In Figure 4, if the current at time of 0 to T1 are not changed much, compared to T1, the equilibrium process of the balanced battery at the end of the T0 can save some time. Compared to the entire battery group, there are

Equation 5: The equilibrium speed increased

$$V_{up} = \frac{T0 - T1}{2 \times T1} \times 100\%$$

Where:

V_{up}= The speed increased

T0= the time at T0 (s)

T1= the time at T1 (s)

Obviously, the equilibrium method proposed in this paper can accelerate the equalisation speed indirectly under the premise of achieving the goal of battery pack equalisation.

4. EXPERIMENTAL VERIFICATION

4.1. Experimental preparation

The experiment uses 3.7V, nominal capacity is 1200mAh 18650 batteries. 7 batteries are labelled, From 1 to 7. Using the Arbin instrument to measure the capacity of the 7 batteries.

Figure 5: Arbin instrument

7 batteries used in the experiment are tested in the thermostat according to the following steps, of which the temperature of the thermostat is set to 25 degrees Celsius.

(1) Charge the battery to 4.2V at 0.5C, then charge the battery at 4.2V voltage until the battery charging current is less than 0.02C.

(2) Discharge the battery to 3V at 0.5C, then discharge the battery at 3V voltage until the discharge current of the battery is less than 0.02C.

(3) Collecting the capacity of batteries.

The capacity of the 7 cells were shown in Table 1.

Table 1: Battery capacity

Battery labeling	1#	2#	3#	4#	5#	6#	7#
capacity /mAh	1214	1122	1206	1187	1214	1247	1225

As shown in Table 1, even if 7 batteries are 1200mAh, but real capacities are also quite different.

After collecting the capacity of the 7 batteries, a balanced experiment is conducted for these batteries. The equilibrium experimental diagram is shown in Figure 6.

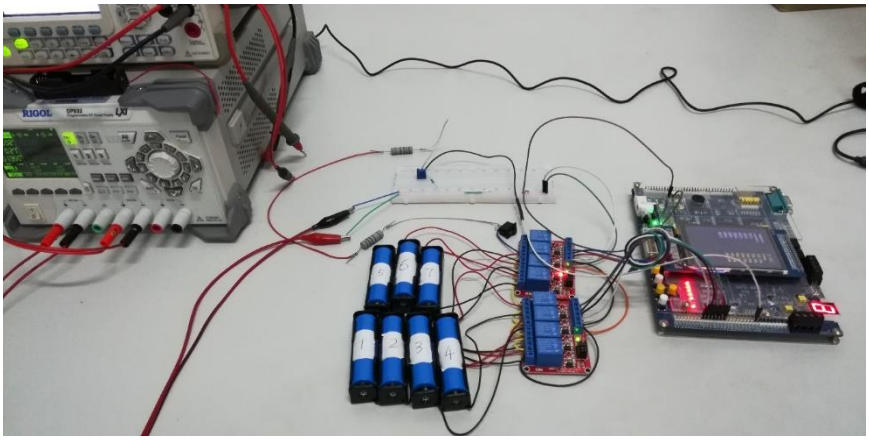

Figure 6: Balance experiment

The MCU we used is STM32F103, and the SOC of the 7 batteries is estimated by the ampere integral method, displayed by the 3.2 inch TFT screen. The equalisation is started when the difference between the maximum and minimum SOC of the battery pack is greater than 1%. The initial SOC of the 7 cells batteries used in the experiment is as shown in Table 2.

Table 2: Initial battery SOC

Battery labeling	1#	2#	3#	4#	5#	6#	7#
SOC/%	79.9	80	79.8	78.9	79.7	78.8	79.9

In the equalisation process, the SOC value of 7 batteries are recorded at every 10s, and the time for the balance of the start and end of the battery in the battery group and the SOC value of the 7 batteries at this time are recorded.

4.2. Analysis of experimental results

When using the traditional equalisation method, it is considered that the SOC value of the balanced battery can hardly be completely equal to the set target value, and the balance ends when the difference between the SOC

value of the balanced battery and the set target value is less than 0.01%. At this point, the 7 batteries SOC changes as shown in Figure 7.

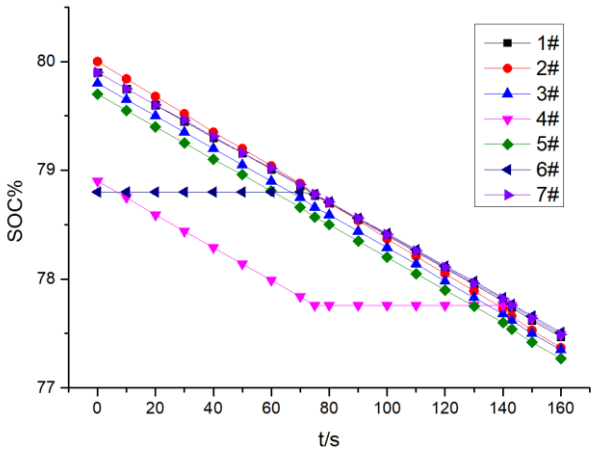

Figure 7: Experimental results use traditional balance methods

As shown in Figure 7, the difference of SOC between 2# and 6# battery reaches the setting condition, all the batteries except 6# are loaded to the load. Until the 75s and 6# battery are balanced. Then 4# battery is balanced in the same way until 143s. At this point, the battery pack reaches a set equilibrium state and ends at equilibrium.

It can be seen that this circuit uses only 7 relays, completes the process of balancing the 7 batteries. Because there is no transfer process of energy in the equilibrium process, the equilibrium conversion efficiency is ideal. Moreover, it can be seen that the balance of 6# battery or 4# battery only needs to control the relays related to the balanced battery, and the balance is more convenient.

In order to prove the superiority of the proposed equalisation method, we use this equilibrium method to carry out the experiment again. That is to say, when the difference between the maximum and minimum SOC of the battery pack is greater than 1%, the balance will be started until the difference between the two SOC is less than 0.5%. At this point, the SOC change of the 7 cells are shown in Figure 8.

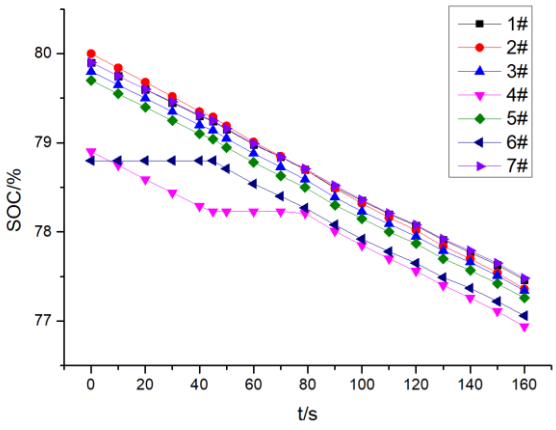

Figure 8: Experimental results using balance method this paper proposed

As shown in Figure 8, 6# battery reaches the set conditions at 45s, and 4# battery reaches the set conditions at 79s, the equilibrium process ends.

Equation 6: The definition of X

$$X = SOC_2 - SOC_6$$

Where:

SOC_2= SOC values of 2# battery

SOC_6= SOC values of 6# battery

Equation 7: The definition of Y

$$Y = SOC_2 - SOC_4$$

Where:

SOC_2= SOC values of 2# battery

SOC_4= SOC values of 4# battery

At 0, 45s, 79s and 160s, the change of X and Y are shown in Table 3.

Table 3: The values change of X and Y

t/s	0	45	79	160
X/%	1.2	0.5	0.43	0.3
Y/%	1.1	1.06	0.5	0.42

As shown in Table 3, although the equilibrium method proposed in this paper does not balance the SOC value of 4# and 6# batteries to the target value, but these batteries will gradually tend to ideal equilibrium over time, basically reaching the target of battery pack equilibrium.

When using the traditional equalisation method to balance the battery, It takes 143s, compare to 79s we used. the equilibrium method proposed in this paper reduces the equilibrium time of 64s and increases the equilibrium speed about 44.8%.

5. CONCLUSION

The equalisation circuit proposed in this paper can well balance the battery pack. Compared with the traditional equilibrium method that equalizing the SOC of the battery to the target value, the equilibrium method proposed in this paper takes full account of the difference of battery capacity in battery group. Therefore, by keeping the corresponding margin, the equilibrium speed can be better improved on the premise of achieving the goal of equalisation.

6. REFERENCES

bouchhima, N., Schnierle, M., Schulte, S. & Kai, P. B. 2016. Active model-based balancing strategy for self-reconfigurable batteries. *Journal of Power Sources,* 322**,** 129-137.

Campestrini, C., Keil, P., Schuster, S. F. & Jossen, A. 2016. Ageing of lithium-ion battery modules with dissipative balancing compared with single-cell ageing. *Journal of Energy Storage,* 6**,** 142-152.

Chen, Y., Liu, X., Cui, Y., Zou, J. & Yang, S. 2016. A MultiWinding Transformer Cell-to-Cell Active Equalisation Method for Lithium-Ion Batteries With Reduced Number of Driving Circuits. *IEEE Transactions on Power Electronics,* 31**,** 4916-4929.

Cui, X., Shen, W., Zhang, Y., Hu, C. & Zheng, J. 2017. Novel active LiFePO 4 battery balancing method based on chargeable and dischargeable capacity. *Computers & Chemical Engineering,* 97**,** 27-35.

Han, W. & Zhang, L. 2017. Battery Cell Reconfiguration to Expedite Charge Equalisation in Series-Connected Battery Systems. *IEEE Robotics & Automation Letters,* 3**,** 22-28.

Huang, W. & Qahouq, J. A. A. 2015. Energy Sharing Control Scheme for State-of-Charge Balancing of Distributed Battery Energy Storage System. *IEEE Transactions on Industrial Electronics,* 62**,** 2764-2776.

Ju, F., Deng, W. & Li, J. 2016. Performance Evaluation of Modularized Global Equalisation System for Lithium-Ion Battery Packs. *IEEE Transactions on Automation Science & Engineering,* 13**,** 986-996.

Kim, D. & Lee, J. 2017. Discharge scheduling for voltage balancing in reconfigurable battery systems. *Electronics Letters,* 53**,** 496-498.

Kim, T., Qiao, W. & Qu, L. 2012. Power Electronics-Enabled Self-X Multicell Batteries: A Design Toward Smart Batteries. *IEEE Transactions on Power Electronics,* 27**,** 4723-4733.

Lee, K. M., Lee, S. W., Choi, Y. G. & Kang, B. 2017. Active Balancing of Li-Ion Battery Cells Using Transformer as Energy Carrier. *IEEE Transactions on Industrial Electronics,* 64**,** 1251-1257.

Morstyn, T., Momayyezan, M., Hredzak, B. & Agelidis, V. G. 2016. Distributed Control for State-of-Charge Balancing Between the Modules of a Reconfigurable Battery Energy Storage System. *IEEE Transactions on Power Electronics,* 31**,** 7986-7995.

Qi, J. & Lu, D. C. 2017. A Preventive Approach for Solving Battery Imbalance Issue by Using a Bidirectional Multiple-Input Ćuk Converter Working in DCVM. *IEEE Transactions on Industrial Electronics,* 64**,** 7780-7789.

Song, C., Lin, N. & Wu, D. 2016. Reconfigurable Battery Techniques and Systems: A Survey. *IEEE Access,* 4**,** 1175-1189.

Wang, S., Shang, L., Li, Z., Deng, H. & Li, J. 2016. Online dynamic equalisation adjustment of high-power lithium-ion battery packs based on the state of balance estimation. *Applied Energy,* 166**,** 44-58.

Wei, J., Dong, G., Chen, Z. & Kang, Y. 2017. System state estimation and optimal energy control framework for multicell lithium-ion battery system. *Applied Energy,* 187**,** 37-49.

Zheng, X., Liu, X., He, Y. & Zeng, G. 2017. Active Vehicle Battery Equalisation Scheme in the Condition of Constant-Voltage/Current Charging and Discharging. *IEEE Transactions on Vehicular Technology,* 66**,** 3714-3723.

169: Calculation method of convective heat transfer coefficient in air-cooled radiator temperature field simulation

JINGWEI LI[1], JIE ZHANG[1], HONG-XI YANG[2]

[1]*Solar Energy Efficient Utilisation Cooperative Innovation Center, Hubei University of Technology, HubeiWUhan, 476103202@qq.com*
[2]*Suizhou Power Grid Corporation, Suizhou,zjmato@163.com*

At present, the general steps for heat sink design of power semiconductor devices are: First, calculate the allowable thermal resistance of the heat sink, then select the corresponding heat sink according to the thermal resistance, and finally test whether the junction temperature of the power device is allowable. Inside. Since there are many approximations to the calculation of the thermal resistance, the resulting thermal resistance is just the average thermal resistance of the heat sink. Therefore, the temperature distribution diagram on the radiator cannot be obtained and the result is lack of intuitiveness. In addition, the heat resistance Rthsa from the surface to the environment of different heat sinks of different materials and shapes varies considerably, so this increases the difficulty of calculating the total heat resistance Rth. The literature took into account the effect of temperature on various losses. Using the equivalent circuit of thermal resistance, the general formula for the temperature of each point of the radiator system was deduced. The method is cumbersome and the practicality is not well.In order to simulate on thermal field of air-cooling radiation，it is necessary to calculate the value of the convection heat transfer coefficient. According to the theory of thermal conduction，the paper establishes power semiconductor device and its physical model of air-cooling radiation，provides the formula of convection heat transfer coefficient and its parameters table of dry air on different conditions. It provides flow chart of convection heat transfer coefficient on simulation. The simulation and experiment verify the calculation formula of convection heat transfer coefficient and the validity of adjustment method.

Keywords: air-cooling radiation;thermal field simulation;convection heat transfer coefficient

1. INTRODUCTION

At present, according to the traditional theory of thermal conduction, there are many factors affecting the convection heat transfer coefficient of the thermal convection. The value of the convection heat transfer coefficient varies in different situations, and the selection of its value is critical to the accuracy of the heat sink temperature field simulation. The literature (Liu, 2013) data has only been used for this purpose, or it has only stated the range of values, and no explicit formula has been given. The literature directly sets the convective heat transfer coefficient h_L of the natural air-cooling under laboratory conditions to 10, and the selection of its value is subject to discussion. In this paper, the workbench software is used to simulate and analyze the power semiconductor and its heat sink. The general calculation formula of convective heat transfer coefficient under forced air cooling is given. It is proved that the selection of the convective heat transfer coefficient is reasonable and practical by experiments.

2. THE THEORETICAL BASIS OF RADIATOR HEAT CONDUCTION

The heat transfer process consists of three basic ways: heat conduction, convection, and radiation. For the sake of simplicity, assume: (1) the radiators are isotropic homogenous continuum; (2) the physical parameters of the radiator (ie density, specific heat capacity, and thermal conductivity) are all constant; (3) After the system is stable, it is steady-state heat dissipation and there is no internal heat source (Wang, 2006).

2.1. Heat conduction

The law of heat conduction is summarised as Fourier's law and its mathematical expression is

$$(1)\varphi = -\lambda A \frac{dt}{dx}$$

Where:

φ = heat (W)

A= cross-sectional area perpendicular to the heat flow direction (m^2)

dt/dx= change rate of the temperature t in the x direction

λ= thermal conductivity coefficient, which is the parameter to characterise the thermal conductivity of the material (W/(m·K))

A negative sign indicates that the heat transfer direction points in the direction of temperature decrease.

2.2. Convection

Thermal convection refers to the heat transfer process caused by the relative displacement between fluid parts due to the macroscopic motion of the fluid and the intermixing of cold and hot fluids. Thermal convection can only occur in fluids, and due to the molecules in the fluid are simultaneously undergoing irregular thermal motion, thermal convection must be accompanied by thermal conduction (Cheng, 2011).

The capacity of the convection heat transfer process can be calculated in terms of the Newton's cooling equation, and the mathematical formula is

$$(2)\varphi = h_c A\left(t_w - t_f\right)$$

Where:

h_c =heat transfer coefficient (W/(m2·℃))

A= solid wall heat exchange area (m^2)

t_f= fluid temperature(℃)

t_w= the solid wall temperature (℃)

The size of the convection heat transfer coefficient is related to many factors in the convective heat transfer process. It depends not only on the physical properties of the fluid, but also on the shape, size, and arrangement of the heat transfer surface, but also has a close relationship with the flow rate.

2.3. Radiation

The way an object transmits its power through electromagnetic waves is called radiation. The object emits radiant energy for various reasons, and the phenomenon of emitting radiant energy due to heat is called thermal radiation.

Heat radiation is essentially different from convection heat transfer and heat transfer (Hu, 2009). It can transfer energy from light to light through the vacuum from one object to another.

In engineering, radiation between two or more objects is usually considered, and each object in the system radiates and absorbs heat at the same time. The net radiative heat transfer between them can be calculated using Stephen Boltzmann's law:

$$(3)\varphi = \delta\varepsilon F_{ES}(T_E^4 - T_S^4)$$

Where:

δ =Stephen Boltzmann constant (0.516 x 10-7 W/(m2.K4))

ε= relative darkness between the surface and the surroundings

F_{ES}= angular coefficient between the device and the surroundings

A= Radiation area (m2)

T_E= thermodynamic temperature of the radiation surface(℃)

T_S= surrounding thermodynamic temperature (℃)

3. APPLICATION OF CONVECTIVE HEAT TRANSFER COEFFICIENT CALCULATION IN ENGINEERING PRACTICE

When the fluid is in direct contact with solid walls at different temperatures, heat transfer due to relative motion is called convection heat transfer. The main factors influencing the convective heat transfer are: (1) the origin of flow and flow, (2) the thermophysical properties of the fluid, and (3) the geometry of the heat transfer surface. Among them, the thermophysical properties of fluids are the most complex and numerous.

Whether in theoretical analysis or experimental research, convection heat transfer problems should be classified and resolved. In this experiment, forced air cooling was applied to the radiator, and the wind direction was parallel to the side wall of the radiator. This convection heat exchange system belongs to no phase change convection heat transfer. First, according to the test conditions, the specific requirements of the model are abstracted, and the average fluid temperature t_f and the wall surface temperature of the radiator t_w are preset, and the arithmetic average temperature between the fluid and the wall surface is $t_m = (t_f + t_w)/2$. Check the table (the thermal physical properties of dry air) at atmospheric pressure, the thermal conductivity λ, the kinematic viscosity v and the Prandtl number P_r, then the parameters of the model of the system, solve the convection heat transfer coefficient h_L.

$$(4)\ h_L = 0.332\frac{\lambda}{L}\left(\frac{U\times L}{\vee}\right)^{1/2}P_r^{1/3}$$

Where:

λ =thermal conductivity

v= kinematic viscosity

P_r= Prandtl number

h_L=convection heat transfer coefficient

U= fluid velocity

L= length o the radiator substrate

Table 1: Thermophysical properties of dry air ($p=1.013\times10^5$ Pa)

t_m/℃	λ/[10^{-2}W·(m· K)$^{-1}$]	v/（10^{-6} m^2·S^{-1}）	Pr
20	2.59	15.06	0.705
30	2.67	16.00	0.701
40	2.76	16.96	0.699
50	2.83	17.95	0.698
60	2.90	18.97	0.696
70	2.96	20.02	0.694
80	3.05	21.09	0.692

In the later stage, the radiator wall temperature is adjusted according to the temperature value obtained from the simulation result. If the wall temperature value and the simulation result are small, the hypothesis is reasonable and the simulation result is reliable. If the set wall temperature value is different from the simulation result, the hypothesis is readjusted.

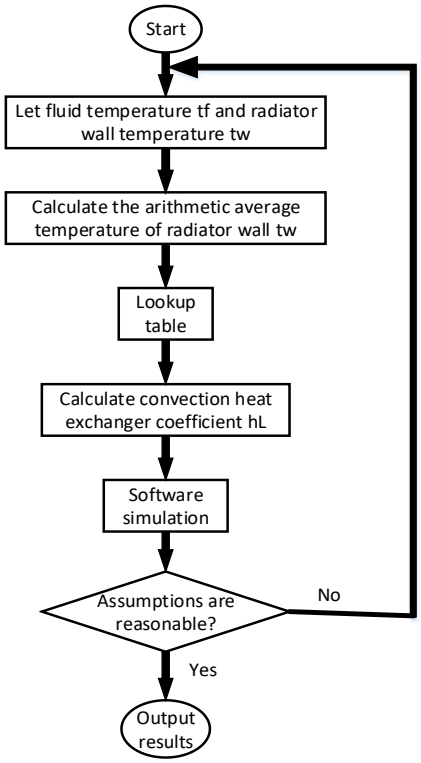

Figure 1: Flow chart of calculating heat transfer coefficient of convection

4. APPLICATION OF CONVECTIVE HEAT TRANSFER COEFFICIENT CALCULATION IN ENGINEERING PRACTICE

The loss of power semiconductor devices will be transmitted to the surrounding in the form of heat, and the die is the main heating part, which is regarded as a constant volume, constant temperature heat source. In engineering applications, when the loss of the device is too large, that is, the temperature is too high, it is necessary to add a radiator and provide forced air cooling to the system to dissipate heat.

Diode (MUR6060) was used for experiments. Refer to the technical documents. The conduction voltage drop is a function of the conduction current and temperature. Under different conditions of conduction current and temperature, the conduction voltage drop is different. When calculating its loss, it should actually measure its conduction voltage drop.

Table 2: F-type radiator related parameters

Board length	Rib thickness	width	Thickness of substrate	Tooth height	Number of teeth
100mm	1.5mm	58mm	4mm	32mm	16mm

System Modeling: The diode is equivalent to a single power source with constant power and is directly attached to the heat sink substrate. Figure 2 shows the physical model of the cooling system.

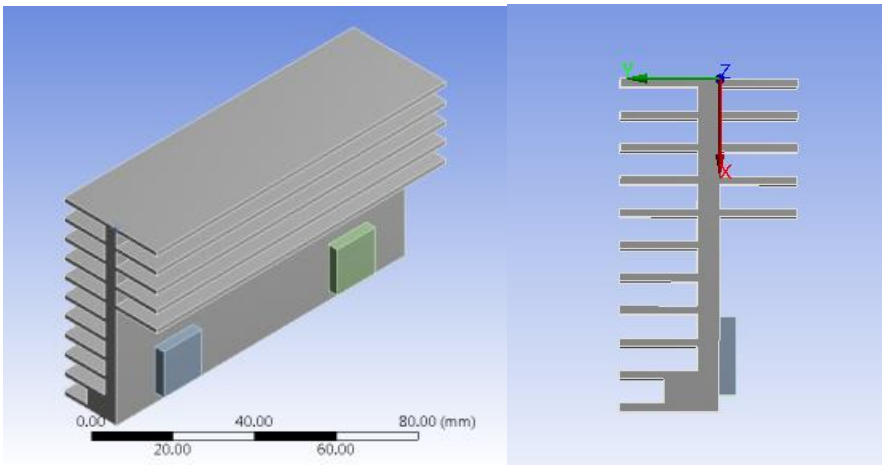

Figure 2: Physical model of radiator system

5. SIMULATION RESULTS AND EXPERIMENTAL RESULTS

After establishing the simulation model, set parameters and impose constraints on it. The heat sink is made of aluminum alloy material with a precision of 1mm. A heat flux is applied to the diode, and a heat convection coefficient is applied to the heat sink. Common cooling methods include natural cooling, forced air cooling, oil cooling, and water cooling (Liu, 2013). The surface of the entire radiator system was selected for convection heat transfer and heat radiation, and the heat radiation emissivity of the smooth aluminum alloy heat sink surface was set at 0.05. The temperature tester is VT04 produced by FLUCK.

A DC fan was added to apply air cooling to the radiator system. The fan air volume was 140.16 CFM (cubic feet per minute) and the wind speed was 5.849 m/s. The convection heat transfer coefficient is calculated according to Equation 4 herein.

Table 3: Experimental conditions for the radiator system

Power consumption P(W)	Convective heat transfer coefficient h_L/(W/m^2·℃)	Simulation temperature T/℃	Measured temperature T/℃
8.540	15.049	45.336	38.5
9.800	15.049	48.964	43.3
11.178	15.049	52.991	47.1
12.570	15.049	57.051	52.5
13.959	15.102	61.016	55.6
15.396	15.102	65.143	59.7
16.692	15.102	68.880	65.8
18.186	15.044	73.331	70.7
19.665	15.044	77.589	73.3

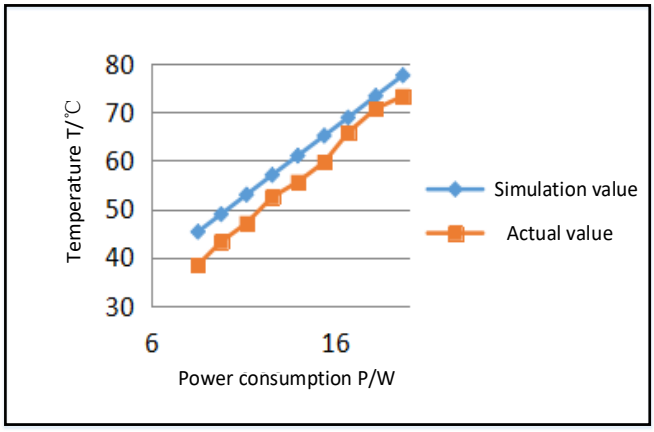

Figure 3: Measuring temperature curve

From the graph, the overall simulation value is slightly higher than the actual value. As the power consumption increases, the actual value gradually approaches the simulation value. In engineering applications, the maximum allowable junction temperature of the diode die is 150°C. In any case, it is not allowed to exceed the rated value of the device. Considering the margin and the worst environment, the junction temperature does not exceed 120°C.

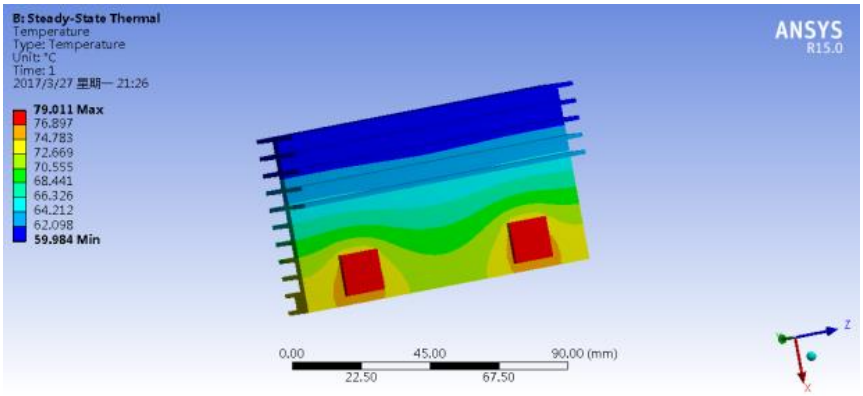

Figure 4: simulation of the radiator

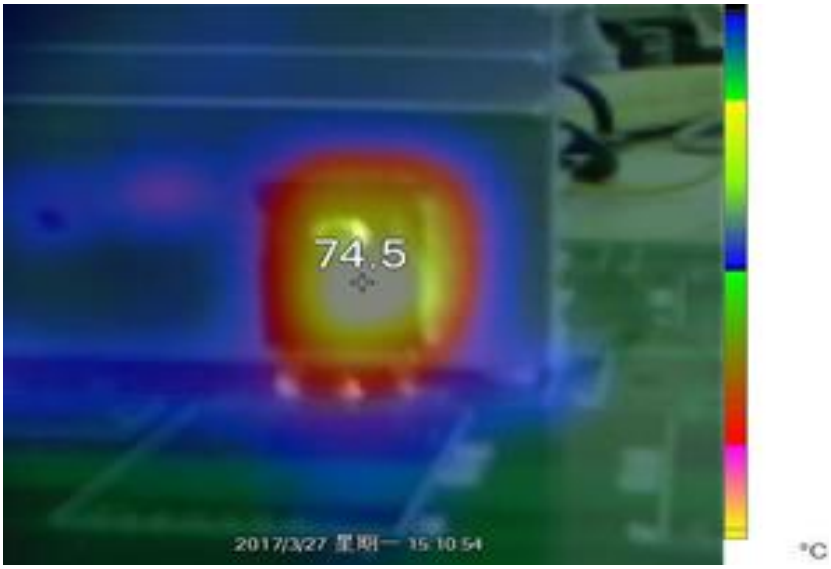

Figure 5:The result of the temperature tester screenshot

6. REFERENCES

Cheng P, Lan H, Luo Y. Rectifier device thermal analysis and the simulation research of the air-cooled radiator [J]. Computer simulation of 2011.11 (28):275-278.

Hu J, Li J, Zou J. Inverter in IGBT module loss calculation and the cooling system design [J]. Journal of electrotechnics. 2009.3 (24):159-163.

Liu J, Huang L. IGBT module thermal analysis based on Ansys software [J]. Power electronic technology / 2013.2 (47):107-108.

Wang H, Zhou G, Li X. Heat transfer [M]. Chongqing: Chongqing University Press, 2006.11:3-6.

170: Research on active equilibrium with balanced power supply

Yu ZHANG[1], Mingming HUANG[2], Tiezhou WU[3]

[1] *Hubei Key Laboratory for High-efficiency Utilisation of Solar Energy and Operation Control of Energy Storage System, Hubei University of Technology, 430068, China, 946411426@qq.com*
[2] *Hubei Key Laboratory for High-efficiency Utilisation of Solar Energy and Operation Control of Energy Storage System, Hubei University of Technology, 430068, China, 2545896156@qq.com*
[3] *Hubei Key Laboratory for High-efficiency Utilisation of Solar Energy and Operation Control of Energy Storage System, Hubei University of Technology, 430068, China, 164228917@qq.com*

The balance of the series lithium ion battery can prevent the overcharge or over-discharge of some single cell in the battery group, so as to prolong the service life of the battery. Aiming at the current active equalisation circuit, it is difficult to achieve equalisation of any single cell in battery pack based on a small number of components. A new active equalisation circuit with balanced power supply is proposed. The circuit is composed of the current mainstream switch array, bidirectional DC-DC converter and balanced power supply. The switch array is divided into two groups, the first group has N+1 switches, in which N is the number of series batteries, which provides access for the balanced single cell battery; the second group has 4 switches and is divided into two groups to achieve the purpose of controlling the polarity of the bidirectional DC-DC circuit. By controlling the switching array and the working state of the bidirectional DC-DC converter, the energy exchange between the single cell and the balanced power supply in the battery group is realised, and then the target of the battery pack is balanced. The balanced power supply can also provide power for load to reduce battery load under the condition that the load needs more power. On this basis, we use MATLAB/SIMULINK software to build the model and simulate it. The simulation results show that, under the premise of using less components (N+1+4 switches and one bidirectional DC-DC converter), the structure can achieve a balanced target for any single cell in the battery group, which proves that the circuit can meet the requirements well.

Keywords: Lithium-ion battery balanced power supply MATLAB/SIMULINK active equalisation

1. INTRODUCTION

Lithium-ion batteries are favoured by electric vehicles because of their excellent performance. Due to differences in production and use, battery packs need to be balanced. The passive equilibrium structure is simple, economical and reliable, but it is subject to many restrictions. Although the cost of active equalisation is high, it is the focus of current research to maximise the use of energy. The use of capacitive or inductive energy storage elements for equalisation, the structure is relatively simple, high conversion efficiency, and easy to implement modular. However, the equilibrium is slower, more components are needed, and cross-battery balancing is difficult to achieve. With multi-winding transformers, the equilibrium speed is faster, but there is a higher voltage and current stress, and there are problems such as large volume, high price, and low conversion efficiency. (Cui et al., 2017) adopts single pair packet structure, which is more flexible but inefficient. By comparing various equalisation methods, (Baronti et al., 2014) finds that single to one equilibria perform well in many respects. The literature (Hannan et al., 2017) uses the flyback converter for equalisation, which is more flexible but requires more switches. The equalisation circuit proposed by (Kim et al., 2014) can reduce the number of switching components, but it is not flexible enough. The literature (Bouchhima et al., 2016) is balanced by partial battery discharge, while the literature (Huang et al., 2015) equaliser the different weights of the battery. These methods are highly efficient and flexible, but the cost is high.

Considering the advantages of active equalisation, a balancing method with balanced power supply is proposed in this paper. With the advantages of switching array and bidirectional DC-DC converter, it simulates the corresponding control strategy with the advantages of multi-use balanced power supply. It is proved that the method can achieve high conversion efficiency by using less components on the premise of realizing flexible equilibrium.

2. EQUILIBRIUM CIRCUIT DIAGRAM AND ITS ANALYSIS AND EVALUATION

2.1. Balanced circuit diagram

Figure 1 is a balanced circuit diagram presented in this paper. It can be seen that it consists of a storage battery pack, a switch array, a bidirectional DC-DC converter and a balanced battery pack.

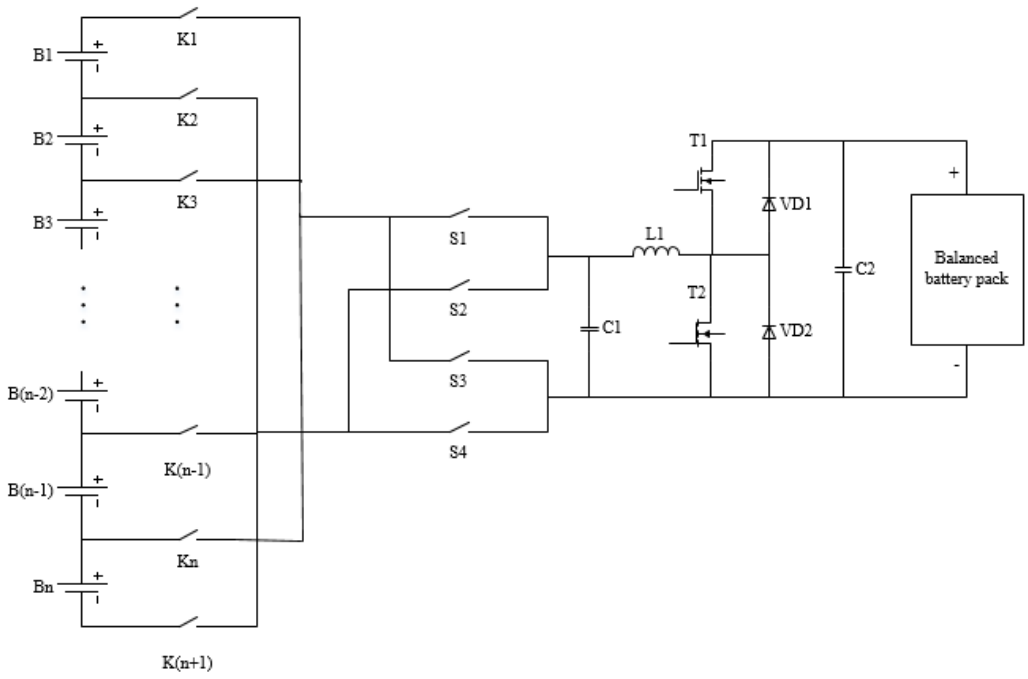

Figure 1: Equilibrium circuit diagram

The balanced power supply is split into several equalisation batteries, and the energy storage battery of each group is balanced. The single cell used in the equalisation battery is the same or similar to the energy storage battery. Balanced battery using single battery, bidirectional DC-DC converter switch in a given PWM control signal duty ratio tends to be very large or very small two extremes, it is generally according to the actual situation, the two and above become a balanced battery-battery series.

The switch array is divided into two groups. The first group has N+1 switches, of which N is the number of battery cells. When connected to a storage battery, the rest of the switches are connected to the anode of the battery and the positive part of the next battery. The second group has four switches, of which S1 and S4 are a group, S2 and S3 are another group, which are connected to the bidirectional DC-DC converter to control the polarity of access. N Series in the battery case, compared with the traditional method for each battery with two switches, the method can reduce the traditional method of N-1 switch number through four control polarity switch. When the number of series batteries is large, the superiority of this method will be more obvious.

The principle of bidirectional DC-DC converter in Figure 1 is very simple. When the switch T1 is always in a state of disconnection, the switch T2, diode VD1 and inductor and capacitor constitute the Boost circuit. Similarly, when the switch T2 is always disconnected, the switch T1, diode VD2 and inductor and capacitor constitute the Buck circuit.

2.2. Analysis and evaluation of working principle

Assuming that the SOC of the battery B1 in the storage battery is too high, it is necessary to transfer the charge to the equalisation battery pack. The switch K1 and K2 that control the positive and negative poles of the B1 battery, and the switch S1 that controls the polarity of the bidirectional DC-DC converter are closed with S4. The bidirectional DC-DC converter operates in the Boost circuit mode. The partial charge of the B1 battery will be transferred to the equalisation battery pack, as shown in Figure 2.

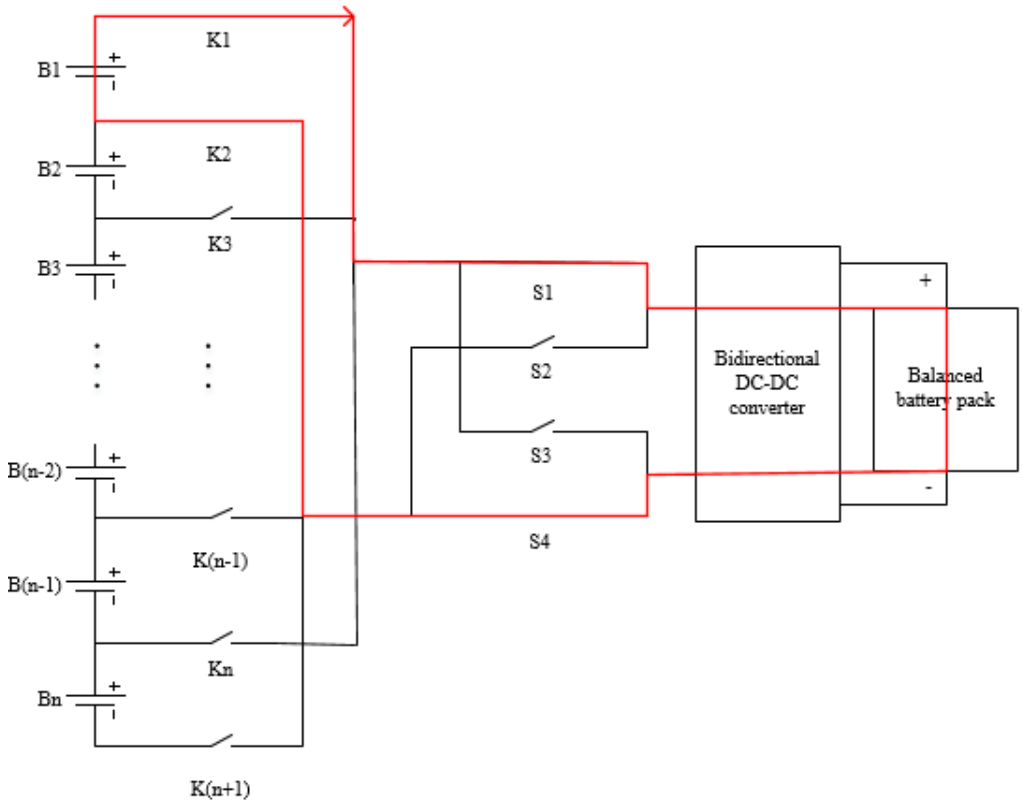

Figure 2: B1 battery balance diagram

When the SOC of the B2 battery in the energy storage battery is low, the switch K2 and K3 of the positive and negative electrodes of the B2 battery are controlled, and the switch S2 and S3 of the control polarity are closed. The bidirectional DC-DC converter operates in the Buck circuit mode, and the charge will be transferred from the balanced battery pack to the B1 battery through the bidirectional DC-DC converter, as shown in Figure 3.

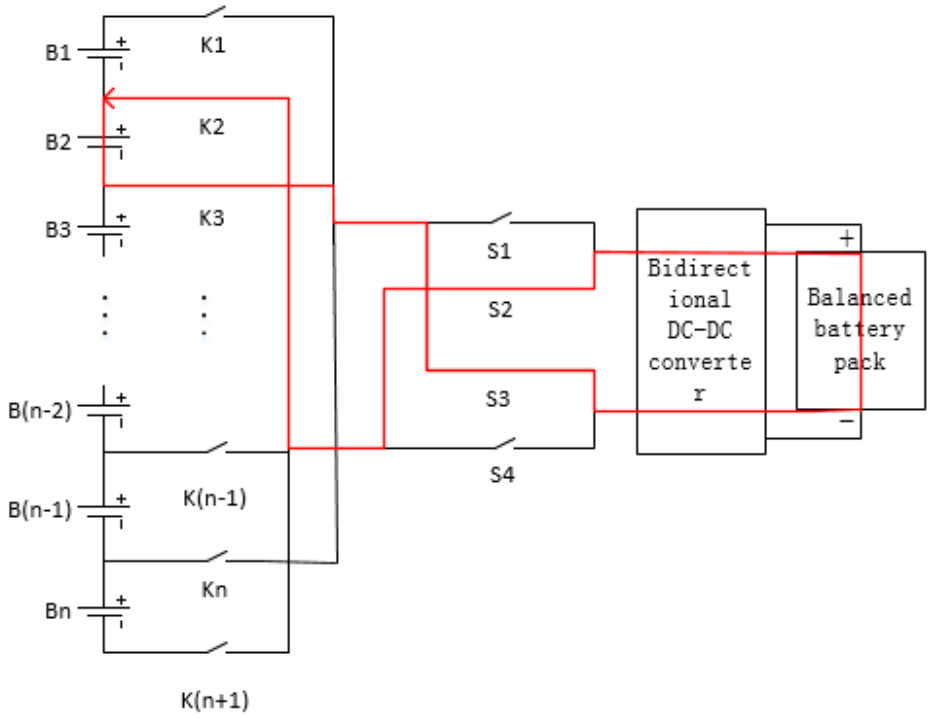

Figure 3: B2 battery balance diagram

Note that when the battery B1 and B2 are balanced, switch K2 is used. The switch K2 can not only control the balance of the battery B1, but also control the B2 balance of the battery. We can see that the balance of battery with switch array and bidirectional DC-DC converter, at any time can be very convenient for the single cell SOC high discharge equilibrium, or of low SOC monomer battery charge equalisation.

In terms of conversion efficiency, the current active equalisation circuit loss is shown in Equation 1.

Equation1: The current active equalisation circuit loss

$$P = P_s + P_m + P_e$$

Where:

P = the total loss (W)

P_s= the switching loss of switch array (W)

P_m= the loss of balanced main device (W)

P_e= the other loss (W)

The equalisation circuit used in this paper, P_S is the loss of four switches, and P_e is mostly the loss of battery internal resistance when balancing. Compared with most of the current equalisation circuits, loss minimisation can basically be achieved. Moreover, because the number of components used in this article is small, more cases are satisfied Equation 2.

Equation 2: This method compares with traditional methods in terms of switching loss and other losses

$$P_s' + P_e' \geq P_s + P_e$$

Where:

P'_s+P'_e= the sum of switching losses and other losses in most of the equalisation circuits. (W)

The P_m In Equation 1 is the loss of bidirectional DC-DC converter here, because the equalisation circuit used in this paper is single to single mode, with small power and small loss. In comparison with most of the current equalisation circuits, more cases are satisfied Equation 3.

Equation 3: This method compares with traditional methods in terms of balanced master loss

$$P_m' \geq P_m$$

Where:

P'_m= Balanced master loss in most equaliser circuits (W)

Because the number of bidirectional DC-DC converters used in this paper is small, the soft switching technology can be used to further reduce the loss.

From the Equation 2 and Equation 3, the equalisation circuit proposed in this paper can theoretically achieve a higher level of conversion efficiency, as shown in Equation 4.

Equation 4: Comparison of the total loss of this method and the traditional method

$$P' \geq P$$

3. MULTIPLE UTILISATION OF BALANCED POWER SUPPLY

Figure 4 is an overall schematic diagram of the balanced power supply in the battery pack of an electric vehicle.

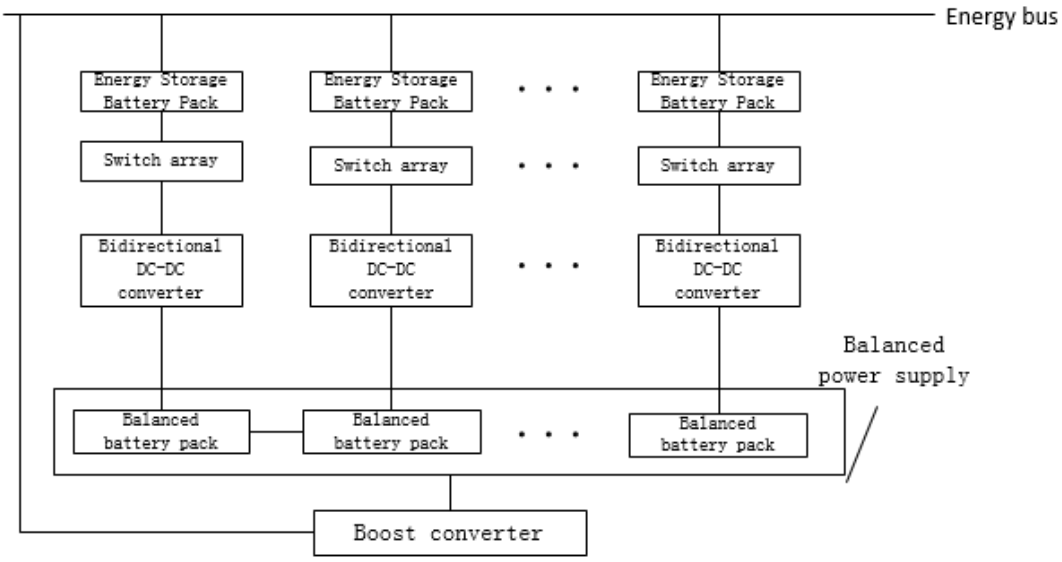

Figure 4: Schematic diagram of balanced power supply in battery pack of EV

It can be seen that each energy storage battery group is connected in series to form an equalizing power supply, and the balanced power supply provides electric power for the electric vehicle through the boost converter. In addition to balancing the battery pack, the balanced power supply can also be an alternate power source for electric vehicles, which can provide electricity for any energy bus at any time. Especially when the electric vehicle is in the hill climbing, the acceleration and so on needs high power, the addition of the backup power can reduce the burden of the energy storage battery group, so as to prolong the service life of the energy storage battery pack. If a battery pack of electric vehicle is out of operation because of damage, the balanced power supply can also give full play to the role of the standby power supply, instead of the damaged energy storage battery group, and improve the reliability of the electric vehicle operation.

Due to the small number of unbalanced battery and unbalanced degree, the method of document (Huang et al., 2015) can be used for equalisation.

4. ANALYSIS OF SIMULATION RESULTS

In order to verify the feasibility of the proposed equalisation circuit, MATLAB/SIMULINK software is used for simulation. The battery can be replaced by a series of four single cell batteries. The battery used in the balanced battery pack and the energy storage battery pack adopts the parameters of the literature (Campestrini et al., 2016), as shown in Table 1.

Table 1: The parameters of simulated batteries

Nominal voltage	capacity	Internal resistance	Charging cut-off voltage
3.7V	2.8Ah	20mΩ	4.2V

The literature (Campestrini et al., 2016) uses a nickel-cobalt-aluminum ternary lithium-ion battery for experiments and finds that the equilibrium charge required during the cycle life of a single cell is about 1.13 Ah. When the battery is used, the battery cycle number of the electric vehicle is 500 times, and the number of the series battery is 135, of which the bus voltage is 500V. The charge required by the battery pack during the first cycle is about 0.31Ah, about 11.1% of the capacity of the single cell. Considering that the lithium ion battery parameters obey the normal distribution and the equilibrium battery pack acts as a medium, the charge of the high SOC single cell battery is transferred to the low SOC battery, so the charge of the balanced battery group required during the first cycle of the energy storage battery group is much smaller than that of the calculated value. Considering cost and control, the two batteries are replaced by two batteries in the simulation.

The initial SOC of the four section of the single energy storage battery is set at 72%, 70%, 68% and 70% respectively, and the SOC of the battery in the equalisation battery is set to 70%. When the difference between the SOC of the single energy storage battery and the average SOC is 1.5%, the equalisation is started. In the actual situation, in order to prevent the occurrence of repeated balance, such as low capacity single cell in its high SOC discharge equilibrium, but after a period of time its SOC may be lower than the average, at this time the charge balance, which will lead to the waste of energy. Therefore, the difference between the SOC of the single cell and the average SOC is balanced to 1%. The balance is interlocked, that is, only one battery can be balanced at any time.

Figure 5 is the SOC curve of the single cell from the top to bottom respectively in the first, second, third and fourth sections of the energy storage battery pack.

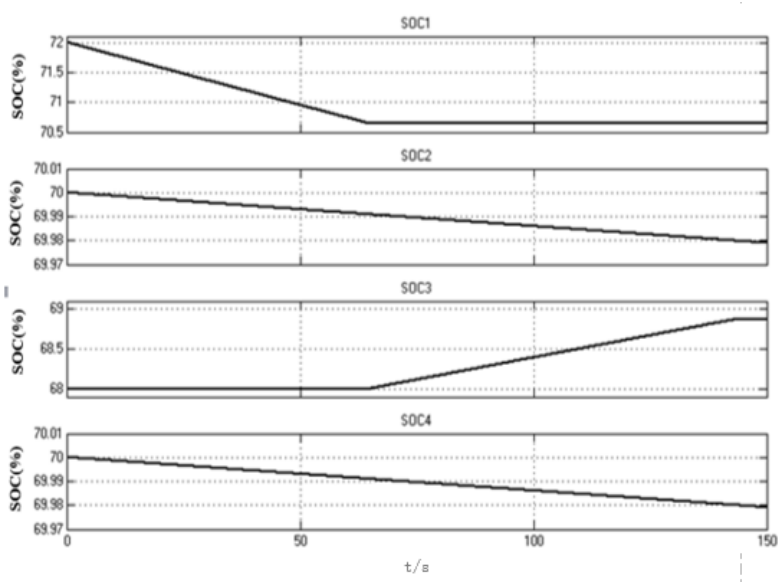

Figure 5: SOC diagram of energy storage batteries

As the battery pack is in the load state, the SOC of the second and fourth batteries gradually decreases, but the drop is not much, so it can be neglected. As you can see from Figure 5, the first part of the battery SOC is falling, and it is in a state of discharge equalisation. Due to the balanced interlocking, even if the third batteries need to be

balanced, they can only start after the first section of the battery is balanced. After about 64S, the charge is about 1.3%, about 36.4mAh. From about 64S, the SOC of the third cell began to rise and was in a state of charge equalisation. At about 143s, its SOC increased by about 0.9%, about 25.2mAh. At this point, the SOC of each battery of the battery pack has reached the set equilibrium condition. Of course, the equalisation time can be reduced by increasing the balanced current. It is also possible to make the battery pack cell closer to the average SOC of the battery group by reducing the set equilibrium threshold, but this will reduce the overall balance conversion efficiency of the battery group.

To balance the change of SOC in battery pack, take one section of two batteries to observe the SOC change, as shown in Figure 6.

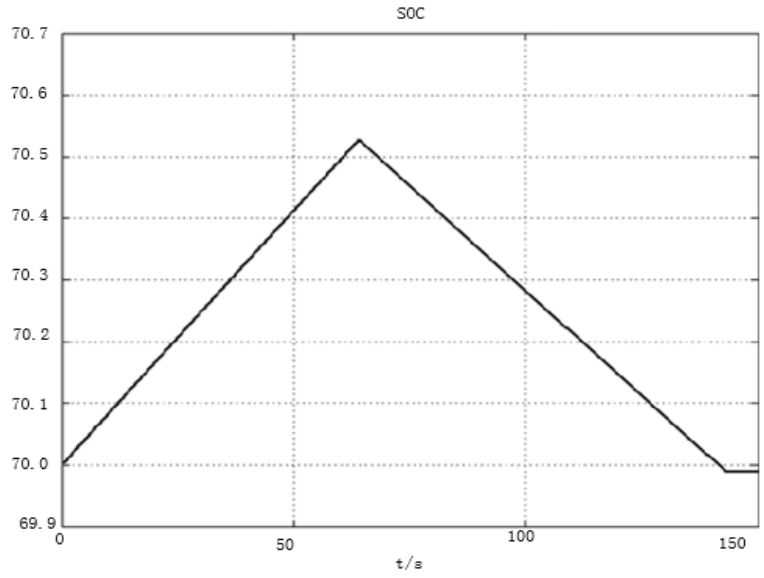

Figure 6: SOC change diagram of single cell for balanced battery pack

As you can see from Figure 6, the SOC of the single cell in the equalisation battery is increased by about 0.53%, because the first cell is discharged at the moment. When the first cell is balanced to a set threshold, the equalisation is stopped. The charge of the equalisation battery pack is about 29.7mAh, and then the third batteries are started and charged evenly, and the SOC of the battery pack is balanced. When the third cell SOC reaches a balanced setting threshold, the balance is completed.

For the first and third batteries, the initial SOC is 2% different from the average SOC of the battery pack. After equalisation, the SOC of the first cell is about 70.7%, and the SOC of the third cell is about 68.9%. In the first section, the battery transfers 1.3% of its charge to the equalisation battery pack, then equalisers the battery and transfers the charge to the third cell. As you can see from Figure 6, since the SOC of the balanced battery group remains the same after two equaliser, it can be considered that the charge of the first battery is transferred to the third cell, and the balanced battery group is only acting as a medium in this case.

The conversion efficiency is calculated below. If there are two single cells B1 and B2, if the partial charge of the B1 battery is transferred to the B2 battery, At the level of charge transfer, the expression of conversion efficiency is shown in Equation 5.

Equation 5 :Balanced efficiency

$$\eta = \frac{Q_g}{Q_1} \times 100\%$$

Where:

Q_1= B1 battery loss of charge(C)

Q_2= the amount of charge obtained by B2 battery(C)

The combination Equation 5, two times equalisation, single battery discharge equalisation and charge equalisation are shown in Table 2 respectively.

Table 2: Equilibrium conditions

	Q_g	Q_l	η
Two equilibrium	25.2mAh	36.4mAh	69.2%
Discharge equalisation	29.7mAh	36.4mAh	81.6%
Charge balance	25.2mAh	29.7mAh	84.8%

In the two equilibrium, Q_g is the power of third batteries, and Q_1 is the first battery loss. When the discharge is balanced, Q_g equalise the amount of power obtained by the battery pack, and Q_1 is the first battery loss. When charging is balanced, Q_g is the power of third batteries, and Q_1 is the power loss of the battery pack. Because the components used in the equalisation circuit are more reasonable, the efficiency of equalisation conversion is at a higher level.

5. CONCLUSION

The active equalisation circuit with balanced power supply proposed in this paper applies the multiple utilisation of the balanced power supply to the N-cell battery storage battery pack in series. The prerequisite for using N+1 + 4 switches and a bidirectional DC-DC converter. Next, to achieve the balance of any single cell. The included balanced power supply can not only balance the battery pack, but also give full play to its advantages of standby power supply, prolong the service life of the battery pack and improve the reliability of the battery pack. Simulations using MATLAB/SIMULINK software confirmed the feasibility of the proposed circuit. Although this circuit solves most of the problems in the active equalisation circuit at the same time, it has the disadvantage that only one cell can be balanced at the same time. This is a problem that needs to be studied and solved in the future.

6. REFERENCES

Wang Y, Zhang C, Chen Z. 2016. An adaptive remaining energy prediction approach for lithium-ion batteries in electric vehicles. Journal of Power Sources, 305, 80-88.

Chen Y, Liu X, Cui Y, et al. 2016. A MultiWinding Transformer Cell-to-Cell Active Equalisation Method for Lithium-Ion Batteries With Reduced Number of Driving Circuits. IEEE Transactions on Power Electronics, 31(7), 4916-4929.

Wei J, Dong G, Chen Z, et al. 2017. System state estimation and optimal energy control framework for multicell lithium-ion battery system. Applied Energy, 187, 37-49.

Qi J, Lu DC. 2017. A Preventive Approach for Solving Battery Imbalance Issue by Using a Bidirectional Multiple-Input Ćuk Converter Working in DCVM. IEEE Transactions on Industrial Electronics, 64(10), 7780-7789.

Lee KM, Lee SW, Choi YG, et al. 2017. Active Balancing of Li-Ion Battery Cells Using Transformer as Energy Carrier. IEEE Transactions on Industrial Electronics, 64(2), 1251-1257.

Zheng X, Liu X, He Y, et al. 2017. Active Vehicle Battery Equalisation Scheme in the Condition of Constant-Voltage/Current Charging and Discharging. IEEE Transactions on Vehicular Technology, 66(5), 3714-3723.

Chen H, Zhang L, Han Y. 2015. System-Theoretic Analysis of a Class of Battery Equalisation Systems: Mathematical Modeling and Performance Evaluation. Vehicular Technology IEEE Transactions on, 64(4), 1445-1457.

Zhang Z, Gui H, Gu DJ, et al. 2017. A Hierarchical Active Balancing Architecture for Lithium-ion Batteries. IEEE Transactions on Power Electronics, 32(4), 2757-2768.

Cui X, Shen W, Zhang Y, et al. 2017. Novel active LiFePO 4 battery balancing method based on chargeable and dischargeable capacity. Computers & Chemical Engineering, 97, 27-35.

Baronti F, Roncella R, Saletti R. 2014. Performance comparison of active balancing techniques for lithium-ion batteries. Journal of Power Sources, 267(4), 603-609.

Hannan MA, Hoque MM, Peng SE, et al. 2017. Lithium-ion battery charge equalisation algorithm for electric vehicle applications. IEEE Transactions on Industry Applications, 53(3), 2541-2549.

Kim MY, Kim JH, Moon GW. 2014. Center-Cell Concentration Structure of a Cell-to-Cell Balancing Circuit With a Reduced Number of Switches. IEEE Transactions on Power Electronics, 29(10), 5285-5297.

Bouchhima N, Schnierle M, Schulte S, et al. 2016. Active model-based balancing strategy for self-reconfigurable batteries. Journal of Power Sources, 322, 129-137.

Huang W, Qahouq JAA. 2015. Energy Sharing Control Scheme for State-of-Charge Balancing of Distributed Battery Energy Storage System. IEEE Transactions on Industrial Electronics, 62(5), 2764-2776.

Campestrini C, Keil P, Schuster SF, et al. 2016. Ageing of lithium-ion battery modules with dissipative balancing compared with single-cell ageing. Journal of Energy Storage, 6, 142-152.

171: Research on SOC estimation method of multi-rotor UAV battery based on improved extended Kalman filter

Yu ZHANG [1], Li-jie WANG[2], Tie-zhou WU[3]

[1] *Hubei Key Laboratory for High-efficiency Utilisation of Solar Energy and Operation Control of Energy Storage System，Hubei University of Technology, 542540666@qq.com*

[2] *Hubei Key Laboratory for High-efficiency Utilisation of Solar Energy and Operation Control of Energy Storage System，Hubei University of Technology, wanglijie778@qq.com*

[3] *Hubei Key Laboratory for High-efficiency Utilisation of Solar Energy and Operation Control of Energy Storage System，Hubei University of Technology, 1297362526@qq.com*

Multi-rotor UAV is a special unmanned rotorcraft with three or more rotor shafts, used in many fields. The Multi-rotor UAV generally uses a battery as a power source, so accurately estimating the Battery State of Charge (SOC) in a Multi-rotor UAV energy management system is crucial, which confirms the Multi-rotor UAV can be operated efficiently and safely. But, because the working condition of Multi-rotor UAV is special, the error of battery SOC is estimated by the current integration method, which has cumulative error. Although the SOC value estimated by the current integration method is verified in actual industrial applications, it does not fundamentally solve the problem that the current integration method relies on the initial value and the accumulated error is large. Kalman filter method estimates battery SOC independent of initial value and does not produce error, and the SOC estimation accuracy can be improved by using the EKF method. Aiming at the special working conditions of the Multi-rotor UAV, the filtering gain of the EKF method is improved for the dynamic adjustment of the filter gain. Effectively improve the tracking performance of the EKF method. The experimental results show that the improved Kalman filter can quickly track the true SOC value when the current mutates, and the tracking effect increases by about 70%.The tracking effect of the estimation process is improved by using the filter gain of the dynamic correction, which improve the real-time performance of the estimated SOC value to ensure that the accuracy of the Multi-rotor UAV SOC value is within 5%, effectively solving the problem of inaccurate estimation of the SOC value of the Multi-rotor UAV in the project.

Keywords: State of Charge; Multi-rotor UAV; Kalman filter

1. INTRODUCTION

Due to its simple structure, good manoeuvrability, and low manufacturing cost, multi-rotor UAVs are widely used in military and civilian neighbourhoods such as reconnaissance and aerial photography. In order to ensure that the Multi-rotor UAV can effectively accomplish specified tasks, the design of its structure, energy management system, and control system is particularly important (Le, 2014:87-91). Currently, multi-rotor UAVs have been miniaturised and lightened with the development of research, but they have not been able to meet the special needs of specific occasions. With the improvement of applications, higher requirements are imposed on the cruising range and stability. Therefore, accurately estimating the SOC in the UAV energy management system is crucial to ensure the efficient and safe drone operation, but also to avoid the impact of overcharge or over discharge drone battery life. But the remaining capacity of the battery is related to many factors, and the working condition of the drone is special, which makes the estimation of the battery SOC value complicated and the accuracy is difficult to guarantee (Li, 2014:361-371).

SOC estimation methods mainly include open circuit voltage method, current integration method, Kalman filter method, and neural network method (Liu, 2015:3533-3535). The current integration method is commonly used in Multi-rotor UAVs, but Multi-rotor UAVs have special operating conditions. Accuracy of the SOC value estimated by the current integration method is not ideal, and it will produce an accumulated error (Wu, 2018:1-11). Although the SOC value estimated by the current integration method will be verified in actual industrial applications, it does not fundamentally solve the problem that the current integration method depends on the initial value and the accumulated error is large. The open-circuit voltage method cannot be used to estimate the SOC value in real-time online. The neural network method is very dependent on the training method and training data, so it has not yet been well used. The Kalman filter estimates the battery SOC independent of the initial value and does not generate errors (Hong, 2011:1461-1469). It is suitable for applications where the current change amplitude is large, and a comprehensive analysis of the Kalman filter method is more suitable for use in MULTI-ROTOR UAVs. Vehicle SOC estimation (Meidoubi, 2016:2391-2402).

This paper first analyses the special working conditions of Multi-rotor UAVs in industrial production. Based on this, it analyses the root cause of estimation of SOC value by current integration method, and proposes to use extended Kalman filter method to estimate the SOC value of Multi-rotor UAVs, aiming at expanding Kalman (Charkhgard, 2010:4178-4187).The filter method has poor tracking effect in industrial production. This paper optimises it, improves its filter gain as the dynamic change gain, and improves the tracking effect of the extended Kalman filter applied to the SOC estimation of the Multi-rotor UAV. Finally, through a series of experiments, the accuracy and effectiveness of the extended Kalman filter algorithm was verified, and the improved tracking performance of the improved Kalman filter algorithm was verified (Li, 2015:88-90).

2. MULTI-ROTOR UAV CONDITION ANALYSIS

The multi-rotor drone has a faster working rhythm change during normal operation, and is basically charged only after the work is over. And because the drone works in the sky, it emphasises the accurate estimation of its lithium battery SOC, ensuring that the body does not fall due to exhaustion. This paper selects INSPIRE2 aerial four-rotor UAV, charging power is 180W, charging current is 6.9A, battery capacity is 4480mAh, charging rate is 1.54C, charging time is generally 3.5 hours, and its working discharge time is 45 minutes. Left and right, the discharge rate is 10C or more (Du, 2015:1385-1395). Figure 1 depicts the charging and discharging changes of the drone within 4 hours, t_1-t_2 is the vertical motion current when the drone is rising, and t_2-t_3 is the current when the drone is moving forward and backward. The discharge current is positive and the charging current is negative. It can be seen that in 4 hours, the drone is charged twice for more than 3 hours, and the running time is only about 1 hour (Du, 2016:477-481). How to fluctuate at such high current and high charging frequency Under the rigorous estimation of the SOC value of the multi-rotor UAV lithium battery is a problem worth studying.

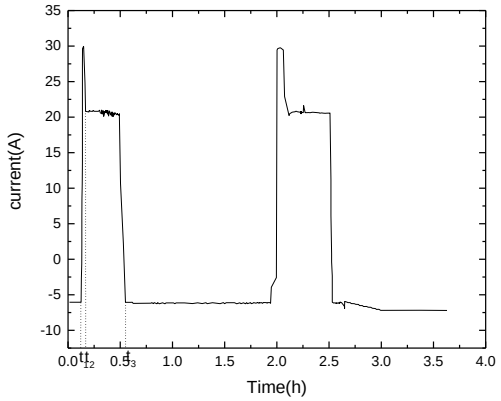

Figure 1: Current variation diagram of actual Multi-rotor UAV(DU.2016:477-481)

The current integration method is a common method for estimating the SOC value. However, the current integration method relies on the initial value and requires a high accuracy of the current measurement. The Multi-rotor UAV cannot guarantee the initial SOC value and current measurement accuracy under special conditions, so the current integral accuracy of estimating the SOC value of the Multi-rotor UAV is not very high. The basic idea of the Kalman filtering method is a constant weighted iterative process, there are two values in the entire filtering process, namely the predicted value of the model and the measured value of the instrument, and then the predicted value and the measured value are performed. Comprehensive weighting gives the best estimate, Kalman filter method does not depend on the initial value and does not produce an accumulated error, which can guarantee the accuracy of the SOC value under special conditions. But the Kalman filter method relies on the battery model, the accuracy of the battery model directly affects the accuracy of the SOC estimation. Therefore, establishing the battery model accurately is the basis for estimating the SOC value by the Kalman filter method.

3. BATTERY MODEL SELECTION

This article uses the Thévenin model to carry on the equivalent to Multi-rotor UAV battery. This model can describe the mutation and gradual change characteristics of the Li-ion battery during charge and discharge. The equivalent circuit diagram is shown in Figure 2, where R_0 describes the resistive characteristics of the lithium battery during charge and discharge, R_p and C_p simulate the gradual capacitance characteristics of the battery. Parameters in the battery equivalent circuit model can be identified by performing intermittent pulse charge and discharge experiments on the battery. Calculate the internal resistance and capacitance of the circuit model by the voltage rise and fall and charge and discharge times of the battery during the charge and discharge process in the experiment (Liu, 2017:1-4).

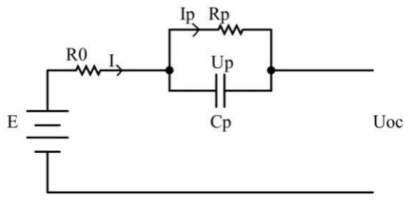

Figure 2: Battery Equivalent Circuit Schematic

In Figure 2, E is the battery electromotive force, R_0 is the battery internal resistance, R_p and C_p are polarisation resistance and polarisation capacitance, U_{oc} is the battery open circuit voltage, I is the total battery current, I_p is the current through the polarisation resistance, U_p is the voltage across the polarisation resistance and polarisation capacitance. The principle of the Kalman filter method shows that in the process of filtering, a state quantity and an observation measure are needed, and the SOC value cannot be measured directly(Gong, 2015:139-140). Therefore, select U_p as the state variable, and perform linearisation and discretisation processing. The equation of state is shown in Equation 1. Select the detected battery terminal voltage U_{oc} for observation, the established observation equation is shown in Equation 2.

Equation 1: Linearisation and discretisation processing state equation.

$$\begin{bmatrix} U_{p,k} \\ SOC_k \end{bmatrix} = \begin{bmatrix} 1-\frac{T}{C_p R_p} & 0 \\ 0 & 1 \end{bmatrix} \begin{bmatrix} U_{p,k-1} \\ SOC_{k-1} \end{bmatrix} + \begin{bmatrix} \frac{T}{C_P} \\ \frac{\eta T}{C} \end{bmatrix} [I_{k-1}] + \begin{bmatrix} w_{1,k-1} \\ w_{2,k-1} \end{bmatrix}$$

Equation 2: Observation equation.

$$[E_k] = [1 \ 0] \begin{bmatrix} U_{p,k} \\ SOC_k \end{bmatrix} + [R_0][I_k] + [U_{oc}] + [v_k]$$

Where:

U_p = the voltage across the polarisation resistance and polarisation capacitance(V)

- $U_{p,k}$ = the value of U_p at time k(V)
- $U_{p,k-1}$= the value of U_p at time $k-1$(V)
- SOC_k = the battery SOC value at time k
- SOC_{k-1} = $k-1$ time SOC value
- T = the system's sampling time
- $w_{1,k-1}$ and $w_{2,k-1}$ = the system noise

E_k = K time electromotive force(V)

- R_p = polarisation resistance(Ω)

C_p = polarisation capacitance(F)

- R_0 = Internal resistance(Ω)

I_k = k moment current(Ah)

The matrix required by the Kalman filter from Equation 1 and Equation 2 is given by Equation 3

Equation 3: The required matrix for Kalman filtering.

$$\begin{cases} X_k = \begin{bmatrix} U_{p,k} \\ SOC_k \end{bmatrix} \\ A_k = \begin{bmatrix} 1-\frac{T}{C_P R_P} & 0 \\ 0 & 1 \end{bmatrix} \\ B_k = \begin{bmatrix} \frac{T}{C_P} \\ \frac{\eta T}{C} \end{bmatrix} \\ C_k = \frac{\partial E}{\partial X} = \begin{bmatrix} \frac{\partial E}{\partial U_p} & \frac{\partial E}{\partial SOC} \end{bmatrix} \end{cases}$$

Among them $\frac{\partial E}{\partial U_P} = 1$, $\frac{\partial E}{\partial SOC} = \frac{\partial U_{OC}}{\partial SOC} + I * \frac{\partial R_0}{\partial SOC}$,

The relationship between R_0 and SOC, U_{oc} and SOC, can be obtained by fitting the charge and discharge data.

4. IMPROVED EXTENDED KALMAN FILTER ALGORITHM FOR ESTIMATING MULTI-ROTOR UAV SOC VALUE

The Kalman filter method is aimed at the optimal estimation of the linear system. The extended Kalman filter algorithm is a generalisation of the traditional Kalman filter algorithm and is suitable for the optimal estimation of the nonlinear system. The battery is a typical nonlinear system, so it needs to use the extended Kalman filter to estimate its remaining capacity (Xing, 2015:52-54). The state equations and observation equations of the system are obtained through the modelling of the battery, and the Kalman filtering process shown in Equation 4 can be obtained by combining the characteristic equations of the Kalman filter method.

Equation 3: Kalman filtering process.

$$\begin{aligned} \hat{X}_{k/k-1} &= A_{k-1}\hat{X}_{k-1/k-1} + B_{k-1}I_k \\ P_{k/k-1} &= A_{k-1}P_{k-1/k-1}A_{k-1}^T + Q_{k-1} \\ K_k &= P_{k/k-1}C_k^T (C_k P_{k/k-1} C_k^T + R_k)^{-1} \\ \hat{X}_{k/k} &= \hat{X}_{k/k-1} + K_k \left[Z_k - H_k \hat{X}_{k/k-1} \right] \\ P_{k/k} &= (I - K_k C_k) P_{k/k-1} \end{aligned}$$

Where:

$\hat{X}_{k/k-1}$ = the estimate of k to k-1 includes k time observations.

$\hat{X}_{k/k}$ = the estimate of k time

A_{k-1}, B_{k-1} = parameter matrices

I_k = the current state of control

$P_{k/k-1}$ = the covariance of $\hat{X}_{k/k-1}$

$P_{k/k}$ = the covariance of $\hat{X}_{k/k}$

K_k = the Kalman Gain

Q_{k-1} = the covariance of the system process

C_k = the coefficient matrix of the observation equation

Z_k = Observation at time k value

R_k = Covariance of measured values

H_k = Mapping matrix of observation space

The initial conditions of the filter equation are initial value SOC_0 of SOC, initial voltage $U_p(0)$ across C_p , and covariance P_0 of estimation error. SOC_0 is obtained by reading the last SOC value. $U_p(0)$ is generally 0 at initialisation and the initial value of the estimated error covariance P_0 is selected according to engineering practice experience. Normally, the accuracy of these initial values does not affect the estimated SOC value very much, because the Kalman filter is very robust to the poor initial accuracy and can be quickly convergence to the real value, if the initial value is reasonable, then the Kalman filter converges to the true value faster. If the value is unreasonable, the convergence rate will be relatively slow, and it takes multiple iterations to converge to the true value, but eventually it will the error caused by the inaccuracy of the initial value is eliminated [7]. This is the reason why the extended Kalman filter method estimates the SOC value of the multi-rotor UAV independent of the initial value. The extended Kalman filter estimates the battery SOC is that when k=1, 2, 3, ..., it loops through Equation 4 to converge the state quantity to the true value.

The specific estimation process is as follows:

1) According to the first formula in Equation 4, the battery-equivalent model is used for prediction, and the state quantity at time k-1 is used to predict the state quantity at time k;

2) According to the second formula in Equation 4, calculate the error covariance matrix of the prediction value, determine the accuracy of the prediction, and prepare for the weight distribution;

3) Calculate the Kalman filter gain according to the third formula in Equation 4, that is, assign the weight to the measured value and the predicted value, and then correct the state quantity through the Kalman filter gain;

4) According to the fourth formula in Equation 4, Kalman's optimal estimation is performed by using this formula, and the predicted state information is used to back-measure, then the difference between the measured value Z_k and the back-calculated value is calculated, and then the comprehensive weighting is performed;

5) According to the fifth formula in Equation 4, this formula is to evaluate the calculated optimal results, calculate the accuracy of the optimal results, and also to prepare for the next moment, to ensure that the follow-up can be repeated go on.

The Kalman filter method estimates the battery SOC value by iterating through the above five steps, so that the SOC value converges to the true value, and there is no dependence on the initial value during the estimation process, and there is no accumulated error. The estimated SOC The value accuracy and stability are higher than the current integration method, but the multi-rotor UAV operating conditions are special, and the frequency of the current mutation is high. Under actual operating conditions, the extended Kalman filter method is used to estimate the SOC's tracking effect when the current is abrupt, resulting in poor SOC estimation. Accuracy and real-time performance. So we need to improve the extended Kalman filter method to speed up the prediction of the algorithm when the current is abrupt, and improve the accuracy and real-time performance of the SOC under special conditions.

Accelerating the prediction speed of the algorithm when the current suddenly changes requires the algorithm to increase the correction range of the SOC value at the moment when the current suddenly changes. From Equation 4, increasing the value of the filter gain K_k can increase the update amount of the state quantity and speed up the algorithm's tracking speed. To improve the prediction speed of the extended Kalman filter algorithm under special

conditions, it is necessary to increase the filter gain at the beginning of the mutation and reduce the filter gain after the mutation, so as to achieve a dynamic correction of the SOC.

Let improved filter gain be K_k' and the state update of the extended Kalman filter algorithm is shown in Equation 5.

Equation 5: Extended Kalman filter algorithm.

$$\hat{X}_{k/k}' = \hat{X}_{k/k-1}' + K_k'\left[Z_k - H_k\hat{X}_{k/k-1}\right]$$

Where:

$\hat{X}_{k/k}'$ = the improved k time observations.

$\hat{X}_{k/k-1}'$ = the improved estimate of k to k-1 includes k time observations.

K_k' = the improved Kalman Gain

Z_k = Observation at time k value

H_k = Mapping matrix of observation space

By Equation 5 available:

Equation 6: Converted equation

$$K_k'\left[Z_k - H_k\hat{X}_{k/k-1}\right] = \hat{X}_{k/k}' - \hat{X}_{k/k-1}'$$

By Equation 4 available:

Equation 7: Converted equation

$$K_k\left[Z_k - H_k\hat{X}_{k/k-1}\right] = \hat{X}_{k/k} - \hat{X}_{k/k-1}$$

Let the filter gain correction function be *W(t)*, which can be obtained from Equation 6 and Equation 7:

Equation 8: Linked equations

$$W(t) = \frac{K_k'\left[Z_k - H_k\hat{X}_{k/k-1}\right]}{K_k\left[Z_k - H_k\hat{X}_{k/k-1}\right]} = \frac{\hat{X}_{k/k}' - \hat{X}_{k/k-1}'}{\hat{X}_{k/k} - \hat{X}_{k/k-1}}$$

$$= \frac{K_k'}{K_k} = \frac{\hat{X}_{k/k}' - \hat{X}_{k/k-1}'}{\hat{X}_{k/k} - \hat{X}_{k/k-1}}$$

The filter gain increases at the beginning of the mutation and increases the correction amplitude. As the mutation progresses, the filter gain gradually decreases, and the normal value is restored after the mutation is over. To find out the variation law of the filter gain correction function under special conditions, this paper Select the experimental data and find the correction function through data fitting. Experimental data is shown in Table 1.

Table 1: Correction function fitting experimental data

t	K'/K	t	K'/K
0	2.001	0.5	1.7822
1	1.6124	1.5	1.4788
2	1.3746	2.5	1.2931
3	1.2292	3.5	1.1792
4	1.1402	4.5	1.1098
5	1.0859	6	1.0525
7	1.0322	8	1.0196

Using the Matlab least square method to fit the experimental data, the functional relationship as shown in Equation 9 can be obtained.

Equation 9: Least Squares Fitting Function Relationship of Experimental Data

$$W(t) = 1.011e^{-0.4909t} + 0.9998$$

Simplify Equation 9 to get:

Equation 10: Simplified equation

$$W(t) = 0.6121^{t} + 0.9998$$

Draw the experimental data graph in Matlab, as shown in Figure 3. The first 6 seconds in Figure 3 is the sudden change of current. The correction function makes the filter gain larger and the correction range of SOC value larger at the beginning of the mutation. After the mutation, the filter gain value returns to normal value. This filter gain can be adjusted dynamically based on the mutation, speeding up the algorithm's tracking speed.

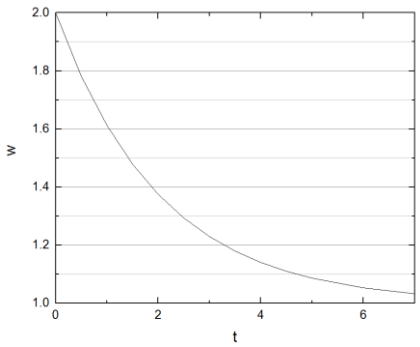

Figure 3: Current variation diagram of actual Multi-rotor UAV

According to the fitting of experimental data, it can be concluded that the correction function conforms to the exponential function, and the dynamic correction function is shown in Equation 11.

Equation 11: Dynamic correction function

$$\delta=1+\varphi\beta^{t}$$

Where:

- β = adjustment factor
- φ = adjustment amplitude factor
- t = the duration of the system mutation

Then, the gain K_k' in the extended Kalman filter algorithm is improved as shown in Equation 12.

Equation 12: Extended gain in Kalman filter algorithm

$$K_k' = \delta K_k$$
$$K_k' = (1+\varphi\beta^{t})P_{k/k-1}C_k^T(C_kP_{k/k-1}C_k^T + R_k)^{-1}$$

Where:

- β = adjustment factor
- φ = adjustment amplitude factor
- t_0 = the time at which the mutation starts
- t' = time at which the mutation ends
- t = the duration of the system mutation = t_0-t'

In Equation 12, β is an adjustment factor, and its value is a number from 0-1. This parameter can adjust the duration of current mutation. If the mutation time lasts for a short time, the value of this parameter is smaller, if the mutation time duration is longer the value of this parameter is long, and the specific value can be determined according to the actual project. φ is the adjustment amplitude factor. This parameter can track the mutation intensity of the system. If the mutation intensity is greater, the value of this parameter is larger and the mutation intensity is smaller. From this, the gain change in the improved extended Kalman filter algorithm can be calculated as shown in Equation 13.

Equation 13: Extended Kalman filter algorithm for gain changes

$$\delta = 1+\varphi(t\to 0)$$
$$\delta=1(t\to\infty)$$
$$K_k'=(1+\varphi)K_k(t\to 0)$$
$$K_k' = K_k(t\to\infty)$$

After improving the extended Kalman filter gain, the system expands the filter gain at the beginning of the mutation to $1+\varphi$ without improvement. The correction range of the system SOC value becomes large and quickly converges to the true value; with the end of the mutation, filtering the gain gradually becomes smaller and eventually returns to K_k. In this way, the dynamic adjustment of the filter gain in the extended Kalman filter algorithm is implemented, and the dynamic amplitude change is corrected, which is favorable for the system to more quickly converge to the true value in the case of mutation and reduce the observation value in the extended Kalman filter algorithm. Hysteresis affects the influence of SOC estimation accuracy and improves the system's tracking ability.

5. EXPERIMENTS AND ANALYSIS

This project has carried out a series of experiments to verify the effect of using the extended Kalman filter to estimate the SOC value of the multi-rotor UAV lithium battery. Based on this, it is proved that the improved filter gain has better tracking effect. The experiment first compares the different results of the extended Kalman filter and the current integration method in estimating the SOC of the lithium battery of the drone. Secondly, the extended Kalman filter method with improved filter gain and the comparative experiment without improvement are made.

In this paper, the algorithm verification program is written by Keil,and the current of the INSPIRE2 aerial four-rotor UAV is collected and simulated by STM32. Finally, the extended Kalman filter method and current integration method are used to calculate the SOC value of the drone. The result is shown in Figure 4.

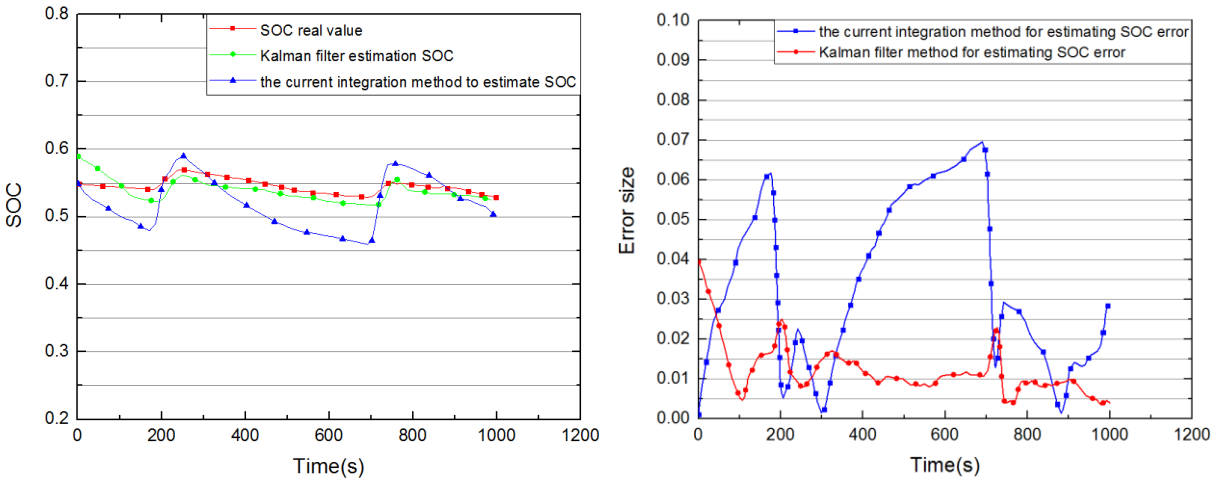

(a) Different methods for estimating curves *(b) Error curve*

Figure 4: Comparison curve of SOC estimation

In order to ensure the accuracy of the current integration method in the experiment, given its initial value is accurate, and the initial value of the Kalman filter method has a large error. The experimental results show that the error of current integration is larger and the maximum error exceeds 7%, and this error range is generated when the initial value is accurate. If the initial value is inaccurate, the error range will be further enlarged. While the Kalman filter method is inaccurate in the initial value, as the number of iterations increases, the estimation result gradually converges to the true value, the error range can basically be controlled within 4%, and the accuracy is obviously higher than current integration. But from the results of the comparison curve can also be seen that the extended Kalman filter method also has some problems. Two circles are marked in Figure 5(a). It can be seen in each circle that the SOC value estimated by the Kalman filter lags behind the true value, resulting in a relatively large error, because when the multi-rotor UAV vehicle current suddenly changes, the observation voltage of the extended Kalman filter is lagging, which leads to the lag of the SOC estimation. In order to solve this problem, the extended Kalman filter method is improved, that is, the adjustment gain in the extended Kalman filter algorithm is set to dynamic gain, in this experiment β=0.5, φ =1, for the improved algorithm experiments were performed and the results are shown in Figure 5(b).

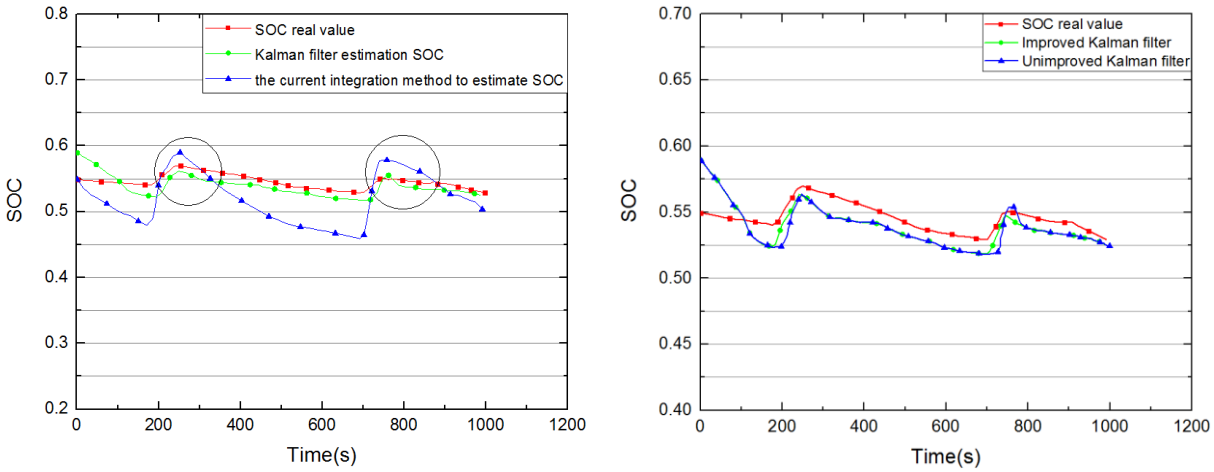

(a) Optimised pre-SOC curve *(b) Optimised SOC curve*

Figure 5: Extended Kalman filter algorithm tracking effect

From the improved experimental results, the accuracy of the SOC estimation is further improved. Compared with the improved Kalman filter algorithm, the tracking effect is better, and the current value can be converged to the true value quickly when the current mutates. To further illustrate that the optimised Kalman filter algorithm has better tracking effect, the SOC value is improved, the SOC value estimated by the pre-Kalman filter method is improved, and the SOC value estimated by the improved Kalman filter method is amplified and compared. The results are shown in Figure 6. The improved Kalman filter can quickly track the true SOC value when the current mutates, and the tracking effect increases by about 70%, so the magnitude of the current change in the Multi-rotor UAV is large. Under the operating conditions, the improved Kalman filter method estimates the SOC value more accurately.

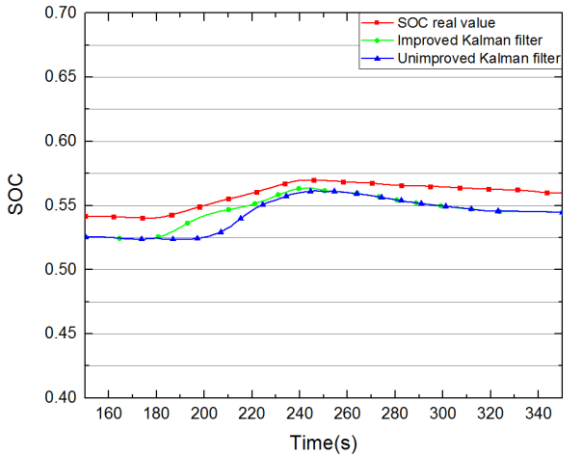

Figure 6: Comparison of tracking effect

6. CONCLUSION

Based on solving practical problems in industrial production, this paper fully analyses the special working conditions of Multi-rotor UAVs and points out the reason why the Ah-hour integration method is inaccurate in estimating its SOC value. It proposes to use Extended Kalman Filter to estimate its battery SOC value, aiming at the traditional expansion. The Kalman filter method has a poor tracking effect, improves its filter gain as a dynamic change gain, improves the real-time performance of the estimated SOC value, ensures that the accuracy of the Multi-rotor UAV SOC value is within 5%, and effectively solves the SOC value estimation of the Multi-rotor UAV in the project.

7. REFERENCES

Le S, Wang Y, Liu S, et al. 2014. Numerical analysis of aerodynamic characteristics of a new hybrid unmanned aerial vehicle[J]. *Computer Simulation*, 31(6): 87-91.

Li P, Zhao Q. 2014. CFD Calculation of Hovering State Rotor/Airfoil Interference Flow Field and Aerodynamic Force[J]. *Journal of Aeronautic*s,35(2):361-371

Liu S, Li Y, Zhao Z, Yu Y, Huang J. 2015. Research and implementation of charge state estimation of lithium battery for electric vehicle based on DSP[J]. *Computer Measurement & Control*, (10), 3533-3535.

Wu T, Wang Y, Xu Y, Guo L, Shi X, He S. 2018. HEV energy optimisation control strategy based on PMP algorithm [J/OL]. *Journal of Automation*: 1-11

Hong W, Rui X, Xiao W, Feng C, Jin X. 2011. State-of-Charge Estimation of the Lithium-Ion Battery Using an Adaptive Extended Kalman Filter Based on an Improved Thevenin Model[J].*IEEE Transactions on Vehicular Technology*, Vol .60 (No. 4), 1461-1469.

Meidoubi A, Oukaour A, Chaoui H, Gualous H, Sabor J, Slamani Y, 2016. State-of-Charge and State-of-Health Lithium-Ion Batteries' Diagnosis According to Surface Temperature Variation[J].*IEEE Transactions on Industrial Electronics*. Vol.63(No.4), 2391-2402.

Charkhgard M, Farrokhi M. 2010. State-of-Charge Estimation for Lithium-Ion Batteries Using Neural Networks and EKF[J]. *Industrial Electronics, IEEE Transactions on*. Vol.57 (No.12), 4178-4187.

Li S, Yu L. 2015. Research on Multivariable Control Structure Design of Aircraft Power System[J]. *Measure and Control Technology,* 34(2): 88-90.

Du Y, Fang J, Sheng W, Lei X. 2015. An autonomous take-off control method for small unmanned helicopters. *Automatic Chemistry*, 38(8):1385-1392.

Du M, Jin F. Design and control of a mini quad-rotor UAV based on embedded system, 2016. *Advanced Materials Research*, 442: 477-481.

Liu J, Zhang J. 2017.A Control Method of Supercapacitor-Battery Hybrid Energy Storage System[J]. *Electric Power Science and Engineering*, 27(001): 1-4.

Gong J, Deng H, Xie Y. 2015. Energy storage technology classification and domestic large-capacity battery energy storage technology comparison. *China Science and Technology Information,* 22(09): 139-140.

Xing M. 2015. China's implementation of new energy vehicles policy and effect analysis [J]. *Economic Research Guide*, (6): 52-54.

172: A study on force-bearing capacity of joints of transmission tower subjected to wind loads

Yinghua BAI[1], Kang SHEN[1], Xianghai TAO[2], Bo CHEN[3]

[1]*Yinghua Bai, School of Civil Engineering, Architecture and Environment, Hubei Univ. of Tech.,Wuhan 430064, China, yhbai750608@163.com.*
[1]*Kang Shen, School of Civil Engineering, Architecture and Environment, Hubei Univ. of Tech.,Wuhan 430064, China, 837980624@qq.com.*
[2]*Xianghai Tao, Zhanjiang Power Supply Bureau, Guangdong Power Grid Corporation Co. Ltd, Zhanjiang 524037,China, cexhtao@163.com*
[3]*Bo Chen, Key Laboratory of Roadway Bridge and Structural Engineering, Wuhan Univ. of Tech.,Wuhan 430070, China, cbsteven@163.com.*

The transmission tower-line system, which is widely used in electric infrastructures across the world, generally possesses a small stiffness and low structural damping. The excessive vibration of a transmission tower-line system subjected to external excitations may induce a damage or failure, which has been frequently reported across the world. The effects of external loads on joint strength of transmission tower-line systems have not been examined in detail. In this regard, the force-bearing capacity of transmission tower joints is actively investigated in this study. A three dimensional analytical model of a tower joint is established with the aid of commercial package ABAQUS. The analytical model of bolt is developed by simulating the pre-stressed forces acting on structural members. A nonlinear contact force model for the interacting between bolts and member is presented to precisely simulate the contact effect subjected to wind loads. A real transmission tower-line system constructed in China is taken as an example to examine the feasibility and reliability of the proposed joint analytical approach. The parametric study is conducted to investigate the effects of various factors on joint strength, such as bolt diameter, bolt strength, pre-stressed force, friction coefficients and etc. The made observations demonstrate that bolt stress is linearly positively correlated with the bolt pre-tightening force under normal service load, while it is linearly negatively correlated with the bolt diameter. The bolt stress of skew member is linearly correlated with bolt pre-tightening force and bolt diameter under the critical load. When the external load increases from the normal service load to the critical load, the bolt stress of oblique members remains linearly related to the bolt pre-tightening force and the bolt diameter, while the bolt preload, bolt diameter, and friction factor have different effects on performance of bolt in major members. The friction interaction among contact surface has little effects on the strength of bolts.

Keywords: transmission tower; joint; bolt strength; preload; bolt diameter,

1. INTRODUCTION

To be a typical spatial steel structure, the transmission tower is widely used as electrical power infrastructures throughout the world. The transmission tower is a high-rise structure with small damping and is prone to strong dynamic excitations, such as earthquakes and wind loadings. It is frequently reported across the world that the excessive vibration of a transmission tower under dynamic excitations may induce the structural damage and even failure. Therefore, it is necessary to evaluate the structural performance of the transmission tower subjected to external loads. Many theoretical and experimental investigations have been carried out during the past two decades for examining the performance of the transmission tower. With regard to the approaches and techniques used for performance evaluation, the transmission tower system is conventionally designed and constructed using appropriate design standards without considering the nonlinear contact interaction among bolts and members. The common approach does not provide deep insights into the joint behaviour under strong excitations. Thus, the nonlinear contact analytical approaches based on fine finite element models have been utilised in the performance evaluation of tower joints across the world. The assessment process need develop or improve a mathematical model of a joint system using nonlinear interaction to describe the contact relationship. Various strength analytical methods have been developed to improve the quality of the finite element model of a tower joint based on different contact models. With regard to the different interaction algorithm used, the effects of various physical parameters on the structural responses can be examined in detail to determine the crucial parameters for structural design and assessment. Under wind load, the bolts of the transmission tower may loosen, slide or even destroy, which will in turn threaten the structural safety. Li Jing (2015) proposed the optimal bolt tightening sequence in the assembly process of experiments. Li Wei (2016) used the software ANSYS to analyse the influence of contact pairs, contact types and contact algorithms. However, the strength assessment of tower joints subjected to wind excitations has not been examined in detail.

To this end, the force-bearing capacity of transmission tower joints is actively investigated in this study. A three dimensional analytical model of a tower joint is established with the aid of commercial package ABAQUS. The analytical model of bolt is developed by simulating the pre-stressed forces acting on structural members. A nonlinear contact force model for the interacting between bolts and member is presented to precisely simulate the contact effect subjected to wind loads. A real transmission tower-line system constructed in China is taken as an example to examine the feasibility and reliability of the proposed joint analytical approach. The parametric study is conducted to investigate the effects of various factors on joint strength, such as bolt diameter, bolt strength, pre-stressed force, friction coefficients and etc. The made observations demonstrate that bolt stress is linearly positively correlated with the bolt pre-tightening force under normal service load, while it is linearly negatively correlated with the bolt diameter. The bolt stress of skew member is linearly correlated with bolt pre-tightening force and bolt diameter under the critical load. When the external load increases from the normal service load to the critical load, the bolt stress of oblique members remains linearly related to the bolt pre-tightening force and the bolt diameter, while the bolt preload, bolt diameter, and friction factor have different effects on performance of bolt in major members. The friction interaction among contact surface has little effects on the strength of bolts.

2. JOINT MODEL OF TRANSMISSION TOWER

2.1. Structural configuration

A real transmission tower-line system constructed in southern coastal mountain areas of China as shown in Figure 1 is taken as an example to illustrate the configuration of the tower-line-mountain coupling model. Figure 2 shows the detailed configuration of a typical joint bolt. The tower is bears the wind load from north to south, with the maximum wind speed of 39.7m/s. And other transmission towers exist in the northwest direction of the tower at 553m and the southeast direction at 532m.

Table 1: Parameters of transmission tower joints

Part Name	Length (mm)	Width (mm)	Depth (mm)	Material Grade
Skew member 1	300	100	8	Q235
Skew member 2	300	90	7	Q235
Skew member 3	200	56	5	Q235
Skew member 4	300	100	8	Q235
Skew member 5	300	90	7	Q235
Skew member 6	200	56	5	Q235
Major member	1000	160	12	Q345
Connection plate	750	400	10	Q235
Bolts in cross member	50	-	20	Q235
Bolts in major member	60	-	20	Q235

The elevation of the tower is 31m and the structural members used in the transmission tower are made of Q235 steel with a yielding stress of 235 MPa. The Young's modulus of steel metal is 2.06×10^{11} N/m^2 and the density is 7800 kg/m^3. Vertical major members, skew members, cross arms and platforms of the tower are formed as a spatial truss tower as shown in Figure 1, respectively. Both the skew members and the major members are fabricated by angle steel members. The inclination θ_1 of the skew member 1 is 40°, and the inclination θ_2 of the skew member 2 is 49°. The precise geometric parameters of all components are listed in Table 1, and the detailed configuration of a typical joint bolt is shown in Figure 2. It should be noted in Table 1 that the lengths of the skew member bolt and the main member bolt are corresponding to the screw length, while the thicknesses of the skew member bolt and the main member bolt are corresponding to the screw diameter. The nut diameter and thicknesses are selected following Chinese design code *GB/T 6170-2000* (National Standard of the People's Republic of China, 2000).

The stress-strain relationship of steel material adopts the two-segment. The Poisson's ratio of the steel is 0.3. The yielding strength of the steel is denoted as f_y, and the ultimate yielding strength of the steel is *denoted as* f_u. The yielding strain of the steel is denoted as ε_s, and the material properties of steel are shown in Table 2.

Table 2: Physical properties of steel materials.

Type	f_y / MPa	f_u / MPa	ε_s	E / MPa
Q345	345	431	0.009	206
Q235	235	293	0.011	206

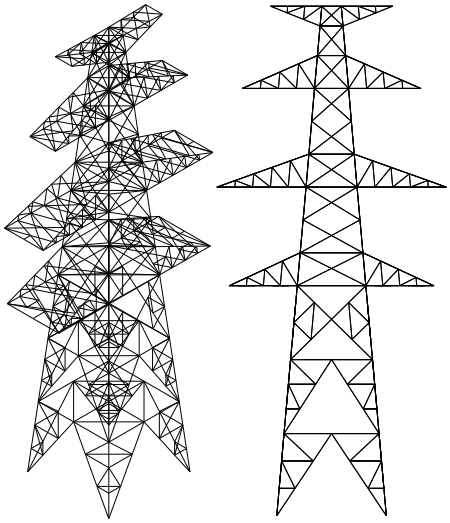

Figure 1: Configuration of example tower

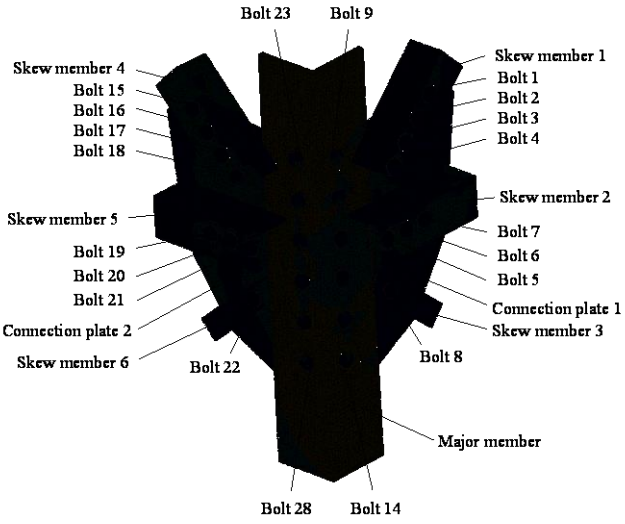

Figure 2: Configuration of example tower joint

2.2. Contact forces and loads of joint bolts

The contact problem presents highly nonlinear properties from the practical viewpoint. Therefore, it is necessary to select a suitable friction theory to evaluate the bolt contact problems Zhao (2015). The Coulomb friction contact model is used in this study. Following the Coulomb friction model, before the two contact surfaces slide, the interface can withstand a certain degree of shear stress, i.e. the state of adhesion. The sliding state is that when the equivalent shear stress on the contact interface reaches the ultimate shear stress and the surface starts to slide. Therefore, the coulomb friction force can be expressed as:

Equation 1: Coulomb friction force

$$\begin{cases} \tau_{\max} = \mu P + b \\ |\tau| \le \tau_{\max} \end{cases}$$

Where:

τ_{max} = the ultimate shear stress (Pa)
τ = the equivalent stress (Pa)
P = the normal stress (N)
b = the contact cohesion (N)
μ = the friction coefficient

It is essential to define the contact of the interaction module because the ABAQUS cannot identify contact problems automatically among different entities. According to *Steel Structure Design Code (GB 50017-2003)* the roughness of the steel paints is determined with a friction factor μ of 0.3. The friction contact diagram is displayed in Figure 3. The value of pre-tightening force Q should be determined according to load intensity as well as joint stiffness. The pre-tightening force applied on the model can be derived based on the torque T. In fact, the torque T is the sum of the frictional resistance moment T_1 between screw-thread and the frictional torque T_2 between the nut annular bottom, that is:

Equation 3: Tightening torque T .

$$T = T_1 + T_2$$

Equation 4: Frictional torque T_1 between screw-thread.

$$T_1 = Q\frac{d_2}{d}\tan(\lambda + \rho)$$

Equation 5: Thread angle λ .

$$\lambda = \arctan(\frac{p}{\pi d_2})$$

Equation 6: Thread equivalent friction angle ρ.

$$\rho = \arctan\mu$$

Equation 7: Friction torque T_2.

$$T_2 = \frac{1}{2}\mu Qd$$

Equation 8: Relationship between torque T and preload Q.

$$T = \frac{1}{2}\left[\frac{d_2}{d}\tan(\lambda + \rho) + \frac{d_m}{d}\mu\right]Qd$$

Equation 9: Preload factor K:

$$K = \frac{d_2}{d}\tan(\lambda + \rho) + \frac{d_m}{d}\mu$$

Where:

Q = the pretightening force (N)
T = the tightening torque (N.m)
T_1 = the rotary pair frictional resistance torque (N.m)
T_2 = the frictional resistance moment between annular end face and bearing surface (N.m)
λ = the thread angle (°)
P = the thread pitch (°)
ρ= the thread equivalent friction angle (°)
d_m = the average diameter of the nut bearing surface (m)
d_2 = the thread diameter (m)
d = the nominal diameter of the bolt (m)
μ = the friction factor of the nut bearing surface.

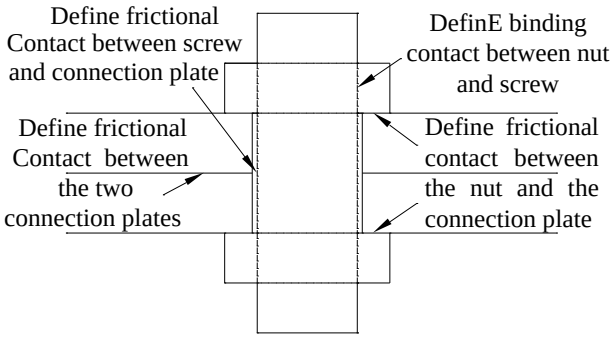

Figure 3: Friction contact diagram

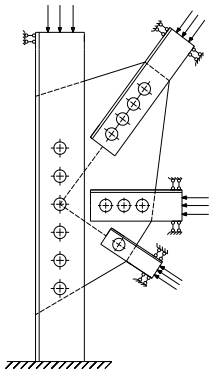

Figure 4: Boundary conditions and applied loads of joint

According to the boundary constraints of the real structure, one side of the main member is fixed and the other is directional bearing which only could move along the axis, the skew member is also considered to be fixed (Chen, Huang and Zhang, 2015; Chen, Xiao, Li and Zhong, 2015; Chen, Xu and Zhao, 2010). The uniform loads along the rod axis are applied at each rod end and the load information is listed in Table 3. The values of bolt torque is

determined based on the *Code for the Construction and Acceptance of 110~500KV Overhead Transmission Lines (GB 50233-2005)*.

Table 3: The load data of each component of the transmission tower joint

Part Name	Critical Load (kN)	Service Load (kN)
Skew member 1	-59.227	-17.76834
Skew member 2	61.460	18.43824
Skew member 3	-6.803	-2.04114
Skew member 4	-132.602	-39.7806
Skew member 5	28.805	8.64174
Skew member 6	-7.565	-2.269716
Main member	-935.926	-280.7778

3. CASE STUDY

Considering the nonlinearity of major members, skew members, gusset plates and bolts, the elastic-plastic characteristics of the material is determined by the von-Mises yield criterion according to the strengthening isotropic theory. The stress distribution of joint components and bolts are computed and displayed in Figures 5 and 6, respectively. It is observed that the stresses in the neighboring areas are much larger than those at other areas. Obviously, the stress concentration of the bolts is very clear because the internal forces of major members and skew members can be transferred to the gusset plates only through bolts.

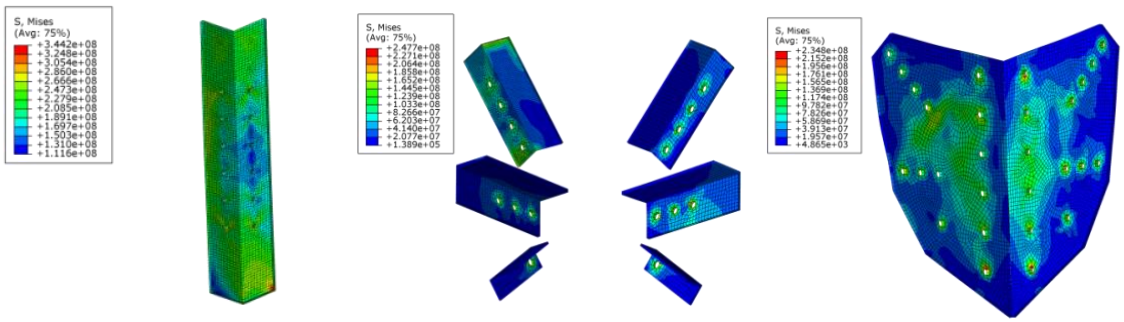

(a) Major member *(b) Skew member* *(c) Gusset plate*

Figure 5: Stress distribution of joint components

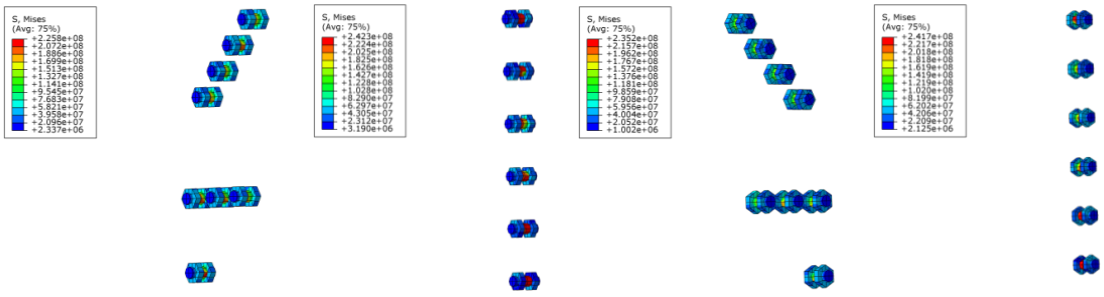

(a) Group 1 *(b) Group 2* *(c) Group 3* *(d) Group 4*

Figure 6: Stress distribution of joint bolts

3.1. Effects of bolt preloads

Transmission towers may collapse under the strong wind load, most of which resulted from the decreased force-bearing capacity of the tower, and the steel yields in the most unfavorable force of the tower. With the continuous action of external excitations, the damage or destruction of the transmission tower may occur. In this paper, according to the bolt torques that specified in the *110~500 kV overhead transmission lines specification*, five pre-tightening forces are selected to investigate the tightness of the bolts, and the effects of pre-tightening force on joint strength. Figure 7 display the variations of bolt stress with pre-loads under normal service loads with a bolt diameter of 20 mm and a friction factor of 0.3. It is seen that the bolt stresses of the group 1 is linearly correlated with the

pre-tightening force under normal service load. Similar observations can be made from the results of the other three groups. When bolt preloads increase from 40MPa to 200MPa, bolt stresses increase from 55MPa to 235MPa. For the second and fourth groups, the stresses of bolt 9, 14 and 28 are about 115MPa under a 40 MPa preload while the counterparts of the bolt 11, 12, 25 and 26 are only 70 MPa. In addition, all of bolt stresses reach by about 235MPa under 200MPa preload.

Displayed in Figure 8 are the variations of bolt stress with pre-loads under critical destruction loads. The critical destruction loads is the loads which induce the collapse of the entire tower. The figures demonstrate the relationship between bolt preload and bolt stress with a bolt diameter of 20 mm and a friction factor of 0.3 subjected to the critical destruction load. The curves indicate that bolt stresses in the first group are positively linear correlated with the bolt pre-tightening force. The maximum bolt stress of the third group is observed at the bolt 18 with a peak value of 160MPa under a preload of 40MPa. As shown in Figure 8, when the pre-tightening force increased from 40 MPa to 200 MPa, the stresses of bolt 9, 10, 13 and 14 almost keep unchanged. When the preload varies from 40 MPa to 160 MPa, the stresses of bolt 11 and 12 increase by about 38%. If the preload increases from 40 MPa to 200 MPa, the bolt stresses in the fourth group (bolt 23, 27 and 28) basically remain unchanged. When the pre-tightening force varies from 40 MPa to 120 MPa, the stresses of the bolt 24, 25 and 26 increase by 24.05%.

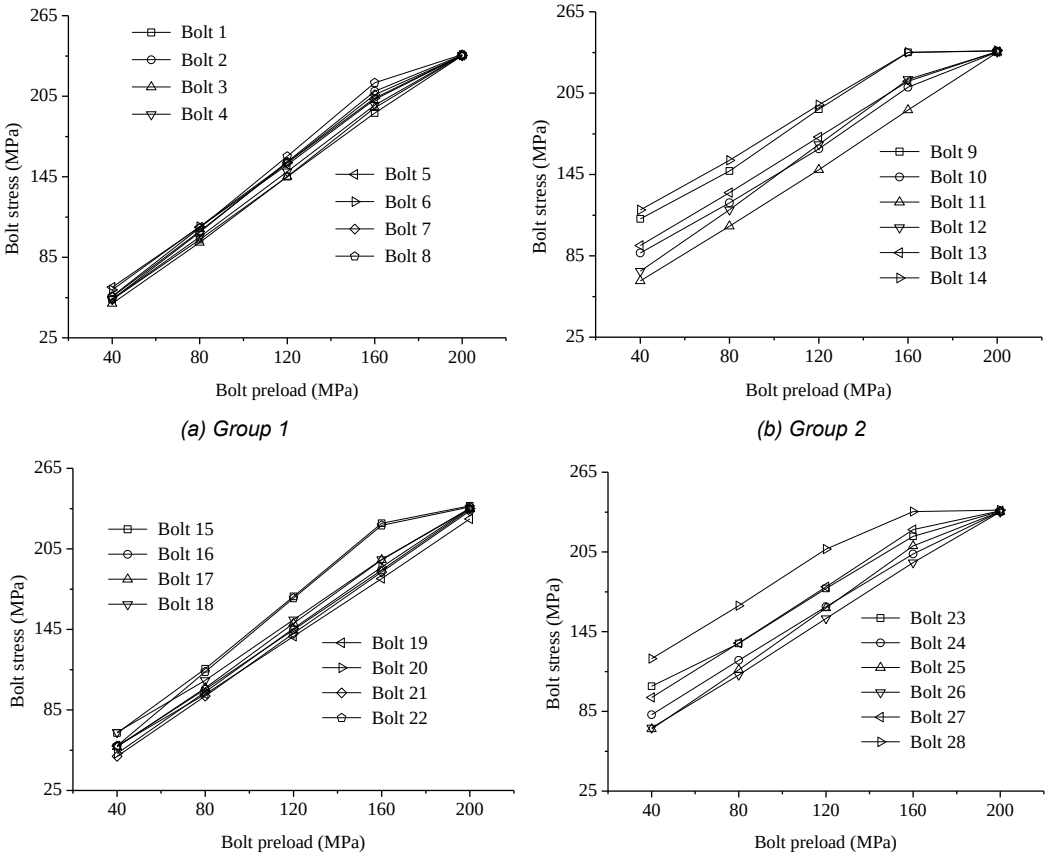

(a) Group 1 *(b) Group 2*

(c) Group 3 *(d) Group 4*

Figure 7: Variations of bolt stress with pre-loads under normal service loads

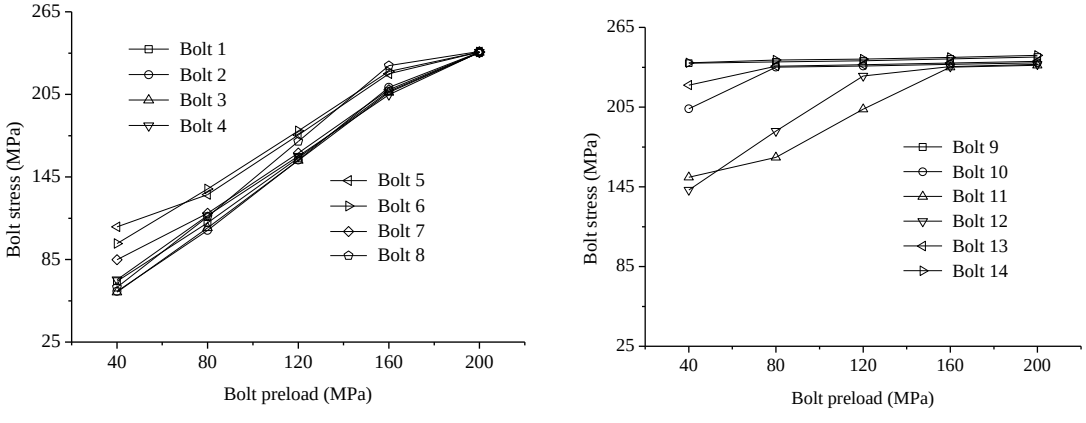

(a) Group 1 *(b) Group 2*

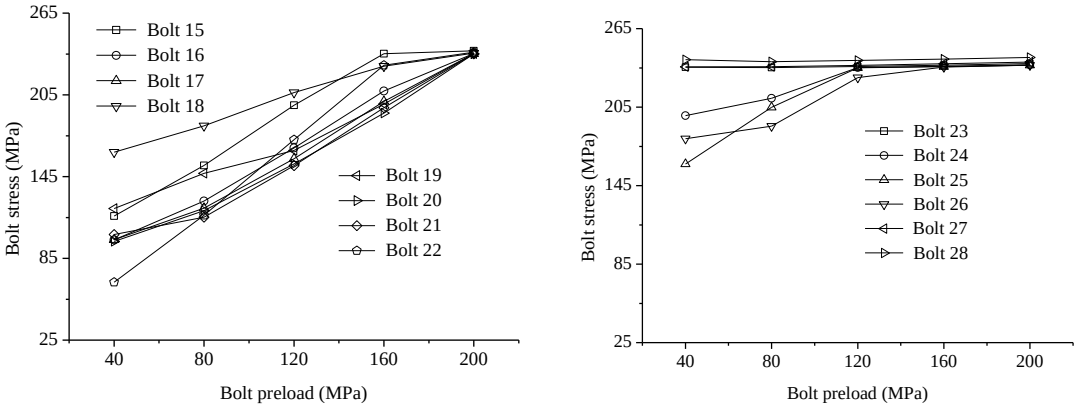

(c) Group 3 *(d) Group 4*

Figure 8: Variations of bolt stress with pre-loads under critical destruction loads

3.2. Effects of friction coefficients

The internal forces of tower joint are transferred through joint bolts when the structure is subjected to wind excitations. The friction coefficient is set at 0.15, 0.20, 0.25, 0.30 and 0.35 to explore the effects of friction contact on joint strength referred to the Chinese specification of steel structure. Depicted in Figure 9 are the variations of bolt stress with friction coefficients under normal service loads. The bolt diameter is 20 mm and the bolt preload is 80 MPa. It is seen that the bolt stresses slowly reduce with the increasing friction coefficients for all the bolts in the gusset plate. The stress changes of bolts in the first and third groups are basically the same, but the stresses of the bolt 15, 18 and 22 in the third group are larger than those in the other bolts. The stress changes of bolts in the second and fourth groups are quite close. The variations of bolt stress with friction coefficients under critical destruction loads are also investigated in this section while the figures are not displayed here due to page limitation. The made observations indicate that the bolt stresses in the first and third groups gradually decrease with the increasing friction coefficient under the critical destruction loads. The maximum stresses can be observed at bolts 5 and bolt with a peak value of about 140 MPa under a friction factor of 0.15. The bolt 18 in the third group has the highest stress of 190 MPa when the friction factor is reached by 0.15. The stresses of the bolt 9, 10, 13 and 14 in the second group keep stable when the friction coefficients increase. Similarly, the stresses of the bolt 23, 27, and 28 in the fourth group do not change with the increasing friction coefficients and the maximum bolt stress reaches by about 240 MPa.

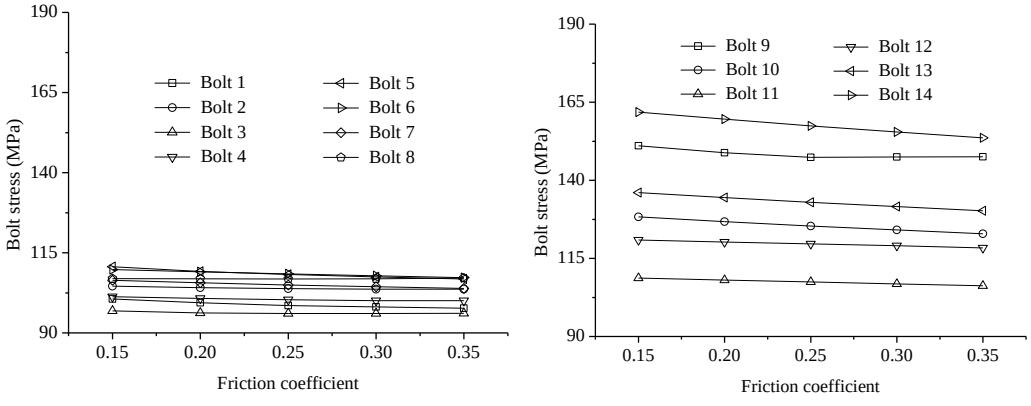

(a) Group 1 *(b) Group 2*

Figure 9: Variations of bolt stress with friction coefficients under normal service loads

3.3. Effects of bolt diameter

The effects of bolt diameter on bolt stress are also examined in this section as shown in Figure 10. The friction coefficient is set at 0.3 and the preload is set at 80 MPa under normal service load.

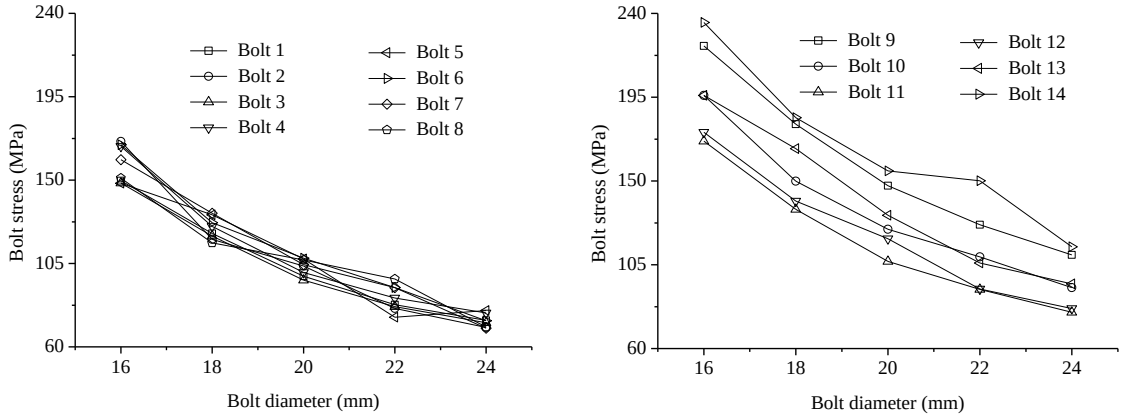

(a) Group 1 *(b) Group 2*

Figure 10: Variations of bolt stress with bolt diameter under normal service loads

The curves in Figure 10 indicate that under normal service load, the bolt stresses and bolt diameters present a negatively linear relationship. The bolt stresses in the first groups gradually reduce with the increase of bolt diameter and similar observations can be made for the bolt group 3. It is found that with the bolt diameter increasing from 16mm to 24 mm, the bolt stresses decreases by about 53%, almost half of the peak value. The stresses of the second and fourth groups are quite close and the bolts 14 and 28 at the edge of the major member have the maximum stresses. When the bolt diameter increases from 16mm to 24mm, the stresses of bolts 14 and 28 reduces by about 48%. The relationship between bolt diameter and bolt stress under the critical destruction loads are also investigated with a friction coefficient of 0.3 and a preload of 80 MPa. The analytical resluts indicate that the bolt stresses in the first group is still negatively linearly correlated with bolt diameters under critical destruction loads. When bolt diameter increases from 16mm to 24 mm, the bolt stresses decrease by about 53%. The bolt stress in the third group increases remarkably, but it still shows a negative linear varying trend. The bolt diameter of bolts 9 and 14 in the second group cannot affect their bolt stresses while the counterparts of bolts 11 and 12 decease by 45.09%. With the bolt diameter increasing from 18 mm to 20 mm, the stresses of bolt 28 keeps stable.

3. CONCLUSIONS

The force-bearing capacity of transmission tower joints is actively investigated in this study based on fine three dimensional finite element analysis with the aid of commercial package ABAQUS. The analytical model of bolt is developed and the nonlinear contact force model for the interacting between bolts and member is presented under wind loads. A real transmission tower-line system constructed in China is taken as an example to examine the feasibility and reliability of the proposed joint analytical approach. The parametric study is conducted to investigate the effects of various factors on joint strength, such as bolt diameter, bolt strength, pre-stressed force, friction coefficients and etc. The made observations demonstrate that the bolt stresses increase with increasing the preloads. When the external loads gradually increases from normal service loads to critical destruction loads, the bolt stress at the connection parts nearby the skew members and the gusset plate still keeps a positive linear relationship. The bolt stresses at connection parts nearby the major member and the gusset plate is directly proportional to the preloads. The bolt stress is linearly positively correlated with the bolt pre-tightening force under normal service load, while it is linearly negatively correlated with the bolt diameter. The bolt stress of skew member is linearly correlated with bolt pre-tightening force and bolt diameter under the critical load. When the external load increases from the normal service load to the critical load, the bolt stress of oblique members remains linearly related to the bolt pre-tightening force and the bolt diameter, while the bolt preload, bolt diameter, and friction factor have different effects on performance of bolt in major members. The friction interaction among contact surface has little effects on the strength of bolts. A protective layer can be applied during the design and construction of the transmission tower to ensure normal contact among different components. The diameters of the bolts at the ends of the major member can be increased to improve the force-bearing capacity of the joint.

4. ACKNOWLEDGEMENT

The writers are grateful for the financial support from the technological project of the Chinese Southern Power Grid Co. Ltd (GDKJXM20161994(030800KK52160004)), the National Natural Science Foundation of China (51678463), the Chenguang Science and Technology Plan of Wuhan (2016070204010107) and Urban-Rural Development of China (2017-K5-003). Corresponding author of the paper is B. Chen.

5. REFERENCES

Li J, Zhao C and Bai Y, et al. Research on the Connection Process of Bolt Sets Based on Joint Sealing. *Mechanical Design & Manufacture*, 2015(6):154-157.

Li W, Duan R and Yang C, et al. Numerical Simulation and Contact Convergence Analysis of Bolt Flange Connection. Journal of Chongqing University, 2016,39(5):10-16.

National Standard of the People's Republic of China. Hexagon nut GB/T6170-2000. China Standard Press, 2000.

Zhao W. Analysis of key bolt connection strength of high-power dish-type solar thermal power generation system. Hunan University of Science and Technology, 2015.

National Standards of the People's Republic of China. Steel Structure Design Code GB 50017-2003. China Planning Press, 2003.

Chen B, Zheng J, Qu WL. Control of wind-induced response of transmission tower-line system by using magnetorheological dampers, International Journal of Structural Stability and Dynamics, 2009, 9(4): 661-685.

Chen C, Wang Q and Liu R, et al. Influence of Bolt Connections on Structural Mode and Transfer Characteristics. Journal of Vibration and Shock, 2014(2):178-182.

Chen B, Zhao SL, Li PY. Application of Hilbert-Huang transform in structural health monitoring: a state-of-the-art review, Mathematical Problems in Engineering, 2014, 317954, 1-23.

Chen Y, Huang H and Zhang Y, et al. Finite Element Analysis of Force Performance of UHVAC Transmission Tower KK Joint. Chongqing Architecture, 2015(11):51-53.

Chen B, Xiao X, Li PY, and Zhong WL. Performance evaluation on transmission-tower line system with passive friction dampers subjected to wind excitations, Shock and Vibration, 2015, 310458, 1-13.

Chen B, Xu YL and Zhao X. Integrated vibration control and health monitoring of building structures: a time-domain approach. Smart Structures and Systems, 2010, 6(7), 811-833.

National Standards of the People's Republic of China. Specification for Construction and Acceptance of 110~500KV Overhead Transmission Lines (GB 50233-2005). China Planning Press, 2005.

Chen B, Xu YL. A new damage index for detecting sudden change of structural stiffness, International Journal of Structural Engineering and Mechanics, 2007, 26(3): 315-341.

173: Control optimisation of hybrid energy storage system based on H-bridge convert

Yuanzhong XU[1], Wanying XIAO[2], Tiezhou WU[3]

[1] *Hubei Key Laboratory for High-efficiency Utilisation of Solar Energy and Operation Control of Energy Storage System, Hubei University of Technology, 430068, China, 443903039@qq.com*

[2] *Hubei Key Laboratory for High-efficiency Utilisation of Solar Energy and Operation Control of Energy Storage System, Hubei University of Technology, 430068, China, 494920275@qq.com*

[3] *Hubei Key Laboratory for High-efficiency Utilisation of Solar Energy and Operation Control of Energy Storage System, Hubei University of Technology, 430068, China, 972537502 @qq.com*

The hybrid energy storage system（HESS）uses Battery-Supercapacitor to suppress the DC bus current fluctuation caused by the load fluctuation. The traditional HESS uses a boost circuit to connect the HESS and the DC bus. However, the Boost circuit has the disadvantages of large output current ripple and interrupted output current. Using the H-bridge DC-DC converter connects the DC bus and the HESS, which can reduce the output current ripple and can stabilise the output current when the load suddenly changes. The proportional gain KP and the integral speed KI of the PI controller will restrict the flexible adjustment when the load is suddenly changed. The improved self-adaptive fuzzy PI controller is used to control the charging and discharging of the battery. The intelligence of the fuzzy control（FC）can be used in combination with the PI control to restrict the current fluctuation caused by the pulse load in quantitative adjustment. To verify the proposed method, a MATLAB/Simulink model was set up. Then the pulse loads were set to be added in 4.0s-7.0s and 10.0s-11.0s.The simulation results show that the system uses the Boost controller and the improved self-adaptive fuzzy PI control strategy can stabilise the output current in 0.3S; Using the H-bridge DC-DC converter and PI control strategy can stabilise the output current in 0.2S; Using the H-Bridge DC-DC converter and the improved self-adaptive PI control strategy can stabilise the output current in the moment of load fluctuation. Therefore, using the H-bridge DC-DC converter and the improved self-adaptive fuzzy PI control strategy can be the best one to stabilise the current fluctuations when the load changes.

Keywords: Hybrid Energy Storage System; PI Controller; Fuzzy Control; H-Bridge DC-DC Controller; Pulse load

1. INTRODUCTION

With environmental pollution and energy shortages becoming increasingly serious, the utilisation of traditional energy needs to be upgraded and reformed. The lead-acid batteries, lithium batteries and flow batteries are commonly used energy storage batteries (Xie et al., 2017). These batteries are of the electrochemical energy storage type and have the advantages of low cost, mature technology, and high energy density. However, there are problems such as low power density, inability to deep discharge and battery pack equalisation. Supercapacitor is electromagnetic energy storage, which has the advantages of fast response, high power density and repeating charge and discharge (Zhang et al., 2015). The storage battery is used as energy type element and the Supercapacitor is used as power type element. A HESS is established, which can combine the advantages of two type batteries to make the energy storage system operate more stably and respond more quickly.

At present, the research on HESS is mainly about capacity allocation and control strategies. This article focuses on the control strategies of HESS. Moreover, the research of control strategies is mainly focused on controllers and intelligent algorithms. Research on controllers uses low-pass filter (LPF) and fuzzy logic controller (FLC) to reduce the dynamic stress and peak power requirements of the battery. A particle swarm optimisation (PSO) algorithm was implemented to tune the membership function (MF) of the fuzzy logic controller to optimise the battery peak current. This method greatly improves the dynamic stress and peak current demand of the battery in the system, and ultimately will prolong the service life of the battery (Chong et al., 2016). The other literature proposes to filter the total load power of the HESS and use the current hysteresis to control the charge and discharge of the battery. The Supercapacitor provides the difference value power, and the complementary Pulse-Width Modulation (PWM) control method is used to enable the power device to achieve soft switching. This method improves the dynamic response capability of the system and reduces the loss when the power frequently changes direction (Wang et al., 2013). In addition, there are scholars using the chip to control the energy storage system, as proposed using C8051F020 as the control chip, through the control of charge and discharge of the supercapacitor to avoid the impact of small current on the battery polarisation, according to the state of charge (SOC) of storage batteries to control the on-off charge switch. The control system that joins the chip runs more intelligently, and the battery supply is more continuous and reliable (Xiao et al., 2016).

Research on control strategies for intelligent algorithms, as mentioned using fuzzy embedded boost converters for photovoltaic in hybrid grid connection systems. 7 fuzzy sets are used, 7 of which are applied to the DC-DC converter. The supercapacitor module is used to balance the DC bus voltage and the remaining power and absorb the energy and send it back to the system when needed. The strategy has a better dynamic response in the transition state (Hassan et al., 2017). The intelligent hybrid control based on PID and fuzzy logic controller to stabilise the three-phase grid-connected output current and photovoltaic voltage. This intelligent hybrid controller has fast and stabilise response without delay, eliminates shocks around the operating point, accurately tracks the maximum power operating point to ensure photovoltaic batteries produce maximum power (Louzazni et al., 2014).

Based on the methods above, this paper improves on the basis of learning and proposes a new type of control strategy. The establishment of an H-bridge DC-DC converter to connect the energy storage system and the DC bus can overcome the drawbacks of the Buck/Boost circuit with large output current ripple and unstable current. Using self-adaptive fuzzy PI controller to control the charge and discharge of the battery, real-time monitoring of the amount of current flowing through the DC bus, using the artificial intelligence of fuzzy control and real-time deviation adjustment of the PI controller to avoid rapid power fluctuation under pulse load. In conclusion, this method can stabilise the output power and promote the energy storage system operate more smoothly.

2. ENERGY STORAGE SYSTEM AND CONTROLLER STRUCTURE

2.1. HESS structure

A HESS generally consists of a storage battery, a supercapacitor, an energy optimisation controller and an inverter. Specific HESS model shown in Figure 1.

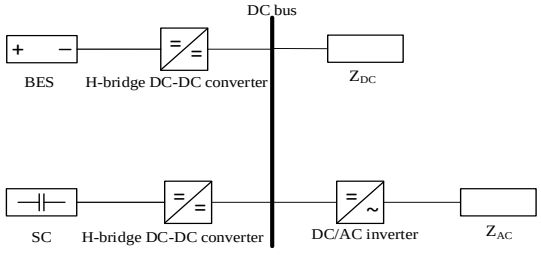

Figure 1: Model of HESS

In Figure 1, BES is the storage battery, SC is the supercapacitor, Z_{AC} is the AC load and Z_{DC} is the DC load. Among them, the output voltage of the storage battery and the supercapacitor is transmitted to the DC bus through the H-bridge DC-DC converter.

HESS has a significant effect on increasing the amount of power in a short period of time. The hybrid energy storage device herein is selected as a supercapacitor and a battery. The supercapacitor is used as high power density devices to support transient process and is used to handle short-term energy shortages. The battery is used for the main power supply requirements of the load. The energy storage of the hybrid energy storage system is calculated as shown in Equation (1):

Equation 1: The energy storage of the hybrid energy storage system . $E_{HESS} = \frac{1}{2} LI^2$

Where:

- L= inductance of the converter(H)
- I = current flowing through the battery(A).

In addition, to prevent overcharge and deep discharge of the battery, the battery SOC should be adjusted between 30% and 90% (Ji et al., 2014), the specific regulation is shown in Equation (2):

Equation 2: The battery SOC regulation. $SOC_{Battery} = \frac{W_O - \int_0^t \eta E(SOC) I dt}{W_t}$

Where:

- W_0 = initial energy value of the battery before discharge(J)
- W_t = energy value at time t(J)
- E(SOC) = electromotive force of the battery
- I = battery charge and discharge current(A).

2.2. H-bridge DC-DC controller structure

The DC-DC controller is used for energy optimisation controllers of DC bus in HESS. The energy flow of the energy storage element is bidirectional. This system is a HESS composed of a battery and a supercapacitor, and belongs to the form of a voltage source. Therefore, a current reversible DC-DC converter is used.

In single-quadrant DC-DC converters, Buck and Boost have the highest efficiency (Jiang et al., 2014). The Buck circuit is a step-down converter. The system voltage must always be higher than the load voltage to make the system work at the maximum power point, which limits the configuration of the system to some extent. The diodes in Boost circuit can be used as anti-reverse diodes to prevent the power on the grid side from flowing back to the PV array which can save anti-counter diodes and improve the system's working efficiency. However, both the Buck circuit and the Boost circuit have the disadvantage of large output current ripple. This system adopts H-bridge DC-DC bidirectional converter, which can reduce the output current ripple to some extent. The specific model is shown in Figure 2.

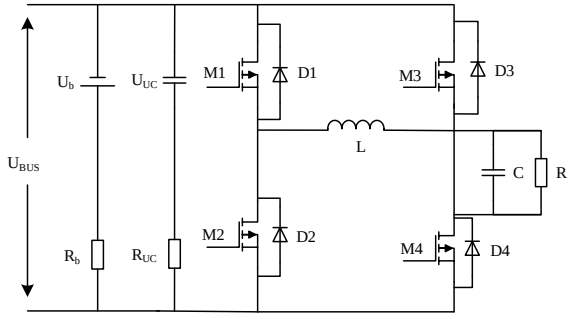

Figure 2 Model of H-bridge converter controller in HESS

As shown in Figure 2, the H-bridge converter consists of four MOS transistors (M1, M2, M3, M4), four diodes (D1, D2, D3, D4) and a capacitor C. U_{UC} is the supercapacitor voltage, R_{UC} is the internal resistance of the supercapacitor, U_b is the battery voltage, R_b is the internal resistance of the battery, and R is the load.

Among them, M1 and M3 as the direction of the control of the output voltage polarity, M2 and M4 as a choke tube to adjust the circuit output voltage size (Xia et al., 2017). When power is supplied to the load, the switches M1 and M4 are turned on simultaneously; when the battery is charged, the switches M2 and M4 are turned on at the same time. The output voltage U_O and the output average voltage U_C are shown in Equation (3).

Equation 3: The output average voltage U_C. $U_C = \frac{T_{on}}{T_S} U_O = \frac{T_{on}}{T_S} U_{BUS}$

Where:

- T_{on} = MOS transistors conduction time(s)
- T_s = MOS transistors one cycle time(s)
- U_o = output voltage(V)
- U_{BUS} = voltage in the DC bus(V).

3. SYSTEM CONTROLLER DESIGN

H-bridge DC-DC converters are used to control the charging and discharging of storage battery and supercapacitor. There are three operating modes: charging mode, discharging mode and standby mode. In the discharging mode: the bus voltage is less than the voltage across the battery and the supercapacitor, so the switch tube M1 and M4 are turned on, and the energy storage system supplies power to the load. In charge mode: The bus voltage is greater than the voltage of the battery and the supercapacitor, so the switch tube M2 and M3 are turned on, and the grid charges the energy storage system. In standby mode: The bus voltage is between the charging voltage and the discharging voltage. In this case, the HESS is not required to supply power to the load. In order to maintain the current circulation, there are two types of switching: (1) M1 Turned on, M4 turns off, and free-wheeling diodes of M1 and M3 form a loop. This state lasts before the next turn-on period of M4; (2) M3 turns on, M2 turns off, and freewheeling diodes of M3 and M1 form a loop. This state lasts before the next conduction period of M2.

3.1. Energy storage battery charge control

The battery is controlled by a PI controller, which compares the DC bus voltage with the energy storage system voltage and considers the battery's SOC. Charge control block diagram shown in Figure 3.

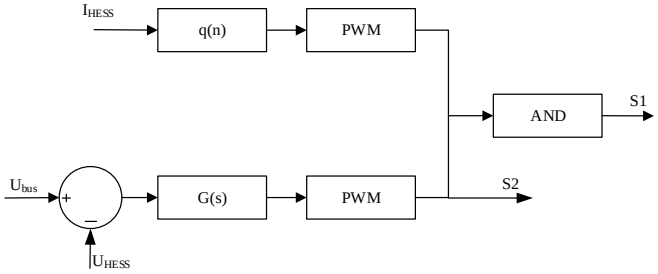

Figure 3: Block diagram of the H-bridge converter controller charge mode

As shown in Figure 3, D1 (duty cycle of MOSFET1) controls the charge rate by receiving a pulse of current in the HESS so that the battery can be quickly charged. The DC bus voltage pulse and the HESS pulse are connected through the AND logic function to jointly control the charging process of the system. The formula for controlling the pulse of M1 receiving hybrid energy storage system is shown in Equation (4).

Equation 4: The formula for controlling the pulse of M1 receiving the HESS.

$$q = (k_a)\exp(\frac{I_{HESS}}{k_{HESS}})^{k_b}$$

Where:

- I_{HESS} = current stored in the HESS(A)
- k_{HESS} = the over-periodic adjustable parameters of the HESS current.
- k_a, k_b = the over-periodic adjustable parameters of the energy storage battery current.

3.2. Energy storage battery discharge control

When the current of the HESS begins to drop through dynamic droop control, the voltage begins to drop slightly and the PI controller allows the battery to discharge and maintain the power required for the pulsed load. The controller keeps the battery's SOC between 30% and 90%. The specific battery discharge control block diagram is shown in Figure 4.

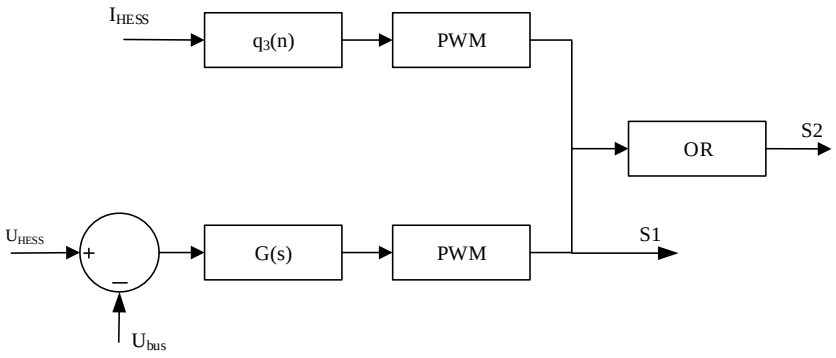

Figure 4; Block diagram of the H-bridge converter controller discharge mode

As shown in Figure 4, D3 (duty cycle of MOSFET3) controls the discharge rate by receiving a pulse of the current in the HESS, enabling rapid discharge of the battery. The DC bus voltage pulse and the HESS pulse are connected through the OR logic function to jointly control the discharge process of the system. The control formula for the pulse of M3 receiving hybrid energy storage system is shown in Equation (5).

Equation 5: The formula for controlling the pulse of M3 receiving the HESS.

$$q_3 = (k_a)\log_{10}(\frac{I_{HESS}}{k_{HESS}})^{k_b}$$

Where:

- I_{HESS} = current stored in the HESS(A)
- k_{HESS} = the over-periodic adjustable parameters of the HESS current.
- k_a, k_b = over-periodic adjustable parameters of the energy storage battery current.

4. SELF-ADAPTIVE FUZZY PI ALGORITHM DESIGN

The PI controller function has a timely suppression effect on the disturbance of the system (Huang et al., 2010), Specific PI adjusts the controlled object output U(t) and the deviation e(t) as shown in Equation (6).

Equation 6: The PI adjusts the controlled object output U(t).

$$U(t) = k_p[e(t) + \frac{1}{T_I}\int e(t)dt]$$

Where:

- e(t) = The systematic deviation
- kp = The proportional gain.

Equation 7: Rewrite U(t) to U(s).

$$U(s) = k_p(1 + \frac{1}{T_I s})E(s)$$

Where:

- Kp = The proportional gain
- 1/TI = The integration speed and kI=1/TI.

In Equations (6) and (7), kp is the proportional gain, 1/TI is the integration speed, and kI=1/TI. The resulting transfer function is shown in Equation (8):

Equation 8 :The resulting transfer function.

$$G_C(s) = \frac{U(s)}{E(s)} = k_p(1 + \frac{1}{T_I s})$$

From (7) and (8), the output U(s) can be rewritten as shown in Equation (9).

Equation 9: rewritten the output U(s).

$$k_p E(s) = U(s)\frac{T_I s}{T_I s+1} = U(s) - \frac{1}{T_I s+1}U(s)$$

Equation 10: Further rewritten the output U(s).

$$U(s) = k_p E(s) + \frac{1}{T_I s+1}U_b(s)$$

In Equation (10), when $U_b(s) = U(s)$, it is PI regulator; When $U_b(s) = 0$, it is P regulator.

From Equation (10), theoretically speaking, e(t) decreases as kp increases when the output and integration speed control are unchanged, but increasing kp is equivalent to increasing the open-loop gain of the system which will cause system oscillation and reduce system stability. Therefore, increasing the fuzzy controller makes the PI controller change kp according to the actual deviation, and the output kp is then adjusted by the PI controller to enhance the dynamic adjustment of the control system.

This fuzzy rule has two input signals: e(t) and U(t), an output signal kp. The fuzzy sets of e(t) and U(t) are e(t)={NB, NM, NS, ZE, PS, PM, PB}, U(t)={N, Z, P}. The domain range is e(t)={-3,-2,-1,0,1,2,3}, U(t)={-1,0,1}. The fuzzy set of the output signal kp is kp={NB,NM,NS,ZE,PS, PM, PB}, the corresponding domain range is kp=[-0.3,0.3].

This fuzzy rule uses the “if-then” form (Shi et al., 2008). The specific fuzzy control statement is: if e(t) is A and U(t) is B, then kp is C. The fuzzy rules are shown in Table 1.

Table1 Rule of Fuzzy Control

U(t) \ e(t)	NB	NS	ZE	PS	PB
N	PB	PM	NS	NM	NB
Z	NM	NS	ZE	PS	PM
P	NB	NM	PS	PM	PB

Among them, NB: Negative Big, NM: Negative Medium, NS: Negative Small, ZE: Zero, PB: Positive Big., PM: Positive Medium, PS: Positive Small. The membership function of the output variable obtained by calling the “fuzzy inference calculation function evalfis( )” in MATLAB is shown in Figure 5 .

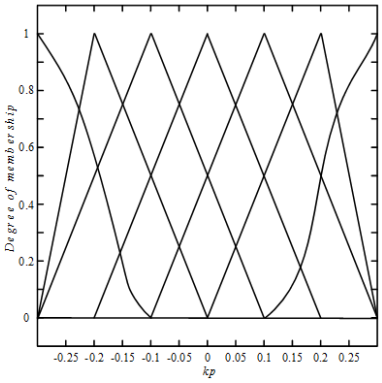

Figure 5: The membership function of the output variable kp

5. COMPARISON AND ANALYSIS OF SIMULATION RESULTS

According to the HESS model in Figure 1 and the H-bridge DC-DC converter model in Figure 2, the model is set up in simulation software matlab/simlink as shown in Figure 6.

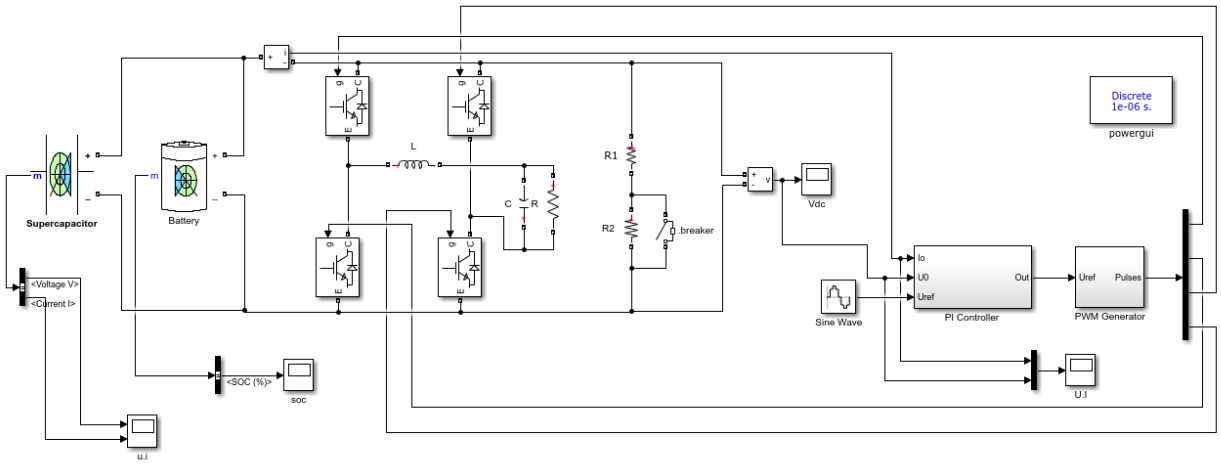

Figure 6: Simulation model of HESS

The simulation was constructed using three situations: a Boost circuit and a PI controller, an H-bridge DC-DC converter and a PI controller, and an H-bridge DC-DC converter and an self-adaptive PI fuzzy controller. Among them, there is Boost circuit rather than H-bridge DC-DC converter is used in order to verify the function of stabilizing the current and voltage of the circuit by H-bridge DC-DC converter. In addition, the latter two situations both use H-bridge DC-DC converters to connect the DC bus and the energy storage battery. The purpose is to verify whether there are differences in fuzzy control algorithms under the same converter conditions. In order to check the dynamic response performance of the three schemes when the load changes abruptly, it is set in 4.0s and 10.0s, the breaker connected with the load acts to make the busbar access the pulse load; the pulse load is removed in 7s and 13s. The specific simulation results are shown in Figure 7 and Figure 8.

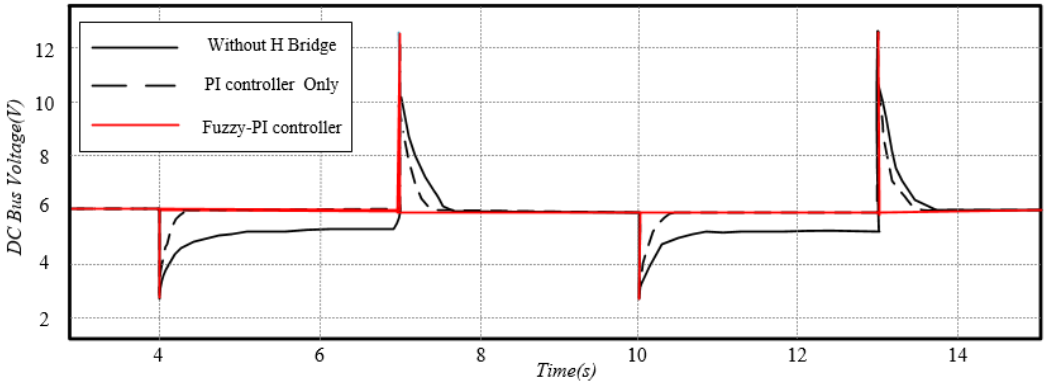

Figure 7: The DC bus voltage output voltage under three conditions

As shown in Figure 7, the stable operating voltage is 6V.When the pulse load is added at 4.0s, the bus voltage is suddenly reduced from 6V to 3V. In systems using Boost circuit and PI controllers, as the black solid line shown in Figure 7, voltages cannot be restored after 3 seconds because there is no efficient converter to control voltage distribution; systems using H-bridge converters and PI controllers , as the black dotted line shown in Figure 7,can stable pulse loads due to H-bridge converters, so the voltage recover to 6V after 0.3s; however, the systems using H-bridge converter and self-adaptive PI fuzzy controller, as the red solid line shown in Figure 7,because the self-adaptive PI fuzzy controller can stabilise instantaneous voltage, so the voltage can be restored to 6V at the moment of load conversion. It can be seen that the H-bridge converter and self-adaptive PI fuzzy controller have a significant role in stabilizing the DC bus voltage during sudden load changes. Whereas, when the pulse load disappears at 7.0s, due to overcurrent, the bus voltage increases to 12.5V rapidly. Nevertheless, the supercapacitor absorbs excess current, so the voltage can be maintained at 6V in the end.

The output current of HESS and battery is shown in Figure 8.

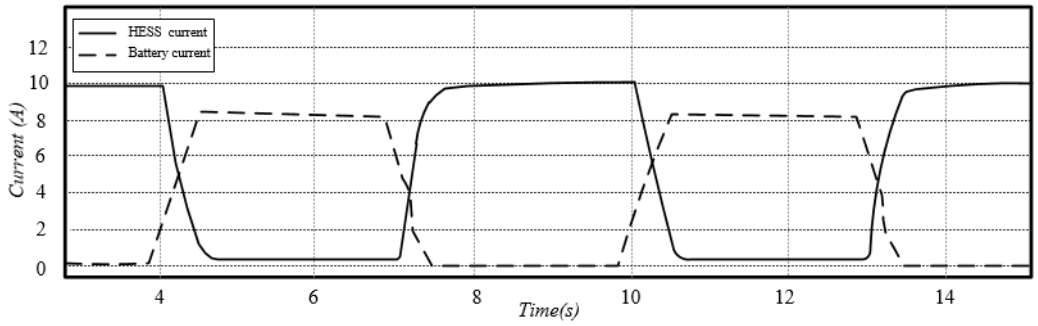

Figure 8: The output current

As shown in Figure 8, the solid lines depict hybrid energy storage current which the maximum is 10A. When the pulse load was applied at 4.0s, the energy storage system was immediately discharged, and the current was descending at a rate of 33 A/s. According to Equations (4) and (5), the discharge rate depends on I_{HESS} and U_{bus}. Lowering the discharge rate slows down the DC bus voltage drop, which can provide more response time for the battery.

Also in Figure 8, the other dotted line is the output current waveform when the battery is powered. When 4.0s is connected to the pulse load, the battery discharge becomes the main power source of the load, hence the battery discharge voltage rises from 0A to 8A. The battery discharge current rate is 26.7 A/s. The constant discharge current during stable operation is 8A.

In some special electrical devices, such as pulse load devices, the current slope of a Li-ion battery can be reduced by increasing the size of the H-bridge converter. However, there must be a weigh between the H-bridge converter and battery life. In the following study, optimisation studies will be conducted to find the optimal battery and H-bridge converter size to provide the best solution for the H-bridge converter and battery life.

6. CONCLUSION

This paper proposes an H-bridge DC-DC converter to control the current variation in the DC bus and HESS, which can mitigate the effect of sudden changes in load power on system stability. By building a simulation model in matlab/simlink, it is shown the different output voltages under three situations. The differences show that the HESS based on H-bridge converters and self-adaptive PI fuzzy controllers perform best when the pulse load accessed. This system maintains the voltage at the target level whatever there is a pulse load or not, so that the DC bus voltage output is stable. In order to further study the feasibility and advantage of this strategy, the size of the H-bridge converter and battery life will be optimised in the future.

7. REFERENCES

Xie W H, 2017. Study on Common Energy Storage Characteristics and Applications[J]. Telecom Power Technology, 34(3):90-95.

Zhang Y Y,2015.Super capacitor energy storage technology development status and prospects[J]. Ningbo Chemical Industry, (3):17-19.

Chong L W, Wong Y W, Rajkumar R K, et al, 2016. An optimal control strategy for standalone PV system with Battery-Supercapacitor Hybrid Energy Storage System[J]. Journal of Power Sources, 331:553-565.

Wang H B,Yang X,Zhang M X, 2013. A Control Strategy of Hybrid Energy Storage System Capable of Suppress- ing Output Fluctuation of Photovoltaic Generation System[J].Power System Technology,37(9):2452-2458.

Xiao X T,Li Y,Xu J Y, 2016. Research on Hybrid Energy Storage Controller of Photovoltaic Supercapacitor and Battery[J]. Electronic Technology, 45(9).

Hassan S Z, LI H, Kamal T, et al, 2017. Fuzzy embedded MPPT modeling and control of PV system in a hybrid power system[C]// International Conference on Emerging Technologies. IEEE, 1-6.

Louzazni M, Aroudam E, 2014. Control and stabilisation of three-phase grid connected photovoltaics using PID-Fuzzy logic[C]// IEEE International Conference on Intelligent Energy and Power Systems. IEEE, 279-284.

Ji Y X,Du H J,Shun H, 2014. A Survey of Charge Estimation Methods[J].Electrical Measurement & Instrumentation, 51(4):18-22.

Jiang W,Chen W,Hu R J, 2014. Charging strategy for super capacitor of photovoltaic generation system[J].Electric Power Automation Equipment, 34(12):31-37.

Xia Y H,Zhao J H,Zhang J H, 2017. Simulation Research and Theoretical Analysis on DC-DC Converter Based on H-Bridge[J].Marine Electric & Electronic Engineering, (12):15-18.

Huang Y R, Qu L G, 2010. PID Controller Parameters Tuning and Implementation[M]. Science Press.

Shi X M, Hao Z Q, 2008. Fuzzy Control and MATLAB Simulation[M]. Beijing Jiaotong University Press.

174: Research on cascaded bidirectional DC-DC converter based on model predictive control

Lujun WANG[1], Jiong GUO[2], Tiezhou WU[3]

[1] *Hubei Key Laboratory for High-efficiency Utilisation of Solar Energy and Operation Control of Energy Storage System, Hubei University of Technology, Nanli Road, Hubei 430068, China, 18611946486@163.com*
[2] *Hubei Key Laboratory for High-efficiency Utilisation of Solar Energy and Operation Control of Energy Storage System, Hubei University of Technology, Nanli Road, Hubei 430068, China, 2362169752@qq.com*
[3] *Hubei Key Laboratory for High-efficiency Utilisation of Solar Energy and Operation Control of Energy Storage System, Hubei University of Technology, Nanli Road, Hubei 430068, China, wtz315@163.com*

The traditional double closed loop PID control method of bidirectional Buck/Boost DC-DC converter is more mature and has better control effect, but the process of setting up PI parameters is rather tedious. The power prediction control based on the model predictive control (MPC) thought is simple and the controller is easy to realise. But the large amount of computation in the control process leads to slower response of the system. Therefore, traditional PID control or power predictive control is difficult to achieve good performance for cascaded bidirectional DC-DC converters. In this paper, a model predictive control method based on reference power is proposed, which takes the duty ratio as input and has weight factor. This method has the advantages of simple and intuitive control process and good control effect. Through the establishment of the system model, the calculation of the reference power, the evaluation of the performance index and the optimisation of the switching state, the performance of the system is optimised, which makes the converter have a faster response speed and a smaller voltage overshoot. In view of the above control methods, a simulation model is built to verify the results. The results show that compared with the traditional PID control method and power prediction control method, the proposed method can improve the dynamic and static performance of the system. The results verify the effectiveness of the proposed control method.

Keywords: Bidirectional DC-DC converter, model predictive control, PID control, duty cycle

1. INTRODUCTION

At present, photovoltaic power generation is mainly used in distributed generation systems (Wu et al., 2013). However, the output of photovoltaic power generation has the disadvantages of randomness, volatility, and unpredictability (Zhang et al., 2015, Mei et al., 2015). In order to enable the photovoltaic power generation system to operate more safely and flexibly, it must be equipped with corresponding energy storage units (Chen et al., 2011). Since the ratio between the voltage of the battery used for energy storage and the bus is generally 10 times or even 20 times (Li et al., 2018, Pang et al., 2016), therefore, a cascaded bidirectional DC-DC converter capable of achieving a high conversion ratio is widely used in a distributed power supply system.

There are several ways to control the converter, including PID control, intelligent control, predictive control and so on (Yu et al., 2015). The most widely used is a traditional PID control method, which has the advantages of simple algorithm and good control effect (Feng et al., 2017). However, the parameter design and selection process of the PID controller is tedious. The designer's experience and skill level directly affect the tracking accuracy and response speed of the converter. Leng and Liu (2018) proposed the idea of predictive control. Its concept is intuitive, it is easy to understand, easy to incorporate system constraints and nonlinear characteristics, and the controller is easy to implement, which are its advantages. It can effectively overcome the effects of time-varying, uncertainties, and interference of the system and is widely used in industrial processes. However, this method requires a lot of calculations, and the control reaction speed has a strong dependence on the controlled chip.

Aiming at the above problems, a model predictive control method based on reference power is proposed in this paper, which takes the duty ratio as input, realises control action through a single controller and can better improve the dynamic performance of the system. Simulated by Matlab/Simulink, confirmed the superiority of this method.

2. WORKING PRINCIPLES OF CASCADED BIDIRECTIONAL DC-DC CONVERTERS

The common distributed power supply system topology is shown in Figure 1. The distributed power supply is connected to the DC bus via an AC/DC converter or a DC/DC converter to supply the load. The battery is connected to the DC bus via a bidirectional DC-DC converter, and bidirectional flow of energy is used to achieve the purpose of suppressing the power fluctuation of the bus and achieving energy storage.

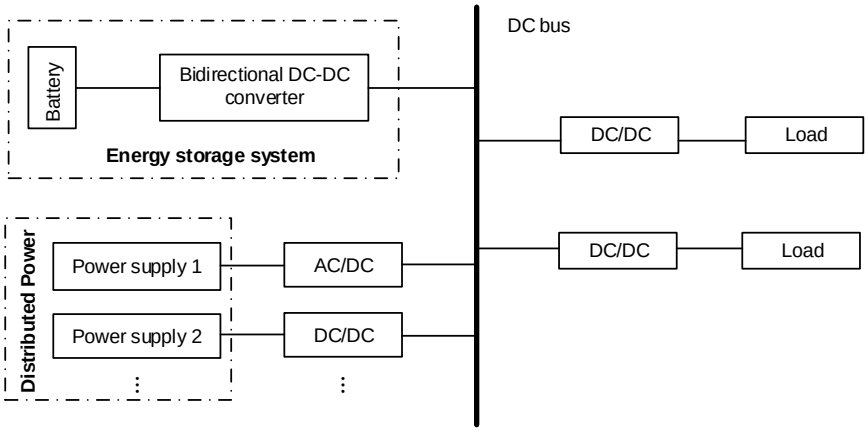

Figure 1: Typical DC distributed power supply system structure

The two-stage converter shown in Figure 2 is obtained by cascading two simple Buck/Boost bidirectional DC-DC converters. In Figure 2, the inverter connected to the battery is called the first stage converter, and the converter connected to the DC bus is called the second stage converter (Mei et al., 2017). The output of the first stage converter is used as the input of the second stage converter. The complexity of the system topology determines the complexity of the control. The stable voltage output of the first stage converter ensures that the input voltage of the second stage converter is constant, so that it is possible for the DC bus voltage to accurately track the reference value to meet the load demand.

The normal operation of the system requires that the bidirectional DC-DC converter can smoothly switch between the boost and buck operating modes (Cavanini et al., 2017, Lin et al., 2015). When the distributed power output power is less than the power required by the load, the DC bus is equivalent to the load, and the battery discharge provides energy for the load. At this moment, both stages of the bidirectional DC-DC converter work in the boost mode. In the first-stage of the converter, S_1 works and S_2 turns off; in the second-stage of the converter, S_3 works, and S_4 turns off. When the output power of the distributed power source is greater than the power required by the load, the DC bus is equivalent to the power source and the battery needs to be charged. At this moment, both stages of the bidirectional DC-DC converter work in the

buck mode. In the first-stage of the converter, S_2 works and S_1 turns off; in the second-stage of the converter, S_4 works, and S_3 turns off.

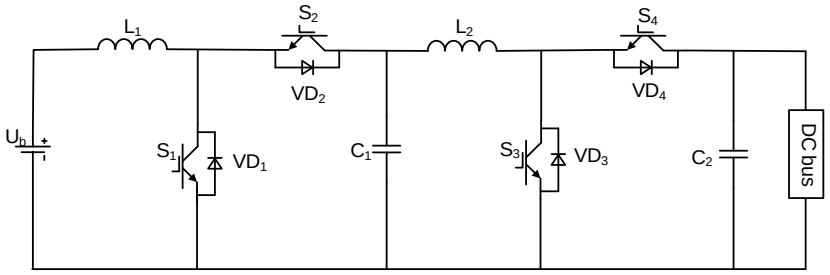

Figure 2: Cascaded bi-directional DC-DC converter circuit topology

3. CONTROL METHOD

3.1. Model predictive control principle analysis

Although the model predictive control has various forms of algorithm implementation, its common features include three important parts: predictive model, rolling optimisation and feedback correction. At time k, considering the system's future limited-time state, using the current time measurement value and the prediction model, and by having the control constraints and the minimisation of the objective function, the current and future optimal control for a limited time can be obtained. At time k+1, this optimisation process is repeated using the measured data after control at time k. The principle of model predictive control is shown in Figure 3. In Figure 3, the horizontal axis is the time region, the vertical axis shows the system output, where Np represents the prediction step size, Nc represents the control step size, and Np ≥ Nc. At time k, the time zone is divided into two parts. The left side is the actual input and output in the past, and the right side is the future prediction input and output. At time k, based on the current measurement information, the Nc-step control variable $\Delta u=[\Delta u(k|k),\Delta u(k+1|k),L,\Delta u(k+N_c-1)|k)]$ is obtained through optimisation to satisfy the target state of the prediction time domain k + Np. However, only the first one of the Nc control variables, which is $\Delta u(k|k)$, is executed at each time. The above process is repeated at time k+1.

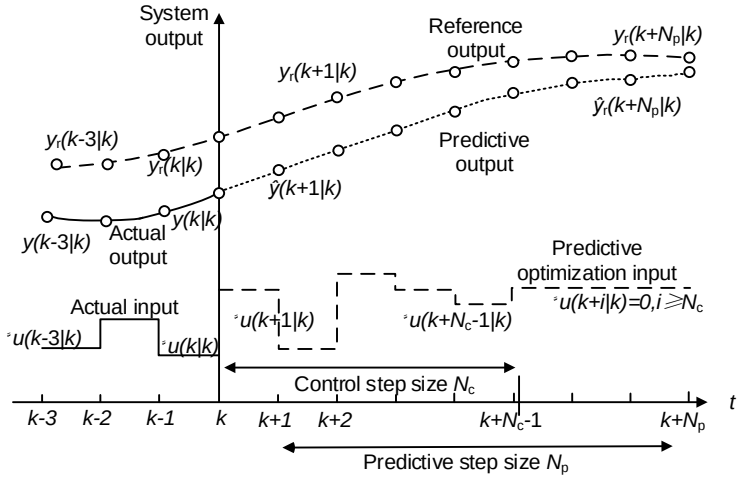

Figure 3: Principle of model predictive control

The model predictive control can directly consider the state of the control process, constraints of the input and output variables, and express it. The design of the controller directly reflects the dynamics of the controlled process. At the same time, the model predictive control converts the control problem into an optimisation problem to solve, considering the future action of the control object.

3.2. Model predictive control design

The model predictive control structure is shown in Figure 4. Firstly, the model predictive controller is input with the set value. Then an appropriate reference trajectory is determined. In the subsequent control process, the model predictive controller will make the state or output of the controlled object follow the reference trajectory as much as possible.

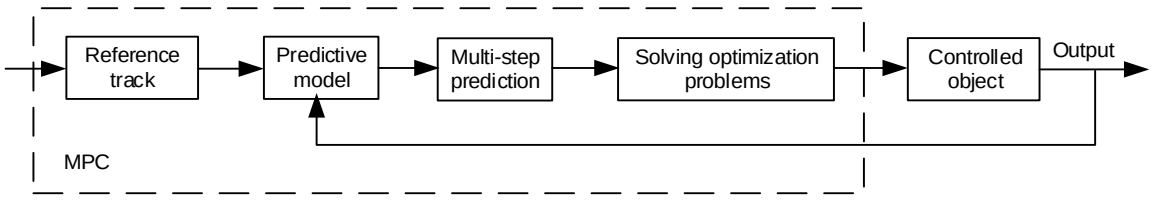

Figure 4: block diagram of model predictive control

Reference trajectory selection and calculation

The reference trajectory of the model predictive control refers to the curve that the state or output of the controlled object needs to be as close to as possible during the entire control process. By selecting a suitable reference trajectory, the controlled object can be guaranteed to have better control characteristics. The fluctuation of the DC bus power will appear as the change of the bus voltage, i.e. the change of the voltage across C_2. Since the voltage change across the bus capacitor C_2 can only be achieved by adjusting the current flowing through the capacitor, and the current across the capacitor cannot be infinitely large, the reference prediction range N is introduced. The filter voltage value U_{p2} at the next sampling time can be calculated by the bus voltage reference value U_2^*, the current bus voltage sampling values U_2 and N. i.e.

Equation 1: The definition of $U_{p2}(k+1)$

$$U_{p2}(k+1) = U_2(k) + \frac{1}{N}\left[U_2^* - U_2(k)\right]$$

Where:

$U_{p2}(k+1)$ = The predictive bus voltage at time of k+1(V)
$U_2(k)$= The bus voltage at time of k(V)
N= The reference prediction range
U_2^*= The reference value of the bus voltage(V)

This is equivalent to making the bus voltage linearly reach the given value U_2^* through N steps. The change in the bus voltage requires that the current flowing through the capacitor C_2 on the bus side be adjusted accordingly.

Equation 2: The relationship between the current flowing through the capacitor C_2 and the voltage across it

$$i_{c2} = C_2 \frac{\mathrm{d}U_2}{\mathrm{d}t}$$

Where:

i_{c2}= Instantaneous current flowing through the capacitor C_2(A)
C_2= The capacitance of C_2(F)
U_2= Instantaneous bus voltage(V)

Equation 3: The first form of calculation of $i_{C2}(k+1)$

$$i_{c2}(k+1) = \frac{C_2}{T_s}\left[U_2(k+1) - U_2(k)\right]$$

Where:

$i_{c2}(k+1)$ = The current flowing through the capacitor C_2 at time of k+1(A)
T_s= The sampling period(s)
$U_2(k+1)$ = The bus voltage at time of k+1(V)

Make $U_2(k+1) = U_{p2}(k+1)$, substituting Equation 1 into Equation 3, get

Equation 4: The second form of calculation of $i_{c2}(k+1)$

$$i_{c2}(k+1) = \frac{1}{N}\left\{\frac{C_2}{T_s}\left[U_2^* - U_2(k)\right]\right\}$$

That is, the current of the capacitor required at the next sampling time is calculated from the bus voltage at the current sampling time. Then Equation 5 can be derived by Kirchhoff's current law.

Equation 5: The definition of i_{dc}

$$i_{dc} = i_p + i_{L2} - i_{c2}$$

Where:

i_{dc}= Instantaneous current flowing through the bus(A)

i_p = Instantaneous current that the distributed power supply delivered to the DC bus(A)

i_{L2} = Instantaneous current flowing through the inductance L_2(A)

Thus, the predicted value of power can be obtained.

Equation 6: The definition of P_2^*

$$P_2^* = P_2(k+1) = U_2^* i_{dc}(k+1)$$

Where:

P_2^*= The reference value of power(W)

$P_2(k+1)$ = power at time of k+1(W)

$i_{dc}(k+1)$= The current flowing through the bus at time of k+1(A)

The establishment of a prediction model

The prediction model is obtained from the equivalent circuit of the bidirectional DC-DC converter corresponding to different switching states of the switch tube. Take the second stage converter as an example for analysis, S_g=1 (g=3,4) represents IGBT conduction, and S_g=0 (g=3,4) represents IGBT turn-off. The equivalent circuit of all switching states when the bidirectional DC-DC converter operates in the Boost mode is shown in Figure 5.

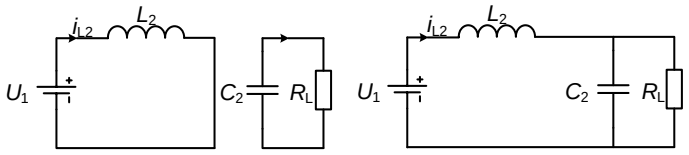

(a)S_3=1, S_4=0 *(b)S_3=0,S_4=0*

Figure 5: Equivalent circuits for Boost model

(1) State 1: S_3=1, S_4=0.

Equation 7 can be obtained according to the equivalent circuit.

Equation 7: The relationship between the voltage across the inductor L_2 and the current flowing through it

$$L_2 \frac{\mathrm{d}i_{L2}}{\mathrm{d}t} = U_1$$

Where:

L_2= The inductance of L_2(H)

i_{L2} = Instantaneous current flowing through the inductance L_2(A)

U_1= Instantaneous intermediate bus voltage(V)

Equation 8: The corresponding discrete form of Equation 7

$$i_{L2}(k+1) = \frac{T_s}{L_2} U_1(k) + i_{L2}(k)$$

Where:

$i_{L2}(k+1)$ = The current flowing through the inductance L_2 at time of k+1(A)

$U_1(k)$= The intermediate bus voltage at time of k(V)

$i_{L2}(k)$= The current flowing through the inductance L_2 at time of k(A)

(2) State 2: S_3=0, S_4=0.

Equation 9 can be obtained according to the equivalent circuit.

Equation 9: The relationship between the voltage across the inductor L_2 and the current flowing through it

$$L_2 \frac{\mathrm{d}i_{L2}}{\mathrm{d}t} = U_1 - U_2$$

Equation 10: The corresponding discrete form of Equation 9

$$i_{L2}(k+1)=\frac{T_s}{L_2}\left[-U_2(k)+U_1(k)\right]+i_{L2}(k)$$

In boost mode, the predictive value of the duty cycle of switch S_3 at time of k+1 can be calculated by Equation 11.

Equation 11: The calculation formula of $u_D(k+1)$ in boost mode

$$u_D(k+1)=1-\frac{U_{p1}(k+1)}{U_{p2}(k+1)}$$

Where:

$u_D(k+1)$ = The predictive value of the duty cycle at time of k+1

$U_{p1}(k+1)$ = The predictive intermediate bus voltage at time of k+1(V)

Similarly, the discrete equations corresponding to all switching states can be obtained when the bidirectional DC-DC converter operates in the buck mode.

(1) State 1: S_4=1, S_3=0.

Equation 12: The discrete form in the first switching state of the buck mode

$$i_{L2}(k+1)=\frac{T_s}{L_2}\left[U_2(k)-U_1(k)\right]+i_{L2}(k)$$

(2) State 1: S_4=0, S_3=0.

Equation 13: The discrete form in the second switching state of the buck mode

$$i_{L2}(k+1)=-\frac{T_s}{L_2}U_1(k)+i_{L2}(k)$$

In buck mode, the predictive value of the duty cycle of switch S_4 at time of k+1 can be calculated by Equation 14.

Equation 14: The calculation formula of $u_D(k+1)$ in buck mode

$$u_D(k+1)=\frac{U_{p1}(k+1)}{U_{p2}(k+1)}$$

Then substituting the discretised Equations 8, 10, 12, and 13 into Equation 15.

Equation 15: The definition of $P_{p2}(k+1)$

$$P_{p2}(k+1)=\left|i_{L2}(k+1)U_{p1}(k+1)\right|$$

Where:

$P_{p2}(k+1)$= The predictive power at time of k+1(W)

The power prediction models corresponding to all switching states can be obtained.

Objective function optimisation

At each control time, the system state in the future time domain can be predicted based on the state space averaging model of the Buck/Boost converter. The predicted values in different states are compared with the reference values, and then the optimal input sequence is solved. Finally, the first control of the optimal input sequence is applied to the controlled object. At the next control moment, the actual state of the controlled object is used instead of the state quantity in the predictive model, and the above process is continuously repeated to ensure the rolling optimisation. The objective function, which is established with duty cycle as input, by adding weighting factor and by using power as the control target, is as Equation 16.

Equation 16: The definition of objective function J

$$J=\sum_{i=1}^{N_p}\left(\alpha\left|P_{p2}(k+1)-P_2^*\right|+\beta\left|u_D(k+1)-u_D^*\right|\right)$$

$$(i=1,2,\cdots,H_p)$$

Where:

J= Target optimisation variable
N_P=The predictive step size
α= The weight factor of power
β= The weight factor of u_D
u_D^*= The reference value of the duty cycle

Taking the bidirectional DC-DC converter operating in boost mode as an example, the process of selecting the switch state by minimizing the objective function is described. Based on the sampled values of the current of the inductor at time of k, the voltage of the intermediate bus, and the voltage of the bus at the end, and the established prediction model, the predicted value of the duty cycle at time of k+1, the predicted battery power at time of k+1, and the reference value of power can be calculated separately. Then according to the objective function, calculate the values of the objective functions corresponding to the switch states S_3=1, S_4=0 and S_3=0 , S_4=0, such as $J_{S3=1\ ,\ S4=0}$ and $J_{S3=0,\ S4=0}$. The switch state that minimises the value of the objective function is selected as the switch state at time k+1. The entire process diagram is shown in Figure 6.

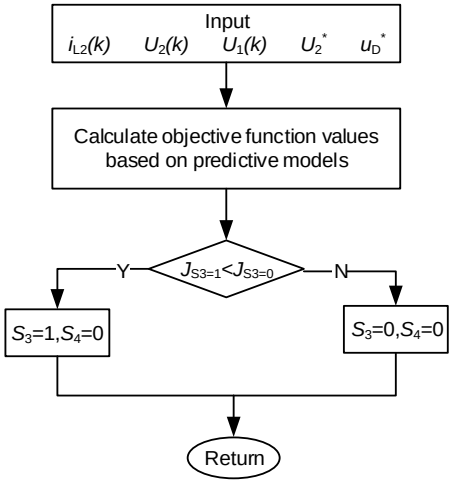

Figure 6: The flow chart of selecting the optimal switching state

Restrictions

In the process of converter response, certain state constraints need to be satisfied, namely, the inductor current and the capacitor voltage and the input duty cycle must be within a certain constraint range.

The state and input constraints for the system model are shown in Equation 17.

Equation 17: The state and input constraints for the system mode

$$\begin{cases} i_{\min} \le i_{L2}(k+i) \le i_{\max} \\ U_{2\min} \le U_2(k+i) \le U_{2\max} \\ U_{1\min} \le U_1(k+i) \le U_{1\max} \\ u_{D\min} \le u_D(k+i-1) \le u_{D\max} \end{cases}$$
$$(i=1,2,\cdots,N_p)$$

Where:

i_{L2}(k+i) = The current flowing through the inductance L_2 at time of k+i(A)
U_2(k+i) = The bus voltage at time of k+i(V)
U_1(k+i) = The intermediate bus voltage at time of k+i(V)

$u_D(k+i)$ = The value of the duty cycle at time of k+i
i_{min}/ i_{max} =The lower/ upper limit of the inductor current(A)
U_{2min} /U_{2max} = The lower/ upper limit of the bus voltage(V)
U_{1min} /U_{1max} = The lower/ upper limit of the intermediate bus voltage(V)
u_{Dmin} / u_{Dmax} = The lower/ upper limit of the value of the duty cycle

The current constraint condition of the inductor L_2 is $0 \le i_{L2} \le 5$ A, the voltage constraint condition of the capacitor C_2 is $0 \le U_2 \le 205$V, the voltage constraint condition of the capacitor C_1 is $0 \le U_1 \le 102$V, and the duty cycle constraint condition is $0.05 \le u_D \le 0.95$.

4. SIMULATION ANALYSIS

4.1. Simulation parameter design

Using Matlab/Simulink software, set up the system model for each of the three control methods. The control frequency is set to 20 kHz. System parameters are shown in Table 1. In the simulation process, the required power of the load P_R is stepped from 200 W to 100 W at time of 0.3 s, and the distributed power output P_V changes from 150 W to 0 W at time of 0.5s. The weight factors α and β in the prediction model are taken as 0.9 and 0.1 respectively, and the duty ratio reference value u_D^* is taken as 0.5.

Table 1: Simulation parameters

Parameters	Value
Battery	50V/32(Ah) , SOC=80%
DC bus/V	U1-ref=100 , U2-ref=200
Inductance /mH	L1=5 , L2=5
The power output by the distributed power supply /W	150

4.2. Analysis of simulation results

Figure 7 shows simulation waveforms for three control methods. As can be seen from Figure7, the three control methods enable the bus voltage to accurately track the given value. Table 2 lists the overshoots σ and response times T_U of the bus under the three control methods when the bus power fluctuates, and the switching time T_{bat} of the battery between charging and discharging.

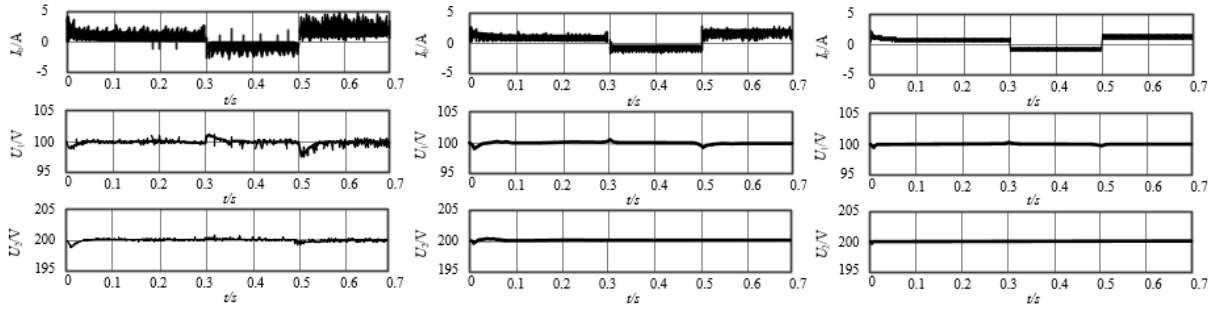

(a) Traditional PID control *(b) Power prediction control* *(c) Power prediction control with duty cycle as input*

Figure 7: Simulation results of the three control methods

Table 2: Analysis of simulation results

Control method	σ (%)		t_{U1}/s	t_{U2}/s	t_{bat}/s
	U_1	U_2			
Traditional PID control	2.5	2	0.07	0.05	0.1
Power prediction control	1	0.92	0.01	0.075	0.075
Power prediction control with duty cycle as input	1.75	1	0.045	0.01	0.05

In summary, all three methods can meet the system's steady-state performance requirements. In terms of dynamic performance, compared with the traditional PID control method and power prediction control method, the power prediction control method with the duty cycle as input makes the dynamic performance of the system greatly improved.

5. CONCLUSION

A state-space averaging model for cascaded buck/boost bidirectional DC-DC converter is established in this paper. And a power prediction control method with duty cycle as input is proposed. The traditional PID control method, power prediction control method, and power prediction control method with duty cycle as input are simulated in Matlab/Simulink. The simulation results show that the traditional PID control can make the system achieve a good control performance. The power prediction control method effectively avoids the setting process of multiple PI parameters in the traditional PID control, greatly simplifies the control structure, and the system dynamic performance is better than the traditional PID control method, but the algorithm requires a larger amount of calculation. The power prediction control method using the duty ratio as the input does not need to set more PI parameters. Compared with the power prediction control, the proposed method can greatly reduce the amount of calculation, make the system response speed faster, and make the output voltage of the converter settle to the set value faster without overshooting.

6. REFERENCES

Cavanini, L., Cimini, G., Ippoliti, G. & Bemporad, A. 2017. Model predictive control for pre-compensated voltage mode controlled DC–DC converters. *Iet Control Theory & Applications,* 11**,** 2514-2520.

Chen, Y., Xu, R., Wang, X. & Hu, X. 2011. Suppression of Voltage Ripple in Bidirectional Buck-Boost Converters. *Power Electronics,* 45**,** 19-21.

Feng, X., Wan, M., Han, L. & Wu, L. 2017. Control Strategy of Bidirectional DC/DC Converter Power System Based on Energy Storage. *Power Electronics***,** 8-10.

Leng, Z. & Liu, Q. 2018. Direct Current and Direct Voltage Model Predictive Control of Buck Converter. *Power Electronics*.

Li, Y., Huo, W., Zhu, Z., Chen, C. & Li, S. 2018. Rapidly convergent cascade battery cell technology. *High Voltage Engineering,* 44**,** 169-175.

Lin, X., Li, R., Ma, Y. & Zhang, J. 2015. Research on high-ratio DC/DC converter in uninterrupted power system. *Urban Construction Theory Research: Electronic Edition*.

Mei, Y., Li, X. & Huang, W. 2017. Model Predictive Control of Cascaded Bidirectional DC-DC Converters. *Journal of Electrical Engineering,* 12**,** 10-15.

Mei , Y., Qi , Y. & Li , X. 2015. Model Predictive Control Method of Bidirectional Converter in Optical Storage System. *Electric Transmission,* 45**,** 31-35.

Pang, Y., Zhang, G., Jiang, X., Wang, C. & Shang, E. 2016. Application of Cascaded Bidirectional Converters in Multi-energy Converters. *Electric Power Construction,* 37**,** 52-57.

Wu, T. F., Kuo, C. L., Sun, K. H., Chen, Y. K., Chang, Y. R. & Lee, Y. D. 2013. Integration and Operation of a Single-Phase Bidirectional Inverter With Two Buck/Boost MPPTs for DC-Distribution Applications. *IEEE Transactions on Power Electronics,* 28**,** 5098-5106.

Yu, Y., Zhang, X., Long, H. & Luo, Q. 2015. Research on Control Strategy for Energy Storage Converters with Distributed Generation. *Modern Machinery***,** 63-66.

Zhang, J., Feng, Yang, W. & Bao , C. 2015. Application of energy storage system in distributed generation. *Naval Architecture*.

175: Capacity allocation of HESS in microgrid based on fuzzy control and ABC algorithm

Yu ZHANG[1], Zhe YAN[2], Tiezhou WU[3]

[1] *Hubei Key Laboratory for High-efficiency Utilisation of Solar Energy and Operation Control of Energy Storage System, Hubei University of Technology, Hongshan District ,Hubei 430068, China,1836726769@qq.com*
[2] *Hubei Key Laboratory for High-efficiency Utilisation of Solar Energy and Operation Control of Energy Storage System, Hubei University of Technology, Hongshan District ,Hubei 430068, China, 956147458@qq.com*
[3] *Hubei Key Laboratory for High-efficiency Utilisation of Solar Energy and Operation Control of Energy Storage System, Hubei University of Technology, Hongshan District ,Hubei 430068, China, 1039144539@qq.com*

Hybrid energy storage system (HESS) is a key component for smoothing fluctuation of power in microgrid. Appropriate configuration of energy storage capacity for microgrid can effectively improve system economy. A new method for HESS capacity allocation in microgrid based on fuzzy control and ABC algorithm is proposed. The method proposed a power allocation strategy based on low pass filter (LPF) and fuzzy control. The strategy coordinates battery and supercapacitor operation and improves battery operation environment. The fuzzy control takes the state of charge (SOC) of battery and supercapacitor as the input, and the correction coefficient of the time constant of the LPF filter as the output. The filter time constant of the LPF is adjusted in real time, and the SOC of the battery and supercapacitor is stable within the limited range, so that the overcharge and over-discharge of the battery can be avoided, and the lifetime of the battery is increased. This method also exploits sub-algorithms for supercapacitor and battery capacity optimisation. Besides, Monte Carlo simulation of the statistic model is implemented to eliminate the influence of uncertain factors such as wind speed, light intensity and temperature. The artificial bee colony (ABC) algorithm is used to optimise the capacity allocation of hybrid energy storage, which avoids the problem of low accuracy and easy to fall into the local optimal solution of the supercapacitor and battery capacity allocation sub-algorithms, and the optimal allocation of the capacity of the hybrid energy storage system is determined. By using this method, the number of supercapacitor required for the HESS is unchanged, and the number of battery is reduced from 75 to 65, which proves the rationality and economy of the proposed method.

Keywords: HESS, fuzzy control , Monte Carlo , ABC algorithm

1. INTRODUCTION

The randomness, volatility and uncertainty of renewable energy such as wind and light have always been the main reasons restricting their large-scale grid connected operation. As an important component of the micro network, the energy storage system can significantly improve the power system's cancellation level of the renewable energy, and reduce the impact of the new energy grid on the grid. It has become one of the key technologies to promote the replacement of the main energy from the fossil energy to the clean energy.

At present, HESS consisting of battery and supercapacitor is used to stabilise the power fluctuation of the microgrid. But the cost of energy storage is high, and choosing the appropriate energy storage capacity is helpful to reduce costs and improve system economy. In order to ensure system reliability and reduce costs, (Shang et al, 2016, 104-117) adopted a particle swarm optimisation algorithm to configure battery capacity in hybrid power system. (Kuperman et al, 2014, 5399-5405) presented a configuration method for supercapacitors based on expected power and energy characteristics on electric trains. (Li, 2013, 20-24) used cost analysis method to propose a HESS capacity allocation scheme to improve its application in large capacity and high power applications. (Han, 2011, 91-97) used the LPF to suppress the output power fluctuation of photovoltaic power generation. And studied the problem of the capacity allocation of the hybrid energy storage system in the photovoltaic power generation under the condition of the variable life of the energy storage device. Considering the state of charge and the power limitation of charge and discharge, (Xiao, 2014, 1-7) proposed a power allocation strategy based on spectrum analysis and established an economic evaluation model, optimised the capacity allocation of diesel generator and energy storage.

The above methods are based on deterministic analysis, which may lead to inconsistent results. Compared with the traditional hybrid energy storage capacity allocation method, statistical analysis takes into account many uncertainties in the configuration process, which improves the conservatism of the traditional algorithm. (Bludszuweit, 2011, 1651-1658) gives a probabilistic method of energy storage capacity allocation based on uncertainty in wind energy prediction. (Yang, 2014, 1-7) studied a capacity allocation method based on cut-off normal distribution method to reduce the prediction error and reduce the cost of wind power. (Jia, 2014, 516-524) The capacity allocation of HESS using statistical methods shows that the optimal capacity can be flexibly selected according to operation requirements.

In this paper, a microgrid with photovoltaic generation and wind power generation is selected as the research object and a method for HESS capacity optimisation based on fuzzy control and ABC algorithm is proposed. This method divides the power required by the HESS into high-frequency and low-frequency parts by using the LPF-based power allocation strategy. The high-frequency power is compensated by the supercapacitor, and the low-frequency power is compensated by the battery; the fuzzy control reduces the charge and discharge cycle of the battery and extends its lifetime. This method also explored the capacity optimisation sub-algorithms for batteries and supercapacitors, and a statistical model is used to describe the rated power and capacity of energy storage equipment. ABC algorithm is used to optimise the capacity configuration of HESS, which avoids the problem of low accuracy and easy to fall into the local optimal solution of the supercapacitor and battery capacity allocation sub-algorithms, and the optimal capacity optimisation of HESS in microgrid is determined. The simulation results verify the rationality and economy of the method.

2. MICROGRID SYSTEM MODEL

2.1. Photovoltaic generation system model

The output power of Photovoltaic array is mainly related to light and temperature and can be expressed as

Equation 1: The output power of Photovoltaic array.

$$P_{PV}(t) = n_{PV} P_r \left(\frac{R_c(t)}{R_r} \right) [1 + k(T_c(t) - T_r)]$$

Where:

n_{pv} = the number of photovoltaic cells
p_r = rated output power of PV array (W)
$R_c(t)$ = light intensity of t moment (Lx)
R_r = rated light intensity under standard environment(Lx)
$T_c(t)$ = temperature of the t moment (℃)
T_r = rated temperature under standard environment (℃)
K = power temperature coefficient

2.2. Wind power generation system model

The output power of wind power model is generally represented by a piecewise function

Equation 2: The output power of wind power.

$$w_t = \begin{cases} 0 & 0 \le v(t) < v_i \, or \, v(t) > v_0 \\ \dfrac{v(t)^3 - v_i^3}{v_r^3 - v_i^3} P & v_i \le v(t) < v_r \\ P_r & v_r \le v(t) < v_0 \end{cases}$$

Where

P_r = Rated power of fan (W)
v_r = rated wind speed of fan (m/s)
v_i and v_o = cut in and cut out wind speed of the fan (m/s)

2.3. HESS model

It is assumed that the battery terminal voltage will remain unchanged throughout the battery charging and discharging process. The working state of the battery is divided into charging and discharging state.

Equation 3: SOC of battery when discharging.

$$SOC_{bat}(t+1) = SOC_{bat}(t) - \Delta t \frac{P_{dbat}}{\eta_d}$$

Equation 4: SOC of battery when charging.

$$SOC_{bat}(t+1) = SOC_{bat}(t) + \Delta t P_{cbat} \eta_c$$

Where:

P_{cbat} and P_{dbat} = the charge and discharge power of the battery in T period (W)
η_c and η_d = the charge and discharge efficiency of the battery in t period

Similarly, when the supercapacitor is charged and discharged, it meets:

Equation 5: SOC of supercapacitor when discharging.

$$SOC_{sc}(t+1) = SOC_{sc}(t) - \Delta t \frac{P_{dsc}}{\eta_d^{'}}$$

Equation 6: SOC of supercapacitor when charging.

$$SOC_{sc}(t+1) = SOC_{sc}(t) + \Delta t P_{csc} \eta_c^{'}$$

Where:

P_{csc} and P_{dsc} = the charge and discharge power of the supercapacitor in T period (W)
$\eta_{c'}$ and $\eta_{d'}$ = the efficiency of charge and discharge for supercapacitor and battery in t period

2.4. Objective function

Microgrid planning requires comprehensive consideration of short-term and long-term costs to achieve optimal economic benefits. Considering the construction cost, operation and maintenance costs and recovery profit, a objective function is established based on the life cycle cost.

Equation 6: Minimum cost.

$$\min C = C_{es} + C_{om} + C_r$$

Where

C_{cap} = the energy storage cost (yuan)
C_{on} = the operation and maintenance costs (yuan)
C_r = the recovery profit

3. HESS POWER ALLOCATION STRATEGY

3.1. Power allocation strategy based on LPF

This paper uses HESS to maintain instantaneous power balance and achieve power distribution. The power distribution is based on the power requirements of the load and the output power of the distributed power supply to calculate the power that the HESS needs to stabilise, as shown in Equation 7. The LPF divides the frequency band into high frequency and low frequency. The low frequency part is provided with power compensation by battery, and the high frequency part is provided with power compensation by supercapacitor. The supercapacitor compensates for the short time high frequency power fluctuation. The battery only needs to compensate for the long time low frequency power fluctuation, which improves the operating environment of the battery and extends its lifetime.

Equation 7: The power that HESS needs to adjust.

$$P_J(t) = P_L(t) - P_{WT}(t) - P_{PV}(t)$$

Where

$P_L(t)$ = Load power at time t (W)

The process of power allocation is first to sample the power that HESS needs to adjust, and the sampling period is 10min. Secondly, the discrete Fourier transform is applied to the sample data P_J =[$P_J(1)$, $P_J(2)$,…, $P_J(t)$,…, $P_J(N)$], and the result of spectrum distribution is obtained.

Equation 8: Fourier transform.

$$\begin{cases} S = DFT(P_J) = [S_J(1), \ldots, S_J(n)] \\ f_J = [f_J(1), \ldots, f_J(n), \ldots, f_J(N)] \end{cases}$$

Where

$DFT(P_J)$ = discrete Fourier transform of data P_J

$S_J(n)$ = the amplitude of the corresponding nth frequency after DFT

Finally, the Fourier inverse transform is used to convert the amplitude frequency results of each compensation band to the time domain, then the power situation of each frequency band can be obtained, and the power instruction of each energy storage device is obtained.

3.2. Time constant adjustment of filtering based on fuzzy control

When the LPF is used, due to the fixed value of the time constant T of the filter, it is very easy to lead to overcharge and over-discharge without considering the SOC of the energy storage unit. In this paper, the SOC is considered and the filter time constant T is corrected according to the SOC of the battery and the supercapacitor, so that the SOC of the units are always stable in a certain range. Therefore, the SOC limit value is set to be

Equation 9: SOC of supercapacitor.

$$SOC_{sc\_min} \le SOC_{sc} \le SOC_{sc\_max}$$

Equation 10: SOC of battery.

$$SOC_{bat\_min} \le SOC_{bat} \le SOC_{sc\_max}$$

In this paper, a fuzzy controller is added on the basis of the LPF control. According to the SOC of the battery and the supercapacitor and the current charge/discharge status of the system, the filter time constant T is changed in real time so that the SOC of the energy storage unit is stable within the limited range. As shown in Figure 1, the steps of fuzzy control are as follows.

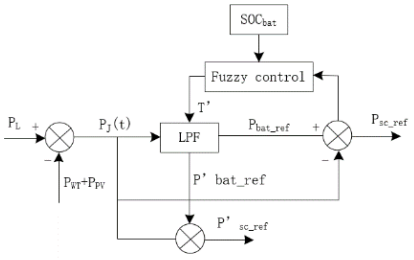

Figure 1: Fuzzy control schematic diagram

a) Establish input, output fuzzy subsets and membership functions

In this paper, SOC_{bat} and SOC_{sc} are selected as input, and the revised filter time constant is the output. First SOC_{bat} and SOC_{sc} are normalised, and the membership degree of SOC of the energy storage units are as follows:

Equation 11: Battery membership degree.

$$\mu_{bat} = \frac{SOC_{bat} - SOC_{bat\text{-}mid}}{SOC_{bat\text{-}mid}}$$

Equation 12: Supercapacitor membership degree.

$$\mu_{sc} = \frac{SOC_{sc} - SOC_{sc\text{-}mid}}{SOC_{sc\text{-}mid}}$$

Where

SOC_{bat_mid} and SOC_{sc_mid} = intermediate values of SOC_{bat} and SOC_{sc}

μ_{bat} and μ_{sc} are used as inputs for fuzzy control, and the fuzzy sets of input are set to {NL, ZE, PL}, the corresponding domains of μ_{bat} are [-m, m], the corresponding domains of μ_{sc} are [-n, n], and m and N are both between 0 and 1. In general, the charge/discharge depth of the supercapacitor is greater than that of the battery, so n › m. $\Delta\varphi$ is the output of fuzzy control and the fuzzy sets are [-0.98, -0.4, 0, 0, 0.4, 0.98]. Whether $P_J(t)$ is greater or less than zero, its input membership function and output membership function are the same, as shown in Figure 2.

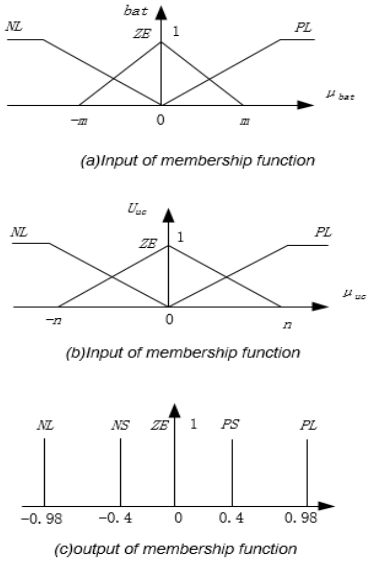

Figure 2: Input/output of membership function

Table 1: Fuzzy control rules ($P_J(t) < 0$)

SOC_{bat}	SOC_{uc}		
	NL	ZE	PL
NL	ZE	NS	NL
ZE	PS	ZE	NS
PL	PL	PS	ZE

Table 2: Fuzzy control rules ($P_J(t) > 0$)

SOCbat	SOCuc		
	NL	ZE	PL
NL	ZE	PS	PL
ZE	NS	ZE	ZE
PL	NL	NS	NE

b) Formulate fuzzy rules

From the case where $P_J(t)$ is greater than zero and less than zero respectively, the fuzzy rules are formulated, as shown in Table 1-2.

c) Defuzzification

The correction coefficient$\Delta\varphi$of reference power is obtained by using the weighted average method for defuzzification calculation, $-1< \Delta\varphi<1$

Equation 13: correction coefficient.
$$\Delta\varphi = \frac{\sum_i \sum_j \mu_{1i}(SOC_{bat})\,\mu_{2i}(SOC_{sc})\,k_{ij}}{\sum_i \sum_j \mu_{1i}(SOC_{bat})\,\mu_{2i}(SOC_{sc})}$$

Equation 14: Revised time.
$$T' = (1+\Delta\varphi)T$$

Where

$\mu_{1i}(SOC_{bat})$ and $\mu_{2j}(SOC_{sc})$ = ith membership value of SOC_{bat} and SOC_{sc}

Δk_{ij} = the corresponding output of two inputs

The control strategy is as follows: The $P_J(t)$is decomposed by LPF. The high and low frequencies of decomposition are used as the initial charge and discharge instructions for supercapacitor and battery P_{sc_ref} and P_{bat_ref}. With the current state of the charge of the battery as the input of the fuzzy controller, the fuzzy adaptive control of the battery is carried out, the modified filter time constant A is output, and the charge and discharge instructions of the battery are further corrected, and P'_{bat_ref} and P'_{sc_ref} are obtained.

When $P_J(t) < 0$, HESS needs to absorb energy, If SOC_{bat} and SOC_{sc} are intermediate values, maintain the default T constant. When SOC_{bat} is a minimum and SOC_{sc} is a maximum, T is properly reduced to increase the charging power of the supercapacitor. When SOC_{bat} is the maximum and SOC_{sc} is a minimum, the T is properly adjusted to increase the charging power of the supercapacitor. When $P_J(t) > 0$, HESS needs to release energy, If SOC_{bat} and SOC_{sc} are intermediate values, maintain the default T constant. When SOC_{bat} is a minimum and SOC_{sc} is a maximum, T is properly adjusted to reduce the charging power of the supercapacitor. When SOC_{bat} is the maximum and SOC_{sc} is a minimum, the T is properly reduced to increase the charging power of the supercapacitor.

4. HESS CAPACITY ALLOCATION METHOD

4.1. Battery capacity allocation sub-algorithms

The battery capacity allocation process is based on the energy stored in the battery and the storage capacity of the battery energy storage system is E^A_{bat}, as shown in Figure 5. First initialise the energy of the battery to the initial SOC i_{SOC}, at each calculation step, the exchanged energy e is calculated. When $e \leq 0$, battery needs to release energy e, regardless of the state of charge, the new SOC is lower than before. When $e > 0$ and $E_{bat}(i-1)+e \leq i_{SOC}$, , battery can obtain energy e, and the

new SOC is higher than before. When $e > 0$ and $E_{bat}(i-1)+e > i_{SOC}$, battery can't obtain energy e, and the new SOC is is equal to that before.

The sub-algorithm takes into account the natural limit of storage capacity of the battery, and the battery cannot be recharged when the maximum SOC is reached. Because deep discharge will reduce the service life of the battery, the range of the SOC of the stored energy is usually set by the discharge depth D_{bat} (75%). During the allocation process, the battery's energy capacity C_{bat} is defined as

Equation 15: Battery's energy capacity.

$$C_{bat} = \frac{E_{bat}^{A}}{D_{bat}}$$

Battery charge and discharge power constraints are

Equation 16: Battery charge and discharge power constraints.

$$\begin{cases} P_{cbat,min} \le P_{bat} \le P_{cbat,max} \\ P_{dbat,min} \le P_{bat} \le P_{dbat,max} \end{cases}$$

Where

P_{cbat} and P_{dbat} = The charging and discharging power of the battery (W)

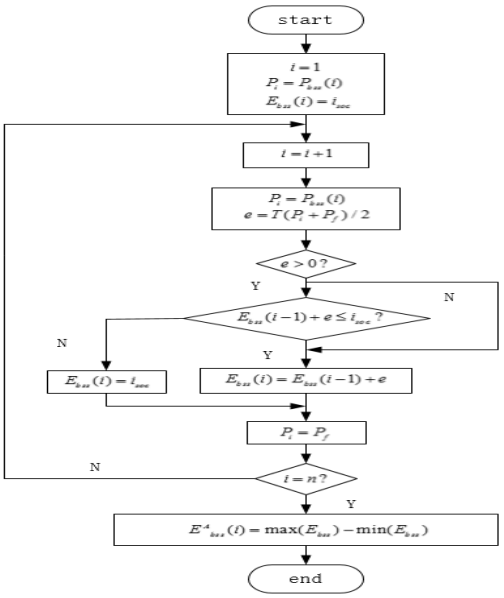

Figure 3: Calculation of battery energy storage system capacity

4.2. Supercapacitor capacity allocation sub-algorithms

The calculation method for energy storage capacity E^{A}_{sc} and energy capacity C_{sc} of the supercapacitor is the same as the battery, i.e.

Equation 18: The storage capacity of supercapacitor.

$$E_{sc}^{A} = \max\left[E_{sc}(t)\right] - \min\left[E_{sc}(t)\right]$$

Equation 19: supercapacitor's energy capacity.

$$C_{sc} = \frac{E_{sc}^{A}}{D_{sc}}$$

Equation 20: supercapacitor charge and discharge power constraints.

$$P_{sc\text{-}max} = \max(\left|P_{sc}(t)\right|)$$

Where

D_{sc} = discharge depth of supercapacitor

4.3. Capacity optimisation based on ABC algorithm

The battery and supercapacitor capacity allocation sub-algorithm is easy to fall into the local optimal solution. To solve this problem, the ABC algorithm is used to further optimise the capacity allocation and get the optimal configuration of HESS capacity. ABC algorithm is an algorithm based on honeybee honey collecting behaviour. The algorithm seeks the optimal

solution by continuously circulating three ways: leading bees search for food in the neighbourhood of the food source, following bees search for food by a certain probability, and investing bees search for new food sources. The probability of food source i being selected is

Equation 22: The probability of food source i being selected.

$$P_i = \frac{F(X_i)}{\sum_{k=1}^{N} F(X_i)}$$

Where

$F(X_i)$ = food fitness

Leading bees and following bees will search for new food sources in the neighbourhood of the food source. When the new food source returns better, give up the original food source, instead, preserve the original food source. The location of the new food source is defined as V_i, the search equation is given by

Equation 23: The location of the new food source.

$$V_{ij}(t+1) = X_{ij}(t) + \mathrm{r} \times \left[X_{ij}(t) - X_{kj}(t) \right]$$

Where

j, r and k = random number, k≠I, and r is between-1 and 1

If a food source is not improved within the set number of iterations, it is explained that the food source is solved locally and the food source is abandoned. The leading bee corresponding to this food source is transformed into a following bee to search for new food sources. The location of its search for a new food source, Z_i is given by

Equation 24: The location of its search for the new food source.

$$Z_i = X_{min} + r \times (X_{max} - X_{min})$$

Where

X_{max} and X_{min} = upper and lower borders in each dimension for the original food chain X_i

The specific flow of artificial bee colony algorithm is as follows:

Step 1：Initialisation. Randomly generate N food sources and calculate the fitness of each food source;

Step 2：Search the neighbourhood of X_i of the food source location of each leading bee, and generate a new food source position V_i according to Equation 22. The fitness of X_i and V_i were calculated respectively, and a better food source location was preserved.

Step 3：According to the selection probability of each food source, a food source was selected and searched in the neighbourhood of the food source position X_i. A new food source V_i was produced according to Equation 23. The fitness of X_i and V_i was calculated, and the better location of food source was retained.

Step 4：Determine whether there is a food source to be abandoned; if so, give up the food source and replace it with the new food source according to the Equation 24. Otherwise, take the next step.

Step 5：Determine if the maximum number of iterations has been reached. If not, return to step 2, otherwise, output the location of the best food source.

The ABC algorithm is used to optimisation the HESS capacity of the microgrid. The specific solution flow is as follows:

Step 1：Initialise the parameters of the artificial bee colony algorithm and read load and distributed power data and calculate their capacity.

Step 2: Randomly generate K optimal allocation scheme and calculate its corresponding life cycle cost C, taking it as fitness.

Step 3：Stochastic generation of K optimal configuration scheme in the neighbourhood of the above initial capacity configuration scheme, and calculate its corresponding life cycle cost C, compared with the fitness above, and retain the optimal allocation scheme;

Step 4：Determine whether the optimisation allocation scheme remain unchanged for continuous I times. If so, the corresponding solution is the local optimal solution, and go to the next step. Otherwise, it will continue to solve its local optimal solution iteratively.

Step 5：Determine whether to reach the maximum number of iterations Nmax, if so, go to the next step. Otherwise, go back to step 2 and recalculate best solution in other places;

Step 6：Comparing the local optimal solutions, calculating the global optimal solution, and output the optimal power and capacity of the HESS.

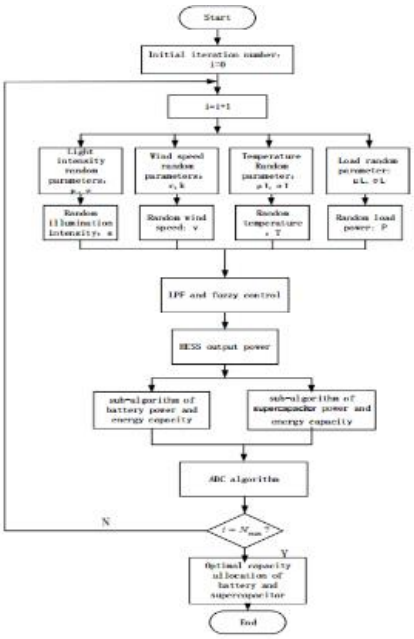

Figure 4: HESS capacity optimisation configuration flow chart

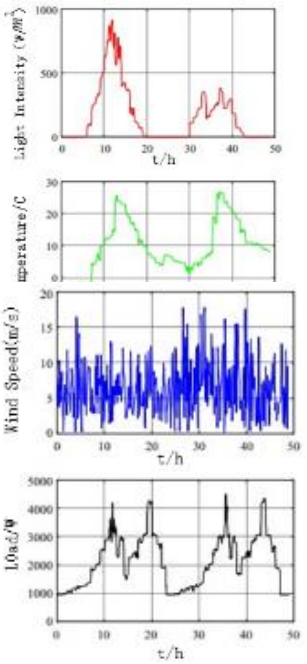

Figure 5: 48 Hours environmental data of microgrid

4.4. HESS configuration flowchart

Taking full consideration of the influence of uncertainties, this paper uses Weibull distribution and normal distribution to define the wind speed and light intensity respectively. The wind speed and light intensity data are randomly generated by Monte Carlo simulation. The flow chart of the optimal configuration of the capacity of the microgrid hybrid energy storage system is shown in Figure 6. The algorithm consists of four parts:

1) A set of random distribution parameters[c, k, μ, σ, μT, σT, μL, σL] are obtained through Monte Carlo simulation. And the data of wind speed and light intensity were generated through statistical analysis.
2) Power system time domain simulation and Control strategy. This section describes the LPF-based power allocation strategy and fuzzy control.
3) The calculation methods for rated power and energy capacity include battery and super capacitor calculation sub-algorithms.
4) Capacity allocation and result analysis of HESS. A large number of random scenarios are generated by Monte Carlo simulation at a certain confidence level, and the capacity allocation results of the hybrid energy storage system are obtained. Then the ABC algorithm is used to optimise the result, and the solution process ends until the iteration number I = Nmax.

5. EXAMPLE ANALYSIS

5.1. System power profile

The 48-hour environmental data with 98% confidence level of the wind, such as light intensity, wind speed, temperature and load profiles are shown in Figure 5. The data of wind speed, temperature and light intensity sampled from every ten minutes are simulated, and the data of PV system, fan and load can be obtained The net load power curve is shown in Figure 6. The result of spectral analysis of net load using LPF algorithm is shown in Figure 7. According to the above, the spectrum analysis results are divided into two components: low frequency and high frequency.

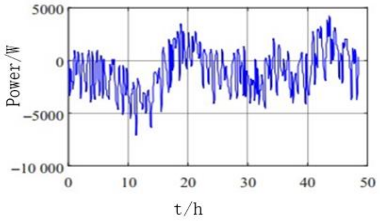

Figure 6: Net load power curve

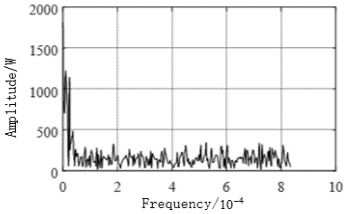

Figure 7: Results of spectrum analysis of net load power

Furthermore, the curves of charge and discharge power of supercapacitor and battery in 48h are shown in Figures 8 and 9. The power of the positive half axis of the time axis indicates the power shortage. The energy storage system compensates the missing system power by discharge, and absorbs the excess power by charging to keep the power of the system stable. The Figure 12 shows that the supercapacitor has a large number of charge and discharge cycles, compensating for short-term high-frequency power fluctuations; and the battery charge and discharge cycle is small, compensating long-term low-frequency power fluctuations. The results show that the LPF allocation strategy based on fuzzy control effectively improves the operating environment of the battery, while the fuzzy control reduces the battery's small charge-discharge cycle and increases its lifetime.

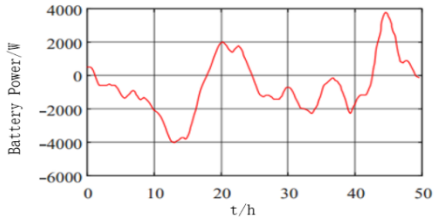

Figure 8: The charge and discharge power of battery

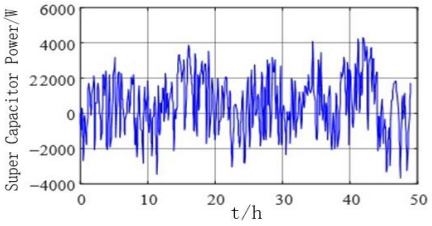

Figure 9: The charge and discharge power of supercapacitor

5.2. HESS configuration and results

Hybrid energy storage system capacity consists of rated power and energy capacity. The rated power is the maximum instantaneous power that the HESS can provide. Energy capacity is defined as the total amount of energy that the HESS can store. Energy storage system is used for 20 years. The SOC limits for battery and supercapacitor are shown in Table 3. The ABC algorithm parameters are set as follows: I=1000, the maximum number of iterations K_{max} = 100; the number of the leading bees m_1=30, and the number of the following bees m_2=10.

Table 3: SOC limit of battery and supercapacitor

Energy storage unit	SOC_{min}	SOC_{max}
battery	0.30	0.80
supercapacitor	0.20	0.95

Table 4 configures the final result for the hybrid energy storage capacity. When the fuzzy control and ABC algorithms are not used, the battery capacity is 39201 W·h, the rated power is 5255W, the energy capacity of the supercapacitor is 36599 W·h, the rated power is 7003W, the minimum cost is 191774.17 yuan. When the fuzzy control is used and the ABC algorithm is not used, the battery capacity is 38243 W h, the rated power is 5133W, the energy capacity of supercapacitor is 36100 W·h, the rated power is 6905W, and the minimum cost is 286949 yuan. After using fuzzy control and artificial swarm algorithm, the battery capacity is 32362 W h, the rated power is 4449W, the energy capacity of supercapacitor is 32362 W·h, the power rating is 5588W, and the minimum cost is 259750 yuan. It can be seen that by fuzzy control and ABC algorithm, both the rated power and the energy capacity of the battery or supercapacitor have been reduced a lot and the minimum cost is dropped by 32023.77 yuan. Compared with the supercapacitor, the number of battery varies greatly depending on the rated power and energy capacity.

Table 4: Final result of HESS capacity allocation

capacity allocation	P_{bat}/W	P_{sc}/W	E_{bat}/(W·h)	E_{sc}/(W·h)	min_C
Fuzzy control and ABC are not used	5255	7003	39201	36599	291774.17
Fuzzy control is used and ABC is not used	5133	6905	38243	36100	286949
Fuzzy control and ABC are not used	4449	5588	32362	32080	259750.4

In this paper, the HESS capacity allocation using fuzzy control and ABC algorithm is relatively economical and reliable. In most cases, this capacity allocation can meet the requirements of the microgrid. When the capacity of battery and supercapacitor is insufficient in rare cases, the demand side controllable load can be used to compensate for additional energy storage capacity requirements.

6. CONCLUSION

On the basis of power supply, energy storage type, power and energy characteristics, a hybrid energy storage capacity allocation method based on fuzzy control and ABC algorithm is proposed in this paper. Hybrid energy storage system aims at stabilizing the power fluctuation of distributed power supply and ensuring the output power of microgrid is within controllable range. Combining the power distribution strategy based on LPF and fuzzy control, the lifetime of the battery is increased by using the complementary characteristics of battery and the supercapacitor, and the stability of the system is improved. The method has also explored the capacity allocation sub-algorithm of battery and supercapacitor, and the optimal capacity allocation of the HESS is finally obtained by using the ABC algorithm. Compared with the traditional capacity configuration method, this method takes into account many uncertain factors in the configuration process, improves the conservative type of the traditional algorithm, and makes the system more economical and reliable.

7. REFERENCES

Shang C, Srinivasan D, Reindl T. 2016. An improved particle swarm optimisation algorithm applied to battery sizing for stand-alone hybrid power systems[J]. International Journal of Electrical Power & Energy Systems, 74:104-117.

Kuperman A, Mellincovsky M, Lerman C, 2014. Supercapacitor Sizing Based on Desired Power and Energy Performance[J]. IEEE Transactions on Power Electronics, 29(10):5399-5405.

LI C, Xiu Y, Zhang M, 2013. Optimal Configuration Scheme for Hybrid Energy Storage System of Super-capacitors and Batteries Based on Cost Analysis[J]. Automation of Electric Power Systems, 37(18):20-24.

Han X, Cheng C, Ji T, 2011. Capacity optimal modeling of hybrid energy storage systems considering battery life [J]. Proceedings of the CSEE, 33(34)： 91-97(in Chinese)

Xiao J, Bai L, Wang C, 2014. Spectrum analysis based capacity optimisation method of energy storage and diesel engines in island microgrids[J]. Power System Technology, 38(9)： 1-7(in Chinese).

Bludszuweit H, Domínguez-Navarro JA, 2011. A probabilistic method for energy storage sizing based on wind power forecast uncertainty[J]. IEEE Transactions on Power Systems, 26(3)： 1651-1658.

Yang S, Li J, Hui D, 2014. Optimal capacity configuration of battery energy storage system to track planned output of wind farm[J]. Power System Technology, 38(6)： 1-7(in Chinese).

Jia HJ, Mu YF, Qi Y, 2014. A statistical model to determine the capacity of battery-supercapacitor hybrid energy storage system in autonomous microgrid[J]. Electrical Power and Energy Systems, 54(1)：516-524.

176: A method of power distribution network classification based on improved grey cluster

Lichao XU[1], Yu YU[1], Yiheng YIN[2]

[1] .Solar Energy Efficient Utilisation Cooperative Innovation Center, Hubei University of Technology,HubeiWUhan,kssdyrh@163.com
[2]. School of Electrical Engineering, Wuhan University,HubeiWuhan,1136869083@qq.com

The classification of distribution network power supply area is an important fundamental work for the planning and construction of distribution network which will directly affects the scale of investment for the construction of power grid. The scientific and reasonable classification of the power supply area can help to make a differentiated aim and plan of distribution network; meanwhile, it can also meet the requirements of reliability and economy so as to prolong the life- cycle of distribution network. Taking three factors into thorough consideration, namely, the development level, construction level, and load level of all the areas, this paper gives a complete index system for the classification of power supply area. According to the relevant data, the authors use the grey polycategory method of the improved whitenisation weight function to classify the area of distribution network. In the process of this, the index weight is obtained by the comprehensive application of AHP and entropy weight, which can prove that the method from this paper is useful according to the result of the classification of power supply in a certain city in Henan. The division of the distribution network power supply area is a key issue in distribution network planning. Due to the actual situation of distribution network in China varies greatly. If the construction is carried out according to a unified standard, it will result in economic and technically unreasonable situations such as inefficient use of equipment assets and serious waste. Scientific and rational distribution network planning is the basic basis for the construction and transformation of power grids, and it is also an important prerequisite for safe, reliable and economical operation of power grids. The division of scientific and reasonable power supply areas for distribution networks and the provision of guiding opinions based on the district results are conducive to improving the investment decision-making level and investment efficiency of power grid planning.

Keywords: distribution network；power supply area division；grey cluster；combination weighting method；diversified planning.

1. INTRODUCTION

At present, most of the literature studies are substation power supply area division and optimal power supply radius (Tang, 2015, Peng, 2015, Li, 2006). The lack of quantitative calculation and analysis methods for the distribution of power supply areas in distribution networks is mainly based on expert experience and qualitative classification, and it is difficult to achieve scientific and effective division. In terms of indicators, the main body of the comprehensive evaluation index system for distribution network planning proposed in Xiao (2008) the literature is the index of distribution network construction level, power supply capacity, etc., and lacks indicators that reflect regional differences. Liu (2012) proposes a comprehensive evaluation index system that takes into account resilience, but does not consider economic indicators that reflect regional characteristics. Although Zhou (2016) proposes a more comprehensive power supply area division index system and calculation method. However, since only the analytic hierarchy process is used to obtain the weights, the obtained power supply partition results are not objective enough. This paper proposes a complete set of power supply partition index system based on comprehensive consideration of the factors that affect the distribution network partition. Based on this, the power supply partition is implemented by using the grey clustering method, and the commonly used triangle whitening weight function is improved. Improve the accuracy of quantitative evaluation. In addition, in terms of index weights, a combination weighting calculation method is proposed, which combines the index weights of the AHP method and the entropy weight method, which avoids the irrationality of mixed weights in the previous calculation methods.

2. INDEX SYSTEM

The primary issue in the allocation of power supply areas is the selection of indicators. In addition to geographical conditions, more relevant factors need to be considered. The index system for the distribution of power supply network regions proposed in this paper is shown in Figure 1. There are certain correlations among various indicators. For example, the higher the level of development of power supply areas, the generally higher level of construction and load levels. vice versa. Therefore, the power supply partition not only needs to calculate the whitening weight function value of the individual indicators with respect to different grey classes, but also needs to calculate the grey clustering coefficients in combination with the index weights, on the basis of which a reasonable partition result can be obtained.

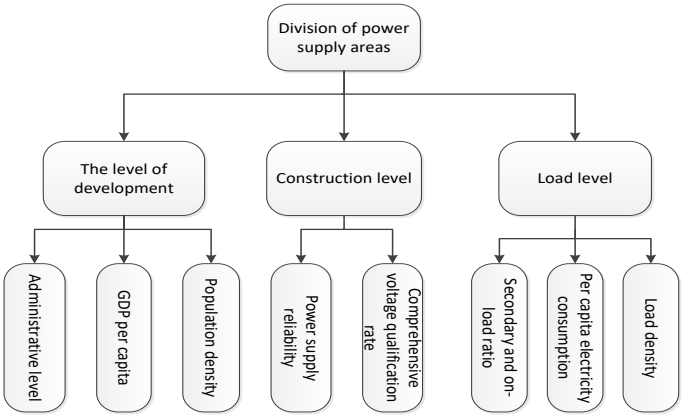

Figure 1: Indexes system of the power supply division

3. IMPROVED GRAY CLUSTERING METHOD APPLIED TO POWER SUPPLY PARTITION

Grey clustering is a method of aggregating some observational indices or observation objects into several definable categories based on the whitening weights function of correlation matrix or grey number (Liu, 2004, Lei, 2009, Li, 2016), in which the most important two parts are the calculation of index weights and the construction of the whitening weights function.

Since the form of the whitening weight function in the grey cluster evaluation method has a decisive influence on the evaluation result, the white point weighting function of the centre point is improved in this paper. There are m clustering indicators, n objects, and s different grey classes (Zhang, 2017). The modelling steps of the grey clustering evaluation model based on the improved centre point triangle whitening weight function are as follows:

3.1. Determine the centre point of the whitening weight function

For the indicator, set its value range to $[a_i, b_i]$. Determine the center point $\lambda_i^1, \lambda_i^2, \ldots, \lambda_i^s$ of ash class *1* to grey class *S* according to the number of grey classes required.

3.2. Determining the whitening weight function for grey class 1 and grey class

Taking the whitening right function of grey class as an example $f_i^s(x)$, (same reason $f_i^1(x)$). In the traditional trigonometric whitening function, when the sample value is greater than the center point, It does not increase with the increase of $f_i^s(x)$, resulting in a lower evaluation value for better index samples, which affects the accuracy of quantitative evaluation. Therefore, this paper improves the functions $f_i^1(x)$ and $f_i^s(x)$ on the basis of the traditional upper measure and lower measure functions respectively. The improved whitening weight function expressions (1) and (2) are shown in Figures 2 (a) and (b), respectively.

(1) $$f_i^1(x)=\begin{cases}0, x\notin[a_i,\lambda^2_i];\\ p(x-\lambda_i^2)/\lambda_i^1-\lambda_i^2, x\in[\lambda_i^1,\lambda_i^2);\\ (p-1)x+\lambda_i^1/\lambda_i^1, x\in[a_i,\lambda^2_i];\end{cases}$$

(2) $$f_i^s(x)=\begin{cases}0, x\notin[\lambda_i^{s-1},b_j];\\ p\ (\lambda_i^{s-1}-x)/\lambda_i^{s-1}-\lambda^s_i, x\in[\lambda_i^{s-1},\lambda^s_i];\\ (1-p)x+p-\lambda_s/1-\lambda_s, x\in[\lambda_i^s,b_i];\end{cases}$$

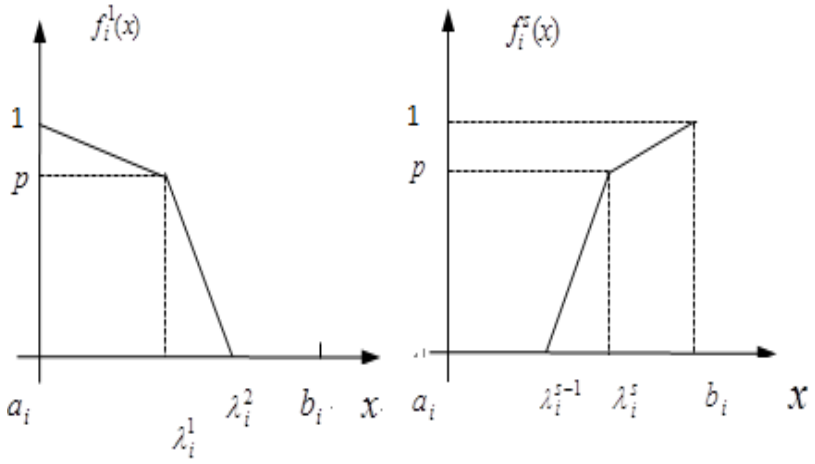

Figure 2: Graph of improved whitenisation weight function

For grey class *1* and grey class, the improved whitening weight function can well reflect the degree of conformity of the sample value to the grey class. The function $f_i^s(x)$ is still used as an example ($f_i^1(x)$ is the same). For the constant *p*, there is *p*∈(0.5,1). By changing the value of *p*, the bias of the whitening weight function can be changed. This can ensure that the grey class coincidence degree $f_i^s(x)$ can be increased as quickly as possible when $x \in [\lambda_i^{s-1},\lambda_i^s]$, inheriting the main features of the traditional measurement function. At the same time, it can continue to maintain incrementality when $x \in [\lambda_i^{s-1},\lambda_i^s]$, to ensure the correctness of $f_i^s(x)$ quantitative assessment.

3.3. Determining the whitening weight function of grey class 2 to grey class

For the grey class *k*(*k*∈{2,3,…,*s*-1}), connect the point $(\lambda_i^k,0)$, the center point $(\lambda_i^{k-1},0)$ of the gray class *k*, and the centre point $(\lambda_i^{k+1},0)$ of the gray class k with a straight line. Get the i indicator. The triangle whitening weight function for gray class *k* is $f_i^k[\lambda_i^{k-1},\lambda_i^k,-,\lambda_i^{k+1}], i=1,2,\ldots,m, k=2,3,\ldots,s-1$ that is

$$f_i^k(x)=\begin{cases}0, x\notin[\lambda^{k-1}_i,\lambda^{k+1}_i];\\ x-\lambda_i^{k-1}/\lambda_i^k-\lambda_i^{k-1}, x\in[\lambda^{k-1}_i,\lambda^k_i];\\ \lambda_i^{k+1}-x/\lambda_i^{k+1}-\lambda_i^k, x\notin[\lambda^k_i,\lambda^{k+1}_i];\end{cases}$$

(3)

3.4. Combination weight w_i calculation

Grey clustering weights can be divided into grey variable weighted clusters and grey fixed weighted clusters. The weight coefficients of variable weight clustering are related to the sample values of the index, emphasizing the difference of the sample values (Liu, 2004), i.e., the more vague data should occupy less weight. The weight of a sample in a weighted

cluster depends on its own importance. It is a fixed value regardless of the sample value of the indicator. This paper proposes a fixed-weight clustering approach that combines subjective and objective weighting methods. It uses the analytic hierarchy process (subjective weighting method) to reflect the importance of the sample, and the entropy weighting method (objective weighting method) to reflect the differences in the sample. Combining these two methods of weighting achieves the complementary effects of weighting and weighted clustering.

Analytic Hierarchy Process

All the factors affecting the division of the distribution network power supply area will be organised and layered, and a multi-level structural model will be established. For each indicator of the same level, a judgment matrix is constructed by comparing the degree of influence on the indicators of the previous level, and the eigenvalues and eigenvectors are solved and the consistency check is performed according to Equations (4) and (5).

$$CI = \frac{\lambda_{\max} - n}{n-1} \quad (4)$$

$$CR = \frac{CI}{RI} \quad (5)$$

In Equations (4) and (5), n is the order of the judgment matrix; λ_{max} is the largest eigenvalue; RI is the average random consistency index. The smaller the CI value, the better the consistency of the judgment matrix. When $CR < 0.1$, the judgment matrix passes the consistency check. If the judgment matrix fails the consistency test, it is necessary to re-evaluate the mutual importance of each index until it passes the consistency check of the judgment matrix. Then, the feature vector corresponding to the largest eigenvalue is the importance ranking of the index with respect to the upper level index. After normalisation, the index weight vector $\alpha = [\alpha_1, \alpha_2, \dots, \alpha_m]$ can be obtained.

Entropy method

- *Indicators are both homogeneous and non-dimensional*

Assume that there are m indexes, each index corresponds to n areas, and an initial matrix $Y = (y_{ij})_{m\times n}$ is obtained, where y_{ij} is the *i-th* index value of the *j-th* area. If there are reverse indicators (that is, the smaller the number is, the better) or moderate indicators (that is, the optimal value of a certain segment in the middle), then m indicators need to be converted into positive indicators (that is, the larger the number, the better) (OuYang, 2013). In addition, the dimensions of different indicators are mostly different, and they must also be dimensionless. The resulting standardised matrix for the indicator data is $X = (x_{ij})_{m\times n}$.

- *Weight calculation*

The entropy value of the *i-th* index

$$E_i = -k\sum_{i=1}^{m} x_{ij} \cdot \ln x_{ij} \quad (6)$$

In Equation (6), to make $0 < E_i < 1$, generally take k=1/ln$n$.

The entropy weight of the *i-th* indicator is

$$\beta_i = \frac{1 - E_i}{m - \sum_{i-1}^{m} E_i} \quad (7)$$

Combination weight

The combination weight is calculated as

$$w_i = \frac{\sqrt{\alpha_i \cdot \beta_i}}{\sum_{i=1}^{m} \sqrt{\alpha_i \cdot \beta_i}} \quad (8)$$

Equation (8) overcomes the fact that only a few weighted indicators caused by the mixed weight calculation result reflect the characteristics of the object being evaluated and cannot reflect the influence of all indicators. Therefore, the resulting mixed weight can reflect the evaluation more fully. The characteristics of the object.

3.5. Calculate grey clustering coefficient σ_j^k

Calculate the clustering coefficient of the object $j(j = 1,2, \dots, n)$ for the gray class $k(k = 1,2, \dots, s)$:

$$\sigma_j^k = \sum_{i=1}^{m} f_i^k(x_{ij}) \cdot w_i \quad (9)$$

In Equation (9), $f_i^k(x_{ij})$ is the i-index *k* grey class whitening weight function, and w_i is the weight of the index *i* in the gray cluster.

3.6. Grey clustering

It is determined by $max_{1\le k\le s}\{\alpha_j^k\} = \alpha_j^{k*}$ that the object *j* belongs to the grey class k^*. When there are multiple objects that belong to the k^* gray class, the merits or ranks of each object are further determined according to the size of the comprehensive clustering coefficient.

4. CASE ANALYSIS

Taking the historical data of the development level, construction level and load level of a city in Henan Province in 2015 as a sample for case analysis.

4.1. The calculation of the whitening right function value

The results of the same-oriented and non-dimensionalied processing of the three first-level indicator data are shown in Table 1.

Table 1 Index data of 12 regions of Xuchang

Area	administrative leve	GDP per capita	Population density	Power supply reliability	Comprehensive voltage qualification rate	Secondary and above loads	Per capita electricity consumption	Load density
A city	94.25	95.46	82.65	96.56	95.23	91.08	91.5	89.46
Changge County	86.25	98.15	69.06	85.92	88.69	84.09	89.92	80.84
Yuzhou County	88.01	91.32	66.65	87.26	90.87	86.11	84.2	77.49
County County	87.33	85.31	65.76	91.17	86.81	83.75	85.17	74.09
A suburb	80.55	77.61	78.35	82.62	83.28	78.59	82.62	73.68
Xiangcheng County	79.32	81.33	66.48	81.01	83.54	83.67	81.01	71.64
Yanling County	79.99	82.23	65.61	79.76	77.36	81.38	78.76	70.74
Changge Rural	62.65	76.64	64.15	73.43	81.07	71.54	75.43	62.66
Xiangcheng Rural	62.78	74.05	62.97	69.87	71.56	66.33	69.87	69.94
Yuzhou Rural	64.01	73.91	63.05	73.95	74.54	68.98	73.95	69.31
Rural areas of a county	60.61	70.86	62.64	68.75	68.63	64.66	68.73	68.91
Yanling Rural	63.99	74.81	61.56	66.32	66.85	65.16	66.32	66.93

According to the indicator data in Table 1, the whitening weight function value is calculated using the grey clustering method based on the improved whitening weight function.

4.2. Weight calculation

Table 2 Indexes weights

Target Layer	Level two indicators	Level three indicators	Index weight	Normalised
Division of power supply areas	Development level（0.4）	Administrative level	0.4	0.16
		GDP per capita	0.4	0.16
		Population density	0.2	0.08
	Construction level（0.2）	Reliability rate of power supply	0.5	0.1
		Comprehensive voltage pass Rate	0.5	0.1
	Load level（0.4）	Second-and above-load ratio	0.4	0.16
		Per capita power consumption	0.2	0.08
		Load density	0.4	0.16

The weight values calculated by the analytical hierarchy process and obtained by the consistency test are shown in Table 2.

The normalised values of the weight in Table 2 is expressed as a vector $\alpha = [0.16,0.16,0.08,0.1,0.1,0.16,0.08,0.16]$

Substituting the indicator data in Table 1 into the entropy weighting method, the weight vector obtained by Equations (6) and (7) is $\beta = [0.26,0.118,0.091,0.095,0.095,0.144,0.095,0.103]$

The combined weight obtained by using Equation (9) is $\omega = [0.206,0.139,0.086,0.098,0.153,0.088,0.13]$(10)

4.3. Power supply area division

The number of types of power supply network power supply areas should be appropriate. It is necessary to avoid excessive types of distribution network construction standards that are complex and difficult to implement, but also to reflect the characteristics of “differentiation” in distribution network planning, and to truly reflect the different regions. The actual characteristics and development needs of the company can be implemented according to local conditions(Peng2015). Based on this, combined with the development status of the distribution network in Henan Province, the types of power supply areas are classified into five categories, *ie* A, B, C, D, E. According to the expert survey, the center point of the whitening weight function determined for each indicator is shown in Table 3. According to the survey conducted by experts, the central points of the determined whitening weight functions are shown in Table 3

Table3 The central point of the whitening weight function

Various grey center points	Grey class Ⅰ	Grey class Ⅱ	Grey class Ⅲ	Grey class Ⅳ	Grey class Ⅴ
administrative level	65	75	85	92	97
GDP per capita	65	74	82	90	95
Population density	60	70	80	90	95
Power supply reliability	70	75	85	95	99
Comprehensive voltage qualification rate	68	75	85	95	99
Secondary and above loads	65	72	80	88	95
Per capita electricity consumption	60	75	80	90	93
Load density	60	70	80	90	95

When calculating the whitening weight function value and grey clustering coefficient of each index for different grey classes, the range of each index is $[60,100]$. The affiliated ash classes in 12 areas of a city are shown in Table 4.

Table 4 Power supply division results of 12 regions of Xuchang

Area	Grey class type	Partition results	Area	Comprehensive score	Grey class type
A city	Grey class Ⅳ	B	Yanling County	Grey class Ⅱ	D
Changge County	Grey class Ⅲ	C	Changge Rural	Grey class Ⅰ	E
Yuzhou County			Xiangcheng Rural		
County County			Yuzhou Rural		
A suburb			Rural areas of a county		
Xiangcheng County	Grey class Ⅱ	D	Yanling Rural		

4.4. Rationality analysis

In order to verify the rationality of the power supply partition results, 12 clusters of a city were clustered using the SPSS system cluster analysis method. When the distance was 5, 12 areas were divided into 4 categories. The clustering results are shown in Table 5.

Table 5 Power supply division results of 12 regions of Xuchang

Area	Partition results	Area	Grey class type
A city	B	Yanling County	D
Changge County	C	Changge Rural	E
Yuzhou County		Xiangcheng Rural	
County County		Yuzhou Rural	
A suburb	D	Rural areas of a county	
Xiangcheng County		Yanling Rural	

Comparing Table 4 and Table 5, it can be seen that the two partitioning methods are identical except for a suburb and other subarea results. The administrative level of a suburb, population density, power supply reliability, comprehensive voltage qualification rate, and the proportion of secondary and above load, the per capita electricity consumption belong to the grey category III, only a few indexes of per capita GDP and load density belong to the grey category II, and then The grey clustering coefficient $\alpha^{II} = 0.235$ for gray class *II* in a certain suburb is calculated by the weight of formula $max_{1\le k\le s}\{\alpha_i^{k*}\} = \alpha_i^{k*}$, and the clustering coefficient $\sigma^{III} = 0.756$ for gray class *III*, which classifies a suburb as a class *C* more reasonable. This fully demonstrates that the proposed power supply partition method is reasonable and effective.

5. CONCLUSION

This paper proposes an improved grey clustering method applied to the power supply partition of distribution networks. Firstly, the commonly used triangle whitening weight function is improved to improve the accuracy of the quantitative evaluation of the method. Second, in terms of index weights, a weight calculation method for combination weighting is proposed, which eliminates only a few of the results caused by previous mixed weight calculation results. The indicators with larger weights reflect the characteristics of the objects being evaluated and do not reflect the impact of all indicators. The example analysis shows that the proposed method can be used to obtain more reasonable partition results. For different types of power supply areas with different sizes, only the index weights and the center points of various grey classes can be adjusted to make a reasonable division using the partition method of this paper.

6. REFERENCES

Tang X, Liu L, Zhang J, 2015 .Method of Power Distribution Network Partition Based on Adaptive Weighted Voronoi Diagram[J]. Power System Technology, 2015, 43(19):83-88.

Peng W, Du X, Shi M, 2015. Distribution Substation Planning Based on Load Region Division[J]. Electric Power Automation Equipment, 2015, 35(1):112-117.

Li Z, Chen J, 2006. Study and Practice about Distribution Network Planning Based on Optimal Partitioning[J].Guangxi Electric Power, 2006,11(4):1-4.

Xiao J, Cui Y, Wang J, et al, 2008. Comprehensive Evaluation Index System and Method for Distribution Network Planning[J]. Automation of Electric Power System, 2008,15(6):36-40.

Liu L, Ma L, Zhu T, 2012. Sythetical Assessment on Distribution Network Planning Scheme Considering Anti-Disaster Ability and Regional Characteristic[J] Power System Technology, 2012, (05):219-225.

Zhou L, Qu G, Liu W, et al, 2016. Methods and Practical Application of Power Supply Area Division for Distribution[J].Power System Technology, 2016, 40(1):242-248.

Liu S, Dang Y, Fang Z, 2004. Grey System Theory and Its Application[M]. Beijing:Science China Press, 2004.

Lei G, Gu W, Yuan X, 2009. Application of Grey Theory in Power Quality in Power Comprehensive Evaluation[J]. Electric Power Automation Equipment, 2009, 37(11):62-65.

Li G, Jiao Y, Liu F, et al, 2016. Comprehensive Evaluation of Big Data Quality in Power Systems with Entropy Weight and Grey System Theory[J]. Electric Power Construction, 2016, 37(12):24-31.

Zhang J, Xu X, Ding M, et al, 2017. Acondition Assesment Method of Power Transformers Based on Fuzzy Analytic Hierarchy Process[J]. Power System Technology, 2017,45(3)1-7

OuYang S, Shi Y, 2013. Application of Improved Entrop Method in Power Quality Assesment[J]. Automation of Electric Power Systems, 2013, 36(21):156-159.

177: Application of PID optimisation control srategy based on particle swarm optimisation (PSO) for battery charging system

Linzhang WU[1], Cuicui ZHOU[2], Tiezhou WU[3], Junjie ZHANG[4]

[1] Hubei Key Laboratory for High-efficiency Utilisation of Solar Energy and Operation Control of Energy Storage System, Hubei University of Technology, 956147458@qq.com
[2] Hubei Key Laboratory for High-efficiency Utilisation of Solar Energy and Operation Control of Energy Storage System, Hubei University of Technology, 1039144539@qq.com
[3] Hubei Key Laboratory for High-efficiency Utilisation of Solar Energy and Operation Control of Energy Storage System, Hubei University of Technology, 1297362526@qq.com
[4]Hubei Key Laboratory for High-efficiency Utilisation of Solar Energy and Operation Control of Energy Storage System, Hubei University of Technology, 1367050754@qq.com

The issue of protecting health of residents of urbanised areas from the effect of excessive particulate matter and toxic components of car exhaust gases imposes the need of introduction of clean electric vehicles to the market. In order to solve the problem of nonlinear and lagging in charging process of electric vehicle battery, an application of PID optimisation control strategy based on particle swarm optimisation (PSO) for battery charging system is studied in this paper. The main goal here is to design a PID controller with a flexible structure and adaptive tuning of its parameters, which leads to improvement of charging efficiency of the battery. The traditional tuning method for PID parameter is difficult to give the appropriate parameters, which affects the battery charging efficiency. PSO is a population-based evolutionary algorithm and is proved to be robust in solving problems featuring nonlinearity, non-differentiability and multi-dimensionality. The advantages of PSO are its relative simplicity and stable convergence characteristic with good computational efficiency. Aim at the defects of basic PSO such as slow convergence speed, low convergence precision and easy to be premature, a modified PSO is proposed by adjustments to the inertia weight, learning factor and local optimum value. And the modified PSO algorithm has stronger global convergence ability in the early stage and stronger local convergence ability in the later stage which can preferably avoid trapping into the local optimal solution. Five different classical functions are selected for optimisation test to verify the feasibility and effectiveness of the modified algorithm. Comparisons are made with the performance indexes of the standard PSO, such as the number of successful search and the average convergence time, and it is shown that the modified PSO algorithm can highly accelerate the PSO for the convergence rate and improve its convergence accuracy. The optimised PID parameters are applied to the battery charging control system. And the experimental results show that the battery charging process possesses better dynamic performance and the charging efficiency of the battery has increased from 86.44% to 91.47%.

Keywords: battery; PID parameters; particle swarm optimisation.

1. INTRODUCTION

PID control is one of the earliest developed control strategies. It has many advantages, such as simple algorithm, high reliability and good robustness, and has been widely applied in the field of industrial process control. The control performance of PID controller is directly related to the optimisation setting of controller parameters, such as K_p, K_i and K_d. The charging circuit of battery is nonlinear and hysteresis loop. The setting process of the conventional PID setting method is complicated. It is necessary to correct the PID parameters according to the empirical formula and several experiments. It is difficult to realise the ideal setting of the parameters. The control system has a long response time and a large overshoot, and it cannot meet the requirements of the current control. The accurate control of the charging parameters (charge voltage and current) of lithium battery can shorten the charging time, improve the charging efficiency of the battery, prolong the service life and reduce the cost. Therefore, it is of great significance to the PID parameter tuning of the battery charging circuit.

Particle Swarm Optimisation (PSO) is a new evolutionary algorithm proposed by Kennedy and Eberhart et al in 1995 (Xiang, 2007:3341-3345). Compared with other optimisation algorithms, this algorithm preserves the global search strategy based on population, and the speed position model is easy to operate. Its unique memory function enables it to dynamically track the current search and can adjust the search strategy according to the search condition. The particle swarm optimisation algorithm is a more efficient parallel algorithm. The concept of search algorithm is concise, clear and easy to implement. It has been widely applied in the field of scientific computing and engineering application.

Aim at the defects of the basic particle swarm optimisation (PSO), such as slow convergence speed and easy to be premature, this paper improves it and the improved particle swarm optimisation is used to optimise the three parameters of PID in the battery charging circuit, and the new PID parameters are applied to the battery charging system. The system has better transition performance, and the experiments show that battery charging efficiency has been significantly improved.

2. BASIC PARTICLE SWARM OPTIMISATION (PSO) ALGORITHM

In 1995, Dr. Kennegy of social psychology and Eberhart of electronic engineering, inspired by Boid model, proposed the particle swarm optimisation (PSO) algorithm after further research on the model and applied it to the optimisation calculation. The PSO algorithm is based on the population with many particles. Each particle consists of two parameters of speed and location. The location represents a solution in the solution space, and the velocity determines the direction and distance of the particle's next move when solving optimisation problems. In addition, each particle has a fitness function to evaluate the current position of the particle. This algorithm initialises a group of random particles, and then finds the optimal solution or approximate optimal solution by iteration. In each iteration, particles update their speed and location by tracking individual extremum and global extremum. The modified velocity and position of each particle can be manipulated according to the following equations (Colomi, 1992):

Equation 1: Velocity of each particle.

$$v(t+1) = v(t) + c_1 r_1 (p_{best} - x(t)) + c_2 r_2 (g_{best} - x(t))$$

Equation 2: Position of each particle.

$$x_{ij}(t+1) = x_{ij}(t) + v_{ij}(t+1)$$

Where：

t = the number of current iteration or generation.

c_1 and c_2 = the acceleration constants and are often set to 2.0.

r_1 andr_2= random number in the range of [0,1].

p_{best}= the best solution found by the particle itself.

g_{best} = the best position among all the neighbour of a particle, that is, global extremum.

The g_{best} is each particle has a velocity represented by a velocity vector $v \in [-v_{max}, +v_{max}]$, which is clamped to a maximum velocity v_{max}. If v_{max} is too big, then the particle may not explore sufficiently beyond local solutions. In general ,the iteration will be aborted when the maximum iteration number is achieved or the particle swam find the global extremum.

Y. Shi and others add the inertia coefficient ω to enhance the ability of particles to jump out of the local extremum, so that the Equation 1 can be changed into:

Equation 3: Velocity of each particle.

$$v(t+1) = wv(t) + c_1 r_1 (p_{best} - x(t)) + c_2 r_2 (g_{best} - x(t))$$

Equation 4: The inertia coefficient.

$$w = w_{\max} - \frac{(w_{\max} - w_{\min})t}{T_{\max}}$$

Where:

ω_{max} = the maximum inertia coefficient.

ω_{min} = the minimum inertia coefficient.

t = the number of current iteration.

T_{max} = the maximum number of iteration.

Nowadays, researchers usually call Equation1 and 2 basic PSO, and Equation 2 and 3 are called standard PSO.

3. IMPROVEMENT OF PARTICLE SWARM OPTIMISATION

In the basic PSO, the inertia weight and acceleration constants are important parameters, which are usually set as constant, but it cannot balance the local search and global search, which leads to problems of slow convergence speed, low convergence precision and local optimal solution. A new PSO algorithm is proposed to in this paper to solve the problems of basic PSO. The convergence speed and convergence accuracy of the algorithm is improved by using the inertia weight of nonlinear decrement, improving the acceleration constants and using adaptive mutation operation for global extremum, and at the same time, it can avoid trapping into the local optimal solution and a more accurate solution is obtained. The concrete improvements are as follows:

3.1. Inertia weight adjustment method

In the PSO, inertia weight ω determines the influence of the particle's prior flight speed on the current flight speed. The selection of the appropriate inertia weight can balance the global and local search ability and improve the performance of the algorithm. Generally, it's beneficial to the local search for using a bigger inertia weight is used in the early search and a smaller inertia weight value in the late search (Wu, 2011). In this paper, the dynamically changed nonlinear inverse tangent decreasing inertia weight is used, such as Equation 5.

Equation 5: nonlinear inverse tangent decreasing inertia weight.

$$w = (w_{start} - w_{end})\arctan\frac{t_{\max} - t}{t_{\max}}$$

Where:

t=the number of current iterations.

T_{max}= the maximum number of iterations.

3.2. Acceleration constants adjustment method

In the PSO algorithm, the acceleration constants c_1 and c_2 determine the influence of particle's experience information and other particle's experience information on particle trajectories. Based on the basis of literature (Kennedy, 2002:1942-1948 vol.4), an improvement has made to improve the accuracy of PSO, c_1 and c_2 are dynamically nonlinear changed when the number of iterations is changed, such as Equation 6 and 7. In the early stage of search, the particle will have a large self-learning ability and a small social learning ability, and the global searching ability will be strengthened when c_1 takes the larger value and c_2 takes the smaller value. The particle will have a large social learning ability and a small self-learning ability, and the global searching ability will be strengthened when c_1 takes the smaller value and c_2 takes the larger value at the later stage of the algorithm.

Equation 6: Acceleration constant C_1.

$$c_1 = 1.3 + 1.2\cos\pi\frac{t}{t_{\max}}$$

Equation 7: Acceleration constant C_2.

$$c_2 = 2 - 1.2\cos\pi\frac{t}{t_{\max}}$$

3.3. Adjustment method of local optimal solution

When the premature convergence is appeared, g_{best} must be the local optimal solution. If the Cauchy mutation is used to change g_{best}, the direction of the particle swarm will be changed and the particle will go into other new regions for searching, so that the particle may find new p_{best} and g_{best}, thus other particles will be driving to escape from the local

extrema, when this cycle repeated, the algorithm will find the global optimal solution, which is the principle of the Cauchy mutation operation for the current local extremum.

As analyzed earlier, the premise of mutation operation for global extremum is to detect the convergence state of the particle and judge whether g_{best} is the global extremum or the local extremum, then the local extremum g_{best} is mutated in the Cauchy way. PSO is either local convergence or global convergence, the phenomenon of "aggregation" of particles will appear. The state of particle swarm can be tracked by observing the overall changes in the fitness of all particles in the swarm. In order to quantitatively describe the state of particle swarm, the definition of fitness variance is given by

Equation 8: Average fitness of particle swarm.

$$f_{avg} = \frac{1}{n}\sum_{i=1}^{n} f_i$$

Equation 9: Fitness variance of particle swarm.

$$\sigma^2 = \frac{1}{n}\sum_{i=1}^{n}\left(\frac{f_i - f_{avg}}{f}\right)^2$$

Equation 10: Value of f in this article.

$$f = \max\left\{\max\left|f_i - f_{avg}\right|, 1\right\} \ldots i \in [1, n]$$

Equation 11: Position of a particle at the time t.

$$\lim_{t \to +\infty} X(t) = P$$

Where：

n= the number of particle swarm.

f_i= the fitness of the ith particle.

f= normalised scaling factor which is used to limit the size of σ^2.

P= the location within the search space.

The definition shows that the convergence of particles means that particles will eventually stay in a fixed position P within the search space (Guo, 2010, 58(5-8):766-775.).

The definition of fitness variance and particle convergence show that σ^2 reflects the degree of aggregation of the particle swarm. The smaller the value is, the more convergent the population will be, on the contrary, the particle swarm will be in a random search stage. As the algorithm continues, the particle swarm continues to converge, and the PSO will achieve global convergence or local convergence when σ^2 is equal to zero or closer to zero (or less than a certain threshold (Wang, 2012(2):31-34)). The g_{best} can be judged as a local optimal solution or a global optimal solution by comparing g_{best} and f_{best} (theoretical optimal value or empirical optimal value). And g_{best} will be subjected to Cauchy mutation if the algorithm appears precocious, when the current global extreme value g_{best} is the local optimal solution.

For individuals, the idea of traditional Cauchy mutation is given by $X_{ij} = (X_{i1}, X_{i2}, \cdots X_{in})$ .The operating formula for the individual Cauchy mutation is given by

Equation 12: Cauchy mutation.

$$x_{ij} = x_{ij} + \eta * C(0,1)$$

Where :

j = 1,2,…n.

η = constant for controlling the variation of the step size.

C(0,1) random number generated by the Cauchy distribution function of t=1.

Currently, the Cauchy mutations introduced in the PSO are all implemented according to Equation 12, and the variable step length parameter η is a fixed constant. The state of the particle swarm can be tracked by studying the overall change in the fitness of all particles in the particle swarm, When the particle is trapped in a local optimum, the variation in the larger step size can help the particle to jump out; When the particles are close to convergence and are searching for the neighbourhood of the optimal solution, the variation in smaller steps can accelerate particle convergence. Therefore, the change of the average speed of population is consistent with its convergence characteristics. In order to overcome the shortcoming of traditional Cauchy mutation step size as a fixed value, the adaptive Cauchy mutation method is proposed in this paper. It uses the group average speed as the parameter of control variable and asynchronous length to mutate the local extremum, which improves the effectiveness of the algorithm. In order to quantitatively describe the overall state of the particle swarm, the definition of the average speed is given below.

Equation 13: Average speed.

$$\overline{v_j} = \frac{1}{n}\sum_{i=1}^{n} v_{ij}$$

Where

n = number of particle swarm.

V_{ij}=e velocity of the ith particle's jth dimension.

According to the foregoing, When the PSO algorithm premature convergence is appeared, the current global extremum g_{best} increases variational disturbances, the g_{best} Perform the following mutation operations:

Equation 14: g_{best} after mutation operations.

$$g_{best} = g_{best} + \overline{v_j} * C(x_{\min}, x_{\max})$$

Where:

j = 1,2,…,n.

C = a random number generated by the Cauchy distribution function of t = 1.

(X_{min}, X_{max}) = the domain of the problem.

Integrating 3.1 ~3.3, this paper proposes an improved PSO algorithm, which dynamically adjusts the inertia weight and learning factors according to the current optimisation process. And the adaptive mutation operation of the global extremum is carried out to avoid the local optimal solution. The improved PSO algorithm has strong global convergence ability in the early stage and has strong local convergence ability in the later stage. To a certain extent, it can solve the problem of slow convergence speed, low precision and easy "prematurity" for basic particle swarm optimisation. To some extent, it can solve the problem of slow convergence speed, low precision and easy "precocious", which can improve the convergence speed, precision and search success rate of particle swarm optimisation algorithm, and the performance test will be carried out by experiments.

4. PERFORMANCE TEST OF IMPROVED PARTICLE SWARM OPTIMISATION

In order to verify the feasibility and effectiveness of the improved algorithm, five different classical functions were used in this paper to perform the optimisation test and compare the performance of the algorithm. These functions represent different optimisation problems, including single peak function to multi-peak function, and low- Dimensional functions to high-dimensional functions, test functions are typically representativeness, it can be targeted to detect a specific function of the algorithm. This program uses MATLAB R2012a version programming.

4.1. Selection of test functions

Equation 15: Sphere function.

$$f_1(X) = \sum_{i=1}^{n} x_i^2 \ldots (-100 \le x_i \le 100)$$

Sphere is a single-peak function, it takes the minimum at $x_i = 0$.

Equation 16: Rosenbrock function.

$$f_2(X) = \sum_{i=1}^{n} 100(x_{i+1}^2 - x_i) + (1 - x_i)^2$$

Rosenbrock is a non-convex and ill-conditioned function, it takes the minimum at x_i=1.

Equation 17: Rastrigin function.

$$f_3(X) = \sum_{i=1}^{n} (x_i^2 - 10\cos(2\pi x_i) + 10) \ldots (-5.12 \le x_i \le 5.12)$$

The Rastrigin function is a multimodal function. The global minimum is taken at $x_i = 0$ (1, 2,.... n), and there are approximately 10n local minimum values in the range of $S = \{x_i \in (-5.12, 5.12), i = 1, 2, ..., 10n\}$.

Equation 18: Griewank function.

$$f_4(X) = \frac{\sum_{i=1}^{n} x_i^2}{4000} - \prod_{i=1}^{n} \cos(x_i / \sqrt{i}) + 1 \ldots (-600 \le x_i \le 600)$$

The Griewank function takes global minimum at $x_i = 0(i = 1,2,...,n)$ and local minimum values at $x_i = k\pi\sqrt{i}, i = 1,2,....n; k = 0,1,2,....n$.

Equation 19: Schaffer function.

$$f_5(X) = 0.5 + \frac{(\sin^2\sqrt{x_1^2 + x_2^2} - 0.5)}{(1 + 0.001(x_1^2 + x_2^2))^2} ... (-100 \le x_i \le 100)$$

The global maximum value of the Schaffer function is (0, 0), and there is an infinite number of global maxima in the range of about 3.14 range from the global maximum. It is difficult to make the global optimisation with strong concussion of the function.

4.2. Performance test

In this experiment, the population size of the particle swarm is n=30, $c_1 = c_2 = 2$, $w_{\max} = 0.9$, $w_{\min} = 0.4$, the maximum speed is $v_{\max}$ =5, and the maximum iteration algebra is 500 times. The optimisation objective of all algorithms is to minimise the function value, it will take 50 times for each function to get the average value. The purpose of the experiment is to compare the performance of the improved particle swarm optimisation algorithm and the basic particle swarm optimisation (PSO) algorithm proposed in this paper. The evaluation indicators are introduced to characterise the performance of the improved PSO algorithm. This paper introduces two evaluation indexes, the number of successful algorithms and the speed of convergence. The simulation results and statistics are shown in Table 1.

It can be seen from the above table that the performance index of the improved particle swarm optimisation algorithm, such as the search success rate, the convergence time, and so on, is greatly improved than the standard particle swarm algorithm, which proves the feasibility and superiority of the algorithm. This method can accelerate the convergence speed of particle swarm optimisation and improve the precision of the algorithm. At the same time, it can effectively solve the problem of "precocious" of the basic particle swarm optimisation (PSO) algorithm, which is easy to be trapped in the local optimality.

Table 1: Benchmark test function comparison experiment results

Benchmark function	Theoretical extremes	Standard PSO		Improved PSO	
		Successful search times	Average convergence time (s)	Successful search times	Average convergence time (s)
Sphere function	0	48	65.9	50	43.2
Rosenbrock function	0	46	82.3	50	44.8
Rastrigin function	0	44	75.4	50	53.2
Griewank function	0	44	84.5	50	56.5
Schaffer function	0	45	96	49	73.4

5. OPTIMISATION OF PID PARAMETERS IN CHARGING CIRCUIT

Figure 1 is a block diagram of the PID parameters optimised by the particle swarm algorithm. The input is a given charging current or voltage, the output is the charging current or the charging voltage value of the battery, and the loop adopts a PID control method to ensure that the charging system has better stability and Dynamic response performance.

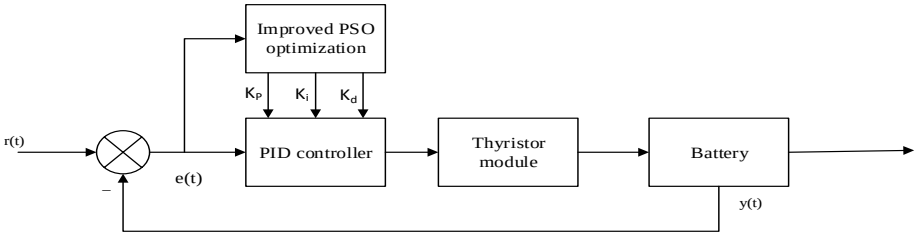

Figure 1: PID parameter diagram of particle swarm optimisation

From the perspective of optimisation, PID controller parameter tuning is to make use of particle swarm optimisation algorithm to optimise the characteristics of (k_p, k_i, k_d) as the basic particles, the three parameter groups automatically evolve in the solution space, and tend to be globally optimal. At this time, the system performance is optimal. In this paper, the PSO algorithm first performs offline learning and then accesses the control system.

5.1. The establishment of charging circuit transfer function

The equivalent model of the battery charging system is shown in Figure 2.

Equation 20: Transfer function of the control system.

$$\frac{U_c(s)}{U_i(s)} = \frac{R_a}{(R_r + Ls)(1 + R_a Cs) + R_a}$$

Where:

R_r = the internal resistance of the rectifier module.

R_a = the internal resistance of the battery pack.

U_i = the ideal voltage of the rectifier device.

U_i = the charge voltage of the battery.

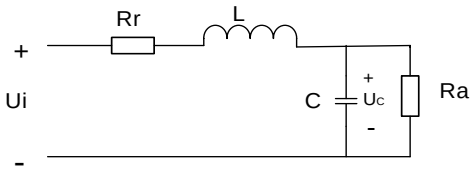

Figure 2: Battery charging system equivalent circuit

In the thyristor rectifier module, the dynamic trigger-rectification part is a purely delayed amplification part. This lag is due to the uncontrolled time of the rectifier module. In a certain range of work, Using linear transformation for the rectifier output U_I and control voltage U_c , U_I Lag behind by $K_s = \Delta U_I / \Delta U_c$, namely

Equation 21: Linear transformation for UI and UC.

$$\frac{U_c(s)}{U_i(s)} = \frac{R_a}{(R_r + Ls)(1 + R_a Cs) + R_a}$$

Where:

U_I = rectifier output voltage.

U_C = control voltage.

K_S = The amount of ΔU_I lagging behind ΔU_C

So the battery charge control transfer function is given by

Equation 22: The battery charge control transfer function.

$$G(s) = \frac{R_a}{R_r + R_a + Ls + R_r R_a Cs} K_s e^{-Ts}$$

With:

L= 50mH, C=5F, R_r≈0.8Ω, R_a ≈0.2Ω， K_S=5, T_S=0.067s, T_1=0.028s, T= T_1+ T_S =0.095 s.

Then, the last controlled transfer function is given by

Equation 23: The last controlled transfer function.

$$G(s) = \frac{e^{-0.095s}}{0.8s + 1}$$

5.2. PID parameter coding

S is the number of particles in the population P, and the position vector of each particle is composed of three control parameters of the PID controller, and the dimension of the particle position vector is D=3. The population can be represented by an S × D matrix

Equation24: The population P..

$$P(S,D)=\begin{vmatrix} K_p^1 & K_i^1 & K_d^1 \\ K_p^2 & K_i^2 & K_d^2 \\ ..... & ..... & ..... \\ K_p^S & K_i^S & K_d^S \end{vmatrix}$$

Considering the diversity of the control system, the range of values of each parameter is determined by the actual problem, and the initial population can be randomly generated within the allowable range of values.

5.3. Fitness function selection

PSO algorithm uses fitness value to evaluate the merits of individual or solution in the process of search evolution. In order to obtain satisfactory transient process dynamic characteristics, this paper uses the error absolute time integral (ITAE) performance index as the parameter to select the adaptive function (C S 1, 2011, 47(17):42-44), and the smaller the adaptation function value J indicates (k_p, k_i, k_d) The more appropriate the parameters, the better the overall performance of the control system.

Equation 25: The adaptive function of the PSO algorithm.

$$J = ITAE = \int_0^\infty t\left|e(t)\right|dt$$

Where:

e(t) = the systematic error, and e(t) = 1-y(t).

5.4. Flow chart for improved PSO optimizing PID parameters

The flow of improved particle swarm optimisation algorithm is shown in Figure 3.

6. EXPERIMENTAL SIMULATION

The battery charge circuit transfer function is $G_1(s)=\frac{e^{-0.095s}}{0.8s+1}$, Z-N method, standard PSO method and improved PSO method are used to set the PID control parameters. Set the population size of particle swarm n=30, $c_1=c_2=2$, $w_{\max}=0.9$, $w_{\min}=0.4$, Maximum speed $v_{\max}$ = 2, the maximum number of iterations is 500, convergence accuracy eps $=10^{-4}$,parameter k_p , k_i , k_d ∈[0,15], the input signal is a step signal, and the PID parameters set by the three methods are simulated in Matlab/Simulink. The system simulation response curve is shown in Figure 3, and the experimental results are shown in Table 2:

Compared with the three groups of PID parameter response curves, the performance parameters such as overshoot, error, and adjustment time of the PID system with improved PSO tuning are significantly reduced, indicating the feasibility and practicality of the improved algorithm. The following is proved by experiment.

Table 2: Comparison of Current Loop Setting Results by Different Methods

Setting method	k_p	k_i	k_d	adaptability	Overshoot σ%	Adjust the time t_s(s)
Z -N	10.1	0.2	0.048	4.6	48.4%	1.2
Standard PSO	5.5	6	0.15	0.233	5%	0.58
Improved PSO	6.71	8	0.247	0.187	2.7%	0.38

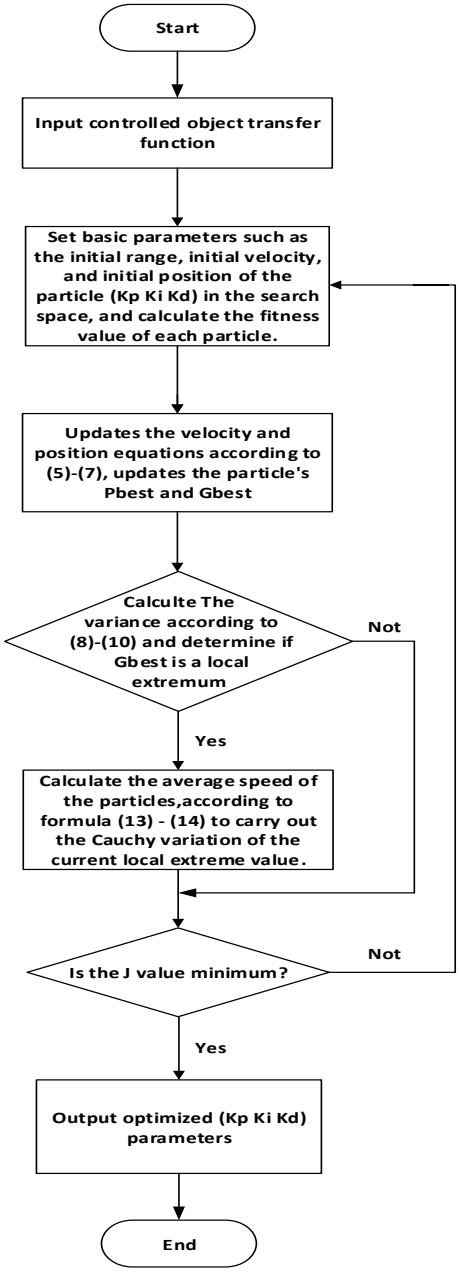

Figure 3: Flowchart of Improved PSO

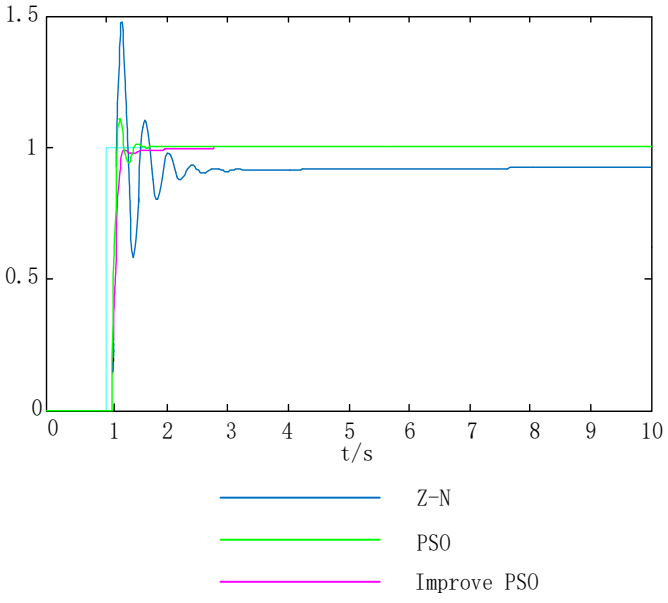

Figure 4: step response curve

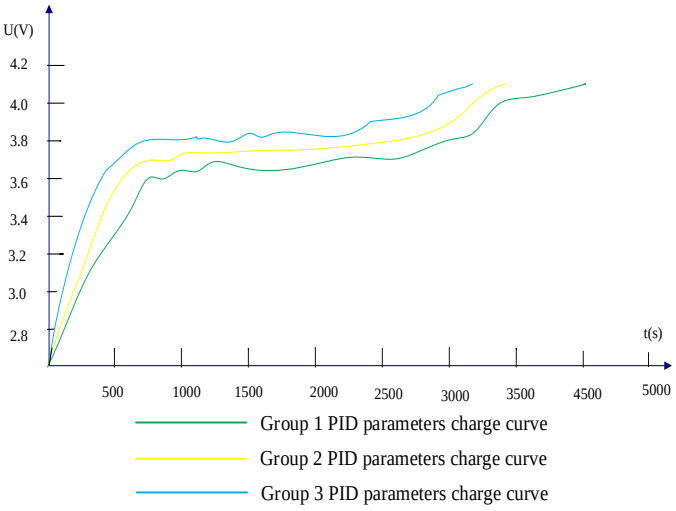

Figure 5: Comparison of Battery Terminal Voltage Changes

7. EXPERIMENTAL VERIFICATION OF BATTERY CHARGING

With TMS320LF2407 DSP as the control centre, an experimental platform was set up to record data such as charging voltage, current, battery terminal voltage and battery temperature rise. The experiment used a lithium-ion battery model of 3.6V/1500mAh and was charged by a constant current method. The experiment set the above three groups of PID parameters, and the battery SOC was 0 before the experiment started. Three charging experiments were carried out with different PID charging parameters. The relevant charging experimental data is summarised in Table 3, in which charging efficiency = discharge power/charge power × 100%, Figure 5 records the battery terminal voltage changes.

Based on the above experimental results, the third group of PID parameter charging control system is better than the former two in terms of charging efficiency, temperature rise, and terminal voltage change during charging, illustrating the optimisation of the PID set by the improved particle swarm optimisation algorithm. The parameters are better, which proves the feasibility and superiority of the improved particle swarm algorithm.

Table 3: Comparison table of charging results of three groups of PID parameters

Response Performance index	Charging time (min)	Charge (Ah)	Discharge power (Ah)	Charging efficiency (%)	Temperature rise (°C)
Z-N method	4576	1.183	0.886	74.89%	6
Standard PSO	3520	1.272	1.10	86.44%	4
Improved PSO	3476	1.478	1.408	91.47%	3

8. CONCLUSION

For the shortcomings such as slow convergence rate, low precision and easy to be premature, the inertia weight, learning factor and local optimal value in the particle swarm optimisation algorithm are improved and a new improved particle swarm algorithm is proposed in this paper. The algorithm has a faster convergence speed and accuracy in the optimisation process. The improved particle swarm optimisation method was applied to optimise the battery charging PID parameters. The simulation shows that the battery charging process has good dynamic performance. The experiment shows that the improved PID parameters after improved calculation are more efficient in the battery charging process. Improved the feasibility and superiority of the algorithm.

9 REFERENCES

Xiang T, Wang J, Liao X, 2007. An improved particle swarm optimizer with momentum[C]// Evolutionary Computation, CEC. IEEE Congress on. IEEE, 2007:3341-3345.

Colorni A, 1992. Distributed Optimisation by Ant Colonies[C]// European Conference on Artificial Life. The MIT Press.

Wu Y, 2011. The Research of VRLA Charger based on Fuzzy Logic Control[D]. University of South China.

Kennedy J, Eberhart R, 1995. Particle swarm optimisation[C]// IEEE International Conference on Neural Networks, Proceedings. IEEE, 2002:1942-1948 vol.4.

Clerc M, 1999. The swarm and the queen: towards a deterministic and adaptive particle swarm optimisation[C]// Evolutionary Computation. CEC 99. Proceedings of the 1999 Congress on IEEE, 2002:1957 Vol. 3.

Guo GH, Wang ZG, 2010. A Modified Particle Swarm Optimisation [J]. Journal of Harbin University of Science & Technology, 58(5-8):766-775.

Wang J, Kang Ly, Li Y, 2012. Simulation of Lead-Acid Batteries Charging System Based on Fuzzy Self-Adaptive PID[J]. Electrical Appliance and Energy Efficiency Management Technology, (2):31-34.

Sundareswaran K, Jayant K, Shanavas TN, 2007. Inverter Harmonic Elimination Through a Colony of Continuously Exploring Ants[J]. IEEE Trans. ind. electron, 54(5):2558-2565.

Chang CS, 2011. Adaptive particle swarm optimisation algorithm with hybrid mutation operator[J]. Computer Engineering & Applications, 5(2):158-177.

Shi Y, Eberhart R, 1998. A modified particle swarm optimizer[M]// Advances in Natural Computation. Springer Berlin Heidelberg, 1998:439-439. IEEE Press, 1998:69-73.

Sundareswaran K, Jayant K, Shanavas TN, 2007. Inverter Harmonic Elimination Through a Colony of Continuously Exploring Ants[J]. IEEE Trans. ind. electron, 54(5):2558-2565.

Arasomwan MA, Adewumi AO, 2013. An Adaptive Velocity Particle Swarm Optimisation for high-dimensional function optimisation[C]// Evolutionary Computation. IEEE, 2013:2352-2359.

Ahmed W, Jamil OM, Shiraz MF, et al, 2013. PSO with Gompertz increasing inertia weight[C]// Industrial Electronics and Applications. IEEE, 2013:923-928.

179: The development of data acquisition terminal based on ARM

JINGYU YANG [1], ZIQIANG XI[1], TINGANG YANG [1]

[1]Solar Energy Efficient Utilisation Cooperative Innovation Center, Hubei University of Technology, Hubei Wuhan,1143236026@qq.com

The development of modern industry is moving toward the integration of large-scale integration and control terminals, the commonly used analog signal 4-20mA in industry still plays a greater role in the current control field. Due to the complexity of data collection outside many systems, the amount of analog collected has become more and more. At present, many design products use single-channel analog acquisition and transmission over industrial buses，pass the data to the superior control unit, then the higher-level unit processes the signal of the lower unit，Send instructions to control direct actions of subordinate units，Because the acquisition passes through the bus, the acquisition will inevitably have an access cycle. When the data collected by the lower level is too much, it will cause time delay for data acquisition. In some demanding industrial control environments, it is likely to cause danger. Because of the increasing contradiction between the acquisition of signal and the integration of control, the integration of multi-channel data acquisition and multi-channel alarm communication becomes more and more important. This article describes the design method and idea with a single ARM controller with 8 analog inputs and 48 switches. It has a certain guiding significance. (Objectives, methods, results, conclusions) This paper designed a multi-channel data acquisition system based on the ARM series STM32F107VX. Using ARM data processing speed, low power consumption, etc., 8 channels of analog quantity and 48 channels of switch were collected. And conversion, and pass the acquisition data to the upper computer through CAN communication. The experimental operation shows that the system has high collection accuracy and fast data processing, and can collect and monitor signals in real time.

Keywords: ARM, Analog acquisition, Switch acquisition, CAN communication

1. INTRODUCTION

The methods used in this paper are local centralised control of multi-channel data acquisition, and some units perform control actions and task processing under pre-designed control principles. The local control unit can also exchange data with the superior control unit, which can not only solve the problem of time delay caused by the superior's excessive access and issuing instructions, and also can ensure that the entire local control process can be monitored and managed by superiors (Zhu, 2013).

2. GLOBAL BLOCK DIAGRAM AND DESIGN IDEAS

The entire controller adopts the block interface design, which facilitates the partial block management and the expansion of the subsequent expansion interfaces, each unit port is designed with 2 analog inputs, or 12-way open and close volume acquisition can satisfy most of the control requirements (Zhao, 2013).The specific peripheral design scheme and design interface are shown in Figure 1. It can be seen that the amount of data directly passes the high-level and low-level detection of open and close operation, all analog interfaces are tested using external resistor resistance variations. By designing a simple constant current source at the device interface, an external voltage detection amount can be easily realised by Ohm's law. Internally, the required voltage is reduced by the way of resistance conversion, After a simple voltage follower and LC filtering, can directly entered into the internal AD of the ARM, at this time, feedback can be made through the judgment of the internal logic of ARM. Finally, the local data is directly transmitted to the upper-level central control device through the port of the communication device of ARM.

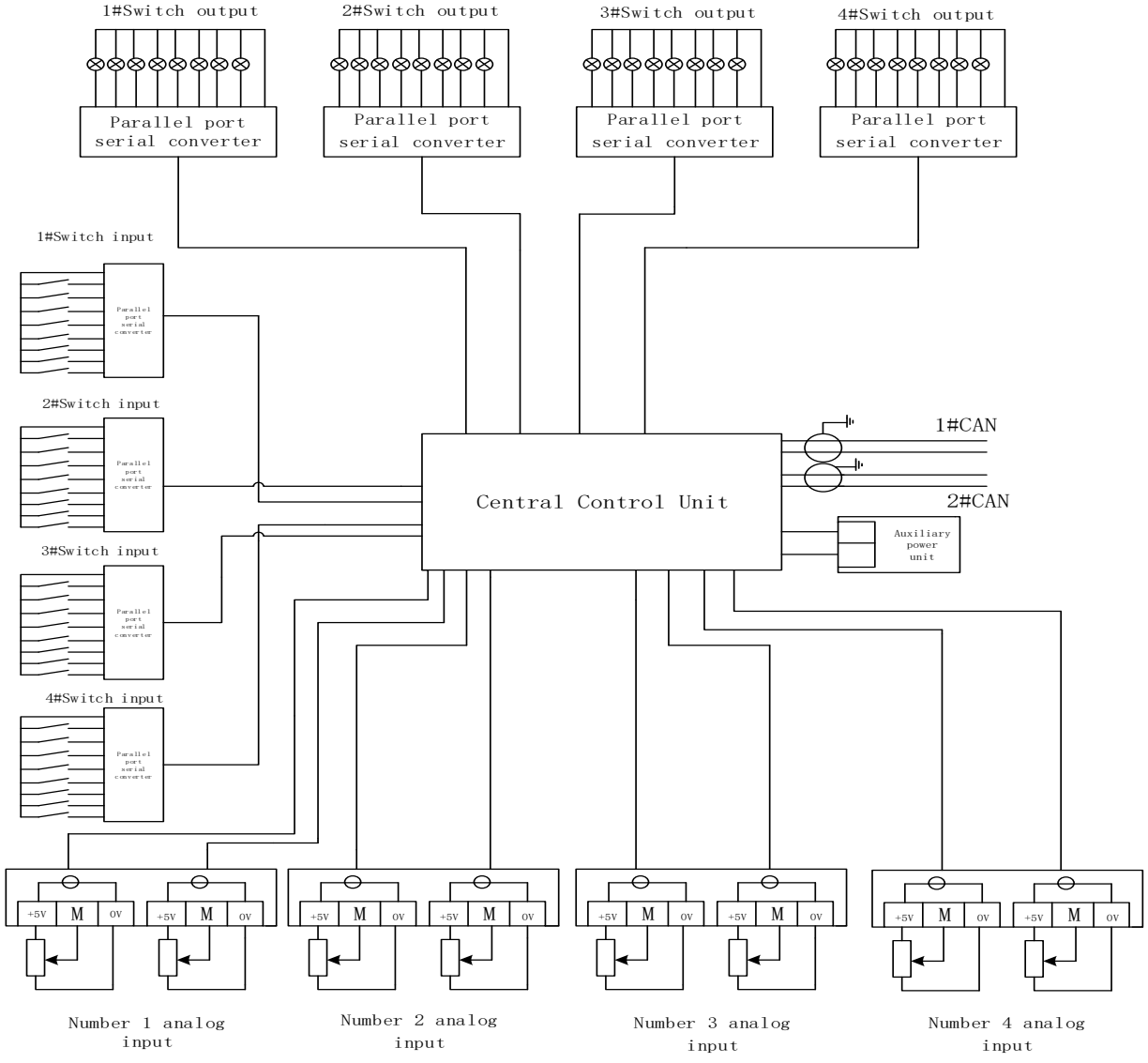

Figure 1: Global design plan for ARM acquisition equipment

This design idea has the advantage of being able to summarise data and parameters step by step through lower-level central control devices. Users who are exempt from the upper-level control unit need to consider designing too many spare interfaces and the additional engineering work brought about in the initial design.

The ARM chip model used in this article is the STM32F107Vx chip. The chip has great advantages in communication and digital-to-analog conversion and universal peripheral interface GPIO. The specific parameters are shown in Table 3 below.

Table 1: STM32F107Vx hardware interface

STM32F107Vx				
Communication interfaces				
SPI	I2C	USART	USB	CAN
3	1	5	Yes	2
GPIO	12-bit ADC		12-bit DAC	
80	16		2	
Ethernet				
Yes				

It can be seen that the chip can fully meet the current design requirements on the hardware level. And because it has Ethernet and dual CAN and other industrial communication interface capabilities, it can also have a larger upgrade and transformation space in the subsequent upgrade and expansion.

3. BOTTOM PROGRAMMING

Since a large part of the chip's GPIO port functions is multiplexed, the number of available interfaces does not fully meet the chip's number in the hardware functional specification in the actual chip interface design and use. In particular, the chip only provides one-way PWM interface, which cannot meet the requirements for driving multiple chips in a multi-strand serial-parallel architecture, must design its own to simulate PWM function, and can output high and low level bottom layer interface uninterruptedly as required.

First, the input direction, input frequency, and input address structure of the GPIO interface must be clearly defined. The 1-channel serial output is changed to the 8-channel parallel output opening and closing volume output control interface design process program as an example. The specific definition method is as follows:

```
GPIO_InitStructure.GPIO_Mode=GPIO_Mode_Out_PP
//Define the output direction of the GPIO port
GPIO_InitStructure.GPIO_Speed=GPIO_Speed_8MHz
//Define the operating frequency of the GPIO port
GPIO_Init(GPIOB,&GPIO_Initstructure);
//Define the data storage unit of GPIO port
```

Second, need to be in the program, design the functional level of the high and low working order, and the storage address of the corresponding data and output data. The corresponding design method is as follows:

```
For (i=0;i<8;i++)
{
  SRCLK1_Low();  //Output low for writing data
  temp1=vaule1&n1;//Take the data value to the first temporary position
  if (temp==1)
  {
SER1_High();  //Write data 1
}
   else
   {
```

```
    SER1_Low();  //Write data 0
   }
   n1=n1<<1;     //Move one bit to the left to prepare for the next data write
}
```

Since the 74H chips used in parallel conversion of each string are 8-bit, the receiving and control loops of the programs are all designed with 8 bits, so each time data of one data unit is received, then start again and prepare to accept the next data bit, 8 cycles as an actual output cycle.

Similarly, to explain the entire process of 8-bit serial read data, the first chip clock output low to read data, 8 parallel data written into 74HC, then the ARM output drive high and low. The data of the serial port reads the first bit into the temporary cell and judges the data of the temporary cell. If the data is high, it writes 1 in the internal register, and otherwise writes 0.Afterwards, the internal data group is shifted to the left by one bit, and the high and low levels for driving are output again, and the recording is judged again. If you cycle 8 times like this, you can rewrite an 8-bit parallel data into an 8-bit serial data through the 74HC unit.

4. HARDWARE CIRCUIT DESIGN

4.1. Page size

Since the current field analog control commonly used in the industry is generally based on resistive passive devices, a current source device is required during analog circuit acquisition to ensure that the peripheral resistors can operate normally， a high-impedance, post-stage differential amplifier was used to complete the voltage conversion of this resistor(He,2014).

The corresponding circuit is shown in Figure 2. The circuit is divided into two unit modules. The first module is an adjustable power supply consisting of a three-terminal regulator chip and a miniature varistor. Its output voltage is calculated as follows:

$$V_{ref} = V_0 \times \frac{R_s + R_{c1} + R_{c2}}{R_s + R_{c1}} \quad (1)$$

Where:

V_0 = a three-terminal fixed-voltage output pin voltage

R_s = a fixed-value lower resistor

R_{C1} = the lower resistor

R_{C2} = the upper resistor

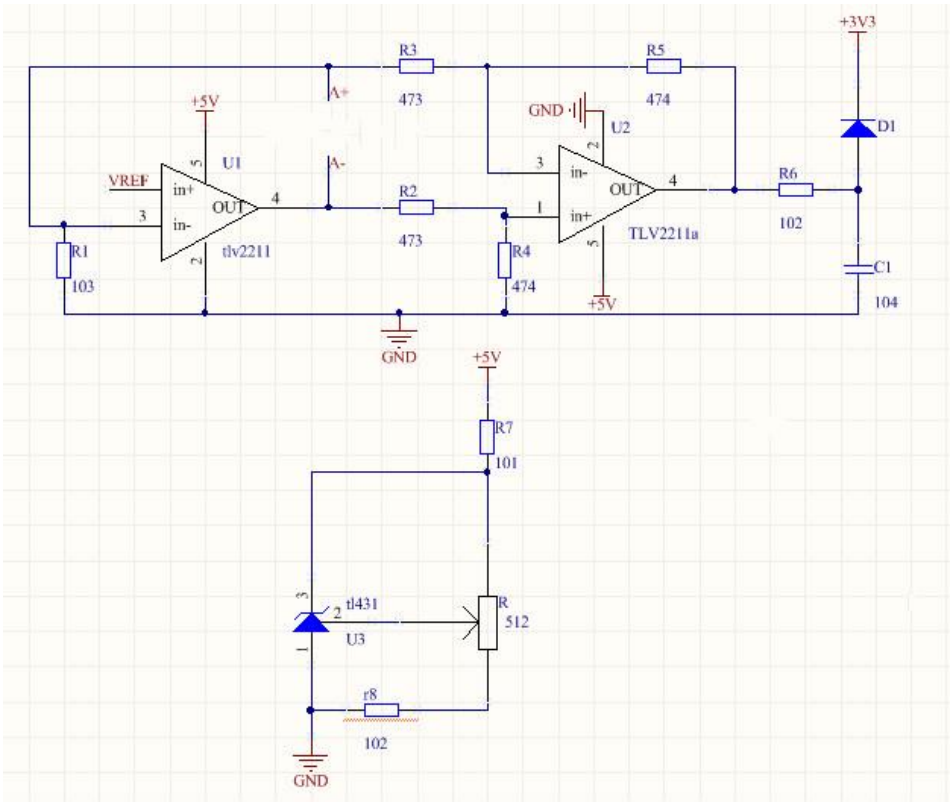

Figure 2: analog acquisition circuit

Since the input resistance of the second level of the differential amplifier circuit is about 50K, and the resistance of the general industrial copper resistor is around several tens to several hundred ohms, the numerical level of the two is not a level, so the second level of the circuit and the The first-order circuit can be approximately equivalent to no current relationship (Zhang, 2004). The output voltage of the second-stage circuit can be directly derived from the basic formula of the proportional difference circuit to derive the corresponding output value. The derivation formula is as follows:

$$V_{out} = (V_+ - V_-)\frac{R_1}{R_2} \quad (2)$$

Where:

R_2 =the negative input of the operational amplifier ground resistance

R_1= the direct input resistance of the negative input

V positive and negative V are the two-end voltage after the resistor on the designed cell is connected, the upper end is positive, and the lower end is negative. R_1 and R_2 are the amplified proportional resistances of the second-stage differential amplifying circuit. The differential operation here is one tenth. Basically, it can meet the theoretical requirements of the input upper and lower limits. The end of the voltage analog input circuit designed a diode for overvoltage protection, the entire circuit overvoltage protection action in the 3.7v or so, can play the internal AD protection.

4.2. I/O volume acquisition interface design

Peripheral opening and closing amount data is controlled through optocoupler isolation. There is no special speed requirement for the optocoupler, but the maximum isolation voltage is required. Therefore, the common optocoupler P627 is selected. Parallel to serial data conversion chip using 74HC165, the typical operating voltage is 5V, at this typical operating voltage, the corresponding input voltage can also work at 5V, operating power consumption in the hundreds of milliwatts level, can basically meet Designed power requirements. The corresponding design circuit diagram is shown in Figure 3.

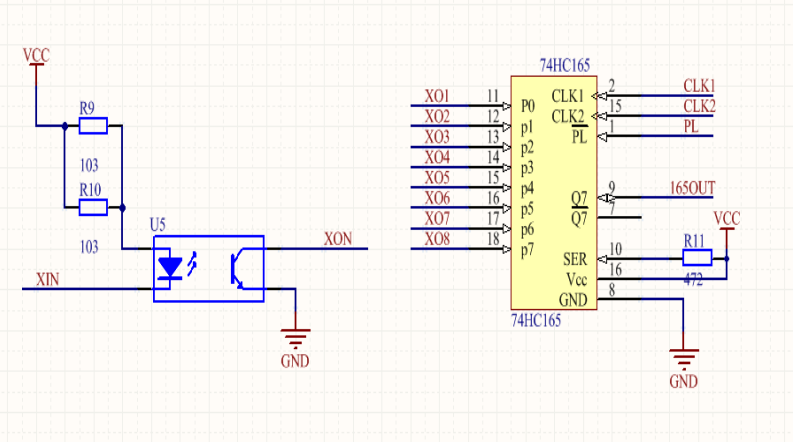

Figure 3: Parallel port acquisition hardware circuit diagram

4.3 Open and close output interface design

The internal output interface of the device needs to meet the power-on stability, so all the internal input interfaces use a single row of resistors to achieve the potential pull-up requirement, considering that the current sink capability of the ARM chip GPIO interface is about 0.3 mA. Exclusion resistance design is generally selected around 10K. In the internal-to-external control, it is generally required to provide relay operating current for the external [re-] respectively. The driving capability of the 74HC595 will not be able to meet this requirement. The chip is also operating at a typical operating voltage of 5V and it can output 5V. Voltage, but the output power needs to be amplified by one stage to drive the relay coil. This circuit uses the design of the external 24V power supply system. The 24V DC power supply is used in the second stage of the amplifier to meet most of the conditions (Figure 4).

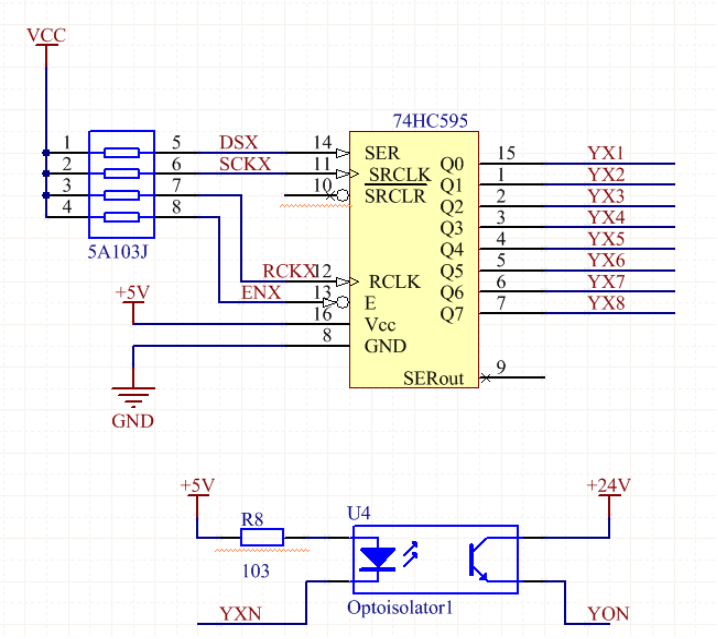

Figure 4: Parallel port to the serial hardware hardware

4.4. Communication Circuit Design

The circuit adopts the communication design structure of the dual CAN circuit. The hardware structures of the two groups of CAN are actually the same type. Therefore, only the design of one of the circuits is explained here. The corresponding circuit is shown in Figure 5 .Through high-speed optocoupler chip to complete the isolation of the main circuit equipment and peripheral wiring circuit, to ensure the stability of the circuit. CAN hardware protocol part uses TJA1050 chip, this chip has a great advantage in the adaptive transmission rate, and strong driving ability. The two ports of T and R use individually-powered 6N137 optocoupler chip. The ON current of the chip is about 10mA, which can reach the communication speed of 10M, and can fully meet the communication requirements of the device in terms of performance.

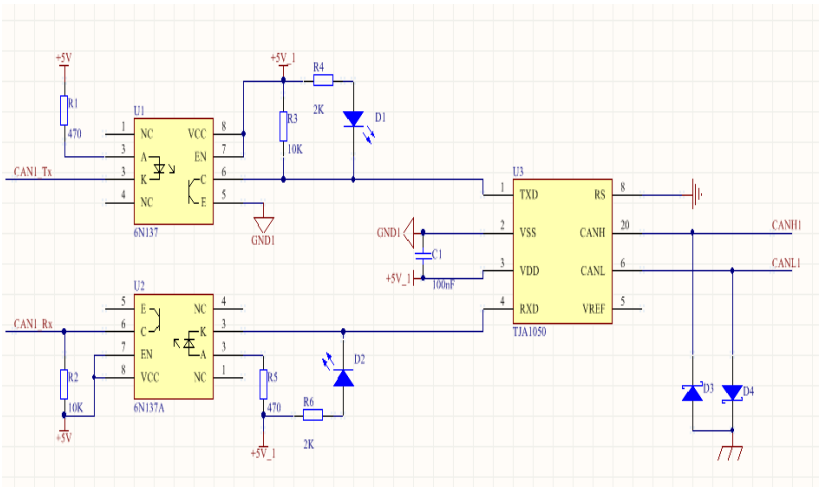

Figure 5: CAN communication hardware circuit diagram

5. CONCLUSION

In the actual operation of the circuit equipment, it can achieve the data upload and acquisition function requirements of multiple channels of zero milliseconds, realise the requirements of the working conditions in the actual operation, and basically reach the design goal.

The equipment does not completely dig out the capabilities of the ARM chip. In the future, for ARM chips with Ethernet interface functions, a local touch control screen can be designed to control the local logic, can also use its D/A function to achieve superior to the next level of analog instrumentation control display, in short, the device has a large space for development and application value.

6. REFERENCES

Zhu J, 2013.Design and implementation of configurable engineering machinery controller [D]. Nanjing: Nanjing University of Science and Technology, 2013.

Zhao J, 2013. Design of Multi-channel Analog Acquisition Module Based on Single Chip Microcomputer[J]. Electronic Quality, 2013, 6(7): 11-14.

He W, 2014. A Configurable Analog Acquisition Module Design [J]. Theory and Methods, 2014, 5 (10): 42-45

Zhang H, Wang L, 2004, Circuit Design of a High Precision Data Acquisition System [J]. Computer Measurement and Control. 2004, (06):575-577.

Collins A J, Foley R N, Herzog C et al.. US Renal Data System 2010 Annual Data Report.[J]. American Journal of Kidney Diseases, 2010, 57(1 Suppl 1).

Needham S, Lee M, Shipkova P. Chemical and Pharmaceutical Structure Analysis 2010: From Data to Biology: Analytical Measurements to Drive Pharmaceutical R&D.[J]. Bioanalysis, 2011, 3(4).

Jamali F. Estimation of Onset of Analgesia from Simulated Data.[J]. The Journal of Clinical Pharmacology (Online), 2011.

Jagust W J. Amyloid Imaging: Liberal or Conservative? Let the Data Decide.[J]. Archives of Neurology, 2011.

Groom C R. Data-Driven High-Throughput Prediction of the 3-D Structure of Small Molecules: Review and Progress. A Response from The Cambridge Crystallographic Data Centre.[J]. Journal of Chemical Information and Modeling, 2011.

Kennedy D N, Ascoli G A, De Schutter E. Next Steps in Data Publishing.[J]. NeuroInformatics, 2011.

180: Study on three-level DC-DC converter for microgrid energy storage system

Qi WANG[1], Changzheng ZHANG[2], Yonghao SHU[3]

[1] *Hubei Collaborative Innovation Center for High efficiency Utilisation of Solar Energy, Hubei University of Technology, Wuhan，430068，P. R. China，2218347970@qq.com*
[2] *Hubei Collaborative Innovation Center for High efficiency Utilisation of Solar Energy, Hubei University of Technology ,Wuhan，430068，P. R. China，longmarch_zhang@163.com*
[3] *Hubei Collaborative Innovation Center for High efficiency Utilisation of Solar Energy, Hubei University of Technology, Wuhan， 430068，P. R. China，996716351@qq.com*

With the rapid rise of new energy generation in microgrid, energy storage receives much concern in dealing with the instability of distributed generation units' output power. As the interface of storage device and power grid, the performance of the energy storage converter directly affects the operation efficiency, reliability and output power quality of the microgrid. Due to the two-level structure of the traditional DC/DC converter has the disadvantages of serious switching loss, low voltage stress and low efficiency, a new type of three-level DC-DC converter is used in this paper. This topology requires no high frequency isolation transformers and secondary circuits, small size, high efficiency and high power density, and each switch tube voltage stress is half of the input voltage, and it can utilise parallel structure to implement fast charge and discharge requirements of super power capacitor. The three-level DC-DC converter topology and operating principle are introduced in detail. The modulation mechanism is analyzed in the case of balance and unbalance of neutral point voltage. Based on the above, a new type of three closed loop control strategy is proposed, which is composed of a double closed-loop and an extra voltage closed-loop. The former is used to maintain stable DC bus voltage, and the latter is to handle the inherent neutral point voltage offset problem of three-level structure in the process of energy storage units charge and discharge. A simulation model of energy storage system is built in MATLAB, and the simulation results validate the feasibility and effectiveness of the three-level converter structure and control strategy.

Keywords: energy storage system, three-level DC-DC converter, bidirectional power flow, neutral point voltage suppression.

1. INTRODUCTION

With the dual development of energy demand and environmental protection, new energy research has become an important topic, and distributed power generation system is a hot research direction. However, the output power of new energy generation such as wind, light greatly influenced by environmental factors, has the shortcomings of variability and uncertainty, leading to poor continuity and stability of renewable energy power generation system. Thus, a certain capacity of energy storage device must be installed to improve the acceptance ability of the system to the distributed generation unit (DG) in the microgrid system. As the core component of energy storage system, DC-DC converter plays an important role in aggregation and transmission of DC power, which guarantees the stability of the bidirectional power flow. Compared with the traditional two-level DC-DC converter, the three-level topology has the advantages of larger output, higher output voltage, more stable operation and faster dynamic response. But the existence of three-level topological structure introduces to the unbalance problem of neutral point voltage, which can cause the switch device to withstand the imbalanced voltage, reduce output performance, and shorten the DC side capacitance's life. At present, the point voltage unbalance suppression method for three-level converters is usually divided into two categories: hardware and software. The main methods of hardware control are to increase capacitance capacity, the bridge arm and the external circuit of boost and buck to adjust charge and discharge of the capacitor. Most of the software control method based on the improvement of modulation algorithms.

In this paper, a novel three-level DC-DC converter topology is introduced to meet the requirements of large capacity of energy storage system. In order to solve the problem of midpoint voltage shift and energy bidirectional flow in a three-level converter, a novel control strategy is proposed on account of operating principle and modulation mechanism of the converter, which can solve the problem quickly. Finally, the simulation results demonstrate that the converter can realise the fast bidirectional power flow to maintain stability of DC bus voltage, and the control method can effectively suppress the neutral point voltage offset in the process of energy storage units charge and discharge.

2. THREE-LEVEL DC-DC TOPOLOGY AND WORKING PRINCIPLE

2.2. Structure of converter topology and operating principle

Figure 1 shows the three level topology of DC-DC converter, which consists of four switches(S_1, S_2, S_3 and S_4), two inductors(L_1 and L_2), one input filter capacitor(C_f), and two output filter capacitors(C_1 and C_2). This converter's advantages are that the device can reduce the voltage stress of the switch tube, the switching loss and the output ripple. Besides, parallel structure, the proportional increase of inductors and switches, can achieve larger power output.

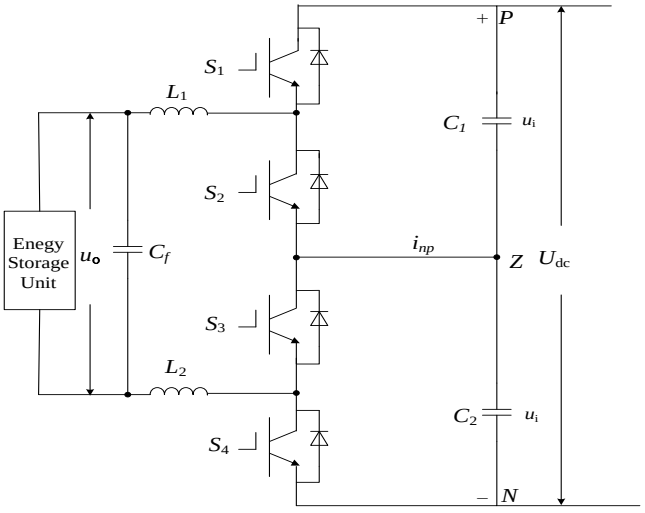

Figure 1: Three-Level DC/DC converter topology

During normal operation of the three-Level DC-DC converter, two switches are on at the same time. Using the number as the opening mark, this converter has six possible switching states: 12, 13, 14, 23, 24, 34. Since 12 and 34 are redundant switch state, there are four effective working stages. Taking the energy storage unit discharging as an example, Figure 2 shows current flow in four operating states. The effects of different working modes on midpoint voltage are as follows: at state 13, the energy storage units charges the upper capacitor C_1 of DC bus, so state 13 can increase u_{c1}; at state 24, u_{c2} is increased; at state 23, this state has no effects on the balance of upper and lower capacitor voltage, because u_{c1}, u_{c2} and u_{dc} are zero; at state 14, because the battery charges capacitor C_1 and C_2, there is no influence on neutral point potential balance. In short, the balanced state of neutral point voltage depends on state 13 and state 24.

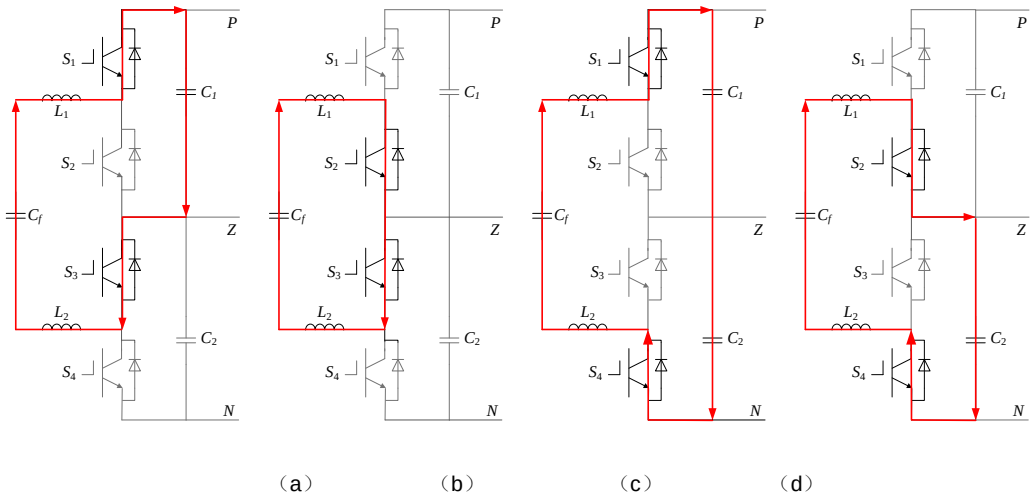

Figure 2: Four operating stages. (a) 13. (b) 23. (c) 14. (d) 24.

2.3. Structure of converter topology and operating principle

Figure 3 shows specific modulation mode under balanced power condition when the energy storage unit is charged. By compared the value of modulated signals (d_1 and d_4) with two phase difference 180° triangular carrier signals (c_1 and c_4), the pulse signal of S_1, S_2, S_3 and S_4 can be obtained. Among them, d_1 and d_4 are same (d_1=d_4=d), and S_2, S_3 trigger signals are complementary to S_1, S_4, respectively. As is seen from Figure 3, the generated voltage fluctuates between 0 and u_i, if modulated signals are less than 0.5. While modulated signals are more than 0.5, generated voltage jumps between u_i and 2u_i. Namely, the converter achieves buck function. On the contrary, when the energy storage unit discharges, the converter achieve boost buck. As a consequence, this converter operates on two working modes: when the energy storage unit discharges, the system operates on boost mode, otherwise, on boost mode.

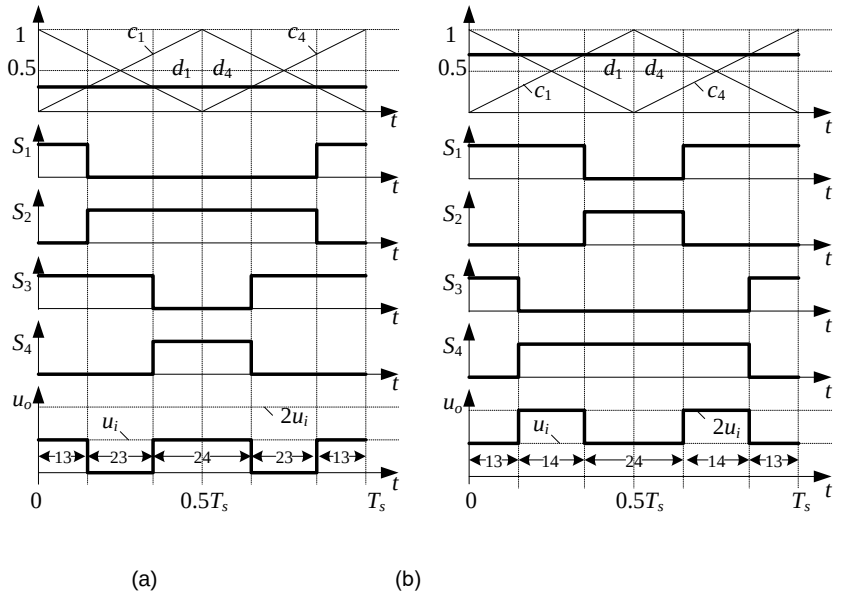

Figure 3: Modulation principle under balanced condition. (a)d_1=d_4<0.5.(b)d_1=d_4>0.5

2.4. Mechanism of unbalance suppression modulation

Based on the aforementioned analysis, operating state 13 and 24 have an opposite impact on neutral-point voltage. Thus, by adjusting the time of state 13 and 24, neutral-point voltage unbalance can be eliminated or suppressed. The unbalance suppression modulation is shown in Figure 4. At the assumption of the system operates on boost mode (d>0.5), when u_{c1}<u_{c2}, the time of state 13 should be extended, and the time of state 24 should be reduced. Namely, d_1 moves up and d_4 moves down (d_1>d_4), so the charge time of the battery for capacitor C_1 is more for capacitor C_2, which is presented in Figure 4(a). On the contrary, when u_{c1}>u_{c2}, from Figure 4(b), it can be seen that d_1 shifts up and d_2 shifts down (d_1<d_4), leading to the increase of u_{c2}. At last, u_{c1} is equal u_{c2}.

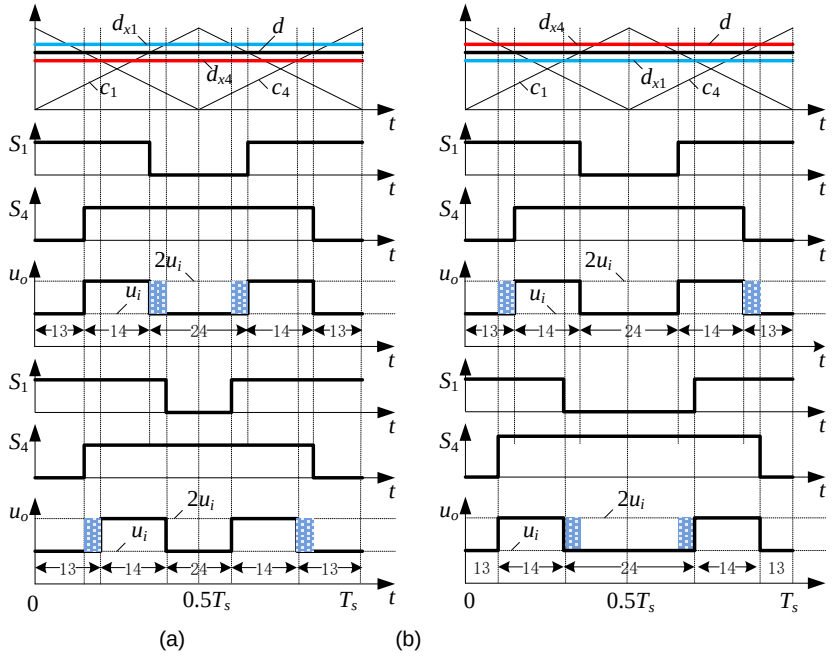

Figure 4: Modulation principle under unbalanced condition. (a)d_1>d_4. (b)d_1<d_4.

Table 1 shows the neutral point potential modulation wave offset under different condition. The offset of d_1 and d_4 is equal, which means the time of state 23 and state 14 remain unchanged, thus there are no effects in the average value of output voltage u_{dc}. It is worth noting that the unbalance only can be suppressed, not be eliminated when d_1'(d_4')>1 or d_1'(d_4')<0.

Table 1 The neutral point potential modulation wave offset

state	d<0.5	d>0.5
u_{c1}>u_{c2}	d_1'=d_1+Δd, d_4'=d_4-Δd	d_1'=d_1-Δd, d_4'=d_4+Δd
u_{c1}<u_{c2}	d_1'=d_1-Δd, d_4'=d_4+Δd	d_1'=d_1+Δd, d_4'=d_4-Δd

3. METHOD OF THREE-LEVEL DC-DC CONVERTER

The control strategy of the energy system is a three closed loop, which aims at maintaining the stability of DC bus voltage and midpoint voltage suppression. The specific scheme is divided into two parts. Figure 5 shows block diagram of the system control. $G_v(s)$, $G_d(s)$ is transfer function of voltage controller. $G_i(s)$ is transfer function of current controller. $G_{di}(s)$ is transfer function of duty-ratio signal to battery current, and $G_{iv}(s)$ is transfer function of battery current to DC bus voltage.

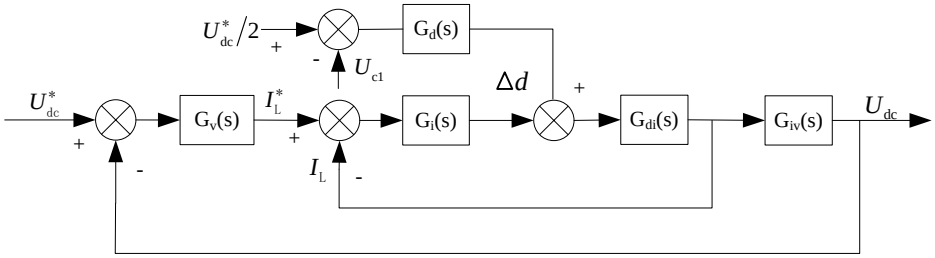

Figure 5: Block diagram of the system control

First, the system utilises a double closed-loop control strategy based on voltage loop and current loop to implement the stability of DC bus. In outer voltage loop, comparing the reference voltage U^*_{dc} with the feedback value U_{dc}, the error signal is handled by voltage controller (PI) to generate the reference current I_L*. In current inner loop, the difference between the reference current and the current feedback value from the inductor L_1 is converted by current controller (PI) to obtain the modulated wave signal *d*. The existence of current inner loop can improve the response speed of stabilizing the voltage of DC bus.

Second, the system introduces to an extra voltage loop to solve the unbalanced problem of midpoint voltage. The output of comparing half of the reference voltage U^*_{dc} with the feedback value U_{c1} is controlled by controller (PI) to generate Δ*d*.

Considering the difference of charge and discharge, by judging the direction of the inductor current I_{L1}, the symbol of Δd can be determined. Figure 6 shows the control and modulation diagram of three level DC-DC storage converter.

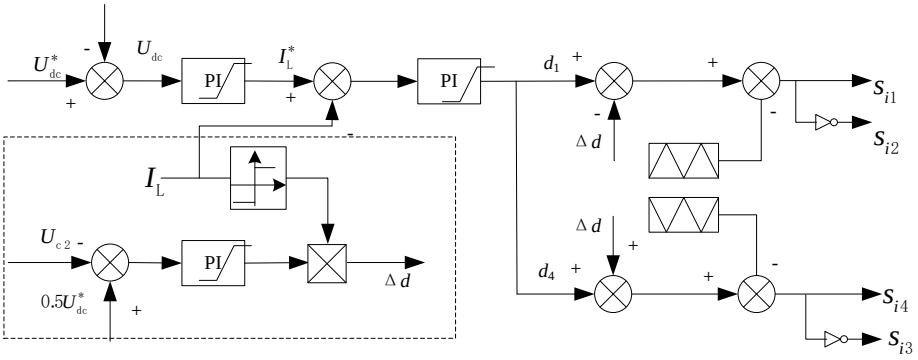

Figure 6: Control and modulation diagram of three-level converters

4. SIMULATION RESULTS

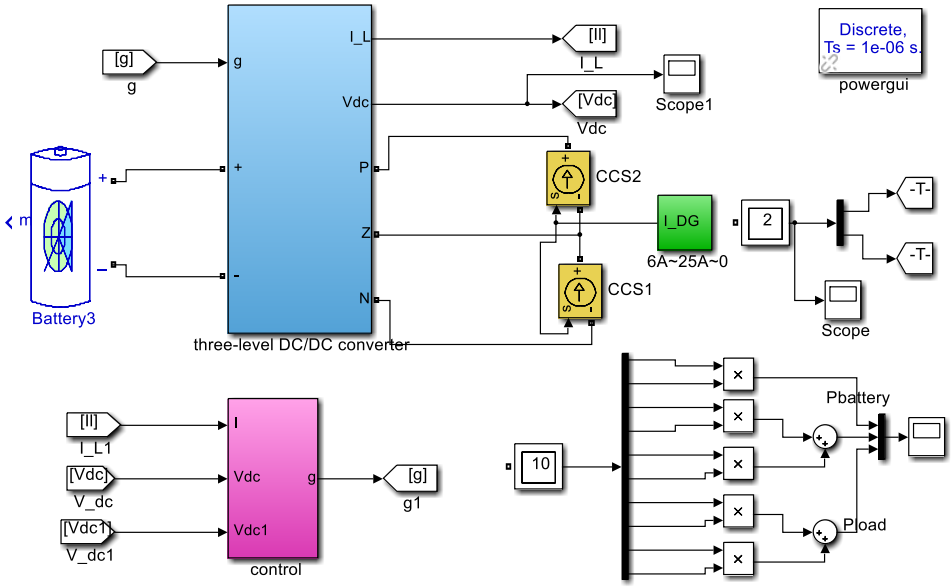

Figure 7: Simulation model of energy storage system

In order to verify the bidirectional power flow and unbalance suppression of DC bus neutral point voltage of three-level DC/DC converter, detailed simulation is accomplished in Matlab/Simulink, and it is shown in Figure 7. The switch frequency in this system is 5 kHz. The output voltage of the battery is 600V. L_1=L_2=1mH, R_1 and R_2 is the upper and lower loads in DC bus, respectively.

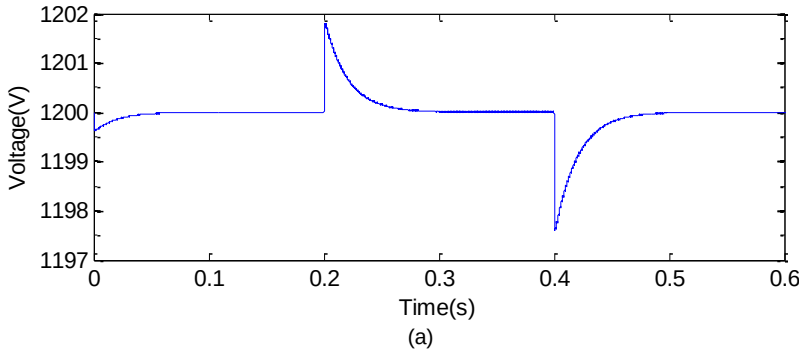

(a)

Figure 8: Voltage and power curve under different power of DG.(a) the waveform of DC bus voltage u_{dc}

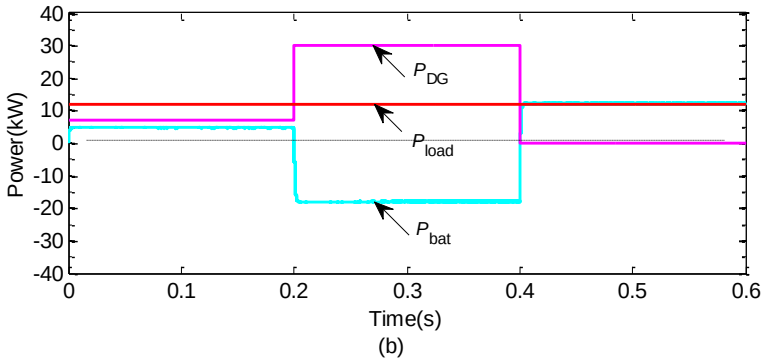

Figure 8: Voltage and power curve under different power of DG. (b) the changing curve of P_{load}, P_{DG} and P_{bat}.

Figure 8 presents the voltage and power curve under different power of DG. Both of the two loads in DC bus are 60 Ω. Using the different current source simulates power fluctuation caused by DG. Given initial current of current source is 6 A in parallel with the capacitor. When t is 0.2s, given current source is 25 A and then current source changes to 0 at 0.4s. Figure 8(a) reveals that DC bus voltage is basically stable at 1200V, even though the power fluctuation of DG is very high. At the assumption of the battery discharge is in positive direction, as can be seen from Figure 8(b), in 0~0.2s, the power of distributed generating unit (P_{DG}) is 7.2kW, and the power of battery (P_{bat}) is 4.8kW, which indicates the battery discharges to ensure that the power of load remains 12kW because of the absence of DG power ($P_{load} = P_{DG}+P_{bat}$). From 0.2~0.4s, P_{DG} is 30kW, whose value is more than P_{load}, resulting in the battery charging ($P_{load} = P_{DG}-P_{bat}$). During 0.4~0.6s, there is no power supply of DG, hence only the battery provides the power required for the load ($P_{load} = P_{bat}$). The results reflect the energy storage unit can follow quickly and keep the load power constant by regulating power flow direction.

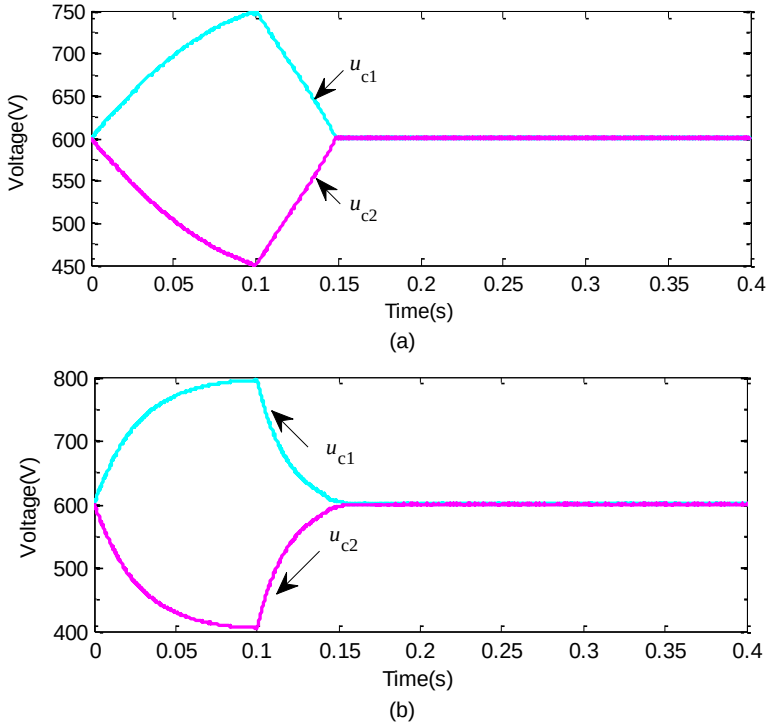

Figure 9: Voltage waveforms of capacitor C_1 and C_2 when R_1=60Ω, R_2=30Ω. (a)d>0.5. (b)d<0.5.

Figure 9 shows voltage waveforms of capacitor C_1 and C_2 when R_1 = 60Ω, R_2 = 30Ω. In Figure 9(a), u_{c1} and u_{c2} appear a trend of divergence before adding the neutral point voltage balance control. After 0.1s, due to the addition of the control, the voltage waves start to converge, and reach consistency at 0.15s. Consequently, the result demonstrates the efficiency of the proposed control in eliminating neutral point voltage unbalance. Figure 9(b) shows voltage waves of capacitor C_1 and C_2 when $d < 0.5$. u_{c1} and u_{c2} reach to be consistent within 0.05s. However, the existence of over-modulation and under-modulation result in the problem that unbalanced voltage couldn't be eliminate completely only by control algorithm. Figure 10 presents voltage waveforms of capacitor C_1 and C_2 when the load power difference of R_1 and R_2 exceeds the adjustment range.

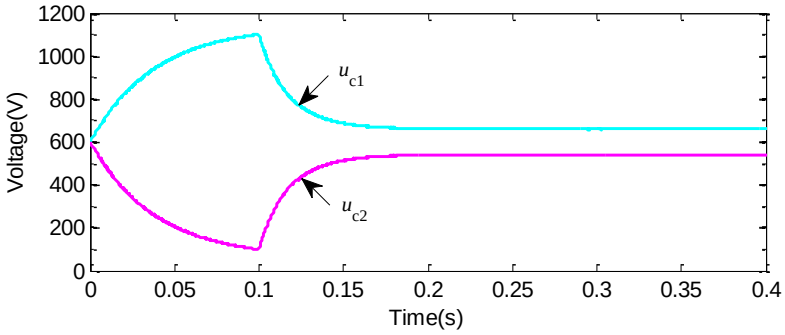

Figure 10: Voltage waves of capacitor C_1 and C_2 when the load power difference exceeds the adjustment range (R_1=600Ω, R_2=20Ω)

5. CONCLUSION

A new type of three-level DC-DC converter for energy storage system of high power microgrid has been introduced in this paper. Based on the structure characteristics, operation principle and modulation mechanism of this topology, a novel control strategy is proposed for achieving bidirectional power flow and DC bus voltage unbalance suppression. From results of analysis simulation, conclusions can be summarised as follows:

1) With the increase of energy storage capacity, the power capacity of the three-level DC-DC converter can be increased easily by parallel structure.

2) The topology of the three-level converter can quickly realise the bidirectional flow of energy to ensure the stability of DC bus voltage.

3) The control scheme of neutral point voltage suppression is easy to implement, and it has good performance for eliminating midpoint voltage fluctuation. Although the overlarge of unbalanced voltage may be beyond the range of modulation, it also can be certain inhibitory action.

4) The control scheme of neutral point voltage suppression has a fast dynamic response and can suppress power quality problems caused by unbalanced load, difference of capacitance parameters in DC side and more, timely.

6. REFERENCES

Akar F, Tavlasoglu Y, Vural B, 2017. An Energy Management Strategy for a Concept Battery/Ultracapacitor Electric Vehicle with Improved Battery Life. IEEE Transactions on Transportation Electrification, 3(1):191-200.

Lai CM, Cheng YH, Hsieh MH and Lin YC, 2018. Development of a Bidirectional DC/DC Converter With Dual-Battery Energy Storage for Hybrid Electric Vehicle System," in IEEE Transactions on Vehicular Technology, 67(2): 1036-1052.

Akar F, Tavlasoglu Y, Ugur E, et al, 2016. A Bidirectional Non-isolated Multi-Input DC–DC Converter for Hybrid Energy Storage Systems in Electric Vehicles. IEEE Transactions on Vehicular Technology, 65(10): 7944-7955.

Kanouda A, Ouchi T, Shimada T, 2015. High efficiency bidirectional DC-DC converter topologies for energy storage systems using high energy density batteries. IEICE Transactions on Fundamentals of Electronics, Communications and Computer Sciences, E98A(2): 460-465.

Shreelekha K and Arulmozhi S, 2016. Multiport isolated bidirectional DC-DC converter interfacing battery and supercapacitor for hybrid energy storage application. International Conference on Electrical, Electronics, and Optimisation Techniques (ICEEOT), Chennai.

Zhu L, Wu H, Xu P, Hu H and Ge H, 2014. A novel high efficiency high power density three-port converter based on interleaved half-bridge converter for renewable energy applications. IEEE Energy Conversion Congress and Exposition (ECCE), Pittsburgh, PA

Lai C M, 2016. Development of a Novel Bidirectional DC/DC Converter Topology with High Voltage Conversion Ratio for Electric Vehicles and DC-Microgrids. Energies, 9(6):410.

Piris-Botalla L, Oggier G G, García, G O, 2017. Extending the power transfer capability of a three-port DC-DC converter for hybrid energy storage systems. Institution of Engineering and Technology, 10(13): 1687-1697.

Singh S, Singh M, Kaushik S C, 2017. Optimal power scheduling of renewable energy systems in microgrids using distributed energy storage system. Iet Renewable Power Generation, 10(9):1328-1339.

Tan L, Wu B, Rivera S, et al, 2015. Comprehensive DC Power Balance Management in High-Power Three-Level DC–DC Converter for Electric Vehicle Fast Charging. IEEE Transactions on Power Electronics, 31(1):89-100.

Wu D, Tang F, Dragicevic T, et al, 2014. Autonomous Active Power Control for Islanded AC Microgrids With Photovoltaic Generation and Energy Storage System. IEEE Transactions on Energy Conversion, 29(4):882-892.

Wang C, Xiong R. He H, et al, 2016. Efficiency analysis of a bidirectional DC/DC converter in a hybrid energy storage system for plug-in hybrid electric vehicles. Elsevier Ltd, 183: 612-622

181: Automatic generation control based on improved particle swarm optimisation algorithm

ZHANG Xuanhao, DING Wenfang

Solar Energy Efficient Utilisation Cooperative Innovation Center of Hubei Province in Hubei University of Technology, Wuhan 430068，China

Most of the load frequency control（LFC）of automatic generation control（AGC）uses the PID controller based on particle swarm optimisation to operate the AGC unit. For the traditional particle swarm optimisation algorithm, it is easy to fall into a local optimal problem. This paper proposes a block chaotic particle swarm optimisation algorithm. By dividing these swarms into several areas, the different particles within the region are limited to different small areas, so that it avoids particle swarm optimisation searching best index in a small area. At the same time, inertia weights based on linear differential decrease strategy are introduced. Different search speeds are used in the early and late stages of search. Large inertia weights are used in the early stage to improve the global search ability of the population, and later the chair group is given a smaller search speed to improve the local search ability of the population by searching near the best value. Then, the partitioned particle swarm optimisation algorithm is combined with the chaotic particle swarm optimisation algorithm to make use of the ergodicity of chaos to stabilise the particle swarm while some particles jump out of the accumulating area, which further solves the problem of the easy prematurity of the traditional particle swarm optimisation algorithm.In this paper, the block chaotic particle swarm optimisation algorithm is investigated for frequency control of a single regional power system. The studied system comprises of various autonomous generation systems such as photovoltaic power generation and diesel engine generator. The simulation experiments show that the frequency can be controlled reposefully by PID controller with block chaotic particle swarm optimisation algorithm.

Keywords: PSO ; chaotic; single-area; load fluctuations; stability

1. INTRODUCTION

In response to the energy crisis and environmental pollution, countries around the world have begun to vigorously develop renewable energies represented by wind and solar energy (Lu, 2011). However, large-scale renewable energy injection will lead to increase the disturbance of the system, which bring new challenges about electric power system automatic generation control. Automatic generation control (AGC) plays a key role in maintaining the balance of generation power and user load power, and it is an important means to ensure the frequency stability of power system and regional power exchange. In the traditional sense, AGC adjust the power of generation by accompanying with the disturbance of lode power. On the one hand, as a part of the traditional power generation have been replaced by the wind turbines and photovoltaic power generation system, which makes the revolving inertia declining, the ability to maintain quality of frequency reduced. At the same time, a large scale of injection about renewable energy has added the demand for frequency adjustment; On the other hand, the power of wind power and photovoltaic power generation can be adjusted rapidly through power electronic equipment, which has great potential to maintain the frequency level of power system (Hu, 2018).

Because of the reliability and maneuverability of PI control, most AGC units at home and abroad use traditional PI control. However, the adjustment of the traditional PID controller parameters is time-consuming, and the controller parameters under certain conditions often cannot be applied to another situation (Zhang, 2016; Xu 2010; Xu, 2014). In recent years, with the development of computer technology, particle swarm algorithm, genetic optimisation algorithm and other intelligent algorithms have been widely applied in the optimisation of controller parameters. Genetic algorithm needs complex operation, and the evolution speed is slow, and it is easy to produce premature convergence (Zhang, 2015). Particle swarm optimisation (PSO) is a global optimisation method based on swarm intelligence theory, through the cooperation and competition between particles in a population of swarm intelligence to guide the optimisation search, fast convergence speed. However, PSO has disadvantages such as low accuracy and easy distribution in the early stage of the algorithm. Under the condition of convergence, as a result of all the particles to the optimal direction, the particle diversity declined and the speed of convergence slowed, the whole swarm is easy to fall into local optimum (Wang, 2009). In research based on particle swarm optimisation algorithm, the literature (Zhou, 2012) proposed adaptive inertia weight chaos particle swarm optimisation (PSO) algorithm, the inertia weight changes as the change of particle fitness, which can improve the convergence speed, when the algorithm into puberty, using chaotic sequence generated a number of replacing part of the poor to adapt to the value of particles help particles to jump out of local optimal; Del Valle (2008) elaborates on the problems of the traditional particle swarm algorithm, which is prone to precocity and late search ability. Chen (2008) divided the optimisation process into two phases, and the PSO algorithm and chaos optimisation algorithm were used to improve the accuracy and robustness of the algorithm. Tang (2007) classified particles after each iteration according to the fitness value, then for different population take different inertial factor optimisation, the algorithm is relatively complex, the optimisation effect is not obvious.

In this paper, the traditional particle swarm is improved, and chaos theory is combined with particle swarm algorithm to solve the problem of weak searching ability and easy to get into local optimum. When the photovoltaic module is added or withdrawn from the system, the algorithm can be used to adjust PID parameters and suppress frequency fluctuation.

2. SINGLE REGIONAL POWER SYSTEM MODEL CONSTRUCTION.

2.1. AGC System Model

A single region grid AGC system control object include: governor, reheat steam turbine, generator and load, the control purpose is to adjust the grid frequency fluctuation to zero as soon as possible by PID controller when the load disturbance occurs. According to the transfer function model of each object, the simulation model is built as follows:

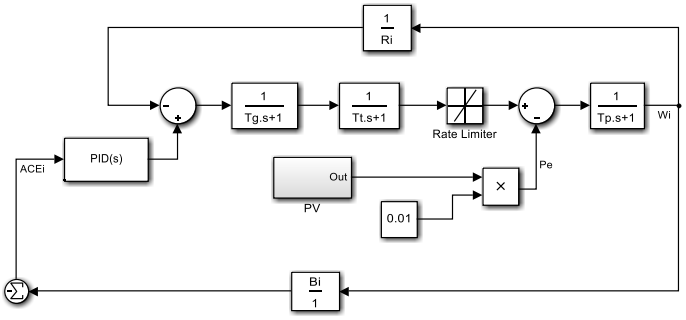

Figure 1: Isolated power system

The parameters for the isolated power system are shown as follows:

$ACE_i = B_i w_i$ the control errors for area i;

T_g the governor time for area i;

T_p inertia constant for area i;

B_i frequency deviations for area i;

R_i the speed regulations for area i;

T_t turbine time constant for area i;

PV Photovoltaic Modules ;

The simulation system takes a regional network modulation system as an example, the system frequency is 50Hz, and the parameters of the power system are taken from Yao (2015). The parameters are as Table 1:

Table 1: System parameters

Area	T_p	T_g	T_t	R
1	70	0.08	0.04	0.05
2	28.6	0.08	0.04	0.05
3	24.3	0.08	0.04	0.05

2.2 Controller Design

PID controller is used to realise AGC system. The controller structure is shown in the figure. K_p, K_i, K_d and N are proportional coefficient, integral coefficient and differential Coefficient, filter coefficient.The transfer function of PID controller is shown in Equation (1).

$$TF_{PID}(s) = K_p + \frac{K_i}{s} + \frac{NK_d s}{s+N} \quad (1)$$

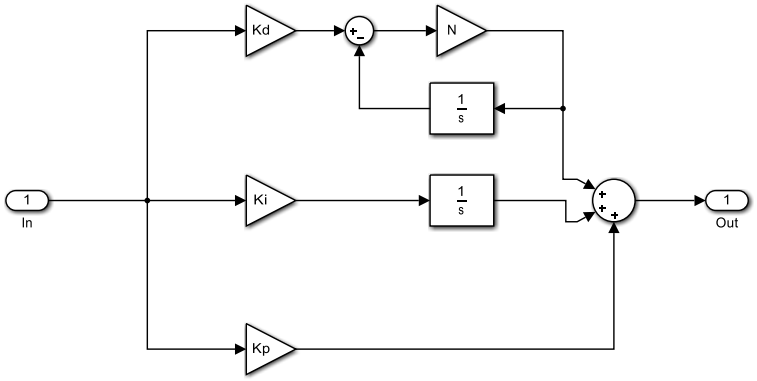

Figure 2: PID controller structure

The target function mainly detects the frequency fluctuation of the power system and sends the results to the PSO algorithm, which can adjust the PID parameters. The traditional calculation method is IAE, ISE, ITAE, ITSE, taking into account the complexity of the single power system and taking ITAE method calculation, the formula is as formula (10),and regional control deviation is as formal ()

$$ITAE = \int_0^{t_0} t|\Delta\omega|dt \tag{2}$$

$$ACE_i = B_i \Delta\omega_i \tag{3}$$

3. IMPROVED PARTICLE SWARM OPTIMISATION DESIGN.

3.1. Standard particle swarm optimisation

Since Kennedy and Eberhart proposed the particle swarm optimisation (PSO) algorithm in 1995, its algorithm has received wide attention due to its simple operation. Each particle in the particle swarm has its own position and velocity, its position $x_i(x_1,x_2,\ldots x_d)$ represents a potential solution in the solution space, velocity v_i $(v_1,v_2,\ldots v_d)$ represents the direction and distance of the particle flight, and the fitness value is calculated by the specific fitness function, and its value represents the fitness of the particle. The particle moves in the solution space and adjusts its position by tracking the current individual extreme value Pb and the global optimal value Pg. Once the position of particle is updated, the fitness value is calculated at the same time, and by comparing the new particle group of fitness value and the individual extremum value to update the position of individual extreme value and global optimal value, the update formula is:

$$v_{ij}(t+1) = wv_{ij}(t) + c_1 r_1 (Pb_{ij} - x_{ij}(t)) + c_2 r_2 (Pg - x(t)) \tag{4}$$

$$Swarm(j,:) = Swarm(j,:) + v_j \tag{5}$$

Where: w is the inertial weight; T is the number of iterations; c_1, c_2 is the learning factor; r_1, r_2 is the random number of uniform distribution between 0 and 1; $v_{ij}(t+1)$ represents the velocity of the particle i in the j dimension in t+1 iteration; $x_{ij}(t+1)$ denotes the displacement of the particle i in the j dimension in t+1 iteration.

3.2 Improved particle swarm optimisation

Traditional particle swarm optimisation (pso) algorithm of inertial factor and learning factor is constant, fail to adjust parameters in the search process of lead to search ability is not strong, late in the search, the particles easily gather near the local optimal value, which would result in algorithm premature. In this paper, we will adopt the real-time adjustment parameter factor optimisation search ability, and use the initial and iterative chaos to avoid the precocity.

In particle swarm optimisation (pso) algorithm, the inertia factor w determines the speed of particles near the optimal value, the larger w, the beneficial to global search, w is small is advantageous to the depth of the local search, so according to the fitness value of real-time adjustment of inertia factor size, will improve the early stage of the algorithm is global search and local search ability and guarantee convergence in a timely manner.

The inertial weight linear differential decreasing adjustment method can be expressed as：

$$\frac{dw(t)}{dt} = \frac{2(w_{\max} - w_{\min})}{t_{\max}} t \tag{6}$$

The integral of (6) is obtained.

$$w(t) = w_{\max} - \frac{2(w_{\max} - w_{\min})}{t_{\max}^2} t \tag{7}$$

W_{max}, W_{min} is the maximum and minimum of inertia weight respectively; t is the maximum number of iterations while t is the current iteration number.

The learning factor gives the particle self-summarisation ability and the ability to learn the global optimal particle. This paper adopts the learning factor optimisation method of asynchronous change. In the early stage of search, the learning factor c_1 takes a larger value, and the learning factor c_2 takes smaller value, which makes the particle global search ability enhanced. At the end of the search, the learning factor c_1 takes a smaller value, and the learning factor c_2 takes a larger value, which makes the particle local search capability enhanced. Its search formula is.

$$c_1 = 2.4 - \frac{1.4t}{t_{\max}} \tag{8}$$

$$c_2 = 0.9 + \frac{1.6t}{t_{\max}} \tag{9}$$

Considering the particles easily plunged into local optimum, when initializing particles, the population is divided into several different areas, for each region respectively carry out intelligent algorithm, can avoid particle gathered in a single region; Combine chaos algorithm and particle swarm optimisation (pso) algorithm, using the characteristics of ergodicity and randomness of chaotic, applied to the search process, when particles trapped in local optimum, chaos perturbation make some particles jump out of local optimal and improve the accuracy of solutions. Logistic chaotic mapping is adopted in this paper.

$$y_{t+1} = \mu y_t (1 - y_t) \quad n = 0,1,2..... \quad 0 \le \mu \le 4 \tag{10}$$

To sum up, the steps of block chaos particle swarm optimisation (SCPSO) are as follows;

Step 1 randomly generates a population of N particles, divides the particle and initializing the velocity and position of each particle.

Step 2 evaluate the fitness value of each particle, and save the best position (P_b) of the individual and the best global location (P_g).

Step 3 use (4) and (5) to update the velocity and position of the particle, update the inertia weight of the particle with Equation (7), and update the learning factor with Equation (8) and (9);

Step 4 calculate the fitness function value of each particle and find the optimal position(P_{gd}).

Step 5 chaotic search for optimal location.

- Map decision variables x^k_j, j = 1, 2, 3.....n to chaotic variables y^k_j. The initial value of chaotic search is P_{gd} the formula as follows:

$$y_j^k = \frac{x_j^k - x_{\min j}^{\ k}}{x_{\max j}^{\ k} - x_{\min j}^{\ k}} \tag{11}$$

In the formula: $P_{gd}^{k}{}_{j}$ is the global optimal position in j dimension, $x_{min}^{k}{}_{j}$ and $x_{max}^{k}{}_{j}$ are the down and up boundary conditions respectively,

- calculate the chaotic variables of the next iteration with Equation (10).

- transform chaotic variables into decision variables.

$$x_j^{k+1} = x_{\min j} + y_j^{k+1}(x_{\max j} - x_{\min j}) \tag{12}$$

- calculate the fitness value of the new solution, and if it is better than the initial solution or the maximum number of iterations, the new solution will be used as the result, otherwise, it will be transferred by Equation (7).

- determines whether the current operation meets the stop condition, and if it is satisfied, stop circulation , otherwise jump to step 3.

Figure 3 is the whole algorithm flow chart

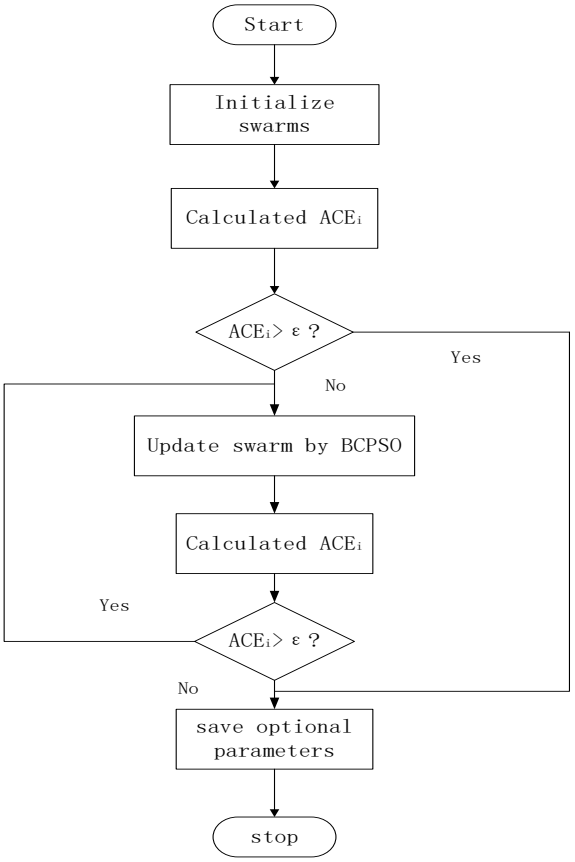

Figure 3: the flow chart of BCPSO and power system model frequency adjustment algorithm:

4. THE EXAMPLE ANALYSIS

In this paper, a single power system is used as the optimised object, and the connection of pv is regarded as the disturbance of the power grid, and the adjustment of the power grid is optimised by Matlab simulation.

The pv model of this paper adopts the pv output curve at T=25℃, S=600W/m^2 and U=25v, and its characteristics are shown in Figure 4:

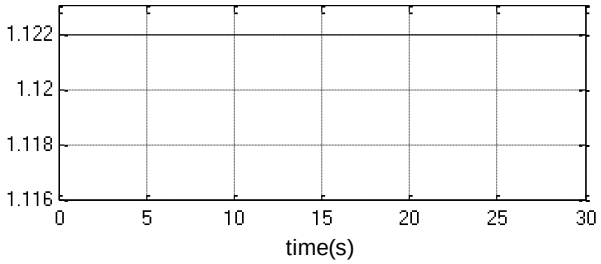

Figure 4: Photovoltaic cell output curve

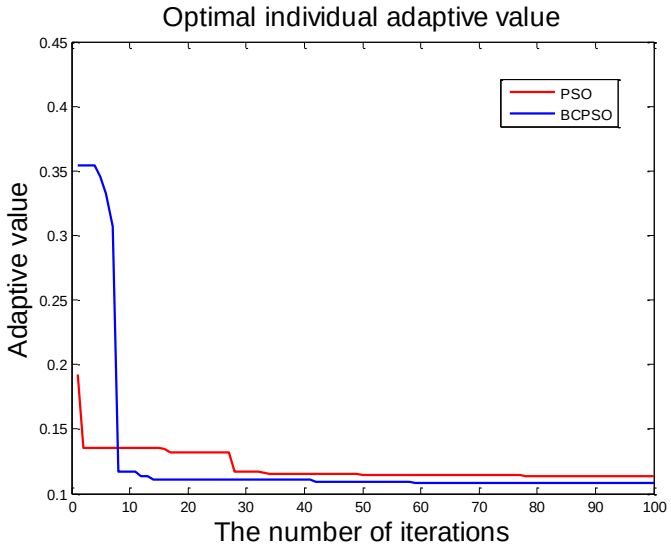

Figure 5: BCPSO adaptive value curve

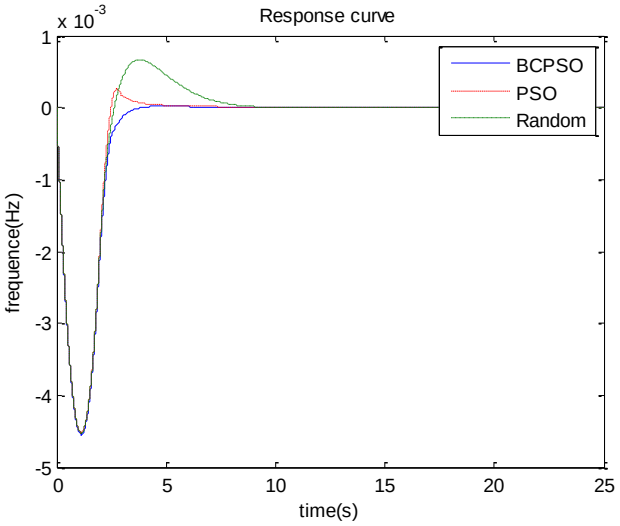

Figure 6: Photovoltaic response curve

Table 2: PID control gain

	Kp	Ki	Kd	Fitness
BCPSO	20	7.4	3.9	0.1081
PSO	28.8	8.1	8	0.1135
Random	14.5	10.4	7.4	

It can be seen from Figure 5 that BCPSO can find the optimal results after 15 iterations, while PSO needs 30 iterations, and both the search precision and the search speed of BCPSO are better than traditional PSO.As can be seen from Figure 6, for the same pv fluctuation, the PID controller with BCPSO parameter has better adjustment effect than that with PSO parameter controller. The BCPSO parameter controller has no positive overshoot, faster adjustment speed and more smooth adjustment curve

5. CONCLUSION

In this paper, with the improved particle swarm optimisation (pso) algorithm, optimise the power system frequency control, the interference is produced by photovoltaic modules, the simulation results prove that: improved particle swarm optimisation algorithm has both the standard particle swarm simple quickness and ergodicity, and it is not easy to fall into local optimum. Using this method, the PID controller can be adjusted and the frequency fluctuation of the system can be smoothed quickly, and its performance is better than the traditional method.

6. REFERENCES

Lu Z, Huang H, Shan B, 2011. High proportion renewable energy power system structure form evolution and power forecast. Electric power system automation, 41 (9): 12-18

Hu Z, 2018. The current situation and prospect of automatic power generation control under the background of large-scale renewable energy access. Power system automation, Vol. 42(8)

Zhang Y, large-scale wind power intervention on the power system AGC control parameters influence north China electric power university, 2016

Xu Y, Li F, Kueck JD, 2010.Adaptive voltage control with distributed energy resources: Algorithm, theoretical analysis, simulation and field test verification. IEEE Trans, Power System, 25(3):1638-1647

Xu Y.and Li F, 2014.Adaptive control of STATCOM for voltage regulation, IEEE Trans，Power Del，29(3):1002-1011

Zhang M, Yang Fan, 2015. Research on PID governing system based on particle swarm algorithm. Control engineering, 22 (6)

Wang W, LI Hei, 2009. Overview of particle swarm optimisation algorithm. Research and development, (301)

Zhou Y, Liu P, Zhao J, et al. 2012. Adaptive particle swarm algorithm based on adaptive inertia weight. Journal of Shandong University,47 (3)

Del Valle Y, Venayagamoorthy G K, Mohagheghi S, et al. 2008.Particle swarm optimisation: basic concepts, variants and applications in power systems. IEEE Trans on Evolutionary Computation, 12(2):171-195.

Chen R, Yu J. 2008. Research and application of chaotic particle swarm optimisation algorithm, journal of system simulation, 20 (3).

Tang X, 2007. Theory and application of chaos particle swarm optimisation algorithm, chongqing university .

Yao X, Li F, 2015. Dynamic gain-tuning control (DGTC) approach for AGC with effects of wind power.IEEE transactions on power systems, 31(5)

Yin L，Zhao X，Mei Z，2016. Optimizing Technology for Micro Grid Operation Based on Chaos Particle Swarm Optimisation Algorithm. Proceedings of the CSU-EPSA, 28(5)

182: Research on large scale electric vehicle charging scheme based on improved genetic algorithm

Xiaohua ZHANG[1], Kang LI[2], Tiezhou WU[3]

[1] *Hubei Key Laboratory for High-efficiency Utilisation of Solar Energy and Operation Control of Energy Storage System, Hubei University of Technology, 1297362526@qq.com*
[2] *Hubei Key Laboratory for High-efficiency Utilisation of Solar Energy and Operation Control of Energy Storage System, Hubei University of Technology, 527763258@qq.com*
[3] *Hubei Key Laboratory for High-efficiency Utilisation of Solar Energy and Operation Control of Energy Storage System, Hubei University of Technology, 534228591@qq.com*

When a large number of electric vehicles randomly access the power system, the peak-to-valley difference and power fluctuation will become more serious, and even exceed the power system's power supply capacity and affordability, which will affect the stable operation of the power grid, make the charging cost too high and hinder the development of electric vehicle industrialisation. Therefore, analysing and optimizing the charging scheduling method for electric vehicles to reduce the adverse effect of charging load on the power grid is very significant in practical applications. In the optimisation of the above problems, satisfying the constraints of peak-to-valley difference, daily load variance, and electric vehicle charging power, a charging model is constructed with the goal of minimizing charging costs. But using a standard genetic algorithm to solve the objective function will cause problems such as inhomogeneous spatial distribution leading to local optimum solutions, premature convergence, and slow operation speeds. Therefore, an improved genetic algorithm is proposed in this paper. Through the introduction of orthogonal operators in population initialisation and crossover operations, the problems such as non-uniform distribution of solution space are overcome, the diversity of species is strengthened, a more optimised charging scheme is obtained, and a more accurate solution set is gained. The experimental simulations compared the improved genetic algorithm with the standard genetic algorithm, showing that the charging cost obtained by the improved genetic algorithm is reduced by 17.1%, the peak-to-valley difference is reduced by 252.6 kW, the variance is reduced by $0.3121*10^5 kW^2$ and the convergence speed has nearly doubled. The experimental results verify the effectiveness of the improved genetic algorithm in solving the EV charging model.

Keywords: genetic algorithm; orthogonal operator; charging cost; convergence speed

1. INTRODUCTION

In order to reduce the influence of the large-scale electric vehicle grid connected to the grid, we should try to avoid the charging in the peak period of the conventional load in the power grid, reasonably disperse the charging load of the electric vehicle, reduce the impact on the other load of the power grid and the construction cost of the unnecessary transmission and distribution, ensure the coordinated development of the electric vehicle and the power grid, and achieve the effect of cutting the peak and filling the valley (Wang, Liu, Zhang, 2017: page 26-32). It is necessary to effectively guide or control the charging of electric vehicles, that is, on the basis of meeting the demand of electric vehicle daily consumption, it is the concept of orderly charging by using practical and effective economic or technical means to guide electric vehicles to carry on the orderly charging (Wang, Ye, 2015: page 65-70).

This paper guides users to adjust the charging behaviour voluntarily through the change of real time price, as shown in Figure 1(Wu, Jiang, Zhang, 2016: page 81-85), the relationship between electricity price and power grid load (Huang, Xiong, Che, 2017: page 30-36). The horizontal axis is taken as a point of 24 hours in a day (Jin, Liu, Chen, 2017: page 31-36).Because the unit dimension is different, the left of the vertical axis is the normal daily load coordinate, the right is the time point of the electricity price (Yang, Fu, 2016: page 19-19). In the same picture, it is more convenient to compare the trend of the two. From Figure 1, it can be seen that the change trend of electricity price and load curve is basically similar (Meng, Liu, Wen, 2017: page 117-128). When the load is at the peak, the electricity price is higher. When the load is in the valley value, the electricity price decreases. When large-scale electric vehicles are randomly connected to the grid, most electric vehicle users may choose to charge the lower electricity price to make the charging cost as small as possible, but this will make the load curve another peak.

Therefore, it is necessary to guide or control the charging of electric vehicles effectively (Guo, Wang, 2017: page 117-128). In this paper, under the influence of real time electricity price, the ordered charging of electric vehicles is regulated through the construction of electric vehicle charging model, and the charging power of electric vehicles is reasonably dispersed to avoid another high peak, ensure the coordinated development of electric vehicles and power grids, and achieve the effect of avoiding peak and filling the valley.

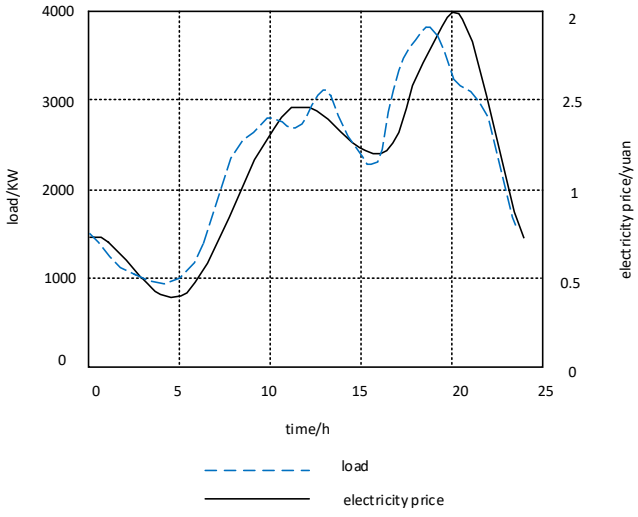

Figure 1: Relationship between load and price

2. ELECTRIC VEHICLE CHARGING MODEL

2.1. Objective function

The ultimate goal of implementing the real-time tariff is to minimise the charging cost from the user side and to reduce the negative effects of a certain scale of electric vehicles coming into the power grid from the grid side. Considering the interests of the two parties, we can guide and encourage the electric vehicle users to adjust the charging time as far as possible through the change of charging electricity price, reach the maximum charging cost while avoiding the superposition of the original peak and refreshment of the peak value during the peak period of the electricity consumption, even use the transfer of the charging load to increase the load curve of the valley period, reduce the peak and valley difference in the current power grid, and further improve the stability of the power grid. This paper builds a charging model with the goal of minimizing charging costs, as shown in Equation 1, the objective function is:

Equation 1: the minimum charging cost

$$\min f = \min \sum_{t=1}^{96} \sum_{i=1}^{N} x_{it} P_i p_t \Delta t$$

Where:

Δt = 24 hours in a day is divided into 96 periods, each of which is 15 minutes (t).

P_t = the price of the t-th period (yuan).

P_i = charging power of the i-th electric vehicle (W).

N = the total number of all electric cars in the area.

X_{it} = 0-1 decision variable, which determines whether the i-th electric car is charged during time period j.

Equation 2: whether the i-th electric car is charged ;

$$x_{it} = \begin{cases} 1 \ , charge \\ 0 \ , idle \end{cases}$$

The charging time of the i-th electric car can be expressed as T_i:

Equation 3: The charging time of the i-th electric car;

$$T_i = \sum_{j=1}^{96} x_{it} \cdot \Delta t$$

Equation 4: the charging time;

$$T_i = \left(S_{en} - S_{st} \right) B_r / P_i$$

Where:

S_{st} = the state of charge at the start of charging.

S_{en} = the actual state of charge at the end of charging.

B_r = the battery capacity.

2.2. Constraint condition

Peak-to-valley difference constraint

If the electric vehicle is connected to the grid for charging, if only charging costs are taken into account, a large number of users will elect to charge at a time when the electricity price is low due to the guidance of real-time electricity prices. Considering from the grid side, a large number of loads are concentrated in a certain period of time, which will increase the system daily load peak-to-valley difference and adversely affect the stability of system scheduling. Therefore, this paper makes the difference between peaks and valleys as small as one of the constraints.

Equation 5: Difference between maximum load and minimum load;

$$L_{\max} - L_{\min} = \Delta L$$

Where:

L_{max} = maximum load.

L_{min} = minimum load.

Equation 6: Difference between maximum load and minimum load;

$$L_{\max} - L_{\min} = \max\left(L_0 + \sum_{i=1}^{N} P_i x_{it} \right) - \min\left(L_0 + \sum_{i=1}^{N} P_i x_{it} \right)$$

Where:

L_0 = the basic load of each period of the grid.

In Equation 6, L_0 is the basic load of each period of the grid, and the initial value of ΔL is defined as the minimum value of the peak-to-valley difference in the past few days. However, this value may be too small, resulting in no solution in Equation

5. If there is no solution, then 0.1 is used. The % step increments by ΔL until there is a solution. If there is no solution, then the value of ΔL is gradually increased by 0.1% step until there is solution.

Daily load variance constraint

The small peak-to-valley difference in power system load during the day does not mean that the total fluctuation of the total system load is small. Therefore, while limiting the size of the peak-to-valley difference, it is also necessary to limit the load fluctuation of the electric vehicle after it is connected to the power grid, so as to ensure the stable operation of the system.

Equation 7: minimum variance;

$$\min \frac{1}{95} \sum_{t=1}^{96} \left(L_t - \mu\right)^2 \leq M$$

Where:

M = Minimum load variance in the past few days.

Equation 8: the average load of the system in a day;

$$\mu = \frac{1}{96} \sum_{t=1}^{96} L_t$$

Where:

L_t = the system load value that superimposed the charging load of the electric vehicle in the t-th period.

Equation 9: system load value;

$$L_t = L_0 + \sum_{i=1}^{N} P_i x_{it}$$

In Equation 9, the initial value of M is defined as the minimum value of the load variance in the past few days, a smaller value may cause Equation 7 to have no solution, if there is no solution the value of M will be gradually increased by 1% steps until there is a solution.

Electric Vehicle Recharge Constraints

The charge of an electric vehicle must meet certain conditions, the actual power can't exceed the total capacity of the battery, but at the same time, it can't be less than the power expected by the user. Let the user of the electric vehicle enter the desired state of charge Sh (the current battery capacity of an electric vehicle to its total battery capacity) into the system when entering the charging station. That is, the actual capacity at the end of charging is not less than that desired by the user, and charging is completed when it is full. It can be expressed as:

Equation 10: the relationship between S_h, $S_{en,i}$;

$$S_h \leq S_{en,i} \leq 1$$

Where:

$S_{en,i}$ = the actual state of charge at the end of the charging of the i-th electric car.

Then put Equation 4 into Equation 10 to get:

Equation 11:

$$\left(S_h - S_{st}\right) B_r / \left(P_i \cdot \Delta t\right) \leq \sum_{t=1}^{96} x_{it} \leq \left(1 - S_{st}\right) B_r / \left(P_i \cdot \Delta t\right)$$

Where:

S_{st} = the actual state of charge of the electric vehicle.

$\sum X_{it}$ = the total duration of charging of the i-th electric vehicle.

In Equation 11, then the restriction of the electric vehicle charging capacity may be converted to the constraint on the charging duration of electric vehicles.

3. IMPROVED GENETIC ALGORITHM FOR SOLVING CHARGE OPTIMISATION MODEL

3.1. Standard genetic algorithm

The genetic algorithm GA (Genetic Algorithm) is a randomised search algorithm that draws on the natural selection and natural genetic mechanisms of the biological world. The algorithm was proposed by the American scholar Holland JH in the 1970s.It treats the possible solutions to the problem as individuals with chromosome strings, a large number of individuals constitute populations, Individual fitness function is used as an evaluation index of the individual's merits, In the process of population evolution, three kinds of genetic operators, selection, crossover, and mutation, are constantly used to continuously solve the problem until a global optimal solution is produced. Genetic algorithms are particularly suitable for dealing with complex and non-linear problems that traditional search methods cannot solve. The general steps to solve the problem with GA: (1) encode the bit string of the desired optimisation parameters; (2) generate the initial population; (3) evaluate the population and determine the fitness value of each individual; (4) The genetic operator is applied to the population to generate a new generation of populations. Genetic operations mainly include: ① Selection, which is the key to GA and reflects the idea of the survival of the fittest in nature; ② Crossover, which is the most important operator in GA, can pass good information to a substring of the next generation to make them have better performance than their parents, so the cross-probability PC should be larger, generally from 0.6 to 0.9; ③ Mutation, which ensures the GA's global search, in order to reduce the randomness of the operation, the mutation probability Pm should be smaller, generally from 0.01 to 0.3.

3.2. Improved genetic algorithm for solving charge model

The standard genetic algorithm uses a stochastic method to generate a set of initial solution populations, the three populations of genetic operators are selected for replication, crossover, and mutation. The population is multi-generationally evolved. This kind of random initialisation may cause the initial solution population to be unevenly distributed in the solution space, and too large a population size will make the calculation slow, thereby affecting the performance of the algorithm and causing problems of “premature convergence” and “searching dullness”. Orthogonal design method is to select some representative points from a large-scale comprehensive experiment to conduct experiments. Combining genetic algorithm with orthogonal experiment design, an orthogonal operator was introduced in the initial population design and genetic manipulation of genetic algorithm to overcome the problem of non-uniform spatial distribution of the solution and to enhance the diversity of species.

Binary Matrix Coding

This article uses the charging plan to be developed as an individual in the genetic algorithm and encodes it in a matrix. This paper describes the allocation of electric vehicles using a 0-1 matrix in a binary coded manner, each row of the matrix is a separate chromosome, and each gene on the chromosome corresponds to the distribution of all electric cars. In addition, for each chromosome, two kinds of information about their respective EV allocations and total charging time are recorded to reduce the calculation of the crossover process. Its specific form is

Equation 12:

$$G_k = \left[V_1, V_2, \cdots, V_t, \cdots, V_{96}\right] = \left[R_1, R_2, \cdots, R_i, \cdots R_N\right]^T = \begin{bmatrix} x_{1,1} & x_{1,2} & \cdots & x_{1,t} & \cdots & x_{1,96} \\ x_{2,1} & x_{2,2} & \cdots & x_{2,t} & \cdots & x_{2,96} \\ \vdots & \vdots & & \vdots & & \vdots \\ x_{i,1} & x_{i,2} & \cdots & x_{i,t} & \cdots & x_{i,96} \\ \vdots & \vdots & & \vdots & & \vdots \\ x_{N,1} & x_{N,2} & \cdots & x_{N,t} & \cdots & x_{N,96} \end{bmatrix}$$

Where:

G_k = the k-th individual in the genetic population, it is an N*96 high-dimension matrix.

$X_{i,t}$ = the i-th row and t-th column element in the encoding matrix, which means the charging state of the i-th electric vehicle at time t, When $X_{i,t}$=0 means not charged; when $X_{i,t}$=1 means charging.

V_t = the t-th column vector in the encoding matrix, which means the charging status of each electric car in the t-th period.

R_i = the i-th row vector in the encoding matrix, which means the charging status of the i-th electric car at various times of the day.

Orthogonal Design Method Initialise to Generate Initial Population

Before the optimal solution is obtained, it is impossible to know where the global optimal solution is located. If the chromosomes of the initial population can be evenly distributed in the feasible solution space, then the algorithm can perform a uniform search in the solution space. Because an orthogonal array specifies a minimum number of combinations that are evenly spread across all combinations of spaces, orthogonal design methods can be used to produce a good initial population.

The individual G_k encoded in this paper is a high-dimensional matrix of N*96, which can be viewed as a 96 factors, N levels of problems, a total of N^{96} combinations. However, in order to avoid charging peak when guiding the charging of electric vehicles, the charging behavior is shifted to the trough period. As shown in Figure 1, for the period from 10:00 to 15:00, it is neither peak nor trough. Therefore, individuals who have a charging schedule at this time are excluded from the initialisation process. That is, individuals with this code "1" are removed. At the same time, according to the constraints of 2.2, when initializing, each initial individual must ensure that each individual satisfies the requirements of the power, that is, the total number of “1” codes in each row must satisfy the Equation 11.

Let N individuals participating in the initialisation be G1, G2,..., GN, where the specific algorithm of $G_k=[V_1^k,V_2^k,\ldots,V_t^k,\ldots,V_{96}^k]$ is as follows:

(1) The remaining individual N satisfying the conditions is divided into S subspaces; denoted as $W_1 = [G_1,G_2,\ldots,G_k]$, $W_2 = [G_{K+1},G_{K+2},\ldots,G_{2k}]$, … $W_s = [G_{nk+1},G_{nk+2},\ldots,G_N]$.

(2) In each subspace, the population is quantified into Q levels. Taking $W_1 = [G_1,G_2,\ldots,G_k]$ as an example, orthogonal crossover operations are performed. As shown in section above, the orthogonal table $L_{M1}(Q^F)$ is selected, for each subspace, M1 individuals are generated so that there can be M1S individuals.

Orthogonal crossover operator design

Let the Q individuals participating in orthogonality be G_1, G_2,..., G_Q, where $G_k = 0$, there will be Q_{96} possible combinations, ie, the sample space size of the offspring individuals is Q_{96}. When Q is very large, it is not possible to perform genetic algorithm operations on Q_{96} individuals one by one. Therefore, we use orthogonal experimental design methods to generate representative M combinations from individual sample spaces to generate offspring individuals. Here, M is generally much smaller than Q_{96}, thereby improving the search efficiency of the algorithm.

For G_1, G_2,..., G_Q, the specific steps for arranging cross-operations using orthogonal experiments are: each parent participating in the coding is considered as a level of orthogonal experimental design, ie Q levels; then each parental individual is divided into F segments, each of which is a factor of orthogonal experimental design, that is, F factors. In this way, the recombination problem of Q parent individuals is transformed into an experimental design problem of Q level and F factor. Then the orthogonal table L_m is constructed, and arranging the orthogonal experimental design will generate M offspring individuals, where Q is a prime number and $M=Q_j$. Specific steps are as follows:

(1) The Q individuals involved in the orthogonality are respectively taken as a level of the orthogonal experimental design, and the k-th level is denoted by $\beta_k, K \in \{1,2,\ldots,Q\}$, then $\beta_K = G_K$.

(2) Let $G_k = [V_1^k,V_2^k,\ldots,V_t^k,\ldots,V_{96}^k]$ be any individual participating in orthogonality, divide the individual G_k into F segments, and use each segment as a factor of orthogonal experimental design, the specific fragmentation operation method is as follows: First, randomly generate F-1 integers, ie $t_1,t_2,\ldots,t_{F-1}$, and satisfies $1<t_1<t_2<t_{F-1}<T$; then the individual $G_k = [V_1^k,V_2^k,\ldots,V_t^k,\ldots,V_T^k]$ is divided into F segments, where each segment represents a factor of the individual G_K;

Equation 13:

$$\begin{cases} f_1 = \left(V_1^k,\cdots,V_{t_1}^k\right) \\ f_2 = \left(V_{t_1+1}^k,\cdots,V_{t_2}^k\right) \\ \cdots \\ f_F = \left(V_{t_{F-1}}^k,\cdots,V_{96}^k\right) \end{cases}$$

Let $t_0 = 0$, $t_F = T$, so the Q levels of the j-th (j = 1, 2, ..., F) factors f_j can be expressed as

Equation 14:

$$\begin{cases} f_j(1) = \left(\beta_{1,t_{j-1}+1}, \beta_{1,t_{j-1}+2}, \cdots, \beta_{1,t_j}\right) \\ f_j(2) = \left(\beta_{2,t_{j-1}+1}, \beta_{2,t_{j-1}+2}, \cdots, \beta_{2,t_j}\right) \\ \cdots \\ f_j(Q) = \left(\beta_{Q,t_{j-1}+1}, \beta_{Q,t_{j-1}+2}, \cdots, \beta_{Q,t_j}\right) \end{cases}$$

(3) the orthogonal table $L_M(Q^F) = [a_{i,j}]_{MxF}$ is constructed, and then the experiment is arranged to generate M offspring individuals according to the orthogonal table $L_M(Q^F)$:

Equation 15:

$$\begin{cases} \left(f_1(a_{1,1}), f_2(a_{1,2}), \cdots, f_F(a_{1,F})\right) \\ \left(f_1(a_{2,1}), f_2(a_{2,2}), \cdots, f_F(a_{2,F})\right) \\ \cdots \\ \left(f_1(a_{M,1}), f_2(a_{M,2}), \cdots, f_F(a_{M,F})\right) \end{cases}$$

Calculating the fitness of each individual, the N individuals with the largest fitness function is select as the initial individuals. Avoiding large computational overhead, any pair of parent individuals should not produce too many offspring individuals after each reorganisation. The number of offspring can be reduced by reducing the number of factors. In this paper, the dimension is 96. In order to avoid the excessive number of individuals resulting from the cross, individual $G_k = [V_1^k, V_2^k, \ldots, V_t^k, \ldots, V_{96}^k]$ is divided into F segments. Each segment is used as a factor of orthogonal experimental design, that is, F factors. Since any two parent individuals cross with probabilities P_c, then Q = 2 constructs an orthogonal table $L_{2K}(2^{2k-1})$, arranges cross-operations according to the orthogonal table, and produces 2^k child individuals .Among them, $2^{k-1} \leq F \leq 2^k-1$, if $F < 2^k-1$, then take the first F column in the orthogonal table. In the process of parent intersections, ensure that each parent crosses and does not repeat operations. The resulting orthogonal array will be reduced, so that there will not be too many individuals, as shown in section above. Note: When individuals cross each row, they must ensure that the total number of "1"s in each row is not changed. That is to ensure that the charging time of electric vehicles is certain. Take k = 3, F = 6.

3.3. Algorithm flow chart

The specific flow chart using the improved genetic algorithm is as follows:

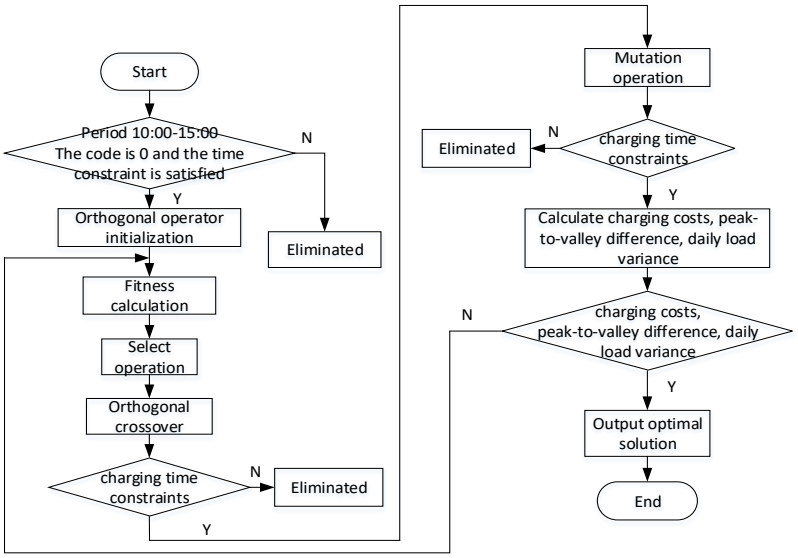

Figure 2: algorithm flow chart

4. SIMULATION

4.1. Charging parameter settings

To simplify the analysis, set the following experimental prerequisites:

1) uniformly assumes the rated battery capacity Br of each electric vehicle 60kWh;
2) using conventional charging mode to charge the electric vehicle, and the charging power during the charging process remains unchanged, the charging power is 7kW, that is, P_i is 7kW;
3) using Monte Carlo simulation method to simulate the charging behaviour of electric vehicles, randomly generate data for multiple electric vehicle charging days, the user's charge demand power obeys the distribution N (0.6, 0.12), and the user desires to leave the charge state 0.8 or 0.9 (Each accounted for 50%) that Sh is 0.8 or 0.9;
4) there are 100 electric vehicles in the area.

4.2. Experimental results and analysis

This paper takes the residential distribution network of a certain place as an example. Based on the established electric vehicle charging model, an improved genetic algorithm is proposed to solve the model, and the accuracy of the improved genetic algorithm and the standard genetic algorithm is compared through experimental simulation. The comparison is shown in Figures 3 and 4. It can be seen that using the improved genetic algorithm to solve the model, the solution is more accurate and the speed is faster than the standard genetic algorithm.

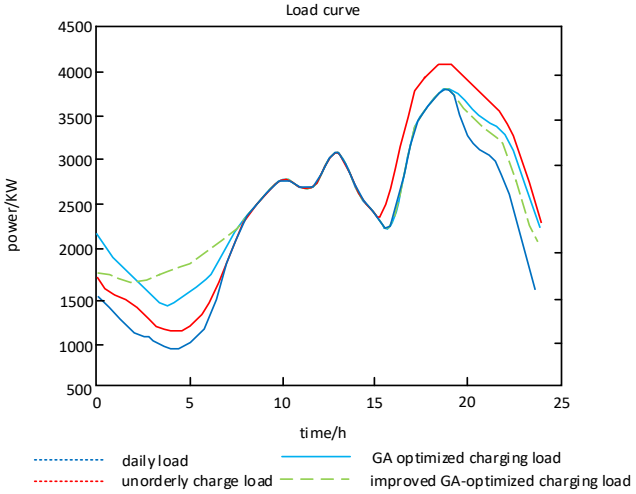

Figure 3: Disordered, GA Optimised, Improved GA Optimised Charging Load Curve

The four curves in Figure 3 are the original daily load curves for the non-superimposed electric vehicle charging, the out-of-sequence charging, the orderly charge of the optimised by the standard genetic algorithm, and the comparison of the ordered charge curve optimised by the improved genetic algorithm. The comparison chart shows that:

1) During the out-of-order charging, the highest peak of the charging curve of the electric vehicle appears at 19:00-21:00 in the evening, which is also the peak period of conventional load. When large-scale electric vehicles are disorderly connected to the grid, the users will cause a large number of electric vehicles to be charged at the peak time according to their own needs, overlapping with the original peak load period of the grid, resulting in the grid's regular load “peak on the peak”. Phenomenon that large-scale electric vehicles will increase the maximum load of the power grid during the disordered charging and further exacerbate the system peak-to-valley difference. It can be seen from Table 1 that the peak-to-valley difference increases from 2920.7 kW to 3005.7 kW at the same time during unregulated charging. The variance of load increased by 0.8196*105 kW^2, which means that the daily load fluctuations aggravated, which resulted in a decrease in the utilisation of power resources, which was not conducive to grid dispatch and stable operation. Combined with the real-time price trend chart in Figure 1, the peak load period of disordered charging, Electric car users will charge higher charges.

2) After solving the charging model with GA, most of the electric vehicle charging load was transferred to the low period of the original load, the grid peak-valley difference was greatly reduced from the previous 3005.7 kW to 2423.3 kW, and the variance was also reduced to out-of-order charging One-half of the variance, in terms of charging costs, was reduced from 6752.3 yuan for disorderly charging to 4362.5 yuan; at the same time, compared with the original daily load, the peak-to-valley difference decreased by 497.4 kW, and the daily load variance decreased by 3.0623*105 kW^2. This shows that the fluctuation of the total load curve is gradually stable, and the characteristics of the original load curve have also been greatly improved. However, as can be seen from Figure 4, the solution process of the genetic algorithm is too slow. It takes about 60 iterations to gradually converge, which greatly reduces the work efficiency of the system. The individuals of the model are composed of a large matrix, and the genetic algorithm is accurate in solving the problem. There is still room for improvement.

3) After solving the charging model with improved GA, we can see from Figure 3 that there are corresponding improvements in each parameter compared to the GA solution. The specific data is shown in Table 1. The peak-to-valley difference is reduced by 252.6 kW, the variance is reduced by 0.3121*105 kW^2, and the charging cost is also reduced by 1157.4 yuan;

this shows that the ordered charging strategy obtained using the improved genetic algorithm is more expensive than the standard genetic algorithm for orderly charging. The strategy is more reasonable and saves money.

The two curves in Figure 4 represent the convergence of the standard GA and the improved GA respectively. The standard GA algorithm is iterated approximately 60 times to obtain the optimal solution. The improved GA algorithm has converged around the 30th generation. For the comparison of the slopes of the two curves, the slope of the improved GA algorithm is larger than that of the standard GA algorithm.

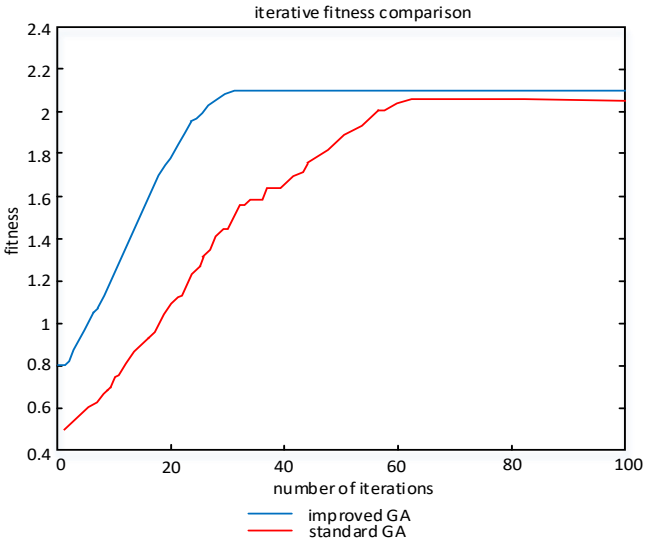

Figure 4: Comparison of improved GA and standard GA convergence curves

The speed at which the curve of the improved GA rises is faster than that of the standard GA, which means that the convergence speed of the improved GA algorithm is faster than that of the standard GA algorithm. Fast, so it has better convergence.

Table 1: Charge costs, peak-to-valley difference, variance comparison in three cases

item	charge costs (yuan)	peak-to-valley difference（kW）	variance（kW^2）
daily routine load	/	2920.7	$7.5666*10^5$
charging unorderly	6752.3	3005.7	$8.3862*10^5$
GA optimised charge orderly	4362.5	2423.3	$4.4977*10^5$
optimise Orderly Charge Based on Improved GA	3205.1	2170.7	$4.1856*10^5$

5. CONCLUSION

This paper studied the problem of using an improved genetic algorithm to solve the charging model of an electric vehicle. The process of establishing the charging model of the electric vehicle is given in this paper, and the method of solving the model is mainly discussed. To solve the problems of poor local search ability, slow convergence rate, and non-uniform spatial distribution in traditional genetic algorithms, this paper introduces the orthogonal experimental design method into the initialisation and cross-operation of genetic algorithms, and proposes an improved positive method. The genetic algorithm is applied and the algorithm is applied to the solution of the charging model of the electric vehicle. The results of numerical experiments show that the optimisation performance of this algorithm is obviously higher than the traditional genetic algorithm, which can effectively reduce the population size and number of searches, accelerate the convergence speed, and at the same time preserve the representative individuals and distribute them uniformly in the solution space. The local optimal solution shows that the charging load of the electric vehicle connected to the grid is less fluctuating at any time, which is more conducive to guiding the orderly use of electric vehicles, optimizing the power investment, and making the electric vehicle charging scheme more economical.

6. REFERENCES

Huang W, Xiong W, Che W, 2017. Application of Fuzzy Control in Hybrid Wind Energy Storage System [J]. Modern Power, 34(1), 30-36.

Jin W, Liu S, Chen Q, 2017. Optimum scheduling of photovoltaic microgrids considering prediction errors [J]. Journal of Anhui University of Technology, 32(2), 31-36.

Wu T, Jiang X, Zhang Q, 2016. Research on Optimisation Method of Electric Vehicle Charging Scheduling under Real-Time Electricity Price[J]. Journal of Wuhan University of Technology, 38(4), 81-85.

Yang K, Fu X, 2016. Research on Energy Management Strategy of Hybrid Electric Vehicle Based on Genetic Algorithm[J]. Industry, 2016(6), 00019-00019.

Guo R, Wang L, 2017. Study on Coupling Inductance of Six-Channel Bidirectional DC-DC Converter in Hybrid Energy Storage System[J]. Transactions of Electrical Engineering, 32(1), 117-128.

Wang Z, Liu Y, Zhang M, 2017. Dynamic Control Strategy of Hybrid Energy Storage System Based on Bidirectional DC/AC Converter[J]. Power System Protection and Control, 45(3), 26-32.

Wang L, Ye X, 2015. Research on Energy Management Strategy Optimisation of Plug-in Hybrid Electric Vehicle Based on Hybrid Energy Storage System[J]. Agriculture Equipment and Vehicle Engineering, 53(7), 65-70.

Meng R, Liu J, Wen B, 2015. Hybrid energy storage control and hierarchical coordinated control strategy for DC microgrid[J]. High Voltage Engineering, 41(7), 2186-2193.

183: A lithium-ion battery active equalisation optimisation method

Tiezhou WU [1], Shengqiao HU[2]

[1] *Hubei Key Laboratory for High-efficiency Utilisation of Solar Energy and Operation Control of Energy Storage System, Hubei University of Technology, 430068, China, Wtz315@163.com*
[2] *Hubei Key Laboratory for High-efficiency Utilisation of Solar Energy and Operation Control of Energy Storage System, Hubei University of Technology, 430068, China, 741609091@qq.com*

Battery Equalisation systems are necessary as cell imbalance can lead to poor performance and safety hazards. The equalisation circuit can be regarded as a DC-DC converter capable of transferring energy between its input and output with a certain efficiency and speed. The input and output of the converter can be a single cell or a entire battery pack. The topological structure of a single cell to a battery pack as input and output respectively has the advantages of short equilibration time and low energy loss. This kind of structure can only balance one battery at one time. In this case, the battery might reach the equilibrium threshold and waits for the balance. The battery health will be further deteriorated during the waiting process. In order to solve this problem, this paper proposes a balanced control strategy to set the action threshold, pre-action threshold and end threshold. The proposed strategy calculates the offset and relative rate of change of each battery's State-Of-Charge (SOC), then predicts the SOC of each cell for a period of time in the future, an appropriate single cell is selected for equalisation to achieve an optimal control of the equaliser. This paper use MATLAB/SIMULINK software to simulate a corresponding circuit controlled by the proposed strategy. Simulation results show that compared with the traditional control strategy in a same circuit, the proposed equalisation control strategy can solve the problem of equalisation time overlap without changing the equalisation circuit and increasing the equalisation current. This result confirms the feasibility of this balanced control strategy.

Keywords: Active equilibrium, Equalisation strategy, Balance time

1. INTRODUCTION

Lithium-ion batteries are used in various applications because of their excellent performance (Cui et al., 2017). Monolithic lithium-ion batteries generally cannot meet actual voltage and current requirements and require multiple batteries to be used in parallel (Lee et al., 2017). Due to inconsistencies in production and use, battery packs must be balanced. Passive equilibrium is simple in structure and easy to control, but it has low equilibrium efficiency and serious heat (Wang et al., 2016, Han et al., 2017, Ju et al., 2016). Active equalisation is to transfer the energy of the higher voltage battery through the energy storage element to the battery with lower voltage (Qi et al., 2017, Chen et al., 2016, Chen et al., 2015). Although the cost is higher, it can achieve the maximum utilisation of energy, which is the current research hotspot (Kim et al., 2014, Kim et al., 2014, Zheng et al., 2017). (Baronti et al., 2014) considers the equalisation circuit as a DC-DC converter that transfers energy between its input and its output with a certain efficiency and speed. The input and output of the converter can be single cells and batteries. The paper verifies that the energy is the balanced method of transmission between single cells has the advantages of high speed of equalisation and low energy loss. (Hannan et al., 2017) uses a bi-directional fly back converter, which effectively reduces the equalisation cost. However, there are problems in which multiple cells require equalisation and equalisation time overlap. (Bouchhima et al., 2016) adopts the partial battery-powered method, and (Huang et al., 2015) assigns the force coefficient to each single cell. Such methods have the advantages of high equilibrium speed, high conversion efficiency, and no overlapping of the equalisation time, but the cost is high. (Zhang et al., 2017) balances the battery composition blocks. (Dong et al., 2015) puts the equalisers in different layers. These layers can be balanced at the same time. The purpose is to accelerate the equalisation speed under the premise of controlling the cost, and to solve the equilibrium time overlapping.

At present, most of the research is focused on the equalisation circuit. In this paper, we improve the control method, set the thresholds of three SOC offsets, and reasonably adjust the working state of the equalisation circuit to avoid the occurrence of the equalisation time overlap. Finally, MATLAB/SIMULINK software was used to simulate the corresponding circuit. By comparing the traditional control strategy, the rationality of the proposed control strategy was verified.

2. CONTROL STRATEGY

2.1. Three-threshold equalisation strategy

The three thresholds proposed in this paper are the ending threshold, the pre-action threshold and the action threshold. Equation (1) is the currently accepted battery SOC definition.

Equation 1 : battery SOC definition

$$SOC = \frac{Q_s}{Q} \times 100\%$$

Where:

- Qs = available battery power (C)
- Q = total capacity under the condition of specific discharge rate (C).

It is easy to know that when the available power of the battery is the same, the SOC of the battery with the larger total capacity is lower. Assume there are batteries B1 and B2, where B1 battery capacity and initial available power are small, but SOC is higher than B2 battery. The SOC drop rate of B1 and B2 batteries can be obtained from Equation (2).

Equation 2: SOC drop rate

$$I = Q\frac{dSOC}{dt}$$

Where:

- I = Discharge current (A)

In the case of an equal-charge discharge, the rate of decline of the SOC of batteries B1 and B2 is inversely proportional to its total capacity. The change of the two battery SOC values over time is shown in Figure 1.

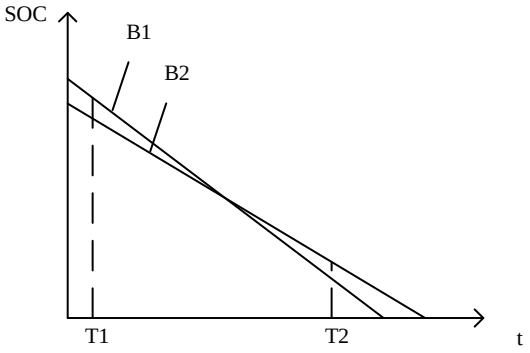

Figure 1: SOC changes in B1 and B2 batteries

The traditional equalisation method begins to transfer the charge of B1 battery to B2 battery at T1, and the SOC of the battery cell is equalised to the average value. Due to the difference in total capacity, the charge of B2 battery may need to be transferred to B1 at the time of T2, battery. And these two equilibria are futile, and the number of such occurrences can be reduced by appropriate control strategies. This paper proposes an ending threshold. When the battery SOC difference is within this threshold, it ends the equalisation, reserves the self-adjusted space for each cell, reduces the number of repeated equalisations, and correspondingly relieves the pressure of the equaliser.

The series battery consists of n cells. The average SOC of each cell is

Equation 3: average SOC of each cell

$$\overline{SOC} = \frac{1}{n}\sum_{i=1}^{n} SOC_i$$

Where:

- SOC_i = SOC of $cell_i$

The SOC offset of each cell is recorded as the difference between the SOC of the cell and the average of the SOC of the battery.

Equation 4: SOC offset of each cell

$$\Delta SOC_i = |SOC_i - \overline{SOC}|$$

In the conventional equalisation control strategy, equalisation starts when the cell SOC offsets reach a set action threshold. For an equalisation circuit that employs energy transfer between cells, it is not possible to equalise multiple cells at the same time, and it may happen that one cell reaches the threshold of action while waiting for the last cell to equalize. In this paper, the pre-action threshold is added based on the action threshold in the traditional equilibrium strategy, as shown in Figure 2.

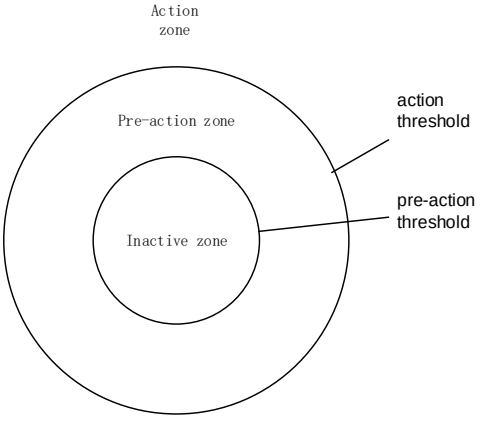

Figure 2: Pre-action threshold diagram

When the SOC offset of the battery cells is small and is in the no-operation zone, no consideration is taken to reduce the calculation amount of the main control unit. When the cell SOC offset reaches the pre-action threshold and is in the pre-action zone, the SOC offset of the maximum elevator battery is taken as ΔSOCmax. At this point, the battery is balanced. The time required is:

Equation 5: time required

$$T_e = \frac{\Delta SOC_{\max} - SOC_{off}}{I_e}$$

Where:

- I_e= equalisation current $_i$
- SOC_{off}=end threshold

The single cell i is in the pre-action zone, its SOC offset is next only to the maximum value, and the time for the battery to reach the action threshold is

Equation 6: time for the battery to reach the action threshold

$$T_a = \frac{SOC_{set} - \Delta SOC_i}{D_i}$$

Where:

- SOCset= action threshold $_i$
- Di = rate of change of the SOC of each cell relative to the average SOC when the cell is in equilibrium

In the equalisation process, the relative change rate of the SOC of the single cell does not change much, and Di is set to be updated after a period of time. According to the above analysis, the equalisation coefficient k (0<k<1) is taken, and when the Equation 7 is satisfied, the equalisation of the cells with the maximum SOC offset is started.

Equation 7: Equilibrium condition of the single cell with the largest SOC offset

$$T_e \geq kT_a$$

After adding the pre-action threshold, the equaliser operates under the condition that the cell SOC offset reaches the action threshold, or the cell with the largest SOC offset is in the pre-action zone and satisfies the Equation (10) equalisation condition.

When using the traditional equalisation control strategy, each cell will be concentrated in a short period of time after the start of equalisation, and the equilibrium of the equaliser will be constant, and the equilibrium of multiple cells will not be completed in a short time, and the equilibrium time will overlap. Happening. The three-threshold control strategy proposed in this paper can dynamically control the battery equalisation threshold, slightly changing the equilibrium time of each cell, and the time interval of the entire equilibrium process will be expanded compared with the traditional equilibrium strategy. The three-threshold equalisation control strategy does not increase the equalisation current, and does not make any changes to the hardware circuit. It merely arranges the equalisation intervals of the individual cells, indirectly accelerates the equalisation speed, and well reduces the occurrence of the equalisation time overlapping.

2.2. Interrupt equilibrium control strategy

The use of a three-threshold equalisation control strategy can cope with the balance of single cells in most battery packs, but it is still possible that some single cells will be too concentrated in dispersion, resulting in a poor balance. As shown in Figure 3, it is assumed that B1 battery has the largest SOC offset, B2 is the next, and B3 is the smallest, where B3 and B2 have a small difference. If a three-threshold equalisation control strategy is used, it may happen that the B3 battery reaches the threshold when equalizing the B2 battery and the equalisation cannot be performed. On the basis of the three-threshold equalisation control strategy, this paper also proposes an interrupt equalisation control strategy to solve such problems.

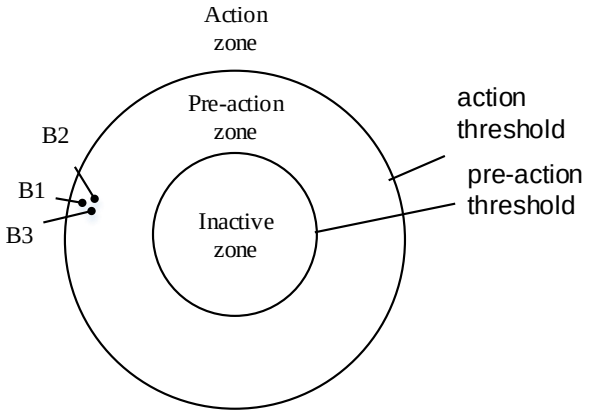

Figure 3: The condition of three threshold equilibrium cannot be dealt with

If the i*th* battery is in equilibrium, the theoretical time required to equalise it to the end threshold is

Equation 8: Theoretical time to end threshold

$$T_{ei} = \frac{\Delta SOC_i - SOC_{off}}{I_e}$$

In the equalisation process, the j*th* cell battery reaches the action threshold. At this time, the SOC offset of the jth cell must be higher than that of the i*th* cell. Therefore, the balance of the single cell of the i*th* cell is interrupted, and the j*th* cell is first balanced. After the SOC offset of the j*th* battery equalises to the end threshold, the ith cell is again equalised. In order to achieve better balanced performance, it is allowed to repeat many times during the interrupt equalisation.

In this case, the equaliser circuit is always in operation, its performance is maximised, and it can be ensured that the SOC offset of any single cell in the battery pack does not exceed the set threshold, i.e. the rate of change of SOC in Equation 2. For each battery cell SOC offset Di, the interrupt equalisation control strategy is used as

Equation 9: usage conditions of Interrupt equilibrium control strategy

$$I_e > \sum_{i=1}^{n} Q_i \times D_i$$

Theoretically satisfying Equation 9, after a period of time, the individual cells in the battery pack will tend to set a balanced state. It can be seen that using the interrupt equalisation control strategy can better solve the problem that the three-threshold equalisation control strategy does not easily solve, but using the interrupt balance control strategy will undoubtedly increase the number of operations and losses of the switching device.

3. EQUILIBRIUM CIRCUITS

Figure 4 is a balanced circuit currently used more generally, the circuit consists of n cells, switch array, cross-current power supply and cross-current load, when the SOC offset of the battery i to meet the equilibrium conditions proposed in this paper, closed switch Ki and K(i+1), if the SOC offset is less than the average value, the KC switch connects the cross current power supply to the single cell battery; if the SOC offset is greater than the average value, the KC switch connects the cross current load to consume the power of the cell.

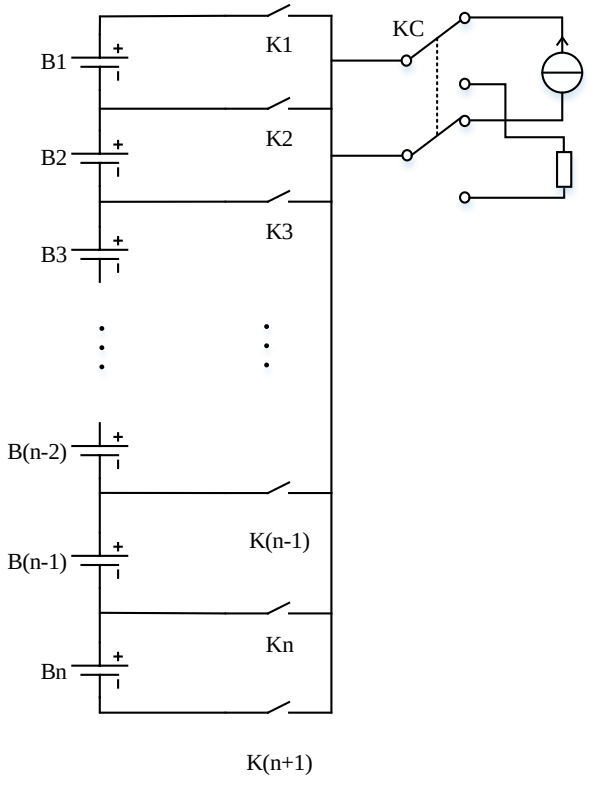

Figure 4: Equilibrium circuit diagram

The circuit in Figure 4 can flexibly balance any single cell in the battery pack. The number of components used in the circuit is small. However, there is a problem mentioned above. That is, only one cell can be balanced at the same time, and equilibrium may occur. Time overlap situation.

4. SIMULATION ANALYSIS

To verify the feasibility of the proposed three-threshold and interrupt equalisation control strategy, MATLAB/SIMULINK software was used to simulate the circuit shown in Figure 4. The energy storage battery is composed of 16 cells in series and the working current of constant current source and constant current load is 1A. The 16 battery parameters are shown in Table 1.

Table 1: The parameters of simulated batteries

nominal voltage	battery capacity	internal resistance	Charging cut-off voltage
3.7V	3Ah	20Mω	4.2V

Among them, the first and the second and the third battery have a corresponding resistance in parallel to simulate the unbalance of the single battery in the battery pack. Table 2 shows the initial SOC of each cell and the relative change rate of SOC when the cell is in equilibrium.

Table 2: Initial SOC and relative conversion rate of SOC in battery pack equilibrium of each single cell

	1st battery	2nd battery	3rd battery	Remaining battery
Initial SOC	68.91%	68.99%	69.02%	70%
Battery SOC rate of change per 100 seconds	0.114	0.138	0.138	0.041

Since the energy storage battery pack in this simulation uses 16 batteries instead, the number is small. When a constant current source is used to charge a single cell, the average value of the battery group has a great influence, which in turn affects the relative change rate of the SOC of each cell. In the case of a large number of battery packs, this effect becomes smaller.

Figure 5 shows the simulation result when using the traditional control strategy for equalisation. The relative threshold of the action threshold is 1% for the single battery SOC. Figure 7 is a simulation result diagram using a three-threshold and interrupt equalisation control strategy. Which take the balance coefficient k is 0.9, the end threshold is the single cell SOC offset is less than 0.5%, the pre-action threshold for the single cell SOC offset reached 0.8%.

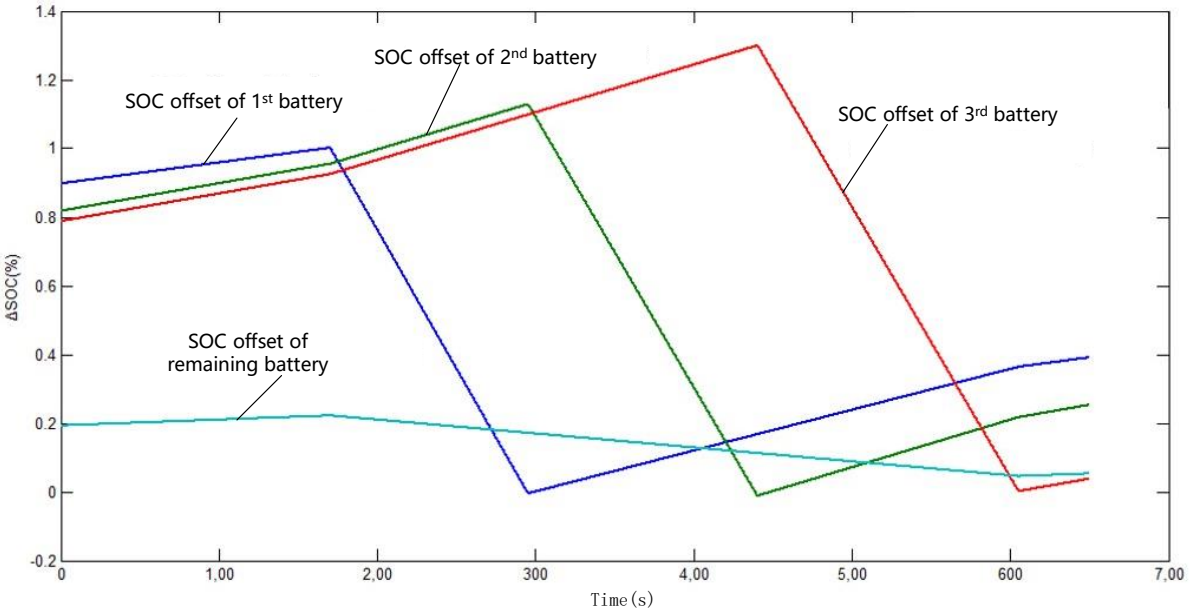

Figure 5: Simulation result diagram of traditional control strategy

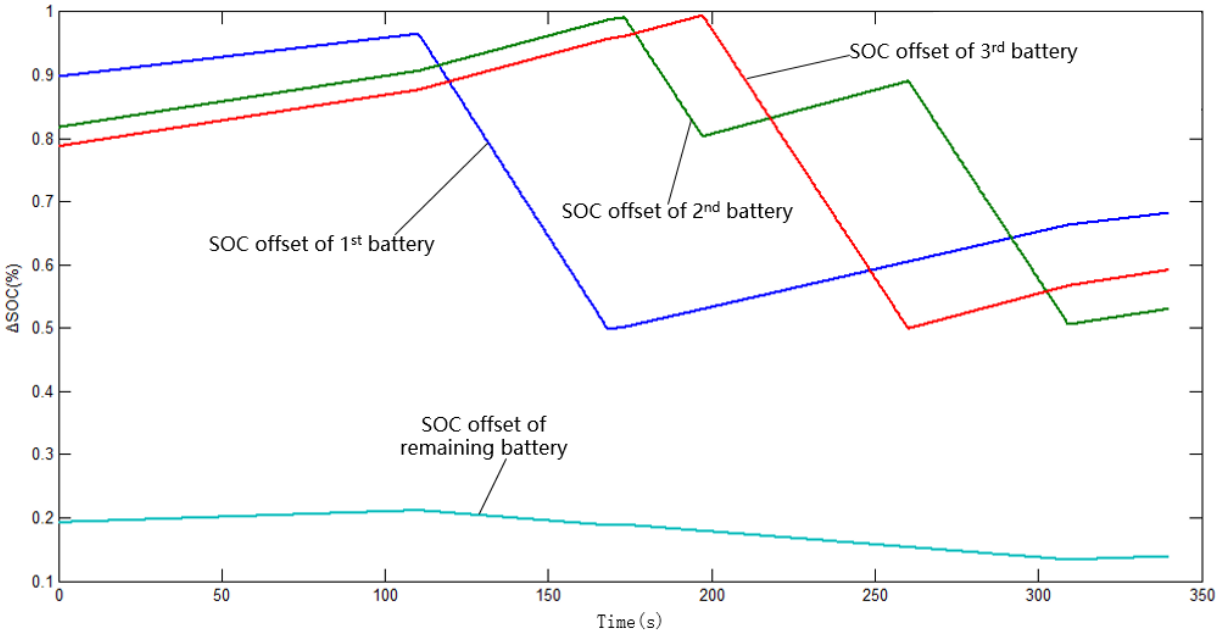

Figure 6: Simulation result diagram of three threshold and interruption equilibrium control strategy

The traditional equalisation control strategy must wait until the cell reaches the action threshold. From Figure 5, it can be seen that when the first cell reaches the action threshold and starts equalisation, the second cell also reaches the action threshold during the equalisation process, since the circuit cannot be used to equalise multiple cells at the same time, resulting in the second quarter. The battery cannot be balanced at this moment. Until about the 295th second, the first battery is balanced until the second battery is equalised. At this time, the SOC offset of the second battery is about 1.13%. In the same way, when the battery is balanced in the second quarter, it cannot balance the battery in the third quarter and it will wait for the equilibrium. Until about 440 seconds, the third battery is balanced after the second battery is balanced. At this time, the third quarter battery SOC offset is about 1.3%. This situation becomes even more severe when the number of stored batteries is high.

As can be seen from Figure 6, since the pre-action threshold is set, when the first battery is in the pre-action zone, Equation (10) is satisfied, even if the first battery SOC offset does not reach the action threshold, the first section will be the battery is balanced. At about 168 seconds, the first battery was balanced. After a period of time, the second battery reaches the action threshold and starts equalisation. The time difference of the middle stagger can be seen from the change curve of the remaining battery SOC offset in Figure 6. However, during the equalisation process of the second battery, the third battery also reaches the threshold of action. At this time, the balance process of the second battery is interrupted until the third battery is equalised to the end threshold, and the second battery is again equalised.

As can be seen from Figure 5 and Figure 6, for the same equalisation circuit, using the three thresholds and the interrupt balance control strategy can ensure that the SOC offsets of the battery cells in the energy storage battery pack are within a set interval, which is a comparative advantage. To solve the problem of overlapping equilibrium time well.

5. CONCLUSION

In this paper, for the problem that there are balance times overlapping in many equalised circuits, three thresholds and interrupt equalisation control strategies are proposed. By reasonably adjusting the working state of the equaliser circuit, it is avoided that the equalisation time overlaps. Using MATLAB/SIMULINK software for simulation, the simulation results confirm that the equalisation control strategy can solve the above problems without changing the equalisation circuit and without increasing the equalisation current. Therefore, the present equalisation control strategy is applied to the corresponding equalisation circuit, and on the premise of guaranteeing the advantages of the equalisation circuit, it is better to avoid the existence of the equilibrium time overlap defect.

6. REFERENCES

Cui X, Shen W& Zhang Y, 2017. Novel active LiFePO 4 battery balancing method based on chargeable and dischargeable capacity. Computers & Chemical Engineering, 97:27-35.

Lee K M, Lee S W& Choi Y G, 2017. Active Balancing of Li-Ion Battery Cells Using Transformer as Energy Carrier. IEEE Transactions on Industrial Electronics, 64(2):1251-1257.

Wang S, Shang L& Li Z, 2016. Online dynamic equalisation adjustment of high-power lithium-ion battery packs based on the state of balance estimation. Applied Energy, 166:44-58.

Han W& Zhang L, 2017. Battery Cell Reconfiguration to Expedite Charge Equalisation in Series-Connected Battery Systems. IEEE Robotics & Automation Letters, 3(1):22-28.

Ju F, Deng W& Li J, 2016. Performance Evaluation of Modularized Global Equalisation System for Lithium-Ion Battery Packs. IEEE Transactions on Automation Science & Engineering, 13(2):986-996.

Qi J& Lu DC, 2017. A Preventive Approach for Solving Battery Imbalance Issue by Using a Bidirectional Multiple-Input Ćuk Converter Working in DCVM. IEEE Transactions on Industrial Electronics, 64(10):7780-7789.

Chen Y, Liu X& Cui Y, 2016. A Multi-winding Transformer Cell-to-Cell Active Equalisation Method for Lithium-Ion Batteries With Reduced Number of Driving Circuits. IEEE Transactions on Power Electronics, 31(7):4916-4929.

Chen H, Zhang L& Han Y, 2015. System-Theoretic Analysis of a Class of Battery Equalisation Systems: Mathematical Modeling and Performance Evaluation. Vehicular Technology IEEE Transactions on, 64(4):1445-1457.

Kim MY, Kim CH& Kim JH, 2014. A Chain Structure of Switched Capacitor for Improved Cell Balancing Speed of Lithium-Ion Batteries. IEEE Transactions on Industrial Electronics, 61(8):3989-3999.

Kim MY, Kim JH& Moon GW, 2014. Center-Cell Concentration Structure of a Cell-to-Cell Balancing Circuit With a Reduced Number of Switches. IEEE Transactions on Power Electronics, 29(10):5285-5297.

Zheng X, Liu X& He Y, 2017. Active Vehicle Battery Equalisation Scheme in the Condition of Constant-Voltage/Current Charging and Discharging. IEEE Transactions on Vehicular Technology, 66(5):3714-3723.

Baronti F, Roncella R& Saletti R, 2014. Performance comparison of active balancing techniques for lithium-ion batteries. *Journal of Power Sources*, 267(4):603-609.

Hannan MA, Hoque MM& Peng SE, 2017. Lithium-ion battery charge equalisation algorithm for electric vehicle applications. *IEEE Transactions on Industry Applications*, 53(3):2541-2549.

Bouchhima N, Schnierle M& Schulte S, 2016. Active model-based balancing strategy for self-reconfigurable batteries. *Journal of Power Sources*, 322:129-137.

Huang W& Qahouq JAA, 2015. Energy Sharing Control Scheme for State-of-Charge Balancing of Distributed Battery Energy Storage System. *IEEE Transactions on Industrial Electronics*, 62(5):2764-2776.

Zhang Z, Gui H& Gu DJ, 2017. A Hierarchical Active Balancing Architecture for Lithium-ion Batteries. *IEEE Transactions on Power Electronics*, 32(4):2757-2768.

Dong B, Li Y& Han Y, 2015. Parallel Architecture for Battery Charge Equalisation. *IEEE Transactions on Power Electronics*, 30(9):4906-4913.

184: Multi-energy body DC micro-grid parallel operation energy management strategy

Li Liao [1], Mei Gao [2], Tiezhou Wu[3]

[1] *Hubei Key Laboratory for High-efficiency Utilisation of Solar Energy and Operation Control of Energy Storage System, Hubei University of Technology, 430068, China, amazon2008@163.com*
[2] *Hubei Key Laboratory for High-efficiency Utilisation of Solar Energy and Operation Control of Energy Storage System, Hubei University of Technology, 430068, China,747105398@qq.com*
[3] *Hubei Key Laboratory for High-efficiency Utilisation of Solar Energy and Operation Control of Energy Storage System, Hubei University of Technology, 430068, China, wtz315@163.com*

The DC microgrid has become an important development direction of the microgrid because of its advantages of easy coordination control, low line cost and no reactive power loss. Energy storages with different power characteristics are solutions to improve the effectiveness and economy of isolated DC microgrid systems. In order to suppress the voltage fluctuation of DC bus and optimise the running status of battery and super capacitor, the hybrid energy storage system (HESS) distributed droop control strategy was adopted. Among them, both the battery unit and the super capacitor unit are set as droop controlled slack terminals. In order to solve the problem of drooping controlling the inconsistency of power characteristics of various terminals, different droop coefficients are selected for different types of energy storage units. Without exceeding the power response range of each energy storage power source, the capacity of each energy storage unit is utilised to the maximum extent. In view of the state of charge (SOC) equilibrium of multi-battery energy storage units, a SOC-based variable droop coefficient control strategy was designed to adjust the power distribution twice, so that the multi-cell energy storage units with higher SOC could bear the burden. Larger power output tasks to achieve a balanced goal. In order to verify the feasibility of the proposed method, a MATLAB/SIMULINK model was built. The simulation results show that compared to the traditional droop control, the improved variable droop coefficient control strategy can effectively suppress the DC bus voltage fluctuation and achieve multi-cell SOC equalisation and supercapacitor Rapid recovery of SOC.

Keywords: DC microgrid, SOC, power characteristics, droop control

1. INTRODUCTION

With the gradual increase of dc-compatible sources and loads, these terminals are connected to a DC microgrid with a certain voltage level（YAO et al., 2015), DC/AC/DC power conversion times are reduced, part of the AC/DC converters are eliminated, and the cost is reduced. Reduce conversion loss (Song et al., 2010). Therefore, DC microgrids are becoming more and more. Typically, an islanded microgrid containing renewable energy and various types of loads, through the energy storage system to reduce power mismatch between renewable energy and load consumption (Zhang et al., 2010). The energy storage unit can be classified according to its power, energy capacity, power change rate (kW/min, W/millisecond), and the like. Among them, the battery has a higher energy capacity, but the rate of change of the output power is low. On the other hand, the supercapacitor has better high power characteristics, but the energy capacity is limited (Li et al., 2014).

The system net power represents the difference between all load consumption and renewable energy within the microgrid. Due to the intermittent nature of renewable energy generation and changes in load, it can be assumed that the hourly power change is a low frequency change, while the power change in minutes, seconds, and milliseconds is a high frequency change (Wang et al., 2010, Li et al., 2016). The main research content of HESS control includes net power decomposition and power scheduling based on ESs characteristics. Currently, most of the research results are how to distribute power between the battery and the super capacitor to reduce the number of charging and discharging of the battery and to suppress power fluctuations. Decomposing the system net power (Mendis et al., 2012, Tummuru et al., 2015, Salmasi F R. 2007). By using a low/high-pass filter (LPF/HPF), the high-frequency component is assigned to the energy storage unit having a high power density. This method also has its disadvantages. The real-time power reference value is inaccurate due to the information lagging behind data transmission and processing results. Another common method is the HESS rule control. The literature (Glavin et al., 2012,Li et al., 2017,Li et al., 2017) is a regular type of control, that is, according to a certain rule, the charging and discharging algorithm of the storage battery and the storage capacitor according to the power fluctuation characteristics and states of various energy storage units. Set to optimise running status in different modes. While the microgrid hybrid energy storage system has both the microgrid topology and the energy storage system needs to be controlled, its operation control strategy is suitable for the combination of the above two methods (Lü et al,. 2015).

The low-frequency component of the net power of the system is mainly allocated to the energy storage unit having a low power change speed, and at the same time, the energy storage unit having a high power change rate such as a super capacitor unit is set to a voltage adjustment (VR) mode for automatically compensating the power high frequency. Component, obviously, compared to the super capacitor unit plus high-pass filter or filterless link scheme, adding the low-pass filter to the controller of the battery unit to decompose the net power can improve the dynamic response speed of the energy storage system. On this basis, this paper designs the local controller of the converter of the energy storage system and proposes a new power scheduling strategy. The simulation verifies the reliability of the system.

All the energy storage units are set as slack terminals with droop control. In the droop control, the deviation and fluctuation of the bus voltage reflect the change of the net power of the system. The bus voltage is used herein to determine the reference voltage of each energy storage unit. At the same time, ESs with high power can automatically compensate for high frequency changes. The energy management system (EMS) in this paper is designed for power storage in DC microgrid with multiple different energy storage units. The power distribution mode is designed to select different modes according to different operating conditions to improve system control. Accuracy and optimisation of the energy management of energy storage units. The local control of the energy storage unit is a bi-directional DC/DC converter that serves as the main component of the system's net power decomposition and scheduling. The power distribution of the battery cell is based on two different droop coefficient algorithms. Based on the first original VP droop control, a second improved variable coefficient droop control is designed to achieve the SOC balance of the battery cell. Improve the cycle life of the battery and the stability of the system's stored energy.

2. DC MICROGRID ENERGY STORAGE STRUCTURE

A schematic diagram of a DC microgrid containing various types of ESs is shown in Figure 1.The typical renewable photovoltaic PV is used in this paper. Each energy storage unit is connected to the DC bus through its respective bi-directional DC/DC converter to achieve two-way transmission of energy. The energy storage unit 1 (ES1) is the energy storage unit with the highest power change speed, and ESm represents the ES unit with the lowest power change rate. The real-time system net work$P_{net}\,(t)$ is expressed as:

Equation 1: The real-time system net work$P_{net}\,(t)$.

$$P_{net}\,(t) = P_{RESs}\,(t) - P_{loads}\,(t)$$

Equation 2 : The relationship between bus voltage and all ESs output power.

$$\frac{dV(t)}{dt} = \frac{1}{CV(t)}\left(P_{HESS}\,(t) - P_{net}\,(t)\right)$$

Where:

P_{Loads}= the power consumption of the load

P_{RESs}=the power generated by the RESs

Among them C and $V(t)$ are the system bus equivalent capacitance and instantaneous bus voltage respectively. Under the condition of excess power, the system bus voltage increases, and vice versa, the bus voltage drops. Any cell can be controlled as the slack cell terminal by adjusting the mode of operation of the inverter of the energy storage unit. This topology can realise plug and play of each energy storage unit (Lu et al., 2013).

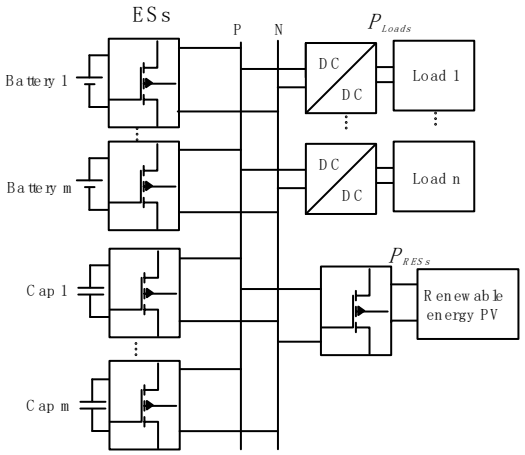

Figure 1: Schematic diagram of a DC microgrid with mixed energy storage

2. DROOP CONTROL OF DC MICROGRID AND IMPROVEMENT OF ITS COEFFICIENT OF VARIATIONPrinciples of droop control

Set to mode 1 in this article. The structure relationship of multiple slack energy storage units adopts droop control. The basic relationship is shown in Equation (3). (Bao et al., 2013)

Equation 3: the relationship between the output power and voltage of the i-th energy storage unit ESi $V_i = V_n - m_i P_{ESi}$

Where:

V_i = the output voltage of theESi

V_n = the bus voltage

m_i = the droop coefficient

P_{ESi} = the output power of theESi

Here, the power of the energy storage unit P_{ESi} represents the output power. That is, the battery or capacitor is in a discharged state, and when it is negative, it is in a charged state.

Equation 4: the droop coefficient $m_i = \frac{\Delta V_{max}}{P_{ESi}^{max}}$

Where:

ΔV_{max}= the maximum allowable change in bus voltage

P_{ESi}^{max}= the droop coefficient based on the ES power capacity

Here$p_i^{max}$is the maximum output power of ESi (i-th ES unit), and ∆V_max is the maximum allowable voltage deviation.

Equation 5: The relationship between the incremental output power Pi and the bus voltage change $\Delta P_i = -\frac{\Delta V_{ESi}}{m_i}$

Equation 6: The HESS output power change $\Delta P_{HESS} = \sum_i^n \Delta P_i = \sum -\frac{\Delta V_{ESi}}{m_i} = -\Delta V \sum \frac{1}{m_i}$

Equation 7: The HESS equivalent droop coefficient $m_{eq} = \frac{-\Delta V}{\Delta P_{HESS}} = \frac{1}{\sum \frac{1}{m_i}}$

Equation 8: The steady state bus voltage

$$V_i = V_n - m_{eq}P_{net} = V_n - \frac{1}{\sum \frac{1}{m_j}} P_{net}$$

Equation 9: The power allocated by the i-th cell ESi

$$P_i = \frac{V_n - V}{m_i} = \frac{m_{eq}P_{net}}{m_i} = \frac{p_i^{max}}{P_{ESs}^{max}} P_{net}$$

P_{ESs}^{max} Is the combined maximum output power of all ESs units. The above derivation shows that the power distribution between ES_i is directly proportional to its respective maximum power. The larger the$P_{ESi}^{max}$of each energy storage unit, the smaller the droop coefficient$m_i$and the faster the charging and discharging speed, the droop control method can be Utilise ES_i power to the maximum and do not exceed the respective power response range. It is suitable to switch to this kind of drooping method when the load changes abruptly. Moreover, the droop control only needs to transmit the voltage signal in real time and can operate normally under communication fault conditions. . After the load tends to be stable, the focus of the system operation control lies on how to handle the energy efficiency and long-term energy support of each energy storage unit. Therefore, a new droop control rule has been designed. The control principle diagram is shown in Figure 2.

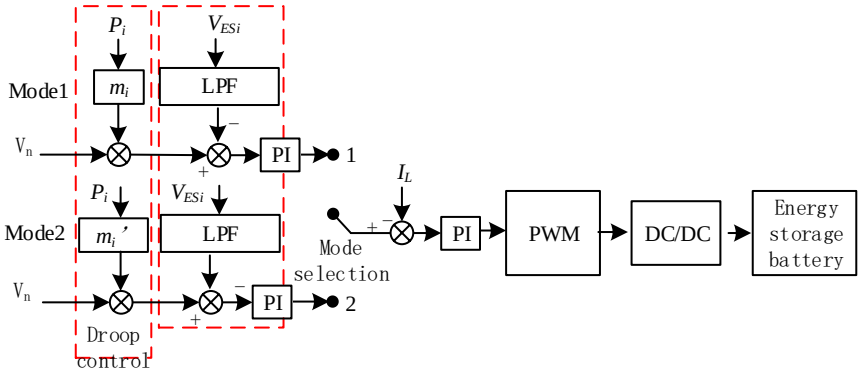

Figure 2: Schematic diagram of energy storage unit control

2.2. Improved variable coefficient droop control

Mode 2 in this system. In the droop control algorithm, in order to ensure the stability and control effect of the independent micro-grid system, a relatively rapid response speed of the energy storage unit and equalisation between the SOCs of the battery cells are specifically designed for the same type of energy storage cells. The droop method 2 is to change the droop coefficient control. The SOC factor of each energy storage unit should be included in the charging and discharging process of the battery droop unit droop coefficient selection rule. The SOC of all battery energy storage units should be calculated in real time.

Equation 10: The real-time average $SOC_{average}$ and the difference between each unit SOC and the average$SOC_{average}$:

$$\Delta SOC_i = SOC_i - \mathrm{SOC}_{average}$$

TakingP_{ESi} as positive, that is, the discharge of the energy storage unit as an example, the corresponding rules are designed. Based on the existing sagging relationship, according to Equation (3)

Equation 11: the improved droop coefficient

$$m_i' = m_i(1 - k' * \Delta SOC_i)$$

Where:

m_i' = SOC-based droop coefficients
m_i = original droop coefficients
k' = adjustment coefficients

The larger k' is, the larger the effect of the deviation of ΔSOC_i is, so that the adjustment k' can obtain different equalisation speeds. When k' is larger, the equalisation speed is faster, but the whole process cannot exceed the maximum charge and discharge current of the battery unit. ΔSOC_i>0, the unit's energy storage SOC is higher than the average, and it can allocate more power. The corrected droop coefficient m_i' is smaller than the original droop coefficient, and the smaller droop coefficient can supply more systems. The power; When ΔSOC_i<0, the unit SOC is lower than the average, the modified

droop coefficient$m_i'$is larger than the original droop coefficient, and the smaller power is allocated. Here, the energy storage unit sets the SOC change range from 10% to 90%, and beyond this range, the output power or power is stopped. This method is suitable for the microgrid load is in a basically stable state and the system communication is normal, the energy balance is implemented for the battery unit, and the system communication failure is switched to the mode 1. When the system DC bus voltage, the super capacitor at this time is in the charging or standby state, for this purpose, the super capacitor SOC recovery mode at this time is designed.

3. NET POWER DECOMPOSITION AND ITS LOWPASS FILTERING UP TO FREQUENCY DESIGN

As shown in Figure 3, the energy storage units of the present system are distributedly controlled, and the power distribution of the respective energy storage units is implemented in the local converters of the energy storage units. The droop voltage compensation value ΔV_{di} is obtained by multiplying the ES output powerP_i by the droop coefficient m_i. According to Equation 3, the ES_iconverter reference output voltageV_{ESi}^*= V_{oi} -ΔV_{di} . The reference voltage V_{ESi}^* is a given value for the DC-DC controller and is tracked with a conventional dual closed-loop PI controller. The battery cell converter voltage feedback loop adds a low-pass filter LPF so that the battery cell only responds to low frequency components of the bus voltage variation.

Equation 12: ES_iThe relationship between the inductor current and the system bus voltage

$$I_{Li}(t) = K_{Pi}\left(V_n - m_i P_i(t) - \frac{\exp\left(-\frac{t}{T_i}\right)}{T_i}V(t)\right) + K_{Ii}\left(V_n - m_i P_i(t) - \frac{\exp\left(-\frac{t}{T_i}\right)}{T_i}V(t)\right)$$

Where:

$I_{Li}(t)$ = the real-time ES_i converter inductor current

K_{Ii} =the ratios-coefficients of ES_iin the voltage outer loop

K_{Pi} =the integral coefficients of ES_iin the voltage outer loop

$\exp\left(-\frac{t}{T_i}\right)$ =The expression of the LPF time domain

T_i, = the time constant of the low-pass filter LPFi ofES_i

Equation 13: theES_i output power is$P_{ESi}(t)$:

$$P_{ESi}(t) = V_{teri}K_{Pi}\left(V_n - m_i P_i(t) - \frac{exp\left(-\frac{t}{T_i}\right)}{T_i}V(t)\right) + V_{teri}K_{Ii}\left(V_n - m_i P_i(t) - \frac{exp\left(-\frac{t}{T_i}\right)}{T_i}V(t)\right)$$

Where:

V_{teri} = the battery terminal voltage

K_{Ii} = the ratios-coefficients of

ES_i in the voltage outer loop

Differentiating the above formula and simplifying the equation, the cut-off frequency ω_{ESi} of the low-pass filter of the battery cell can be obtained according to the net power variation value ΔP_{net} and the maximum power constraint condition.

4. BUS VOLTAGE DROP COMPENSATION AND POWER DISTRIBUTION COMPENSATION

When the microgrid operates independently, the output power fluctuations of the intermittent power generation and the load-carrying load transiently interfere with the microgrid's motion and the busbar voltage will drop. To ensure reliable operation of voltage-sensitive critical loads during their lifetime, the bus bars must be eliminated as far as possible. The voltage drop deviation was added in the text control strategy to achieve a bus voltage drop compensation loop. As shown in Figure 3, the difference between the nominal bus voltage V_n and the actual voltage V_{dc} is processed by the PI controller to generate a voltage recovery compensated ΔV_{vc}signal. On the other hand, in order to eliminate power distribution errors, the output power of each cell is tracked in real time, and a power distribution compensation loop is added to the control loop. As shown in Figure 3, the difference between the reference output power and the actual output power is determined by another PI. The controller performs processing and constitutes a power distribution voltage compensator. The power distribution-voltage compensator is added to the forward path of the voltage loop and compared with the rated voltage at the integration point to obtain the reference output voltage of the unit ES_i. In summary, the bus voltage compensation and power distribution compensation loop are used to eliminate the bus voltage deviation and power distribution error, respectively.

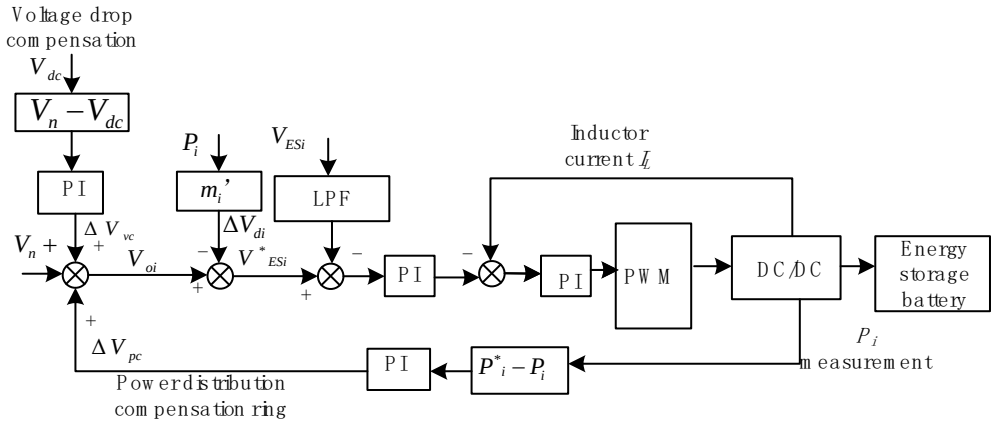

Figure 3: Voltage Compensation and Power Distribution Error Compensation Source Diagram

5. SIMULATION VERIFICATION

Table 1: simulation parameter setting table

Simulation parameters	DC bus voltage	Allowable voltage fluctuation range	PV maximum generating power (under standard conditions)	Battery Bidirectional DC-DC Converter Inductor Lb/Computation Power
Value	400V	±20V	2.5KW	100μH/5KW
Supercapacitor bi-directional DC-DC converter Lsc/compute power	Battery rated voltage	Super capacitor terminal voltage	Load1	Load2
100μH/5KW	200V	60V	80Ω	80Ω

Set up the model and set the parameters in the simulation software for simulation. The simulation parameters are shown in Table 1 above, and the original simulations are shown in Figure 4 below.

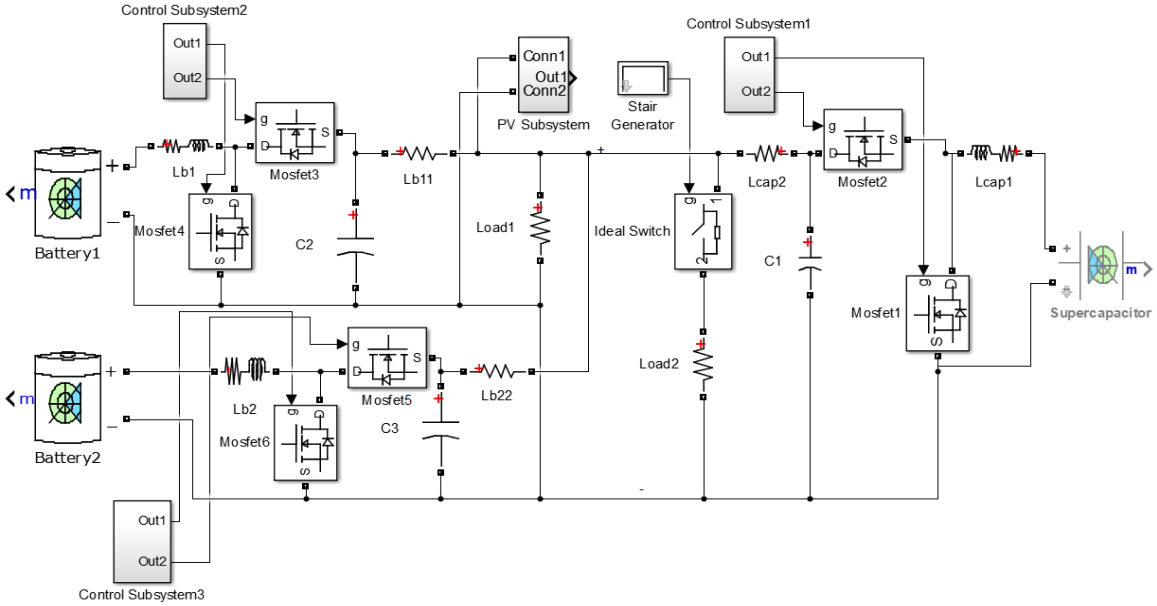

Figure 4: Droop control simulation

Condition 1: In condition 1, the HESS control is performed in a distributed manner. This simulation is to verify the system bus voltage regulation and power distribution in the distributed simulation control. The simulation results of the system bus voltage and the output power of the energy storage unit are shown in Figure 6. At the beginning, input load 1, battery cell 1 and super capacitor, and the power consumption is 2 kW. Since the supercapacitors UC and the battery have the same power capacity, the theoretical distribution power between them is the same. Before the system bus voltage stabilises, initialisation takes 0.08 seconds, and the system bus voltage stabilises at 397.5V, deviating from the nominal 2.5V. At t = 0.2 s, load 2 is input, the total load power produces a step change, and the load consumption increases to 4 kW. Due to the system power imbalance as described in (2), the system bus voltage drops immediately. It can be seen that the system bus voltage suddenly drops by 8.5V. When it is detected that the bus voltage is decreasing, the output power of the energy storage unit converter will increase correspondingly. Because the LPF is added to the voltage feedback loop of the cell converter, it responds to the low-frequency changes in the bus voltage. Therefore, the battery output power is gradually increased. In contrast, the UC output power increased by 2.5 kW in 0.21 seconds, which is much higher than the battery unit's response speed. At 0.3 s, the system bus voltage is stable at 396 V with a deviation of 4 V. This simulation verifies the effectiveness of droop control.

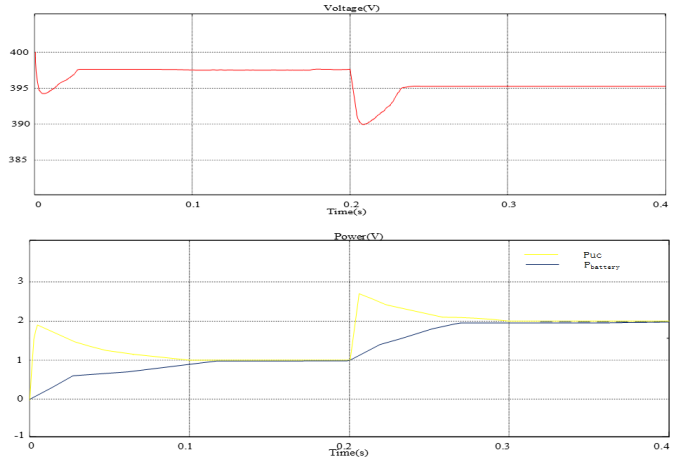

Figure 6: HESS basic droop control simulation

Condition 2: The bus voltage deviation compensation is implemented in the secondary control, which can minimise the bus voltage deviation from the rated value. After loading the voltage compensation control loop, the load load curve is still the same as 1 as shown in Figure 7. With bus voltage recovery, the system voltage is stable at 400 volts, with almost zero deviation. When the load power is increased to 4 kilowatts for 0.2 seconds, the supercapacitor ES1 reacts quickly, while the lithium ion battery cell ES2 output power gradually increases. During the transition period, it can be observed that the bus voltage drops by 5.5V. The system bus voltage recovers to the rated value quickly after the transition process, which shows the effectiveness of voltage compensation.

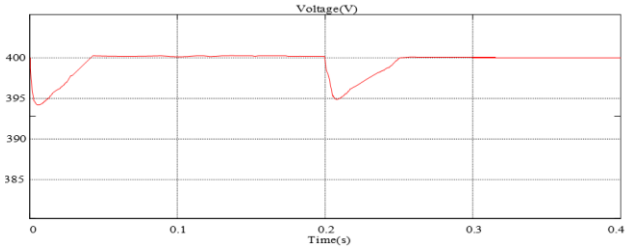

Figure 7: Voltage Compensation

Condition 3: This simulation verifies that power distribution is compensated to minimise power allocation errors. In this operating condition, a power loop is added to achieve power distribution compensation. ES1 is used to compensate for high frequency changes, so the ES1 reference power is given zero at steady state. The simulation results are shown in Figure 8. The blue dotted line indicates the ES1 power reference. The case of the loading curve of Case 3 is consistent with Cases 1 and 2. After the initialisation is completed, the system bus voltage with the bus voltage offset compensation function is stable at the rated value. The ES1 output power with power distribution compensation is stable at zero. ES2 compensates for system load consumption of 2kW. When the load 2 is input at 0.2 s, the bus voltage drop increases due to the system power imbalance. The ES1 immediately responds to the bus voltage change and the output power immediately increases, re-balancing the system power. In contrast, ES2's output power gradually increases because it only responds to changes in the low-frequency bus voltage. The minimum voltage of the bus voltage observed during the transition is 391.5 V and reaches the rated voltage at 0.26 seconds. After the transition is complete, the ES1 output power using power distribution compensation is reduced to zero.

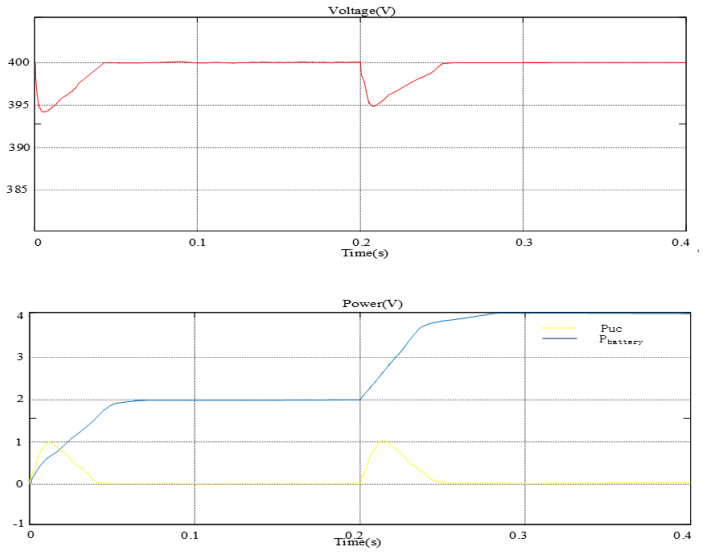

Figure 8: Power distribution compensation simulation

Condition 4: The system is in variable coefficient droop mode. In the simulation, a battery cell with the same capacity is added. Except that the other parameters of the SOC are the same as those of the ES2, the two battery cells are assigned ESb2, ESb3, and the initial SOC is 80% and 40%, respectively. Other parameter settings are the same as those of the working condition 1. During the simulation operation, two different energy storage units can automatically distribute the load power according to the modified power load command and quickly balance the SOC of different energy storage units. Instead of using a variable-coefficient droop mode, the battery cells are always at a large variance.

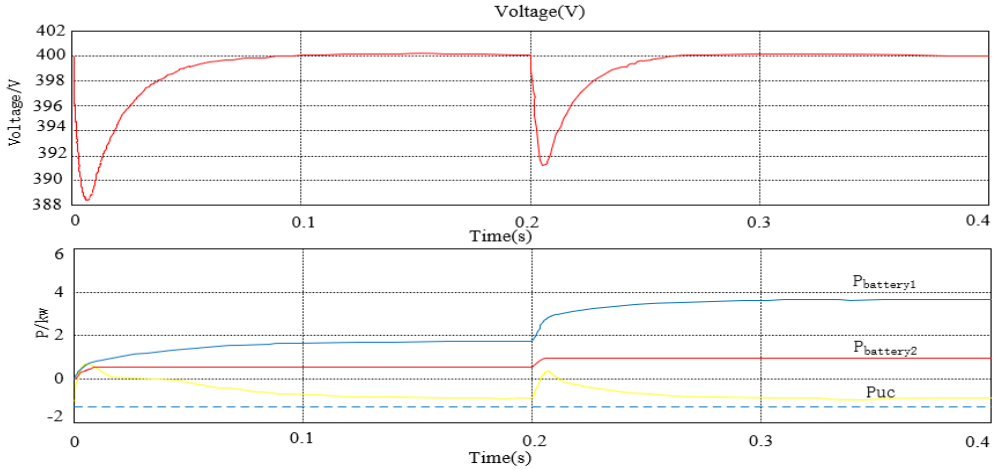

Figure 9: Droop mode power simulation with improved variable parameters

Condition 5: The system is in variable coefficient droop mode. Using the improved variable coefficient droop mode simulation, a battery cell with the same capacity is added in the simulation to verify the trend of SOC changes when two battery cells are operating in parallel. The two SOCs have the same SOC and other parameters, ES2 and ES3 initial SOC. They are 80% and 40% respectively. Other parameter settings are the same as operating conditions 1. During the simulation operation, two different energy storage units can automatically distribute the load power and quickly balance the SOC of different energy storage units according to the revised power load command. For simplicity, the two SOC differential amplification coefficients K take one. From the simulation diagram, we can see that the output capacitance of the supercapacitor is -1.25KW, which is the charging state; 2 battery cells are in the discharged state; the output power of the battery cell 1 is greater than the output power of the battery cell 2. Before 0.2s, both powers when the output tends to be stable, the power is about 1.7KW and 0.5KW respectively; after 0.2s, another load is input, the power is 3.95KW and 1.3KW respectively, and the output power is consistent with formula (4.18), which shows that the variable coefficient improves the sagging strategy. Effectiveness.

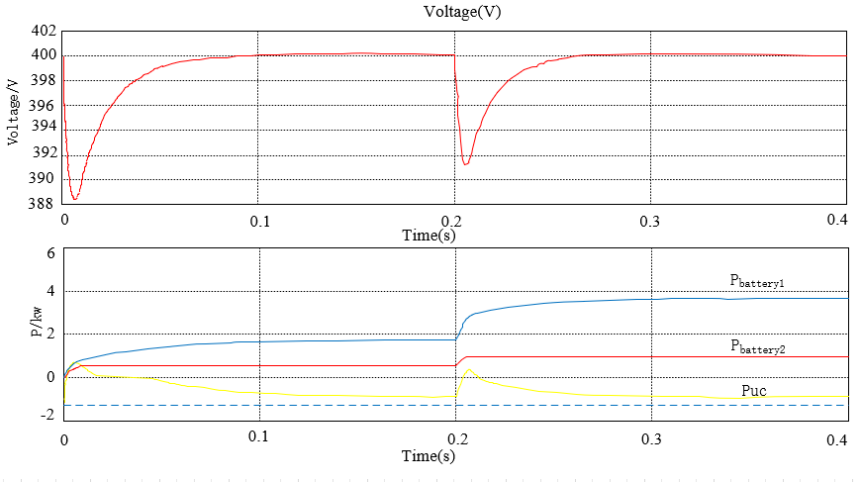

Figure 10: Droop mode loading power simulation with improved variable parameters

Effect comparison: The partial simulation diagram cannot completely see the change of the output power of the two battery cells with the SOC change, set the same condition 5, the simulation set time lengthened, it can be seen that the output power of the two battery units As time changes slowly approach, the SOC values of the two battery cells tend to converge. See Figure 11(b). Without the addition of a variable parameter (decline coefficient), the waveforms show that the output power of the two battery packs does not change much, and there is no rapid and consistent trend as shown in Figure 11(a).

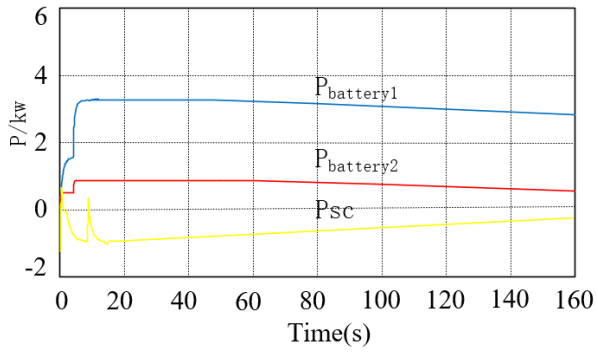

(a)

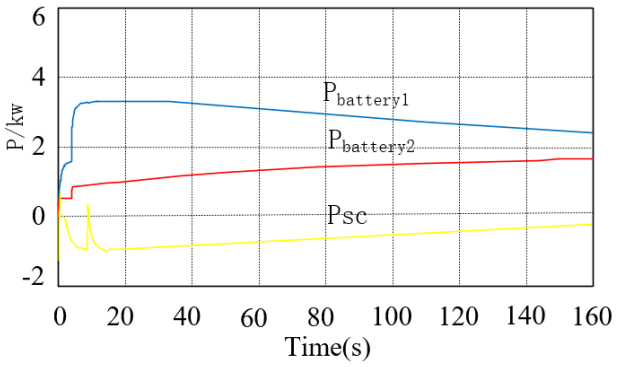

(b)

Figure 11: Droop mode power simulation with improved variable parameters

6. CONCLUSION

Based on this, HESS DC was proposed. Improve system control accuracy and reliability. The system net power decomposition and power storage unit power scheduling are implemented at the equipment level. Moreover, bus voltage compensation and power distribution compensation are designed to eliminate voltage deviation and power distribution error under the control loop. The proposed method was verified by Matlab simulation examples. Based on the analysis of sagging method, a variable coefficient sagging method is proposed. The improved sagging method adaptively changes

the sagging coefficient of the energy storage unit based on the SOC of the remaining energy of the energy storage unit, so that the battery output with large remaining capacity is more efficient. High power, to achieve the balance of the remaining battery power, while dynamically adjusting the droop coefficient and bus reference voltage. Finally, the proposed new sagging method is verified by simulation. The simulation results show that this new sagging method is feasible.

7. REFERENCES

Yao G, Chen S, Wang W 2015.Review of Distributed Power Supply Access to DC Microgrid [J]. *Electrical Engineering and Energy Efficiency Management*, (4):1-6.

Song Q, Zhao W, Liu W, 2013,Research Review of Intelligent DC Distribution Network [J]. Proceedings of the CSEE, 33(25):9-19

Amjadi Z, Williamson S S. 2010, Power-Electronics-Based Solutions for Plug-in Hybrid Electric Vehicle Energy Storage and Management Systems [J]. *IEEE Transactions on Industrial Electronics*, 57(2):608-616.

Zhang G, Tang X, Qi Z. 2010: Research on Battery Supercapacitor Hybrid Storage and its application in MicroGrid[C]// Asia-Pacific Power and Energy Engineering Conference. IEEE, 1-4.

Li B, Chen W, Liang S. 2014. An energy storage capacity optimisation method to suppress the output fluctuation of photovoltaic system [J]. *Power System Protection and Control,* (22):45-50.

Wang C, Yu B, Xiao J. 2012.Optimisation of energy storage system capacity for smooth output of renewable energy generation systems [J]. *Proceedings of the CSEE*, 32(16):1-8.

Li W, Xu C, Qi H,. 2016Hybrid Energy Storage Frequency Dividing Coordinated Control Strategy in DC Micro-grid System [J]. *Journal of China Electrotechnical Society*, 31(14):84-92.

Mendis N, Muttaqi K M, Perera S. 2012 Active power management of a super capacitor-battery hybrid energy storage system for standalone operation of DFIG based wind turbines[C]. Industry Applications Society Meeting. IEEE,:1-8.

Tummuru N R, Mishra M K, Srinivas S. 2015. Dynamic Energy Management of Renewable Grid Integrated Hybrid Energy Storage System [J]. *IEEE Transactions on Industrial Electronics*, 62(12):7728-7737.

Salmasi F R. 2007. Control Strategies for Hybrid Electric Vehicles: Evolution, Classification, Comparison, and Future Trends [J]. IEEE Transactions on Vehicular Technology, 56(5):2393-2404.

Glavin M E, Hurley W G. 2012. Optimisation of a photovoltaic battery ultracapacitor hybrid energy storage system [J]. Solar Energy, 86(10):3009-3020.

Li H, Huang Y, Ma F. 2017. Coordinated control strategy of hybrid energy storage system based on state of charge [J]. China.electricity, 50(1):158-163

Li P, Duan K, Dong Y, 2017.Energy management strategy of photovoltaic DC microgrid with distributed hybrid energy storage system [J]. Power System Protection and Control, 45(13):42-48.

Lü Z, Wu Z, Dou X, 2015. Self-adaptive droop control of isolated DC microgrid based on discrete consistency [J]. Proceedings of the CSEE, 35(17): 4397-4407.

Lu X, Sun K, Huang L, 2013. Load power dynamic allocation method with bus voltage drop compensation in DC microgrid energy storage system [J]. Proceedings of the CSEE, 33(16): 37-46.

Bao W, Hu X, Li G,. 2013. Improved droop control based on virtual impedance in stand-alone microgrid[J]. Power System Protection and Control, (16):7-13.

185: DC micro grid coordination control strategy based on hybrid energy storage

WU Tiezhou, CHEN Huang

Hubei Collaborative Innovation Center for High-Efficiency Utilisation of Solar Energy, Hubei University of Technology, Wuhan Hubei 430068, China

Due to intermittency, uncertainty and real-time change of load of power output of distributed micro grid, hybrid energy storage device should be used to meet the needs of power balance. This paper proposes a hybrid energy storage system composed of several battery and super capacitor to meet the needs of both power and energy at the same time. And a power allocation method based on the SOC parameter was put forward by combining the droop control method with the SOC parameter of different hybrid energy storage subsystem. The above strategy verified by experiments show that it can allocate storage battery and super capacitor output value, effectively reduce the battery charge and discharge times, prolong its service life.

Keywords: *micro grid; hybrid energy storage; soc*

1. INTRODUCTION

With the fossil energy crisis and environmental pollution becoming increasingly serious, clean renewable energy has become the inevitable choice of energy structure adjustment (Lu, 2016). But the output power instability of the solar energy, wind energy and other forms of distributed energy has caused some impacts to the power system planning operation. A hybrid energy storage system consisted of a battery and a super capacitor can solve the problem (Li, 2016; Zhang, 2016; Zhongjing, 2015; Zhang, 2014; Sun, 2016) to a certain extent. Micro-grid solitary network operation using super capacitor to smooth fluctuations in the frequency of high power, and network operation with the battery to stabilise the lower frequency of power (Sun, 2016; Song, 2014; Mendis, 2014; Xiao, 2015), through the joint action of the two micro-grid to improve the power quality And the grid to run the schedulability, while reducing the battery charge and discharge cycles, improve the battery life (Wen, 2015).

In order to meet the demand for large-scale distributed generation units and loads in micro grids, multiple hybrid energy storage subsystems need to be connected in parallel to the micro grid (Wu, 2013; Zhi, 2016), for the problems of how to allocate power amongst multiple hybrid energy storage subsystems , how to coordinate control and distribute power in the different types of energy storage components within hybrid energy storage subsystems Based on the island operation of the dc micro network as the research object, based on the analysis of working principle of the parallelled type hybrid energy storage system, on the basis of combining the traditional droop control with the hybrid energy storage subsystem SOC information between different hybrid energy storage subsystem, proposes a power allocation method based on SOC (Tummuru, 2015). Control system with dc bus voltage, the super capacitor voltage and battery charged status to determine conditions (Wang, 2015), automatic switch work mode. Advantage of the characteristics of super capacitor voltage can't mutate, achieve the smooth control of the battery current, reduce the battery charge and discharge time, prolong the service life of battery (Xie, 2016).

2. THE BASIC STRUCTURE AND WORKING PRINCIPLE OF MICRO - GRID

2.1. System structure

As shown in Figure 1 for typical scenery complementary dc micro grid simplification structure. Main parts are: dc bus, wind power generation unit, photovoltaic cell, hybrid energy storage system, the load. In this system, all units are directly connected to the dc bus through the converter Photovoltaic array and wind turbines are connected to the dc bus through the converter, in order to use of wind and solar power better, general control its operation in the maximum power point. Hybrid energy storage system composed of multiple subsystems in parallel. This article will battery via bi-directional DC - DC2 converter connected to the super capacitor hybrid energy storage system, after the bi-directional DC - DC1 converter is connected to a DC bus.

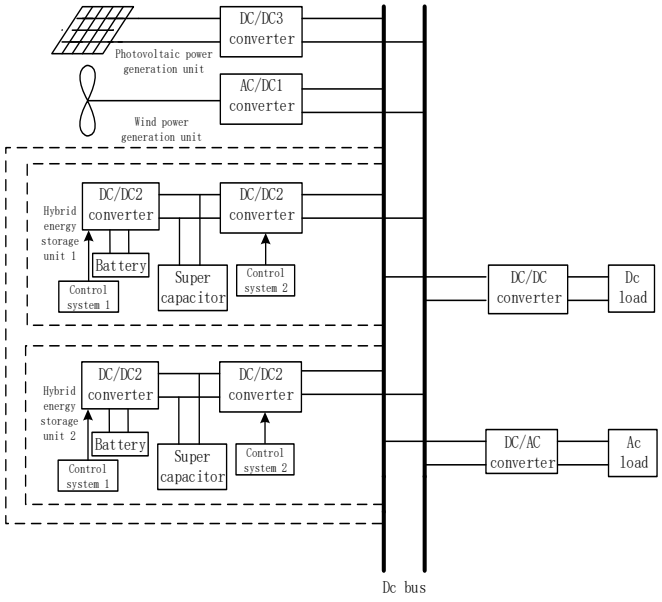

Figure 1: Simplified dc micro grid system structure

2.2. Working principle

In an island mode, the stable operation of the micro grid is guaranteed by the hybrid energy storage system. When the power of micro grid of the power generation section provided is greater than the load demand, the extra power is absorbed by a hybrid energy storage system. On the contrary, hybrid energy storage system absorbs surplus power. As the super capacitor is a power-type energy storage component, it can provide a higher power instantly, so the super capacitor is

connected to the DC bus by the bi-directional DC/DC converter 1, fluctuations in the high-frequency part of DC bus power is balanced by charge and discharge of the super capacitor. However, due to the lack of capacity of super capacitor the response to low frequency power fluctuations will lead to the lack of capacity of the super capacitor so it can not compensate for bus power fluctuations. The battery is added for energy storage, the charge and discharge of the battery is controlled according to the voltage of the super capacitor in order to make the super capacitor voltage maintained within the normal working range.so the super capacitor and indirectly compensates DC bus power fluctuations of the low frequency part. At the same time, when the distributed power generation unit can not provide power (such as a short period of time there is no wind or solar energy), the power is provided by a hybrid energy storage system to load alone to maintain the stability of the micro grid.

3. HYBRID ENERGY STORAGE SYSTEM CONTROL STRATEGY

3.1. The control strategy of hybrid energy storage subsystem

The control block diagram of the hybrid energy storage subsystem is shown in Figure 2. In the figure, U_{dc_ref} is limit voltage, U_{dc} is real-time bus voltage, U_b is battery terminal voltage , U_{sc} is super capacitor terminal voltage, U_{iref} and I_{oi} are respectively mixed energy storage unit of the converter output voltage reference and export current. k_i is droop coefficient(The subscript “i” represents the i th hybrid energy storage subsystem)

In the DC micro grid, because there is no reactive power flow, the voltage becomes the only indicator of the power balance of the system. When the power of the micro grid system changes, the voltage on the DC bus will fall or rise in order to maintain the power balance of the micro grid. When the DC bus voltage fluctuates, the energy storage system will be put into operation, absorbing or releasing power to make the bus voltage tends stable. Therefore, the DC bus voltage changes can be collected to reflect the system net power changes, so as to control the various energy storage unit charge and discharge. The power balance in the system is achieved by maintaining a constant DC bus voltage. The general idea of the control strategy is: to ensure the DC bus voltage quality under the premise of the use of super capacitors and batteries to stabilise the bus voltage changes in the high-frequency components and low-frequency components.

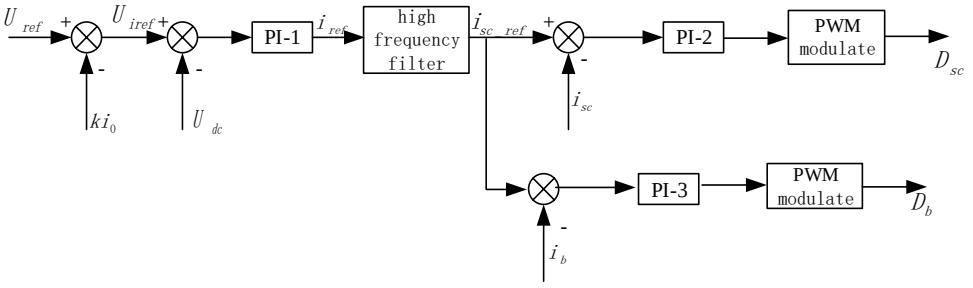

Figure 2: The control strategy of hybrid energy storage subsystem

When the net power of the system is changed, the reference voltage U_{iref} of the hybrid energy storage unit is obtained by voltage drooping control. U_{iref} is compared with the real-time bus voltage U_{dc} through the voltage outer loop PI-1 controller to obtain the reference value i_{ref} of the hybrid energy storage unit current, through high-frequency filter, i_{ref} is changed into the

Reference value i_{sc_ref} of the super capacitor, the difference between i_{sc_ref} and the feedback ultracapacitor i_{sc} transits the current inner loop PI-2 controller of the capacitor, and then the switching duty cycle D_{sc} of the bi-directional DC / DC converter of ultracapacitor can be obtained from PWM circuit. Because the response speed of the battery is slow and its reference current i_{b_ref} cannot be tracked timely by i_b , which will lead to the increase of the bus voltage fluctuations. Taking into account the characteristics of the rapid response of the super capacitor, in the control strategy proposed in this paper, the super capacitor is not only used to respond to the high frequency components, but also indirectly respond to the dynamic unresponsive power of the battery, which means to compare the current reference value i_{sc_ref} of the ultracapacitor with the feedback current i_b of the battery , its deviation transits current inner loop PI-2 controller of the

battery, and then the switching duty cycle of the bi-directional DC / DC converter of the battery can be obtained from the PWM circuit.

The hybrid energy storage unit has a corresponding control system to control the bi-directional DC-DC converter. The control system 1 for the bi-directional DC-DC1 converter automatically switches the DC-DC1 mode of operation via the DC bus voltage information. Control system 1 control flow chart shown in Figure 3, ΔU_{dc} is the DC bus voltage to allow fluctuations in the value. In order to avoid the battery overcharge and over discharge, its SOC is generally maintained between 20% to 80%.

If the battery voltage fluctuation value is within the allowable range, if the SOC_{bat} > 80%, it means that the energy storage system energy is excessive, so control the bidirectional DC-DC1 converter to discharge the energy storage system; if the battery of the state of charge is between 20% and 80%, bidirectional DC-DC1 converter stops working, to avoid frequent battery charge and discharge. When the DC bus voltage fluctuation value exceeds the allowable range, the DC bus voltage is stabilised by the super capacitor.

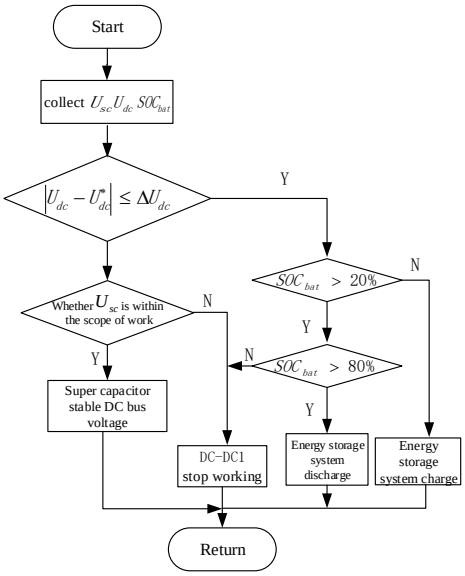

Figure 3: The control flow chart of control system 1

DC-DC2 converter control system 2 control the battery charge and discharge so that the super capacitor voltage is maintained within the normal working range, the system control flow chart is shown in Figure 4. If the super capacitor voltage is maintained within the normal working range, and the battery SOC is not in the normal working range, then the battery stops working; if the super capacitor voltage is not within the normal working range, the battery SOC work in the normal range, then the battery maintains super capacitance voltage.

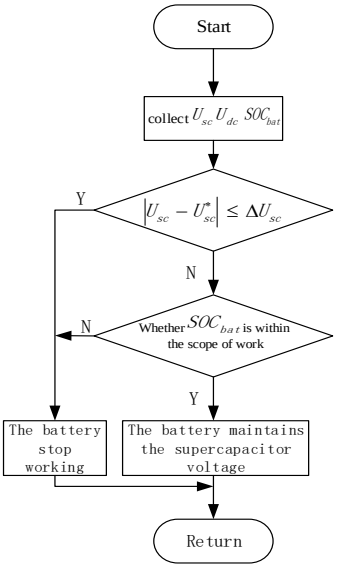

Figure 4: The control flow chart of control system 2

3.2. Power allocation between the hybrid energy storage subsystem

In the parallel hybrid energy storage system, the output capacity of different subsystems is different. In order to achieve a reasonable allocation of load power between the various hybrid energy storage unit subsystems, output size is determined according to its output capacity. When the total hybrid energy storage system power shortage (surplus), The remaining capacity of large hybrid energy storage unit should be more output, the remaining capacity of small hybrid energy storage unit should absorb more, the remaining capacity should be less small output, the remaining capacity should be large output. This paper through the energy storage converter output current to reflect the size of its commitment to the size of power.

The droop expression in the DC microgrid is:

$$U_{dc} = U_{ref} - k_i I_{oi} \quad (1)$$

Where k_i is the droop coefficient of the i-th hybrid energy storage subsystem converter. k_i is determined by the maximum output current $I_{oi\_\max}$ of the energy storage converter and the maximum allowable voltage fluctuation value $\Delta U_{\max}$:

$$k_i = \frac{\Delta U_{\max}}{I_{oi\_\max}} \quad (2)$$

In this paper, the power allocation method based on hybrid energy storage subsystem SOC is deduced. It can be seen from Equation 1 that when the bus voltage fluctuates, the output change of the i-th hybrid energy storage subsystem is:

$$\Delta I_{oi} = \frac{\Delta U}{k_i} \quad (3)$$

The output of the entire hybrid energy storage system changes:

$$\Delta I_o = \sum_{i=1}^{n} \Delta I_{oi} = \Delta U \sum_{i=1}^{n} \frac{1}{k_i} \quad (4)$$

Where n represents the number of hybrid energy storage subsystems in the system;

The equivalent drooping coefficient k_{eq} of the hybrid energy storage system is:

$$k_{eq} = \frac{\Delta U}{\Delta I_o} = \frac{1}{\sum_{i=1}^{n} \frac{1}{k_i}} \quad (5)$$

Thus, the equivalent droop control equation for the hybrid energy storage system is:

$$U_{dc} = U_{ref} - k_{eq} I_o \quad (6)$$

Where I_0 is the output value of the hybrid energy storage system.

When the system voltage fluctuates, the output of the first hybrid energy storage subsystem is:

$$I_{oi} = \frac{\Delta U}{k_i} = \frac{k_{eq}}{k_i} I_o = \frac{I_{oi\_\max}}{I_{o\_\max}} I_o \quad (7)$$

Where $I_{o\_\max}$ is the maximum output current of the micro grid hybrid energy storage system. It can be seen from Equation 7 that when the system bus voltage fluctuates, the output of the different hybrid energy storage subsystem is proportional to its maximum output current. Therefore, this paper proposes to set the maximum output current according to the SOC information of different hybrid energy storage subsystem, and then determine its drooping coefficient.

4. EXPERIMENTAL VERIFICATION AND RESULT ANALYSIS

In order to verify the validity of the control strategy proposed in this paper, we set up the experimental platform of DC micro grid. Set the micro-grid voltage level as 400V, the range of maximum voltage fluctuation is ± 10V, the fixed force of the distributed power is1.6kW. The hybrid energy storage system consists of two subsystems in parallel. When the SOC of the two subsystems is 0.75 and 0.25.1 seconds respectively, the system load increases from the rated load of 1.6kW to 2.4kW; 2 seconds, the load is reduced to 0.8kW.

4.1. Analysis of results

The experimental results are shown in Figures 5-7. Among them, Figure 5 shows the system bus voltage change map, Figure 6 shows the mixed energy storage system output curve. Figure 7 shows the output curve for different types of energy storage elements in a hybrid energy storage subsystem.

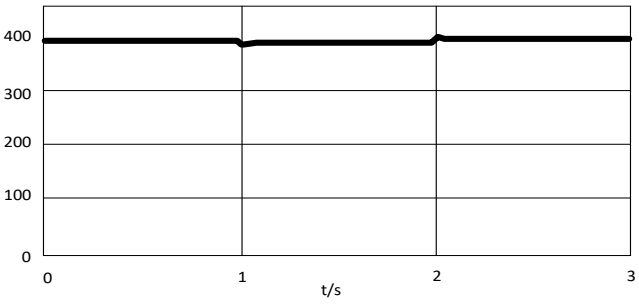

Figure 5 Busbar voltage variation

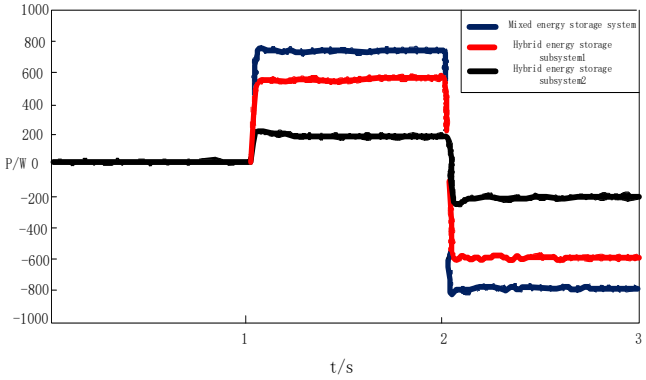

Figure 6: Hybrid energy storage system power output

It can be seen from Figure 5, at 1 second and 2 seconds the bus voltage has a slight fluctuation, but at 1.1 seconds and 2.1 seconds achieve steady state is achieved, steady-state voltage is396V and 405V, respectively, in the process the largest voltage fluctuation is +7V. It can be seen that the system bus voltage is within the range of the maximum voltage fluctuation regardless of increase or decrease of the load. Also, since the SOC of the two hybrid energy storage subsystems set in advance is 0.75 and 0.25, respectively, it can be seen from Equation 7 that the output ratio of the two subsystems under the state of discharge and charge / should be 3: 1 and 1: 3. It can be seen from Figure 6, from 0.5 to 1 second period, the output of the two subsystems were 570W and 190W; from 2 to 3 seconds, the output of the two subsystems were -215W and -645W, which is consistent with the theory.

When the system load suddenly increased at 1 second, the system net power low frequency component is very small, so the bus voltage changes in the low frequency component is also very small. it can be seen from Figure 7, when the load loading, the super capacitor quickly outputs to maintain stability of the bus voltage, along with the stability of the voltage, the net power of low-frequency components began to rise, the battery output gradually increased, while the output of the super capacitor is gradually reduced. Similarly, at 2-second system load suddenly reduced, the super capacitor quickly absorbs the system's remaining energy, while the battery's output gradually increases until it reaches steady state.

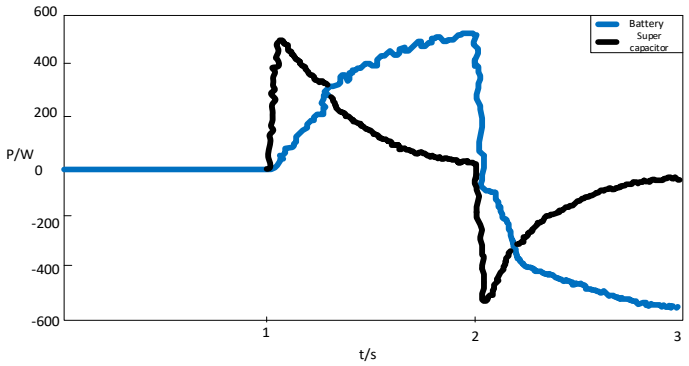

Figure 7: Battery and super capacitor power output

5. CONCLUSION

The energy storage system plays a very important role in maintaining the safety and stability of micro grid operation. In this paper, a hybrid energy storage system based on super capacitor and battery is proposed for the power quality of micro grid and its control strategy. The experimental results show that the control strategy proposed in this paper has the following advantages: 1) Power allocation between hybrid energy storage subsystems to meet the needs of large-scale distributed power generation units and loads. 2) Use super capacitor to response to the high voltage components of bus voltage fluctuations, and use battery to compensate the lack of power capacity of the super capacitor to achieve the battery charge and discharge current optimisation, and effectively reduce the battery charge and discharge times to extend its service life. 3) Using the SOC information of each hybrid energy storage subsystem to set its drooping coefficient, it is possible to realise the reasonable distribution of the net power of the system among the subsystems. 4) The use of DC bus and super capacitor voltage information automatically for energy distribution, thus improving the reliability of the system.

6. REFERENCES

Lu Y, Xu J. Wind power hybrid energy storage capacity configuration based on wavelet packet decomposition[J]. Power System Protection and Control, 2016, 44(11):149-154.

Li K, Qin W, Zhang H, Xu Z.Control Strategy for Microgrid Energy Management System Including Hybrid Energy Storage[J] .Proceedings of the CSU - EPSA, 2016, 28(10):85-91.

Zhang Q, Li X, Yang M, Cao Y, Li P. Capacity Determination of Hybrid Energy Storage System for Smoothing Wind Power Fluctuations with Maximum Net Benefit[J]. Transactions of China Electrotechnical Society, 2016, 31(14):40-48.

Zhongjing MA, Jiang W. A Novel Droop Control Strategy for Direct Current Microgrid[J]. 2015, 49(9):16-18.

Zhang C, Dong J, Liu J. A Control Strategy for Battery-Ultracapacitor Hybrid Energy Storage System[J]. Transactions of China Electrotechnical Society, 2014, 29(4):335-340.

Sun J, Dou X, Zhang Z. DC Peer-to-Peer Coordinated Control Strategy of Hybrid Energy Storage System for Microgrid[J]. Transactions of China Electrotechnical Society, 2016, 31(4):194-202.

Song Z, Hofmann H, Li J, et al. Energy management strategies comparison for electric vehicles with hybrid energy storage system[J]. Applied Energy, 2014, 134(C):321-331.

Mendis N, Muttaqi K M, Perera S. Management of Battery-Supercapacitor Hybrid Energy Storage and Synchronous Condenser for Isolated Operation of PMSG Based Variable-Speed Wind Turbine Generating Systems[J]. IEEE Transactions on Smart Grid, 2014, 5(2):944-953.

Xiao J, Wang P, Setyawan L. Hierarchical Control of Hybrid Energy Storage System in DC Microgrids[J]. IEEE Transactions on Industrial Electronics, 2015, 62(8):1-1.

Wen B, Qin W, Han X.Control Strategy of Hybrid Energy Storage Systems in DC Microgrid Based on Voltage Droop Method[J].Power System Technology, 2015(4):892-898.

Wu Y, Pan W, Feng M, Bao S. Power Control Strategy for Microgrid Based on Hybrid Energy Storage System[J].Proceedings of the CSU-EPSA, 2013, 25(2):109-114.

Zhi L, Zhang H, Xiao X. Research on the Improved Droop for Improving the Dynamic Characteristics of DC Microgrid[J]. Transactions of China Electrotechnical Society, 2016, 31(3):31-39.

Tummuru N R, Mishra M K, Srinivas S. Dynamic Energy Management of Hybrid Energy Storage System With High-Gain PV Converter[J]. IEEE Transactions on Energy Conversion, 2015, 30(1):150-160.

Wang S, Tang Y, Shi J, et al. Design and advanced control strategies of a hybrid energy storage system for the grid integration of wind power generations[J]. Renewable Power Generation Iet, 2015, 9(2):89-98.

Xie J, Qiu X, Ren L, et al. Capacity Configuration Model of Hybrid Energy Storage System Considering DC Distribution Benefit[J]. Electric Power Construction, 2016.

186: Li-ion battery SOC estimation based on RTS - IEKPF algorithm

Tiezhou WU[1], Xinyu DU[2], Fuchao XIANG[3]

[1] *Hubei Key Laboratory for High-efficiency Utilisation of Solar Energy and Operation Control of Energy Storage System, Hubei University of Technology, 430068, China, 1792935600@qq.com*
[2] *Hubei Key Laboratory for High-efficiency Utilisation of Solar Energy and Operation Control of Energy Storage System, Hubei University of Technology, 430068, China, 935978339@163.com*
[3] *Hubei Key Laboratory for High-efficiency Utilisation of Solar Energy and Operation Control of Energy Storage System, Hubei University of Technology, 430068, China,543206584@qq.com*

Compared with traditional fuel vehicles, electric vehicles have the advantages of saving energy resources and environmental protection. Therefore, the electric vehicles have been widely studied and promoted. As the main energy source for electric vehicles, the power battery can realise reliable management and control of the battery pack. It can provide the required power for the vehicle while achieving the best performance. The state of charge (SOC) of the battery is one of the core parameters of the battery management system (BMS). The accuracy of the SOC may directly affect the cycle life of the battery and the performance of the BMS. The instantaneous high-current charge and discharge of the battery will increase the nonlinearity of the battery while working. To estimate the SOC of the lithium battery by using the Kalman filter method will engender fairly great error. The particle filter method is not limited by the system model or noise distribution, and it has high practicability. However, it can affect the filtering that the particle itself may face degradation and depletion. In order to obtain higher precision of SOC estimation, a new estimation method is proposed here. It is called RTS-IEKPF algorithm, in combination with the IEKPF algorithm and RTS optimal smoothing, which uses an iterative EKF algorithm to generate a particle filter recommended distribution (IEKPF algorithm), and applies the RTS fixed interval optimal smoothing algorithm to a nonlinear system. RTS smoothing has good inhibition to suppress observation noise. It can stabilise the filtering result in the environment with large observation noise, accelerate the convergence speed of the algorithm and improve the precision of estimation. According to the experimental results, the battery model has a higher precision in estimation, and the RTS-IEKPF algorithm has better tracking filtering performance as well as higher estimation accuracy when estimating SOC.

Keywords: SOC estimation; particle filter; optimal smoothing

1. INTRODUCTION

Compared with traditional fuel vehicles, electric vehicles have the advantage of saving energy resources and environmental protection (Song et al., 2015). Therefore, the electric vehicles have been widely studied and promoted. As the main energy source for electric vehicles, the power battery can realise reliable management and control of the battery pack. It can provide the required power for the vehicle while achieving the best performance. The state of charge (SOC) of the battery is one of the core parameters of the battery management system (BMS). The accuracy of the SOC may directly affect the cycle life of the battery and the performance of the BMS.

There are many methods used to estimate SOC before (Merwe et al., 2001, Yu et al., 2013), and each has its own advantages and disadvantages. Taking into account the nonlinear characteristics of the battery, an extended Kalman filter (EKF) algorithm is proposed (Fang et al., 2014). The algorithm has low requirements on the accuracy of the initial value, and it can suppress the system noise better, and the estimation accuracy is higher. However, the accuracy of the algorithm depends on the accuracy of the model, and the high-order terms of the nonlinear function are ignored. When the system exhibits a highly nonlinear characteristic, a large linearisation error occurs. The particle filter method is not limited by the system model and the noise distribution. As a non-parametric simulation method, the particle filter method has strong applicability. However, it can affect the filtering that the particle itself may face degradation and depletion. In order to obtain higher accuracy of SOC estimation, a new estimation method is proposed here. Based on the EKF algorithm and the particle filter method, the iterative filtering theory (Li et al., 2005) and the optimal smoothing idea are introduced. The iterative EKF algorithm is used to generate the proposed particle filter distribution (IEKPF algorithm), the RTS fixed-interval optimal smoothing algorithm is applied in the nonlinear system, combined with the IEKPF algorithm, proposes an RTS-IEKPF algorithm that integrates the RTS optimal smoothing IEKPF algorithm. RTS smoothing has good ability to suppress observation noise. It can stabilise the filtering result in the environment with large observation noise, accelerate the convergence speed of the algorithm and improve the accuracy of estimation.

2. SOC CALCULATION FORMULA

Battery SOC is an important parameter, it is used to describe the remaining battery capacity and reflect the battery power consumption. Using the SOC calculation formula (Mao et al., 2014) with coefficient correction and discretizing the formula, the following formula can be:

Equation 1: The SOC calculation.

$$SOC(k+1) = SOC(k) - \frac{\eta_i \Delta t}{\eta_T (1-\eta_n) Q_n} i(k)$$

Where:

SOC(k+1) = the SOC value of the battery at the time

i(k) = is the current value at the time of k-k+1T= equilibrium time (h)

Qn = represents the rated capacity of the battery（Ah）

η_i, η_T, η_n = respectively indicate the charge and discharge rate, temperature, and the correction factor of the battery capacity

3. BATTERY MODELING AND PARAMETER IDENTIFICATION

3.1. Battery equivalent model

Common battery equivalent models include electrochemical models, equivalent circuit models, and neural network models. Taking into account that the battery equivalent model has a greater impact on the accuracy of the Kalman filter algorithm, the built model requires a small amount of calculation and high accuracy. A composite electrochemical model was obtained by combining several electrochemical models of Shepherd, Unnewehr universal, and Nernst (Pan et al., 2014), and after being discretised its expression is shown in Equation 2.

Equation 2: Chemical model expression.

$$E(k) = k_0 + \frac{k_1}{SOC(k)} + k_2 SOC(k) + k_3 \ln[SOC(k)] + k_4 \ln[1 - SOC(k)] - Ri(k)$$

Where:

E(k) = the terminal voltage of the battery at time k

R = the internal resistance of the battery (Ω)

i(k) = is the current value at the time of k-k+1T = equilibrium time (h)

k_0、k_1、k_2、k_3、k_4= the battery equivalent model parameters to be identified

Select SOC(k) as the state variable, written as X_k=SOC(k); select E(k) as the output variable, written as y_k=E($k_)$; select current $i_{L(k)}$ as the input variable, written as u_k=i_L(k). Adding the process noise W_k and the observed noise V_k to the state equation and the observation equation respectively, the state space model equation of the battery can be established as shown in Equations 3 and 4.

Equation 3: the state equation.

$$x_{k+1} = x_k - \frac{\eta_i \Delta t}{\eta_T (1-\eta_n) \mathrm{Q}_n} u_k + w_k$$

Where:

x_k= the state variable
u_k= the output variable(i_L(k))
W_k = the process noise

Equation 4: the observation equation.

$$y_k = k_0 + \frac{k_1}{x_k} + k_2 x_k + k_3 \ln(x_k) + k_4 \ln(1-x_k) - R u_k + v_k$$

Where:

y_k= the output variable
v_k= the observed noise

3.2. Method of parameter identification

The parameters k_0、k_1、k_2、k_3、k_4 are very important in the estimation process of the battery SOC. By charging and discharging the battery, the voltage and current in the process of discharging from the fully charged state to a discharge cut off voltage at a certain discharge rate are recorded. The corresponding SOC values are obtained by least-squares fitting.

Least square method (Li, 2015) is a common method in system parameter identification, which has the advantages of simple calculation, fast convergence, and easy programming. Using online recursive least squares method that introduces forgetting factor λ ($0 < \lambda < 1$) to identify these parameters online (Zhou et al., 2015).

Equation 5: The least squares iteration formula:

$$\begin{cases} \hat{\theta}(k) = \hat{\theta}(k-1) + K(k)[y(k) - \varphi^T(k)\hat{\theta}(k-1)] \\ K(k) = \frac{1}{\lambda} p(k-1)\varphi(k) + \varphi^T(k)\, p(k-1)\varphi(k) \\ p(k) = \frac{1}{\lambda}[I - K(k)\varphi^T(k)]p(k-1) \end{cases}$$

Where:

$\lambda_{(k)}$ = variable forgetting factor
K(k)= gain vector
p(k)= covariance matrix.

The observation Equation 4 is expressed as a vector in the form shown in Equation 6

Equation 6: the observation equation expressed as a vector

$$y_k = \varphi(k) \cdot \theta(k)^T + v_k$$

Where:

$$\varphi(\mathrm{k}) = [1, \frac{1}{x_k}, x_k, \ln(x_k), \ln(1-x_k), -u_k]$$
$$\theta(\mathrm{k}) = [k_0, k_1, k_2, k_3, k_4, \mathrm{R}]$$

In Equations 5 and 6, if the parameter matrices $p(0)$ and $\theta(0)$ are given at the initial time, we can get the unknown parameters k_0、k_1、k_2、k_3、k_4 in $\theta(k)$.

4. PARTICLE FILTER ALGORITHM BASED ON RTS-IEKF

Equation 7: Battery state equation.

$$x_k = f(x_{k-1}, u_k) + \omega_k$$

Equation 8: observation equation.

$$y_k = h(x_k, u_k) + v_k$$

4.1. Particle filter algorithm

The core idea of the particle filter algorithm is to approximate the posterior probability distribution of the system state by approximating the weighted sum of sample particles randomly propagating in the state space, and to replace the integral operation by sample summation. The sampling of the algorithm and the schematic diagram of the particle propagation process are shown in Figure 1 (Wang et al., 2014).

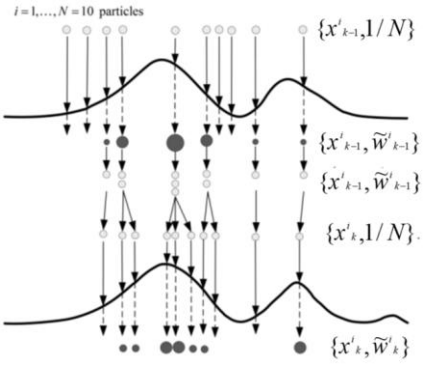

Figure 1: particle filter algorithm

Figure 1 show, x_k^i represents the state of the i sampled particle at time k, and its corresponding weight is w_k^i.

At time k -1, N equal-weight particles $\left\{x_{k-1}^i, 1/N\right\}$ are randomly sampled from the prior probability distribution of the state; the particle weights are updated according to the likelihood function to obtain $\left\{x_{k-1}^i, \tilde{w}_{k-1}^i\right\}$; then resampling is performed, large-weight particles are duplicated, and the weights are discarded Smaller particles, and set the resampling particle weight to $1/N$;Then at the next moment, the system state transition model predicts the particle state at time k , and updates the particle weight when the observed value arrives to obtain the weighted particle set $\left\{x_k^i, \tilde{w}_k^i\right\}$ at time k .

4.2. IEKPF algorithm based on RTS optimal smoothing

RTS (Rauch-Tung-Striebel smoother) fixed interval smoothing (Cao, 2012, Sarkka, 2008) algorithm is proposed by Rauch et al. It is a simple and effective optimal smoothing algorithm based on Kalman filtering algorithm and the minimum variance estimation of the system state is achieved by recursively using all measured values within a fixed time interval [0, T], which has a good ability to suppress observation noise. Here, the generalisation is applied to a nonlinear system. Considering the system time step is [0, T], the nonlinear system is first subjected to IEKF filtering to obtain the maximum posterior estimation of the state and variance, and then the RTS optimal smoothing algorithm is used to correct the filtering. As a result, a new proposed distribution function RTS-IEKF is generated thereby. The design idea of the RTS-IEKF recommendation distribution is as follows:

(1) IEKF filter
a) State prediction and iterative initialisation.
State forecast:

Equation 9: State forecast

$$\begin{cases} \hat{x}_{k|k-1} = f(x_{k-1|k-1}, u_{k-1}) \\ P_{k|k-1} = F_k P_{k-1|k-1} F_k^T + R_k \end{cases}$$

Where:

$\hat{X}_{k|k,0}$ (the iterative initial values of the state vector)= $\hat{x}_{k|k,k-1}$

$P_{k|k,0}$ (the iterative initial values of its covariance)= $P_{k|k,k-1}$

Fk= $\left.\frac{\partial f(x_k)}{\partial x_k}\right|_{x_k}$

Rk= $\left.\frac{\partial f(w_k)}{\partial w_k}\right|_{w_k}$

Iterative initialisation: $\hat{x}_{k|k,0} = \hat{x}_{k|k-1}, P_{k|k,0} = P_{k|k-1}$

b) Iteratively update status and variance:

Equation 10: Iteratively update status

$$\hat{x}_{k|k,i+1} = \hat{x}_{k|k,i} + P_{k|k,i} H_{k,i}^T Q_k^{-1}[y_k - h(\hat{x}_{k|k,i}, u_k)] - P_{k|k,i} P_{k|k-1}^{-1}(\hat{x}_{k|k,i} - \hat{x}_{k|k-1})$$

Where:

I = i corresponds to the current number of iterations

Q_k = the observation noise covariance matrix

$\hat{X}_{k|k,i+1}$ = The updated state estimate after the ith iteration

Equation 11: Iteratively update variance

$$P_{k|k,i} = P_{k|k-1} - P_{k|k-1} H_{k,i}^T [H_{k,i} P_{k|k-1} H_{k,i}^T + Q_k]^{-1} H_{k,i} P_{k|k-1}$$

Where:

$P_{k|k,i}$ = Covariance matrix updated after the ith iteration

Among them, subscript i corresponds to the current number of iterations, Q_k is the observation noise covariance matrix, and $X_{k|k,i+1}$, $P_{k|k,i}$ are updated state estimates and their covariance matrices after the ith iteration.

c) Storage of filtering results: The filtering results at various times within the storage time interval [0, T] are used for the optimal smoothing of the next step.

(2) RTS fixed interval smoothing

a) Initialisation: Initialise the state and variance of the smoother with the filtering result at the moment k=T.

Equation 12: Initialisation

$$\begin{cases} \hat{x}_{T|T}^s = \hat{x}_{T|T}^f \\ P_{T|T}^s = P_{T|T}^f \end{cases}$$

Where:

F = represents IEKF filtering

S = represents RTS smoothing

b) Smoothing correction: Time K = T-1,T-2,…,0, smoothing correction formula for state and variance:

Equation 13: smoothing correction formula for state

$$\begin{cases} \hat{x}_{k|T}^s = \hat{x}_{k|k}^f + K_k^s(\hat{x}_{k+1|T}^s - x_{k+1|k}^f) \\ P_{k|T}^s = P_{k|k}^f + K_k^s(P_{k+1|T}^s - P_{k+1|k}^f)(K_k^s)^T \end{cases}$$

Equation 14: smoothing correction formula for variance

$$K_k^s = P_{k|k}^f F_{k+1|k} (P_{k+1|k}^f)^{-1}$$

Where:

K_k^s = the smoothing gain at time k

$F_{k+1|k}$ = the Jacobian matrix of the system state transition

$x_{k+1|k}^f$ = the one-step predicted values of IEKF state

$P_{k+1|k}^f$ = the one-step predicted values of covariance

$\hat{x}_{k|k}^f$ = the IEKF filtered state estimates

$P_{k|k}^f$ = the IEKF filtered state covariance

$\hat{x}_{k|T}^s$ = the state vectors at time k after the smoothing of RTS

$P_{k|\mathrm{T}}^s$ = the state covariances at time k after the smoothing of RTS

It can be seen that the smoothing starts from $k = T-1$ to $k = 0$, and is gradually reversed by $\hat{x}_{T|T}^s$ to obtain $\hat{x}_{T-1|T}^s$, $\hat{x}_{T-2|T}^s$,…, $\hat{x}_{0|T}^s$ in sequence.

(3) Generate RTS-IEKF Recommendation Distribution

According to the steps (1) and (2), the state vector and covariance at each moment are smoothly modified to obtain the corrected state and variance sequence as $\left\{\hat{x}_{k|T}^s, P_{k|T}^s\right\}, k = 1,2,\ldots,T$, thereby constructing the RTS-IEKF recommended distribution function as follows:

Equation 15: the RTS-IEKF recommended distribution function. $$q(x_k \mid x_{k-1}, y_k) = N(x_k; \hat{x}^s_{k|T}, P^s_{k|T})$$

It can be seen that the smoothing correction is the processing after the filtering process. In the realisation, the slow smoothing lag problem is implemented, and the time interval $[0, \mathrm{T}]$ is segmentally smoothed, and the smoothing step length $T_s = T/3$ is obtained.

From the above steps, it can be seen that the introduction of iterative filtering theory and smoothing correction makes the RTS-IEKF recommendation distribution utilise the system observation information better and improve the suppression ability of observation noise. Therefore, from the proposed distribution generated by RTS-IEKF, the sampled particles are more in line with the system's true posterior probability distribution and the estimated performance of particle filtering is improved.

The main idea of the RTS-IEKPF algorithm is to update each particle in the filtered particle set $\left\{ x_k^i \right\}_{i=1}^N$ by integrating the RTS smoothing correction into the IEKF filtering at the time k, and to predict the particle's $\hat{x}_k^{i,s}$ and $P_k^{i,s}$ (superscript indicates the smoothing result). Then, generate the recommended distribution function and sample the generated particle set from it, and update the particle weights and normalise them. Then conduct particle propagation at the next moment.

5. EXPERIMENTAL VERIFICATION AND RESULT ANALYSIS

5.1. Recursive least squares parameter identification and model validation

The parameter identification results obtained by online parameter identification using recursive least squares method will be used as the input of models and algorithms built at the time of SOC estimation. However, the parameter obtained at the end of the identification process is a constant. In order to simplify the process of parameter identification, the result of parameter identification takes the updated value finally obtained by the algorithm.

From the above，the parameters that need to be identified in the model include the parameters k_0、k_1、k_2、k_3、k_4 and the internal resistance R of the battery, as described in Figure 2, when the current shown in Figure 2(a) is used to perform constant current intermittent discharge of the battery. The obtained battery terminal voltage curve is shown in Figure 2(b). The final result of the parameter identification result:

$k_0 = -19.8573$ $k_1 = -30.8021$、k_2、$= 7.0016$、$k_3 = -30.4230$、$k_4 = -0.9886$ and $\mathrm{R} = 0.0162$.

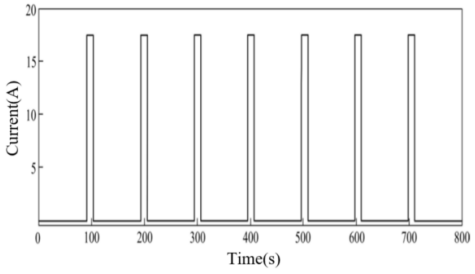

(a) Current variation curve

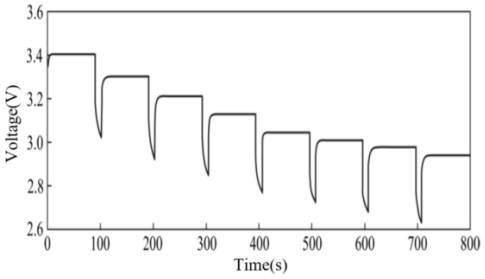

(b) Voltage change curve

Figure 2: Discharge test current and voltage curve

In order to verify the accuracy of the battery model built, the battery was discharged under the discharge current conditions given in Figure 2(a). The actual terminal voltage data of the battery collected on the experimental equipment is compared with the voltage output data of the model, and the comparison of the experimental results is shown in Figure 3. Figure 3 shows the verification result of the model output voltage. The experimental results show that the accuracy of the composite electrochemical model is very high.

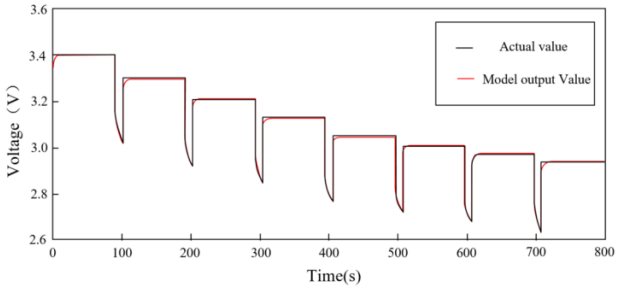

Figure 3: Comparison between model output voltage and actual value

5.2 RTS-IEKPF estimation SOC experiment and result analysis

To verify the proposed tracking performance of the RTS-IEKPF algorithm, a nonlinear discrete system as shown in the following Equation 16 was used for simulation experiments, and compared with other nonlinear filtering methods: PF, EKPF, and IEKPF.

Equation 16: nonlinear discrete system expression.

$$x_k = 1 + \sin(0.4\pi k) + 0.5x_{k-1} + w_k$$

$$y_k = \begin{cases} 0.2x_k^2 + v_k, & k \le 30 \\ 0.5x_k - 2 + v_k, & k > 30 \end{cases}$$

Simulation experiment conditions: Set the initial value to $x_0 = 1.0$, and x_k obeys $p(x_0) \sim \mathrm{N}(0, 0.75)$. Set the time step of each simulation to T=60s, and set the number of particles to $N = 200$. The variance R and Q of the process noise and the observed noise are 0.75 and 0.001, respectively. The resulting curve is shown in Figure 4.

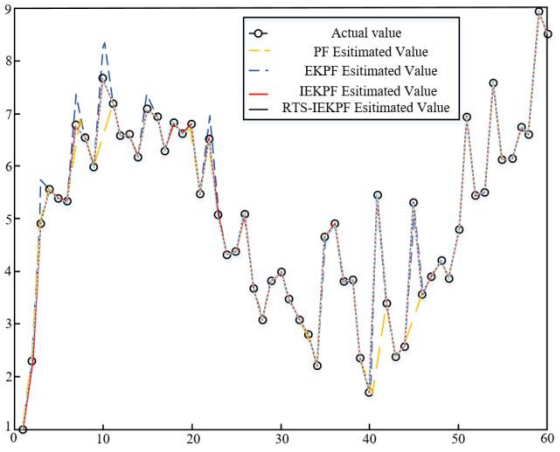

Figure 4: Comparison of simulation results

Figure 4 shows the comparison curve. It can be seen that there are large estimation errors of the PF algorithm and EKPF algorithm, and the tracking performance of the algorithm is unstable. The estimation results of the RTS-IEKPF algorithm and the IEKPF algorithm are in good agreement with their true values, but the RTS-IEKPF algorithm continuously integrates new system observation information and smooths the correction when generating the recommended distribution, and makes the predicted result closer to its actual value, and the tracking performance of the algorithm is the best.

Using the above three filtering algorithms for 100 Monte Carlo simulations, the results obtained are shown in Table 1. Among them, the RMS error is defined as:

Equation 17: Root mean square error definition

$$\cdot RMSE = \sqrt{\frac{1}{T}\sum_{k=1}^{N}(x_k - \hat{x}_k)^2}$$

Where:

$\hat{X}_k$ = average

T= Sample number

Table 1: Comparison Chart of the estimated result data

Filtering algorithm	PF	EKPF	IEKPF	RTS-IEKPF
RMSE mean value	0.50719	0.29415	0.07528	0.04008
RMSE Variance	0.06958	0.01524	0.00628	0.00151
Average elapsed time (s)	0.42672	2.85670	6.34260	3.22630

The RMSE mean and variance of the RTS-IEKPF algorithm are minimal , at the running time, the RTS-IEKPF algorithm is slightly longer than the average running time of the PF algorithm and the EKPF algorithm, but compared with the IEKPF algorithm, the time of operation is much shorter, only 50% of its running time.

In order to verify the effectiveness of the proposed algorithm in estimating battery SOC, a battery test platform consisted of Arbin-BT2000 equipment, PC, and lithium-ion batteries was selected for verification. Using different currents to charge and discharge the battery, BT2000 was used to record the experimental data. Based on the recorded data, PF, EKPF, IEKPF, and the proposed RTS-IEKPF algorithm were used to estimate the SOC of the battery. The estimated results of the comparison curve are shown in Figure 5 (As shown in (a)), the error curve of the estimation result is shown in Figure 5(b).

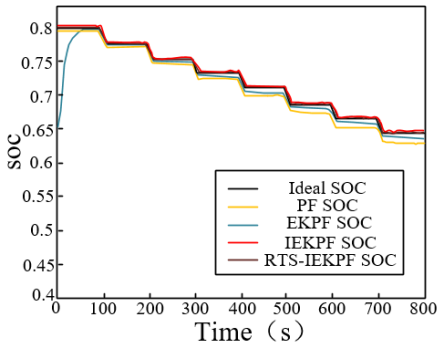

(a) Comparison of SOC estimation results

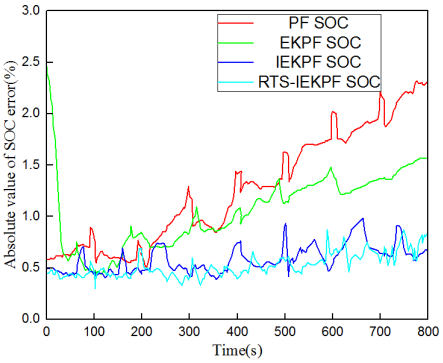

(b) Error Comparison of SOC Estimation Results

Figure 5: SOC estimation results for several different estimation algorithms

From the experimental results shown in Figure 5, it can be seen that the estimated trend curves of the four estimation methods are close to the actual value curve. The estimation errors of the PF and EKPF algorithms are relatively large. In

terms of the overall situation, the error of the PF algorithm is larger than that of the EKPF algorithm. The error of the EKPF algorithm is larger than that of the IEKPF algorithm. The error of the RTS-IEKPF algorithm is the smallest, and the fluctuation of the error is not very large. This is mainly because the RTS-IEKPF algorithm has the advantages of the other three algorithms at the same time, and because the latest system observation information is continuously integrated and smoothed during the generation of the recommended distribution, the generated predicted particles are more in line with the true distribution of their states. Improve the tracking performance of the algorithm .In general, when using the RTS-IEKPF algorithm proposed in this paper to estimate SOC, the algorithm's estimation accuracy and performance are obviously better than other algorithms.

4. CONCLUSION

The estimation of the battery SOC is one of the key factors for predicting the operating status of the electric vehicle energy storage unit. In this paper, the complex electrochemical model of the battery is established, and the parameters of the model are identified online by using the recursive least square method. The concept of optimal smoothing is introduced based on the IEKF algorithm, an algorithm based on RTS optimal smoothing IEKPF, RTS-IEKPF, is proposed. A new particle filter proposed distribution function, RTS-IEKF, is designed. By smoothing the IEKF filter results, the tracking performance of the predicted particles and the estimation accuracy of the algorithm are improved. The experimental results show that the battery model has higher accuracy, and the RTS-IEKPF algorithm has better tracking filtering performance, and has higher estimation accuracy when estimating the SOC.

5. REFERENCES

Song S, Lin Q, Lin X F, 2015. Modeling and Optimisation of Pure Electric Vehicle's LiFeP04 Battery Pack. Computer Measurement and Control. 23(5), 1713-1716.

Merwe R V D, Doucet A, Freitas N D, et al, 2001. The Unscented Particle Filter. Advances in Neural Information Processing Systems. 13, 584-590.

Yu H-B, Wang G-H, Sun Y et al, 2013, Particle filtering algorithm of state estimation on fusion of UKF and EKF[J]. System Engineering and Electronics. 35(7), 1375-1379.

Fang H, Wang Y, Sahinoglu Z, et al, 2014. State of charge estimation for lithium-ion batteries: An adaptive approach. Control Engineering Practice. 25(1), 45-54.

Li S, 2015. Study on Parameter Identification of the Equivalent Circuit Model in Lithium-ion Battery in Electric Car. Beijing Institute of Technology.

Ma0 H-F Wan G , Wang L, et al, 2014. Estimation of battery SOC based on Kalman filter correction algorithm. Power Technology. 38(2), 298-302.

Pan W, Liu X, 2014. Research on Estimating SOC of Lithium-ion Battery Based on Improved Kalman Filter. Computer Simulation. 31(3), 148-150.

Zhou D, Ravey A, Gao F, et al, 2015. Online estimation of state of charge of Li-ion battery using an iterated extended Kalman particle filter. Transportation Electrification Conference and Expo.

Wang F-S, Lu M-Y Zhao Q-J, et al, 2014. Chinese Journal of Computers. 37(8), 1679-1694.

Li L Q, Ji H B, Luo J H, 2005. The iterated extended Kalman particle filter. IEEE International Symposium on Communications and Information Technology. 1213-1216.

Cao B, 2012. Research on Improved Algorithms and Applications based on Particle Filter. Xi’an Institute of Optics and Precision Mechanics of CAS.

Sarkka S. Unscented Rauch--Tung--Striebel Smoother, 2008. IEEE Transactions on Automatic Control. 53(3), 845-849.

187: Study on photovoltaic grid-connected fast harmonic compensation technology for three-phase voltage unbalance

Tiezhou WU[1], Zhenyu YANG[2], Cuicui ZHOU[3]

[1] *Hubei Key Laboratory for High-efficiency Utilisation of Solar Energy and Operation Control of Energy Storage System, Hubei University of Technology, 430068, China, 470155230@qq.com*
[2] *Hubei Key Laboratory for High-efficiency Utilisation of Solar Energy and Operation Control of Energy Storage System, Hubei University of Technology, 430068, China,903313780@qq.com*
[3] *Hubei Key Laboratory for High-efficiency Utilisation of Solar Energy and Operation Control of Energy Storage System, Hubei University of Technology, 430068, China, 1039144539@qq.com*

Because the basic structure of the photovoltaic grid-connected inverter is the same as the active power filter, a unified control of the photovoltaic grid-connected inverter and the active filter can be realised. At present, the unified control system is mainly based on the detection method of three-phase voltage balance when compensating for the side harmonics of the power grid. However, in actual working conditions, the three-phase voltage imbalance may occur from time to time. At this time, the detection error of the voltage phase angle is large， harmonic response slows down, the actual compensation will have a large delay, reducing the system's harmonic compensation speed, resulting in poor side-by-side harmonic filtering effect. Aiming at the problem of harmonic compensation speed reduction, an improved harmonic detection method is proposed in this paper. When the three-phase grid voltage shows unbalanced phenomena such as phase shift and amplitude variation, the positive and negative sequence voltages are park-transformed at the same time. Through the current average module to get the fundamental wave voltage, and then accurately calculate the positive phase voltage phase angle, to ensure the speed of harmonic detection to improve the harmonic dynamic compensation effect. The simulative study of the improved harmonic detection algorithm is carried out by building a simulation model of a PV grid-connected and active power filtering unified control system in MATLAB/Simulink. The simulation results show that the improved harmonic detection algorithm can accurately extract the voltage phase， perform harmonic compensation quickly and increase the compensation speed of the entire system by 0.057s when the three-phase voltage is unbalanced.

Keywords: Three-phase voltage unbalance, PV grid-connected, Harmonic compensation, Park transformation

1. INTRODUCTION

Photovoltaic power generation system will be affected by weather and environmental factors, so photovoltaic power generation will be restricted by illumination. However, the active power filter is not limited by these restrictions, and it is more convenient to operate. Before the unified control, the control strategies of the two control systems should be analysed. MPPT technology and DC converter are used to output stable DC energy, which is converted into AC energy by modulation technology. Finally, the active power energy is transferred to the grid. In the operation of active power filter, the stability of DC energy can guarantee the stable output of AC power, so the above two functions can be realised only by using a certain control strategy.

The unified control strategy is mainly embodied in the synthesis algorithm of the instruction current. When the light intensity is suitable, photovoltaic cell starts to output the DC power, but the system only outputs the active grid-connected current [6]. When the light intensity is weak or the photovoltaic cell is in the absence of light, the photovoltaic cell has no output, so there is no energy transmission to the power grid. In this moment, the active power filter function is realised by the adjustment algorithm, detecting harmonic currents in power grid and compensating reactive power and harmonics in power system by a certain control technology. When the illumination is not enough, the system has excess capacity, and two functions can be realised at the same time. First, the active current is still generated by the MPPT technology, then the compensation current is generated by the harmonic and reactive power detection techniques, and finally the two kinds of currents are synthesised. While the photovoltaic capacity is injected into the grid to the maximum extent, the remaining capacity is used in the active power filter. The control structure diagram with photovoltaic power generation and active power filter is shown in Figure 1.

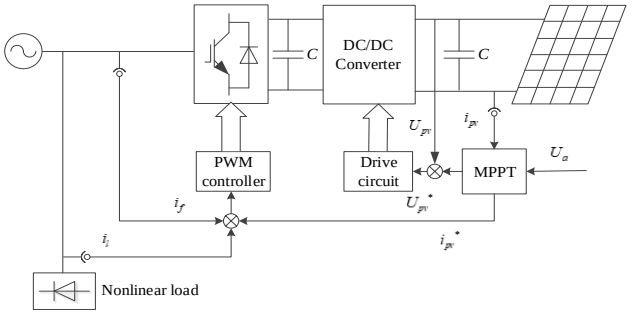

Figure 1: unified control structure block diagram

In view of the different working conditions above, the control strategy can be adjusted in time to make the photovoltaic power system work in the optimal state, which can not only reduce the investment of equipment, improve the utilisation of equipment, but also can make rapid compensation to the harmonics of the system, and improve the power quality of the power grid [9-10].

2. IMPROVED HARMONIC DETECTION ALGORITHM

In traditional i_p、i_q, low pass filter is needed. Because of the characteristic of digital low pass filter, it takes a long time to track the signal of the system. The dynamic performance is not very good, and the detection time of harmonic current has several times of periodic delay. The traditional detection method is based on the situation when the three-phase voltage is symmetrical, but in the operation of the power system, the voltage imbalance usually occurs, so it is necessary to adopt a new detection method to deal with the above situation. And in the general current control mode or active damping technology, all the closed-loop control is in the d,q coordinate system, but the traditional current detection method, the harmonic current instruction value is in the three phase coordinate system, so it is not easy to control. In this paper, the harmonic current detection method is improved, that is to calculate the harmonic current instruction value in the two phase d,q coordinate system, then, after the closed-loop control is adopted, the harmonic current instruction value is inverse transformed to obtain the three-phase harmonic current value, and then the inverter is controlled.

When the three-phase voltage is asymmetric, the phase angle obtained from the single-phase phase-locked loop is traditionally used as the phase angle of the standard rotation vector, which will reduce the accuracy of the measurement. The positive sequence part of the unbalanced three-phase voltage can be expressed as:

Equation 2: $\begin{bmatrix} U_{a1} \\ U_{b1} \\ U_{c1} \end{bmatrix}$ $\begin{bmatrix} U_{a1} \\ U_{b1} \\ U_{c1} \end{bmatrix} = \begin{bmatrix} U^{+}\sin(\omega t+\varphi_u^{+}) \\ U^{+}\sin(\omega t+\varphi_u^{+}-\frac{2}{3}\pi) \\ U^{+}\sin(\omega t+\varphi_u^{+}+\frac{2}{3}\pi) \end{bmatrix}$

The negative sequence part of the three-phase voltage can be expressed as

Equation 2: $\begin{bmatrix} U_{a2} \\ U_{b2} \\ U_{c2} \end{bmatrix}$ $\begin{bmatrix} U_{a2} \\ U_{b2} \\ U_{c2} \end{bmatrix} = \begin{bmatrix} U^{-}\sin(\omega t+\varphi_u^{-}) \\ U^{-}\sin(\omega t+\varphi_u^{-}-\frac{2}{3}\pi) \\ U^{-}\sin(\omega t+\varphi_u^{-}+\frac{2}{3}\pi) \end{bmatrix}$

The zero sequence voltage of the three-phase voltage is U_0 , $\varphi_u^{+}=\varphi_u$, and

Equation 3: U_a, U_b, U_c $\begin{cases} U_a = U_{a1}+U_{a2}+U_0 \\ U_b = U_{b1}+U_{b2}+U_0 \\ U_c = U_{c1}+U_{c2}+U_0 \end{cases}$

So $U_0 = 1/3(U_a+U_b+U_c)$, u_a^{*}、u_b^{*}、u_c^{*} are the sum of positive sequence voltage and negative sequence voltage. When the grid voltage with the similar ip、iq transform, then the average value calculation module is used to get the Equation (4).

Equation 4: $\begin{bmatrix} \overline{U_p} \\ \overline{U_q} \end{bmatrix}$ $\begin{bmatrix} \overline{U_p} \\ \overline{U_q} \end{bmatrix} = \begin{bmatrix} \sqrt{3}U_1^{+}\cos\varphi_u^{+} \\ -\sqrt{3}U_1^{+}\sin\varphi_u^{+} \end{bmatrix}$

Unbalanced grid voltage can also lead to unbalanced current. i_a、i_b、i_c are three phase load current, can be expressed as

Equation 5: i_a, i_b, i_c $\begin{cases} i_a = \sum_{k=1}^{\infty}\sqrt{2}I_{km}\sin(k\omega t+\varphi_{uk}) \\ i_b = \sum_{k=1}^{\infty}\sqrt{2}I_{km}\sin[k(\omega t-\frac{2}{3}\pi)+\varphi_{uk}] \\ i_c = \sum_{k=1}^{\infty}\sqrt{2}I_{km}\sin[k(\omega t+\frac{2}{3}\pi)+\varphi_{uk}] \end{cases}$

Where $k = 6n\pm 1$, k is a positive integer. After the average current calculation module is adopted and according to the transformation formula of ip and iq, as Equation (6), then the fundamental active current and the fundamental reactive current can be obtained.

Equation 6: $\begin{bmatrix} i_p \\ i_q \end{bmatrix}$ $$\begin{bmatrix} i_p \\ i_q \end{bmatrix} = C_{32} C' \begin{bmatrix} i_a \\ i_b \\ i_c \end{bmatrix}$$

Where

Equation 7: C_{32} $$C_{32} = \sqrt{\frac{2}{3}} \begin{bmatrix} 1 & -1/2 & -1/2 \\ 0 & \sqrt{3}/2 & -\sqrt{3}/2 \end{bmatrix}$$

Equation 8: C' $$C' = \begin{bmatrix} \sin(\omega t + \varphi_{uk}) & -\cos(\omega t + \varphi_{uk}) \\ -\cos(\omega t + \varphi_{uk}) & -\sin(\omega t + \varphi_{uk}) \end{bmatrix}$$

Where $\sin(\omega t + \varphi_{uk})$ $\cos(\omega t + \varphi_{uk})$ can be obtained by the phase-locked module of the voltage.

Then through inverse transformation, can be obtained as

Equation 9: $\begin{bmatrix} i_{af} \\ i_{bf} \\ i_{cf} \end{bmatrix}$ $$\begin{bmatrix} i_p \\ i_q \end{bmatrix} = C_{32} C' \begin{bmatrix} i_a \\ i_b \\ i_c \end{bmatrix}$$

Then the Grid connected instruction current can be expressed as

Equation 10: $\begin{bmatrix} i_p \\ i_q \end{bmatrix}$ $$\begin{bmatrix} i_p \\ i_q \end{bmatrix} = \sqrt{3} \begin{bmatrix} \sum_{k=1}^{\infty} I_{km} \cos[(1 \mp k)\omega t \mp \varphi_{uk}] \\ \sum_{k=1}^{\infty} \pm I_{km} \sin[(1-k)\omega t - \varphi_{uk}] \end{bmatrix}$$

When $k = 6n+1$, take the minus sign. When $k = 6n-1$, take the positive sign. Bring $k = 6n \pm 1$ into Equation (10), derive the Equations (11) and (12) through calculation.

Equation 11: i_p $$\begin{aligned} i_p = \sqrt{3}[&I_1 \cos(-\varphi_{1u}) + I_5(\cos 6\omega t + \varphi_{5u}) + \\ &I_7 \cos(-6\omega t - \varphi_{7u}) + I_{11} \cos(12\omega t + \varphi_{11u}) \\ &+ I_{13}(-12\omega t - \varphi_{13u}) + \cdots \end{aligned}$$

Equation 12: i_q $$\begin{aligned} i_q = \sqrt{3}[&I_1 \cos(-\varphi_{1u}) + I_5(\cos 6\omega t + \varphi_{5u}) + \\ &I_7 \cos(-6\omega t - \varphi_{7u}) + I_{11} \cos(12\omega t + \varphi_{11u}) \\ &+ I_{13}(-12\omega t - \varphi_{13u}) + \cdots \end{aligned}$$

It can be seen from the above formula that after the coordinate transformation of the grid current, the active current is changed from the original $6n \pm 1$ to the harmonic $6n$ times. The reactive current changed from the original to even harmonics, such as 4 / 6 / 10 / 12 and so on. According to the orthogonality of sinusoidal and cosine functions, the integral of sinusoidal and cosine functions in a period is 0, but there will be one cycle delay. By studying the integration method, it is found that the minimum common multiple of each harmonic cycle can be used as the integral interval, and the integral value is also zero, so the current integral module can be used to filter. The schematic diagram of the integral module is shown in Figure 2.

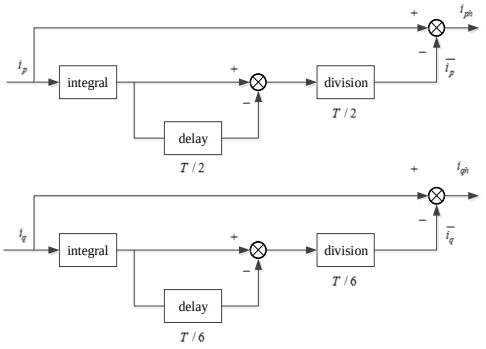

Figure 2: Principle of current mean calculation

At this time, the minimum common multiple of the AC component of active current is $T/6$, the minimum common multiple of AC component of reactive current is $T/2$. The DC component after the AC component is filtered by mean value is (13).

Equation 13:

$$\begin{bmatrix} \overline{i_p} \\ \overline{i_q} \end{bmatrix} \qquad \begin{bmatrix} \overline{i_p} \\ \overline{i_q} \end{bmatrix} = \frac{1}{T}\begin{bmatrix} \int_t^{t+T/6} i_p dt \\ \int_t^{t+T/2} i_q dt \end{bmatrix} = \sqrt{3}\begin{bmatrix} I_1 \cos(-\varphi_1) \\ I_1 \sin(-\varphi_1) \end{bmatrix}$$

Compared with the traditional low-pass filtering method, the delay current average method for harmonic current detection is shorter and easier to be realised digitally. Therefore, in the case of voltage imbalance, the harmonic current detection algorithm block diagram is shown in Figure 3.

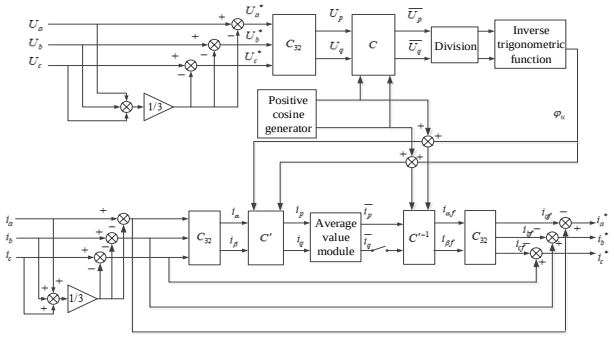

Figure 3: Three-phase unbalanced current detection algorithm

As a result of the asymmetry of three-phase voltage, phase shift and amplitude change, will lead to the detection error of harmonic current become larger, or even failure. Therefore, the improved detection algorithm can shorten the detection time and improve the accuracy of harmonic current detection. According to Equation (6), the following matrix is obtained by matrix transformation

Equation 14:

$$\begin{bmatrix} \overline{i_p} \\ \overline{i_q} \end{bmatrix} \qquad \begin{bmatrix} \overline{i_p} \\ \overline{i_q} \end{bmatrix} = C_{32}C'\begin{bmatrix} i_{af} \\ i_{bf} \\ i_{cf} \end{bmatrix}$$

In order to obtain harmonic instruction current value in d and q coordinates, the difference between Equation (6) and Equation (14) obtained to Equation (15).

Equation 15: $\begin{bmatrix} i_{ph} \\ i_{qh} \end{bmatrix}$

$$\begin{bmatrix} i_{ph} \\ i_{qh} \end{bmatrix} = \begin{bmatrix} i_p - \bar{i}_p \\ i_q - \bar{i}_q \end{bmatrix} = C_{32}C' \begin{bmatrix} i_a - i_{af} \\ i_b - i_{bf} \\ i_c - i_{cf} \end{bmatrix} = C_{32}C' \begin{bmatrix} i_{ah} \\ i_{bh} \\ i_{ch} \end{bmatrix}$$

Where iph、iqh is harmonic instruction current in d and q coordinate system. It can be seen from (15) that the harmonic instruction current can be calculated first in d and q coordinate system, and then the three-phase harmonic instruction current can be obtained by inverse transformation. Thus, it is convenient to realise closed-loop control of instruction current in d and q coordinate system, as well as other applications. Then the algorithm in Figure 3 is improved to get the current detection algorithm as shown in Figure 4.

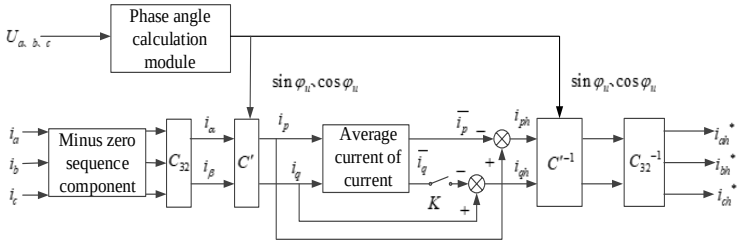

Figure 4: improved harmonic current detection algorithm

The improved ip、iq detection method can realise the phase angle detection when the voltage is unbalanced in three-phase grid, and ensure the accuracy of harmonic detection. At the same time, the average current value module is used instead of the low pass filter to reduce the delay time when the voltage is unbalance. In order to realise the closed loop control of harmonic current, the harmonic instruction current in d and q coordinates is calculated, and then the three-phase harmonic current is obtained by inverting the inverter.

3. PHOTOVOLTAIC GRID CONNECTED AND HARMONIC CURRENT SYNTHESIS INSTRUCTION ALGORITHM

The instruction current is composed of two parts: one is the active current of the PV grid connected, the two is the harmonic instruction current from the load side. At this time the inverter consists of three working states, one is independent photovoltaic power generation, the two is independent active filtering, and the three is simultaneous photovoltaic grid and active filtering. When the active filter and PV grid are conducted at the same time, the synthetic command current Equation (16)

Equation 16: i_{ref}^*

$$i_{ref}^* = i_{pv}^* + i_h(t)$$

Where i*pv is active instruction current of photovoltaic grid connected power generation, obtained by MPPT technology. The harmonic command current is obtained by the improved harmonic detection algorithm, and the harmonic current will be affected by the capacity of the inverter and other factors. The schematic diagram of the combined instruction algorithm of photovoltaic grid-connected and active filter is shown in Figure 5.

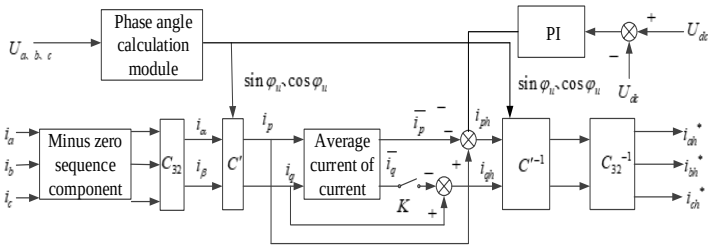

Figure 5: unified control of synthetic command current map

The unified system can provide grid connected active current, and provide reactive harmonic current with polarity opposite to the power grid harmonic. And the full compensation of harmonic and reactive power can be realised

4. SIMULATION RESEARCH AND RESULT ANALYSIS

In MATLAB/Simulink environment, the simulation model of photovoltaic grid-connected and active power filter unified control system is built. The simulation model mainly includes three-phase power supply, an uncontrolled rectifier bridge with inductance resistance to simulate nonlinear load, photovoltaic solar array, harmonic current detection module. Verify the control strategy mentioned above. The main parameters in the unified control model are Table 1.

Table 1: simulation model of the main parameters

Simulation parameters	parameter values
Phase voltage of three phase power supply	220V/50HZ
Total capacity of three phase system	30KVA
DC side voltage of photovoltaic inverter	700V
DC side voltage PI controller parameters	Kp=5.5 Ki=9.1
Parameter of quasi PR controller	Kp=2 Kr=15
LCL filter parameters	L1=0.15mH L2=0.1mH C=5uF
DC side capacitance of photovoltaic inverter	C=4700 uF
Uncontrolled rectifier bridge load	L=2mH R=25

In order to verify the feasibility of unified control of active power filter and grid connected photovoltaic system, a unified control model is established. Firstly, the harmonic wave caused by the nonlinear load is compensated , and then photovoltaic grid connected power generation is carried out .Simulation results shown in Figure 6.

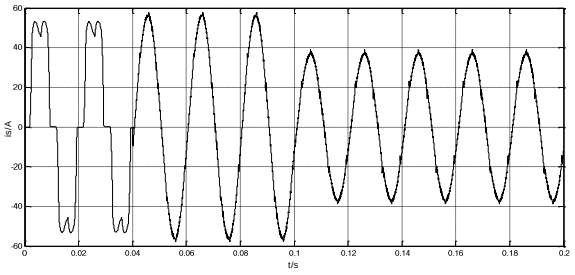

Figure 6: Photovoltaic grid-connected and active filter unified control simulation

The system is put into operation in 0.04 seconds, the active power filtering is conducted first. It can be seen from the image above that the “saddle wave” caused by nonlinear load shows a sinusoidal wave shape after active power filtering, and the harmonic content is obviously reduced. PV grid-connected begins at 0.1s. When both active filtering and photovoltaic grid are simultaneously carried out, the unified control system inputs active current to the power system, so the active current from the grid drops from 56.63A to 38.21A. The above results verify the feasibility of the unified control function.

In the traditional harmonic detection method, the harmonic current has at least one period delay due to the detection characteristics of the low-pass filter. Based on the average current detection algorithm, the minimum delay can be reduced to one sixth of a period. In the traditional detection method, the low pass filter uses a two order filter with cut-off frequency of 20HZ. The improved detection algorithm is compared with the traditional detection algorithm for the active current and reactive current contrast, as shown in Figures 7 (a), (b) and 8 (a) (b).

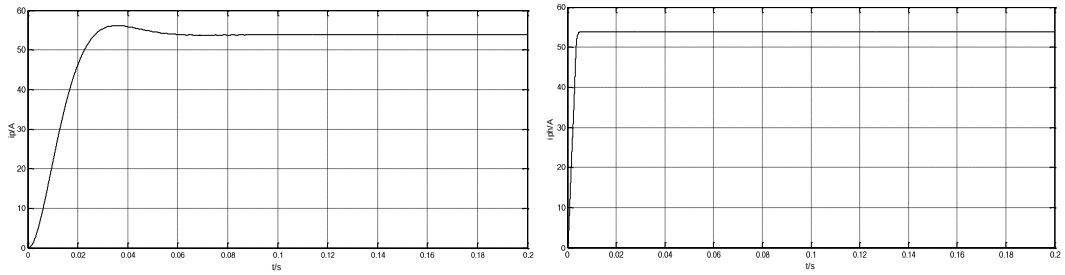

Figure 7: (a) Conventional detection method Active current curve

Figure 7: (b) Improved detection algorithm active current curve

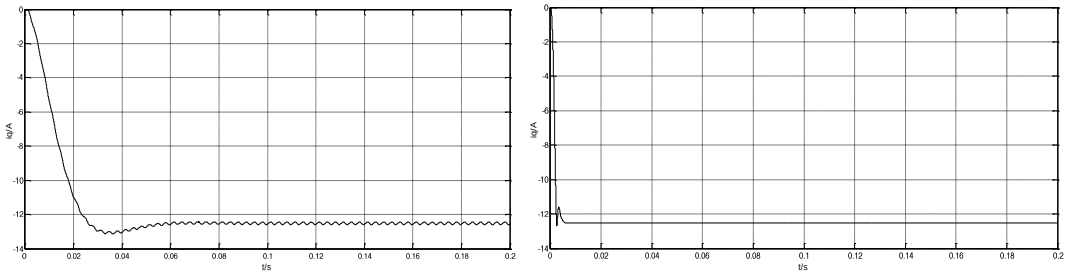

Figure 8: (a) Traditional detection algorithm reactive current curve

Figure 8: (b) Improved detection algorithm reactive current curve

By comparing the two diagrams, it can be found that when the active power filter is applied, In the traditional harmonic detection method, The detected active and reactive currents are not stable until 0.06s and there is a certain overshoot. It shows that harmonic detection has a delay of nearly three periods. From Figures 7 and 8 (b), we can see that the active and reactive currents at 0.0033s are stable and there is no overshoot. Because the harmonic detection methods are usually based on three-phase grid voltage balance. However, there are negative sequence and zero sequence voltage components when the grid voltage is unbalanced. Therefore, the detection of voltage phase angle is more error, or even invalid. Therefore, avoid common phase-locked loops to determine phase angle. The single-phase short-circuit fault of three-phase power supply is adopted to simulate the three-phase voltage imbalance, when single-phase short-circuit occurs, three phase voltage will have negative sequence and zero sequence voltage components. The simulation shows a single-phase grounding short circuit in 0.1s. Figure 9 shows the three-phase voltage waveform before and after the single-phase grounding short circuit fault.

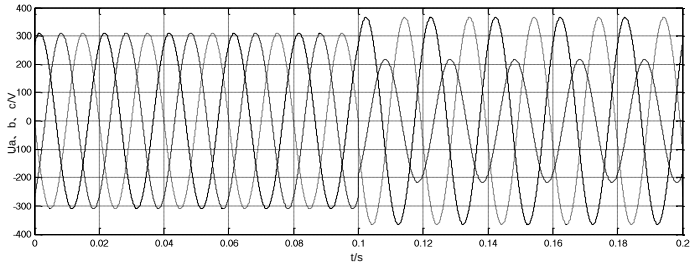

Figure 9: Single-phase ground short-circuit fault before and after the grid voltage waveform

As can be seen from the figure above, the three-phase voltage imbalance at 0. 1s, in this case the phase locked loop will lock the voltage deviation. In order to verify the proposed harmonic detection method can extracted accurately, the voltage phase angle when the three-phase voltage is unbalance, and the initial phase angle of the three-phase power supply voltage is 60 degrees. The initial phase angle of the three phase supply voltage is 60 degrees. Figure 10 is the phase angle extracted from the traditional phase-locked loop and the improved detection method.

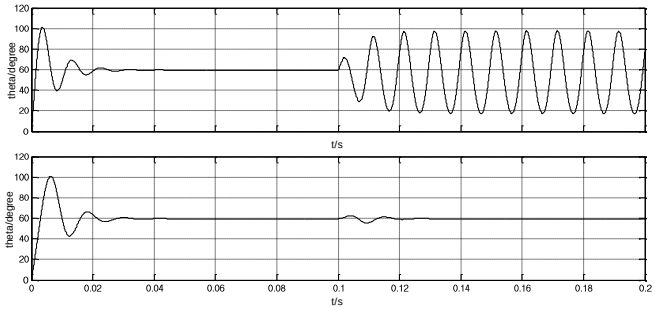

Figure 10: Comparison of traditional phase-locked and improved detection extraction phase angle

It can be seen from the above diagram that the voltage phase angle can be accurately extracted in two ways before the single phase short circuit fault occurs in 0.1s. However, in the 0.1s failure, the traditional phase-locked loop module can produce a large amplitude sinusoidal oscillation, and the improved detection method can still accurately extract the voltage phase. When the voltage of three-phase power grid is unbalanced, the traditional phase-locked loop cannot accurately lock phase angle of positive-sequence voltage, so the effect of compensation will become very poor and even ineffective. Figure 11 (a) (b) compares the harmonic compensation effect between the traditional harmonic detection method and the improved harmonic detection method when the three-phase voltage is unbalanced. Figure 12 is the FFT analysis diagram of the compensation effect of the improved harmonic detection method when the three-phase voltage is unbalanced.

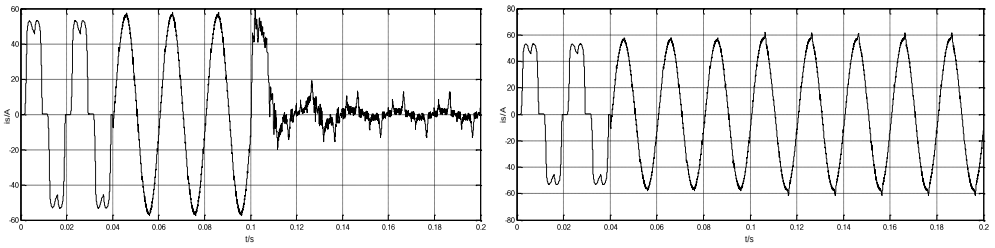

Figure 11(a): Three-phase voltage unbalance The traditional harmonic detection method compensates the effect

Figure 11(b): Three-phase voltage unbalance improved harmonic detection method to compensate for the effect

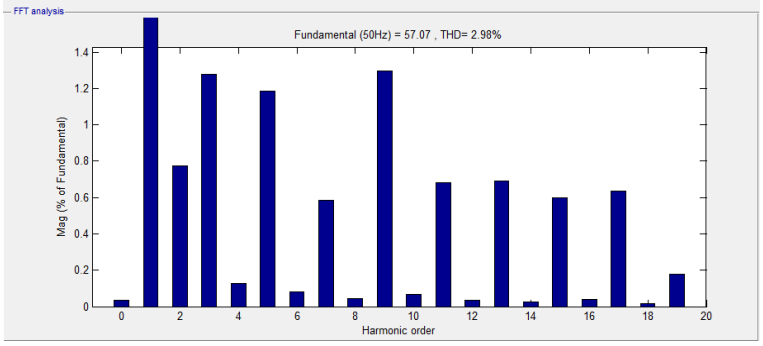

Figure 12: Improved harmonic detection method compensation effect FFT analysis

From Figure 11(a), it can be seen that when the three-phase voltage appears single-phase grounding short circuit, due to the deviation of the three-phase voltage amplitude, and the three-phase voltage is no longer the standard positive sequence voltage, the zero sequence and negative sequence voltage appear, so the compensation effect is obviously invalid at this time, and the traditional harmonic detection method cannot deal with this situation at this time. It can be seen from Figure 11(b) that the improved detection method can detect harmonics accurately and compensate for harmonics even though the voltage is unbalanced. As we can see from the FFT analysis of Figure 12, although the total harmonic content now is 2.98%, which is larger than the total harmonic content of 1.84% in equilibrium state, it is still in the safe range. The results show that when the three-phase voltage is unbalanced, the detection method can detect the harmonic accurately and suppress the harmonics.I.

5. CONCLUSION

In this paper, an improved harmonic detection method based on photovoltaic grid-connected unified control strategy is proposed, which can still detect harmonics and carry out harmonic suppression quickly and accurately, when the voltage of three phase network is unbalanced. The simulation results show that the system realises the unified control of PV grid connected and active power filter. The improved harmonic detection method can detect harmonic accurately, and the compensation effect is good and the time delay is short. This method has a good compensation accuracy and speed.

6. REFERENCES

Gao Z-Z, Wang L-Z, Zhao L-C, et al. Research on Control Strategy of Photovoltaic Inverters under Grid Unbalance Condition[J]. Power Capacitor and Reactive Compensation, 2016, 37(1):71-75.

Tian P, Xuan W, Niu Y. Harmonic Resonance Restraint of LCL Photovoltaic Grid-connected Inverter Based on Notch Control[J]. Power System Protection and Control, 2016, 44(14):82-88.

Liu S, Li C, Li Q, et al. Characteristic Analysis and Sensitivity Calculation of Series Harmonic Resonance in Power System[J]. Power System Protection and Control, 2015(9):21-27.

Noroozian R, Gharehpetian G B. An investigation on combined operation of active power filter with photovoltaic arrays[J]. International Journal of Electrical Power & Energy Systems, 2013, 46: 392-399.

Li M. Harmonic Suppression Method for Electric Vehicle Charging Station Based on Y/Y and Y/Δ Transformers[J]. Journal of Electric Power Science and Technology, 2014, 29(2):82-88.

Zaveri N, Chudasama A. Control strategies for harmonic mitigation and power factor correction using shunt active filter under various source voltage conditions[J]. International Journal of Electrical Power & Energy Systems, 2012, 42(1): 661-671.

Zhang Z, Zhang L, Wang B, et al. Design and implementation of three-phase photovoltaic grid-connected inverter voltage ring[J]. Power Electronics Technology, 2017(11):20-23.

Jiang W, Wu Z, Li W, et al. Control Strategy for Suppression of Negative-sequence Current Grid-connected Inverter when Grid Is Asymmetric[J]. Transactions of China Electrotechnical Society, 2015, 30(16):77-84.

Trinh Q N, Lee H H. An advanced current control strategy for three-phase shunt active power filters[J]. Industrial Electronics, IEEE Transactions on, 2013, 60(12): 5400-5410.

Zhang X, Ma Y, Li R, et al. Repetitive Control Strategy of Grid-connected Inverter in Two-phase Static Coordinate System[J]. Transactions of China Electrotechnical Society, 2016, 31(9):85-91.

Xie Z, Wang X, Zhang X, et al. Harmonic Damping Based Harmonic Suppression Optimisation Strategy for Three-phase LCL Grid-connected Inverter[J]. Electric Power System Automation, 2015, 39(24): 96-103.

You Y, Song Z. New method for calculating converter current command under unbalanced grid[J]. Power Electronics Technology, 2017(6): 71-74.

189: Constant power constant voltage startup procedures for VSC-LCC based hybrid pseudo bipolar HVDC system

Yu YU[1], Hongliang LI[2], Ziqiang XI[3]

[1] Yu YU, Hubei Collaborative Innovation Center for High efficiency Utilisation of Solar Energy, Hubei University of Technology, Wuhan，430068，P. R. China，minetoybox@163.com

[2] Hongliang LI, Hubei Collaborative Innovation Center for High efficiency Utilisation of Solar Energy, Hubei University of Technology, Wuhan，430068，P. R. China， Leectric@outlook.com

[3] Ziqiang XI, Hubei Collaborative Innovation Center for High efficiency Utilisation of Solar Energy, Hubei University of Technology, Wuhan， 430068，P. R. China，695936405@qq.com

Hybrid bipolar HVDC technology is a new research hotspot for the grid-connected of new energy power generation system. In order to reduce the undesired impacts and damages on the HB-HVDC system and the connected AC system during the startup procedures, appropriate startup control strategy should be dedicatedly designed. There are three steps in the startup procedures. Firstly, the VSC and LCC are both locked, the inverter parallel diodes of the VSC are used for charging the capacitance in the DC side by uncontrolled rectifier. Secondly, when the dc voltage achieves 0.52pu, the VSC converter is unlocked, the controlled variable of active power is DC voltage and the controlled variable of passive power is passive power with the instruction value of 1.0pu. The DC voltage will continue to rise. Thirdly, when the DC voltage achieves to the instruction value, the switch in parallel with the current limiting resistor is closed and the resistor exits, the voltage will keep stability. Then, the LCC inverter is unlocked with the constant DC voltage control, the voltage instruction is 1.0pu. At the same time, the VSC converter uses active power as the controlled variable of active power with the instruction value increasing from zero to 1.0pu. The entire startup procedures are complete. The steady-state control strategy and start-up strategy are proposed based on the deduced quasi-steady state mathematic model of the hybrid pseudo bipolar HVDC system. The hybrid pseudo bipolar HVDC simulation system is built in PSCAD/EMTDC, and the effectiveness of the proposed steady-state control strategy and start-up strategy are illustrated. The entire startup process is smooth and stable, and the control strategy of the hybrid pseudo bipolar HVDC system is perfect. After startup, the system tracks target reference accurately and operates stably.

Keywords: Pseudo bipolar, LCC-HVDC, VSC-HVDC, HB-HVDC, Start-up procedures.

1. INTRODUCTION

HB-HVDC (hybrid bipolar high voltage direct current) transmission technology is a combination of conventional and flexible DC transmission. That is, one end of a HB-HVDC system uses a thyristor based LCC (line commutation converter), and the other end uses a VSC (voltage source converter) based on IGBT (Insulated Gate Bipolar Transistor) or GTO (Gate Turn-Off Thyristor). HB-HVDC technology combines the advantages of the two HVDC transmission technologies. The control is highly flexible and the cost is low. It has a good application prospect in the energy convergence of renewable energy generation, asynchronous grid interconnection, and long-distance transmission, becoming a new research hotspot (Wang et al, 2017).

The start-up control process of the hybrid HVDC system is the precondition and basis for the normal operation of the system. Serious overvoltage and overcurrent phenomena will occur when the hybrid HVDC system is started without a special start-up control strategy, which endangers the safety of the converter device. Therefore, the start-up control of the hybrid HVDC system needs to be studied. Ye, An, Pei, Han & Qi (2017) give the starting characteristics and steps of the conventional LCC-HVDC system. Other literature (Yu et al, 2016; Ni et al, 2017; Guo et al, 2016) studied the start-up control of VSC-HVDC and revealed the cause of over-current generated by VSC during the start-up process. Since a hybrid DC transmission system is a combination of voltage source converter and current source converter, none of these startup methods can be applied directly to the hybrid DC system. Omar (2010) and Fan et al (2014) give a start-up control method of a single-stage LCC-VSC hybrid HVDC transmission system. Ni (2017) gives a study of start-up control of a HB-HVDC power transmission system. Up to now, there is no literature to study in detail of the start-up process of pseudo dual-stage VSC-LCC HVDC system.

At present, new energy power generation has been vigorously developed in China. The VSC-LCC hybrid HVDC system is well-suited for the generation and grid interconnection of renewable energy, and asynchronous AC grid interconnection. In this paper, the start-up control of a pseudo bipolar VSC-LCC hybrid HVDC system is studied. The VSC-LCC hybrid HVDC is a hybrid HVDC system that uses VSC and LCC on the rectifier inverter side, respectively. The VSC can accurately control the size of the transmitted active power. The voltage of the AC system bus can be stabilised by compensating the reactive power of the AC system. The LCC converter on the inverter side retains the advantages of low DC switching losses, low investment, mature technology, and simple control. This topology is suitable for occasions where the receiving end grid is strong and has a wide range of application prospects (Ramírez, Castellanos and Calderón, 2017; Suzuki et al, 1997; Liu & Xu, 2016; Lei, Wang & Zeng, 2013; Tang, Xu & Xue, 2013).

This paper presents the topological structure and mathematical model of a pseudo bipolar VSC-LCC HVDC system. A cooperative control strategy is needed between the rectifier side VSC and the inverter side LCC in the pseudo bipolar VSC-LCC hybrid HVDC system to ensure the power balance between the two stations. This paper proposes a three-section startup scheme to complete a process from a shutdown condition to normal operation. Finally, a pseudo bipolar VSC-LCC hybrid HVDC system model is established in the PSCAD/EMTDC simulation software. The simulation results prove that the three-section start-up control scheme proposed in this paper is feasible, and the whole start-up process is smooth and stable without over-voltage or over-current phenomena. The strategy, which is designed for the hybrid DC system in this paper, is proved to be correct and reasonable. After the startup is complete, the system operates stably by accurately tracking the target reference value.

2. TOPOLOGICAL STRUCTURE AND MATHEMATICAL MODEL OF PSEUDO BIPOLAR VSC-LCC HYBRID HVDC SYSTEM

2.1. Topological structure

The pseudo bipolar system, not as traditional bipolar DC transmission system, but composed of a VSC converter. This structure is called a pseudo bipolar structure (Liu et al, 2015). The topological structure of a double-end pseudo bipolar VSC-LCC hybrid DC transmission system is shown in Figure 1. The AC system 1 is connected to a three-phase two-level bridge-type VSC converter by a transformer T1. The system side of transformer T1 is provided with an AC circuit breaker S1 and a current limiting resistor with a parallel switch. There is a characteristic harmonic filter between transformer T1 and the VSC converter. The shunt capacitor C is provided in the DC side of VSC converter to stabilise the DC voltage and filter out some of the harmonics. The voltage regulated capacitor C is grounded on the DC side. The 12-pulse LCC converter with the intermediate point on the inverter side is connected to the AC system 2 via transformers T2 and T3. The smoothing reactor is provided on the DC side of the LCC converter, and the shunt filter which filters characteristic harmonics is provided in the AC side.

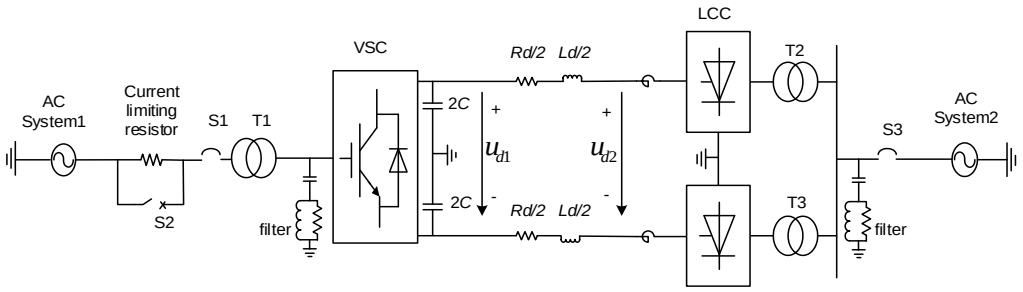

Figure 1: The topology of a VSC-LCC hybrid pseudo bipolar HVDC

2.2. Mathematical model

The rectifier side of pseudo bipolar VSC-LCC hybrid DC transmission system is a three-phase two-level bridge-type VSC. The d- and q-axis components of AC system 1 voltage in the dq rotating coordinate system are u_{sd} and u_{sq}, the d- and q-axis components of the voltage fundamental wave of the VSC rectifier network are u_d and u_q, the d- and q-axis components of the grid current are i_{sd} and i_{sq}, the equivalent resistance and inductance of transformers and phase reactors are R and L, respectively. When the AC voltage of the system 1 is three-phase balanced, set its voltage direction $\dot{U}_S$ to the direction of the d-axis, then $U_S = u_{sd}$, u_{sq} = 0, and the active power delivered from the rectifier side is p_{d1}, and the emitted reactive power is q_{c1}. δ is the angle between system voltage and output voltage of converter station. Then the rectifier side VSC mathematical model is as follows:

$$L\frac{\mathrm{d}i_{sd}}{\mathrm{d}t} = -Ri_{sd} - \omega Li_{sq} + u_{sd} - u_d \tag{1}$$

$$L\frac{\mathrm{d}i_{sq}}{\mathrm{d}t} = -\mathrm{R}i_{sq} + \omega Li_{sd} + u_{sq} - u_q \tag{2}$$

$$\mathrm{C}\frac{\mathrm{d}u_{d2}}{\mathrm{d}t} = \frac{3}{2}(i_q\cos\delta - i_d\sin\delta) + i_d \tag{3}$$

$$p_{d1} = \frac{3}{2}U_S i_{sd} = \frac{3}{2}u_{sd}i_{sd} \tag{4}$$

$$q_{c1} = -\frac{3}{2}U_S i_{sq} = -\frac{3}{2}u_{sd}i_{sq} \tag{5}$$

A 12-pulse converter is used on the inverter side. It consists of two 6-pulse converter units with a voltage phase difference of 30°, which are connected in series on the DC side and in parallel on the AC side. The no-load line voltage on the valve side of the transformer T2 is U_2, the DC voltage on the inverter side is U_{d2}, the DC current is I_d, active power transmitted from the inverter station is P_{d2}, the consumed reactive power is Q_{c2}, the single commutative reactance is X_{r1}, the power factor angle is φ, the trigger angle is β, arc extinction advance angle is γ, and the commutation overlap angle is μ. Then the LCC mathematical model on inverter side is as follows:

$$U_{d2} = 2.7U_2\cos\beta + \frac{6}{\pi}X_{r1}I_d \tag{6}$$

$$\text{or } U_{d2} = 2.7U_2\cos\gamma - \frac{6}{\pi}X_{r1}I_d \tag{7}$$

$$P_{d2} = U_{d2} I_d \tag{8}$$

$$Q_{c2} = P_{d2} \tan\varphi \tag{9}$$

$$\cos\varphi = \frac{1}{2}[\cos\alpha + \cos(\alpha + \mu)] \tag{10}$$

Where u_{d1} and u_{d2} are the DC voltage on converter station and inverter station, L_d and R_d are the equivalent inductance and resistor on DC line, respectively. Then the mathematical model is as follows:

$$I_d = \frac{U_{d1} - U_{d2}}{R_d} \tag{11}$$

Equation (1) - Equation (11) is the mathematical model of VSC-LCC hybrid HVDC system. In the following, the control strategy of hybrid HVDC system startup process is designed based on this mathematical model.

3. CONTROL STRATEGY OF PSEUDO BIPOLAR VSC-LCC HYBRID HVDC SYSTEM

In order to realise the stable operation, the rectifier and inverter sides need to be coordinated in the HB-HVDC system (Oni and Davidson, 2016; Huang, 2015; PSCAD User's Guide, 2009).

At present, new energy grid-connected technology and asynchronous grid interconnection have entered a stage of rapid development, and various new VSC-HVDC topologies and control methods have emerged. In this paper, the control of VSC on the converter side includes internal control and external control. The inner loop controller is a d-q decoupled direct current controller and the outer loop controller is a constant active and reactive power controller (Ni et al, 2017). The reference value of d-axis and q-axis current in the inner loop controller are provided by the outer loop controller. The basic control method is shown in Figure 2.

The control on the rectifier side adopts the double closed loop controller. Inner loop adopts d-q decoupled direct current control method and the outer loop adopts constant active and reactive power control. Active control variable is first switched to active power after DC voltage. The outer loop controller provides reference value of the d-axis and q-axis current for the inner loop controller. The basic control method is shown in Figure 2.

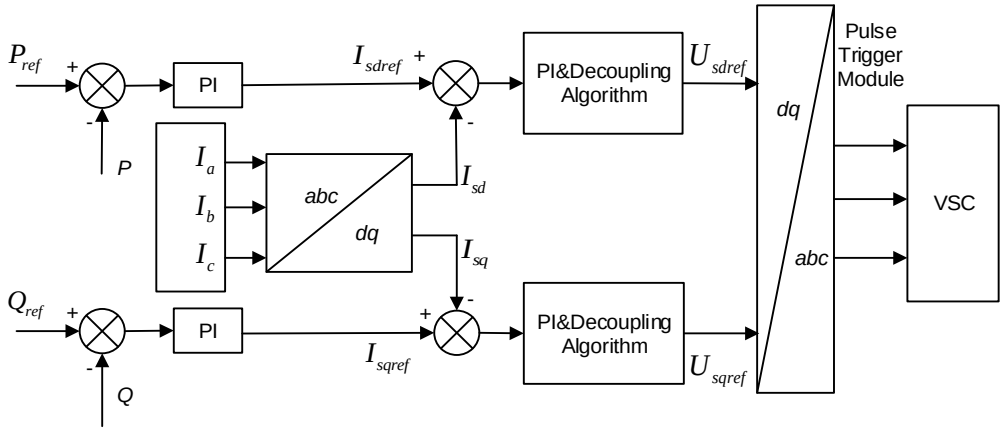

Figure 2: Inner and outer ring control of direct current control

The inner loop controller realises feedforward compensation to the grid voltage and independent decoupling control of d and q axis currents, which improves the dynamic performance of the entire system. Equation (12) gives the desired fundamental voltage output on the AC side of the VSC:

$$\begin{cases} u_{sdref} = u_{sd} - K_{P1}(i_{sdref} - i_{sd}) - K_{I1}\int (i_{sdref} - i_{sd})dt + \omega L i_{sq} \\ u_{sqref} = u_{sq} - K_{P2}(i_{sqref} - i_{sq}) - K_{I2}\int (i_{sqref} - i_{sq})dt - \omega L i_{sd} \end{cases} \tag{12}$$

Where i_{sdref} and i_{sqref} are the current reference value provided from the outer loop. K_{P1} and K_{P2} are the proportional constant, K_{I1} and K_{I2} are the integral constant, in the PI controller of inner current controller.

The LCC converter adopts PI loop controller to control DC voltage on the inverter side. The control block diagram shown in Figure 3.

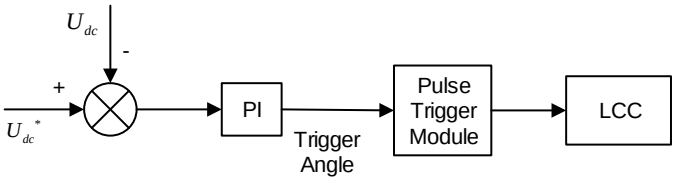

Figure 3: control block diagram of α in LCC

4. START CONTROL STRATEGY FOR VSC- LCC HYBRID HVDC SYSTEM

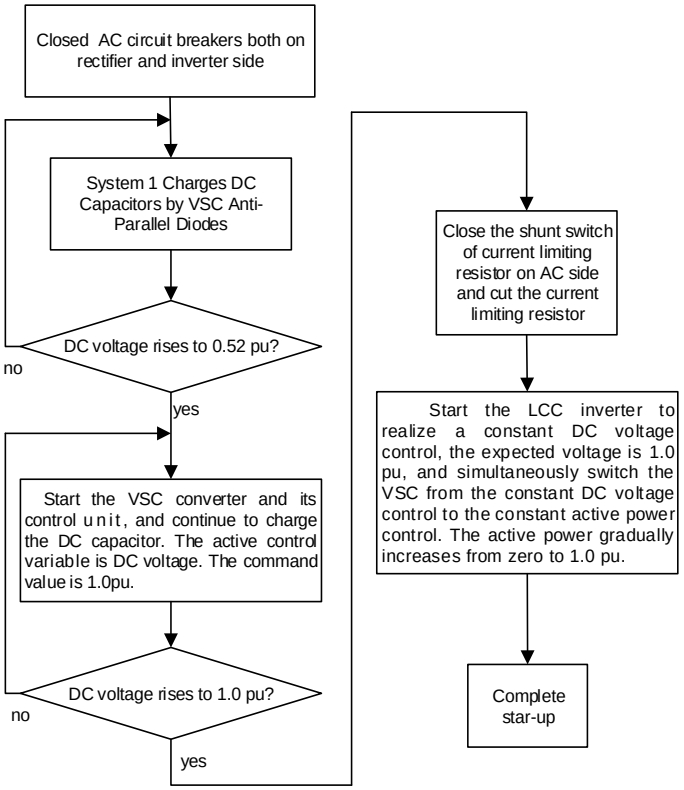

Figure 4: flow diagram of start-up procedures

The hybrid HVDC system shouldn't generate excessive charging overcurrent or overvoltage during the start-up process, but also requires that the DC voltage can quickly reach the normal operating voltage (Ni et al, 2017). Therefore, it is necessary to design a reasonable startup control strategy to complete the smooth start.

The start-up problem of the hybrid HVDC system has its particularity: the start conditions of both end of the converter station have their own characteristics. Before the sending end VSC converter starts, it must have voltage on its DC side. An auxiliary power can be used to charge the DC side capacitor, but it is unrealistic and uneconomical in the hybrid DC transmission field. The solution in this paper is to connect a current limiting resistor in series in the charging circuit during startup. The system uses the anti-parallel diode to realise the uncontrolled rectification to charge the DC capacitor. Current limiting resistor is cut at specific time to reduce losses. The start-up control of the receiver LCC inverter mainly includes the process of changing the LCC from the outage state to the operating state and the transmission power from zero to a given value. In order to reduce overcurrent and overvoltage during startup, and reduce the impact on the AC system during startup, the current regulator on the inverter side gradually increases the DC current from zero to the setting value.

The rectifier station and the inverter station need collaborative control to ensure that the active power flow keeping balance on both side and the DC voltage unchanged. The start-up control strategy of the VSC-LCC hybrid HVDC system adopted in this paper is shown in Figure 4. The system 1 uses the anti-parallel diode as uncontrolled rectifier to charge the DC capacitor. When the DC voltage reaches 0.52 pu (0.2 s), the converter control link is started, in which the active control variable is DC voltage and the reactive control variable is reactive power. The command value is 1.0 pu and the DC voltage will continue to rise. When the DC voltage is stable to the command value (0.9s), the shunt switch of current limiting resistor is closed to cut the resistor on the AC side and the voltage remains stable. At 1.0s, the LCC converter is put to realise the constant DC voltage control and the voltage reference is 1.0pu. At the same time, the active control variable on VSC side is switched from DC voltage to active power, and the active power command value gradually increases from zero to 1.0 pu. Realizing the power flow gradually flows from the VSC side to the LCC side, the entire startup process is complete.

5. SIMULATION OF START PROCESS

In this paper, VSC-LCC hybrid HVDC system model is built in PSCAD/EMTDC simulation software (PSCAD User's Guide, 2009) to verify the effectiveness of the startup and control strategy. The rectifier side is a voltage source converter with a three-phase two-level bridge structure. The LCC on the inverter side is composed of two 6-pulse converter units with a phase difference of 30°, which are connected in series on the DC side and in parallel on the AC side. The basic parameters of the topology of the hybrid HVDC system are shown in Table 1.

Table 1: Parameters of the hybrid HVDC system

	Rectifier side	Inverter side
Converter station rated capacity /MVA	480	480
AC bus voltage / kV	220	220
Converter transformer rated capacity / MVA	480(T1)	240（T2, T3）
Converter transformer ratio （kV/kV）	220/240	220/169.5
Converter transformer leakage reactance （pu）	0.1	0.1
DC line parameters (π-type lumped parameter, positive and negative symmetry)		
DC voltage/ kV		400
DC line equivalent resistance /Ω		2.78
Equivalent inductance /H		0.0318
Equivalent capacitance /μF		11.55

Start the control strategy according to the above, the simulation waveform as shown:

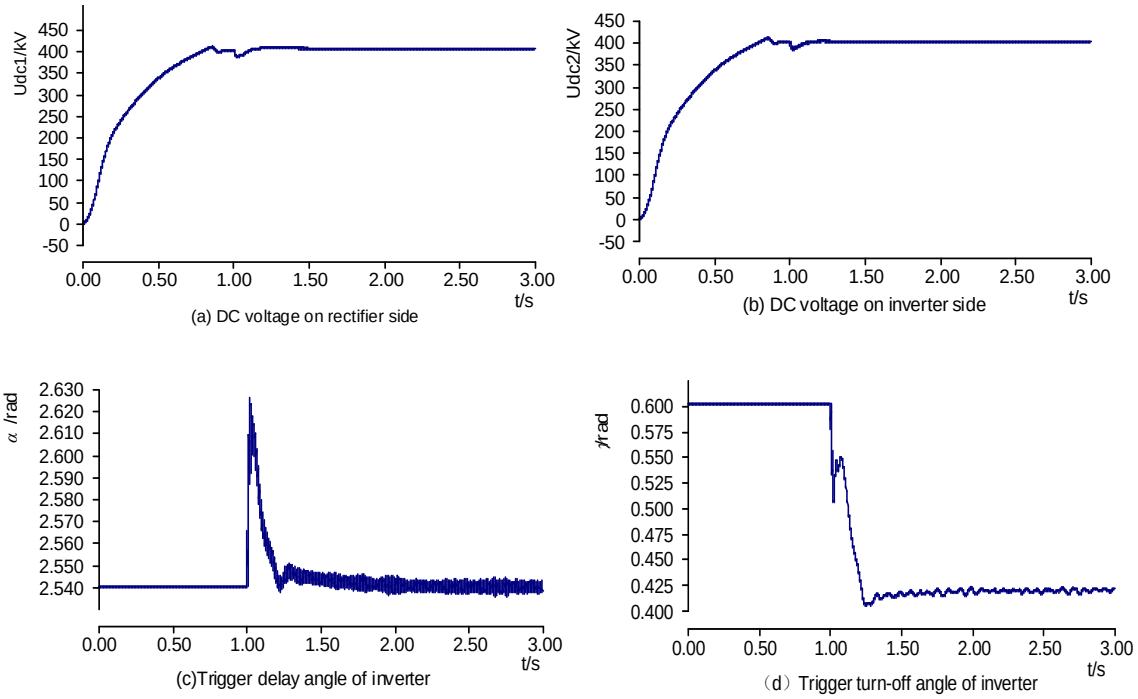

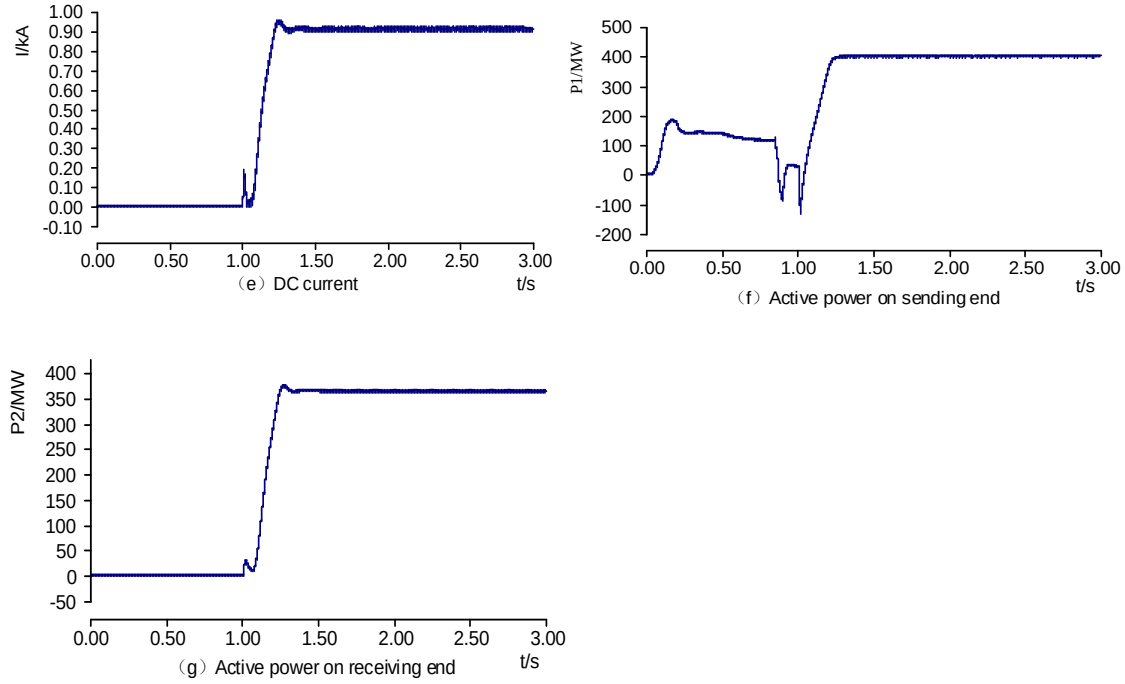

Figure 5: The simulation waveforms of the start-up and the steady state

Figure 5(a) and (b) are the DC voltage variation curves on the rectifier and inverter side respectively during startup. Between 0s-0.2s, the anti-parallel diode is adopted as uncontrolled rectifier to charge the DC capacitor. The voltage rises steadily to 0.52 pu. The VSC converter is started at 0.2s and the DC side voltage continues to rise. When the DC voltage rises steadily to 1.0 pu (0.9s), the current limiting resistor is cut. The LCC will be put to control DC voltage at 1.0s and the expected voltage value is 1.0pu. The DC voltage will stabilise at 400kV after small fluctuation.

Figure 5(c) is the trigger delay angle change curve on the inverter side during start-up process. At 1.0 s, the LCC inverter is put into the DC voltage control system with a control expectation of 1.0 pu. Delayed trigger angle rapidly changes to 146° (2.54 rad), which is the normal operation value, from the initial 151 ° (2.63rad).

Figure 5(d) is the curve of turn-off angle of inverter during start-up. Starting from the moment of 1.0s, the turn-off angle gradually changes from 28.6° (0.5rad) to 24° (0.42ad), which is the normal operation value. The turn-off angle is always greater than zero, thus no commutation failure has occurred during the inversion process.

Figure 5(e) is the DC current curve during start-up. Between 1.0s-1.2s, the active power gradually increases from zero to 1.0 pu and the DC current follows the active power increasing from zero to 1.0 pu without overcurrent. The controller has a quick response and performs well in the system.

Figure 5(f) is the active power change curve on the sending end during the start-up process. Before the LCC inverter is connected to the network, the AC system on sending end has charged the DC capacitor. After the LCC inverter is connected to the network, the active power gradually increases from zero to 1.0 pu. After the moment of 1.2s, the active power rises to the rated value, and the steady-state performance is good.

Figure 5(g) shows the active power change curve of the receiving end during the start-up process. After the LCC inverter is connected to the grid (0.2s), the active power rises from zero to 1.0 pu without apparent overshoot. The entire system enters steady-state operation after the moment of 1.2s. The active power rises to the rated value, and the steady-state characteristics are good. The simulation results verify the effectiveness of the startup and system control strategy proposed in this paper.

6. CONCLUSION

In this paper, a pseudo-bipolar VSC-LCC hybrid HVDC topology composed of VSC and LCC on is constructed. The corresponding start-up control strategy is designed based on its steady state mathematical model. The conclusions are as follows:

(1) The VSC-LCC hybrid HVDC system is well-suited for the interconnection of new energy and the interconnection of asynchronous grids. The VSC side can independently and quickly control the size of the active power and reactive power, and can dynamically compensate the reactive power of the AC system to stabilise the voltage of the AC system bus. The inverter side adopts LCC converter. Since the advantages of low switching loss, low investment, mature technology and simple control, it is applicable to the occasion where the receiving end grid is strong.

(2) The smooth start control scheme proposed in this paper is feasible. The entire startup process is smooth and stable. At the same time, the control strategy of the hybrid HVDC system is perfect and clear. After the startup is complete, the system can maintain the stable operation by accurately tracking the target reference value.

7. ACKNOWLEDGEMENT

Project Supported by the Natural Science Foundation of Hubei Province (2017CFB298).

8. REFERENCES

Wang Y, Zhao W, Yang J, Wang N, Lu Y, Li H. Hybrid high-voltage direct current transmission technology and its development analysis [J]. Automation of Electric Power Systems, 2017, 41(07):156-167.

Ye H, An T, Pei W, Han C, Qi Z. Multi-scale modeling and simulation of transients for VSC-HVDC and AC systems [J]. Proceedings of the CSEE, 2017, 37(07):1897-1909.

Yu Z, Xu A, Gu C, Wang G, Zhao Y. Based on PSCAD/EMTDC fault simulation of VSC-HVDC line [J]. Control Engineering of China, 2016, 23(02):299-302.

Ni X, Zhao C, Guo C, Liu D. Effects of LCC-HVDC on system strength of VSC-HVDC in hybrid dual-infeed HVDC system [J]. Power System Technology, 2017, 41(08):2436-2442.

Guo C, Ni X, Zhao C. A quantitative evaluation method on interaction analysis of hybrid multi-infeed HVDC system [J]. Proceedings of the CSEE, 2016, 36(07):1772-1780.

Omar K. A hybrid LCC-VSC HVDC transmission system supplying a passiveload[D].Oshawa:University of Ontario Institute of Technology, 2010.

Fan X, Guan L, Xia C, Li F, Rao H, Li L. Control of VSC-HVDC in AC/DC hybrid transmission with wind farms integrated [J]. Proceedings of the CSEE, 2014, 34(28):4781-4790.

Ni X, Guo C, Zhao C, Lu Y, Tong K, Xuan J. Effects of LCC-HVDC control mode on the operating characteristic of dual-infeed hybrid HVDC system [J]. Power System and Clean Energy, 2017, 33(01):24-30.

Ramírez M, Castellanos R and Calderón JG, "Modified teaching-learning based optimisation algorithm and damping of inter-area oscillations through VSC-HVDC," 2017 19th International Conference on Intelligent System Application to Power Systems (ISAP), San Antonio, TX, USA, 2017, pp. 1-6.

Suzuki H, Nakajima T, Izumi K, et al. Development and testing of prototype models for a high performance 300 MW self-commutated AC/DC converter[J]. IEEE Transactions on Power Delivery,1997, 12(4): 1589-1601.

Liu S, Xu Z. Study on stable operating region of VSC-HVDC connected to weak AC systems [J]. Proceedings of the CSEE, 2016, 36(01):133-144.

Lei X, Wang H, Zeng N. Simulation research on operation characteristics of hybrid multi-terminal HVDC system with LCC and VSC [J]. Advanced Technology of Electrical Engineering and Energy, 2013, 32(2): 48-52.

Tang Y, Xu Z, Xue Y. Control design of multi-terminal HVDC based on modular multilevel converter [J]. High Voltage Engineering, 2013, 39(11). 2773-2782

Liu S, Xu Z, Li W, Wu C, Wang X, Li L, You G. VSC-HVDC AC voltage-frequency coordination control strategy for improving AC system transient stability [J]. Proceedings of the CSEE, 2015, 35(19):4879-4887.

Oni OE and Davidson IE, "Harmonie distortion of LCC-HVDC and VSC-HVDC link in eskom's cahora bassa HVDC scheme," 2016 IEEE International Conference on Renewable Energy Research and Applications (ICRERA), Birmingham, 2016, pp. 484-489.

Huang S, Wang H, Liao W, Huang S. Control strategy based on VSC-HVDC series topology offshore wind farm for low voltage ride through [J]. Transactions of China Electrotechnical Society, 2015, 30(14):362-369.

PSCAD User's Guide[Z]. HVDC Research Centre Inc., Winnipeg, Canada, 2005.Xia Changliang, Song Zhanfeng. Wind energy in China: current scenario and future perspectives[J]. Renewable and Sustainable Energy Reviews, 2009, 13(8): 1966-1974.

190: Online parameter identification based on split battery model

Tiezhou WU[1], Shan HAO [2], Chun CHANG[3]

[1] *Hubei Key Laboratory for High-efficiency Utilisation of Solar Energy and Operation Control of Energy Storage System, Hubei University of Technology, 430068, China, 1348980399@qq.com*
[2] *Hubei Key Laboratory for High-efficiency Utilisation of Solar Energy and Operation Control of Energy Storage System, Hubei University of Technology, 430068, China, 935978339@qq.com*
[3] *Hubei Key Laboratory for High-efficiency Utilisation of Solar Energy and Operation Control of Energy Storage System, Hubei University of Technology, 430068, China, 543206584@qq.com*

The battery state of charge (SOC) estimation is still one of the key technologies to be solved in the battery management system. The estimation accuracy plays a decisive role in other key issues such as vehicle safety management, residual power monitoring, and battery pack equalisation control. The second-order RC model is a common battery model for SOC estimation. However, there are mutual interferences between the state variables of the traditional second-order RC model, which causes unnecessary oscillations in the initial SOC estimation and affects the stability and accuracy of estimation. Although the split battery model (SBM) can effectively solve this problem, the parameter identification of the model still uses offline parameter identification, which cannot effectively track the model parameters affected by temperature, resulting in low identification accuracy and poor tracking performance. To solve this problem, this paper first analyses how the model solves the problem of mutual interference between state variables; then, through the measurement data and curve simulation obtained by the battery detection system, an OCV-SOC relationship curve is established; then a online parameter identification method, Recursive Least-Squares with Forgetting Factor(FFRLS) based on split battery model is proposed, to make up for the problem that the original offline parameter identification cannot solve the model parameters influenced by temperature, so as to achieve rapid mode parameters identify and improve the recognition accuracy on-line; finally the Unscented Kalman Filter(UKF) algorithm is used to estimate the SOC and verify the effect of the parameter recognition. This article takes a 3.3V 20Ah lithium iron phosphate battery as the research object, through parameter identification comparison experiments and SOC estimation and verification experiments, verifying that FFRLS can effectively improve the estimation accuracy of the model parameters and improve the SOC estimation effect.

Keywords: SOC, second-order RC model, Split battery model, FFRLS, UKF

1. INTRODUCTION

Lithium-ion batteries are an important source of power for pure electric vehicles. Among them, lithium iron phosphate batteries are favoured by many battery manufacturers because of their high specific energy, high specific power, good safety, and long life span (Mao, 2016). In the management of lithium iron phosphate battery, SOC estimation is still one of the key technologies to be solved in the battery management system. The estimation accuracy plays a decisive role in other key issues such as vehicle safety management, remaining power monitoring, and battery pack equalisation control (Schacht, 2017).

According to the existing research, there are two main factors influencing the accuracy of SOC estimation: battery model and estimation algorithm. The literature（Wang, 2016, Wu, 2016,Liang, 2017) introduced several typical battery models, mainly internal resistance model, impedance model, Thévenin model, PNGV model, GNL model, etc. These models or structures are too simple to properly model the dynamic and static characteristics of the battery with low accuracy, or the structure is too complex and the amount of calculation is too large. The literature（Wu, 2016）adopts an improved second-order RC model, taking into account the influence of temperature on the accuracy, and the parameter identification effect has been improved. It is worth pointing out that the battery models used in the above references all use the RC terminal voltage and SOC as the state variables, ignoring the uncertainty relationship between the two, which affects the convergence speed and accuracy of the SOC estimation. The literature（Yang, 2017）proposed a split battery model that can effectively solve this problem. However, the offline identification method is still used for parameter identification of the model. It is unable to effectively track the model parameters affected by many factors, resulting in low identification accuracy.

Based on the split battery model, this paper first analyses the model and then proposes a parameter identification method based on recursive least-squares method with forgetting factor. The on-line identification of the parameters of the model compensates for the problems that cannot be solved by the off-line parameter identification influenced by SOC, temperature, etc., thereby improving the identification accuracy of the model parameters. This paper takes a 3.3V 20Ah lithium iron phosphate battery as the research object, through the parameter identification and comparison experiments and SOC estimation verification experiments, verifying the effectiveness of the proposed method, and the SOC estimation accuracy has improved.

2. SPLIT BATTERY MODEL

2.1. Interference between State Variables

The second-order RC equivalent circuit model is shown in Figure 1, where $U_{(t)}$ is the open-circuit voltage of the battery, $U_{(t)}$ is the battery terminal voltage, R_0 is the internal resistance of the battery, and R_1、C_1、R_2、C_2 are the internal resistance and capacitors formed two RC networks that simulated battery electrochemical polarisation and concentration polarisation respectively (Xia, 2017).

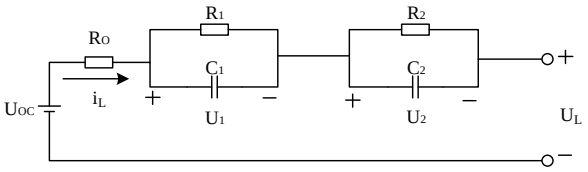

Figure 1: The second-order RC equivalent circuit model

According to the zero input response and zero state response of the RC network and SOC definition, the state equation of the second-order RC equivalent circuit model can be expressed as：

Equation 1:

$$\begin{bmatrix} U_{1,k+1} \\ U_{1,k+1} \\ SOC_{k+1} \end{bmatrix} = \begin{bmatrix} e^{-\frac{T_s}{R_1C_1}} & & \\ & e^{-\frac{T_s}{R_2C_2}} & \\ & & 1 \end{bmatrix} \begin{bmatrix} U_{1,k} \\ U_{2,k} \\ SOC_k \end{bmatrix} + \begin{bmatrix} R_1(1-e^{-\frac{T_s}{R_1C_1}}) \\ R_2(1-e^{-\frac{T_s}{R_2C_2}}) \\ \eta T_s / C_{cap} \end{bmatrix} I_k$$

Where:

- T_s = sampling time(s)
- η = coulomb efficiency
- C_{cap} = is battery capacity(Ah)

According to the voltage loop, the output equation can be expressed as

Equation 2:

$$U_{L,k+1} = U_{OC}(SOC_{k+1}) + U_{1,k+1} + U_{2,k+1} + R_0 I_{k+1}$$

It can be obtained from Equations 1 and 2 that the equation of state contains two state variables: RC terminal voltages and SOC, where the SOC can be calculated from the definition, and the SOC can also be derived from the relationship between OCV and SOC. In the Kalman filter theory, the Kalman gain is a very important value, which determines the weight between the above two SOC estimation methods and has an important influence on the estimation accuracy of the SOC (Phan,2017). The expression of the Kalman gain K_k can be expressed by Equation 3, where P_k^- is the prediction state covariance. According to the characteristics of the covariance matrix, the definition of P_k^- can be given by Equation 4, where $p_{ij,k}^-$ is the covariance of each item in the covariance matrix. The out-of-diagonal terms can be further written out, as shown in Equation 5, where $\rho_{ij,k}$ reprents the correlation coefficient and $\left|\rho_{ij,k}\right| \le 1$. Specially, $\rho_{ij,k} > 0$ indicates the positive correlation between U_{RC} and SOC, $\rho_{ij,k} < 0$ indicates the negative correlation and $\rho_{ij,k} = 0$ indicates no correlation.

Equation 3:

$$K_k = P_k^- C_k^T (C_k P_k^- C_k^T + \hat{R}_{k-1})^{-1}$$

Equation 4:

$$P_k^- = \left\{p_{ij,k}^-\right\}_{(n+1)\times(n+1)}, p_{ij,k}^- = p_{ji,k}^-, i, j = 1,2\cdots, n+1$$

Equation 5:

$$p_{ij,k} = \rho_{ij,k}\sqrt{p_{ii,k}}\sqrt{p_{jj,k}}, \quad i, j = 1,2,\cdots, n+1 \& i \neq j$$

From the above analysis, it can seen that the diagonal terms $\rho_{ij,k}$ contains the information of the statevariables U_{RC} and the SOC, and the values of them affect the Kalman gain even the final SOC estimation result.

Although there is correlation between U_{RC} and SOC, there is no clear correlation. Taking the charging process as an example, when C_1 or C_2 is not full, U_{RC} and the SOC continues to increase, the two are positively correlated; When C_1 or C_2 is full, U_{RC} does not change, but SOC continues to increase, and the corresponding correlation coefficient gradually decreases to zero; Considering the case where the charging current is small, $e^{-\frac{T_s}{R_i C_i}} U_i$ ratios greater than $R_i I_i (1 - e^{-\frac{T_s}{R_i C_i}})$, U_{RC} is a downward trend, and the SOC is still increasing. The discharge process is similar to the above analysis. It can be seen that there is no clear correlation between U_{RC} and SOC, so measures must be taken to eliminate mutual interference between the variables.

2.2. Split battery model analysis

In order to eliminate the mutual interference between state variables, a split battery model based on the second-order RC model is proposed. The second-order RC model was divided into two submodels:SOC submodel and U_{RC} submodel, and the state-space equations are shown as Equations 6~9:

The U_{RC} submodel:

Equation 6:

$$\begin{bmatrix} U_{1,k+1} \\ U_{2,k+1} \end{bmatrix} = \begin{bmatrix} e^{-\frac{T_s}{R_1C_1}} & \\ & e^{-\frac{T_s}{R_2C_2}} \end{bmatrix} \begin{bmatrix} U_{1,k} \\ U_{2,k} \end{bmatrix} + \begin{bmatrix} R_1(1-e^{-\frac{T_s}{R_1C_1}}) \\ R_2(1-e^{-\frac{T_s}{R_2C_2}}) \end{bmatrix} \begin{bmatrix} I_k & SOC_k \end{bmatrix}$$

Equation 7:

$$U_{L,k} = \begin{bmatrix} 1 & 1 \end{bmatrix} \begin{bmatrix} U_{1,k} & U_{2,k} \end{bmatrix}^T + \begin{bmatrix} R_0 & \frac{dU_{OC,k}}{dSOC_k} \end{bmatrix} \begin{bmatrix} I_k & SOC_k \end{bmatrix}^T$$

The SOC submodel:

Equation 8:

$$SOC_{k+1} = SOC_k + \begin{bmatrix} \frac{\eta T_s}{C_{cap}} & 0 & 0 \end{bmatrix} \begin{bmatrix} I_k & U_{1,k} & U_{2,k} \end{bmatrix}^T$$

Equation 9:

$$U_{L,k} = \frac{dU_{OC,k}}{dSOC_k} SOC_k + \begin{bmatrix} R_0 & 1 & 1 \end{bmatrix} \begin{bmatrix} I_k & U_{1,k} & U_{2,k} \end{bmatrix}^T$$

From the above two state space equations, the state variables are divided into two parts: only contains the state variable of U_{RC} and only contains the state variable of SOC. In Equation 6,SOC is input vector of the U_{RC} submodel and U_{RC} is output vector, Similarly, in Equation 8, U_{RC} is input vector of the SOC submodel and SOC is output vector. Therefore, the split battery model consisting of two submodels constitutes a complete battery model. The operating mechanism of the model is shown in Figure 2.

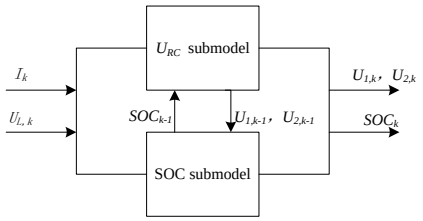

Figure 2: Block diagram of split battery model

The split battery model uses two sub-models to effectively avoid the interference problem between state variables. The following analysis of the Kalman gains of the two submodels illustrates how the split battery model solves this problem. The Kalman gain expressions for the two submodels of U_{RC} and SOC can be written separately from Equation 3, as shown in Equations 10 and 11 :

Equation 10:

$$\begin{bmatrix} K_{11,k} \\ K_{12,k} \end{bmatrix} = \frac{1}{\sum_{i=1}^{2}\sum_{j=1}^{2} p_{ij,k}^{-} + r_{1,k}} \begin{bmatrix} p_{11,k}^{-} + p_{12,k}^{-} \\ p_{21,k}^{-} + p_{22,k}^{-} \end{bmatrix}$$

Equation 11:

$$K_{2,k} = \frac{p_{2,k}^{-} \frac{dU_{OC,k}}{dSOC_k}}{p_{2,k}^{-} (\frac{dU_{OC,k}}{dSOC_k})^2 + r_{2,k}}$$

Where:

- $r_{1,k}$ = the measurement covariance of the U_{RC} submodel
- $r_{2,k}$ = the measurement covariance of the SOC submodel

As illustrated in Equation 10, $K_{1,k}$ is related only to covariance $p_{ij,k}^{-}$ and measurement covariance $r_{1,k}$ of U_{RC} ;It can be seen that $K_{2,k}$ is influenced by three factors: variance of SOC($p_{2,k}^{-}$), measurement covariance of SOC($r_{2,k}$), and change rate of open circuit voltage($dU_{OC,k}/dSOC_k$) which is particularly significant.. Especially for lithium iron phosphate batteries, the OCV-SOC curve is relatively flat over a large SOC range, which means the rate of change of the open circuit voltage is very small, even close to zero. If the measurement covariance is also small, the value of SOC is relatively large, and the weight of the SOC estimated by the open circuit voltage is large, which directly leads to a large SOC estimation error.

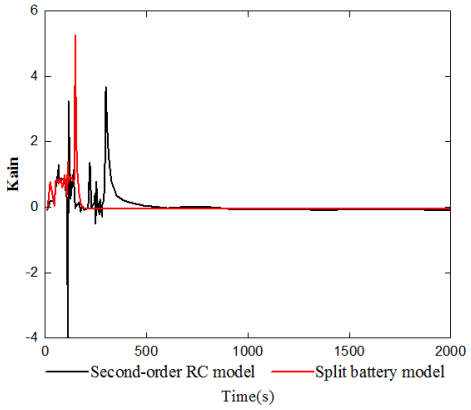

Figure 3: Kalman gain curve

Experiments were conducted on a 3.3 V 20 Ah lithium iron phosphate battery, and different battery models were used for comparison experiments. The experimental results are shown in Figure 3. Figure 3 shows the Kalman gain variation curves for the two models. It can be clearly seen that when the second-order RC model is used, the initial Kalman gain variation is more severe; when the split battery model is used, the Kalman gain early variation is significantly smaller. It shows that the split battery model can effectively reduce the Kalman gain early oscillation. However, although the split battery model can effectively improve the SOC estimation accuracy, the traditional method of estimating the parameters of the model still uses the offline identification method, least-squares method, which cannot meet the problem because the model parameters are affected by many factors. So there is room for improvement.

3. MODEL PARAMETER IDENTIFICATION

3.1. Recursive least squares method with forgetting factor

The basic principle of the least-squares method is to minimise the sum of squared errors. In the case that observation data are not provided, the least-square method is a simple and effective parameter identification method, but for time-varying systems, this will lead to the parameters cannot be well tracked (Qiang, 2014). The recursive least squares method can identify the parameters online, but as the data is continuously iteratively updated, the data is saturated, and the gain matrix P_k and K_k becomes smaller and the correction effect becomes worse (Wu, 2016). In view of this phenomenon, based on the recursive least squares method, the forgetting factor λ (0<λ≤1) is introduced, and the algorithm recursive formula is shown as:

Equation 12:

$$\begin{cases} e_k = y_k - \varphi_k^{\ T}\hat{\theta}_{k-1} \\ \lambda_k = 1 - \dfrac{1}{1+\varphi_{k-1-l}^{T} P_{k-1}\varphi_{k-1-l}} \dfrac{e_k^2}{R} \\ K_k = \dfrac{P_{k-1}\varphi_k}{\lambda_k + \varphi_k^{\ T} P_{k-1}\varphi_k} \\ \hat{\theta}_k = \hat{\theta}_{k-1} + K_k e_k \\ P_k = \dfrac{1}{\lambda_k}(P_{k-1} - K_k \varphi_k^{\ T} P_{k-1}) \end{cases}$$

Where:

- $\lambda_{(k)}$ = variable forgetting factor
- $e_{(k)}$ = innovation
- l = step length
- P_k = covariance matrix.

Perform a series of processing to Equation 12 such as bilinear transformation and discretisation for Equation 2. The difference equation of the available system is as follows:

Equation 13:

$$\begin{aligned} U(k) &= (1-a_1-a_2)U_{oc}(k) + a_1U(k-1) + a_2U(k-2) + \\ &\quad a_3I(k) + a_4I(k-1) + a_5I(k-2) \\ &= a_0 + a_1U(k-1) + a_2U(k-2) + a_3I(k) + \\ &\quad a_4I(k-1) + a_5I(k-2) \end{aligned}$$

the corresponding model of the least squares form is:

Equation 14:

$$\begin{cases} y(k) = U(k) = \varphi^T(k)\theta \\ \varphi(k) = \left[1, U(k-1), U(k-2), I(k), I(k-1), I(k-2)\right]^T \\ \theta = \left[a_0, a_1, a_2, a_3, a_4, a_5\right]^T \end{cases}$$

use MATLAB to solve the above process programming, program flow chart shown in Figure 4:

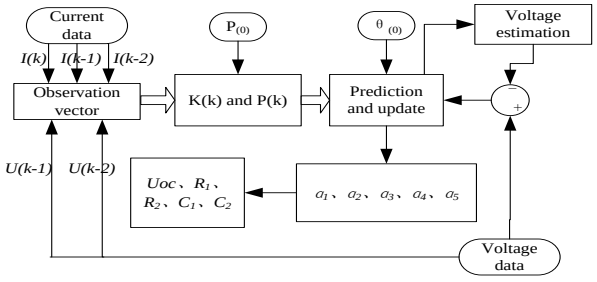

Figure 4: Flow chart of parameter identification

3.2. Parameter identification verification experiment

In order to verify the effect of the least square method with forgetting factor on the second-order RC model parameter identification, the simulation experiment and the actual experiment were compared with the off-line parameter identification results. The equipment used in the experiment was an Arbin BT2000 battery test system. The experimental object was a lithium iron phosphate battery with a nominal voltage of 3.3V and a rated capacity of 20 Ah. In order to ensure that the experimental results are more representative, the experiment was conducted under the conditions of SOC=50% and a temperature of 25°C. The experimental current data uses a simulated dynamic current curve as shown in Figure 5.

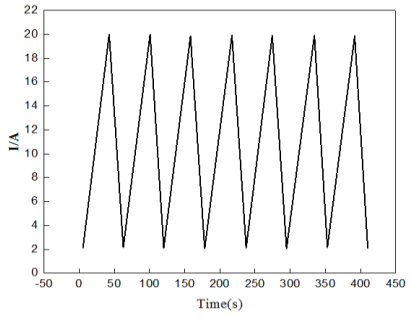

Figure 5: Simulated dynamic current curve

The parameter identification results are given in Figure. 6, where Figure 6(a) is the voltage part of the model parameters, Figure 6(b) is the resistance part of the model parameters, and Figure 6(c) is the capacitance part of the model parameters.

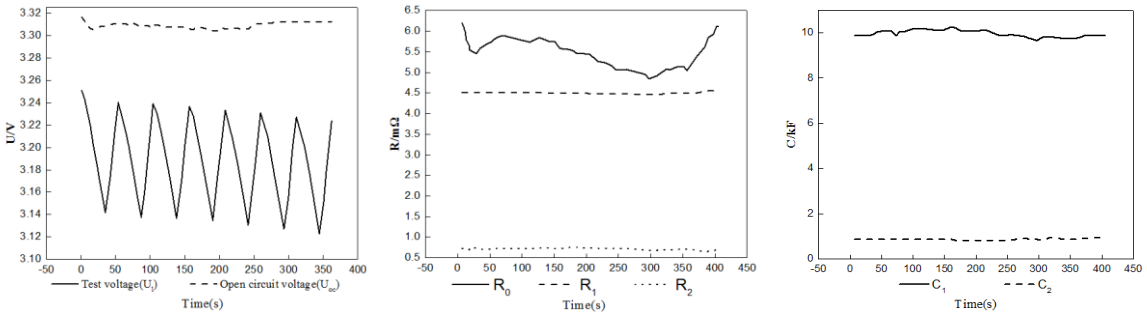

(a) (b) (c)

Figure 6: Model parameter identification results

To verify the accuracy of the experimental results, a second-order RC simulation model as shown in Figure 7 was built in the simulink. And by comparing the value of the battery terminal voltage in the simulation experiment and the actual experiment, the accuracy of the parameter identification result is verified. Figure 8 shows the comparison of simulation data and experimental data.

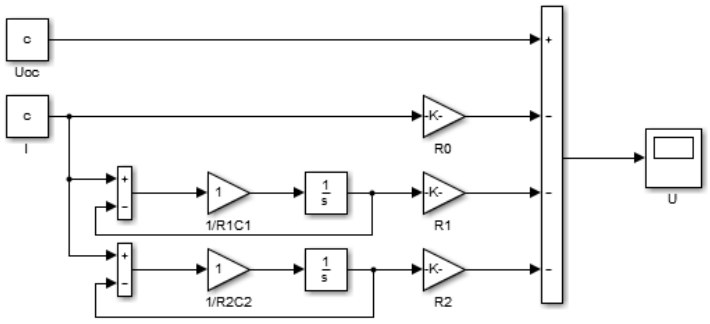

Figure 7: The second-order RC simulation model

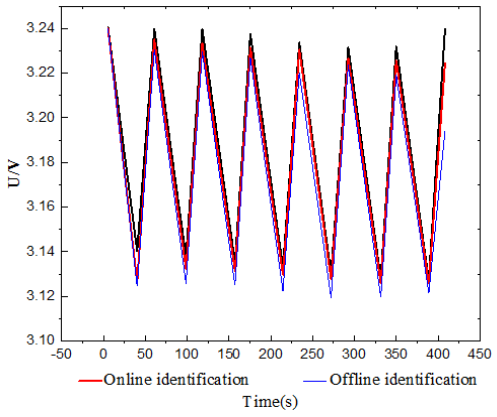

Figure 8: Comparison of simulation data and experimental data

From Figure 8, it can be seen intuitively that the simulation data of on-line parameter identification is closer to the experimental data, and the specific error calculation is shown in Table 1. The error calculation in Table 1 shows that the parameter identification effect using the least-square method with forgetting factor is significantly better than the offline parameter identification. Therefore, the following will draw on this result to further improve the battery SOC estimation results.

Table 1: Error calculation

Error	Offline	Online
Maximum absolute error	42.3mV	18.7mV
Average absolute error	10.8mV	6.1mV
Root mean square error	9.3mV	7.5mV
Maximum relative error	2.16%	0.54%

4. SOC VERIFICATION EXPERIMENT

4.1. SOC estimation algorithm

In order to verify the on-line parameter identification effect of the split battery model, the unscented Kalman filter algorithm was used to estimate the battery SOC. Unscented Kalman filtering algorithm uses the idea of probability distribution, which is more accurate than the extended Kalman's first-order Taylor expansion (Li, 2016). The specific algorithm is shown in Table 2:

Table 2: Unscented Kalman filter algorithm

Step	Formula
Initial value calculation	$\bar{x} = E(x_0), p_0 = E(x_0 - \bar{x})(x_0 - \bar{x})^T$
Create Sigma points	$x^i_{(k-1)} = \begin{cases} \bar{x}(k-1) + \left[\sqrt{(L+\lambda)p(k-1)}\right], & i = 1,\cdots,L \\ \bar{x}(k-1) - \left[\sqrt{(L+\lambda)p(k-1)}\right], & i = L+1,\cdots,2L+1 \end{cases}$
Time update	$x^i_{k\|k-1} = f(x^i_{k-1}), \bar{x}^-_k = \sum_{i=0}^{2L} \omega^m_i x^i_{k\|k-1}$
	$P_{k\|k-1} = \sum_{i=0}^{2L} \omega^e_i (x^i_{k\|k-1} - \bar{x}^-_k)(x^i_{k\|k-1} - \bar{x}^-_k)^T + Q_k$
	$y^i_{k\|k-1} = g(x^i_{k\|k-1}), \bar{y}^-_k = \sum_{i=0}^{2L} \omega^m_i \left[g(x^i_{k\|k-1}) + v_{k-1}\right] = \sum_{i=0}^{2L} \omega^m_i y^i_{k\|k-1}$
Measurement update	$p_{\bar{y},k} = \sum_{i=0}^{2L} \omega^e_i (y^i_{k\|k-1} - \bar{y}^-_k)(y^i_{k\|k-1} - \bar{y}^-_k)^T + Q_k$
	$p_{\bar{x}\bar{y},k} = \sum_{i=0}^{2L} \omega^e_i (x^i_{k\|k-1} - \bar{x}^-_k)(y^i_{k\|k-1} - \bar{y}^-_k)^T$
	$K = p_{\bar{x}\bar{y},k} p_{\bar{y},k}^{-1}, \bar{x}_k = \bar{x}^-_k + K(y_k - \bar{y}^-_k), p_{k\|k} = p_{k\|k-1} - K p_{\bar{y},k} K^T$

Where

- $k|k-1$ = estimated value based on the k-1 time
- $\bar{x}_k$ = the optimal estimate
- $\bar{x}^-_k$ = priori estimation of input
- $\bar{y}^-_k$ = priori estimation of output
- ω^m_i = the weight used for the mean weighting
- ω^e_i = the weight used for the covariance weighting
- $p_{\bar{x}\bar{y},k}$ = cross-covariance matrix
- Q_k = the process noise covariance
- K = Kalman gain

In conjunction with the split battery model, Figure 9 shows an SOC estimation framework based on the unscented Kalman filter algorithm.

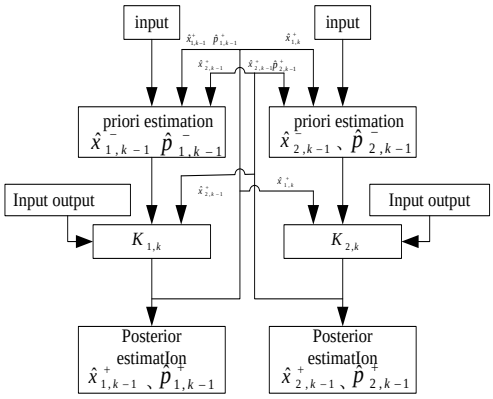

Figure 9: Algorithm estimation framework

4.2. Experimental results and analysis

In order to verify the model parameter identification method and the SOC estimation algorithm used above, the experiment was performed under the battery discharge state, and the initial SOC was set to 50% and the reference value was 70%, which was obtained the SOC curve as shown in Figure 10(a). Both methods have certain oscillations during the initial estimation, due to the split battery model, the oscillation tends to flatten after 200s, accelerating the SOC estimation speed. Compared with the reference curve, the SOC estimation curve using the off-line parameter identification method can quickly converge to the reference value at first, However, when the battery SOC changes significantly, that is, when the time t=1100s, the SOC estimated by the offline identification method deviates significantly from the reference value, and the estimation accuracy decreases remarkably. Compared with the off-line parameter identification method, the on-line parameter identification method is getting closer and closer to the reference value over time, and the estimation accuracy is obviously improved.

Figure 10(b) shows the SOC estimation error curves for the two methods. It is clear from the Figure that Although the SOC estimation error using the offline identification method is zero at a certain time, this is because the SOC value finally estimated by the offline identification parameter method has an intersection with the reference value, and after this time, the SOC estimation error continues to increase,and continue to increase. The SOC estimation error using the online parameter identification method gradually decreases. Calculate the error when the SOC estimation curve tends to be stable for a period of time, the maximum SOC estimation error using off-line parameter identification reached 15.7%, the average error was 5.3%, and the average error with on-line parameter identification was only 1.8%. Thus, on the basis of the split battery model, the online parameter identification method with least-square method with forgetting factor can effectively improve the SOC estimation accuracy.

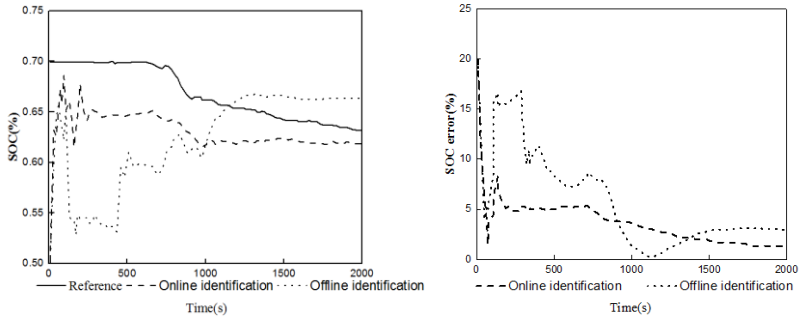

(a) SOC estimate *(b) SOC estimation error*

Figure 10: SOC estimation result

5. CONCLUSION

The equivalent circuit model of the power battery is an important part of the battery SOC estimation. The novel split battery model can effectively improve the initial Kalman gain oscillation and speed up the estimation. This paper further improves the parameter identification of the model, and adopts the least squares method with forgetting factor, which can effectively improve the problem of inaccurate parameter estimation due to the influence of the external environment or the internal parameters of the battery. The algorithm used to implement a simple UKF algorithm, and gives an estimation framework based on the split battery model, the experiment shows that the SOC estimation error is small. This paper takes a step forward in the research of SOC estimation based on the split battery model, and has further implications for the further application of this model.

6. REFERENCES

Mao G, Liu J, Zhao P, 2016. Study on Storage Performance of LiFePO4 Battery. Power Technology, 40(5), 971-972.

Schacht-Rodriguez R, Ortiz-Torres G, García-Beltrán C D, et al. 2017. SOC estimation using an Extended Kalman filter for UAV applications International Conference on Unmanned Aircraft Systems.

Wang,M, JJ Li, X Wu, et al, 2016. Research progress of lithium ion battery model. Power Technology , 50(5),95-98.

Wu CG, Li SM, Pan Y, 2016. Comparison of EKF and UKF Applied in Nonlinear Navigation System. Journal of Changchun University of Science & Technology.

Liang Q, Yu CM, Wang SL, et al. 2017. Study on Internal Resistance of Aviation Aerobic Lithium Batteries Based on PNGV Circuit Model. Power Journal, 15(2),153-158.

Wu T, Luo M, Zhang Q, et al. 2016. Battery SOC Estimation Based on Iterative Extended Kalman Filtering Algorithm. Power Electronics Technology, 50(5),95-98.

Yang J, Xia B, Shang Y, et al. 2017. Adaptive State-of-charge Estimation Based on a Split Battery Model for Electric Vehicle Applications. IEEE Transactions on Vehicular Technology, PP(99),1-1.

Xia B, Sun Z, Zhang R, et al. 2017. A cubature particle filter algorithm to estimate the state of the charge of lithium-ion batteries based on a second-order equivalent circuit model. Energies, 10(4).

Phan M Q, Vicario F, Longman R W, et al. 2017. State-Space Model and Kalman Filter Gain Identification by a Kalman Filter of a Kalman Filter. Journal of Dynamic Systems Measurement & Control, 140(3).

Qiang N, Ji Wang, Shide Li, et al. 2014. Estimation of State of Charge of Lithium Battery in Energy Storage System. Journal of Electric Power, (6),468-472.

Chunguang Wu, Shuangming L I, Pan Y , 2016. Comparison of EKF and UKF Applied in Nonlinear Navigation System. Journal of Changchun University of Science & Technology.

Li Zhang, Shuaishuai Niu, Zhengyu Niu, et al. 2016. Research on Adaptive Parameter Identification and SOC Estimation of Li-ion Battery. Journal of Electronic Measurement and Instrument, 30(1):45-51.

191: HESS power optimised distribution based on genetic algorithm

Tiezhou Wu[1], Li Ji[2]

[1] Hubei Key Laboratory for High-efficiency Utilisation of Solar Energy and Operation Control of Energy Storage System, Hubei University of Technology, Nanli Road, Hubei 430068, China,444152656@qq.com
[2] Hubei Key Laboratory for High-efficiency Utilisation of Solar Energy and Operation Control of Energy Storage System, Hubei University of Technology, Nanli Road, Hubei 430068, China, 2580264581@qq.com

Energy storage system is one of the key technologies of electric vehicle promotion. A single storage battery can't meet the power demand of the electric vehicle, so the speed of electric vehicles can't be improved, limiting the development of electric vehicles. Therefore, the energy storage system of electric vehicles must be combined with two or more kinds of energy storage structures to form a hybrid energy storage system, giving full play to the advantages of various energy storage technologies. In this paper, a hybrid energy storage system consisting of battery and super capacitor is used to meet the two demands of electric vehicle's power and energy simultaneously. The hybrid structure can switch between Battery/SC and SC/Battery working mode, the control is more flexible, but it increases the difficulty of energy management of hybrid power. The operating mode of Hybrid Energy Storage System of battery and super capacitor is not conducive to optimal power allocation of different operating modes. A HESS power hierarchical management optimised strategy has been proposed. The working mode of HESS is discussed hierarchically, an optimal mode of output power of energy storage system is set and energy management strategy is designed based on different hierarchies. Genetic algorithm is utilised to optimise power allocation in order to improve the overall efficiency of the system on the basis of hierarchical energy management strategy. HESS simulation mode and experiment platform are built to simulate and experiment, the result of simulation and experiment show that, under the road condition of EUDC and UDDC, optimised HESS using the genetic algorithm can reduce 1.1% and 0.8% of the overall loss compared with that of the traditional hysteresis control. The optimised HESS using genetic algorithm can effectively reduce the loss of the system, realise power optimal distribution. It can also follow the demand of power in time and the super capacitor compensate or absorb peak power to ensure battery safety.

Keywords: electric vehicle, genetic algorithm, HESS, power optimal distribution

1. INTRODUCTION

Energy storage system is one of the key technologies for the extension of electric vehicles. It is difficult for single battery to meet the power demand of electric vehicles, and the loss is great, thus the velocity of electric vehicles cannot be lifted, which is a barrier for their development (Wang, et al, 2016). So the energy storage system of electric vehicles must combine two or more energy storage structures to constitute hybrid energy storage systems so as to exploit the advantages of each energy storage technology to the full (Farshid, et al, 2016).

The research object of this paper is the hybrid energy storage system which is the mixed use of battery and super capacitor of electric vehicles, the two combined is called composite power supply which includes Battery/SC structure, SC/Battery structure and hybrid structure etc. (Ephrem, et al, 2016. Deng, et al, 2016). The hybrid structure can switch between the Battery/SC and SC/Battery structures, and the control is more flexible, but it increases the difficulty to manage (Choi, et al, 2014. Huseyin, et al, 2016). For the problem, the state of power of different composite power supply is discussed and managed hierarchically. The output power and energy optimal mode of energy management system is built. Because it is a real-time control, the demand for operating velocity is high. Genetic algorithm is selected to monitor the hybrid energy storage system and to realise optimal distribution of the power output of battery and super capacitor. The system efficiency is improved while protecting battery and super capacitor.

2. TOPOLOGY AND WORKING MODE OF HESS

The circuit structure of the hybrid energy storage energy management system is shown as Figure 1, switch S1 controls the output of SC and select Li/SC or SC/Li operating mode. Switch S2 controls the output of battery pack to stop them from over discharge (Shin, et al, 2016). DC-DC inverter is of buck-boost structure which boosts for battery pack and bucks for super capacitors; power diode makes SC recycle braking-energy (Sathish, et al, 2016).

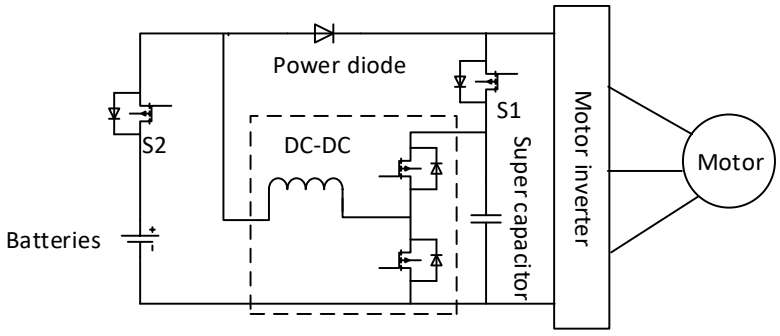

Figure 1: Working mode of composite power source

In this paper, the design of hybrid composite power source has four types of power output working modes and 2 types of recycling braking-energy modes. SC separate output mode, boost hybrid working mode, battery separate output mode, buck hybrid working mode, SC separate recycling mode and joint recycling mode are included. In order to make the system recycle braking-energy as much as possible, if the voltage of SC is higher than the superior limit value during output , SC separate output mode is utilised; when the vehicle is braking ,if SC voltage is lower than the superior limit value, SC separate recycling mode is preferred. These 2 modes are only concerned with SC voltage and must be enforced. They are defined as the top-level mandatory mode.

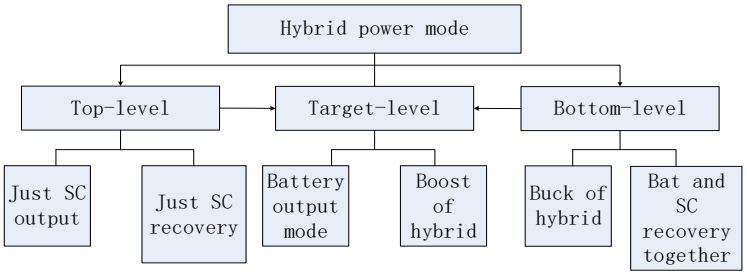

Figure 2: Stratification of hybrid power operating mode

To prevent the battery pack from over discharging, when the state of power is lower than lower limit value, SC/Battery buck hybrid working mode is utilised in which SC charges battery pack or provides energy for the inverter. When the vehicle is braking, joint recycling mode is only used when the voltage of SC is higher than the superior limit value. In order to simplify control, constant power buck control is done by this hierarchy to DC-DC. To prolong the life of the battery, usage of these two working modes needs to be avoided. This hierarchy is defined as special underlying mode.

Two working modes left are battery separate output mode and Battery/SC boost hybrid working mode. The working mode with minimum loss needs to be selected. Genetic algorithm is utilised by this layer to search for minimum loss of the system, meanwhile realizing compensation for SOC if SC and optimal realisation of system power distribution, therefore, the layer is defined as the target-layer optimisation mode. Stratification of HESS working mode is shown as Figure 2.

3. THE STRATEGY AND OPTIMISATION OF ENERGY MANAGEMENT

3.1. The equivalent model of lithium battery and SC

Power distribution of battery and SC needs to be based on the state of charge, otherwise there will be irreversible damage to them, even destroying energy storage system (Chen, et al, 2016). So before power distribution, SOC value of battery and SC needs to be known (Hooman, et al, 2016). Figure 3 shows the selected equivalent model of the lithium-ion battery and super capacitor (Xiao, et al, 2016) .In this figure, R1 and Rs1 is the internal resistance of Lithium battery and super capacitor respectively. R2 and Rs2 is the polarised internal resistance of Lithium battery and super capacitor respectively, Cb and Cs is polarised capacitance of Lithium battery and super capacitor respectively.

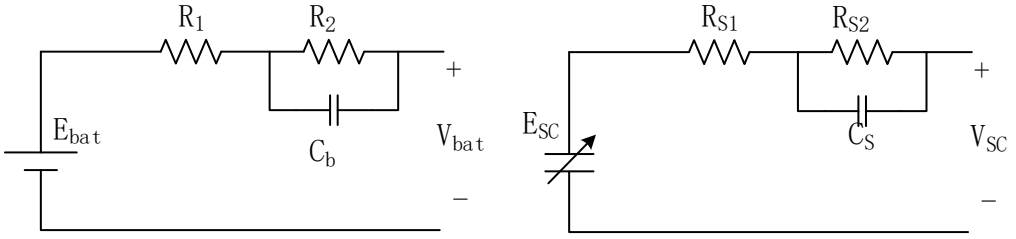

（a) Battery equivalent circuit *(b) SC equivalent circuit*

Figure 3: battery and SC equivalent circuit mode

3.2. Building energy management mode

SOC value of battery and SC is the critical step to select HESS working mode, the calculative mode is as follows:

Equation 1: SOC value of battery and SC.

$$S_{bat} = S_{b0} - [\eta \int_0^t I_{bat}(t)dt] / C_b$$

$$S_{SC} = S_{S0} - [\eta \int_0^t I_{SC}(t)dt] / C_S$$

Equation 2: The output power of electric vehicles under operation.

$$P_o = \omega_1 \eta_1 P_{bat} + \omega_2 \eta_2 P_{SC}$$

Equation 3: the conversion efficiency.

$$0 < \omega_1 \le 1, -\frac{P_{bat}\eta_1}{P_{SC}\eta_2} < \omega_2 \le 1$$

Where:

S_{bat} = the SOC of batteries

S_{b0} = initial SOC of batteries

S_{SC} = the SOC of SC

S_{S0} = initial SOC of SC

P_{bat} = the maximum output power of battery (kW)

P_{SC} = the maximum output power of super capacitor (kW)

P_o = the output power of the energy storage system (kW)

ω_1 = weight coefficient of battery

ω_2 = weight coefficient of SC

η_1, η_2 = the conversion efficiency of the two DC-DC converters (the conversion efficiency is also amortised, namely the inverter is regarded as ideal component without loss)

When $\omega_1 = 0, \omega_2 \neq 0$,, for the top level, super capacitor is utilized individually to provide or absorb power .The super capacitor actively discharge so as to shift to the target layer for optimizing. Super capacitor discharging individually belongs to abnormal working situation under which it should be enforced to other operating mode or the electric vehicle needs to be stopped (stalled).

When $\omega_1 > 0, \omega_2 = 0$, the system is of only battery output working mode, when $\omega_1 > 0, \omega_2 > 0$,, the system is of boost hybrid working mode . The energy management strategy of the target-layer not only needs to achieve selecting and switching of operating modes but also needs to reach the required power for start-stop and acceleration of electric vehicles in the shortest time. Therefore, the corresponding power of only battery working mode has only one solution, And the boost hybrid working mode corresponds to multiple solutions, thus comparisons are needed to search for optimisation.

In order to realise optimisation-searching and mode-selecting functions of genetic algorithm, the initial value of EV is set as the corresponding solution of battery individually output mode, that is $\omega_1 > 0, \omega_2 = 0$. Then genetic algorithm is used to find solution to the target function, the initial value is continually updated until the minimum value of the target function is got .Current ω_1 and ω_2 is outputted ,according to which the output power of DC-DC inverter is assured, namely the output power of battery and super capacitor .

Global stratificated energy management and optimisation is shown as Figure 4, when on the top-level or bottom-level, energy management strategy makes the working mode draw close to or switch to the target-level by charging/discharging or compensating for the SOC of battery. Then, the power distribution is realised by genetic algorithm. The output form of energy management and optimisation algorithm is the power output of battery and super capacitor. On the top-level or bottom-level, the logic threshold is utilised to control the super capacitor to absorb or output power. On the target-level genetic algorithm is used to optimise the output power of battery pack and the super Capacitor provides the remaining power to achieve optimal power distribution.

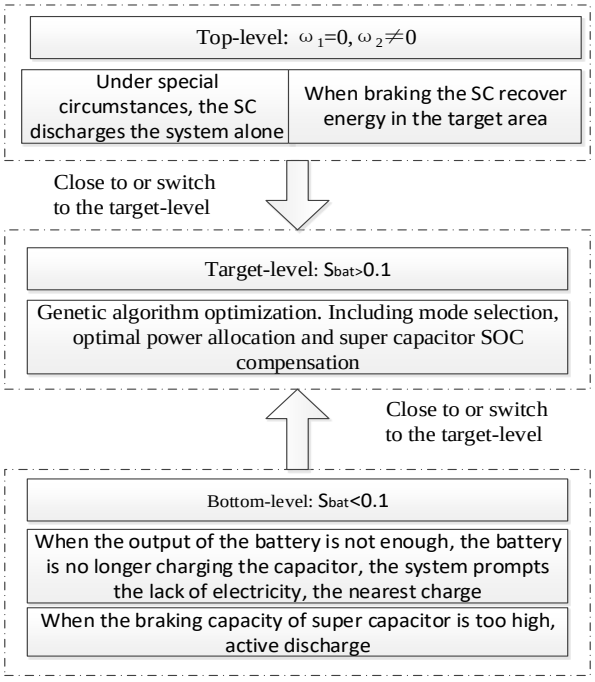

Figure 4: Global stratificated energy management and optimisation

The target function and other constraints is set as:

Equation 4: The target function.

$$f = \min \left| P_o - P_d \right|$$

Equation 5: Other constraints.

$$\begin{cases} P_{bat} = V_{bat} I_{bat} \\ P_{SC} = V_{SC} I_{SC} \\ P_d = V_0 I_d \\ P_o = V_0 I_o \\ 0 \le \left| I_{bat} \right| \le I_{bat\max} \\ 0 \le \left| I_{SC} \right| \le I_{SC\max} \\ 0 < S_{SC} \le 1 \\ 0 < S_{bat} \le 1 \end{cases}$$

Where:

P_d = the power needed when the system is accelerating or starting (kW)

t = time (min)

V_0 = the rated voltage of the motor of EV (V)

I_d = the referent current when the motor is under operation (including start-stop) (A)

I_o = the real current when the motor is under operation (including start-stop) (A)

When the controller is operating, the current and voltage should be tested continuously and SOC needs to be estimated. Then the constraints of the target function are determined so as to control the working condition of energy storage system. $S_{SC\max}$ and $S_{SC\min}$ is defined as superior limit value and lower limit value respectively. Reaching or exceeding the superior limit value, the super capacitor will be no longer charged. Reaching or below the lower limit value, super capacitor will no longer discharge. When SOC of the battery is below 0.1, the system alarms, then the energy storage system needs charging and it will not be charged by the battery any more. Here are some of the working conditions of electric vehicles.

(1) when $S_{SC} \ge S_{SC\max}$, $S_{bat} > 0.1$, the system will not compensate for the power of SC. It depends that SC inputs certain amount of power and discharge initiatively. The weight coefficients satisfy:

Equation 6: The weight coefficients

$$0 < \omega_1 \le 1, 0 \le \omega_2 \le 1$$

（2）when $S_{SC\min} < S_{SC} < S_{SC\max}$, $S_{bat} > 0.1$, the system is of battery only output mode or boost hybrid operating mode, which satisfies:

Equation 7: The weight coefficients

$$0 < \omega_1 \le 1, -\frac{P_{bat}\eta_1}{P_{SC}\eta_2} < \omega_2 \le 1$$

（3）when $S_{SC} \le S_{SC\min}$, $S_{bat} > 0.1$, according to operating situation of EV, the power of SC can be compensated, which satisfies:

Equation 8: The weight coefficients

$$0 < \omega_1 \le 1, -\frac{P_{bat}\eta_1}{P_{SC}\eta_2} < \omega_2 \le 0$$

3.3. The optimised algorithm of model

To ensure that SC has enough power and energy storage system can provide the power demand of EV, with corresponding SOC, The energy storage system should reach the power demand at the fastest speed. The genetic algorithm is selected to optimise energy management.

The optimisation searching process is based on working area with high-efficiency and switching of working modes. Initial value corresponds to battery only output mode, and other values corresponds to boost hybrid working mode. Optimal distribution of output power is as the constraint to make the power response of EV as fast as possible.

Step 1: the initial output power is generated randomly, forming initial population;

Step 2: read SOC of the battery and super capacitor so as to caculate the applicable function value of each power value;

Step 3: new generation of population is generated by selecting, crossing and variation.

Step 4: judge whether the population stops conditions, if not satisfied go back to step 2, if satisfied, execute next step;

Step 5: the optimal individual is selected from current population as the optimal solution of optimised problem.

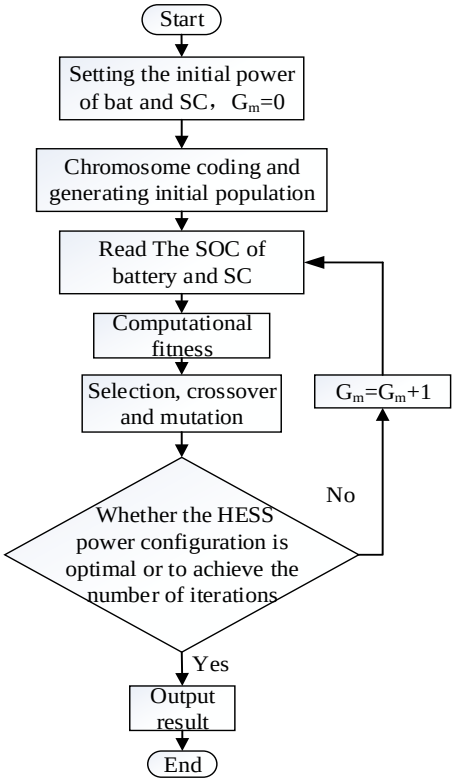

Figure 5: Flow chart of genetic algorithm

4. SIMULATION AND EXPERIMENTS

HESS EV simulation model is built in advisor to verify the power distribution problem of hybrid power supply in conventional working mode. The simulation is done under EUDS (European Urban Driving Schedule) and UDDC (Urban Dynamometer Driving Schedule). The complete vehicle quality is 1297kg.

Figure 6 is the speed variations of the electric vehicle under EUDS and UDDC. For EUDC, it is in a moderate speed in most of the time, while for UDDC, the speed varies dramatically, under which circumstance the output power of the energy storage system also changes dramatically, thereby to control the output current is extremely important.

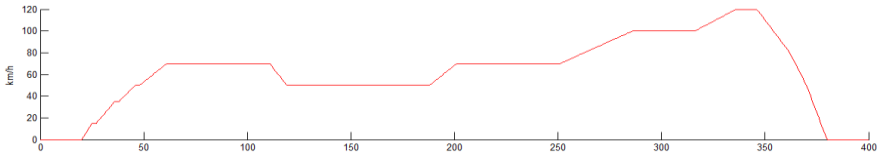

(a) Velocity variations of EUDC cycle

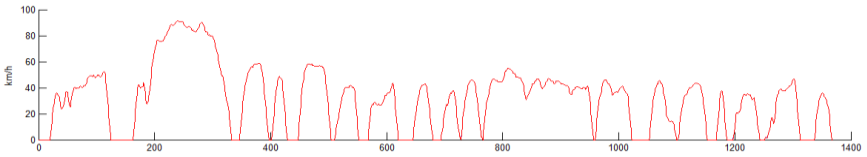

(b) Velocity variations of UDDC cycle
Figure 6: the speed variations of the electric vehicle under EUDS and UDDC

Figure 7 is the results comparisons of EUDC, hysteresis control is selected for making comparisons. The sudden increase of battery output power will severely shorten its life. HESS with genetic algorithm can compensate SOC of SC after 200s, which can smoothly increase the battery output power and effectively guarantee the safety of batteries. Meanwhile Super Capacitor SOC is maintained above 0.5%, even though the output power of the battery can increase slightly with stratificated genetic algorithm, But the final power consumption of super capacitor decreases by 6.8%.

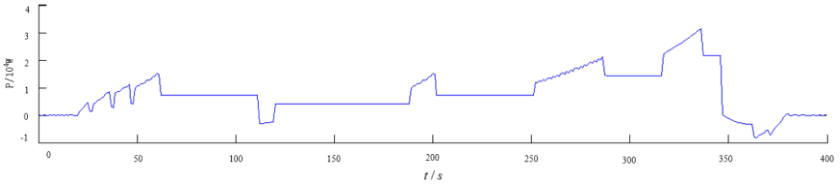

(a) Power demand of EUDC

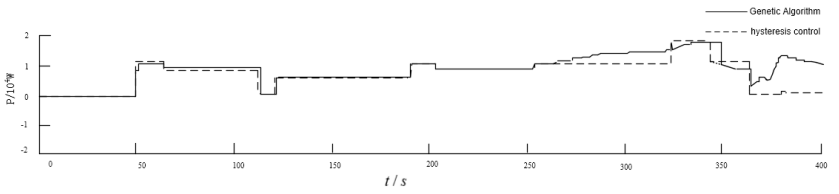

(b) Lithium power output of EUDC

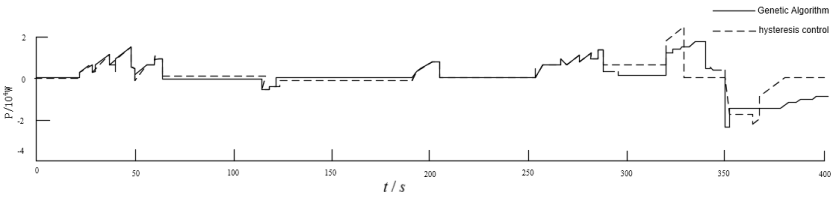

(c) SC power output of EUDC

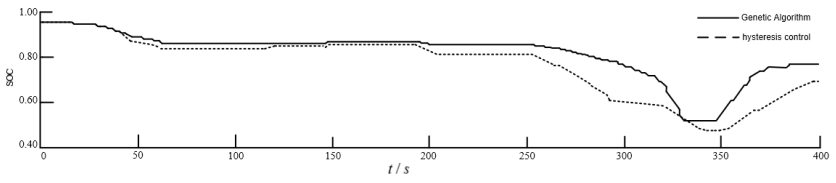

(d) SC SOC value of EUDC
Figure 7: simulation comparisons of EUDS

Figure 8 is the result comparisons of UDDC. For the energy management strategy based on two algorithms, when SOC value is higher than the superior limit value 0.9, super capacitor discharges depending on the circumstances. Compared with hysteresis control, the super capacitor using genetic algorithm outputs power faster with less loss. The power output of the battery is slightly higher than or approximately the same as hysteresis control result. When the battery output is with virtually no increase, using genetic algorithm can achieve optimisation of the system. It can be seen from SOC curves, between 200s and 300s, the power of SC decreases sharply. Then the braking-energy is recycled when the electric vehicle brakes. During the process, the loss of energy stratificated management system with genetic algorithm is 4.5% less than that of the energy management system with hysteresis control.

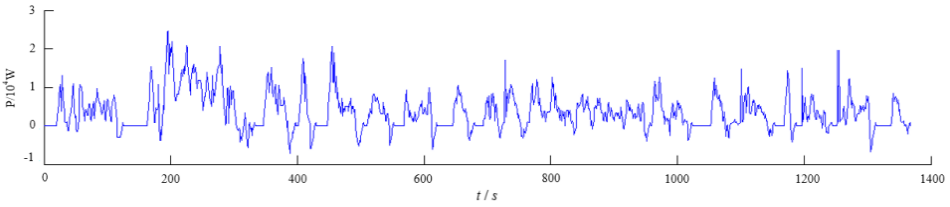

(a) UDDC power demand

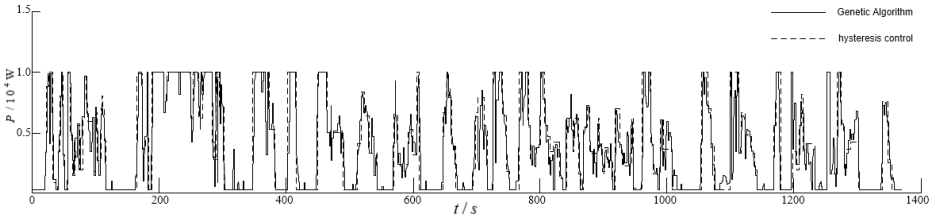

(b) UDDC Lithium battery output power

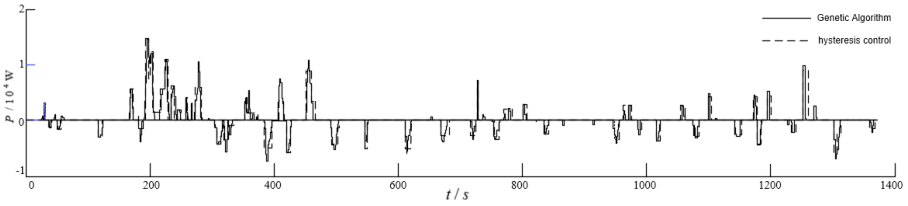

(c) UDDC super capacitor output power

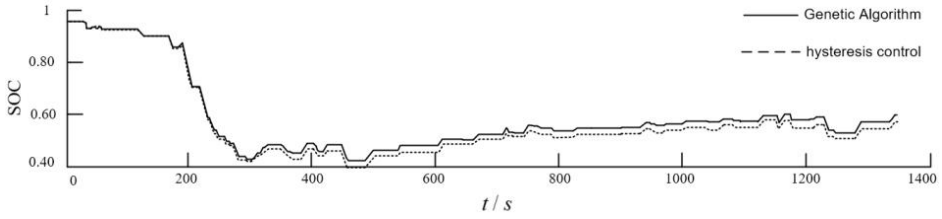

(d) UDDC SOC of SC

Figure 8: UDDS simulation results comparison

In order to further verify that the energy management system can effectively reduce the loss of the system by using genetic algorithm, and achieve the purpose of rapid response. Build a small power HESS system to verify. The nominal voltage of the battery pack is 136V, the maximum output power is limited to 80W, and the maximum voltage of the super capacitor is designed to be 252V. Arbin BT2000 is used to control the charge and discharge of battery and super capacitor. The test results are shown in Figure 9.

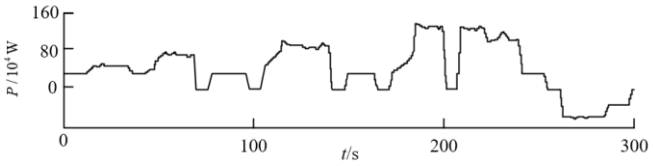

(a) experiment power demand

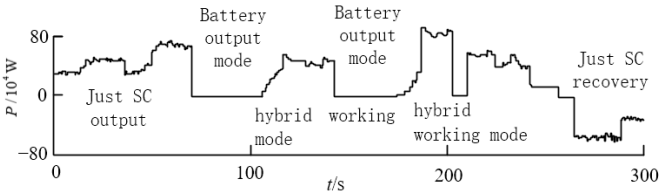

(b) output power of SC pack

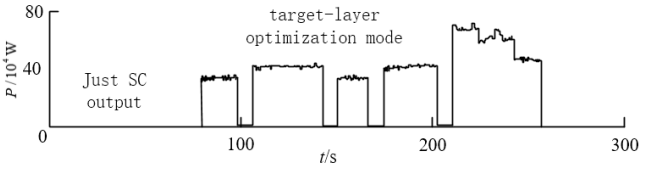

(c) battery output power

Figure 9: experimental results

Figure 9 verifies the SC separate output mode SC separate recovery mode and optimisation mode of hybrid composite power source optimised by hierarchical genetic algorithm. Under the optimisation mode, it can automatically switch all the working modes of the battery and achieve the optimal power allocation and super capacitor SOC compensation. Because the special mode will affect the battery life, special mode is not used in the experiment. The test results and simulation results show that the hybrid power supply optimised by the genetic algorithm can follow the power demand effectively. The supercapacitor provides or absorbs the peak power in time to optimise the energy management and ensure the battery safety.

5. CONCLUSION

HESS working mode of electric vehicles is complex to switch, which is unfavourable to optimal power distribution of different working modes. Thus, an optimised method for HESS management based on genetic algorithm is proposed. HESS working mode is discussed hierarchically and power output optimal model of energy management system is built, thereby realizing energy management and optimisation. Under EUDC and UDDC road conditions, optimised HESS using the genetic algorithm can reduce 1.1% and 0.8% of the overall loss compared with that of the traditional hysteresis control. HESS using genetic algorithm can effectively reduce the loss of the system and realise optimal power distribution. And it can follow the power demand in time to provide or absorb peak power by the super capacitor to ensure the safety of batteries.

6. REFERENCES

Wang B, Xu J, WRJ, Gang BG, 2016. Adaptive Sliding-Mode with Hysteresis Control Strategy for Simple Multi-Mode Hybrid Energy Storage System in Electric Vehicles [J]. IEEE Transactions on Industrial Electronics, 2017, 64(2):1404-1414.

Farshid N, Ebrahim F, Teymoor Gi, 2016. An Efficient Regenerative Braking System Based on Battery/Supercapacitor for Electric, Hybrid and Plug-In Hybrid Electric Vehicles with BLDC Motor [J]. IEEE Transactions on Vehicular Technology, 2017, 66(5):3724-3738.

Ephrem C, Matthias P, Pawel M, Ali E, 2016. Electrochemical and Electrostatic Energy Storage and Management Systems for Electric Drive Vehicles: State-of-the-Art Review and Future Trends [J]. IEEE Journal of Emerging and Selected Topics in Power Electronics, 4(3): 1117-1134.

Deng J X, Shi J, Liu Y, Tang Y J, 2016. Application of a hybrid energy storage system in the fast charging station of electric vehicles [J]. IET Generation, Transmission & Distribution, 10(4):1092-1097.

Choi M, Lee J, Seo S, 2014. Real-Time Optimisation for Power Management Systems of a Battery/Supercapacitor Hybrid Energy Storage System in Electric Vehicles [J]. IEEE Transactions on Vehicular Technology, 63(8): 3600-3611.

Huseyin A Y, Shen J Y, Shi C, Metin G, Alireza K, 2015. Power Split Control Strategy for an EV Powertrain With Two Propulsion Machines [J]. IEEE Transactions on Transportation Electrification, 1(4): 382-390.

Shin C, Yoo K, Kim D K, Lee J Y, 2016. Current limiting circuit for low-cost HESS [J]. Electronics Letters, 52(1):64 – 66.

Sathish K K, Mahesh K. M, Abhisek U, Hoay B G, 2016. DC Grid Voltage Regulation Using New HESS Control Strategy [J]. IEEE Transactions on Sustainable Energy, IEEE, 2017:1-1.

Chen Z, He Y, Ma C B, 2016. Quantitative Efficiency and Temperature Analysis of Battery-Ultracapacitor Hybrid Energy Storage Systems [J]. IEEE Transactions on Sustainable Energy, 7(4): 1791-1802.

Hooman S, Xavier F, 2016. Battery Current's Fluctuations Removal in Hybrid Energy Storage System Based on Optimized Control of Supercapacitor Voltage [J]. IEEE Embedded Systems Letters, 8(3): 53-56.

Xiao J F, Wang P, Leonardy S, 2016. Multilevel Energy Management System for Hybridisation of Energy Storages in DC Microgrids [J]. IEEE Transactions on Smart Grid, 7(2): 847-856.

192: Research on self-compensating dynamic droop control strategy of microgrid energy storage system

Rui PENG[1], Ziqiang XI[2], Jie ZHANG[3], Cheng XU[4]

[1] *Rui Peng, Hubei Collaborative Innovation Center for High efficiency Utilisation of Solar Energy, Hubei University of Technology, Wuhan，430068，P.R. China，1013305543@qq.com*

[2] *Ziqiang Xi, Hubei Collaborative Innovation Center for High efficiency Utilisation of Solar Energy, Hubei University of Technology, Wuhan，430068，P.R. China，695936405@qq.com*

[3] *Jie Zhang, Hubei Collaborative Innovation Center for High efficiency Utilisation of Solar Energy, Hubei University of Technology, Wuhan，430068，P.R. China，zjmato@.com*

[4] *Cheng Xu, Hubei Collaborative Innovation Center for High efficiency Utilisation of Solar Energy, Hubei University of Technology, Wuhan，430068，P.R. China，xch657279145@163.com*

In order to take advantage the energy storage system in maintain the power balance of microgrid system, an improved state of charge(SOC) based dynamic droop control method with self-compensation for energy storage systems was proposed in this paper. As the droop coefficient of traditional droop control is too large, which lead to bus voltage deviation, and the fixed droop coefficient is applied to charge and discharge control of energy storage system, which would cause overcharge and over-discharge of battery. For this issue,a new dynamic droop coefficient is designed based on the system power balance relationship, and the output power of the energy storage system is proportional to their respective SOC values. In addition，the voltage compensation algorithm was deduced to eliminate the bus voltage deviation caused by droop control. Finally, an improved droop control of the energy storage system is obtained. The above method reduces the control complexity compared to the conventional secondary control. For this purpose, multiple groups of small-capacity energy storage systems are used to balance distributed power (DG) and load power to control bus voltage stability. To analyse the stability of the three power grid modes: power shortage, system power excess, and partial power system fault removal in the microgrid system. Finally, the proposed control structure was verified by Matlab / Simulink simulation. The simulation results show that in three different modes of the microgrid, the energy of the energy storage system can always be distributed proportionally according to the SOC value, and finally satisfy the SOC balance and power balance. Compared with traditional droop control, the DC bus voltage fluctuation of microgrid is smaller and the precision of the power distribution is higher.

Keywords: energy storage unit, energy storage unit remaining capacity, droop control, power balance

1. INTRODUCTION

With the development of renewable energy, utilise the Distributed Generation to effectively use Renewable energy (Hu, 2010; Zhang, 2012; Li, 2015), the use of micro-grid structure can effectively solve the impact of distributed generation (Guo, 2016; Diaz, 2014). With the increasing use of DC microgrid, DC micro-sources (photovoltaic, energy storage, etc.) and DC loads can be directly connected to DC bus. Therefore, the power loss of power electronic devices has become increasingly prominent (Li, 2016).

The DC microgrid bus voltage is a key indicator reflecting the stability of the system. The energy storage system can maintain the microgrid bus voltage stability and power balance. However, there is a problem of "overcharging and over-discharging" of batteries in energy storage systems. At present, the use of droop control in energy storage systems can alleviate this problem (Xiang, 2017; Zhou, 2018; Shivram. 2017). Lu et al (2014) improves the output current distribution accuracy by reducing the DC output voltage. Yang et al (2016) designed droop control with voltage change rate $\dot{V}$ to reduce the influence between voltage and current, so that the current load distribution accuracy was improved. Zhi et al (2016) uses a resistive virtual impedance to achieve steady-state power distribution in a DC microgrid and compensates for virtual impedance to improve stability. This method first meets the distribution accuracy requirements, and then uses the compensation control to stabilise the DC bus voltage. Chen (2016) and Chiang (2016) adopt the definite droop coefficient, and the output power of the battery is automatically distributed according to a definite proportion, which easily causes problems such as overcharge and over-discharge of the battery. Chen (2016) and Chiang (2016) adopts a fixed droop coefficient, and the output power of each battery is fixed, which will cause overcharge and over-discharge of the battery. Mi (2017) and Shivram (2017) apply fuzzy droop control to dynamically adjust load power distribution as well as fast equalisation based on the charged state of each storage unit (SOC).

Based on the above analysis, this paper presents a self-compensating dynamic droop control strategy. The state of charge (SOC) of the battery is considered as a state quantity, and the droop coefficient of the exponent of the SOC is designed. In addition, A voltage compensation algorithm was proposed to compensate for the DC bus voltage deviation. The output power of each group of batteries is distributed in proportion to the nth power of SOC, and the power balance state is finally achieved.

2. DC MICROGRID STRUCTURE AND CONTROL ANALYSIS

Figure 1 shows the typical structure of a DC microgrid. Each unit is connected with DC bus by power electronic device. This paper mainly studies distributed power generation systems and energy storage systems to provide load power. The remaining energy of the system is temporarily not considered into the grid, and it is preferentially input into the energy storage system.

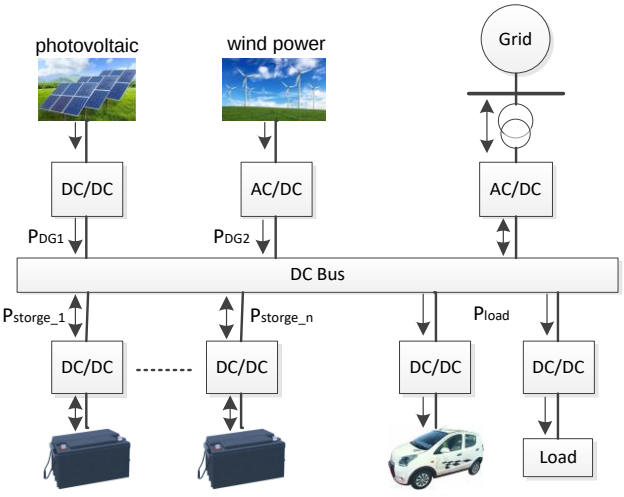

Figure 1: Structure of DC microgrid

Equation 1: Convention droop control.

$$u_{dc} = u_{dc}^{*} - Ri_{dc}$$

Where:

u_{dc} = Output DC Voltage of Converter (V)

u_{dc}^{*} = Converter output voltage reference (V)

i_{dc} = Converter output current (A)

R= Droop coefficient

Figure 2 shows a simplified model of the n-group energy storage system. The output current of any two groups of converters:

Equation 2: Output current of any two groups of converters.

$$\frac{i_{dci}}{i_{dcj}} = \frac{R_j}{R_i} + \frac{R_{linej}(R_i - R_j)}{R_i(R_i + R_{linei})}$$

Where:

i_{dci} / i_{dcj} = The group i/j(i/j=1、2…n, and $i \neq j$) converter output current (A)

R_{linei} / R_{linej} =The group i/j(i/j=1、2…n, and $i \neq j$) converter line impedance (Ω)

R_i / R_j = The group i/j(i/j=1、2…n, and $i \neq j$) converter droop coefficient

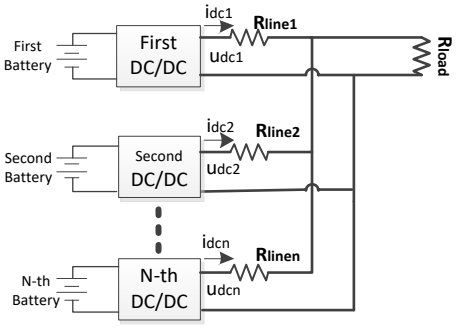

Figure 2: Simplified Model of the n-group energy storage System

In traditional droop control analysis, usually assumed $R_{linei} = 0$.When the traditional droop coefficient is large, the bus voltage has a large deviation. When the traditional droop coefficient is small, which affects the power distribution accuracy. Therefore, the traditional droop control often chooses an appropriate droop coefficient. This traditional droop control method can lead to overcharge and over-discharge problems and affect battery life. To solve this problem, the self-compensating dynamic droop control is designed to solve the problem and maintain the stability of the system.

3. SELF-COMPENSATING DYNAMIC DROOP CONTROL

According to the physical relation of the power balance of the system, the mathematical model is established, and self-compensated droop control based on SOC is deduced.

3.1. Self-compensating dynamic droop control

Equation 3: Power relationship between source and load of microgrid system.

$$\Delta P = \Delta u_{dc} \cdot \left(i_{dc}^{*} - \Delta i_{dc}\right) + u_{dc}^{*} \cdot \Delta i_{dc}$$

Where:

ΔP = The difference between actual power and rated power of the system (W)

Δu_{dc} = Bus voltage deviation (V)

Δi_{dc} =Output current variation(A)

i_{dc}^{*} =Output current rating (A)

Taking two energy storage systems as an example, the output power of two energy storage systems is proportional to the values of SOC_1 and SOC_2.

Equation 4: Output (absorption) power.

$$P_1 = \Delta P \frac{SOC_1^n}{SOC_1^n + SOC_2^n}$$

$$P_2 = \Delta P \frac{SOC_2^n}{SOC_1^n + SOC_2^n}$$

Where:

P_1 / P_2 = The first or second group of energy system output (absorption) power (W)

Simultaneous (3) and (4) formula has:

Equation 5: Output (absorption) power.

$$P_1 = \frac{\Delta u_{dc} \cdot (i_{dc}^* - \Delta i_{dc}) \cdot (SOC_1^n + SOC_2^n)}{SOC_1^n} + u_{dc}^* \cdot \Delta i_{dc} \cdot \frac{SOC_1^n}{SOC_1^n + SOC_2^n}$$

$$P_2 = \frac{\Delta u_{dc} \cdot (i_{dc}^* - \Delta i_{dc}) \cdot (SOC_1^n + SOC_2^n)}{SOC_2^n} + u_{dc}^* \cdot \Delta i_{dc} \cdot \frac{SOC_2^n}{SOC_1^n + SOC_2^n}$$

Take P_1 as an example, it is transformed that:

Equation 6: Bus voltage and power relationship.

$$u_{dc} = u_{dc}^* - \frac{1}{i_{dc}^* - \Delta i_{dc}} \cdot \frac{SOC_1^n + SOC_2^n}{SOC_1^n} \cdot P_1 + \frac{u_{dc}^* \cdot \Delta i_{dc}}{i_{dc}^* - \Delta i_{dc}}$$

The new droop control formula based on the Equations (5) to (6) is:

Equation 7:Self-Compensating Dynamic Droop Control.

$$u_{dc} = u_{dc}^* - \frac{m_o}{i_{dc}^* - \Delta i_{dc}} \cdot \frac{SOC_1^n + SOC_2^n}{SOC_1^n} \cdot P_1 + \frac{u_{dc}^* \cdot \Delta i_{dc}}{i_{dc}^* - \Delta i_{dc}} \cdot m_o$$

Where:

m_o = Initial droop coefficient

The self-compensating dynamic droop control is based on the battery SOC value to establish a new droop coefficient, and design bus voltage compensation algorithm.

3.2. Improved droop control stability analysis

According to the system power balance, an improved droop control strategy is deduced, and the self-compensating dynamic droop control block diagram based on SOC is designed. As shown in Figure 3. The V-P droop control is established, the power sampling value is passed through a low-pass filter, and the processed power value is introduced into the droop controller.

According to the control block diagram shown in Figure 3, the voltage closed-loop transfer function is:

Equation 8:the voltage closed-loop transfer function.

$$V_{dc}(s) = G_1(s)V_{dc}^*(s) - G_2(s)P_{out}(s) - Z_0(s)I_{dc}(s)$$

Where:

$G_1(s)$ = Output voltage closed-loop tracking transfer function.

$G_2(s)$ = Output power closed-loop tracking transfer function.

$Z_0(s)$ = Equivalent output impedance of converter.

Equation 9:

$$\begin{cases} G_1(s) = \dfrac{G_{cc}G_{vc}K_{pwm}(1+G_{bc})}{(Ls+r)\cdot cs + G_{cd} + G_{cc}K_{pwm}\cdot cs + G_{cc}G_{vc}K_{pwm}} \\ G_2(s) = \dfrac{G_{droop}G_{lf}G_{cc}G_{vc}K_{pwm}P_{out}}{(Ls+r)\cdot cs + G_{cd} + G_{cc}K_{pwm}\cdot cs + G_{cc}G_{vc}K_{pwm}} \\ G_1(s) = \dfrac{(Ls+r) + G_{cc}K_{pwm}}{(Ls+r)\cdot cs + G_{cd} + G_{cc}K_{pwm}\cdot cs + G_{cc}G_{vc}K_{pwm}} \end{cases}$$

Equation 10:

$$\begin{cases} G_{vc} = k_{pv} + \dfrac{k_{iv}}{s} \quad , \quad G_{cc} = k_{pi} + \dfrac{k_{ii}}{s} \\ G_{lf} = \dfrac{1}{\tau s + 1} \quad , \quad G_{bc} = \dfrac{\Delta i_{load}}{i^*_{load} - \Delta i_{load}} \cdot m_o \\ G_{droop} = \dfrac{m_o}{i^*_{load} - \Delta i_{load}} \cdot \dfrac{\sum_{j=1}^{n} SOC_j^n}{SOC_i^n} \\ G_{cd} = \begin{cases} 1 - D & \text{Boost state} \\ D & \text{Buck state} \end{cases} \end{cases}$$

Where:

G_{droop} = Dynamic droop coefficient.

G_{vc} / G_{cc} =Voltage outer loop transfer function of PI/Current inner loop transfer function of PI.

Δi_{load} = Difference between actual load current and load rated current.

k_{pv} / k_{iv} = Voltage outer loop ratio(integral) value.

k_{pi} / k_{ii} = Current Inner loop ratio(integral) value.

D/L/C/r= The set duty cycle of the converter/Low-side inductance/High-side capacitance/Line impedance.

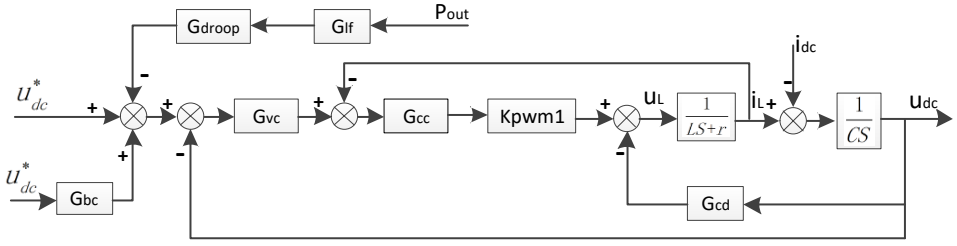

Figure 3: Self-compensating droop control block diagram

Without considering the effect of line impedance on power distribution accuracy, self-compensating droop control introduces SOC exponential state quantities. Therefore, it is necessary to analyse the influence of $\left(SOC_1 / SOC_2\right)^n$ on stability of the system, according to (8), we can obtain

Equation 11:

$$s^5 + as^4 + bs^3 + cs^2 + ds + e = 0$$

Where:

$$a = \frac{(\tau rc + Lc) + K_{pwm} k_{pi} \tau c}{\tau Lc} \cdot \frac{m_o \left(SOC_1^n + SOC_2^n\right)}{(i^*_{load} - \Delta i_{load}) SOC_1^n} .$$

$$b = \frac{K_{pwm}\left(k_{ii}\tau c + k_{pi} c + k_{pi} k_{pv} \tau\right) + rc + G_{cd}\tau}{\tau Lc} \cdot \frac{m_o \left(SOC_1^n + SOC_2^n\right)}{(i^*_{load} - \Delta i_{load}) SOC_1^n} .$$

$$c = \frac{K_{pwm}[\tau\left(k_{ii} k_{pv} + k_{pi} k_{iv}\right) + k_{ii} c + k_{pi} k_{pv}] + G_{cd}}{\tau Lc} \cdot \frac{m_o \left(SOC_1^n + SOC_2^n\right)}{(i^*_{load} - \Delta i_{load}) SOC_1^n}$$

$$d = \frac{K_{pwm}(k_{ii}k_{iv}\tau + k_{ii}k_{pv} + k_{pi}k_{iv})}{\tau Lc} \cdot \frac{m_o\left(SOC_1^n + SOC_2^n\right)}{(i_{load}^* - \Delta i_{load})SOC_1^n} .$$

$$e = \frac{K_{pwm}k_{ii}k_{iv}}{\tau Lc} \cdot \frac{m_o\left(SOC_1^n + SOC_2^n\right)}{(i_{load}^* - \Delta i_{load})SOC_1^n} .$$

Take two energy storage systems as an example, the SOC of the battery is transmitted to the droop controller through the local low-bandwidth communication line. The effects of different initial droop coefficients m_o and n on the stability of the system are analysed and appropriate values m_o and n are designed. Microgrid system parameters as shown in Table 1.

Table 4: Microgrid system partial parameters

parameter	value
Initial of SOC_1 discharge/charge/%	90/45
Initial of SOC_2 discharge/charge/%	80/40
Low pass filter cutoff frequency/ rad^{-1}	120
The first converter output voltage u_{dc1} /V	160
The second converter output voltage u_{dc2} /V	160
DC bus voltage u_{load} /V	380
Initial droop coefficient	0.02
Switch frequency/kHz	10
Inverter low-voltage side inductor L/mH	3.5
Converter high-voltage side capacitor C/mF	0.88

Each energy storage system different SOC values, and the SOC value of exponent n is gradually.

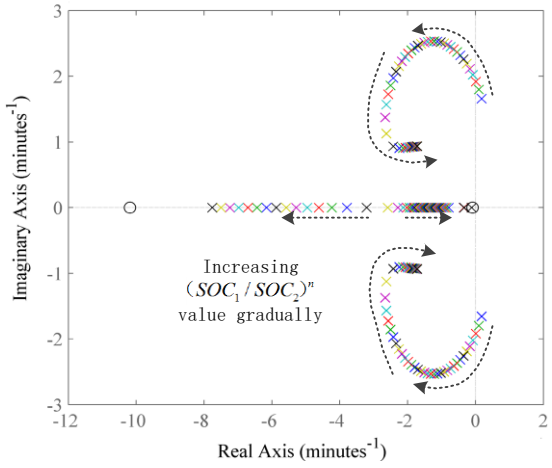

Figure 4: Closed-loop dominant poles with poles with different gains, n(0.1-5)

According to Equations (11) and (12), the closed-loop dominant pole distribution with gradually increasing $\left(SOC_1 / SOC_2\right)^n$ value is obtained by self-compensating dynamic droop control. As shown in Figure 4, according to the distribution of the poles, when the initial values of SOC_1 and SOC_2 are fixed, the $\left(SOC_1 / SOC_2\right)^n$ gradually increases as the value of n increases. It can be seen from the distribution of poles that with the increase of SOC, the pole gradually approaches the virtual axis from the left side of the virtual axis, and when the M value is too small, the poles are distributed on the right side of the virtual axis, and the system is unstable. So the n value should belong to 1 to 5.

4. SIMULATION ANALYSIS

In order to verify the effectiveness of the proposed control strategy, a simulation model for analysis is established in Matlab / Simulink. The storage system was divided into 2 groups or 3 groups with a battery capacity of 4.0 Ah. The rated output

power of photovoltaic is 28.88 kW, the maximum permissible output power is 31.16 kW, and the minimum permissible output power is 26.6kW. When analysing the instability of the system caused by the fluctuation of DG output power, the stability of the system is maintained according to the control strategy in this paper.

4.1. System power shortage

In the normal operation of DC microgrid, the power required by the system is mainly provided by photovoltaic. The simulation results show that the power of the system cannot meet the load power, and the influence of n value on the discharge of the storage system is analysed.

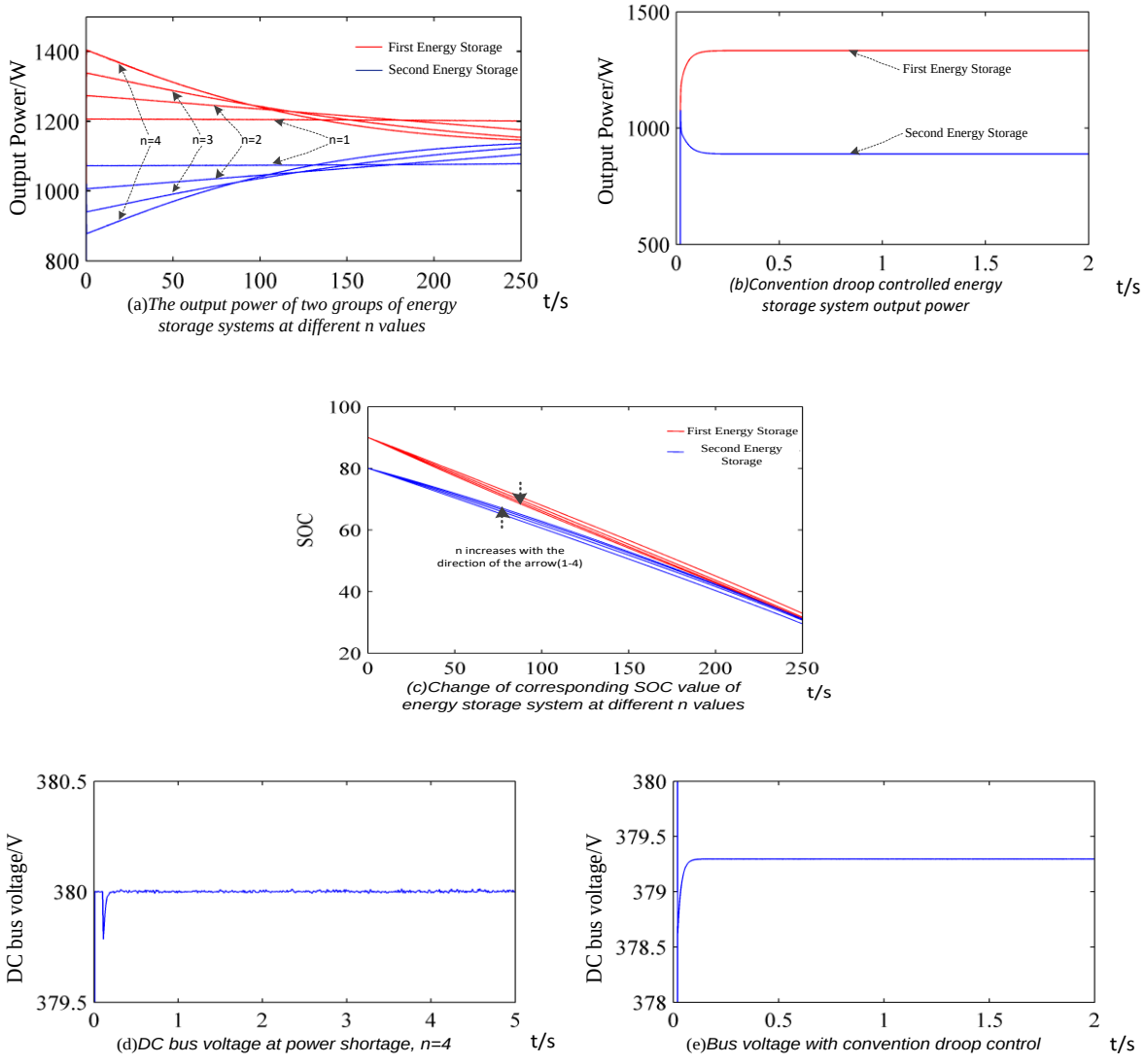

Figure 5: System power shortage simulation results

As shown in Figure 5(a), the DC microgrid system is operating normally. The system power is unbalanced at 0.1 s, the DG power is reduced from 28.88 kW to 26.6 kW, and the output power of the energy storage system is adjusted rapidly and about 2.28 kW of power is released to ensure the normal operation of the system. As can be seen from Figure 5(a), the output power of each energy storage system is directly proportional to its respective SOC value. As the value of n increases, the difference between the initial output power of the two groups of energy storage systems gradually increases and the final output power tends to be equal. The larger the value of n, the faster the output power is approaching equal. Compared with Figure 5(b), the output power of the conventional droop control energy storage system is always at a fixed ratio, and there is a problem of over-discharge. From Figure 5(c), it can be seen that as the value of n increases, the SOC of the two groups of energy storage systems approaches the same value, but according to Figure 4, the value of n can be obtained in the range of 1 to 5.

From Figure 5(d), when the power system generates power fluctuations, the bus voltage responds quickly and the voltage fluctuation is small, stable at 380V. Compared with the traditional droop control shown in Figure 5(e), it can be seen that the DC bus voltage is reduced, and the bus voltage is reduced to 379.3 V after stabilisation. The self-compensating droop control proposed in this paper uses the self-compensation algorithm to compensate the voltage reduction value and reduce the control complexity.

4.2. System power excess

The influence of excessive power on the stability of microgrid is analysed by simulation. As shown in Figure 6(a), the output power of the system increases from 28.88 kW to 31.16 kW at 0.1 seconds. The energy storage system quickly absorbs about 2.28 kW of system excess power.

In addition, the self-compensating dynamic droop control proposed by this paper, as the value of n gradually increases, the difference between the initial absorption power gradually increases, and the initial absorption power of each energy storage system is inversely proportional to the SOC value. The absorption power of the two sets of energy storage systems tends to be nearly equal and eventually converges. Compared to Figure 6(b), conventional droop controlled energy storage systems absorb power at a fixed rate and there is overcharging. As can be seen from Figure 6(c) that SOC tends to be equal with the increase of n value.

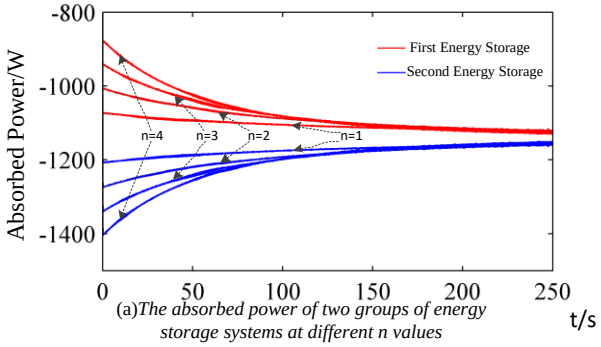

(a)*The absorbed power of two groups of energy storage systems at different n values*

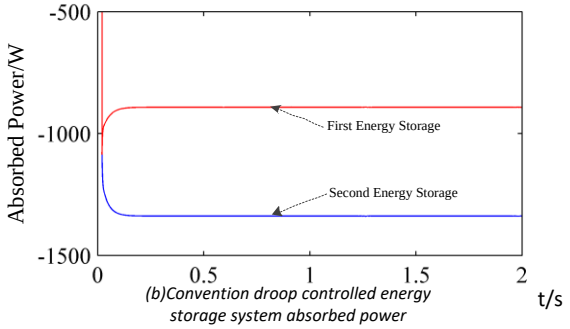

(b)Convention droop controlled energy storage system absorbed power

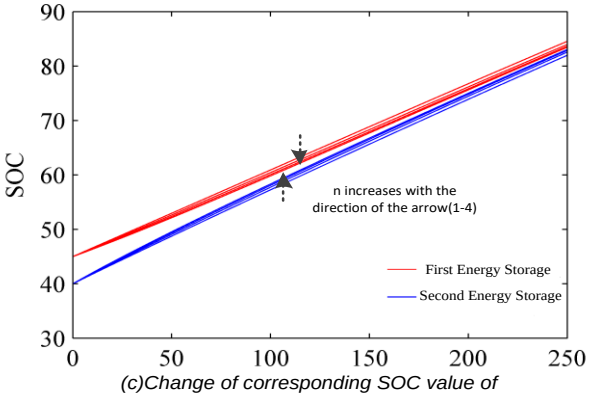

(c)Change of corresponding SOC value of energy storage system at different n values

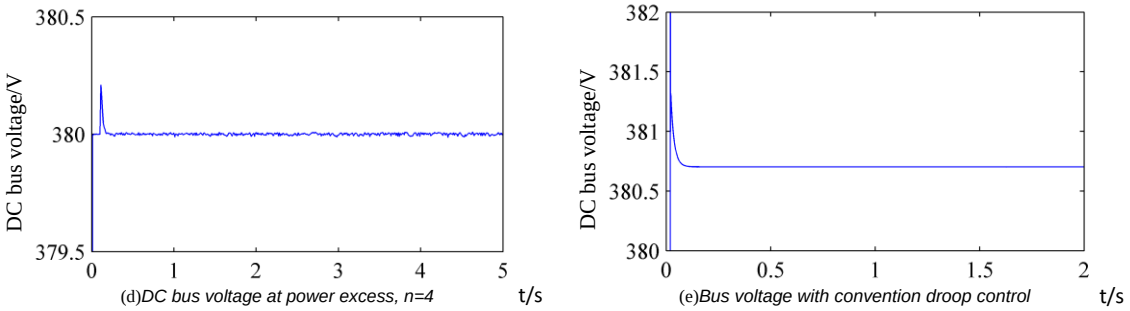

Figure 6: System power excess simulation results

It can be seen from Figure 6(d) that when the power of the power generation system increases, the self-compensating dynamic droop control is adopted in this paper, the energy storage system is quickly started, the bus voltage fluctuation is small, and it is stable at 380V. Compared with Figure 6(e), the traditional droop control, bus voltage due to droop coefficient is too large, the bus voltage rises to 380.7V. The self-compensation algorithm is used to eliminate the voltage increase and reduce the control complexity.

4.3. Partial battery fault removal

When part of the storage system exits due to a failure, the remaining energy storage system quickly adjusts the output power to maintain the stability of the system. Using the simulation of three energy storage systems, the initial SOC of the third energy storage system is 85, which is obtained from Figure 7(a). When the DC microgrid is at 0.1 s, the output power of the generation system is reduced, and the initial output power of the three sets of energy storage systems is proportional to the SOC value. And the output power tends to be equal gradually. At 30 seconds, the third group of energy storage systems exits operation. The remaining energy storage system quickly adjusts the output power to keep the system stable. The remaining energy storage system output power is proportional to the SOC at this time. As shown in Figure 7(b), when the third group of energy storage systems stops working, the DC bus voltage responds quickly and the voltage is stabilised at 380V. It can be seen that the self-compensating dynamic droop control strategy proposed in this paper can maintain the bus voltage stability and solve the voltage deviation problem caused by droop control.

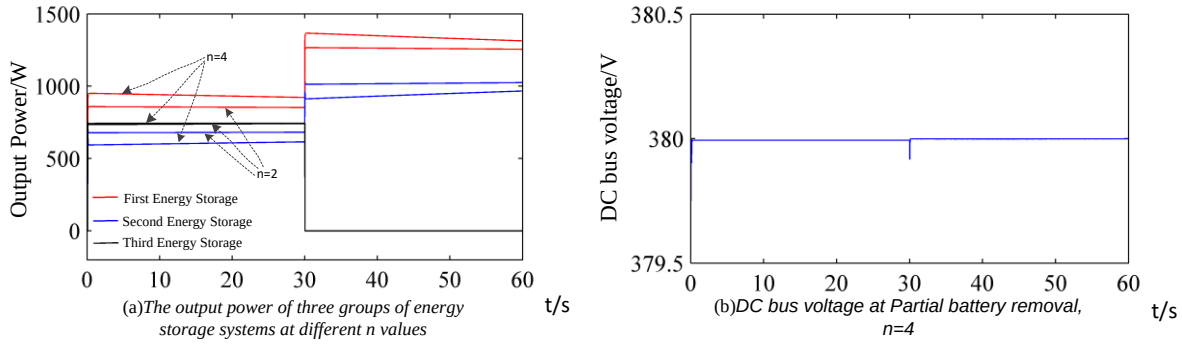

Figure 7: Some battery faults eliminate simulation results

5. CONCLUSION

In this paper, the self-compensating dynamic sag control strategy is proposed, in which uses multiple small-capacity energy storage systems to maintain the DC bus voltage stability of the microgrid and reduce the current of the converter in a single group of energy storage systems. In the case where the SOC values of multiple energy storage systems are different, in order to prevent the batteries from being overcharged and over-discharged, the energy storage system distributes the power proportionally according to their respective SOC values, thereby achieving SOC equalisation and power balance design requirements. At the same time, the self-compensating dynamic droop control strategy can improve the accuracy of power distribution. The voltage compensation algorithm can stabilise the bus voltage at the rated value, reducing the complexity of the control. The simulation results show that this strategy can use the renewable energy storage system to maintain the reliable operation of the microgrid under three different operating modes.

6. REFERENCES

Hu X ,Wang L, Gong, C, 2010. Harmonic analysis and suppression strategies of grid current for renewable energy grid integration system. Proceedings of the CSEE, 30 (S), 167-170.

Zhang Q, Peng C, Chen Y, 2012. A control strategy for parallel operation of multi-inverters in microgrid. Proceedings of the CSEE, 32 (25), 126-132.

Li W, Gu Y, Wang Y, 2015. Control architecture and hierarchy division for renewable energy DC microgrids. Automation of Electric Power Systems, 39(9), 156-163.

Guo L, Zhang S, Li X, 2016. Hierarchical coordination control for DC microgrid considering time-of-use price. Power System Technology, 40(7), 1992-2000.

Diaz NL, Dragicevic T, Vasquez JC, 2014. Intelligent distributed generation and storage units for DC microgrids-a new concept on cooperative control without communications beyond droop control. Transactions on Smart Grid, 5(5), 2476-2485.

Li X, Guo L, Wang C, 2016. Key technologies of DC microgrids: an overview. Proceedings of the CSEE, 36(1), 2-17.

Xiang Y, Fu M, Zhang A, 2017. Small signal stability analysis of AC/DC hybrid microgrid under isolated island operation, 38(1), 96-105.

Zhou X, Zhou L, Chen Y, 2018. A microgrid cluster structure and its autonomous coordination control strategy. Electrical Power and Energy Systems, 1(7), 69-80.

Shivam, Ratna D, 2017. Intelligent Distributed Control Techniques for Effective Current Sharing and Voltage Regulation in DC Distributed Systems. Electrical Engineering, 42, 5071-5081.

Lu X, Josep M.G, Sun K, 2014. An Improved Droop Control Method for DC Microgrids Based on Low Bandwidth Communication with DC Bus Voltage Restoration and Enhanced Current Sharing Accuracy. Transactions on Power Electronics, 29(4), 1800-1812.

Yang J, Jing X, Wu X, 2016. An Improved Load Current Sharing Control Method in DC Microgrids. Power System Technology. Proceedings of the CSEE, 36(1), 59-67.

Zhi N, Zhang H, Xiao X, 2016.Research on the Improved Droop Control Strategy for Improving the Dynamic Characteristics of DC Microgrid,Transactions of China Electrotechnical Society, 31(3), 31-39.

Chen M, Zha X, Jing X, 2016.Research on Parallel Control Strategy of Hybrid Energy Storage Units in DC Microgrid. Transactions of China Electrotechnical Society, 31(2), 142-149.

Chiang H-C, Jen K-K, You G-H, 2016. Improved Droop Control Method with Precise Current Sharing and Voltage Regulation. IET Power Electronics, 9(4), 789-800.

Mi Y, Wu Y, Ji H, 2017. Coordinative Control Based on Dynamic Load Allocation Among Multiple Energy Stroages for Islaned DC Microgris. Electric Power Automation Equipment,37(5), 170-176.

Shivam, R D, 2017. Intelligent Distributed Control Techniques for Effective Current Sharing and Voltage Regulation in DC Distributed Systems. Arab J Sci, 43, 5071-5081.

193: Control strategy of bidirectional convertor in DC/AC hybrid microgrid

Cheng XU [1], Jie ZHANG[1], Yunhao JIANG[1], Rui PEANG[1]

[1]Hubei Collaborative Innovation Center for High-efficiency Utilisation of Solar Energy, Hubei University of Technology, xch657279145@qq.com
[1] Hubei Collaborative Innovation Center for High-efficiency Utilisation of Solar Energy, Hubei University of Technology,274870985@qq.com
[1] Hubei Collaborative Innovation Center for High-efficiency Utilisation of Solar Energy, Hubei University of Technology,407307716@qq.com
[1] Hubei Collaborative Innovation Center for High-efficiency Utilisation of Solar Energy, Hubei University of Technology,1013305543@qq.com

The AC/DC hybrid power supply system can not only provide power for DC loads, but also can supply AC power equipment, and can also reduce power electronic components to improve power quality. Therefore, it is suitable for using in new energy buildings. The bidirectional DC/AC converter is an important device for realizing the power exchange between the DC sub-microgrid and the AC sub-microgrid in an AC/DC hybrid microgrid, and it is also a key device for maintaining the stable operation of the hybrid microgrid. The relationship between power and voltage in the microgrid is in line with PU droop characteristics. This paper proposes an improved droop control strategy that determines the power shortage (excess) value based on the relationship between the DC side capacitance and the voltage across AC and DC and delivers the corresponding power accordingly. To ensure the power balance in the microgrid system and maintain the stability of the system.

Keywords: AC-DC Hybrid Microgrid,Bidirectional DC/AC Converter,Improved droop control,Power balance

1. INTRODUCTION

With the vigorous promotion of new energy buildings and the vigorous development of DC power equipment, it is necessary to build an AC/DC hybrid microgrid that can directly supply power for DC power equipment and AC power equipment for new energy buildings. Compared with AC distribution networks and DC distribution networks, AC-DC hybrid microgrids have AC busses and DC busbars. They can directly supply AC power equipment and DC power equipment, reducing DC/AC, AC/DC conversion. In this way, the impact of power electronic switching devices on the power quality of the power grid can be reduced. The hybrid microgrid is divided into three parts: AC-DC sub-microgrids, DC sub-microgrids and bidirectional DC/AC converters. The normal operation of the hybrid microgrid must satisfy two aspects. On the one hand, it must ensure that the AC sub-microgrid and the DC sub-microgrid can operate stably at the same time; on the other hand, a bidirectional DC/AC converter is required to realise the power in the sub-network. The reasonable two-way flow between the networks, to achieve the overall coordinated operation of the AC-DC hybrid microgrid system. The development of AC/DC hybrid micro-grid and bi-directional DC/AC converter as the core device for AC side and DC side power exchange control strategy is the key to determine the stability of hybrid micro-grid and power quality.

In the AC/DC hybrid microgrid, the DC bus voltage stability, AC bus voltage and frequency stability are important indicators reflecting the stable operation of the hybrid microgrid system. Because of the intermittent nature of distributed energy, maintaining power balance within the system is particularly important. Ding *et al* (2015) proposed DC/AC converters in AC/DC hybrid microgrid to have three main functions in the operation of microgrid: First, when the microgrid system is running off-grid, the DC/AC converter must maintain the voltage and frequency of the AC side stability. Second, in the grid-connected operation, the DC/AC converter can transfer the DC side excess power to the grid. Third, it ensures the stable operation of the system when the grid-connected operation and the off-grid operation are switched. Tang *et al* (2013) suggest that droop control does not require the communication between each micro-source, automatically adjusts the output according to the bus voltage signal, improves the system stability, and is widely used in various distributed energy systems. Liu *et al* (2014) proposed a segmented droop control strategy to avoid the frequent switching of current direction due to the small range fluctuation of load or micro-source supply when the bi-directional converter works in equilibrium, affecting the lifespan and power of power electronic devices quality. Because the AC sagging characteristic is P-f and Q-V sagging, and the DC sagging characteristic is PV sagging, in order to unify the two sagging characteristics into a unified coordinate system, Xie *et al* (2016) unitises the signal quantities in the two sagging characteristics to facilitate the establishment of AC sagging. The relationship between AC characteristics and DC droop characteristics, Bouthaina *et al* (2016) adopts the AC-DC hybrid microgrid system with energy storage unit to incorporate the SOC of the energy storage unit into the reference signal of the DC/AC converter, which improves the stability of the system. Yu *et al* (2017) uses a voltage-type virtual synchronous generator to control the operation of a bidirectional DC/AC converter to achieve an even distribution of energy in the energy storage unit, but does not take into account the difference in SOC of each energy storage unit. Wang *et al* (2017) DC microgrid uses droop control to adjust the random fluctuation of high-frequency power, and the variable droop coefficient can suppress the fluctuation of DC voltage.

In AC/DC hybrid microgrids, capacitive charging and discharging are generally used to achieve power fluctuation stabilisation, but the power fluctuations of the capacitors are not linearly related to voltage fluctuations. The traditional droop control generally uses a fixed droop coefficient, and describes the relationship between power and voltage as a linear relationship. In order to ensure the microgrid control is more accurate, an improved droop control can be used.

2. AC-DC HYBRID MICROGRID SYSTEM

2.1. The structure of AC and DC hybrid microgrid

The AC-DC hybrid microgrid consists of two sub-micronets: a DC sub-microgrid and an AC sub-microgrid. The two sub-microgrids are connected by a bidirectional DC/AC converter and connected to the public power grid. Figure 1 is a schematic diagram of the AC-DC hybrid microgrid studied in this paper. The AC sub-microgrid in the AC/DC hybrid microgrid contains AC bus, AC load and diesel generator; the DC sub-microgrid has energy storage unit, DC load, photovoltaic power generation unit, wind power generation equipment and DC bus, among which the energy storage unit the photovoltaic power generation unit is passed through a DC/DC converter, and the wind power generation unit is connected to the DC bus through the AC/DC converter. The energy storage unit is used to regulate the power balance of the system, and the DC/DC converter it uses can control the bidirectional flow of power. Papers exceeding the page limit will need to revised and resubmitted.

AC-DC hybrid microgrids can work under both grid-connected and off-grid conditions. Under the grid-connected conditions, the AC sub-microgrid in the AC/DC hybrid microgrid is directly connected to the public power grid, and the large grid supports the voltage and frequency. In order to maintain the stable operation of the hybrid microgrid, only the DC bus in the sub-microgrid needs to be guaranteed. The voltage is stable. Under off-grid conditions, because the microgrid has lost

the support of the large grid, the micro-sources and DC-AC converters in the AC sub-microgrid need to adjust the output according to the voltage and frequency of the AC bus.

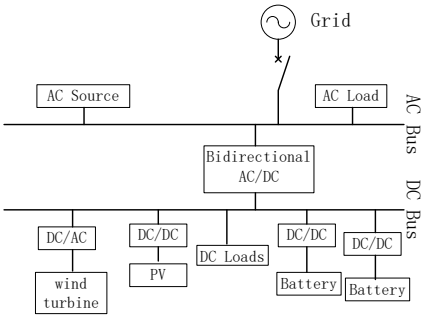

Figure 1: Simplified Schematic of AC-DC Hybrid Microgrid

2.2. AC drooping characteristics

In the AC microgrid, the droop characteristics of P-f and Q-U are shown in Equation (1) & (2):

Equation 1: P-f drooping characteristics

$$f = f_n - \frac{P_{ac} - P_n}{a}$$

Equation 2: Q-U drooping characteristics

$$U_{ac} = E_0 - \frac{Q}{b}$$

where,

f = AC bus voltage frequency(Hz)

f_n = AC bus nominal frequency (Hz)

P_{ac} = AC sub-micro network output power(W)

P_n =AC sub-micro network output nominal power

U_{ac} =AC bus voltage(V)

E_0 =AC bus nominal voltage(V)

Q =AC sub-micro-grid output reactive power

a , b drooping coefficient

2.3. DC droop characteristics

In the DC microgrid, there is no need to consider the issue of reactive power and frequency. The P-U droop characteristic is shown in Equation (3):

Equation 3: P-V drooping characteristics

$$U_{dc-ref} = U_{dc} - m \cdot \Delta P$$

where,

U_{dc} = DC bus voltage (V)

U_{dc-ref} =DC bus nominal voltage (V)

m = drooping coefficient

ΔP =Power fluctuation (W)

3. CONTROL METHOD OF BI-DIRECTIONAL DC-AC CONVERTER IN AC-DC HYBRID MICROGRID

Microgrids can operate under both grid and island conditions. When the microgrid is in grid-connected condition, the AC side voltage and frequency are supported by the public power grid. At this time, ensuring the stability of the DC bus voltage

ensures the stable operation of the microgrid. When the AC/DC hybrid microgrid is separated from the public grid and the microgrid system is operating under island conditions, due to the loss of support from the public grid, not only the DC bus voltage stability but also the AC bus voltage and frequency stability must be ensured at this time.

The AC/DC hybrid microgrid is different from the traditional "source-grid" type microgrid, which can be regarded as a "net-net" type microgrid, so the control of the bidirectional DC/AC converter in the hybrid microgrid will be similar to that of the general DC/AC. When the DC sub-micro network transmits power to the AC side, the DC sub-micro network can be regarded as a micro source at this time; similarly, when the AC side transmits power to the DC side, the AC sub-micro network should also be regarded as a DC micro's source of the web. However, in both cases, the droop characteristics that DC/AC follows are different.

3.1. Droop control of bidirectional DC/AC converters

In general, droop control is widely used in systems with many micro-sources. By using the bus voltage as a reference, the output of each micro-source is adjusted according to the droop characteristics, and the bus voltage is maintained stable.

In the research of this paper, when the AC-DC hybrid work is connected to the grid, the AC bus voltage and frequency are supported by the public power grid. In this case, only the stability on the DC side needs to be considered. The output power of the bi-directional DC/AC converter corresponds to the bus voltage, and the DC output characteristic of the bi-directional DC/AC converter complies with the DC droop characteristic. Figure 2 shows the relationship between the transmission power of the bidirectional DC/AC converter and the DC bus voltage.

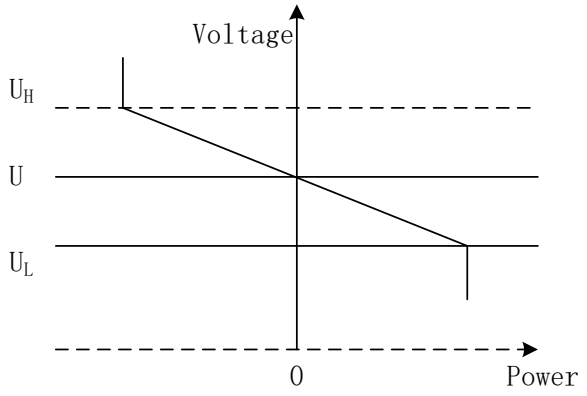

Figure 2

If the loss of the bidirectional converter is ignored, the active power balance in the microgrid is as follows:

Equation 4: AC side power balance

$$P_{\text{grid}} = \sum P_{ac,i}^{\text{load}} - P_{dcac}$$

Equation 5: DC side power balance

$$\sum P_{dc,j} = P_{dc,i}^{load} + P_{dcac}$$

P_{grid} = Power exchange between the microgrid and the public power grid(W)

$P_{ac,i}^{load}$ =Active power consumed by AC side load i (W)

P_{acdc}= power transmissed by Bidirectional converter (W)

$P_{dc,j}$ =DC side micro-source j output power (W)

$P_{dc,i}^{load}$ =DC side load i consumes power (W)

Due to the limitation of the rated power of the bidirectional DC/AC converter, when the fluctuation of the bus voltage exceeds a limit value, the power transmitted by the bidirectional DC/AC converter is limited to the rated value.

When the AC/DC hybrid microgrid works in off-grid mode, due to the loss of public grid support, the load requirements in the microgrid system, the stability of the AC microgrid voltage and frequency, and the stability of the DC microgrid voltage

all need to be handled by the system. The source and the energy storage unit ensure that, at this time, the power balance of the micro-grid system is particularly important, and the loss of the converter is ignored. The power balance formula in the AC/DC hybrid micro-grid is as follows Equation 6.

Equation 6: Microgrid system power balance

$$\sum P_{dc,i}+\sum P_{ac,i}+\sum P_{s,i}=\sum P_{dc,i}^{load}+\sum P_{ac,i}^{load}$$

where,

P_{dc} = The power provided by the micro source on the DC side (W)

P_{ac} = The power provided by the micro source on the AC side(W)

P_s = Energy provided by energy storage unit (W)

In the off-grid state, the droop characteristics of the DC microgrid did not change. The relationship between the AC microgrid P-f and Q-V is shown in the following Figure 3:

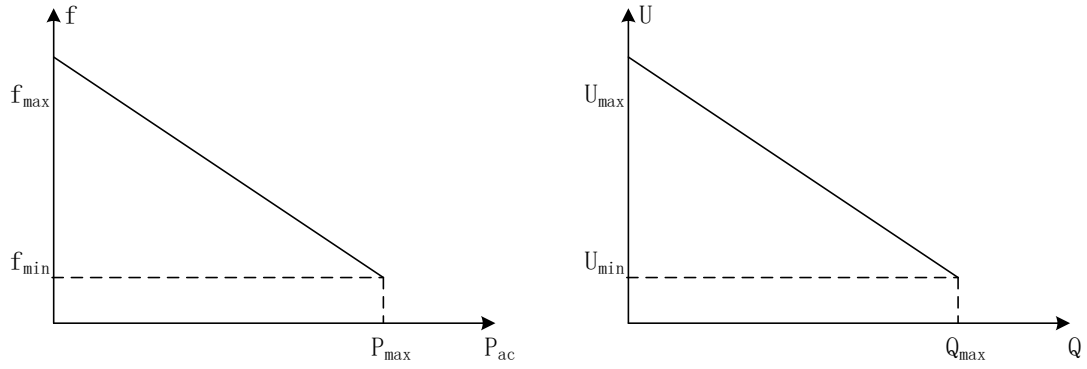

(a)P-f characteristic curve *(b)Q-U characteristic curve*

Figure 3: AC droop characteristics

In the AC-DC hybrid microgrid, the power transfer on both sides of the AC and DC is achieved through the charging and discharging of DC bus capacitors. According to the principle of power balance, the DC side output (absorption) power and the AC side absorption (output) power are equal, and the stored energy on the DC side bus capacitance is Equation 7.

Equation 7: Capacitor stored energy

$$W_C=\frac{1}{2}C_{dc}U_{dc}^2$$

Equation 8: The relationship between power fluctuation and voltage

$$\frac{dW_C}{dt}=\frac{1}{2}C_{dc}\frac{dU_{dc}^2}{dt}=\Delta P$$

where,

W_C = DC bus capacitance stored energy

C_{dc} = DC bus capacitance (F)

U_{dc} = DC bus voltage (V)

4. IMPROVED DROOP CONTROL OF BIDIRECTIONAL DC/AC CONVERTERS

Figure 4 shows a schematic diagram of the converter's grid connection. In the figure, the inverter is simplified as a voltage source Us ∠ δ , which is connected to the grid E ∠ 0° through a connection line with an impedance of R+jX.

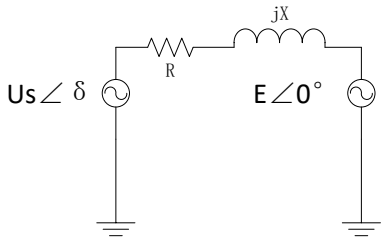

Figure 4 shows a schematic diagram

The inverter output active P and reactive Q are respectived by Equation 9 and Equation 10.

Equation 9:

$$P=\frac{E}{R^2+X^2}\left[R\left(U_s\cos\delta-E\right)+XU_s\sin\delta\right]$$

Equation 10:

$$Q=\frac{E}{R^2+X^2}\left[X\left(U_s\cos\delta-E\right)-RU_s\sin\delta\right]$$

Synchronous type 9 and 10 can be obtained

Equation 11:

$$U_s\sin\delta=\frac{XP-RQ}{E}$$

Equation 12:

$$U_s\cos\delta-E=\frac{RP+XQ}{E}$$

This article studies the low-voltage microgrid system. In the low-voltage microgrid system, there is a difference between the line characteristics and the high-voltage network, that is, $X \square R$. In this case, X is ignored. At this time, it can be considered as $\sin\delta=\delta$, $\cos\delta=1$, the above formula becomes Equation 13 and Equation 14.

Equation 13:

$$\delta\approx\frac{-RQ}{U_sE}$$

Equation 14:

$$U_s-E\approx\frac{RP}{E}$$

Therefore, the sagging characteristics of the active voltage and reactive frequency on the AC side are become Equation 15 and Equation 16.

Equation 15: Q-f drooping characteristics

$$f-f_0=k_{qi}\left(Q-Q_0\right)$$

Equation 16: P-U drooping characteristics

$$U-U_0=-k_{pi}\left(P-P_0\right)$$

According to the P-U droop characteristics analysed above, a bidirectional DC/AC converter control strategy is designed. This article uses the power outer loop, current inner loop control strategy. The reference value of the power outer loop is calculated based on the AC-DC bus voltage. The controller schematic is shown in Figure 5. In the schematic diagram of the controller, S is the state quantity. When S=1, the sign microgrid is in off-grid mode; when S=0, the microgrid is connected to the large power grid.

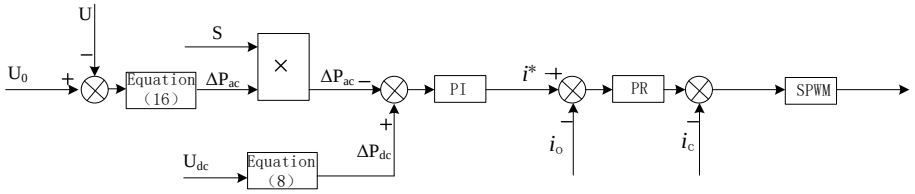

Figure 5: Control schematic

The main task of the bi-directional DC/AC converter is to transmit active power. Therefore, considering the limit of the capacity of the converter, the maximum value of reactive power is set to $Q_{\max} = \sqrt{S_{\max}^2 - P_{\max}^2}$, where $S_{\max}$ is the maximum apparent power of the converter, and the power is inactive. The reference value of power is calculated using the AC frequency-reactive power (fQ) droop characteristic curve.

5. SIMULATION ANALYSIS

In order to verify that the improved droop control strategy can realise the mutual support of the AC and DC sides of the AC-DC hybrid microgrid, a simulation platform was built on Matlab/Simulink to verify the simulation.

In the simulation, the initial operation mode of the AC/DC hybrid microgrid is that the power provided by the micro-source on the DC side is equal to the power consumed by the DC load, the AC side is also in a power balance state, the DC bus voltage is stable running at a rated voltage of 400V, and the interior of the hybrid microgrid is self power balance. At this time, the output current of the AC-DC bidirectional power converter is 0. When t = 1 s, the DC side power excess (shortage), resulting in changes in the system DC bus voltage, this paper gives the micro-grid operation results under two different conditions of the power surplus and shortage of the DC side.

Figure 6 shows the simulation results of AC-DC hybrid microgrid system with excess DC side power. Figure 6(a) is the DC bus capacitor voltage waveform diagram, the initial state of the system for each sub-network power balance operating state, bi-directional DC / AC converter does not transmit power at t = 1s, DC side power excess, this time causing the DC bus When the voltage rises, the bi-directional DC/AC converter starts to work, and the DC side excess power is transferred to the AC side, so that the DC side bus voltage is restored to the rated value of 400V.

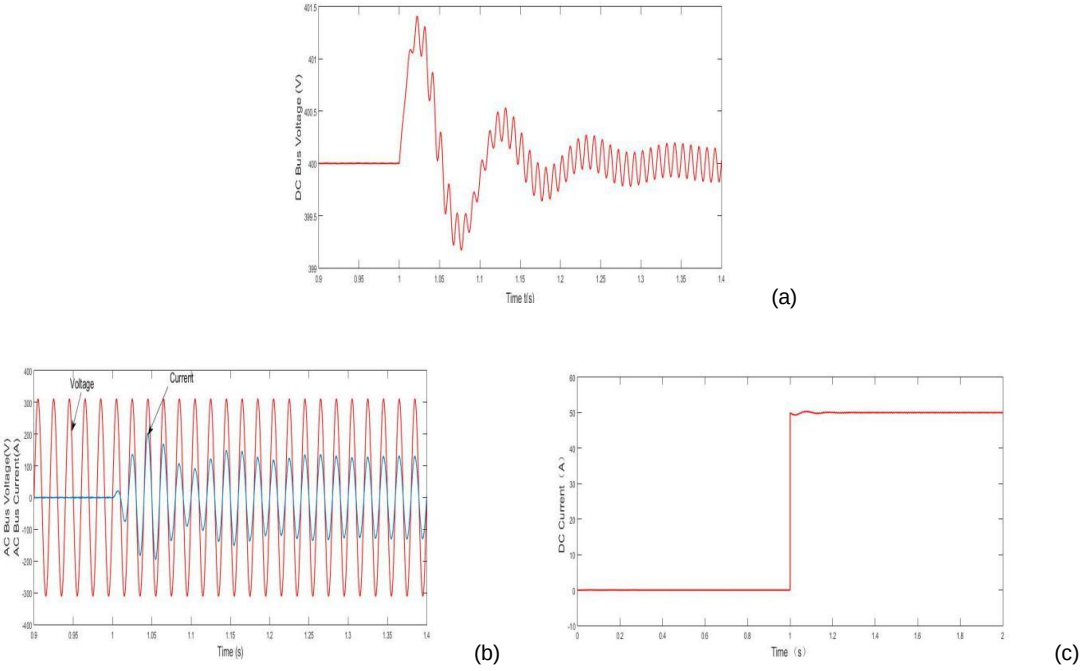

Figure 6: Inversion mode

Figures 6(b) and (c) respectively shows the output and input current of the DC/AC converter when there is excess power on the DC side.

Figure 7 shows the simulation results of AC-DC hybrid microgrid system on the DC side power shortage. The initial state of the system is the power balance state in each sub-network. The bi-directional DC/AC converter does not transmit power. At t = 1 s, the DC-side power shortage causes the DC bus voltage to drop, and the bidirectional DC/AC converter starts. Work, transfer power from the AC side to the DC side, and restore the DC bus voltage to the rated value of 400V.

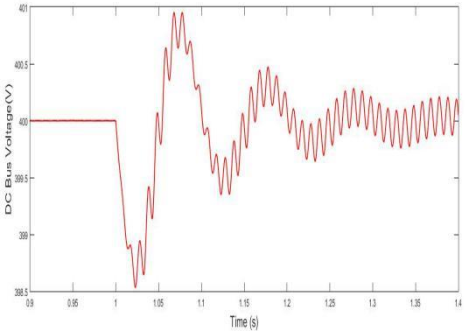

(a)

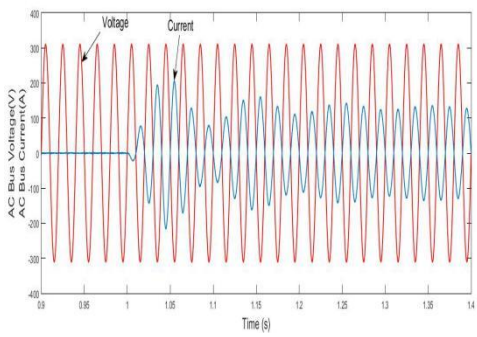

(b)

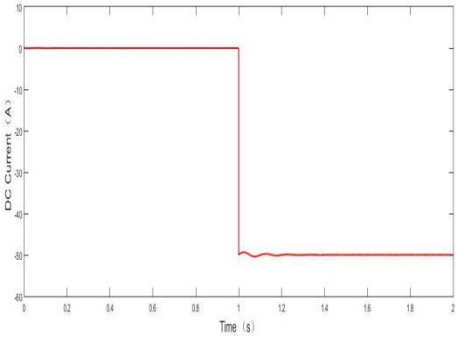

(c)

Figure 7: Rectification mode

Figures 7(b) and (c) respectively shows the input and output current of the DC/AC converter when the DC side power is insufficient.

6. CONCLUSION

For the bidirectional flow of energy in AC/DC hybrid microgrids, an improved droop control strategy is adopted based on the relationship between the DC side capacitance and the AC/DC voltage on both sides, and a simulation platform is built to verify the simulation. Through simulation, it is verified that the improved droop control adopted in this paper has the following advantages: (1) The bidirectional DC/AC converter can exchange the power balance in the microgrid system through the power, whether it is the power shortage on the DC side or the excess power, thus ensuring micro the stable operation of the power grid; (2) The control system adjusts the droop coefficient in real time according to the AC and DC bus voltage signals in the microgrid; (3) The droop coefficient of the droop control used in this paper is adjusted according to the voltage change rate, which relieves the impact on the system caused by power mutation.

With the vigorous development of new energy buildings, AC-DC hybrid microgrids will be a trend of development. Bidirectional DC/AC converters are of great significance to the operation of AC/DC hybrid microgrids. The research of this paper is in hybrid AC/DC microgrids. It has very good prospects.

7. REFERENCES

Ding M, Tian L, Pan H, Zhang X, Zhou J, 2015.Research on control strategy of hybrid AC/DC microgrid.*Power System Protection and Control,* 43(09):1-8.

Tang L, Zeng C, Miao H, Xu W, Yang Y, 2013.One novel control strategy of the AC / DC bi-directional power converter in micro-grid.*Power System Protection and Control,* 41(14):13-18

Liu J, Qin W, Han X, Liu X, Zhu X, 2014.Control Method of Interlink-Converter in DC Microgrid. *Power System Technology,* 38(02):304-310.

Xie W, Zhu Y, Du S, Xia R, 2016. Power Control of Interconnected Converters in AC/DC Hybrid Microgrid. *Electric Power Construction,* 37(10):9-15.

Bouthaina M, Rachid C, Erol K, Kamel EH. Design and control of a stand-alone hybrid power system[J].International Journal of Hydrogen Energy, 2016, 41(29):12485-12496

Yu J; Ming W; Yang L; Hongbin W, 2017.IEEE International Conference on Energy Internet (ICEI)/Operating Characteristic Analysis of Hybrid AC/DC Microgrid under Energy Internet.Beijing: IEEE

Wang Y, Hei Y, Fu Y, Shi K, 2017. Adaptive Virtual Inertia Control of DC Distribution Network Based on Variable Droop Coefficient. *Automation of Electric Power Systems,* 41(08):116-124.

Sun X, Lü Q*, 2012.* Improved PV Control of Grid-Connected Inverter in Low Voltage Micro-Grid.Transactions of China Eelectrltechnical Society, 27(08):77-84.

Tang L, Zeng C, Miao H, Xu W, Yang Y, 2013.One novel control strategy of the AC / DC bi-directional power converter in micro-grid.*Power System Protection and Control,* 41(14):13-18

Yang J, Jin X, Yang X, Wu X, 2017.Overview on Power Control Technologies in Hybrid AC-DC Microgrid.*Power System Technology*, 41(1):29-39

195: A fuzzy control constant polarisation voltage charging method for lithium-ion batteries

Xiaohua ZHANG[1], Pengcai SONG[2], Zhenyu YANG[3], Jie DENG[4]

[1] Hubei Collaborative Innovation Center for High-efficiency Utilisation of Solar Energy, Hubei University of Technology, Wuhan China, zxh.hbgd@163.com
[2]Hubei Collaborative Innovation Center for High-efficiency Utilisation of Solar Energy, Hubei University of Technology, Wuhan China, 1121191624@qq.com
[3]Hubei Collaborative Innovation Center for High-efficiency Utilisation of Solar Energy, Hubei University of Technology, Wuhan China, 903313780 @qq.com
[4]Hubei Collaborative Innovation Center for High-efficiency Utilisation of Solar Energy, Hubei University of Technology, Wuhan China, 593263495@qq.com

Electric car is the future development trend of the automobile industry. Currently, the electric car's energy storage components are mainly batteries. Various types of, batteries have been studied for many years, compared with traditional lead-acid and nickel-cadmium batteries, lithium-ion battery has the advantage of high energy ratio, long life, low pollution and high operating voltage characteristics. The polarisation during charging is the main factor affecting the fast charging efficiency of lithium-ion batteries. Although the current charging method for lithium-ion batteries is faster, the methods of improving the charging efficiency and prolonging the life by controlling the polarisation of the battery need to be further improved. Therefore, in this paper an alternate fast charging technology which can maintain constant polarisation voltage is proposed. Based on the traditional lithium battery RC equivalent circuit model，the charging process of lithium battery is simulated. The charging current, the initial state-of-charge (SOC), the initial polarisation state, the cycle life and other aspects are analysed. The relationship between the polarisation voltage and SOC is established. The polarisation voltage is divided into different sections, and it is controlled within constant threshold value. On the basis of this study, the fuzzy control algorithm is used to control the charging polarisation voltage to optimise the fast charging of the battery, so that the charging current can adapt to the SOC rechargeable current of the lithium-ion battery at any time. The experimental results show that compared with the traditional constant-current constant-voltage charging(CC-CV) method, the proposed constant polarisation charging method can greatly shorten the charging time by about 20% and therefore the charging efficiency is improved, while there is no obvious difference in temperature rise.

Keywords: lithium-ion battery; constant polarisation; fuzzy control; charging time; cycle life

1. INTRODUCTION

Normal charging methods are usually controlled by current or voltage control, or follow the law of Maas law (Abdel-Monem 2017). The current control is a widely used method, using a small current to charge the battery which can effectively prevent a substantial increase in voltage and temperature. This charging method has a difficulty in choosing a suitable charging current to balance the charging time and capacity (Cousland 2010; Chambon 2017; Paul 2017; Liu 2017) It is difficult to ensure that the battery is safe to charge. Using the voltage control method in which the battery is charged with a constant voltage, This method can effectively prevent the battery from being overcharged (Peters 2017), but this method has a large current in the initial charging, it would reduce the battery life. Constant current constant voltage charging method combines two control methods to improve the charging performance and safety. In the meanwhile, Maas law has also been widely used, which calculates the charging current of the battery by the Maas three-law, but the law is designed for lead-acid battery, not for lithium-ion battery. In recent years, some intelligent charging methods, such as fuzzy control, ant colony genetic algorithm and other methods have been proposed by applying the intelligent control algorithm to control the charging current trajectory in order to enhance the battery charging speed (Zhang 2010; Wei 2017; Torchio 201; 5 Gopaluni 2013; Zhang). Although these control algorithms can increase the charging speed and charging efficiency, their structure is complex and the calculation time is too long, so it is difficult to meet fast change in the demand during the lithium-ion battery charging.

Therefore, a fast charging technology that can maintain constant polarisation voltage is propsed in this paper. This method first uses the resistor-capacitor (RC) polarisation voltage circuit model to estimate the charge polarisation voltage, which is used to simulate the lithium-ion battery charging process, but also analyzes the linear and non-linear influencing factors on the polarisation voltage (Tsang 2010; Mills 2015; Fathabadi 2014 Dogger 2011). In addition, the lithium-ion battery current, state-of-charge (SOC), charging time and polarisation voltage are also considered (Maher 2014; Yang 2016; Panchal 2016). On the basis of the charging time and SOC, the polarisation voltage is analyzed and the relationship between the polarisation voltage, the current and SOC is found (Ling 2015). Finally, this paper presents a method based on the control of the polarisation voltage using fuzzy control technology for lithium-ion battery fast charging method, which can make the charging current adapt to the current state of the battery current. This method can not only have a certain effect on the lithium-ion battery charging technology, but also has a certain reference value for the design of electric vehicle charging device.

2. THE CHARACTERISTICS OF CHARGE POLARISATION VOLTAGE

2.1. Polarisation voltage estimation

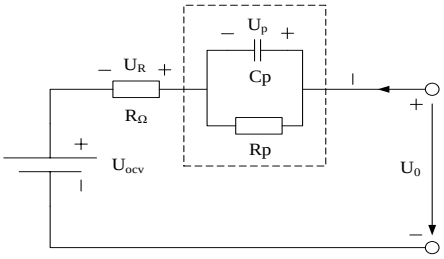

Figure1: Lithium-ion battery "Davein" equivalent circuit diagram

The lithium-ion may be represented to the "Davein" equivalent circuit model, as shown in Figure 1, to describe the lithium-ion battery charge and discharge process. The electromotive force in the lithium-ion battery model is equal to the open circuit voltage (U_{OCV}), and the inherent electrical conductivity and its polarisation effects in the chemical structure are represented by an ohmic internal resistance and a resistor-capacitor (RC) network. The voltage balance equation is:

Equation 1: The voltage balance equation

$$U_O = U_{OCV} + U_P + U_R$$

Where:

U_O = the terminal voltage of the lithium-ion battery (V)

U_{OCV} = the open circuit voltage (V)

U_P = the polarisation voltage of the battery (V)

U_R = the ohmic voltage drop (V)

Through the experience we know that the open circuit voltage is a function of state-of-charge (SOC). When the SOC is known, there is a balanced equation to get the polarisation voltage, which can be expressed as:

Equation 2: the polarisation voltage

$$U_P = U_O - f_{OCV-SOC}(SOC) - U_R$$

Where:

$f_{OCV-SOC}(SOC)$ = the open circuit voltage as the function of SOC (V)

Assuming that the open-circuit voltage is linearly related to SOC in a fixed time interval, the SOC is segmented and can be linearised based on the curve to fit the equation:

Equation 3:The SOC is segmented

$$f_{OCV-SOC} = \begin{cases} H(0) \times SOC + B(0), & 0 < soc \le 10\% \\ H(1) \times SOC + B(1), & 10\% < soc \le 20\% \\ \vdots & \vdots \\ H(8) \times SOC + B(8), & 80\% < soc \le 90\% \\ H(9) \times SOC + B(9), & 90\% < soc \le 100\% \end{cases}$$

Where:

H and B = the slope and intercept of the line, respectively.

It can accurately calculate the open circuit voltage, while the ohmic voltage drop product U_R can be given, through the product of the battery current and resistance, so the polarisation voltage U_P can be calculated from Equation 2.

2.2. Polarisation analysis

Polarisation of the battery is caused by many reasons, including linear and non-linear factors.Based on the "Davidin" model, it can be seen that the characteristics of the polarisation voltage amplitude are related to the parameters of the RC. Figure 2 shows, the polarisation volatge of an n-order RC model.

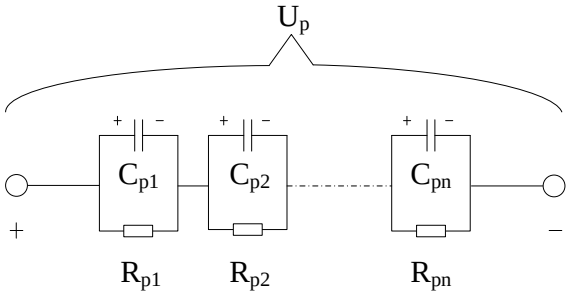

Figure 2: Polarisation voltage of an n-order RC model

Based on the n-order RC model, the polarisation voltage of a lithium-ion battery can be expressed as:

Equation 4: The polarisation voltage of a lithium-ion

$$u_P(t) = \sum_{i=1}^{n} \left(U_{pi}(0) \times \exp(-t/R_{Pi}C_{Pi}) + I \times R_{Pi}(1 - \exp(-t/R_{Pi}C_{Pi})) \right)$$

Where:

$U_{Pi}(0)$ = the initial polarisation voltage in the RC model (V)

I = the battery charging current(A)

Assuming that the RC model reaches the saturation state after a certain charging time, Equation 4 can be changed to:

Equation 5: The change of polarisation voltage

$$U_P = U_P(0) + I \times R_{P1} + I \times R_{P2} + \cdots + I \times R_{Pk} + I \times R_{Pk+1}(1 - \exp(-t/R_{Pk+1}C_{Pk+1})) + \cdots + I \times R_{Pn}(1 - \exp(-t/R_{Pn}C_{Pn}))$$

Where:

$U_P(0)$ = the total initial polarisation voltage of the n-order RC model (V)

The saturation time constant must be satisfied:

Equation 6: The saturation time constant $3R_{P0}C_{P0} < \cdots < 3R_{P(k-1)}C_{P(k-1)} < 3R_{Pk}C_{Pk} < T$

Where:

T = the total charge time (S)

In the RC model, the high frequency concentrated components must reach a saturation state T before the low frequency component is in an unsaturated state. Equation 5 can be simplified to

Equation 7: The change of Equation 5 $U_P = U_P(0) + I \times A_1 + I \times A_2 + \cdots + I \times A_k + I \times A_{k+1} + \cdots I \times A_N$

Where:

$$A_k = \begin{cases} R_{Pk}, & 0 < k \le K \\ R_{Pk+1}(1 - \exp(-T/R_{Pk+1}C_{Pk+1})), & K+1 \le k < N \end{cases}$$

In which $A_1 \cdots A_n$ represents the linearity of the polarisation voltage, indicating that the same charge current, the different RC model requirements under the battery polarisation.

However, the charge polarisation is not only related to the parameters of the RC model, but also to the non-linear factors such as the current, the initial SOC, the duration, and the number of battery cycles. Consider all the factors that charge the polarisation voltage at the specified time as in Equation 8:

Equation 8: All the factors that charge the polarisation voltage $U_P = f_{U_{P-t}}(I, t, K_{SOC}, K_I, B_{SOH}, B_{P0^-}, A_1, A_2, \cdots, A_N)$

Where:

K_I = the charge factor

K_{SOC} = the initial SOC state coefficient

B_{SOH} = the battery cycle number

B_{P0^-} = the initial polarisation state coefficient

It can be seen from Equation 8 that the initial polarisation state and the degree of aging have a double effect on the polarisation voltage in the nonlinear effect, whereas the battery current and SOC have no effect on the polarisation voltage. Therefore, the main effect of the battery charge polarisation voltage is the battery current and the initial SOC.

3. FUZZY CONTROL CONSTANT POLARISATION CHARGING METHOD

3.1. Constant polarisation charge control strategy

Ohmic resistance and polarisation caused by the loss of over-voltage can be used to quantify the lithium-ion battery charging efficiency and charging capacity. From an electrochemical point of view, the polarisation voltage is an indirect measure of the chemical reaction rate. According to the previous analysis,consider the electrochemical principle, one can control the polarisation voltage to effectively control the battery electrolyte concentration and electrode reaction rate. From the electrical point of view, one can control the charge current to maintain the polarisation voltage at a specified value, thus controlling the charging fficiency, so that it can adapt to different SOC, battery aging and initial polarisation state. Hence, when the charging conditions change, lithium-ion battery current state can be automatically optimised for charging current.

3.2. The reference value of the polarisation voltage reference control

Based on the "charge polarisation characteristics" described above, it is shown that the establishment of the amplitude of the polarisation voltage is related to the parameters, current, initial SOC, initial time and battery aging of the RC model. From Equation (8), current I can be given:

Equation 9: The battery charging current

$$I = \left[U_P - U_P(0) - B_{P0^-} - B_{SOH}\right] \Big/ \left[K_{SOC} \times K_I \times (A_1 + A_2 + \cdots A_N)\right]$$

Based on Equation 9, the appropriate charge current can be obtained from the initial SOC state, health condition and initial polarisation state of the lithium ion battery. The energy efficiency of the charging can also be obtained by the current I and the interruption voltage. So one can also control the charge polarisation to optimise the charge capacity, charging time, charging life.

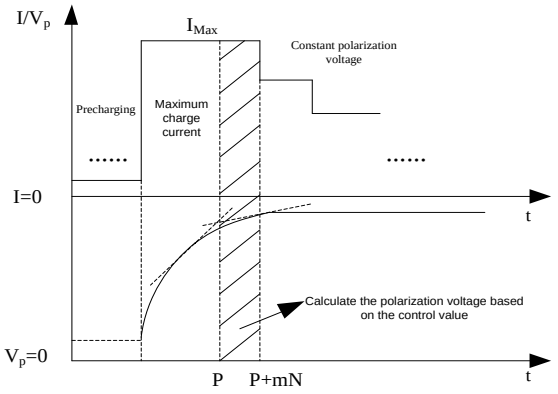

Figure 3: Principle of maximum current selection method

The maximum current for the polarisation characteristics of lithium-ion batteries is determined by the maximum current method. The chargeable current of the battery depends on the SOC of the battery, so the maximum charge current should be at the minimum SOC stage of the polarisation voltage. The maximum current selection method is to determine the method of controlling the polarisation voltage when the battery is charged with the maximum charge current at the maximum acceptable charge capacity. This method can be based on lithium-ion battery charging conditions in the initial charge phase of the battery with the maximum charge current charging automatically search for the minimum polarisation voltage, but also a reasonable increase in charge current, thereby shortening the charging time.

Lithium-ion battery charging capacity varies with the SOC, lithium-ion battery can be within the SOC with an acceptable maximum current charge, the establishment of the minimum polarisation voltage to determine the control polarisation voltage .The principle of maximum current selection is shown in Figure 3, and the polarisation voltage (U_{PC}) control value is selected by Equation 10.

Equation 10: Polarisation voltage error rate of change

$$M = \partial Err_{U_P} \Big/ \partial SOC$$

Where:

Err_{U_P} = the polarisation voltage error between the target value and the feedback value

Assuming that the maximum charge current is I_{max} and the control polarisation voltage is U_P .As shown in Figure 3, it is shown that the sampling interval of the polarisation voltage is from P to (P + mN). The average polarisation voltage is defined as the following equation:

Equation 11: The average polarisation voltage

$$U_{PG} = \bar{U}_P = \left[\sum_{i=0}^{m} U_P(m \times N)\right] \Big/ m$$

Therefore, we can control the polarisation voltage through the U_{PG} trajectory to accommodate the charging current under different SOC.

3.3. Polarisation charge control based on fuzzy control algorithm

In summary, the factors that affect the charge polarisation voltage include not only the linear part but also the nonlinear coefficient, however, the nonlinear factor is a variable. Conventional closed-loop control, such as calculus control, has difficulties in implementing polarisation voltage control. In order to solve this problem, the use of fuzzy control algorithm to control the charge polarisation voltage, is used to regulate the charge current. Based on the fuzzy control method. The polarisation voltage error (Err_{U_P}) range and its rate of change ($\partial Err_{U_P} / \partial SOC$) can be established. A closed-loop control system is designed to find the relationship between the corresponding polarisation voltage and the output current. Through the target polarisation voltage control, the charge current is adjusted to achieve lithium-ion battery charge and polarisation control. The fuzzy control logic diagram is shown in Figure 4.

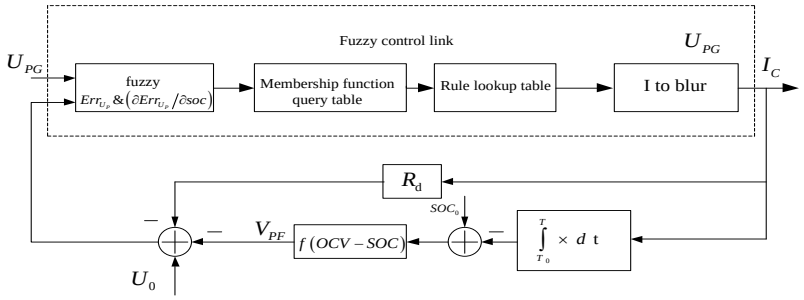

Figure 4: Fuzzy control logic flow chart

Table 1: Polarisation voltage error classification

quantitative level	-5	-4	-3	-2	-1	-0
value (mV)	≤-5	(-5,-4]	(-4,-3]	(-3,-2]	(-2,-1]	(-1,-0]
Quantitative level	-0	1	2	3	4	5
value (mV)	[0,1)	[1,2)	[2,3)	[3,4)	[4,5)	≥-5

As shown in Figure 4, the system output is the charge current I_C , the control output is the polarisation voltage U_{PG} . The feedback function from the I_C to the U_{PG} is known and is controlled by fuzzy logic. The value of the polarisation voltage between the target value and the feedback value and its SOC change rate are input variables as fuzzy logic control. Then, based on the fuzzy rules, the algorithm can give the output current I_C . The feedback polarisation voltage V_{PF} can be estimated from SOC, OCV and charge current.

Based on the basic principle of fuzzy control, the polarisation voltage error (Err_{U_P}) can be divided into several levels, as shown in Table 1.

Polarisation voltage error can be divided into six categories, positive (PB), positive (PS), positive zero (PO), negative zero (NO), negative (NS), negative (NB):

$$PB = \frac{0.1}{+3} + \frac{0.6}{+4} + \frac{1.0}{+5}$$

$$PS=\frac{0.7}{+1}+\frac{1.0}{+2}+\frac{0.7}{+3}+\frac{0.2}{+4}$$

$$PO=\frac{1}{+0}+\frac{0.8}{+1}+\frac{0.4}{+2}+\frac{0.1}{+3}$$

$$NO=\frac{0.1}{-3}+\frac{0.4}{-2}+\frac{0.8}{-1}+\frac{1}{-0}$$

$$NS=\frac{0.2}{-4}+\frac{0.7}{-3}+\frac{1.0}{-2}+\frac{0.7}{-1}$$

$$NB=\frac{1.0}{-5}+\frac{0.6}{-4}+\frac{0.1}{-3}$$

And the rate of change in the polarisation voltage error($\partial Err_{U_P}/\partial soc$) can be divided into different levels, as shown in Table 2.

Table 2: $\partial Err_{U_P}/\partial soc$ *classification*

Quantitative level	-1	0	1
value (mV)	≤-10	(-10,10)	≥10

Table 3: SOC output current gradient classification

ΔI level	-2	-1	0	1	2
value (A/soc)	-4/dsoc	-4/3dsoc	0	4/3dsoc	-4/dsoc

Table 4: Fuzzy logic control table

$\partial Err_{U_P}/\partial soc$ / Err_{U_P}	NB	O	PB
NB	PB	PB	O
NS	PB	PS	O
NO	PS	O	O
PO	O	O	NS
PS	O	NS	NB
PB	O	NB	NB

The function of each class can be expressed as:

$$PB=\frac{1.0}{+2} \quad O=\frac{1}{0} \quad NB=\frac{1.0}{-2}$$

According to the polarisation voltage hysteresis for the output current frequency adjustment method, the minimum SOC sampling rate is taken as the basic event control unit (*dsoc*), and the output current change rate (ΔI) is divided into five stages based on the fuzzy set value range definition, as listed in Table 3.

When Err_{U_P} or $\partial Err_{U_P}/\partial soc$ is high, the charge current will drop to a lower polarisation voltage. When Err_{U_P} or $\partial Err_{U_P}/\partial soc$ is too high, the charge current change rate also needs to rise. The specific logic control table is shown in Table 4. The charge current is adjusted by controlling the polarisation voltage.

4. EXPERIMENTS AND RESULTS ANALYSIS

First, the relationship between constant polarisation and charge current is experimentally verified. The LiMn2O4 battery with capacity of 72Ah was selected as the experimental object, and it was charged by adding a fuzzily controlled constant polarisation charging method. In the constant polarisation charging mode, after the initial polarisation voltage was set to a fixed value, Fuzzy control in the charging process can maintain the polarisation voltage in the set fixed value. The battery charging curve is shown in Figure 5. It can be seen that the charging current fluctuates obviously during the initial charging phase (0 to 500s), and the mid-charging period (500-3500s) fluctuates little and decreases rapidly at the end of charging (3500s-4500s). In addition to the ohmic voltage, the battery terminal voltage is different, the open circuit voltage remains constant. It can be concluded that the fuzzy control can be adjusted to keep the polarisation voltage fluctuating around a set constant value, although a certain control hysteresis begins, but during the control process, the polarisation voltage can be kept constant by adjusting the charge current.

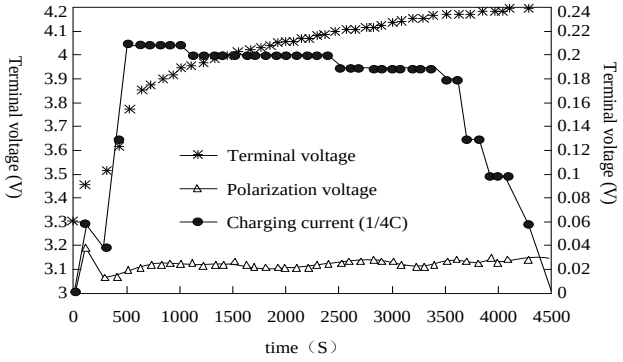

Figure 5: Charge curve using the constant polarisation fuzzy control

In order to verify the charging performance of the constant polarisation charging method using fuzzy control, the same lithium-ion batteries were randomly divided into three groups, namely, experimental sample batteries 1, 2 and 3, and three experiments were carried out under the same external conditions, using the experimental platform as shown in Figure 6.

Figure 6: Lithium-ion battery fast charge and discharge test platform

In Experiment 1, Sample Battery 1 was first charged with the proposed fuzzy control constant polarisation method until the capacity was charged to 100%, the polarisation voltage control value was 30mV, and then discharged at 0.3C current until the battery terminal voltage was reduced to 3.0V. The experiment was repeated 100 times.

In Experiment 2 and Experiment 3, Sample Battery 2 and 3 were respectively charged with constant current-constant voltage (CC-CV) charging method, and the constant current was 0.3C and 1C, respectively. Then, these two sample batteries was subjected to a discharge experiment in the same manner as in the first experiment, and the same experiment were repeated for one hundred times. All experiments were carried out under the same room temperature, and the results of the three charging modes were shown in Table 5.

Table 5: Comparison of Constant Polarisation Charge Mode and CC-CV Charge Mode

Battery number	Charging method	Chargecapacity (%)	Charging time (s)	Maximumtemperature rise (℃)	Maximum current (C)
1	Constant Polarisation	100%	5760	6	1
2	CC-CV(mode 2)	100%	11520	5	0.3
3	CC-CV(mode 3)	100%	4320	8	1

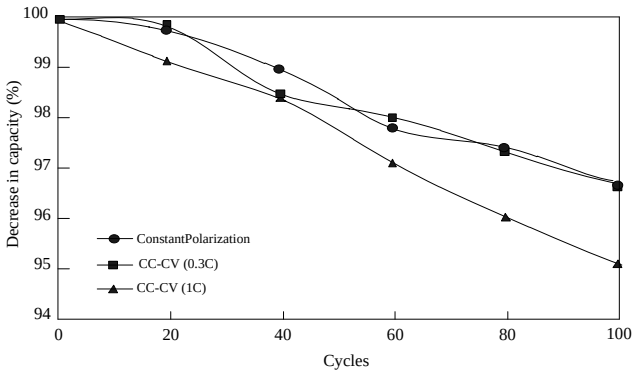

Figure 7: Comparison of the charging capacity of the three methods

As can be seen from Table 5, all charging methods can be fulfilled with lithium-ion battery, the temperature rise for the CC-CV (0.3C) mode, but the batteries were fully charged for a long time. CC-CV(1C) significantly reduced the charging time, but the temperature rise is very high. In contrast, Constant Polarisation shows a significant improvement on the charging time and temperature rise. Figure 7 shows a comparison of the capacity reductions of the three charging methods. It can be found that the charging life is remarkably reduced when the constant current reaches 1C. From Table 5, it can be found that constant current constant voltage charging method control is relatively simple, this charging method to solve the charging speed and battery life is not good. The proposed fuzzy control constant polarisation charging method can significantly shorten the charging time compared to CC-CV (0.3C) mode, while maintain the almost same battery life. This shows that the fuzzy control of the constant polarisation method can simultaneously improve the charging time and battery life..

5. CONCLUSION

In this paper, the classic "Davidin" model is used to study the polarisation characteristics of lithium ion batteries. The factors influencing the polarisation voltage are analyzed and calculated, such as charging current, initial SOC, initial polarisation state and lifetime. Based on the analysis of the polarisation characteristics under the combined effect of these influencing factors, the relationship between the influencing factors and the polarisation voltage is summarised. At the same time, the effects of current, initial SOC, initial polarisation state and polarisation influences of battery life. In this paper, a constant polarisation voltage charging method based on fuzzy control algorithm is proposed, and the polarisation voltage is regarded as the control target to improve the charging effect of the battery. Experiments show that compared with the traditional CC-CV method, the fuzzy control of the constant polarisation charging method can significantly shorten the charging time, the lithium-ion battery life has no significant impact, to improve the charging speed while ensuring the battery life.

6. REFERENCES

Abdel-Monem M, Trad K, Omar N, et al. 2017.Influence analysis of static and dynamic fast-charging current profiles on ageing performance of commercial lithium-ion batteries. Energy,120,179-191.

Cousland, A.W.， Ciaravolo, R.J.; Blieden, G.; Hosseinzadeh, N, 2010. "Design of a battery charger and charging management system for an electric vehicle". Universities Power Engineering Conference (AUPEC), 2010 20th Australasian, vol., no., pp.1,6, 5-8 Dec.

Chambon P, Curran S, Huff S, et al, 2017. Development of a range-extended electric vehicle powertrain for an integrated energy systems research printed utility vehicle. Applied Energy, 191,99-110.

Paul N, Wandt J, Seidlmayer S, et al, 2017,Aging behavior of lithium-ion phosphate based 18650-type cells studied by in situ neutron diffraction. Journal of Power Sources, 345,85-96.

Liu K, Li K, Yang Z, et al, 2017. An advanced Lithium-ion battery optimal charging strategy based on a coupled thermoelectric model. Electrochimica Acta, 225,330- 344.

Peters JF, Baumann M, Zimmermann B, et al, 2017. The environmental impact of Li-Ion batteries and the role of key parameters-A review, Renewable & Sustainable Energy Reviews, 67, 491-506.

Zhan C P, Zhang C N, Liu J Z, and Sharkh S M, .2010. “Identification of dynamic model for lithium-ion batteries used in hybrid electric vehicles”. High Technol. Lett., vol. 16, no. 1, pp. 6–12, Jan.

Wei J, Dong G, Chen Z, et al, 2017. System state estimation and optimal energy control framework for multicell lithium-ion battery system, Applied Energy, 187, 37-49.

Torchio M, Nicolas A, Davide M, et al, 2015. Raimondo Real-time model predictive control for the optimal charging of a lithium-ion battery. American Control Conference (ACC), 1-3 July 2015, 4536-4541.

Gopaluni R B and Braatz R D, 2013. State of charge estimation in Li-ion batteries using an isothermal pseudo two-dimensional model. Proceedings of the 10th IFAC International Symposium on Dynamics and Control of Process Systems, pp,135–140.

Zhang Z, Wang J, Wang X, 15 November 2015. An improved charging/discharging strategy of lithium batteries considering depreciation cost in day-ahead microgrid scheduling. Energy Conversion and Management, Volume 105, Pages 675-684.

Tsang K M, Sun L, Chan W L, December 2010. Identification and modelling of Lithium ion battery.Energy Conversion and Management, Volume 51, Issue 12, Pages 2857-2862.

Mills A, Al-Hallaj S, 2015. Simulation of passive thermal management system for lithium-ion battery packs.Power Sources, 141 (2015), pp. 307–315

Fathabadi H, 2014. High thermal performance lithium-ion battery pack including hybrid active passive thermal management system for using in hybrid/electric vehicles Energy, 70 (2014), pp. 529–538.

Dogger J D, Roossien B, Nieuwenhout F D J. 2011. Characterisation of li-ion batteries for intelligent management of distributed grid-connected storage, IEEE Trans Energy Convers, 26 (2011), pp. 256–262.

Maher K, Yazami R, 2014. A study of lithium ion batteries cycle aging by thermodynamics, J Power Sources, 247 (2014), pp. 527–533.

Yang X-H, Tan S-C, Liu J, 2016. Thermal management of Li-ion battery with liquid metal, Energy Convers Manage, 117 (2016), pp. 577–585.

Panchal S, Dincer I, Agelin-Chaab M, Fraser R, Fowler M, 2016. Thermal modeling and validation of temperature distributions in a prismatic lithium-ion battery at different discharge rates and varying boundary conditions, Appl Therm Eng, 96 (2016), pp. 190–199.

Ling Z, Wang F, Fang X, Gao X, Zhang Z, 2015. A hybrid thermal management system for lithium ion batteries combining phase change materials with forced-air cooling, Appl Energy, 148 (2015), pp. 403–409.

196: An improved voltage feedforward SVM method for STATCOM in wind plant with multi cells cascaded

Huimei LIU[1], Lan XIONG[2]

[1]Hubei Collaborative Innovation Center for High-efficiency Utilisation of Solar Energy, Hubei University of Technology, Wuhan, 430068, P. R. China; 1038785711@qq.com
[2]Hubei Collaborative Innovation Center for High-efficiency Utilisation of Solar Energy, Hubei University of Technology, Wuhan, 430068, P. R. China; xusbl@hotmail.com

Static Synchronous Compensator（STATCOM）is considered an effective means to keep the voltage stable at the connection point between a wind power plant and the grid. The dc voltage imbalance of a cascaded STATCOM in a wind power generation system will affect the quality of output voltage waveform and the operation of the STATCOM. To solve the problem of the dc voltage imbalance, the usual approach is to add some special control algorithms to the controller, making the controller rather complex and bringing extra parameters that should be adjusted. This paper proposes to use a voltage feedforward space vector modulation (FFSVM) method in a cascaded STATCOM. This method can obtain perfect output waveform under the condition of dc voltage imbalance and make them converge. This paper extends its utilisation from a two-cell cascaded inverter into a STATCOM with three or above cells cascaded in one phase. Considering the fact that the dc voltage differences among the cells in a STATCOM are small, some extreme situations of the dc voltage distribution are excluded, and the vector selection is simplified. Thus the application method of FFSVM in a multi-cell cascaded STATCOM is developed. If the number of cells increases further, there will be more output vectors, but the method of vector selection is still applicable. A simulation model of a three-phase three-cell cascaded STATCOM is built in Matlab/Simulink. Simulation results verify that a cascaded STATCOM adopting the proposed modulation method can accurately output waveforms, and simultaneously suppresses dc voltage divergence by using output vectors conducive to convergence.

Keywords: wind power generation systems, cascaded STATCOM, FFSVM, three cells

1. INTRODUCTION

In wind power generation systems, the random variation of wind speed causes the output power fluctuation of wind plants. If the capacity of wind power accounts for a large proportion in the grid, the voltage of the access point will fluctuate and even exceed the limit, affecting the stability of the power grid. Deploying a STATCOM in a wind power generation system can provide reactive support and improve the stability and the power quality. Cascaded STATCOM can directly synthesise high voltage output with low voltage cells, which can meet the demand of high voltage and large capacity reactive power compensation, but its operating principle requires that the voltages of inter-phase and the dc voltage of each cell keep balance and stable. Many research results on dc voltage balance control algorithms have been published, and their main ideas can be summed up as a two-stage dc voltage control of inter-phase balance and balance among the cascaded cells, which superimposes an active power control on the reactive power control. This approach can suppress the dc voltage imbalance, but it also makes the controller algorithm more complex, and there may be conflicts among multiple control targets under certain conditions.

The H-bridge cascaded STATCOM usually adopts modulation methods such as carrier-based phase shift modulation (PS-PWM), level shift modulation (LS-PWM) and multilevel space vector modulation (SVM), but all of them take the dc voltage balance as the assumption. Under the condition of unbalanced dc voltages of cells, the output waveform quality of STATCOM will decline. A method to obtain a high-quality output waveform under the condition of unbalanced dc voltages in cascaded inverter by adjusting the modulation ratio has been presented, but it does not suppress the imbalance of the dc voltage.

A voltage feedforward space vector modulation (FFSVM) method can deal with the output waveform modulation under dc voltage imbalance in a single-phase H-bridge cascaded structure, and automatically suppresses this imbalance at the same time. In this paper, the use of the modulation method is extended from a two-cell cascaded inverter to a multi-cell inverter and is applied in a three-phase STATCOM. Simulation results are presented to verify that the proposed method is feasible and effective for a three-phase multi-cell STATCOM.

2. VOLTAGE FEEDFORWARD SPACE VECTOR MODULATION FOR TWO CELLS

The structure topology of a single-phase two-cell cascaded STATCOM is shown in Figure 1, the two cells' dc voltages are U_{dc1} and U_{dc2} respectively. Since a cell can output three levels, the output levels of two cells include 0, $\pm U_{dc1}$, $\pm U_{dc2}$, $\pm(U_{dc1}-U_{dc2})$ and $\pm(U_{dc1}+U_{dc2})$. Taking the value of output levels as partition nodes, the scope of the output voltage u_{out} can be divided into several sections.

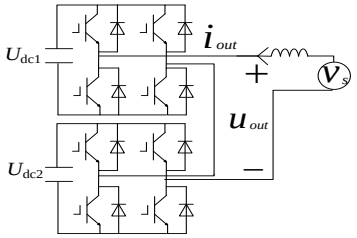

Figure 1: Topology of a single-phase two-cell cascaded inverter

Table 1 gives out the partition levels and the corresponding vectors in various circumstances of U_{dc1} and U_{dc2} when u_{out} is greater than zero. P_i and V_i (i=1, 2, 3, 4) are the output levels and vectors respectively. The levels and vectors can be analogised when u_{out} is below zero.

Table: 1 Partition levels under different relations of the two cells' dc voltages

Dc voltage ratio of cells	P_1	V_1	P_2	V_2	P_3	V_3	P_4	V_4
$U_{dc2} \le U_{dc1} < 2 \cdot U_{dc2}$	$U_{dc1}-U_{dc2}$	[1,-1]	U_{dc2}	[0, 1]	U_{dc1}	[1, 0]	$U_{dc1}+U_{dc2}$	[1,1]
$2 \cdot U_{dc2} \le U_{dc1}$	U_{dc2}	[0, 1]	$U_{dc1}-U_{dc2}$	[1,-1]	U_{dc1}	[1, 0]	$U_{dc1}+U_{dc2}$	[1,1]
$U_{dc1} < U_{dc2} < 2 \cdot U_{dc1}$	$U_{dc2}-U_{dc1}$	[-1,1]	U_{dc1}	[1, 0]	U_{dc2}	[0, 1]	$U_{dc1}+U_{dc2}$	[1,1]
$2 \cdot U_{dc1} \le U_{dc2}$	U_{dc1}	[1, 0]	$U_{dc2}-U_{dc1}$	[-1,1]	U_{dc2}	[0, 1]	$U_{dc1}+U_{dc2}$	[1,1]

In every switching period, the output voltage reference M is compared with the output levels (P_i, i=1, 2, 3, 4) to find out the two partition levels near M. The two vectors corresponding to these two partition levels are used as the output vectors, and the duties of these two output vectors are calculated. As shown in Figure 2, when M is between P_2 and P_3, the duties of the two output vectors corresponding to P_2 and P_3 are t_1 and t_2 respectively. The normalised switching period is 1, and then t_1 and t_2 can be solved from Equation 1.

Equation 1: 3 principle of vector duty ratio

$$\begin{cases} M \times 1 = P_2 \times t_1 + P_3 \times t_2 \\ t_1 + t_2 = 1 \end{cases}$$

Where

M=the output voltage reference

P_2, P_3=the two selected levels

t_1=the duty of the first vector in a period

t_2=the duty of the second vector in a period

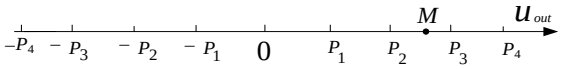

Figure 2: Partition of two-cell output voltage sections

In this modulation algorithm, the output vectors and their duties are determined and calculated according to the actual instantaneous values of all cells' dc voltages. Hence, the modulation result becomes more accurate because the dc voltage differences are considered.

In cascaded STATCOM, the ac output terminals of the cells are connected in series. In every switching period, the variation of the dc voltage of a cell depends on its output level and the direction of output current. Take the current direction in Figure 1 as positive. When the output level of a cell and the output current are both positive or negative, the dc voltage of the cell will rise, whereas it will decline. Therefore in vector selection, the controller of the STATCOM firstly detects the direction of the inverter's output current. Then it should exclude those vectors leading to dc voltage divergence as far as possible, and uses the adjacent non-conflicting vectors as an alternative. In this way the STATCOM can accurately output the voltage waveform, and suppresses the dc voltage imbalance simultaneously.

3. VOLTAGE FEEDFORWARD SPACE VECTOR MODULATION FOR THREE CELLS

The topology of a three-phase three-cell STATCOM is displayed in Figure 3. When the modulation method described in Section 2 is used in an inverter with three or above cells cascaded in one phase, the vector selection will become difficult. The increase of the cell number leads to a sharp increase in the number of output vectors, making the vector selection algorithm rather complex. In the case of three cells with unequal dc voltages, the number of the output vectors increases to 13 when u_{out} is greater than zero. And in the case of four cells, the number of the output vectors even increases to 40. The sequence of the partition levels will be complex and change frequently with the instantaneous values of dc voltages. The comparison of the output reference and the partition levels will take a relatively long time.

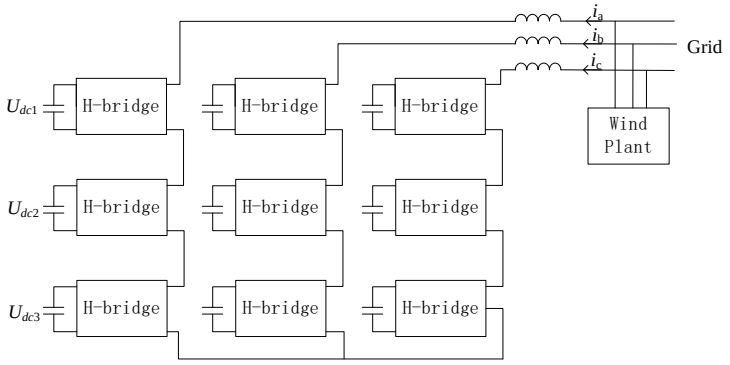

Figure 3: Topology of three-phase three-cell cascaded STATCOM

Table 2 gives out the partition levels in the case of $U_{dc1}<U_{dc2}<U_{dc3}$ when u_{out} is greater than zero as an example. The corresponding vectors can be easily deduced from the levels. For example, the level $U_{dc1}+U_{dc2}- U_{dc3}$ indicates a vector [1,1,-1]. The levels and vectors can be analogised for $u_{out}< 0$.

Considering the fact that the dc voltage differences are not large in the practical operation of a cascaded STATCOM, the following assumption is made to simplify the vector selection:

Equation 2 Upper limit of dc voltage difference of all cells

$$\max(U_{dc1},U_{dc2},U_{dc3})-\min(U_{dc1},U_{dc2},U_{dc3})<\min(U_{dc1},U_{dc2},U_{dc3})/2$$

Where

U_{dc1}=dc voltage of the first cell

U_{dc2}=dc voltage of the second cell

U_{dc3}=dc voltage of the third cell

This assumption means the difference between the maximum and the minimum of all the dc voltagesis less than half of the minimum. With the above condition, some extreme conditions are excluded and the sequence of the levels becomes relatively fixed. Actually, if the modulation takes effect from the beginning of the STATCOM operation, those extreme situations will not appear.

On comparison of Table 1 and Table 2, it can be seen that the number of output vectors increases by (13-4) × 2 = 18 when all the dc voltages are unequal. Anyway, the increase of the number of partition levels brings less output harmonic.

Table 2: Partition levels under different relations of the three cells' dc voltages

Dc voltage relationship of cells		Partition levels in the scope of output voltage		
$U_{dc1}<U_{dc2}<U_{dc3}$	$U_{dc3}-U_{dc2}>U_{dc2}-U_{dc1}$ ($U_{dc1}\neq U_{dc2}$)	$P_1=U_{dc2}-U_{dc1}$ $P_4=U_{dc1}+U_{dc2}-U_{dc3}$ $P_7=U_{dc1}+U_{dc3}-U_{dc2}$ $P_{10}=U_{dc1}+U_{dc2}$ $P_{13}=U_{dc1}+U_{dc2}+U_{dc3}$	$P_2=U_{dc3}-U_{dc2}$ $P_5=U_{dc1}$ $P_8=U_{dc3}$ $P_{11}=U_{dc1}+U_{dc3}$	$P_3=U_{dc3}-U_{dc1}$ $P_6=U_{dc2}$ $P_9=U_{dc2}+U_{dc3}-U_{dc1}$ $P_{12}=U_{dc2}+U_{dc3}$
	$U_{dc3}-U_{dc2}>U_{dc2}-U_{dc1}$ ($U_{dc1}=U_{dc2}$)	$P_2=P_3=U_{dc3}-U_{dc1}$ $P_7=P_8=P_9=U_{dc3}$ $P_{11}=P_{12}=U_{dc1}+U_{dc3}$	$P_4=U_{dc1}+U_{dc2}-U_{dc3}$ $P_{10}=U_{dc1}+U_{dc2}$ $P_{13}=U_{dc1}+U_{dc2}+U_{dc3}$	$P_5=P_6=U_{dc1}$
	$U_{dc3}-U_{dc2}<U_{dc2}-U_{dc1}$ ($U_{dc2}\neq U_{dc3}$)	$P_1=U_{dc3}-U_{dc2}$ $P_4=U_{dc1}+U_{dc2}-U_{dc3}$ $P_7=U_{dc2}$ $P_{10}=U_{dc1}+U_{dc2}$ $P_{13}=U_{dc1}+Ud_{c2}+U_{dc3}$	$P_2=U_{dc2}-U_{dc1}$ $P_5=U_{dc1}$ $P_8=U_{dc3}$ $P_{11}=U_{dc1}+U_{dc3}$	$P_3=U_{dc3}-U_{dc1}$ $P_6=U_{dc1}+U_{dc3}-U_{dc2}$ $P_9=U_{dc2}+U_{dc3}-U_{dc1}$ $P_{12}=U_{dc2}+U_{dc3}$
	$U_{dc3}-U_{dc2}<U_{dc2}-U_{dc1}$ ($U_{dc2}=U_{dc3}$)	$P_2=P_3=U_{dc3}-U_{dc1}$ $P_9=U_{dc2}+U_{dc3}-U_{dc1}$ $P_{13}=U_{dc1}+U_{dc2}+U_{dc3}$	$P_4=P_5=P_6=U_{dc1}$ $P_{10}=P_{11}=U_{dc1}+U_{dc2}$	$P_7=P_8=U_{dc2}$ $P_{12}=U_{dc2}+U_{dc3}$
$U_{dc1}=U_{dc2}=U_{dc3}=U$		$P_1=U$	$P_2=2U$	$P_3=3U$

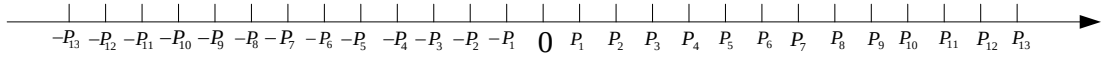

Figure 4: Partition of three-cell output voltage scope

The partition sections of the condition $U_{dc1}<U_{dc2}<U_{dc3}$ in Table 2 are shown in Figure 4. In order to make the dc voltage convergent, the first and the second cell need to charge, while the third cell needs to discharge. According to Section 2, the direction of the output current and the output vector determine the charge and discharge state of all cells, and the output vectors that are not conducive to the convergence should be eliminated. For example, when $i_a>0$, if the output vector V_3=[-1,0,1] ($P_3=U_{dc3}-U_{dc1}$) is used, then the first cell will discharge and the third cell will charge, making the difference of their dc voltages greater. Therefore, V_3 (P_3) should be eliminated. Similarly, $-P_1$, $-P_4$, $-P_5$, $-P_6$, $-P_7$, $-P_9$, $-P_{10}$, $-P_{11}$, $-P_{12}$, P_1, P_2, P_7, P_8, P_9, P_{11}, P_{12} are also eliminated. Figure 5 shows the remaining ten output levels.

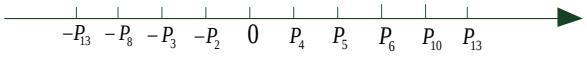

Figure 5: Output scope partition after eliminating conflicting vectors

If the cell number increases, there will be more the partition sections of the output voltages cope. Applying the improved modulation algorithm and eliminating the output vectors leading to dc voltage divergence, a cascaded STATCOM can get accurate waveform and suppress dc voltage divergence at the same time.

The improved FFSVM method selects output vectors according to the actual instantaneous values of all cells' dc voltages and a criterion of the convergence of dc voltages, and excludes unpractical initial conditions to simplify the complexity of vector selection. With this modulation method, the dc voltage balance control of the cells in one phase is irrelevant to the active and reactive power control scheme. Therefore, the system control method can be simplified. For a three-phase inverter, it is still necessary to consider the phase-to-phase balance control. On the other hand, the output current determines the charge-discharge speed of all cells, and thus affects the speed of dc voltage convergence. The larger the current is, the faster all cells'dc voltages tend to be convergent.

4. SIMULATION RESULTS

To verify the feasibility of the presented method, a three-phase three-cell cascaded STATCOM is built in Matlab/Simulink, and the control block diagram is depicted in Figure 6. U_{dck} (k=1, 2, …, 9) respectively represents the dc voltages of the ninecells, V^*_{dc} is the reference of one cell's dc voltage, V_s is the grid voltage, i^*_q is reactive current command, i_{out} is the output current.

In order to control the average value of the dc voltages of the cells in each phase, three PI controllers are used. The results are multiplied by the phase factor of the three-phase grid voltage. After a d-q transformation, the references of active current and inactive current are summed up to get the reference of output current. The current loop uses a proportional control, and the feedforward of the grid voltage is added to the output voltage reference to offset the disturbance of the grid voltage.

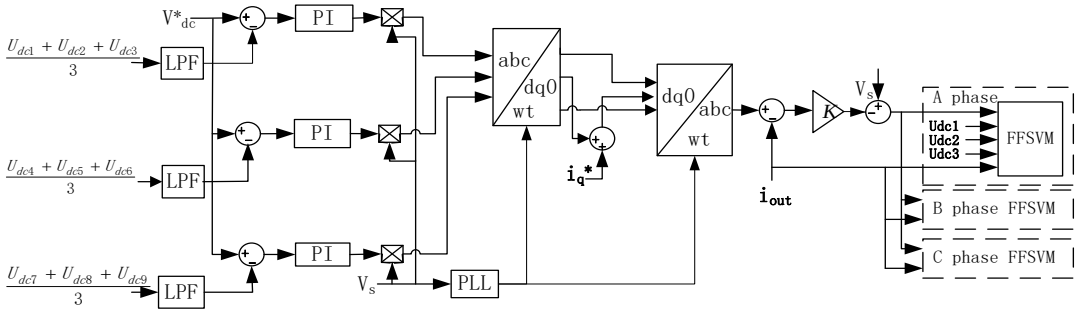

Figure 6: Three-phase STATCOM control diagram

Table 3: Parameters of system simulation

Parameter	Value	Parameter	Value
Grid voltage	690V	Ac filter inductor	4 mH
Line frequency	50Hz	Dc capacitance of cells	4700 μF
Switching frequency	10 kHz	Reference of dc voltage	205 V

Table 3 gives out the main simulation parameters of the system. In order to test the effectiveness of the modulation method, different resistances are connected to the dc of the cells to emulate the causes of the dc voltage divergence, and the initial values of the dc voltages of the cells are also set different to create an initial state of apparent divergence. The initial values of dc voltages and dc resistance of all cells are in Table 4. Figure 7 (a) and (b) respectively show the output line voltage of the cascaded STATCOM and its harmonic analysis. As can be seen from Figure 7(b), the amplitude of the fundamental wave is 1075.8V, and the THD is 22.39%. Because the switching frequency of the STATCOM is 10 kHz, harmonics at the frequency of 10 kHz and 20 kHz are relatively high.

Table 4: Dc resistances and initial values of dc voltages of cells

Parameter	Value in phase A	Value in phase B	Value in phase C
Dc resistance	330 Ω, 260 Ω, 250 Ω	260 Ω, 200 Ω, 200 Ω	260 Ω, 200 Ω, 200 Ω
Initial value of dc voltage	254 V, 236 V, 200 V	245 V, 263 V, 209 V	145V, 163 V, 173 V

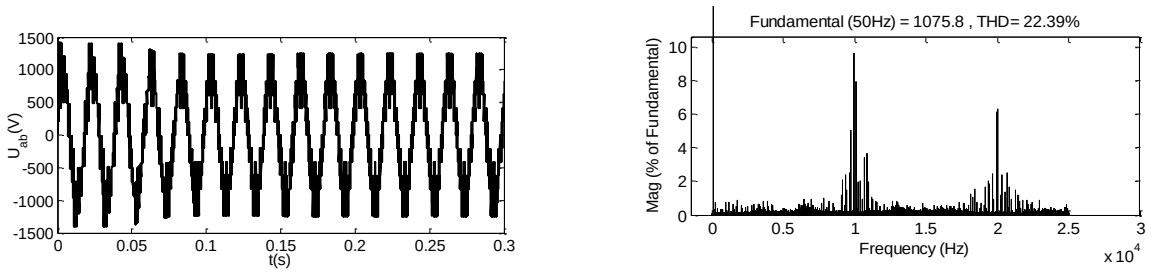

(a) *(b)*

Figure 7: Waveform of output line voltage U_{ab} and its harmonic analysis (a) Waveform of output line voltage U_{ab} (b) Harmonic analysis of output line voltage U_{ab}

Figure 8 shows the waveforms of the grid voltage and the inverter's output current. Figure 9 shows the dc voltage of all cells. In the simulation, the feedforward of the grid voltage works from the beginning, but the PI control of the average of dc voltages does not work until 0.05s. Since the output current is very small, only a slow trend of convergence appears in the dc voltages in each phase. As the PI controllers start to at 0.05s, the output current of the STATCOM increases dramatically, and convergence processes in all three phases are obviously accelerated. Soon the dc voltages of all cells reach the reference value. The current of phase A is the smallest, and the convergence of phase A is correspondingly the slowest. At 0.15s, the STATCOM begins to output reactive power, and the dc voltages are still well kept in a consistent state.

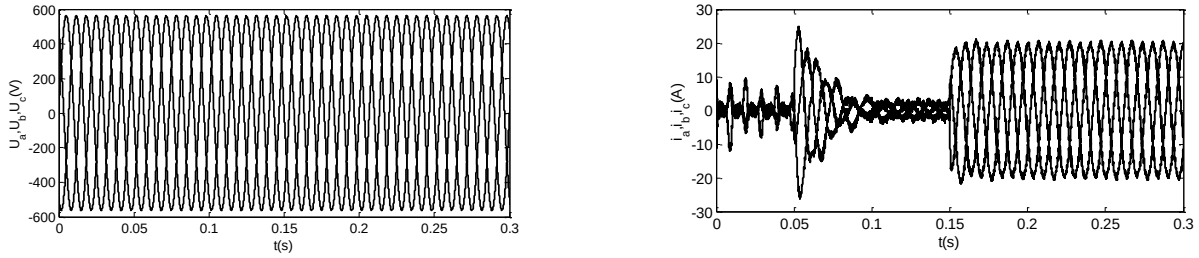

(a) *(b)*

Figure 8: Waveforms of the grid voltage and the output current (a) Waveforms of the grid voltage (b) Waveforms of the inverter's output current

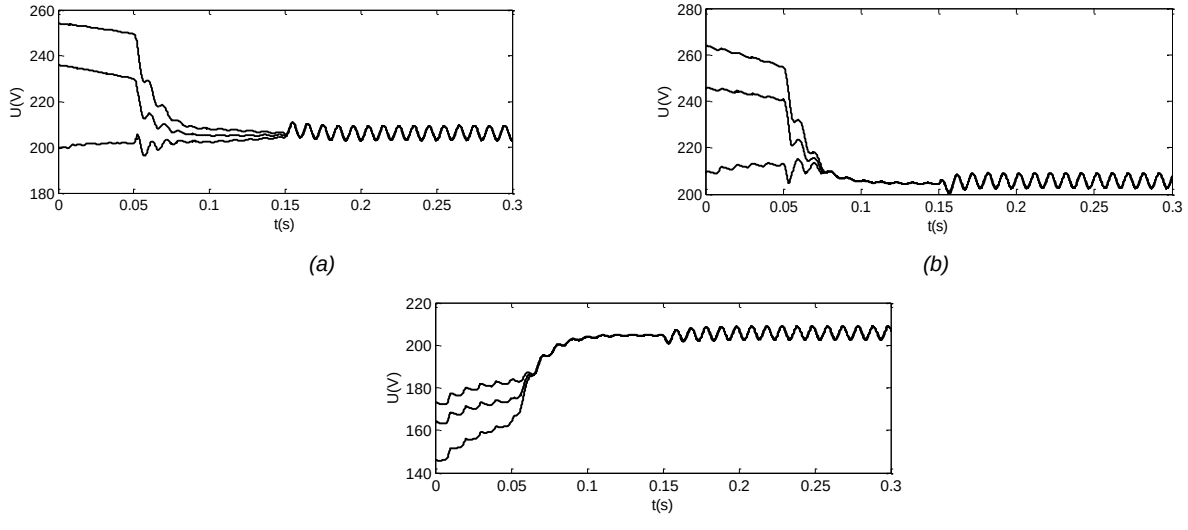

(a) *(b)*

(c)

Figure 9: Waveforms of all cells. (a)Waveforms of the dc voltages in phase A. (b) Waveforms of the dc voltages in phase B (c) Waveforms of the dc voltages in phase C

The simulation results verify that a cascaded STATCOM with three or above cells adopting the improved modulation method can accurately output waveforms according to the voltage reference, and selects output vectors conducive to dc voltage convergence to keep the dc voltage balance.

5. CONCLUSION

In this paper, the FFSVM method is applied to a multi-cell cascaded STATCOM based on a single-phase two-cell FFSVM method.The FFSVM method is modified according to the operation of STATCOM, and becomes applicable to the STATCOM with three or above cells cascaded in one phase. By adopting the improved modulation method and using vectors conducive to dc voltage convergence, a STATCOM has good output waveforms, and does not need extra dc voltage balance control algorithm.

6. REFERENCES

Chen L. Research on cascaded H-bridge based STATCOM and its control strategy [D]. China University of Mining and Technology, 2014.

Cho Y, Labella T, Lai J S, Seneskym K. A carrier-based neutral voltage modulation strategy for multilevel cascaded inverters under unbalanced dc sources[J]. IEEE Transactions on Industrial Electronics, 2014, 61(2): 625-636.

Efika I B, Nwobu C J, Zhang L. Reactive power compensation by modular multilevel flying capacitor converter-based STATCOM using PS-PWM[C]//IET International Conference on Power Electronics, Machines and Drives, 2014:1-6.

Ghias A M Y M, Pou J, Ciobotaru M, et al. Voltage-balancing method using phase-shifted PWM for the flying capacitor multilevel converter[J]. IEEE Transactions on Power Electronics, 2013, 29(9):4521 - 4531.

Jiang D, Zhang Z. Control scheme of three-phase H-bridge cascaded STATCOM[J]. High Voltage Engineering, 2011, 37(8): 2024-2025.

Leon J I, Vazquez S, Watson A J, Franquelo L G, Wheeler P W and Carrasco J M. Feed-forward space vector modulation for single-phase multilevel cascaded converters with any dc voltage ratio[J]. IEEE Transactions on Industrial Electronics, 2009, 56(2): 315-325.

Leon J I, Portillo R, Franquelo L G, et al. New space vector modulation technique for single-phase multilevel converters[C]//IEEE International Symposium on Industrial Electronics, 2007:617-622.

Shao R. Research on voltage feedforward space vector modulation strategy for cascaded STATCOM [D]. Hubei University of Technology, 2016.

Tao X, Li Y, Song Y, et al. Improved dc-link voltage balancing method for cascaded H-bridge rectifier[J]. High Voltage Engineering, 2012, 38(2): 505-506.

Tsunoda A, Hinago Y, Koizumi H. Level- and phase-shifted PWM for seven-level switched-capacitor inverter using series/parallel conversion[J]. IEEE Transactions on Industrial Electronics, 2014, 61(8):4011-4021.

Wang Z, Yu K, Zhou X. Control strategy for dc Bus voltage balance in cascaded H-bridge multilevel converters[J]. Proceedings of the CSEE, 2012, 32(6):56-63.

Zheng B, Xu Z. Research on control strategy of STATCOM based on cascaded H-Bridge[J]. Electrical Engineering, 2014(12): 21-22.

Zou C, Wang B, Application of STATCOM in Wind Farm [J]. Electric Drive, 2008, 38 (12): 46-49.

198: Research on the optimal operation strategy of CCHP-ORC systems

Yufang CHANG[1], Hao XIE[2], Wencong HUANG[3]

[1] Hubei Collaborative Innovation Canter for High-efficiency Utilisation of Solar Energy, Hubei University of Technology, changyf@hbut.edu.cn
[2] School of Electrical and Electronic Engineering, Hubei University of Technology, 516891609@qq.com
[3] School of Electrical and Electronic Engineering, Hubei University of Technology, huangwc@hbut.edu.cn

The ratio of electricity to thermal energy output is a very important impact for the performances of the combined cooling, heating, and power (CCHP) system, and the system efficiency would reach the maximum value if the energy outputs of the CCHP systems just match the energy requirements of users. However, this ideal situation is rare to be achieved in practice because the load demands change with a lot of factors. To further improve the using efficiency of the excess thermal energy from the combined cooling, heating, and power system, an active method, which adds the organic Rankine cycle (ORC) equipment in the CCHP system, is proposed. A complementary configuration of this CCHP-ORC is also investigated. The obviously feature of the CCHP-ORC system is that the ratio of electricity to thermal energy output can be adjusted through changing the loads of the electric chiller and the ORC equipment dynamically. The CCHP-ORC system is a multiple input and multiple output (MIMO) system. The system dynamics can be described in a matrix form to facilitate the optimisation-based energy flow coordination. The optimal energy injection and flow are determined by optimizing various dispatch factors. The optimisation problem of minimizing the evaluation criteria function is solved using sequential quadratic programming (SQP) algorithms by designing the multi-objective functions and determining constraints. Comprehensive case studies are conducted based on a hypothetical CCHP-ORC system. The study results reveal that the effectiveness and economic efficiency of the proposed approaches outperform those obtained from conventional CCHP systems.

Keywords: Combined cooling, heating and power (CCHP), Organic Rankine cycle (ORC), Matrix modelling, Energy flow, Optimal operation strategy

1. INTRODUCTION

A CCHP system is an integrated energy supply system, which can also be referred to the trigeneration system. It provides the building users electricity, cooling energy and heating energy by installing the power generation unit (PGU) (Shi 2017; Liu 2014). The CCHP system makes use of the rejected heat from the PGU to generate thermal energy for cooling and heating demands (Murugan 2016; Wang 2010). So the overall fuel energy utilisation efficiency of CCHP systems can reach 70%-90%, which is significantly higher than that of separation production (SP) systems (Mohamed 2015). CCHP systems have been broadly applied in office buildings, hotels, hospitals, commercial malls, and other building types.

The traditional CCHP system consists of a PGU, a heat recovery system, an absorption chiller, an auxiliary boiler, and a heating unit (Fumo 2009). PGU is adopted to generate electricity to meet the building users' electricity demand. The heat recovery system recovers the rejected heat from the PGU and provides the thermal energy for the building users' cooling and heating demands. The absorption chiller is used to absorb the recovered heat and provide cooling. The auxiliary boiler is installed in the system to provide thermal energy as a back-up. The heating unit provides heating to the building users by using the recovered heat. In order to better satisfy the energy demand and more conveniently adjust energy supply, a new CCHP system structure is proposed in Fang (2012), in which both absorption and electric chillers are installed. Four typical CCHP systems with existing technologies for various size ranges are illustrated in Liu (2012). With the development of the renewable energy, a solar CCHP system is studied in Wu (2006), Tora (2011), Meng (2010), Calise (2013) and Nosrat (2011). A new integrated SOFC-trigeneration system is researched in Wang (2009) and Baghernejad (2016). A realistic biomass-trigeneration system is developed in Fong (2014). In recent years, some researchers add orgic Rankine cycle (ORC) equipments in the traditional CCHP, SOFC-trigeneration, solar-trigeneration, biomass-trigeneration systems to further improve the energy utilisation efficiency (Arnavat 2014; Fang 2012; Huang 2013).

When a specific type of system structure is determined and implemented, the operation strategy is the second important factor for the CCHP system design. There are two popular operation strategies (Al-Sulaiman 2013; Mago & Chamra 2009; Mago 2009): one is the following the electric load (FEL) which can be referred to the electric demand management (EDM); the other is the following the thermal load (FTL) which can also be referred to the thermal demand management (TDM) (Cao 2014). However, both of the FEL and FTL strategies inherently waste a certain amount of energy (Fang 2012). Therefore, it is necessary to design an optimal operation strategy to improve the energy utilisation efficiency by reducing the energy waste. The design of system evaluation criteria is one of the emerging research aspects.

For an existing CCHP system, when the electricity to thermal energy requirement ratio of building users is exactly equal to the output ratio of the PGU, the maximum efficiency of the CCHP system will be achieved (Arnavat 2014). However, this ideal situation rarely happens due to the random variation of energy requirements. The energy supplies are always unbalanced with the energy requirements. When the supply is less than the demand, adding extra energy (fuel or electricity) is a direct treatment. However, when the supply excesses the demand, the situation becomes complicated. If surplus electricity is supplied, it can be sold back to power grid or converted to thermal energy. Similarly, the excess thermal energy can be stored in thermal storage units or converted to electricity by some special equipment, such as organic Ranking cycle (ORC), mixed refrigerant cycle, Kalinna cycle, and ammonia absorption refrigeration cycle (Jing 2012). ORC products have been presented on the market since the beginning of the 1980s (Arnavat 2014). ORC is one of prime movers which can be used to operate trigeneration plants. The ORC is similar to the steam Rankine cycle but uses an organic working fluid instead of water. A steam Rankine cycle can be used when a high temperature waste heat temperature is available while ORC can be used when a low-temperature waste heat is available (Huang 2013). ORC generation technology has been most widely used in low-temperature heat generation field. In this paper, an active excess thermal energy treatment method which uses an ORC to convert the excess thermal to electricity is investigated.

In recent years, some researches focused on the ORC system (Arnavat 2014; Fang 2012; Huang 2013; Hajabdollahi 2012). Fang et al. (2012) proposed a complementary structure and an operation strategy for a CCHP-ORC system Arnavat. Huang et al. (2013) studied a biomass fuelled trigeneration system integrated with ORC, and the results showed that this system is more environment friendly than conventional biomass trigeneration system. Al-Sulaiman et al. (2013) analysed three trigeneration systems: combined SOFC with ORC, combined biomass combustor with ORC, and combined solar collectors with ORC, and the result could help to identify which system has the best thermoconformed performance under different operation conditions. Li et al. (2016) presented a novel CCHP-ORC system with heat pumps and established the system model under an idealised operating condition. These above researches show that the ORC technology has advantages in using the thermal energy and its combination with trigeneration system has good application prospects. SOFC will have a potential application in the future due to less air pollution compared with fossil fuel systems. Biomass fuel and solar energy are renewable energy sources, researches on the feasibility of these two renewable energy sources are on ongoing. In addition, the maximum trigeneration-exergy efficiencies of the SOFC-ORC trigeneration system, biomass-ORC trigeneration system, and solar-ORC trigeneration system are below 40% (Li 2016). So we are going to adopt the CCHP-ORC structure which uses the gas turbine as PGU, an ORC as waste heat recycle equipment, an electric and an absorption chiller as hybrid chillers. The advantages of our CCHP-ORC system are higher energy utilisation, and the electricity to thermal energy output ratio of the proposed CCHP-ORC system dynamic adjustability.

From the perspective of control theory, the CCHP-ORC system can be treated as the connection between the energy input and the building users' demand. We could use transfer function to describe this input-output relation. Because the energy input includes fuel and electricity from the power grid, and the building users' demand includes cooling, heating and power,

the CCHP-ORC system is a multiple input and multiple output (MIMO) system. The system model is a matrix form and represents an interface between different energy infrastructures and loads. Liu et al. (2013) proposed a matrix modelling approach to describe the CCHP system dynamics, energy conversion, and energy flow. Chicco et al. presented an input-output matrix approach aiming at modelling small-scale trigeneration equipment by taking into account the interactions among plant components and external energy networks (Chicco 2009). These researches show that the matrix modelling approach is more comprehensive and systematic.

The motivation of this work is to make full use of the excess thermal energy produced by the PGU and improve the energy utilisation efficiency. Furthermore, a comprehensive and systematic matrix modelling approach is proposed to describe the CCHP-ORC system. The optimal operation strategy will be obtained by solving a well-constructed optimisation problem by taking into account various evaluation criteria and facility constraints.

This paper is organised as follows. The configuration and matrix modelling of the CCHP-ORC system is described in Section 2. In Section 3, the performance criteria for the CCHP-ORC system is presented and the optimisation problem is established. Finally, the effectiveness of the proposed system configuration and operation strategy are verified through a case study of a hypothetical office building in Section 4. Section 5 concludes this paper.

2. SYSTEM CONFIGURATION AND MATRIX MODELING

In this section, an optimal CCHP-ORC structure and an intuitive matrix modelling of the CCHP-ORC system will be introduced. In order to make full use of energy and improve the flexibility of energy supply, the configuration of the CCHP-ORC system is presented in Figure 1.

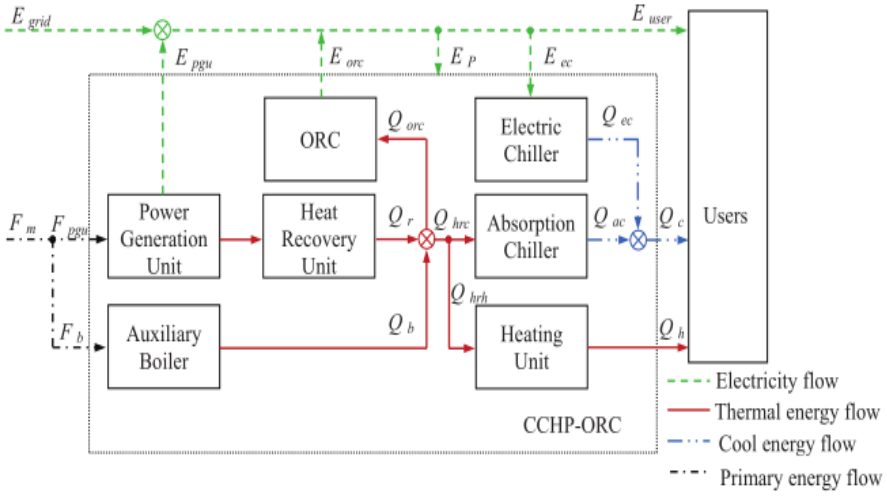

Figure 1: Structure diagram of a CCHP-ORC system.

In addition to traditional equipment, including the PGU, the heat recovery system, the auxiliary boiler, the absorption chiller, and the heating unit, a complementary ORC and an electric chiller are added as important components which can not only utilise the excess thermal energy but also dynamically adjust the electricity to thermal energy output ratio of the entire system.

2.1. Efficiency matrices of system components

The energy conversion of the components in the CCHP-ORC system can be described using efficiency matrices, namely coupling matrices. In this paper, u is a equipment set and equipment m ∈ u, F, E, Q_c, and Q_h denote the fuel, electricity, cooling energy, and heating energy, respectively. The input and the output of the component m are defined as $V_i^m = \left[F_i^m E_i^m Q_{ci}^m Q_{hi}^m\right]^T$ and $V_o^m = \left[F_o^m E_o^m Q_{co}^m Q_{ho}^m\right]^T$, respectively. So the input-output relation of the component m can be described as

Equation 1:The input-output relation of component m

$$V_0^m = H^m V_i^m$$

Where:

- V_i^m = input of component m

- V_o^m = output of component m
- H^m = efficiency matrix of the component m

2.2. Dispatch matrices of system

The dispatch matrices indicate the energy flow between the components in the system. Usually, the dispatch factors exist at the bifurcations of the system. For example in Figure 1, the thermal energy produced by the heat recovery system and the auxiliary boiler will be separated into three parts: One for the absorption chiller, one for the heating unit and the last one for the ORC. So, at the ORC side, we have

Equation 2: The relationship between system input and ORC input

$$V_i^{orc} = \begin{bmatrix} 0 \\ 0 \\ 0 \\ \alpha_{orc}\left[\alpha_{pgu}\left(1-\eta_{pgu}\right)\eta_{hrs}+\alpha_b\eta_b\right] \end{bmatrix} \begin{bmatrix} F_m \\ E_{grid} \\ 0 \\ 0 \end{bmatrix} = T_{orc}V_i$$

Where:

- α_{orc} = dispatch factor for the ORC
- α_{pgu} = dispatch factor for the PGU
- α_b = dispatch factor for the auxiliary boiler
- η_{pgu} = efficiency factor for the PGU
- η_b = efficiency factor for the auxiliary boiler
- η_{hrs} = efficiency factor for the HRS
- T_{orc} = The dispatch matrix for ORC

According to the Figure 1, by following the similar procedure, the dispatch matrices for the PGU, the auxiliary boiler, electric chiller, heat recovery system, heating unit and absorption chiller can be defined as the dispatch matrices for the PGU, the auxiliary boiler, electric chiller, heat recovery system, heating unit and absorption chiller can be defined. So the T_{pgu}, T_b, T_{ec}, T_{hrs}, T_h, T_{ac} can be obtained.

2.3. Conversion matrices of system

The CCHP-ORC system modelled in a matrix form can be viewed as an input-out model. The conversion matrix of the CCHP-ORC system describes the relationship between the input and the output, and represents the energy flow procedure of the system. From Figure 1, the system input and output are defined as

Equation 3: The system input

$$V_i^{orc} = \begin{bmatrix} F_m & E_{grid} & Q_{ci} & Q_h \end{bmatrix}^T = \begin{bmatrix} F_m & E_{grid} & 0 & 0 \end{bmatrix}^T$$

Equation 4: The system output

$$V_o = \begin{bmatrix} F_o & E_{user} & Q_c & Q_h \end{bmatrix}^T = \begin{bmatrix} 0 & E_{user} & Q_c & Q_h \end{bmatrix}^T$$

Then the conversion matrix of the CCHP-ORC system, G, can be defined as

Equation 5: The relationship between system input and output

$$V_o = GV_i$$

Where:

- G = conversion matrix of the CCHP-ORC system

In order to obtain the conversion matrix G, the expression of the output elements, E_{user}, Q_c, and Q_h, should be written as functions of the system input. Without the loss of generality, the parasitic electricity E_p can be assumed to be a constant and further assumed to be zero. According to the Figure 1, based on the relationship between elements. The conversion matrix of the CCHP-ORC system can be obtained.

Equation 6: conversion matrix of the CCHP-ORC system

$$G = \begin{bmatrix} 0 & 0 & 0 & 0 \\ G_{21} & \alpha_{user} & 0 & 0 \\ G_{31} & \alpha_{ec} COP_{ec} & 0 & 0 \\ G_{41} & 0 & 0 & 0 \end{bmatrix}$$

Where:

- $G_{21}=\alpha_{user}\alpha_{pgu}\eta_{pgu}+\alpha_{pgu}\left(1-\eta_{pgu}\right)\eta_{hrs}\alpha_{orc}COP_{orc}\alpha_{user}+\alpha_{b}\eta_{b}\alpha_{orc}\eta_{orc}\alpha_{user}$
- $G_{31}=\alpha_{ec}\alpha_{pgu}\eta_{pgu}COP_{ec}+[\alpha_{pgu}\left(1-\eta_{pgu}\right)\eta_{hrs}+\alpha_{b}\eta_{b}]\alpha_{orc}COP_{orc}\alpha_{ec}COP_{ec}$ $+[\alpha_{pgu}\left(1-\eta_{pgu}\right)\eta_{hrs}+\alpha_{b}\eta_{b}]\alpha_{ac}COP_{ac}$
- $G_{41}=[\alpha_{pgu}\left(1-\eta_{pgu}\right)\eta_{hrs}+\alpha_{b}\eta_{b}]\alpha_{h}\eta_{h}$

The main objective of this paper is to determine the dispatch factors and the system input to optimise the performance criteria objective function.

3. OPTIMAL OPERATION STRATEGY DESIGN

Having the whole system modelled in a matrix form, we can formulate the operation strategy design as an optimisation problem. The objective function and associated constraints will be illustrated in the rest of this section.

3.1. Performance criteria for the CCHP-ORC system

Evaluation of a CCHP system may contain many factors, including primary energy consumption, energy conversion efficiency, total cost of the system, environmental impact, life cycle assessment, combination of multiple factors, etc. In this paper, three popular criteria, i.e., primary energy consumption, the total cost of the system, and the environmental impact are adopted to evaluate the performance of the CCHP-ORC system.

Primary energy consumption (PEC)., PEC is a direct and common indicator to reflect the operating efficiency of a CCHP-ORC system. PEC is defined as

Equation 7: The definition of PEC

$$PEC = \frac{E_{user}+E_p}{\eta_e\eta_{grid}}+\frac{Q_c}{COP_{ec}\eta_e\eta_{grid}}+\frac{Q_h}{\eta_h\eta_b}$$

Where:

- E_p = the parasitic electricity
- η_e = the generation efficiency of the grid power plant
- η_{grid} = the transmission efficiency of grid

Hourly total cost (HTC). In order to obtain the optimal energy flow and operation strategy for every hour, HTC is adopted as a key element in the operation strategy optimisation. HTC of the CCHP-ORC system is defined as

Equation 8: The definition of HTC

$$HTC = E_{grid}C_e + E_{grid}C_{ca}\mu_c + F_mC_f + F_m\mu_f C_{ca} + \frac{\sum_{k=1}^{t} N_k C_k}{8760L}$$

Where:

- C_e = the unit prices of electricity
- C_f = the unit prices of the fuel
- C_a = the carbon tax rate
- C_k = the initial capital cost of each equipment
- μ_e = the carbon conversion factors of the the electricity
- μ_f = the carbon conversion factors of the the fuel

- N_k = the installed capacity of each equipment
- I = the number of equipments included in the CCHP-ORC system
- L = the life of each equipment

Carbon dioxide emission (CDE), Greenhouse gas emission control is an emerging topic in the CCHP system design. In a CCHP-ORC system equipped with fossil-fuel combustion units, CDE serves as an indicator of environment impacts and can be calculated as

Equation 9: The definition of CDE

$$CDE = E_{grid}\mu_e + F_m\mu_f$$

Where:

- μ_e = the carbon conversion factors of the electricity
- μ_f = the carbon conversion factors of the fuel

Performance evaluation criteria (EC) function. To comprehensively evaluate the system performance, we define a performance evaluation criteria function as a weighted summation of the three above mentioned criteria. Specifically, the hourly EC function is defined as

Equation 10: The definition of EC

$$EC_{hour} = \omega_1 PEC + \omega_2 HTC + \omega_3 CDE$$

Where:

- ω_1 = the weights of PEC
- ω_2 = the weights of HTC
- ω_3 = the weights of CDE

Three weights' Satisfaction is added to 1, and each of them between 0 and 1.

3.2. Optimisation problem formulation

As mention in Section 2, dispatch factors and energy inputs are the variables that need to be adjusted to coordinate the energy flow of the system, meet the building demand and minimise the objective function. Thus, the dispatch factors and system energy inputs can be selected as decision variables. The system energy inputs include F_m and E_{grid}. Thus, the optimiser consisting of all the decision variables can be defined as

Equation 11: the decision variables

$$x = \left[\alpha_{pgu}\ \alpha_{user}\ \alpha_{ac}\ \alpha_{orc}\ F_m\ E_{grid}\right]^T$$

By using the defined optimiser x and compare those factors with those of SP system, the EC_{hour} function in Equation 10 can be redefined as a linear function of the optimiser x as

Equation 12: The objective function

$$EC_{hour} = \omega_1 \frac{Bx}{PEC^{SP}} + \omega_2 \frac{Cx+L}{HTC^{SP}} + \omega_3 \frac{Dx}{CDE^{SP}}$$

Where:

- $B = [0\ 0\ 0\ 0\ 1\ 1/(\eta_e^{SP}\eta_{grid})]$
- $C = [0\ 0\ 0\ 0\ C_f + \mu_f C_{ca}\ C_e + \mu_e C_e]$
- $D = [0\ 0\ 0\ 0\ \mu_f\ \mu_e]$
- $L = \frac{\sum_{k=1}^{t} N_k C_k}{8760L}$

$EC_{hour}(x)$ will serve as the objective function of the optimisation-based operation strategy design. ω_1, ω_2 and ω_3 can be set according to different evaluation requirements. For example, ω_3 would be set relatively higher if more emphases are put on the environmental aspect.

In the sense of balance, Eqn. 5 will serve as the equality constraint of the optimisation problem. And the inequality constraints include the bound of the decision variables, various capacities of system components, and thresholds of the components output. The decision variables can be separated into two parts: one consists of dispatch factors, and the other consists of system input. To facilitate the later derivation, we define α dispatch factor vector as $\alpha = \left[\alpha_{pgu}\ \alpha_{user}\ \alpha_{ac}\ \alpha_{orc}\right]^T$,and

In this paper, we assume that no electricity would be sold back, thus the constraints for fuel and electricity input can be represented by $\beta = \left[F_m \; E_{grid} \right]^T$,they have to satisfy

Equation 13: linear inequality constraints seeing as the bounds of the decision variables.

$$-\alpha \le 0, \alpha - 1 \le 0.$$
$$-\beta \le 0$$

The output upper bound of the element m can be denoted as $\bar{V}_o^m$,similarly the lower bound of element m can be denoted as V_o^m , The lower bound of a component implies that the output will be cut down when the expected output of the component is lower than this bound. In this paper, the lower bound can be set as 5 percent of the maximum capacity of each component. Combined Equation 1, the bounding conditions for component output can be represented by

Equation 14: linear inequality constraints seeing as the bounds of the decision variables.

$$H^m V_i^m - \bar{V}_o^m \le 0$$
$$- \quad V_o^m - H^m V_i^m \le 0$$

Therefore, Equation 13 is the linear inequality constraints, and Equation 14 is the nonlinear inequality constraint of the optimisation problem. The optimal solution can be obtained by solving

Equation 15: The goal of optimisation

$$min\, x \;\; \omega_1 \frac{Bx}{PEC^{SP}} + \omega_2 \frac{Cx+L}{HTC^{SP}} + \omega_3 \frac{Dx}{CDE^{SP}}$$
s.t Eqn.5, Eqn.11, and Eqn.12

4. CASE STUDY

4.1. Simulation parameters

In this section, a CCHP-ORC system is installed for a hypothetical office building in Wuhan, Hubei, China. We chose EnergyPlus to analyse energy consumption of this building. This building is assumed to operate all year around and have five floors with a total construction area of 6000m^2.The first floor consists of 400m^2 exhibition halls and 800m^2 office rooms. The second to the fifth floors are office rooms. Table 1 shows a set of technical parameters of the installed CCHP-ORC system for the hypothetical building.

Table 1: System coefficient

Symbol	Variable	Bedroom
η_{pgu}	Efficiency of PGU in CCHP-ORC system	0.35
η_e^{SP}	Generation efficiency SP system	0.40
η_h	Efficiency of heating unit	0.78
η_b	Efficiency of auxiliary boiler	0.78
η_{hrs}	Efficiency of heat recovery system	0.81
COP_{orc}	Coefficient of performance of ORC	0.17
COP_{ac}	Coefficient of performance of absorption chiller	0.72
COPec	Coefficient of performance of electric chiller	2.98
η_{grid}	Transmission efficiency of local grid	0.92
μ_e	CO_2 emission conversion factor of electricity (g/kW h)	970
μ_f	CO_2 emission conversion factor of natural gas (g/kW h)	218
C_c	Carbon tax rates (yuan/kW h)	0.00002
C_e	Electricity rates (yuan/kW h)	0.642
C_f	Natural gas rates (yuan/kW h)	0.375
C_{pgu}	Unit price of PGU (yuan/kW h)	6800
C_b	Unit price of auxiliary boiler (yuan/kW h)	300
C_h	Unit price of heating unit (yuan/kW h)	200

C_{ac}	Unit price of absorption chiller (yuan/kW h)	1200
C_{ec}	Unit price of electric chiller (yuan/kW h)	970
C_{orc}	Unit price of ORC (yuan/kW h)	12000
L	Facilities' lives (year)	20
ω_1	Coefficient of PEC	0.6
ω_2	Coefficient of HTC	0.3
ω_3	Coefficient of CDE	0.1

4.2. Test result

SQP algorithms have been proved highly effective for solving general constrained problems with smooth objective and constraint functions. In this paper, we chose SQP algorithms to solve the optimisation problem established in Section 3.2. In order to accelerate the convergence, some feasible initial points which are calculated from FEL and FTL strategies are manually designated. So the local optimal solution can be avoided and the convergence time is significantly reduced. The constructed optimisation problem is solved in MATLAB by using fmincon .m. The computer used to solve this problem is configured with 2.6384 GHz Intel Core i5-3230M processor and 4 GB 1067 MHz memory. Time elapsed for each step of optimisation is about 0.25s. This time is much shorter than one hour, in other words, the optimal energy flow and operation strategy for the next hour can be quickly obtained at the beginning of this hour. Thus, we can say that the optimisation method is appropriate for practical use.

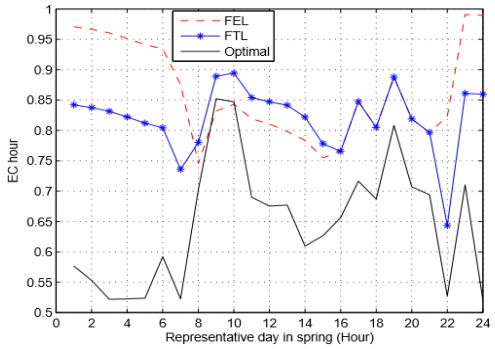

Figure 2: Comparison of three strategies in a spring day.

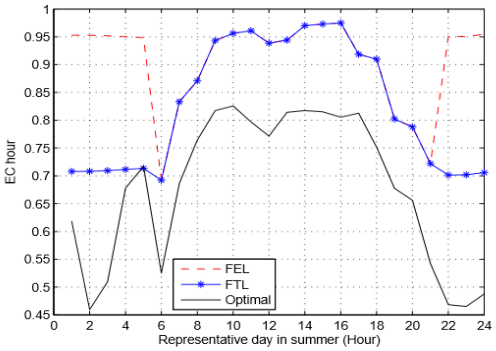

Figure 3: Comparison of three strategies in a summer day.

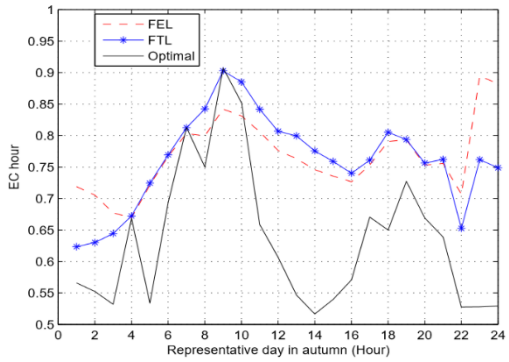

Figure 4: Comparison of three strategies in a autumn day.

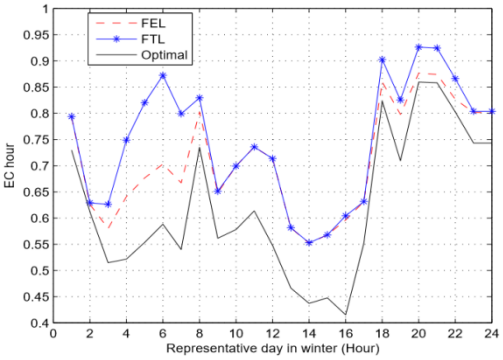

Figure 5: Comparison of three strategies in a winter day.

The performance comparison of FEL, FTL, and the proposed optimal operation strategy is shown in Figures 2 to 5 which includes spring, summer, autumn, and winter, respectively. From Figures 2 to 5, it can be noticed that the EC_{hour} value of the proposed optimal energy flow and operation strategy is obviously less than those of the FEL and FTL strategies. In spring, summer, and autumn, especially in the morning and in the evening, the optimal energy flow has excellent performance, while in the middle of a day, the advantage is not that evident. In winter, the performance in the middle of a day is much better than that of in the morning and in the evening.

The reason for the proposed optimal operation strategy performing better than FEL and FTL strategies is that both FEL and FTL strategies are inevitably wasting energy. When operating at FEL mode, electricity for the building is firstly satisfied, and then if the thermal provided by PGU cannot meet the thermal demand, the auxiliary boiler will be activated, if the thermal supply exceeds the thermal demand, the excess thermal will be wasted. When operating at FTL mode, the thermal

requirements is firstly satisfied, and then if the electricity provided by PGU cannot meet the electricity demand, additional electricity should be purchased from the power grid, if the electricity provided by PGU is sufficient, a certain amount of electricity will be wasted.

5. CONCLUSION

A complementary configuration of the CCHP-ORC system is investigated to further improve the utilisation efficiency of the excess thermal energy from the CCHP system. A comprehensive and systematic matrix modelling approach is proposed to describe the CCHP-ORC system. The matrix model includes efficiency matrices of system components, system conversion matrix and dispatch factors. The optimal operation strategy is obtained by solving the optimisation problem. Both economic and environmental factors are considered in the objective function of the optimal operation strategy design. The weights of economic and environmental factors can be changed according to different requirements. At last, an illustrative case study is conducted to show that the effectiveness and economic efficiency of the proposed approaches outperform those obtained from conventional CCHP systems. The main problem of the CCHP-ORC system is high investment cost of the ORC. However, the unit price of the ORC will continually decline because of the technology maturing in recent years. Therefore, the CCHP-ORC system will be more attractive and valuable. In addition, all calculation in this paper is based on an accurate load profile. While in practical applications, accurate load profile does not exist. Therefore, in the future work, accurate load forecasting should be considered. In a further step, excess electricity sold back feature can be considered. In recent years, with the development of the renewable energy including solar energy, wind energy and tide energy, more and more renewable energy should be incorporated into the CCHP system to make the trigeneration system more efficient.

6. REFERENCES

Shi Y., Liu M., Fang F., 2017, Combined Cooling, Heating, and Power Systems: Modelling, Optimisation, and Operation, John Wiley & Sons, 2017.

Liu M., Shi Y., Fang F., 2014, Combined cooling, heating and power systems: A survey, Renewable and Sustainable Energy Reviews 35 (2014) 1–22.

Murugan S., Horak B., 2016, Tri and polygeneration systems-A review, Renewable and Sustainable Energy Reviews 60 (2016) 1032–1051.

Wang J., Jing Y., Zhang C., 2010, Optimisation of capacity and operation for CCHP system by genetic algorithm, Applied Energy 87 (4) (2010) 1325–1335.

Mohamed A., Mohamed H., Hasan A., Siren K., 2015, The performance of small scale multi-generation technologies in achieving cost-optimal and zero-energy office building solutions, Applied Energy 152 (15) (2015) 94–108.

Fumo N., Mago P., Chamra L., 2009, Analysis of cooling, heating, and power systems based on site energy consumption, Applied Energy 86 (6) (2009) 928–932.

Fang F., Wang Q., Shi Y., 2012, A novel optimal operational strategy for the CCHP system based on two operating modes, IEEE Transactions on Power Systems 27 (2) (2012) 103–141.

Liu M., Shi Y., Fang F., 2012, A new operation strategy for CCHP systems with hybrid chillers, Applied Energy 95 (7) (2012) 164–173.

Wu D., Wang R., 2006, Combined cooling, heating and power: A review, Process in Energy and Combustion Science 32 (2006) 459–495.

Tora E., Halwagi M., 2011, Integrated conceptual design of solar-assisted trigeneration systems, Computers and Chemical Engineering 35 (2011) 1807–1814.

Meng X., Yang F., Bao Z., Deng N. S. J., Zhang Z., 2010, Theoretical study of a novel solar trigeneration system based on metal hydrides, Applied Energy 87 (2010) 2050–2061.

Calise F., Accadia M., Palombo A., Vanoli L., 2013, Dynamic simulation of a novel high-temperature solar trigeneration system based on concentrating photovoltaic/thermal collectors, Energy 61 (2013) 72–86.

Nosrat A., Pearce J., 2011, Dispatch strategy and model for hybrid photovoltaic and trigeneration power systems, Applied Energy 88 (2011) 3270–3276.

Wang J., Dai Y., Gao L., Ma S., 2009, A new combined cooling, heating501 and power system driven by solar energy, Renewable Energy 34 (2009) 2780–2788.

Baghernejad A., Yaghoubi M., Jafarpur K., 2016, Exergoeconomic comparison of three novel trigeneration systems using SOFC, biomass and solar energies, Applied Thermal Engineering 104 (2016) 534–555.

Fong K., Lee C., 2014, Investigation on zero grid-electricity design strategies of solid oxide fuel cell trigeneration system for high-rise building in hot and humid climate, Applied Energy 114 (2014) 426–433.

Arnavat M., Bruno J., Coronas A., 2014, Modeling of trigeneration configurations based on biomass gasification and comparison of performance, Applied Energy 114 (2014) 845–856.

Fang F., Wei L., Liu J., Zhang J., Hou G., 2012, Complementary configuration and operation of a CCHP-ORC system, Energy 46 (1) (2012) 211–220.

Huang Y., Wang Y., Rezvani S., Mcllveen-Wright D., Anderson M., Mondol N. H. J., Zacharopolous A., 2013, A techno-economic assessment of biomass fuelled trigeneration system integrated with organic Rankine cycle, Applied Thermal Engineering 53 (2013) 325–331.

Al-Sulaiman F. A., Dincer I., Hamdullahpur F., 2013, Thermoeconomic optimisation of three trigeneration systems using organic rankine cycles: Part I-Formulations, Energy Conversion and Management 69 (2013) 199–208.

Mago P., Chamra L., 2009, Analysis and optimisation of CCHP systems based on energy, economical, and environmental considerations, Energy Buildings 41 (10) (2009) 1099–1106.

Mago P., Fumo N., Chamra L., 2009, Performance analysis of CCHP and CHP systems operating following the thermal and electric load, Energy Research 33 (9) (2009) 852–864.

Cao S., Mohamed A., Hasan A., Siren K., 2014, Energy matching analysis of on-site micro-cogeneration for a single-family house with thermal and electrical tracking strategies, Energy and Buildings 68 (2014) 351–363.

Jing Y., Bai H., Wang J., 2012, Multi-objective optimisation design and operation strategy analysis of BCHP system based on life cycle assessment, Energy 37 (1) (2012) 405–416.

Hajabdollahi H., 2012, Investigating the effects of load demands on selection of optimum CCHP-ORC plant, Applied Thermal Engineering 87 (2015) 547–558.

Li Z., Li W., Xu B., 2016, Optimisation of mixed working fluids for a novel trigeneration system based on organic rankine cycle installed with heat pumps, Applied Thermal Engineering 96 (2016) 750–762.

Liu M., Shi Y., Fang F., 2013, Optimal power flow and PGU capacity of CCHP systems using a matrix modelling approach, Applied Energy 102 (2) (2013) 794–802.

Chicco G., Mancarella P., 2009, Matrix modelling of small-scale trigeneration systems and application to operational optimisation, Energy 34 (2009) 261–273.

200: Research on key techniques for surface defect detection of solar cells based on convolutional neural network

Juan WANG[1], Linkang CAI [2], Min LIU*[3] , Bin DENG[4] ,Hao SHI[5], Kaiwen CHENG[6]

[1] *Hubei Key Laboratory for High-efficiency Utilisation of Solar Energy and Operation Control of Energy Storage System, Hubei University of Technology, Wuhan, 430068, P. R. China ,happywj@hbut.edu.cn*
[2] *Hubei Key Laboratory for High-efficiency Utilisation of Solar Energy and Operation Control of Energy Storage System, Hubei University of Technology, Wuhan, 430068, P. R. China, 362961694@qq.com*
[3] *Hubei Key Laboratory for High-efficiency Utilisation of Solar Energy and Operation Control of Energy Storage System, Hubei University of Technology, Wuhan, 430068, P. R. China, 463467853@qq.com*
**Corresponding author*

At present, the defect detection of solar cells still depend on manual completion. The common surface defects are classified into four types: appearance defects, colour defects, cracks, and silk screen defects. For the detection of solar cell surface defects, there are hidden issues, low accuracy, and manual dependence. Therefore, fast and accurate locking of defects is the most critical step for improving the detection of surface defect defects. The convolutional neural network (CNN) with multilayer network architectures has a strong ability to extract the data features of the surface image and good pertinence to the detection of surface defects of solar cells. In this paper, it focuses on the key technology of surface defect detection for solar cells based on CNN. It will provide the technical support for establishing automatic intelligent detection system to detach from manual detection. The main research contents are: Firstly, by summarizing various imaging methods and common defect types on the surface of solar cells, the imaging methods and defect models are analysed to establish the relationship between them. Secondly, It is designed that a good visual acquisition system of solar cells by analysing the mechanism of common defect types and combining the surrounding environment to collect the image of battery surface in real time. Finally, the acquired image features are extracted and the new feature image reconstructed by using CNN. Then the reconstructed image and defect image of the algorithm are compared to detect the surface defects. The experimental results demonstrate that this research content of technology can be used for on-line detection of solar cell surface defects. It has higher detection accuracy, lower algorithm complexity and real-time performance than the traditional method.

Keywords: Convolutional neural network (CNN), Solar cells, Defect detection, Surface image

1. INTRODUCTION

The current solar cells can be classified into single crystal silicon solar cells, polycrystalline silicon solar cells, and amorphous silicon solar cells, depending on the materials used. According to different detection methods, solar cell surface defect detection methods can be divided into three categories: artificial visual inspection, physical detection and machine vision inspection. The limitation of artificial visual inspection is relatively large, and it is easily affected by personal factors and environmental factors, and there are few application. Typical physical method tests include the following: Tsuzuki K et al. proposed the use of sound waves for defect detection, mainly to make the solar cells vibrate to generate sound waves, and to perform defect detection based on comparison and analysis with sound waves generated by non-defective solar cells. Sawyer (2005) uses laser scanning technology to detect the continuity of the resistance in the crystal silicon that is forward-biased by the laser scanning. If the crack exists, the resistance discontinuity occurs; In addition, a detection method based on resonant ultrasonic vibration is proposed in Byelyayev (2005). And the detection method based on optical deep-level transient spectroscopy analysis proposed in Zhang (2009).

Compared with physical detection methods, the detection method of solar cell surface defects based on machine vision is more convenient and faster, and it is also one of the main methods currently used for defect detection. According to different mathematical modelling ideas, the existing detection methods based on machine vision can be divided into a variety of types based on gradient features, clustering algorithms, frequency domain analysis, matrix decomposition and machine learning. The relevant representative work is briefly described as follows. In Anwar (2014) and Gao (2016), a detection method based on the defect gradient feature was proposed, aiming at the feature that the brightness of the solar cell surface defects and the rest of the solar cell surface are significantly different, that is, there is a high gradient at the junction between the two, and then the gradient is used. The features are combined with anisotropic diffusion algorithm, mean shift algorithm, and particle swarm optimisation algorithm to detect defects. In Tsai (2015) and Agroui (2017), a cluster-based defect detection method is proposed. The main idea of this type of method is to distinguish the defect area from the non-defect area by a clustering algorithm. Finally, a threshold segmentation algorithm is used to obtain a defect-only area. Binary image; In Tsai (2012) and Wang (2014), a defect detection method based on frequency domain analysis is proposed. The core idea of this type of method is to transform the input image into frequency domain through Fourier transform or wavelet transform and then process it, and then inverse transform. Return to the time domain to get the final result; In Lu (2005) and Yao (2013), a method of defect detection based on matrix decomposition is proposed. The basic idea of this method is to decompose the input image into a matrix containing a large number of repeated features and a matrix of singular features through a matrix decomposition algorithm. Is the defect-free image part, the latter represents the image part containing the defect area; In Demant (2017) and Wang (2014), a machine-learning-based defect detection method is proposed, in which the main machine learning methods used include: support vector machines, independent component analysis, and deep learning.

In this paper, we propose a method for surface defect detection of solar cells based on deep learning. Firstly, the image of the surface of the cell to be detected is acquired; then, the surface image is pre-processed to remove noise and gate lines that affect the detection; secondly, the CNN trained by the training set is used for defect detection; Whether to contain the result of the defect. Solar cell defect detection process shown in Figure 1:

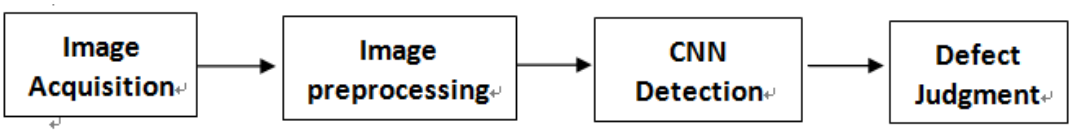

Figure1: Defect inspection process

2. CNN STRUCTURE MODEL

A machine learning based model usually contains two parts: a feature representation and a classifier. The CNN model itself contains a feature extraction stage. The extracted features can reflect the image feature information more comprehensively, saving manpower selection time and making up for the inadequacy of manually extracting features that cannot be adjusted according to the new data set. Therefore, the CNN model is used. Defect detection research has a dual meaning of theory and application.

As shown in Figure 2, the basic structure of CNN is divided into 7 layers (Lecun 2011): layer 1 is the input stage; layer 2-5 is the feature extraction stage, and layer 2 and layer 3 are the extraction stage of the first feature. Layer 4 and Layer 5 are the extraction phase of the second feature. Each node is connected to the local neighbourhood of the previous layer. The feature integration of the lower level extraction is transformed into the higher level feature representation; Layer 6 and The 7th layer is the classification stage. CNN uses two layers of fully connected neural networks as classifiers. In addition, the common classifiers in image processing are polynomial logistic regression or radial basis function networks.

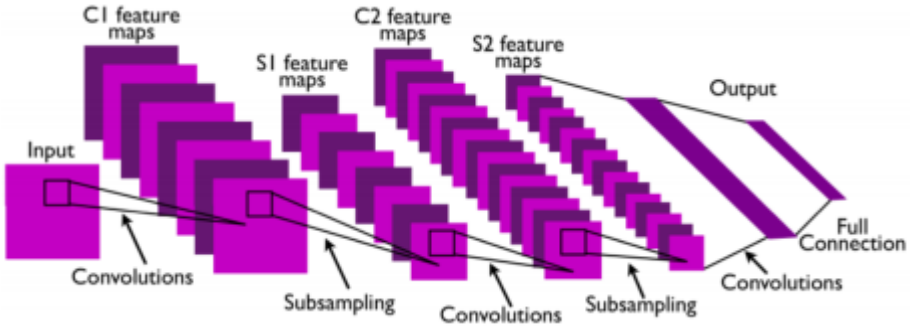

Figure 2: CNN structure model

The 7-layer structure of CNN includes an input layer, a convolution layer, a down-sampling layer, a fully-connected layer, and an output layer. The first layer is the input layer, and the input image size should be unified to N*N. Layers 2 and 4 are convolutional layers. By performing convolution on the previous layer, multiple feature maps are obtained. That is, the previous layer is convolutionally processed with multiple trainable convolution kernels, respectively. The size is k*k, plus an offset b. After an excitation function f, a feature map equal to the number of convolution kernels is obtained. The size of the feature map is (N-k+1)*(N-k+1). The calculation process can be expressed by Equation 1:

Equation 1: Convolution calculation

$$x_j^l = f\left(\sum_{i \in M_j} x_i^{l-1} \times k_{ij}^l + b_j^l\right)$$

Where:

x = Convolution layer

l= Number of layers (Floor)

k= Convolution kernel

M_J= The jth characteristic diagram

b= Offset

Layers 3 and 5 are down sampling layers, sub-sampling each feature map of the previous convolutional layer, converting high-level representations of the previous layer to low-resolution representations to reduce data processing time and not Loss of useful information, that is, the weighted summation or the maximum value of the neighbourhood of m*m in each feature map is calculated, and an offset b is added. After an excitation function f, the input is obtained and input. When the same number of feature maps, the size of the feature map becomes $(N-k+1)/m$. The down sampling layer is calculated as:

Equation 2: Convolution calculation.

$$x_j^l = f(\beta_j^l down(x_j^{l-1}) + b_j^l)$$

Where:

x = Sampling layer

l= Number of layers (Floor)

j= Feature number

down（·）= Down-sampling function

β= Weights

b= Offset

Layer 6 is a fully connected neural network layer, a classifier, which combines the feature maps obtained from the previous layer as a feature vector input network for learning. The 7th layer is the output layer, and the corresponding mark is output.

3. PRETREATMENT

3.1. Solar cell surface image pre-processing

Solar cell surface image pre-processing mainly includes two steps: image noise reduction and raster line deletion. In order to suppress noise interference, this paper adopts the anisotropic diffusion method and the median filtering method to perform noise reduction. This section mainly introduces the work of removing the gate line. When the human eye observes the solar cell, as shown in Figure 1, even if it is a non-defective solar cell, the white grid lines, especially the thicker ones, will attract the attention of the human eye. Therefore, in order to ensure the grid The line portion is not detected as a

significant area during visual saliency detection, resulting in subsequent erroneous detection (the detection method in this paper mainly relies on visual saliency to locate the defect area), and the white bus bar lines and sub-gate lines need to delete.

Figure 3: Solar cell surface image

Calculation of the original image $I(x_i, y_p)$ in each row and each column and the luminance:

Equation 3: Calculate the sum of brightness

$$SH_i = \sum_{P=1}^{K} I(x_i, y_p) \quad i \in (1, H)$$

Equation 4: Calculate the sum of brightness

$$SV_j = \sum_{q=1}^{H} I(x_q, y_j) \quad j \in (1, K)$$

Where:

SH_i =The brightness of the pixels in the i-th row

SV_j = The brightness of the pixel in the j-th column

H= rows

K= columns

The brightness of each row and column and the threshold processing to delete the main and secondary gate lines in the image:

Equation 5: Delete primary and secondary gate lines.

$$I'(x_i, y) = \begin{cases} I(x_i, y), & SH_i \le \frac{1}{H} \sum_{i=1}^{H} SH_i \\ 0, & others \end{cases} \quad i \in (1, H)$$

Equation 6: Delete primary and secondary gate lines.

$$I'(x, y) = \begin{cases} I(x, y), & SV_J \le \frac{1}{K} \sum_{j=1}^{K} SV_j \\ 0, & others \end{cases} \quad j \in (1, K)$$

In addition, in order to prevent the deletion of the gate line from affecting the detection (if the defect area intersects with the gate line, the gate line deletion operation will destroy the integrity of the defect area), and the gate line needs to be filled after the gate line is deleted. The least square method is mainly adopted for curve fitting to perform padding, ie, the pixel values of the grid region are estimated using the pixel values of the pixels on both sides of the grid line, so that the padding region and the adjacent region achieve natural docking. Mark the pre-processed image as $I_p(x, y)$.

3.2. Training set production and expansion

In general, the neural network obtains the desired result by inputting data, and they can well relate the results through the data. It is to learn a certain amount of data and use the learned rules to predict unknown data. Therefore, the classification algorithm needs sufficient training samples and test samples. However, in practical applications, the number of sample sets is small and the types are large. As a result, theoretically effective learning methods are not ideal for applications.

During the production and processing of solar cells, due to improper operation, defects such as broken gates, missing corners, colour differences, dirt, cracks, etc. may occur on the surface of the solar cell slice, thereby reducing the service life of the solar cell slice and affecting its working efficiency. Therefore, in order to make CNN's detection effect more accurate, we use LabelImg to label the training solar cells and rotate the images to expand the sample set, making the training and recognition more accurate. As shown in Figure 4, LabelImg is used to label and rotate defective images:

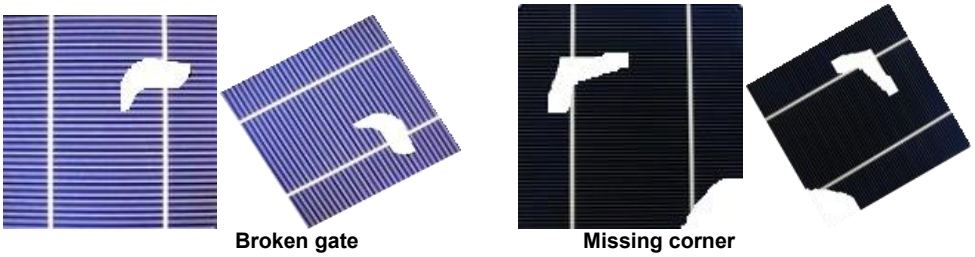

Figure 4: Defect Image of LabelImg Label Rotation

3.3. Parameter selection

The classical CNN model consists of 7 layers, including the input layer, convolutional layer, sampling layer, fully connected layer, and output layer. There are also 2 down-sampling layers between the 2 convolution layers for a total of 7 layers of networks (Wang 2014). The simplified network model synchronises the convolution and down-sampling. The convolution process traverses the pixels in the image at step intervals. The down-sampling process takes the upper left pixel of each n*n region (n is the step size). Only five layers are left, which greatly reduces the complexity of the network. The network model includes input layer, convolution layer, full connection layer, and output layer. The convolution layer can be regarded as a trainable feature extractor and can be composed of one or more layers. The full connection layer and the output layer can constitute trained classifiers. For the key image processed in this paper, set the network input image size to 28*28. The size of the convolution kernel is chosen to be odd and the images can be fully overlapped without loss of information. When the size is chosen as 3*3, there are too few overlapping units and there is no redundant calculation. When the selection size is 7*7, there are too many overlapping units. Therefore, the size of the convolution kernel chosen in this paper is 5*5.

This article has experimented with the number of hidden layer nodes. The experimental results are listed in Table 2. By training the CNN models with different numbers of hidden layer nodes, the corresponding recognition accuracy rate and the identification of the consumption time are statistically compared. It is found that the greater the number of hidden nodes, the longer the recognition consumption time and the shortest recognition time when the number of nodes is 50. However, the correct rate is low; when the hidden unit is 100, the optimum is achieved, and when the number of nodes is 100 or more, the correct rate is not improved.

Table 1: Number of hidden units, correct rate and identification time

Hidden nodes	Correct rate /%	Time/s
40	93.1	0.12
60	95.2	0.23
100	97.6	0.235
130	98.1	0.241
160	97.2	0.254

For a multi-layer network, the error surface may contain multiple local minima. The initialisation of the network weight determines the direction from which the network training starts from the error surface. If each step is modified along the direction of the fastest decrease of the error surface. The weight vector can reach the minimum error point at the fastest speed. Therefore, the initialisation of weights is extremely important to avoid network congestion and shorten the training time of the network.

In this paper, experiments are performed on the recognition rates under different training algebras. The experimental results are listed in Table 2. Using the mean square error as the cost function, the training error decreases as the number of training times increases, but the error rate on the test set decreases first and then increases. This indicates that increasing the training algebra will cause the network to excessively train the training set. Because the Sigmoid function has a linear feature in the case of small input, initializing the network weight to a small random number makes the decision surface formed at the early stage of the training smooth. As the training progresses, the weights begin to increase, the nonlinear characteristics of the Sigmoid function begin to appear, resulting in continuous increase in the complexity of the decision-making surface, and ultimately leading to an over-complex decision-making surface in the late training period. This article limits overtraining by setting the maximum algebra.

Table 2: Recognition rate of iterations

Number of iterations	Mean Square Error	Recognition rate /%
2000	123.73	63.2
3000	293.64	72.1
4000	161.32	97.3

When the gradient just begins to fall, the network appears as a very smooth function, there is no problem of local extremum. After training for a certain time, the weights changed through continuous learning will evolve the network into a network that can represent highly nonlinear functions. There are many local minima (Lecun 2011). Therefore, in the early training period, the weights in the CNN should be initialised to a random number close to 0, which can avoid the network reaching saturation prematurely due to the large parameters, and can effectively reduce the probability that the search stays at the local minimum value; The value ensures that the network has a certain level of learning ability.

After the above experiments, the network parameters of this paper are shown in Table 3:

Table 3: CNN parameters

Convolution kernel size	Number of hidden layer nodes	Learning rate	Number of iterations
5*5	130	0.04	4000

4. EXPERIMENTAL RESULTS AND ANALYSIS

Our experiment is based on the Ubuntu system, using the TensorFlow framework to achieve the detection of solar cell surface defects. Before defect detection, it is necessary to manually perform defect classification and labelling on the battery. The result of manual authentication is used as verification of the later CNN identification. In order to ensure the correctness of the experiment, we uniformly used 600 28*28-size solar cell images, including 300 defective and non-defective images. First of all, these images are divided into three groups. Each group contains defective images and non-defective images. Then the trained CNN recognition network is used to identify each group of images and detect defect maps in each group. Finally, the detection results are compared with the results of the previous manual identification to obtain the recognition rate of each group.

The first time we tested on three groups of solar battery image test set, test results can be a very high detection accuracy. But when we test again, the accuracy rate is very low, this is one of the biggest problems our experiment. We have been improving our experiments, but there has been no solution to the problem of the experimental results. So the results did not show in this article, I will continue to improve our experiment, to achieve the desired results

5. SUMMARY

In this article, we use CNN to detect solar cell surface defects. Collected solar cell surface images, using the median filter and the anisotropic diffusion of the image noise reduction process, using the least squares based curve fitting to fill the surface of the grid line. In order to simulate the diversity of defects when expanding the training set samples, we use LabelImg to rotate and label the surface images. In the selection of the convolution kernel, the setting of the learning rate, and the number of iterations, we compare several sets of experiments to select the network parameters that are most beneficial to the results. The deficiencies in this paper are that the type of defect cannot be detected, and there are subtle errors in the detection of some subtle defects. The deep learning network that we have trained can effectively detect the defects of solar cells. But our experiments also have shortcomings, sometimes detecting precision can reach the idea accuracy, sometimes the result is unsatisfactory, we will continue to work hard.

8. ACKNOWLEDGEMENTS.

This work was supported in part by National Natural Science Foundation of China (61471162, 61501178, 61571182, 11605051, 41601399, 61601177); Program of International science and technology cooperation (2015DFA10940); Science and technology support program (R & D) project of Hubei Province (2015BAA115); PhD Research Startup Foundation of Hubei University of Technology (BSQD2015023，BSQD13029, BSQD13032, BSQD14028, BSQD14033); Open Foundation of Hubei Collaborative Innovation Center for High-Efficiency Utilisation of Solar Energy (HBSKFZD2015005，HBSKFTD2016002)；Key projects of Hubei Key Laboratory for High-efficiency Utilisation of Solar Energy and Operation Control of Energy Storage System（HBSEES201701).

6. REFERENCES

Sawyer, D. E., & Kessler, H. K. (2005). Laser scanning of solar cells for the display of cell operating characteristics and detection of cell defects.IEEE Transactions on Electron Devices, 27(4), 864-872.

Byelyayev, A. (2005). Stress diagnostics and crack detection in full-size silicon wafers using resonance ultrasonic vibrations.

Zhang, X., Hu, J., Wu, Y., & Lu, F. (2009). Direct observation of defects in triple-junction solar cell by optical deep-level transient spectroscopy.Journal of Physics D Applied Physics, 42(14), 145401-145405

Anwar, S. A., & Abdullah, M. Z. (2014). Micro-crack detection of multicrystalline solar cells featuring an improved anisotropic diffusion filter and image segmentation technique. Eurasip Journal on Image & Video Processing, 2014(1), 1-17.

Gao, X., & Abousleman, G. P. (2016). Automatic solar panel recognition and defect detection using infrared imaging. SPIE Defense + Security(Vol.9476, pp.94760O).

Tsai, D. M., Li, G. N., Li, W. C., & Chiu, W. Y. (2015). Defect detection in multi-crystal solar cells using clustering with uniformity measures.Advanced Engineering Informatics, 29(3), 419-430.

Agroui, K., Pellegrino, M., & Giovanni, F. (2017). Analysis techniques for photovoltaic modules based on amorphous solar cells. Arabian Journal for Science & Engineering, 42(1), 1-7.

Tsai, D. M., Wu, S. C., & Li, W. C. (2012). Defect detection of solar cells in electroluminescence images using fourier image reconstruction. Solar Energy Materials & Solar Cells, 99(99), 250-262.

Wang, Z. (2014). Research on detection technology for solar cells multi-defects in complicated background. Journal of Information & Computational Science, 11(2), 449-459.

Lu, C. J., & Tsai, D. M. (2005). Automatic defect inspection for lcds using singular value decomposition. International Journal of Advanced Manufacturing Technology, 25(1-2), 53-61.

Yao, M. H., Jie, L. I., & Wang, X. B. (2013). Solar cells surface defects detection using rpca method. Chinese Journal of Computers, 36(9), 1943-1952.

Demant, M., Welschehold, T., Oswald, M., Bartsch, S., Brox, T., & Schoenfelder, S., et al. (2017). Microcracks in silicon wafers i: inline detection and implications of crack morphology on wafer strength. IEEE Journal of Photovoltaics, 6(1), 126-135.

Wang, X. B., Jie, L. I., Yao, M. H., Wen-Xiu, H. E., & Qian, Y. T. (2014). Solar cells surface defects detection based on deep learning. Pattern Recognition & Artificial Intelligence, 27(6), 517-523.

Lecun, Y., Kavukcuoglu, K., & Farabet, C. (2011). Convolutional networks and applications in vision. IEEE International Symposium on Circuits and Systems (Vol.14, pp.253-256). IEEE.